U.S.NRC
United States Nuclear Regulatory Commission
Protecting People and the Environment

NUREG/CR-7019
PNNL-18713, Rev. 1

Results of the Program for the Inspection of Nickel Alloy Components

Office of Nuclear Regulatory Research

U.S.NRC
United States Nuclear Regulatory Commission
Protecting People and the Environment

NUREG/CR-7019
PNNL-18713, Rev. 1

Results of the Program for the Inspection of Nickel Alloy Components

Manuscript Completed: April 2010
Date Published: August 2010

Prepared by
S.E. Cumblidge, S.R. Doctor, P.G. Heasler, and T.T. Taylor

Pacific Norhwest National Laboratory
P.O. Box 999
Richland, WA 99352

I. Prokofiev, NRC Project Manager

NRC Job Code N6593

Office of Nuclear Regulatory Research

Abstract

The U.S. Nuclear Regulatory Commission (NRC) executed agreements with organizations in Japan, Sweden, South Korea, Finland, and the United States to establish the Program for the Inspection of Nickel Alloy Components (PINC). A series of round-robin tests was conducted by teams from Europe, Japan, Korea, and the United States. The teams examined a series of test blocks designed to simulate cracked piping dissimilar metal welds and bottom-mounted instrumentation tube penetrations. The round-robin tests were carried out to determine the effectiveness of a variety of nondestructive testing techniques for the detection of simulated stress corrosion cracking. These round robin tests were conducted using nickel-based alloys, such as Alloy 600. In these tests, 22 test blocks, 19 containing simulated primary water stress corrosion cracking and 3 blanks, were used. The teams used techniques ranging from conventional ultrasonic techniques to experimental potential drop methods. The results were then scored to allow for comparisons between the techniques. The conclusions and recommendations presented in this report are based on the probability of detection, false call probability, and sizing statistics measured in the round robin studies.

The highest-performing technique for detection and length sizing, for both dissimilar metal welds and bottom-mounted instrumentation nozzles, was the use of eddy current testing on the cracked surface. Ultrasonic testing showed that it could be used effectively for detection and length and depth sizing. The effective detection of flaws in bottom-mounted instrumentation nozzles by eddy current and ultrasound shows that it may be possible to reliably inspect these components in the field. The high variability in the team performances suggested that the skill of the team conducting the test is a very important factor in the quality of the examination. This suggests that some form of strict inspector qualification, such as a performance demonstration program, is required to ensure that the inspections are effective. This evaluation also shows that it may be beneficial to tie the inspection interval length to the crack growth rates in the materials of interest. Materials with very high crack growth rates may require inspections at every outage to provide a sufficient improvement factor.

This body of work suggests that several NDE techniques need to be used in tandem to ensure adequate flaw detection and sizing from the noncracked surfaces. Eddy current provided the highest performance for flaw detection from the cracked surface. The round-robin results from this effort showed that a combination of conventional and phased array ultrasound provided the highest performance for accurate depth sizing in dissimilar metal piping welds. It is worth noting that eddy current is not universally applicable for dissimilar metal welds, as many welds are in locations that do not allow for inner diameter inspections. If access to the flawed surface is not possible, a combination of phased array ultrasound and conventional ultrasound appears to be the most effective alternative.

Foreword

Between November 2000 and March 2001, leaks were discovered in Alloy 600 control rod drive mechanism (CRDM) nozzles and associated Alloy 182 J-groove attachment welds in several pressurized-water reactors (PWRs). Destructive examination of several CRDMs showed that the leaks were the result of primary water stress corrosion cracking (PWSCC). By mid-2002, over 30 leaking CRDM nozzles had been reported in the United States. Moreover, during this same time, a circumferential hairline crack was detected in the first weld between the reactor vessel nozzle and the A loop hot leg piping at another PWR that was subsequently determined to be PWSCC. Such events, both domestic and international, made it apparent that additional research was necessary to address the problem of stress corrosion cracking (SCC) in nickel-based alloys in PWR components.

The U.S. Nuclear Regulatory Commission (NRC) executed agreements with organizations in Japan, Sweden, South Korea, Finland, and the United States to establish the Program for the Inspection of Nickel Alloy Components (PINC). The Pacific Northwest National Laboratory (PNNL) assisted NRC with the coordination of PINC with two primary objectives:

1. Compile a knowledge base on cracking in Alloy 600 and similar nickel-based alloys in nuclear power plants (NPPs) including the crack morphology and non-destructive examination (NDE) responses.

2. Identify and quantitatively assess capabilities of current and emerging NDE techniques to detect, size, and characterize tight cracks using NDE mock-ups with PWSCC simulations.

The PINC participants identified, ranked, and determined which component configurations should be considered for the study. A series of test blocks with cracks were then designed and fabricated to simulate the selected component configurations. This report describes the results of the round robin tests that were performed to assess the NDE effectiveness and reliability.

The first primary objective of the study was to produce an electronic resource on PWSCC in nickel-based alloys. This included documenting the material generated in support of an improved understanding of (1) PWSCC morphology, (2) NDE responses to PWSCC, and (3) the capability of NDE to reliably detect and accurately size PWSCC. This information should prove to be a valuable resource for the problem of SCC in nickel-based alloys in NPP components.

With regard to the second primary objective (i.e., investigate the capability of various NDE methods to detect and size the through-wall extent of PWSCC), the report describes the efforts of the PINC participants to detect and measure the lengths of cracks. The surface conditions, access to both sides of the weld, and inspection conditions for the PINC specimens provided the inspectors with less challenging conditions than would be expected in field inspections of PWR components. Although the inspection conditions were less challenging, team performance was highly variable. This supports performance demonstration efforts in the nuclear industry to ensure adequate qualification of inspectors. The variability in team performance should be factored in the decisionmaking process when applying the results of this study.

Nonetheless, some firm conclusions could be made. For example, eddy current inspection from the cracked surface demonstrated the highest probability of detection for the examination of the dissimilar metal weld specimens. None of the NDE techniques in this round robin study demonstrated the capability to accurately measure the depths of flaws in dissimilar metal welds to ASME Section XI Code requirements. The study suggests that, in certain situations, examinations would be improved through the use of several NDE techniques to ensure adequate flaw detection and sizing.

Contents

Figures

Tables

Executive Summary

The U.S. Nuclear Regulatory Commission (NRC) executed agreements with organizations in Japan, Sweden, South Korea, Finland, and the United States to establish the Program for the Inspection of Nickel Alloy Components (PINC). The objectives of the PINC program participants are:

- To join together for cooperative research.
- To address the problem of primary water stress corrosion cracking (PWSCC), a form of degradation observed in some pressurized water reactor pressure boundary components. Specifically, the research was designed primarily to understand the morphology of PWSCC cracks, to assess nondestructive evaluation (NDE) techniques for detecting and characterizing cracks with such morphology, and to distinguish them from other types of flaws or other innocuous weld conditions. This program provided data that enabled a quantitative assessment of available NDE techniques to detect and size PWSCC in nickel-based alloys.

The PINC participants identified and ranked all PWSCC and component configurations for consideration for study in the PINC framework. The three areas that were ranked highest were bottom-mounted instrumentation (BMIs), dissimilar metal welds (DMWs), and control rod drive mechanisms (CRDMs). The BMIs were identified as top priority because it is not easy to replace a reactor pressure vessel bottom head and repairs are challenging, as was learned at the South Texas Project. The issue of dissimilar metal welds was considered to also be very important based on the cracking that had been experienced at V.C. Summer and Ringhals. The CRDM issue was also assigned a high priority because of the number of plants world wide that have experienced cracking and the Davis-Besse event. However, the low availability of CRDM assemblies and the need to complete the PINC round robin in a timely fashion made it possible to address only the dissimilar metal welds and the bottom-mounted instrumentation nozzles. Dissimilar metal piping weld assemblies were available immediately so this round-robin study was able to start first.

The PINC was focused on studying two aspects of PWSCC. One was to document the crack morphology and NDE responses of PWSCC and compare these data with methods to simulate PWSCC for NDE capability studies. The other was to study the capability of various NDE methods to detect and size the through-wall extent of PWSCC. The studies involving NDE capability were carried out as international round robins with PINC participants. The results are, in some cases, discussed with reference to the requirements of ASME Code, Section XI, Appendix VIII. It should be noted that the round robin study was not designed to constitute an Appendix VIII compliant demonstration.

This report describes the efforts of the PINC participants to assess the capability of NDE techniques to detect and characterize the through-wall depth and length of PWSCC in dissimilar metal welds and in bottom-mounted instrumentation penetration tubes and J-groove welds. Based upon the information that was developed from conducting round-robin exercises on DMW samples and BMI nozzles, this study provided the following conclusions and recommendations. The conclusions and recommendations presented in this report are based

on the probability of detection, false call probability, and sizing statistics measured in the round robin studies.

Probability of Detection Performance

Dissimilar Metal Weld Pipe Specimen Round Robin Probability of Detection Performance

The conclusions that may be inferred from the experimental results for the dissimilar metal welds pipe specimens are as follows:

1. **Conclusion**: Eddy current inspection from the cracked surface demonstrated the highest probability of detection (POD) for all flaws in the DMW round robin.
    - **PINC Recommendation**: The results of this study show that eddy current inspection are the preferred detection technique for dissimilar metal welds, where conditions allow access to the same surface from which the crack originates and where the surface conditions allow for ECT testing.
2. **Conclusion**: The POD results for the DMW round robin show significant variability in POD performance based upon technique, procedure, and team.
    - **PINC Recommendation**: The results illustrate the usefulness of performance demonstration as a means to help ensure the reliability of DMW inspections.
3. **Conclusion**: The potential-drop techniques that were used in the DMW round robin demonstrated the lowest POD performance.
    - **PINC Recommendation**: The potential-drop techniques used in the DMW round robin need further development before use as detection techniques in inservice inspection programs.

Bottom-Mounted Instrumentation Round Robin Probability of Detection Performance

The conclusions that may be inferred from the experimental results for the bottom mounted instrumentation tube specimens are as follows

1. **Conclusion**: Inspections using a single cross-coil eddy-current probe achieved a high POD and a low false call rate. These examinations were performed with multiple frequencies, with the highest frequency used being 300–400 kHz.
    - **PINC Recommendation**: The results of this study suggest that single cross-coil probe eddy current using frequencies of 300–400 kHz are the preferred method for finding surface-breaking flaws in BMI J-groove welds.
2. **Conclusion**: Inspections using adaptive phased array ultrasound were able to detect all baseline difficulty flaws and none of the challenging flaws (baseline and challenging flaws are defined in Section 4.2.2).

- **PINC Recommendation**: While adaptive phased array ultrasound was slightly less effective than eddy current testing, the results of this study suggest that adaptive phased array ultrasound can be effectively used to find flaws in BMI welds.

3. **Conclusion**: The inspections using array eddy-current techniques used in this BMI round robin study had a reduced POD and a much higher false call rate compared to the higher frequency cross-coil ECT examinations.
    - **PINC Recommendation**: The results of the BMI round-robin study show that the procedures using array ECT probes operating at 100–200 kHz used in this round robin test require further development for detection in inservice inspection programs.

4. **Conclusion**: The closely coupled potential-drop technique was able to detect thermal fatigue flaws and SCC flaws with a POD of 50%. For weld solidification flaws, the POD was 0%. No false calls were made by the inspectors using this technique.
    - **PINC Recommendation**: The results of the BMI round-robin study show that the closely coupled potential-drop technique requires further development before it can be used for detection of flaws in inservice inspection programs.

5. **Conclusion**: Induced-current potential drop was used on only one baseline difficulty test block and two challenging test blocks, possibly skewing the results. There are not enough inspections on baseline difficulty test blocks to draw meaningful conclusions on the POD performance on these test blocks.
    - **PINC Recommendation**: Further testing needs to be performed to determine if ICPD can be used for inservice inspection.

Sizing Performance

Dissimilar Metal Weld Pipe Specimen Sizing Performance

The conclusions that may be inferred from the experimental results indicate the following:

1. **Conclusion**: None of the NDE techniques in this round robin study demonstrated the capability to accurately depth size flaws in dissimilar metal welds to ASME Section XI code standards. The average depth sizing for all techniques tended to slightly undersize the flaws and had standard deviations and RMSE errors of approximately 7 mm. Two techniques came close to meeting ASME Section XI standards.
    - **PINC Recommendation**: The depth sizing of flaws should be improved. The use of phased array UT and conventional ultrasound together showed the most promise.

2. **Conclusion**: Eight teams length-sized flaws with an RMSE within the ASME Section XI standard of 0.75 inch (19 mm). Teams that used phased array UT and eddy current achieved higher accuracy than teams that used conventional UT and potential-drop techniques.

- **PINC Recommendation**: Phased array UT or a combination of eddy-current techniques and conventional UT are the preferred method for length sizing.

Bottom-Mounted Instrumentation Weld Sizing Performance

The conclusions that may be inferred from the experimental results indicate the following:

1. **Conclusion**: Cross-coil eddy current, adaptive phased array ultrasound, and closely coupled probe potential-drop techniques were able to accurately length-size the flaws in the J-groove welds (RMSE of 2.45–4.70 mm).
    - **PINC Recommendation**: These techniques can be used to length-size flaws in BMI J-groove welds.

2. **Conclusion**: The test block geometry made depth-sizing using ultrasound difficult, and not enough data was collected in this round-robin test to accurately determine the effectiveness of the depth-sizing techniques.
    - **PINC Recommendation**: More work should be performed to determine the depth-sizing capabilities of the various techniques.

Based on the round-robin tests, including detection and length-sizing capabilities, several techniques need to be used in tandem for flaw detection and sizing in dissimilar metal welds comparable to ASME Section XI. Eddy current testing had the highest POD performance, and a combination of conventional and phased array ultrasound was the only technique that provided RMSE depth-sizing capabilities close to Section XI requirements. It is worth noting that eddy current is not universally applicable for dissimilar metal welds, as many welds are in locations or have surface conditions that do not allow for ID inspections. If ID access is not possible, a combination of phased array ultrasound and conventional ultrasound appears to be the most accurate alternative.

General Conclusions

1. **Conclusion:** The surface conditions, access to both sides of the weld, and inspection conditions for the PINC specimens provided the inspectors with less challenging conditions than would be expected in field inspections of nuclear power plant components.
    - **PINC Recommendations**: The probability of detection and sizing results should be considered an upper bound for the inspection techniques.

2. **Conclusion**: Inspection procedures and teams with formal NDE qualifications tended to have a higher POD and lower false call rate than teams and procedures with no formal qualifications.
    - **PINC Recommendation**: As NDE inspections are carried out by qualified inspectors, the probability of detection and length sizing results for the qualified teams and procedures should be considered the most representative of field inspections.

3. **Conclusion:** An analysis of the POD curves generated by the PINC round robin testing showed that the procedures improved safety by factors of 1.1 to 1.5 for a 10 year interval and by factors of 1.3 to 2.1 for a four year interval. (These safety factors use the crack growth rates for stress corrosion cracks in stainless steel welds.)
    - **PINC Recommendation:** Effective NDE techniques may need to be combined with inspection intervals selected based on the crack growth rates. The analysis should be refined using PWSCC crack growth rates in nickel-based alloys.

Acknowledgments

There have been significant contributions made by a number of people and organizations to accomplish this study. The authors acknowledge special appreciation to Deborah Jackson and Carol Moyer of the NRC for their leadership in helping organize and start the PINC and Iouri Prokofiev for his leadership. George Schuster (retired) of Pacific Northwest National Laboratory (PNNL) was the initial leader and chairman of the Data Analysis Group and the Atlas Information Tool task group. The authors also acknowledge the hard work and effort of the round-robin invigilators who reviewed inspection procedures and monitored the work of inspection teams, and they thank members of the Data Analysis Group who worked diligently to ensure that the very large set of data was correct and suggested the analysis that was performed.

The following companies participated in the PINC dissimilar metal weld round robin and should be acknowledged for their significant contributions:

- European Inspection Teams
  a. FORCE Institute
  b. Wesdyne TRC (two teams)
  c. Tecnatom
  d. VTT (two teams)
- Korean Inspection Teams
  a. Korea Plant Service and Engineering Company
  b. Doosan Heavy Industries
  c. Sean-UMI-ANSCO
  d. Seoul National University
  e. Korea Hydro & Nuclear Power Company
- Japanese Inspection Teams
  a. Tohoku University – Three Teams
     - Fracture and Reliability Research Institute
     - Institute of Fluid Science
     - Department of Nanomechanics
  b. Mitsubishi Heavy Industries, Ltd., Takasago Research & Development Center – Two Teams
     - Ultrasonic testing team
     - Eddy-current testing team

The following companies participated in the PINC BMI weld round robin and are acknowledged for their significant contributions:

- European Inspection Team
  - Wesdyne TRC

- Korean Inspection Team
  - Korea Plant Service and Engineering Company
- Japanese Inspection Teams
  a. Tohoku University – Three Teams
     - Fracture and Reliability Research Institute
     - Institute of Fluid Science
     - Department of Nanomechanics
  b. Mitsubishi Heavy Industries, Ltd, Takasago Research & Development Center – Two Teams
     - Ultrasonic testing team
     - Eddy-current testing team
- United States Inspection Team
  - The Electric Power Research Institute

The authors acknowledge the following organizations who have participated in the PINC.

Organizations from Japan

- Japan Nuclear Energy Safety Organization (JNES)
- Japan Power Engineering and Inspection Corporation (JAPEIC)
- Tohoku University
- Mitsubishi Heavy Industries, Ltd (MHI)
- KANSAI Electric Power Company

Organizations from Europe

- Swedish Radiation Safety Authority (SSM)
- Swedish Qualification Centre (SQC)
- Wesdyne TRC, Sweden
- VTT, Finland
- Force Institute, Denmark
- Wesdyne TRC, Sweden
- Tecnatom, Spain
- Helsinki University of Technology

Organizations from South Korea

- Korea Institute of Nuclear Safety (KINS)
- Korea Atomic Energy Research Institute (KAERI)
- Korea Plant Services & Engineering Co. Ltd. (KPS)
- Sungkunkwan University
- Korea Electric Power Research Institute (KEPRI)

Organization from the United States

- Electric Power Research Institute

Finally, the authors thank Ms. Kay Hass for typing and editing the seemingly endless versions and revisions of this document.

Acronyms and Abbreviations

AC	alternating current
ACPD	alternating current potential drop method
ASME	American Society of Mechanical Engineers
BMI	bottom-mounted instrumentation
BWR	boiling water reactor
CCPPD	closely coupled probe potential drop method
Circ	circumferential
COD	crack-opening displacement
conv.ut	conventional ultrasonic testing
CRDM	control rod drive mechanism
DAG	Data Analysis Task Group
DC	direct current
DCPD	direct current potential drop method
DE	destructive evaluation
DMW	dissimilar metal welds
ec	eddy current testing
ECT	eddy current testing
EdF	Électricité de France
EDM	electro-discharge machining
em	electromagnetic inspection techniques
EPRI	Electric Power Research Institute
FCP	false call probability
ICPD	induced-current potential-drop method
ID	inner diameter
IDSCC	interdendritic stress corrosion cracking
ISI	inservice inspection
JAPEIC	Japan Power Engineering and Inspection Corporation
JNES	Japan Nuclear Energy Safety Organization
KAERI	Korea Atomic Energy Research Institute
KEPRI	Korea Electric Power Research Institute
KINS	Korea Institute of Nuclear Safety
KPS	Korea Plant Services & Engineering Co. Ltd.
Len	length
LOCA	loss-of-coolant accident
Meas	measured
MHI	Mitsubishi Heavy Industries, Ltd

NA2	North Anna Unit 2
NDE	nondestructive evaluation
No.	number
NRC	Nuclear Regulatory Commission
OD	outer diameter
PD	potential drop method
PINC	Program for the Inspection of Nickel Alloy Components
PNNL	Pacific Northwest National Laboratory
POD	probability of detection
PWR	pressurized water reactor
PWSCC	primary water stress corrosion cracking
PZR	pressurizer
RMSE	root mean square error
RPV	reactor pressure vessel
RVHP	reactor vessel head penetration
SB	surface-breaking
SCC	stress corrosion cracking
SKI	Swedish Nuclear Power Inspectorate
SQC	Swedish Qualification Center
SSM	Swedish Radiation Safety Authority
std dev	standard deviation
TFC	thermal fatigue cracks
TG	Task Group
TOFD	time-of-flight diffraction
Tol	tolerance
UE	Uddcomb Engineering
USP	ultrasonic shot peening
UT	ultrasonic testing
WJP	water jet peening
WSC	weld solidification cracks

1.0 Introduction

Stress corrosion cracking in nickel alloy materials has occurred world-wide in a number of nuclear power plants and is seen as a serious issue affecting the reliable and safe operation of nuclear power plants. Stress corrosion cracking in dissimilar metal welds is often referred to as primary water stress corrosion cracking (PWSCC) or interdendritic stress corrosion cracking (IDSCC). For this report the term primary water stress corrosion cracking (PWSCC) will be used. PWSCC degradation has resulted in breaches of the pressure boundary and caused leakage in several dissimilar metal welds (Bamford 2000; Bamford et al. 2002; Jenssen et al. 2002a; Jenssen et al. 2002b), control rod drive mechanism nozzle penetration weldments (Frye et al. 2002; Lang 2003), and bottom-mounted instrumentation nozzle penetration weldments (Halpin 2003). Reliable detection of PWSCC is challenging because the geometries, materials, and configurations are not conducive to reliable nondestructive evaluation (NDE) and the service-induced cracking exhibits very tight and very complex branching in the nickel-based welds.

The U.S. Nuclear Regulatory Commission (NRC) executed agreements with organizations in Japan, Sweden, South Korea, the United States, and Finland to establish the Program for the Inspection of Nickel Alloy Components (PINC). The objectives of the PINC program participants are:

- To join together for cooperative research.
- To address the problem of PWSCC. Specifically, the research was designed primarily to understand the morphology of PWSCC cracks, to assess NDE techniques for detecting and characterizing cracks with such morphology, and to distinguish them from other types of flaws or other innocuous weld conditions. This program provided data that enabled a quantitative assessment of available NDE techniques to detect and size PWSCC in dissimilar metal welds.

PINC program participants organized the project into a Steering Committee, two task groups, and the Data Analysis Group, as illustrated in the following organizational chart (Figure 1.1).

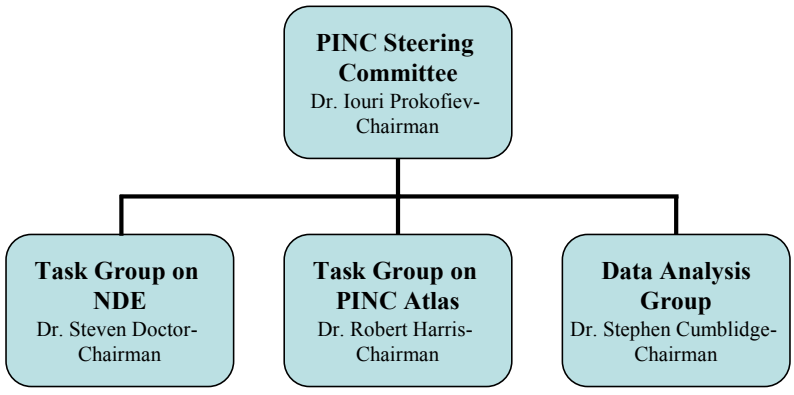

Figure 1.1 Organization Chart for Steering Committee and Task Groups

1.1 PINC Steering Committee

Steering Committee Members

Deborah Jackson was the original Chairman from the NRC, in 2004 she was replaced by Carol Moyer, and in 2007 Carol Moyer was replaced by Iouri Prokofiev
Katsumi Kono
Suck-Chull Kang was the initial representative from KINS. In May 2007 he was replaced by Myungho Song and in May 2008 he was replaced by Haedong Chung
Pentti Kauppinen
Peter Merck
Naoki Chigusa was the initial representative from Kansai Electric Power Company. He was replaced by *Mr. Hiraoka.*
Masanobu Iwasaki was the substitute for Dr. Chigusa. In June 2008, he was replaced by *Mr. Taniguchi*.
Tetsuo Shoji
Jack Spanner
Esa Leskelä

Non-Voting Members
Rob Harris
Steven Doctor
Stephen Cumblidge

The Steering Committee of the Program provides guidance for the project and its implementation and:

- Advises the Task Groups on program implementation and recommends related actions.
- Monitors the program progress, collects, coordinates, and assimilates the results of projects (Task Groups) addressing specific aspects of the problem, and promotes practical implementation of program results at the national level.
- Provides a forum for exchanging information among group members on related work underway and planned activities. The Steering Committee develops strategies to deal with matters requiring coordination with members.
- Assures that the efforts of the Task Groups and of the program as a whole remain focused on specific technical issues that have been agreed to by PINC members as well as ensuring that the work is progressing to an agreed upon time schedule.
- Provides a final report documenting the results of this program and providing specific recommendations for inspection of PWSCC.

1.2 Task Group on NDE

Task Group (TG) NDE Members

Steven Doctor – Chairman
Ichiro Komura
Katsumi Kono
Kwangsik Yoon
Kyungcho Kim
Sung Sik Kang
Pentti Kauppinen
Peter Merck
Tommy Zettervall
Shuji Tanioka
Jack Spanner

This Task Group (TG)-NDE has the following objectives:

- Develop designs of round-robin studies that need to be conducted in order to quantify the effectiveness of NDE for the detection and characterization of PWSCC.
- Review and assess methods to simulate the NDE responses from implanted flaws that will mimic the NDE response from service-induced PWSCC for use in round-robin studies.
- Review available mockups for use in the round-robin studies and, if new assemblies are needed, ensure that they are developed.
- Develop a test plan for each intended round-robin study.
- Coordinate the PINC inspection teams so that a schedule can be developed for circulating the assemblies and ensure it is followed.
- Use invigilators to oversee the round-robin inspections in each country and to ensure uniformity of guidance for each team.
- Coordinate receipt of inspection results.

1.3 Task Group on PINC Atlas

Task Group Atlas Members

Robert Harris – Chairman
Seiji Asada
Joo Youl Hong
Tae Hyun Lee
Iouri Prokofiev
Brian Rassler
Myung Ho Song
Boyd Taylor

Kwangsik Yoon
Masanobu Iwasaki
Kyungcho Kim
Sung Sik Kang
Tetsuo Shoji
Shuji Tanioka
Hännu Hanninen
Karen Gott

The objective of the TG-Atlas technical subgroup is to produce a final product of the PINC program that is an electronic resource of information on PWSCC in nickel-based alloys used in nuclear power plant applications. This will include documenting the material that has been generated in support of an improved understanding of (1) the morphology of PWSCC, (2) NDE responses to PWSCC, and (3) the capability of NDE to reliably detect and accurately size PWSCC.

- The TG-Atlas group is taking the following as input:
  - Results of the activities of the other task groups
  - Presentations of PINC members
  - Submissions from PINC members
  - Available open literature
- The TG-Atlas will produce an Atlas in electronic form as output that will be provided to all PINC participants.
- The Atlas will be user-friendly and permit additions by users.
- The Atlas will document the following:
  - PWSCC morphology
  - PWSCC NDE results from real PWSCC and simulated PWSCC
  - Round-robin test results
  - To the extent practicable, contrasting morphology and NDE results from other types of cracking and noise sources that are likely to be confused with PWSCC
  - References and links to the open literature.

1.4 Data Analysis Group

Data Analysis Group Members

Stephen Cumblidge – Chairman
Steven Doctor, Invigilator U.S.
Pat Heasler
Peter Merck
Tommy Zetterwall, Invigilator Europe

Ichiro Komura, Invigilator Japan
Kazunobu Sakamoto
Kyung-Cho Kim, Invigilator Korea
Myung Ho Song
Yongsik Kim
Sung Sik Kang
Pentti Kauppinen
Jack Spanner
Anders Brunn

This group is responsible for:

- Coordinating the analysis of the data that was generated during the round-robin trials conducted under TG-NDE
- Coordinating the need for oversight of destructive testing
- Assembling the data and information for inclusion into the Atlas
- Developing a final report on the round-robin trials for submitting to the Steering Committee.

The PINC surveyed the program participants to identify and rank all PWSCC and component configurations for consideration to be studied in the PINC framework. The three areas that were ranked highest were the bottom-mounted instrumentation, dissimilar metal piping welds, and control rod drive mechanisms. The bottom-mounted instrumentation (BMI) areas were identified as top priority because it is not easy to replace a reactor pressure vessel bottom head and repairs are challenging, as learned at the South Texas Project nuclear power plant. The issue of dissimilar metal welds (DMWs) was considered to also be very important, based on the cracking experienced at the V.C. Summer and Ringhals plants. The control rod drive mechanism (CRDM) issue was also ranked high because of the Davis-Besse event and the number of plants worldwide that have experienced cracking. However, the limited availability of CRDM assemblies and the need to complete the PINC round robin in a timely fashion made it possible to address only the DMWs and the BMI nozzles. It was also thought that the NDE techniques used for BMIs would be used on CRDMs and, as a result, would be addressing the CRDM inspection issues. DMW assemblies were available immediately, so this round-robin study was able to start first.

The PINC program focused on studying two aspects of PWSCC: (1) document the crack morphology of PWSCC and (2) study the capability of various NDE methods to detect and size the through-wall extent of PWSCC. The studies involving NDE capability were carried out as international round robins with PINC program participants.

This report documents the study of NDE inspection capability to detect and measure the length and through-wall extent of PWSCC in DMWs. The report is organized as follows.

Section 1 provides introductory material and explains the organization of the PINC program. Section 2 describes the test blocks used by the PINC program, including photographs of the test blocks, schematic drawings of product forms, and dimensions of the test blocks. Section 2 also gives the coordinate system used in the round-robin test. Section 3 describes the nondestructive testing techniques used to examine the test blocks in the round-robin trials. Section 4 describes the scoring procedure used for the analysis in this report, the information on probability of detection (POD) results, and the sizing performance for the NDE techniques/ procedures used. Section 5 provides a discussion on how the POD results relate to the integrity of the systems. Section 6 contains the experiences in the international community with cracking in nickel-based components in reactors. Section 7 compares the eddy current responses found for the various flaw types with PWSCC found in the North Anna 2 reactor pressure vessel head. Section 8 discusses the results and highlights the conclusions and recommendations that can be drawn.

2.0 Test Block Descriptions

This section of the report describes the test blocks used for conducting the PINC round-robin tests. Section 2.1 describes the test blocks used for the dissimilar metal weld tests. The test blocks used in the bottom-mounted instrumentation tube tests are described in Section 2.2. Section 2.3 describes the flaw implantation procedures used to produce the test blocks. Section 2.4 describes the flaw locations in the test blocks.

2.1 Dissimilar Metal Weld Round-Robin Test Blocks

Participants in the PINC have offered more than 30 test blocks for use in round-robin tests of NDE effectiveness. The test blocks used in the PINC round robin tests have 68 cracks in nickel-base weld metal that are intended to simulate PWSCC in a variety of component geometries. The test blocks were divided into two categories that were circulated, inspected, and analyzed separately. These two categories are described in Table 2.1.

Table 2.1 Test Block Categories

Typical Component	Thickness/Tube Inner Diameter (ID)
Mid-thickness dissimilar metal weld	Wall thickness range 4.1 to 4.7 cm
Bottom-mounted instrumentation	Tube ID < 2.8 cm

2.1.1 Available Mid-Thickness Dissimilar Metal Weld Test Blocks

Table 2.2 cross-references the photographs, drawings, and coordinate systems provided in this section for the dissimilar metal weld test blocks.

Table 2.2 Index of Photographs, Drawings, and Coordinate Systems for PINC Test Blocks in Mid-Thickness Dissimilar Metal Weld Round-Robin Test

PINC Reference No.	Photograph	Drawing	Coordinate System
PINC 2.1	Figure 2.1	Figure 2.9	Figure 2.13
PINC 2.2	Figure 2.2	Figure 2.9	Figure 2.13
PINC 2.3	Figure 2.3	Figure 2.9	Figure 2.13
PINC 2.4	Figure 2.4	Figure 2.10	Figure 2.14
PINC 2.5	Figure 2.5	Figure 2.10	Figure 2.14
PINC 2.6	Figure 2.6	Figure 2.10	Figure 2.14
PINC 2.9	Figure 2.7	Figure 2.11	Figure 2.15
PINC 2.10	Figure 2.8	Figure 2.12	Figure 2.16

Table 2.3 presents the block dimensions used in the PINC dissimilar metal weld round robin. Each block is described as a cylindrical shell, even the nozzle blocks PINC 2.9 and 2.10. The x, y, and z dimensions describe the volume that could be inspected. For those inspections in which an inspection volume was not recorded, the volumes listed in Table 2.3 were used.

Table 2.3 Dissimilar Metal Weld Test Block Dimensions

Test Block	Thickness of Weld Butter, mm	Inner Radius, mm	Outer Radius Axial, mm	Axial Dimension, mm	Circum-ferential Dimension, degrees	Inspection Volume					
						X1, mm	X2, mm	Y1, mm	Y2, mm	Zl, mm	Z2, mm
PINC 2.1	5	149	195	400	70.0	-119.1	119.1	-40	40	0	46
PINC 2.2	5	149	195	400	70.0	-119.1	119.1	-40	40	0	46
PINC 2.3	5	149	195	400	70.0	-119.1	119.1	-40	40	0	46
PINC 2.4	5	149	195	130	120.0	-204.2	204.2	-65	65	0	46
PINC 2.5	5	149	195	130	120.0	-204.2	204.2	-65	65	0	46
PINC 2.6	5	149	195	130	120.0	-204.2	204.2	-65	65	0	46
PINC 2.9	5	151	193	550	360.0	-1212.6	1212.6	-40	40	0	42
PINC 2.10	5	151	193	220	360.0	-1212.6	1212.6	-40	40	0	42

All available photographs for mid-thickness DMW test blocks are shown in this section.

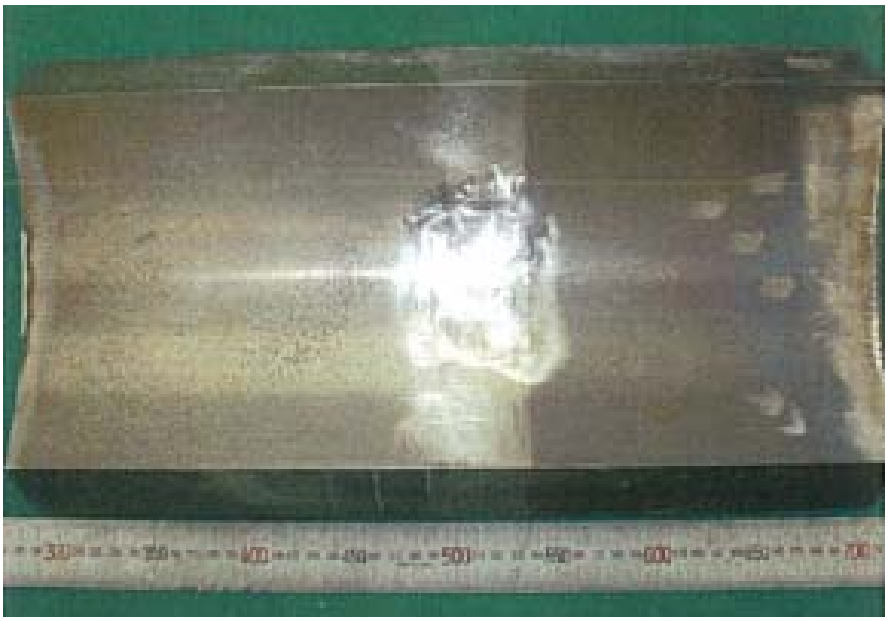

Figure 2.1 PINC Block 2.1 from Japan Nuclear Energy Safety Organization (JNES) – Pressurizer (PZR) Surge Line to Safe-End Dissimilar Metal Weld

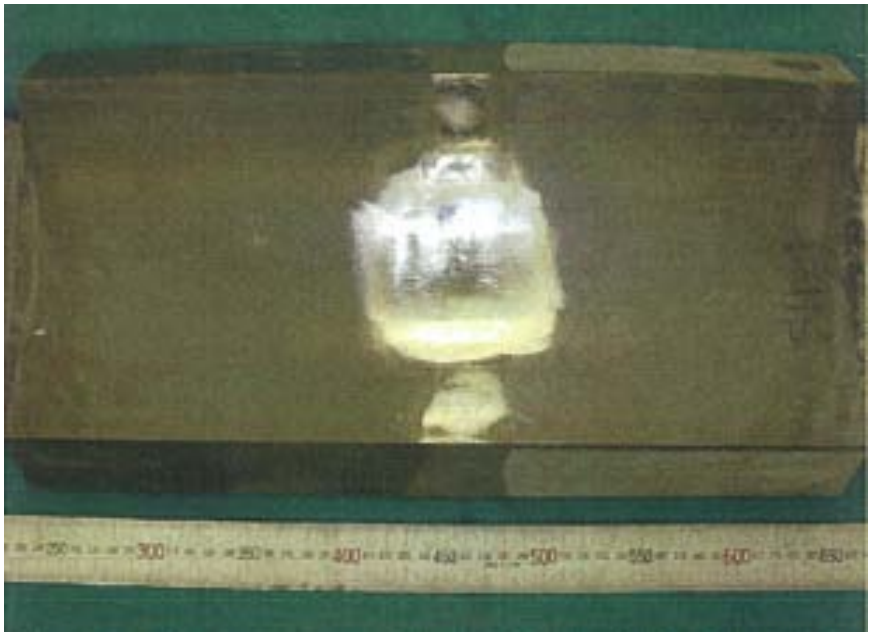

Figure 2.2 PINC Block 2.2 from JNES – PZR Surge Line to Safe-End Dissimilar Metal Weld

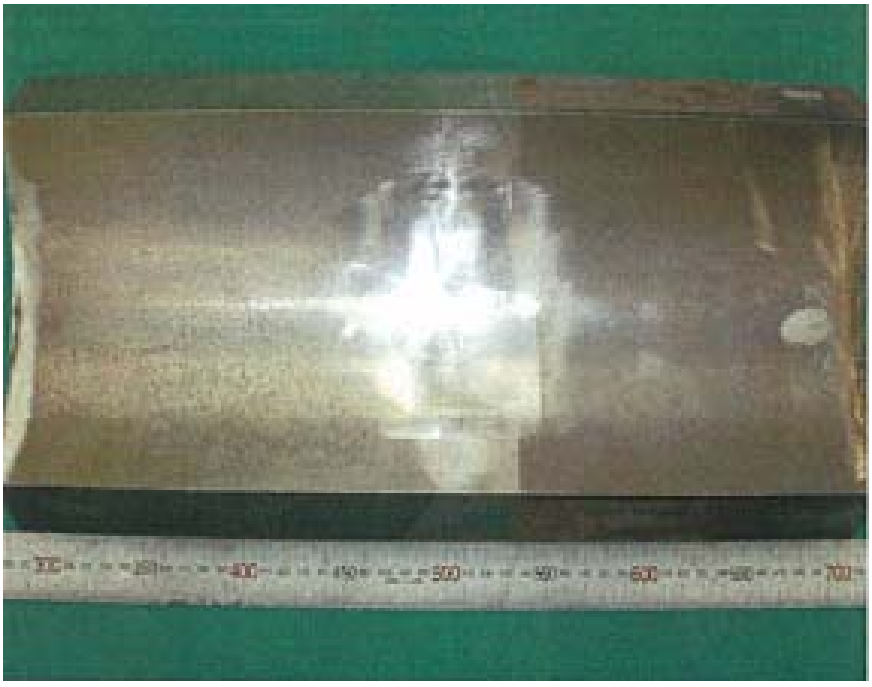

Figure 2.3 PINC Block 2.3 from JNES – PZR Surge Line to Safe-End Dissimilar Metal Weld

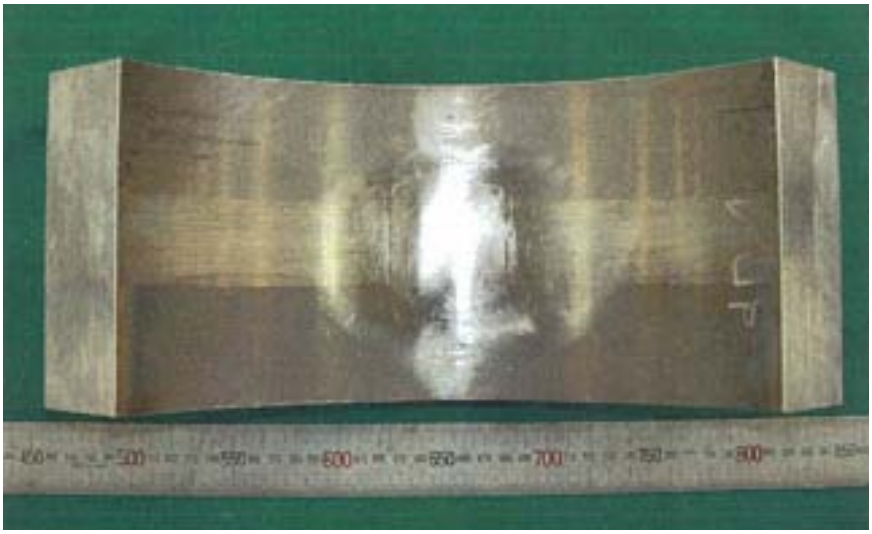

Figure 2.4 PINC Block 2.4 from JNES – PZR Surge Line to Safe-End Dissimilar Metal Weld

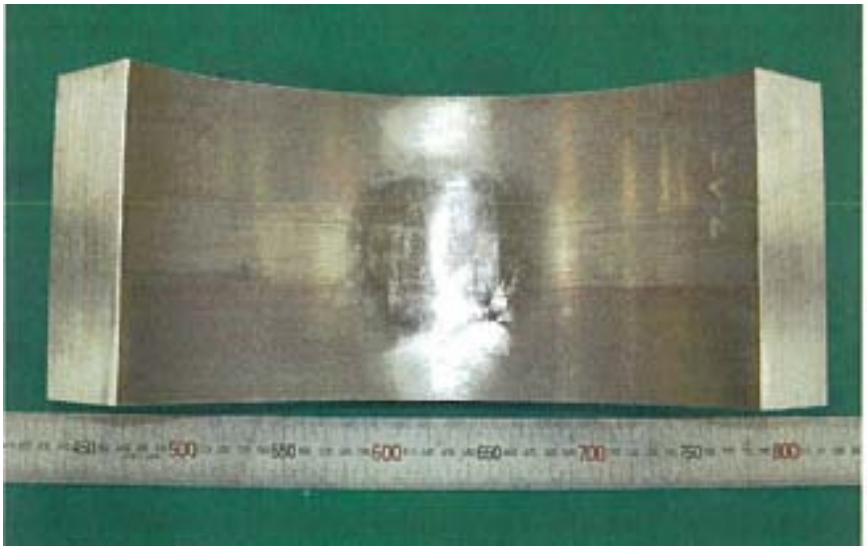

Figure 2.5 PINC Block 2.5 from JNES – PZR Surge Line to Safe-End Dissimilar Metal Weld

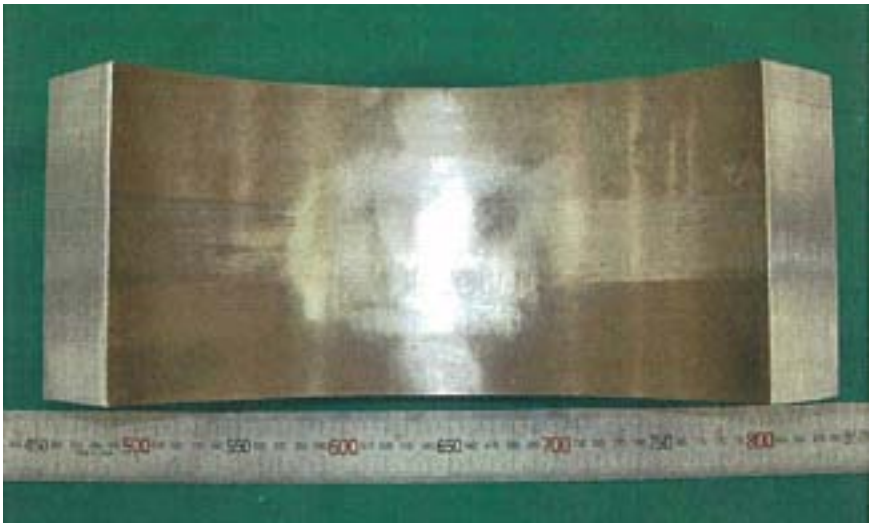

Figure 2.6 PINC Block 2.6 from JNES – PZR Surge Line to Safe-End Dissimilar Metal Weld

Figure 2.7 PINC Block 2.9 from Swedish Qualification Center (SQC)

Figure 2.8 PINC Block 2.10 from SQC

2.1.2 Schematic Drawings for Mid-Thickness Dissimilar Metal Welds

Schematic drawings are provided to give product form configuration and dimensions for the test blocks. The three test blocks PINC 2.1, 2.2, and 2.3 have similar configurations, as shown in Figure 2.9. The three test blocks PINC 2.4, 2.5, and 2.6 are likewise similar to each other, as shown in Figure 2.10. The dimensions of the SQC test block from the Swedish Radiation Safety Authority (SSM) are shown in Figure 2.11 and Figure 2.12. All units are in millimeters for Figures 2.9–2.12.

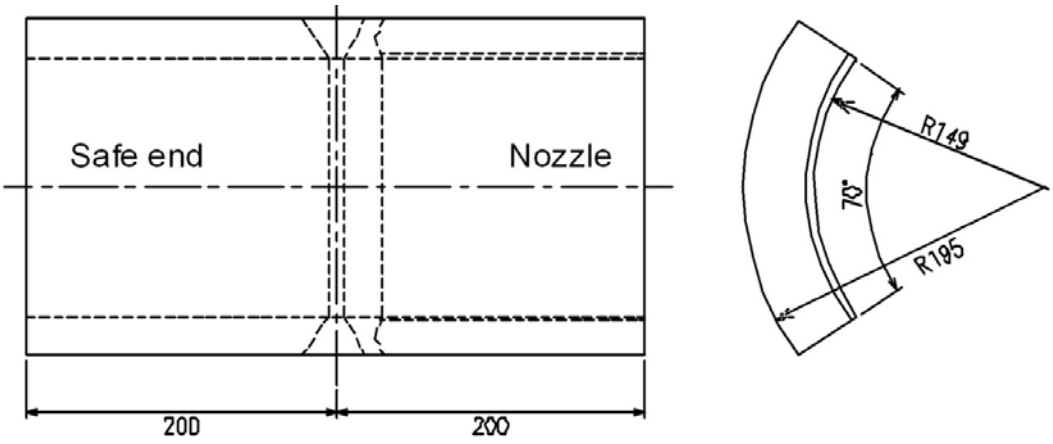

Figure 2.9 PINC Test Blocks 2.1 through 2.3 (JNES No. SH1 to SH3) – PZR Surge Line to Safe-End Dissimilar Metal Weld Test Blocks

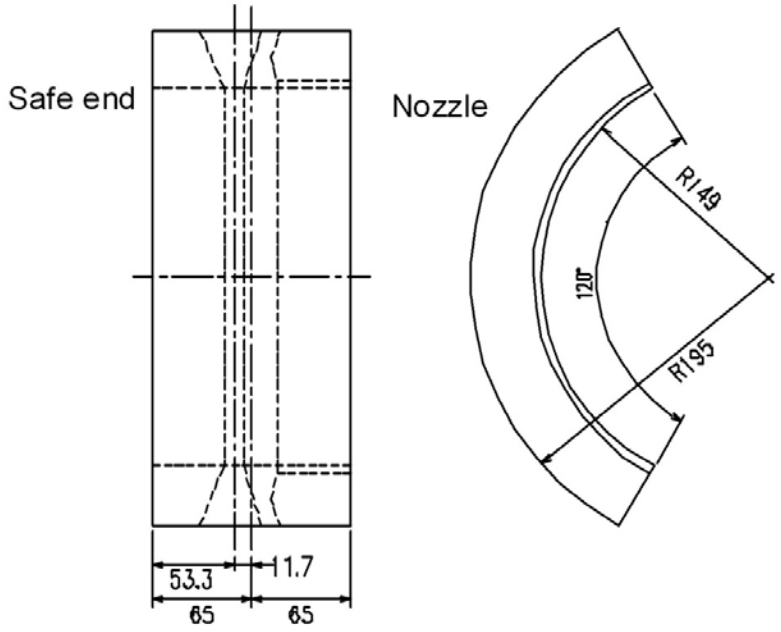

Figure 2.10 PINC Test Blocks 2.4 through 2.6 Test Blocks (JNES No. ST1 to ST3) – PZR Surge Line to Safe-End Dissimilar Metal Weld Test Blocks

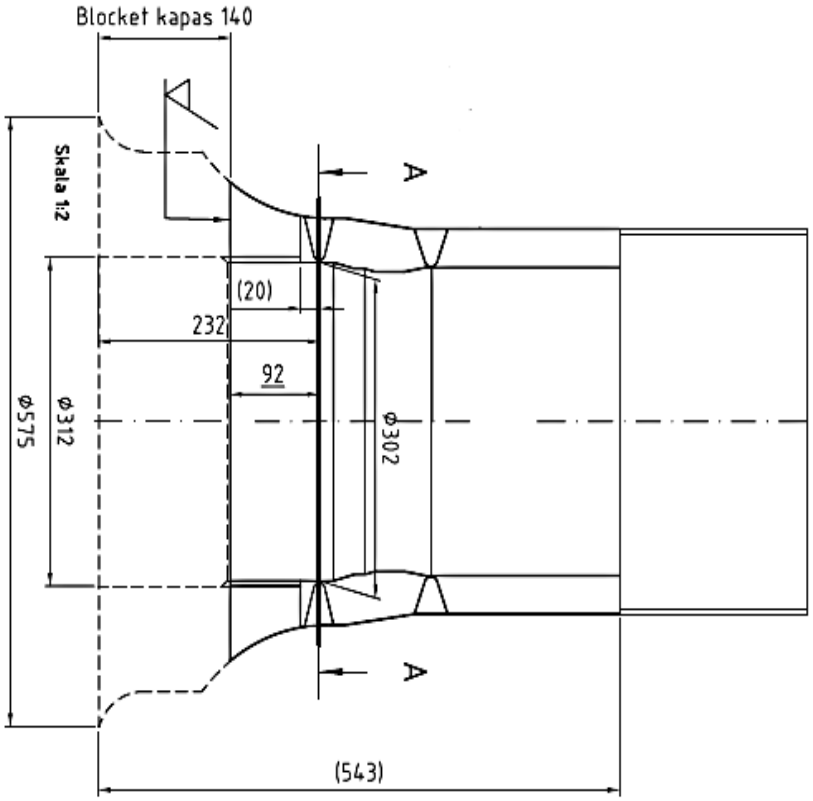

Figure 2.11 PINC Block 2.9 from Swedish Radiation Safety Authority (SSM)

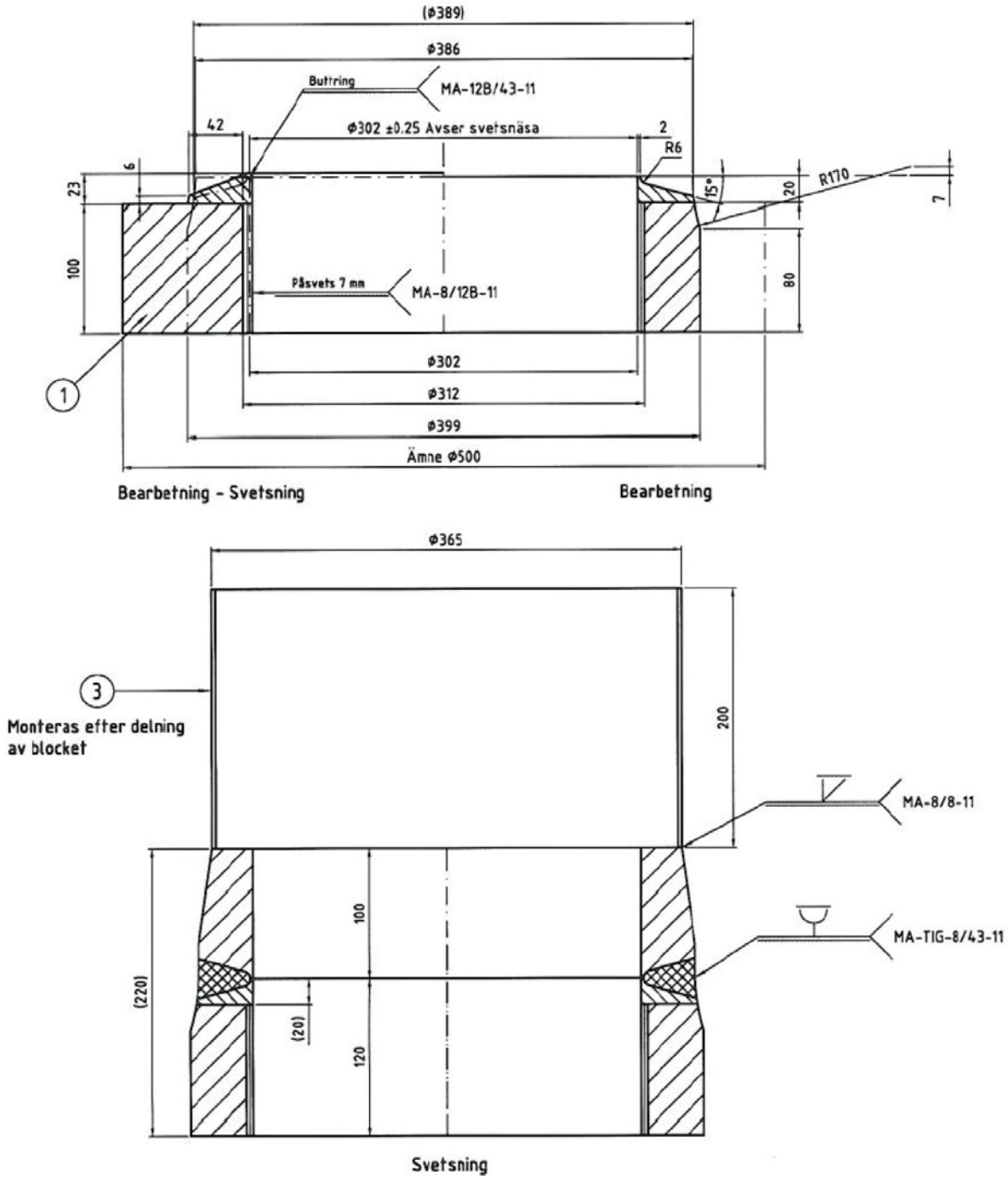

Figure 2.12 PINC Block 2.10 from SSM

2.1.3 Coordinate Systems for Mid-Thickness Dissimilar Metal Welds

This section documents the coordinate system for use in the mid-thickness dissimilar metal weld round-robin test. The reader should pay careful attention to the documented coordinate system

for each test block. The convention for increasing X (always along the weld) and Y (always across the weld) varies from test block to test block.

Figure 2.13 shows the coordinate system for test blocks PINC 2.1, 2.2, and 2.3. The *x-axis* increases clockwise when viewed from the stainless steel side and starts at the midpoint of the weld length. The *y-axis* increases toward the carbon steel side and starts at the weld centerline. The *z-axis* starts at the outside surface and increases into the part. Figure 2.14 shows the coordinate system for test blocks PINC 2.4, 2.5, and 2.6. This coordinate system uses the same convention as that shown in Figure 2.13.

For PINC 2.9, the *x-axis* increases counterclockwise around the part when viewed from the stainless steel side and starts at a scribe line on the part, as shown in Figure 2.15. The *y-axis* starts at the DMW centerline and increases toward the stainless steel side. For PINC 2.10, the *x-axis* increases counterclockwise around the part when viewed from the stainless steel side and starts at a set of punch marks on the part, as shown in Figure 2.16.

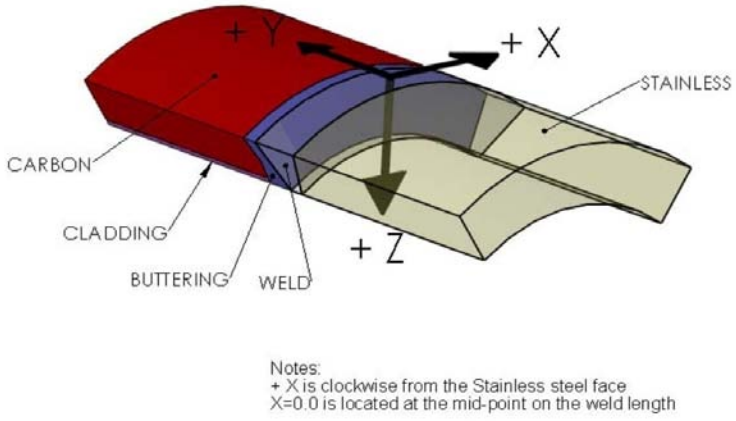

Figure 2.13 Coordinate System for PINC Test Blocks 2.1, 2.2, and 2.3

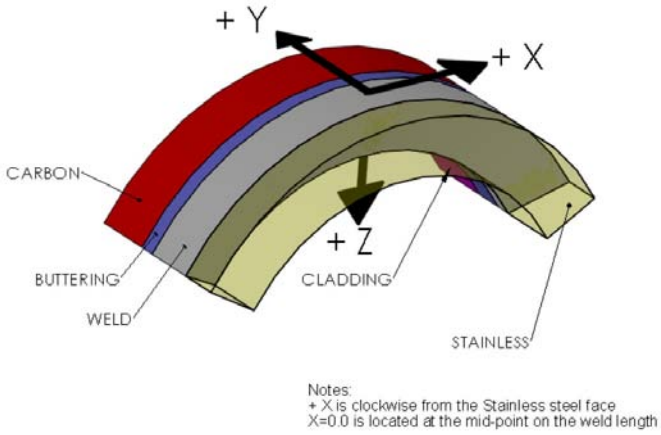

Figure 2.14 Coordinate System for PINC Test Blocks 2.4, 2.5, and 2.6

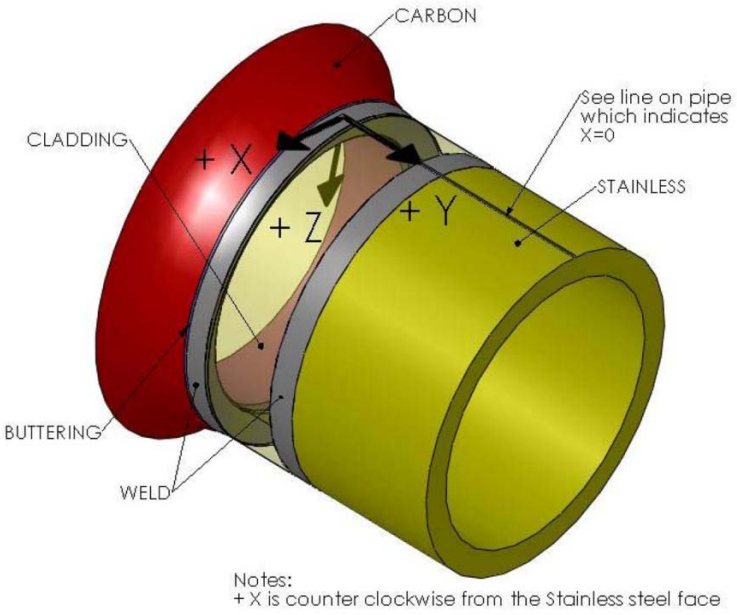

Figure 2.15 Coordinate System for PINC Test Block 2.9 from SSM/SQC

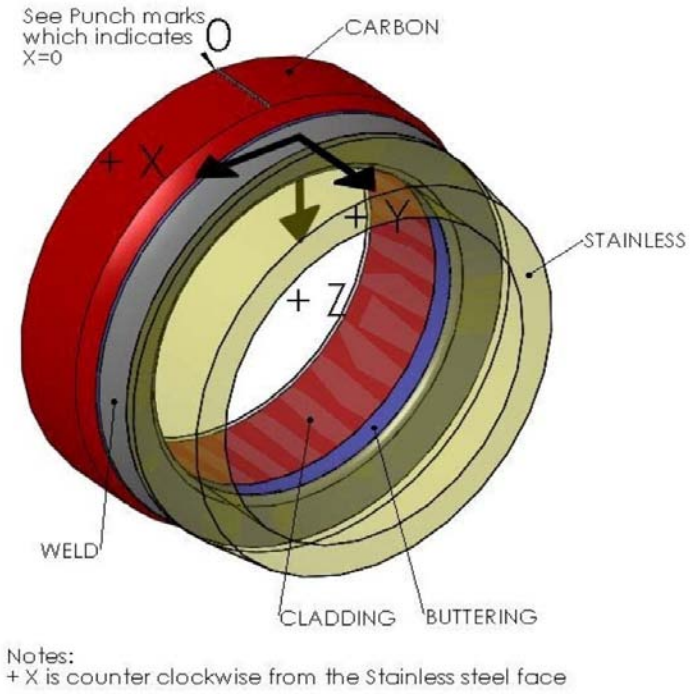

Figure 2.16 Coordinate System for PINC Test Block 2.10 from SSM/SQC

2.2 Bottom-Mounted Instrumentation Round-Robin Test Blocks

Fourteen test blocks were selected for the round-robin test on NDE effectiveness for degradation in BMI nozzle penetration seal welds. Table 2.4 references the photographs and drawings for the test blocks. Test blocks 5.4 and 5.5 did not contain cracks in the weld metal and were not used in the round-robin test studies. An extra test block was provided by KINS, and was not in the original test design. Although the test block was optional, all teams were encouraged to try to include this test block in their inspection schedule. The extra test block is shown in Figure 2.30.

Table 2.4 Test Blocks for BMI Round Robin

ID	Provider	Test Block	Photograph	Drawing
PINC 5.1	KINS	Penetration W17	Figure 2.27	Figure 2.31
PINC 5.2	KINS	Penetration W22	Figure 2.28	Figure 2.32
PINC 5.3	KINS	Penetration W46	Figure 2.29	Figure 2.33
PINC 5.6	SSM/SQC	F3.537.2	No Photograph	Figure 2.34
PINC 5.7	NRC/PNNL	WNP1.BMI.1	Figure 2.17	Figure 2.35
PINC 5.8	NRC/PNNL	WNP1.BMI.2	Figure 2.18	Figure 2.36
PINC 5.9	NRC/PNNL	WNP1.BMI.3	Figure 2.19	Figure 2.37
PINC 5.10	NRC/PNNL	WNP1.BMI.4	Figure 2.20	Figure 2.38
PINC 5.11	NRC/PNNL	WNP1.BMI.5	Figure 2.21	Figure 2.39
PINC 5.12	NRC/PNNL	WNP1.BMI.6	Figure 2.22	Figure 2.40
PINC 5.13	JNES	BMI No 1	Figure 2.23	Figures 2.41 & 2.42
PINC 5.14	JNES	BMI No 2	Figure 2.24	Figures 2.41& 2.42
PINC 5.15	JNES	BMI No 3	Figure 2.25	Figures 2.41 & 2.42
PINC 5.16	JNES	BMI No 4	Figure 2.26	Figures 2.41 & 2.42

Figure 2.17 PINC 5.7 from PNNL – WNP-1 BMI Nozzle Penetration 1

Figure 2.18 PINC 5.8 from PNNL – WNP-1 BMI Nozzle Penetration 2

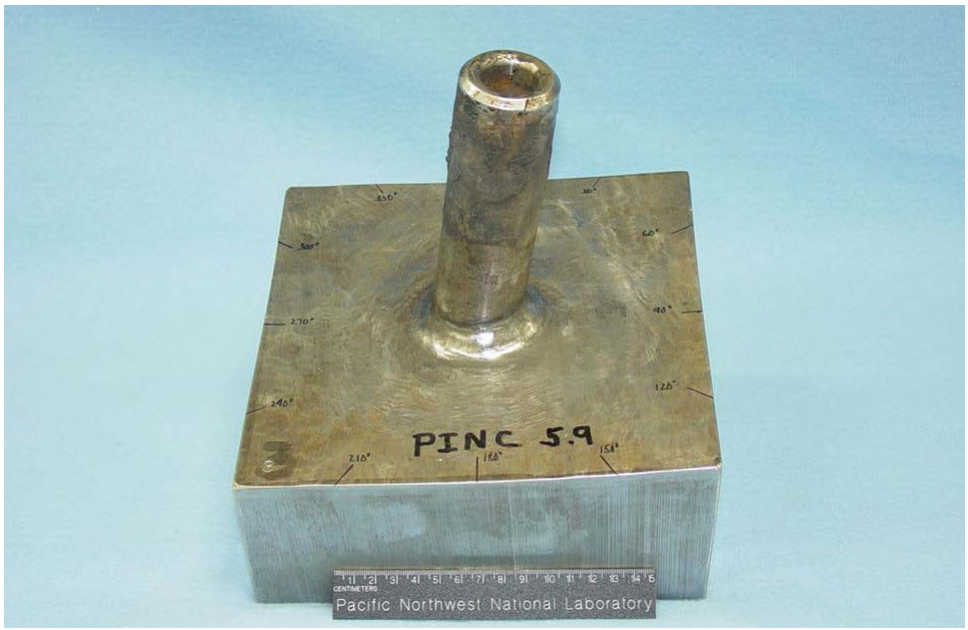

Figure 2.19 PINC 5.9 from PNNL – WNP-1 BMI Nozzle Penetration 3

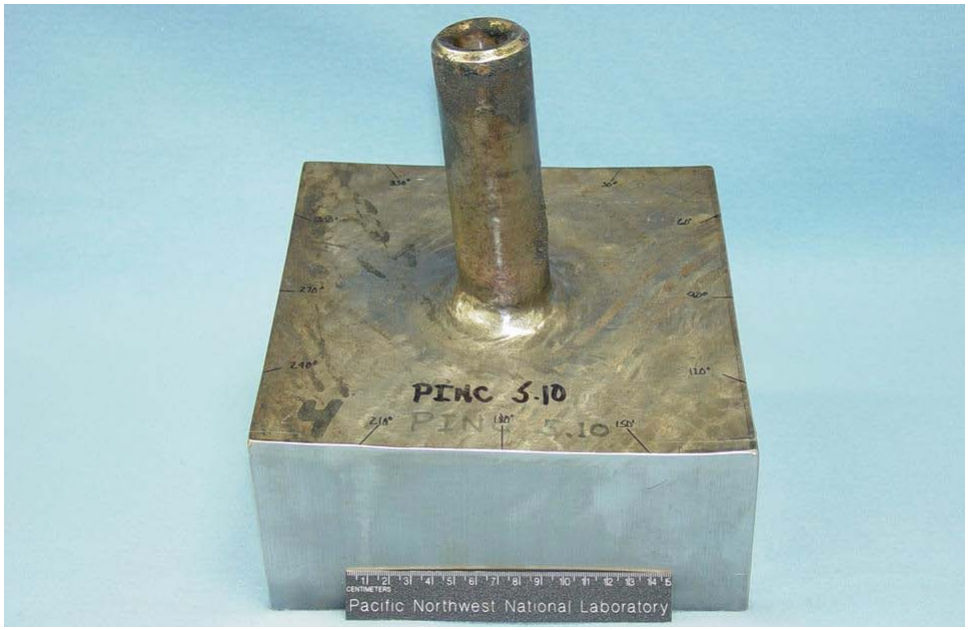

Figure 2.20 PINC 5.10 from PNNL – WNP-1 BMI Nozzle Penetration 4

Figure 2.21 PINC 5.11 from PNNL – WNP-1 BMI Nozzle Penetration 5

Figure 2.22 PINC 5.12 from PNNL – WNP-1 BMI Nozzle Penetration 6

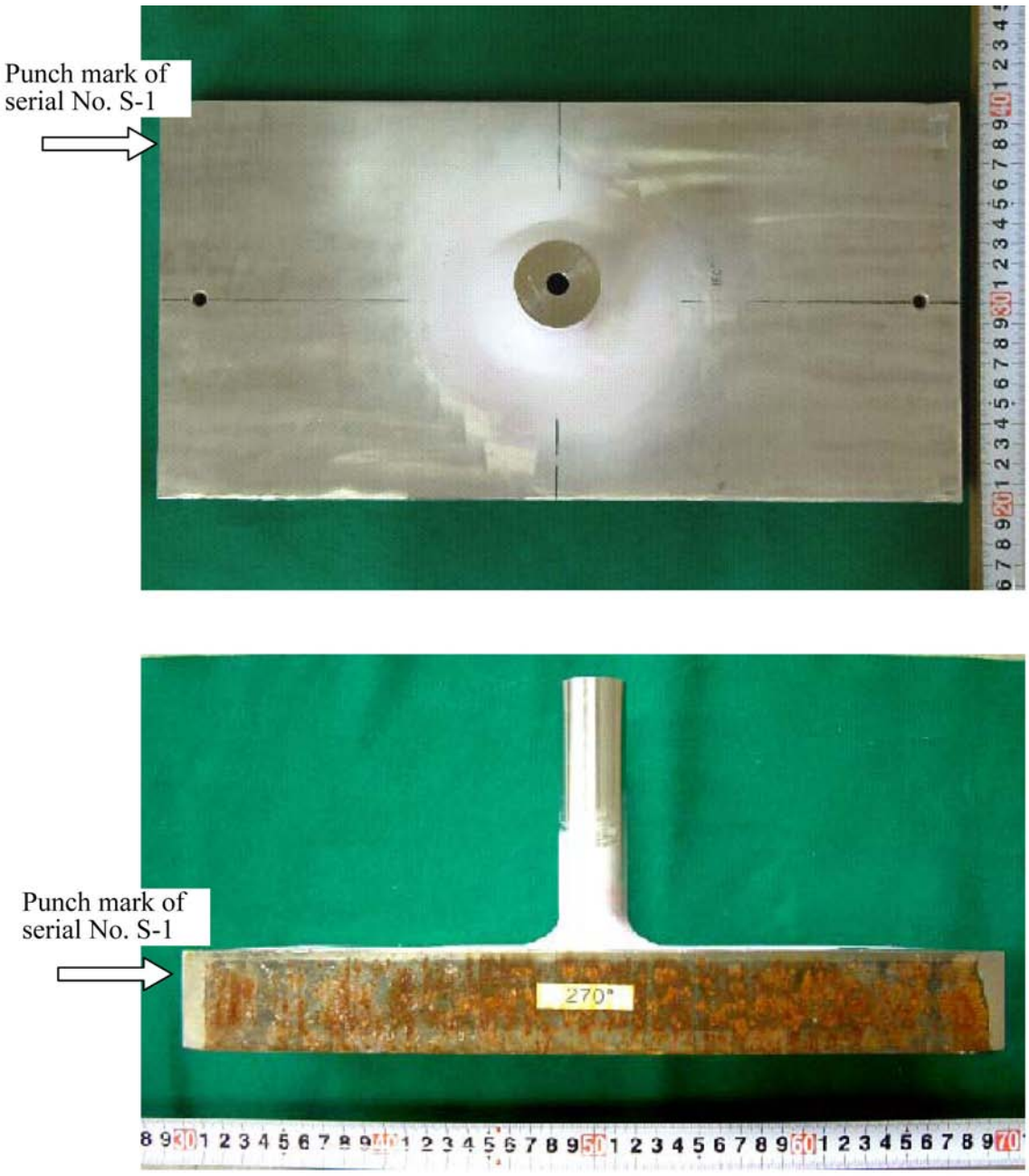

Figure 2.23 PINC 5.13 from JNES – BMI Nozzle Test Block No. 1

Figure 2.24 PINC 5.14 from JNES – BMI Nozzle Test Block No. 2

Figure 2.25 PINC 5.15 from JNES – BMI Nozzle Test Block No. 3

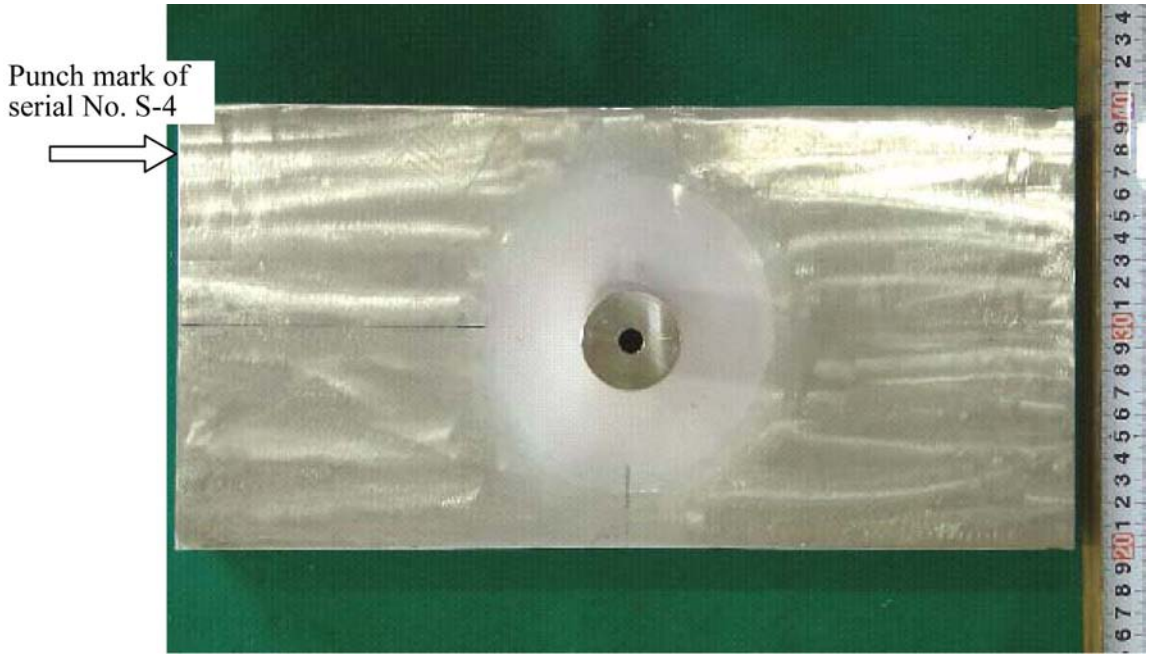

Figure 2.26 PINC 5.16 from JNES – BMI Nozzle Test Block No. 4

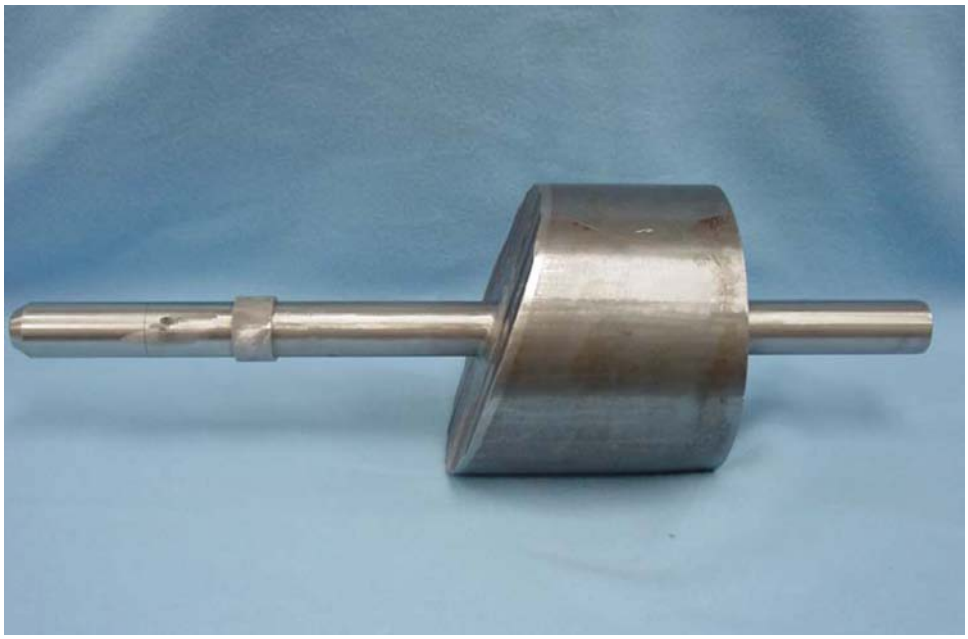

Figure 2.27 PINC 5.1 from KINS – BMI Nozzle Test Block

Figure 2.28 PINC 5.2 from KINS – BMI Nozzle Test Block

Figure 2.29 PINC 5.3 from KINS – BMI Nozzle Test Block

Figure 2.30 Extra Block from KINS – BMI Nozzle Test Block

2.2.1 Schematic Drawings for BMI Test Blocks

Schematic drawings are provided to give product form configuration and dimensions for the test blocks. The first three test blocks from KINS have the configurations shown in Figures 2.31, 2.32, and 2.33. The outside diameter of the BMI penetration tubes is 38 mm, and the inside diameter is 15.5 mm. PINC 5.6 has the configuration shown in Figure 2.34. The outside diameter of the tube is 47 mm; the inside diameter is 25 mm. The six test blocks PINC 5.7 through PINC 5.12 are similar to each other and, as shown in Figures 2.35 through 2.40, the outside diameter of the tube is 44 mm and the inside diameter is 15.9 mm. The four test blocks from JNES have a tube outside diameter of 38.1 mm and an inside diameter of 9.5 mm. Their configuration is shown in Figures 2.41 and 2.42. The units in Figures 2.31–2.33 are in inches, and the units in Figures 2.34–2.42 are in millimeters.

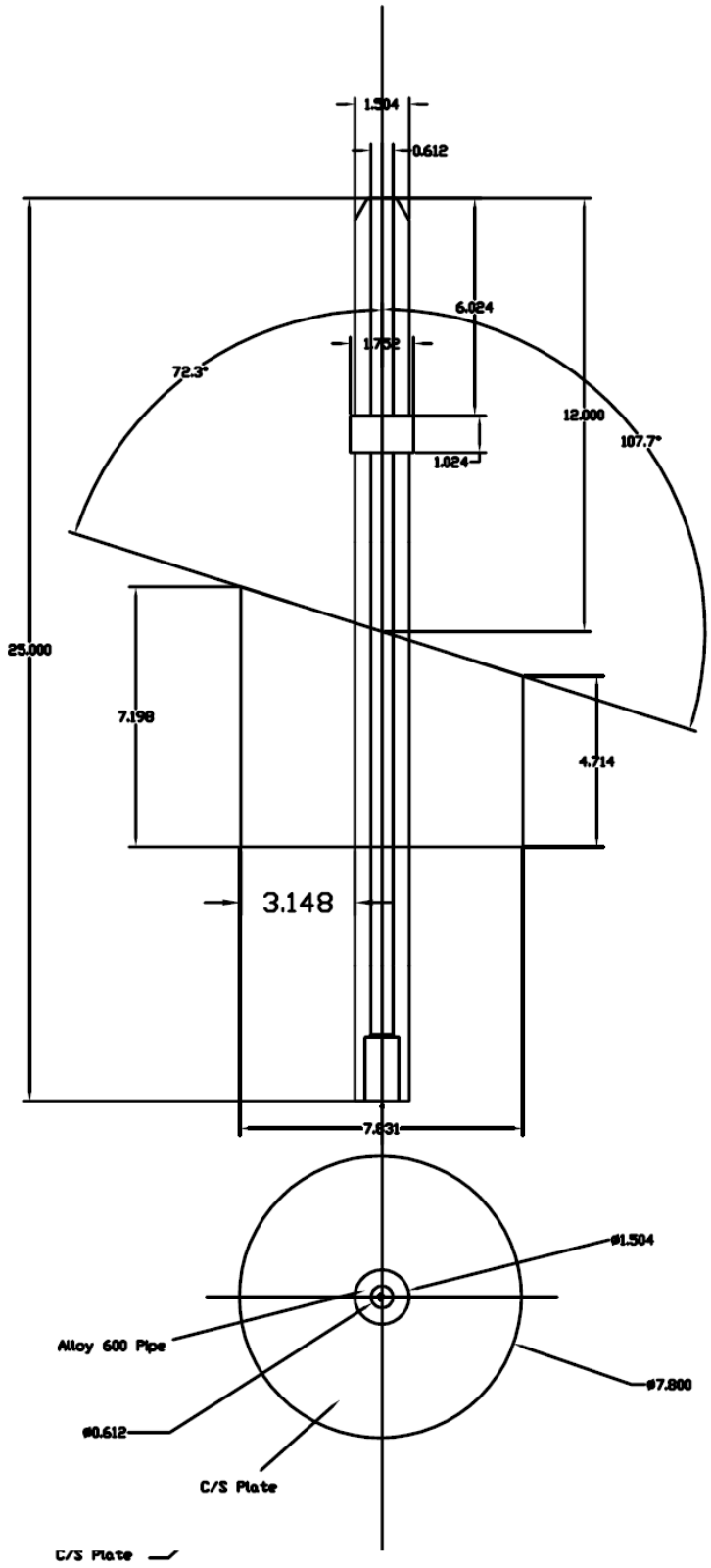

Figure 2.31 PINC 5.1 from KINS

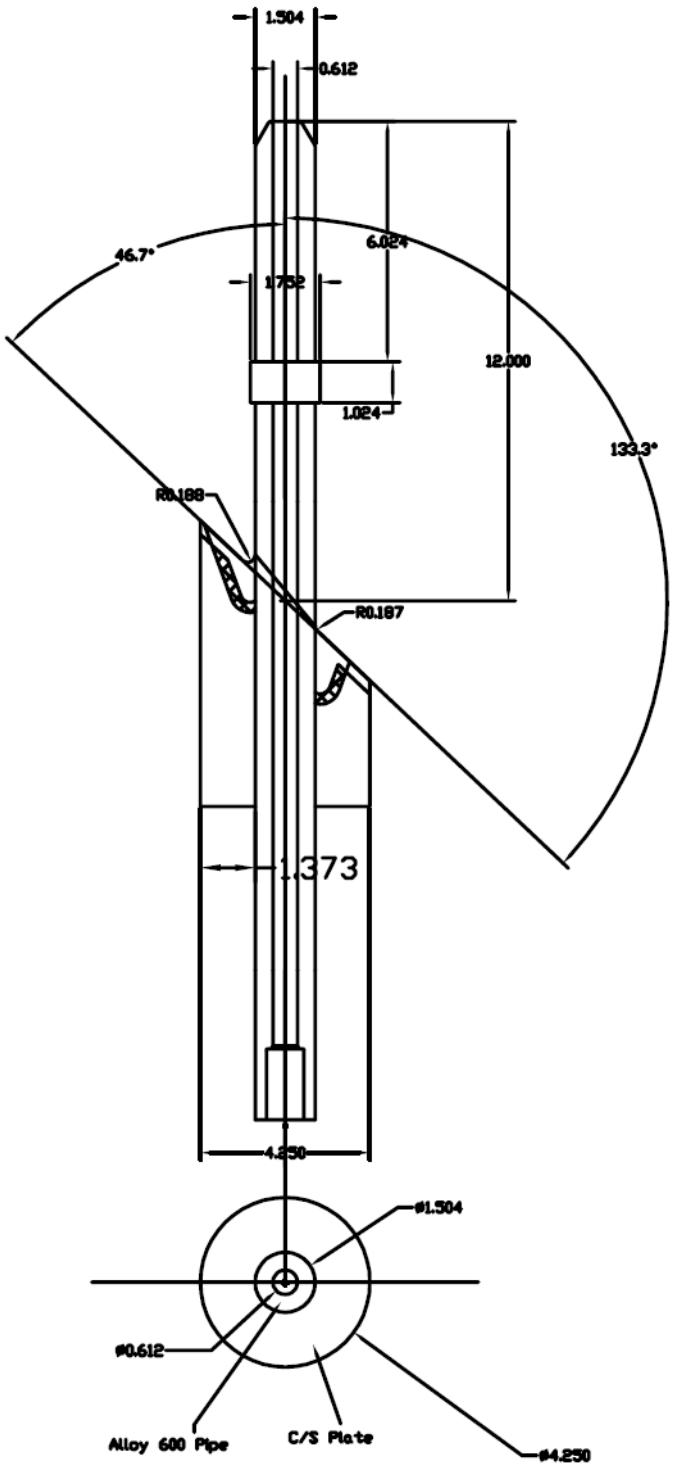

Figure 2.32 PINC 5.2 from KINS

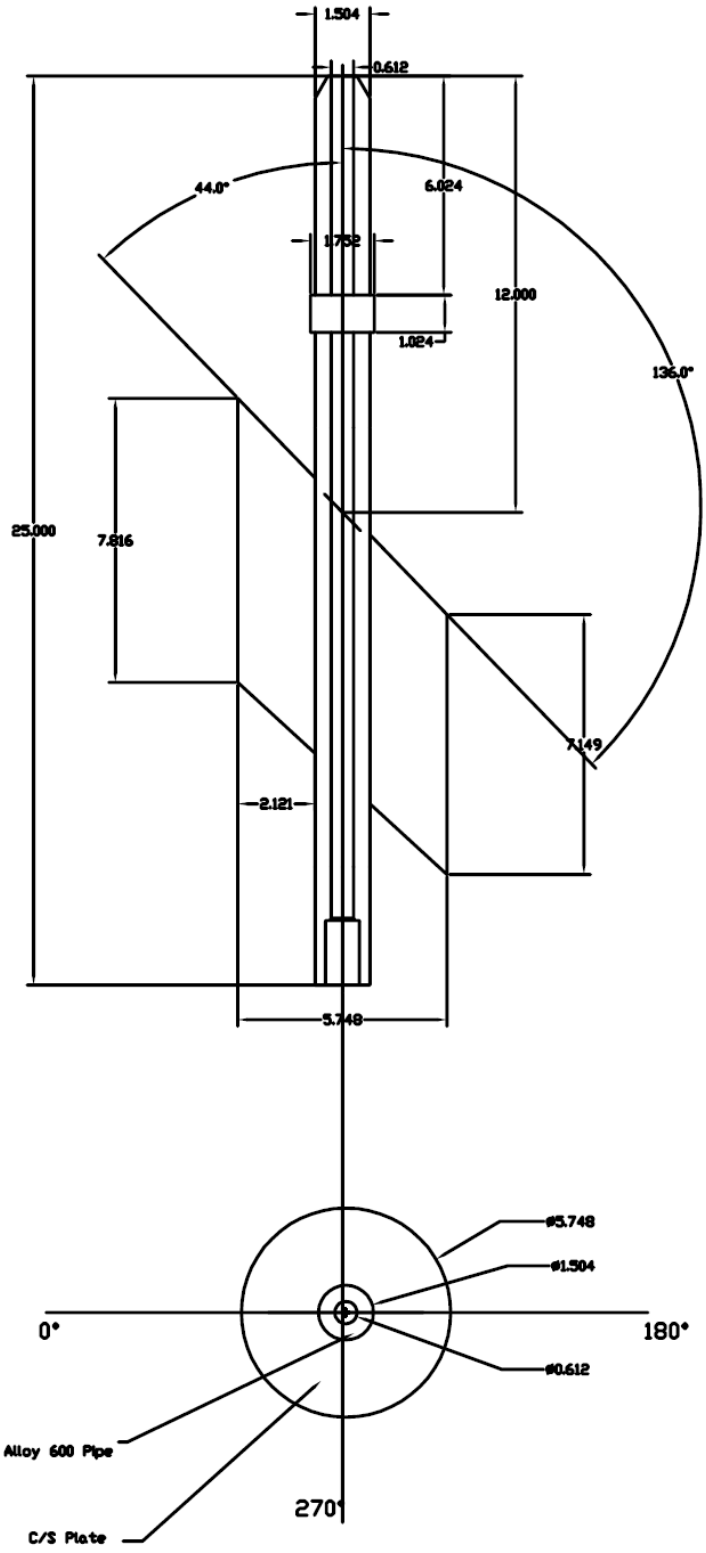

Figure 2.33 PINC 5.3 from KINS

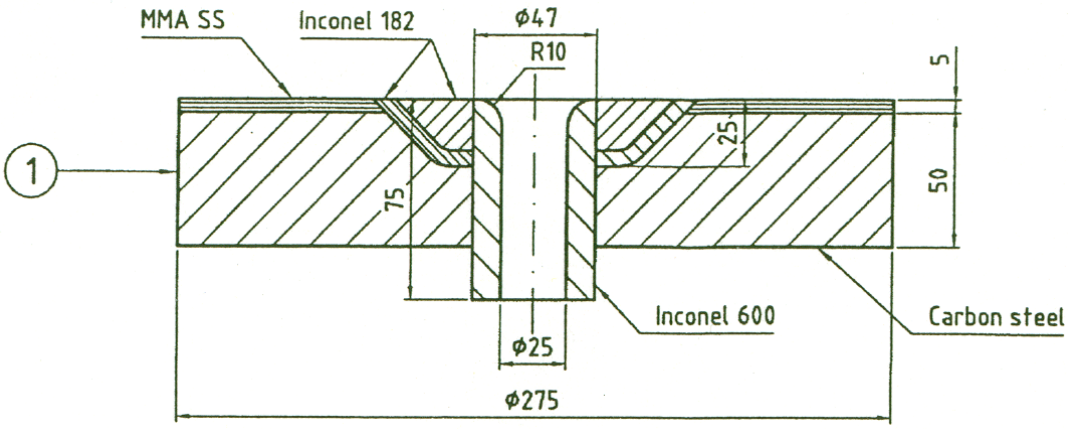

Figure 2.34 PINC 5.6 from SSM/SQC

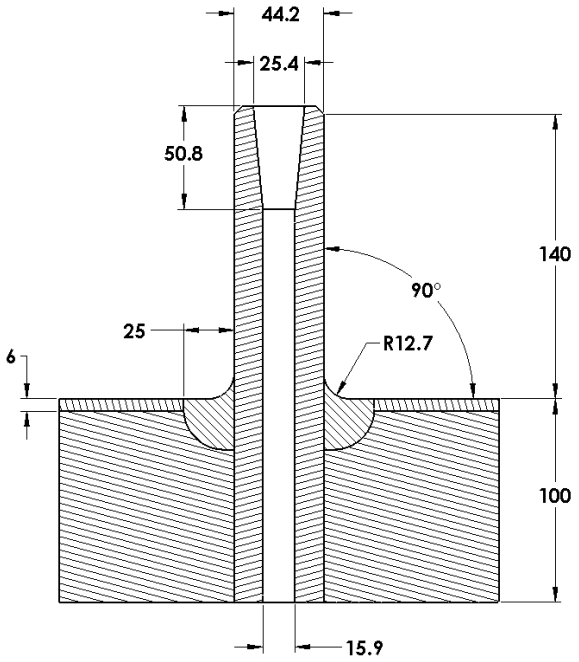

Figure 2.35 PINC 5.7 from NRC/PNNL

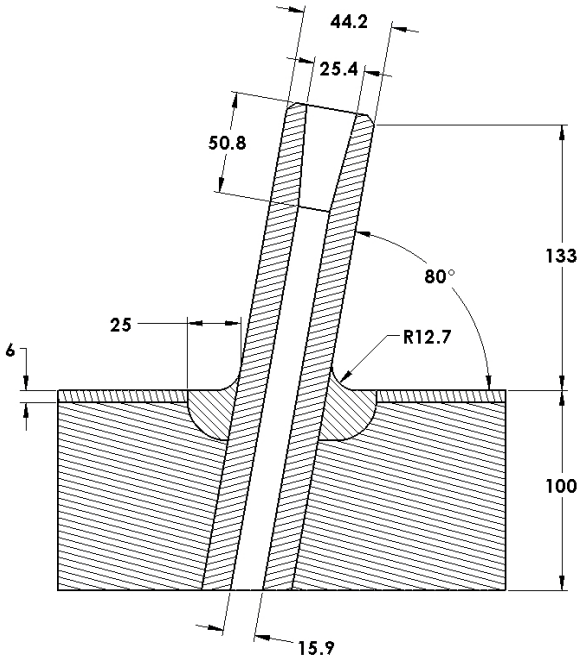

Figure 2.36 PINC 5.8 from NRC/PNNL

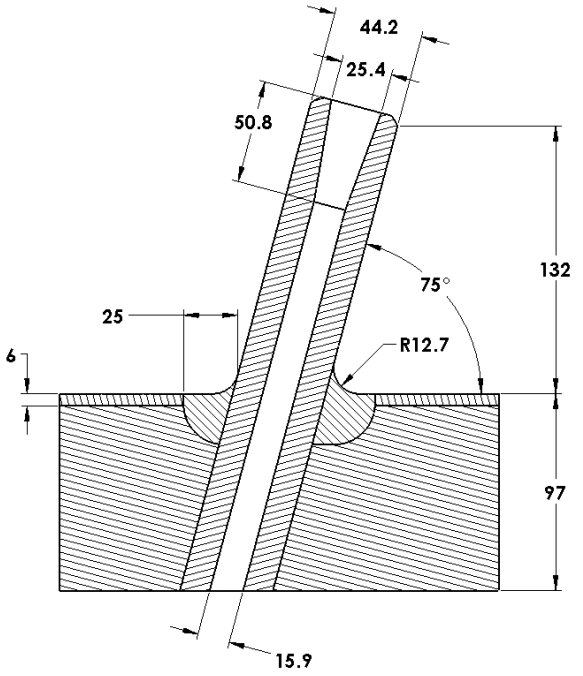

Figure 2.37 PINC 5.9 from NRC/PNNL

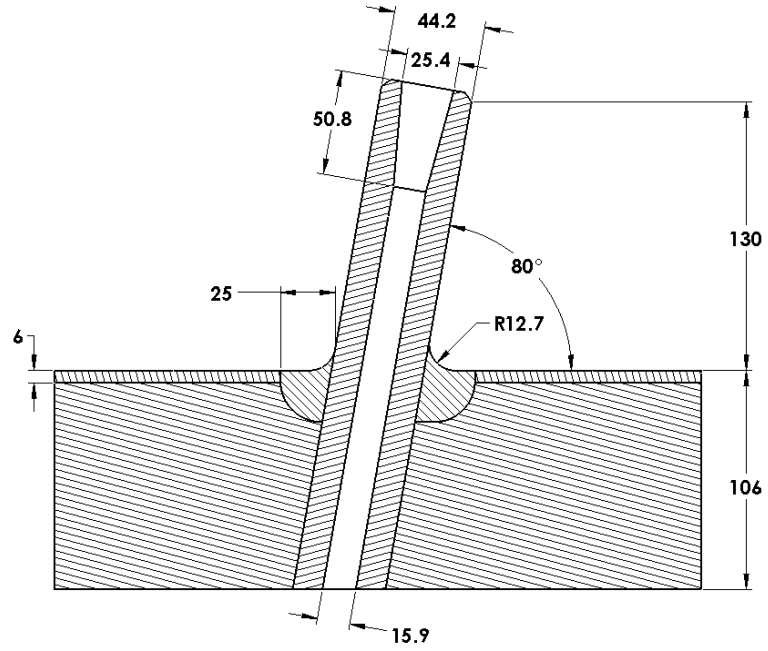

Figure 2.38 PINC 5.10 from NRC/PNNL

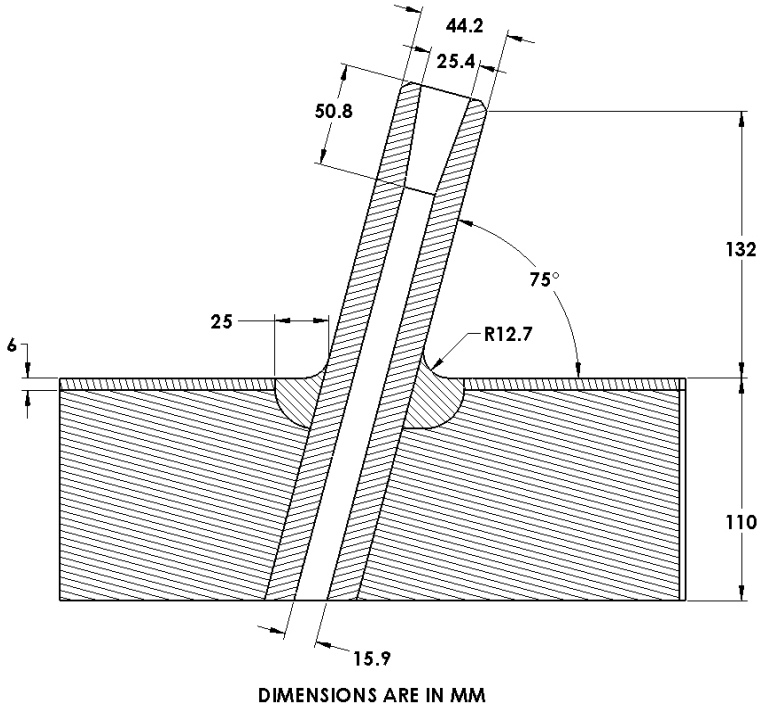

Figure 2.39 PINC 5.11 from NRC/PNNL

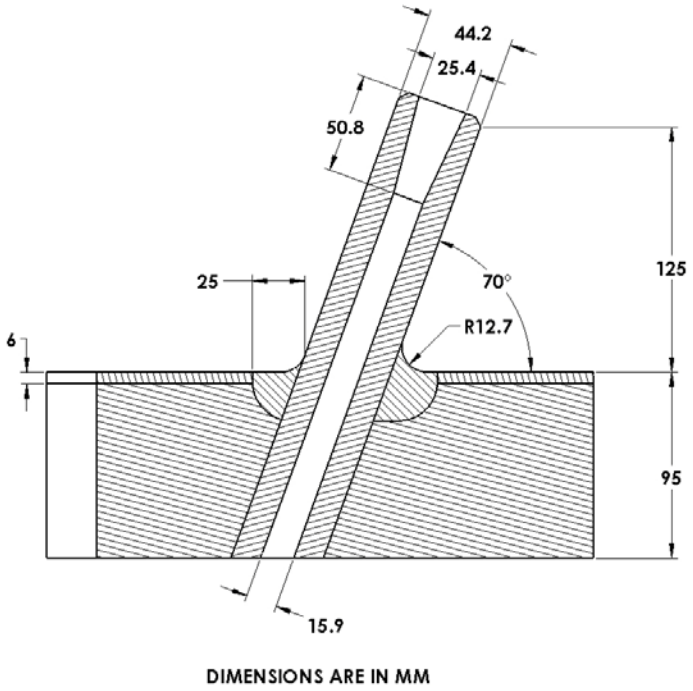

Figure 2.40 PINC 5.12 from NRC/PNNL

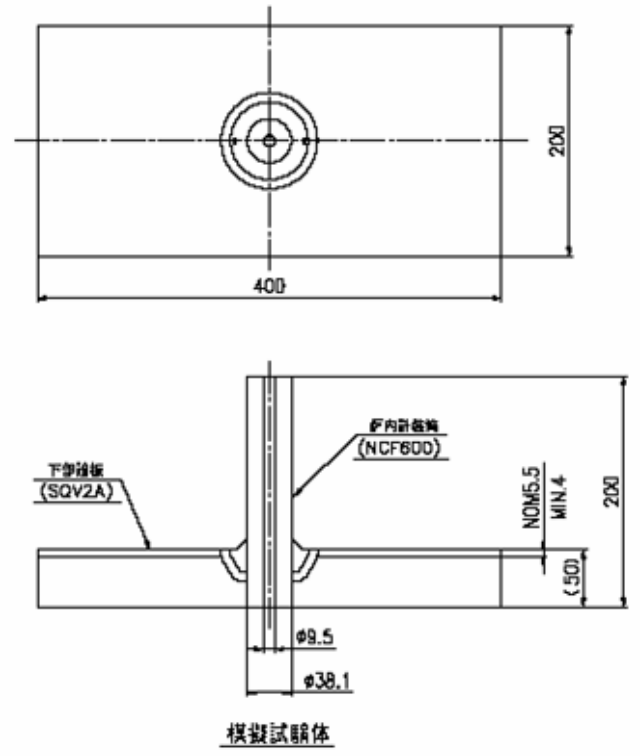

Figure 2.41 Test Blocks PINC 5.13 through 5.16 from JNES

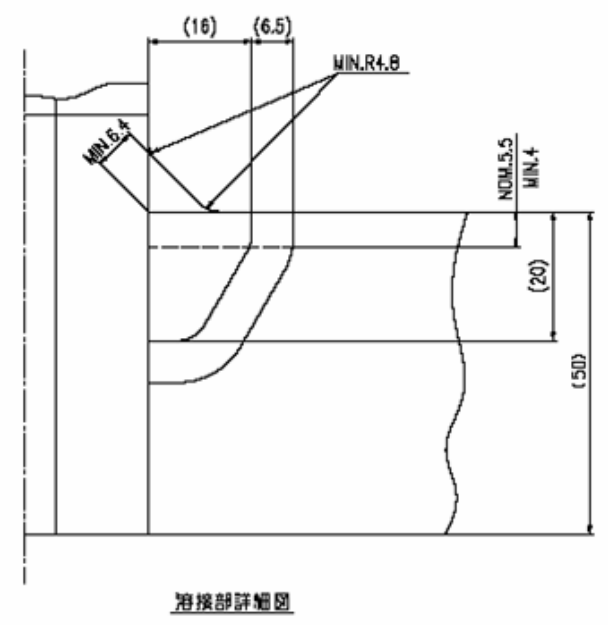

Figure 2.42 Seal Weld Configuration for PINC 5.13 through 5.16 from JNES

2.2.2 Coordinate Systems for BMI Round Robin

This section documents the coordinate system for use in the bottom-mounted instrumentation nozzle penetration seal weld round-robin test. Figure 2.43 shows the coordinate system for the first three test blocks, PINC 5.1 through 5.3. The circumferential axis increases clockwise when viewed from the top of the test block and starts at the 0-degree mark on the part. The radial axis starts at the center of the tube. The Z dimension for PINC 5.1 through 5.3 is measured from one of two areas as follows.

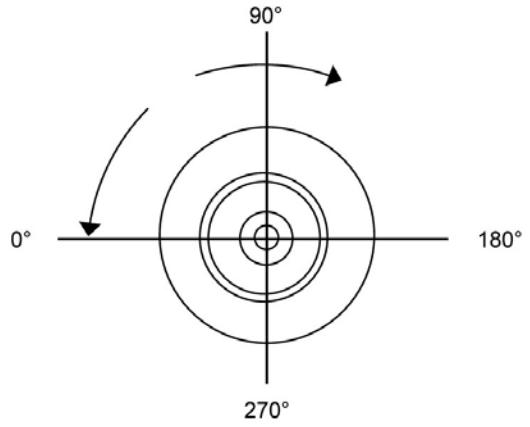

Figure 2.43 Coordinate System for PINC 5.1 through 5.3 from KINS

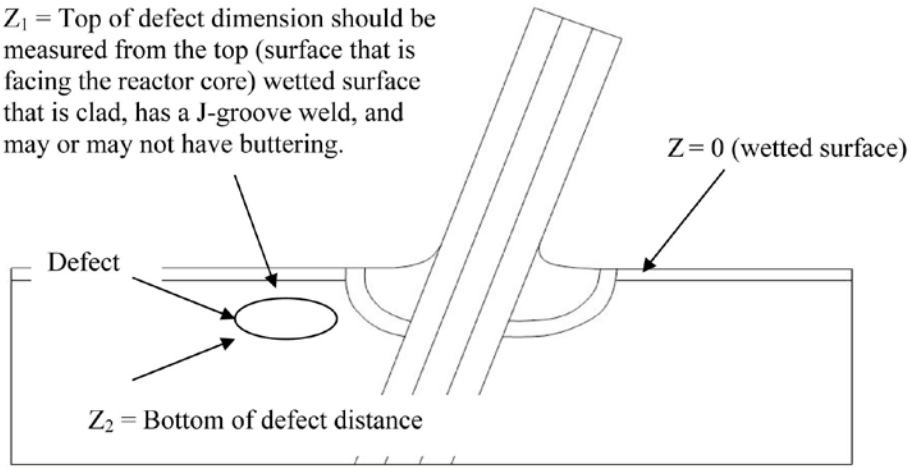

Figure 2.44 Z Dimension for BMI Blocks

For measuring defects in the J-groove weld, the Z dimension should be measured from the top (surface that is facing the reactor core) wetted surface that is clad, has a J-groove weld, and may or may not have buttering. The surface is curved; therefore, the Z dimension is reported relative to the angular location around the specimen. Figure 2.44 is an illustration of the Z dimension.

For measuring defects within the BMI tube, the Z dimension should be measured from the top of the tube down, as shown in Figure 2.45.

Figure 2.46 shows the coordinate system for the fourth test block, PINC 5.6. The circumferential axis increases counterclockwise when viewed from the top of the test block and starts at the 0-degree mark on the part. The radial axis starts at the center of the tube.

For PINC test blocks 5.7–5.12, the zero Θ is defined by a hole drilled into the cladding, with Θ going clockwise when looking down on the specimen, as shown in Figure 2.47. The radial axis starts at the center of the tube. For PINC text blocks 5.7–5.12, when defects in the J-groove weld are measured, the Z dimension should be measured from the top (the surface facing the reactor core) wetted surface that is clad, J-groove, and has buttering. The surface is curved; therefore, the Z dimension is reported relative to the angular location around the specimen.

For PINC test blocks 5.13–5.16, the circumferential axis increases clockwise around the part when viewed from the top of the test block and starts at the 0° punch mark direction on the side surface of the test block, as shown in Figure 2.48. The radial axis starts at the center of the tube.

For the axial coordinate system of PINC 5.13–5.16, the Y = 0 position is the top of the test block. The length for "Y+" is measured along the surface of the test block, as shown in Figure 2.49.

For PINC test blocks 5.13–5.16, when defects in the J-groove weld are measured, the Z dimension should be measured from the top (the surface facing the reactor core) wetted surface that is clad, J-groove, and has buttering. The surface is curved; therefore, the Z dimension is reported relative to the angular location around the specimen.

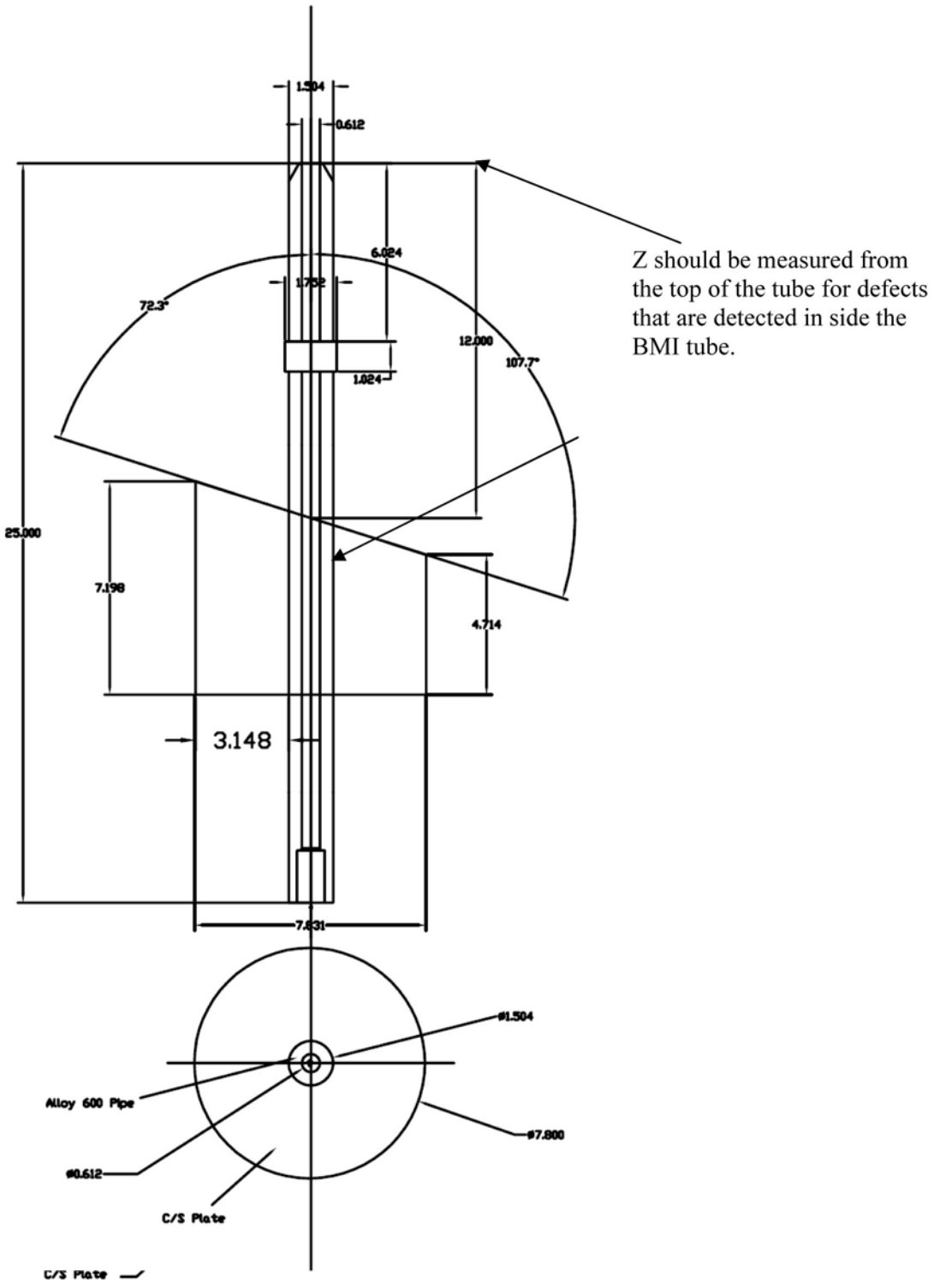

Figure 2.45 Coordinate System for PINC 5.1–5.3

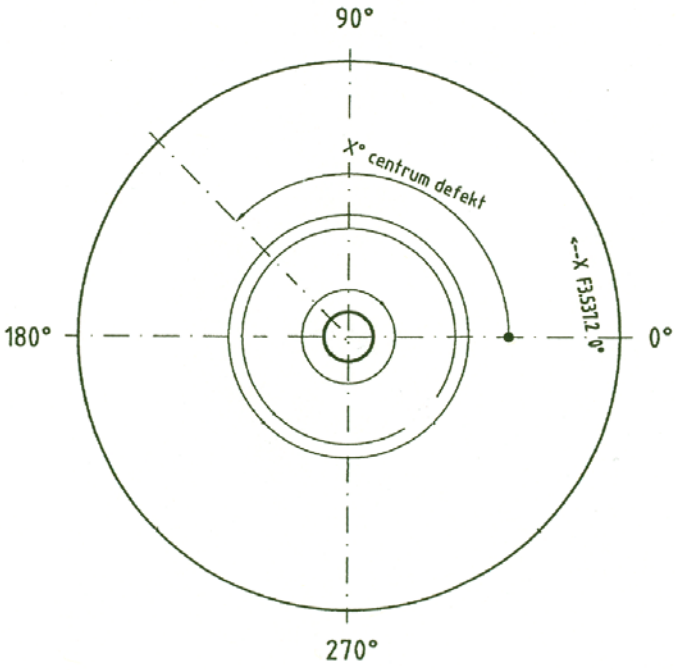

Figure 2.46 Coordinate System for PINC 5.6 – SSM/SQC F3.537.2

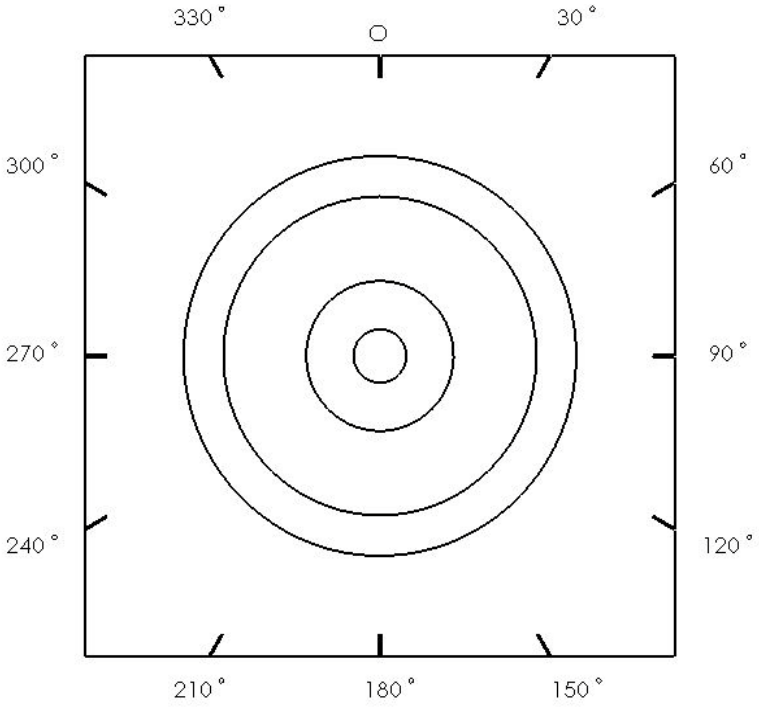

Figure 2.47 Coordinate System for Test Blocks PINC 5.7–5.12

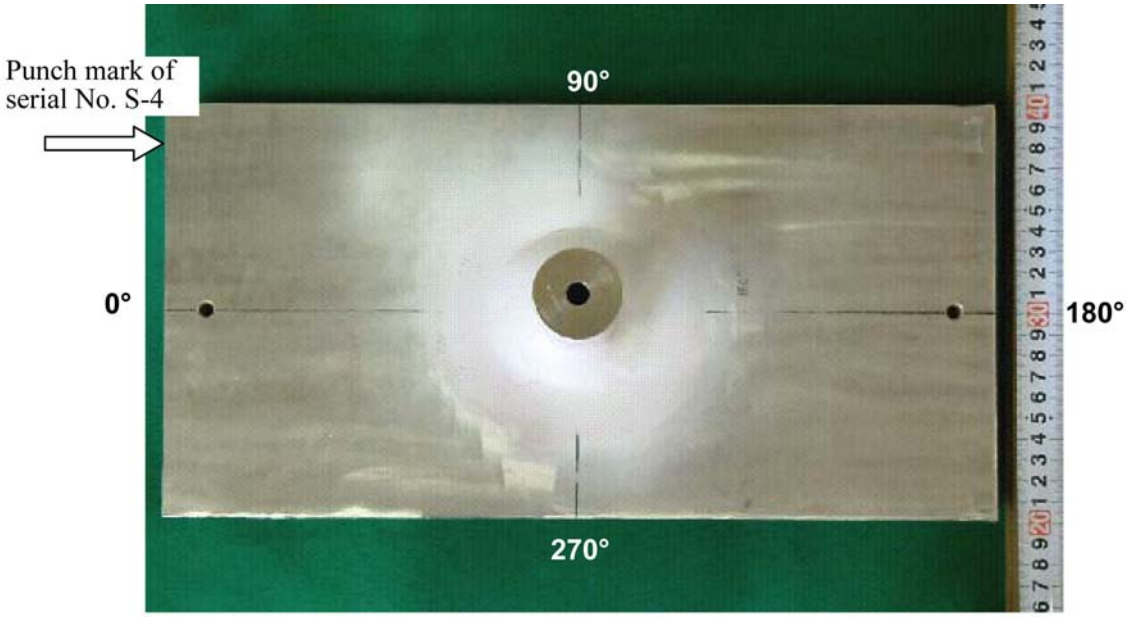

Figure 2.48 Circumferential Coordinate System for Test Blocks PINC 5.13–5.16

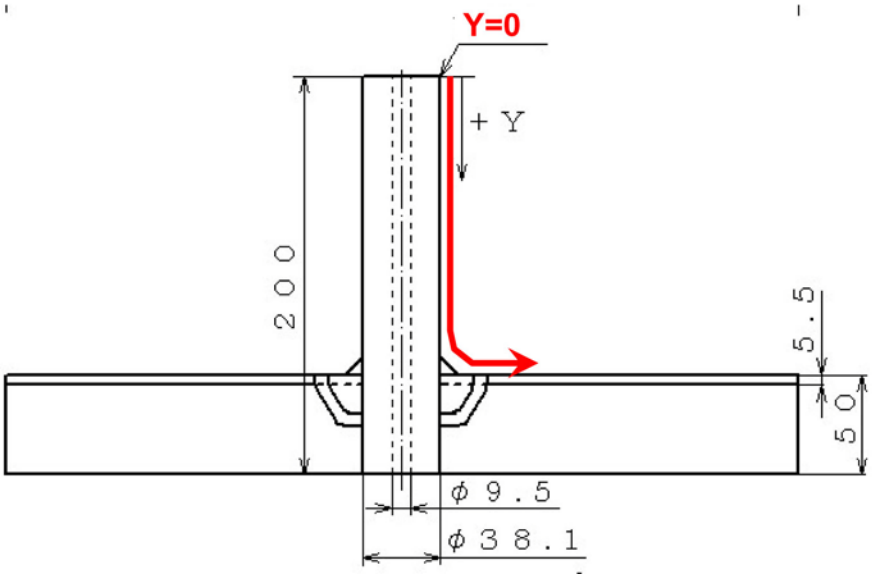

Figure 2.49 Axial Coordinate System for Test Blocks PINC 5.13–5.16

2.3 Description of Fabrication Techniques Used in Developing PINC Test Blocks

This section describes how the flaws were introduced into the various PINC test specimens. The implantation techniques are important because one of the goals of the PINC is to understand what makes the flaws easier or more challenging to detect. Each flaw manufacturing technique produces flaws with a different morphology. The variety of flaw manufacturing techniques used in the PINC BMI test blocks allows for an analysis of the difficulty in detecting the different types of cracks.

2.3.1 Flaw Fabrication in Test Blocks 5.1–5.3

Most of the cracks used in test blocks 5.1, 5.2, and 5.3 were produced by first creating the flaws in coupons and then welding the coupons containing the flaws into the welds. One example of a crack that was fabricated into a weld is shown in Figure 2.50.

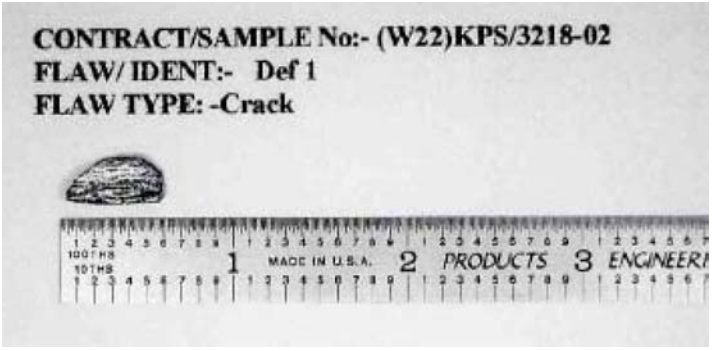

Figure 2.50 Example Flaw Coupon as Used for Test Blocks 5.1–5.3

Other flaw types such as porosity and lack of fusion were introduced into the weld using the same technique. Flaw types such as weld undercut were cut directly into the penetration tube. The undercut flaw is shown in Figure 2.51.

This method of crack fabrication is commonly used and is well understood. The use of coupons does pose one possible issue—the effects of the additional welding on the ultrasonic and electrical properties at the weld–sample interface.

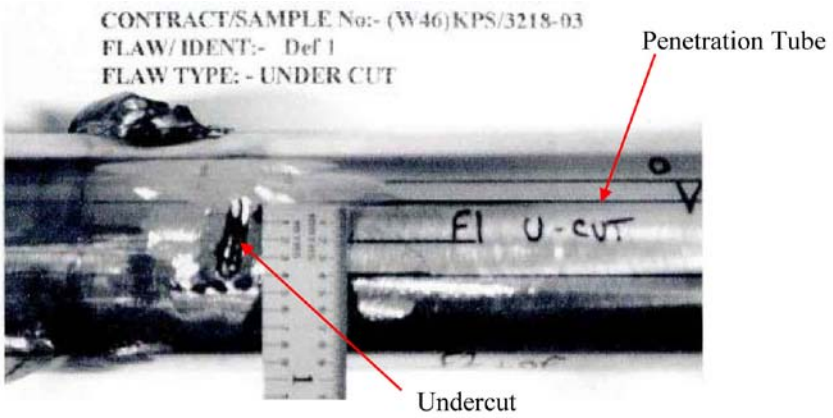

Figure 2.51 Example Weld Undercut Flaw as Used in Test Blocks 5.1–5.3

These flaws were implanted in the penetration tubes and welds of the BMI samples. Additionally, weld flaws can be introduced into the samples during the welding process. Sample 5.3 has implanted cracks, undercut, and a lack of fusion weld flaw. The placement of these flaws is shown in Figure 2.52.

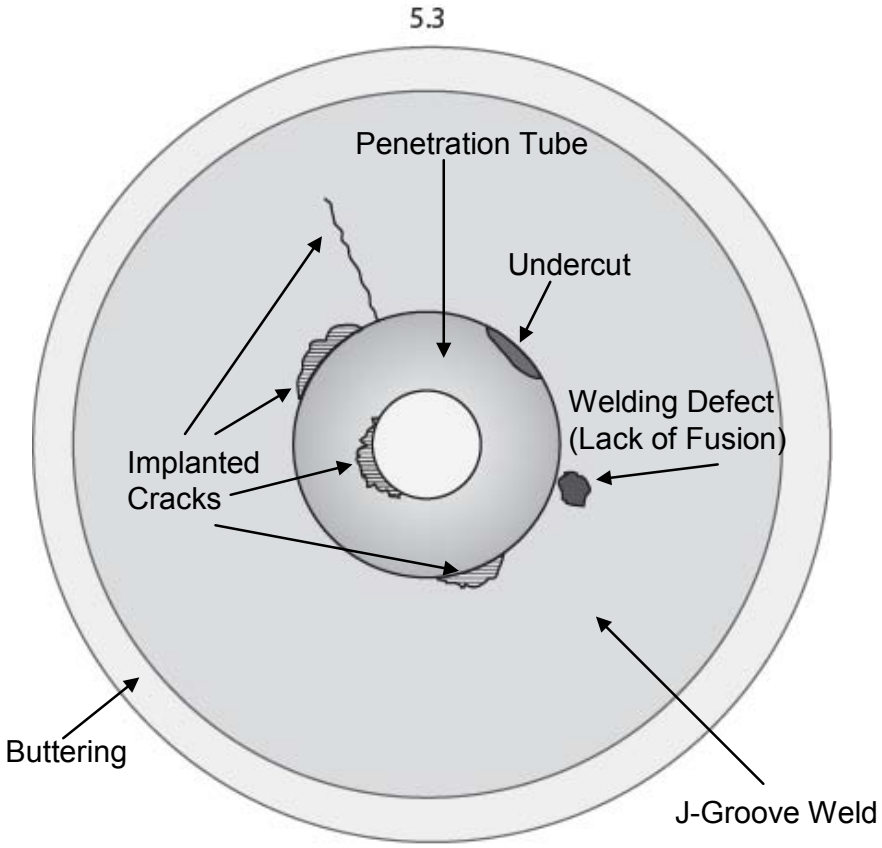

Figure 2.52 Flaw Placement in Test Block 5.3

2.3.2 Flaw Fabrication in Test Blocks 2.9, 2.10 and 5.6

The flaws in test blocks 2.9, 2.10, and 5.6 were fabricated via a weld-solidification process. The region where the crack was fabricated was excised and then filled in with “poisoned” weld metal that is designed to crack on cooling. The cracks in these test blocks were designed to simulate the eddy current responses found for cracks in the 182 weld metal in the Ringhals 4 reactor (SQC 2003). The eddy current responses for the fabricated cracks were checked to ensure they were similar to the responses in real stress corrosion cracks (SCC) that occurred in nickel alloy material.

Possible issues with this style of crack fabrication are similar to those for the fabricated flaws used in test blocks 5.1–5.3—the weld fabrication zone can possibly be detected in an eddy current or a visual examination. A visual examination of the cracked areas showed no disturbance of the surface caused by the implantation process and that the weld solidification cracks were surface-breaking. The flaws in Block 5.6 at 45, 180, 225, 255, and 315 degrees were clearly detected in photographs, and the flaw at 135 degrees had a possible crack-like indication. A sample weld solidification crack in test block 5.6 is shown in Figure 2.53.

2.3.3 Flaw Fabrication in Test Block 5.7

The flaws in test block 5.7 were fabricated using an in situ thermal fatigue process. This process is able to introduce flaws into the material without the weld fabrication problems associated with the coupon insertion or weld-solidification cracking. It is also possible to control crack properties such as crack opening displacement (COD) and crack depth with a high level of precision. The thermal fatigue cracks are very expensive, however, so only two such flaws were ordered. Because of an accident during the fabrication of one of the flaws, three flaws are present in test block 5.7. Only two have the proper pedigree involving length and depth, however. All three flaws in test block 5.7 were confirmed as surface-breaking using visual examination. Photography of the flaws showed that the flaws at 15 degrees and 300 degrees consisted of multiple small cracks spaced closely together. The flaw at 15 degrees is shown in Figure 2.54.

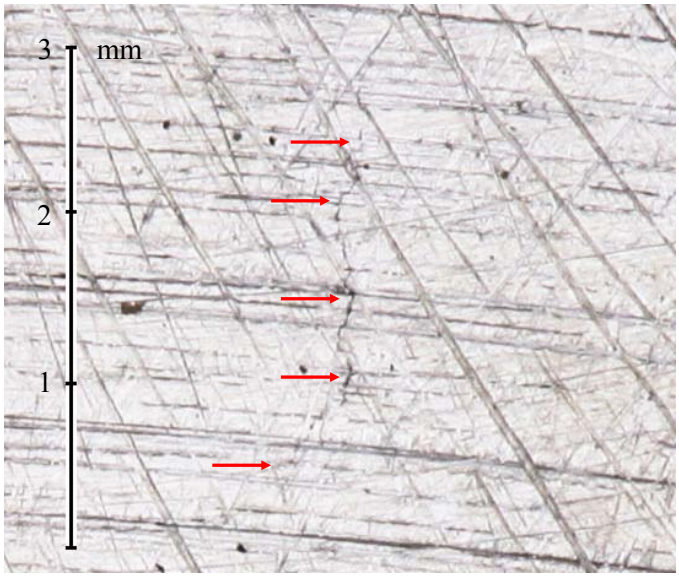

Figure 2.53 Weld Solidification Crack in Test Block 5.6 at 45 Degrees

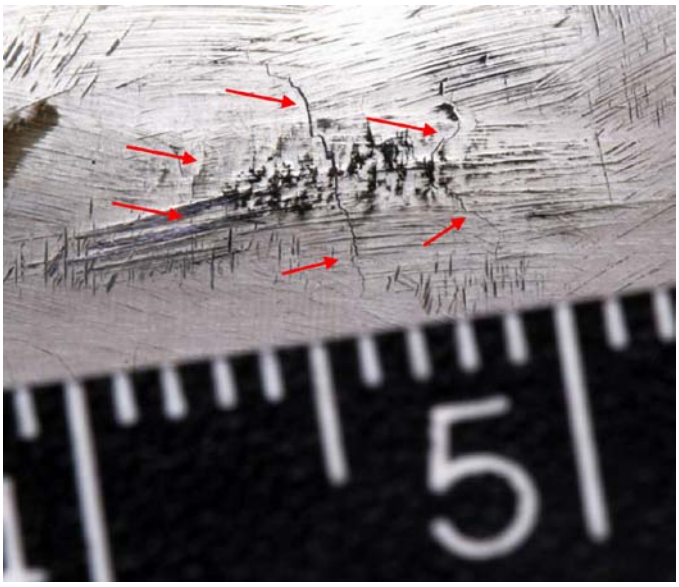

Figure 2.54 Thermal Fatigue Cracks in Test Block 5.7

2.3.4 Flaw Fabrication in Test Block 5.8

Test block 5.8 had a weld repair, but no crack or other flaws, fabricated into the weld. This test block is designed to control for the issues caused by the flaws fabricated via welding flawed coupons into the test blocks and the weld-solidification cracks. The inspection of test block 5.8 provides important insight to determine if the inspectors are finding the fabrication regions and not the cracks themselves.

2.3.5 Flaw Fabrication in Test Blocks 5.9 and 5.10

The flaws in test blocks 5.9 and 5.10 were fabricated using a weld-solidification cracking process similar to the process used in test block 5.6. The difference between test block 5.6 and test blocks 5.9 and 5.10 is that the flaws in test blocks 5.9 and 5.10 were tailored to be more challenging to detect. These flaws are designed to mimic difficult-to-detect indications such as those found in the North Anna 2 nozzle 31. It is worth noting that the indications with challenging to detect NDE responses in North Anna 2 were later found to be less than 8 mm deep.

A careful visual examination using high-resolution macro photography found no evidence of surface-breaking flaws in test blocks 5.9 or 5.10. This is in contrast to the weld solidification flaws in test block 5.6, where flaws were visible on the surface. Test blocks 5.9 and 5.10 were then examined using fluorescent dye penetrant testing. The penetrant testing of test block 5.9 showed no indications of any surface-breaking flaws. The penetrant testing of test block 5.10 found no linear indications, but two small spots of penetrant appeared at locations consistent with the crack implantation regions of 255 and 315 degrees. During the destructive examination of sample 5.10 the crack was revealed to have a limited surface-breaking component, and it is now believed that the PT indication near 315 degrees may have come from a welding defect such as porosity. The results of the penetrant testing are shown in Figure 2.55.

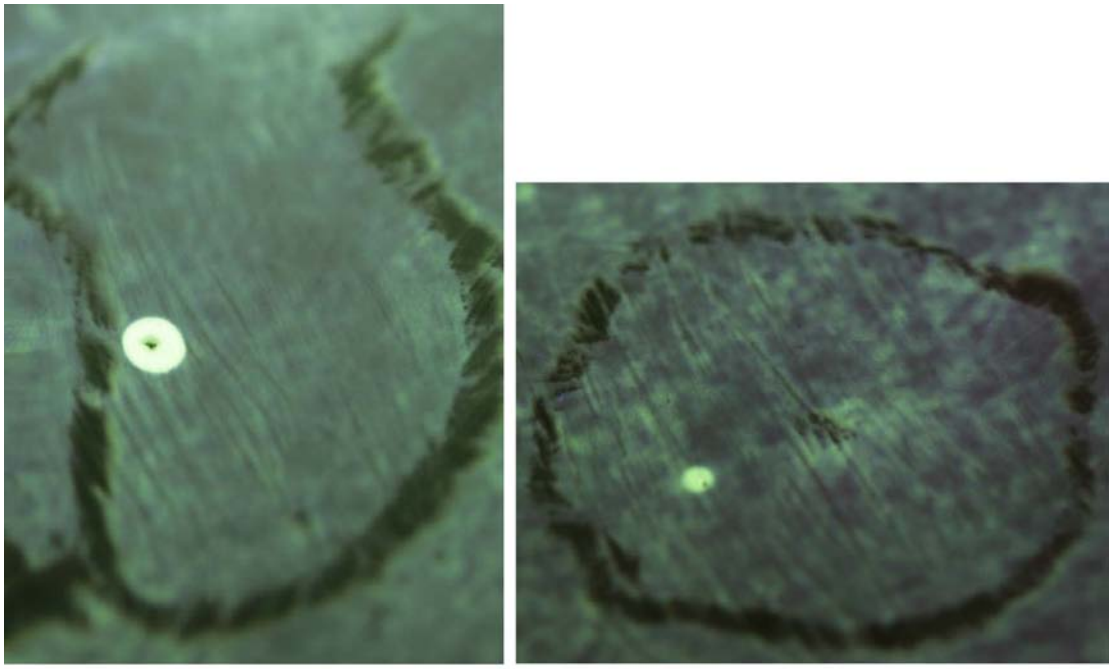

Figure 2.55 Penetrant Testing Results for Test Block 5.10

2.3.6 Test Blocks 5.11 and 5.12

No flaws were present in test blocks 5.11 or 5.12. These test blocks were included in the study to provide blank BMI specimens to help discern the false call rate for the inspectors.

2.3.7 Flaw Fabrication in Test Blocks 2.1–2.6 and 5.13–5.16

For the test blocks 2.1–2.6 and 5.13–5.16, the flaws were fabricated using laboratory-grown stress corrosion cracking (SCC). The geometry of the test blocks before preparing the SCC is shown in Figure 2.56. In the case of BMI test blocks, the penetration tubes were cut off before preparing the SCC, and the tubes were re-welded after preparing the SCC. Figure 2.57 shows the procedure for preparing laboratory SCC in a piping sample. Figure 2.58 and Figure 2.59 show typical examples of laboratory-induced SCC in the case of these BMI test blocks.

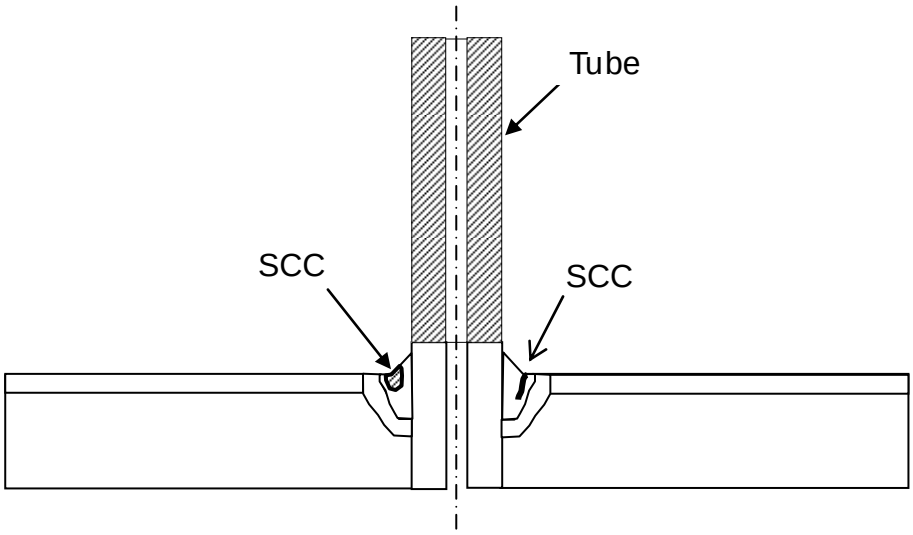

Figure 2.56 BMI Test Blocks for Preparing SCC

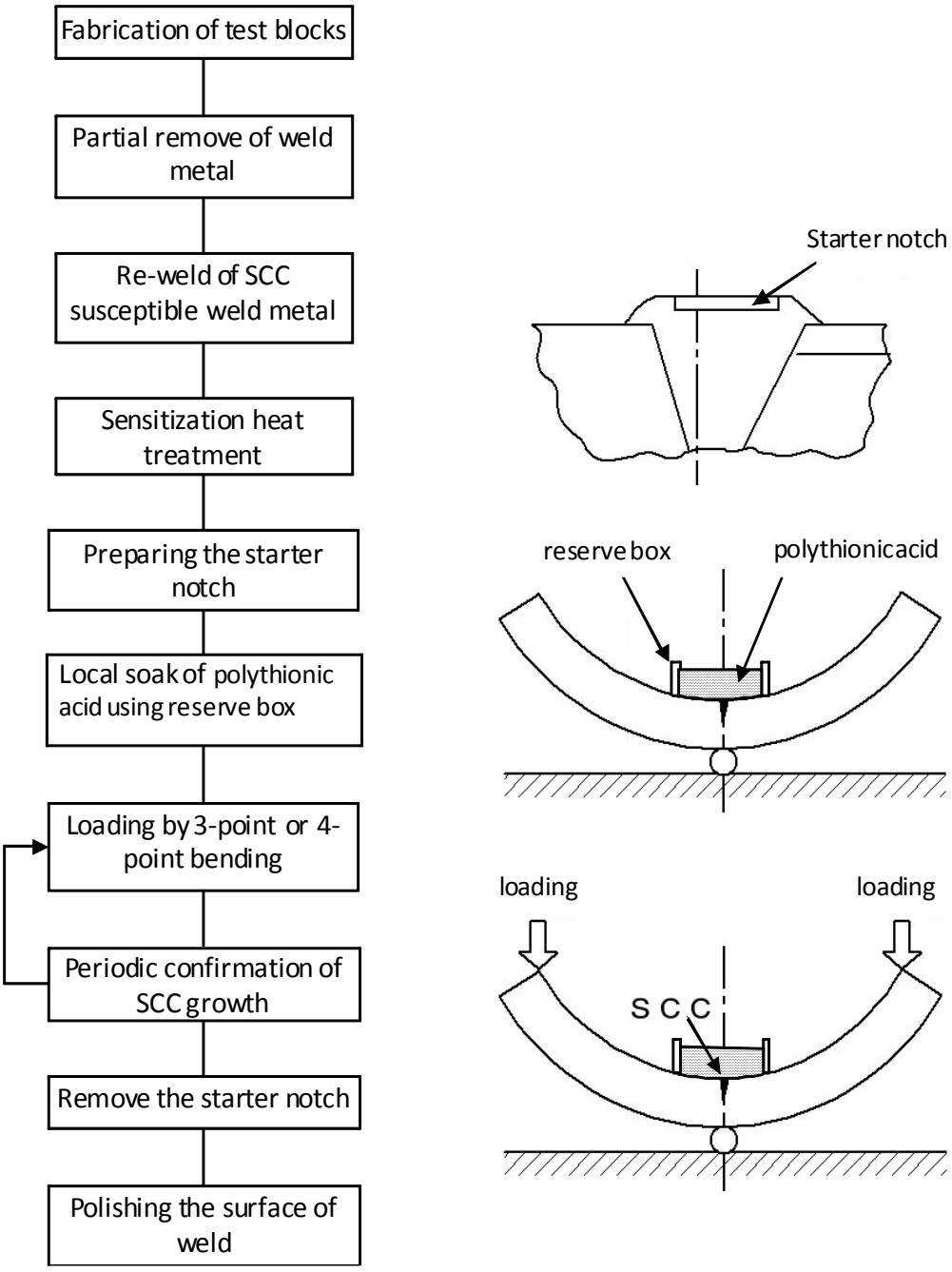

Figure 2.57 Procedure for Preparing Laboratory SCC in a Sample Piping Specimen

Figure 2.58 Example of Laboratory-Induced SCC in BMI Test Block (parallel to the weld)

Figure 2.59 Example of Laboratory-Induced SCC in BMI Test Block (perpendicular to the weld)

2.4 Description of True States for the Test Blocks

The flaws in each test block were documented during the construction of each block, and this documentation was used to provide the locations, lengths, and depths of each flaw. Test blocks 2.1–2.6, 5.2, and 5.13–5.16 were destructively examined to validate these parameters, and the true-state information reflects the destructive test results. Test block 5.10 received a limited destructive validation to determine the crack characteristics such as COD and depth. The destructive testing results for test blocks 2.1–2.6 are contained in Appendix A; the destructive results for test blocks 5.2, 5.10 and 5.13–5.16 are contained in Appendix B.

2.4.1 Description of the True State Used for Dissimilar Metal Weld Round-Robin Test Blocks

Drawings and photographs of the test blocks were provided to the participating teams of inspectors. Information on the actual test specimens is limited to drawings and schematics that were useful for inspection planning. Table 2.5 lists some of the important parameters of the round-robin test of mid-thickness (40–50 mm) dissimilar metal welds. Table 2.6 details how many of each sample were used in the study. It is important to note that test block 2.9 had two flaws that did not have appropriate documentation. These flaws, named F9.13 and F9.14, were left in the test block from a previous set of tests. As the exact position, depth, and sizes are not known, they are not used for POD or sizing regressions.

2.4.2 Description of the True State Used for Bottom-Mounted Instrumentation Round-Robin Test Blocks

The objectives of the round-robin test include simulating the NDE responses from PWSCC by selecting manufactured cracks with appropriate NDE responses. This includes both peak response and indication length. The degradation initiation sites associated with through-wall leaks from observed PWSCC show cracks as short as 4 mm. Therefore, fabricated cracks in the test blocks have a range of crack lengths, including some short cracks to simulate this condition. Some unexpected fabrication flaws were expected to be present in the test blocks, and PNNL fingerprinted the blocks, locating the cracks to separate them from the unexpected fabrication flaws. Inspection teams were instructed to expect fabrication flaws and a range of crack properties in the test blocks.

The test assemblies from Sweden, Japan, and the United States all have the cracks located in the J-groove weld or buttering. Three of the Korean assemblies have cracks in the penetration tubes and at the interface between the penetration tube and the J-groove weld. In one additional assembly provided by Korea, the location of the cracks is unknown. For sample 5.10, flaw 3 was identified as being smaller than was specified in the true state documentation, and was less than one millimeter in depth. Flaw 6 appeared to be mostly embedded, with a small section breaking the surface.

Table 2.7 and Table 2.8 show the test blocks and cracks used in the BMI study.

Table 2.5 Available Cracks in the PINC Mid-Thickness Dissimilar Metal Weld Test Blocks as Provided by JNES and SQC

Flaw Number	PINC Reference Number	X1	X2	Y1	Y2	Z1	Z2	Flaw Orientation	Depth, mm	Length, mm	Tilt
SHCC1	PINC 2.1	−17.0	10.5	0.6	3.1	41.2	46	C	5.8	21.0	0
SHCC2	PINC 2.2	−26.2	28.8	0.3	4.6	34.3	46	C	13.5	42.0	0
SHCC3	PINC 2.3	−53.7	59.5	0.3	4.2	30.0	46	C	17.8	86.5	0
STCC1	PINC 2.4	−1.7	−0.7	7.0	24.0	41.1	46	A	4.9	17.0	0
STCC2	PINC 2.5	−1.3	2.2	−7.0	31.0	33.7	46	A	13.3	38.0	0
STCC3	PINC 2.6	−7.3	2.6	−6.0	36.0	24.5	46	A	23.2	42.0	0
F9.1	PINC 2.9	57.3	95.6	−5.0	1.2	7.0	42	C	35.0	30.0	−10
F9.2	PINC 2.9	518.7	544.3	−4.0	−2.4	24.0	42	C	18.0	20.0	−5
F9.3	PINC 2.9	707.4	745.7	−13.2	−7.0	19.0	42	C	23.0	30.0	15
F9.4	PINC 2.9	875.8	898.8	−3.0	−1.4	33.0	42	C	9.0	18.0	−10
F9.5	PINC 2.9	990.3	1009.5	−3.1	−2.0	36.0	42	C	6.0	15.0	10
F9.6	PINC 2.9	1128.4	1154.0	−3.1	0.4	32.6	42	C	9.4	20.0	−20
F9.7	PINC 2.9	168.4	194.0	−18.7	−17.0	35.8	42	C	6.2	20.0	15
F9.8	PINC 2.9	360.4	386.0	−18.0	−16.3	35.8	42	C	6.2	20.0	−15
F9.9	PINC 2.9	613.1	638.6	−19.0	−15.0	36.0	42	C	6.0	20.0	10
F9.10	PINC 2.9	1054.3	1079.9	−18.0	−18.0	36.0	42	C	6.0	20.0	0
F9.11	PINC 2.9	791.6	814.6	−16.0	−16.0	30.0	42	C	12.0	18.0	0
F9.12	PINC 2.9	1199.2	1224.7	−14.0	−9.5	16.6	42	C	25.4	20.0	−10
F9.13*	PINC 2.9	417	435	0	24	NA	NA	NA	NA	NA	NA
F9.14*	PINC 2.9	293	317	−21	−11	NA	NA	NA	NA	NA	NA
F10.1	PINC 2.10	151.6	151.6	−20.0	0.0	22.0	42	A	20.0	20.0	0
F10.2	PINC 2.10	252.6	254.9	−20.0	0.0	32.0	42	A	10.0	20.0	10
F10.3	PINC 2.10	350.3	350.3	−12.0	0.0	36.0	42	A	6.0	12.0	0
F10.4	PINC 2.10	448.0	454.8	−20.0	0.0	12.0	42	A	30.0	20.0	10
F10.5	PINC 2.10	805.1	805.1	−16.0	−7.0	30.0	42	A	12.0	12.0	0
F10.6	PINC 2.10	902.1	906.1	−20.0	0.0	24.0	42	A	18.0	20.0	−10
F10.7	PINC 2.10	1003.8	1003.8	−20.0	0.0	17.0	42	A	25.0	20.0	0

C = circumferential, A = axial.

*Not used for POD or sizing (see page 2.39)

Table 2.6 Round-Robin Test Blocks for Mid-Thickness (40–50 mm) Dissimilar Metal Weld

Number of SSM test blocks	2
Number of JNES test blocks	6
Total length of weld to be inspected	4 meters

Table 2.7 Flaws Used for Surface Inspections in BMI Test Blocks

Test Block	Flaw	Θ1, °	Θ2, °	r1, mm	r2, mm	Z1, mm	Z2, mm	SB*	Orient
5.1	Surf5.1.5	268	304	20	23.6	1	10	no	Circ.
5.2	Surf5.2.3	148	155	19.3	27.3	0	14.1	yes	Axial
5.3	Surf5.3.3	130	160	19.1	27.7	0	8	yes	Circ.
5.3	Surf5.3.6	338	338	19.1	30	0	10	yes	Axial
5.6	Surf5.6.1	45	45	24	28	0	2	yes	Axial
5.6	Surf5.6.2	131	139	34	34	0	2	yes	Circ.
5.6	Surf5.6.3	225	225	55	60	0	2	yes	Axial
5.6	Surf5.6.4	310	320	58	58	0	5	yes	Circ.
5.6	Surf5.6.5	245	265	30	30	0	5	yes	Circ.
5.6	Surf5.6.6	180	180	35	41	0	1.5	yes	Axial
5.7	Surf5.7.1	162	168	42	42	0	2	yes	Circ.
5.7	Surf5.7.2	15	15	34	37	0	3	yes	Axial
5.7	Surf5.7.3	300	300	32	40	0	NA	Yes	Axial
5.8	No Flaw	NA	NA	NA	NA	NA	NA	NA	NA
5.9	Surf5.9.1	15	15	43	47	0	1	yes	Axial
5.9	Surf5.9.2	75	75	33	36	0	6	yes	Axial
5.9	Surf5.9.3	193	197	44	44	0	3	yes	Circ.
5.9	Surf5.9.4	345	345	45	49	0	7	yes	Axial
5.10	Surf5.10.1	39	51	33	33	0	9	yes	Circ.
5.10	Surf5.10.2	72	78	45	45	0	7	yes	Circ.
5.10	Surf5.10.3†	225	225	39	41	0	0.4	yes	Axial
5.10	Surf5.10.4	251	259	46	46	0	2	yes	Circ.
5.10	Surf5.10.5	285	285	36	40	0	2	yes	Axial
5.10	Surf5.10.6†	315	315	46	48	0	4.5	yes	Axial
5.11	No Flaw	NA	NA	NA	NA	NA	NA	NA	NA
5.12	No Flaw	NA	NA	NA	NA	NA	NA	NA	NA
5.13	Surf5.13.1	349	7.8	34.7	36.9	0	2.2	yes	Circ.
5.13	Surf5.13.2	175	188	33.3	36.1	0	2.4	yes	Circ.
5.14	Surf5.14.1	340.1	22.5	29.8	36.6	0	10.5	yes	Circ.
5.14	Surf5.14.2	166.9	194.8	29	31.4	0	2.1	yes	Circ.
5.15	Surf5.15.1	87.7	91.1	25.1	36.4	0	3.5	yes	Axial
5.15	Surf5.15.2	265.3	270.8	25	35.2	0	3.3	yes	Axial
5.16	Surf5.16.1	88.9	95.5	22.4	38.8	0	10.9	yes	Axial
5.16	Surf5.16.2	268.9	275.9	23.2	36.6	0	5.8	yes	Axial

*SB = surface-breaking, † Determined by destructive evaluation to be too small for use in scoring

Table 2.8 Flaws Used for Penetration Tube Inspections in BMI Test Blocks

Test Block	Flaw	Θ1, °	Θ2, °	r1, mm	r2, mm	Z1, mm	Z2, mm	SB	Orient
5.1	Tube5.1.1	8	44	19.1	21.7	299.1	306.4	no	Circ.
5.1	Tube5.1.2	68	112	10.3	19.1	304.8	304.8	no	Circ.
5.1	Tube5.1.3	202	202	7.5	12.2	310.7	338.6	yes	Axial
5.1	Tube5.1.4	209	245	15	19.1	309.1	315.7	no	Circ.
5.1	Tube5.1.5	268	304	19.8	23.6	303	303	no	Circ.
5.1	Tube5.1.6	303	339	14.7	19.1	299.9	299.9	no	Circ.
5.2	Tube5.2.1	15	70	17.4	23.7	294.1	307.9	no	Circ.
5.2	Tube5.2.2	90	93	18.6	21.1	305.2	352.7	no	Axial
5.2	Tube5.2.3	100	107	7.5	10.7	296	321.6	yes	Axial
5.2	Tube5.2.4	148	155	19.3	27.3	327.1	341.2	no	Axial
5.2	Tube5.2.5	220	290	7.5	19.1	304.5	317	yes	Circ.
5.2	Tube5.2.6	305	350	14.4	19.7	290.4	297.6	no	Circ.
5.3	Tube5.3.1	13	43	16.3	19.1	293.5	293.5	no	Circ.
5.3	Tube5.3.2	86	116	21.6	27.7	307.2	313.3	no	Circ.
5.3	Tube5.3.3	130	160	19.1	27.7	315.2	322.8	no	Circ.
5.3	Tube5.3.4	191	227	7.5	21.7	315.9	315.9	yes	Circ.
5.3	Tube5.3.5	269	313	19.1	29.6	300.2	310.4	no	Circ.
5.3	Tube5.3.6	338	338	19.1	29.9	293	303.8	no	Axial

*SB = surface-breaking

3.0 Techniques and Procedures Descriptions

The teams conducting the examinations used a wide mix of nondestructive techniques, ranging from standard methods such as conventional ultrasonic inspection to experimental techniques such as potential drop. Because there was a wide variety in techniques and the application of those techniques, comparing the effectiveness of the individual techniques would result in a very complex matrix. PNNL has divided the different techniques used in the DMW and BMI round-robin tests into two broad categories—ultrasonic and electromagnetic.

Within the ultrasonic category, the following methods were used:

- conventional ultrasound
- conventional phased array
- adaptive phased array
- time-of-flight diffraction (TOFD).

Within the electromagnetic category, the following methods were used:

- eddy current
- potential-drop methods, including both direct current (DC) and alternating current (AC) methods, and modified variations of these techniques.

3.1 Ultrasonic Techniques

Ultrasonic techniques use beams of high-frequency sound to interrogate the materials. Ultrasonic techniques are capable of inspecting a volume of material to determine the location, size, and depth of flaws. During inservice inspection (ISI) outages at nuclear power plants, ultrasonic methods are used in the examination of piping welds; hence, their use in the PINC DMW round robin. Most ultrasonic inspections of piping welds are performed from the outside of the pipe, looking for cracks initiating in the inner pipe surface. Some ultrasonic inspections are conducted from the inner diameter of a pipe, and from the wetted surface of J-groove welds and the inner diameter of penetration tubes.

3.1.1 Conventional Ultrasound

Conventional ultrasonic techniques use a transducer mounted on a wedge to produce an ultrasonic beam with a specific fixed angle in the material. Typical angles used for ultrasonic inspection of nuclear components include 30-, 45-, and 60-degree beams that use both longitudinal and shear wave modes of propagation. The ultrasonic transducers can be used to manually scan a test object, or the search unit may be designed to fit in a mechanized scanning fixture and the data collected electronically. A conventional ultrasonic transducer examining a specimen from the outer diameter (OD) is shown in Figure 3.1.

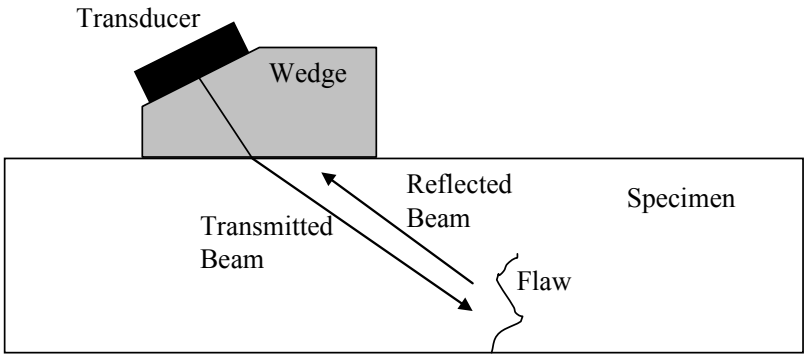

Figure 3.1 Conventional Ultrasonic Testing

Conventional ultrasound is one of the most common and time-tested techniques used to examine reactor components. Inspectors and regulating agencies have a great deal of experience with the capabilities and limitations of conventional ultrasound. The disadvantages of conventional ultrasonic techniques are that they can be time-consuming to apply because a detailed inspection may require many separate examinations using different angles and different frequencies.

3.1.2 Phased Array Ultrasound

Phased array ultrasound is a newer ultrasonic technique that is achieving greater acceptance for performing ISI at nuclear power plants. Unlike a conventional ultrasonic transducer, a phased array ultrasonic transducer consists of several individual elements. These elements are excited to transmit individually at specific time delays, allowing one transducer to emit a beam at many angles and focused at several depths. Phased array beam forming is shown schematically in Figure 3.2.

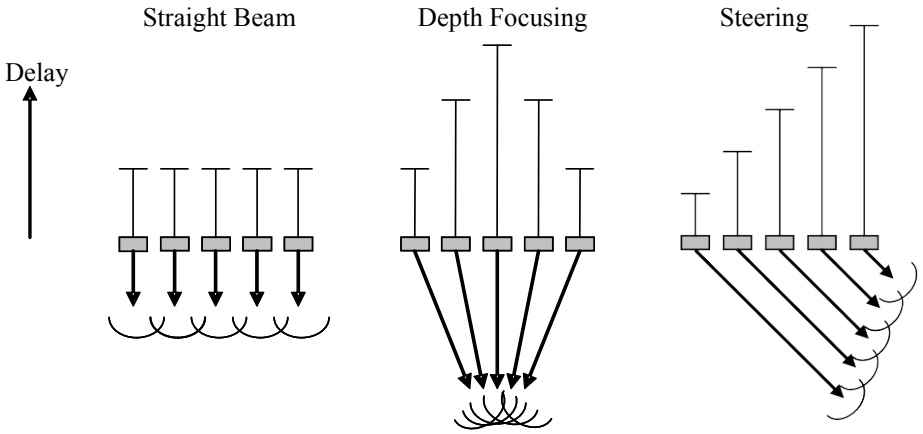

Figure 3.2 Use of Delays to Steer and Focus Ultrasonic Beams in Phased Array Transducers

Phased array ultrasound offers several advantages over conventional ultrasound because a single phased array transducer can be used to emit many angles almost simultaneously. This versatility allows the inspector to examine a sample much more quickly. Because phased array ultrasound requires sophisticated electronics to control the individual elements, it also provides electronic data-recording capabilities. The main disadvantages of phased array ultrasound are the increased expense of transducers and sophisticated electronics over conventional ultrasonic probes and the relative newness of, and lack of experience with, the technique. As with conventional ultrasound, phased array UT is normally used from the outer diameter of a pipe. Phased array ultrasound can be used from the wetted surface of a J-groove weld or the inner diameter of a penetration tube.

3.1.3 Adaptive Phased Array Ultrasound

Adaptive phased array ultrasound uses the versatility of phased array technology to allow for detailed inspections of samples with irregular surfaces. The system first measures the surface profile using an initial scan and then corrects the delay laws used to focus the beam through the irregular surface. The adaptive phased array technique offers the additional benefit of working on a variety of sample configurations, unlike conventional ultrasonic testing (UT) that would require a custom probe and/or wedge for each surface profile. Adaptive phased array UT testing is normally performed from the cracked surface.

3.1.4 Time-of-Flight Diffraction

Time-of-flight diffraction is a well-established ultrasonic technique that is very useful in crack detection and sizing. The TOFD technique uses two transducers that face each other to detect cracks in the material. When arranged properly, a surface lateral wave travels between the two transducers and a back-wall signal is produced by the beam bouncing off of the far side of the sample. If a surface-breaking flaw is present between the two transducers, it will interrupt either the lateral wave or the back-wall wave, and the tip of the flaw will produce a secondary signal, which is also detectable. The TOFD setup is a very powerful technique for detection and length and depth sizing of flaws. TOFD can be used from the ID or OD of a pipe or other component. A diagram of the TOFD technique is given in Figure 3.3.

TOFD has some disadvantages, however. The TOFD arrangement has a large footprint and is not useful for inspections that have limited access to a component. For TOFD to work properly, the transducers generally need to be on a level and relatively flat surface. The region of interest for most reactor inspections is at or near a weld; if the weld has not been machined flat, the weld crown and other geometrical features associated with welds may make TOFD unusable. Also, TOFD is less sensitive to flaws that are parallel to the plane of the transducers.

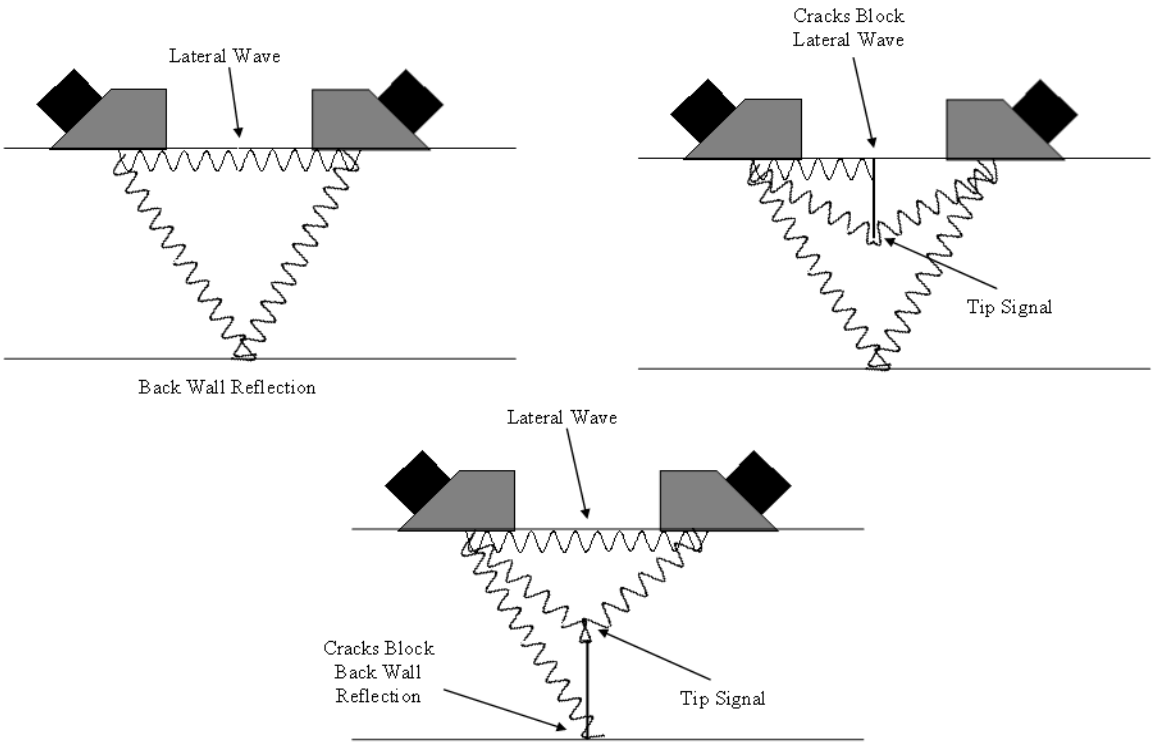

Figure 3.3 Time-of-Flight Diffraction Technique

3.2 Electromagnetic Techniques

Electromagnetic techniques detect flaws by inducing electromagnetic currents in the sample and measuring how the flaws affect the induced current. Electromagnetic techniques are often very useful at detecting surface-breaking flaws but are not typically used to depth-size flaws.

3.2.1 Eddy Current

Eddy current inspection uses a coil or coils held very close to a surface. An AC current is passed through the coil. The AC current creates a cyclical magnetic field around the coil. When this magnetic field intersects with a conducting material, such as steel or stainless steel, electrical currents are induced in the materials. These currents make their own magnetic fields, which interact with the magnetic field generated by the coil. The changes in resistance and inductive reactance in the coil allow one to measure the electrical properties of the material. Breaks in the surface, such as cracks, affect the eddy currents in the materials and can be measured using the eddy current system. An eddy current test setup is shown schematically in Figure 3.4.

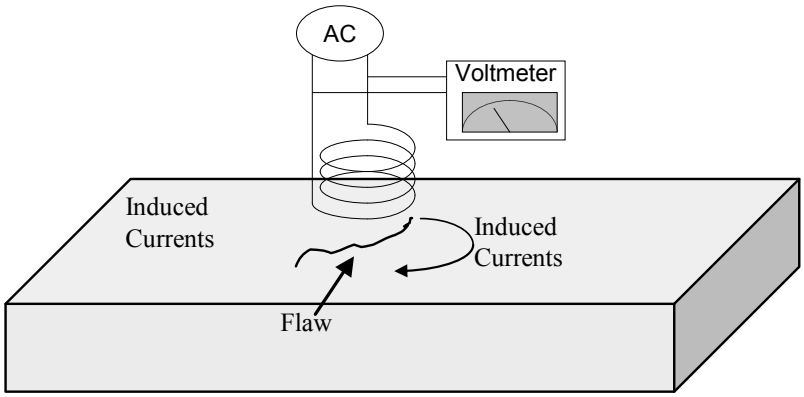

Figure 3.4 Eddy Current Diagram

Eddy current testing (ECT) is very effective at detecting surface-breaking flaws, but usually only from the same surface at which the flaw originates. For piping welds ID inspections are required. Using eddy current inspection for through-wall examinations is possible only with thin materials such as steam generator tubes and is not possible for most reactor piping. ECT is one of the most common techniques used to inspect samples where the possible cracked surface is accessible to inspectors. The main weakness of eddy current inspection is that it is a surface and near-surface examination only and cannot be performed through more than a few millimeters of metal. The technique is not capable of characterizing the through-wall size of cracks more than a few millimeters in depth.

3.2.2 Potential-Drop Techniques

Although there are several implementations of potential-drop techniques, they all function by passing a current (AC or DC, depending on the technique) through the specimen and use several probes to measure the electrically induced voltage of the material (see Figure 3.5). Flaws in the material affect the electrical voltage and current, and this effect can be measured. Some potential-drop measurements need to be made from the surface broken by the crack, but some implementations can be used through the entire thickness of a pipe. Potential-drop techniques are not commonly used in reactor inspections. The potential drop technique has many variations, some of which are used from the ID and some from either side of a pipe or component. The variations used in this round-robin test are as follows:

- alternating current potential-drop (ACPD) method
- direct current potential-drop (DCPD) method
- closely coupled probe potential-drop (CCPPD) method using direct current
- induced current potential-drop (ICPD) method using induction alternating current.

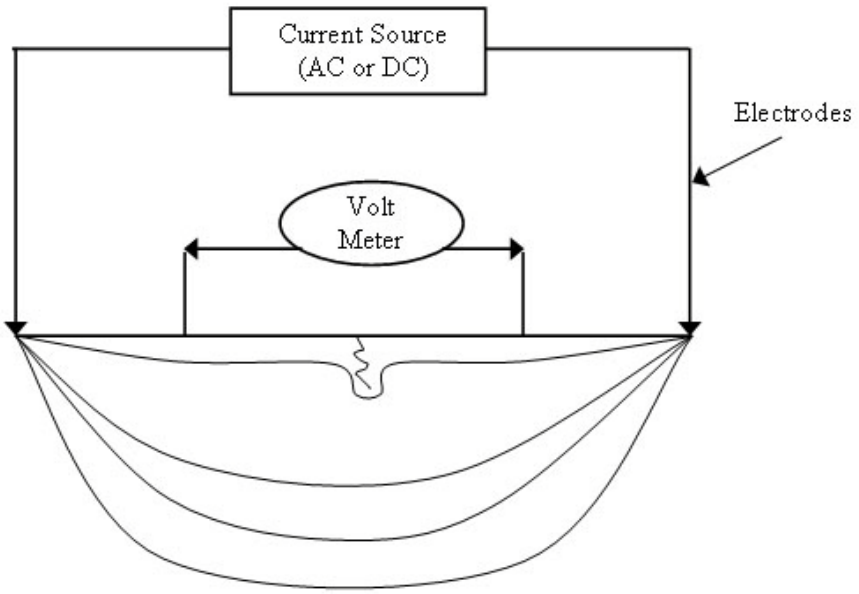

Figure 3.5 Four-Probe Potential-Drop Measurement

4.0 Analysis of Performance

After the teams had completed the round-robin testing, the data were collected, examined, and scored to determine the effectiveness of the various techniques. This section describes the scoring criteria used to analyze the data and the results. Section 4.1 describes the scoring procedures used in the round-robin tests. Section 4.2 contains the probability of detection results for the DMW and BMI examinations. Finally, Section 4.3 details the length- and depth-sizing results for the DMW and BMI round-robin tests.

4.1 Scoring Procedure Used for PINC Round Robins

This section describes how inspection results were compared to the true state of the DMW and BMI test blocks. Specifically, this section describes (1) the method used to determine whether or not an individual flaw was detected; (2) if the flaw was detected, what depth and length size should be assigned to it; (3) unintended defects (flaws that occurred during the test block fabrication process that were not intended to be part of the test block); and (4) the methodology used to determine false calls (i.e., indications not associated with any known flaw).

Scoring merges the inspection results with the true-state results by associating inspection indications with true-state flaws. The scoring procedure is summarized by the flowchart in Figure 4.1.

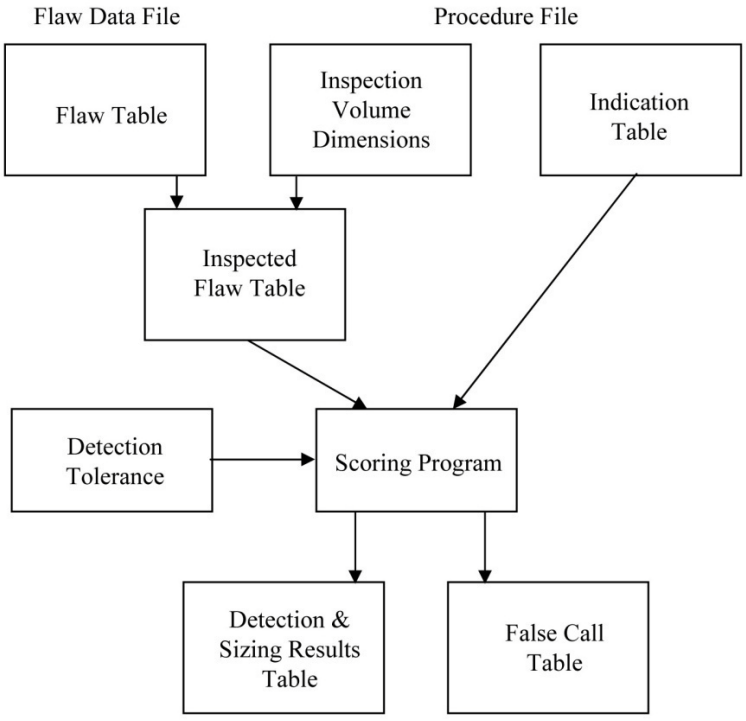

Figure 4.1 Scoring Procedure for PINC Round Robins

The first step of the scoring process consisted of uniquely identifying the flaws in the inspected volume of the weld. For this analysis, a table of flaws was developed for each test specimen. The *inspection volume* field indicated in the portable document format (PDF) file record for inspections was then compared with the flaw table for each specimen to determine which flaws fell within the inspected volume. These flaws are then placed in the *inspected flaw table*.

The next step of the scoring process compared the entries in the *inspected flaw table* to the entries in the *indication table* (the indications that were recorded on inspection data sheets) to determine which flaw cuboids intersected with which indication cuboids.

A tolerance box was defined around each flaw to account for possible location error. Figure 4.2 shows the probability of detection versus size of tolerance for the DMW round robin, and Figure 4.3 shows the same information for the BMI round-robin results. As can be seen in Figure 4.2 and Figure 4.3, there is not much improvement in detection for tolerances larger than 10 mm. The exception is for the tube examinations of the BMI samples, which have closely spaced flaws. Therefore, for the analysis used in this report, a tolerance box of 10 mm was used to score the DMW and BMI results. Without use of a tolerance box, location errors might be misclassified as non-detections. Once the tolerance is defined, ΔX, ΔY, and ΔZ, then the flaw cuboid, X1, X2; Y1, Y2; Z1, Z2, becomes

$$(X_1 - \delta X, X_2 + \delta X, Y_1 - \delta Y, Y_2 + \delta Y, Z_1 - \delta Z, Z_2 + \delta Z) \quad (4.1)$$

A list of all indications not intersecting with any flaws was compiled and was termed the *false call table*. The *false call table* was compiled after the intersecting flaw–indication cuboids had been identified for each indication.

The scoring process therefore resulted in two outputs—the detection of flaws, including the length and through-wall depth determined for each flaw, and a list of false calls.

Finally, detection and sizing information were appended to all flaws in the *inspected flaw table*, using the intersection information, to produce the *detection and sizing results* table.

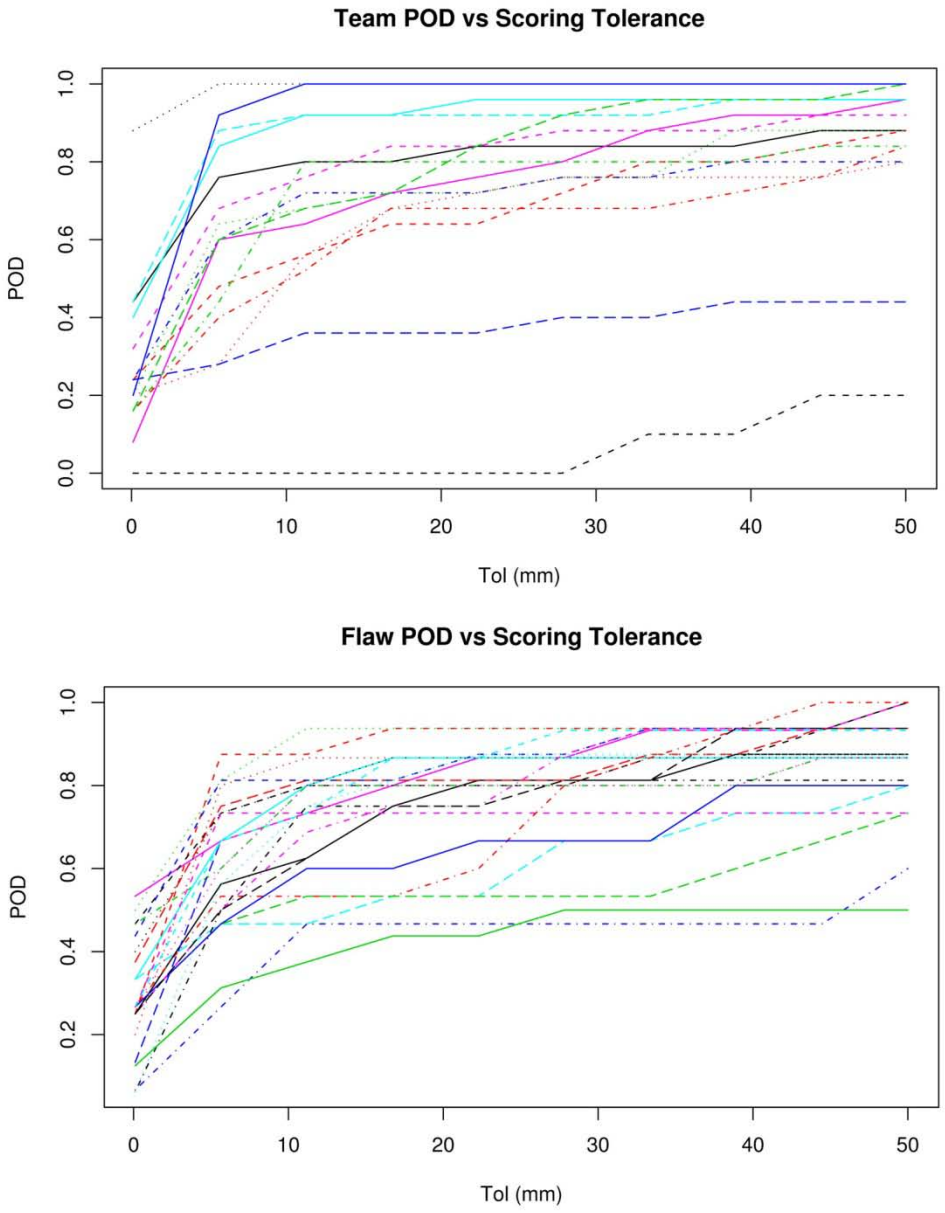

Figure 4.2 Probability of Detection versus Scoring Tolerance for Teams and Flaws for DMW Round Robin

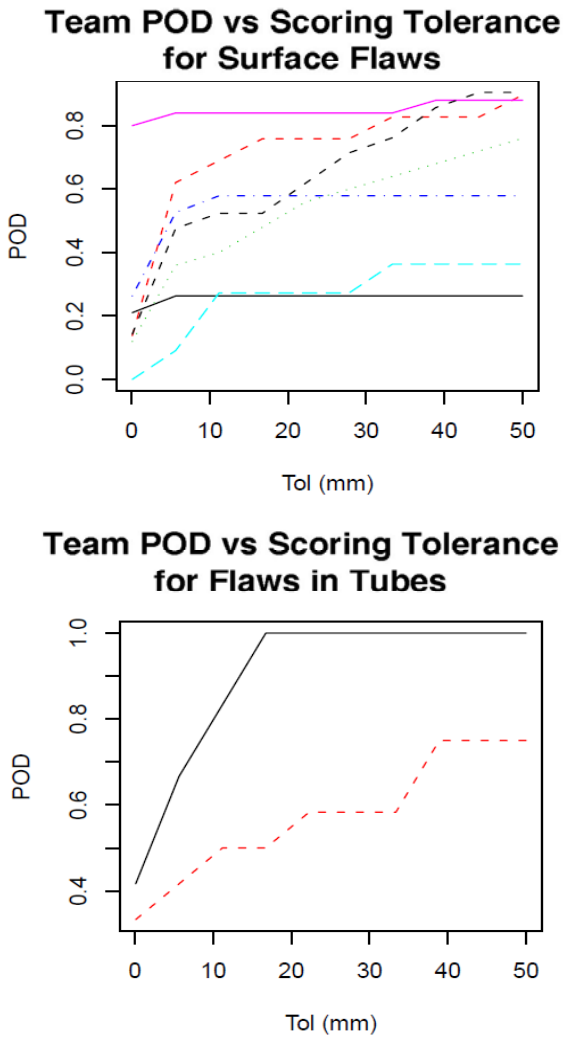

Figure 4.3 Probability of Detection versus Scoring Tolerance for All Teams and Flaws in BMI Round Robin

4.1.1 Definitions of False Call Probability and Probability of Detection

False call probability (FCP) and probability of detection quantify inspection performance on blank (un-flawed) versus flawed material. The FCP is the probability that an inspector will call a flaw in a blank unit of material, while POD is the probability that an inspector will call a flaw in a flawed unit of material. With these definitions, (FCP, POD) measure the capability for inspection to correctly classify units of material as unflawed or flawed. Another equivalent term for FCP is false positive probability while POD is equivalent to 1 minus false negative probability.

POD is frequently expressed as a function of various flaw, material, or inspection variables that might affect detection performance. For example, in PINC, POD is considered to be a function of flaw size, so the expression POD(S) is used to represent the probability of calling a detection in a unit of material than contains a flaw of size S.

One would expect POD(S) to be a monotonically increasing function of flaw size S. Also, one should note that using the false call probability as the POD for a flaw of size zero (POD(0) = FCP) follows from the definition of FCP and POD. When the S = 0 point is included on the POD curve, this curve provides the most basic description of inspection efficacy. An inspection that is no more effective than guessing will have a flat POD curve. More specifically, if the POD for flaws of size S is equal to FCP, (POD(S) = FCP) then flaws of this size aren't really being detected by the inspection procedure.

To be able to calculate FCP and POD, one has to define the applicable unit of material. We call this unit of material the grading unit; In other words, each grading unit in the round robin study will generate a detection statistic when inspected. For inspection of dissimilar metal weldments, the ideal grading unit would be an entire weld, but a round robin test that used whole weldments as the experimental unit would be too costly. Due to cost constraints, the grading unit used is the length of a flaw plus an allowance for sizing error.

To produce unbiased estimates of FCP and POD, the blank and flawed grading units must be identical in all important respects (except that the flawed grading units contain a flaw). Also, if multiple grading units are to be placed in a single weldment, they must be separated from each other by a sufficient distance. These constraints caused problems in defining blank grading units in the PINC specimens. Since reasonable blank grading units could not be defined, we constructed a probability model (described in the next section), to estimate FCP from available PINC false call statistics.

4.1.2 Calculation of FCP

In the PINC inspections, a false call is defined as a call that does not intersect with a flawed grading unit. These false calls were used to estimate a false call rate, λ_{fc} (false calls per meter)

$$\lambda_{fc} = \frac{\#\text{False Calls}}{\text{Length of Material Inspected}} \tag{4.2}$$

Using this rate and the assumption that false calls are randomly (i.e., Poisson) distributed one can then calculate the probability that a call would intersect a blank grading unit of length L_{gu}. Assuming that the average length of a false call is L_{fc}, the probability of a false call intersecting the grading unit is

$$\text{FCP} = \Pr(\text{Grading Unit Intersection}) = 1 - \exp(-\lambda_{fc}(L_{gu} + L_{fc})) \tag{4.3}$$

4.1.3 Logistic Regression model for POD

In PINC, a logistic regression model was used to relate POD to flaw size, S. Flaw size represents either depth or length. The logistic regression model is given by

$$\text{POD}(S) = \text{logistic}(\beta 1 + \beta 2 S) \tag{4.4}$$

where $\beta = (\beta 1, \beta 2)$ are unknown parameters to be determined by the regression algorithm and the function, logistic(x) is defined as

$$\text{logistic}(x) = \frac{1}{1+\exp(-x)} \tag{4.5}$$

Estimates produced by the algorithm are maximum-likelihood estimates. The regression fits included data for flaw size zero (i.e., the FCP estimates described in the last section). In the regression fit plots, you will sometimes see a data point at S = 0 and that represents false call data.

4.1.4 Scoring Example for Single Flaws

For all inspections of the DMW test blocks and the inspections of the weld surface of the BMI test blocks, the scoring was performed using a 10-mm scoring box. This section presents the scoring results for a single inspection, so the reader can more easily understand the scoring process. The example used is an inspection of test block 2.9.

This test block was selected because it contains each type of scoring situation, including missed flaws, false calls, and hits on poorly documented flaws. The team has inspected the entire block (and this is the case for almost all inspections in the round robin), so all flaws in the block should be included in the scoring procedure. The indications called by the inspection team (using their labeling system) are summarized in Table 4.1.

Table 4.1 Test Block PINC 2.9 Inspection Results

Indication ID	X1, mm	X2, mm	Y1, mm	Y2, mm	Z1, mm	Z2, mm	X max, mm	Y max, mm	Z max, mm
1	51	86	−7	−7	16	43	75	1	51
1a	66	108	19	19	35	43	81	2	66
2	163	190	−19	−19	37	43	176	3	163
3	271	304	−18	−18	31	43	298	4	271
4	375	439	14	14	28	43	412	5	375
5	496	527	−1	−1	28	43	513	6	496
6	686	732	−9	−9	27	43	708	7	686
7	787	807	−18	−18	37	43	798	8	787
8	860	880	−5	−5	37	43	870	9	860
9	972	999	−4	−4	36	43	979	10	972
10	1047	1067	−18	−18	38	43	1058	11	1047
11	1105	1125	−4	−4	35	43	1111	12	1105
12	1173	1201	−6	−6	20	43	1180	13	1173

The scoring result is summarized visually by Figure 4.4. Figure 4.4 shows the results in the X, Y plane, the plane most relevant to our scoring definition. The locations of the indications called by the inspection team are shown as black rectangles in Figure 4.4. The test block

contains 12 flaws used for scoring (shown in red) and 2 poorly documented flaws that were not intentionally placed in the test block for the PINC studies but still are detectable (shown in blue). When the intersections between the called indications and the actual flaw locations are compared, one can determine how well the team performed.

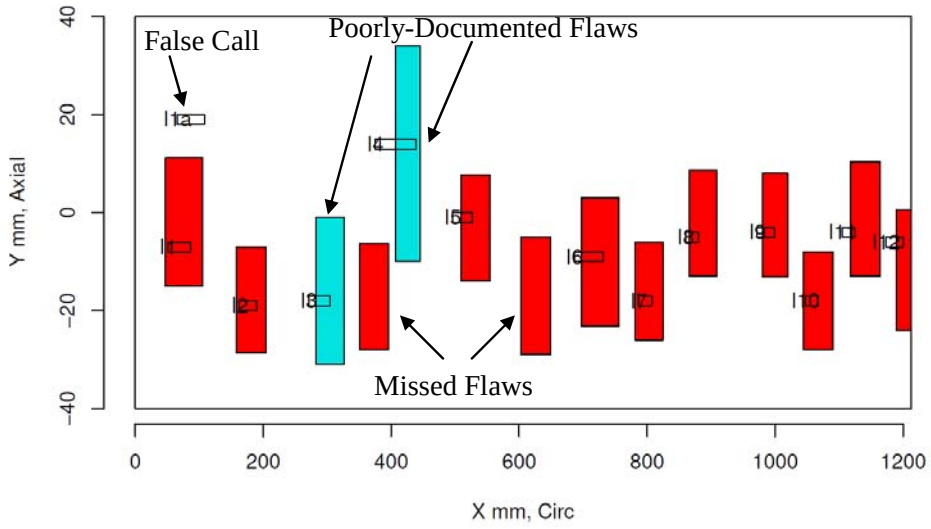

Figure 4.4 Scoring Inspection Results of Test Block 2.9 with 10-mm Tolerance

The scored results are presented in Table 4.2 (detection results). In Table 4.2, each row describes a flaw in the block. From Table 4.2, we see that Flaws 9.8 and 9.9 were not detected, while flaws 9.1–9.7 and 9.10–9.14 were detected and are scored as hits, and the supplied lengths and depths were used to evaluate the length and depth sizing capabilities of the technique. Both of the poorly documented flaws were detected but are not used for depth or length sizing. Missing the poorly documented flaws would not have been counted against the inspection because the exact locations of the poorly documented flaws are not known.

The team conducting the examination successfully detected ten of the flaws used for scoring and both poorly documented flaws. Additionally, the team missed two flaws and made one false call. Appendix C of this report provides the scoring results of all teams that participated in the PINC DMW round-robin tests using this style of plots of indications versus flaw location.

Table 4.2 Detection Results for Sample Inspection of PINC Test Block 2.9

Flaw No.	Detection 0 = no 1 = yes	X1, mm °	X2, mm °	Indication ID from Data Sheet of Team 67
F9.1	1	57.3	95.6	1
F9.2	1	518.7	544.3	5
F9.3	1	707.4	745.7	6
F9.4	1	875.8	898.8	8
F9.5	1	990.3	1010	9
F9.6	1	1128	1154	11
F9.7	1	168.4	194	2
F9.8	0	360.4	386	NA
F9.9	0	613.1	638.6	NA
F9.10	1	1054	1080	10
F9.11	1	791.6	814.6	7
F9.12	1	1199	1225	12
F9.13*	1	293	317	4
F9.14*	1	417	435	3

NA = Not applicable.
*Not used for POD or sizing (see page 2.39).

4.1.5 Scoring Process for Multiple Closely Spaced Cracks

As the Data Analysis Task Group (DAG) reviewed the data from the PINC round-robin exercise, members of the DAG recognized that the test blocks used in the BMI did not contain a single crack; rather, the test blocks contained multiple cracks. In fact, many cracks in the test blocks used for the PINC BMI were close together. The DAG decided to analyze the PINC BMI data using a set of proximity rules that would account for the multiple flaws in the test blocks.

The DAG used the American Society of Mechanical Engineers (ASME) Section XI IWA-3400 rules for linear surface flaws to account for the multiple flaws that were close together. The scoring process was the same as that described in Section 4.1.1.

Section XI, IWA-3400 of the ASME Code states the following:

> *(a)* Linear flaws detected by surface (PT/MT) or volumetric (RT) examination methods shall be considered single linear surface flaws provided the separation distance between flaws is equal to or less than the dimension *S*, where *S* is determined as shown in Figure IWA-3400-1.
> *(b)* The overall length of a single and discontinuous linear flaw shall be determined as shown in Figure IWA-3400-1.

Figure 4.5 is a reproduction of IWA-3400-1 to show the methodology used to determine whether multiple flaws in a PINC BMI test block should be combined as one flaw with length or whether the flaws should be considered as single individual flaws.

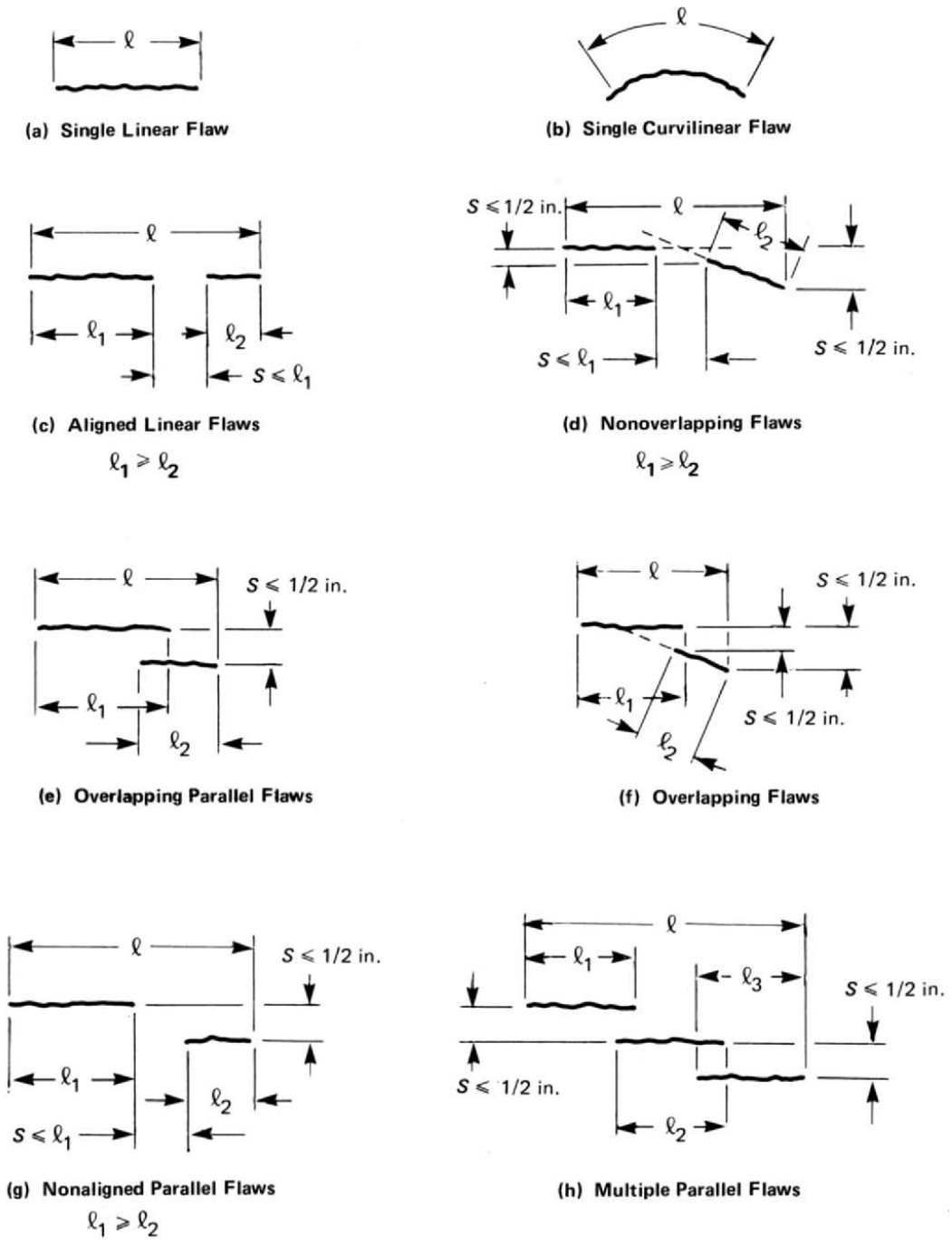

Figure 4.5 Methodology for Determining Singularity or Multiplicity of Linear Surface Flaws. Reprinted from ASME 2007 BPVC Section XI, Figure IWA-3400-1, by permission of The American Society of Mechanical Engineers. All rights reserved.

Once the rules of IWA-3400 were applied to the test blocks, the scoring process described under Section 4.1.1 was used on the test blocks.

One can see from Figure 4.6 that test block 5.1 has six individual flaws that are very close in proximity. Figure 4.7 shows that using the rules of IWA-3400, the six individual flaws in test block 5.1 could be considered as two.

This procedure was not carried out for Sample 5.2, based on the destructive evaluation results.

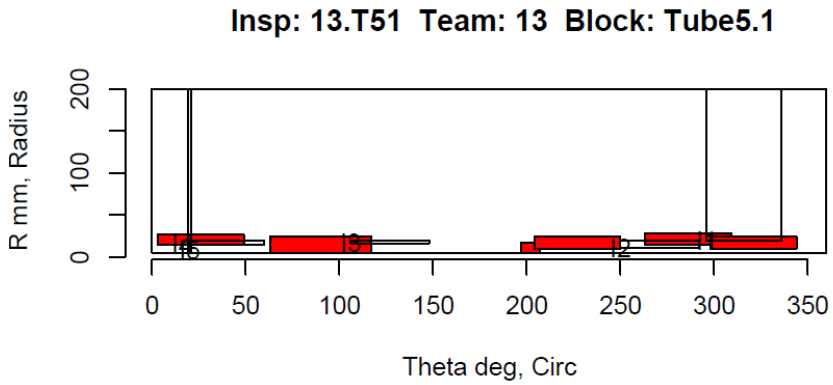

Figure 4.6 Test Block 5.1 –Individual Flaws

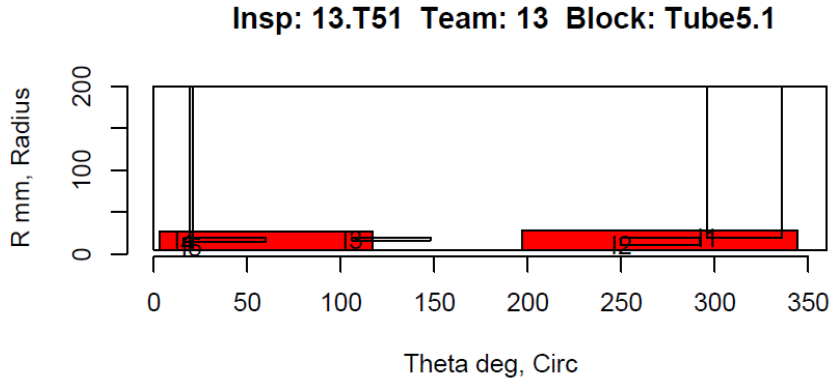

Figure 4.7 Test Block 5.1 – Individual Flaws Combined Under Rules of IWA-3400

4.2 Evaluation of Detection Capability for the PINC Round Robin

4.2.1 Probability of Detection Results for the PINC DMW Round Robin

The goal of the PINC is to determine which techniques are the most effective and to try to understand the physical basis for the high performance of the most effective inspection techniques. To allow for a statistical analysis of the techniques, the data were organized and grouped by team, technique, and flaw orientation.

As stated in Section 4.1, a tolerance of 10 mm was used to analyze the data in the round-robin tests. The 10-mm tolerance was chosen based upon the observation that, when reviewing Figure 4.2, many of the team tolerance curves seemed to approach an asymptote at roughly 10 mm. The 10-mm value should also be roughly equal in magnitude to the position measurement error of the inspection procedures. For simple cylindrical blocks such as PINC 2.1-2.6, this tolerance is probably greater than the measurement error. But for PINC test blocks 2.9 and 2.10, which are nozzles with a non-constant outer radius, a 10-mm tolerance may correctly describe procedure measurement error.

Tables 4.3 and 4.4 summarize the POD when using a 10-mm tolerance. In Table 4.3, note that two teams (70 and 96) detected all flaws, while one team (43) missed all of the flaws. Table 4.3 also indicates if the inspection procedure and teams performing the inspections have formal nondestructive testing qualifications. The definition of "formal qualifications" for the teams and procedures was left up to the individual invigilators, and is meant to discriminate between NDE professionals and NDE researchers with little or no practical NDE experience. The exact qualifications and/or certifications for each team cannot be given without violating the confidentiality of the inspections. Possible qualifications or certifications for each inspection procedure and personnel include but are not limited to:

Procedures:

- Qualifications given by the Czech Republic
- Japan Electric Association JEAC 4207-2008 : Ultrasonic Examination for Inservice Inspection of Light Water Cooled Nuclear Power Plant Components
- ASME Code Section XI Appendix VIII

Personnel:

- Japanese Industrial Standard (JIS) Z 2305:2001, which is consistent with ISO 9712:1999
- ASNT TC-1A and CP189
- ASME Code Section XI Appendix VIII

Also listed is the data collection method used by the inspectors. The three possibilities are "Manual," "Automated," and "Manual+Encoded." A manual exam is one where the inspector uses their own hands to move the probe and records the position of the probes using rulers or other scales. An automated inspection is one where an electronic scanner is used to move the probes and record their positions using encoders. A "Manual+Encoded" scan is one where the probe is moved by hand, possibly in a track or with the aid of a manual scanner, and the positional data is recorded using encoders.

The "No. of Observations" column in Table 4.3 describes the number of flaws inspected by each team. Notice all flaws were inspected by each team except teams 43 and 16. Also listed is the data collection method. Figure 4.8 shows the POD and false call rates for the techniques. The procedures and teams with formal qualifications are identified. Table 4.4 describes the POD for each flaw. The flaws in test blocks 2.2 and 2.3 had the highest POD of 87%. The lowest POD seems to be associated with axial flaws; flaw F10.3 was most difficult to detect with a POD of 37%.

Finally, Table 4.5 summarizes the false calls experienced in each of the blocks. The false call rate is determined by dividing the number of false calls by the total length of blank material. For example, for PINC test block 2.1 has a total of 2.985 meters of blank material (in 16 inspections); thus, the number of false calls divided by 2.985 meters of blank material equals 3.015 false calls per meter. The false call rate varies from 0.6 false call per meter to 4 false calls per meter. A rate of about 2 false calls per meter is an approximation for this round robin.

Appendix D of this report contains plots that show the location of indications (*hits*) and the location of actual flaws. In Appendix D, false calls and detections from the scoring are summarized by "*hitograms"*. The hitogram plots show indication intensity in each block, with the top plot describing false calls and the bottom, detections. The false call hitogram can be used to identify hot spots in the blocks—spots that may contain an unidentified or unintended flaw or reflector. An examination of the false call plots in Appendix D should convince the reader that no hot spots existed in the blocks, except possibly for one in PINC 2.9 at X = 400, Y = 10.

Table 4.3 DMW POD by Teams with 10-mm Tolerance in DMW Test Blocks

Team	No. of Observations	POD	False Calls per Meter of Weld Inspected	Qualified Team	Qualified Procedure	Data Collection
13	27	0.815	0.577	X	X	Automated
16	2	1.000	0.000			Manual
22	27	0.556	4.838		X	Automated
28	27	0.704	2.561	X	X	Automated
30	27	0.667	0.573	X	X	Manual
38	27	0.889	3.699			Manual+Encoded
39	27	0.630	2.277		X	Automated
43	10	0.000	3.08			Manual+Encoded
48	27	0.556	1.446	X	X	Manual
63	27	0.815	0.598		X	Automated
65	27	0.333	5.182			Manual
66	27	0.889	1.423	X		Manual+Encoded
67	27	0.741	0.569			Manual
70	27	1.000	0.437	X		Manual+Encoded
72	27	0.519	3.965	X	X	Automated
82	27	0.741	2.277		X	Automated
96	27	1.000	0.569	X	X	Automated

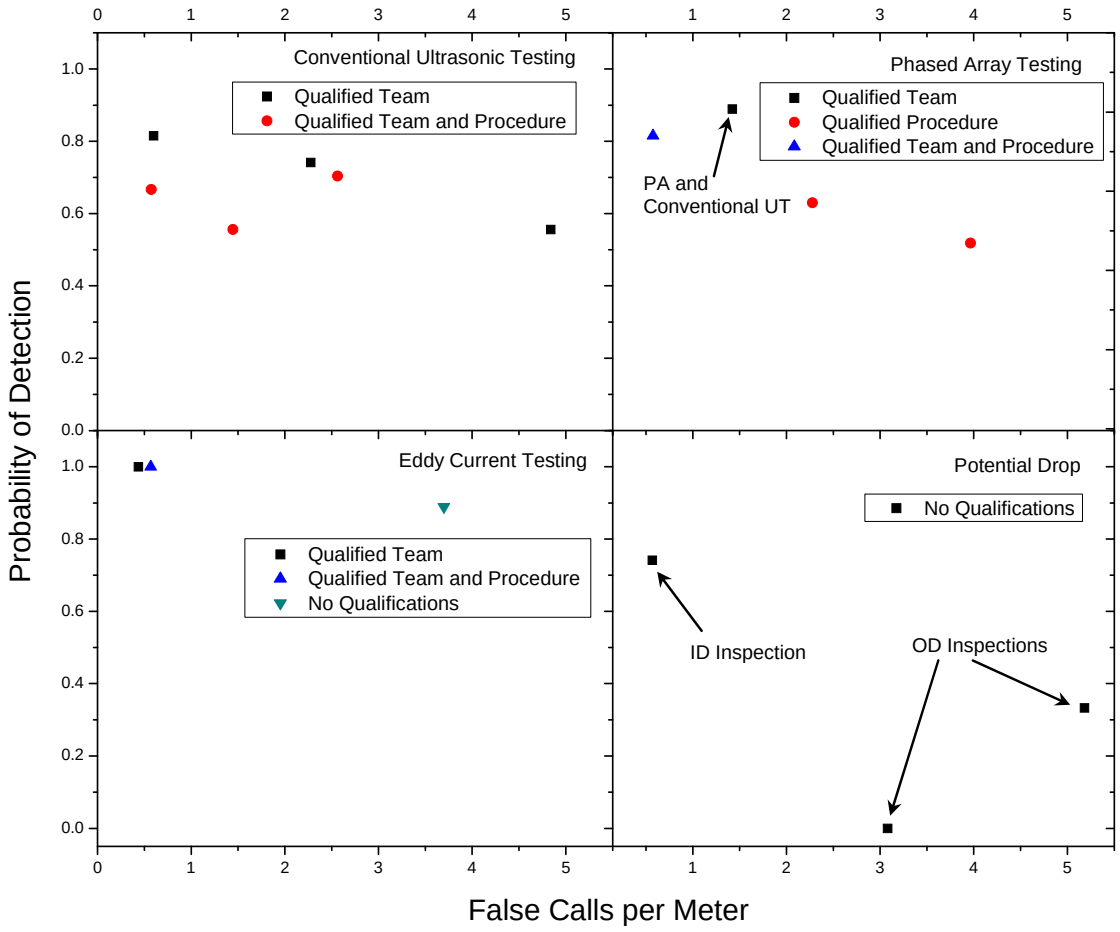

Figure 4.8 DMW Probability of Detection and False Call Rates in DMW Test Blocks for the Inspection Techniques Showing Qualifications

Table 4.4 Probability of Detection by Flaws in DMW Test Blocks

Flaw	No. of Observations	POD	Type	Depth, mm	Length, mm
PINC 2.1.SHCCl	16	0.625	C	5.8	21.0
PINC 2.2.SHCC2	16	0.875	C	13.5	42.0
PINC 2.3.SHCC3	16	0.875	C	17.8	86.5
PINC 2.4.STCC1	15	0.400	A	4.9	17.0
PINC 2.5.STCC2	15	0.467	A	13.3	38.0
PINC 2.6.STCC3	15	0.733	A	23.5	42.0
PINC 2.9.F9.1	15	0.800	C	35.0	30.0
PINC 2.9.F9.2	15	0.800	C	18.0	20.0
PINC 2.9.F9.3	15	0.800	C	23.0	30.0
PINC 2.9.F9.4	15	0.800	C	9.0	18.0
PINC 2.9.F9.5	15	0.800	C	6.0	15.0
PINC 2.9.F9.6	15	0.733	C	9.4	20.0
PINC 2.9.F9.7	15	0.800	C	6.2	20.0
PINC 2.9.F9.8	15	0.533	C	6.2	20.0
PINC 2.9.F9.9	15	0.467	C	6.0	20.0
PINC 2.9.F9.10	15	0.600	C	6.0	20.0
PINC 2.9.F9.11	15	0.733	C	12.0	18.0
PINC 2.9.F9.12	15	0.800	C	25.4	20.0
PINC 2.10.F10.1	16	0.750	A	20.0	20.0
PINC 2.10.F10.2	16	0.750	A	10.0	20.0
PINC 2.10.F10.3	16	0.375	A	6.0	12.0
PINC 2.10.F10.4	16	0.812	A	30.0	20.0
PINC 2.10.F10.5	16	0.812	A	12.0	12.0
PINC 2.10.F10.6	16	0.688	A	18.0	20.0
PINC 2.10.F10.7	16	0.625	A	25.0	20.0

C = circumferential; A = axial

Table 4.5 Summary of False Calls in DMW Test Blocks

	No. of Flaws	No. of Inspections	Block Length, meters	Blank Length, meters	No. of Flaw Calls	False Calls per Meter	FCP*
PINC 2.1	1	16	0.240	2.985	9	3.105	0.26
PINC 2.2	1	16	0.240	2.555	5	1.957	0.18
PINC 2.3	1	15	0.240	1.614	1	0.620	0.06
PINC 2.4	1	15	0.408	5.180	11	2.123	0.19
PINC 2.5	1	15	0.408	5.311	11	2.071	0.19
PINC 2.6	1	15	0.408	5.215	9	1.726	0.16
PINC 2.9	12 (14)	16	1.213	11.574	46	3.974	0.33
PINC 2.10	7	16	1.213	18.069	40	2.214	0.20

*FCP = false call probability

A very important variable for crack detection is the depth of the crack. Deep cracks present more surface area for ultrasonic reflection, disrupt electrical flow more than shallow cracks, and are easier to detect in the presence of geometrical features. Because crack depth is very important in all aspects of crack detection, all POD results for the DMW examinations are given in terms of crack depth.

Another important variable in any round-robin test is the skill level of the team performing the test. Often, even when test blocks, techniques, and other variables are identical, some teams will do significantly better than others based on skill level. Section 4.2.1.1 scores each individual team, with their accuracy counted against crack depth.

The results are scored by technique in Section 4.2.1.2. The techniques are broken into four groups—eddy current testing, phased array ultrasonic testing, conventional ultrasonic testing, and potential-drop testing. The PODs for each technique are scored against the depth of the cracks.

The crack orientation is an important consideration in crack detection. The ability of some techniques to detect cracks is sensitive to crack orientation, and the pipe geometry affects the application of some techniques. Section 4.2.1.3 examines the effects of crack orientation on the flaw PODs based on technique.

Finally, Section 4.2.1.4 describes the probability of detecting small flaws and the relationship between POD for small flaws and service experience in the United States.

4.2.1.1 Probability of Detection Curves for Teams

Although the inspection technique and flaw characteristics are very important in flaw detection, the skill of the operator often is at least as important as the equipment used in the examination. The POD results sorted by team are shown in Table 4.6. Additionally, the teams are grouped by detection technique to allow for an easy comparison of team performance within the different techniques in Table 4.7 and Table 4.8. The probability of detection is given for 5-mm-deep flaws, 10-mm-deep flaws, and 15-mm-deep flaws, along with the false call probability (FCP) and data collection method. The POD data are plotted versus depth in Figure 4.9, with the FCP given as the zero value. When more than one detection technique is identified for detection (as with team 66), these techniques were used in tandem. It is worth noting that most teams used the same techniques for detection and sizing. The exceptions are teams 82 and 96, which used TOFD for depth sizing on flaws found using conventional UT (82) or eddy current (96).

Team variability was notable in the phased array examinations, with teams 13 and 66 outperforming teams 39 and 72. Team 63 did much better than the other teams using conventional UT. All eddy current teams had a high POD, but team 38 had a high false call probability. Notice that teams 70 and 96 performed nearly identically, with a POD close to 1.0 for small flaws.

When examining manual vs. automatic data collection for conventional UT, it appears that automated data collection has an advantage over manual data collection. More data is needed before team variability can be ruled out.

Table 4.6 Individual Team PODs Listed versus DMW Flaw Depth Sorted by Team Number

Team	POD for Flaw Depth: 5 mm	10 mm	15 mm	False Call Probability	Detection Technique	Data Collection
13	0.37	0.83	0.98	0.07	Phased Array UT	Automated
22	0.52	0.52	0.53	0.51	Conventional UT	Automated
28	0.42	0.6	0.76	0.26	Conventional UT	Automated
30	0.24	0.43	0.65	0.11	Conventional UT	Manual
38	0.78	0.96	0.99	0.36	Eddy Current	Manual+Encoded
39	0.36	0.47	0.59	0.26	Phased Array UT	Automated
43	0	0	0	0.31	Potential Drop	Manual+Encoded
48	0.24	0.42	0.61	0.13	Conventional UT	Manual
63	0.37	0.79	0.96	0.08	Conventional UT	Automated
65	0.3	0.32	0.33	0.28	Potential Drop	Manual
66	0.62	0.94	0.99	0.14	Phased Array+Conventional UT	Manual+Encoded
67	0.32	0.45	0.6	0.2	Potential Drop	Manual
70	1	1	1	0.04	Eddy Current	Manual+Encoded
72	0.41	0.47	0.54	0.35	Phased Array UT	Automated
82	0.44	0.53	0.61	0.35	Conventional UT	Automated
96	1	1	1	0.06	Eddy Current	Automated

Table 4.7 Individual Team PODs Listed versus DMW Flaw Depth Sorted by ID Technique

Team	POD for Flaw Depth: 5 mm	10 mm	15 mm	False Call Probability	Detection Technique	Data Collection
38	0.78	0.96	0.99	0.36	Eddy Current	Manual+Encoded
70	1	1	1	0.04	Eddy Current	Manual+Encoded
96	1	1	1	0.06	Eddy Current	Automated
67	0.32	0.45	0.6	0.2	Potential Drop	Manual

Table 4.8 Individual Team PODs Listed versus DMW Flaw Depth Sorted by OD Technique

Team	POD for Flaw Depth: 5 mm	10 mm	15 mm	False Call Probability	Detection Technique	Data Collection
22	0.52	0.52	0.53	0.51	Conventional UT	Automated
28	0.42	0.6	0.76	0.26	Conventional UT	Automated
30	0.24	0.43	0.65	0.11	Conventional UT	Manual
48	0.24	0.42	0.61	0.13	Conventional UT	Manual
63	0.37	0.79	0.96	0.08	Conventional UT	Automated
82	0.44	0.53	0.61	0.35	Conventional UT	Automated
66	0.62	0.94	0.99	0.14	Phased Array + Conventional UT	Manual+Encoded
13	0.37	0.83	0.98	0.07	Phased Array UT	Automated
39	0.36	0.47	0.59	0.26	Phased Array UT	Automated
72	0.41	0.47	0.54	0.35	Phased Array UT	Automated
43	0	0	0	0.31	Potential Drop	Manual
65	0.3	0.32	0.33	0.28	Potential Drop	Manual

4.2.1.2 Probability of Detection Results for Procedures

While there was variation between teams for each technique, the examination technique had a large impact on the probability of detection. Eddy current was the highest performing technique, detecting almost all of the flaws and making few false calls. Conventional ultrasound and phased array UT appeared to be an effective combination, but only one team used this technique, so team variability may be a factor. Using either conventional ultrasound or phased array UT alone gave similar results. Potential-drop techniques had the lowest performance, with the possible exception of team 67. It should be noted that eddy current tests were performed from the ID of the test blocks while the UT techniques were applied from the outside surface of the test blocks. The results for inspection procedures are presented in Table 4.9.

Table 4.9 Probability of Detection Summary for Procedures in DMW Test Blocks

Procedure	POD for Flaw Depths of			False Call Probability	ID/OD
	5 mm	10 mm	15 mm		
Eddy Current	0.88	1.00	1.00	0.17	ID
Conventional UT and Phased Array UT	0.62	0.94	0.99	0.14	OD
Conventional UT	0.36	0.51	0.67	0.23	OD
Phased Array UT	0.36	0.51	0.66	0.24	OD
Conventional UT and TOFD	0.44	0.53	0.61	0.35	OD
Potential Drop	0.29	0.33	0.38	0.25	Both

Figure 4.10 shows these POD values and regressions based on the inspection results. The values are plotted against sample sizes. Each POD curve is surrounded by a 95% confidence bound.

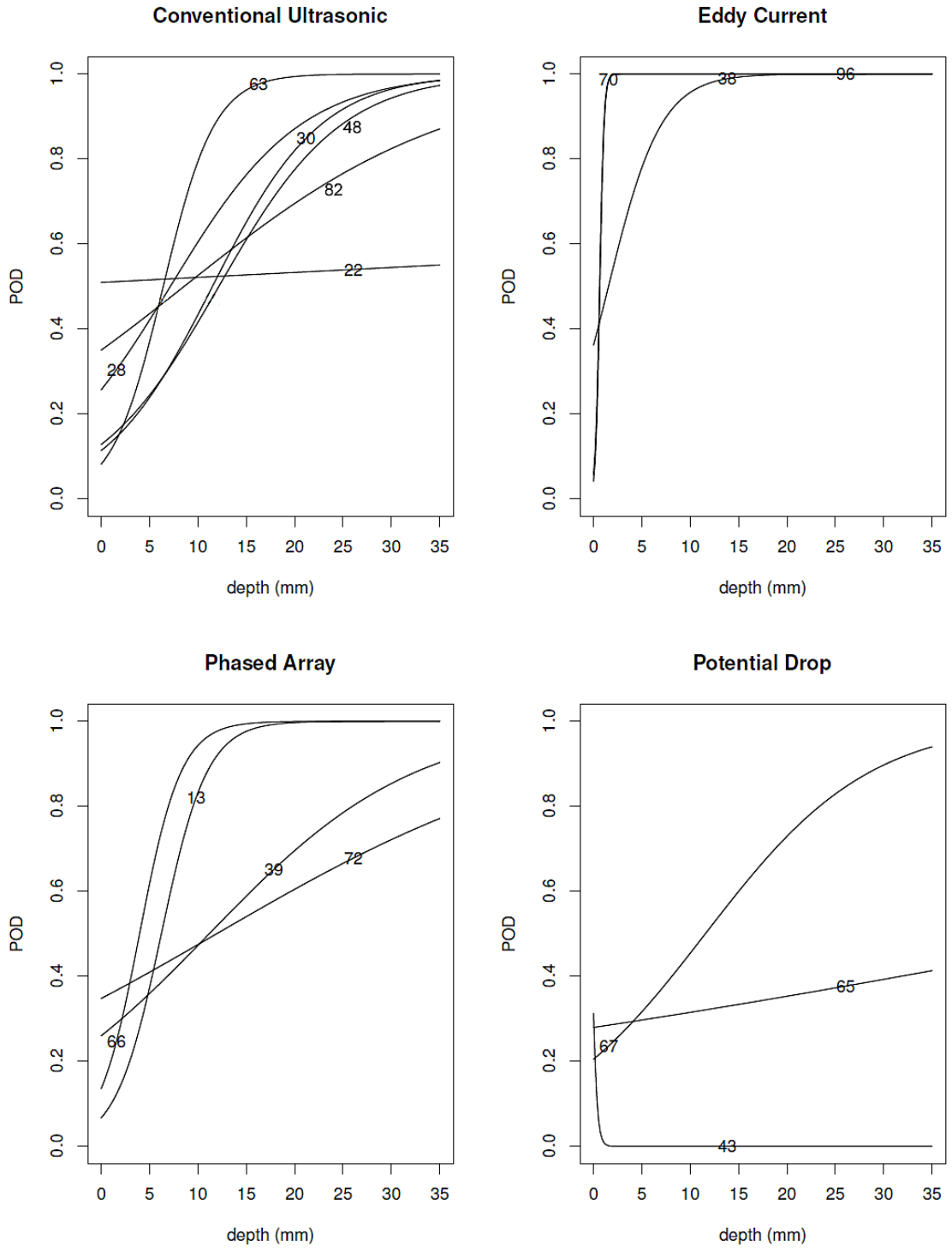

Figure 4.9 Probability of Detection Plotted versus the Crack Depth in DMW Test Blocks

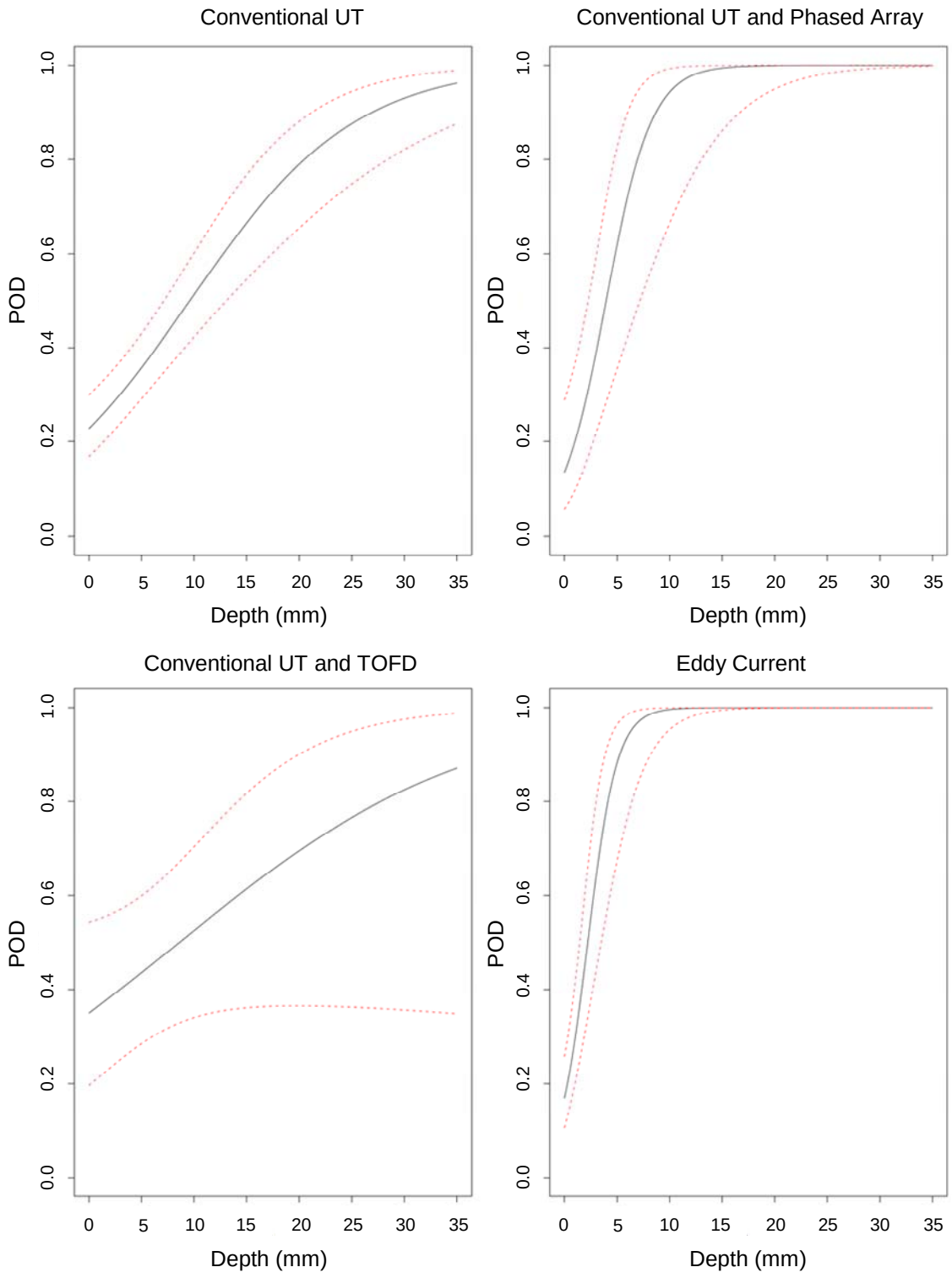

Figure 4.10 Probability of Detection Curves for Detection Procedures in DMW Test Blocks

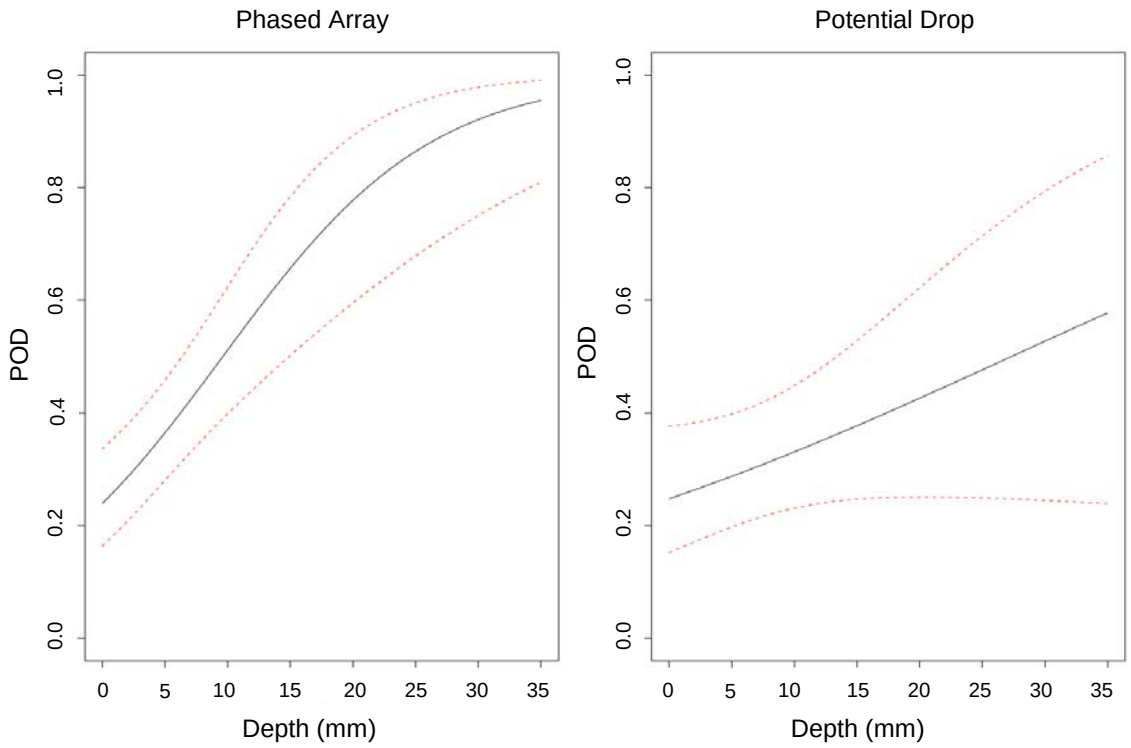

Figure 4.10 (continued)

4.2.1.3 Effects of Flaw Orientation on Dissimilar Metal Weld Detection Probability

As some techniques are more easily applied along the length of a pipe as opposed to around a pipe, it is important to examine the POD of flaws based on their orientation. The POD results are shown in Table 4.10 and Table 4.11. As flaw orientation might be expected to affect each procedure differently, POD curves for ultrasonic and electromagnetic procedures were computed separately. The results are plotted in Figure 4.11.

Table 4.10 Probability of Detection for Circumferential Flaws as a Function of Depth in DMW Test Blocks

Procedure	POD for Flaw Depths of			False Call Probability
	5 mm	10 mm	15 mm	
Eddy Current	0.92	1.00	1.00	0.17
Ultrasound	0.41	0.61	0.61	0.23
Potential Drop	0.28	0.35	0.43	0.23

Table 4.11 Probability of Detection for Axial Flaws as a Function of Depth in DMW Test Blocks

Procedure	POD for Flaw Depths of			False Call Probability
	5 mm	10 mm	15 mm	
Eddy Current	0.80	0.99	1.00	0.17
Ultrasound	0.32	0.45	0.59	0.21
Potential Drop	0.24	0.27	0.32	0.20

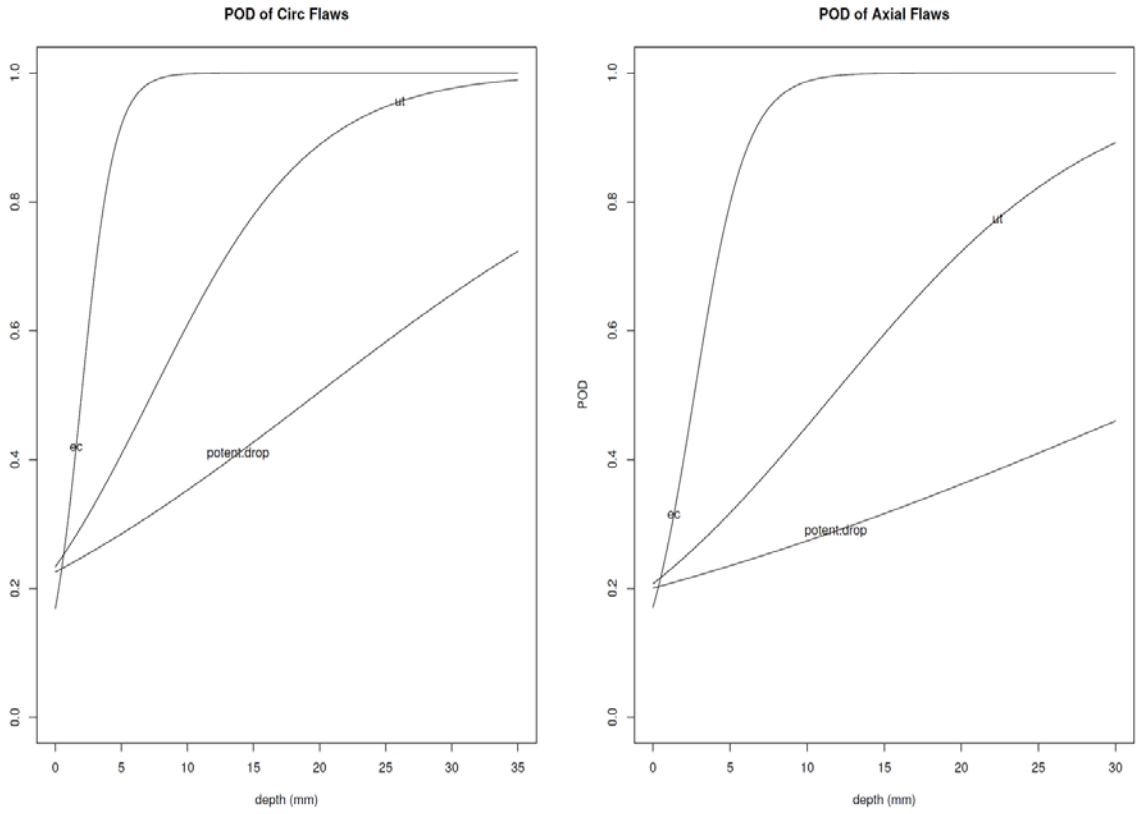

Figure 4.11 Probability of Detection Curves for Flaw Orientation in DMW Test Blocks

The results show that circumferential flaws in these blocks were somewhat easier to detect than axial flaws using ultrasound, especially for cracks close to 10 mm deep. Eddy current was largely unaffected but does show an 11% greater chance of seeing a 5-mm-deep circumferential flaw than a 5-mm-deep axial flaw. Circumferential flaws were somewhat more detectable with the potential-drop technique as well.

4.2.1.4 Probability of Detection for Small Flaws and Service Experience

As shown in Table 4.9, the probability of detection results for small flaws, flaws that are 4 to 5 mm (approximately 10% through-wall) are as follows:

- Eddy current examinations have a detection rate of 88%.
- The Team that used both conventional UT and phased array UT had a 62% chance of finding a 5-mm-deep crack.
- Teams that used conventional UT and TOFD had a 44% chance of detecting a 5-mm-deep crack.
- Teams that used conventional UT or phased array UT techniques demonstrated a 37% detection rate for 5-mm-deep cracks.
- Potential-drop techniques exhibited a 29% chance of finding 5-mm-deep cracks.

With the exception of eddy current inspection techniques that are typically used for examination of vessel nozzles using the vessel inspection tool, the detection performance for small flaws was low. Because PWSCC is a very aggressive degradation mechanism that has demonstrated very fast crack growth rates, it is not surprising that service experience has shown that PWSCC either has usually grown through-wall or has been detected after cracks are greater than 20% through-wall.

4.2.2 Probability of Detection Results for the BMI Round Robin

The flaws in the BMI test blocks were evaluated by eight teams using several techniques. The goal of the PINC BMI round robin was to determine which techniques are the most effective and to understand the physical basis for the techniques' performance. No two teams used identical techniques, although some groupings can be made.

There are several approaches to evaluating the abilities of the different teams to detect the fabricated cracks in the test blocks. The data analysis is complicated by two factors—not all teams examined the same test block set, and some of the test blocks had flaws that proved to be more challenging to find than was expected. The average POD, as shown in Table 4.12 for each test block, shows that test blocks 5.9 and 5.10 were the most challenging. The other test blocks have roughly the same POD of close to 0.8. Test blocks 5.1–5.3 are difficult to interpret because there were too few observations and the error was too large to allow one to draw conclusions on their difficulty. The results for each team and each sample are given in Appendix E. A hitogram showing the numbers of hits and misses and the false call densities for each sample is given in Appendix F.

Test blocks 5.6, 5.7, and 5.13–5.16 can be considered "baseline" difficulty, while test blocks 5.9 and 5.10 can be considered "challenging." It should be noted that test blocks 5.9 and 5.10 were designed to mimic difficult-to-detect indications found in the North Anna 2 Nozzle 31 J-groove weld. During subsequent destructive evaluation these indications could were not confirmed as being caused by PWSCC. The flaw manufacturer for test blocks 5.9 and 5.10 used a process to make the flaws more challenging to detect. All teams inspected the challenging test blocks, 5.9 and 5.10, and the different teams also examined different numbers of the baseline test blocks.

To determine which teams are the most affected by the varying proportion of challenging to baseline test blocks, the number of baseline and challenging flaw observations was tallied and is shown in Table 4.13.

Table 4.12 Probability of Detection for Each Test Block in BMI Test Blocks

Test Block	POD	Observations
5.1	0.50	2
5.2	0.50	2
5.3	0.25	4
5.6	0.75	24
5.7	0.81	21
5.9	0.18	28
5.10	0.18	28
5.13	0.70	10
5.14	0.90	10
5.15	0.70	10
5.16	0.90	10

Table 4.13 Number of Baseline and Challenging Flaw Observations for Each Team in BMI Test Blocks

	Flaw Difficulty		
Team	Baseline Flaw Observations	Challenging Flaw Observations	% Baseline Observations
16	11	8	0.58
373	21	8	0.72
38	17	8	0.68
66	11	8	0.58
67	3	8	0.27
70	17	8	0.68
99	13	8	0.62

Most teams appear to have a ratio of 50–60% of baseline flaws. Team 67 faced a more challenging test than the others and this was noted in the data analysis.

4.2.2.1 Probability of Detection Curves for Teams Using a Strict Tolerance Box

The round-robin data were analyzed using a statistical regression to determine the POD for each technique. An upper and lower 95% confidence boundary was calculated using the POD and the number of flaw observations at each flaw size. It is worth noting that the effect of the challenging test blocks is somewhat mitigated in these regressions because all but two of the flaws in the challenging test blocks are less than 5 mm in length. All regressions include the results for both baseline and challenging flaws. The regressions allow one to draw conclusions about the usefulness of the different techniques for finding flaws of various lengths.

4.2.2.2 Probability of Detection for BMI Tube Examinations

The interiors of the penetration tubes were examined by two teams, 13 and 70. Many of the flaws in test blocks 5.1–5.3 were very close to one another, resulting in some flaws being considered one flaw by ASME Code proximity rules. The results for Team 70 (provided in Appendix E) show some calls made on calibration notches in the penetration tubes. These calls on the calibration notches were not considered hits, as the notches are not representative of flaws that would be encountered in the field. The calls on the calibration notches were not counted as false calls because the notches were present in the penetration tubes. Team 70 used a surface technique and is only scored using surface breaking flaws, and thus has fewer observations than Team 13. The results of the tube examinations are presented in Table 4.14.

Table 4.14 Probability of Detection Scores for Tube Examinations in BMI Test Blocks

Team	Detection Technique	Observations	POD	False Calls per Test Block	Qualified Team	Data Collection
13	ECT and TOFD	17	0.53	1.7		Automatic
70	ECT	4	0.5	0.67	X	Automatic

Given the low number of observations, it is challenging to draw meaningful results from the examinations. Team 13 achieved a higher POD than Team 70, but with more false calls. An examination of the data shows that the teams made calls that grouped multiple flaws together, which is understandable given the tight flaw spacing. When the tube examinations are scored using ASME Code proximity rules, the POD results improve. The POD results for the combined flaws are given in Table 4.15.

Table 4.15 Probability of Detection Scores for Tube Examinations for Flaws Combined Using ASME Rules in BMI Test Blocks

Team	Detection Technique	Observations	POD	False Calls per Test Block	Qualified Team	Data Collection
13	ECT and TOFD	12	0.83	1.7		Automatic
70	ECT	4	0.5	0.67	X	Automatic

For the tube examinations, the results show low PODs with an insufficient number of observations to draw strong conclusions. Some of the flaws are detectable, but a more extensive test would need to be performed to quantify the effectiveness of the ECT and TOFD techniques. The regressions for the tube interiors are given in Figure 4.12.

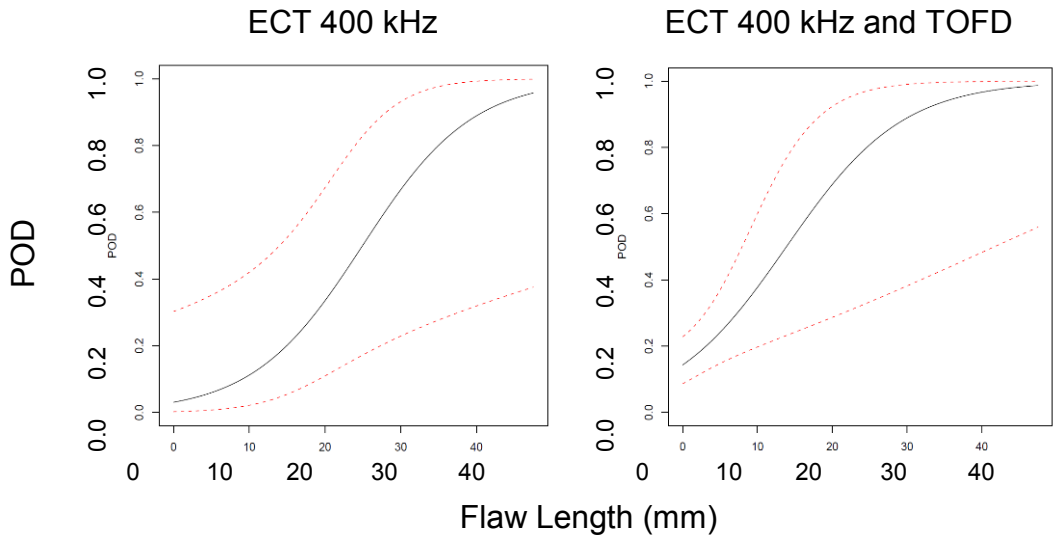

Figure 4.12 Probability of Detection Regression for Examinations of the Penetration Tube Interiors in BMI Test Blocks

4.2.2.3 Probability of Detection for BMI Weld Surface Examinations

The data were analyzed by comparing the true-state information with fixed scoring boxes determined as described in Section 5. This scoring method yields the following results for each team and is given in Table 4.16.

Table 4.16 Probability of Detection and False Call Rates for Each Team Using a 10-mm Tolerance Box in BMI Test Blocks

Team	Detection Technique	Observations	POD	False Calls per Sample	Qualified Team	Data Collection
16	CCPPD	19	0.26	0.00		Manual
373	ECT 300 kHz	29	0.72	0.15		Automatic
38	Array ECT 100 kHz	25	0.4	4.80		Manual
66	Adaptive Phased Array UT	19	0.58	0.00	X	Automatic
67	ICPD	11	0.27	0.67		Automatic
70	ECT 400 kHz	25	0.84	0.00	X	Automatic
99	Array ECT 200 kHz	21	0.43	2.50		Automatic

The straight POD scores correlate very closely with the percentage of baseline flaws examined by each team. When the POD results are analyzed with the baseline and challenging flaws separated out, a trend becomes clear. Teams 66, 70, and 373 were very effective at finding the baseline flaws, with PODs at or near 100%. Teams 16 and 38 showed improved performance on the baseline flaws, but were still below 50%. Teams 67 and 99 showed greatly improved performance on the baseline samples. For the challenging samples, no team performed

strongly. The highest scoring team was Team 70, which achieved a POD of 0.40. Teams 16, 38, 66, and 99 were unable to detect the challenging flaws. The baseline and challenging flaw PODs are given in Table 4.17.

Table 4.17 Probability of Detection Results in BMI Test Blocks for Baseline and Challenging Flaws with Upper and Lower 95% Confidence Levels (CL)

	Baseline	Challenging
Team	POD	POD
16	0.45	0.00
373	0.85	0.38
38	0.59	0.00
66	1.00	0.00
67	0.67	0.13
70	1.00	0.50
99	0.69	0.00

The examinations showed some clear high-performing techniques and techniques that need to be developed further before they are useful for reliably finding flaws in BMIs. The POD regression results for each technique for selected flaw lengths (including borderline and challenging flaws) are given in Table 4.18.

Cross-coil probe eddy current at 300–400 kHz proved to be very effective at finding the flaws in the test blocks. The high-frequency eddy current was also able to find a small fraction of the challenging flaws as well. The 400-kHz eddy current outperformed the 300-kHz eddy current in both the baseline and in the challenging flaws, and the 400-kHz examinations had a lower false call rate. The POD regressions for the two cross-coil eddy-current inspections are shown in Figure 4.13.

Table 4.18 Probability of Detection Regression Results for 5-, 10-, and 15-mm Flaws in BMI Test Blocks

	Detection	POD for Flaw Lengths of:			
Team	Technique	5	10	15	FCP
16	CCPPD	0.04	0.21	0.59	0.01
373	ECT 300 kHz	0.31	0.83	0.98	0.03
38	Array ECT 100 kHz	0.44	0.55	0.65	0.34
66	Adaptive Phased Array UT	0.21	0.96	1.00	0.00
67	ICPD	0.25	0.79	0.98	0.03
70	ECT 400 kHz	0.80	1.00	1.00	0.01
99	Array ECT 200 kHz	0.37	0.58	0.76	0.21

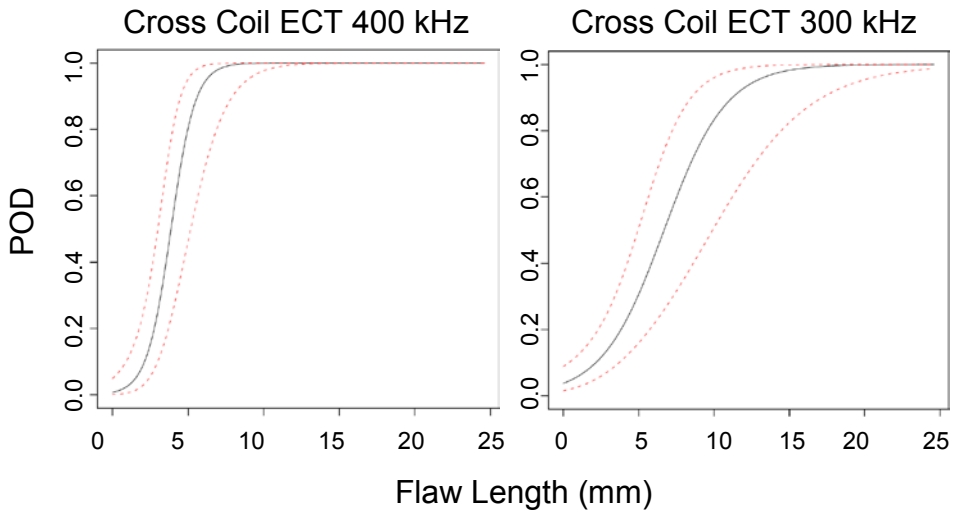

Figure 4.13 Probability of Detection Regressions for Cross-Coil Eddy-Current Techniques with 95% Confidence Intervals in BMI Test Blocks

The results for the array eddy-current techniques were relatively poor compared to the cross-coil probe eddy current, and both array eddy current examinations had a very high false call rate. The array eddy current used lower frequencies than the cross-coil probes, which may have contributed to the poor performance. The POD regressions are shown in Figure 4.14.

The POD regressions for the potential-drop techniques show that they are able to detect longer flaws in test blocks, although the 95% confidence interval is very large based on the small number of test blocks in the tests. It is interesting that the potential-drop techniques were able to outperform the array ECT techniques. The POD regressions for the potential-drop techniques are shown in Figure 4.15.

The adaptive phased array ultrasound provided perfect detection of all flaws in the baseline difficulty test blocks and missed all flaws in the challenging test blocks. The POD regression curve shows the adaptive phased array technique has a very high probability of detecting flaws greater than 10 mm in length. The POD results for the adaptive phased array technique for all flaws are shown in Figure 4.16.

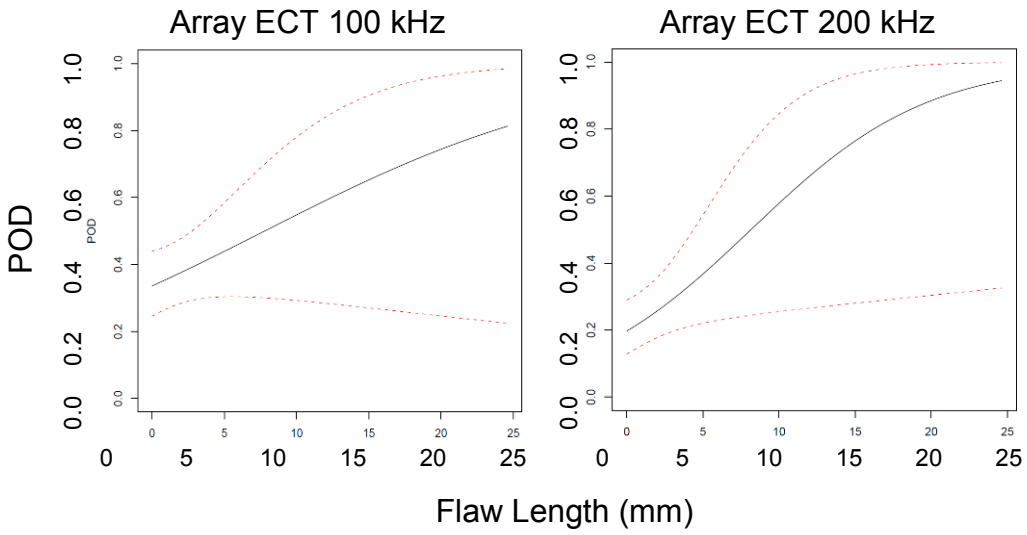

Figure 4.14 Probability of Detection Regressions in BMI Test Blocks for Array Eddy-Current Techniques

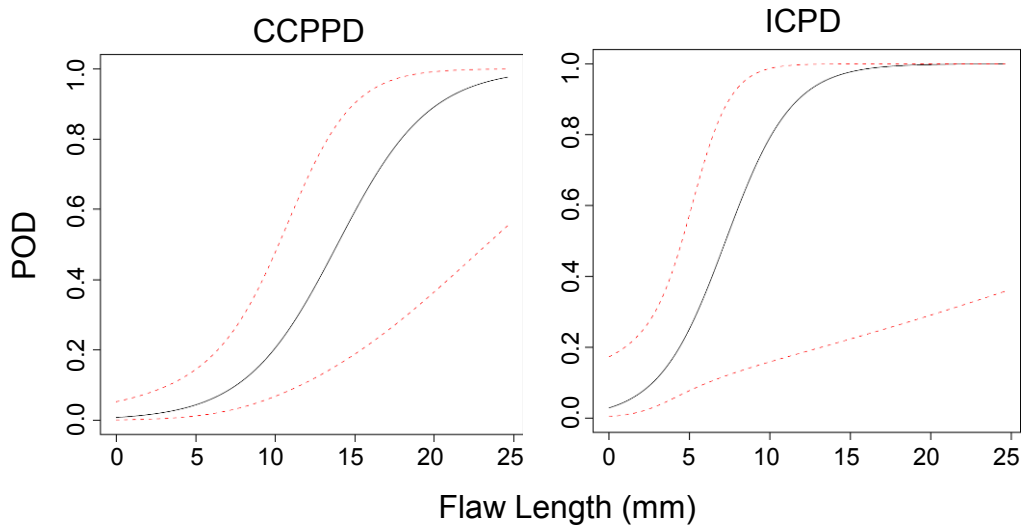

Figure 4.15 Probability of Detection Regressions in BMI Test Blocks for Potential-Drop Techniques

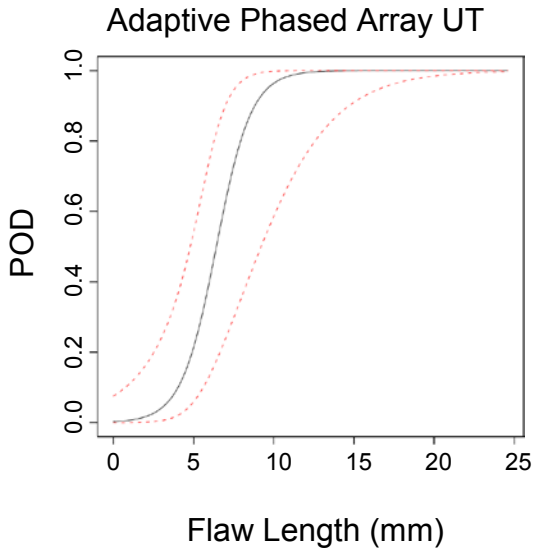

Figure 4.16 Probability of Detection Regression in BMI Test Blocks for Adaptive Phased Array Technique

4.2.2.4 Probability of Detection versus BMI Test Block Flaw Characteristics

It is important to understand the crack morphologies and characteristics that make flaws reliably detectable or challenging to find during inservice inspections. The destructive analysis results of BMI test blocks are shown in Appendices A and B. The usual crack characteristics that are commonly considered important for NDE reliability include crack length, depth, and COD. The true-state information contained the crack lengths and depths, and the destructive examinations for test blocks 5.13–5.16 contain information on the CODs for these test blocks.

To better understand the crack characteristics, PNNL performed a series of fingerprinting examinations of the surfaces of test blocks 5.6–5.16. These fingerprinting measurements were performed in a laboratory with the true-state information available to the inspectors. A 5-MHz eddy current examination was performed using a pancake-style coil. The eddy current system was calibrated before each examination to ensure consistent results. The flaws were analyzed and the maximum voltage for each flaw was recorded. The PNNL fingerprinting results for the flaws in the surfaces of test blocks 5.6-5.16, along with the crack lengths, depths, crack POD, and flaw fabrication technique, are tabulated in Table 4.18. The complete fingerprinting results are shown in Appendix G.

When the data for the surface examinations were analyzed, the overall POD for each flaw was largely independent of flaw length, depth, or flaw orientation. The single largest influence in the flaw POD was the test block identification. All flaws that were not in test blocks 5.9 and 5.10 have a POD of approximately 0.8, and the flaws in test blocks 5.9 and 5.10 had much lower overall PODs. In test blocks 5.9 and 5.10, the largest influence in the flaw POD was the flaw length. The flaw depth was not an important variable for flaw detection in these test blocks. The crack PODs for the various crack fabrication techniques are plotted against their length in Figure 4.17 and against their depth in Figure 4.18.

Table 4.19 BMI Flaw Probability of Detection and Important Parameters

Test Block	Flaw	Radial Location, °	PNNL ECT Magnitude, V	POD	Flaw Length, mm	Flaw Depth, mm	Flaw Orientation	Fabrication Technique
5.6	1	45	0.72	0.75	4	2	Axial	Weld Solidification
5.6	2	135	1.74	0.75	5	2	Circ.	Weld Solidification
5.6	3	180	1.07	0.75	5	2	Axial	Weld Solidification
5.6	4	225	1.25	0.75	10	5	Circ.	Weld Solidification
5.6	5	255	NR	0.75	11	5	Circ	Weld Solidification
5.6	6	315	1.44	0.75	6	1.5	Axial	Weld Solidification
5.7	1	15	2.35	0.71	4	2	Circ.	Thermal Fatigue
5.7	2	165	1.67	0.86	8	3	Axial	Thermal Fatigue
5.7	3	300	2.32	0.86	NA	NA	Axial	Thermal Fatigue
5.9	1	15	0.51	0.29	4	1	Axial	Weld Solidification
5.9	2	75	NR	0.14	3	6	Axial	Weld Solidification
5.9	3	195	NR	0.14	3	3	Circ.	Weld Solidification
5.9	4	345	1.33	0.14	4	7	Axial	Weld Solidification
5.10	1	45	2.69	0.14	7.5	9	Circ.	Weld Solidification
5.10	2	75	1.79	0.00	5	7	Circ.	Weld Solidification
5.10*	3	225	NR	0.00	3.5	0.4	Axial	Weld Solidification
5.10	4	255	1.9	0.43	7	2	Circ.	Weld Solidification
5.10	5	285	NR	0.14	4.5	2	Axial	Weld Solidification
5.10*	6	315	1.96	0.00	1.5	4.5	Axial	Weld Solidification
5.13	1	0	2.45	0.80	8	2	Circ.	Induced SCC
5.13	2	180	1.62	0.60	12	2	Circ.	Induced SCC
5.14	1	0	3.92	1.00	14	11	Circ.	Induced SCC
5.14	2	180	1.39	0.80	14	2	Circ.	Induced SCC
5.15	1	90	2.94	0.80	12	4	Axial	Induced SCC
5.15	2	270	4.01	0.60	13	3	Axial	Induced SCC
5.16	1	90	4.42	1.00	16	11	Axial	Induced SCC
5.16	2	270	7.08	0.80	19	6	Axial	Induced SCC

* During DE, Flaws 5.10 3 and 5.10 6 were determined to be too small for use in scoring.

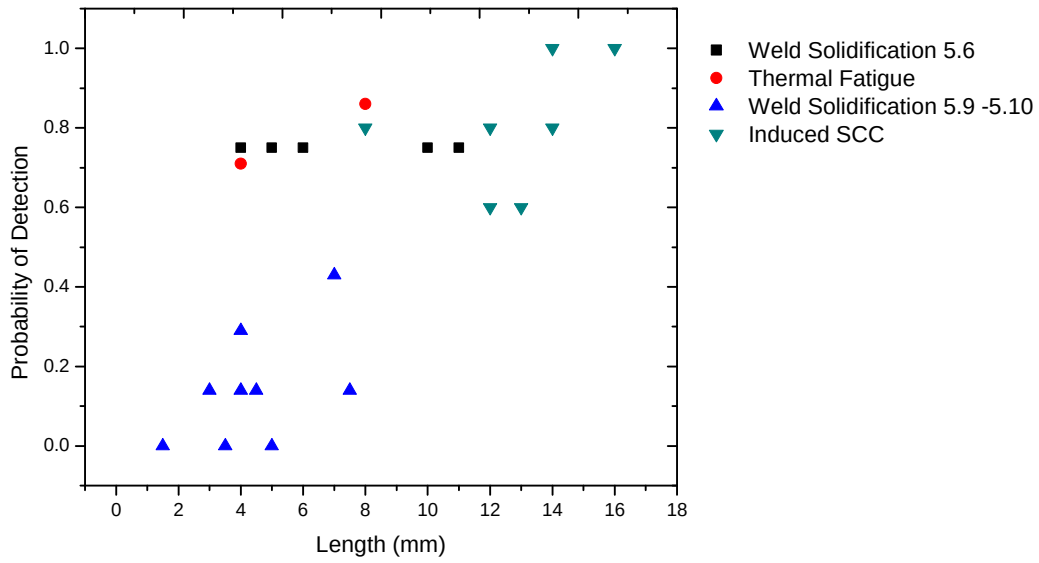

Figure 4.17 BMI Flaw Probability of Detection versus Flaw Length for Each Flaw Fabrication Technique

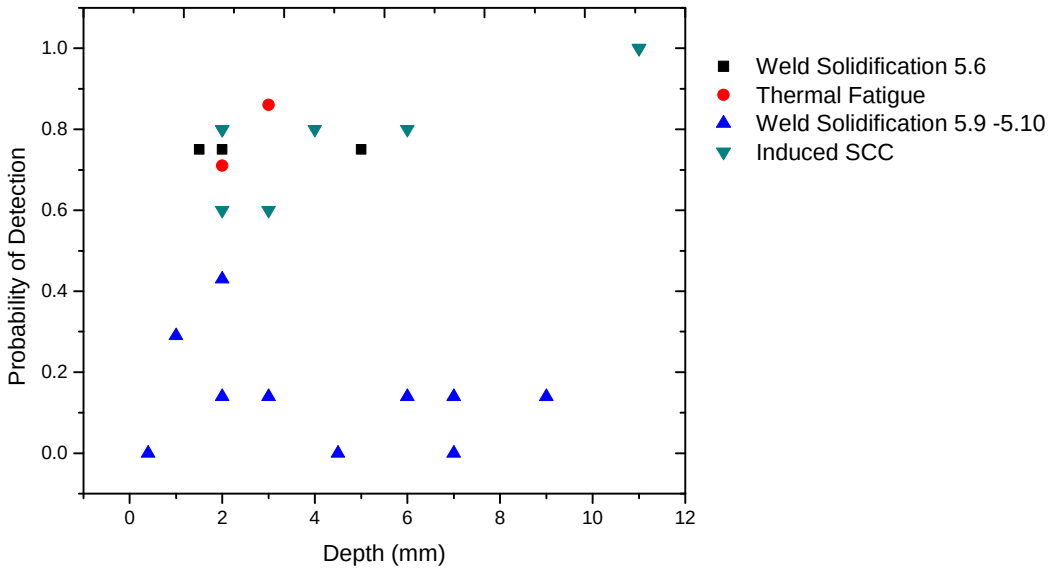

Figure 4.18 BMI Flaw Probability of Detection versus Flaw Depth for Each Flaw Fabrication Technique

Because one of the main goals of the PINC is to discover what makes a crack easy or difficult to detect, the flaws in test blocks 5.9 and 5.10 provided an opportunity to explore what it is about these flaws that make them different from the thermal fatigue, other SCC, and the weld-solidification flaws fabricated into other test blocks. Sample 5.10 was destructively analyzed, and the results are given in Appendix B.

4.3 Sizing Results as Measured by the PINC Round Robin Exercises

4.3.1 Sizing Results from the PINC DMW Round Robin

This section of the report discusses the sizing capability that was measured from the DMW round robin data. One of the goals of the PINC is to determine which techniques are the most effective at characterizing the through-wall depth and length of PWSCC. Some statistical analysis of crack length and depth characterization is provided in this section so that conclusions may be drawn concerning crack characterization capability. The data have been grouped by team, technique, and flaw orientation for a statistical analysis.

Linear regression was used to analyze sizing data that was developed under the PINC DMW round robin. PNNL defined an error relation between the measured and true sizes of the flaws by the following regression formula:

$$M_i = B1 + B2 \times T_i + E_i \tag{4.6}$$

where M_i represents the measured size associated with flaw i
T_i represents the true size of flaw i
E_i represents the measurement error in sizing flaw i

B1 and B2 are the regression parameters usually associated with the Y intercept and slope of the linear regression. Ideal performance for sizing would occur when B1 = 0, B2 = 1 and E_i = 0. To compare two different regression fits, and to order a set of regression fits (from most accurate to least accurate as an example), PNNL used the metric of root mean square error (RMSE). RMSE is a statistic that summarizes the three deviations of regression analyses from their respective ideals. RMSE is defined by

$$RMSE^2 = \frac{\sum_i (M_i - T_i)^2}{n} \tag{4.7}$$

where all the variables are the same as in the preceding descriptions and n is the total number of flaws.

4.3.1.1 Summary of Flaw Depth Characterization for All Flaws and All Teams

According to ASME Code requirements, any indication that is determined to be SCC is not allowable in dissimilar metal welds. The practice in most U.S. nuclear power plants where PWSCC has been detected or is expected is to perform a mitigation technique such as weld overlay or mechanical stress improvement. Before applying the mitigation technique, depth sizing of flaws is important because one does not want to perform a mitigation technique that would place the flaw in a region of tensile stress that would possibly make the welded joint integrity worse after applying the mitigation technique.

Table 4.20 presents the combined results of all teams for characterizing the depth of flaws. Figure 4.19 provides regression plots of measured flaw size versus the true-flaw depths for the teams that participated in the round robin, with the team number printed on the top of the appropriate inspection plot. The design true-flaw depths have been supplied by the host country that provided the test blocks.

Table 4.20 Summary of Depth Sizing Results on All Flaws in DMW Test Blocks

	Intercept		Slope					
Team	Intercept	Std Dev of Intercept	Slope	Std Dev of Slope	Standard Error	RMSE	No. of Observations	Inspection Technique
13	6.91	2.13	0.57	0.12	4.46	5.72	20	Phased Array UT
22	9.17	3.64	0.14	0.23	6.94	10.09	14	Conventional UT
28	4.99	3.44	0.52	0.18	5.75	7.82	15	Conventional UT
30	9.09	3.33	0.40	0.19	6.39	8.16	16	Conventional UT
38	NA	NA	NA	NA	NA	NA	0	Eddy Current
39	1.66	1.33	0.76	0.07	2.62	4.01	15	Phased Array UT
16	NA	NA	NA	NA	NA	NA	2	Potential Drop
43	NA	NA	NA	NA	NA	NA	0	Potential Drop
48	12.94	2.20	0.17	0.11	3.10	7.87	13	Conventional UT
63	6.33	1.90	0.62	0.11	4.06	5.19	20	Conventional UT
65	NA	NA	NA	NA	NA	NA	0	Potential Drop
66	1.61	1.40	0.93	0.08	3.15	3.18	22	Phased Array UT + Conventional UT
67	0.98	1.93	0.21	0.13	4.20	11.47	19	Potential Drop
70	NA	NA	NA	NA	NA	NA	0	Eddy Current
72	10.41	4.78	0.44	0.24	7.70	9.13	12	Phased Array UT
82	7.07	3.06	0.53	0.23	5.85	6.59	17	Conventional UT
96	6.21	1.59	0.55	0.10	4.07	5.58	25	TOFD + Conventional UT + Eddy Current
All	5.34	0.84	0.56	0.56	0.56	7.07	208	

Table 4.20 shows that some teams had accurate sizing results. Team 66 used phased array UT and tip-diffraction techniques and performed well in both detection and sizing. All teams that used the phased array UT technology performed better than teams that used conventional ultrasonic methods. Teams that used electromagnetic methods did not perform well at all in depth sizing. Figure 4.19 presents the depth sizing regression analysis, including 95% confidence bounds, from all teams.

Two teams attempted depth sizing but were not included in the regressions. Team 16 examined two cracks and did not have enough information to allow for a statistical regression. Team 38 was only able to measure the first three millimeters of the surfaces, and only had information on a small region of the samples. Team 38 was able to attempt to depth size flaws that were less than 3 mm in depth and could refer to deeper flaws as “deeper than 3 mm.” The depth sizing results for Team 38 are summarized in Figure 4.20 and the depth sizing results for Team 16 are summarized in Table 4.21.

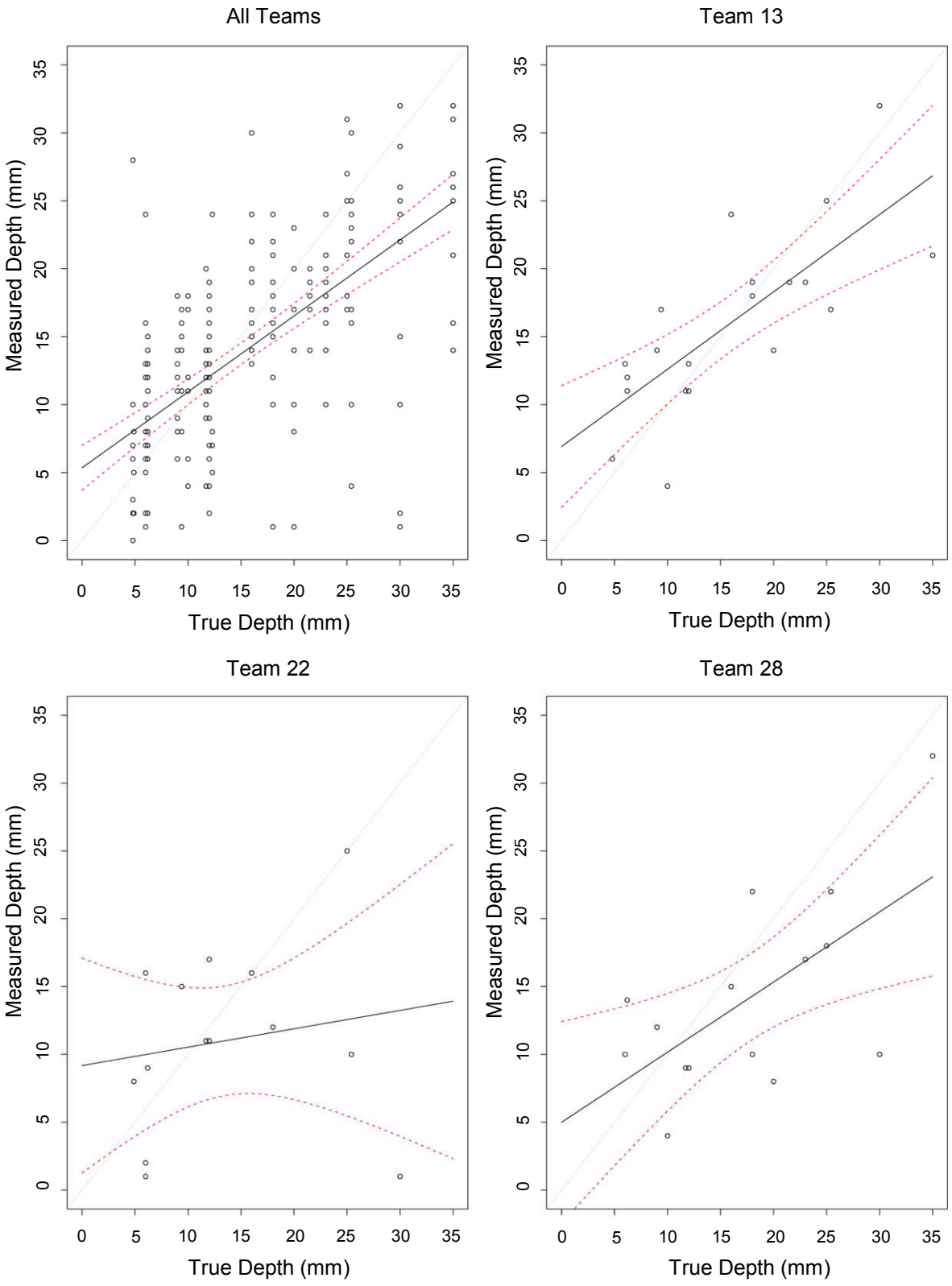

Figure 4.19 Depth Sizing Regression in DMW Test Blocks

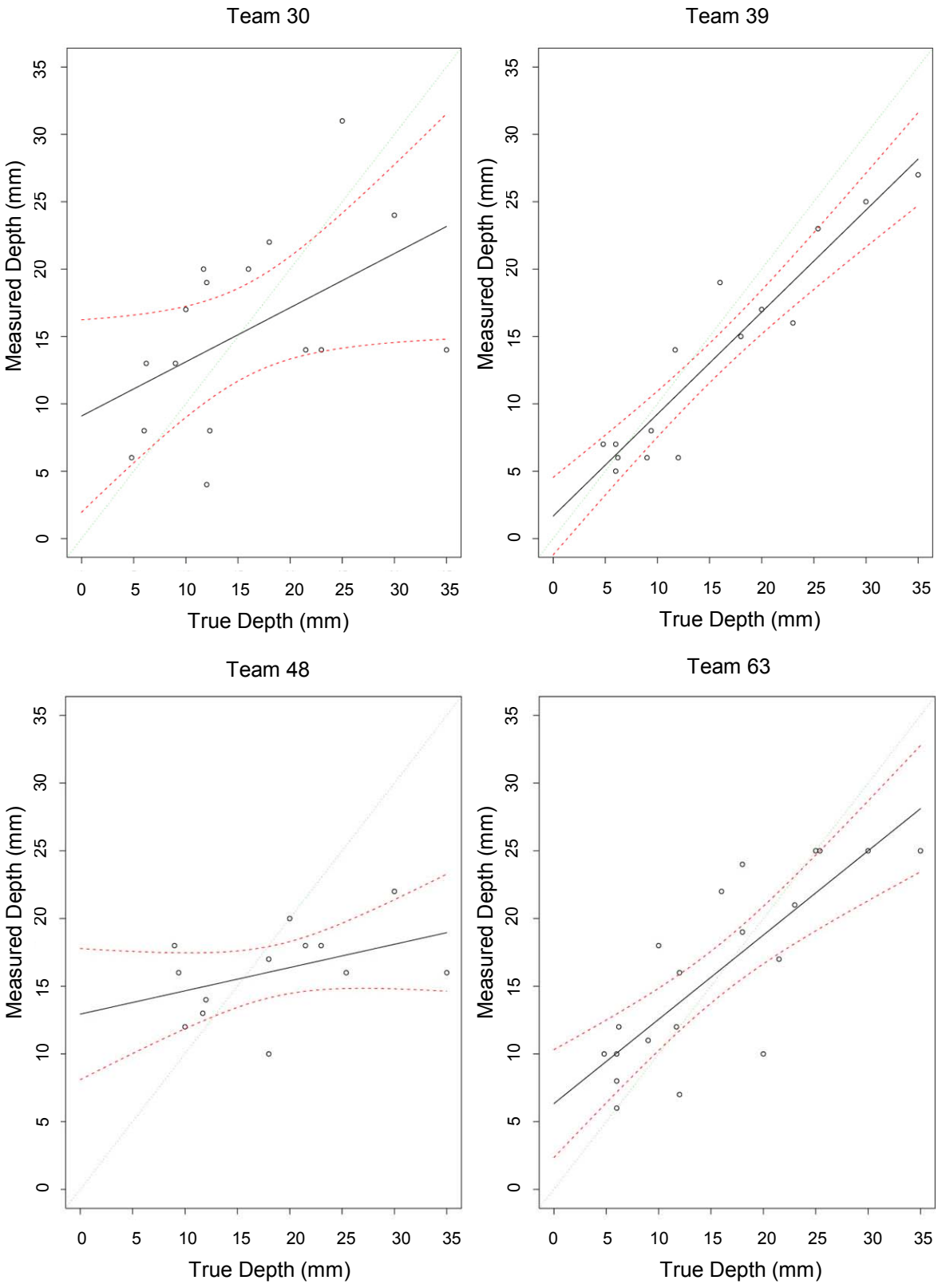

Figure 4.19 (continued)

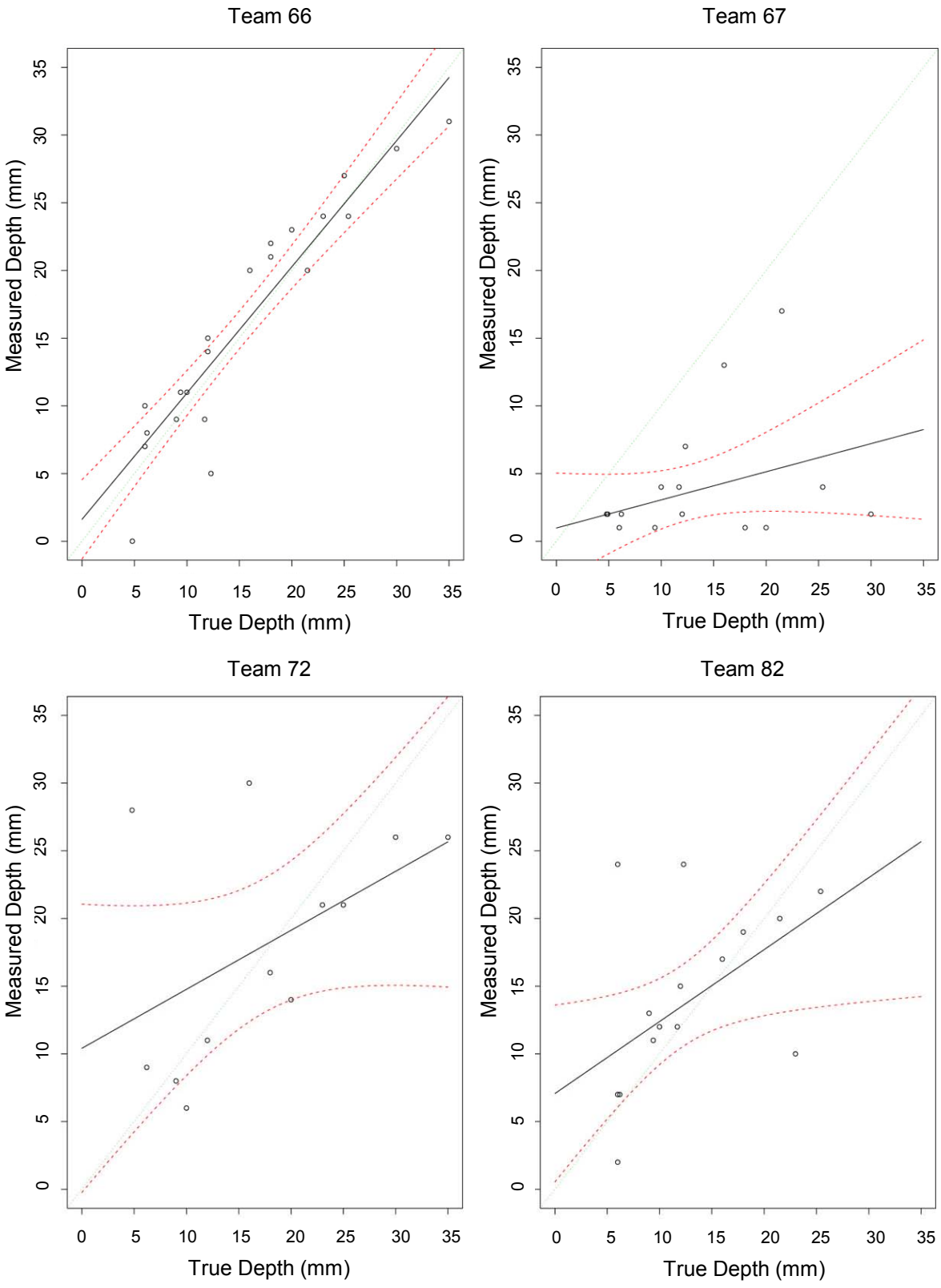

Figure 4.19 (continued)

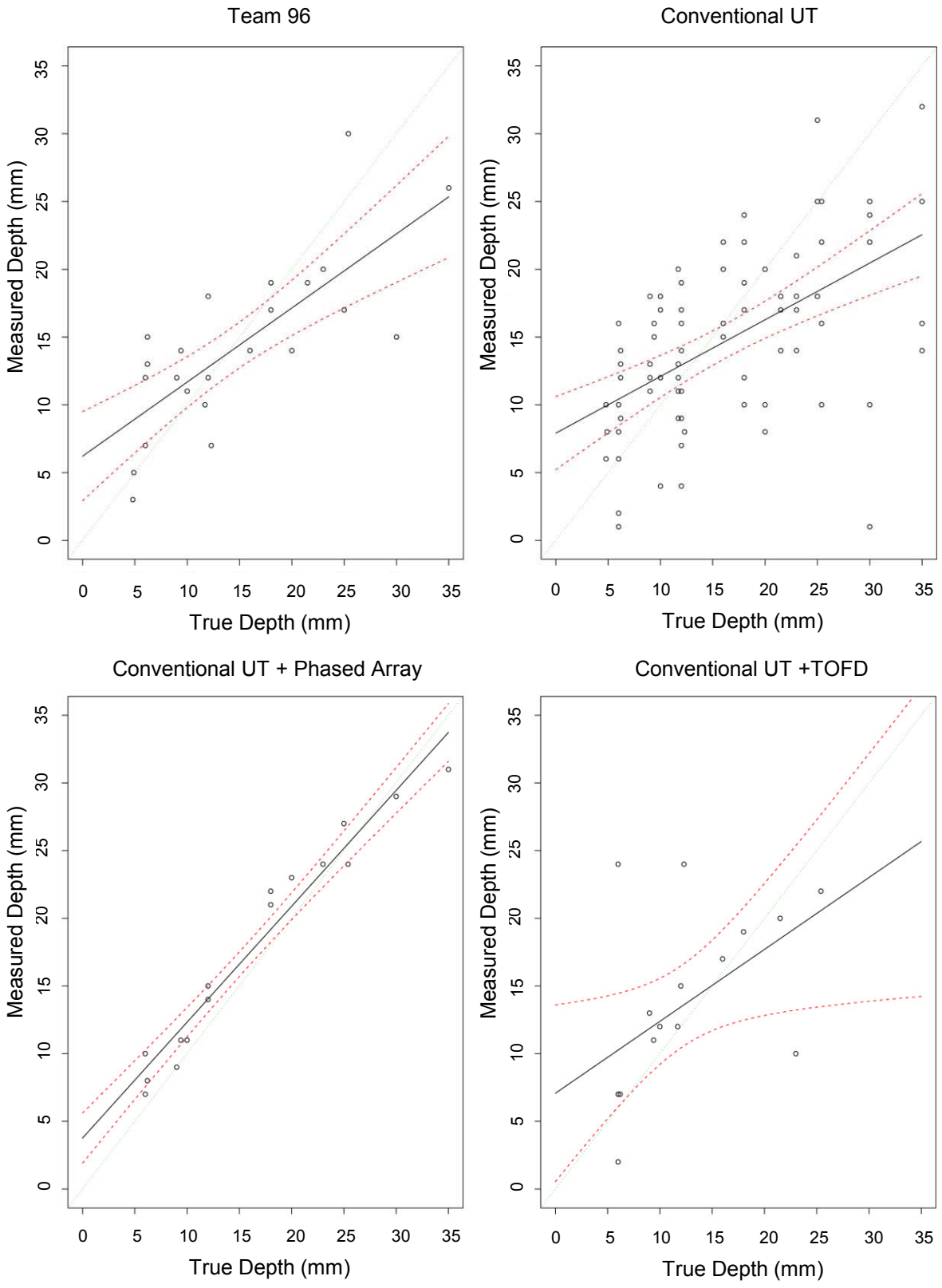

Figure 4.19 (continued)

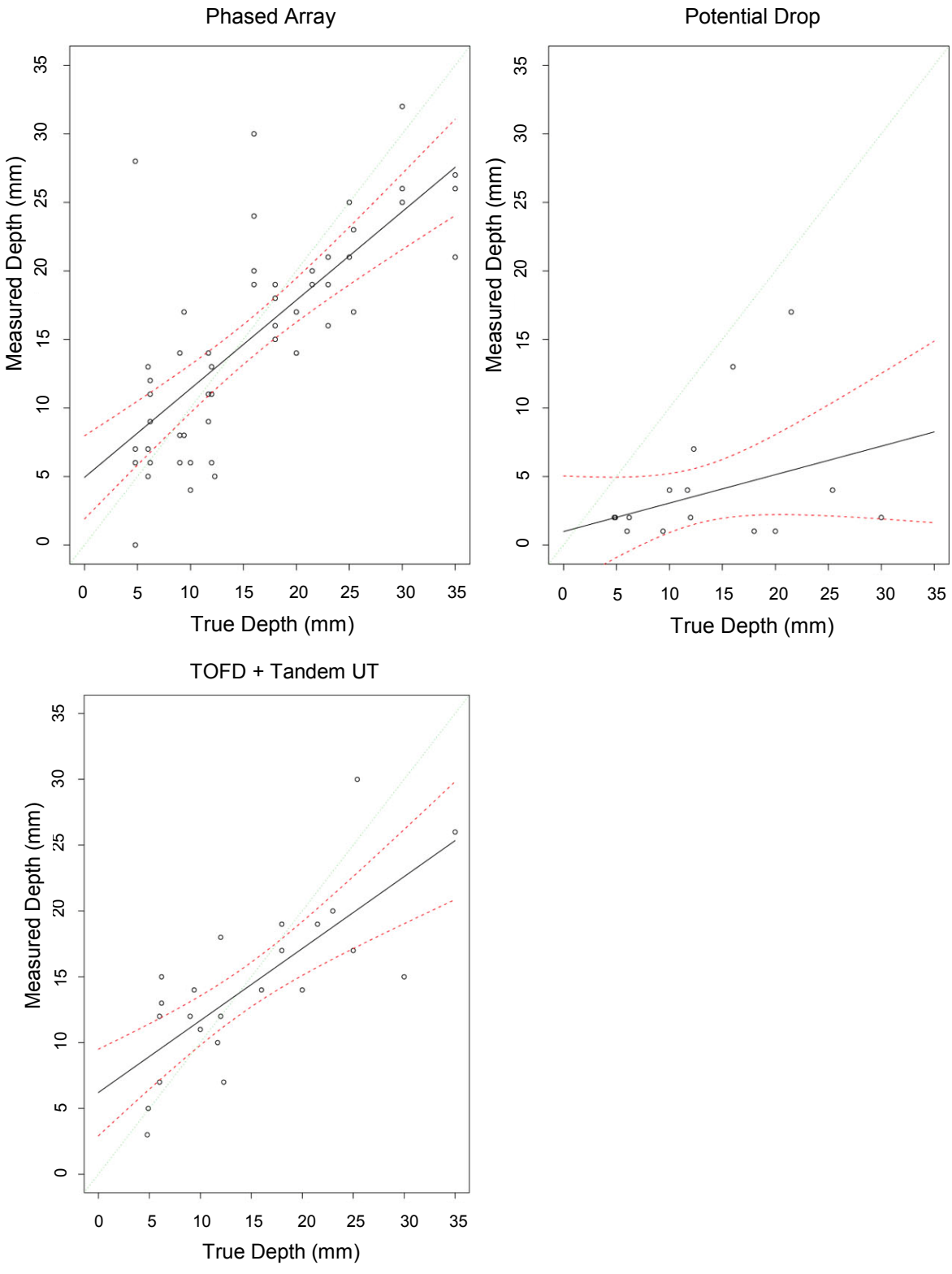

Figure 4.19 (continued)

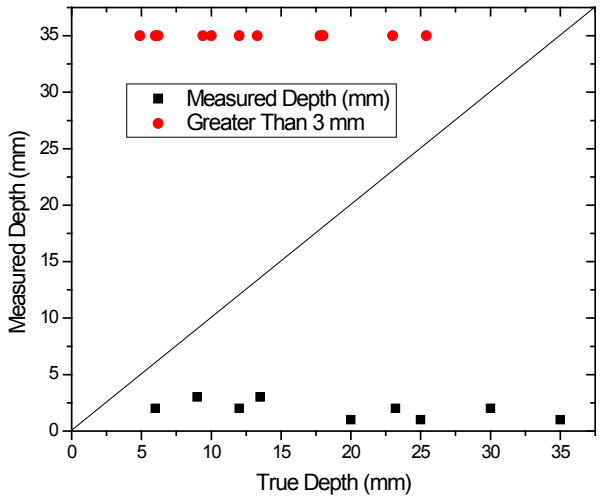

Figure 4.20 Dissimilar Metal Weld Depth Sizing Results for Team 38

Table 4.21 Dissimilar Metal Weld Depth Sizing Results for Team 16

Flaw ID	Measured Depth (mm)	True Depth (mm)
PINC 2.1	3.6	5.8
PINC 2.4	2.6	4.9

4.3.2 Flaw Length Sizing in Dissimilar Metal Welds

Table 4.22 and Table 4.23 provide a summary of the length sizing results for the PINC DMW round robin. Table 4.22 summarizes the length sizing results for circumferential flaws and Table 4.23 summarizes the length sizing results for axial flaws. Figure 4.21 and Figure 4.22 provide regression plots of the length sizing results for the teams that participated in the round robin. Figure 4.21 summarizes the length sizing results for circumferential flaws and Figure 4.22 summarizes the length sizing results for axial flaws. A review of the information in Table 4.22 and Table 4.23 shows that eddy current techniques were the most accurate for length sizing flaws followed by phased array ultrasonic techniques. Conventional ultrasonic and potential-drop techniques were poor at length sizing. Appendix VIII of Section XI of the ASME Code states that examination procedures, equipment, and personnel be qualified for length sizing when the RMSE of the flaw-length measurements compared to the true flaw lengths do not exceed 0.75 in. (19 mm). A review of the data in Table 4.22 and Table 4.23 shows that half (8 out of the 16 teams) would have passed a performance demonstration test. Table 4.24 shows the length sizing results for Team 16.

Table 4.22 Summary of Length Sizing Results for Circumferential Flaws in DMW Test Blocks

Team	Intercept	Std Dev of Intercept	Slope	Std Dev of Slope	Standard Error	RMSE	No. of Obser-vations	Inspection Technique
13	30.54	7.54	0.51	0.23	14.98	24.09	13	Phased Array UT
22	16.72	9.86	0.35	0.28	18.46	22.44	10	Conventional UT
28	12.10	5.43	0.71	0.15	10.01	11.78	11	Conventional UT
30	6.66	6.55	0.65	0.17	11.02	13.54	9	Conventional UT
38	17.43	3.72	-0.08	0.11	7.65	24.28	14	Eddy Current
39	3.14	2.46	0.84	0.07	4.89	5.78	13	Phased Array UT
16	NA	NA	NA	NA	NA	NA		CCPPD
43	NA	NA	NA	NA	NA	NA	0	Potential Drop
48	169.10	23.84	-2.26	0.88	18.95	91.60	7	Conventional UT
63	2.24	2.75	0.83	0.08	5.30	6.62	12	Conventional UT
65	61.30	19.56	-0.60	0.45	26.02	47.67	6	Potential Drop
66	12.46	3.35	0.74	0.10	6.65	9.63	13	Phased Array UT + Conventional UT
67	0.13	2.02	0.90	0.06	3.92	4.94	11	Potential Drop
70	7.08	2.06	0.93	0.06	4.33	6.74	15	Eddy Current
72	24.79	13.53	0.46	0.32	18.94	22.91	6	Phased Array UT
82	28.76	4.77	-0.17	0.15	9.74	24.47	13	Conventional UT
96	4.51	1.23	0.87	0.04	2.58	3.56	15	Conventional UT + Eddy Current
All	19.13	3.13	0.48	0.09	22.61	25.01	168	

Note: All measurements are in millimeters.

Table 4.23 Summary of Length Sizing Results for Axial Flaws in DMW Test Blocks

Team	Intercept	Std Dev of Intercept	Slope	Std Dev of Slope	Standard Error	RMSE	No. of Obser-vations	Inspection Technique
13	20.70	13.08	0.23	0.55	12.62	14.08	7	Phased Array UT
22	-0.81	14.86	0.71	0.85	5.53	7.39	4	Conventional UT
28	5.40	17.13	1.05	0.91	6.62	8.67	6	Conventional UT
30	20.16	5.13	0.00	0.19	5.19	12.78	7	Conventional UT
38	-2.93	5.48	0.78	0.22	6.14	10.18	9	Eddy Current
39	NA	NA	NA	NA	NA	7.14	2	Phased Array UT
16	NA	NA	NA	NA	NA	NA		
43	NA	NA	NA	NA	NA	NA	0	Potential Drop
48	11.34	0.76	0.23	0.03	0.71	9.77	6	Conventional UT
63	6.07	3.47	0.20	0.15	3.80	13.34	8	Conventional UT
65	NA	NA	NA	NA	NA	30.30	3	Potential Drop
66	17.24	2.23	-0.13	0.09	2.66	14.64	9	Phased Array UT + Conventional UT
67	-0.13	1.39	0.86	0.06	1.66	3.92	8	Potential Drop
70	15.13	1.63	0.62	0.07	2.03	7.95	10	Eddy Current
72	17.50	10.35	0.38	0.55	4.00	7.14	6	Phased Array UT
82	6.68	10.12	0.56	0.33	8.20	10.67	4	Conventional UT
96	4.49	2.11	0.72	0.09	2.63	4.11	10	Conventional UT + Eddy Current
All	11.85	2.27	0.38	0.09	8.68	10.55	99	

Note: All measurements are in millimeters.

Table 4.24 Dissimilar Metal Weld Length Sizing Results for Team 16

Flaw ID	Measured Length (mm)	True Length (mm)
PINC 2.1	25	21
PINC 2.4	16	17

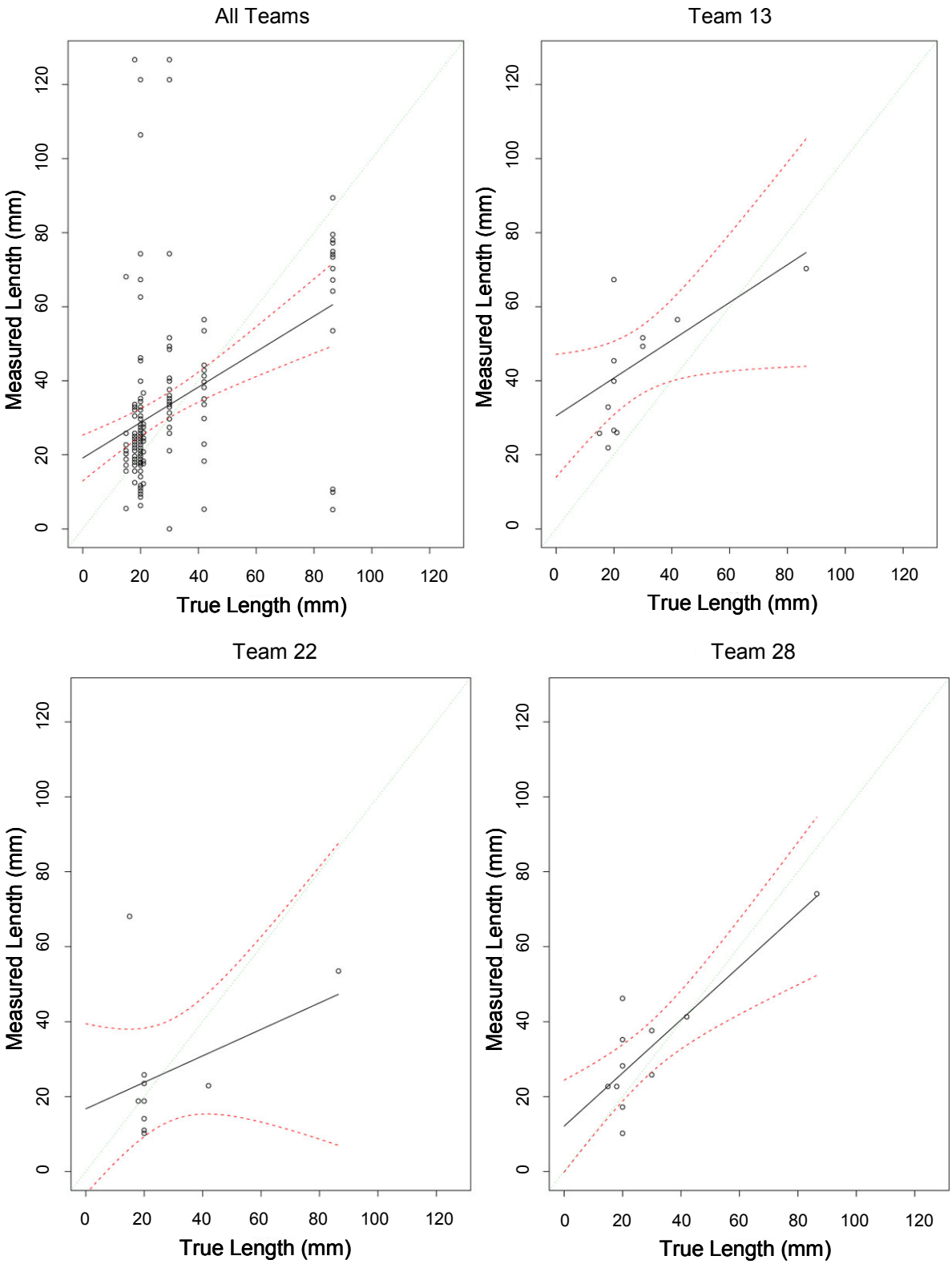

Figure 4.21 Results of Length Sizing on Circumferential Flaws in DMW Test Blocks

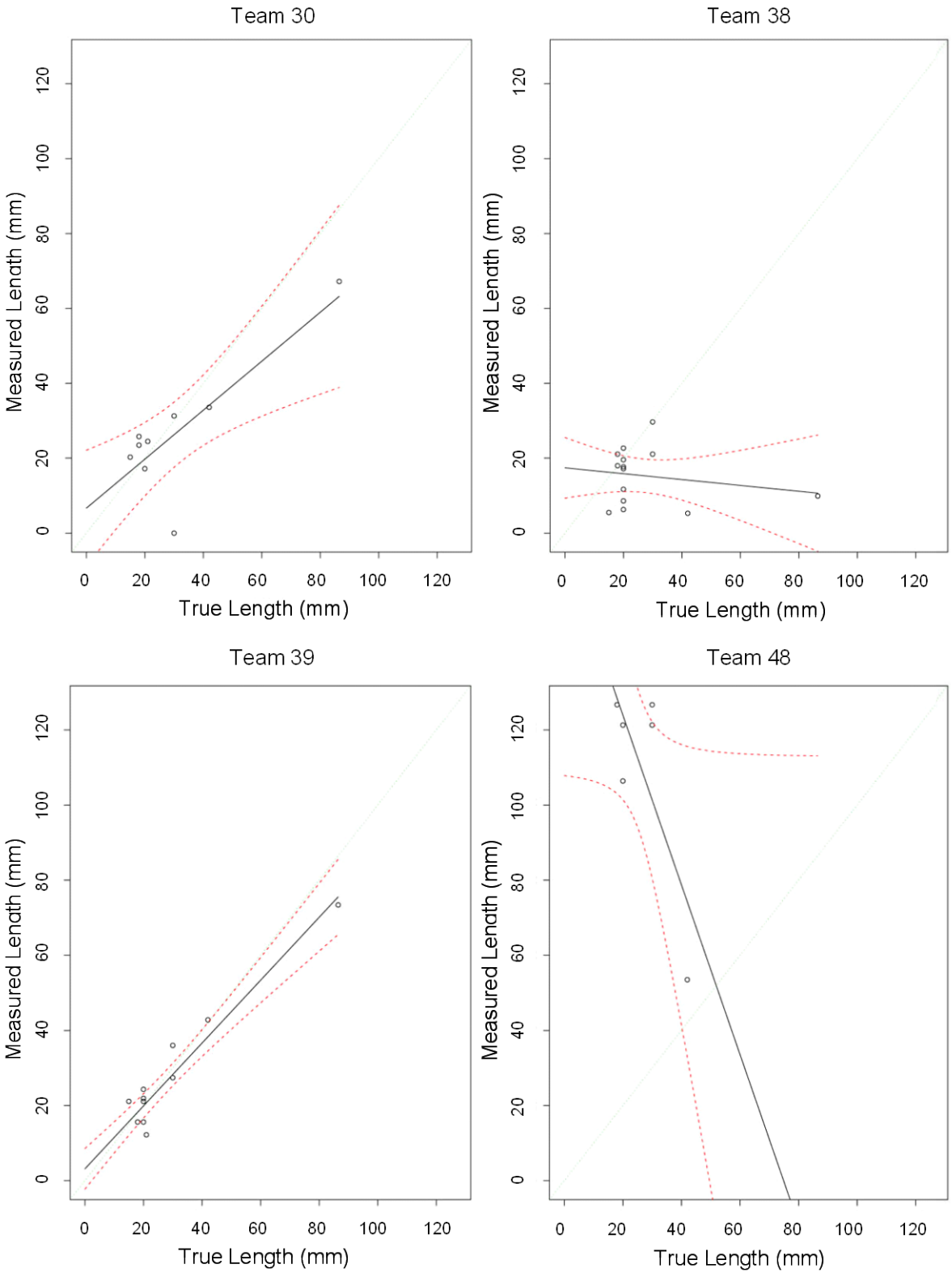

Figure 4.21 (continued)

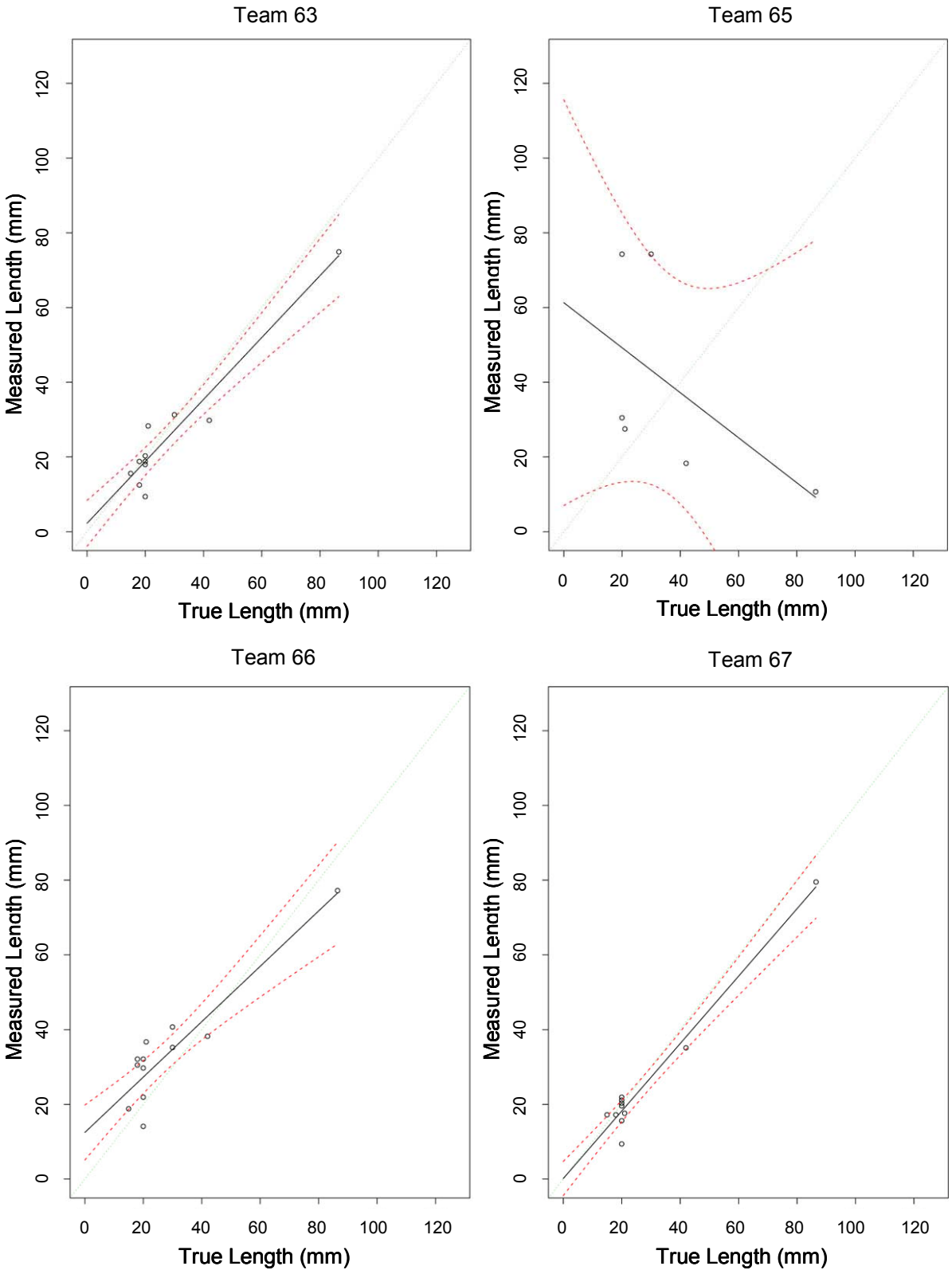

Figure 4.21 (continued)

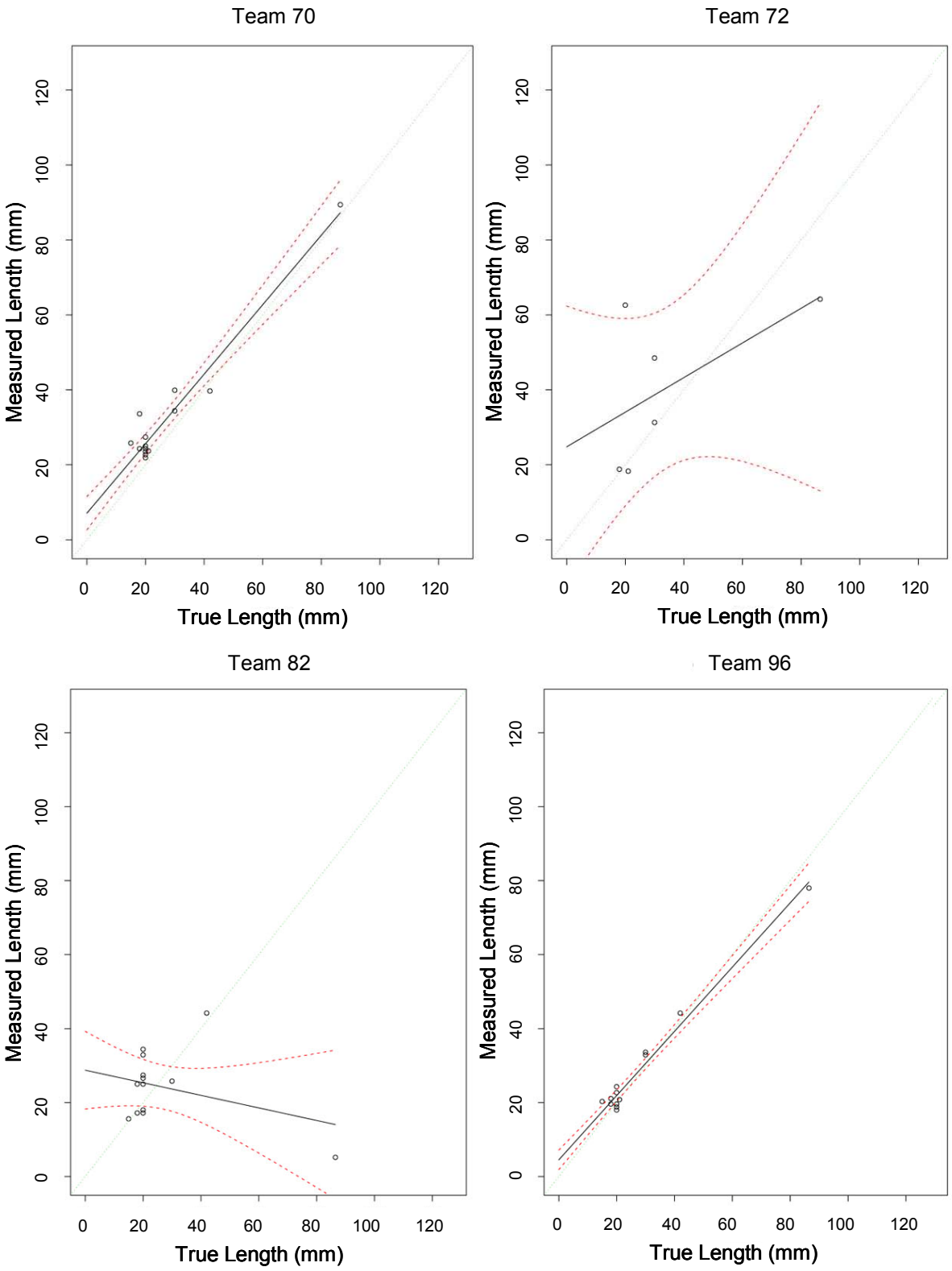

Figure 4.21 (continued)

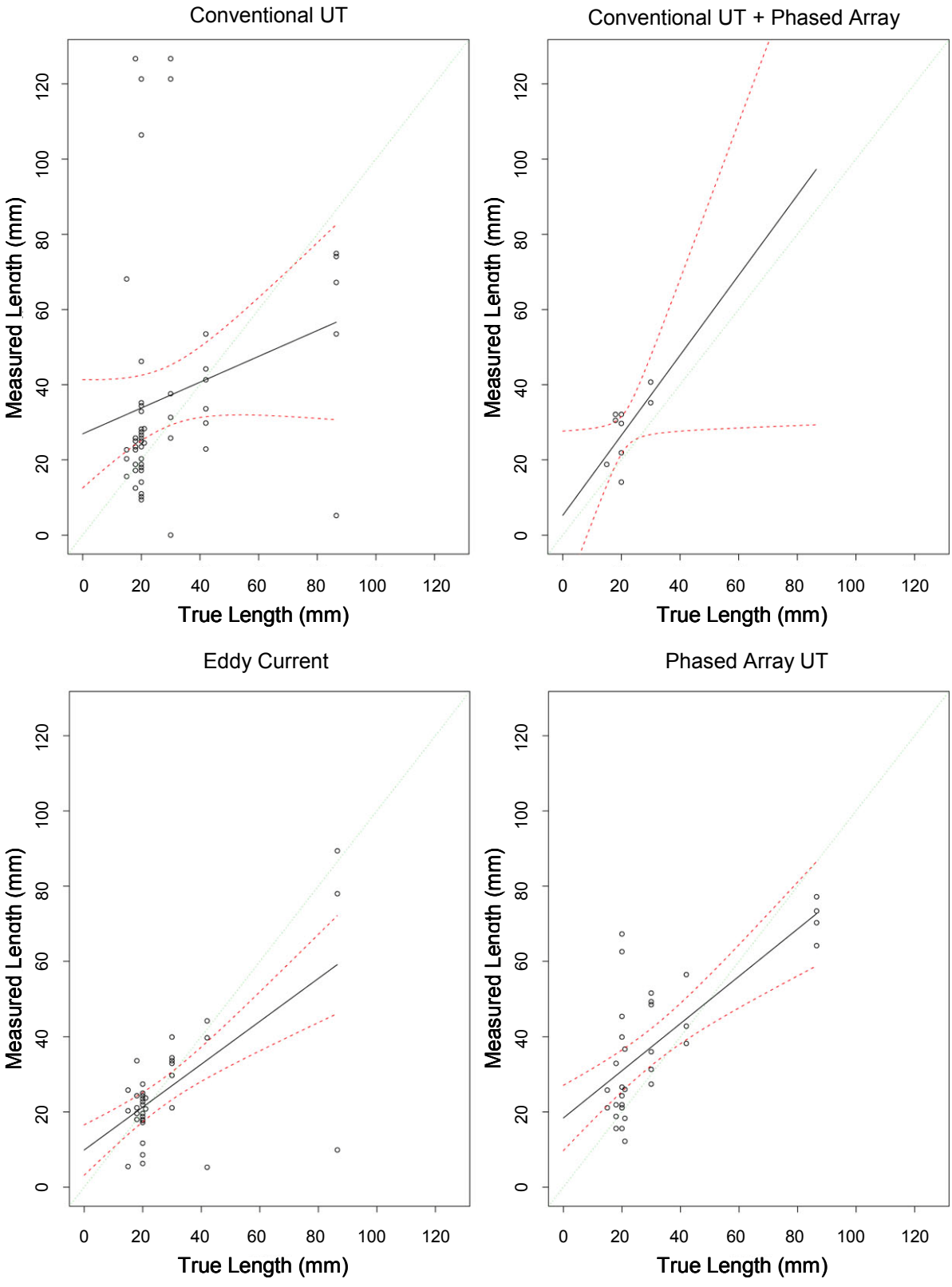

Figure 4.21 (continued)

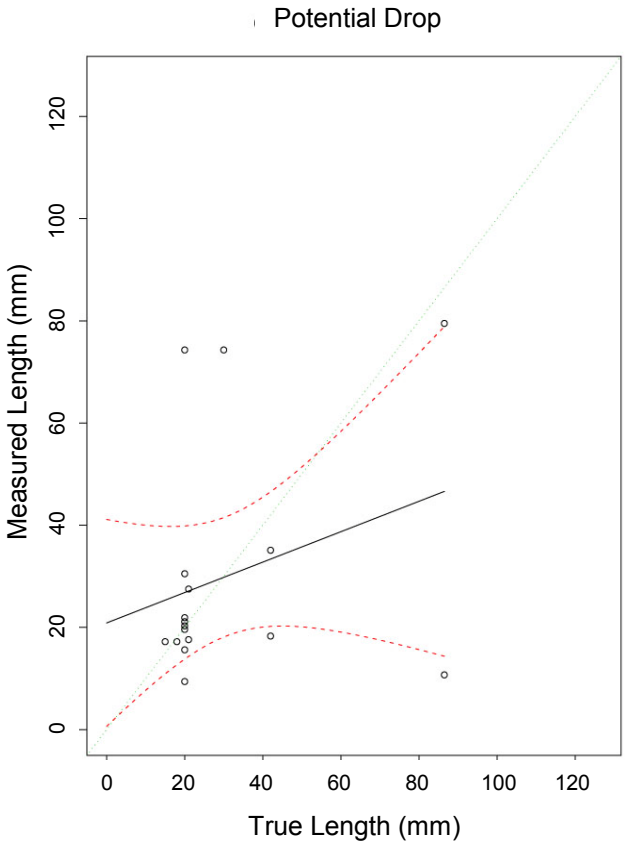

Figure 4.21 (continued)

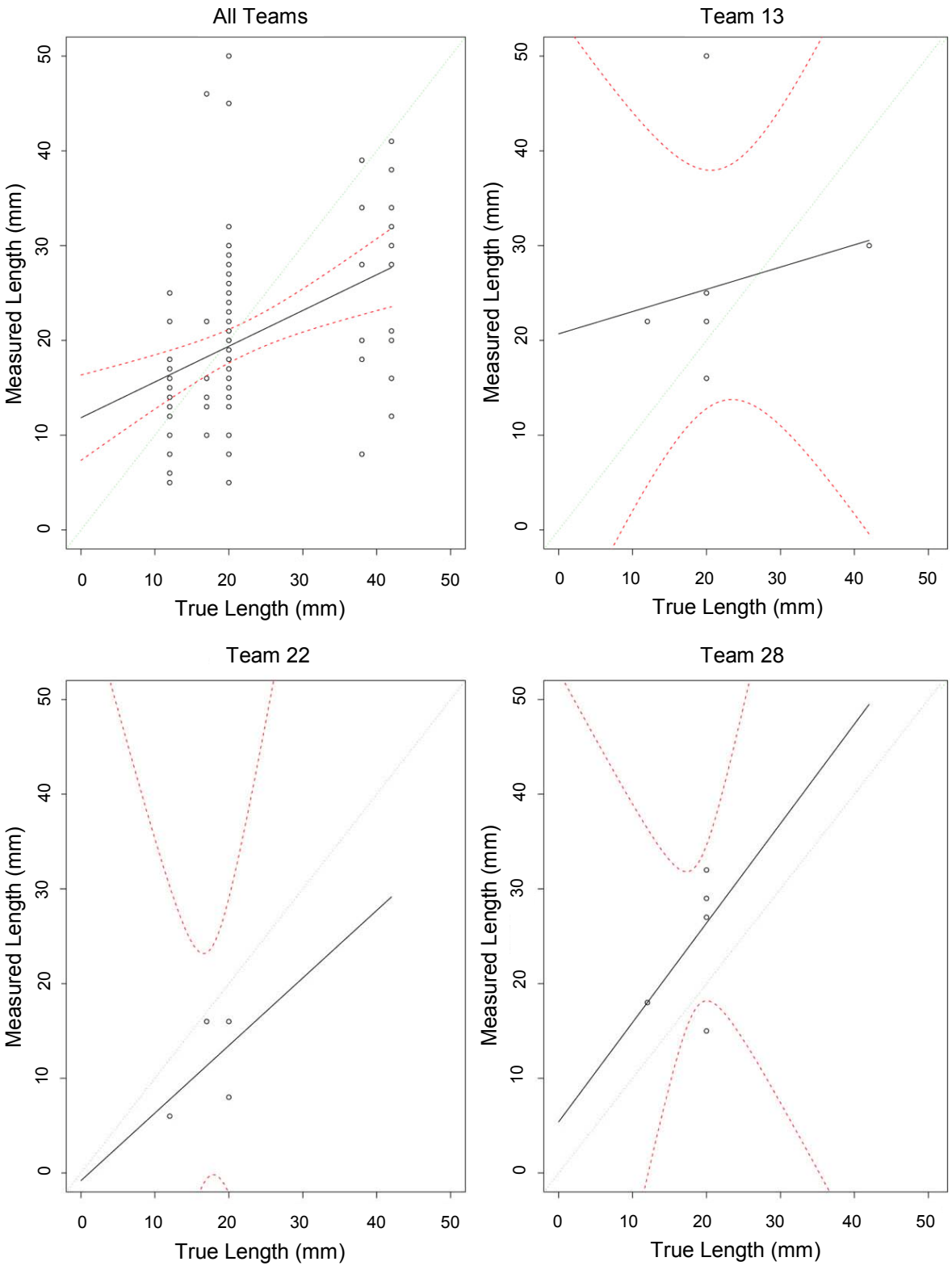

Figure 4.22 Results of Length Sizing on Axial Flaws in DMW Test Blocks

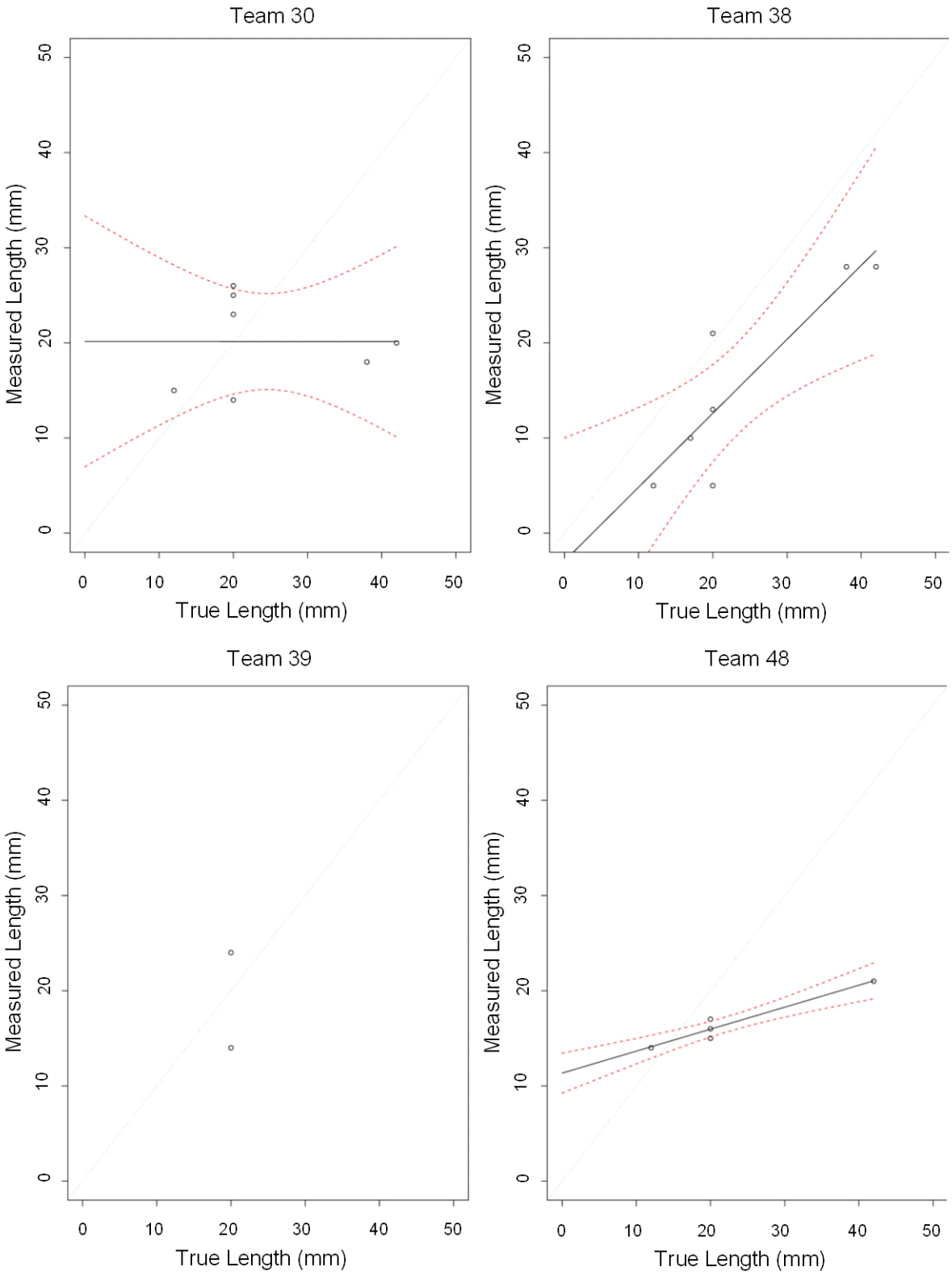

Figure 4.22 (continued)

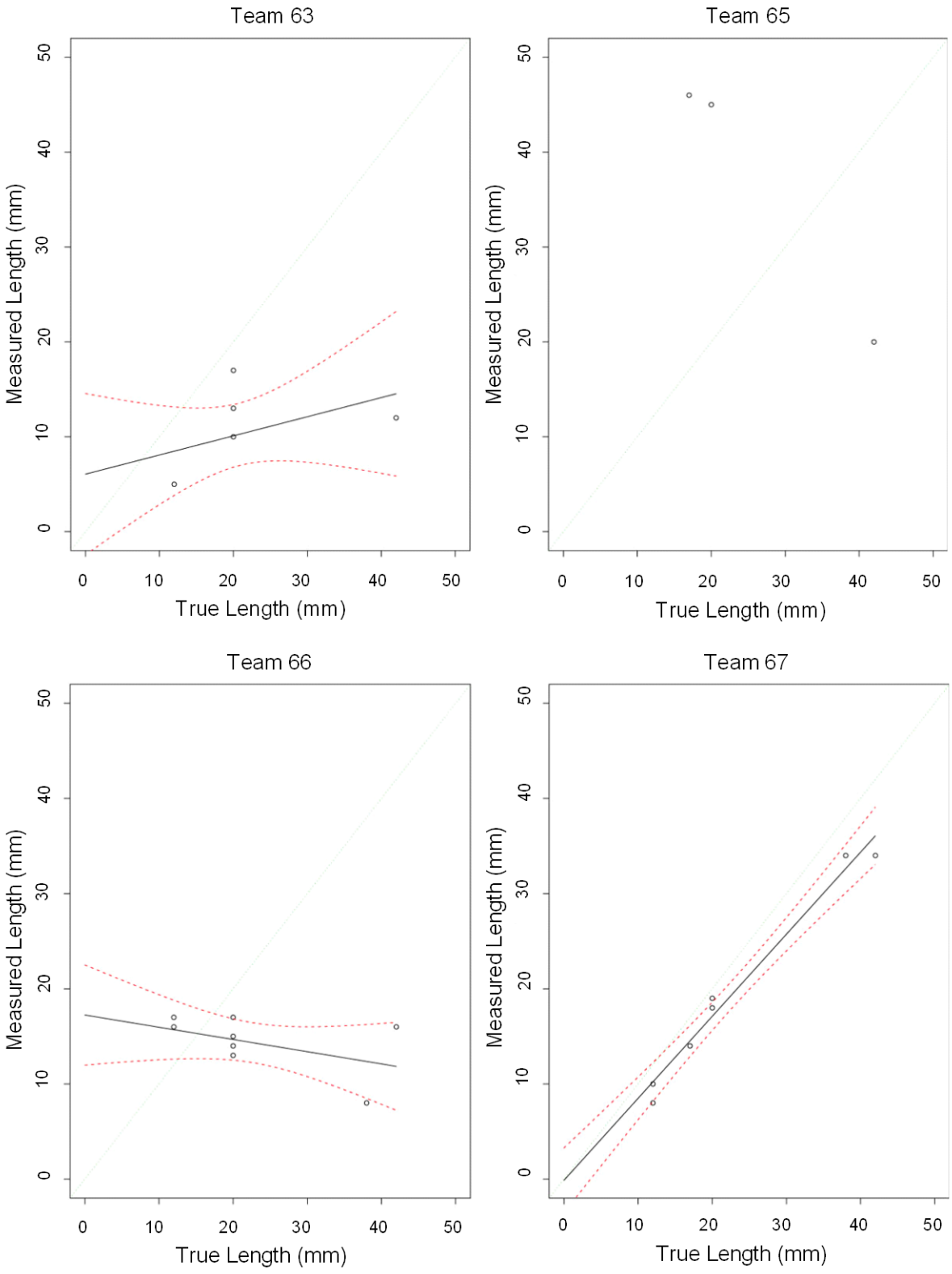

Figure 4.22 (continued)

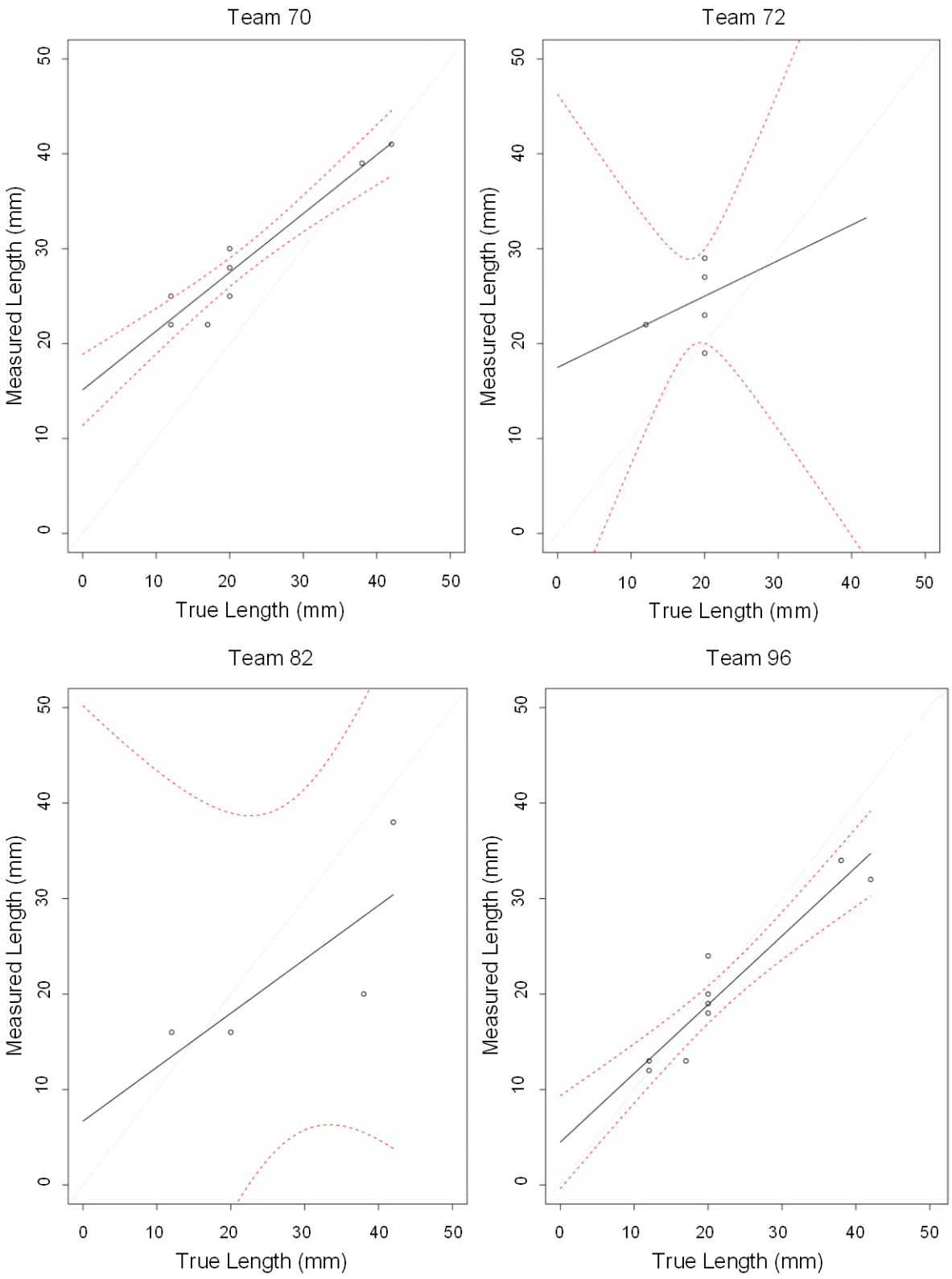

Figure 4.22 (continued)

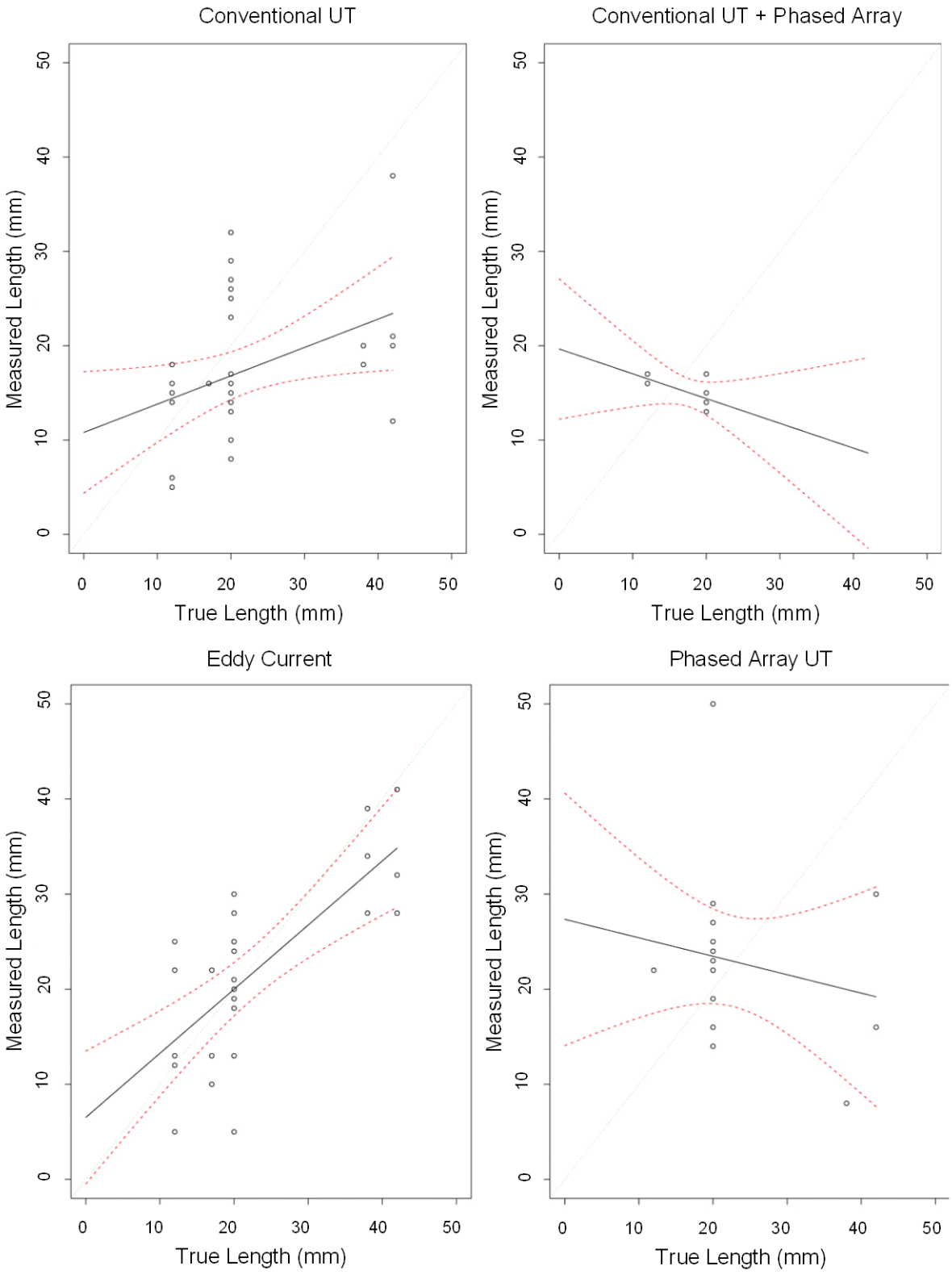

Figure 4.22 (continued)

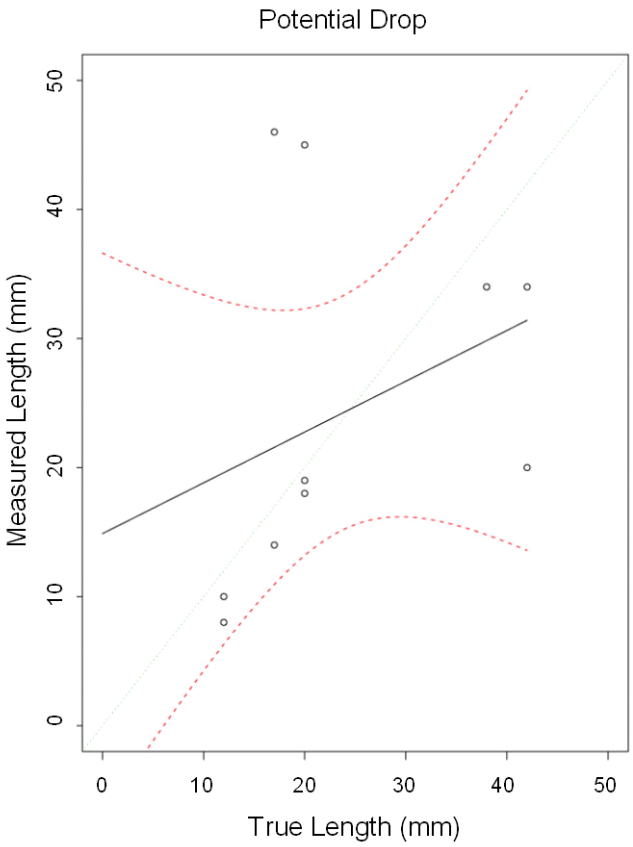

Figure 4.22 (continued)

4.3.3 Sizing Results from the PINC BMI Round Robin

For each detected flaw, the ability of the NDE techniques to accurately characterize the flaw was evaluated. This section describes the depth-sizing and length-sizing accuracy for the inspections in the round-robin tests. The depth-sizing results were sparse and a detailed regression was not performed. The length-sizing results for each inspection were scored using a length-sizing regression and 95% confidence intervals were determined.

4.3.3.1 Tube Examinations

The small number of flaws detected by the tube examinations makes drawing conclusions from the data difficult. An additional challenge in the flaw length sizing was caused by the proximity of the flaws to one another; the teams had occasionally combined multiple flaws into one. Length-sizing results for team 13 are shown in Table 4.25. Team 70 found two flaws, and a detailed regression was not possible. The length-sizing regression showed that the techniques had a very large RMSE and a large standard deviation. Flaws tended to be undersized by both teams.

Table 4.25 Length-Sizing Results for BMI Penetration Tube Examinations

Team	Observations	Technique	RMSE, mm	Standard Deviation, mm	Bias, mm
13	10	ECT and TOFD	16.53	11.84	−11.54

The length-sizing regressions show little relationship between the flaw size and the called indication lengths. The 95% confidence bounds for the tube sizing regressions are so large that they cannot be meaningfully interpreted. Examinations of more flaws by additional teams would be needed for a better length-sizing assessment for examination of flaws in the interior of the penetration tubes.

4.3.3.2 Surface Examinations

Depth sizing was performed by four teams on some flaws. As not all flaws were depth sized by any team and there were so few depth sizing attempts, the statistical regressions were not performed for the depth-sizing results. The teams, techniques, and errors are summarized in Table 4.26 and plotted in Figure 4.23.

Table 4.26 Summary of Depth Sizing Results for BMI Surfaces

Team	Observations	Technique	RMSE, mm	Bias, mm
All	29		3.47	1.67
16	3	CCPPD	5.17	4.5
38	7	Array ECT 100 kHz	5.25	3.86
66	7	Adaptive Phased Array	1.52	1.52
373	12	TOFD	2.24	0.88

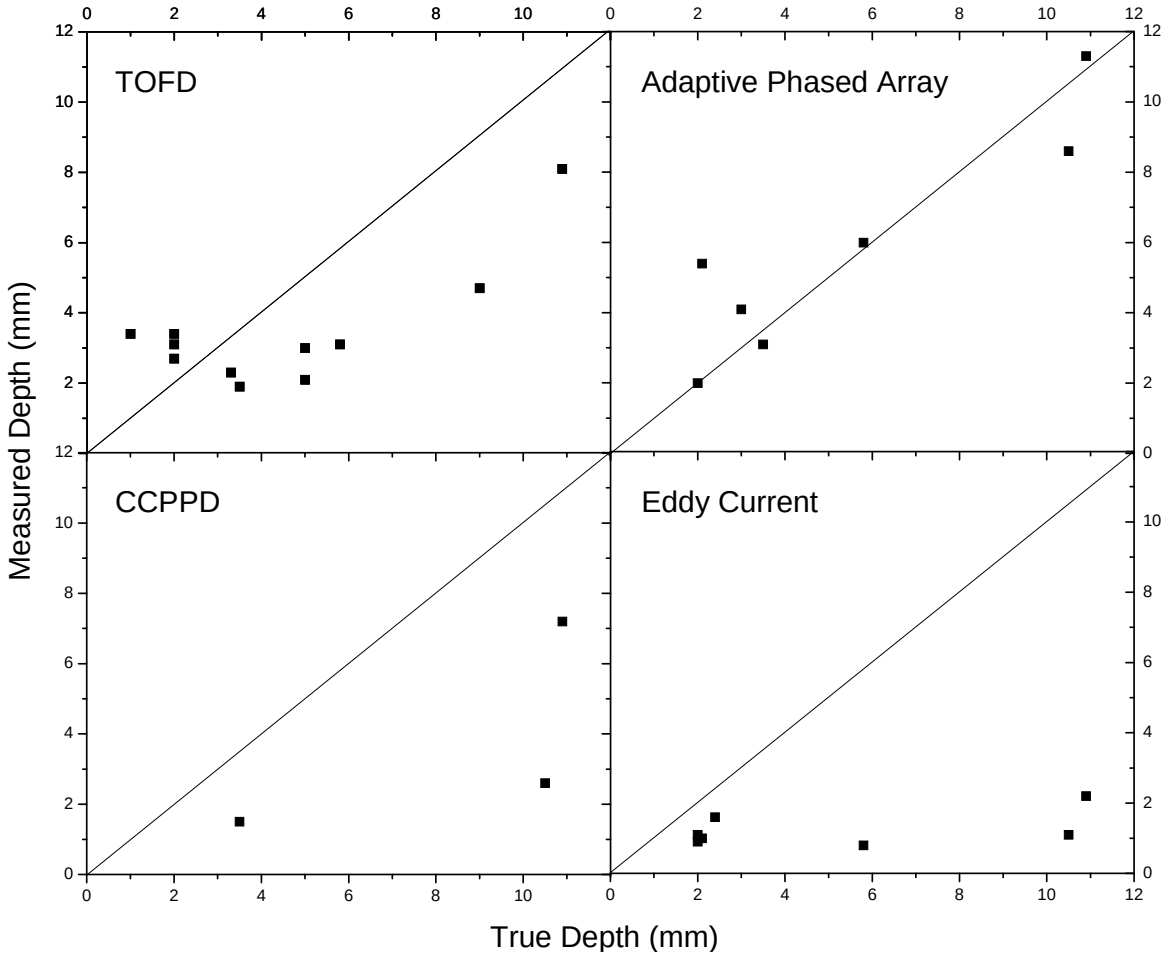

Figure 4.23 Depth Sizing Results for BMI Surfaces

The length-sizing results for the surface examinations contained enough observations to allow for a complex length-sizing regression. The results for each technique were analyzed, and the RMSE, standard deviation, bias, and 95% confidence intervals were determined.

The length-sizing results for the surface examinations showed that some techniques were able to accurately measure the lengths of the flaws. Team 16 had the most accurate length sizing, although it had only five observations in the data set. Several other teams achieved an RMSE of less than 5 mm. The results for each team are given in Table 4.27.

The cross-coil eddy current tests were able to accurately length-size the flaws that were detected, both with RMSEs on the order of 4 mm. The 400-kHz probe examination outperformed the 300-kHz but not by a statistically significant margin. The length-sizing regression for the cross-coil ECT is shown in Figure 4.24.

Table 4.27 Length-Sizing Results for Surface Examinations in BMI Test Blocks

Team	Observations	Technique	RMSE, mm	Standard Deviation, mm	Bias, mm
All	79		11.7	11.53	2.01
16	5	CCPPD	2.45	2.45	-0.1
373	20	Cross Coil ECT 300 kHz	3.94	3.94	-0.18
38	10	Array ECT 100 kHz	32.28	28.33	15.48
66	11	Adaptive Phased Array	4.7	4.55	-1.19
67	3	ICPD	5.46	1.86	-5.13
70	21	Cross Coil ECT 400 kHz	3.76	2.92	2.37
99	9	Array ECT 200 kHz	4.33	4.07	-1.49

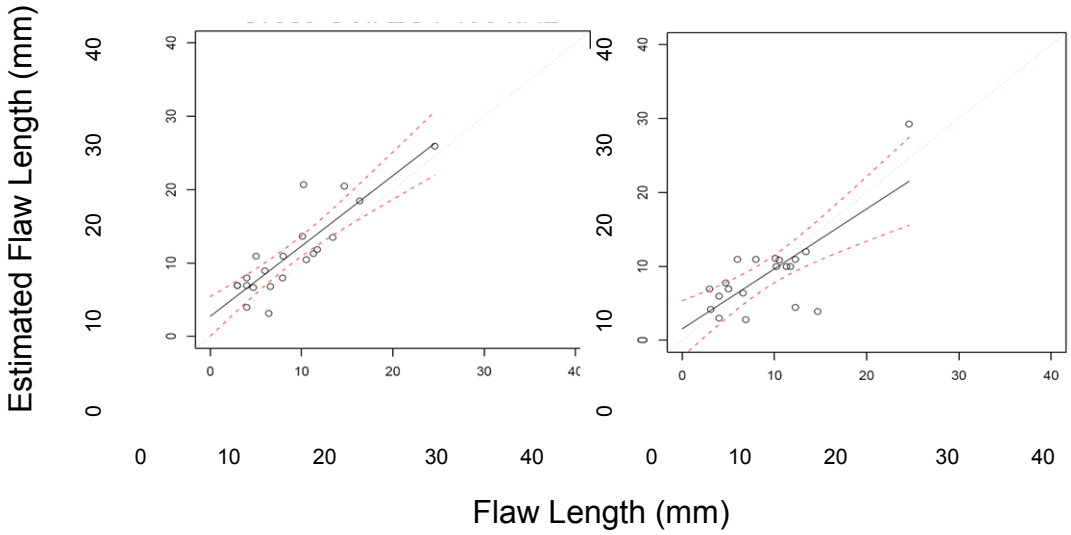

Figure 4.24 Length-Sizing Results for Cross-Coil Eddy-Current Probes in BMI Test Blocks

The array eddy current techniques were less effective than the cross-coil probes in this BMI round robin at length-sizing the flaws. The 200-kHz array outperformed the 100-kHz array probes. The length-sizing regression for the array probes is given in Figure 4.25.

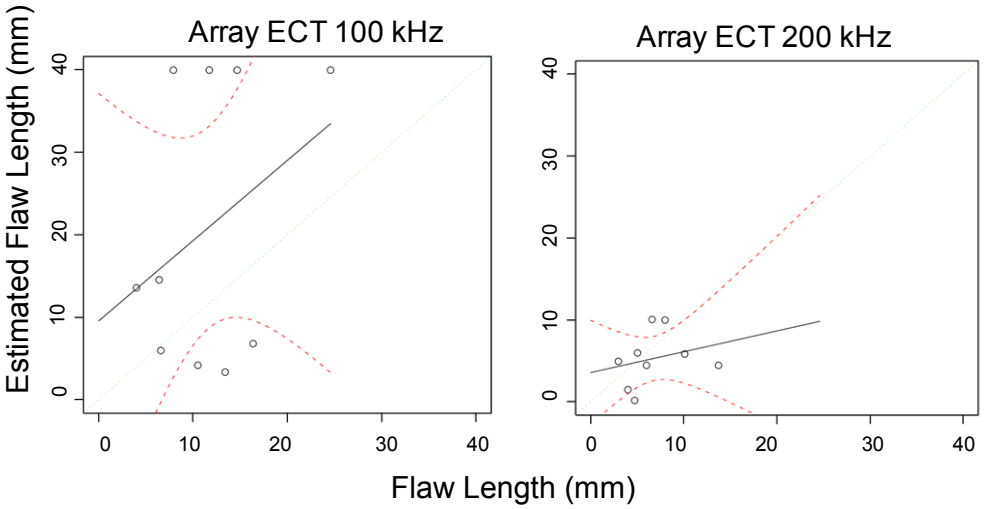

Figure 4.25 Length Sizing Results for Array Eddy-Current Probes in BMI Test Blocks

The length-sizing results for the closely coupled probe potential-drop (CCPPD) technique were very accurate, having the lowest RMSE error and standard deviation of any of the techniques, including the cross-coil eddy-current examinations. There were not enough observations for the induced current potential-drop (ICPD) to perform a meaningful analysis. The length-sizing results for the potential-drop techniques are presented in Figure 4.26.

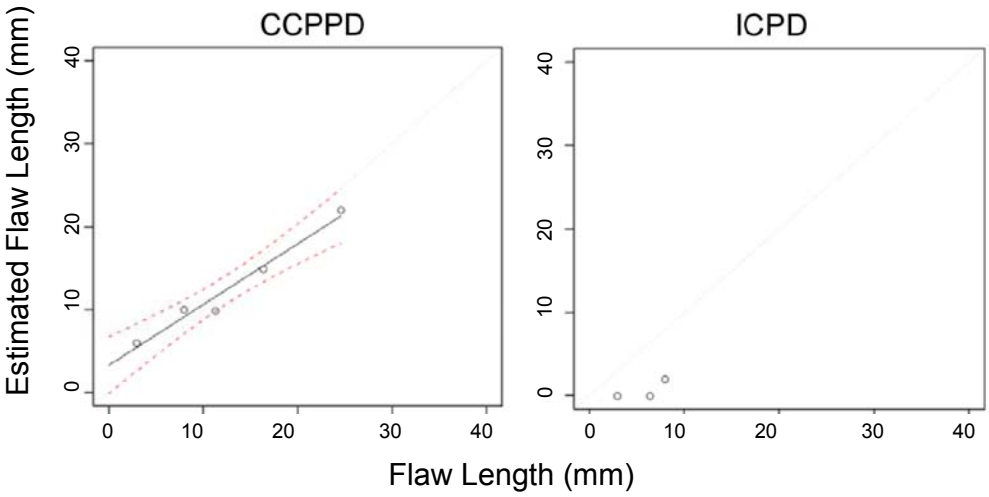

Figure 4.26 Length Sizing Results for Potential-Drop Techniques in BMI Test Blocks

The phased array examinations also were able to accurately size the flaws in the BMI test blocks. The RMSE was on the order of 5 mm, which is very similar to the results for the cross-coil eddy current examinations. The length-sizing results for the phased array examinations are presented in Figure 4.27.

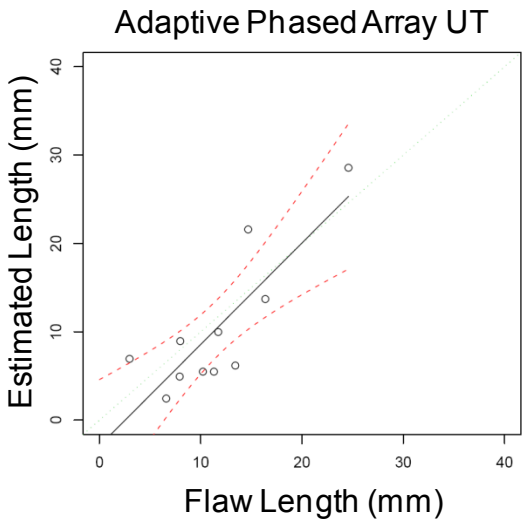

Figure 4.27 Length-Sizing Results for Adaptive Phased Array Ultrasound Techniques in BMI Test Blocks

5.0 Impact of PWSCC Detection and Sizing Performance with Respect to Component Integrity

Inservice inspections should detect degradation (e.g., cracking, wall thinning) before the degradation affects the component's integrity and functional requirements. The key elements of an inspection program include

1. an inspection method that ensures reliable detection and accurate sizing of flaws
2. an inspection program that addresses those locations that are most likely to experience degradation and/or whose failure could have the greatest impacts on the safety and operability of the plant
3. an inspection frequency such that degradation can be detected before it grows to unacceptable levels between successive inspections.

The PINC round-robin exercises described in this report have established probabilities of detection and sizing accuracies of a variety of inspection methods. The PINC round-robin exercises demonstrate that some of these methods can detect PWSCC cracks with relatively high detection probabilities (see Section 4.0). The timely detection of cracks in the field is, however, more difficult because PWSCC is characterized by long periods during which cracks initiate, which are then followed by relatively high crack growth rates. Therefore, even a very reliable inspection method can prove to be ineffective in preventing the failure of a component if the inspections are not conducted often enough to detect the degradation prior to loss of component integrity or function. As an example, an inspection may be performed just before a crack initiates and then the crack grows to a through-wall depth before the next cycle of the periodic inspections. An effective inspection program, therefore, requires an inspection interval consistent both with the smallest detectable crack and with the growth rates for this PWSCC crack.

Probabilistic fracture mechanics computer codes can predict reductions in component failure probabilities that result from a given inspection program as characterized by a given probability of detection and inspection frequency. Future calculations could be performed for components subject to degradation by PWSCC using available computer codes such as PRAISE (Harris et al. 1992) and PROLOCA (Rudland et al. 2006). Such calculations were beyond the scope of work for the present report, so results of similar calculations (Khaleel et al. 1995; Khaleel and Simonen 2009) for intergranular stress corrosion cracking of welds in stainless steel piping were applied as an alternative. These calculations are based on PWR piping welds at 288°C (550°F).

Although the cracking mechanism did not exactly match the current PWSCC concerns, the key features of an incubation period for crack initiation and a potentially rapid growth rate of the initiated cracks were addressed. Results of the calculations were used only to establish relative failure probabilities (i.e., with and without inspection); therefore, conclusions drawn from the calculations should be insensitive to inputs for the cracking mechanism. It should also be noted here that the calculations (Khaleel and Simonen 2009) did not address flaw sizing errors but rather assumed that any detected crack would be repaired without consideration of the measured flaw depth.

Probability of detection curves were a key input, and Figure 5.1 (the curve is taken from Khaleel and Simonen 2009 and the PINC data curve has been added) provides the curves used in the calculations. These curves are labeled *marginal*, *good*, *very good*, and *advanced* and cover a wide range of flaw detection capabilities, as exhibited in the round robin described in this report. These curves also cover the capabilities exhibited by inspection teams for qualification by ASME Section XI Appendix VIII performance demonstrations. The marginal and good POD curves describe teams that would have little chance of meeting the performance demonstration requirements. The very good and advanced POD curves would cover a range of teams that would likely and readily meet the requirements. The advanced POD curve would also represent the potential limit of current technology. The POD curve labeled *PINC DMW data* corresponds to the average performance of the *Conventional UT*, *Phased Array UT*, and *Conventional UT and Phased Array* from Table 4.6 as calculated by Khaleel and Simonen (2009). These performance curves were chosen because they approximate current field practice.

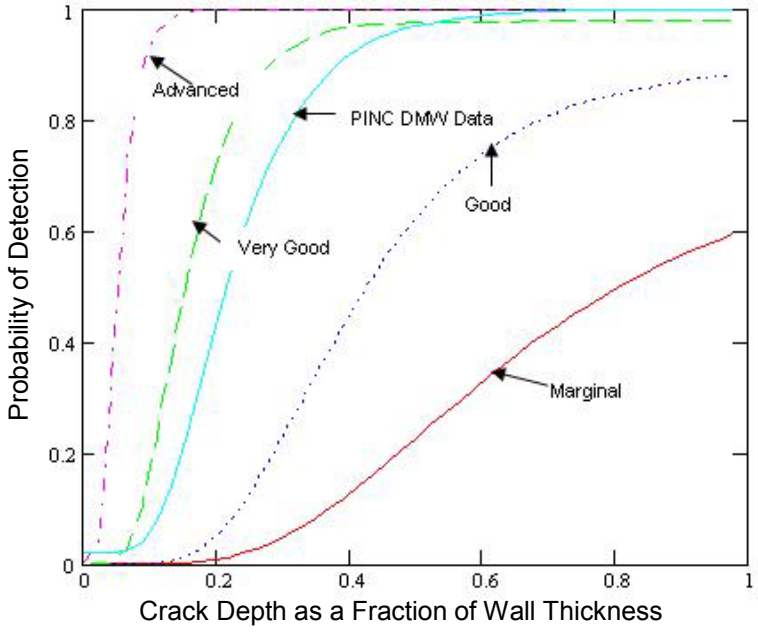

Figure 5.1 Probability of Detection Curves from Round Robin and Curves Used for Probabilistic Fracture Mechanics Evaluations

Evaluations were performed only for the POD data for dissimilar metal welds. Table 5.1 lists the same inspection teams and POD performance levels as given by Table 4.6 of the present report. In each case, the POD performance level for each team was represented by one of the four POD curves (e.g., *very good*) that most closely approximated the POD curve for the team of interest. This allowed results of the available probabilistic fracture mechanics calculations to be applied for the teams listed in Table 5.1.

Table 5.1 Probabilistic Fracture Mechanics Results for Individual Team PODs from PINC for DMW (based on calculations for "Intermediate Pipe" with wall thickness of 0.84 inch)

Team	POD for Flaw Depths of:			False Call Probability	Detection Technique	Selected POD Curve	Improvement Factor in Structural Reliability			
	5 mm	10 mm	15 mm				1 Yr Interval	2 Yr Interval	4 Yr Interval	10 Yr Interval
13	0.37	0.83	0.98	0.07	Phased Array UT	Very Good	4	3.1	1.8	1.4
22	0.52	0.52	0.53	0.51	Conventional UT	Good	2.5	2	1.4	1.2
28	0.42	0.6	0.76	0.26	Conventional UT	Good	2.5	2	1.4	1.2
30	0.24	0.43	0.65	0.11	Conventional UT	Good	2.5	2	1.4	1.2
38	0.78	0.96	0.99	0.36	Eddy Current	Very Good	4	3.1	1.8	1.4
39	0.36	0.47	0.59	0.26	Phased Array UT	Good	2.5	2	1.4	1.2
43	0	0	0	0.31	Potential Drop	Marginal	1.5	1.4	1.3	1.1
48	0.24	0.42	0.61	0.13	Conventional UT	Good	2.5	2	1.4	1.2
63	0.37	0.79	0.96	0.08	Conventional UT	Very Good	4	3.1	1.8	1.4
65	0.3	0.32	0.33	0.28	Potential Drop	Marginal	1.5	1.4	1.3	1.1
66	0.62	0.94	0.99	0.14	Phased Array + Conventional UT	Very Good	4.0	3.1	1.8	1.4
67	0.32	0.45	0.6	0.2	Potential Drop	Good	2.5	2.0	1.4	1.2
70	1	1	1	0.04	Eddy Current	Advanced	6.0	4.4	2.1	1.5
72	0.41	0.47	0.54	0.35	Phased Array UT	Good	2.5	2.0	1.4	1.2
82	0.44	0.53	0.61	0.35	Conventional UT	Good	2.5	2.0	1.4	1.2
96	1	1	1	0.06	Eddy Current + Conventional UT	Advanced	6.0	4.4	2.1	1.5

Four inspection intervals were addressed (1, 2, 4, and 10 years) covering a range of intervals, from inspections at every outage to the standard 10-year interval prescribed by the ASME Code Section XI. The final four columns give Improvement Factor in Structural Reliability, which is defined as the ratio of the calculated failure probability for no ISI to the failure probability given ISI for the indicated combination of POD curve and inspection interval. The failure criterion used in this evaluation was that a pipe may fail by either breakage or leakage. For example, an advanced POD curve in combination with a 1-year inspection interval gives an improvement factor of 6.0. Based on the definition of factor of improvement, this example shows that given six failures with no ISI inspection, an ISI program that required inspections on a 1-year interval would reduce the six failures to one failure.

Clearly the advanced POD curve with a 1-year ISI interval gives the largest improvement factor of 6.0. On the other hand, the marginal POD curve in combination with a 10-year ISI interval gives the smallest improvement factor of 1.1. This factor of 1.1 provides essentially no benefit (only a 10% reduction in the number of failures). Any benefit comes only in the unlikely case that an inspection is performed at the most favorable time when a growing crack is at a relatively large and detectable size.

The trends of Table 5.1 are consistent with the larger set of results of Khaleel and Simonen (2009) that address fatigue failures in addition to stress corrosion cracking. These results show only a few cases that give improvement factors of 10 or larger, and then only for the highest performing of the POD curves and short ISI intervals. In this regard, a reduction in failure probability by a factor of ten should be considered an effective mitigation measure for active degradation mechanisms, particularly if augmented ISI is used in combination with other forms of mitigation (e.g., stress improvement, water chemistry improvements). In other cases, an inspection program with an improvement factor significantly less than a limiting level of 10 still could provide a valuable contribution to structural integrity. In such cases, the benefits of ISI would provide a means to verify the effectiveness of other mitigating measures.

The current evaluation for PWSCC indicates that the better round-robin POD performance levels in combination with relatively small inspection intervals could make an effective contribution to component integrity. However, additional probabilistic fracture mechanics calculations are recommended to support the preliminary conclusions. These evaluations would not require an extrapolation from calculations originally performed to address IGSCC and would include inputs to address residual stresses and crack growth rates for welds and materials of concern for nickel-alloy components, such as alloy 600 and 82/182 weld metals and alloy 690 and the associated 52/152 weld metals.

This evaluation does show that it may be beneficial to tie the inspection interval length to the crack growth rates in the materials of interest. Materials with very high crack growth rates may require inspections at every outage to provide a sufficient improvement factor.

6.0 Field Experience with PWSCC

Cracking observed in the early 1990s in reactor components in France and other countries was attributed to PWSCC, leading to replacement of reactor vessel heads, piping, and other components. Leakage was discovered at the Oconee plant in the United States from a control rod drive mechanism penetration fabricated using Alloy 600, resulting in deposits of boric-acid crystals on the vessel head. Further investigation led to the identification of PWSCC cracks in the reactor penetration tubes and attachment J-groove welds. Circumferential cracking of CRDM nozzles has been identified at Oconee Units 2 and 3 and Crystal River Unit 3. An extreme consequence of such cracking was illustrated by the discovery of wastage on the Davis-Besse reactor vessel head. More recently, boric-acid deposits and NDE indications found on the South Texas Project BMI nozzles have been attributed to PWSCC. Cracks also have been found in reactor nozzle hot-leg DMWs at the V.C. Summer plant in the United States and at the Ringhals plant in Sweden, providing further evidence that PWSCC is a generic concern.

Circumferential cracking associated with safe-end piping welds is important because of the potential for a large loss of coolant inventory, and the cracking of CRDM nozzle welds and circumferential cracking of CRDM nozzle base metal is important because of the potential for control rod ejection and loss-of-coolant accident (LOCA). Recent events at nuclear stations related to damage in Alloy 600 base material and Alloy 182/82 welds have prompted industry initiatives directed at reexamining the damage mechanisms, damage morphology, and examination practices of the affected components. These events have given high visibility to the PWSCC phenomenon and high priority to work on understanding this cracking mechanism.

NRC Generic Letter 97-01 (1997) provides a summary of the domestic and international cracking experience on reactor pressure vessel heads from PWSCC. Various aspects of the problem of PWSCC cracking have also been addressed by a number of research programs within the United States and in other countries. The data collected to date, however, are sparse, and the significant factors leading to crack initiation and governing crack growth rate are not well understood. Complicating factors include chemistry variations in the nickel-base alloy components, evolution of the primary water chemistry within an operating cycle, and residual stresses and possible embedded flaws resulting from weld repairs. In addition, detection and characterization of PWSCC-related flaws through NDE have proven to be particularly difficult in components with complicated geometries. The occurrences of cracking in the United States have been identified initially through indirect means, specifically the discovery of boric-acid deposits resulting from through-wall cracking in the primary system pressure boundary. Such leakage degrades a layer of plant defense-in-depth and should be prevented whenever possible.

Although many different aspects of this issue need to be addressed, NRC proposed research concentrated in two interrelated areas. Task 1 focused on characterizing the morphology of PWSCC cracks, which has been identified as a contributing factor to the difficulties experienced in detecting and sizing cracks in the field. As part of the characterization, work addressed refining the ability to distinguish PWSCC cracks from other flaws with similar features, such as hot cracks in welds. Task 2 focused on the nondestructive testing aspects, including such

topics as the manufacture and simulation of PWSCC cracks in test assemblies for use in assessing the effectiveness and reliability of NDE techniques.

The research addresses the nickel-base alloys used as pressurized water reactor (PWR) pressure boundary components including dissimilar metal welds and reactor pressure vessel (RPV) head penetrations. Primarily, the research focused on the Alloy 600/182/82 group of materials, but replacement materials (Alloys 690/152/52) were not excluded.

6.1 Swedish Experience

Sweden has applied a qualitative risk-based approach to inservice inspection for many years. It is based upon a matrix combining potential risk of damage in a given system with the consequences of failure, and the anticipated severity of subsequent radioactive release. The matrix is illustrated in Table 6.1.

Table 6.1 Risk-Damage Matrix

	Consequence Index		
Damage Index	**High (I)**	**Medium (II)**	**Low (III)**
High (1)	A	A	B
Medium (2)	A	B	C
Low (3)	B	C	C

The consequence index expresses in a qualitative manner the likelihood that a crack or other degradation process will result in fuel damage, discharge of large amounts of radioactive substances, or other forms of damage that could lead to health problems or an accident. In nuclear power plants, the consequence index is determined mainly by the margin to such consequences as the result of a break or malfunction of the specific component or part of a system. Two aspects are important when determining the assignment of the consequence index:

- system margins – how many system circuits are essential in relation to the number available
- thermal margins – how much the fuel can be heated up in relation to acceptable margins.

The damage index expresses in a qualitative manner the likelihood for crack formation or other degradation process occurring in the specific component or system part. The damage index is determined by the loading, environment, and material in relation to the dimensions of the component. Components or parts that may be exposed to loads or other conditions known to result in damage or degradation should be assigned the highest damage index. Components not expected to be subjected to loads or other conditions that will result in damage are assigned damage index II, and components exposed to minimal loads or other benign operational conditions are assigned damage index III.

In systems in which stress corrosion cracking cannot be excluded, the following conditions are considered reason for assigning damage index I to a component:

- high temperatures (>150°C) and high carbon content (>0.04%) in stainless steel, including stabilized austenitic stainless steels
- high temperatures (>150°C) and cold-worked stainless steel that has not had a subsequent heat treatment
- high temperatures (>150°C) and nickel-base alloys such as Alloys 600, and X-750 with compositions and heat treatments that experience has shown are sensitive to stress corrosion cracking
- high neutron fluence (5.10^{20} n/cm^2, E > 1 MeV).

The criteria were first adopted by the Swedish Nuclear Power Inspectorate (SKI) regulations SKIFS 1994:1 concerning mechanical components in nuclear facilities and have been applied since that date. In the more recent versions of the regulations, the specific conditions listed above are no longer included as part of the regulations but are included in the utilities documentation approved by SKI.

In the current version of the regulations concerning mechanical components (SKI 2005, SKIFS 2005:2), the use of quantitative risk-based inspection programs is permitted. One of the utilities has been granted permission to apply a modified version of the Westinghouse Owners Group methodology but did not have any SCC-sensitive materials to be considered.

The inspection interval is determined on the assumption that a crack exists in the component or system of a size for which the applicable inspection method has been qualified. The inspection interval is then calculated as the time required for the crack to grow to a critical size using crack propagation data for the specific material/environment combination. The same crack propagation data are used when a crack is found in a component to permit the component being kept in service until a planned repair or replacement can be performed. Qualification of inspection techniques has to be performed using realistic (not geometric) cracks in test blocks made from typical material. Inspection qualification is required for NDE systems that inspect Class 1 and 2 mechanical components.

6.1.1 Development of Inspection Qualification for PWSCC in Sweden

When the PWSCC cracking was found in safe ends in Ringhals 3 and 4 in 2000, destructive examination showed that the NDE system had underestimated the crack depths. The NDE systems used at Ringhals 3 and 4 had been qualified. SQC and Swedish utility Ringhals began to evaluate the inspection results in accordance to qualification to determine why eddy current and through-wall sizing did not work as expected. The results of the investigation showed that all defects were found with UT; however, the investigation showed that the prerequisites of defect type and knowledge of defect simulation failed.

The results of the investigation described above led to a research project, sponsored by Swedish utilities, to investigate the degradation mechanism (e.g., PWSCC) and to develop a simulation technique to be used for test-piece simulations. The independent organization, SQC Qualification Centre, led the project that compared the destructive evaluation (DE) results from the field cracks to known simulation methods. The real cracks were tight and had branches in

directions, making it very hard for NDE systems to follow the crack propagation. Important conclusions (Wåle 2002) were that the cracks were oriented both axially and circumferentially to the welds. The cracks were found in weld material of the type Alloy 182 and Alloy 82. The cracks were located in the weld material and the buttering. The area of the cracks is repaired regions. One characteristic of the PWSCC cracks is that the crack width decreases close to the surface. This type of crack has been found in both PWR- and boiling water reactor (BWR) types of reactors.

In 2005, SKI initiated another project to investigate statistics of all cracks in Swedish plants, including the PWSCC. This was an update of the report published in 1995 (Ekstrom and Wåle 1995) but now with 10 more years of data and experience (Wåle 2006). The report describes and evaluates the morphology of different mechanisms and is also an important tool when developing NDE systems for different damage mechanisms. This report also included an evaluation of the PWSCC morphology.

6.1.2 Simulated PWSCC Cracks

Cooperation between the qualification body, inspection companies, crack simulation companies, and licensees made it possible to develop a new technique to produce cracks with better agreement to real PWSCC cracks.

One task within the project was to identify relevant crack characteristics to handle when simulating cracks. These were identified as the crack width at the surface, unbroken ligament (both in depth and length), crack morphology as the most important, and specific characteristics for the PWSCC mechanism. Different simulation techniques were tried and compared to the DE result of the real field cracks. The technique that most closely resembled service-induced cracks was a new type of solidification crack technique. The solidification technique to produce these cracks involved a mechanical tightening process. This process achieved a realistic simulation of the unbroken ligaments characteristic of the PWSCC mechanism.

One of the significant outcomes that developed from the new crack specification was that all qualified procedures for detecting and sizing PWSC cracking needed to be requalified. In the subsequent process to requalify the NDE systems, the result was that all inspection companies had to reconstruct their procedure to be able to characterize and size the defects in light of improved understanding of the crack morphology.

6.1.3 Comparison of the Signal Response from the UT and EC Inspection in the Plants and the Response from the Inspections of the Simulated Cracks

After establishing a technique to simulate PWSCC cracks, a task was initiated that characterized and mapped the defect characteristics of the PWSCC found in Alloy 182 that affect the NDE signal response (SQC 2003). The results for this task are shown in Table 6.2 and Table 6.3. Table 6.2 provides the results to UT signal responses, and Table 6.3 provides the results for eddy current signals. These variables should be taken into account when manufacturing simulated cracks to be used for detecting with pulse echo, sizing with pulse echo–TOFD, and also when using eddy current.

Table 6.2 Defect Characteristics Found Significant for Ultrasonic Testing

Defect Characteristics	Parameter Study
Defect width in depth	Min/max > 5 µm–0.3 mm
Unbroken ligaments in depth	Number of ligaments: 4–17 Size: 0.14 mm–0.8 mm
Unbroken ligaments in length	0.6 mm–2 mm
Crack tip radius	7 µm–40 µm
Width at surface	10 µm–35 µm
Surface roughness	Rz = 187 µm–471 µm λ0 = 456 µm–650 µm
Branching	0.25–0.60/mm
Crack shape in depth	Winding

Table 6.3 Defect Characteristics Found Significant for Eddy Current Testing

Defect Characteristics	Parameter Study
Defect width at the surface (electrical contact between the surface of the crack)	10 µm–35 µm
Unbroken ligaments at the surface	Length = 1 mm–4 mm Depth = 0.6 mm–2 mm
Unbroken ligaments in the depth	Number: 2–9 Size: 0.14 mm–0.80 mm
Crack shape in depth	Winding
Crack shape in length	Winding

6.2 United States Experience

The experience in the Unites States with primary water stress corrosion cracking (PWSCC) is extensive and includes PWSCC in components ranging from pressurizer components to bottom mounted instrumentation nozzles. A detailed list of experiences with cracking in Alloy 600 material is contained in Appendix H. This appendix uses information from NUREG-1823, *U.S. Plant Experience With Alloy 600 Cracking and Boric Acid Corrosion of Light-Water Reactor Pressure Vessel Materials,* published in April 2005.

One of the first incidents of PWSCC in the U.S. was the discovery of leaks in pressurizer instrument nozzles (in 1986 at San Onofre Nuclear Generating Station, Unit 3) and heater sleeves (in 1987 at Arkansas Nuclear One). In 1989, 20 leaking heater sleeves were found at Calvert Cliffs, Unit 2 (8 additional sleeves had non-leaking, axial crack indications). These incidents of field cracking were correlated with temperature. The vulnerability of these components may have been enhanced by the higher temperatures at the pressurizer penetrations than other components, such as vessel head penetrations.

Stress corrosion cracking of a dissimilar piping weld occurred at V.C. Summer in 2000. The cracking was discovered during visual testing, in which a large quantity of boric acid deposits

(≈ 160 kg) were discovered. The cracking was investigated using ultrasonic inspections, eddy current, and visual testing.

Control rod drive mechanism nozzles and other vessel head penetration nozzles welded to the upper reactor vessel head are may be subject to primary water stress corrosion cracking. The issue is a potential safety concern because a nozzle with sufficient cracking could break off during operation. This would compromise the integrity of the reactor coolant system pressure boundary—one of three primary barriers that protect the public from exposure to radiation. The break may also result in the ejection of a control rod, which could damage nearby components.

On August 3, 2001, the NRC issued Bulletin 2001-01, "Circumferential Cracking of Reactor Pressure Vessel Head Penetration Nozzles" (NRC 2001), to licensed holders of U.S. PWRs following the discovery of cracked and leaking nozzles in 2000 and 2001. In the bulletin, the staff requested information from PWR licensees about the structural integrity of these nozzles at their facilities. In response to the bulletin, licensees provided their plans for inspecting their nozzles and the outside surfaces of their upper reactor vessel heads to determine whether any nozzles were leaking. Inspections by licensees during fall 2001 revealed vessel head penetration nozzle cracks at Three Mile Island Unit 1, Crystal River Unit 3, North Anna Unit 1, and Oconee Unit 3.

On August 9, 2002, the NRC issued Bulletin 2002-02, "Reactor Pressure Vessel Head and Vessel Head Penetration Nozzle Inspection Programs" (NRC 2002). The bulletin suggested that visual inspections of upper reactor vessel heads and their nozzles may need to be supplemented with non-visual nondestructive examinations to ensure that the structural integrity and leakage integrity of the nozzles is maintained. Bulletin 2002-02 requested that PWR licensees provide information about their inspection programs and plans to supplement existing visual inspections with volumetric and surface examinations. Licensees responded with descriptions of inspection plans for at least the first refueling outage following the issuance of the bulletin. Many did not offer any long-term inspection plans but instead opted to follow guidance being developed by the Materials Reliability Program, an industry-sponsored research organization.

Inspections performed at several PWRs in 2002, including those performed at the Davis-Besse Nuclear Plant, found leakage and cracks in vessel head penetration nozzles or J-groove welds that have required repairs or prompted the replacement of the vessel head. As a result of continuing concerns regarding licensee inspection programs in this area, the NRC issued an order on February 11, 2003, to all PWR licensees in the United States (NRC 2003). The order requires specific inspections of the vessel head and associated penetration nozzles based on their susceptibility to PWSCC. The order may be accessed at the following address on NRC's website: http://www.nrc.gov/reactors/operating/ops-experience/vessel-head-degradation/vessel-head-degradation-files/order-rpv-inspections.pdf.

Twenty-six units were identified by the Electric Power Research Institute (EPRI) Materials Reliability Program as having a high susceptibility to nozzle cracking. Inspections by licensees performed after issuance of the latest bulletin and order revealed nozzle or J-groove weld cracks and/or leaks at Oconee Unit 2, North Anna 2, Arkansas Nuclear One Unit 1, St. Lucie Unit 2, Milestone Unit 2, and Beaver Valley Unit 1. The utilities owning the Oconee, Surry,

Davis-Besse, and North Anna nuclear stations have replaced or are in the process of replacing their upper reactor vessel heads. Approximately 20 other units have announced plans to have their upper reactor vessel heads replaced within the next few years. A detailed list of experiences with cracking in Alloy 600 material is contained in Appendix H. This appendix uses information from NUREG-1823, *U.S. Plant Experience With Alloy 600 Cracking and Boric Acid Corrosion of Light-Water Reactor Pressure Vessel Materials,* published in April 2005.

One instance of a bottom mounted instrumentation nozzle developing stress corrosion cracking in the US occurred at the South Texas Project Unit 1 in 2003. The cracking was discovered by visual inspection of the lower RPV head, which showed boric acid deposits. While there has only been one instance of cracking of a BMI in U.S. reactors, the bottom head cannot be easily repaired and it would be challenging to replace.

6.3 Japanese Experience

In the history of operation of PWR plants in Japan, which started in 1970, PWSCC had not been experienced with the exception of steam generator (SG) tubing until the early 2000s.

In 2003, a trace of leakage was found by visual inspection at the top of the PRZ where the safe-end was welded with nickel alloy material to a relief valve nozzle in Tsuruga 2 plant. PWSCCs including through-wall crack were identified in the DMW by the subsequent investigations. It could be the first PWSCC failure that occurred in the nickel components other than SG tubing in Japan.

The following year (2004), another leak was found at vessel head penetration (CRDM nozzle) of Ohi 3 plant. This failure was also attributed to PWSCC at the weld with nickel-alloy material.

In 2007, DMW failure was found in larger sizes of DMW of SG nozzles of Mihama 2 plant by ECT, which was performed prior to the mitigation process. Similar PWSCC indications have been found in several other plants as a result of ECT for SG nozzles. Furthermore, an ECT indication due to PWSCC was found in a DMW of a reactor vessel (RV) outlet nozzle of Ohi 3 in 2008.

In all, Japan experienced two different types of failures within the pressure boundary among three categories of nickel-alloy components; that is, DMW, CRDM, and BMI. Another indication was found in a BMI nozzle bore of the Takahama 1 plant in 2003, although it was thought to be spurious and was not confirmed as a true defect or PWSCC.

In the following paragraphs, a more detailed description is presented for each category.

6.3.1 DMW

Failures of DMWs of alloy 600 materials in overseas plants (i.e., V. C. Summer and Ringhals 3 and 4) were reported in 2000. Since then, Japanese PWR utilities were concerned about the possible occurrence of PWSCCs in such components. Unfortunately, similar phenomenon was first identified in one of the Japanese PWR plants three years later.

Tsuruga 2 stopped operation for its 13th annual inspection on September 5, 2003. Four days later, there was a trace of leakage observed at the relief valve nozzle located at the top of the PRZ after removal of insulation materials. Subsequent investigation identified multiple axial cracks at two locations (90° and 315°) in DMW connecting safe-end to the nozzle, which included a through-wall crack. The following UT inspections performed for other nozzles of the PRZ revealed another axial crack indication in one of three safety valve nozzles.

Detailed investigation including destructive examination was made on the defected relief valve nozzle weld to show the following results.

- Cracks were interdendritic and branched in nickel-base weld metal.
- Repair welding made during fabrication of PRZ might cause higher residual stress to initiate PWSCC with plant operating stress.
- Cracks were axial and extended only in the weld metal. Therefore, the detected cracks did not cause safety issues.

It could be the first PWSCC failure that occurred in the nickel components other than SG in Japan.

Affected nozzles were finally repaired by welding with replacement safe-end spool pieces and alloy 690 weld metal.

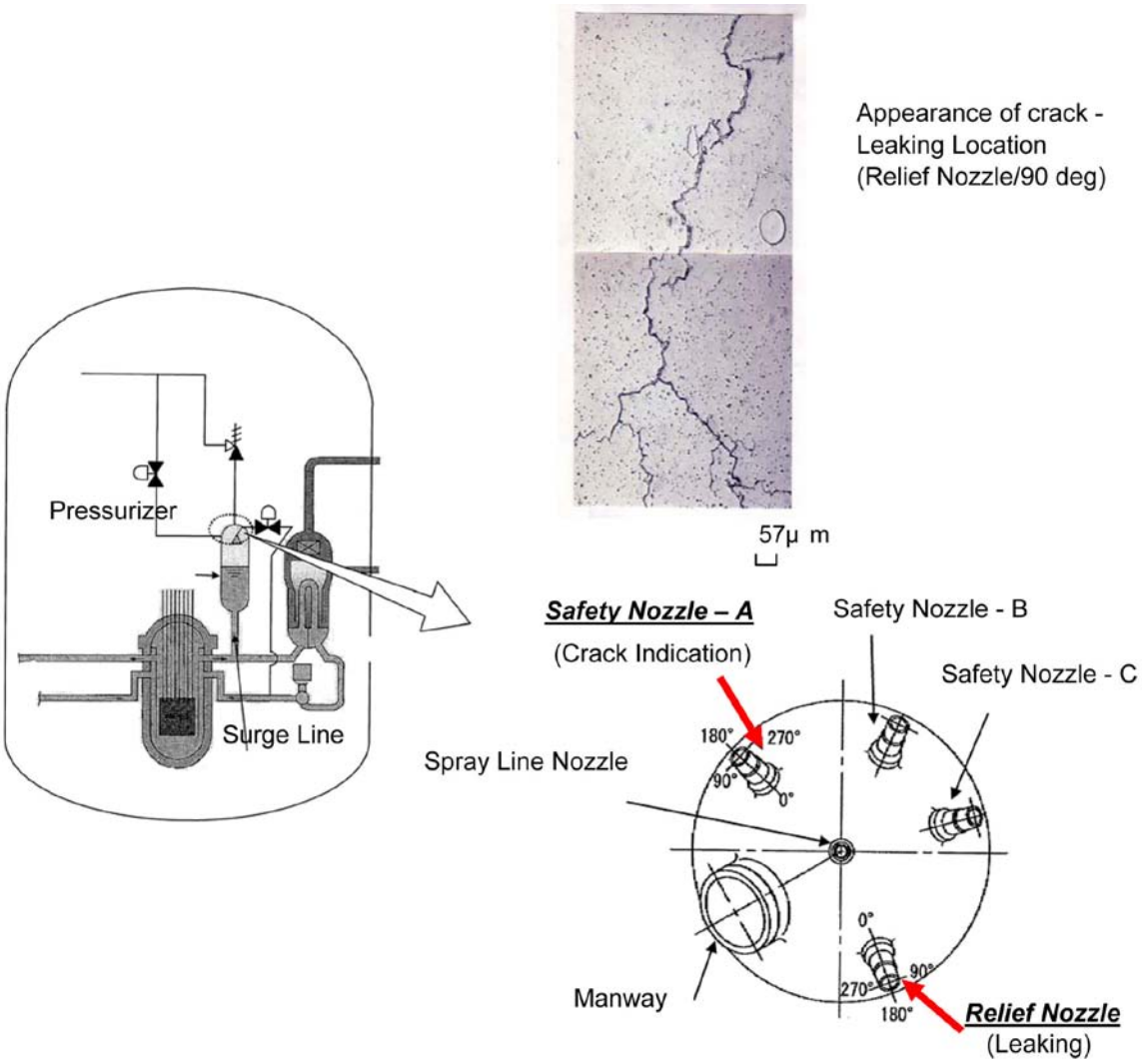

Figure 6.1 DMW Failures of Pressurizer Nozzles in Tsuruga 2

In the continued efforts of preventive maintenance of nickel-alloy components by Japanese PWR utilities, ultrasonic shot peening (USP) was determined to apply to alloy 600 DMWs of SG nozzles for mitigation. When conducting USP, the inside surface of the SG nozzle was to be inspected by ECT and VT before USP operation to ensure the effectiveness of mitigation.

In September 2007, when inside surface of inlet nozzle of A-SG in Mihama 2 plant was scanned by ECT prior to USP, 13 indications were detected. One of them was also identified by VT. In addition, PT was applied to verify all 13 Indications as relevant Indications. The largest was 17 mm in length by PT, and approximately 13 mm in depth by UT. These defects were further investigated by micro printing and by destructive methods. The results were as follows.

- The largest crack was formed with multiple small axial cracks of length from 3 mm to 5 mm.
- Maximum depth of the crack was about 11.5 mm.

- Cracks were considered to be intergranular in nature.
- One of cracks was different from the others in location; that is, all the cracks were within nickel-base material except one that was found in a stainless steel safe-end.

Similar ECT indications have been found in several other plants during their USP efforts that followed operation at Mihama 2. Alloy 600 DMWs of SG nozzles have been inspected as listed in Table 6.4.

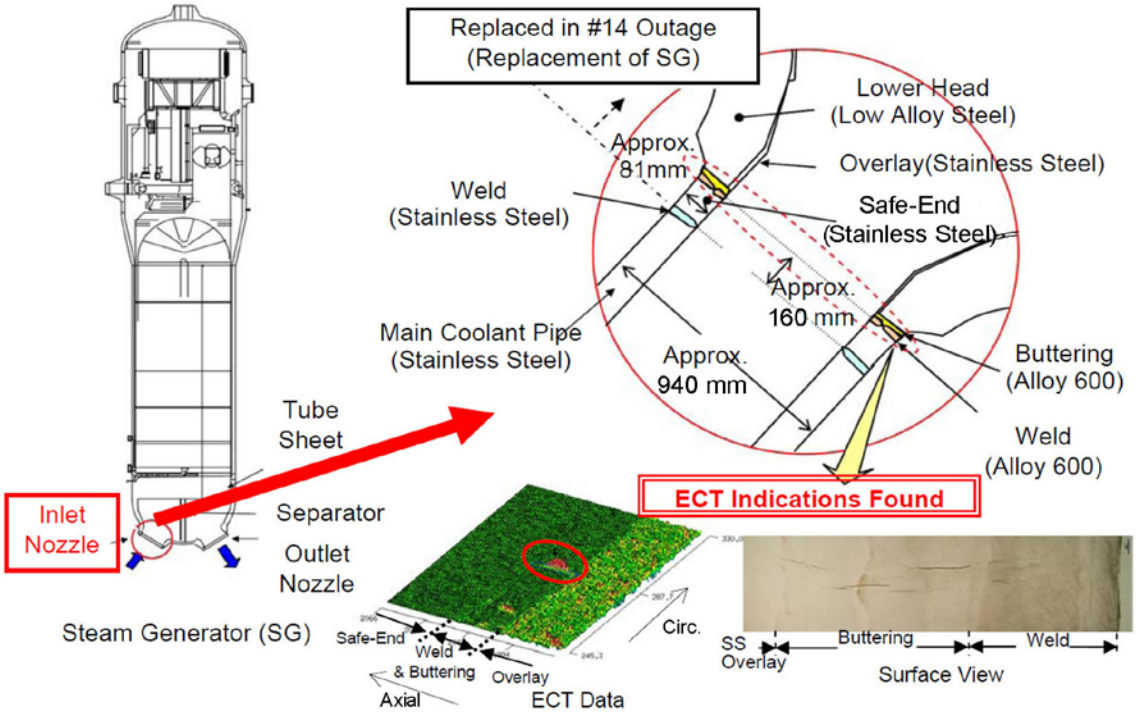

Figure 6.2 DMW Failure of Steam Generator Nozzle in Mihama 2

Table 6.4 SG Nozzle DMW Inspection Results

Plant	Material	Operating Hours (as of Dec. 31, 2008)[(a)]	SG Replacement	Inspection Result[(b)]	Remarks
Takahama 3	Alloy 600/132	179 x 10^3	---	**X**	
Takahama 4	Alloy 600/132	178 x 10^3	---	**X**	
Sendai 2	Alloy 600/132	174 x 10^3	---	**X**	
Tsuruga 2	Alloy600/132	152 x 10^3	---	**X**	
Tomari 1	Alloy 600/132	148 x 10^3	---	**X**	
Tomari 2	Alloy 600/132	133 x 10^3	---	**X**	
Ohi 3	Alloy 600/82	124 x 10^3	---	---	
Ohi 4	Alloy 600/82	122 x 10^3	---	---	
Genkai 3	Alloy 600/82	115 x 10^3	---	---	
Ikata 3	Alloy 600/82	109 x 10^3	---	---	
Takahama 2	Alloy 600/82	104 x 10^3	Yes	**X**	
Genkai 1	Alloy 600/82	102 x 10^3	Yes	**X**	Defect was shallow enough to be removed by grinding
Ohi 1	Alloy 600/82	97 x 10^3	Yes	---	
Mihama 2	Alloy 600/82	96 x 10^3	Yes	**X**	
Genkai 4	Alloy 600/82	90 x 10^3	---	---	

(a) Hours after SG replacement for the plants with SG replaced.
(b) **X**: Indication detected, ---: No indication

To DMWs of RV nozzles, a water jet peening (WJP) process has been applied in Japan since 2005. A small crack indication was detected in a DMW of one of the RV outlet nozzles by ECT performed prior to WJP at Ohi 3 in March 2008. This was verified by VT to be branched and considered to be similar to PWSCCs that had been found in DMWs of SG nozzles. No indications were detected in the other three outlet nozzles and four inlet nozzles of the Ohi 3 RV.

The depth of this crack could not be sized well by UT. It was decided that the crack would be removed by grinding, with the assumption that the crack was relatively shallow. Then, the grinding and ECT/VT process was iterated. This sequence, though, continued much more than anticipated. It ended up with the concavity of about 21 mm in depth, to ensure the crack had been completely removed.

The plant resumed operation in November 2008.

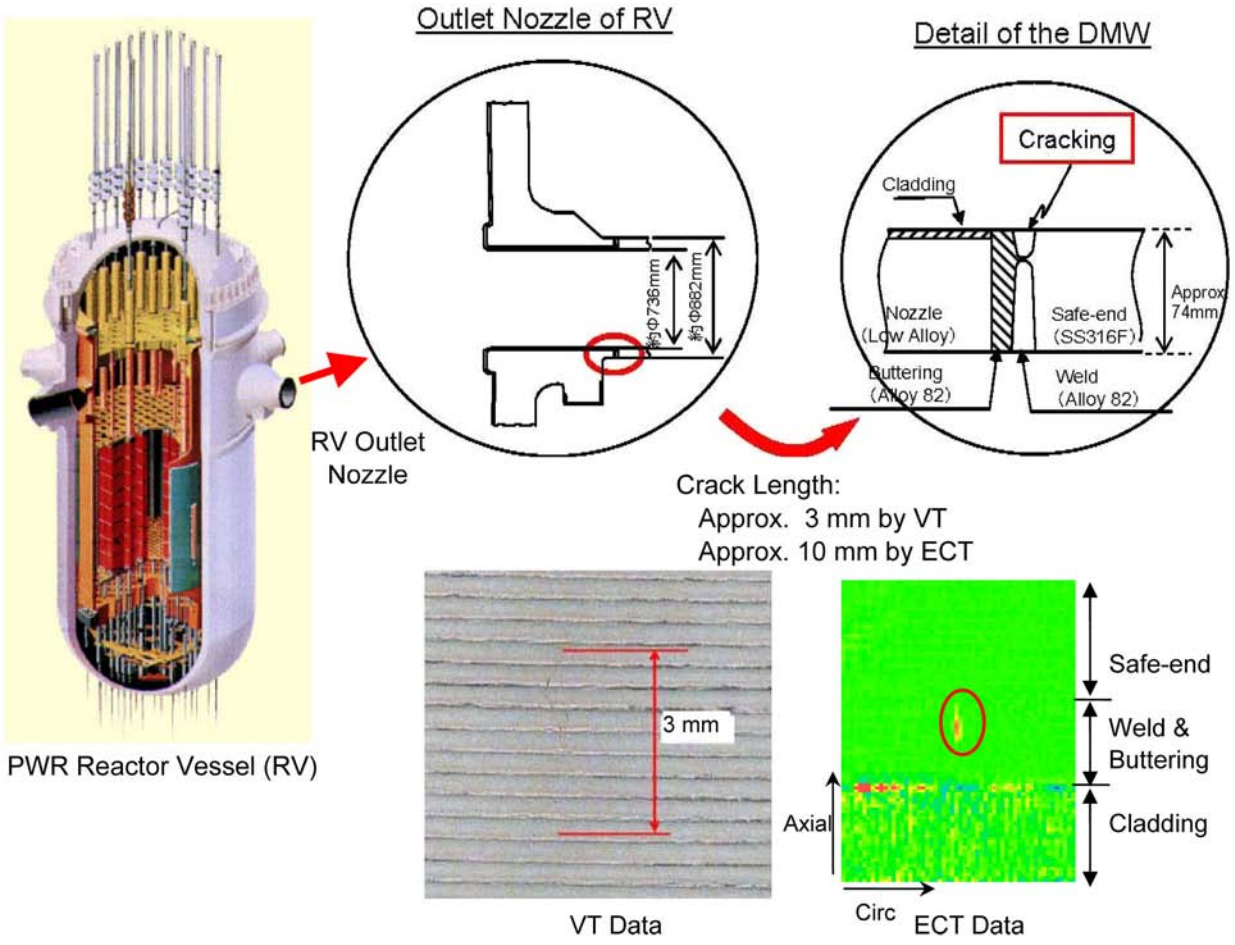

Figure 6.3 DMW Failure of Reactor Vessel Outlet Nozzle in Ohi 3

6.3.2 CRDM

Base materials (Alloy 600) of reactor vessel head penetrations (RVHPs) have been inspected in Japan since the early 1990s, and understanding of the inherent susceptibility to PWSCC of Alloy 600 materials led to preventive vessel head replacements for older Japanese PWR plants. However, it had not been well recognized that possible failure at J-groove welds could pose any short-term risk, until the Ohi 3 event.

On May 4, 2004, bare metal visual testing performed during the tenth annual inspection outage of the Ohi 3 plant revealed a sign of leakage at the CRDM nozzle. There were boric deposits at two nozzle locations, No.47 and No.67. However, subsequent investigation including PT, ECT, UT, and He leak testing revealed that there was no indication of a defect at No. 67 CRDM, and that a defect existed at the J-groove weld of No. 47 CRDM nozzle that caused leaking. Metallographic analysis revealed that cracks branched along the dendrite within the J-weld, and the root cause was considered as follows.

- High tensile residual stress due to no buffing after grinding in a particular area on the J-weld.
- Crack initiated by PWSCC. (The possibility for the initial crack to be other defects such as weld defects cannot be denied.)
- The crack went through the J-weld from the J-weld surface in the radial direction (upper side) due to PWSCC in the plant operating condition.
- Crack passed through the connected root between the J-weld and the nozzle.

In order to maintain the integrity for the RCS pressure boundary and protect PWSCC propagation, weld repair had been performed to the affected weld by using alloy 690 weld material before restart of the plant. This vessel head was replaced during the 12th annual inspection outage of Ohi 3.

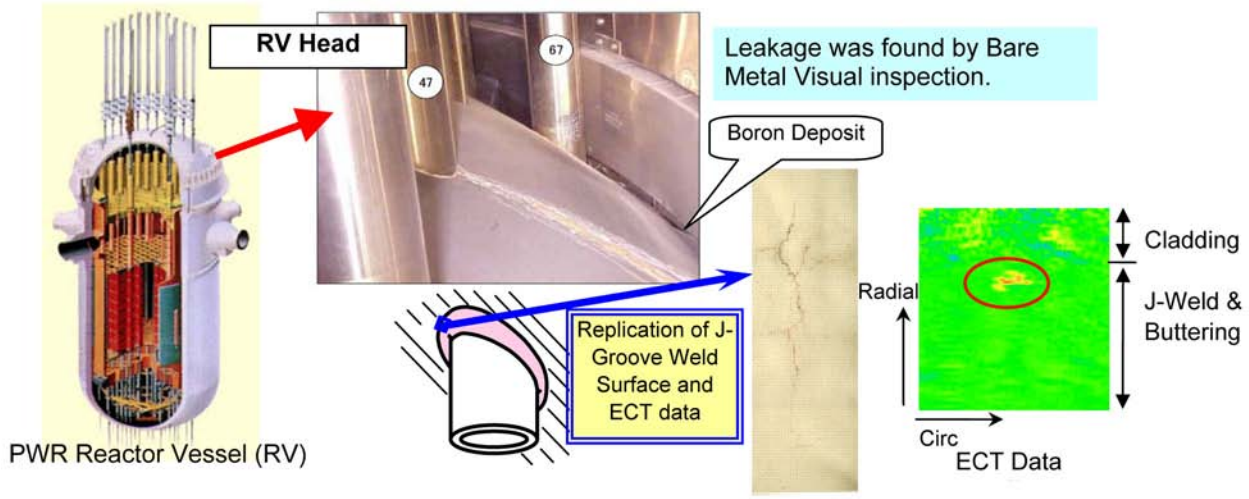

Figure 6.4 Failure of CRDM J-Groove Weld in Ohi 3

6.3.3 BMI

Among the many components to which alloy 600 material is applied, BMI is considered as one of the most important parts because of its difficulty of repair and replacement. In most of the PWR plants in Japan, BMI nozzle material of alloy 600 was used, and inspection and mitigation efforts have been made on such components. In addition, attention has also been paid to J-groove welds of BMIs recently as well as those of CRDM. To date, no defect indications have been found in either nozzle base materials or J-groove welds of BMIs with one exceptional phenomenon as described below.

WJP was performed to BMIs of Takahama 1 plant during its 21st annual inspection outage in 2003. Prior to WJP operation, inner surfaces of all 50 nozzles had been inspected by the ECT method. With this prior inspection, one small indication was found at No. 48 nozzle. It was an axial indication of approximately 32 mm in length. Estimated depth, assuming that indication was a crack, was less than 1 mm.

Eventually, the area concerned was ground in case in the next outage. Retesting with ECT after grinding verified that the indication had been completely eliminated.

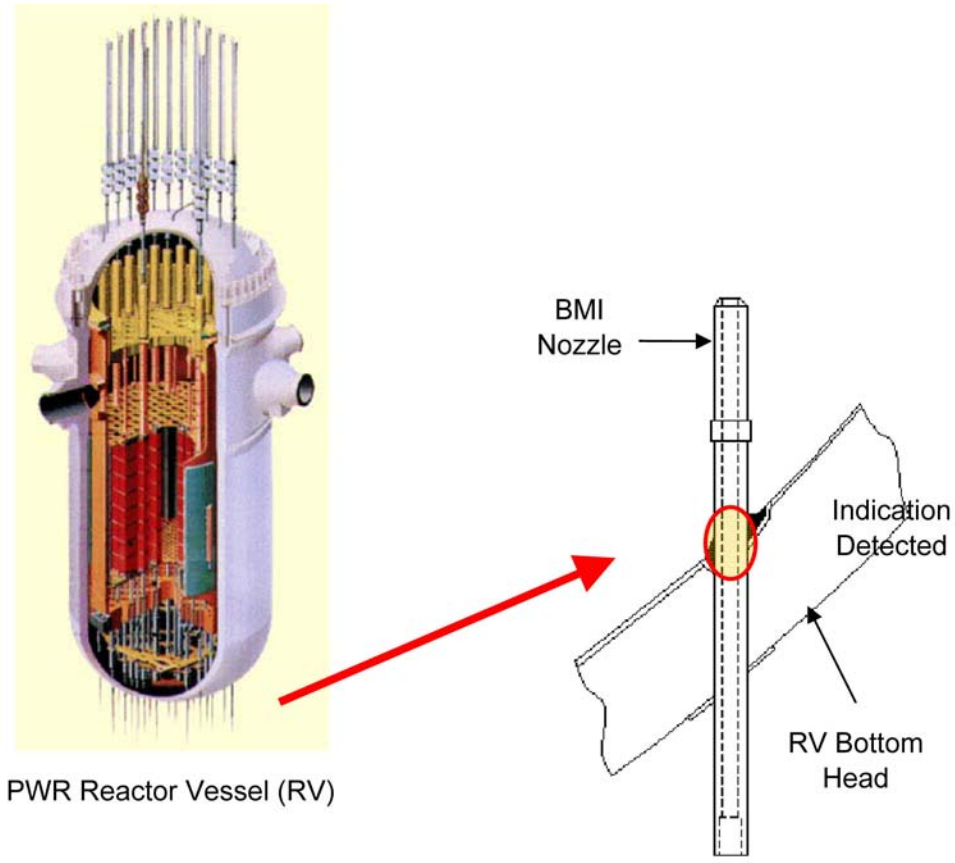

Figure 6.5 Spurious ECT Indication Found in BMI of Takahama

7.0 Parametric Studies – NDE Responses and Flaw Morphology (NA2 and Simulated Flaws)

One of the objectives of the PINC is to assess methods for manufacturing test blocks and mockups with flaws that adequately simulate the NDE response from PWSCC. Existing test blocks offered by the PINC participants were analyzed to determine if the objective of the program could be supported by the available cracks in offered test blocks. PINC documents included the design of the test blocks with available photographs and drawings. Sufficient preexisting test blocks were available for a round-robin test of dissimilar metal welds.

The most important needed product form to add to the open test blocks was Alloy 182/82 seal weld metal and buttering of CRDM and BMI assemblies. A blind test was proposed using 50-mm × 50-mm cracked and blank weld metal coupons with a holder for presenting the cracked and blank coupons to the inspectors. The EPRI NDE Center reported good results with a very similar coupon and mockup system.

7.1 Manufactured Flaw Nondestructive Testing Responses

PNNL proposed to procure the coupons with three different surface finishes—as-welded, hand-ground, and machined smooth. Two different crack orientations were proposed—along and across the weld lay. Three different crack types were proposed—thermal fatigue cracks (TFC), stress corrosion cracks (SCC), and weld solidification cracks (WSC). The cracks in the coupons were proposed to have CODs that fell into four size categories. Cracks with COD less than 20 microns would be very difficult to detect for eddy current and visual testing, and cracks with COD between 20 and 50 microns would be difficult to detect for most systems. Larger cracks should not be missed when using a state-of-the-art eddy current or visual testing system. Clearly, 50 or more coupons would be needed to fill out the test matrix. Furthermore, some or all of the crack types should have duplicates to measure repeat performance of the inspection technology. For cracks on as-welded surfaces, some of the circumferential cracks would need to be located along the fusion line of the weld passes and some located away from the fusion line.

Before PNNL ordered the Alloy 182 weld metal mockup, a simple parametric study was performed. The study was used to refine specifications and quality requirements for the cracks and coupons, especially the selection of appropriate lengths for the cracks to be used in the blind test. Figure 7.1 shows the three cracked Alloy 182 weld metal coupons received at PNNL. The coupon on the right has a thermal fatigue crack that is 5.3-mm long and 2.3 mm deep. The thermal fatigue crack was introduced into the coupon with controlled thermal fatigue loading (Kemppainen et al. 2003). The crack was grown with natural thermal fatigue introduced by cyclic application of high-frequency inductive heating coils and water cooling jets. In this process, the typical heating time is 2–5 seconds and typical cooling time 5–10 seconds. Because the crack is introduced directly into the test material, the crack shape and form are affected by local properties, especially inhomogeneities or stress risers. The cracks tend to grow in the weakest locations in discontinuous segments or with some branching. Figure 7.2 shows the image of the artificially grown stress corrosion crack on the surface of the coupon.

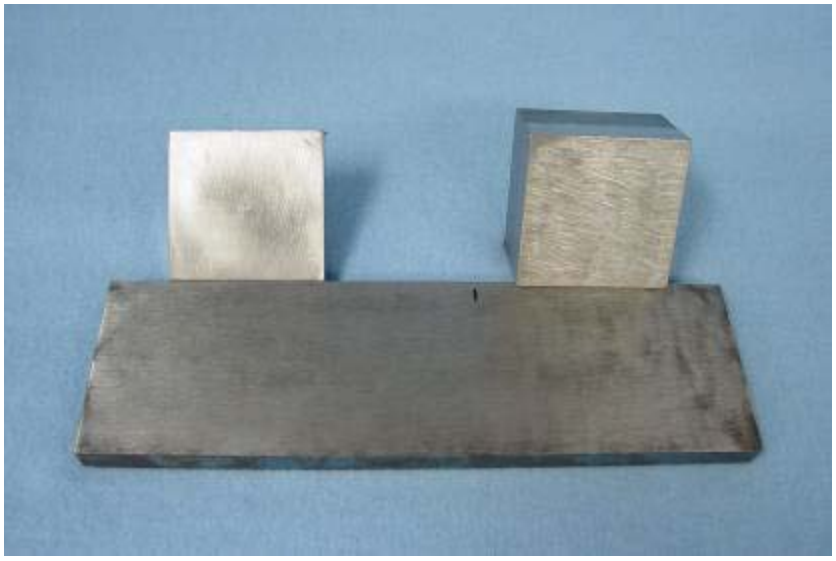

Figure 7.1 Three Cracked Weld Metal Coupons with Thermal Fatigue Crack on the Left, Weld Solidification Crack on the Right, and Laboratory Stress Corrosion Crack at Center

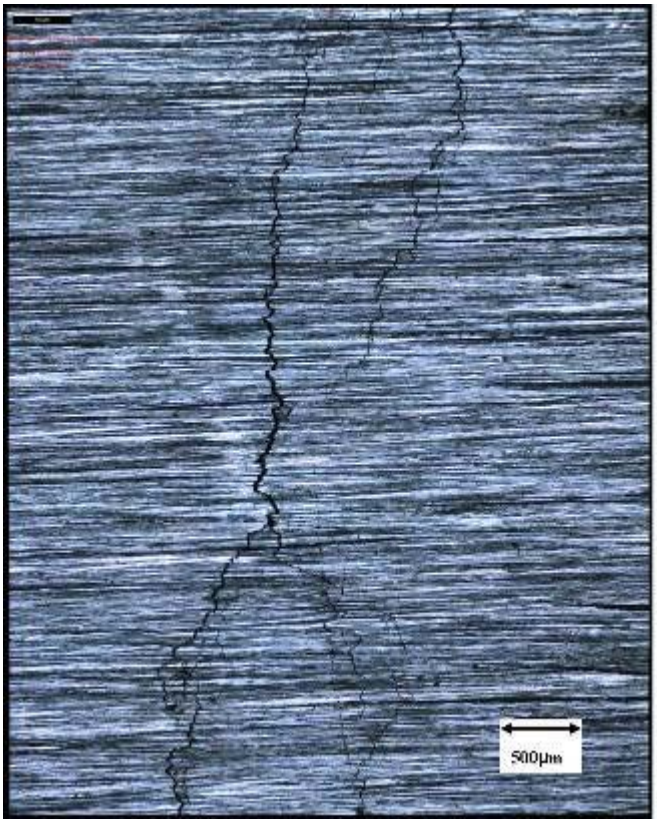

Figure 7.2 Artificially Grown Stress-Corrosion Crack in Coupon of Alloy 182 Weld Metal

Although not visible at this magnification, the coupon on the left in Figure 7.1 has a weld solidification crack that is 10 mm long and 2 mm deep. Such a crack is introduced by performing a weld and adjusting the weld chemistry to produce a centerline crack that is bounded by the fused metal (Watson and Edwards 1996). The technique uses a machined notch to form a cavity with the length and depth of the desired crack. This cavity is filled with poisoned weld metal that cracks starting at the bottom of the notch. The crack breaks the surface, is interdendritic, and has some branching.

A laboratory-grown stress corrosion crack is in the coupon at the center of Figure 7.2. The main crack is 28 mm long with a mean crack opening dimension of 50 microns. Growing SCC (Daniels et al. 2003) involves the manufacture of a test piece that is suitable for the application of tensile stress. The stressed test piece is subjected to a corrosive agent to produce the required crack. Figure 7.4 shows a portion of the laboratory-grown stress corrosion crack purchased by PNNL.

The eddy current responses and noise levels were recorded from the three manufactured cracks at 350 kHz. Figure 7.3 shows eddy current response from the laboratory-grown SCC in Alloy 182 weld metal. The indication is 45% of the calibration electro-discharge machining (EDM) notch. The length of the indication is 25 mm with a secondary crack on the lower edge of the image. The main crack is 28 mm (1.1 in.) long. The depth of the crack is unknown (because the SCC is laboratory-grown with limited control of the cracking process). Figure 7.4 provides a signal-to-noise analysis of eddy current response from the laboratory-grown SCC. The noise level is set to 2.5% of the calibration EDM notch, giving the indication a signal-to-noise ratio of 18.1.

Figure 7.5 shows the eddy current response from a thermal fatigue crack in Alloy 182 weld metal. The indication is 58% of the calibration EDM notch. The length of the indication is 4 mm using loss of signal. The crack is 5.2 mm (0.2-in.) long and 2.3 mm (0.1-in.) deep. Figure 7.6 provides a signal-to-noise analysis of eddy current response from the TFC. The noise level is set to 2.5% of the calibration EDM notch, giving the indication a signal-to-noise ratio of 23.1.

Figure 7.7 shows the eddy current response from a WSC in Alloy 182 weld metal. The indication is 39% of the calibration EDM notch. The length of the indication is 12 mm using loss of signal. Figure 7.8 provides a signal-to-noise analysis of eddy current response from the weld solidification crack. The noise level is set to 3.5% of the calibration EDM notch, giving the indication a signal-to-noise ratio of 11.2.

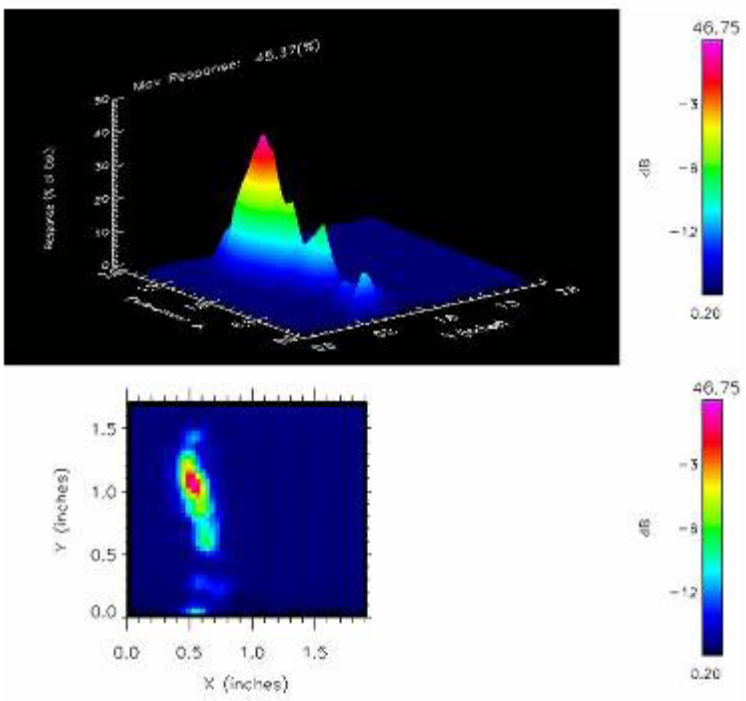

Figure 7.3 Eddy Current Response from Laboratory-Grown Stress Corrosion Crack in Alloy 182 Weld Metal

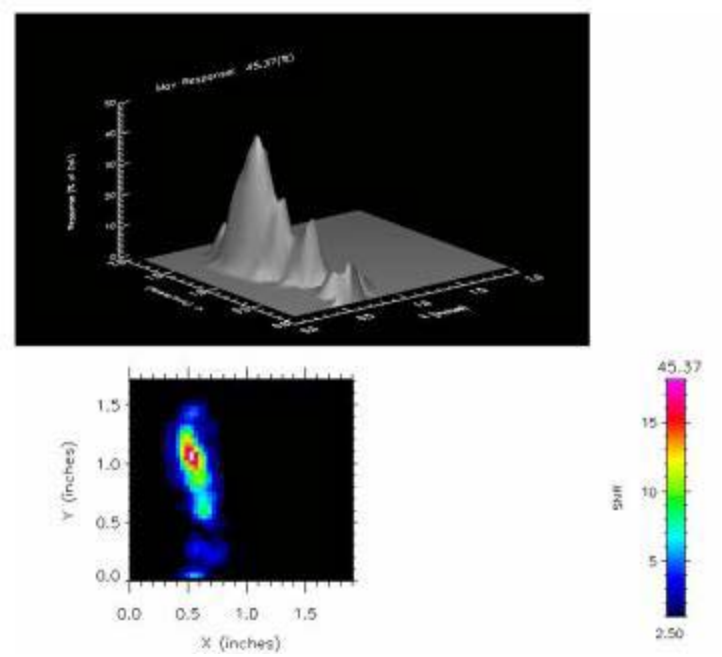

Figure 7.4 Signal-to-Noise Analysis of Eddy Current Response from Laboratory-Grown Stress Corrosion Crack in Alloy 182 Weld Metal

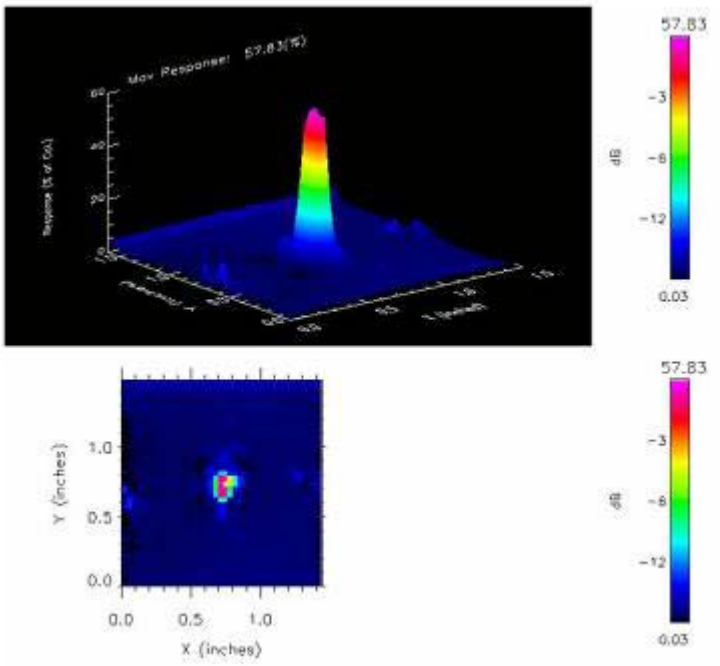

Figure 7.5 Eddy Current Response from Thermal Fatigue Crack in Alloy 182 Weld Metal

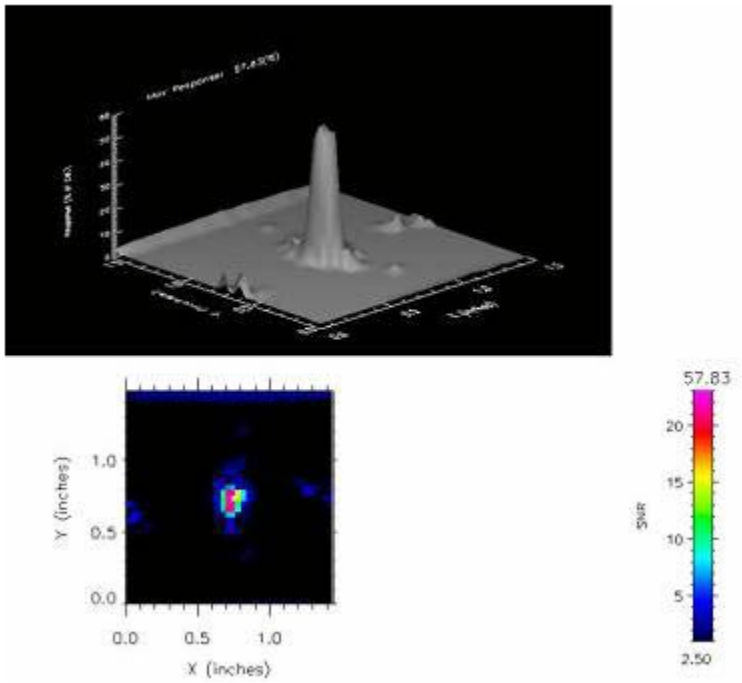

Figure 7.6 Signal-to-Noise Analysis of Eddy Current Response from Thermal Fatigue Crack in Alloy 182 Weld Metal

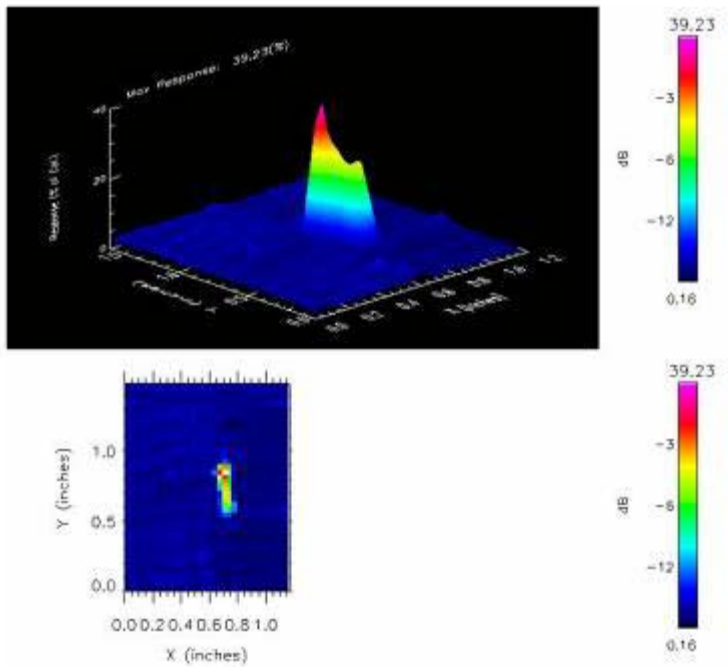

Figure 7.7 Eddy Current Response from Weld Solidification Crack in Alloy 182 Weld Metal

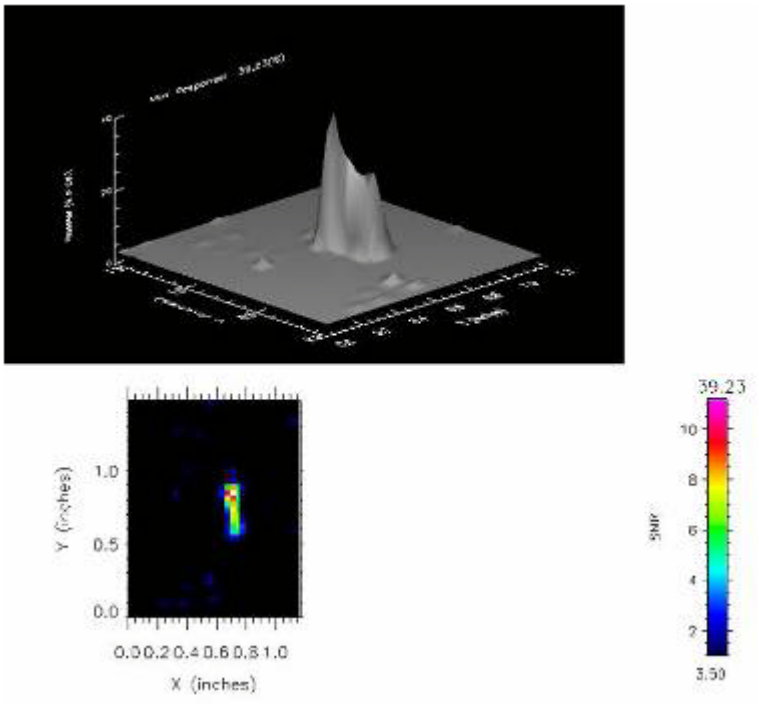

Figure 7.8 Signal-to-Noise Analysis of Eddy Current Response from Weld Solidification Crack in Alloy 182 Weld Metal

7.2 North Anna 2 Flaw Responses

PNNL examined the J-groove weld of a removed-from-service control rod drive nozzle, North Anna 2 (NA2) Nozzle 31, which contained PWSCC. The nozzle was inspected under a joint NRC and EPRI effort to characterize the NDE effectiveness for control rod drive examinations. Nozzle 31 was inspected using a wide variety of NDE techniques, but this section focuses on the eddy current responses of the PWSCC and the destructive validation of the PWSCC. The J-groove weld was examined using a 350-kHz cross-coil eddy-current probe. The nozzle was scanned twice, once with the probe at a 0-degree rotation and again with the probe rotated 45 degrees. Sixteen eddy current indications clustered in four regions of interest were found.

Dye penetrant examinations of the NA2 nozzle showed that three flaws, at 200, 215, and 225 degrees, were surface-breaking cracks. Then the four regions were destructively examined to validate the four regions of interest. First, the regions were cut out and examined using optical microscopy to determine if the flaws were surface-breaking. The regions were cut at depths of 6–8 mm below the wetted surface to determine if any of the flaws penetrated into the weld. When cracks deeper than 6–8 mm were found, the welds were further sectioned to determine how deeply they had propagated. Six indications were found that had penetrated into the weld, and two were found to have propagated entirely through the weld and into the buttering region. One crack was confirmed as the cause of the leak in the nozzle. The eddy current results and the destructive evaluation of these eddy current examinations are summarized in Table 7.1.

Table 7.1 North Anna 2 Eddy Current Responses and Destructive Validation

Indication	Angle	Length	Max Voltage	% EDM Notch	Confirmed PWSCC?	Depth
1	45°	2 mm	2.1	20%	No	< 6 mm
2	50°	5 mm	1.9	18%	No	< 6 mm
3	55°	4 mm	3.3	32%	No	< 6 mm
4	65°	2 mm	1.8	18%	No	< 6 mm
5	70°	4 mm	2.2	21%	No	< 6 mm
6	75°	3 mm	2.5	24%	No	< 6 mm
7	80°	3 mm	2.3	22%	No	< 6 mm
8	130°	4 mm	2.3	22%	No	< 6 mm
9	145°	10 mm	3.2	31%	Yes	< 25 mm
10	155°	8 mm	3.3	32%	Yes	Through-Weld Leaking
11	160°	14 mm	4.1	40%	Yes	< 25 mm
12	170°	5 mm	2.6	25%	No	< 6mm
13	200°	8 mm	4.6	45%	Yes	< 25 mm
14	215°	10 mm	1.8	18%	No	< 6 mm
15	225°	9 mm	4.6	45%	Yes	< 25mm
16	255°	7 mm	4.2	41%	Yes	Through-Weld Not Leaking

The response range for 16 crack indications in CRDM nozzle number 31, from the removed-from-service top head of the North Anna 2 reactor pressure vessel, is 18% to 45% of the calibration response. The response range for the three manufactured cracks is 39% to 58%. The manufactured cracks were representative of only the upper portion of the response range for the crack indications in nozzle 31. The eddy current response from the PWSCC initiation site for a proven leakage path in North Anna 2 nozzle 31 is 32% of the calibration.

It is worth noting that each of the confirmed PWSCC cracks greater than 6–8 mm in depth was found by the inservice examination that was performed prior to the pressure vessel head being removed from service.

7.3 Comparison of Eddy Current Response of Manufactured Flaws and for PWSCC in North Anna 2

The eddy current responses for the manufactured flaws were compared to the six confirmed instances of PWSCC in the nozzle 31 J-groove weld. As there were only six flaws characterized in nozzle 31, this comparison is not definitive, but it is still useful to discuss.

The noise levels in the eddy current data from scans of Alloy 182 weld metal are determined by surface roughness and, to a lesser extent, by fabrication flaws. The noise level in the eddy current scans of North Anna 2 nozzle 31 was 6% of the calibration EDM notch, and the level was 2.5% to 3.5% for the Alloy 182 coupons. Factors of two are important in simulating inspection conditions.

The lowest responses from crack indications in North Anna 2 nozzle 31 that were confirmed with dye penetrant testing were 18% of calibration. The error in manufactured crack responses for the simulation of such PWSCC indications is a factor of 4 to 8 in signal-to-noise ratio.

Figure 7.9 provides a summary of the eddy current response distributions for 13 crack indications in the North Anna 2 nozzle 31, 3 manufactured cracks, and 9 EDM notches. The 0.5-mm EDM notch and 1.0-mm EDM notch approximately bracket the crack indication distribution. The responses from manufactured cracks are representative of PWSCC crack indications producing the largest NDE responses.

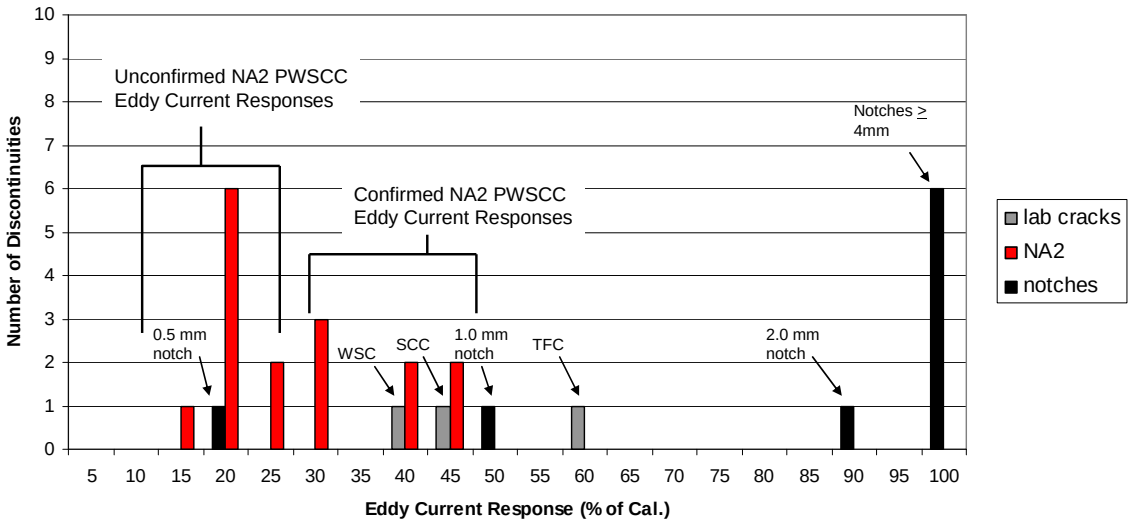

Figure 7.9 Eddy Current Response Distributions for 13 Crack Indications in North Anna 2 Nozzle 31, 3 Manufactured Cracks, and 9 Electro-Discharge Machined Notches

After destructive evaluation of the NA2 nozzle 31, it was determined that the confirmed PWSCC had eddy current responses of 31% or greater relative to the calibration notch. A destructive evaluation of the sample showed no evidence that the low-amplitude indications were caused by PWSCC. All low-amplitude indications (25% and below) were shown to be less than 6 mm deep. Only one low-response indication, the same that was confirmed using dye penetrant, could be found using optical microscopy. The remaining indication may or may not be cracks but could be surface irregularities. Based on the destructive validation, the weld solidification cracks and the induced stress corrosion cracks are a reasonable, but not conservative, approximation of the response of PWSCC in the nickel-based alloys. The through-weld leaking flaw had an eddy current response of 31%, which is less than the 40–45% found for the implanted flaws. The thermal fatigue flaws produce a large response compared to the eddy current response found in nozzle 31.

8.0 Conclusions and Recommendations from PINC Round Robins

Inservice inspections, which are scheduled during maintenance outages at nuclear power plants, serve as an important layer of the defense-in-depth philosophy. For ISI to be effective, the nondestructive examination techniques used during ISI must demonstrate high probabilities for crack detection. Demonstrating a high quality of flaw detection and sizing using nondestructive technology will become increasingly important as nuclear power plants age and as nuclear power plants are operated for longer periods of time. Effective ISI procedures should be able to detect and correctly size flaws with a high degree of accuracy so decision makers at nuclear power plants may make informed "run, repair, or replace" decisions.

The dissimilar metal weld round-robin exercises that were conducted as part of the PINC are an important part of the process in assessing nondestructive testing methods because the data that are developed in the round-robin testing offer insight into capabilities of current nondestructive methods used to detect PWSCC and insight into the capabilities of more experimental nondestructive methods. These insights may then be used in developing regulatory positions and help direct additional research plans.

This section of the report describes the conclusions that may be inferred from the PINC round robin results and then offers recommendations agreed on by the international PINC Steering Committee that address PWSCC-specific issues.

8.1 Probability of Detection Performance

8.1.1 Dissimilar Metal Weld Pipe Specimen Round Robin Probability of Detection Performance

The conclusions that may be inferred from the experimental results for the dissimilar metal welds pipe specimens are as follows:

1. **Conclusion**: Eddy current inspection from the cracked surface demonstrated the highest probability of detection (POD) for all flaws in the DMW round robin.
    - **PINC Recommendation**: The results of this study show that eddy current inspection are the preferred detection technique for dissimilar metal welds, where conditions allow access to the same surface from which the crack originates and where the surface conditions allow for ECT testing.

2. **Conclusion**: The POD results for the DMW round robin show significant variability in POD performance based upon technique, procedure, and team.
    - **PINC Recommendation**: The results illustrate the usefulness of performance demonstration as a means to help ensure the reliability of DMW inspections.

3. **Conclusion**: The potential-drop techniques that were used in the DMW round robin demonstrated the lowest POD performance.

    - **PINC Recommendation**: The potential-drop techniques used in the DMW round robin need further development before use as detection techniques in inservice inspection programs.

8.1.2 Bottom-Mounted Instrumentation Round Robin Probability of Detection Performance

The conclusions that may be inferred from the experimental results for the bottom mounted instrumentation tube specimens are as follows

1. **Conclusion**: Inspections using a single cross-coil eddy-current probe achieved a high POD and a low false call rate. These examinations were performed with multiple frequencies, with the highest frequency used being 300–400 kHz.

    - **PINC Recommendation**: The results of this study suggest that single cross-coil probe eddy current using frequencies of 300–400 kHz are the preferred method for finding surface-breaking flaws in BMI J-groove welds.

2. **Conclusion**: Inspections using adaptive phased array ultrasound were able to detect all baseline difficulty flaws and none of the challenging flaws (baseline and challenging flaws are defined in Section 4.2.2).

    - **PINC Recommendation**: While adaptive phased array ultrasound was slightly less effective than eddy current testing, the results of this study suggest that adaptive phased array ultrasound can be effectively used to find flaws in BMI welds.

3. **Conclusion**: The inspections using array eddy-current techniques used in this BMI round robin study had a reduced POD and a much higher false call rate compared to the higher frequency cross-coil ECT examinations.

    - **PINC Recommendation**: The results of the BMI round-robin study show that the procedures using array ECT probes operating at 100–200 kHz used in this round robin test require further development for detection in inservice inspection programs.

4. **Conclusion**: The closely coupled potential-drop technique was able to detect thermal fatigue flaws and SCC flaws with a POD of 50%. For weld solidification flaws, the POD was 0%. No false calls were made by the inspectors using this technique.

    - **PINC Recommendation**: The results of the BMI round-robin study show that the closely coupled potential-drop technique requires further development before it can be used for detection of flaws in inservice inspection programs.

5. **Conclusion**: Induced-current potential drop was used on only one baseline difficulty test block and two challenging test blocks, possibly skewing the results. There are not enough inspections on baseline difficulty test blocks to draw meaningful conclusions on the POD performance on these test blocks.

- **PINC Recommendation**: Further testing needs to be performed to determine if ICPD can be used for inservice inspection.

8.2 Sizing Performance

8.2.1 Dissimilar Metal Weld Pipe Specimen Sizing Performance

The conclusions that may be inferred from the experimental results indicate the following:

1. **Conclusion**: None of the NDE techniques in this round robin study demonstrated the capability to accurately depth size flaws in dissimilar metal welds to ASME Section XI code standards. The average depth sizing for all techniques tended to slightly undersize the flaws and had standard deviations and RMSE errors of approximately 7 mm. Two techniques came close to meeting ASME Section XI standards.
    - **PINC Recommendation**: The depth sizing of flaws should be improved. The use of phased array UT and conventional ultrasound together showed the most promise.
2. **Conclusion**: Eight teams length-sized flaws with an RMSE within the ASME Section XI standard of 0.75 inch (19 mm). Teams that used phased array UT and eddy current achieved higher accuracy than teams that used conventional UT and potential-drop techniques.
    - **PINC Recommendation**: Phased array UT or a combination of eddy-current techniques and conventional UT are the preferred method for length sizing.

8.2.2 Bottom-Mounted Instrumentation Weld Sizing Performance

The conclusions that may be inferred from the experimental results indicate the following:

1. **Conclusion**: Cross-coil eddy current, adaptive phased array ultrasound, and closely coupled probe potential-drop techniques were able to accurately length-size the flaws in the J-groove welds (RMSE of 2.45-4.70 mm).
    - **PINC Recommendation**: These techniques can be used to length-size flaws in BMI J-groove welds.
2. **Conclusion**: The test block geometry made depth-sizing using ultrasound difficult, and not enough data was collected in this round-robin test to accurately determine the effectiveness of the depth-sizing techniques.
    - **PINC Recommendation**: More work should be performed to determine the depth-sizing capabilities of the various techniques.

Based on the round-robin tests, including detection and length-sizing capabilities, several techniques need to be used in tandem for flaw detection and sizing in dissimilar metal welds comparable to ASME Section XI. Eddy current testing had the highest POD performance, and a combination of conventional and phased array ultrasound was the only technique that provided

RMSE depth-sizing capabilities close to Section XI requirements. It is worth noting that eddy current is not universally applicable for dissimilar metal welds, as many welds are in locations or have surface conditions that do not allow for ID inspections. If ID access is not possible, a combination of phased array ultrasound and conventional ultrasound appears to be the most accurate alternative.

8.3 General Conclusions

1. **Conclusion:** The surface conditions, access to both sides of the weld, and inspection conditions for the PINC specimens provided the inspectors with less challenging conditions than would be expected in field inspections of nuclear power plant components.
    - **PINC Recommendations**: The probability of detection and sizing results should be considered an upper bound for the inspection techniques.

2. **Conclusion**: Inspection procedures and teams with formal NDE qualifications tended to have a higher POD and lower false call rate than teams and procedures with no formal qualifications.
    - **PINC Recommendation**: As NDE inspections are carried out by qualified inspectors, the probability of detection and length sizing results for the qualified teams and procedures should be considered the most representative of field inspections.

3. **Conclusion:** An analysis of the POD curves generated by the PINC round robin testing showed that the procedures improved safety by factors of 1.1 to 1.5 for a 10 year interval and by factors of 1.3 to 2.1 for a four year interval. (These safety factors use the crack growth rates for stress corrosion cracks in stainless steel welds.)
    - **PINC Recommendation:** Effective NDE techniques may need to be combined with inspection intervals selected based on the crack growth rates. The analysis should be refined using PWSCC crack growth rates in nickel-based alloys.

9.0 References

NRC Order EA-03-009. 2003. "Order Modifying Licenses (Effective Immediately)." U.S. Nuclear Regulatory Commission, Washington, D.C.

Bamford WH, et al. 2000. *Integrity Evaluation for Future Operation: Virgil C. Summer Nuclear Plant Reactor Vessel Nozzle to Pipe Weld Regions*. WCAP-15615, Rev. 0, Westinghouse Engineering.

Bamford WH, J Foster, KR Hsu, L Tunon-Sanjur and A McIlree. 2002. "Alloy 182 Crack Growth and Its Impact on Service-Induced Cracking in PWR Plant Piping." In *10th International Conference on Environmental Degradation of Materials in Nuclear Power Systems - Water Reactors*, NACE, Houston, Texas.

Daniels W, P Roscoe, DR Tice, C Waites and C Udell. 2003. *Qualification of Inspection for SCC*. Nuclear Engineering International.

Ekstrom P and J Wåle. 1995. *Crack Characterization for In-service Inspection Planning*. SKI Report 95:70, Swedish Nuclear Power Inspectorate, Stockholm, Sweden.

Frye CR, ML Arey, RR Robinson and DE Whitaker. 2002. "Evaluation and Repair of Primary Water Stress Corrosion Cracking In Alloy 600/182 Control Rod Drive Mechanism Nozzles." In *Proceedings of ICONE10, 10th International Conference on Nuclear Engineering*, April 14–18, 2002, Arlington, Virginia. American Society of Mechanical Engineers, New York.

Halpin ED. 2003. *Bottom Mounted Instrumentation Penetration Indications*. STP Unit 1 Licensee Event Report (LER) 03-003, ADAMS, ML031681316, June 11, 2003.

Harris DO, DD Dedhia and SC Lu. 1992. *Theoretical and User's Manual for pc-PRAISE, A Probabilistic Fracture Mechanics Computer Code for Piping Reliability Analysis*. NUREG/CR-5864, UCRL-ID-109798, U.S. Nuclear Regulatory Commission, Washington, D.C.

Jenssen A, K Norrgard, G Embring, J Lagerstrom and DR Tice. 2002a. "Assessment of Cracking in Dissimilar Metal Welds." In *10th International Conference on Environmental Degradation of Materials in Nuclear Power Systems - Water Reactors*. NACE, Houston, Texas.

Jenssen A, K Norrgard, C Jansson, J Lagerstrom, G Embring and P Efsing. 2002b. "Structural Assessment of Defected Nozzle to Safe-End Welds in Ringhals-3 and -4." In *Fontevraud V International Symposium*. SFEN.

Kemppainen M, I Virkkunen, J Pitkänen, R Paussu and H Hänninen. 2003. "Advanced Flaw Production Method for In-service Inspection Qualification Mock-ups." *Journal of Nuclear Engineering and Design* 224:105–117.

Khaleel MA and FA Simonen. 2009. *Evaluations of Structural Failure Probabilities and Candidate Inservice Inspection Programs*. PNNL-13810, Pacific Northwest National Laboratory, Richland, Washington.

Khaleel MA, FA Simonen, DO Harris and DD Dedhia. 1995. "The Impact of Inspection on Intergranular Stress Corrosion Cracking for Stainless Steel Piping." In *Risk and Safety Assessments: Where Is the Balance?*, PVP-Vol. 296, pp. 411–422. American Society of Mechanical Engineers, New York.

Lang TA. 2003. "Significant Corrosion of the Davis-Besse Nuclear Reactor Pressure Vessel Head." In *ASME Pressure Vessels and Piping Conference*. July 20–24, 2003, Cleveland, Ohio.

NRC. 2001. *Circumferential Cracking of Reactor Pressure Vessel Head Penetration Nozzles*. NRC Bulletin 2001-01, U.S. Nuclear Regulatory Commission, Washington, D.C.

NRC. 2002. *Reactor Pressure Vessel Head and Vessel Head Penetration Nozzle Inspection Programs*. NRC Bulletin 2002-02, U.S. Nuclear Regulatory Commission, Washington, D.C.

NRC Generic Letter 97-01. 1997. *Degradation of Control Rod Drive Mechanism Nozzle and Other Vessel Closure Head Penetrations*. U.S. Nuclear Regulatory Commission, Washington, D.C.

Rudland DL, H Xu, G Wilkowski, P Scott, N Ghadiali and F Brust. 2006. "Development of a New Generation Computer Code (PRO-LOCA) for the Prediction of Break Probabilities for Commercial Nuclear Power Plants Loss-of-Coolant Accidents." In *2006 Proceedings of the ASME Pressure Vessels and Piping Conference*, July 23–27, 2006, Vancouver, British Columbia, Canada. American Society of Mechanical Engineers, New York.

SKI. 2005. *Statens kärnkraftinspektions föreskrifter om mekaniska anordningar i vissa kärntekniska anläggningar, (Regulations Concerning Mechanical Equipment)*. SKIFS 2005:2, Swedish Nuclear Power Inspectorate, Stockholm, Sweden.

SQC. 2003. *Project PostDAS - Final Report, Test Specimen Report*. Report Nr RAPP0115/03, Swedish Qualification Center (SQC), Stockholm, Sweden.

Wåle J. 2002. *Karakterisering av IDSCC i Alloy 182, Delmåi 1 i Projekt DAS182*. Rapport Nr 10521100-1, Det Norske Veritas AB, Stockholm, Sweden.

Wåle J. 2006. *Crack Characterisation for In-service Inspection Planning - An Update*. SKI Report 2006:24, Swedish Nuclear Power Inspectorate, Stockholm, Sweden.

Watson PD and RL Edwards. 1996. "Fabrication of Test Specimens Simulating IGSCC for Demonstration and Inspection Technology Evaluation." In *14th International Conference on NDE in the Nuclear Pressure Vessel Industries*. September 24–26, 1996, Stockholm, Sweden.

Appendix A

Destructive Data Analysis for Dissimilar Metal Weld Pipe Specimens

Appendix A

Destructive Data Analysis for Dissimilar Metal Weld Pipe Specimens

Destructive analysis was performed on the PINC dissimilar metal weld samples PINC 2.1 to 2.6 donated to verify the depth of the cracks. This appendix documents the results of the destructive tests that were performed. The destructive analysis was conducted by JNES. The samples were sectioned and examined to precisely determine the length and depth of the grown crack. Other important parameters such as crack opening displacement were recorded. The crack morphology was examined via polishing and the use of optical microscopy.

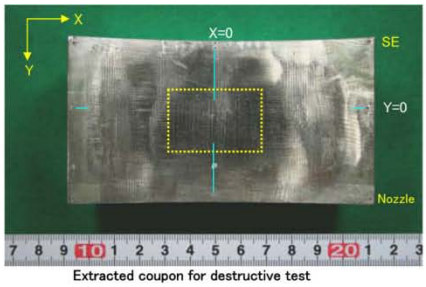

Extracted coupon for destructive test

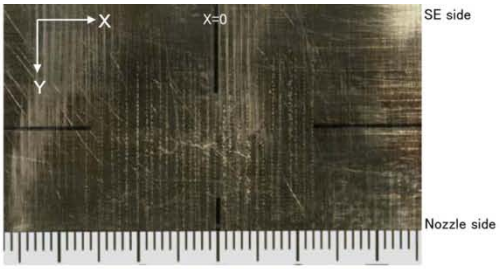

Enlarged surface view of SCC

(1) Profile of SCC ●: Measured on sliced cross section □: Measured on breaked crack △: Internal crack

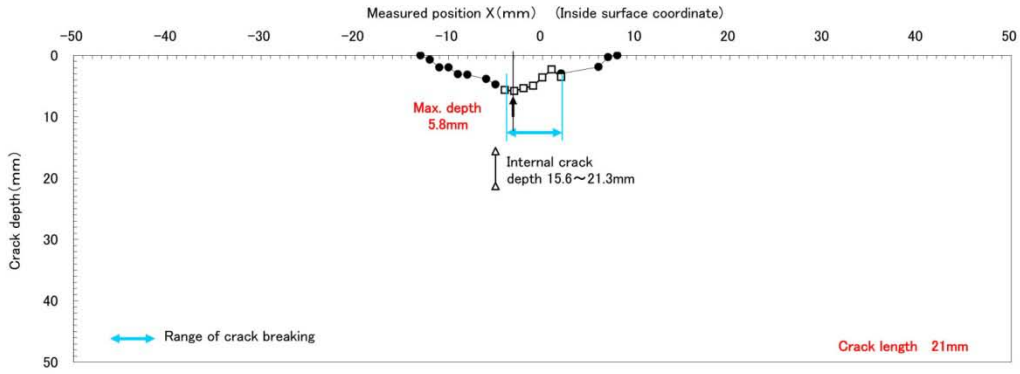

(2) Measured data of SCC

Measured on sliced cross section											
Position (mm)	X=−13	X=−12	X=−11	X=−10	X=−9	X=−8	X=−6	X=−5	X=2	X=6	X=7
Depth (mm)	0.0	0.7	2.0	2.0	3.1	3.2	3.9	4.8	2.9	1.9	0.3
Opening (μm)	0	<5	<5	<5	<5	<5	30	50	10	<5	<5
Inclination from depth direc.(Deg)	0	−9	16	15	18	6	14	−1	13	10	−8

Measured on sliced cross section	
Position (mm)	X=8
Depth (mm)	0.0
Opening (μm)	0
Inclination from depth direc.(Deg)	0

Measured on breaked crack							
Position (mm)	X=−4	X=−3	X=−2	X=−1	X=0	X=1	X=2
Depth (mm)	5.6	5.8	5.4	5.0	3.6	2.3	3.5

Length(mm)	21

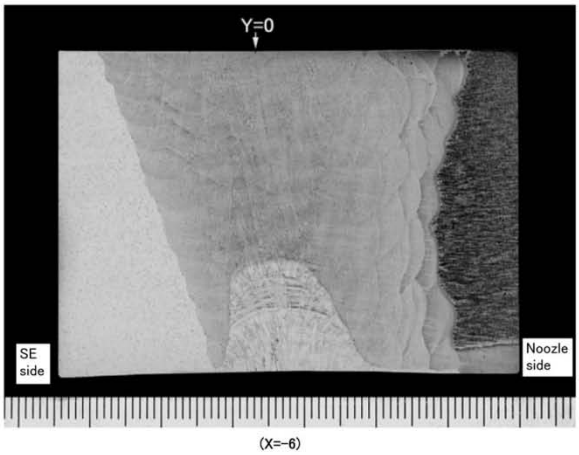

(X=−6)

Results of destructive test on PINC2.1 test block (SH-1)

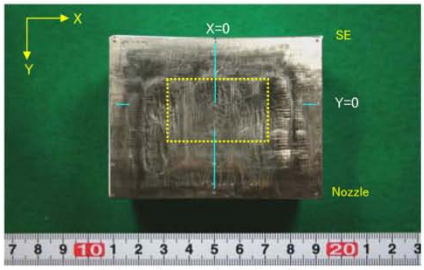

Extracted coupon for destructive test

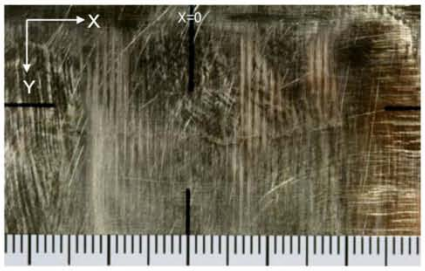

Enlarged surface view of SCC

(1) Profile of SCC ●: Measured on sliced cross section □: Measured on breaked crack

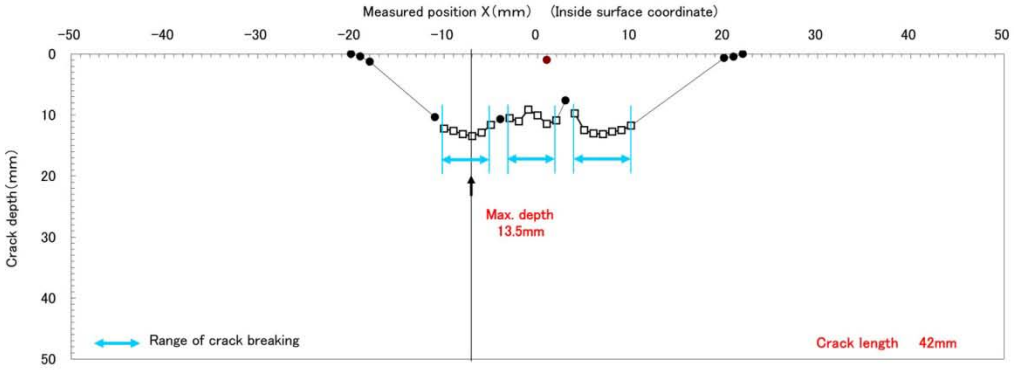

(2) Measured data of SCC

Measured on sliced cross section											
Position (mm)	X=−20	X=−19	X=−18	X=−11	X=−5	X=−4	X=2	X=3	X=10	X=20	X=21
Depth (mm)	0.0	0.4	1.3	10.4	10.9	10.7	10.5	7.6	11.7	0.7	0.4
Opening (μm)	0	<5	<5	<5	<5	10	30	<5	10	<5	<5
Inclination from depth direc.(Deg)	0	15	−7	10	12	7	6	15	10	−5	−1

Measured on sliced cross section	
Position (mm)	X=22
Depth (mm)	0.0
Opening (μm)	0
Inclination from depth direc.(Deg)	0

Length (mm)	42

Measured on breaked crack						
Position (mm)	X=−10	X=−9	X=−8	X=−7	X=−6	X=−5
Depth (mm)	12.2	12.6	13.2	13.5	12.9	11.6

Measured on breaked crack						
Position (mm)	X=−3	X=−2	X=−1	X=0	X=1	X=2
Depth (mm)	10.5	11.1	9.2	10.1	11.5	10.9

Measured on breaked crack				
Position (mm)	X=4	X=5	X=6	X=7
Depth (mm)	9.7	12.5	13.0	13.1

Measured on breaked crack			
Position (mm)	X=8	X=9	X=10
Depth (mm)	12.8	12.5	11.8

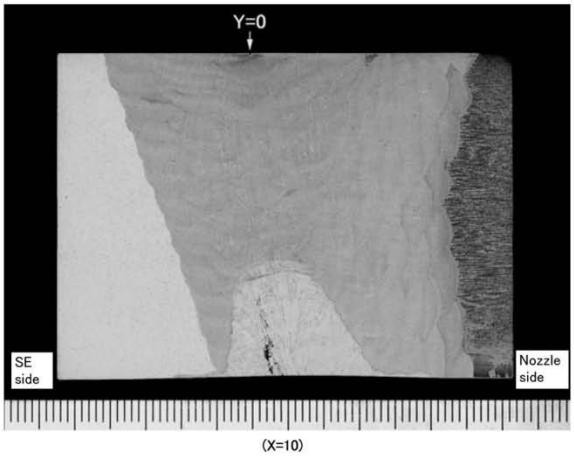

(X=10)

Results of destructive test on PINC2.2 test block (SH-2)

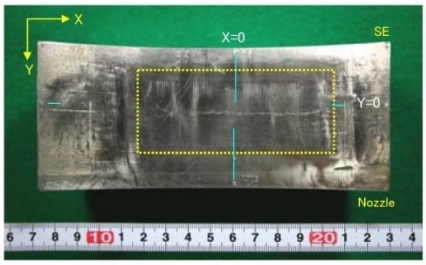

Extracted coupon for destructive test

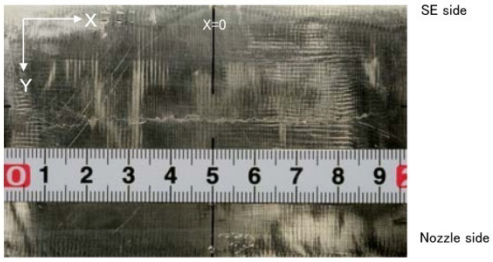

Enlarged surface view of SCC

(1) Profile of SCC ●: Measured on sliced cross section □: Measured on breaked crack

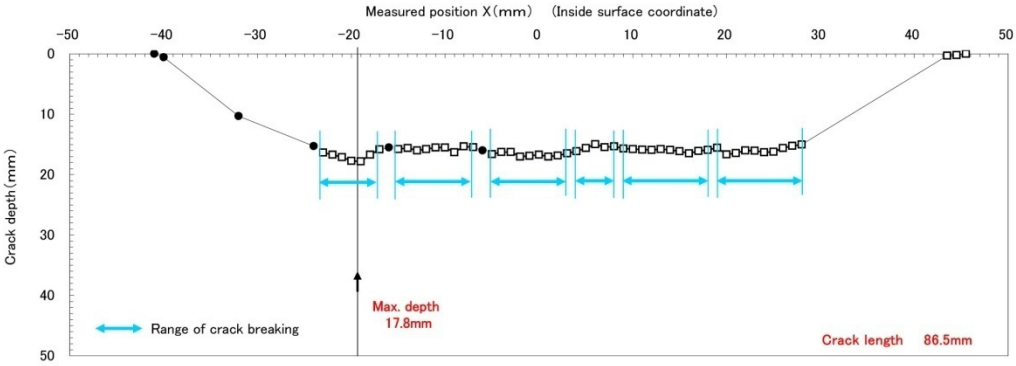

(2) Measured data of SCC

Measured on sliced cross section											
Position (mm)	X=-41	X=-40	X=-32	X=-24	X=-17	X=-16	X=-7	X=-6	X=3	X=8	X=18
Depth (mm)	無	0.6	10.3	15.3	15.4	15.5	15.3	16.0	15.7	15.3	15.9
Opening (μm)	無	<5	25	65(150)	100	100	70	490	790	105(280)	275(420)
Inclination from depth direc.(Deg)	無	0	0	2	7	7	6	3	9	7	3

( ) means supplementary value which include the drop out of crystal by the polishing of sliced cross section.

Measured on sliced cross section				
Position (mm)	X=28	X=43.5	X=44.5	X=45.5
Depth (mm)	15.0	0.3	0.2	無
Opening (μm)	20(490)	<5	<5	無
Inclination from depth direc.(Deg)	2	8	-24	無

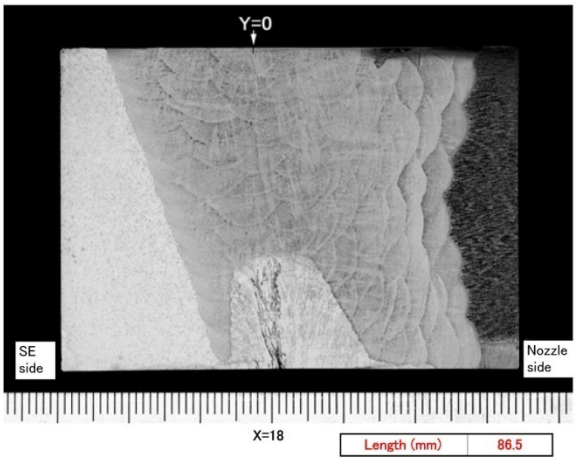

Measured on breaked crack				
Position (mm)	X=-23	X=-22	X=-21	X=-20
Depth (mm)	16.4	16.7	17.1	17.7

Measured on breaked crack				
Position (mm)	X=-19	X=-18	X=-17	X=-15
Depth (mm)	17.8	16.7	15.8	15.8

Measured on breaked crack				
Position (mm)	X=-14	X=-13	X=-12	X=-11
Depth (mm)	15.6	16.0	15.8	15.5

Measured on breaked crack				
Position (mm)	X=-10	X=-9	X=-8	X=-7
Depth (mm)	15.5	16.3	15.3	15.5

Measured on breaked crack												
Position (mm)	X=-5	X=-4	X=-3	X=-2	X=-1	X=0	X=1	X=2	X=3	X=4	X=5	X=6
Depth (mm)	16.6	16.3	16.3	17.0	16.9	16.7	17.0	16.8	16.5	16.1	15.6	15.0

Measured on breaked crack											
Position (mm)	X=7	X=8	X=9	X=10	X=11	X=12	X=13	X=14	X=15	X=16	X=17	X=18
Depth (mm)	15.5	15.3	15.7	15.8	15.9	15.9	15.8	15.9	16.5	16.5	16.1	15.9

Measured on breaked crack										
Position (mm)	X=19	X=20	X=21	X=22	X=23	X=24	X=25	X=26	X=27	X=28
Depth (mm)	15.7	16.7	16.5	16.0	16.0	16.3	16.2	15.6	15.2	15.0

Results of destructive test on PINC2.3 test block (SH-3)

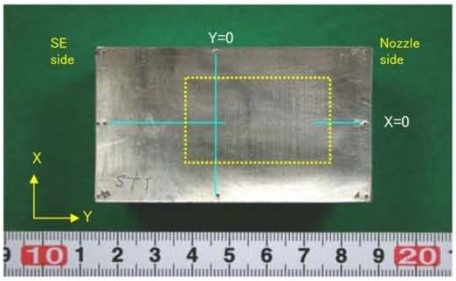

Extracted coupon for destructive test

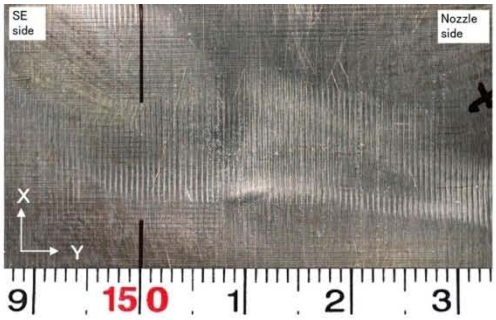

Enlarged surface view of SCC

(1) Profile of SCC ●: Measured on sliced cross section □: Measured on breaked crack

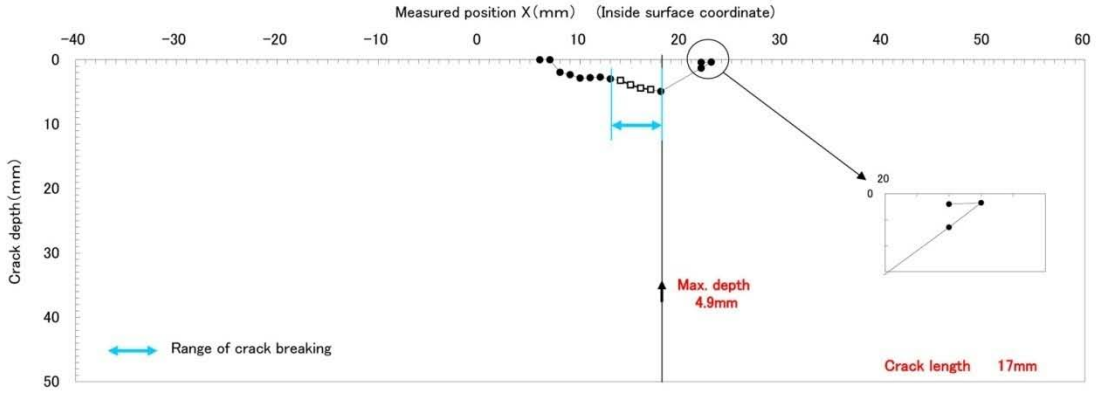

(2) Measured data of SCC

Measured on sliced cross section										
Position (mm)	Y=6	Y=7	Y=8	Y=9	Y=10	Y=11	Y=12	Y=13	Y=18	Y=22
Depth (mm)	0.0	0.00	2.0	2.3	2.9	2.8	2.7	3.0	4.9	1.3
Opening (μm)	0	0	1	5	2	1	13	2	97	embeded
Inclination from depth direc.(Deg)	0	0	−8	8	7	0	4	0	4	—

Measured on sliced cross section		
Position (mm)	Y=23	Y=24
Depth (mm)	0.4	0.0
Opening (μm)	embeded	0
Inclination from depth direc.(Deg)	—	0

Measured on breaked crack				
Position (mm)	Y=14	Y=15	Y=16	Y=17
Depth (mm)	3.2	3.9	4.4	4.6

Length (mm)	17

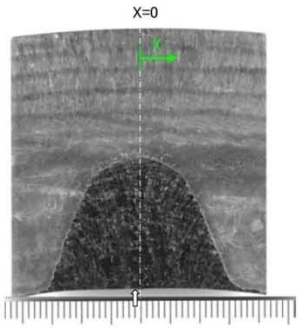

(Y=13) (etched)

Results of destructive test on PINC2.4 test block (ST-1)

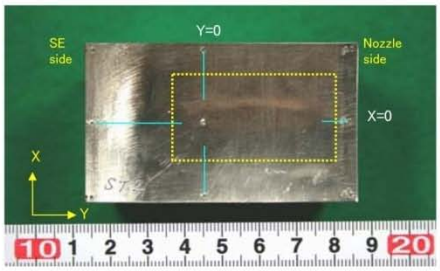

Extracted coupon for destructive test

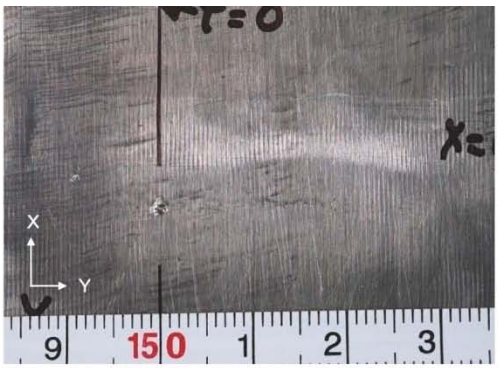

Enlarged surface view of SCC

(1) Profile of SCC ●: Measured on sliced cross section □: Measured on breaked crack △: Internal

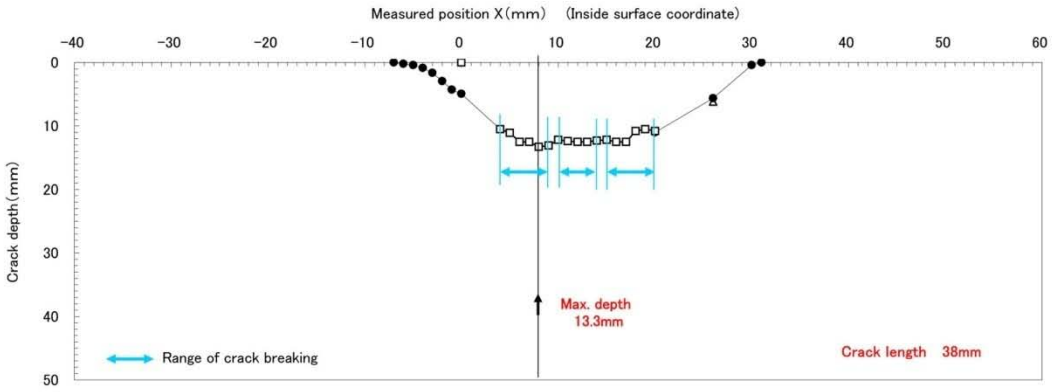

(2) Measured data of SCC

Measured on sliced cross section										
Position (mm)	Y=−7	Y=−6	Y=−5	Y=−4	Y=−3	Y=−2	Y=−1	Y=0	Y=4	Y=9
Depth (mm)	0.0	0.2	0.4	0.9	1.6	2.9	4.3	4.9	＊10.6/10.5	＊10.6/13.1
Opening (μm)	0	2	2	2	4	2	3	13	361	12
Inclination from depth direc.(Deg)	0	−9	25	−18	−24	−2	−8	9	0	−2

＊: A/B means (depth on cross section)/(depth on breaked crack).

Measured on sliced cross section										
Position (mm)	Y=10	Y=14	Y=15	Y=20	Y=26	Y=30	Y=31			
Depth (mm)	＊7.1/12.2	12.3	12.2	＊11.0/10.8	5.6	0.4	0.0			
Opening (μm)	7	19	14	9	11	3	0			
Inclination from depth direc.(Deg)	13	1	0	1	3	44	0			

Measured on breaked crack						
Position (mm)	Y=4	Y=5	Y=6	Y=7	Y=8	Y=9
Depth (mm)	10.5	11.1	12.5	12.5	13.3	13.1

Measured on breaked crack					
Position (mm)	Y=14	Y=10	Y=11	Y=12	Y=13
Depth (mm)	12.3	12.2	12.4	12.5	12.5

Measured on breaked crack						
Position (mm)	Y=15	Y=16	Y=17	Y=18	Y=19	Y=20
Depth (mm)	12.2	12.5	12.5	10.8	10.5	10.8

Length (mm)	38

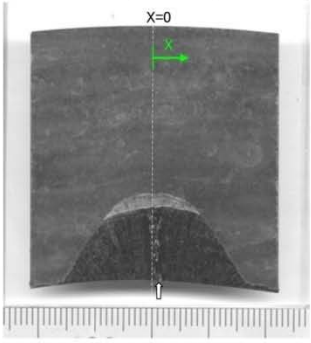

(Y=15) (etched)

Results of destructive test on PINC2.5 test block (ST-2)

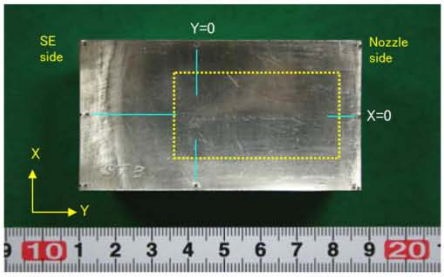

Extracted coupon for destructive test

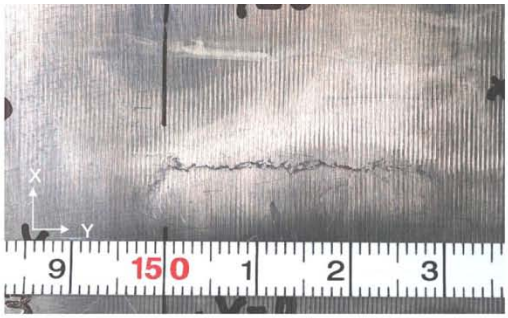

Enlarged surface view of SCC

(1) Profile of SCC ●: Measured on sliced cross section □: Measured on breaked crack

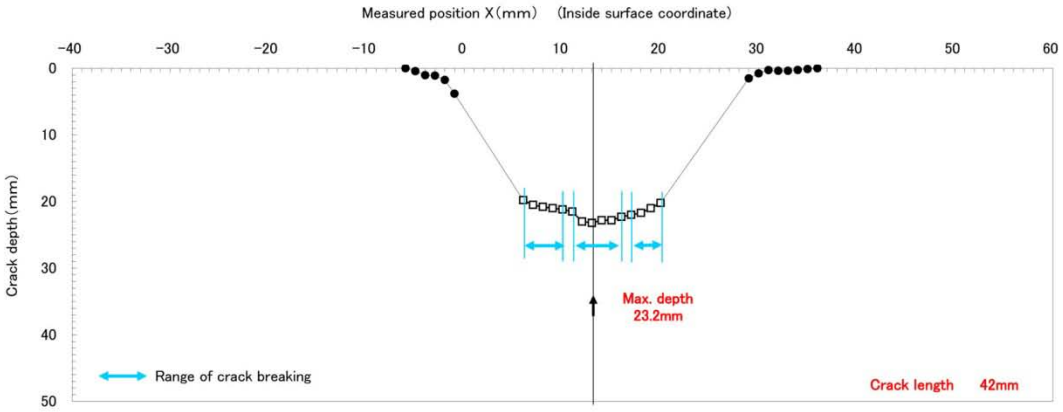

(2) Measured data of SCC

Measured on sliced cross section										
Position (mm)	Y=−6	Y=−5	Y=−4	Y=−3	Y=−2	Y=−1	Y=6	Y=10	Y=11	Y=16
Depth (mm)	0.0	0.4	1.1	1.1	1.8	3.8	＊19.3/19.8	＊20.7/21.2	21.5	＊21.4/22.3
Opening (μm)	0	1	59	18	4	18	87	198	45	686
Inclination from depth direc.(Deg)	0	−8	−29	14	−11	1	−1	−3	−5	2

＊: A/B means (depth on cross section)/(depth on breaked crack).

Measured on sliced cross section										
Position (mm)	Y=17	Y=20	Y=29	Y=30	Y=31	Y=32	Y=33	Y=34	Y=35	Y=36
Depth (mm)	＊21.2/22.0	20.2	1.5	0.8	0.3	0.4	0.4	0.3	0.1	0.0
Opening (μm)	114	97	33	3	3	4	1	37	embeded	0
Inclination from depth direc.(Deg)	4	0	1	3	11	−2	2	−15	—	0

Measured on breaked crack					
Position (mm)	Y=6	Y=7	Y=8	Y=9	Y=10
Depth (mm)	19.8	20.5	20.8	21.0	21.2

Measured on breaked crack					
Position (mm)	Y=11	Y=12	Y=13	Y=14	Y=15
Depth (mm)	21.5	23.0	23.2	22.8	22.8

Measured on breaked crack					
Position (mm)	Y=16	Y=17	Y=18	Y=19	Y=20
Depth (mm)	22.3	22.0	21.7	21.0	20.2

Length (mm)	42

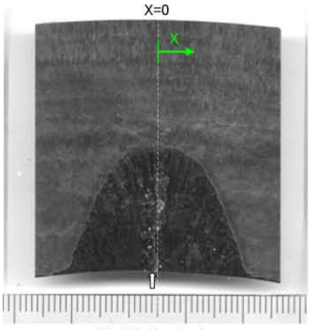

(Y=11) (etched)

Results of destructive test on PINC2.6 test block (ST-3)

Enlarged surface view of SCC

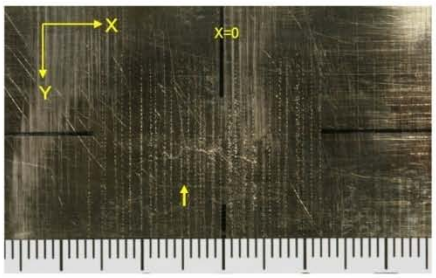

Macro. photo of cross section

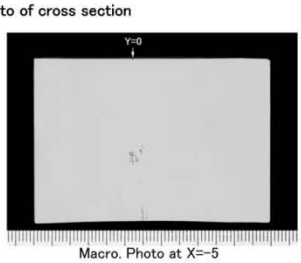

Macro. Photo at X=-5

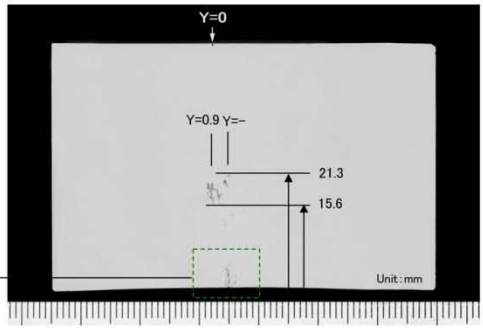

Micro. photo of cross section

Position (X=-5)

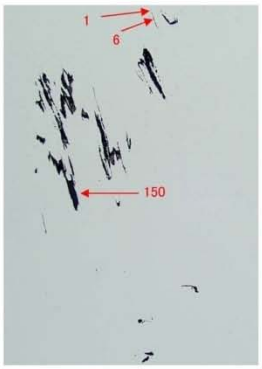

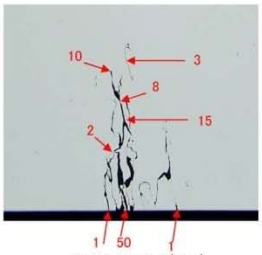

Crack opening (μ m)

Ⅰ. Crack tip

Ⅱ. Middle position

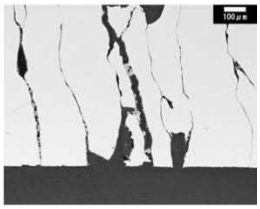

Ⅲ. Surface

Measured on sliced cross section	
Position (mm)	X=−5
Depth (mm)	4.8
Opening (μ m)	50
Inclination from depth direc.(Deg)	−1

Typical crack opening data of PINC2.1(SH-1) test block at X=-5.

Enlarged surface view of SCC

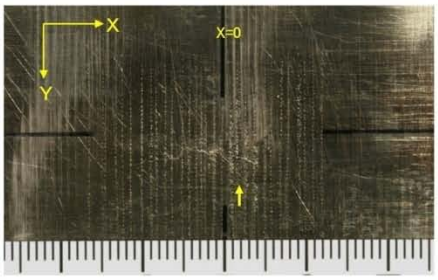

Macro. photo of cross section

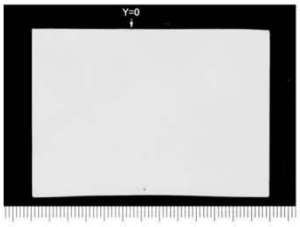

Macro. Photo at X=2

Micro. photo of cross section

Ⅰ. Crack tip

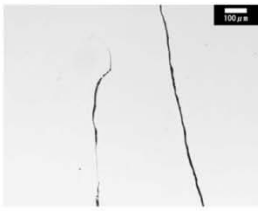

Ⅱ. Middle position

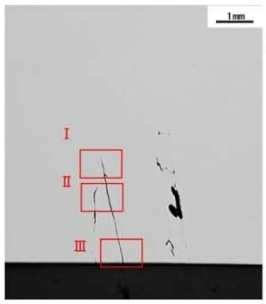

Position (X=2)

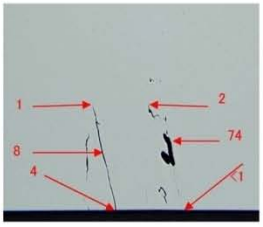

Crack opening(μm)

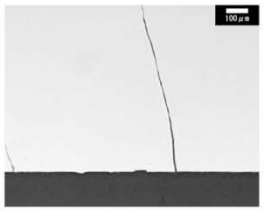

Ⅲ. Surface

Measured on sliced cross section	
Position (mm)	X=2
Depth (mm)	2.9
Opening (μm)	10
Inclination from depth direc.(Deg)	13

Typical crack opening data of PINC2.1(SH-1) test block at X=2.

Enlarged surface view of SCC

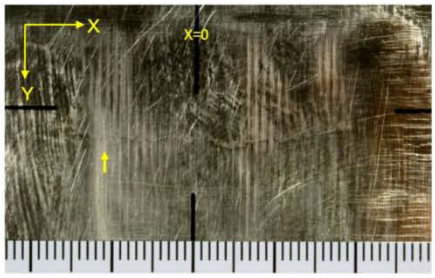

Macro. photo of cross section

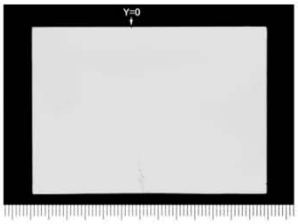

Macro. Photo at X=-11

Micro. photo of cross section

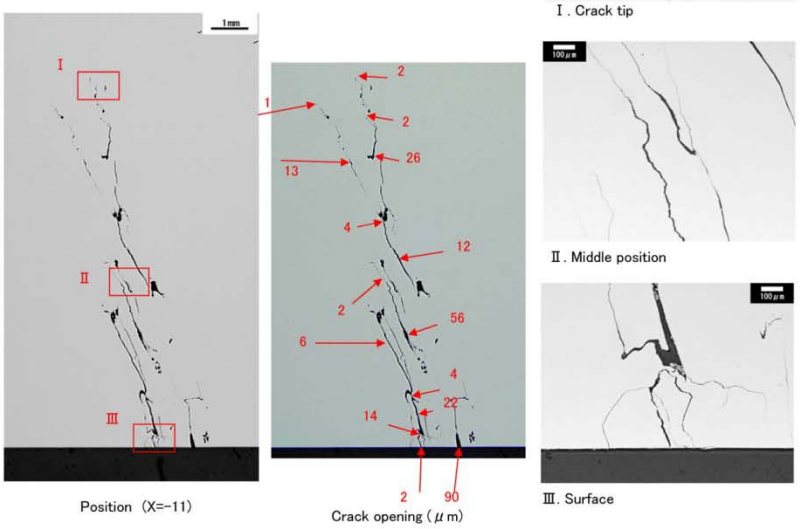

Measured on sliced cross section	
Position (mm)	X=-11
Depth (mm)	10.4
Opening (μm)	<5
Inclination from depth direc.(Deg)	10

Typical crack opening data of PINC2.2(SH-2) test block at X=-11.

Enlarged surface view of SCC

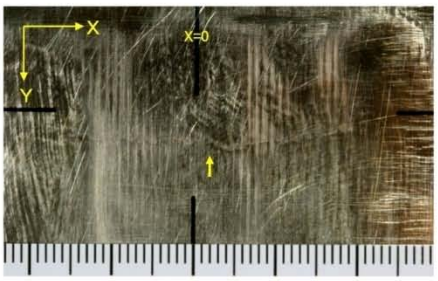

Macro. photo of cross section

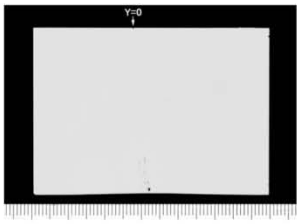

Macro. photo at X=2

Micro. photo of cross section

Ⅰ. Crack tip

Ⅱ. Middle position

Ⅲ. Surface

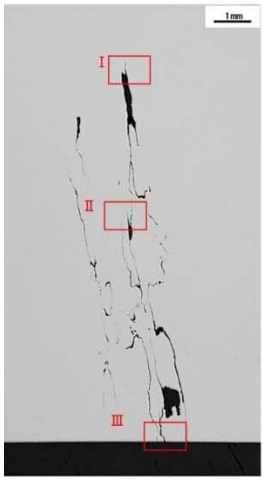

Position (X=2)

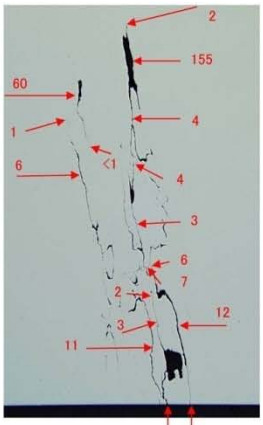

Crack opening (μm)

Measured on sliced cross section	
Position (mm)	X=2
Depth (mm)	10.5
Opening (μm)	30
Inclination from depth direc.(Deg)	6

Typical crack opening data of PINC2.2(SH-2) test block at X=2.

Enlarged surface view of SCC

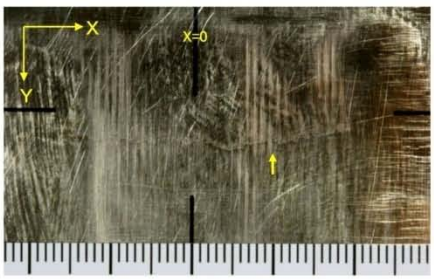

Macro. photo of cross section

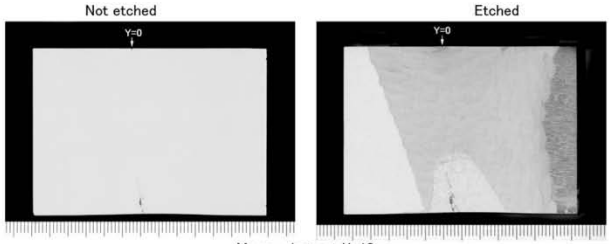

Macro. photo at X=10

Micro. photo of cross section

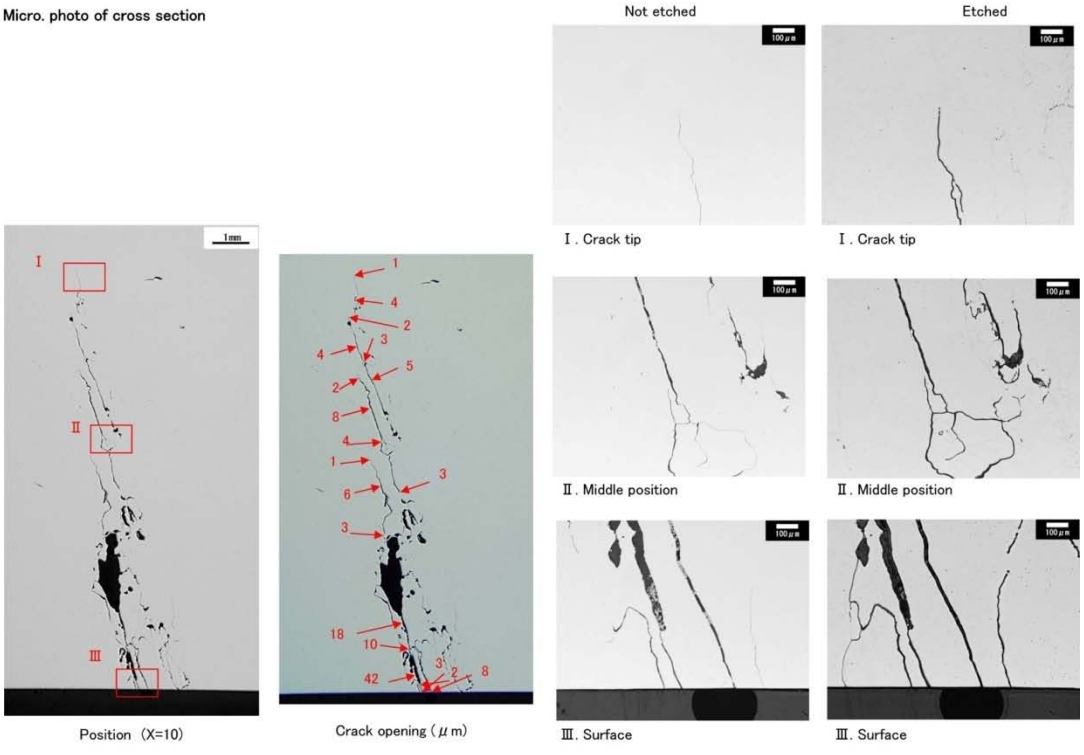

Measured on sliced cross section	
Position (mm)	X=10
Depth (mm)	11.7
Opening (μ m)	10
Inclination from depth direc.(Deg)	10

Typical crack opening data of PINC2.2(SH-2) test block at X=10.

Enlarged surface view of SCC

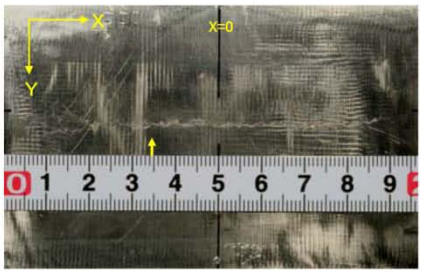

Macro. photo of cross section

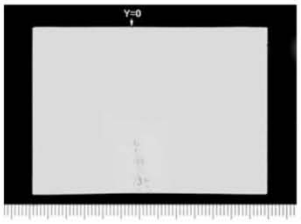

Macro. photo at X=−16

Micro. photo of cross section

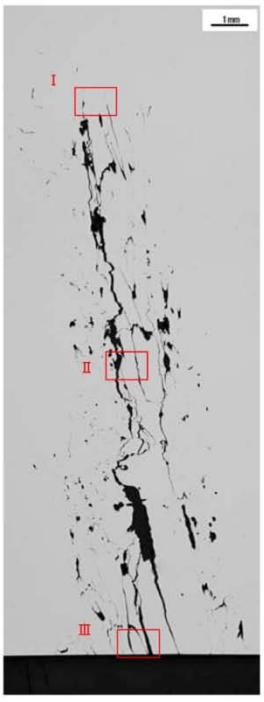

Position (X=−16)

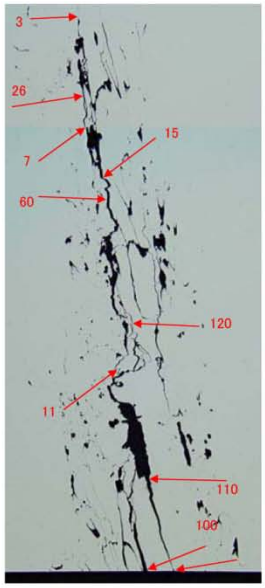

Crack opening (μ m)

Ⅰ. Crack tip

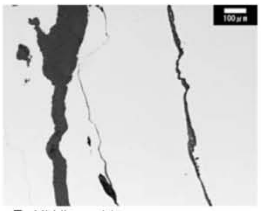

Ⅱ. Middle position

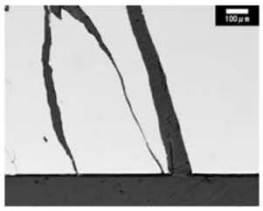

Ⅲ. Surface

Measured on sliced cross section	
Position (mm)	X=−16
Depth (mm)	15.5
Opening (μ m)	100
Inclination from depth direc.(Deg)	7

Typical crack opening data of PINC2.3(SH-3) test block at X=-16.

Enlarged surface view of SCC

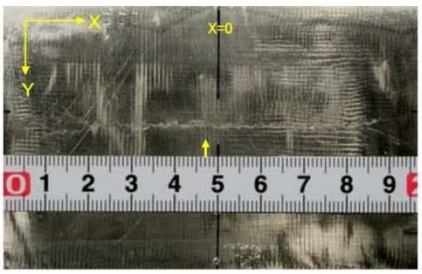

Macro. photo of cross section

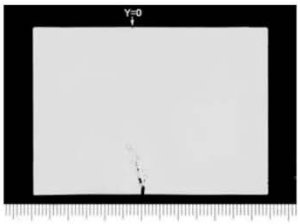

Macro. photo at X=3

Micro. photo of cross section

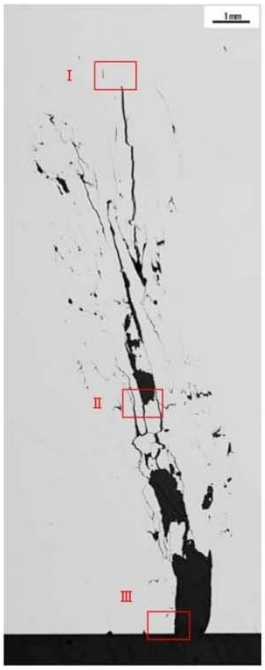

Position (X=3)

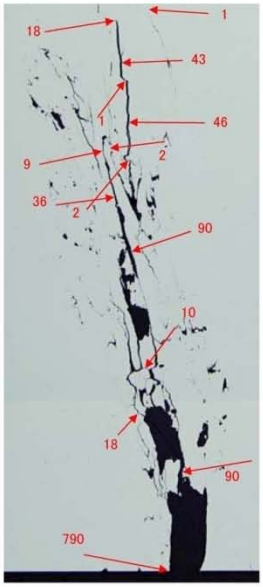

Crack opening (μ m)

Ⅰ. Crack tip

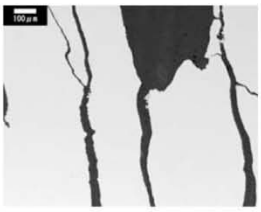

Ⅱ. Middle position

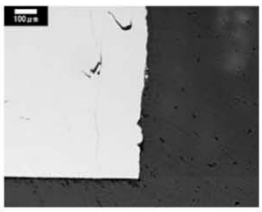

Ⅲ. Surface

Measured on sliced cross section	
Position (mm)	X=3
Depth (mm)	15.7
Opening (μ m)	790
Inclination from depth direc.(Deg)	9

Typical crack opening data of PINC2.3(SH-3) test block at X=3.

Enlarged surface view of SCC

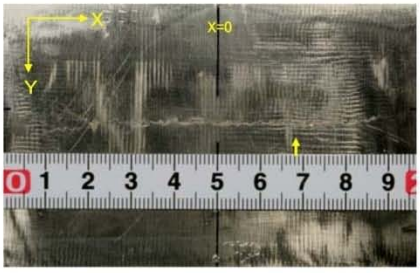

Macro. photo of cross section

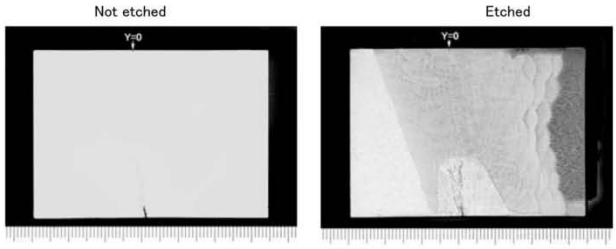

Macro. photo at X=18

Micro. photo of cross section

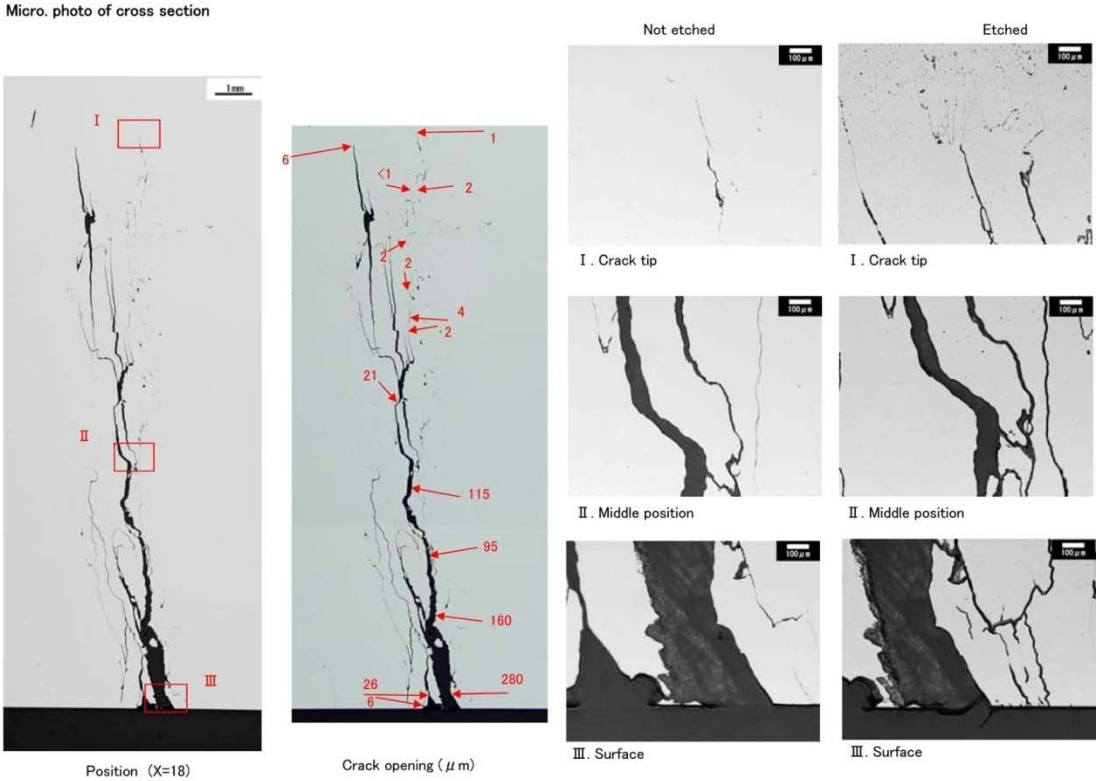

Position (X=18)

Crack opening (μm)

Measured on sliced cross section	
Position (mm)	X=18
Depth (mm)	15.9
Opening (μm)	275(420)
Inclination from depth direc.(Deg)	3

( ) means supplementary value which include the drop out of crystal by the polishing of sliced cross section.

Typical crack opening data of PINC2.3(SH-3) test block at X=18.

Enlarged surface view of SCC

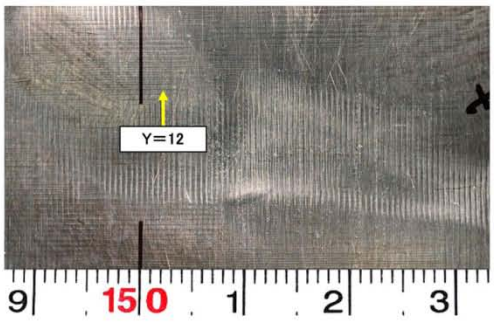

Macro. photo of cross section

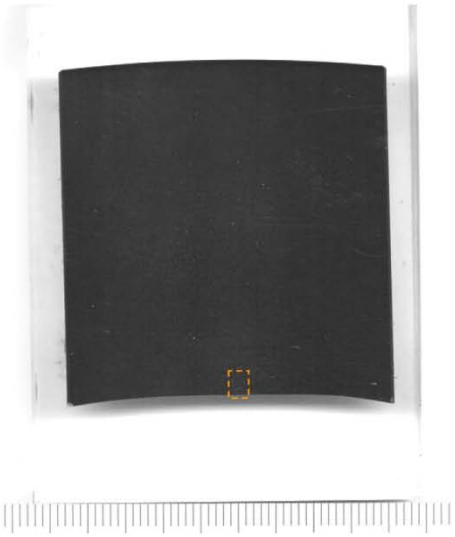

Micro. photo of cross section

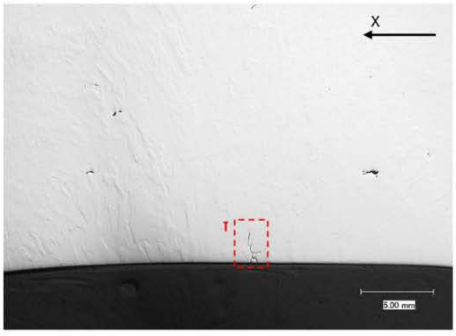

Position (Y=12)

I . Whole crack

Measured on sliced cross section	
Position (mm)	Y=12
Depth (mm)	2.7
Opening (μ m)	13
Inclination from depth direc.(Deg)	4

Typical crack opening data of PINC2.4(ST-1) test block at Y=12. (Page 1/2)

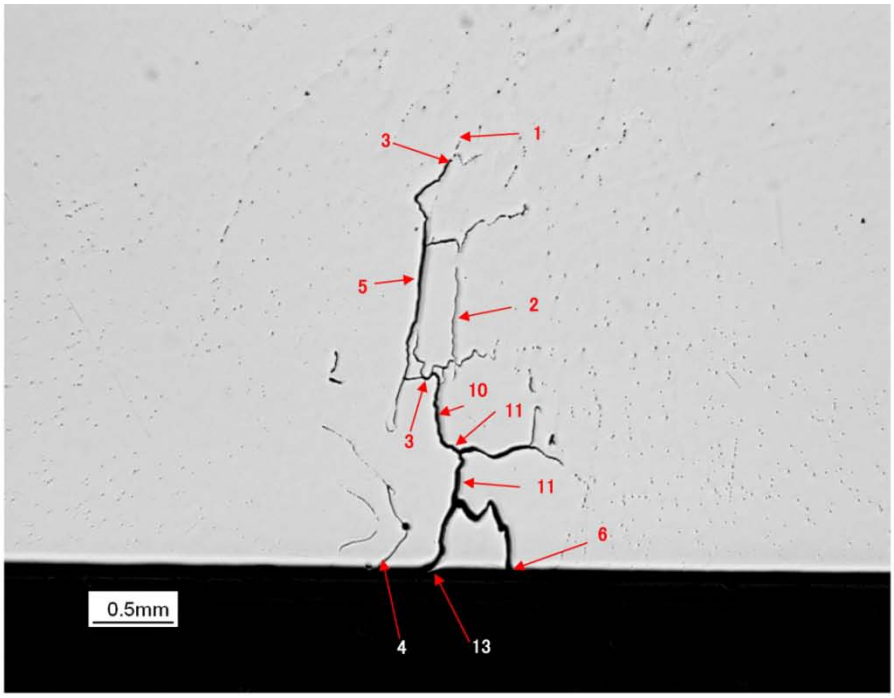

Crack opening（μm）

Typical crack opening data of PINC2.4(ST-1) test block at Y=12.　(Page 2/2)

Enlarged surface view of SCC

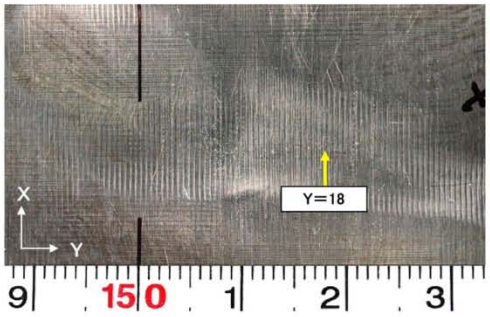

Macro. photo of cross section

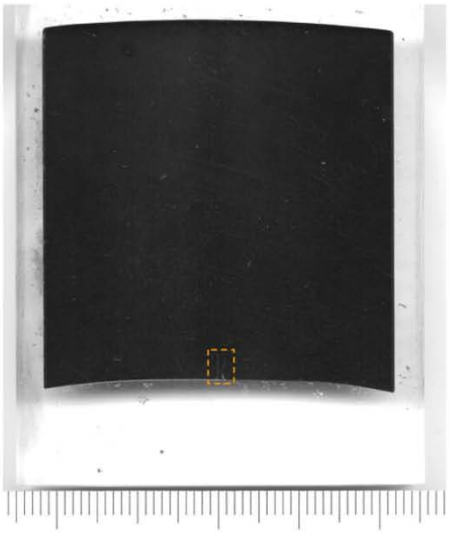

Micro. photo of cross section

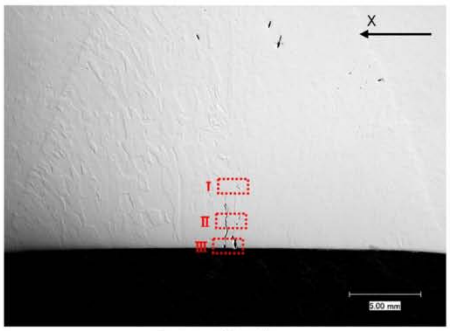

Position（Y=18）

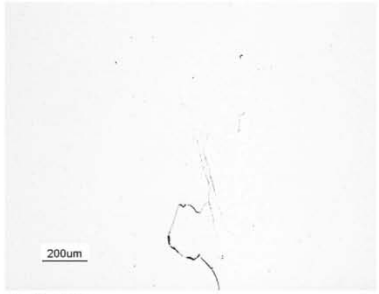

Ⅰ. Crack tip

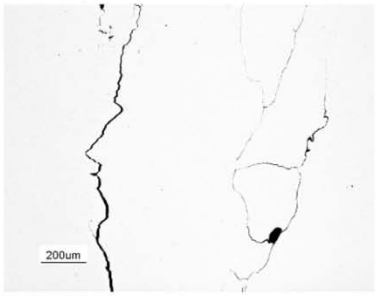

Ⅱ. Middle position

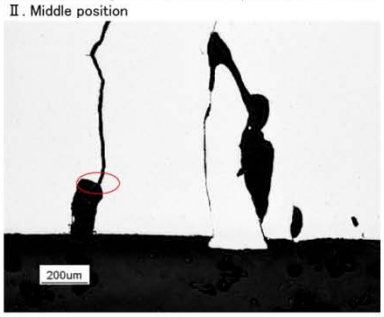

Ⅲ. Surface

Measured on sliced cross section	
Position (mm)	Y=18
Depth (mm)	4.9
Opening (μm)	14 (97)
Inclination from depth direc.(Deg)	4

( ) means supplementary value which include the drop out of crystal by the polishing of sliced cross section.

Typical crack opening data of PINC2.4(ST-1) test block at Y=18. (Page 1/2)

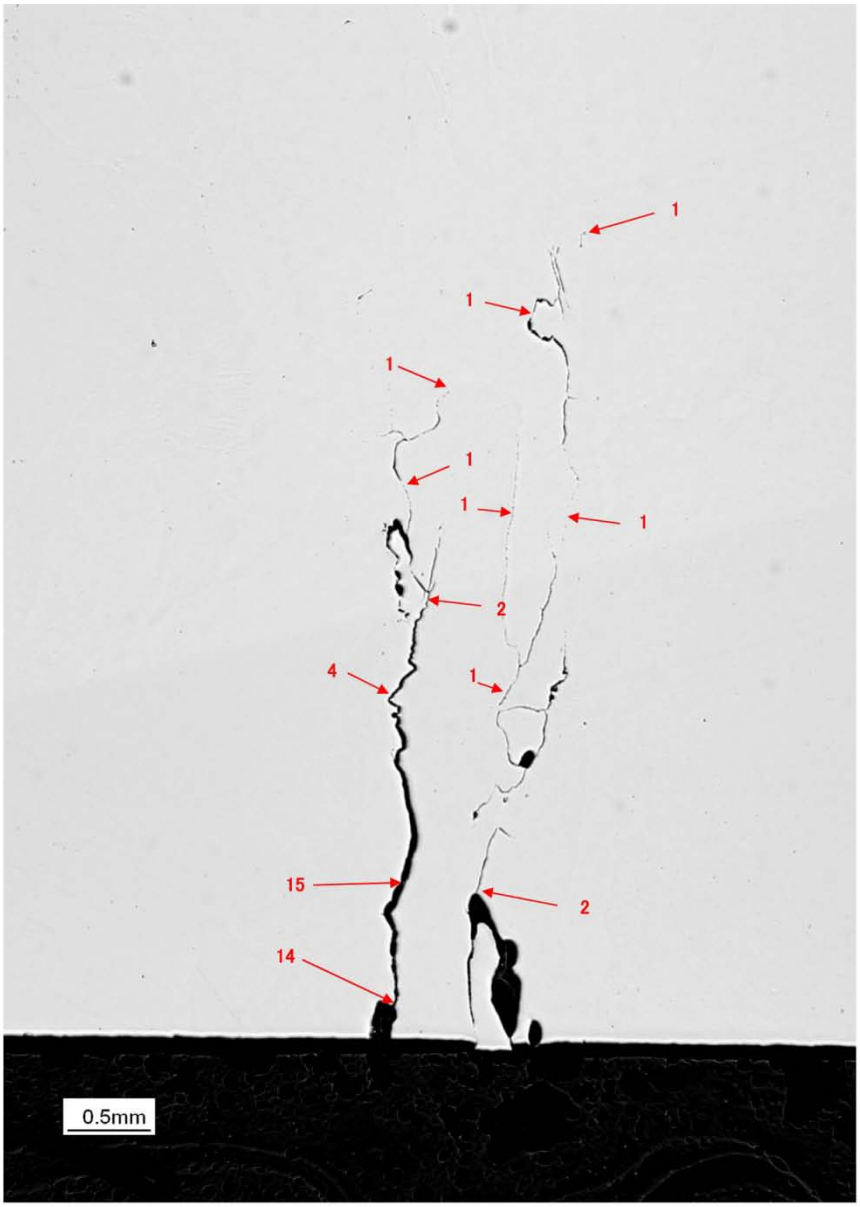

Crack opening （μm）

Typical crack opening data of PINC2.4(ST-1) test block at Y=18.　(Page 2/2)

Enlarged surface view of SCC

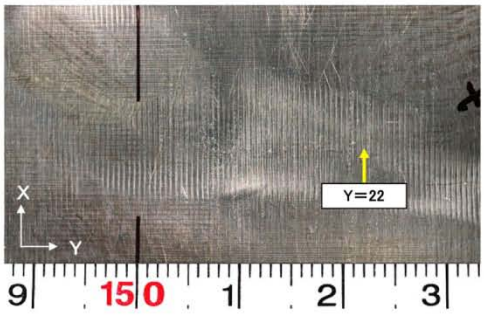

Macro. photo of cross section

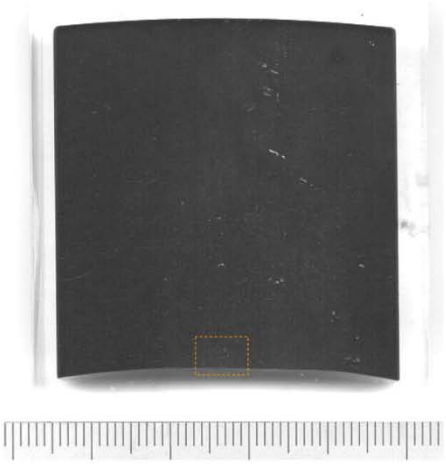

Micro. photo of cross section

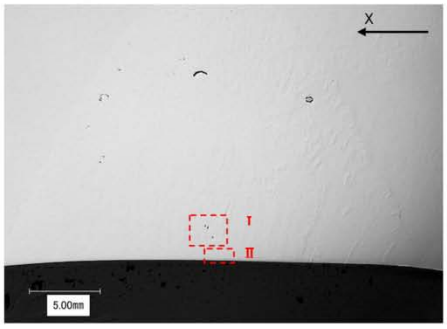

Position (Y=22)

Ⅰ. Crack tip

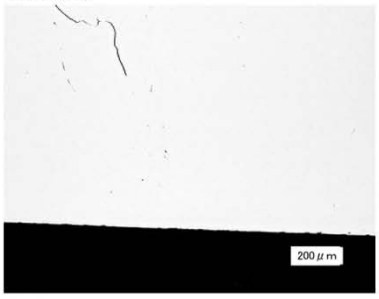

Ⅱ. Surface

Measured on sliced cross section	
Position (mm)	Y=22
Depth (mm)	1.3
Opening (μ m)	embeded
Inclination from depth direc.(Deg)	—

Typical crack opening data of PINC2.4(ST-1) test block at Y=22. (Page 1/2)

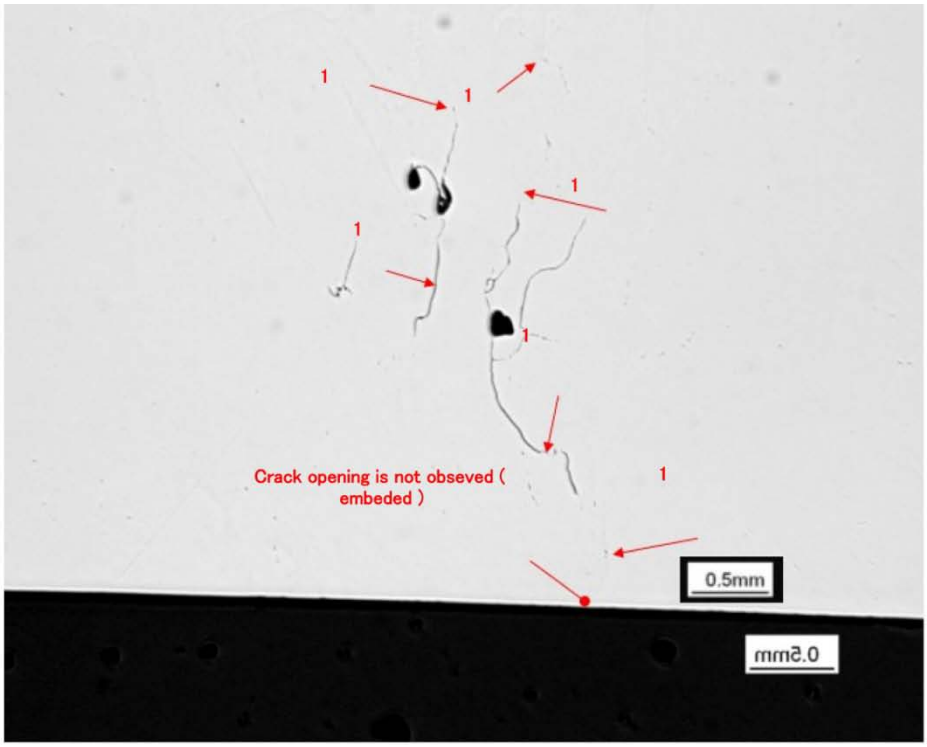

Typical crack opening data of PINC2.4(ST-1) test block at Y=22. (Page 2/2)

Enlarged surface view of SCC

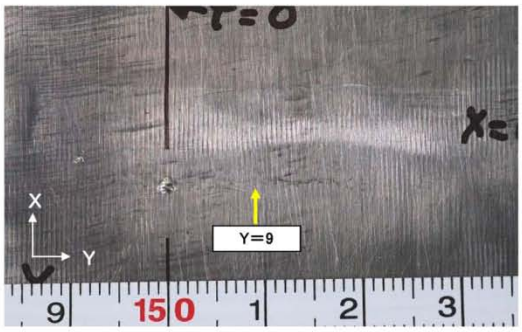

Macro. photo of cross section

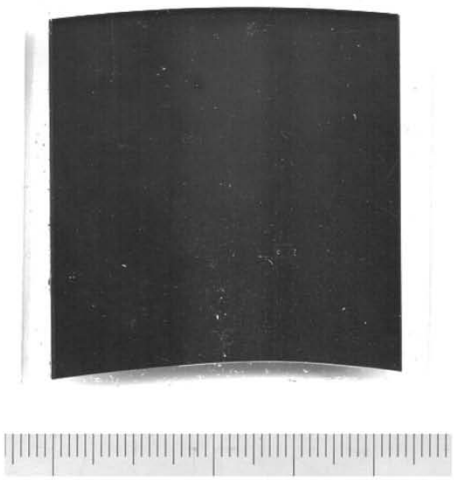

Micro. photo of cross section

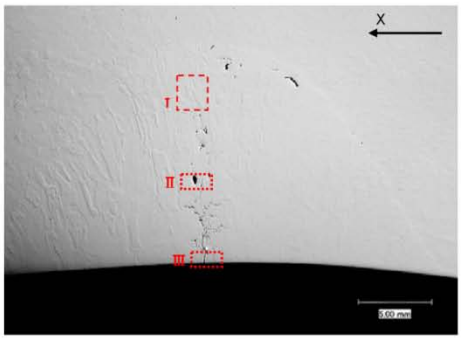

Position (Y=9)

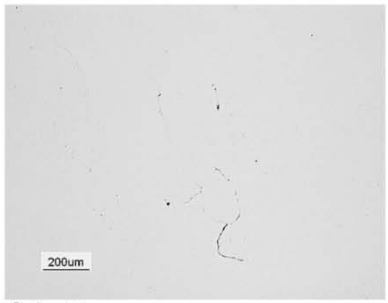

Ⅰ. Crack tip

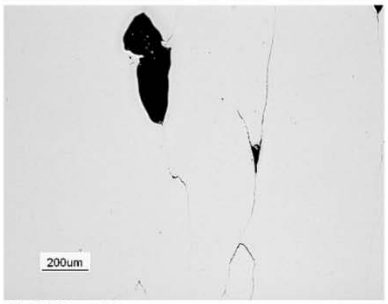

Ⅱ. Middle position

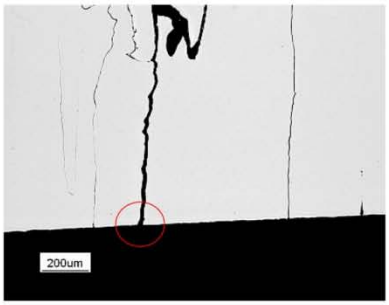

Ⅲ. Surface

Measured on sliced cross section	
Position (mm)	Y=9
Depth (mm)	10.6
Opening (μ m)	12
Inclination from depth direc.(Deg)	-2

Typical crack opening data of PINC2.5(ST-2) test block at Y=9. (Page 1/2)

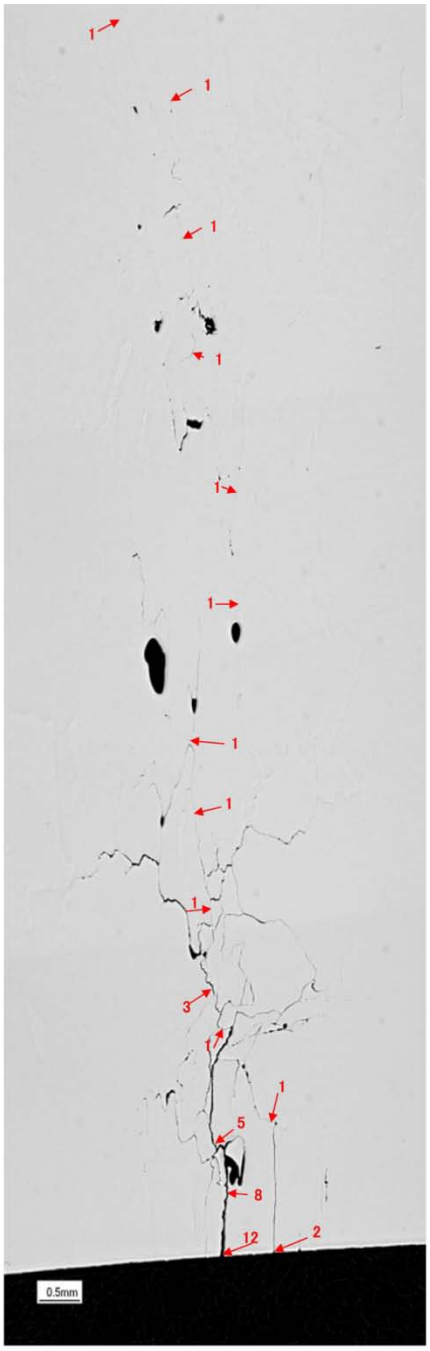

Crack opening (μ m)

Typical crack opening data of PINC2.5(ST-2) test block at Y=9. (Page 2/2)

Enlarged surface view of SCC

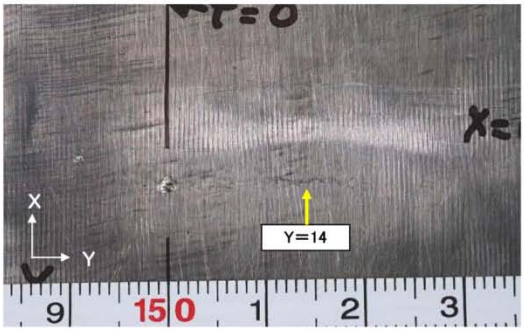

Macro. photo of cross section

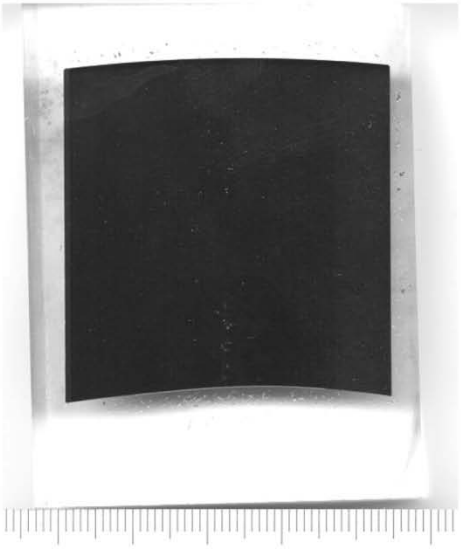

Micro. photo of cross section

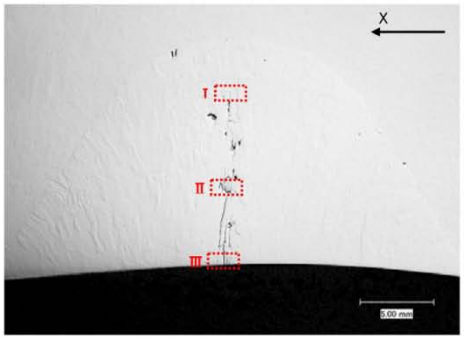

Position （Y=14）

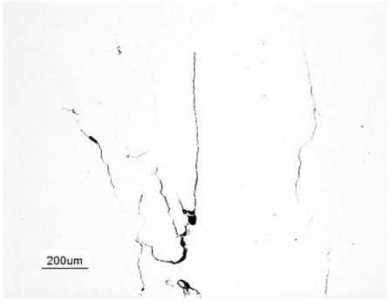

Ⅰ. Crack tip

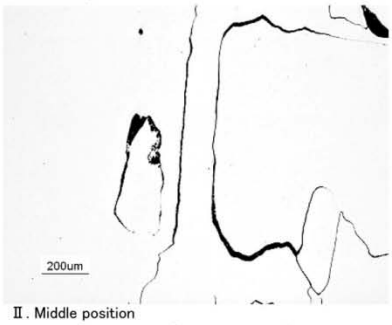

Ⅱ. Middle position

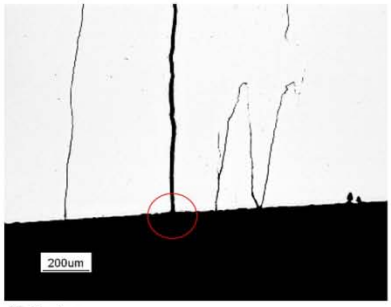

Ⅲ. Surface

Measured on sliced cross section	
Position (mm)	Y=14
Depth (mm)	12.3
Opening (μ m)	19
Inclination from depth direc.(Deg)	1

Typical crack opening data of PINC2.5(ST-2) test block at Y=14.　(Page 1/2)

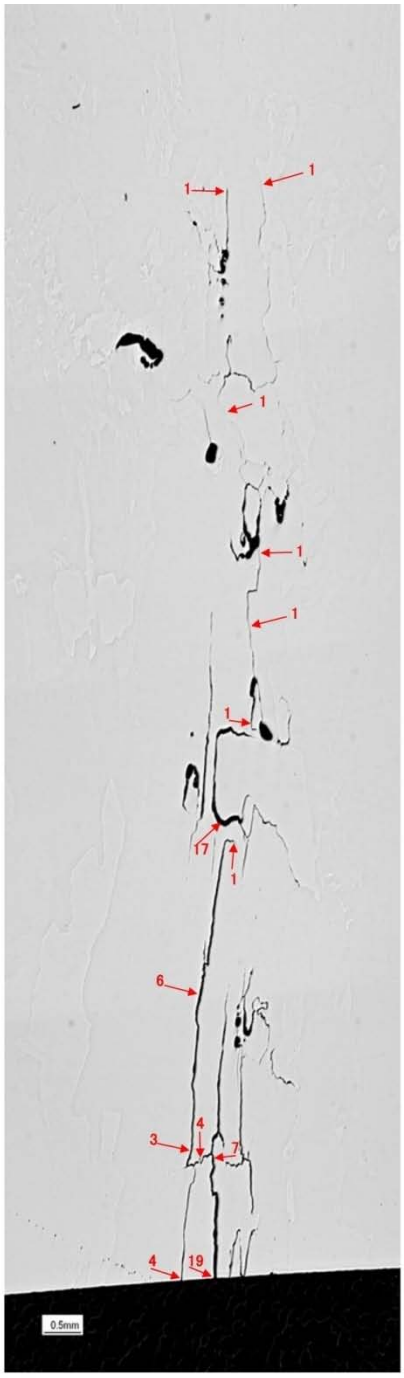

Crack opening (μ m)

Typical crack opening data of PINC2.5(ST-2) test block at Y=14. (Page 2/2)

Enlarged surface view of SCC

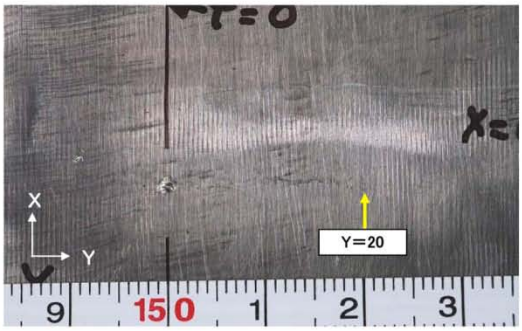

Macro. photo of cross section

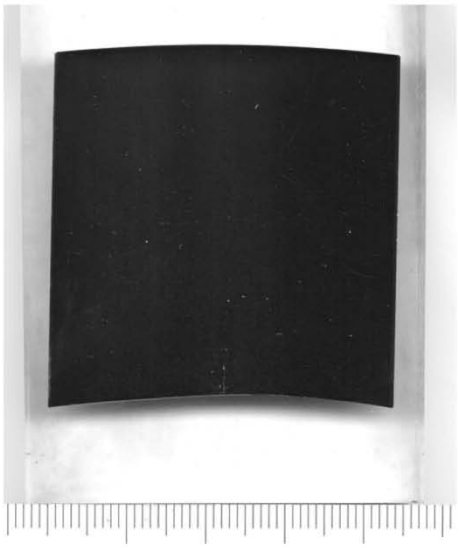

Micro. photo of cross section

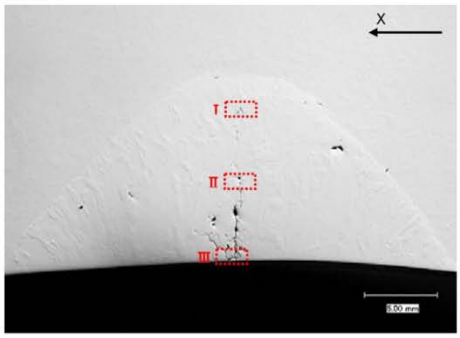

Position （ Y=20 ）

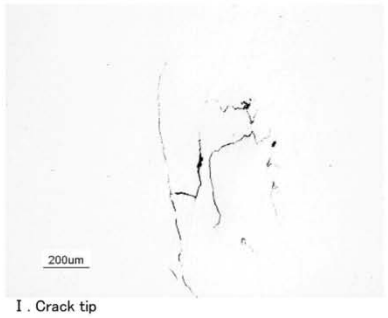

Ⅰ. Crack tip

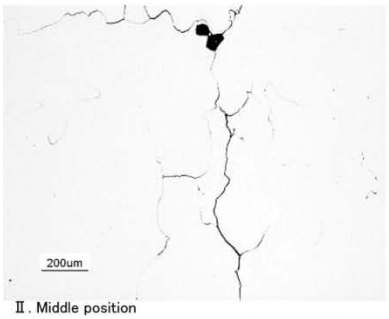

Ⅱ. Middle position

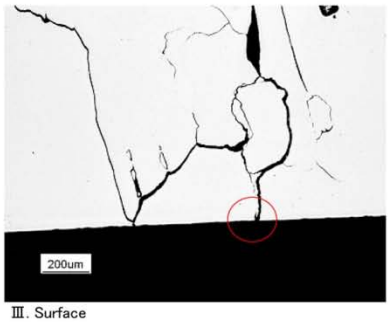

Ⅲ. Surface

Measured on sliced cross section	
Position (mm)	Y=20
Depth (mm)	11.0
Opening (μ m)	9
Inclination from depth direc.(Deg)	1

Typical crack opening data of PINC2.5(ST-2) test block at Y=20.　(Page 1/2)

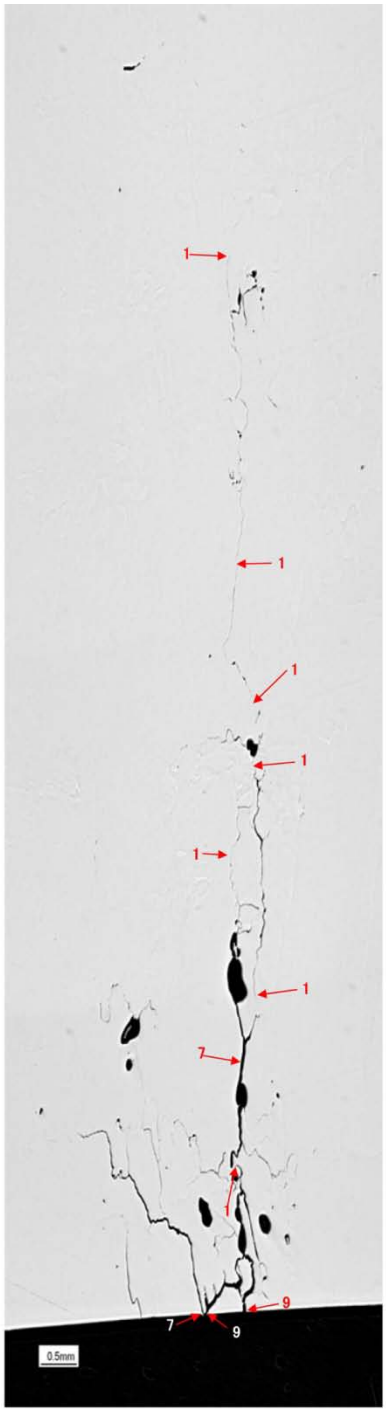

Crack opening (μ m)

Typical crack opening data of PINC2.5(ST-2) test block at Y=20. (Page 2/2)

Enlarged surface view of SCC

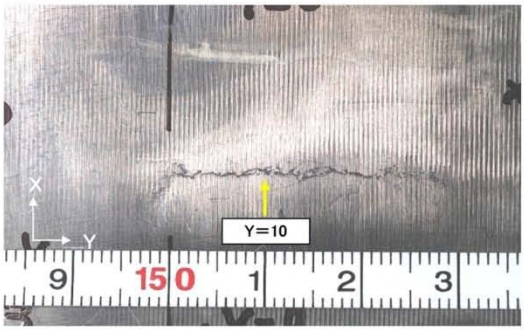

Macro. photo of cross section

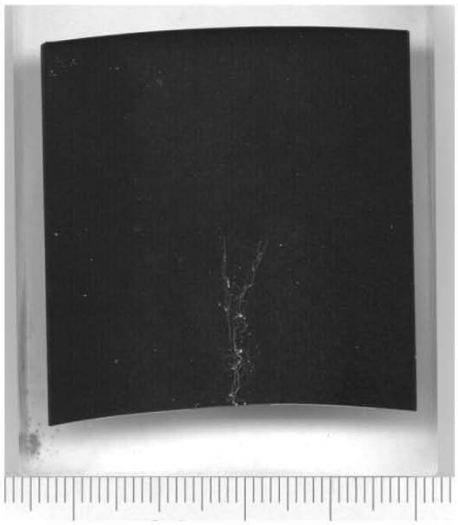

Micro. photo of cross section

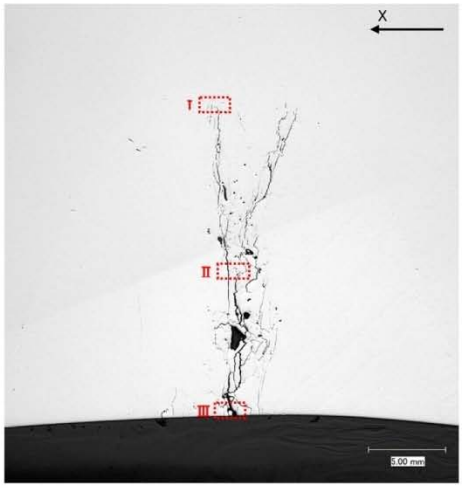

Position （Y=10）

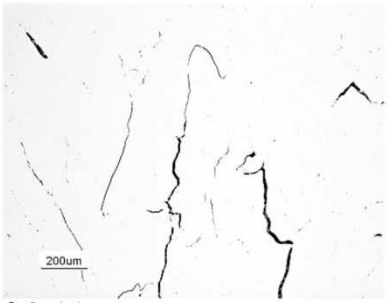

Ⅰ. Crack tip

Ⅱ. Middle position

Ⅲ. Surface

Measured on sliced cross section	
Position (mm)	Y=10
Depth (mm)	(20.7)
Opening (μ m)	198
Inclination from depth direc.(Deg)	−3

（ ）means measured on

Typical crack opening data of PINC2.6(ST-3) test block at Y=10.　(Page 1/2)

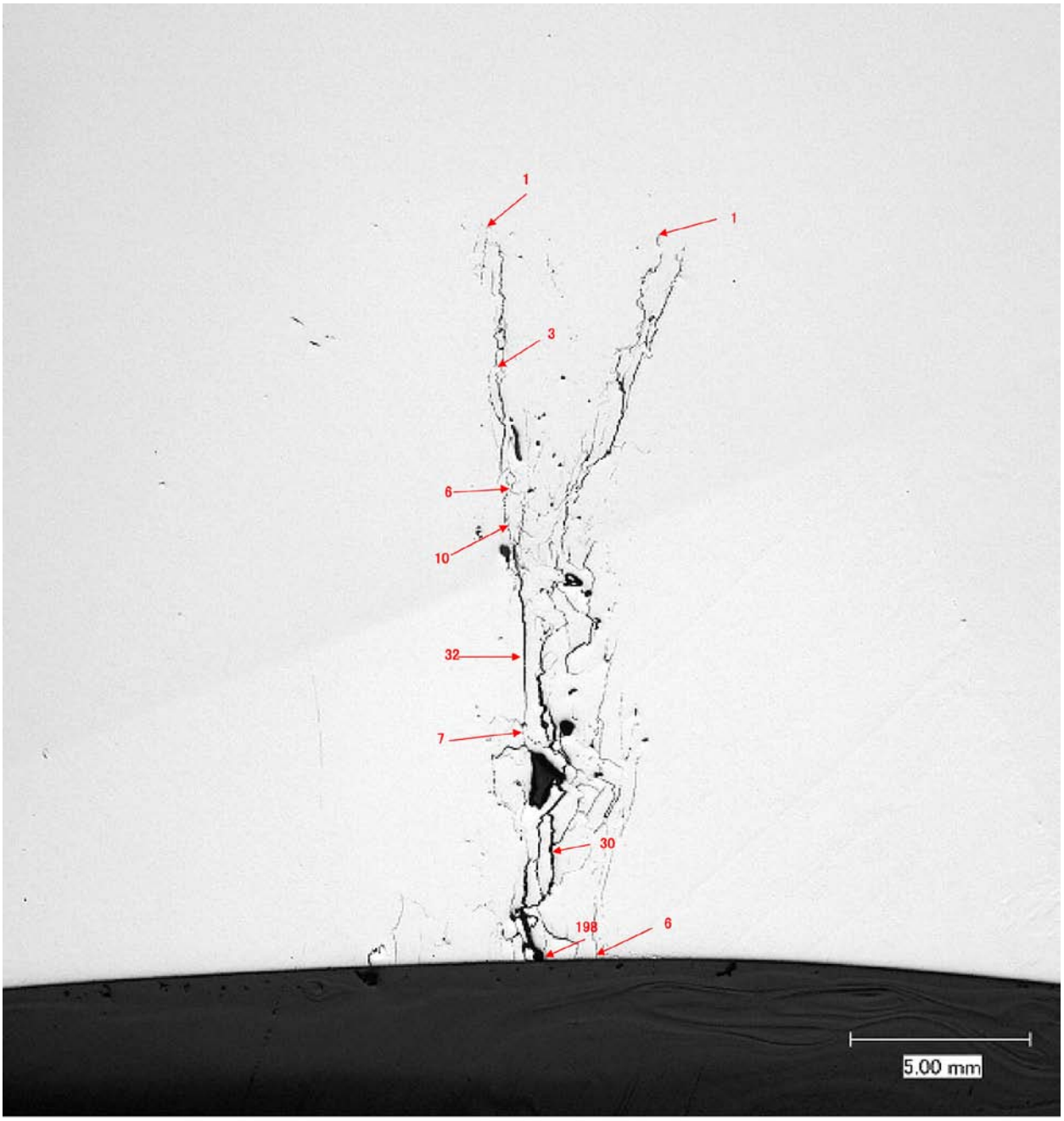

Crack opening (μ m)

Typical crack opening data of PINC2.6(ST-3) test block at Y=10. (Page 2/2)

Enlarged surface view of SCC

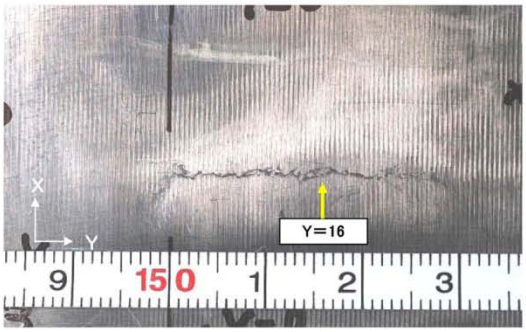

Macro. photo of cross section

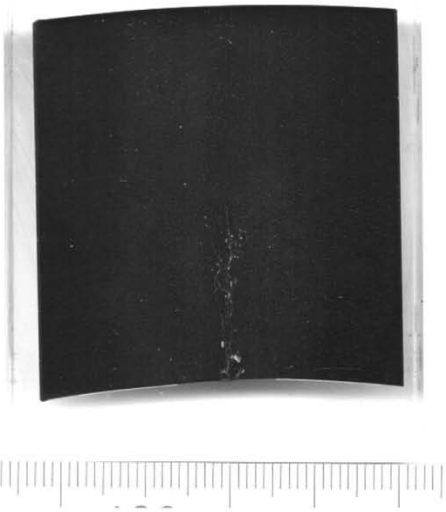

Micro. photo of cross section

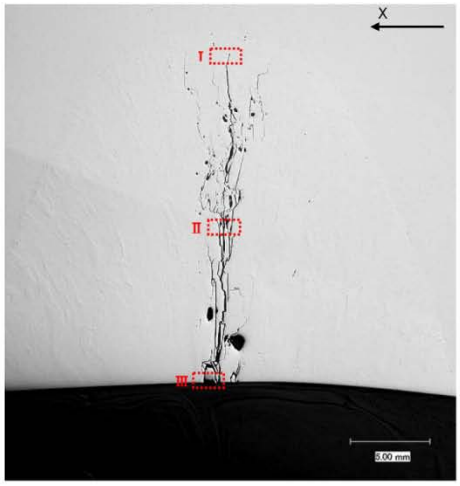

Position （Y=16）

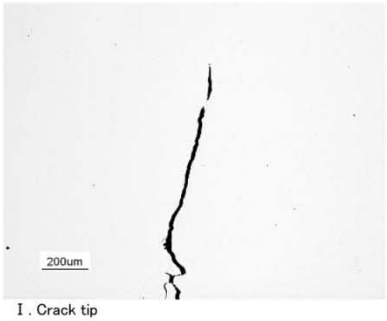

Ⅰ. Crack tip

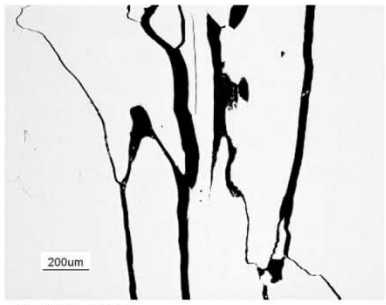

Ⅱ. Middle position

Ⅲ. Surface

Measured on sliced cross section	
Position (mm)	Y=16
Depth (mm)	(21.4)
Opening (μ m)	686
Inclination from depth direc.(Deg)	2

Depth measured on breaked crack is 22.3mm

Typical crack opening data of PINC2.6(ST-3) test block at Y=16. (Page 1/2)

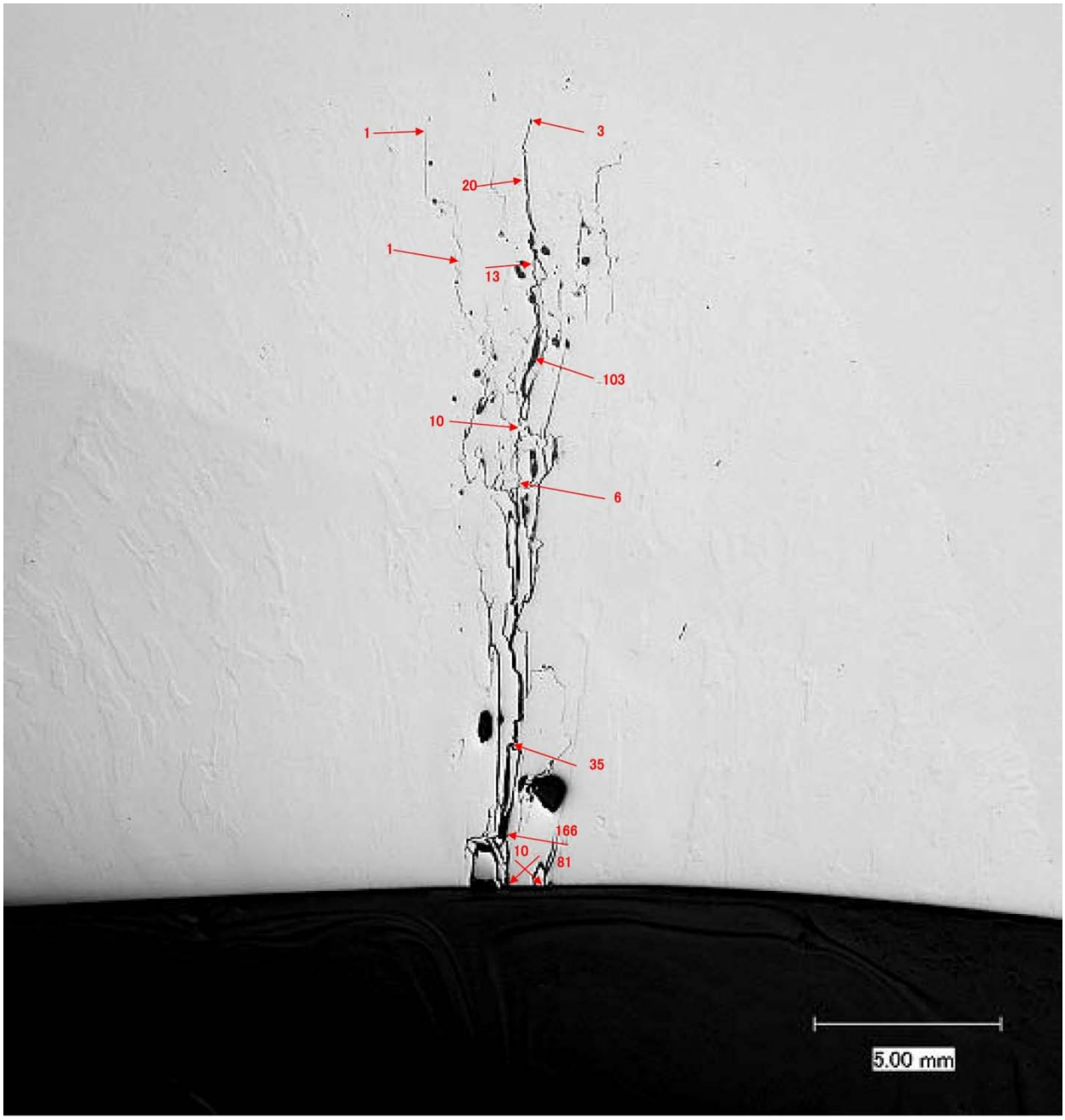

Crack opening (μ m)

Typical crack opening data of PINC2.6(ST-3) test block at Y=16. (Page 2/2)

Enlarged surface view of SCC

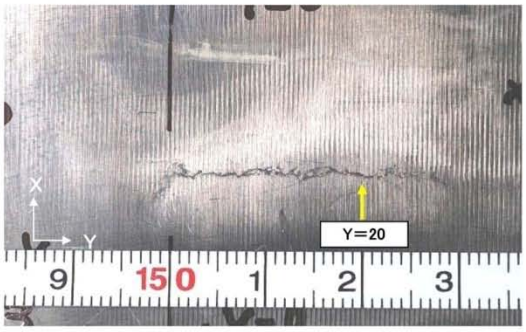

Macro. photo of cross section

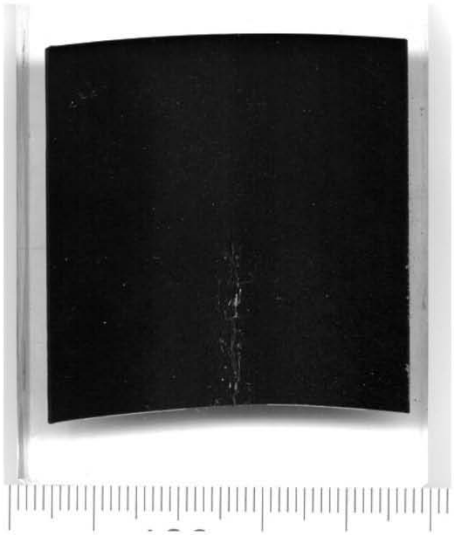

Micro. photo of cross section

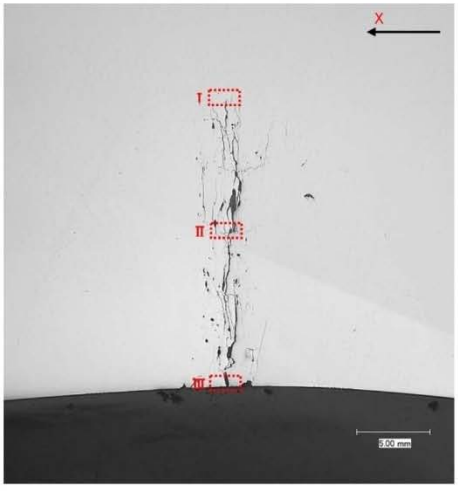

Position （Y=20）

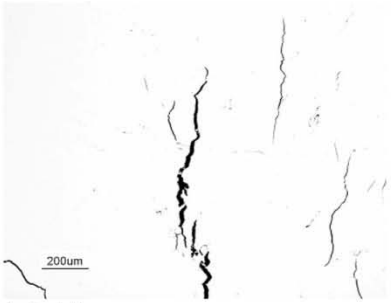

Ⅰ. Crack tip

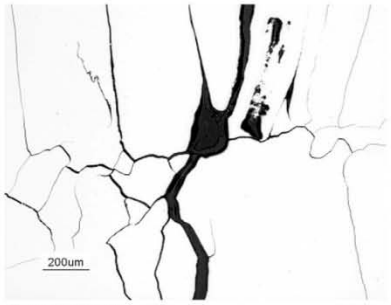

Ⅱ. Middle position

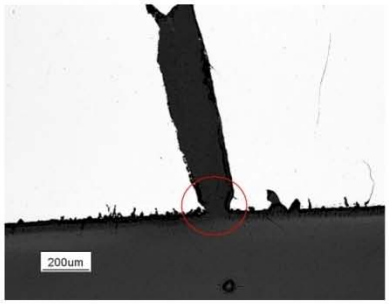

Ⅲ. Surface

Measured on sliced cross section	
Position (mm)	Y=20
Depth (mm)	20.2
Opening (μ m)	97
Inclination from depth direc.(Deg)	0

Typical crack opening data of PINC2.6(ST-3) test block at Y=20.　(Page 1/2)

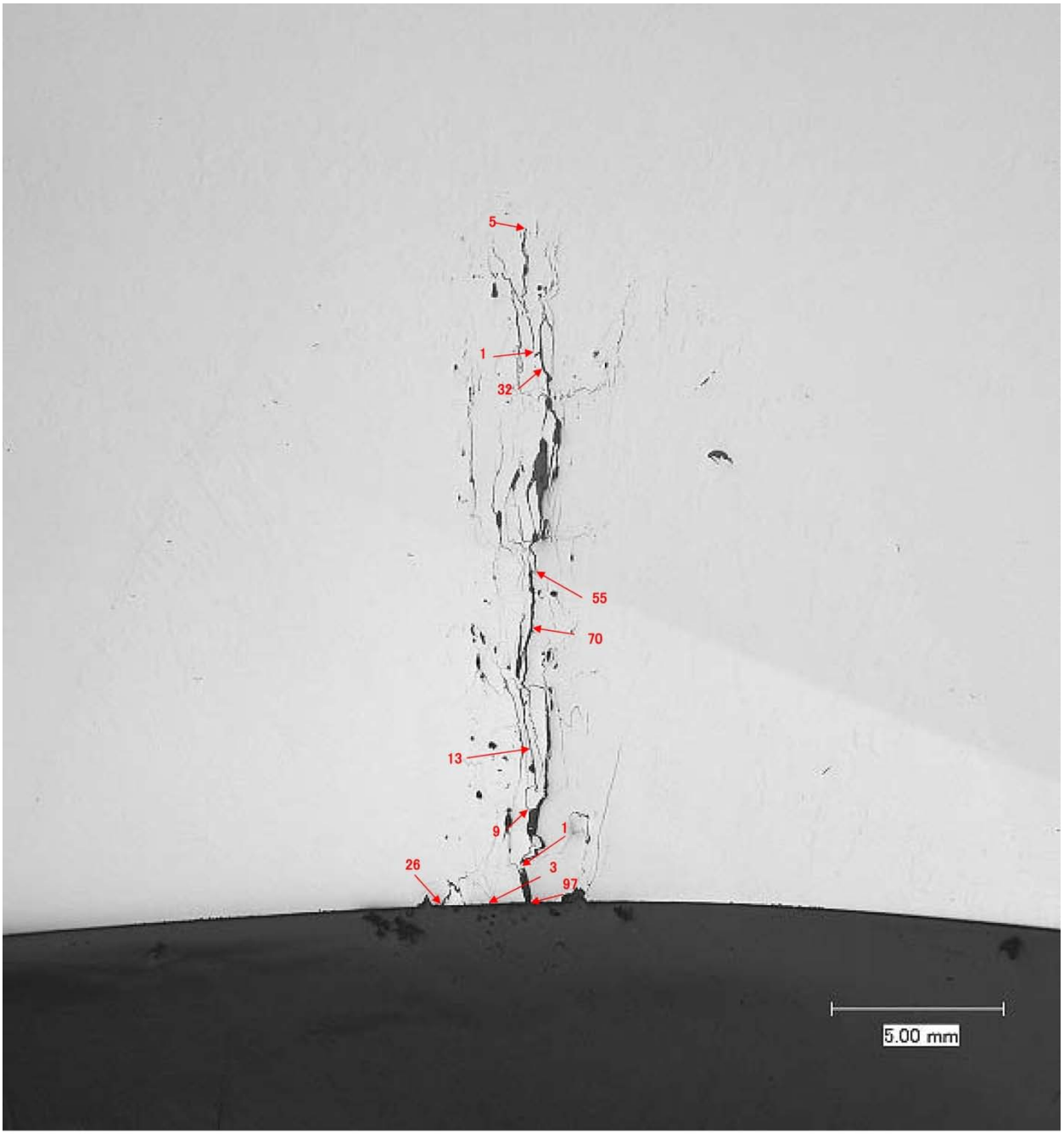

Crack opening (μ m)

Typical crack opening data of PINC2.6(ST-3) test block at Y=20. (Page 2/2)

Appendix B

Destructive Analysis of BMI Samples

Appendix B

Destructive Analysis of BMI Samples

B.1 Destructive Analysis of Sample 5.2

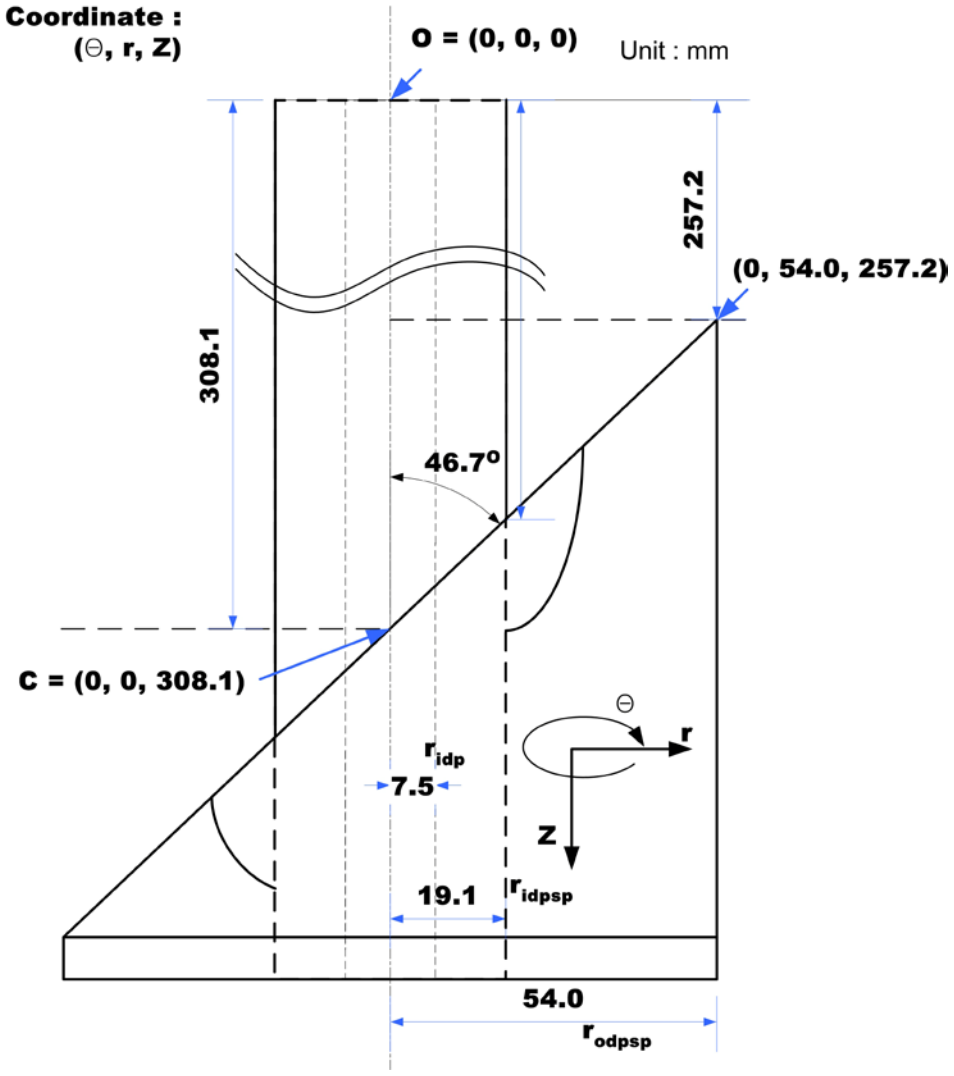

Figure 1 Analysis of BMI Sample Position

List of Symbols

O	:	Origin coordinate of BMI sample
C	:	Center coordinate
r_{idp}	:	I.D. radius of pipe
r_{idpsp}	:	I.D. radius of pipe support plate
r_{odpsp}	:	O.D. radius of pipe support plate
r_{m1}	:	Minimum radial extent measured from pipe inner surface
r_1	:	Minimum radial extent of flaw, $r_1 = r_{idp} + r_{m1}$
r_{m2}	:	Maximum radial extent measured from pipe inner surface
r_2	:	Maximum radial extent of flaw, $r_2 = r_{idp} + r_{m2}$
Z_{m1}	:	Minimum measured vertical position
Z_{m2}	:	Maximum measured vertical position
Z_1	:	Minimum vertical position of flaw measured from origin O
Z_2	:	Maximum vertical position of flaw measured from origin O
θ_1	:	Minimum measured circumferential extent
θ_2	:	Maximum measured circumferential extent
$\mathbf{r_{min}}$	:	Minimum radial extent
$\mathbf{r_{max}}$	:	Maximum radial extent
$\mathbf{Z_{min}}$	:	Minimum vertical position from origin O
$\mathbf{Z_{max}}$	:	Maximum vertical position from origin O
$\boldsymbol{\theta}_{\mathbf{min}}$	:	Minimum circumferential extent
$\boldsymbol{\theta}_{\mathbf{max}}$	:	Maximum circumferential extent

1. Circumferential Crack, Surface Crack of Pipe O.D.

Position of Flaw

Flaw No.	Circ. Extent (deg)	Radial Extent (mm)		Vertical Position (mm)	
	θ	r_1	r_2	Z_1	Z_2
#1-10	305	-	-	-	-
#1-09	310	15.8	17.1	296.0	297.4
#1-08	315	15.8	18.7	295.8	297.6
#1-07	320	14.4	18.2	294.0	297.1
#1-06	325	15.0	18.9	292.7	296.4
#1-05	330	14.7	19.5	292.0	295.8
#1-04	335	14.9	19.6	291.4	295.6
#1-03	340	15.8	19.7	290.9	294.0
#1-02	345	16.0	19.7	290.4	293.3
#1-01	350	-	-	-	-

Final Results of Destructive Test on BMI Test Sample

BMI Test Block Number	Circ. Extent (deg)		Radial Extent (mm)		Vertical Position (mm)	
	θ_{min}	θ_{max}	r_{min}	r_{max}	Z_{min}	Z_{max}
Flaw No. #1	305	350	14.4	19.7	290.4	297.6

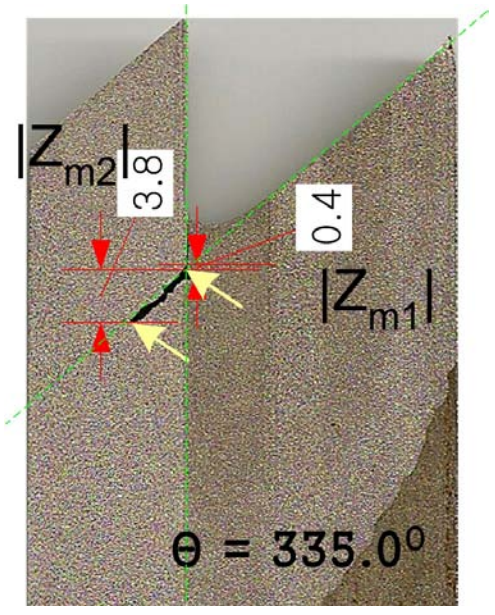

Figure 2 Flaw #1 Surface Crack of Pipe O.D.

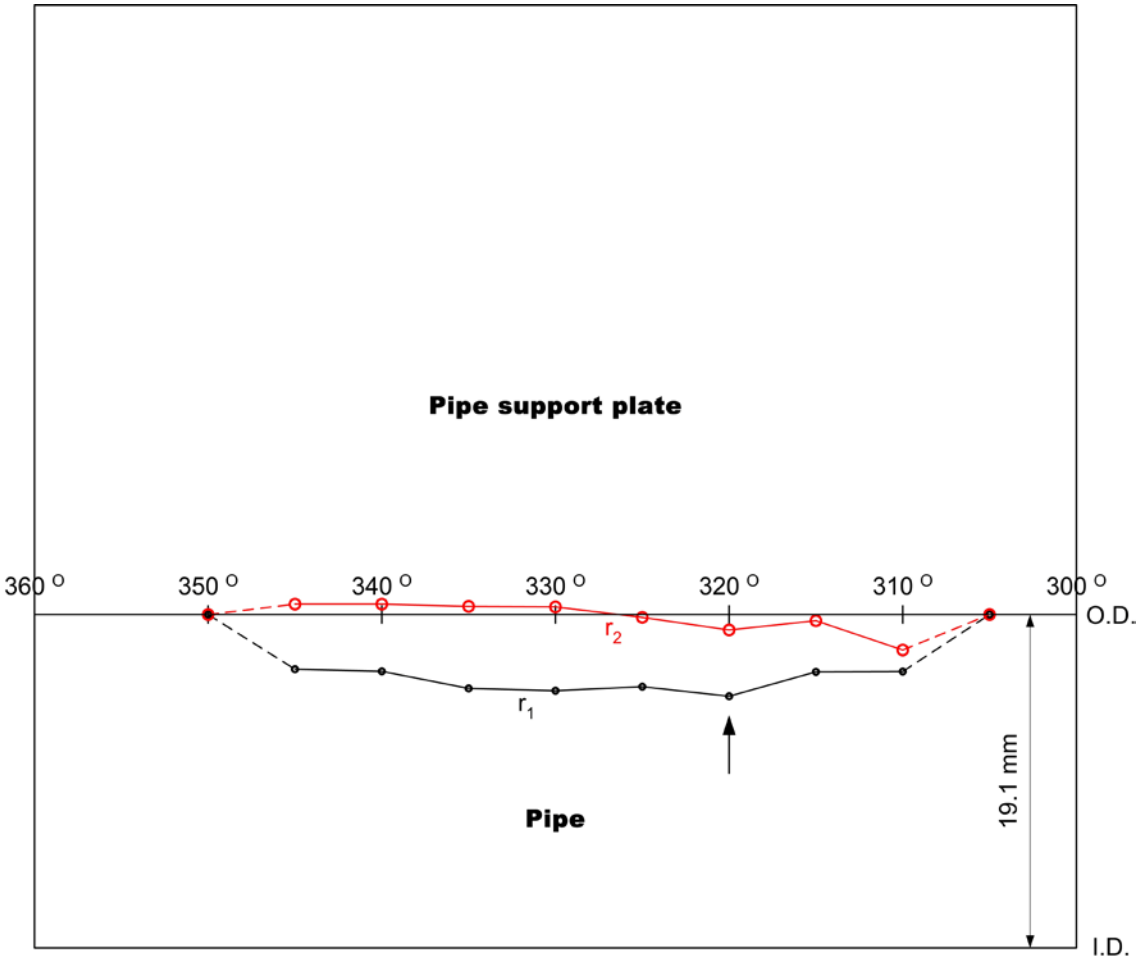

Figure 3 Depth Profile of Flaw #1 Using r_1 and r_2

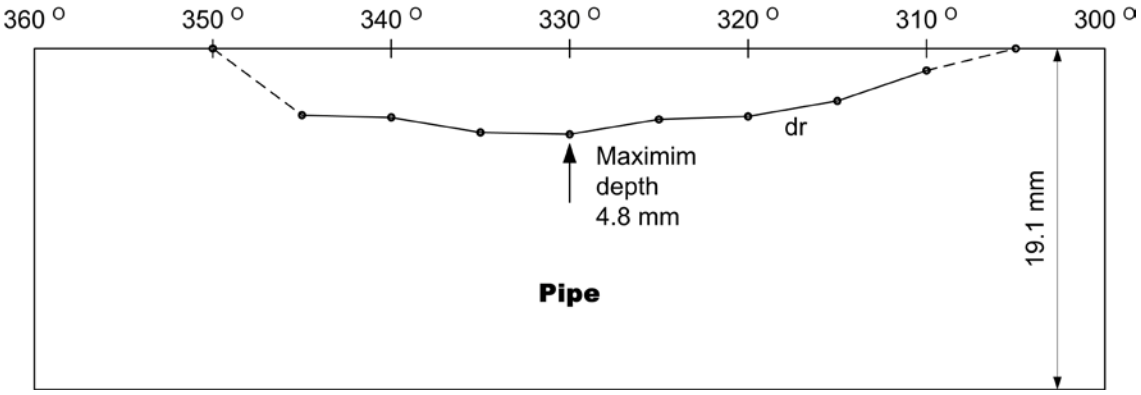

Figure 4 Depth Profile of Flaw # 1 Using dr (= $r_2 - r_1$)

2. Circumferential Crack, Through Wall Crack

Position of Flaw

Flaw No.	Circ. Extent (deg) θ	Radial Extent (mm) r	Vertical Position (mm) Z_1	Vertical Position (mm) Z_2
#2-13*	225	9.2*	314.5	313.9
#2-12*	230	18.9*	317.0	313.5
#2-11	235	19.1	314.7	312.4
#2-10	240	19.1	313.0	312.1
#2-09	245	19.1	311.9	311.5
#2-08	250	19.1	310.6	310.9
#2-07	255	19.1	308.9	310.0
#2-06	260	19.1	307.8	310.1
#2-05	265	19.1	306.4	309.8
#2-04	270	19.1	305.4	309.6
#2-03	275	19.1	304.5	309.2
#2-02*	280	15.8*	305.4	309.8
#2-01*	285	11.3*	307.0	309.6

* : Not perfectly through wall crack

Final Results of Destructive Test on BMI Test Sample

BMI Test Block Number	Circ. Extent (deg) θ_{min}	Circ. Extent (deg) θ_{max}	Radial Extent (mm) r_{min}	Radial Extent (mm) r_{max}	Vertical Position (mm) Z_{min}	Vertical Position (mm) Z_{max}
Flaw No. #2	220	290	9.2	19.1	304.5	317.0

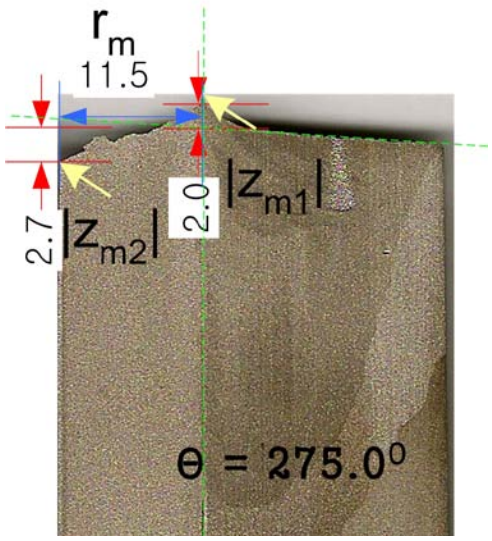

Figure 5 Flaw #2 Through Wall Crack

3. Axial Crack, 0.05” from Interface J-weld and Nozzle O.D.

Position of Flaw

Flaw No.	Circ. Extent (deg)		Radial Extent (mm)		Vertical Position (mm)	
	θ_1	θ_2	r_1	r_2	Z_1	Z_2
#3-01	-	-	-	-	-	-
#3-02	150	154	19.9	27.3	327.1	334.0
#3-03	149	153	19.8	25.9	329.6	335.3
#3-04	148	155	19.3	24.9	331.7	337.6
#3-05	149	155	19.5	21.9	334.9	337.8
#3-06	151	155	21.2	22.6	339.3	341.2
#3-07	-	-	-	-	-	-

Final Results of Destructive Test on BMI Test Sample

BMI Test Block Number	Circ. Extent (deg)		Radial Extent (mm)		Vertical Position (mm)	
	θ_{min}	θ_{max}	r_{min}	r_{max}	Z_{min}	Z_{max}
Flaw No. #3	148	155	19.3	27.3	327.1	341.2

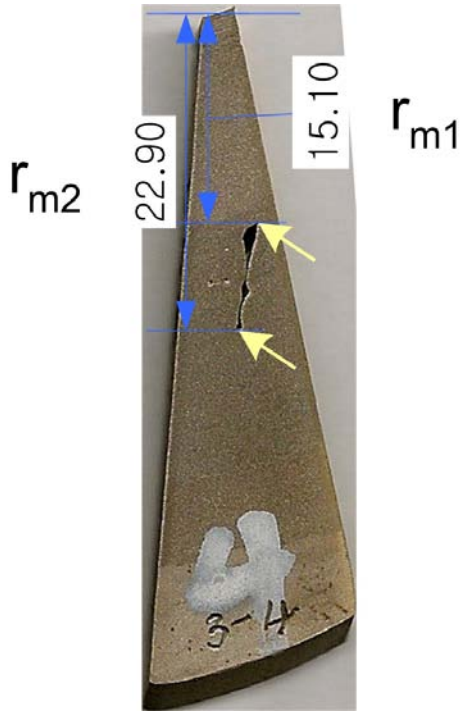

Figure 6 Flaw #3 Interface J-weld and Nozzle O.D.

3A. Axial Crack, I.D. Notch on Carbon Steel Plate

Position of Flaw

Flaw No.	Circ. Extent (deg)		Radial Extent (mm)		Vertical Position (mm)	
	θ_1	θ_2	r_1	r_2	Z_1	Z_2
#3A-initial	89.6	91.7	19.0	19.7	305.2	305.9
#3A-01	89.6	91.7	19.0	19.7	308.0	308.6
#3A-02	89.7	91.8	19.0	20.5	310.8	311.5
#3A-03	90.0	91.9	19.1	20.8	313.6	314.2
#3A-04	90.2	91.9	19.0	20.7	316.4	317.0
#3A-05	90.5	92.1	18.8	20.4	319.2	319.8
#3A-06	90.5	92.1	19.0	20.7	322.0	322.6
#3A-07	90.5	92.0	19.1	20.8	324.7	325.3
#3A-08	90.5	92.0	19.0	20.8	327.5	328.0
#3A-09	90.6	91.9	19.1	20.9	330.3	330.7
#3A-10	90.7	92.1	19.1	21.1	333.1	333.6
#3A-11	89.7	92.5	18.6	20.4	335.5	336.4
#3A-12	89.9	91.9	18.8	20.0	338.3	339.0
#3A-13	89.9	91.8	18.9	20.2	341.0	341.7
#3A-14	89.9	91.8	18.9	20.2	343.8	344.4
#3A-15	89.9	91.8	18.9	20.3	346.5	347.2
#3A-16	89.9	91.8	18.9	20.4	349.3	349.9
#3A-17	89.9	91.8	18.9	20.3	352.0	352.7

Final Results of Destructive Test on BMI Test Sample

BMI Test Block Number	Circ. Extent (deg)		Radial Extent (mm)		Vertical Position (mm)	
	θ_{min}	θ_{max}	r_{min}	r_{max}	Z_{min}	Z_{max}
Flaw No. #3A	89.6	92.5	18.6	21.1	305.2	352.7

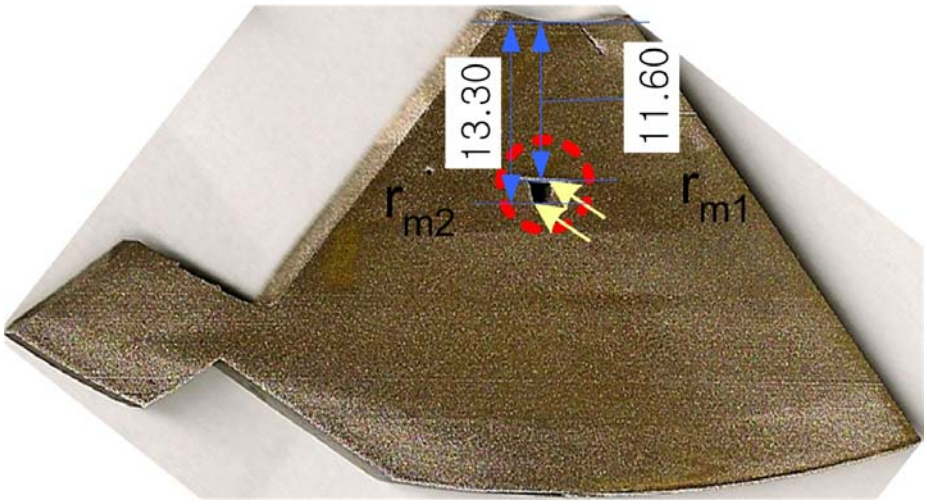

Figure 7 Flaw #3A I.D. Notch on Carbon Steel Plate

4. Slag Crack, 0.02” from Interface J-weld and Nozzle O.D.

Position of Flaw

Flaw No.	Circ. Extent (deg)	Radial Extent (mm)		Vertical Position (mm)	
	θ	r_1	r_2	Z_1	Z_2
#4-10	20	21.1	22.8	297.4	299.8
#4-09	25	19.9	23.7	294.1	301.9
#4-08	30	19.8	23.7	296.7	304.1
#4-07	35	19.6	23.7	297.2	305.2
#4-06	40	19.7	23.6	297.0	305.7
#4-05	45	19.7	23.5	299.2	306.8
#4-04	50	17.4	21.0	300.9	307.9
#4-03	55	19.8	22.6	300.8	307.9
#4-02	60	21.2	21.5	304.6	305.6
#4-01	65	21.2	21.9	306.1	306.8

Final Results of Destructive Test on BMI Test Sample

BMI Test Block Number	Circ. Extent (deg)		Radial Extent (mm)		Vertical Position (mm)	
	θ_{min}	θ_{max}	r_{min}	r_{max}	Z_{min}	Z_{max}
Flaw No. #4	15	70	17.4	23.7	294.1	307.9

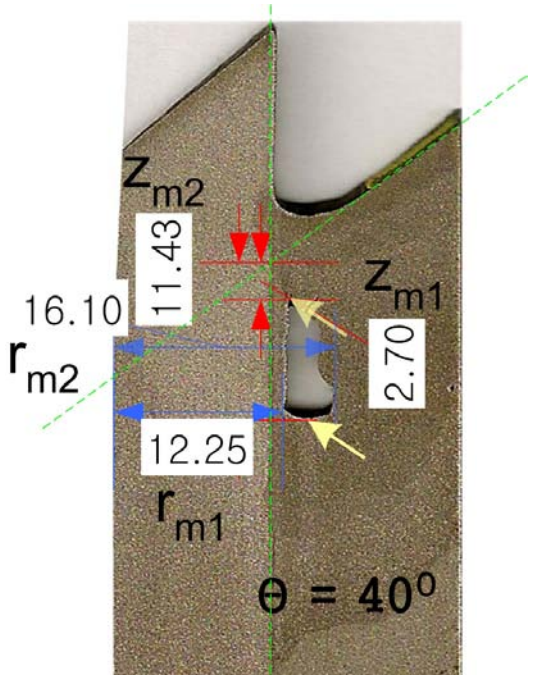

Figure 8 Flaw #4 508 from Interface J-weld and Nozzle O.D.

5. Axial Crack, Surface Crack of Pipe I.D.

Position of Flaw

Flaw No.	Circ. Extent (deg)		Radial Extent (mm)		Vertical Position (mm)	
	θ_1	θ_2	r_1	r_2	Z_1	Z_2
#5-01	102	106	8.4	9.5	296.0	296.8
#5-02	100	107	7.5	10.7	298.3	300.1
#5-03	100	107	7.5	10.2	301.1	302.6
#5-04	100	107	7.5	10.2	303.8	305.4
#5-05	100	107	7.5	10.2	306.6	308.1
#5-06	100	107	7.5	10.3	309.3	310.9
#5-07	100	107	7.5	9.8	312.1	313.5
#5-08	100	107	7.5	10.3	314.8	316.4
#5-09	100	107	7.5	10.5	317.6	319.2
#5-10	100	107	7.5	9.3	320.3	321.6

Final Results of Destructive Test on BMI Test Sample

BMI Test Block Number	Circ. Extent (deg)		Radial Extent (mm)		Vertical Position (mm)	
	θ_{min}	θ_{max}	r_{min}	r_{max}	Z_{min}	Z_{max}
Flaw No. #5	100	107	7.5	10.7	296.0	321.6

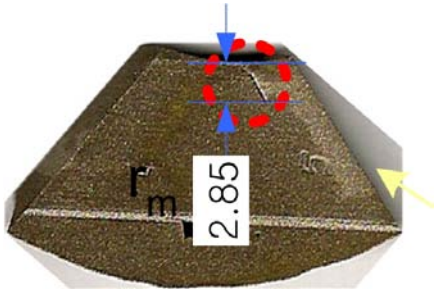

Figure 9 Flaw #5 Surface Crack of Pipe I.D.

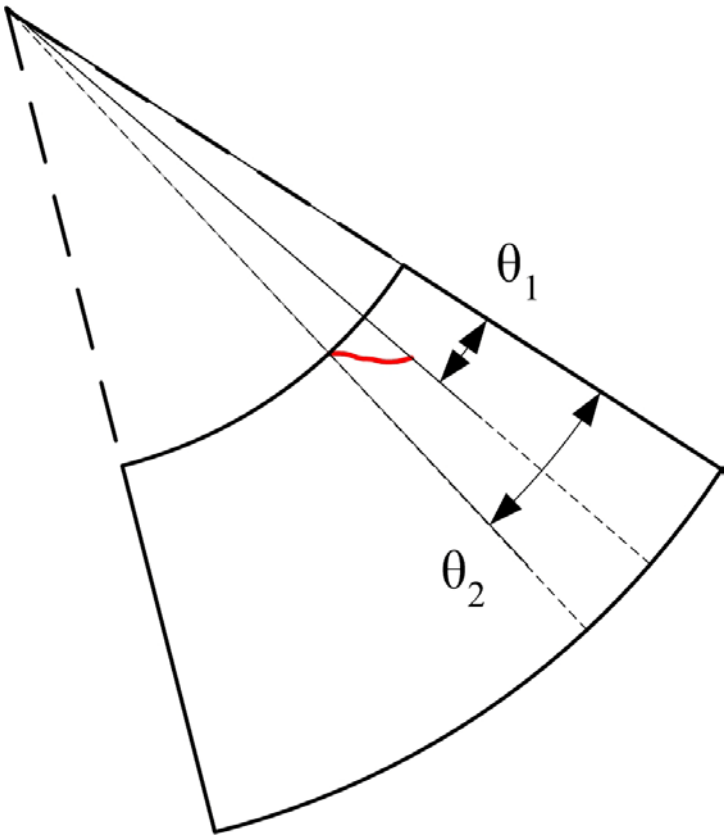

Figure 10 Flaw #5 Angle of crack

B.2 Destructive Analysis of Sample 5.10

The six flaws had a consistent profile. Four of the six flaws, 1, 2, 4, and 6, had a shallow surface-breaking component and disconnected segments deeper into the material. Flaw 3 was very shallow and flaw 5 was continuous.

The surface and profile of Flaw 1 showed that the flaw was reasonably discontinuous on the surface and is not continuous until the first 2 mm of weld. The surface-breaking segment measured at the cut surface only penetrated 0.6 mm into the weld. One team was able to detect Flaw 1.

Flaw 2 is very discontinuous at the surface, and the surface-breaking component of the crack is a mere 0.2 mm into the weld. At a depth of 1.5 mm, the flaw becomes continuous and much wider. Flaw 2 can almost be considered an embedded flaw, as the surface-breaking component is so tight and shallow. No teams were able to detect Flaw 2.

Flaw 3 is the smallest measured using DE, with three small surface-breaking components and a measured depth of 0.35 mm. No teams were able to detect Flaw 3.

Flaw 4 had a discontinuous surface profile along the surface and along the cross section, but the surface-breaking segment of the crack was almost 1-mm deep. Also, the flaw has a "T"-shaped profile that would make it more easily detectable by eddy current systems that are sensitive to the orientation of the crack. Three teams detected Flaw 4.

Flaw 5 was continuous along the surface and the cross section into the weld. One team was able to detect Flaw 5.

Flaw 6 was challenging to characterize at the surface with a scanning electron microscope, and is not continuous through the cross section. This flaw may be considered an embedded flaw, as the surface-breaking component penetrates only 0.2 mm into the material.

The measured properties are listed in Table B.1 along with the PINC round-robin PODs for the flaws are summarized in Table B.1. It should be noted that the crack CODs were measured after the surface was polished.

Table B.1. Measured Properties for Flaws in 5.10

Flaw	Length (mm)	Depth	COD	SB Depth	POD
5.10-1	7.5	9	28	0.6	0.14
5.10-2	5	7	12	0.2	0.00
5.10-3	0.8, 3.5	0.35	15	0.35	0.00
5.10-4	7	2	32	0.95	0.43
5.10-5	4.5	2	12	2	0.14
5.10-6	1.6	4.5	10	0.2	0.00

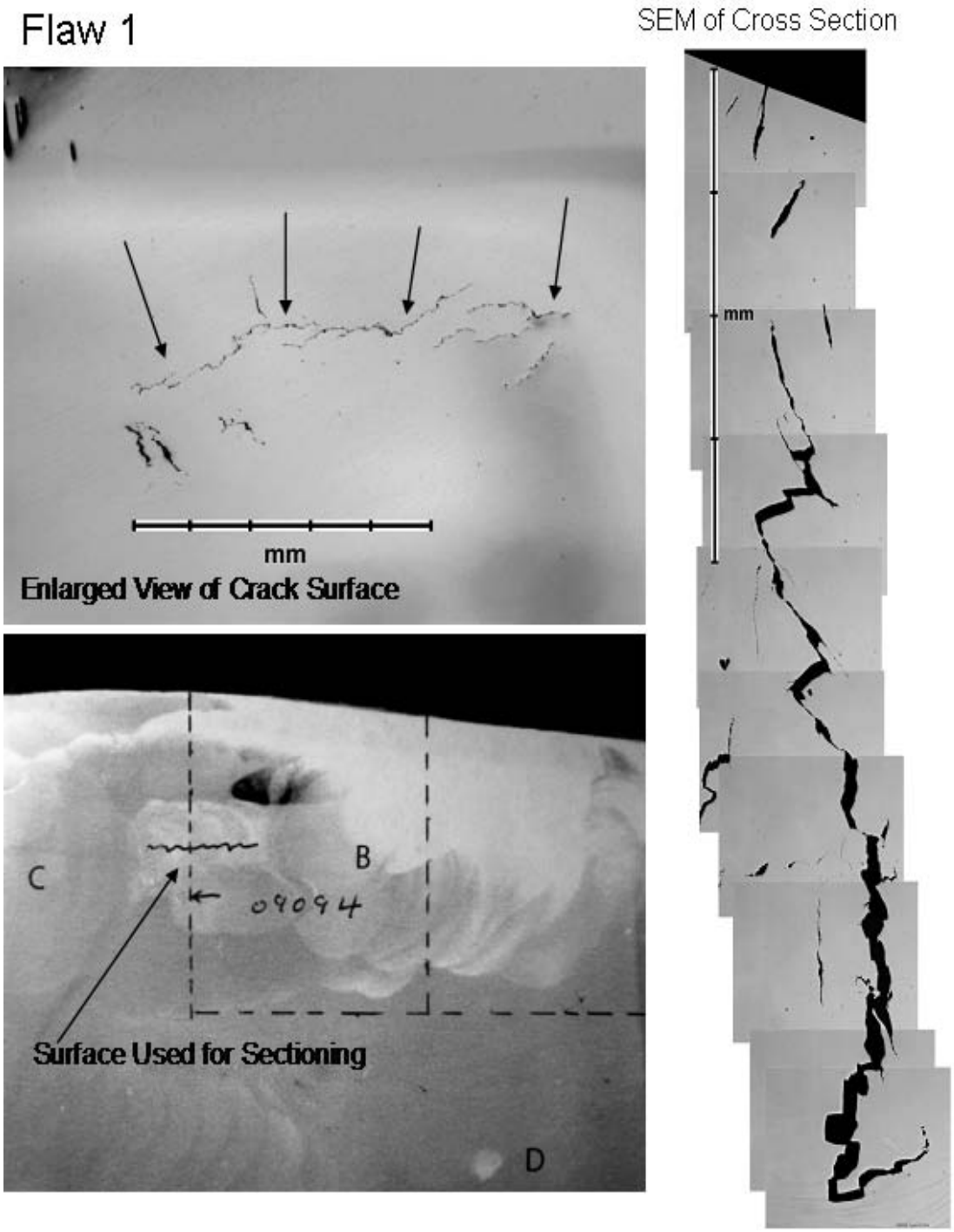

Flaw 1

Measured Length	7.5 mm
COD at Surface	28 μm
Depth of Surface Breaking Segment	0.6 mm
Total Depth	9 mm

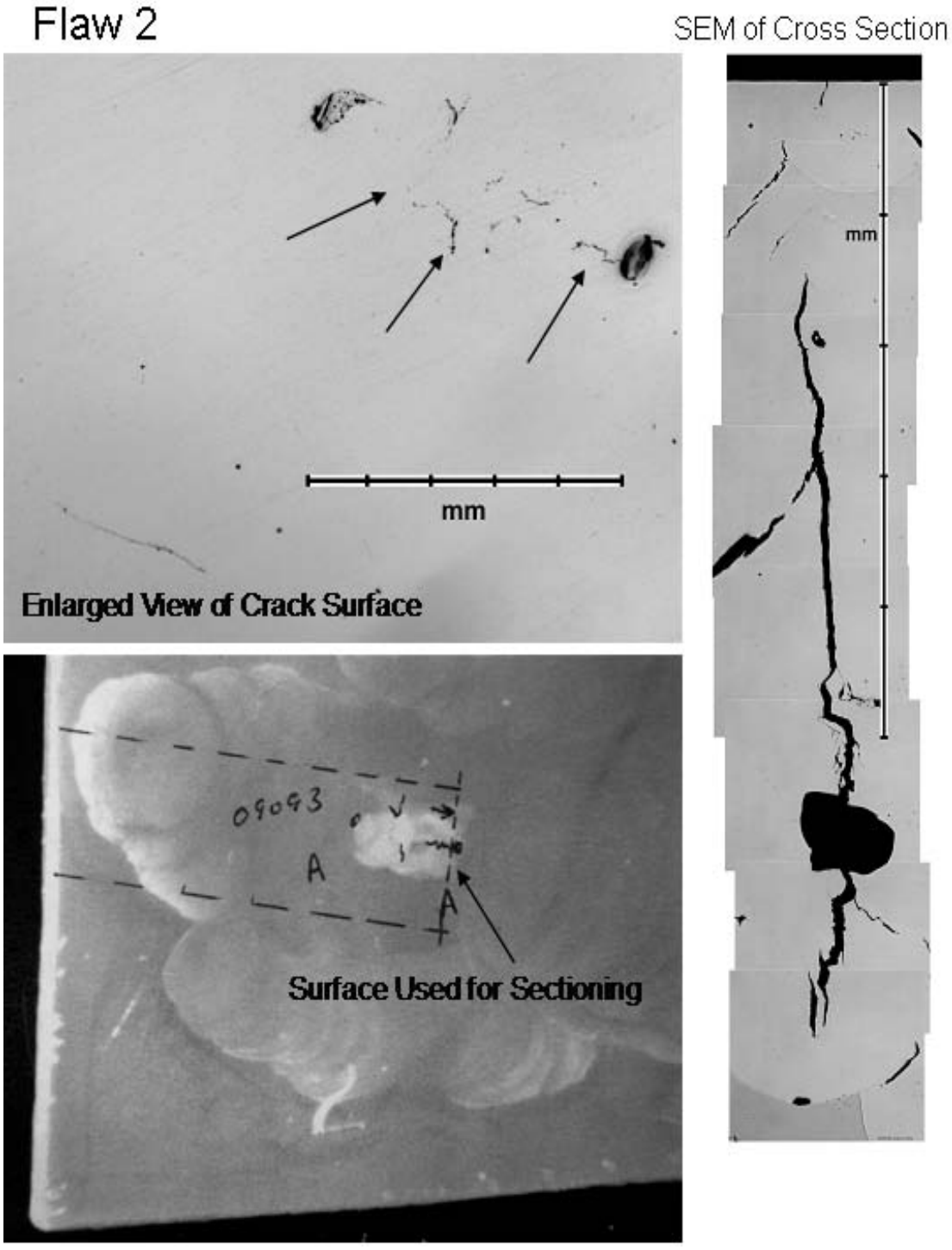

Flaw 2

Measured Length	5 mm
COD at Surface	12 μm
Depth of Surface Breaking Segment	0.2 mm
Total Depth	7 mm

Flaw 3

SEM of Cross Section

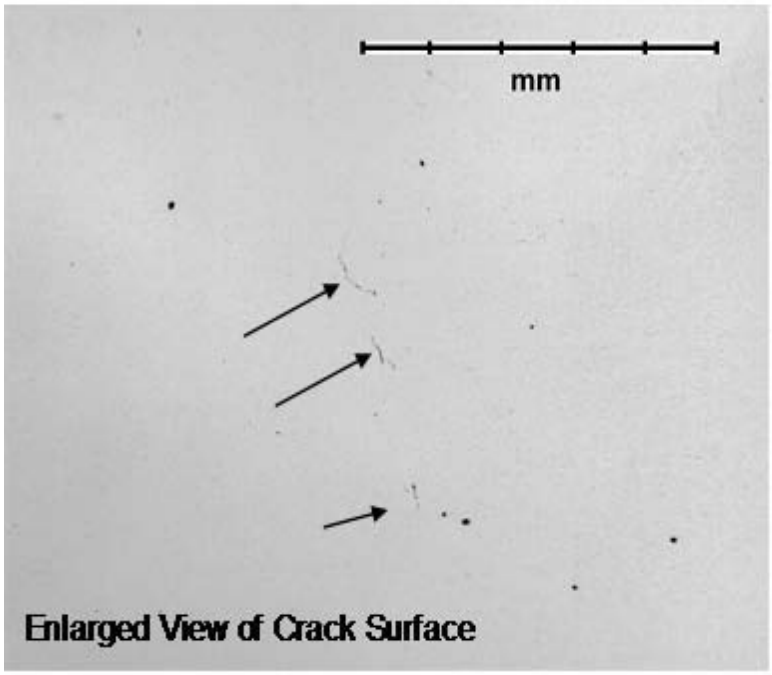

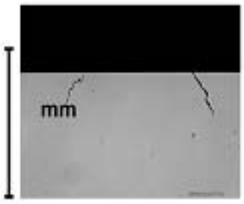

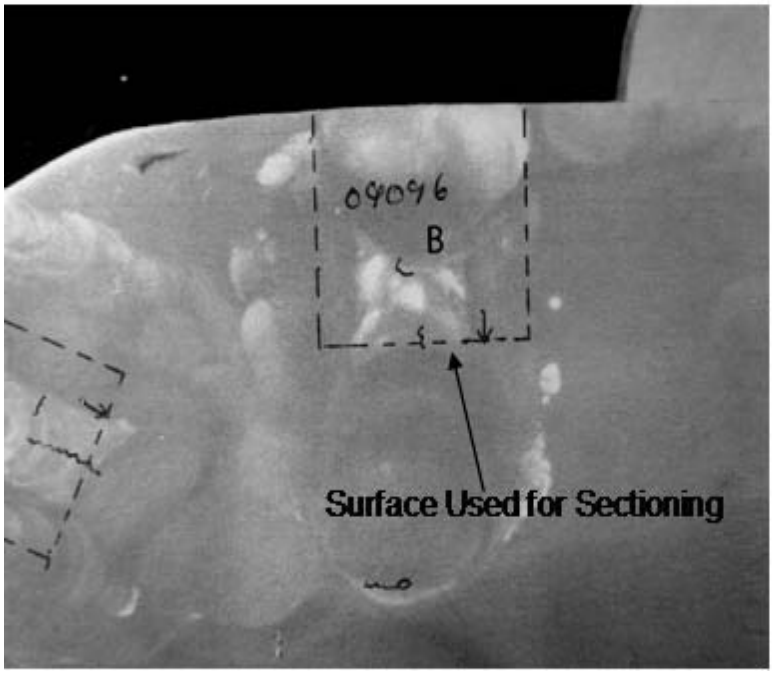

Flaw 3

Measured Length	3.5 mm
COD at Surface	15 µm
Depth of Surface Breaking Segment	0.35 mm
Total Depth	0.35 mm

Flaw 4

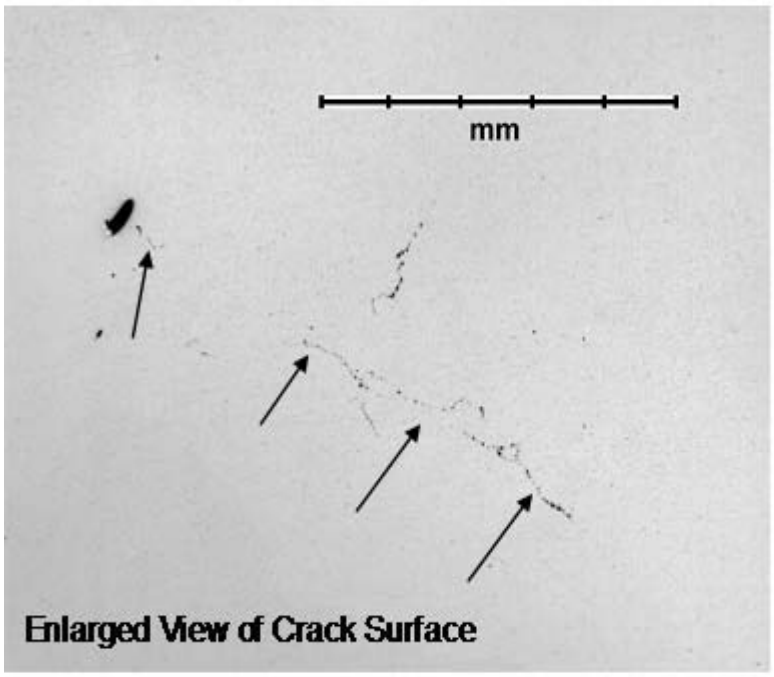

SEM of Cross Section

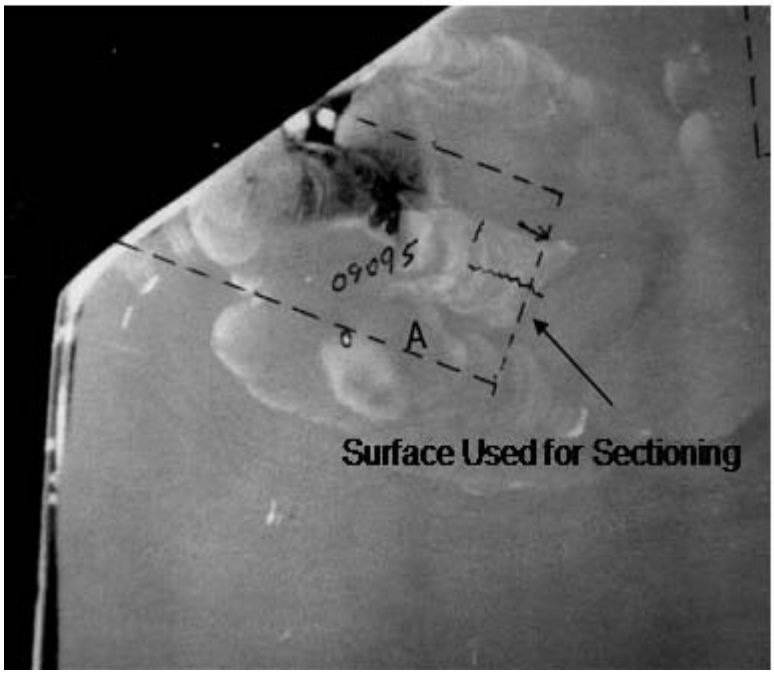

Flaw 4

Measured Length	7 mm
COD at Surface	32 μm
Depth of Surface Breaking Segment	0.9 mm
Total Depth	2 mm

Flaw 5

SEM of Cross Section

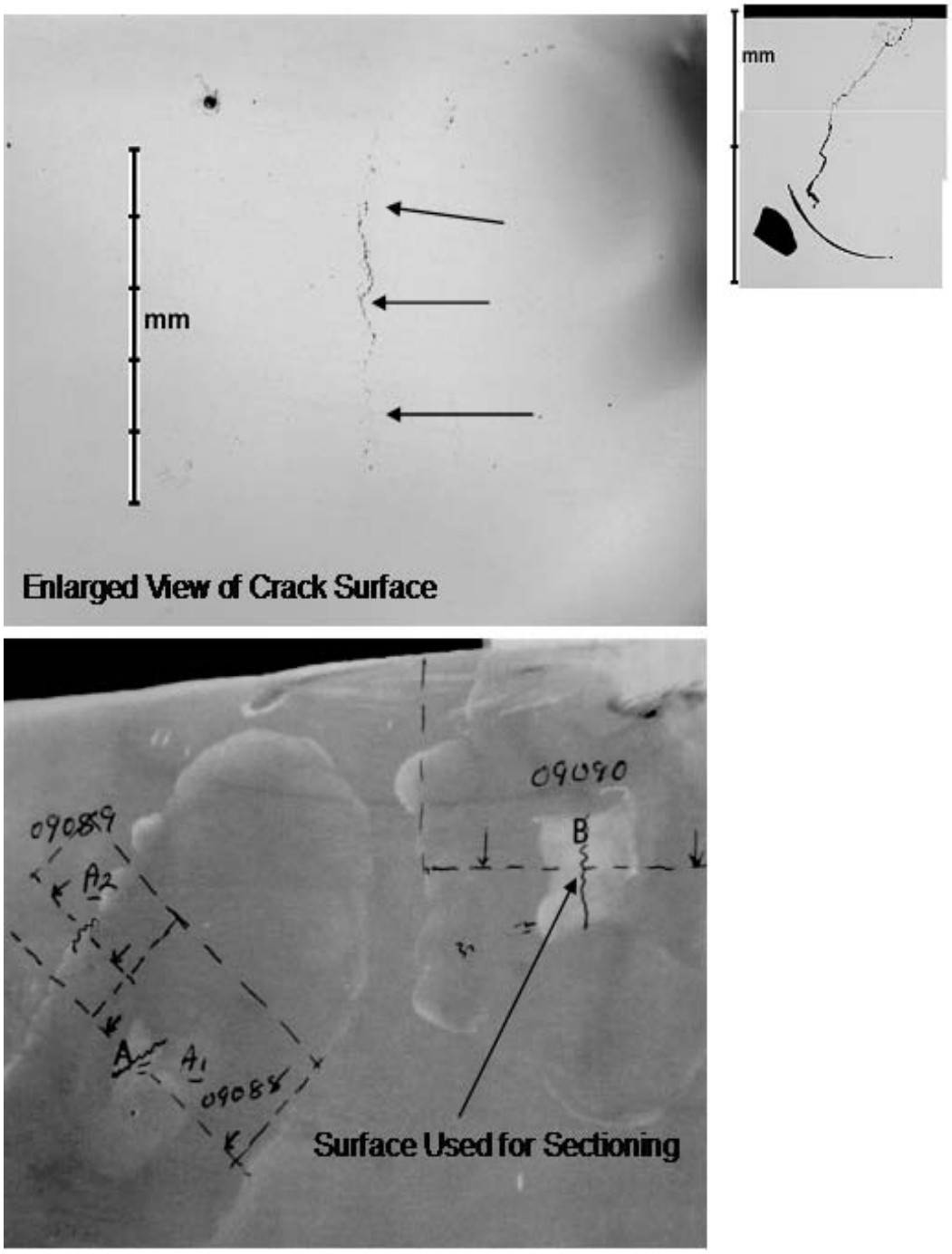

Flaw 5

Measured Length	4.5 mm
COD at Surface	12 μm
Depth of Surface Breaking Segment	1.5 mm

Total Depth 2 mm

Flaw 6

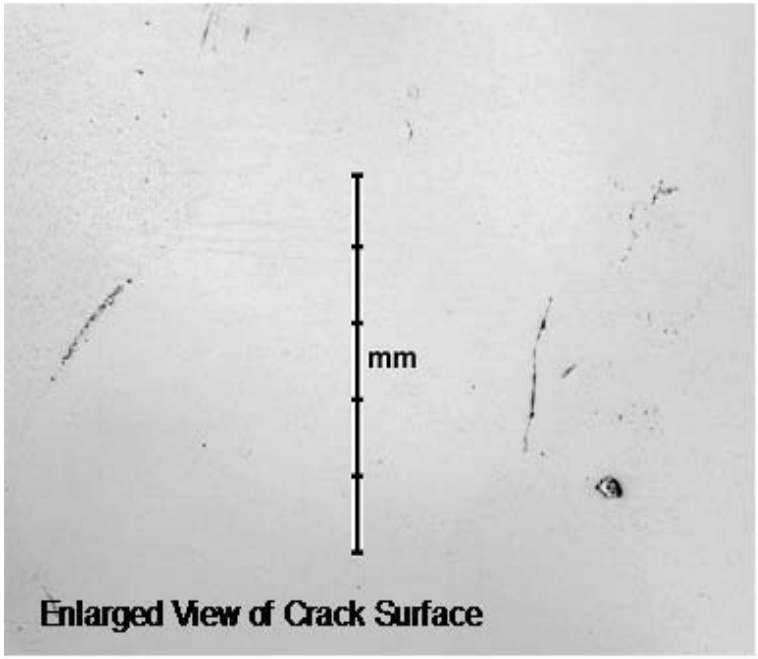

SEM of Cross Section

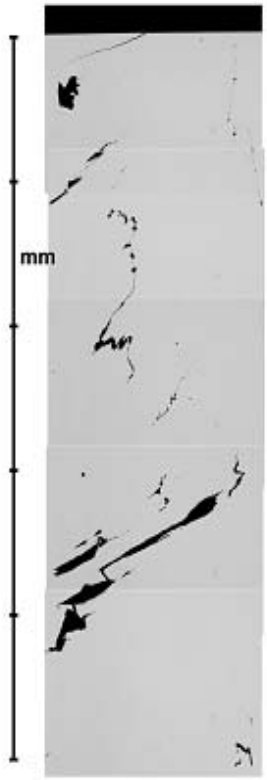

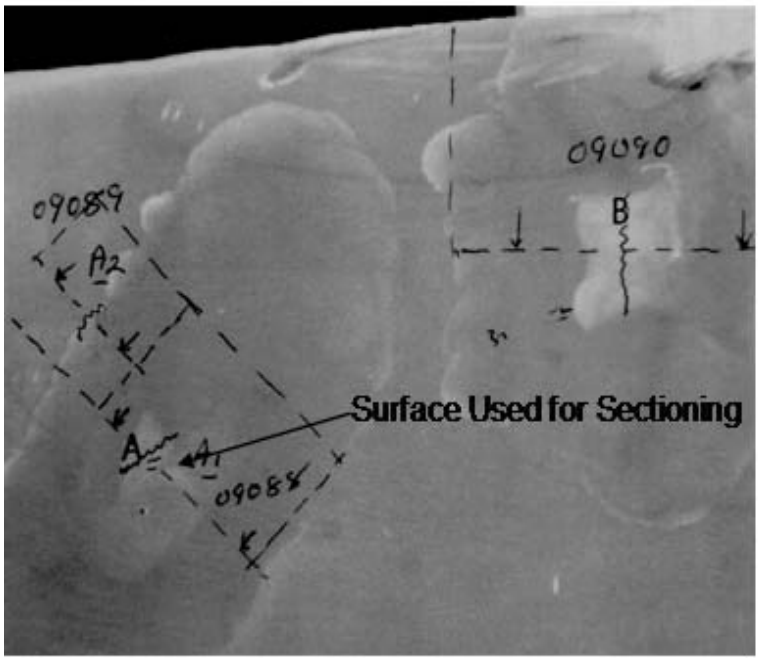

For flaw 6, there was a surface blemish and an apparent crack.

Flaw 6

Measured Length	1.6 mm
COD at Surface	10 μm
Depth of Surface Breaking Segment	0.2 mm
Total Depth	4.5 mm

B.3 Destructive Analysis of Sample 5.11–5.16

Final Results of Destructive Test on JNES BMI Test Block

		Circum. Extent (deg.)		Radial extent (mm)		Depth (mm)		Vertical position (mm)	
PINC Test Block Number (Puch mark number)	Defect Number	Θ1	Θ2	r1	r2	Z1	Z2	Y1	Y2
PINC 5.13 (S-1)	5.13-1	-11.0	7.8	34.7	36.9	0.0	2.2	147.0	149.1
	5.13-2	175.0	188.0	33.3	36.1	0.0	2.4	147.4	150.5
PINC 5.14 (S-2)	5.14-1	-19.9	22.5	29.8	36.6	0.0	10.5	147.2	157.3
	5.14-2	166.9	194.8	29.0	31.4	0.0	2.1	146.8	148.5
PINC 5.15 (S-3)	5.15-1	87.7	91.1	25.1	36.4	0.0	3.5	143.0	148.5
	5.15-2	265.3	270.8	25.0	35.2	0.0	3.3	143.3	149.6
PINC 5.16 (S-4)	5.16-1	88.9	95.5	22.4	38.8	0.0	10.9	138.1	156.5
	5.16-2	268.9	275.9	23.2	36.6	0.0	5.8	139.7	150.8

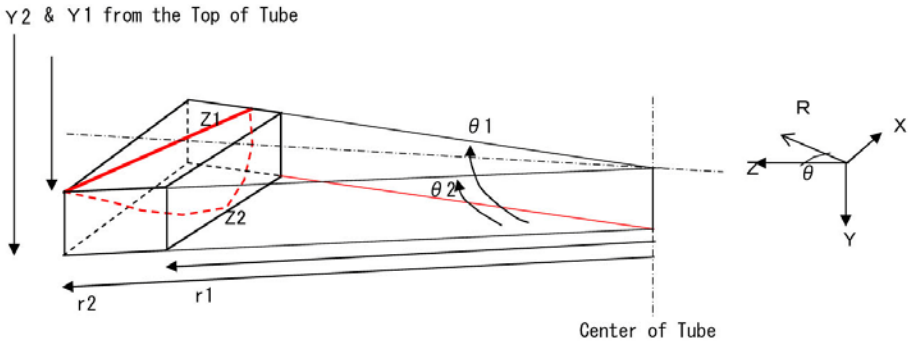

(1) Overview

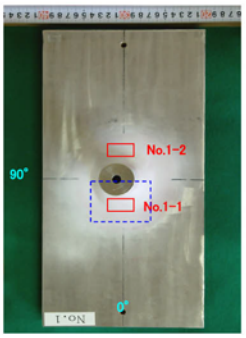

1

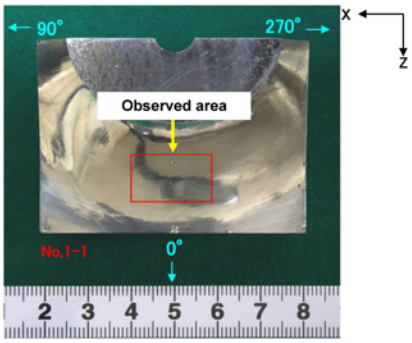

(2) Profile of SCC　　○:Measured on sliced cross section

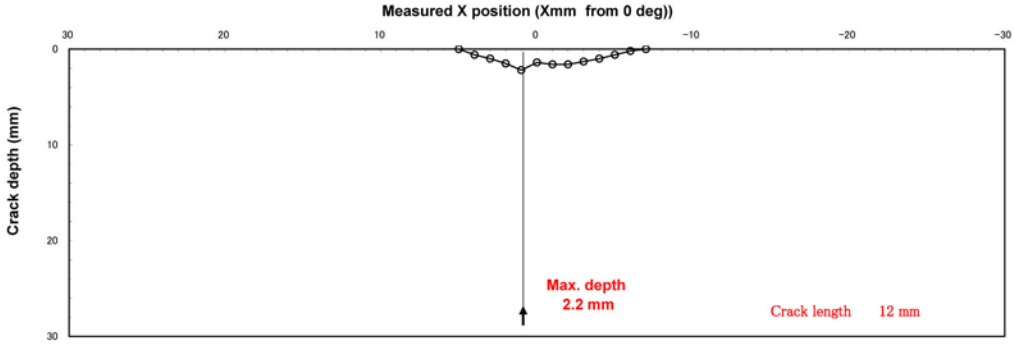

(3) Measured data of SCC

Position (mm)		X=5.0	X=4.0	X=3.0	X=2.0	X=1.0
Depth (mm)	d	0.0	0.6	1.0	1.5	2.2
Opening (μm)		0	2	3	3	2
Tilt (deg) (*)		—	-1	2	14	-27
Position of surf. opening (mm)	X	5.0	4.0	3.0	2.0	1.0
	Y	—	147.4	147.3	147.2	147.1
	Z	—	36.5	36.0	36.0	35.7
Position of crack tip (mm)	X	5.0	4.0	3.0	2.0	1.0
	Y	—	148.1	148.3	148.8	149.1
	Z	—	36.5	36.0	36.4	34.7

Position (mm)		X=0.0	X=-1.0	X=-2.0	X=-3.0	X=-4.0
Depth (mm)	d	1.4	1.6	1.6	1.3	1.0
Opening (μm)		3	31	2	2	2
Tilt (deg) (*)		-5	8	-5	-5	-2
Position of surf. opening (mm)	X	0.0	-1.0	-2.0	-3.0	-4.0
	Y	147.0	147.0	147.2	147.2	147.1
	Z	35.5	35.7	36.1	36.0	35.8
Position of crack tip (mm)	X	0.0	-1.0	-2.0	-3.0	-4
	Y	148.4	148.8	148.8	148.4	148.1
	Z	35.4	35.9	36.0	35.9	35.7

Position (mm)		X=-5.0	X=-6.0	X=-7.0		
Depth (mm)	d	0.6	0.2	0.0		
Opening (μm)		3	1	0		
Tilt (deg) (*)		4	-32	—		
Position of surf. opening (mm)	X	-5.0	-6.0	-7.0		
	Y	147.1	147.3	—		
	Z	35.7	36.1	—		
Position of crack tip (mm)	X	-5.0	-6.0	-7.0		
	Y	147.7	147.4	—		
	Z	35.8	36.0	—		

(*) Measured from Y coordinate (+ : clockwise)

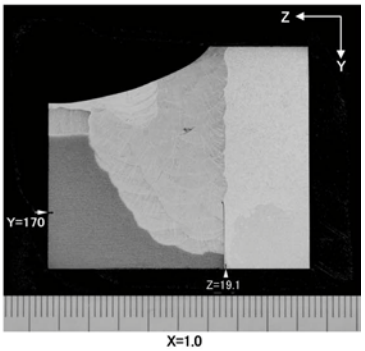

X=1.0

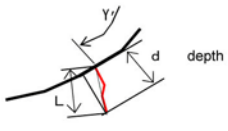

Results of destructive test on PINC 5.13-1 (parallel to weld)

Max depth	Za	Zb	Ya	Yb	L	d
	35.67	34.65	147.1	149.1	2.245	2.2

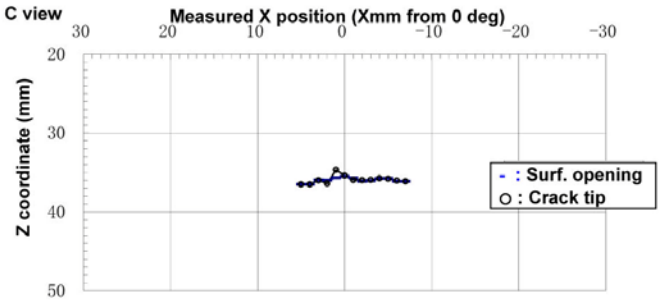

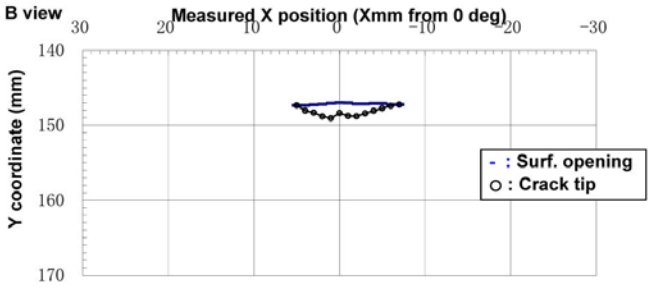

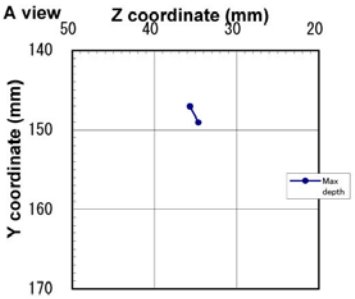

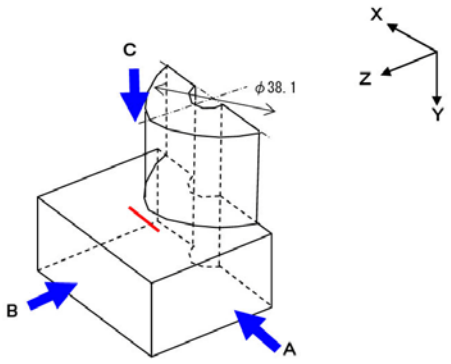

Overview

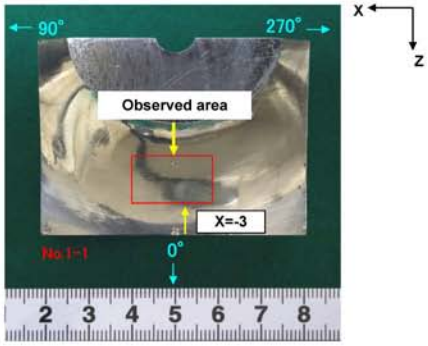

Macro. photo of cross section

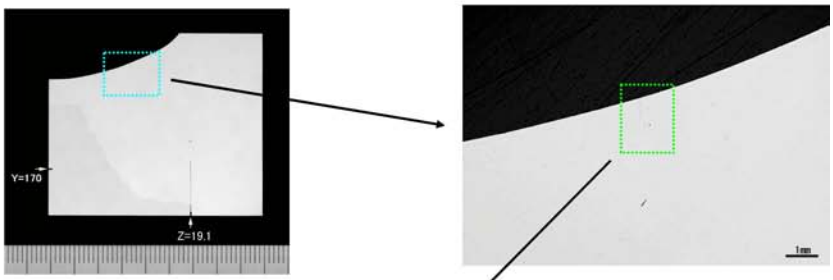

Micro. photo of cross section

1-2-3

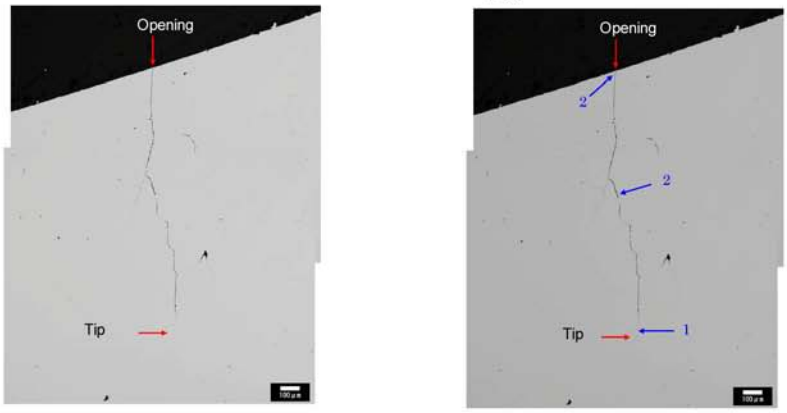

Position (mm)		X=-3.0
Depth (mm)	d	1.3
Opening (μm)		2
Tilt (deg) (°)		-5
Position of surf. opening (mm)	X	-3.0
	Y	147.2
	Z	36.0
Position of crack tip (mm)	X	-3.0
	Y	148.4
	Z	35.9

Typical crack opening data of PINC 5.13-1 (parallel to weld)
(X=- 3.0)

Overview

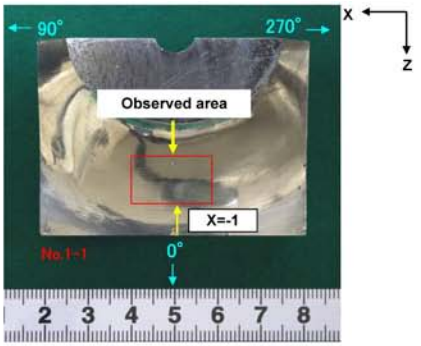

Macro. photo of cross section

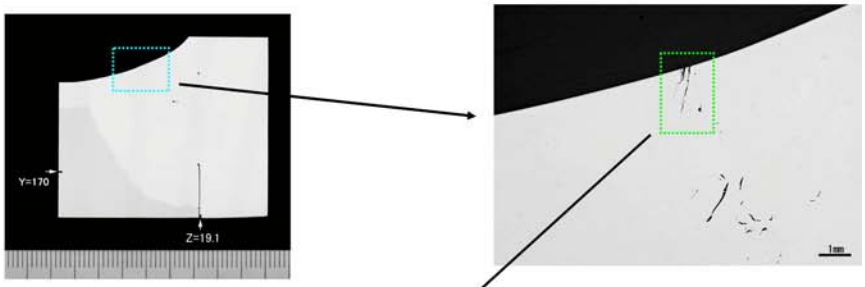

Micro. photo of cross section

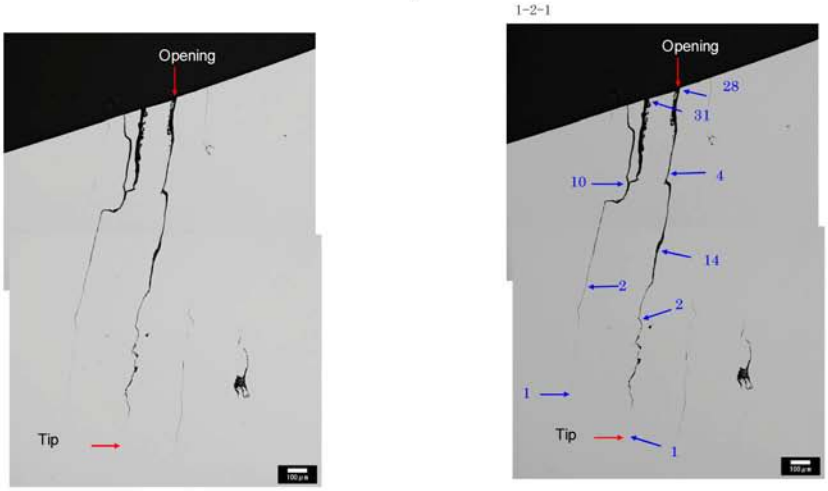

Position (mm)		X=−1.0
Depth (mm)	d	1.6
Opening (μm)		31
Tilt (deg) (°)		8
Position of surf. opening (mm)	X	−1.0
	Y	147.0
	Z	35.7
Position of crack tip (mm)	X	−1.0
	Y	148.8
	Z	35.9

Typical crack opening data of PINC 5.13-1 (parallel to weld)
(X=-1.0)

Overview

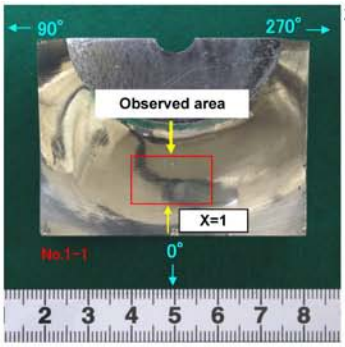

Macro. photo of cross section

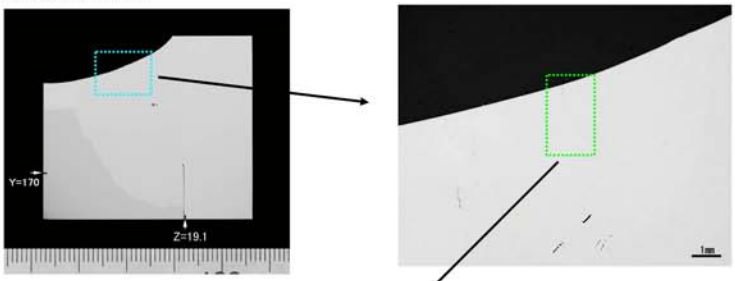

Micro. photo of cross section

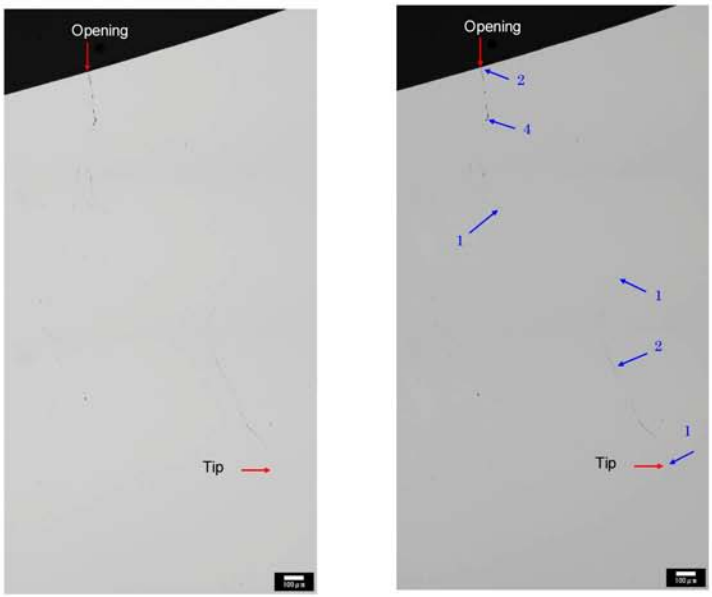

Position (mm)		X=1.0
Depth (mm)	d	2.2
Opening (μm)		2
Tilt (deg) (*)		−27
Position of surf. opening (mm)	X	1.0
	Y	147.1
	Z	35.7
Position of crack tip (mm)	X	1.0
	Y	149.1
	Z	34.7

Typical crack opening data of PINC 5.13-1 (parallel to weld)
(X=1)

Overview

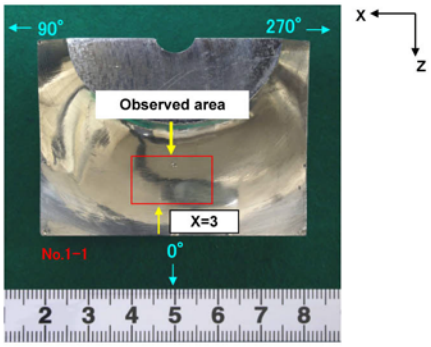

Macro. photo of cross section

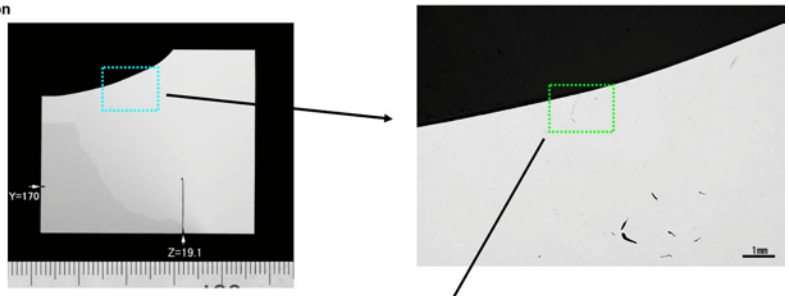

Micro. photo of cross section

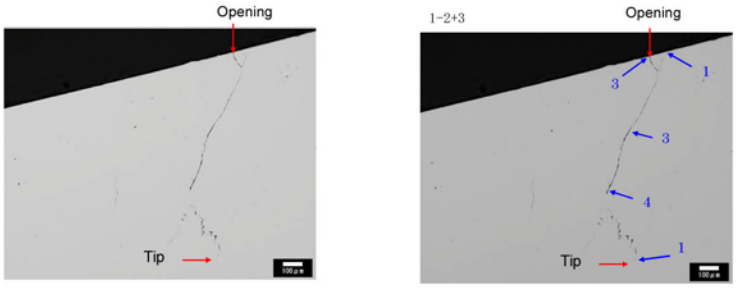

Position (mm)		X=3.0
Depth (mm)	d	1.0
Opening (μm)		3
Tilt (deg) (°)		2
Position of surf. opening (mm)	X	3.0
	Y	147.3
	Z	36.0
Position of crack tip (mm)	X	3.0
	Y	148.3
	Z	36.0

Typical crack opening data of PINC 5.13-1 (parallel to weld)
(X=3)

(1) Overview

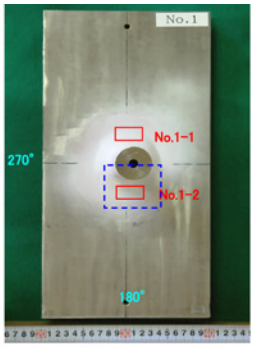

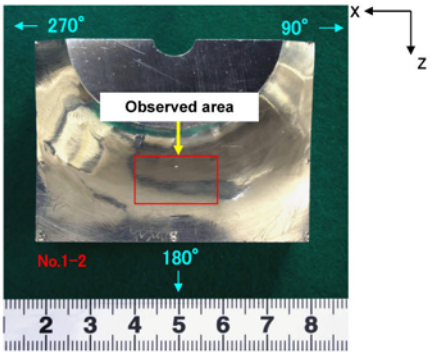

(2) Profile of SCC　　○ : Measured on sliced cross section

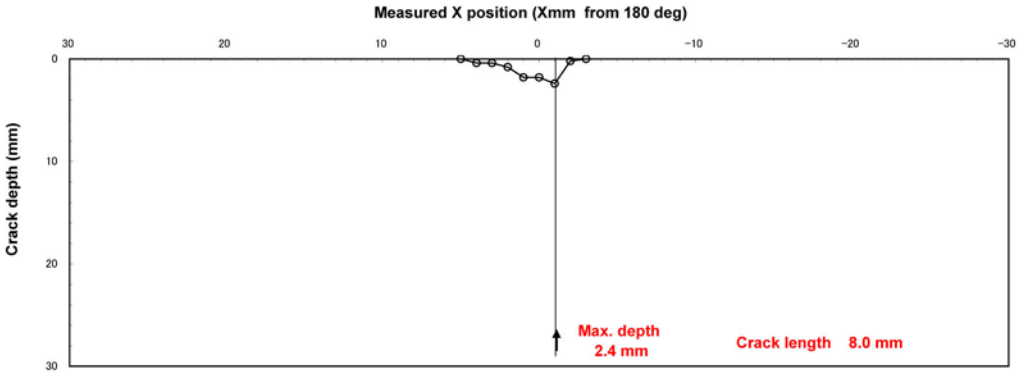

(3) Measured data of SCC

Position (mm)		X=5.0	X=4.0	X=3.0	X=2.0	X=1.0
Depth (mm)	d	0.0	0.4	0.4	0.8	1.8
Opening (μm)		0	3	1	1	2
Tilt (deg) (*)		—	-6	38	-6	8
Position of surf. opening (mm)	X	5.0	4.0	3.0	2.0	1.0
	Y	—	148.3	147.4	147.6	148.1
	Z	—	35.8	33.1	33.7	34.9
Position of crack tip (mm)	X	5.0	4.0	3.0	2.0	1.0
	Y	—	148.8	147.9	148.4	150.1
	Z	—	35.7	33.6	33.6	35.2

Position (mm)		X=0.0	X=-1.0	X=-2.0	X=-3.0	
Depth (mm)	d	1.8	2.4	0.2	0.0	
Opening (μm)		1	2	1	0	
Tilt (deg) (*)		29	20	25	—	
Position of surf. opening (mm)	X	0.0	-1.0	-2.0	-3.0	
	Y	147.8	147.7	147.8	—	
	Z	34.1	34.0	34.3	—	
Position of crack tip (mm)	X	0.0	-1.0	-2.0	-3.0	
	Y	150.3	150.5	148.1	—	
	Z	35.5	35.0	34.5	—	

(*) Measured from Y coordinate (+ : clockwise)

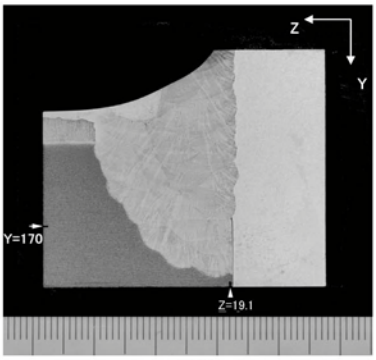

X=5.0

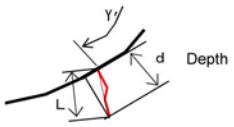

Results of destructive test on PINC 5.13-2 (parallel to weld)

Max depth	Za	Zb	Yb	Yb	L	d
	34.0	35.0	147.7	150.5	2.93	2.4

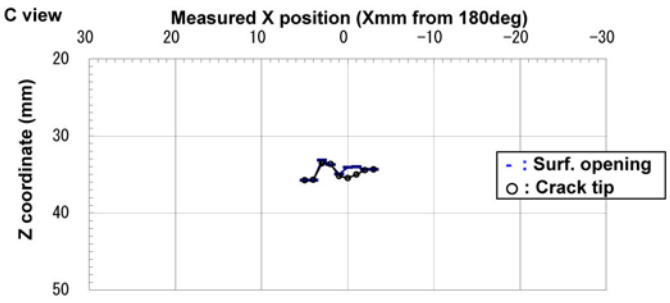

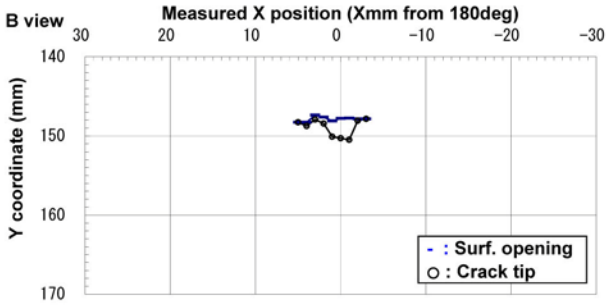

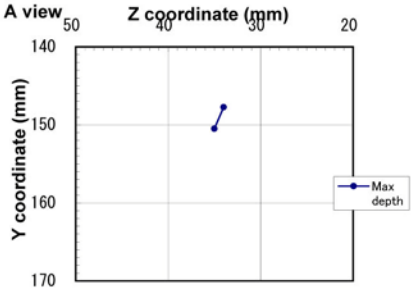

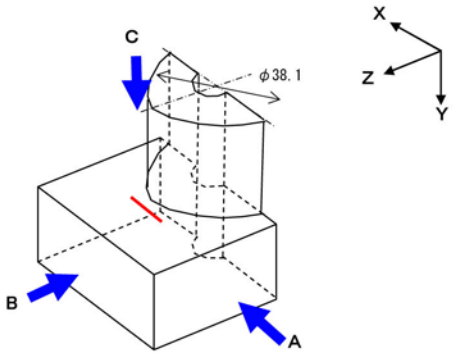

Overview

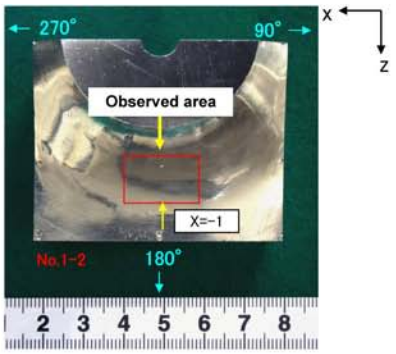

Macro. photo of cross section

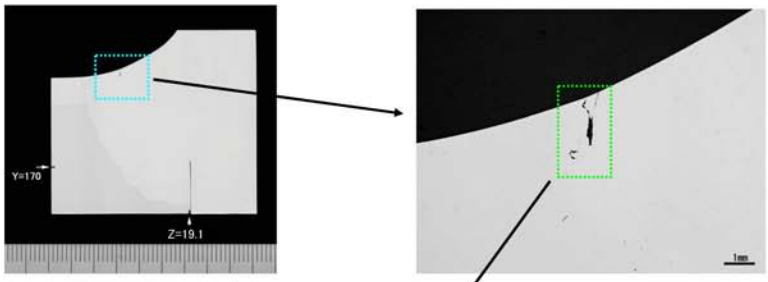

Micro. photo of cross section

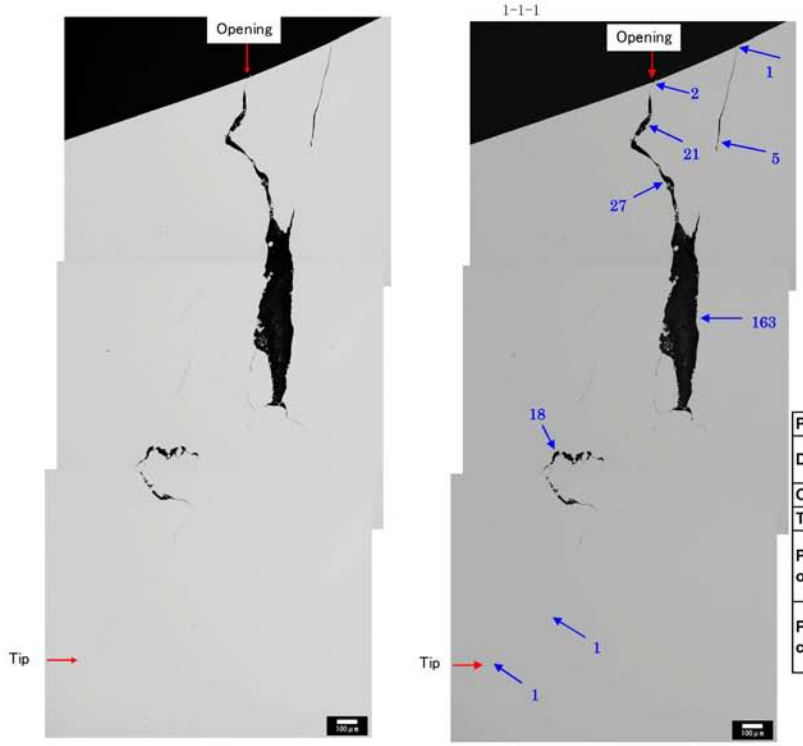

Position (mm)		X=-1.0
Depth (mm)	d	2.4
Opening (μm)		2
Tilt (deg) (*)		20
Position of surf. opening (mm)	X	-1.0
	Y	147.7
	Z	34.0
Position of crack tip (mm)	X	-1.0
	Y	150.5
	Z	35.0

Typical crack opening data of PINC 5.13-2 (parallel to weld)
(X=-1.0)

Overview

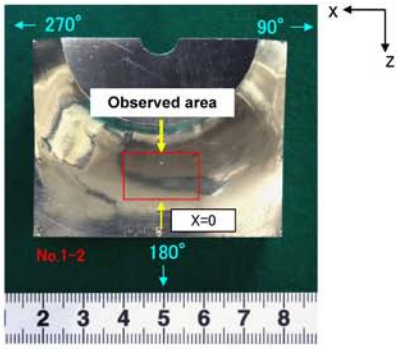

Macro. photo of cross section

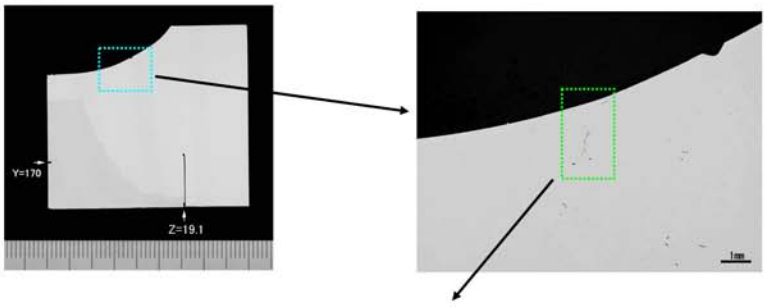

Micro. photo of cross section

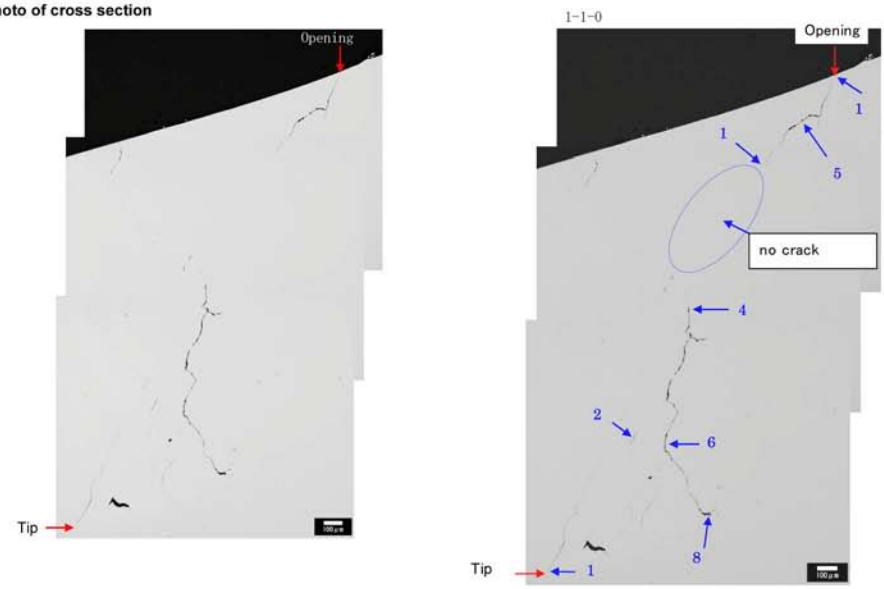

Position (mm)		X=0.0
Depth (mm)	d	1.8
Opening (μm)		1
Tilt (deg) (*)		29
Position of surf. opening (mm)	X	0.0
	Y	147.8
	Z	34.1
Position of crack tip (mm)	X	0.0
	Y	150.3
	Z	35.5

Typical crack opening data of PINC 5.13-2 (parallel to weld)
(X=0)

(1) Overview

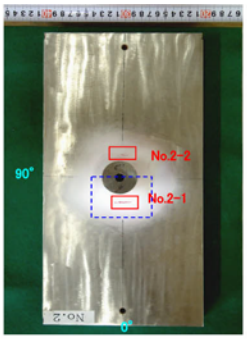

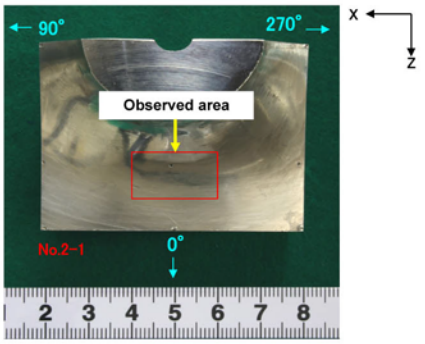

(2) Profile of SCC　　○: Measured on sliced cross section

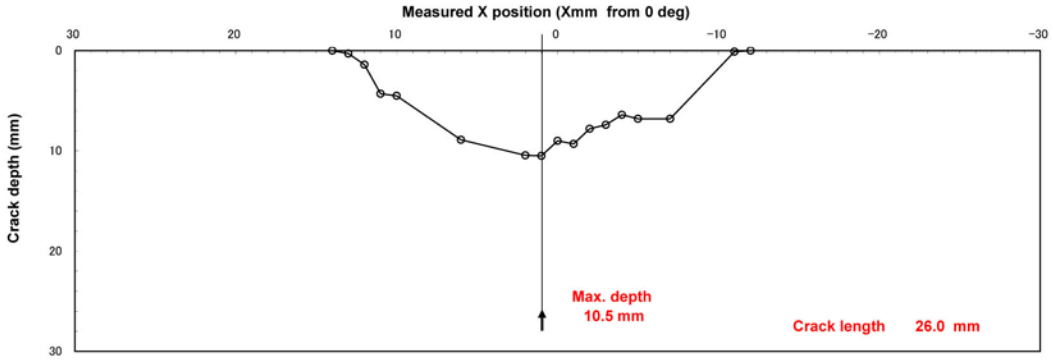

(3) Measured data of SCC

Position (mm)		X=14.0	X=13.0	X=12.0	X=11.0	X=10.0
Depth (mm)	d	0.0	0.3	1.4	4.3	4.5
Opening (μm)		0	2	1	2	4
Tilt (deg) (*)		—	-43	-23	-10	-12
Position of surf. opening (mm)	X	14.0	13.0	12.0	11.0	10.0
	Y	—	147.9	147.9	147.8	147.4
	Z	—	33.8	34.1	33.9	33.1
Position of crack tip (mm)	X	14.0	13.0	12.0	11.0	10.0
	Y	—	148.1	149.2	152.2	151.9
	Z	—	33.6	33.5	33.1	32.2

Position (mm)		X=6.0	X=2.0	X=1.0	X=0.0	X=-1.0
Depth (mm)	d	8.9	10.5	10.5	9.0	9.3
Opening (μm)		8	210	7	17	10
Tilt (deg) (*)		-15	-20	-19	-20	-22
Position of surf. opening (mm)	X	6.0	2.0	1.0	0.0	-1.0
	Y	147.3	147.4	147.3	147.3	147.5
	Z	33.2	33.4	33.2	33.2	33.6
Position of crack tip (mm)	X	6.0	2.0	1.0	0.0	-1.0
	Y	155.9	157.2	157.3	155.8	156.1
	Z	30.8	29.7	29.8	30.1	30.1

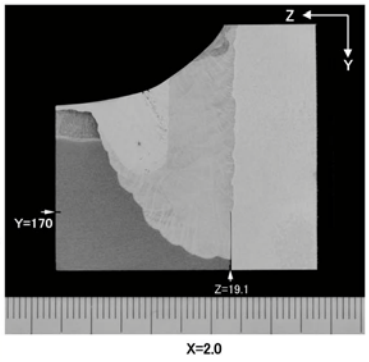

Position (mm)		X=-2.0	X=-3.0	X=-4.0	X=-5.0	X=-7.0	X=-11.0	X=-12.0
Depth (mm)	d	7.8	7.4	6.4	6.8	6.8	0.1	0.0
Opening (μm)		19	38	13	13	8	2	0
Tilt (deg) (*)		-17	-24	-25	-22	-18	20	—
Position of surf. opening (mm)	X	-2.0	-3.0	-4.0	-5.0	-7.0	-11.0	-12.0
	Y	147.2	147.3	147.2	147.2	147.4	147.9	—
	Z	32.9	33.2	32.9	32.8	33.1	33.5	—
Position of crack tip (mm)	X	-2.0	-3.0	-4.0	-5.0	-7.0	-11.0	-12.0
	Y	154.7	154.0	153.0	153.6	153.9	148.0	—
	Z	30.7	30.1	30.2	30.3	30.9	33.5	—

(*) Measured from Y coordinate (+ : clockwise)

Results of destructive test on PINC 5.14-1 (parallel to weld)

Max depth	Za	Zb	Ya	Yb	L	d
	33.15	29.78	147.3	157.3	10.52	10.5

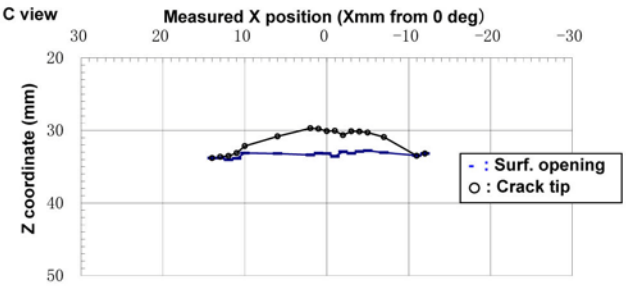

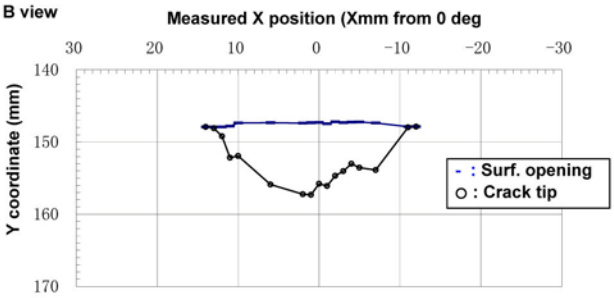

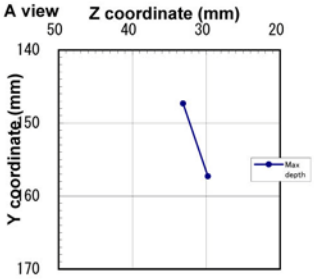

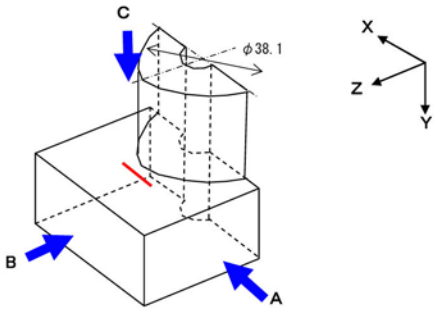

Overview

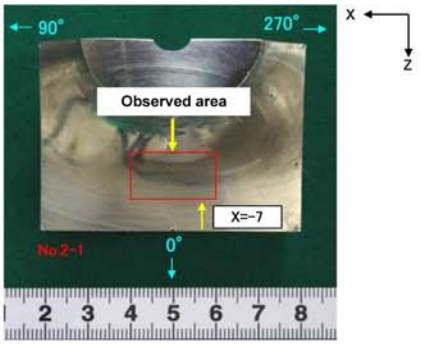

Macro. photo of cross section

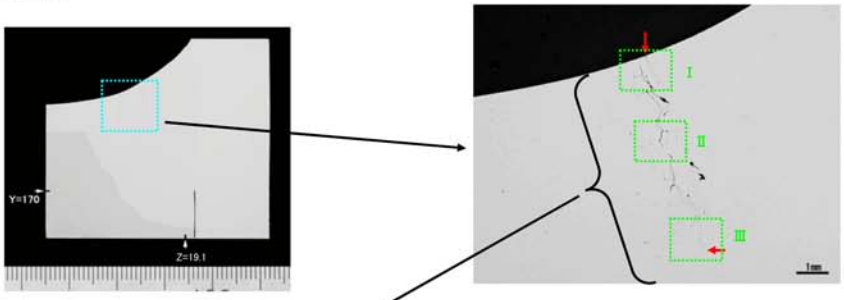

Micro. photo of cross section

Surf. opening

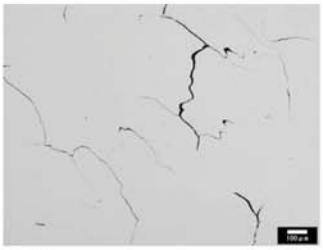

Middle

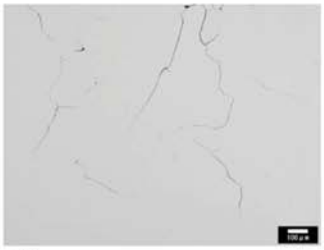

Tip

2-2 -7

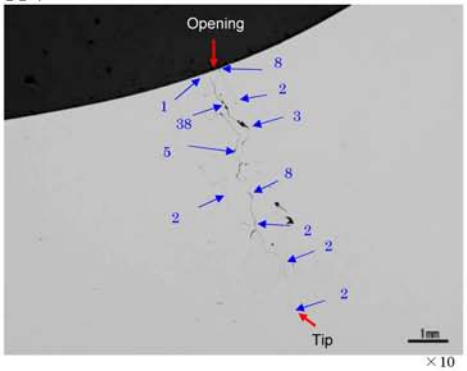

×10

Position (mm)		X=-7.0
Depth (mm)	d	6.8
Opening (μm)		8
Tilt (deg) (*)		-18
Position of surf. opening (mm)	X	-7.0
	Y	147.4
	Z	33.1
Position of crack tip (mm)	X	-7.0
	Y	153.9
	Z	30.9

Typical crack opening data of PINC 5.14-1 (parallel to weld)
(X= -7)

Overview

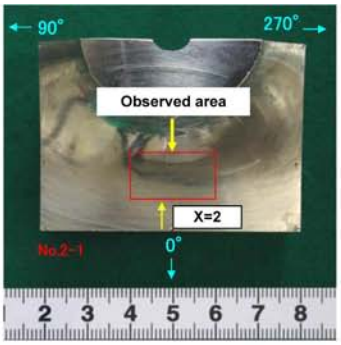

Macro. photo of cross section

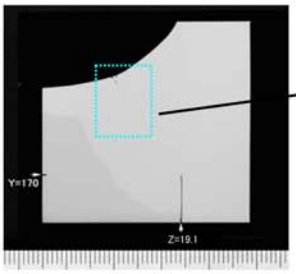

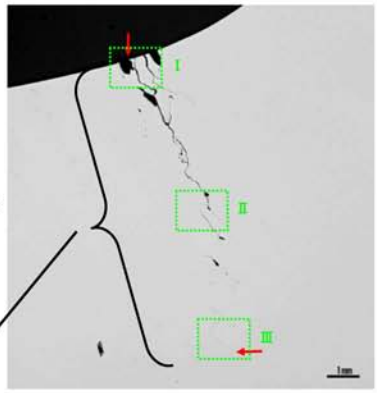

Micro. photo of cross section

Surf. opening

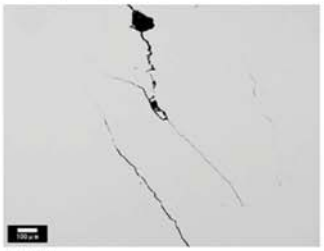

Middle

Tip

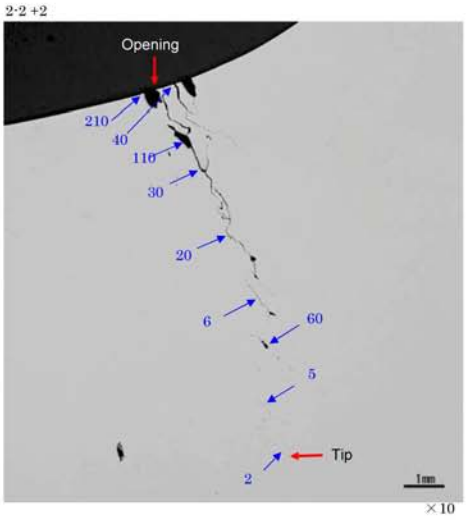

Position (mm)		X=2.0
Depth (mm)	d	10.5
Opening (μm)		210
Tilt (deg) (*)		-20
Position of surf. opening (mm)	X	2.0
	Y	147.4
	Z	33.4
Position of crack tip (mm)	X	2.0
	Y	157.2
	Z	29.7

Typical crack opening data of PINC 5.14-1 (parallel to weld)
(X=2)

(1) Overview

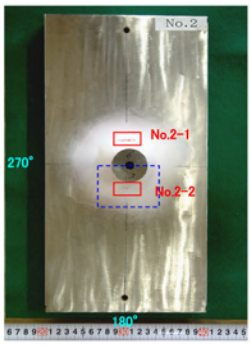

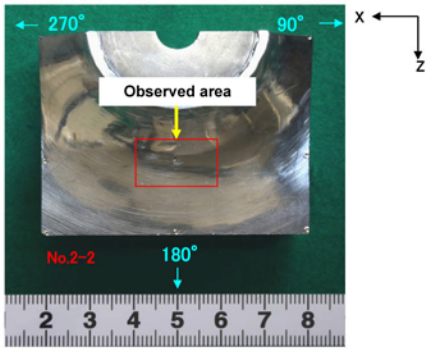

(2) Profile of SCC　　○: Measured on sliced cross section

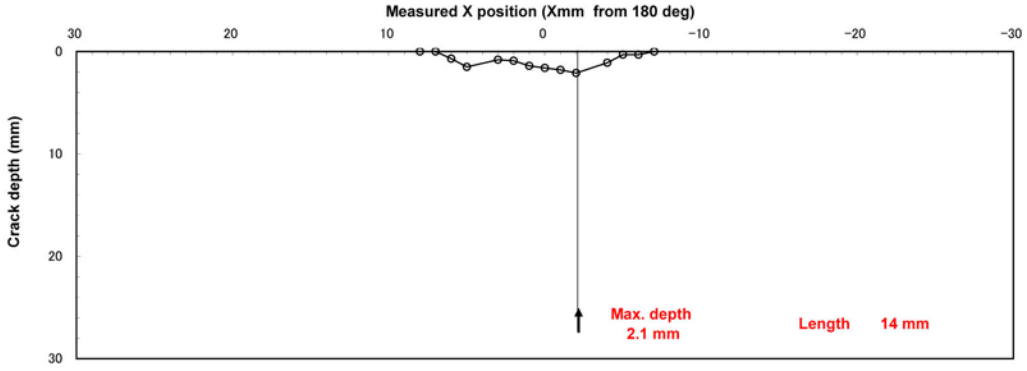

(3) Measured data of SCC

Position (mm)		X=8.0	X=7.0	X=6.0	X=5.0	X=3.0
Depth (mm)	d	0.0	0.0	0.7	1.5	0.8
Opening (μm)		0	0	3	8	7
Tilt (deg) (*)		—	—	-43	-55	-79
Position of surf. opening (mm)	X	8.0	7.0	6.0	5.0	3.0
	Y	—	—	147.1	147.1	147.1
	Z	—	—	30.4	30.3	30.4
Position of crack tip (mm)	X	8.0	7.0	6.0	5.0	3.0
	Y	—	—	147.6	148.1	147.3
	Z	—	—	29.9	28.9	29.1

Position (mm)		X=2.0	X=1.0	X=0.0	X=-1.0	X=-2.0
Depth (mm)	d	0.9	1.4	1.6	1.8	2.1
Opening (μm)		9	2	5	3	17
Tilt (deg) (*)		-65	-36	-64	-54	-56
Position of surf. opening (mm)	X	2.0	1.0	0.0	-1.0	-2.0
	Y	147.0	147.3	147.4	147.3	147.2
	Z	30.3	30.9	31.4	31.1	30.9
Position of crack tip (mm)	X	2.0	1.0	0.0	-1.0	-2.0
	Y	147.5	148.4	148.3	148.5	148.5
	Z	29.4	30.1	29.4	29.5	29.0

Position (mm)		X=-4.0	X=-5.0	X=-6.0	X=-7.0	
Depth (mm)	d	1.1	0.3	0.3	0.0	
Opening (μm)		4	3	3	0	
Tilt (deg) (*)		-67	-48	-76	—	
Position of surf. opening (mm)	X	-4.0	-5.0	-6.0	-7.0	
	Y	147.0	146.8	146.9	—	
	Z	30.5	30.0	30.0	—	
Position of crack tip (mm)	X	-4.0	-5.0	-6.0	-7.0	
	Y	147.6	147.0	147.0	—	
	Z	29.1	29.7	29.6	—	

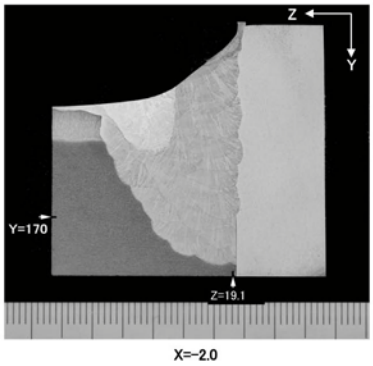

X=-2.0

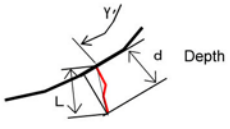

(*) Measured from Y coordinate (+ : clockwise)

Results of destructive test on PINC 5.14-2 (parallel to weld)

Max depth	Za	Zb	Ya	Yb	L	d
	30.9	29.0	147.2	148.5	2.3	2.1

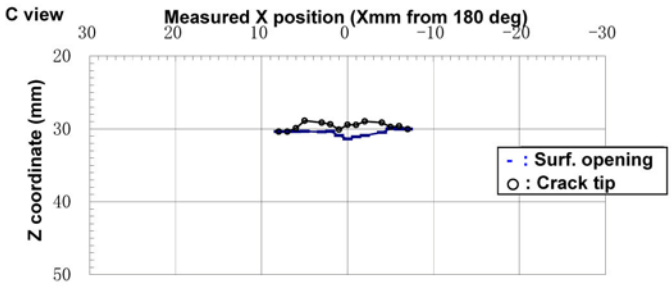

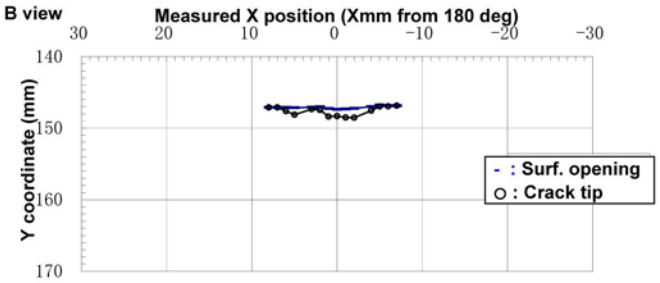

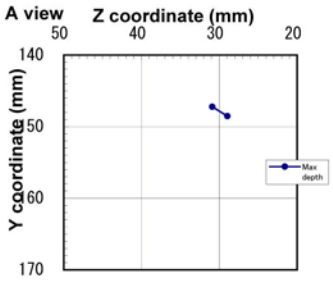

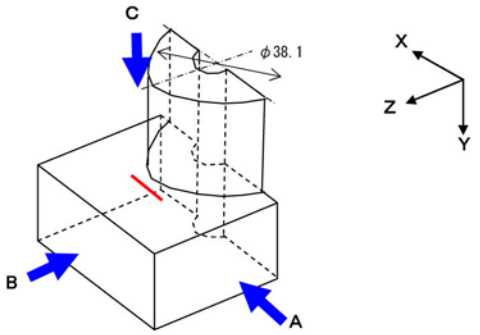

Overview

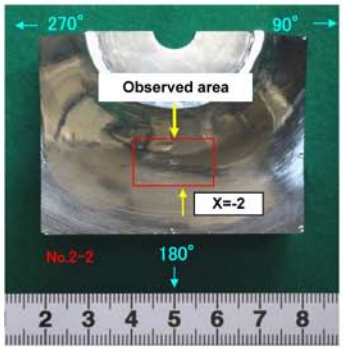

Macro. photo of cross section

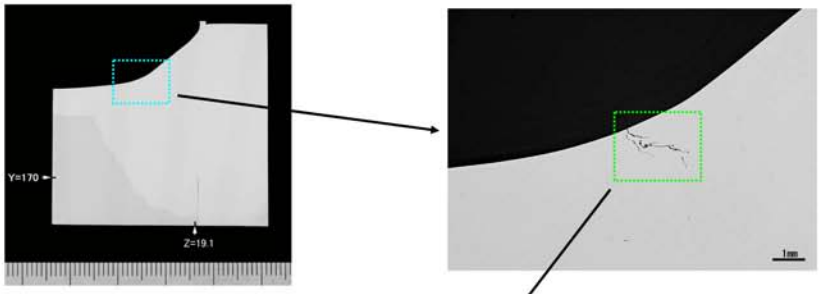

Micro. photo of cross section

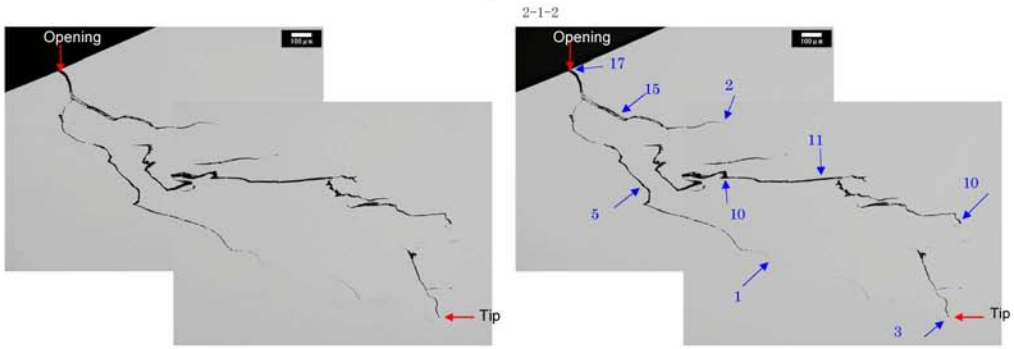

Position (mm)		X=-2.0
Depth (mm)	d	2.1
Opening (μm)		17
Tilt (deg) (°)		-56
Position of surf. opening (mm)	X	-2.0
	Y	147.2
	Z	30.9
Position of crack tip (mm)	X	-2.0
	Y	148.5
	Z	29.0

Typical crack opening data of PINC 5.14-2 (parallel to weld)
(X=-2)

Overview

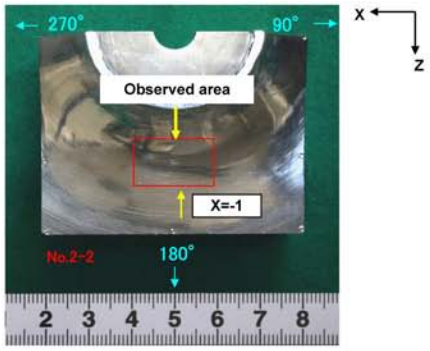

Macro. photo of cross section

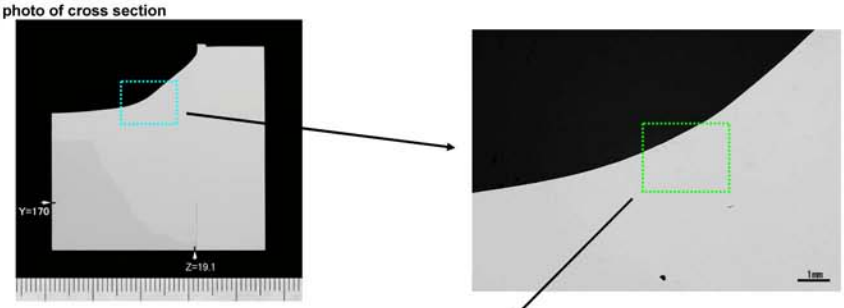

Micro. photo of cross section

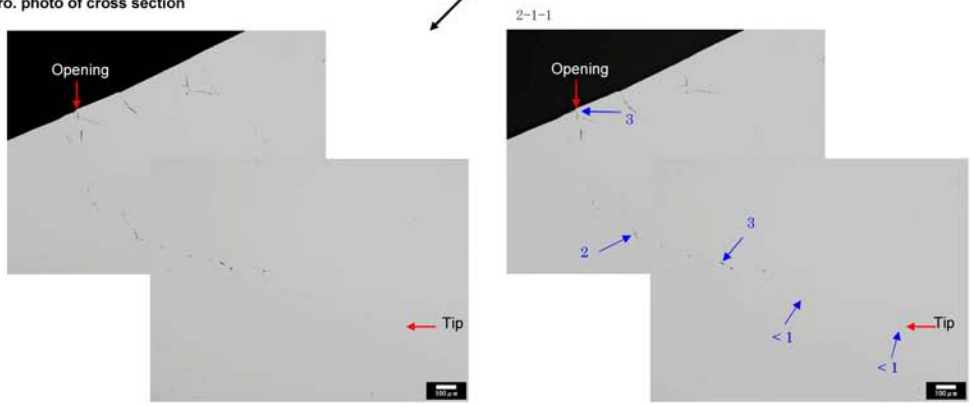

Position (mm)		X=-1.0
Depth (mm)	d	1.8
Opening (μm)		3
Tilt (deg) (°)		-54
Position of surf. opening (mm)	X	-1.0
	Y	147.3
	Z	31.1
Position of crack tip (mm)	X	-1.0
	Y	148.5
	Z	29.5

Typical crack opening data of PINC 5.14-2 (parallel to weld)
(X=-1)

Overview

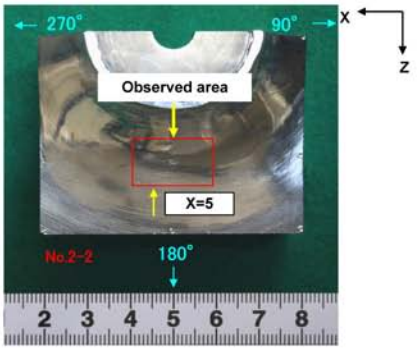

Macro. photo of cross section

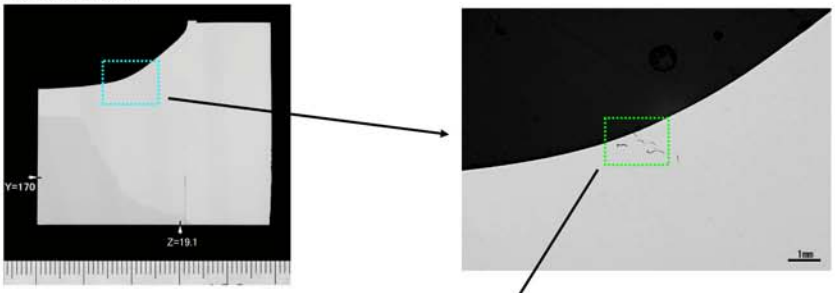

Micro. photo of cross section

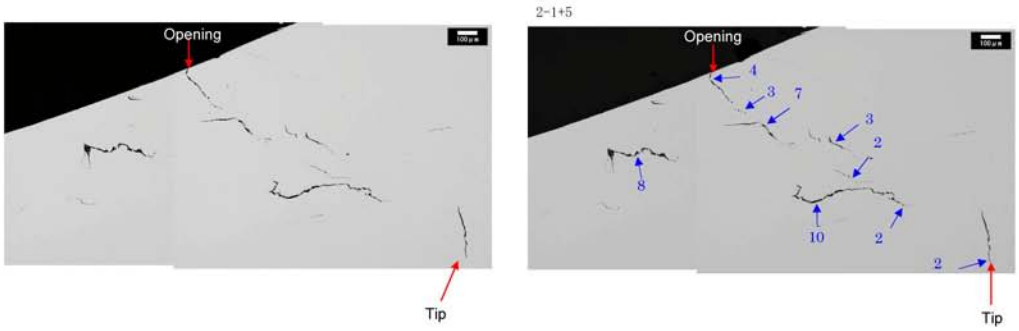

Position (mm)		X=5.0
Depth (mm)	d	1.5
Opening (μm)		8
Tilt (deg) (°)		−55
Position of surf. opening (mm)	X	5.0
	Y	147.1
	Z	30.3
Position of crack tip (mm)	X	5.0
	Y	148.1
	Z	28.9

Typical crack opening data of PINC 5.14-2 (parallel to weld)
(X=5)

(1) Overview

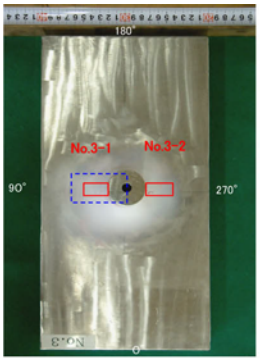

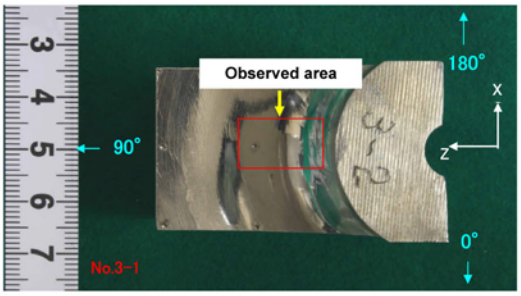

(2) Profile of SCC　　○:Measured on sliced cross section

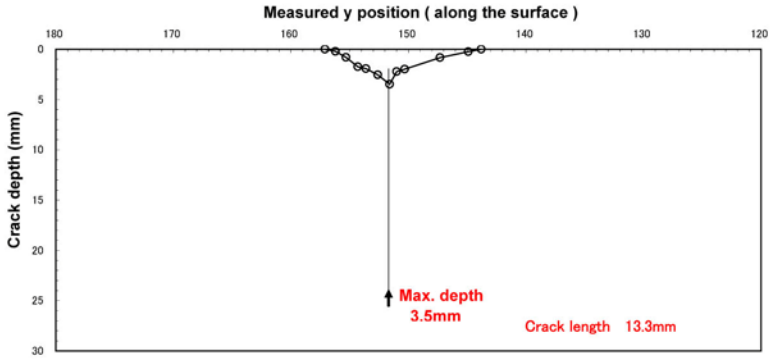

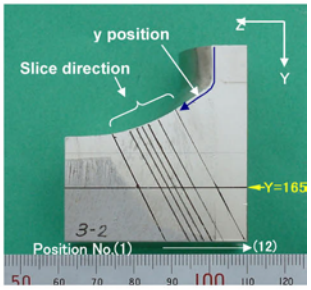

(3) Measured data of SCC

Position		(1)	(2)	(3)	(4)	(5)
Depth (mm)	d	0.0	0.2	0.8	1.7	1.9
Opening (μm)		0	0	3	2	2
Tilt (deg) (*)		—	17	10	-29	-14
Position of surf. opening (mm)	y	157.1	156.2	155.3	154.3	153.6
	X	—	-1.3	-0.7	-1.0	-1.2
	Y	148.5	148.2	147.9	147.7	147.4
	Z	36.3	35.5	34.6	33.7	32.9
Position of crack tip (mm)	X	—	-1.4	-0.9	0.0	-0.7
	Y	—	148.4	148.7	149.2	149.1
	Z	—	35.4	34.2	33.0	32.0

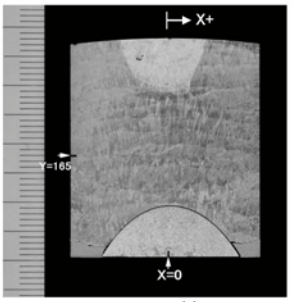

Postition (6)

Position		(6)	(7)	(8)	(9)	(10)	(11)	(12)
Depth (mm)	d	2.5	3.5	2.2	2.0	0.8	0.2	0.0
Opening (μm)		2	6	3	2	2	3	0
Tilt (deg) (*)		-1	10	-10	3	-10	-9	—
Position of surf. opening (mm)	y	152.6	151.6	151.0	150.3	147.3	144.9	143.8
	X	-0.3	-0.5	0.2	-0.9	-0.3	-0.4	—
	Y	146.8	146.6	146.0	145.9	144.9	143.5	143.0
	Z	32.2	31.3	30.6	29.6	28.1	25.8	25.1
Position of crack tip (mm)	X	-0.2	-1.1	0.6	-1.0	-0.2	-0.3	—
	Y	149.0	149.7	148.0	147.6	145.7	143.7	—
	Z	31.0	29.7	29.6	28.7	27.7	25.7	—

(*) Measured from radial coordinate of 90 deg. (+ : clockwise)

Results of destructive test on PINC 5.15-1 (perpendicular to weld)

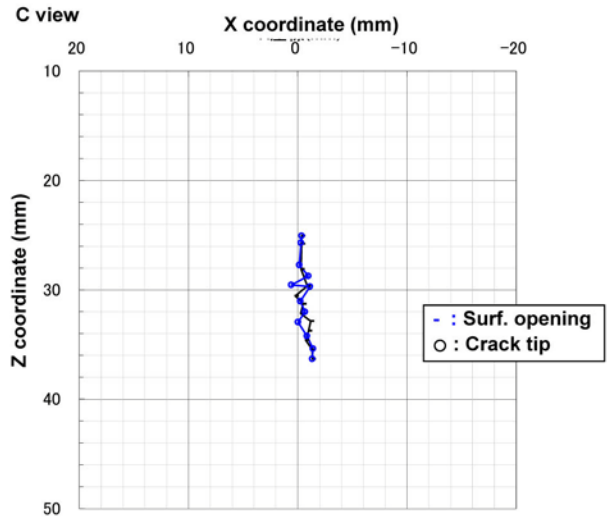
C view
X coordinate (mm)
20
10
0
−10
−20
10
20
30
40
50
Z coordinate (mm)
- : Surf. opening
○ : Crack tip

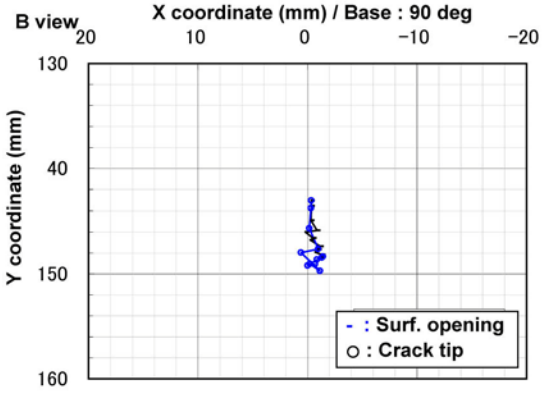
B view
X coordinate (mm) / Base : 90 deg
20
10
0
−10
−20
130
40
150
160
Y coordinate (mm)
- : Surf. opening
○ : Crack tip

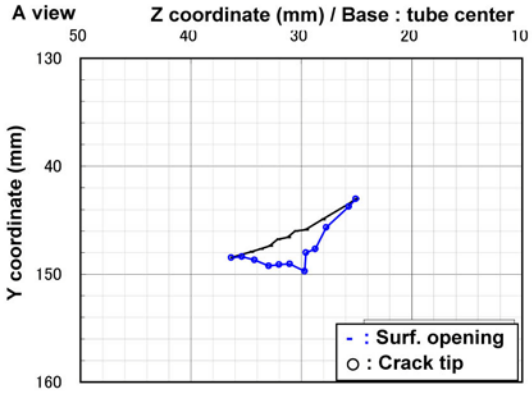
A view
Z coordinate (mm) / Base : tube center
50
40
30
20
10
130
40
150
160
Y coordinate (mm)
- : Surf. opening
○ : Crack tip

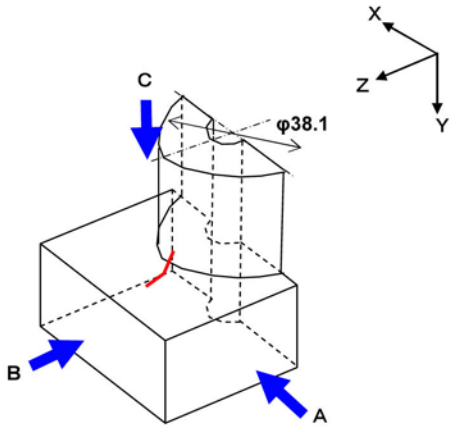
X
Z
Y
C
φ38.1
B
A

Overview

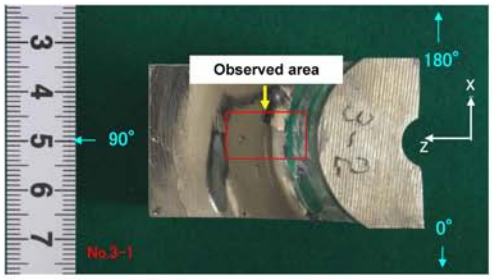

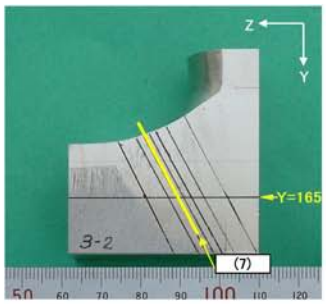

Macro. photo of cross section

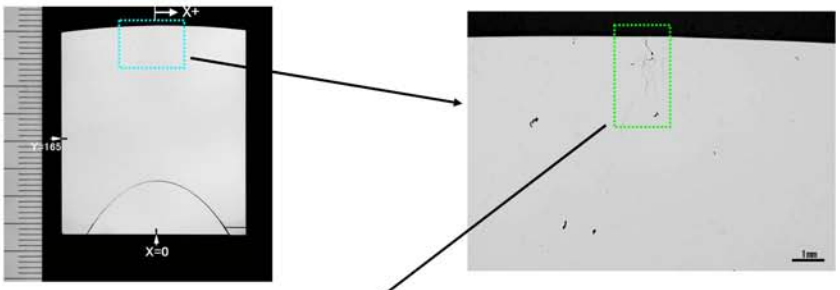

Micro. photo of cross section

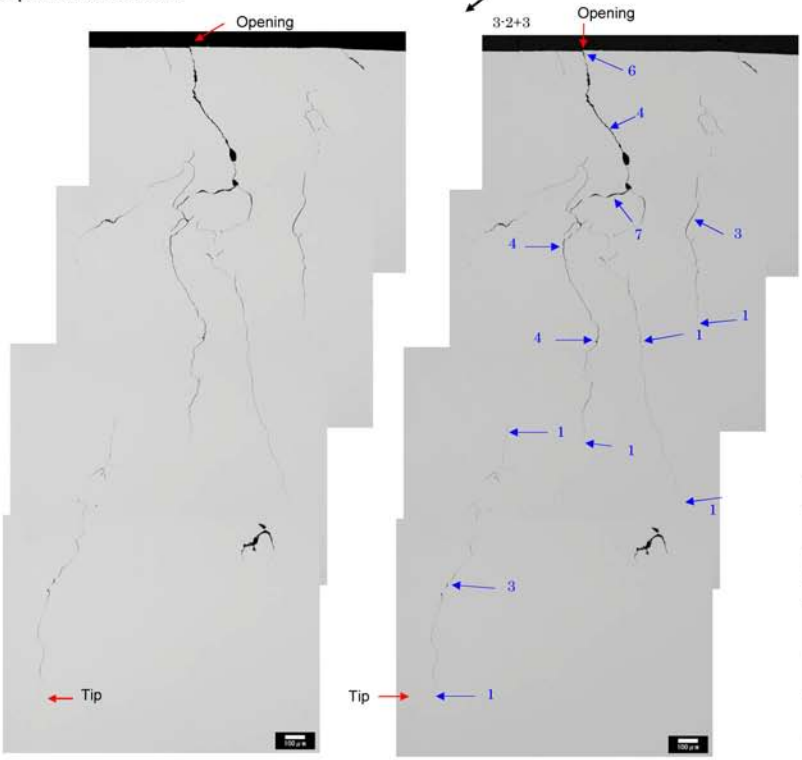

Position		(7)
Depth (mm)	d	3.5
Opening (μm)		6
Tilt (deg) (°)		10
Position of surf. opening (mm)	y	151.6
	X	-0.5
	Y	146.6
	Z	31.3
Position of crack tip (mm)	X	-1.1
	Y	149.7
	Z	29.7

Typical crack opening data of PINC 5.15-1 (perpendicular to weld)
(Position = (7))

Overview

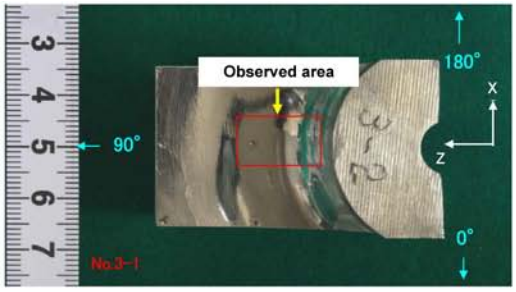

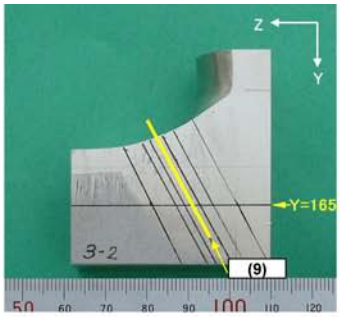

Macro. photo of cross section

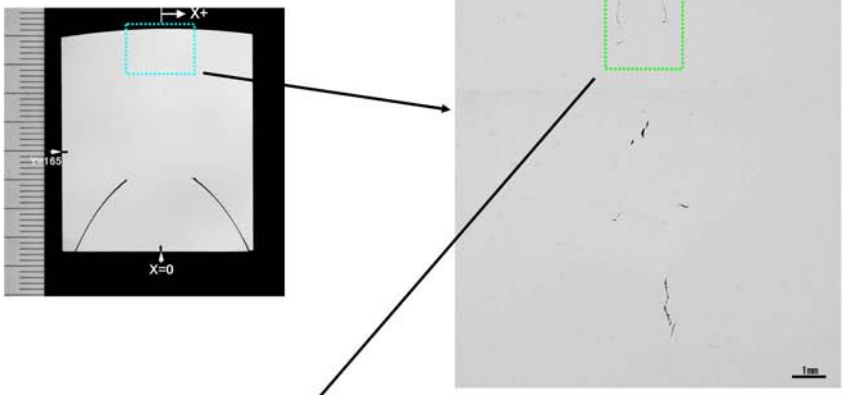

Micro. photo of cross section

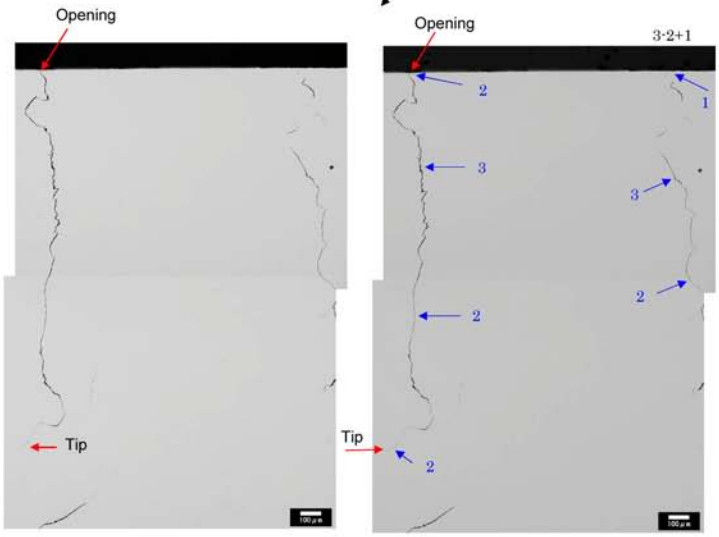

Position		(9)
Depth (mm)	d	2.0
Opening (μm)		2
Tilt (deg) (*)		3
Position of surf. opening (mm)	y	150.3
	X	-0.9
	Y	145.9
	Z	29.6
Position of crack tip (mm)	X	-1.0
	Y	147.6
	Z	28.7

Typical crack opening data of PINC 5.15-1 (perpendicular to weld)
(Position = (9))

(1) Overview

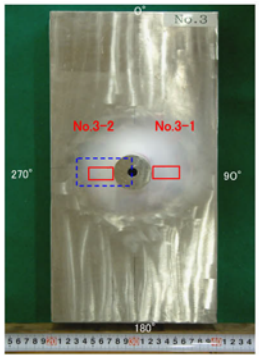

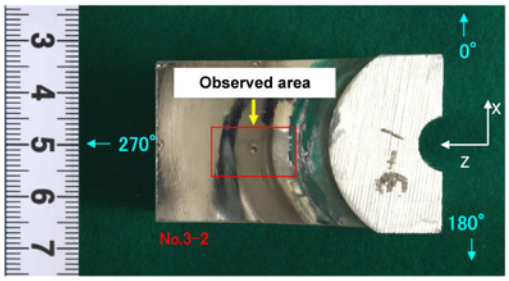

(2) Profile of SCC ○ : Measured on sliced cross section

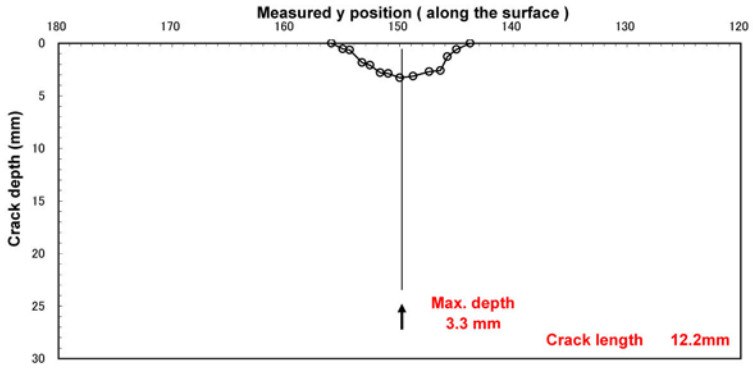

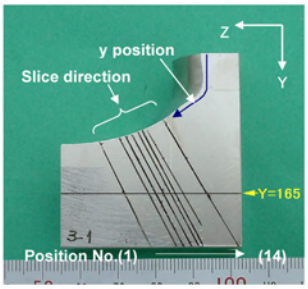

(3) Measured data of SCC

Position		(1)	(2)	(3)	(4)	(5)
Depth (mm)	d	0.0	0.5	0.6	1.8	2.1
Opening (μm)		0	1	1	2	1
Tilt (deg) (*)		—	3	-12	-5	10
Position of surf. opening (mm)	y	156.0	155.0	154.4	153.3	152.6
	X	—	0.4	0.3	-0.2	0.1
	Y	148.7	148.5	148.2	147.7	147.7
	Z	35.2	34.3	33.5	32.7	31.7
Position of crack tip (mm)	X	—	0.3	0.5	-0.1	-0.3
	Y	—	149.0	148.8	149.3	149.6
	Z	—	34.1	33.2	31.9	30.8

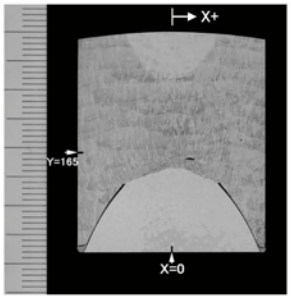

Position (8)

Position		(6)	(7)	(8)	(9)	(10)	(11)	(12)	(13)	(14)
Depth (mm)	d	2.8	2.9	3.3	3.1	2.7	2.6	1.3	0.6	0.0
Opening (μm)		3	131	2	14	3	3	12	1	0
Tilt (deg) (*)		5	18	-7	13	-1	0	22	26	—
Position of surf. opening (mm)	y	151.7	151.0	150.0	148.8	147.4	146.4	145.8	145.0	143.8
	X	-0.1	0.6	-0.4	0.4	-0.8	-0.8	-1.6	-1.7	—
	Y	146.9	146.8	146.1	145.9	145.1	145.1	144.4	143.9	143.3
	Z	31.1	30.2	29.5	28.6	28.0	27.0	26.4	25.6	24.9
Position of crack tip (mm)	X	-0.3	-0.4	0.0	-0.4	-0.8	-0.8	-2.1	-2.0	—
	Y	149.4	149.3	149.1	148.7	147.5	147.4	145.5	144.4	—
	Z	29.9	28.9	28.0	27.2	26.8	25.9	25.8	25.4	—

(*) Measured from radial coordinate of 270 deg. (+ : clockwise)

Results of destructive test on PINC 5.15-2 (perpendicular to weld)

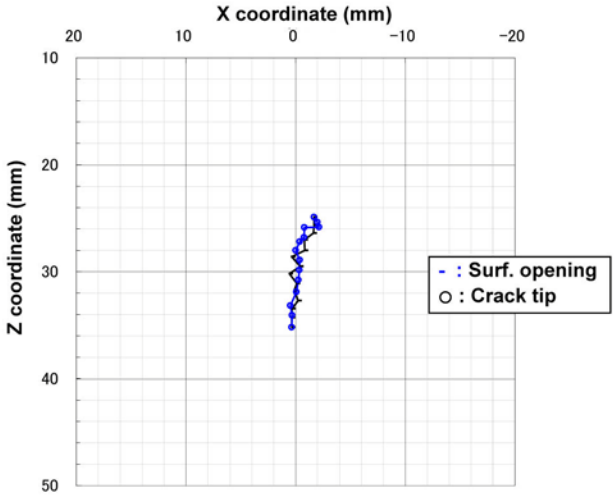
X coordinate (mm)
20
10
0
−10
−20
10
20
30
40
50
Z coordinate (mm)
- : Surf. opening
○ : Crack tip

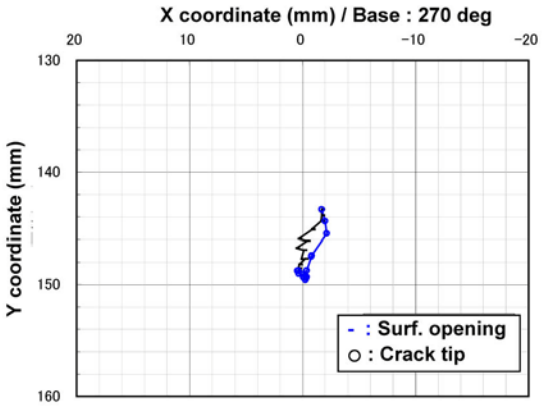
X coordinate (mm) / Base : 270 deg
20
10
0
−10
−20
130
140
150
160
Y coordinate (mm)
- : Surf. opening
○ : Crack tip

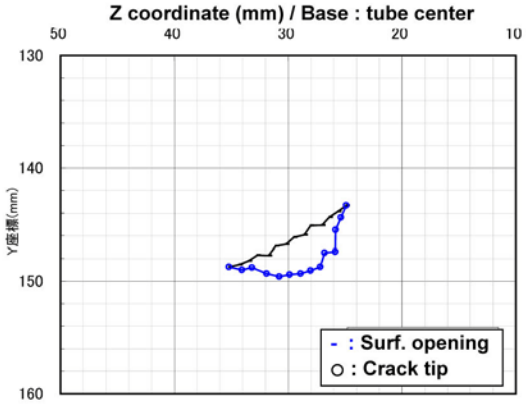
Z coordinate (mm) / Base : tube center
50
40
30
20
10
130
140
150
160
Y座標(mm)
- : Surf. opening
○ : Crack tip

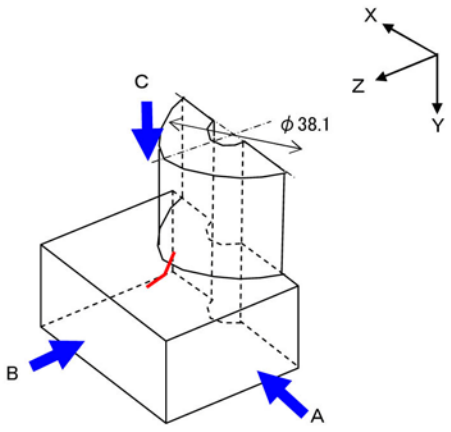
X
Z
Y
C
ϕ38.1
B
A

Overview

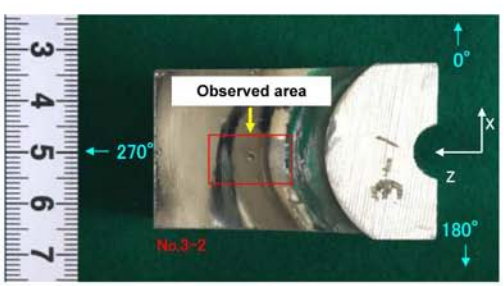

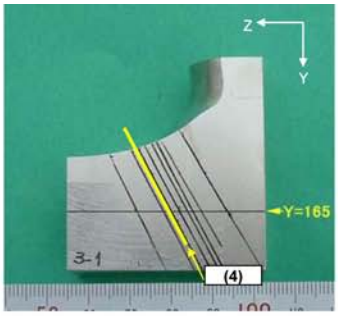

Macro. photo of cross section

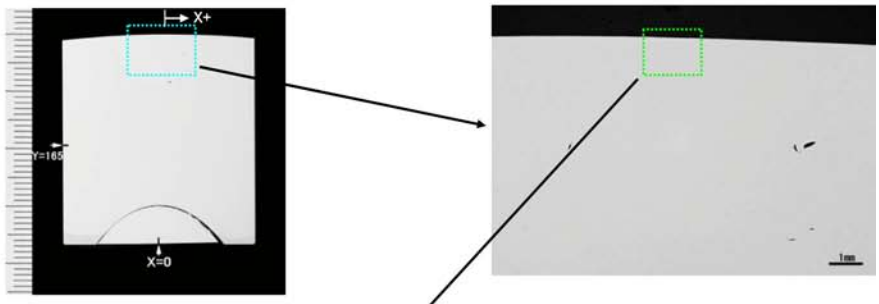

Micro. photo of cross section

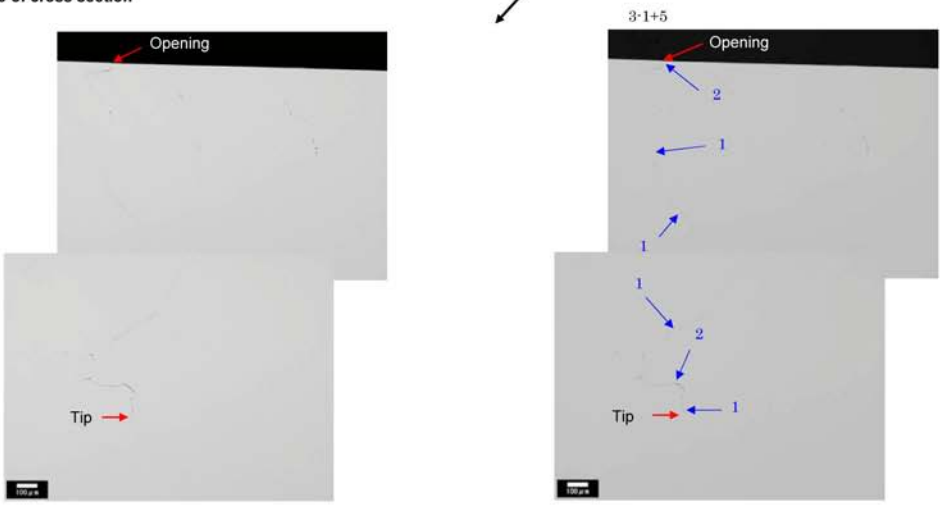

Position		(4)
Depth (mm)	d	1.8
Opening (μm)		2
Tilt (deg) (°)		-5
Position of surf. opening (mm)	y	153.3
	X	-0.2
	Y	147.7
	Z	32.7
Position of crack tip (mm)	X	-0.1
	Y	149.3
	Z	31.9

Typical crack opening data of PINC 5.15-2 (perpendicular to weld)
(Position = (4))

Overview

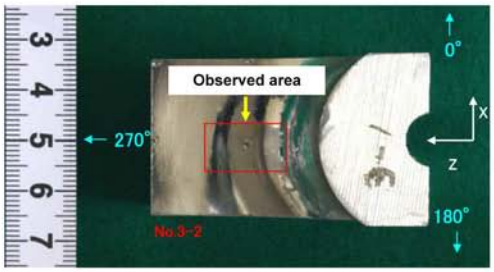

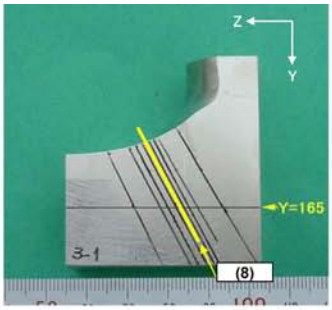

Macro. photo of cross section

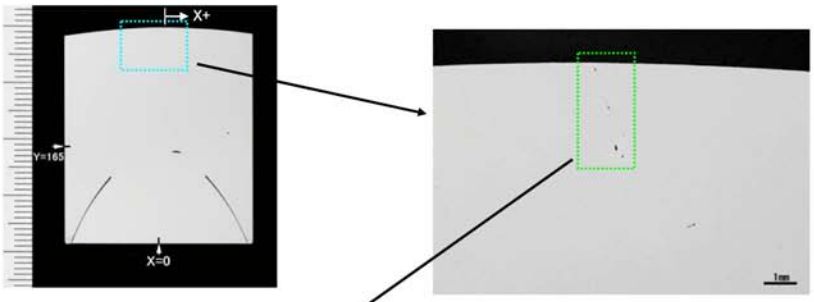

Micro. photo of cross section

3-1+1

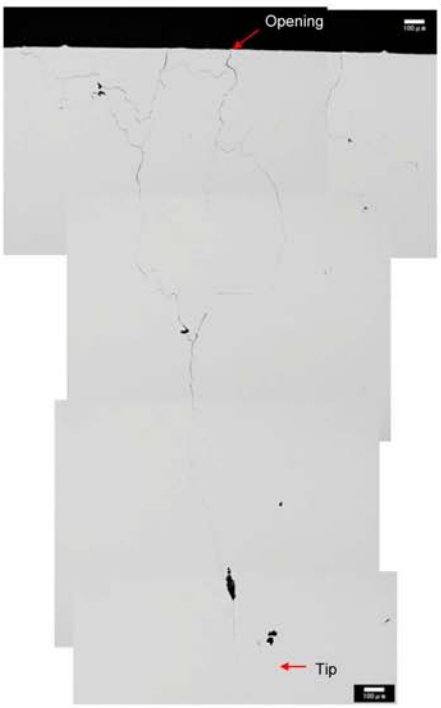

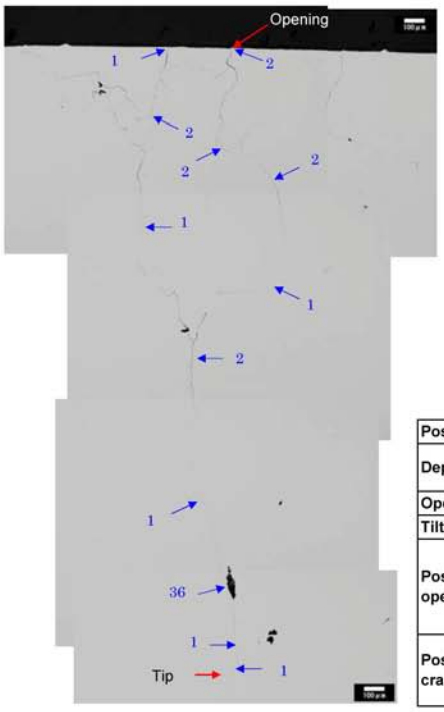

Position		(8)
Depth (mm)	d	3.3
Opening (μm)		2
Tilt (deg) (°)		-7
Position of surf. opening (mm)	y	150.0
	X	-0.4
	Y	146.1
	Z	29.5
Position of crack tip (mm)	X	0.0
	Y	149.1
	Z	28.0

Typical crack opening data of PINC 5.15-2 (perpendicular to weld)
(Position = (8))

(1) Overview

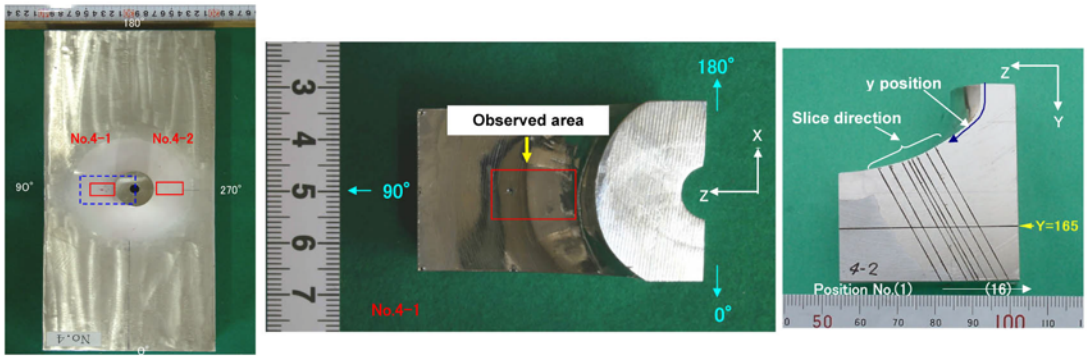

(2) Profile of SCC ○ : Measured on sliced cross section

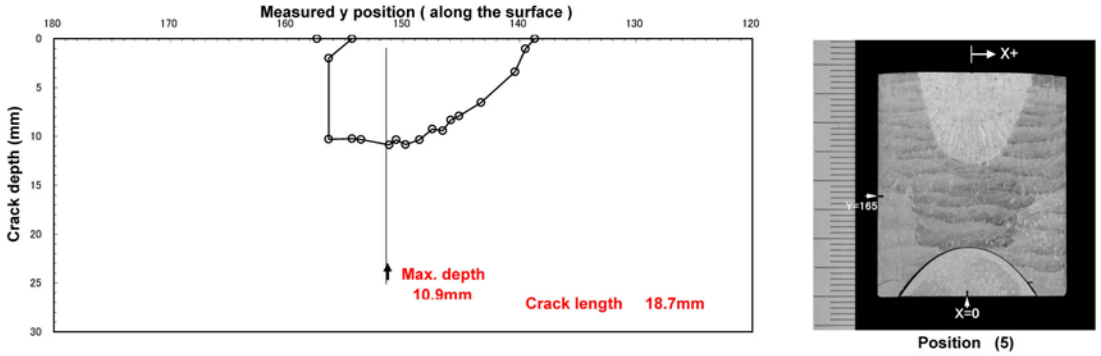

(3) Measured data of SCC

Position		(1)	(2)		(3)	(4)	(5)	(6)	(7)	(8)
Depth (mm)	d	0.0	8.3		10.2	10.3	10.9	10.4	10.8	10.4
Opening (μm)		0	Embeded		2	4	15	5	11	17
Tilt (deg) (*)		—	-		5	3	4	0	2	3
Position of surf. opening (mm)	y	157.4	156.4		154.4	153.6	151.2	150.6	149.8	148.6
	X	—	-1.1	-1.1	1.2	0.8	0.7	0.1	1.2	1.4
	Y	147.5	147.3	149.0	146.8	146.6	145.6	145.4	144.9	144.6
	Z	38.8	37.9	37.0	36.2	35.3	32.8	31.9	31.1	30.3
Position of crack tip (mm)	X	—	1.2		0.3	0.2	0.0	0.1	0.9	0.9
	Y	—	156.5		156.0	155.9	155.3	154.7	154.6	153.9
	Z	—	33.3		31.6	30.6	27.9	27.2	26.3	25.6

Position		(9)	(10)	(11)	(12)	(13)	(14)	(15)	(16)
Depth (mm)	d	9.3	9.4	8.3	7.9	6.6	3.4	1.0	0.0
Opening (μm)		528	5	90	339	5	3	1	0
Tilt (deg) (*)		5	4	17	-1	-3	24	16	—
Position of surf. opening (mm)	y	147.5	146.6	145.9	145.2	143.3	140.4	139.5	138.7
	X	2.0	2.0	2.0	0.0	-0.3	1.3	2.2	—
	Y	144.0	143.7	143.0	142.8	141.3	139.3	138.7	138.1
	Z	29.6	28.7	28.1	27.1	25.9	23.9	23.2	22.5
Position of crack tip (mm)	X	1.3	1.3	-0.5	0.1	0.0	-0.2	1.9	—
	Y	152.3	152.2	150.5	149.9	147.2	142.3	139.6	—
	Z	25.4	24.5	24.3	23.6	23.0	22.4	22.8	—

(*) Measured from radial coordinate of 90 deg. (+ : clockwise)

Results of destructive test on PINC 5.16-1 (perpendicular to weld)

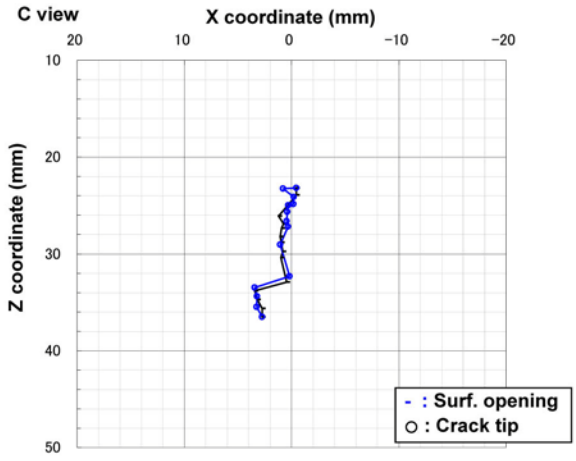
C view
X coordinate (mm)
20
10
0
−10
−20
10
20
30
40
50
Z coordinate (mm)
- : Surf. opening
○ : Crack tip

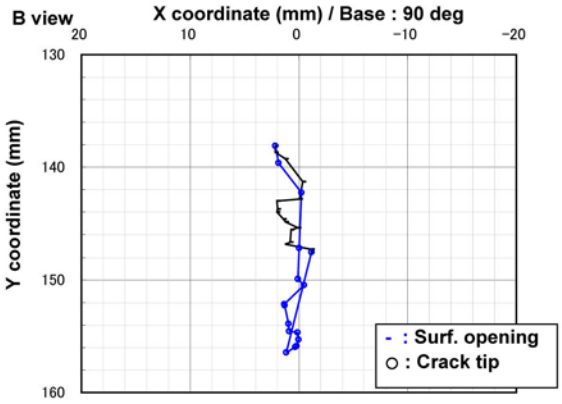
B view
X coordinate (mm) / Base : 90 deg
20
10
0
−10
−20
130
140
150
160
Y coordinate (mm)
- : Surf. opening
○ : Crack tip

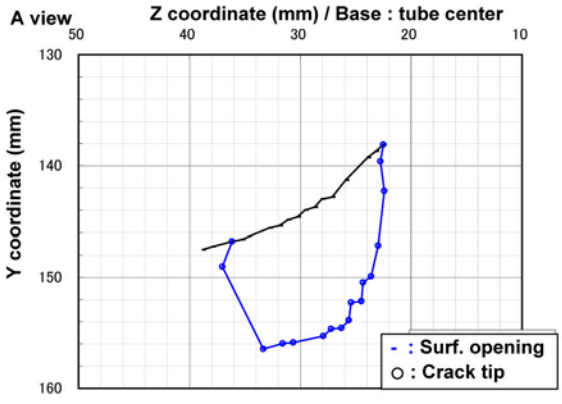
A view
Z coordinate (mm) / Base : tube center
50
40
30
20
10
130
140
150
160
Y coordinate (mm)
- : Surf. opening
○ : Crack tip

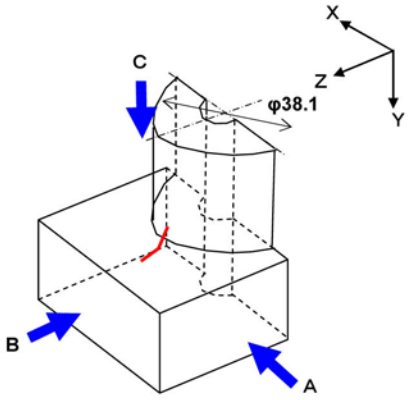
X
Z
Y
C
φ38.1
B
A

Overview

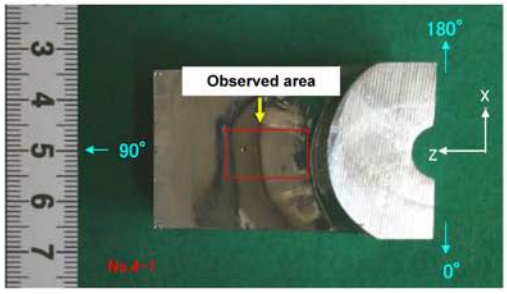

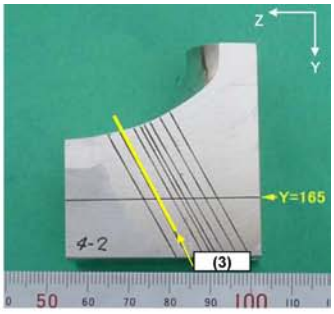

Macro. photo of cross section

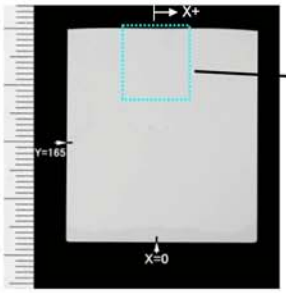

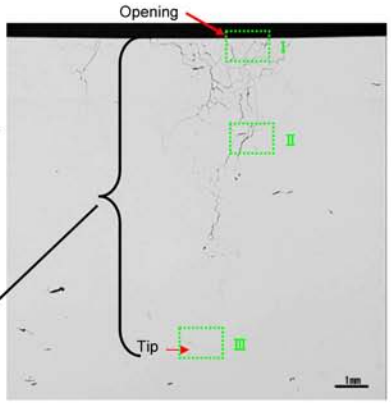

Micro. photo of cross section

Surface opening

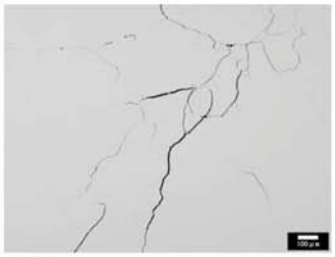

Middle

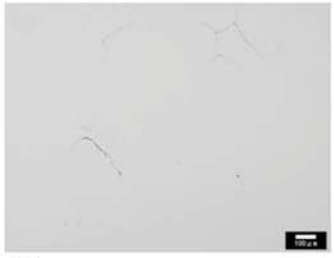

Tip

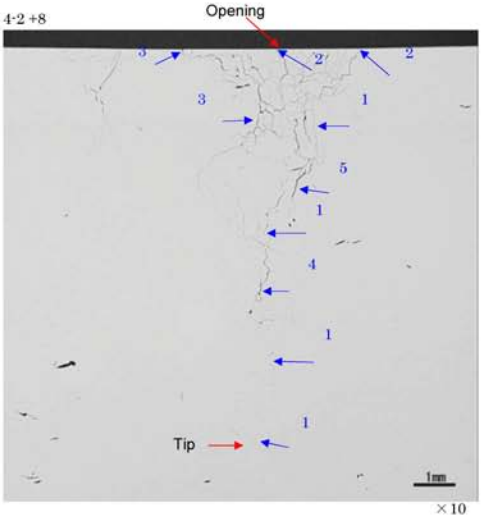

Position		(3)
Depth (mm)	d	10.2
Opening (μm)		2
Tilt (deg) (°)		5
Position of surf. opening (mm)	y	154.4
	X	1.2
	Y	146.8
	Z	36.2
Position of crack tip (mm)	X	0.3
	Y	156.0
	Z	31.6

Typical crack opening data of PINC 5.16-1 (perpendicular to weld)
(Position = (3))

Overview

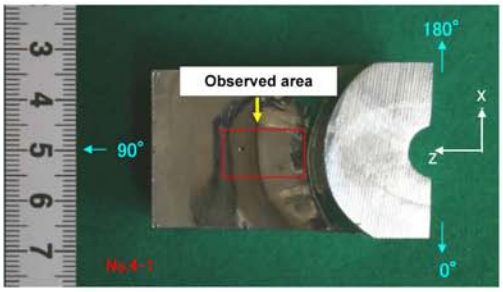

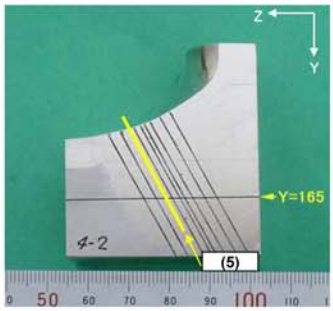

Macro. photo of cross section

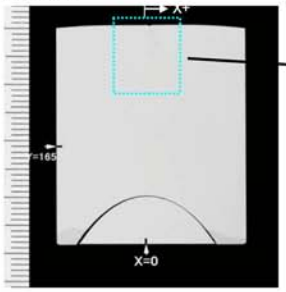

Opening

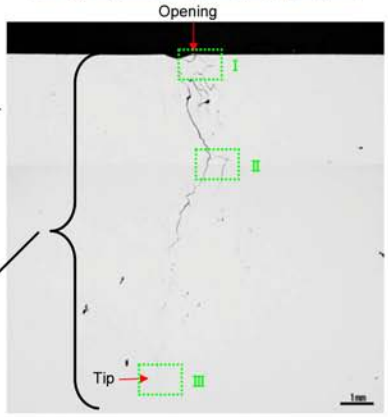

Micro. photo of cross section

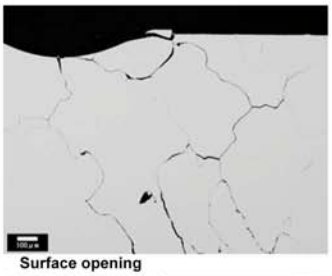

Surface opening

Middle

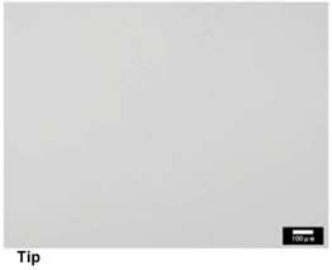

Tip

4-2 +4

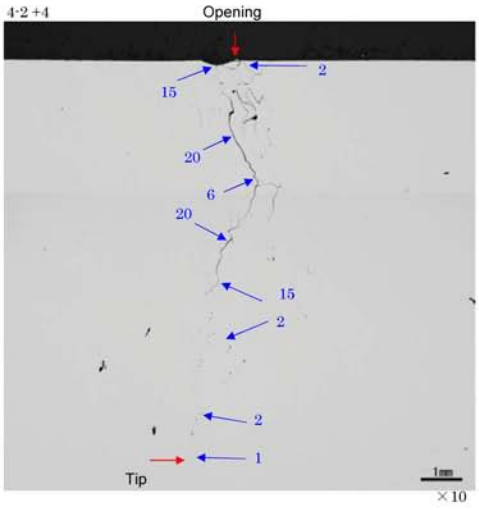

×10

Position		(5)
Depth (mm)	d	10.9
Opening (μm)		15
Tilt (deg) (*)		4
Position of surf. opening (mm)	y	151.2
	X	0.7
	Y	145.6
	Z	32.8
Position of crack tip (mm)	X	0.0
	Y	155.3
	Z	27.9

Typical crack opening data of PINC 5.16-1 (perpendicular to weld)
(Position = (5))

Overview

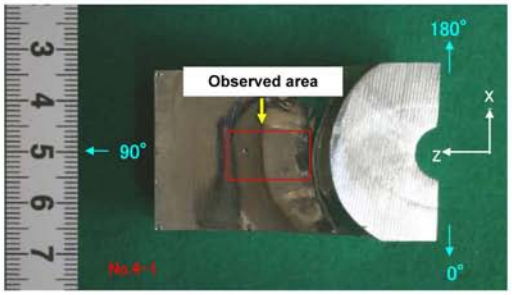

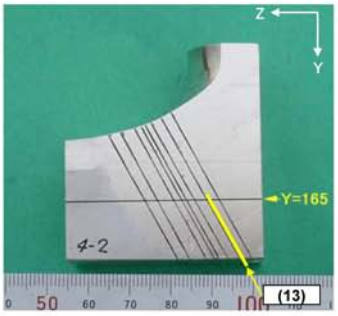

Macro. photo of cross section

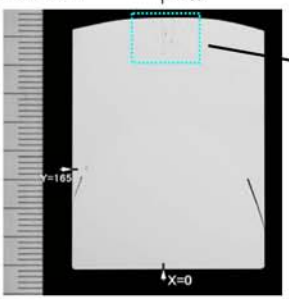

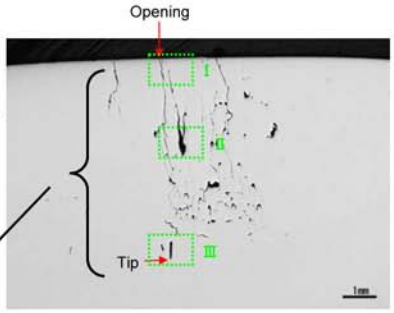

Micro. photo of cross section

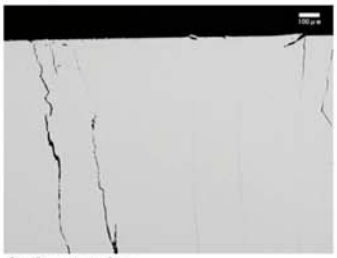

Surface opening

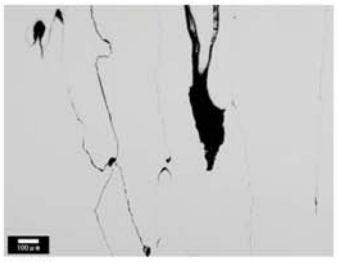

Middle

Tip

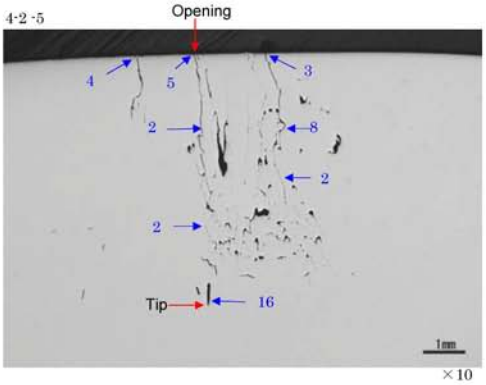

×10

Position		(13)
Depth (mm)	d	6.6
Opening (μm)		5
Tilt (deg) (°)		-3
Position of surf. opening (mm)	y	143.3
	X	-0.3
	Y	141.3
	Z	25.9
Position of crack tip (mm)	X	0.0
	Y	147.2
	Z	23.0

Typical crack opening data of PINC 5.16-1 (perpendicular to weld)
(Position = (13))

(1) Overview

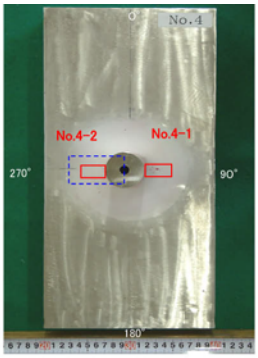

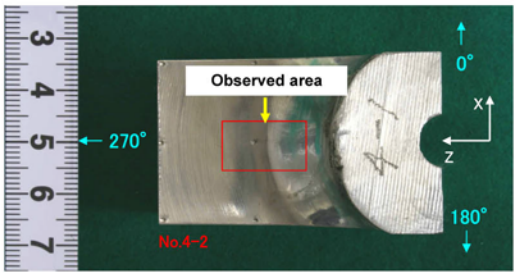

(2) Profile of SCC ○ : Measured on sliced cross section

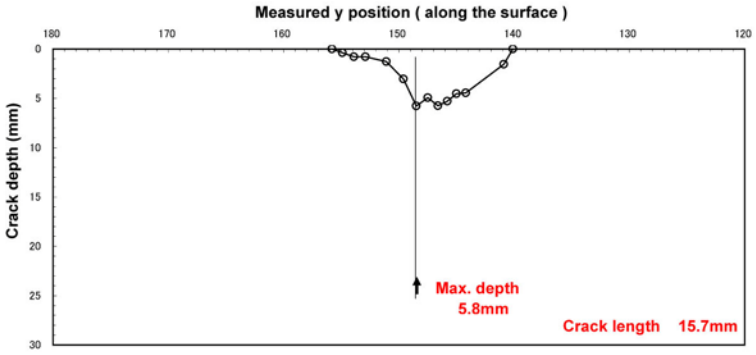

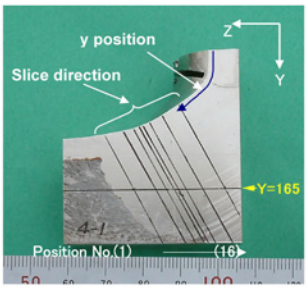

(3) Measured data of SCC

Position		(1)	(2)	(3)	(4)	(5)
Depth (mm)	d	0.0	0.4	0.8	0.8	1.3
Opening (μm)		0	1	1	3	3
Tilt (deg) (*)		—	-55	-1	0	12
Position of surf. opening (mm)	y	155.8	154.9	153.9	152.9	151.1
	X	—	2.7	3.2	3.4	0.4
	Y	148.1	147.8	147.7	147.5	147.3
	Z	36.5	35.6	34.7	33.8	32.9
Position of crack tip (mm)	X	—	3.3	3.2	3.4	0.2
	Y	—	148.2	148.4	148.2	148.5
	Z	—	35.5	34.4	33.5	32.3

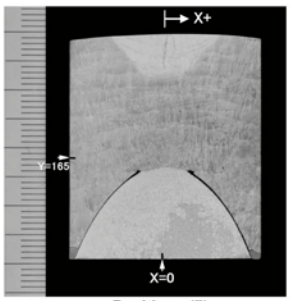

Position (7)

Position		(6)	(7)	(8)	(9)	(10)	(11)	(12)	(13)	(14)
Depth (mm)	d	3.0	5.8	5.0	5.7	5.3	4.5	4.5	1.5	0.0
Opening (μm)		9	8	10	7	4	8	32	13	0
Tilt (deg) (*)		-1	5	6	7	7	12	18	-39	—
Position of surf. opening (mm)	y	149.6	148.5	147.5	146.6	145.8	145.0	144.2	140.9	140.1
	X	1.0	0.8	0.9	1.1	0.9	0.7	1.2	-0.4	—
	Y	146.3	145.6	145.5	144.7	144.4	143.4	142.9	140.3	139.7
	Z	30.4	29.8	28.8	28.2	27.3	26.9	26.1	23.9	23.2
Position of crack tip (mm)	X	1.0	0.3	0.4	0.4	0.3	-0.2	-0.2	0.8	—
	Y	149.0	150.8	149.9	149.8	149.2	147.4	146.9	141.7	—
	Z	29.0	27.2	26.6	25.6	25.0	24.9	24.1	23.2	—

(*) Measured from radial coordinate of 270 deg. (+ : clockwise)

Results of destructive test on PINC 5.16-2 (perpendicular to weld)

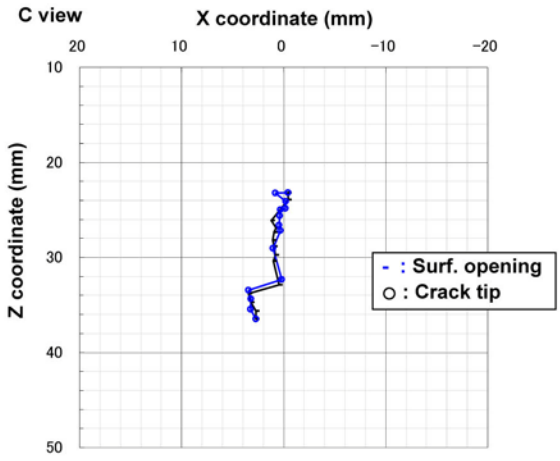
C view
X coordinate (mm)
20
10
0
−10
−20
10
20
30
40
50
Z coordinate (mm)
- : Surf. opening
○ : Crack tip

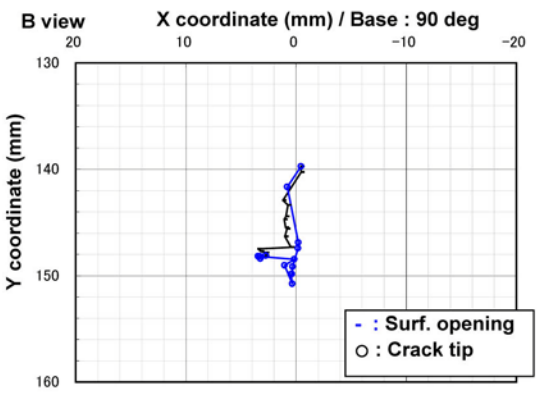
B view
X coordinate (mm) / Base : 90 deg
20
10
0
−10
−20
130
140
150
160
Y coordinate (mm)
- : Surf. opening
○ : Crack tip

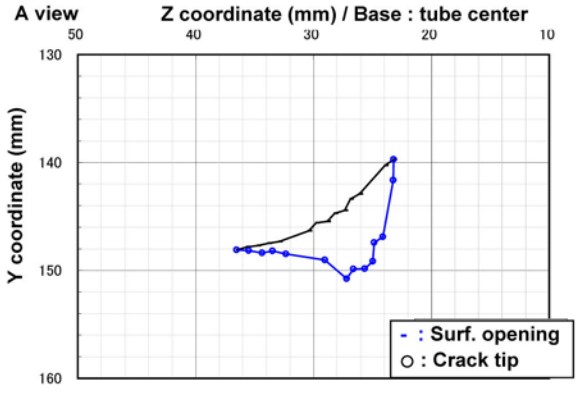
A view
Z coordinate (mm) / Base : tube center
50
40
30
20
10
130
140
150
160
Y coordinate (mm)
- : Surf. opening
○ : Crack tip

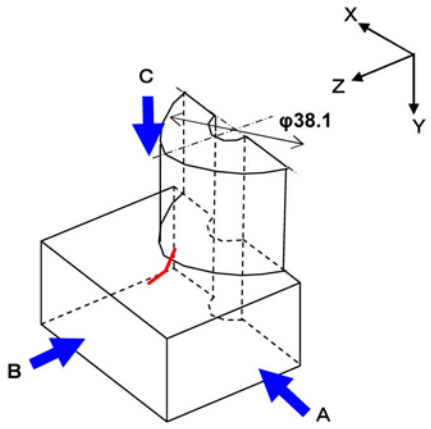
X
Z
Y
C
φ38.1
B
A

Overview

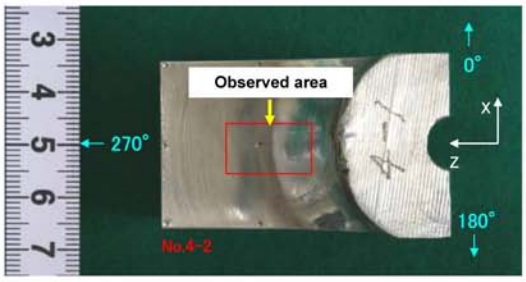

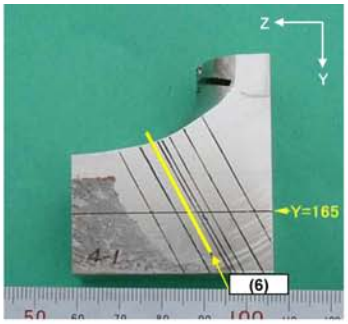

Macro. photo of cross section

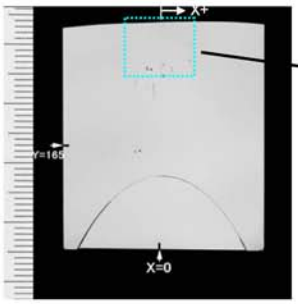

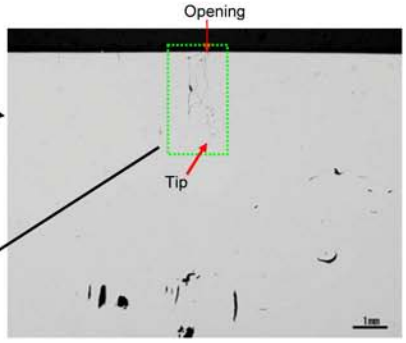

Micro. photo of cross section

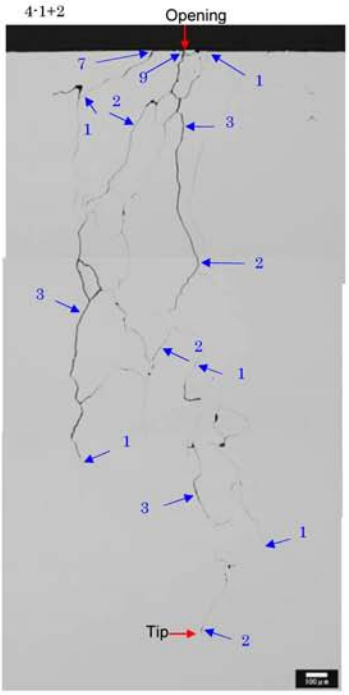

Position		(6)
Depth (mm)	d	3.0
Opening (μm)		9
Tilt (deg) (°)		-1
Position of surf. opening (mm)	y	149.6
	X	1.0
	Y	146.3
	Z	30.4
Position of crack tip (mm)	X	1.0
	Y	149.0
	Z	29.0

Typical crack opening data of PINC 5.16-2 (perpendicular to weld)
(Position = (6))

Overview

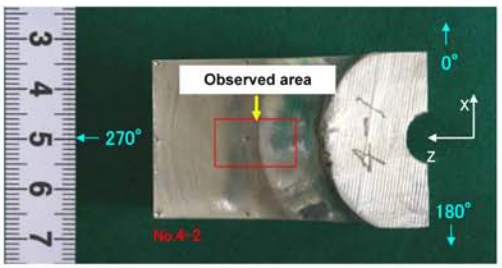

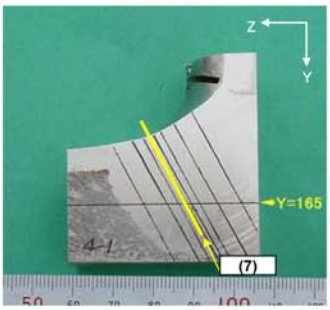

Macro. photo of cross section

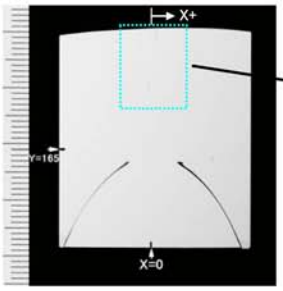

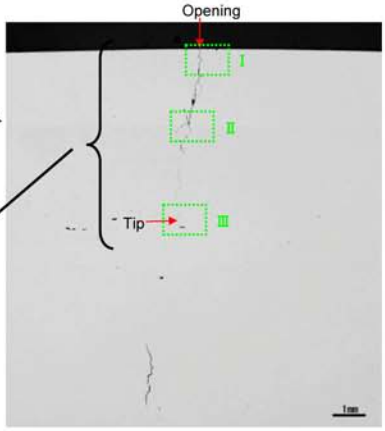

Micro. photo of cross section

Surface opening

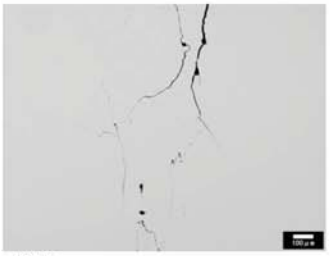

Middle

Tip

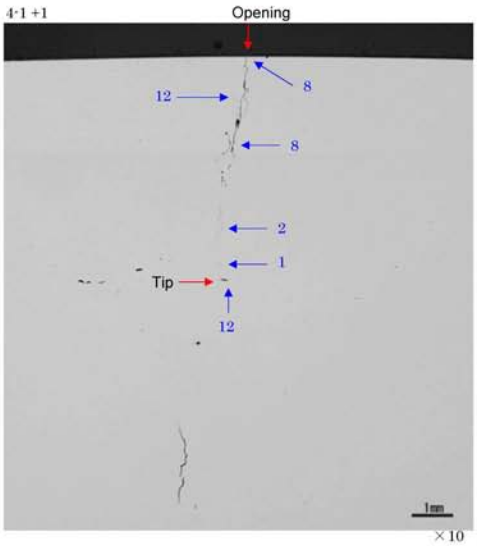

Position		(7)
Depth (mm)	d	5.8
Opening (μm)		8
Tilt (deg) (*)		5
Position of surf. opening (mm)	y	148.5
	X	0.8
	Y	145.6
	Z	29.8
Position of crack tip (mm)	X	0.3
	Y	150.8
	Z	27.2

Typical crack opening data of PINC 5.16-2 (perpendicular to weld)
(Position = (7))

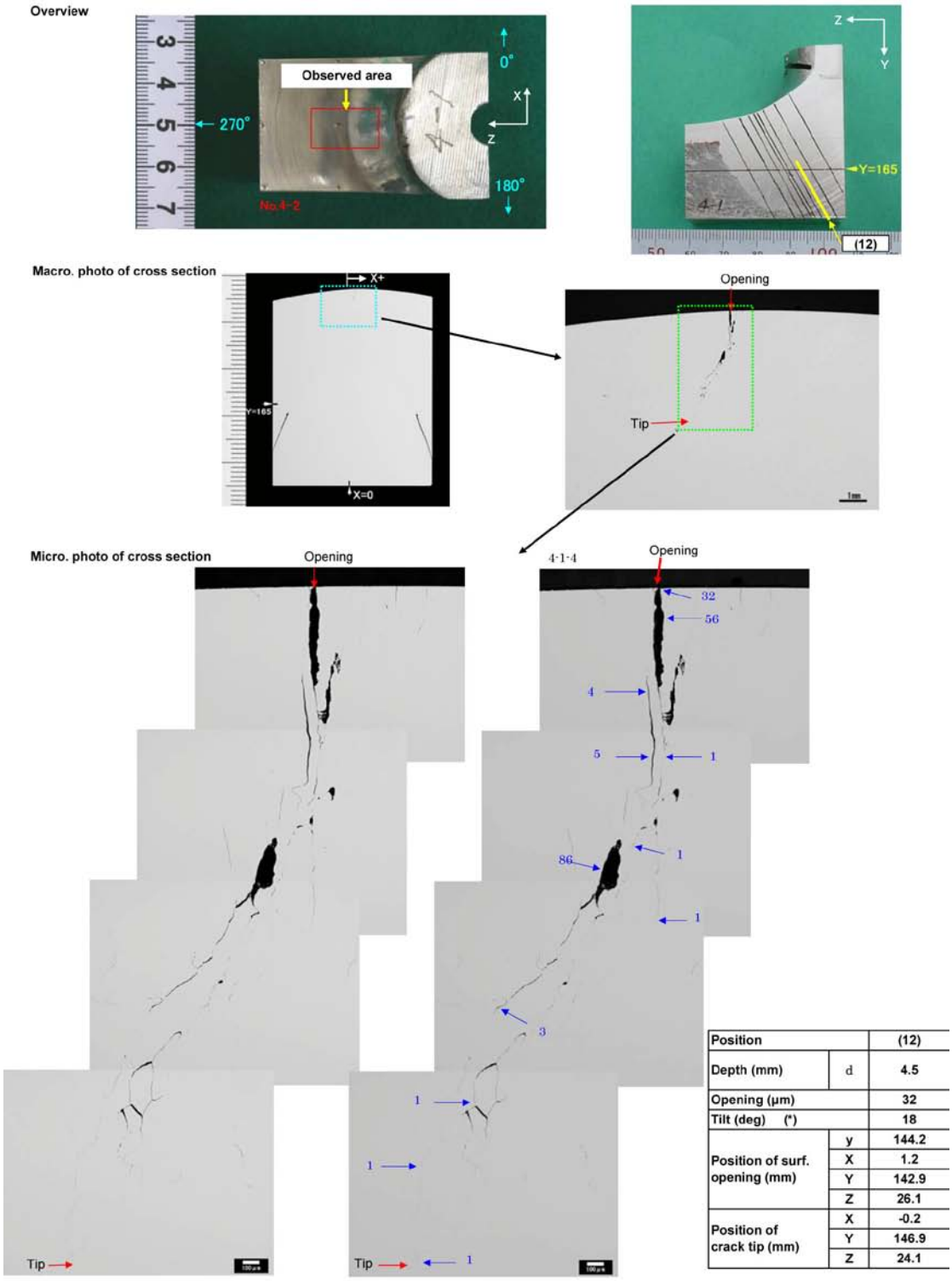

Position		(12)
Depth (mm)	d	4.5
Opening (μm)		32
Tilt (deg) (°)		18
Position of surf. opening (mm)	y	144.2
	X	1.2
	Y	142.9
	Z	26.1
Position of crack tip (mm)	X	-0.2
	Y	146.9
	Z	24.1

Typical crack opening data of PINC 5.16-2 (perpendicular to weld)
(Position = (12))

Appendix C

Inspection Plots for Dissimilar Metal Weld Samples

Appendix C

Inspection Plots for Dissimilar Metal Weld Samples

Table of Contents

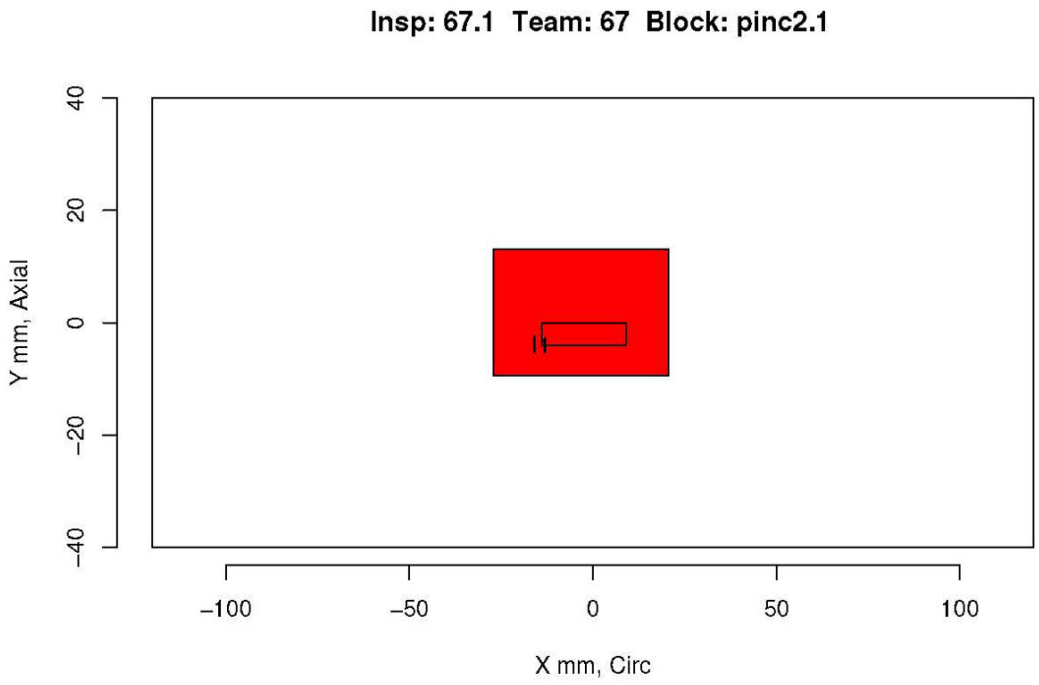
Insp: 67.1 Team: 67 Block: pinc2.1
Y mm, Axial
40
20
0
−20
−40
−100
−50
0
50
100
X mm, Circ

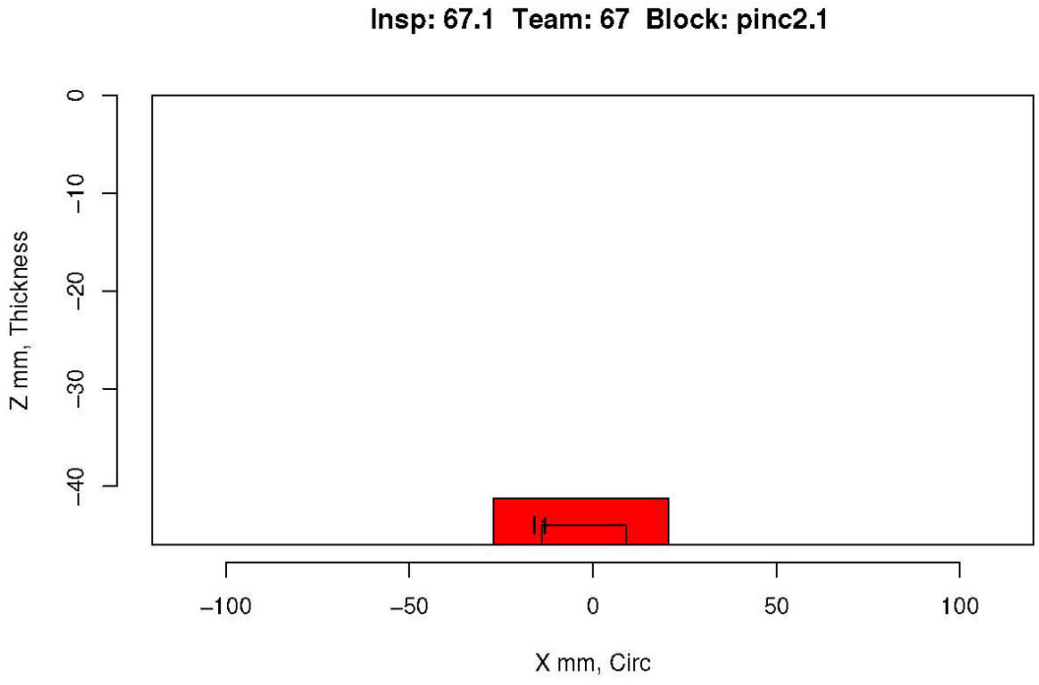
Insp: 67.1 Team: 67 Block: pinc2.1
Z mm, Thickness
0
−10
−20
−30
−40
−100
−50
0
50
100
X mm, Circ

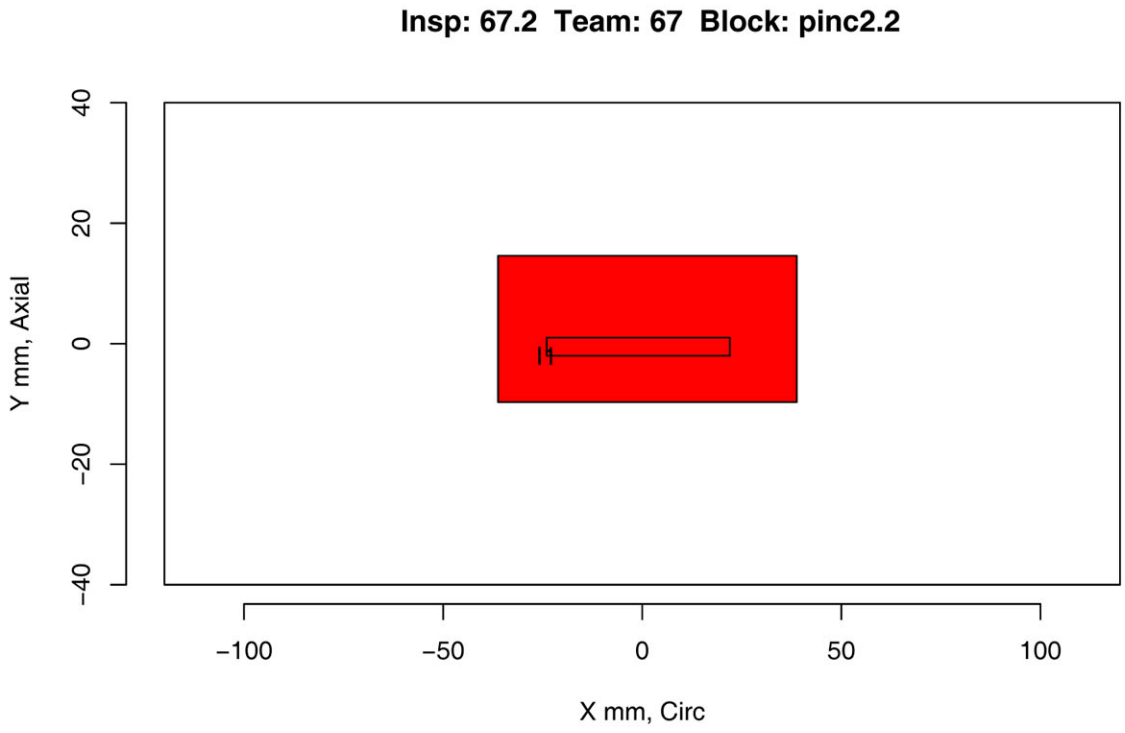
Insp: 67.2 Team: 67 Block: pinc2.2
Y mm, Axial
40
20
0
−20
−40
−100
−50
0
50
100
X mm, Circ

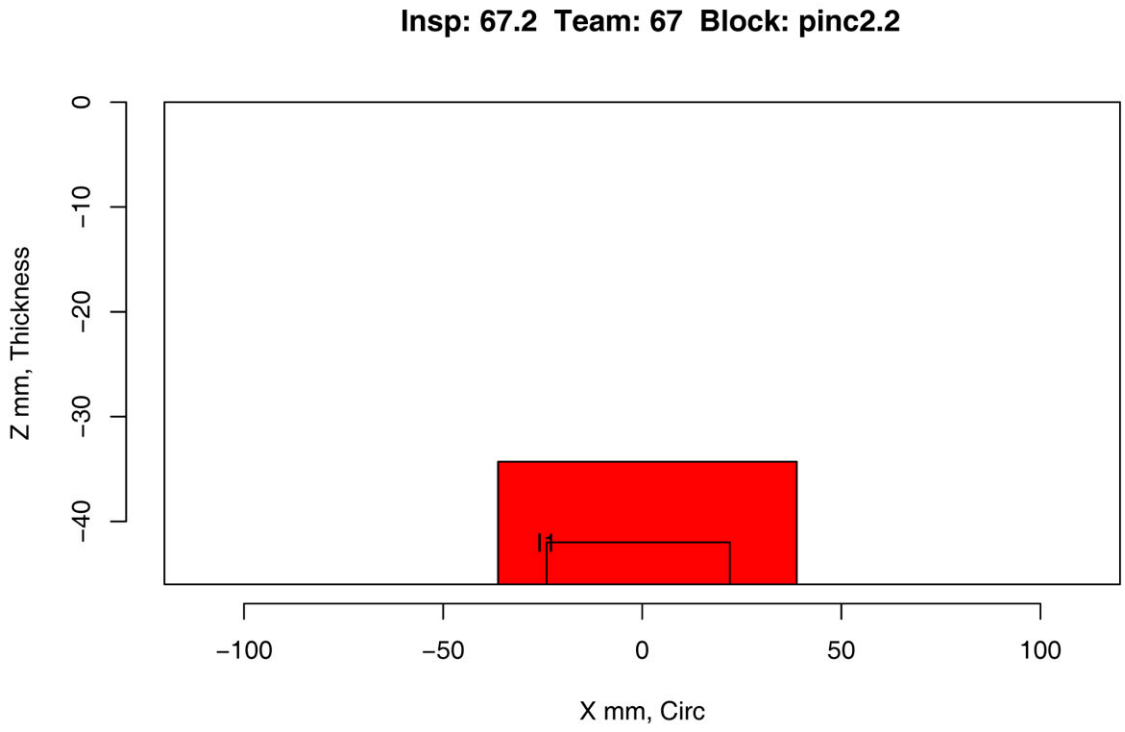
Insp: 67.2 Team: 67 Block: pinc2.2
Z mm, Thickness
0
−10
−20
−30
−40
−100
−50
0
50
100
X mm, Circ

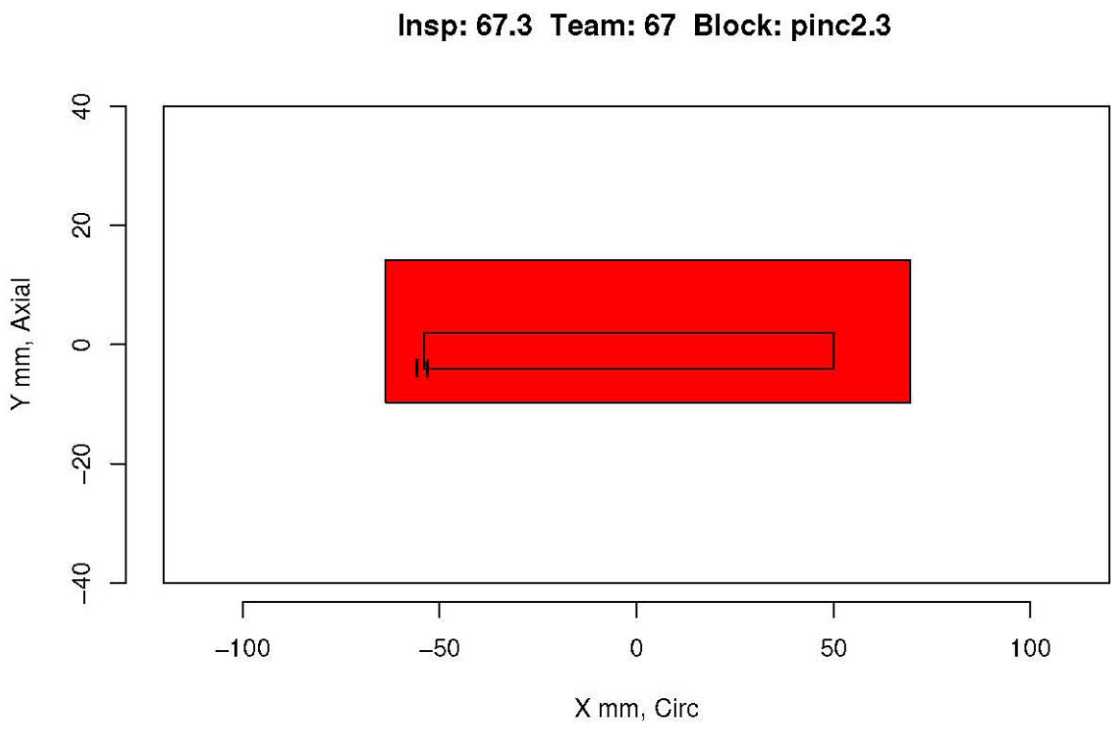
Insp: 67.3 Team: 67 Block: pinc2.3
Y mm, Axial
40
20
0
−20
−40
−100
−50
0
50
100
X mm, Circ

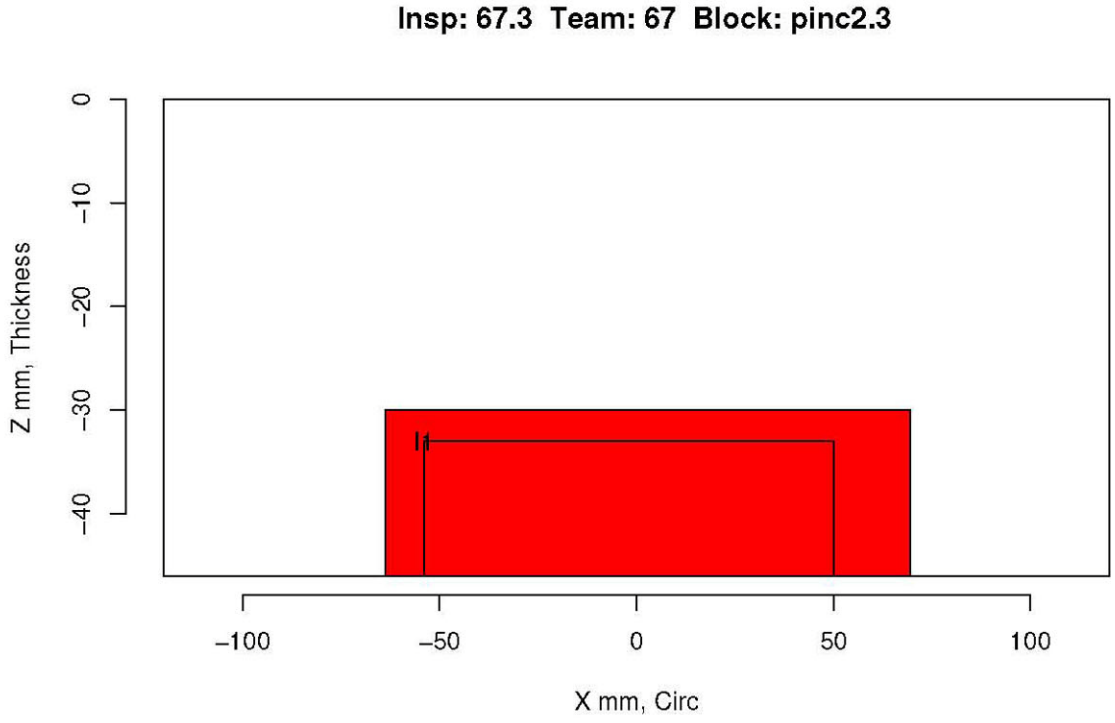
Insp: 67.3 Team: 67 Block: pinc2.3
Z mm, Thickness
0
−10
−20
−30
−40
−100
−50
0
50
100
X mm, Circ

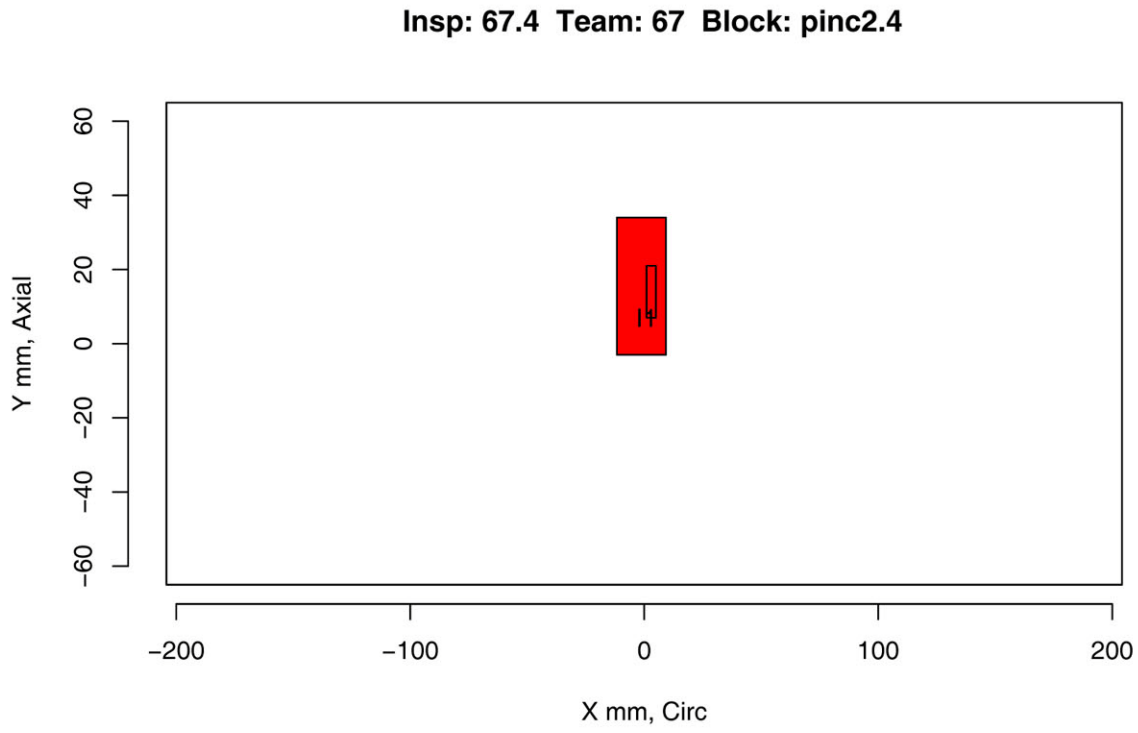
Insp: 67.4 Team: 67 Block: pinc2.4
Y mm, Axial
60
40
20
0
−20
−40
−60
−200
−100
0
100
200
X mm, Circ

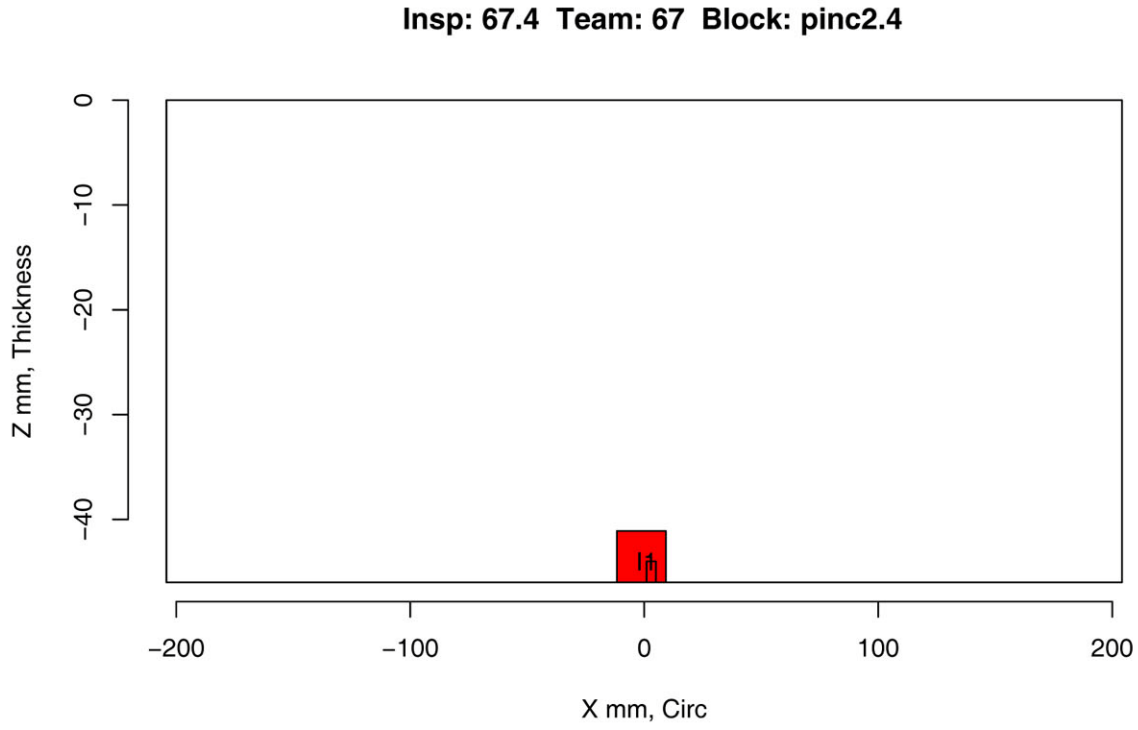
Insp: 67.4 Team: 67 Block: pinc2.4
Z mm, Thickness
0
−10
−20
−30
−40
−200
−100
0
100
200
X mm, Circ

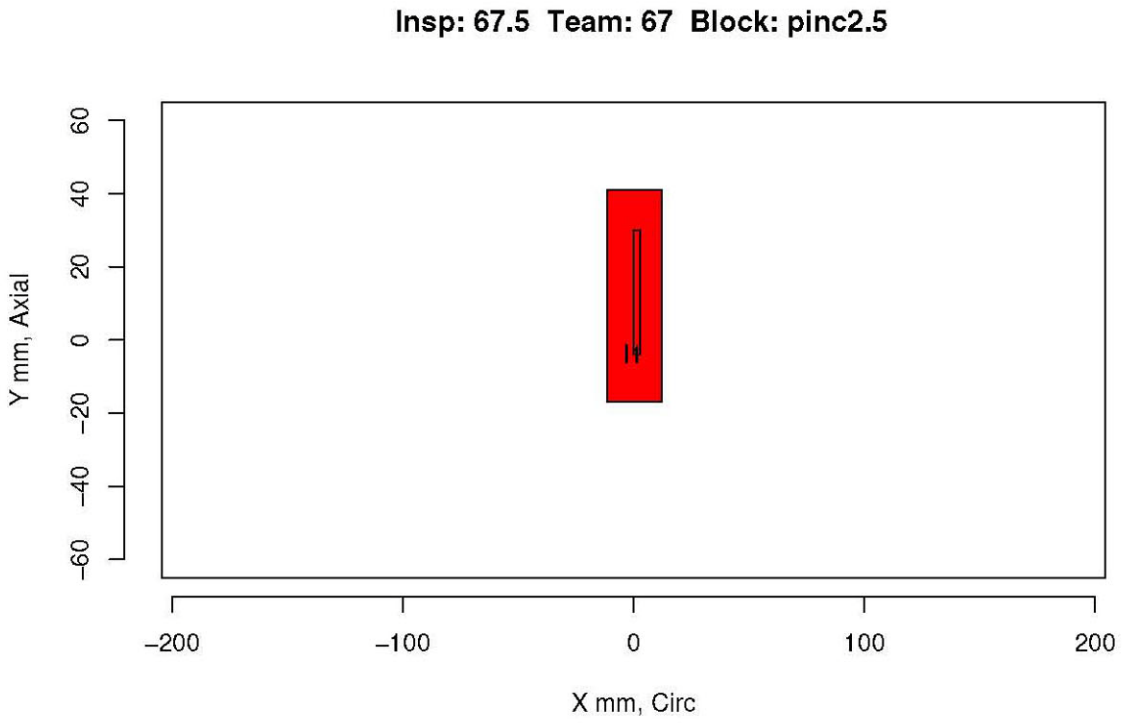
Insp: 67.5 Team: 67 Block: pinc2.5
Y mm, Axial
60
40
20
0
−20
−40
−60
−200
−100
0
100
200
X mm, Circ

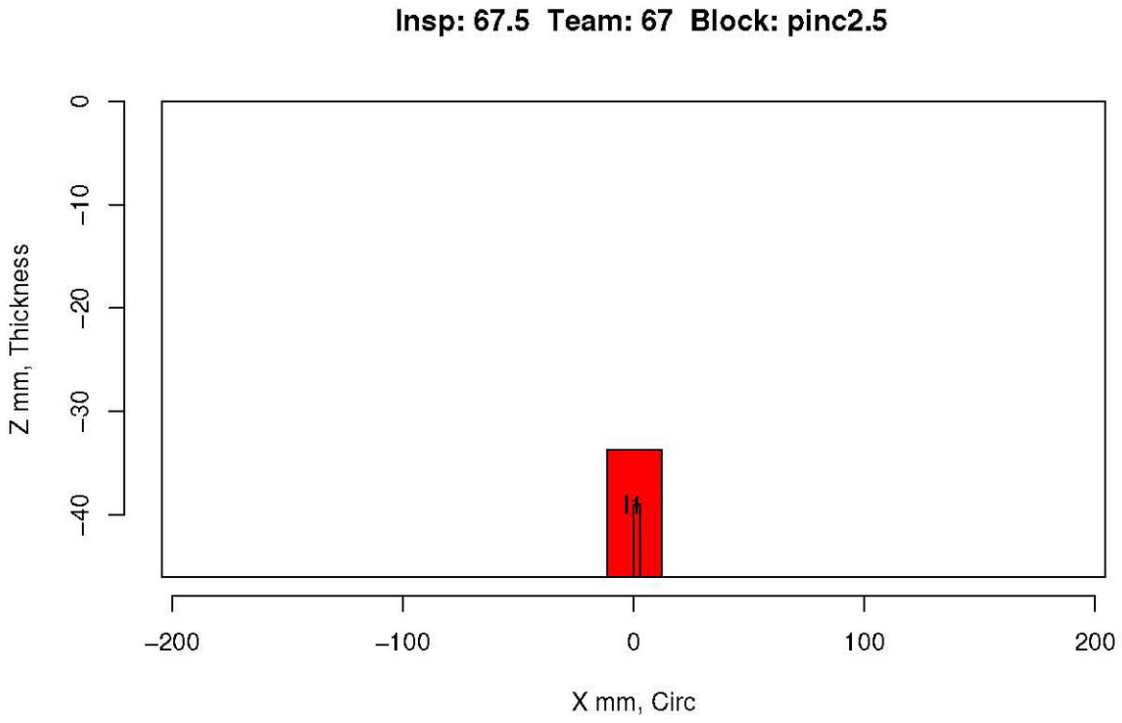
Insp: 67.5 Team: 67 Block: pinc2.5
Z mm, Thickness
0
−10
−20
−30
−40
−200
−100
0
100
200
X mm, Circ

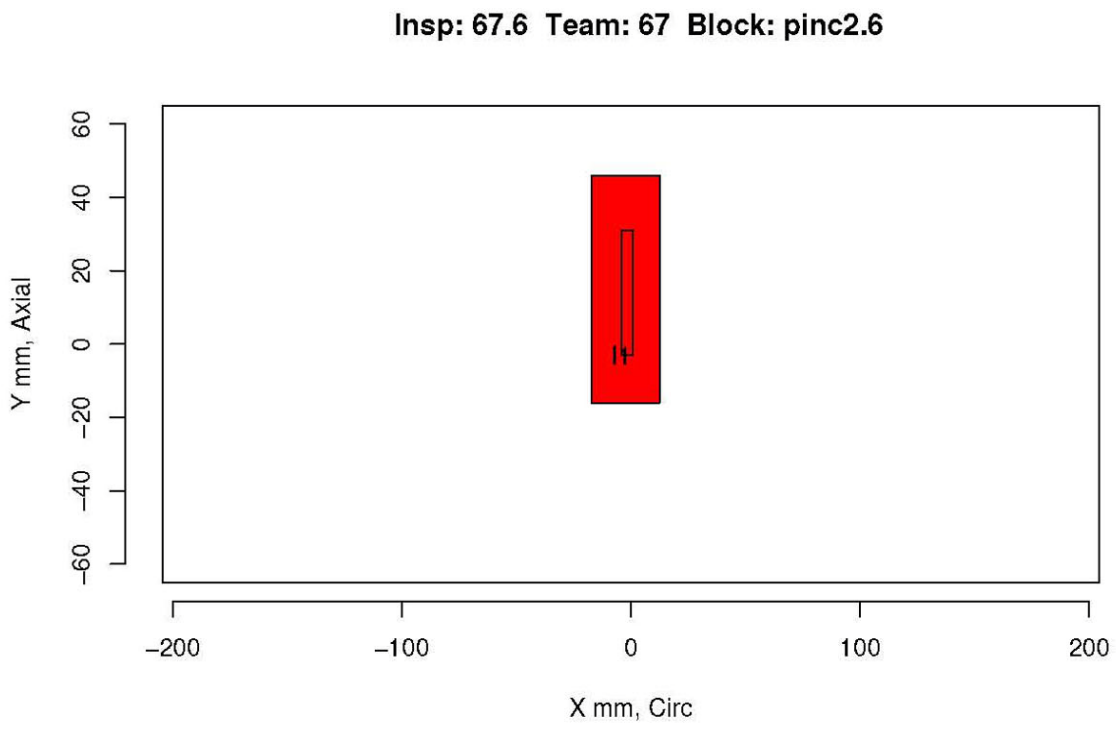
Insp: 67.6 Team: 67 Block: pinc2.6
Y mm, Axial
60
40
20
0
−20
−40
−60
−200
−100
0
100
200
X mm, Circ

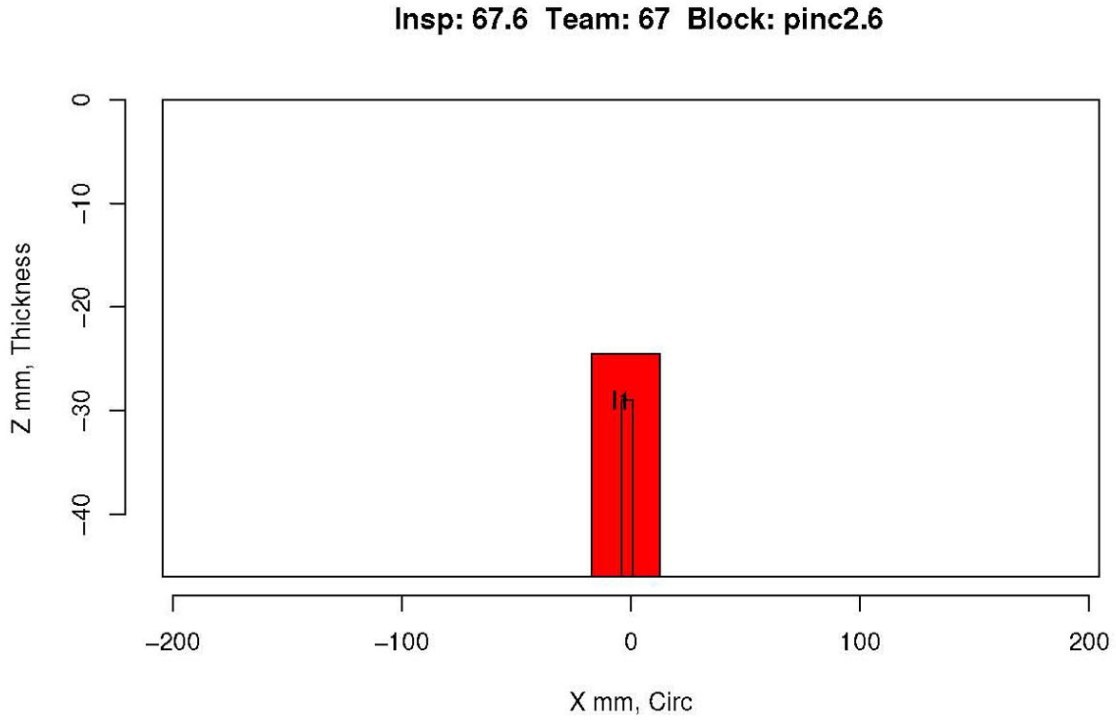
Insp: 67.6 Team: 67 Block: pinc2.6
Z mm, Thickness
0
−10
−20
−30
−40
−200
−100
0
100
200
X mm, Circ

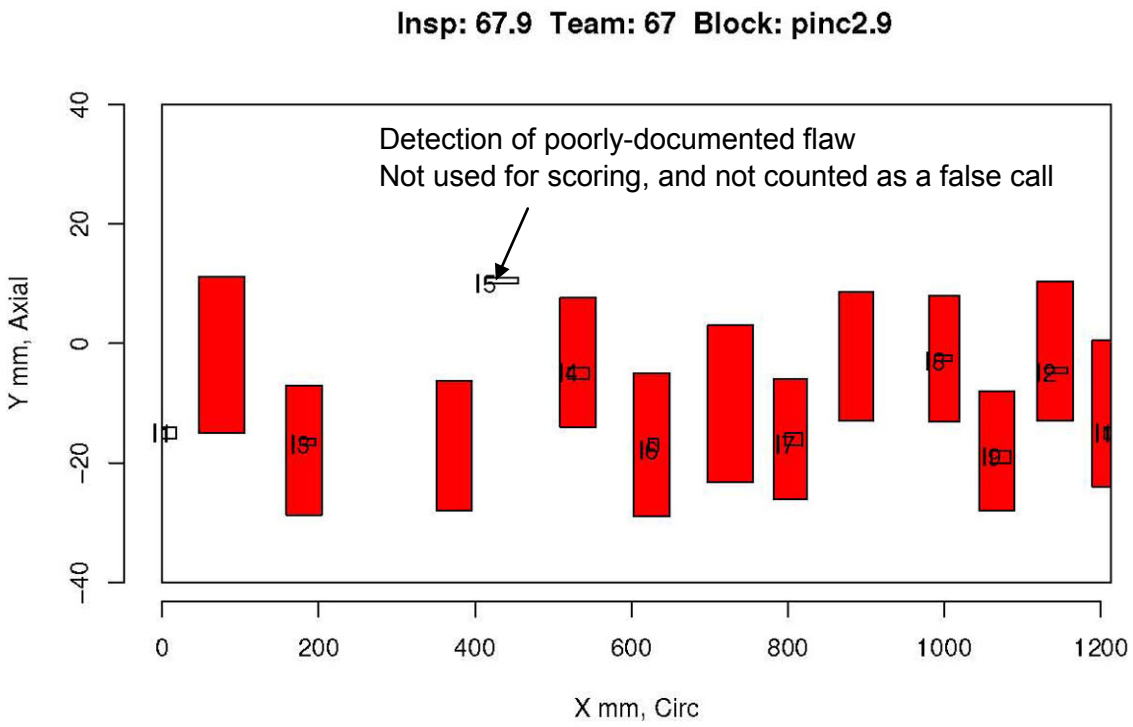
Insp: 67.9 Team: 67 Block: pinc2.9
Detection of poorly-documented flaw
Not used for scoring, and not counted as a false call
Y mm, Axial
40
20
0
-20
-40
0
200
400
600
800
1000
1200
X mm, Circ

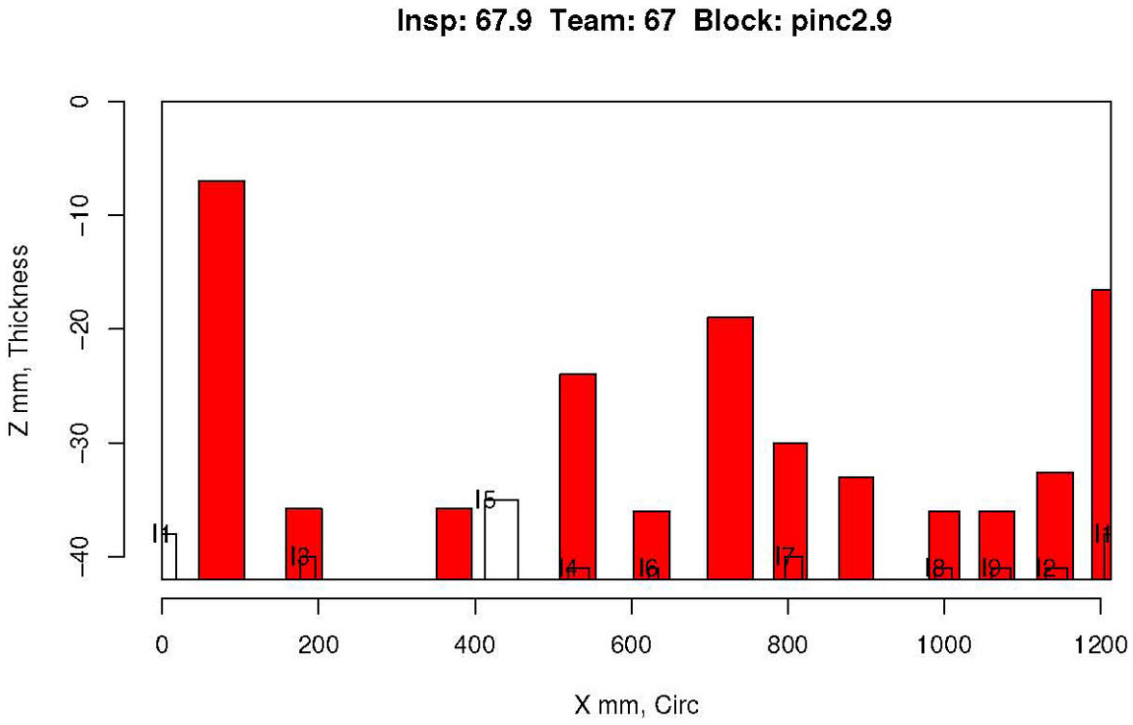
Insp: 67.9 Team: 67 Block: pinc2.9
Z mm, Thickness
0
-10
-20
-30
-40
0
200
400
600
800
1000
1200
X mm, Circ

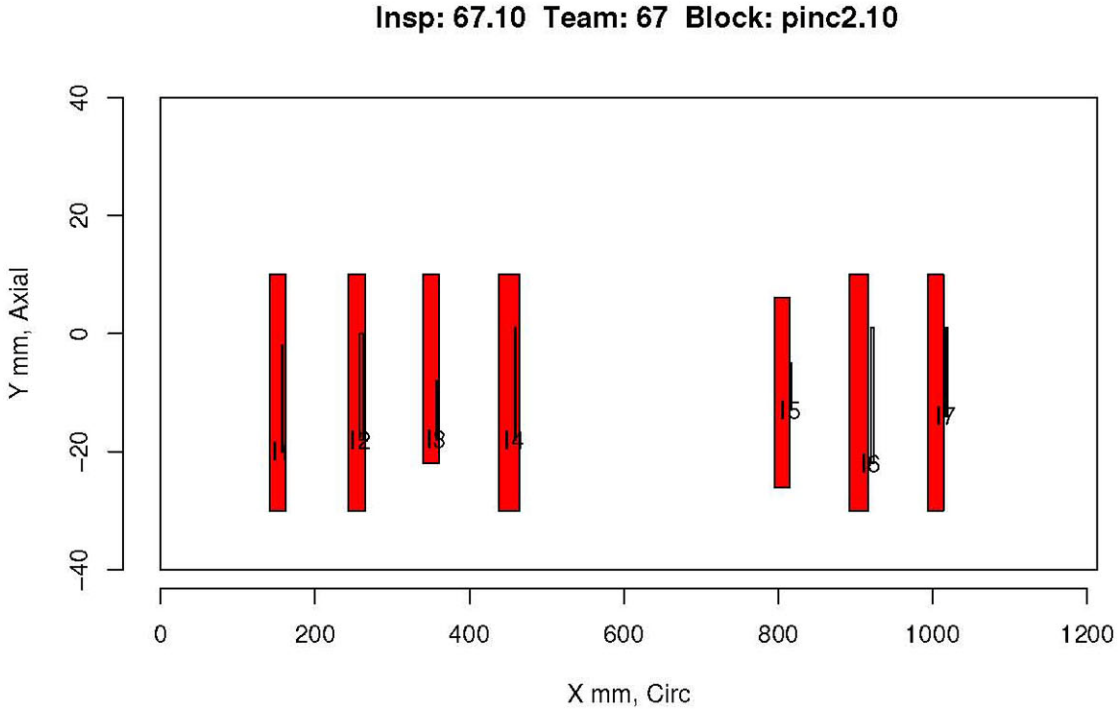
Insp: 67.10 Team: 67 Block: pinc2.10
Y mm, Axial
40
20
0
−20
−40
I1
I2
I3
I4
I5
I6
I7
0
200
400
600
800
1000
1200
X mm, Circ

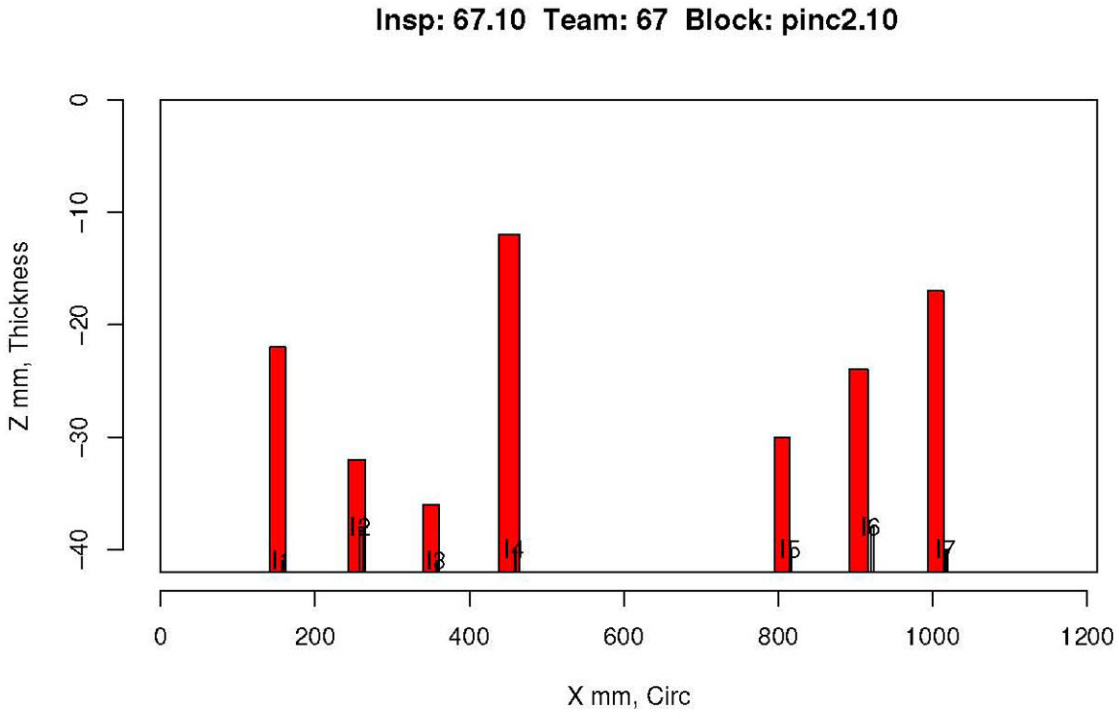
Insp: 67.10 Team: 67 Block: pinc2.10
Z mm, Thickness
0
−10
−20
−30
−40
I1
I2
I3
I4
I5
I6
I7
0
200
400
600
800
1000
1200
X mm, Circ

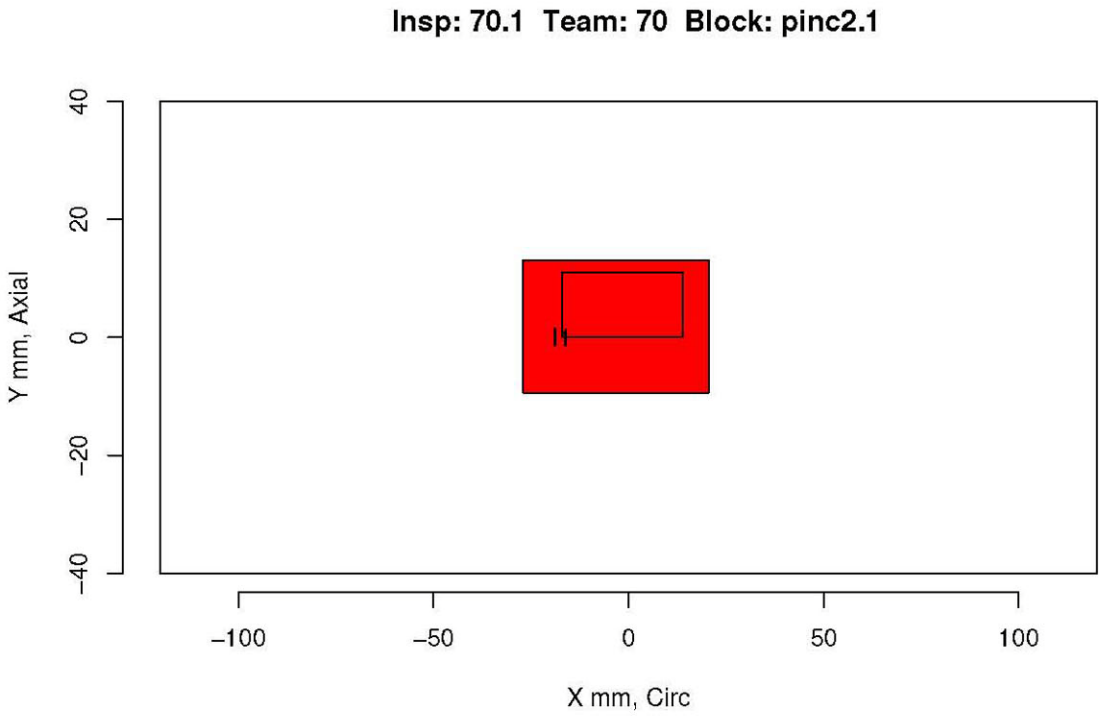
Insp: 70.1 Team: 70 Block: pinc2.1
Y mm, Axial
40
20
0
−20
−40
−100
−50
0
50
100
X mm, Circ

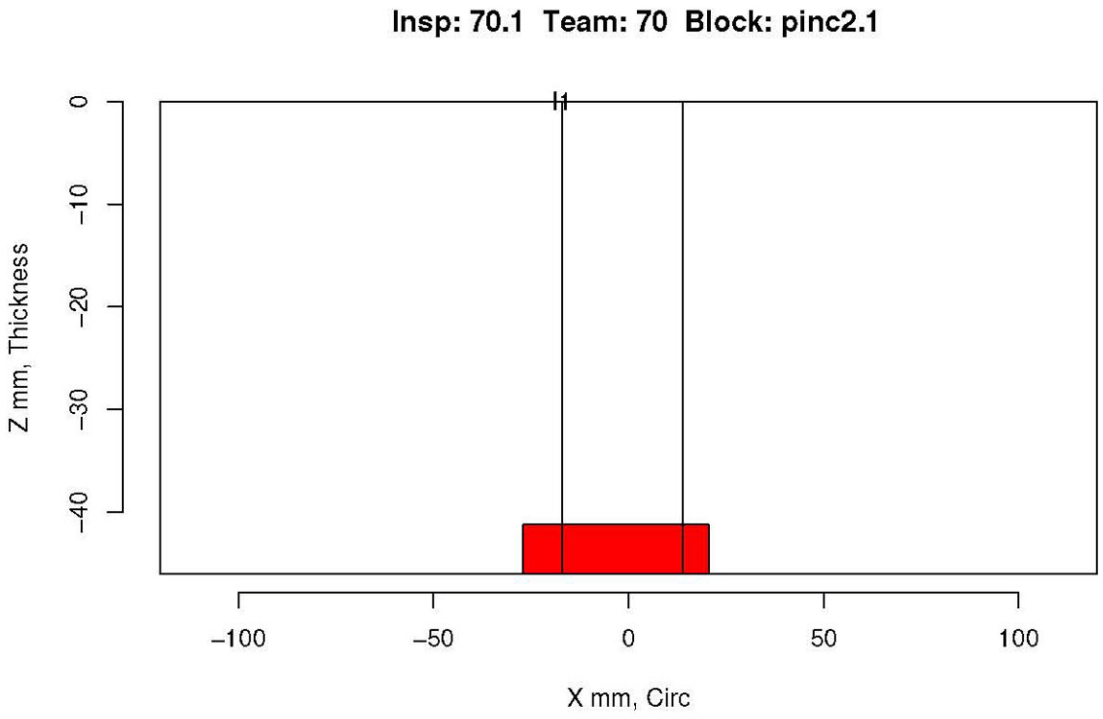
Insp: 70.1 Team: 70 Block: pinc2.1
Z mm, Thickness
0
−10
−20
−30
−40
−100
−50
0
50
100
X mm, Circ

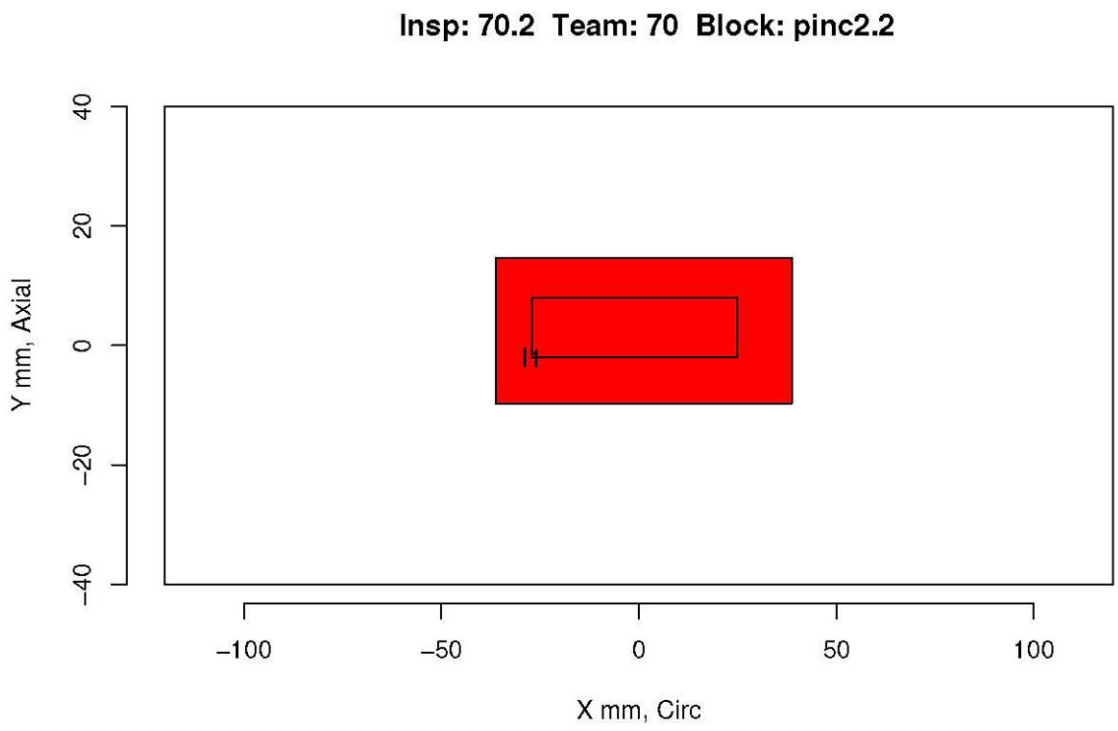
Insp: 70.2 Team: 70 Block: pinc2.2
Y mm, Axial
40
20
0
−20
−40
−100
−50
0
50
100
X mm, Circ

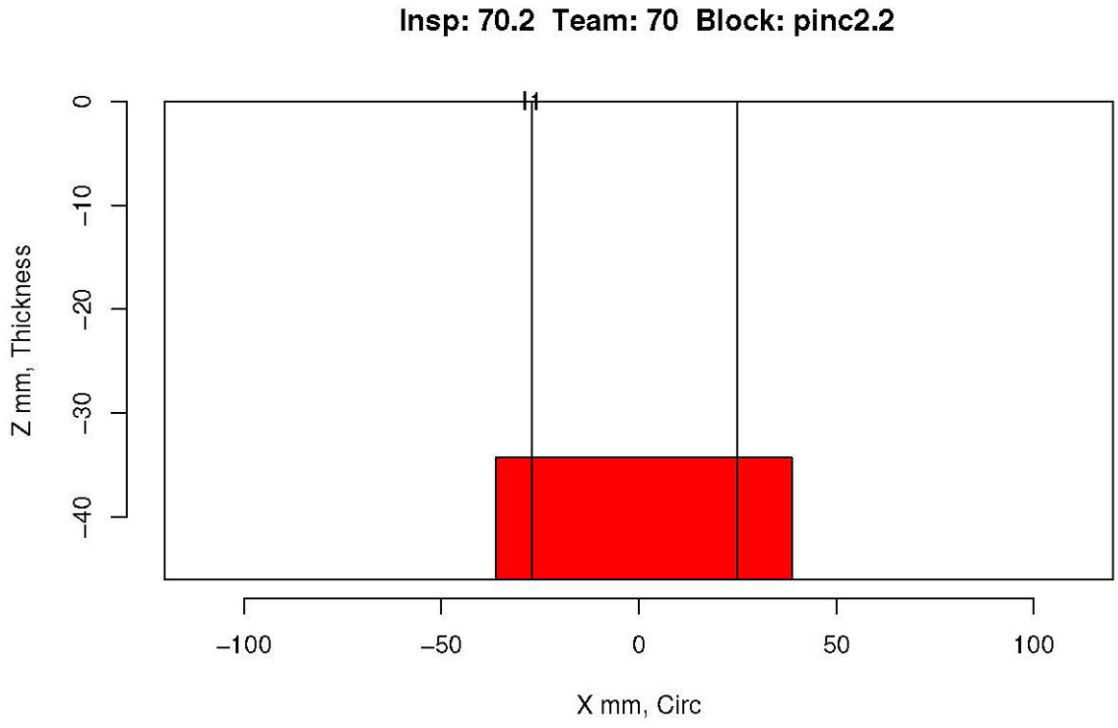
Insp: 70.2 Team: 70 Block: pinc2.2
Z mm, Thickness
0
−10
−20
−30
−40
−100
−50
0
50
100
X mm, Circ

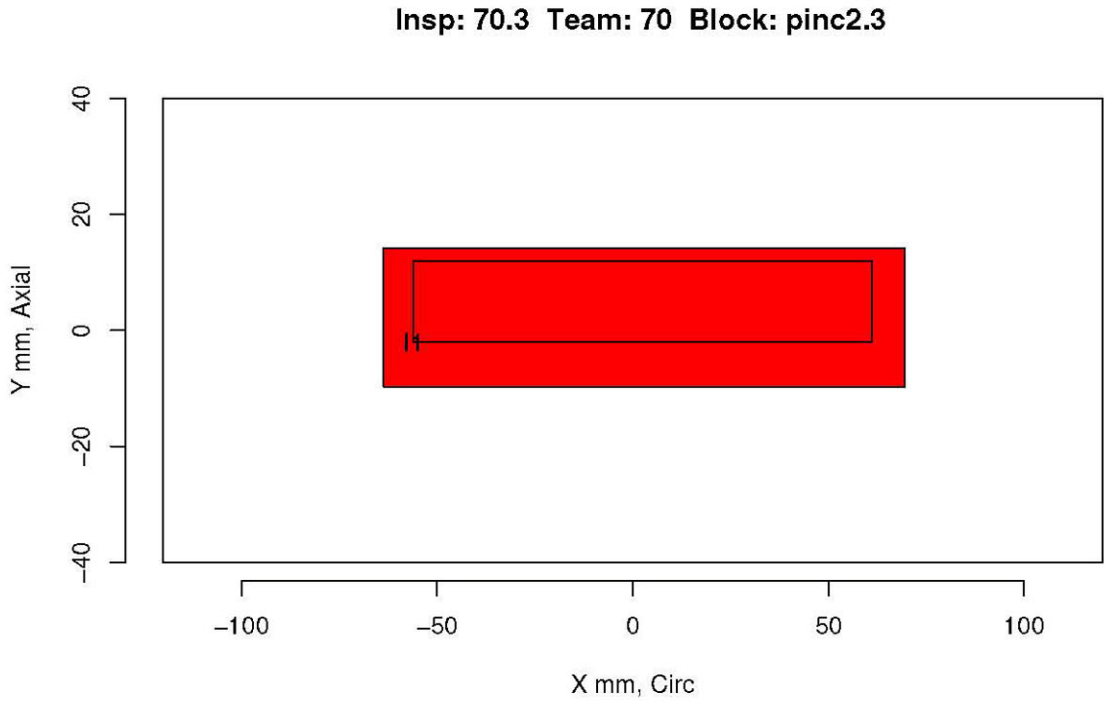
Insp: 70.3 Team: 70 Block: pinc2.3
Y mm, Axial
40
20
0
−20
−40
I1
−100
−50
0
50
100
X mm, Circ

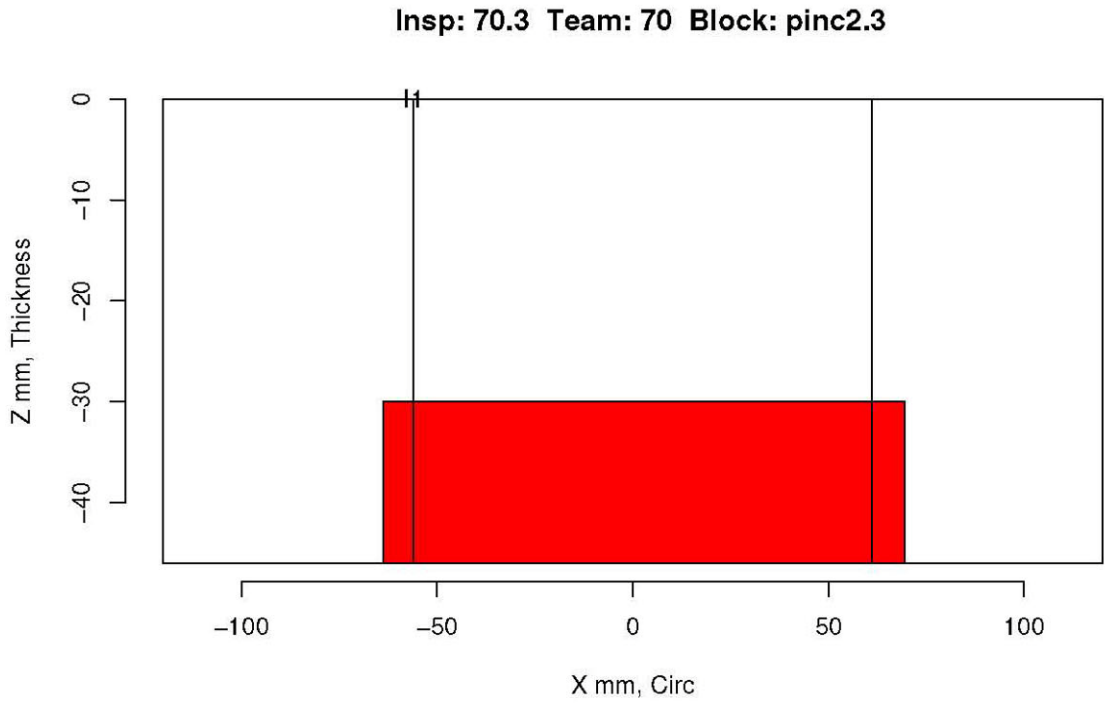
Insp: 70.3 Team: 70 Block: pinc2.3
Z mm, Thickness
0
−10
−20
−30
−40
I1
−100
−50
0
50
100
X mm, Circ

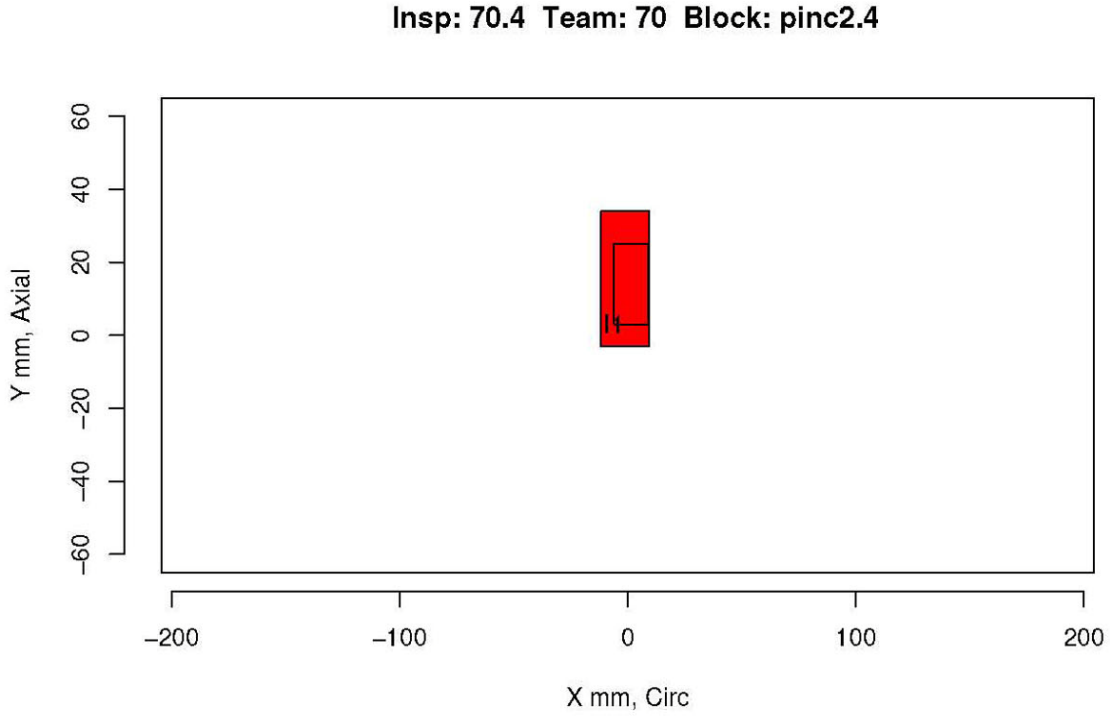
Insp: 70.4 Team: 70 Block: pinc2.4
Y mm, Axial
60
40
20
0
−20
−40
−60
−200
−100
0
100
200
X mm, Circ

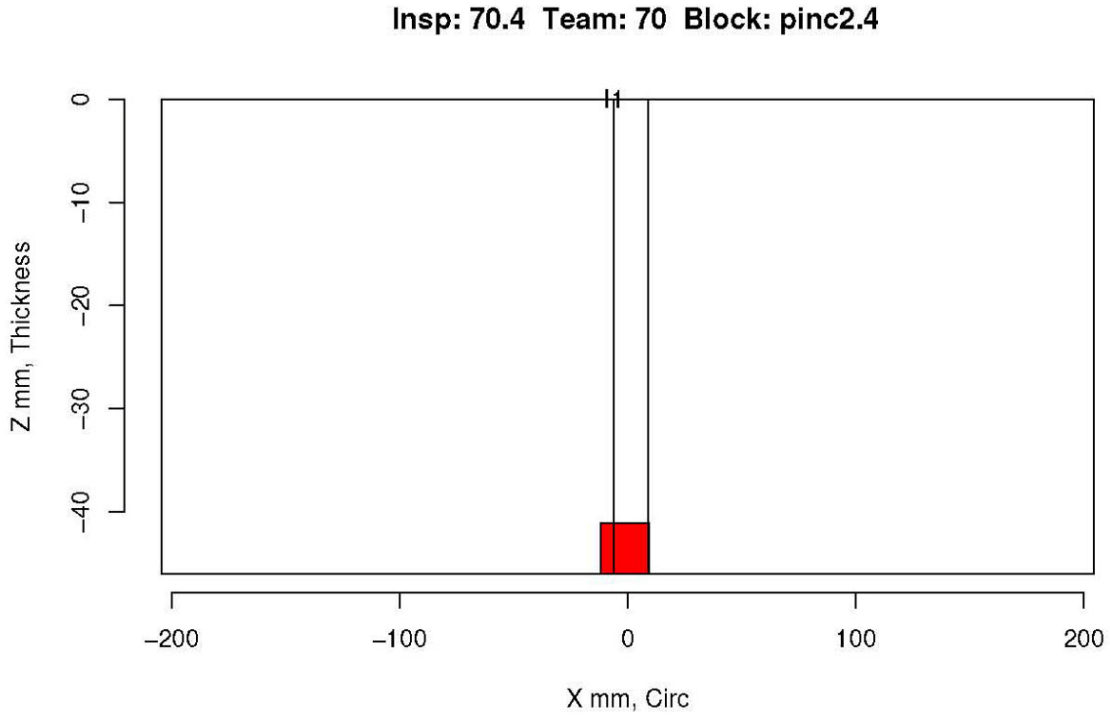
Insp: 70.4 Team: 70 Block: pinc2.4
Z mm, Thickness
0
−10
−20
−30
−40
−200
−100
0
100
200
X mm, Circ

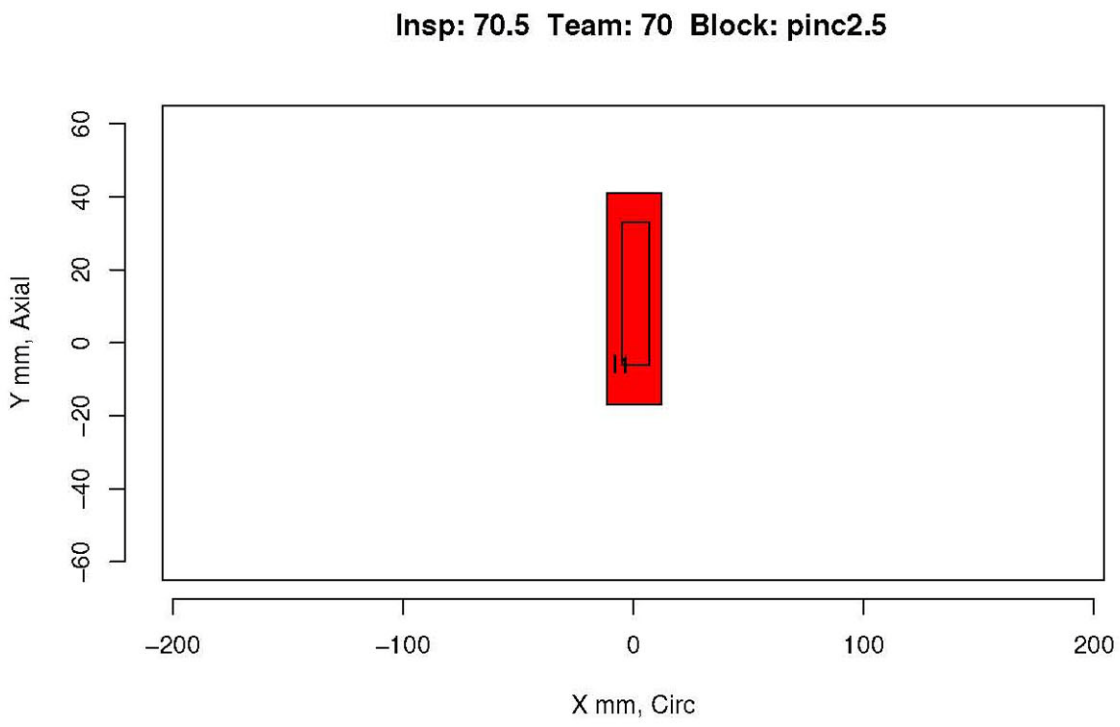
Insp: 70.5 Team: 70 Block: pinc2.5
Y mm, Axial
60
40
20
0
−20
−40
−60
−200
−100
0
100
200
X mm, Circ

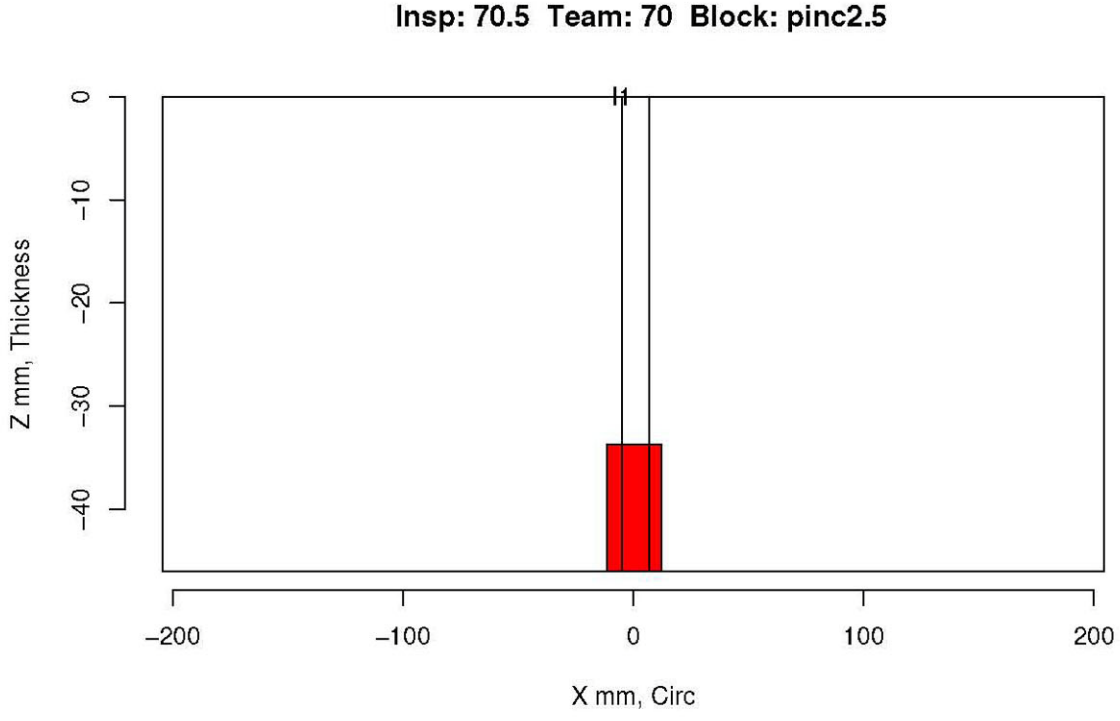
Insp: 70.5 Team: 70 Block: pinc2.5
Z mm, Thickness
0
−10
−20
−30
−40
−200
−100
0
100
200
X mm, Circ

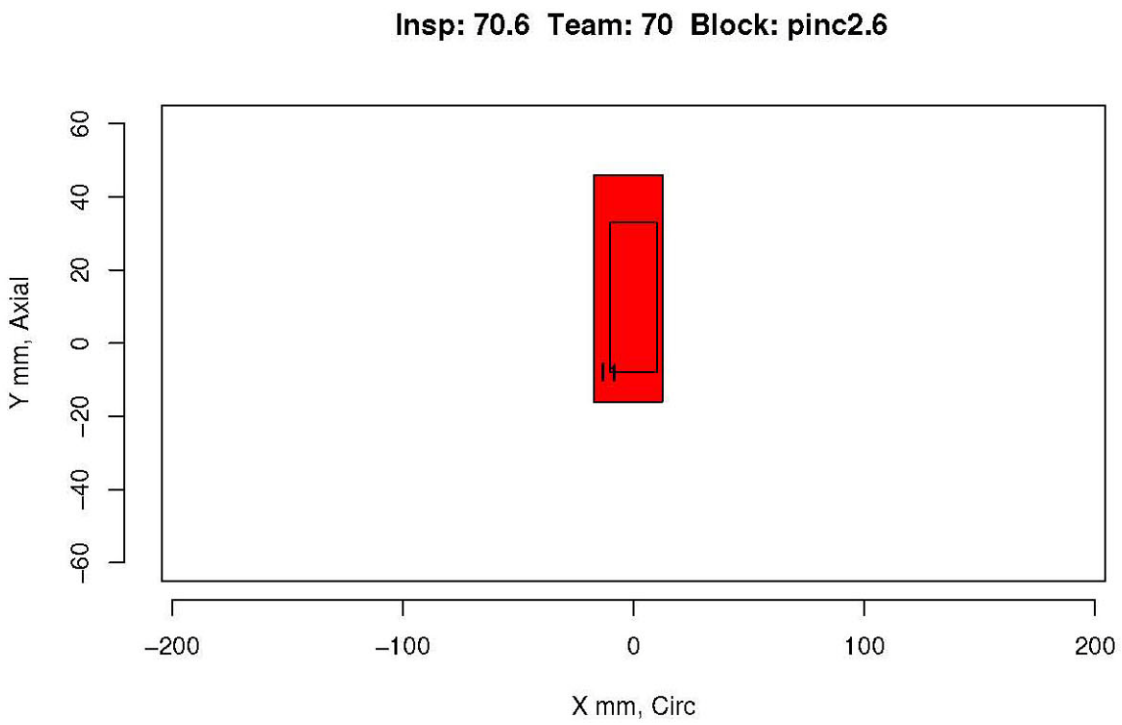
Insp: 70.6 Team: 70 Block: pinc2.6
Y mm, Axial
60
40
20
0
−20
−40
−60
−200
−100
0
100
200
X mm, Circ

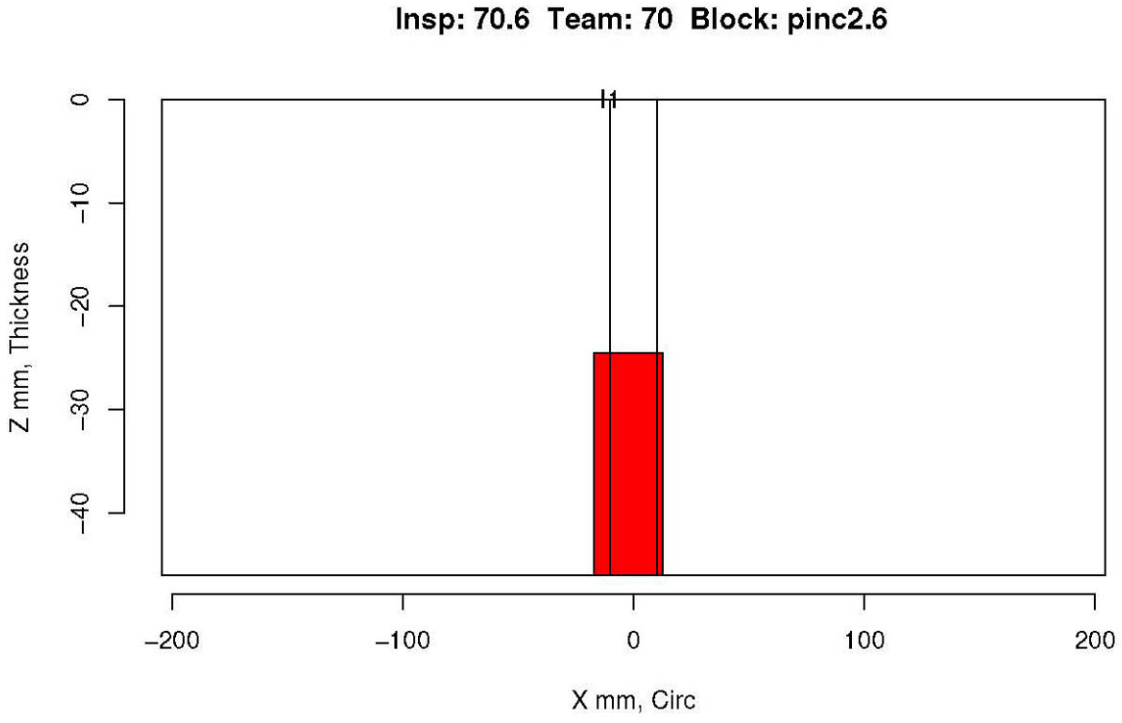
Insp: 70.6 Team: 70 Block: pinc2.6
Z mm, Thickness
0
−10
−20
−30
−40
−200
−100
0
100
200
X mm, Circ

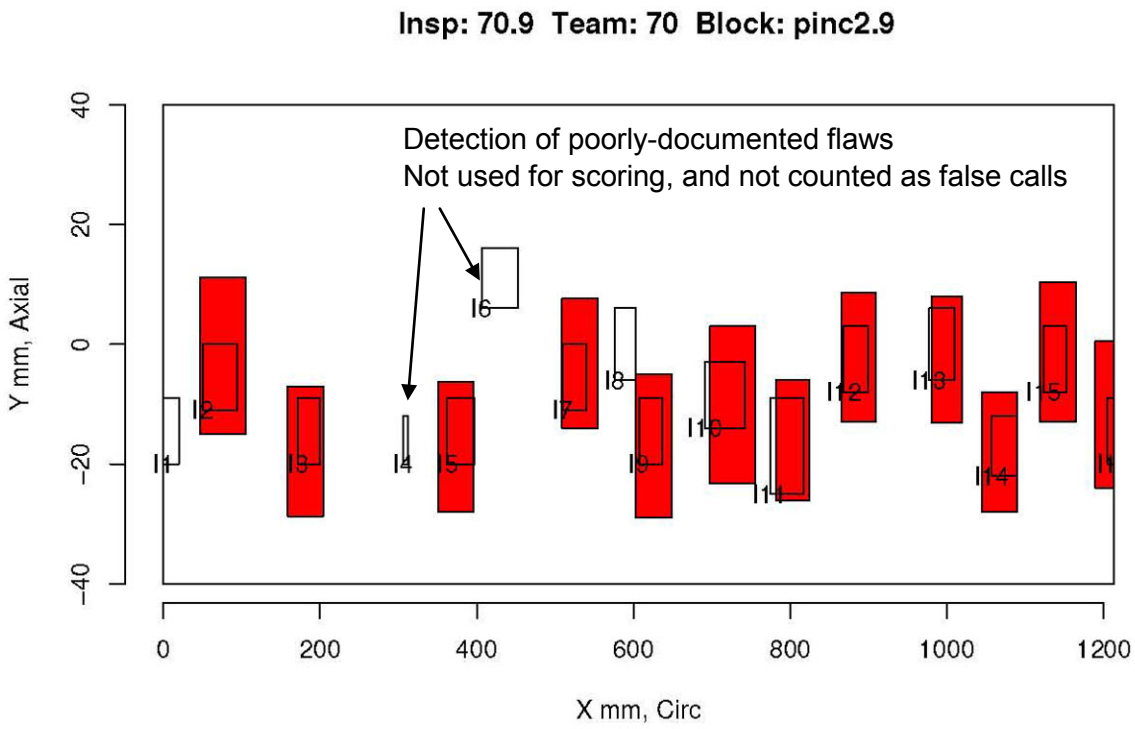
Insp: 70.9 Team: 70 Block: pinc2.9
Detection of poorly-documented flaws
Not used for scoring, and not counted as false calls
Y mm, Axial
X mm, Circ
40
20
0
-20
-40
0
200
400
600
800
1000
1200

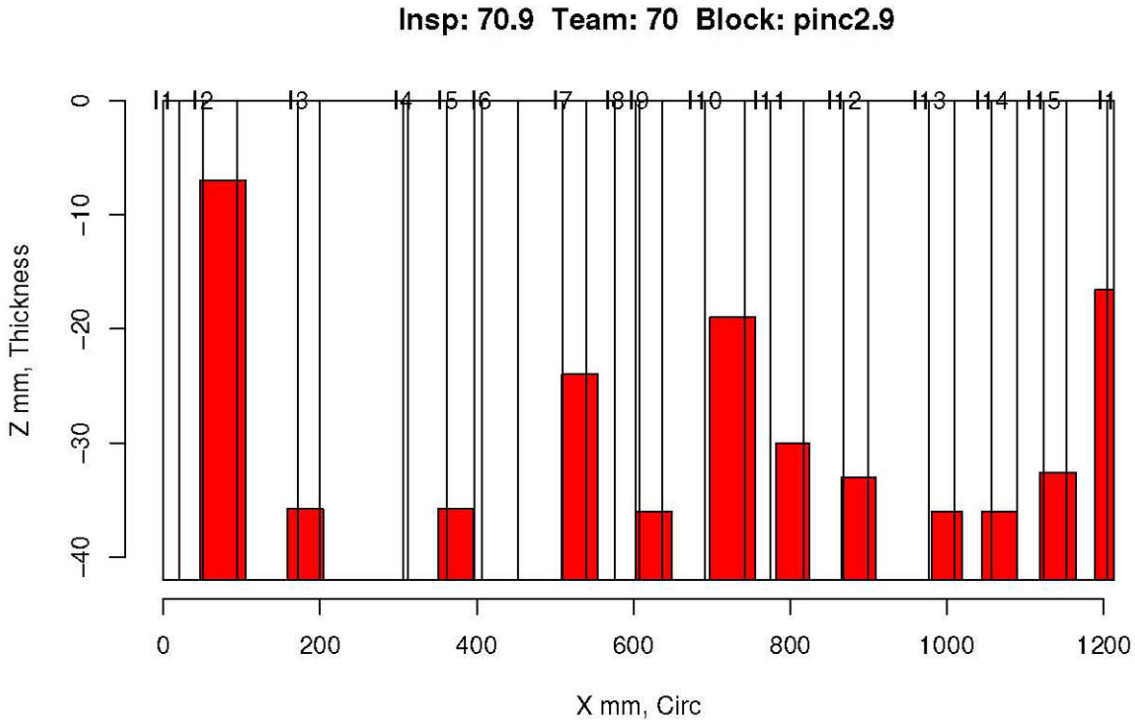
Insp: 70.9 Team: 70 Block: pinc2.9
Z mm, Thickness
X mm, Circ
0
-10
-20
-30
-40
0
200
400
600
800
1000
1200

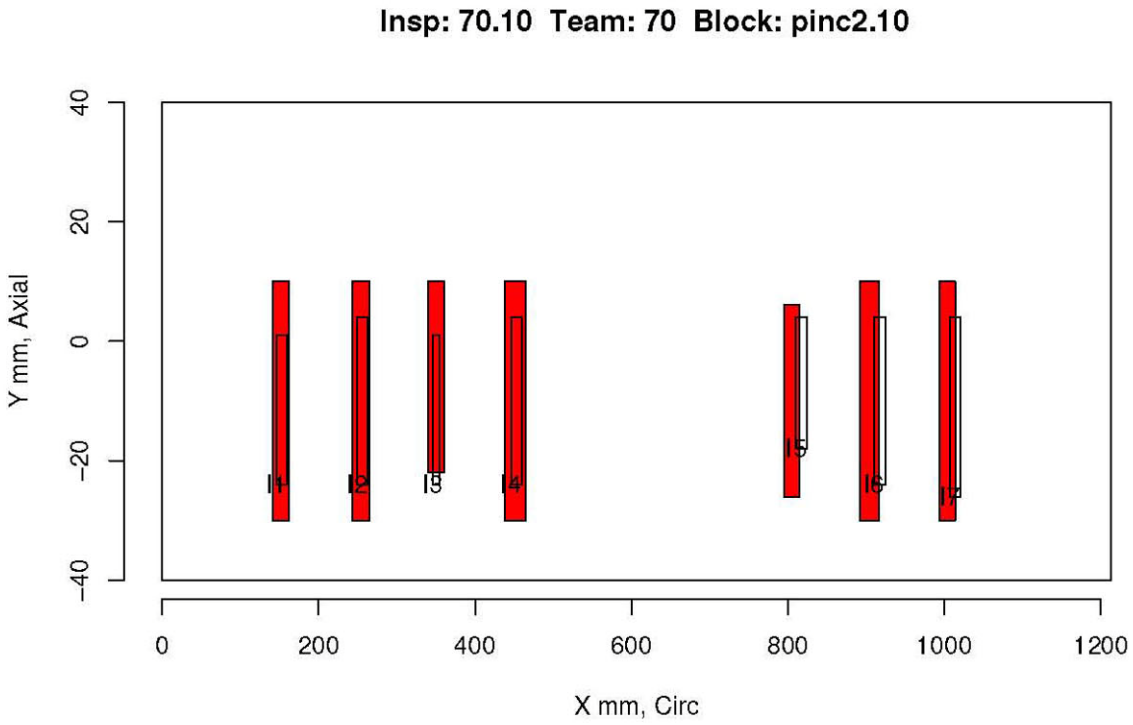
Insp: 70.10 Team: 70 Block: pinc2.10
Y mm, Axial
40
20
0
-20
-40
I1
I2
I3
I4
I5
I6
I7
0
200
400
600
800
1000
1200
X mm, Circ

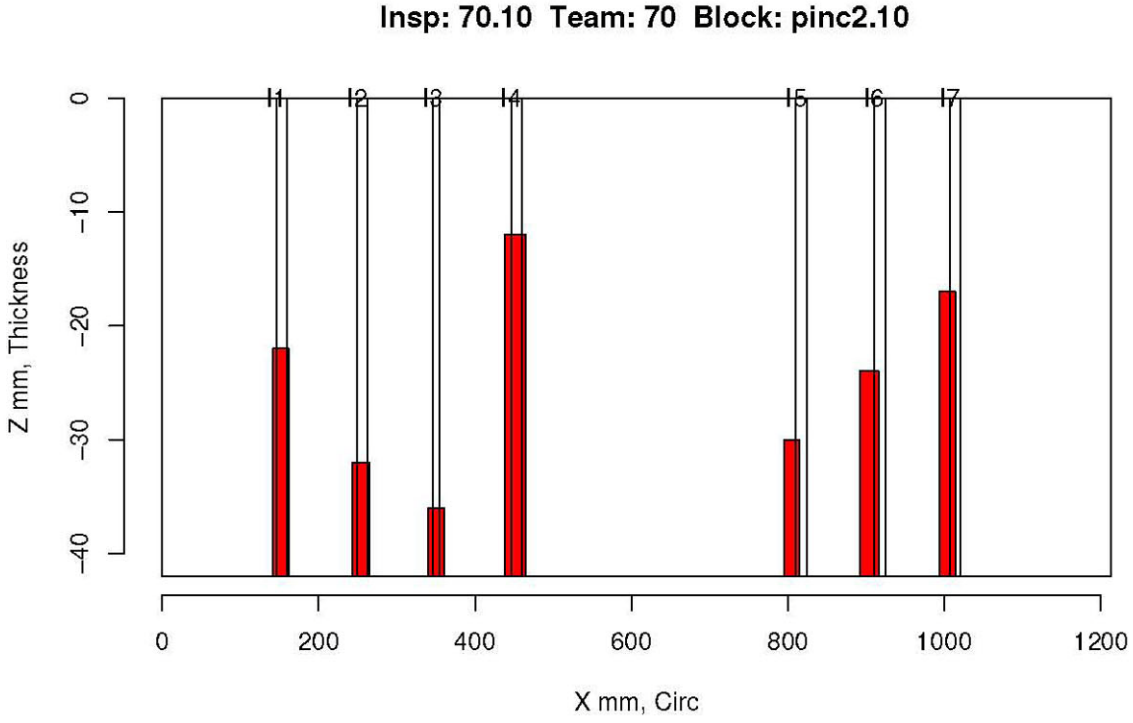
Insp: 70.10 Team: 70 Block: pinc2.10
Z mm, Thickness
0
-10
-20
-30
-40
I1
I2
I3
I4
I5
I6
I7
0
200
400
600
800
1000
1200
X mm, Circ

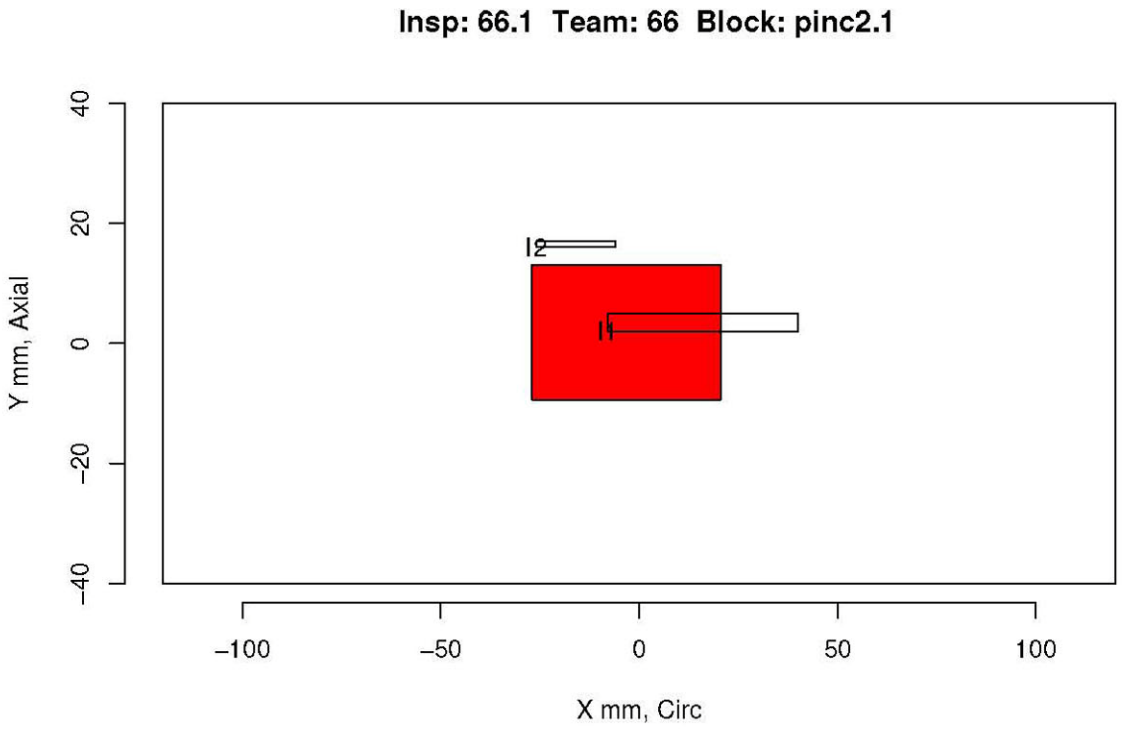
Insp: 66.1 Team: 66 Block: pinc2.1
Y mm, Axial
40
20
0
-20
-40
-100
-50
0
50
100
X mm, Circ

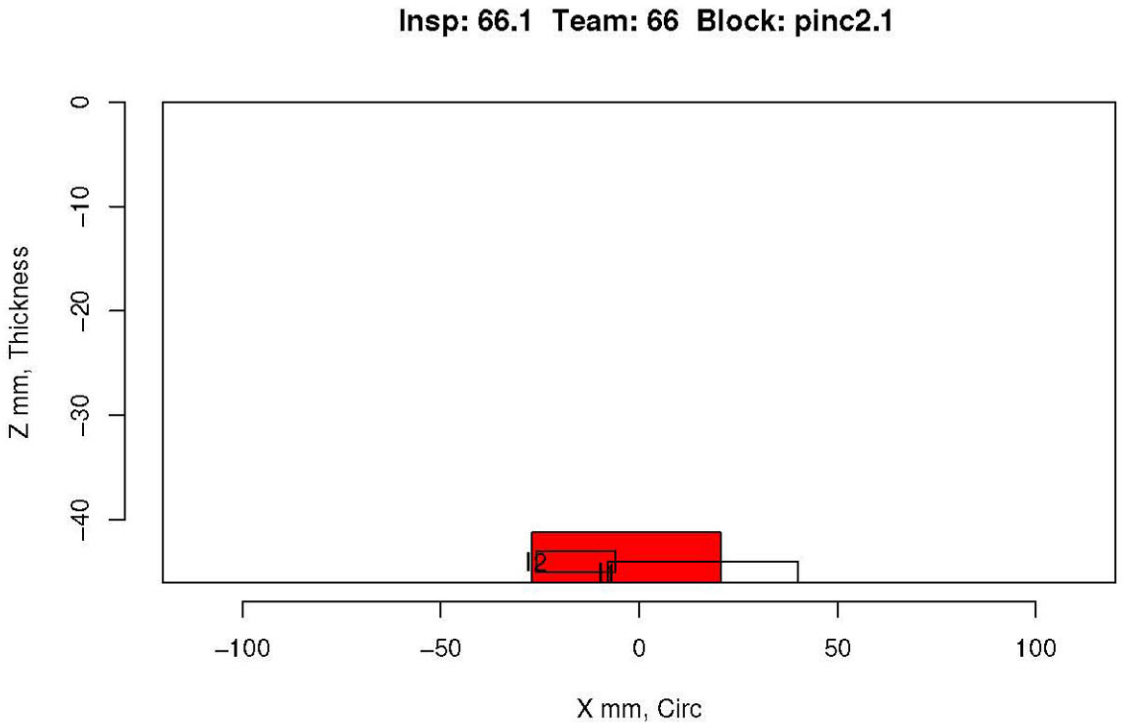
Insp: 66.1 Team: 66 Block: pinc2.1
Z mm, Thickness
0
-10
-20
-30
-40
-100
-50
0
50
100
X mm, Circ

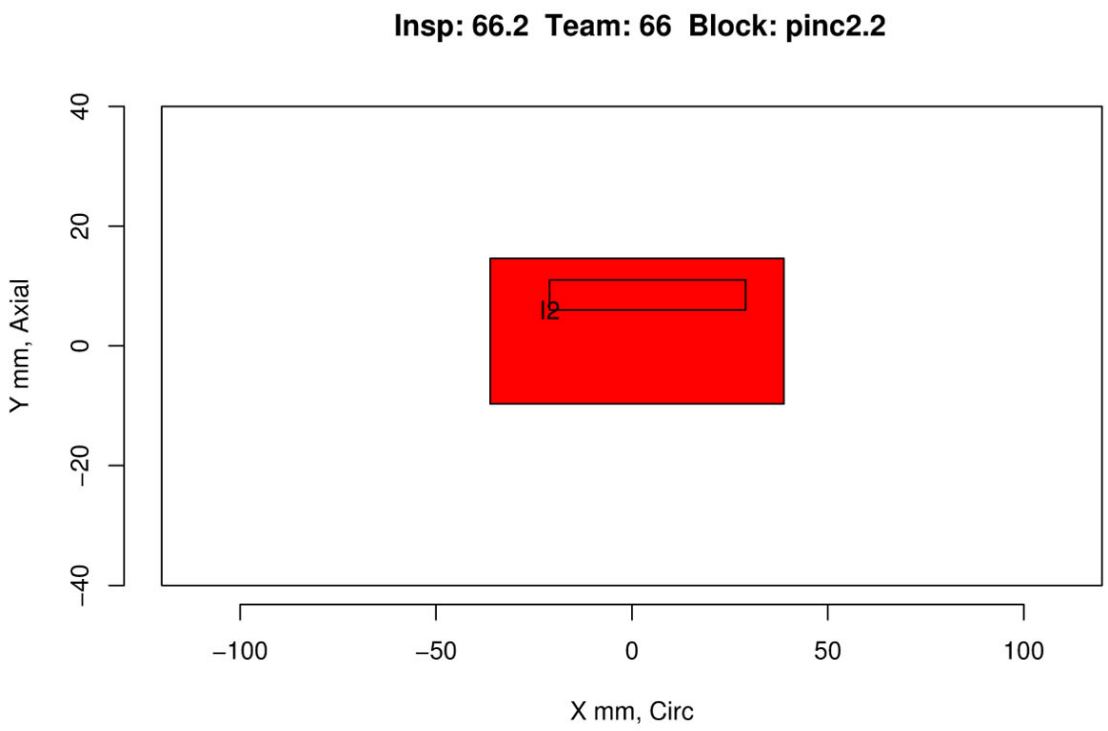
Insp: 66.2 Team: 66 Block: pinc2.2
Y mm, Axial
40
20
0
−20
−40
I2
−100
−50
0
50
100
X mm, Circ

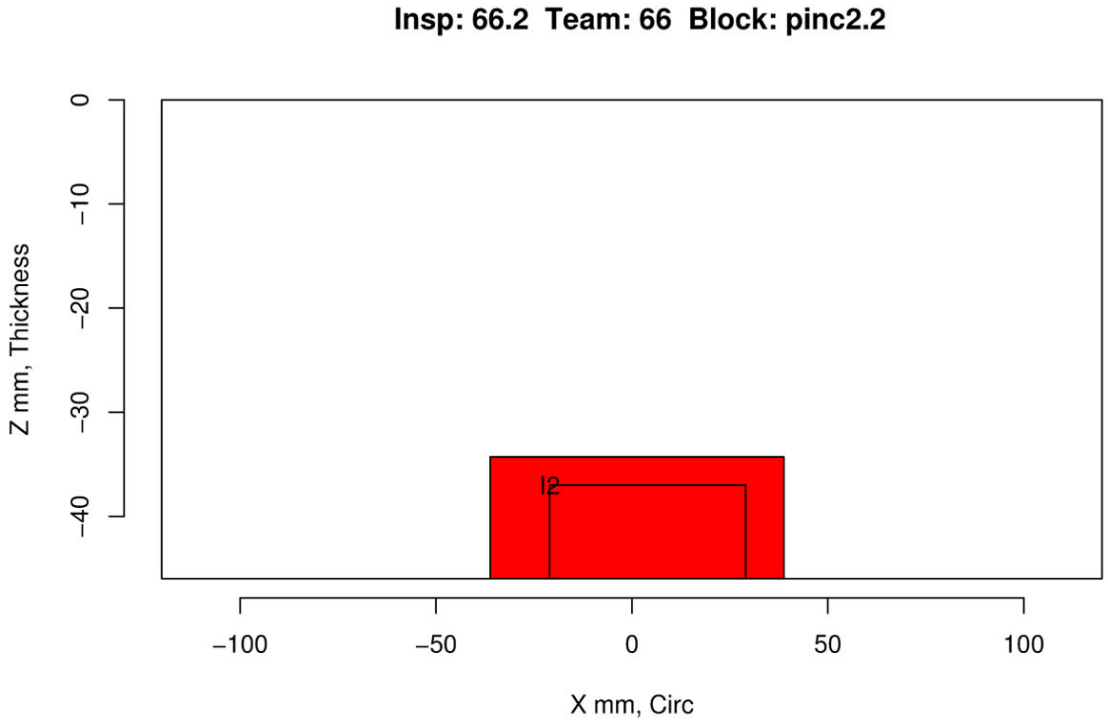
Insp: 66.2 Team: 66 Block: pinc2.2
Z mm, Thickness
0
−10
−20
−30
−40
I2
−100
−50
0
50
100
X mm, Circ

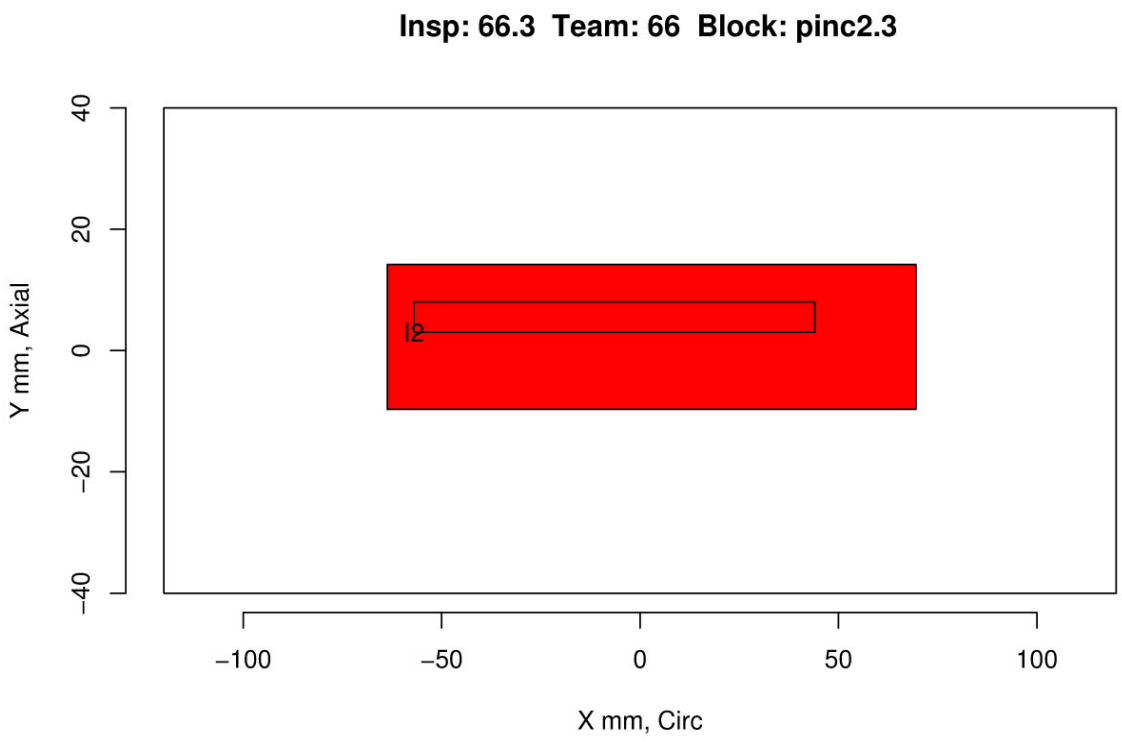
Insp: 66.3 Team: 66 Block: pinc2.3
Y mm, Axial
40
20
0
−20
−40
I2
−100
−50
0
50
100
X mm, Circ

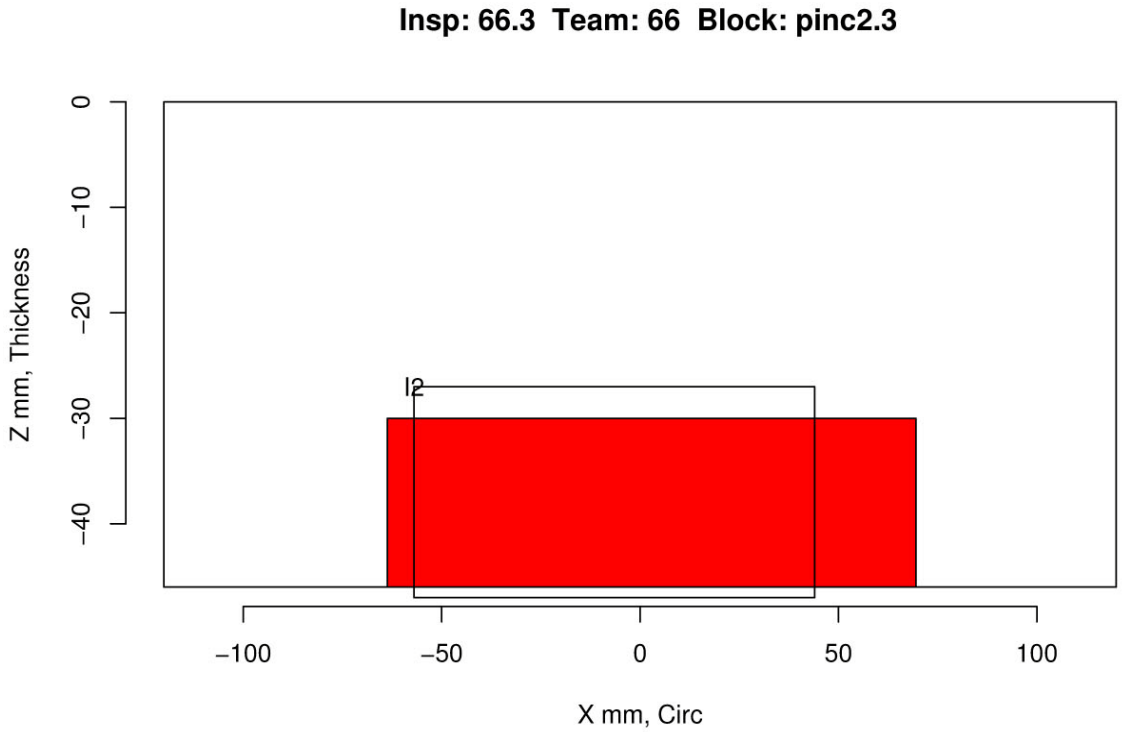
Insp: 66.3 Team: 66 Block: pinc2.3
Z mm, Thickness
0
−10
−20
−30
−40
I2
−100
−50
0
50
100
X mm, Circ

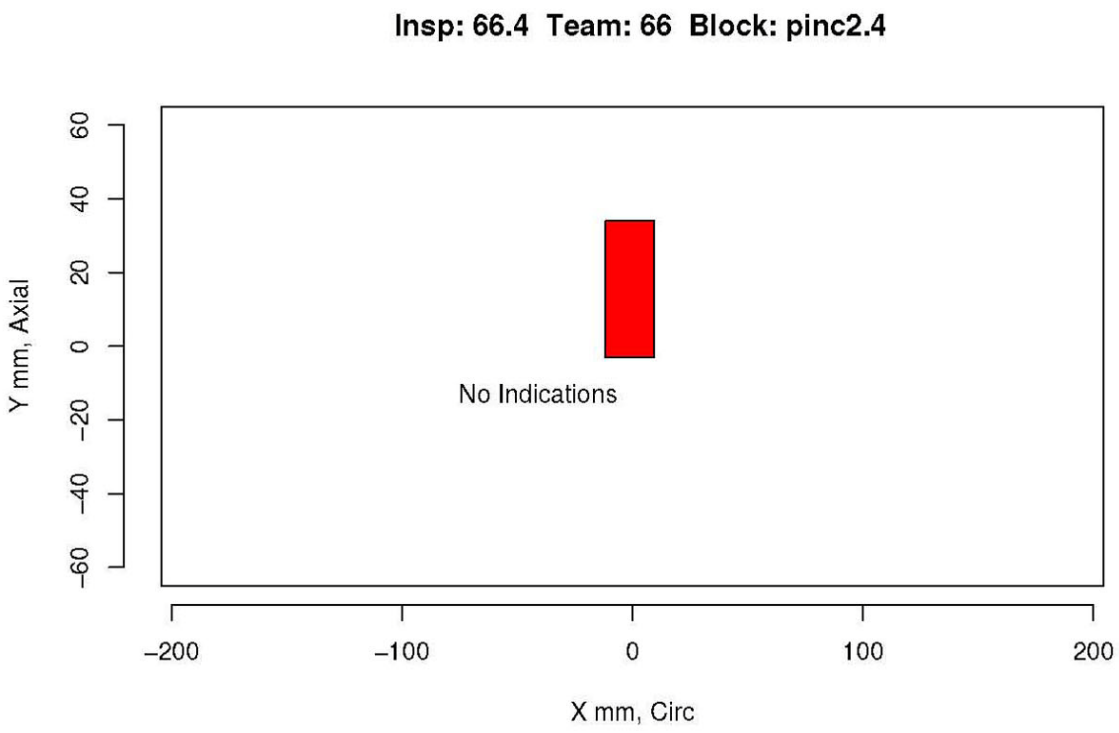
Insp: 66.4 Team: 66 Block: pinc2.4
Y mm, Axial
60
40
20
0
−20
−40
−60
No Indications
−200
−100
0
100
200
X mm, Circ

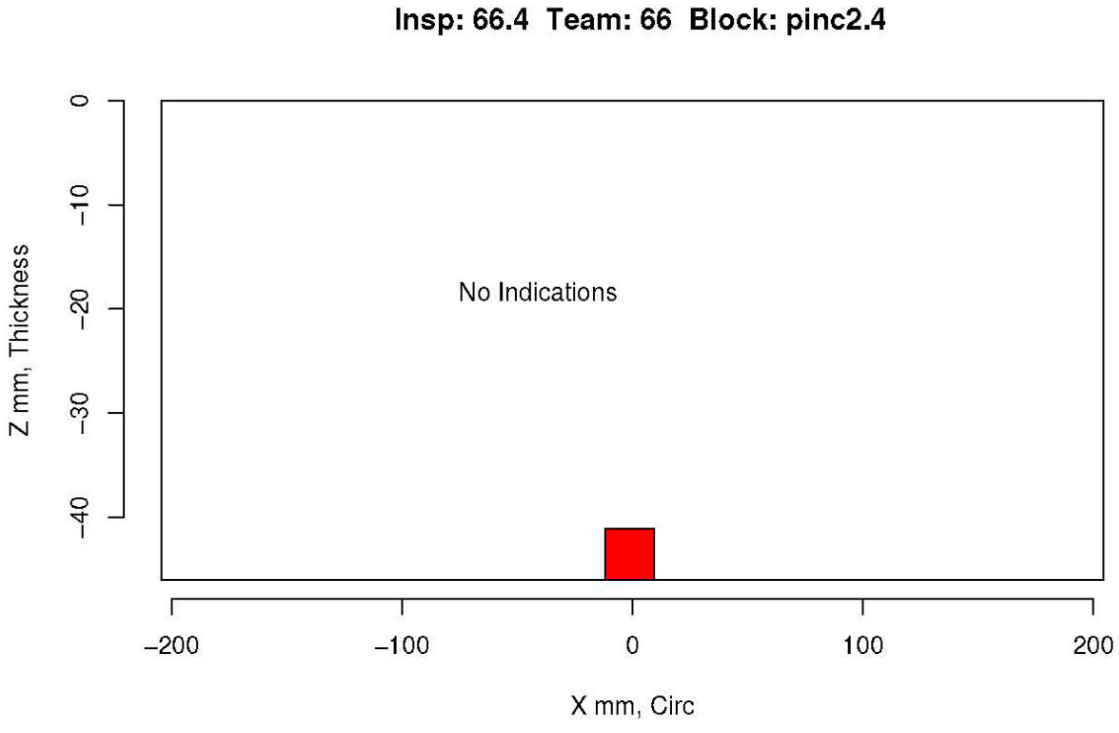
Insp: 66.4 Team: 66 Block: pinc2.4
Z mm, Thickness
0
−10
−20
−30
−40
No Indications
−200
−100
0
100
200
X mm, Circ

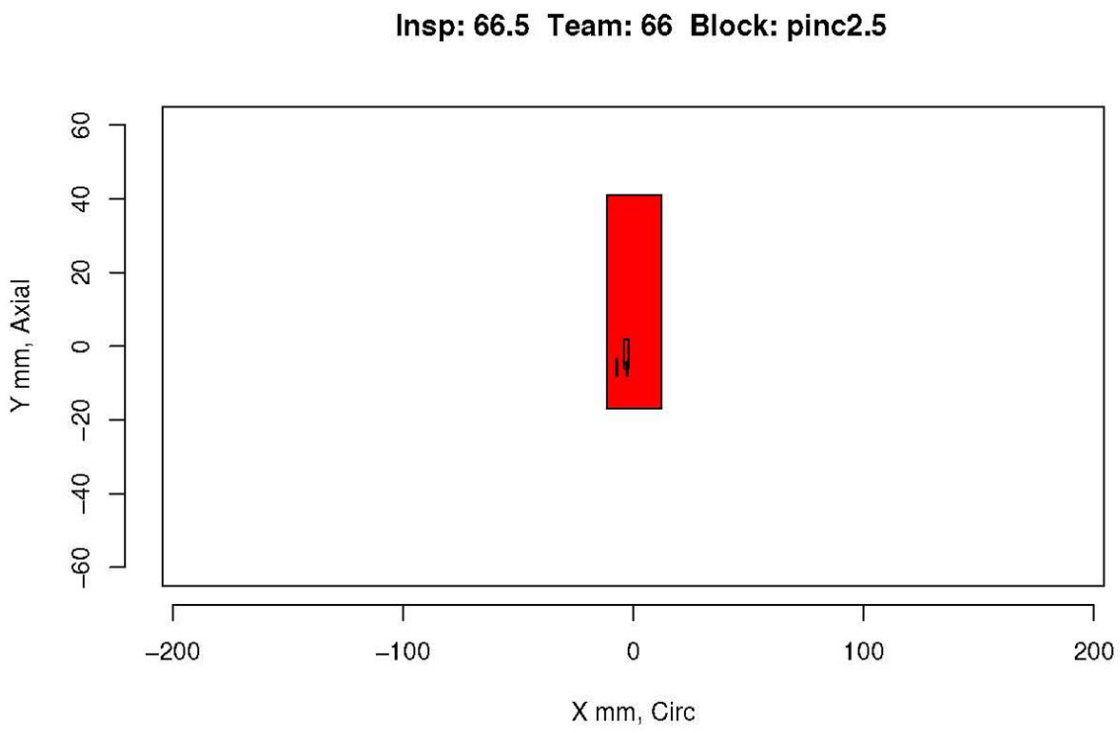
Insp: 66.5 Team: 66 Block: pinc2.5
Y mm, Axial
60
40
20
0
−20
−40
−60
−200
−100
0
100
200
X mm, Circ

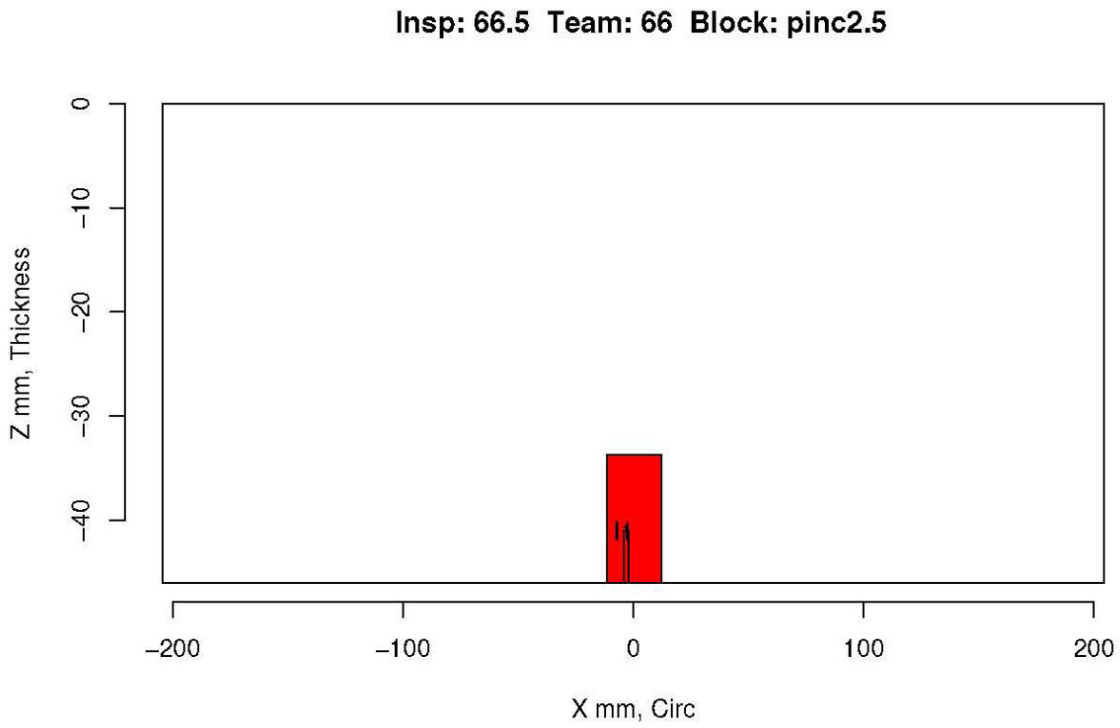
Insp: 66.5 Team: 66 Block: pinc2.5
Z mm, Thickness
0
−10
−20
−30
−40
−200
−100
0
100
200
X mm, Circ

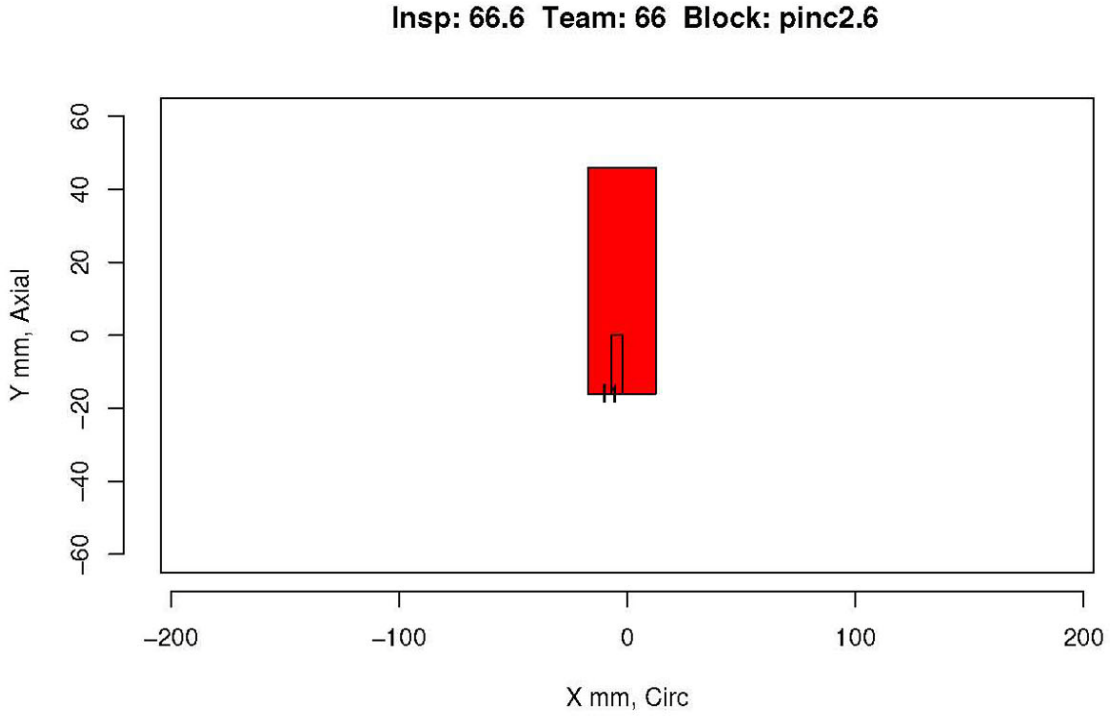
Insp: 66.6 Team: 66 Block: pinc2.6
Y mm, Axial
60
40
20
0
−20
−40
−60
−200
−100
0
100
200
X mm, Circ

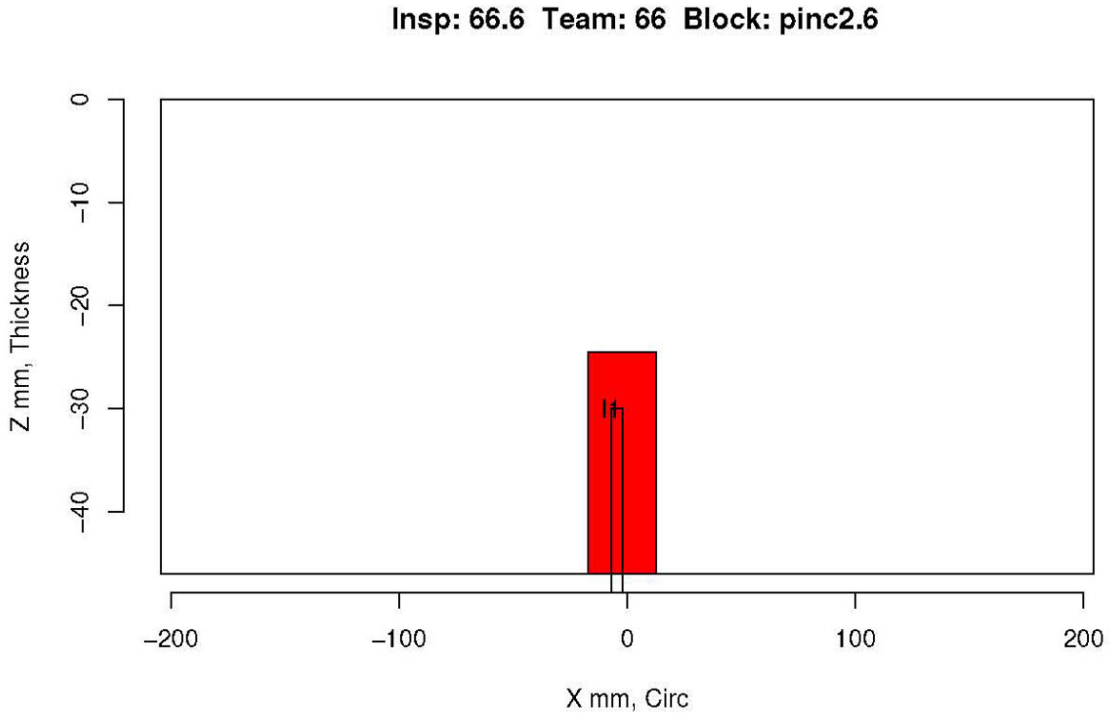
Insp: 66.6 Team: 66 Block: pinc2.6
Z mm, Thickness
0
−10
−20
−30
−40
−200
−100
0
100
200
X mm, Circ

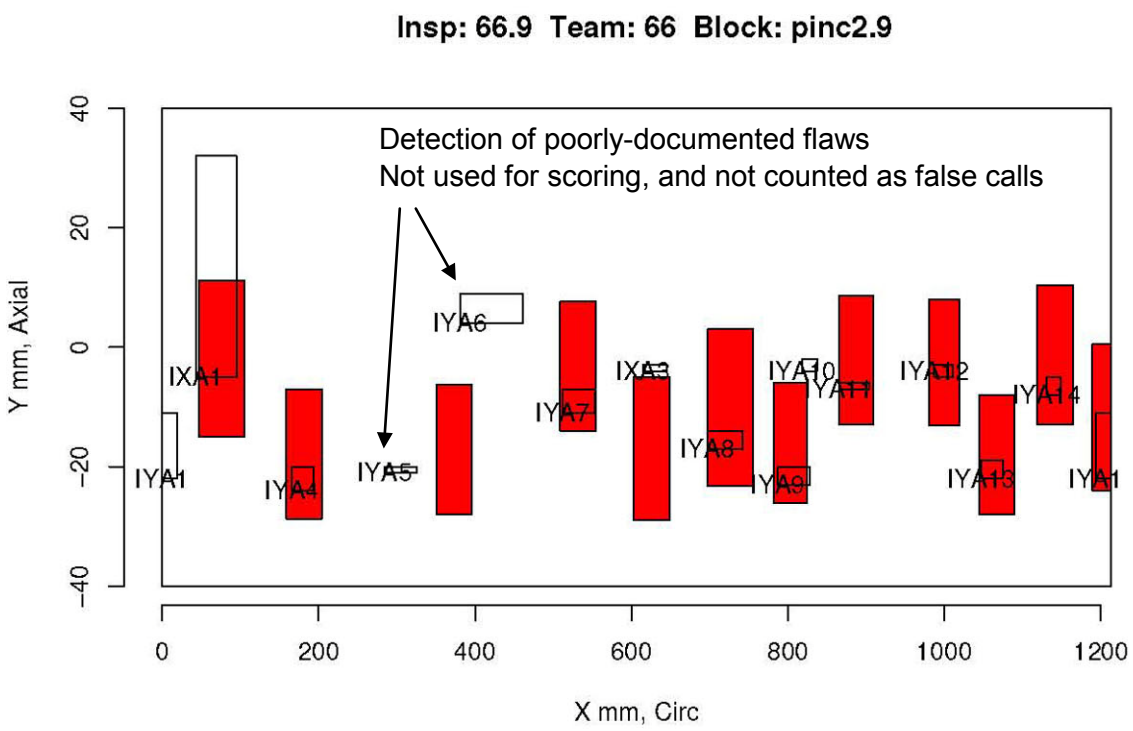
Insp: 66.9 Team: 66 Block: pinc2.9
Detection of poorly-documented flaws
Not used for scoring, and not counted as false calls
Y mm, Axial
X mm, Circ
IXA1
IYA1
IYA4
IYA5
IYA6
IYA7
IXA3
IYA8
IYA9
IYA10
IYA11
IYA12
IYA13
IYA14
IYA1
40
20
0
-20
-40
0
200
400
600
800
1000
1200

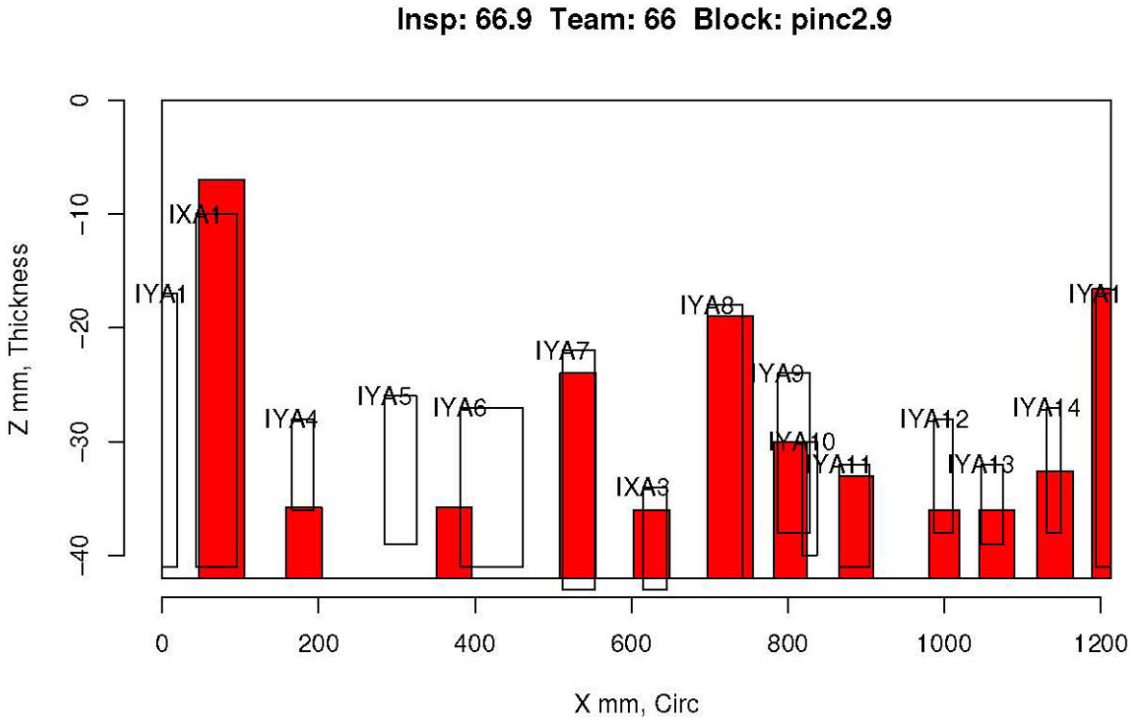
Insp: 66.9 Team: 66 Block: pinc2.9
Z mm, Thickness
X mm, Circ
IXA1
IYA1
IYA4
IYA5
IYA6
IYA7
IXA3
IYA8
IYA9
IYA10
IYA11
IYA12
IYA13
IYA14
IYA1
0
-10
-20
-30
-40
0
200
400
600
800
1000
1200

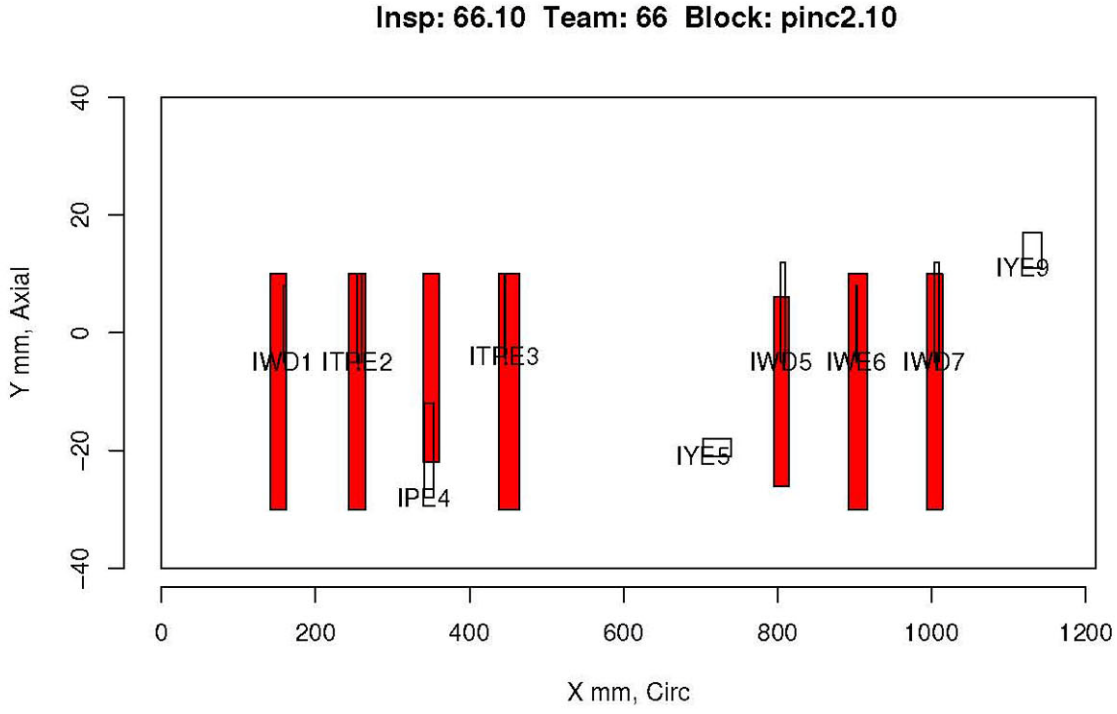
Insp: 66.10 Team: 66 Block: pinc2.10
Y mm, Axial
40
20
0
-20
-40
IWD1
ITRE2
IPE4
ITRE3
IYE5
IWD5
IWE6
IWD7
IYE9
0
200
400
600
800
1000
1200
X mm, Circ

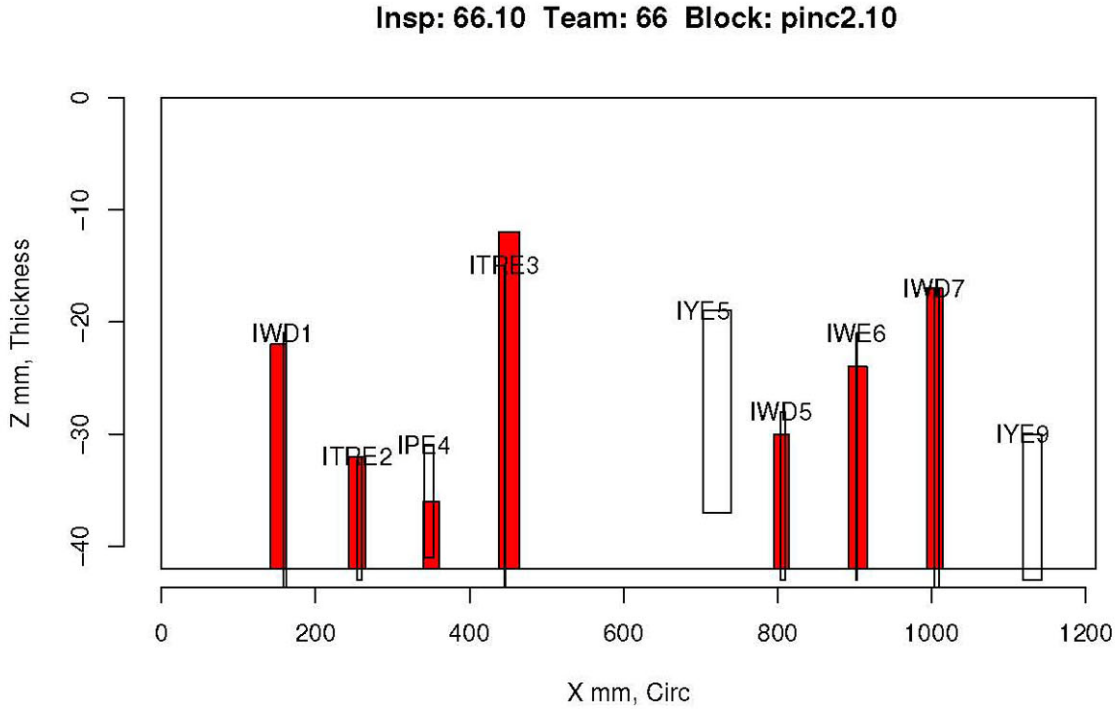
Insp: 66.10 Team: 66 Block: pinc2.10
Z mm, Thickness
0
-10
-20
-30
-40
IWD1
ITRE2
IPE4
ITRE3
IYE5
IWD5
IWE6
IWD7
IYE9
0
200
400
600
800
1000
1200
X mm, Circ

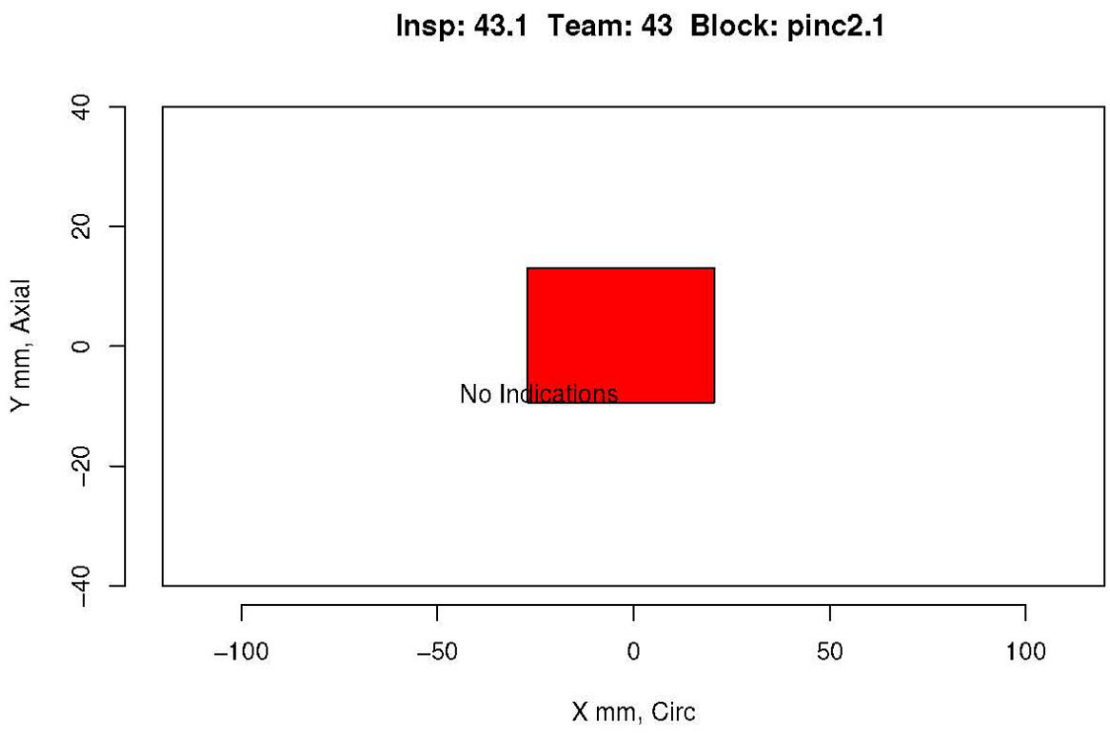
Insp: 43.1 Team: 43 Block: pinc2.1
Y mm, Axial
40
20
0
−20
−40
No Indications
−100
−50
0
50
100
X mm, Circ

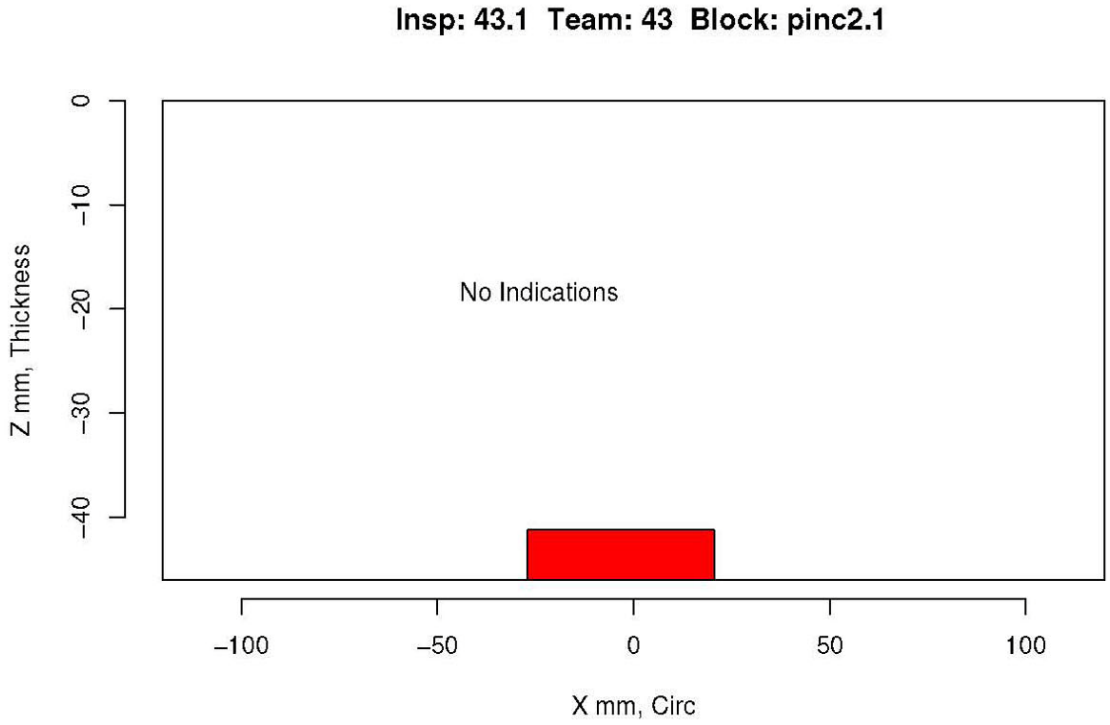
Insp: 43.1 Team: 43 Block: pinc2.1
Z mm, Thickness
0
−10
−20
−30
−40
No Indications
−100
−50
0
50
100
X mm, Circ

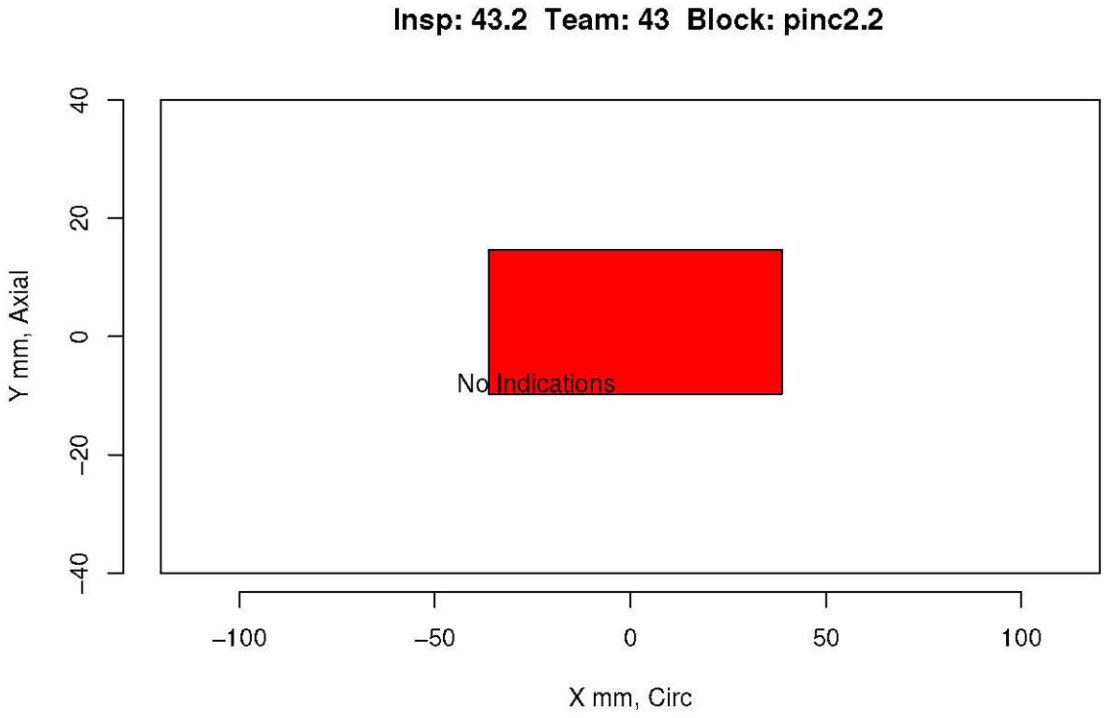
Insp: 43.2 Team: 43 Block: pinc2.2
Y mm, Axial
40
20
0
−20
−40
No Indications
−100
−50
0
50
100
X mm, Circ

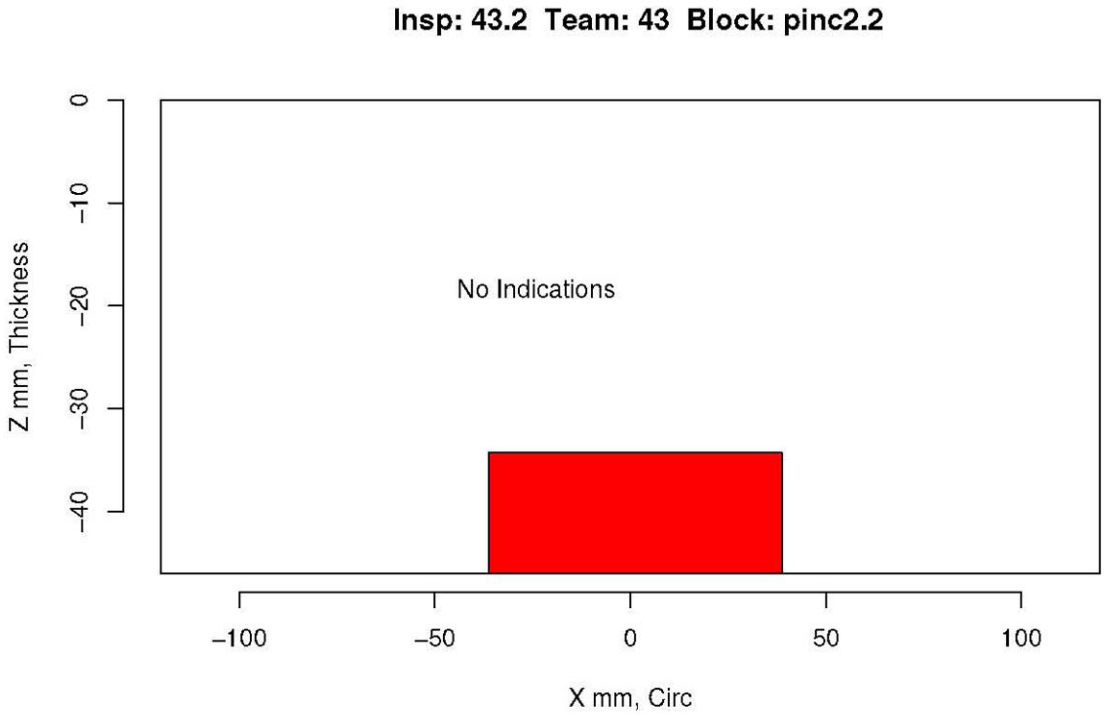
Insp: 43.2 Team: 43 Block: pinc2.2
Z mm, Thickness
0
−10
−20
−30
−40
No Indications
−100
−50
0
50
100
X mm, Circ

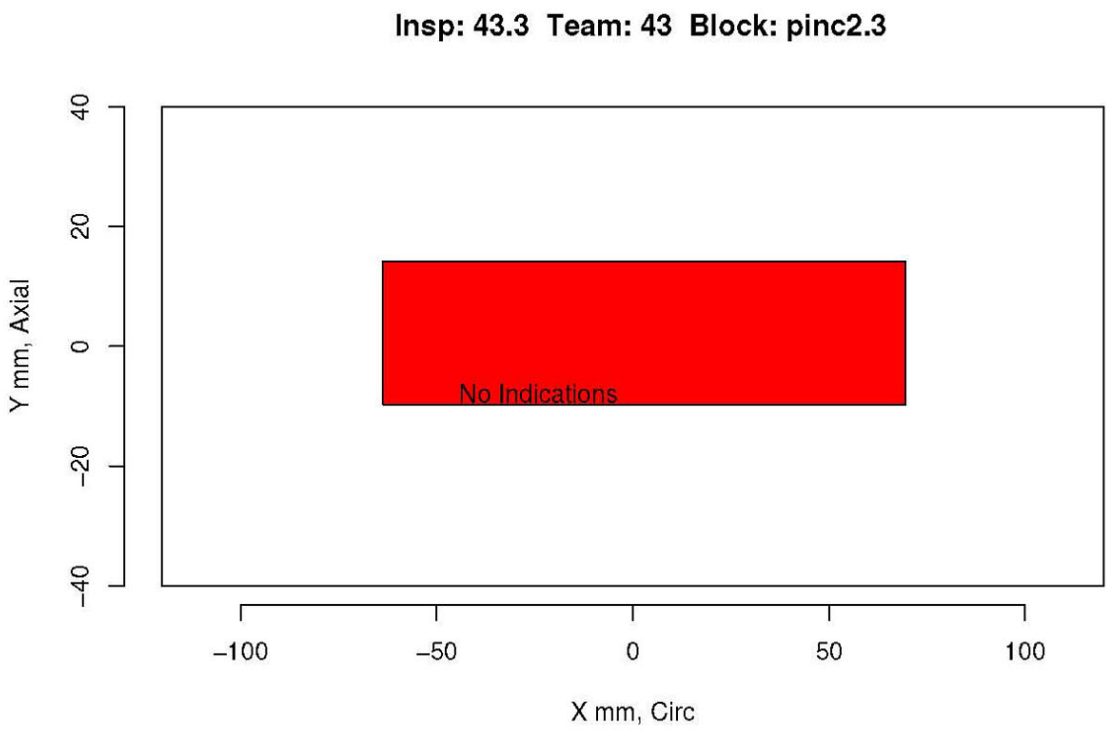
Insp: 43.3 Team: 43 Block: pinc2.3
Y mm, Axial
40
20
0
−20
−40
No Indications
−100
−50
0
50
100
X mm, Circ

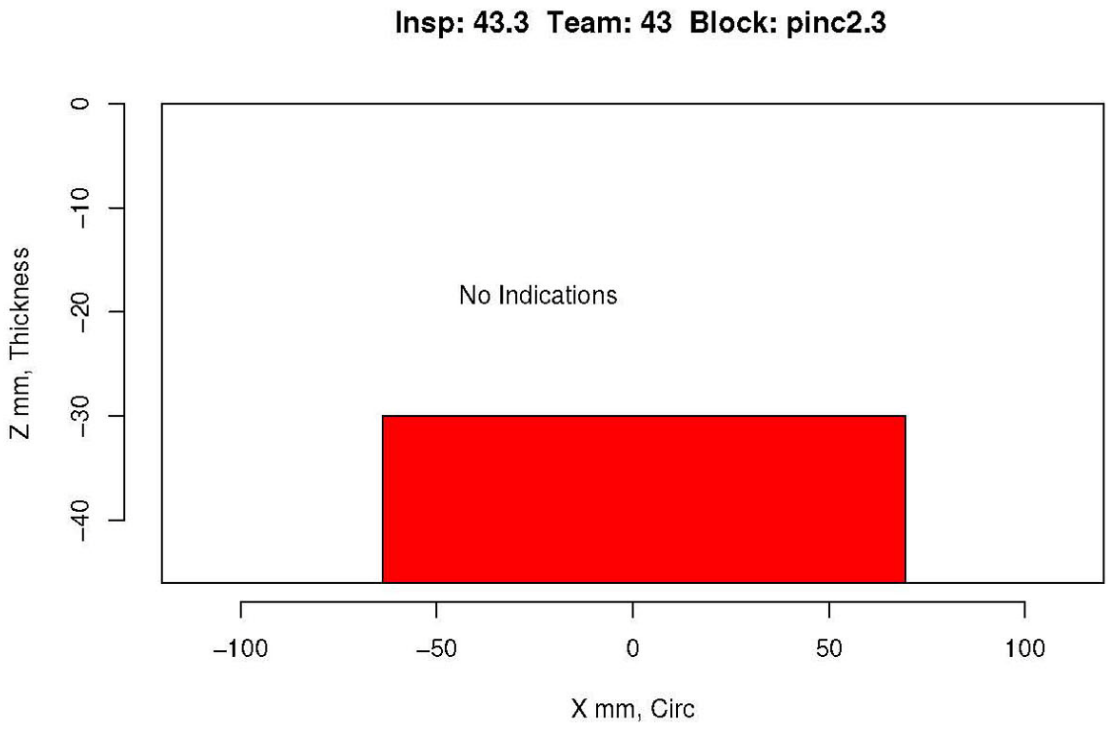
Insp: 43.3 Team: 43 Block: pinc2.3
Z mm, Thickness
0
−10
−20
−30
−40
No Indications
−100
−50
0
50
100
X mm, Circ

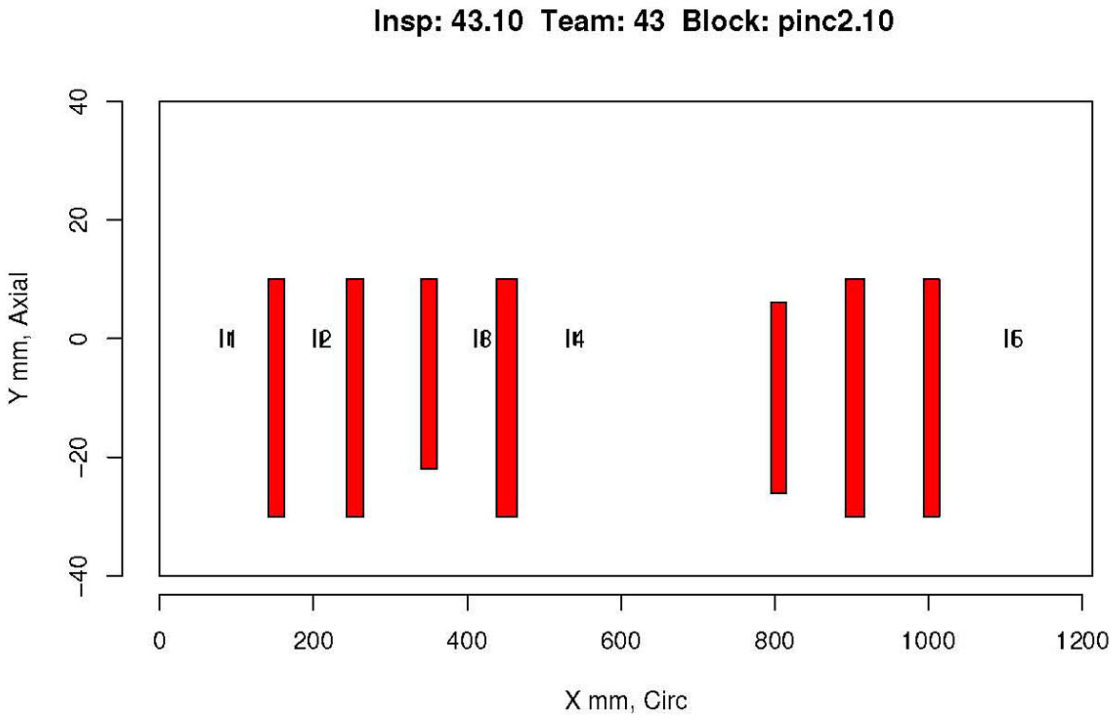
Insp: 43.10 Team: 43 Block: pinc2.10
Y mm, Axial
40
20
0
-20
-40
I1
I2
I3
I4
I5
0
200
400
600
800
1000
1200
X mm, Circ

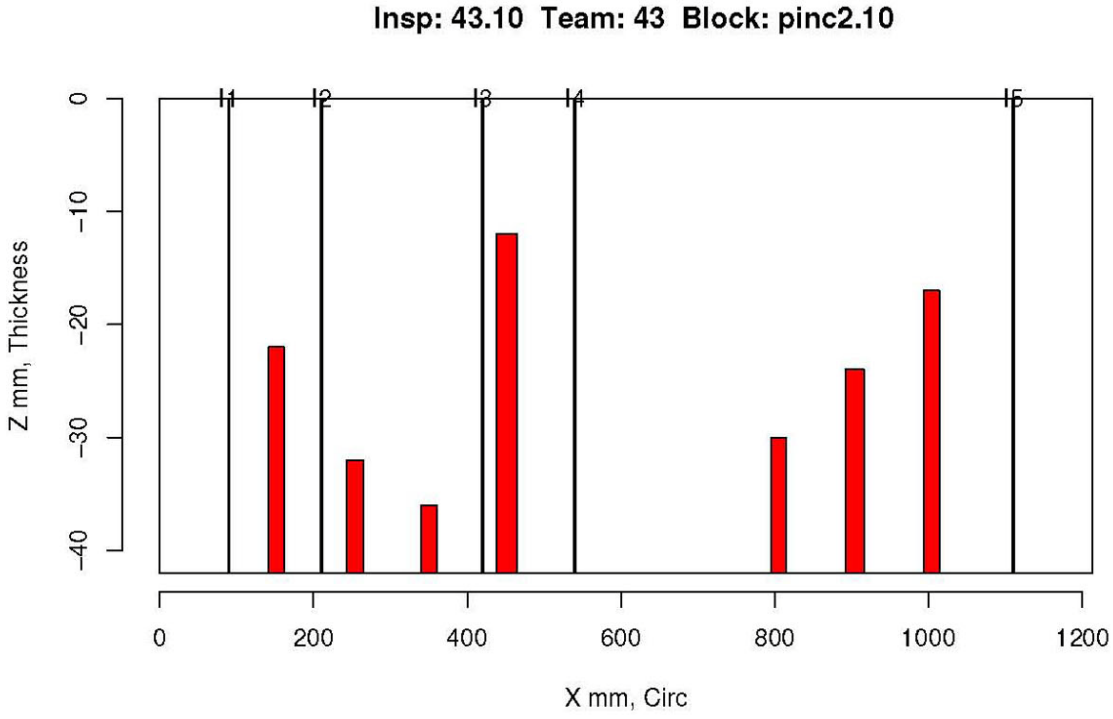
Insp: 43.10 Team: 43 Block: pinc2.10
Z mm, Thickness
0
-10
-20
-30
-40
I1
I2
I3
I4
I5
0
200
400
600
800
1000
1200
X mm, Circ

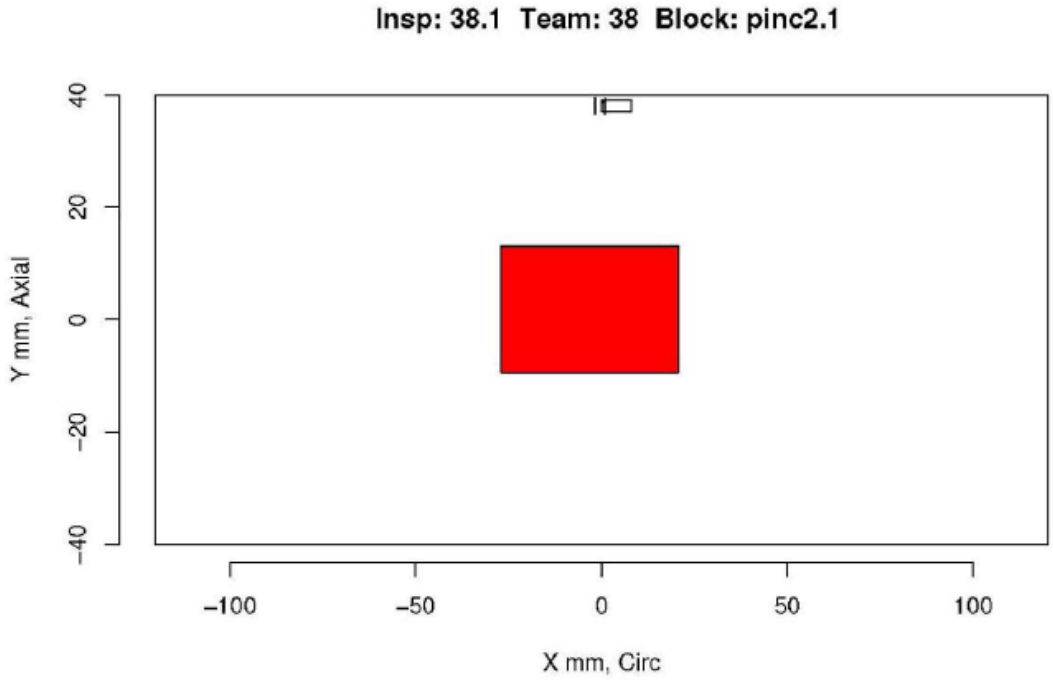
Insp: 38.1 Team: 38 Block: pinc2.1
Y mm, Axial
40
20
0
-20
-40
-100
-50
0
50
100
X mm, Circ

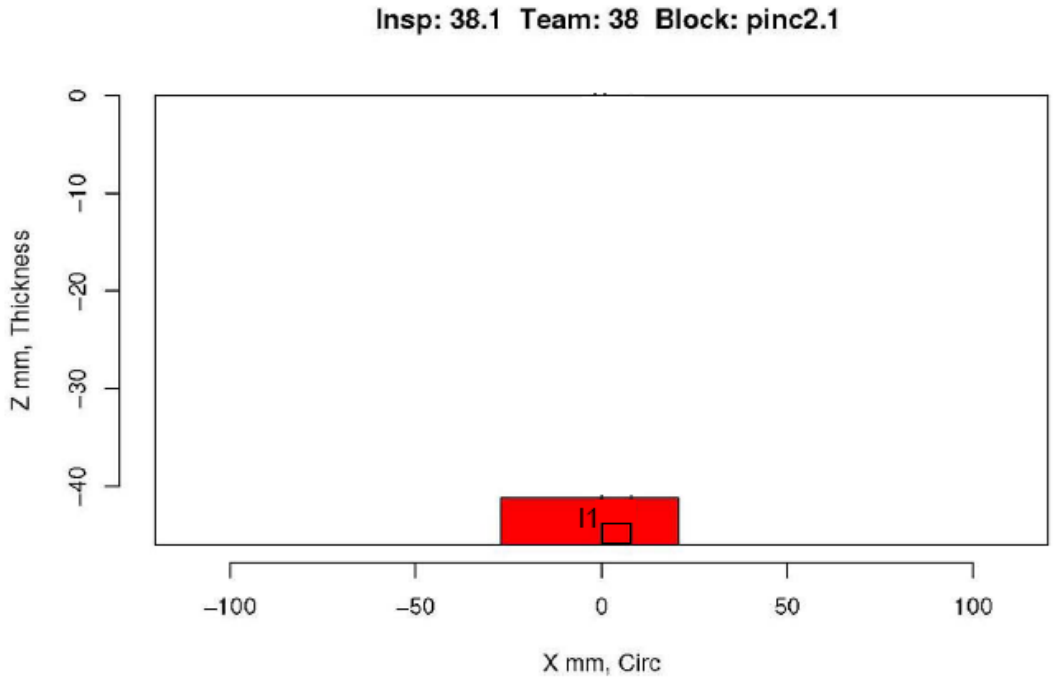
Insp: 38.1 Team: 38 Block: pinc2.1
Z mm, Thickness
0
-10
-20
-30
-40
I1
-100
-50
0
50
100
X mm, Circ

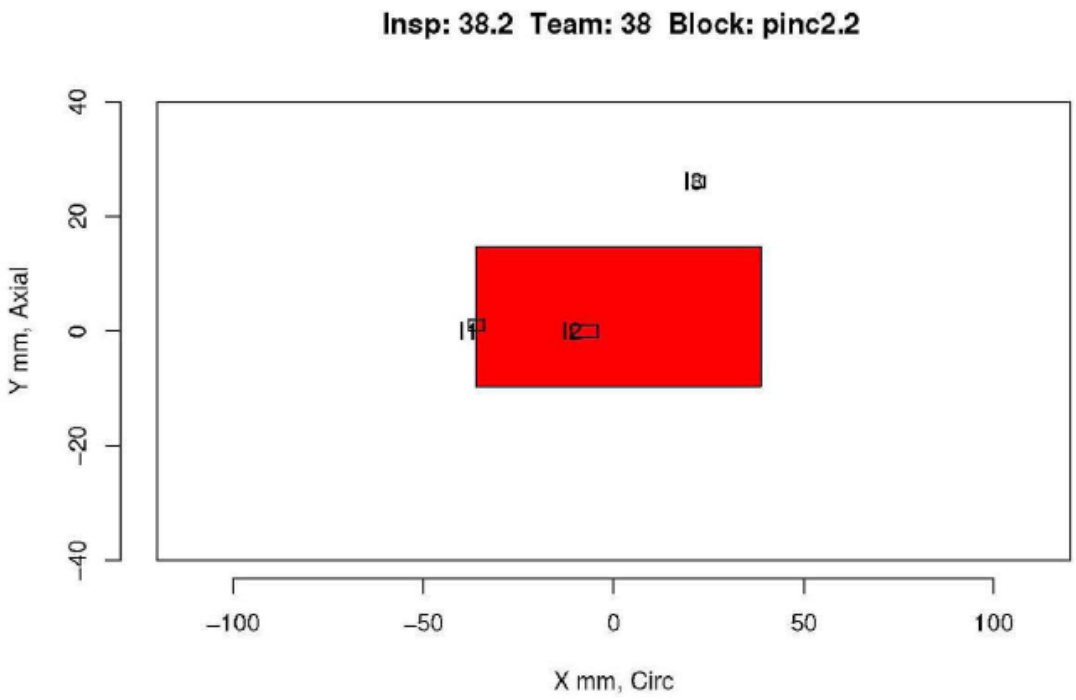
Insp: 38.2 Team: 38 Block: pinc2.2
Y mm, Axial
40
20
0
−20
−40
I1
I2
I3
−100
−50
0
50
100
X mm, Circ

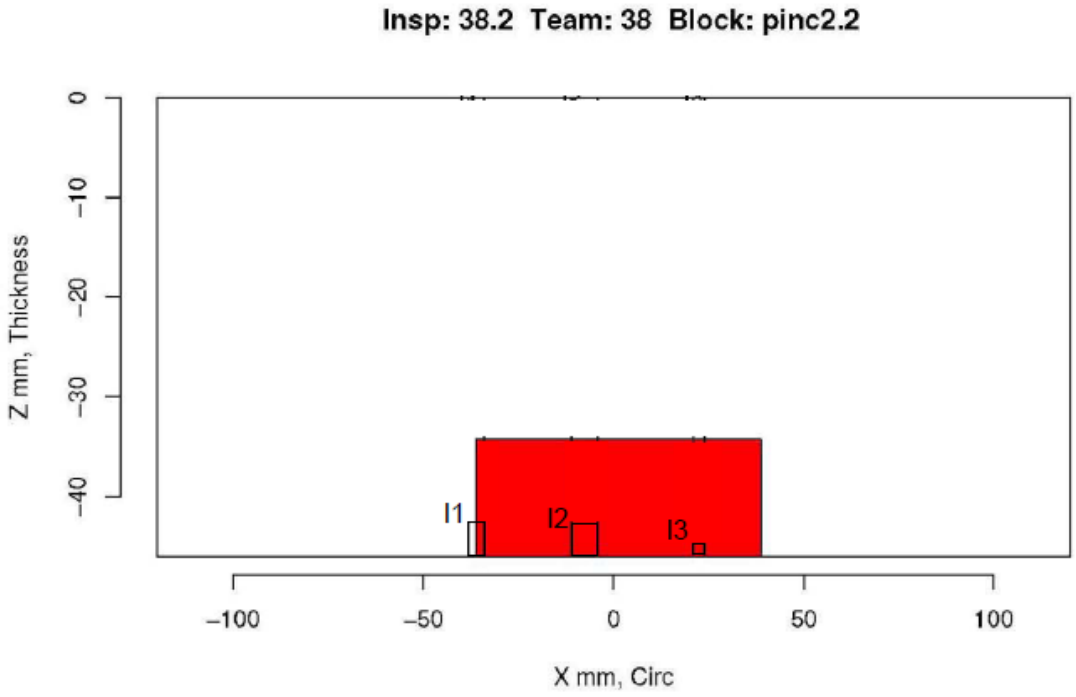
Insp: 38.2 Team: 38 Block: pinc2.2
Z mm, Thickness
0
−10
−20
−30
−40
I1
I2
I3
−100
−50
0
50
100
X mm, Circ

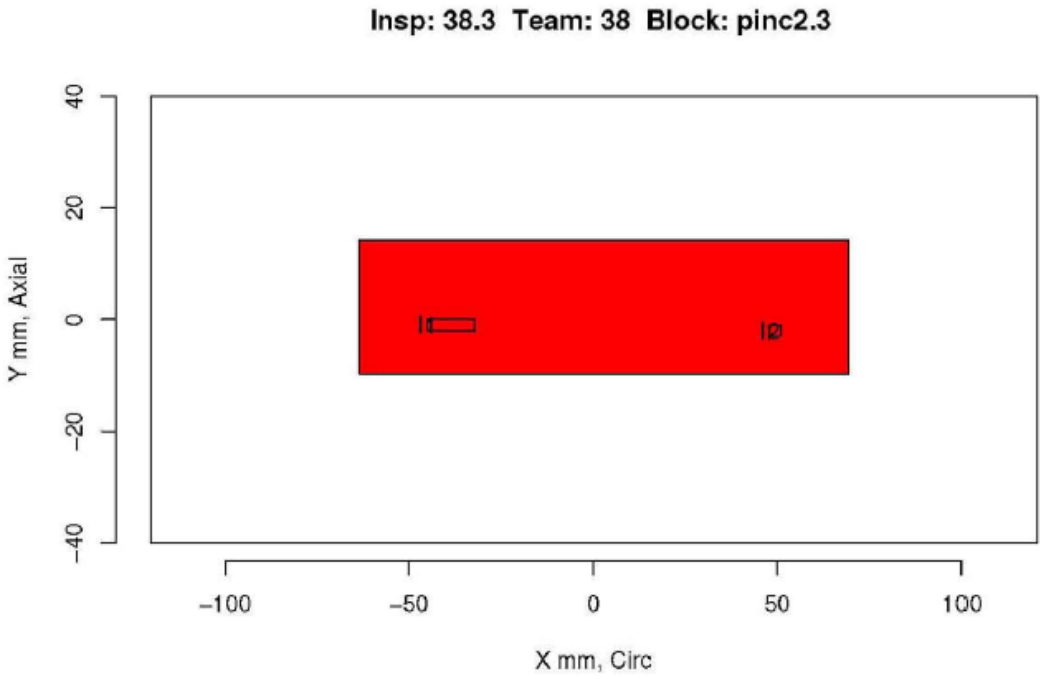
Insp: 38.3 Team: 38 Block: pinc2.3
Y mm, Axial
40
20
0
−20
−40
I1
I2
−100
−50
0
50
100
X mm, Circ

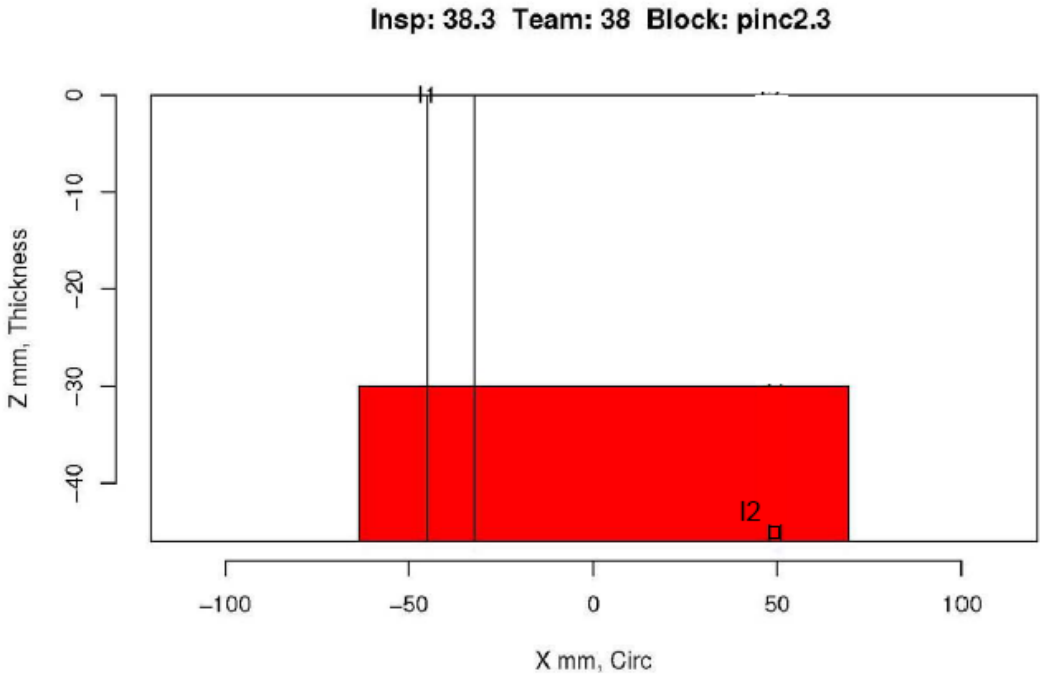
Insp: 38.3 Team: 38 Block: pinc2.3
Z mm, Thickness
0
−10
−20
−30
−40
I1
I2
−100
−50
0
50
100
X mm, Circ

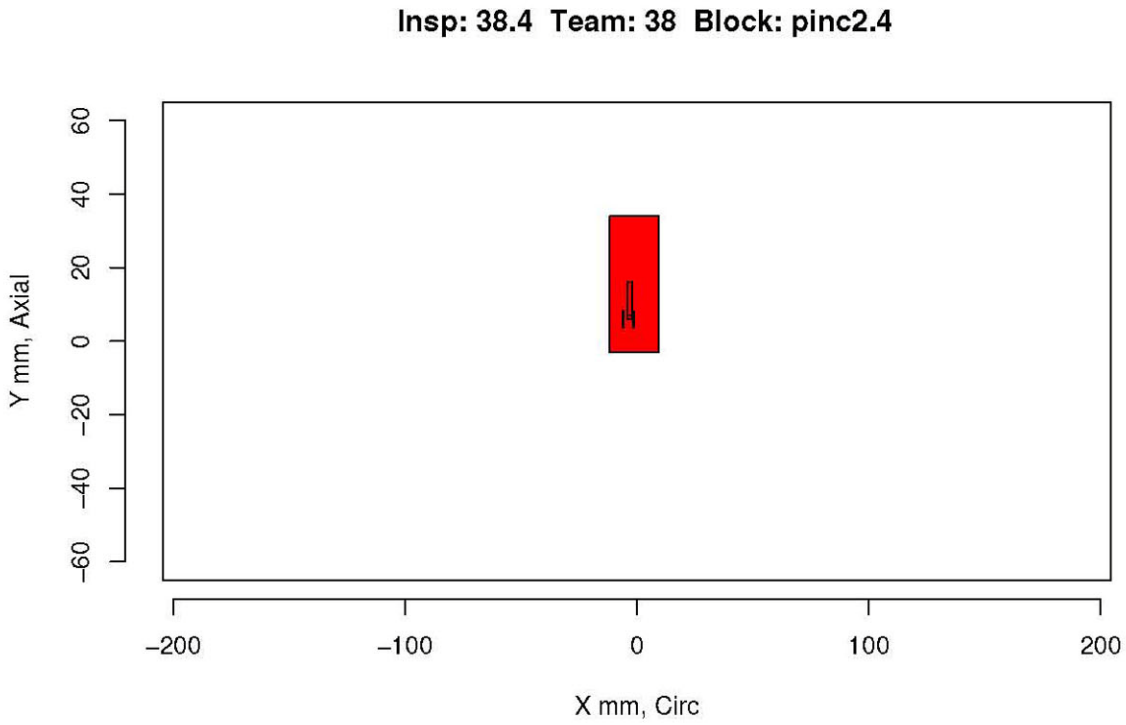
Insp: 38.4 Team: 38 Block: pinc2.4
Y mm, Axial
60
40
20
0
−20
−40
−60
−200
−100
0
100
200
X mm, Circ

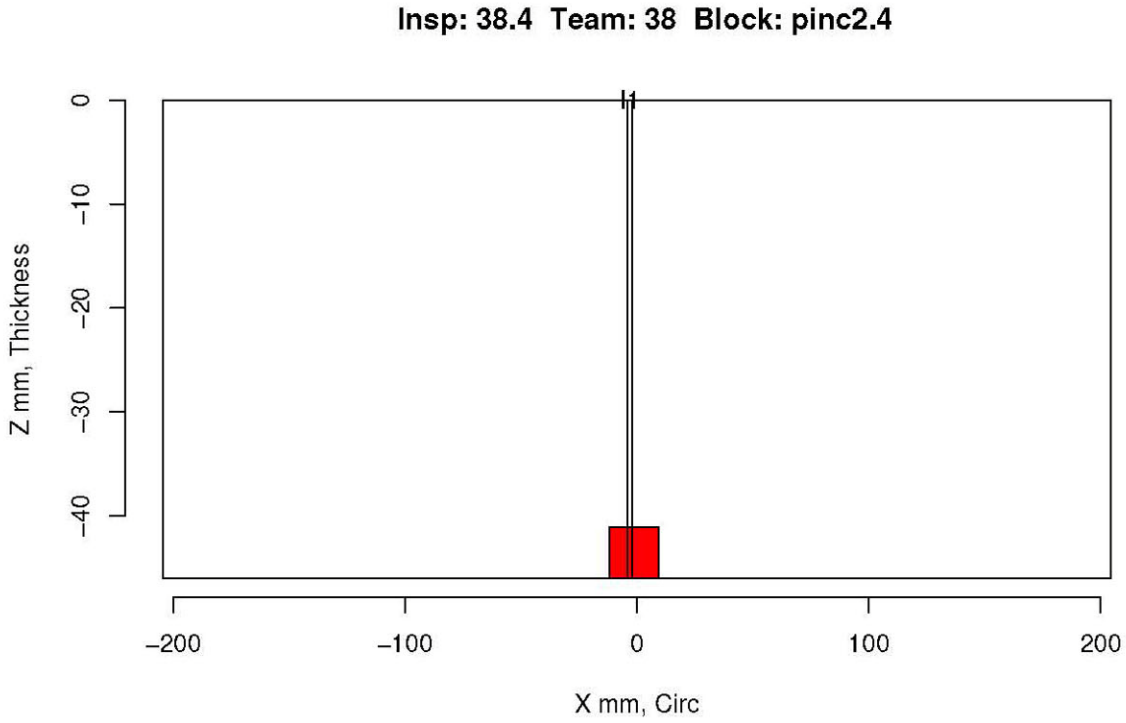
Insp: 38.4 Team: 38 Block: pinc2.4
Z mm, Thickness
0
−10
−20
−30
−40
−200
−100
0
100
200
X mm, Circ

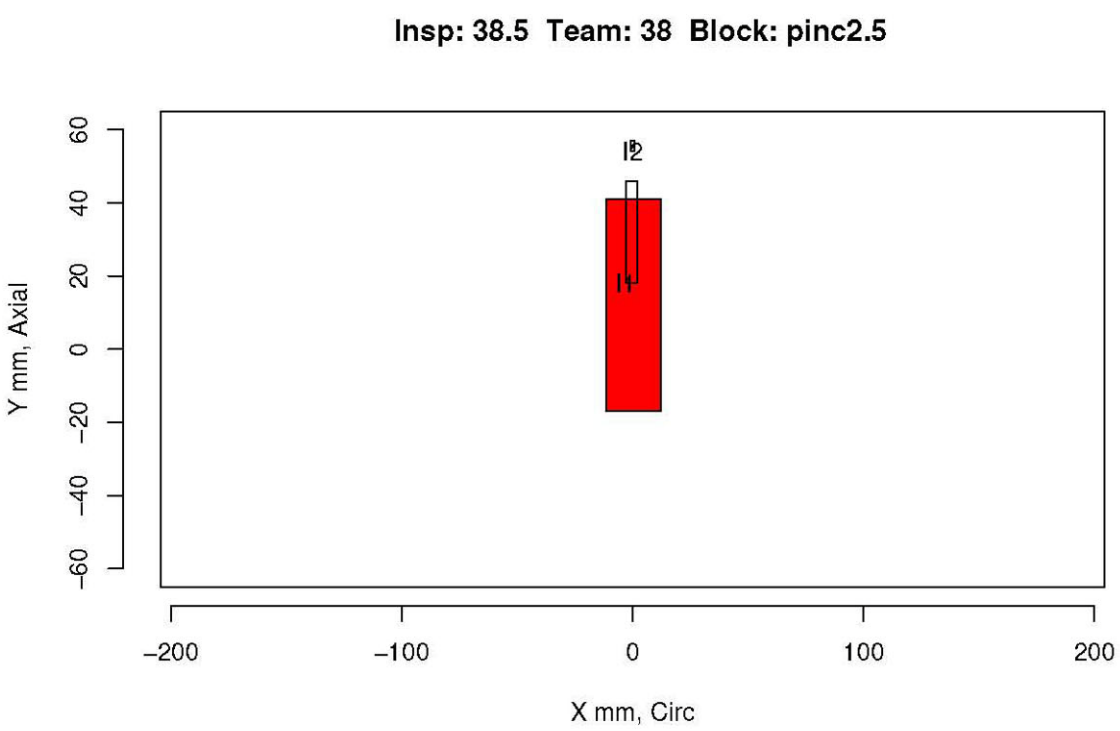
Insp: 38.5 Team: 38 Block: pinc2.5
Y mm, Axial
60
40
20
0
−20
−40
−60
−200
−100
0
100
200
X mm, Circ

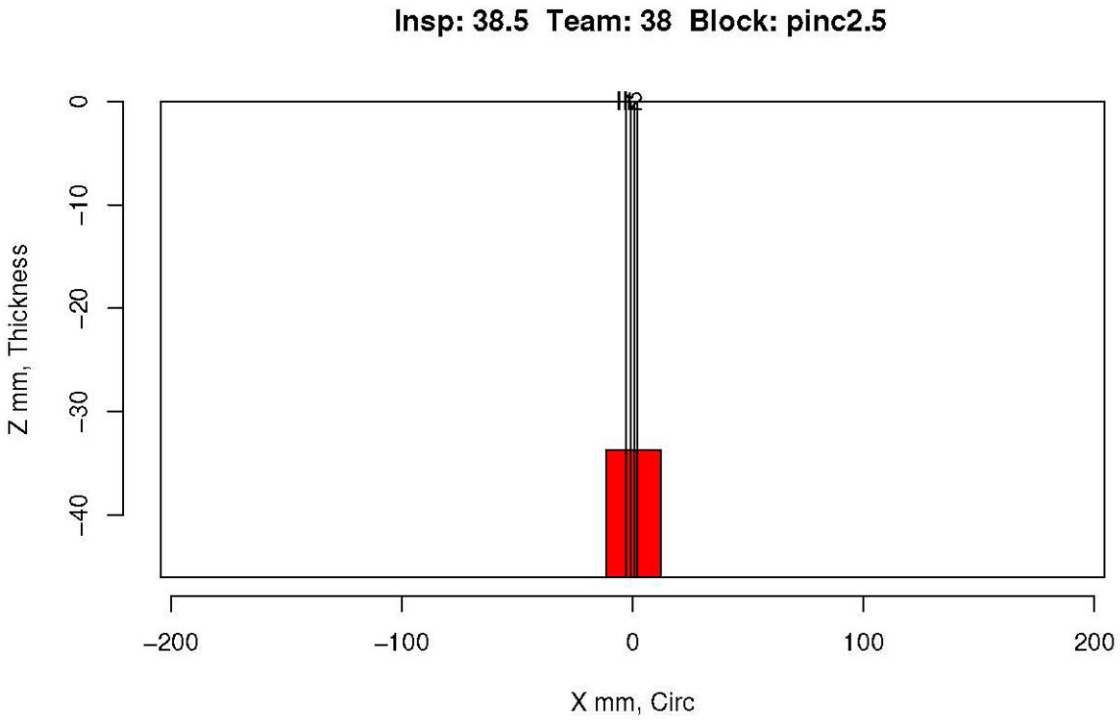
Insp: 38.5 Team: 38 Block: pinc2.5
Z mm, Thickness
0
−10
−20
−30
−40
−200
−100
0
100
200
X mm, Circ

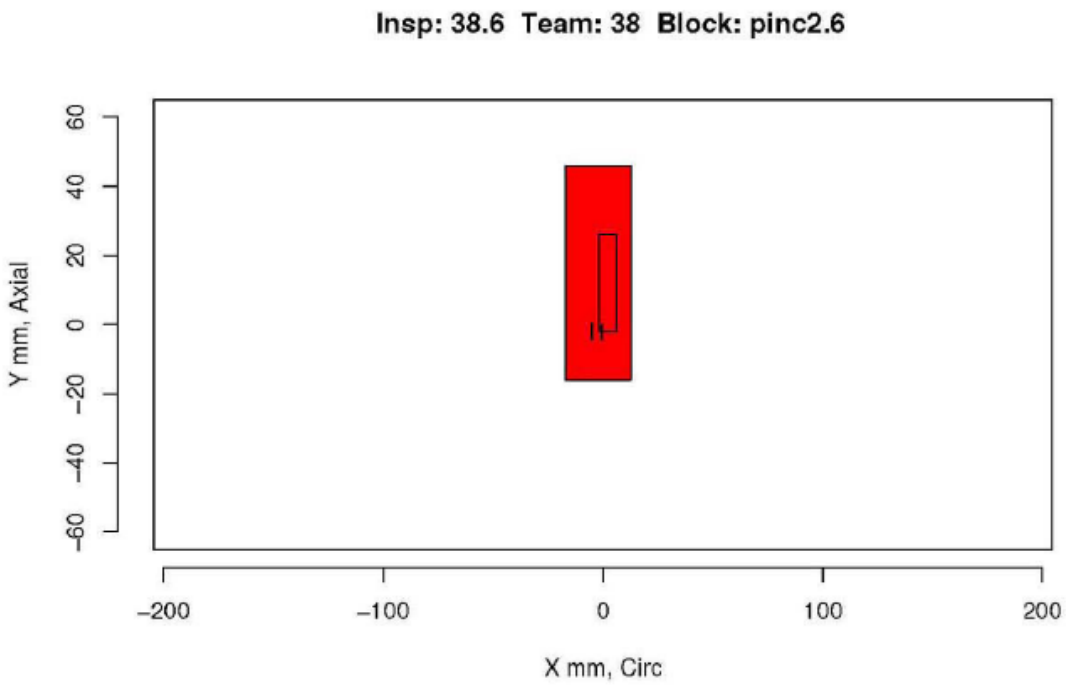
Insp: 38.6 Team: 38 Block: pinc2.6
Y mm, Axial
60
40
20
0
-20
-40
-60
I1
-200
-100
0
100
200
X mm, Circ

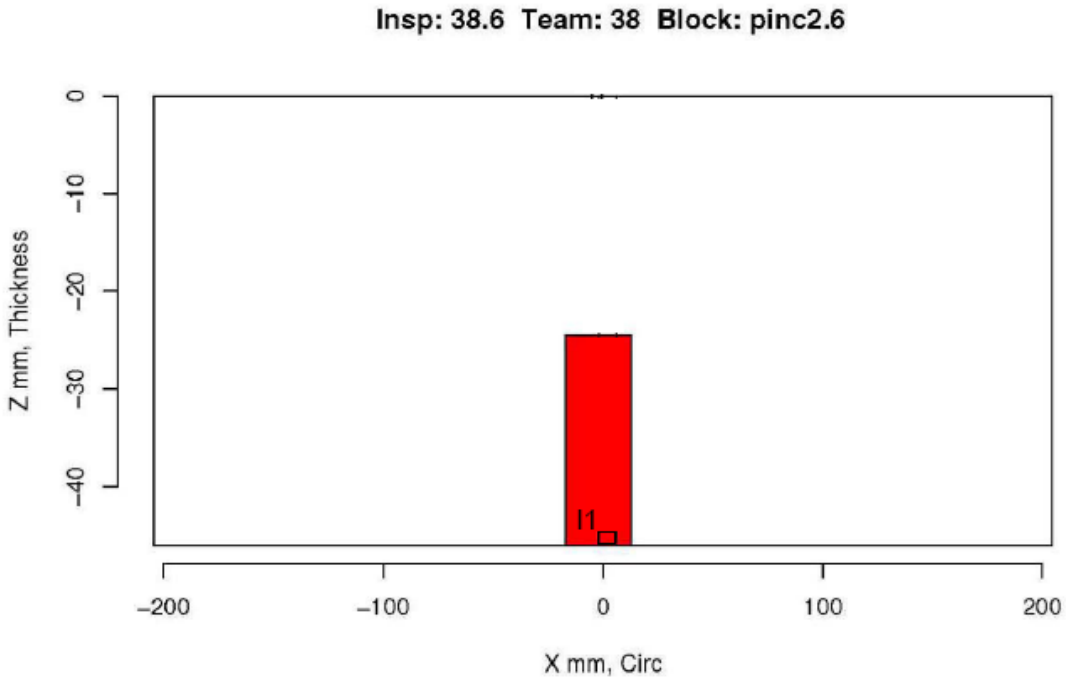
Insp: 38.6 Team: 38 Block: pinc2.6
Z mm, Thickness
0
-10
-20
-30
-40
I1
-200
-100
0
100
200
X mm, Circ

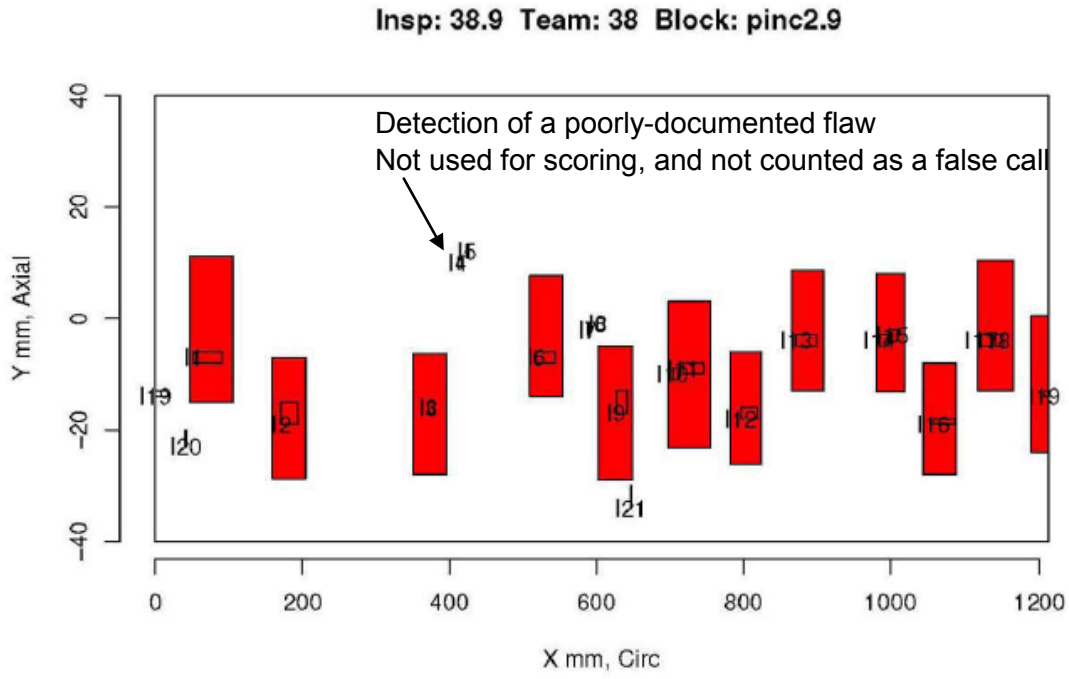
Insp: 38.9 Team: 38 Block: pinc2.9
Detection of a poorly-documented flaw
Not used for scoring, and not counted as a false call
Y mm, Axial
X mm, Circ

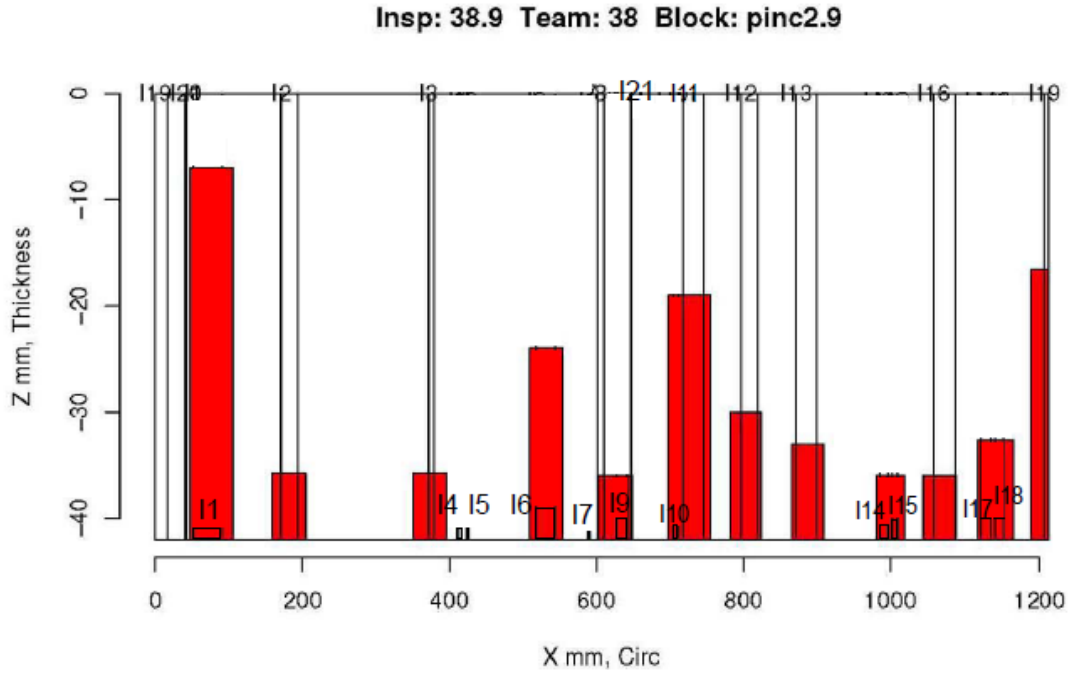
Insp: 38.9 Team: 38 Block: pinc2.9
Z mm, Thickness
X mm, Circ

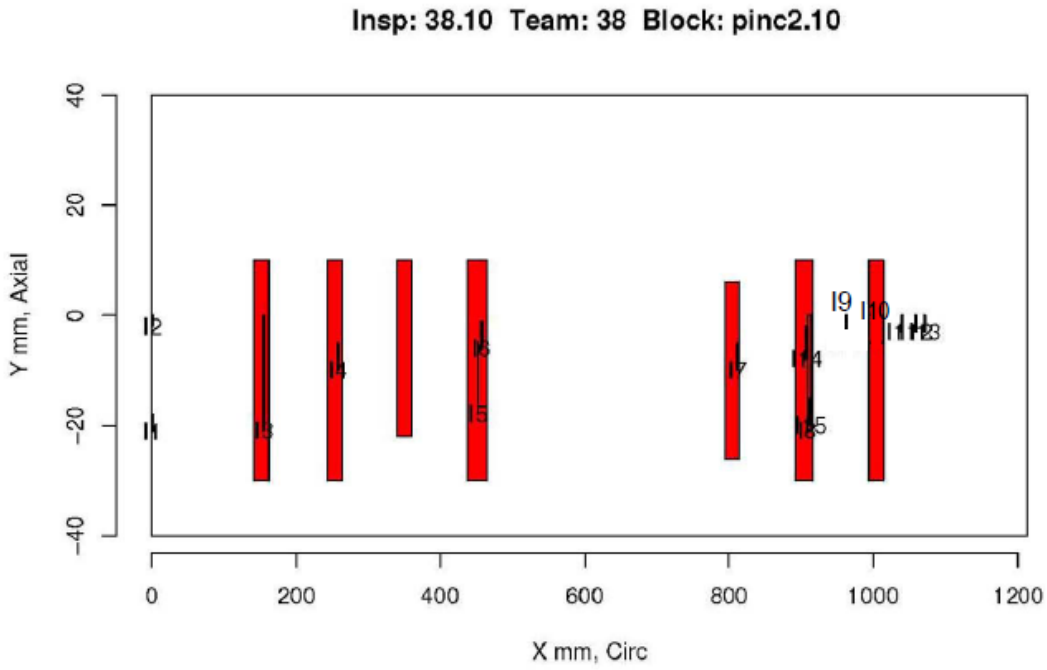
Insp: 38.10 Team: 38 Block: pinc2.10
Y mm, Axial
X mm, Circ
40
20
0
-20
-40
0
200
400
600
800
1000
1200

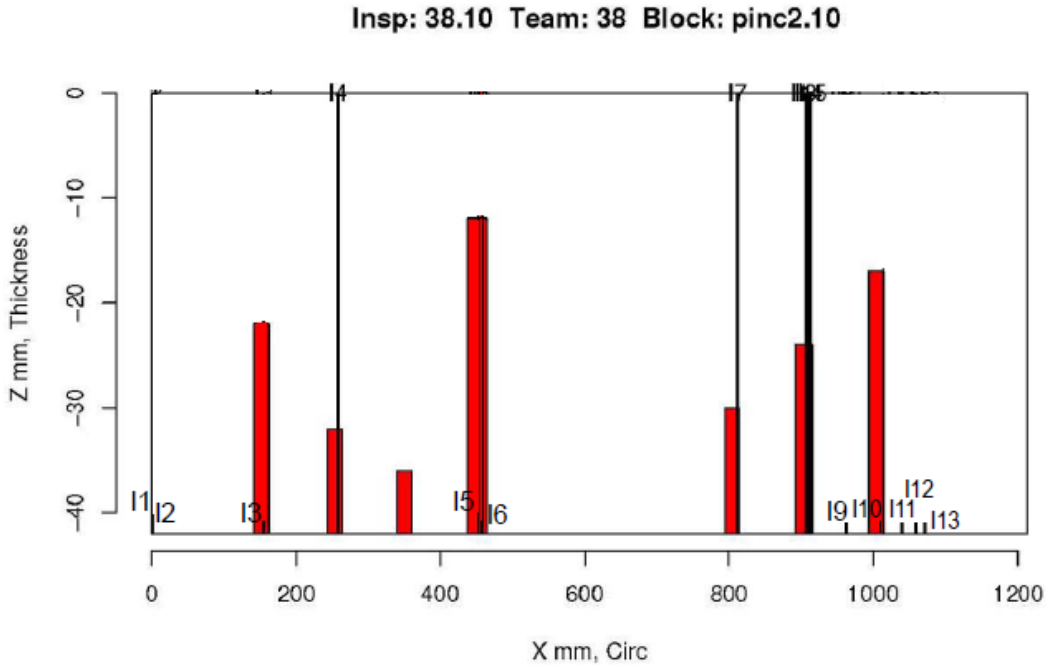
Insp: 38.10 Team: 38 Block: pinc2.10
Z mm, Thickness
X mm, Circ
0
-10
-20
-30
-40
0
200
400
600
800
1000
1200

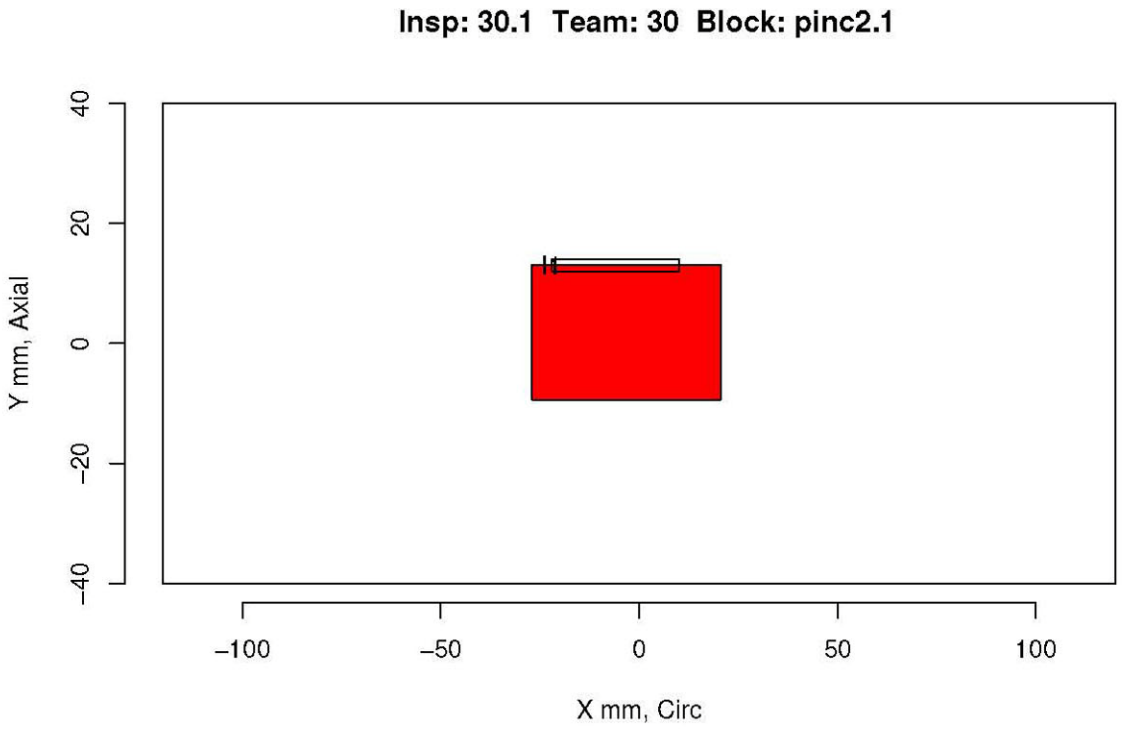
Insp: 30.1 Team: 30 Block: pinc2.1
Y mm, Axial
40
20
0
−20
−40
−100
−50
0
50
100
X mm, Circ

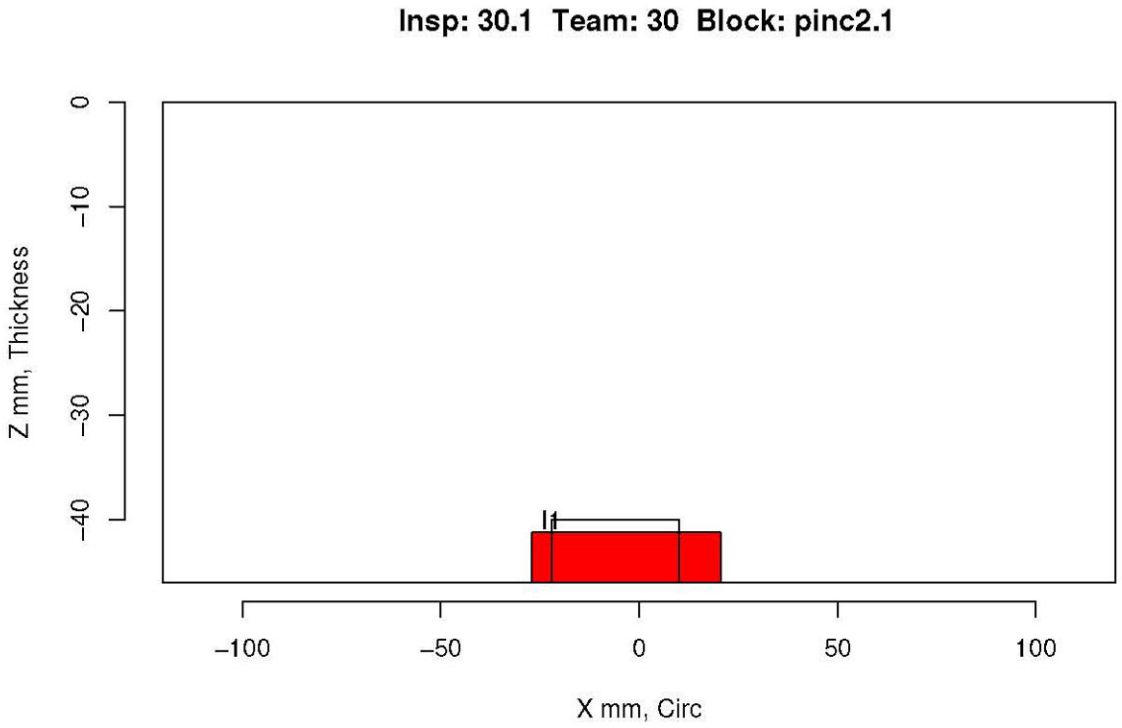
Insp: 30.1 Team: 30 Block: pinc2.1
Z mm, Thickness
0
−10
−20
−30
−40
−100
−50
0
50
100
X mm, Circ

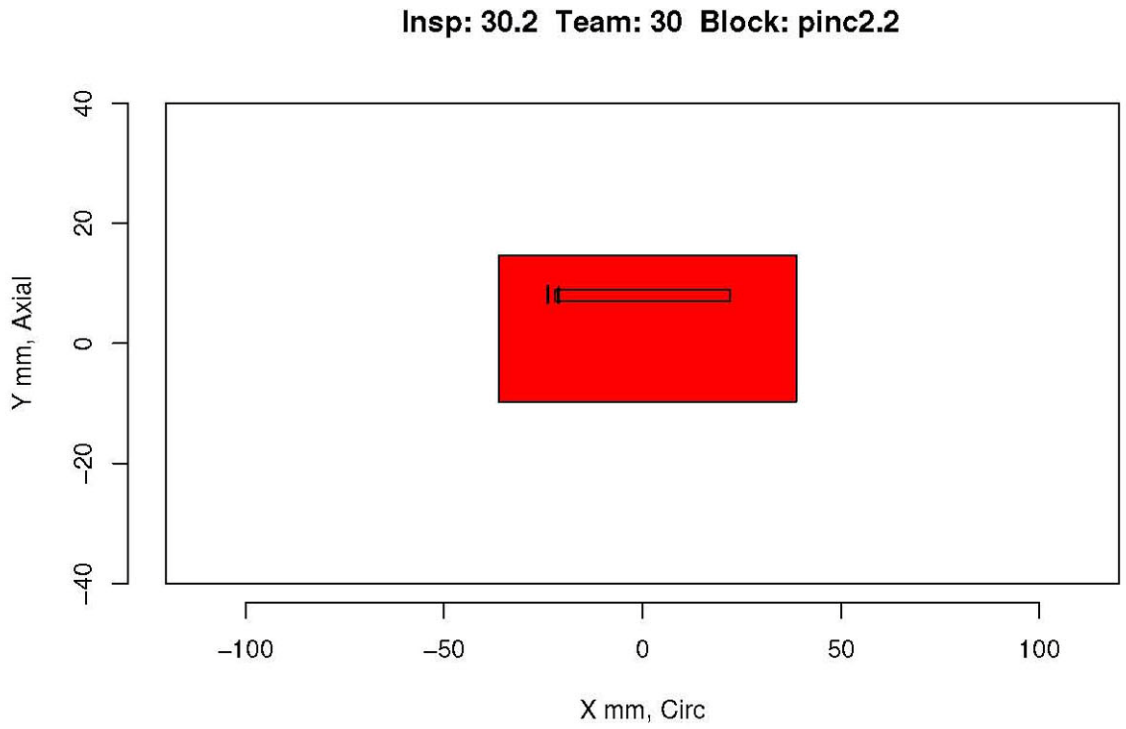
Insp: 30.2 Team: 30 Block: pinc2.2
Y mm, Axial
40
20
0
-20
-40
-100
-50
0
50
100
X mm, Circ

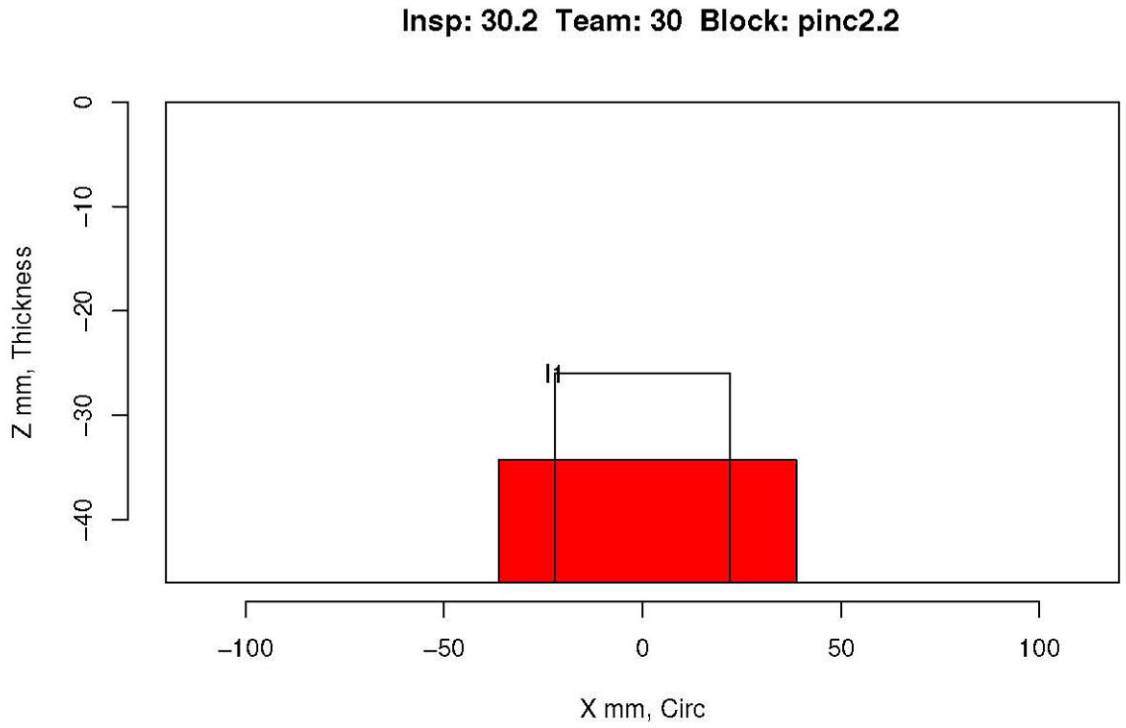
Insp: 30.2 Team: 30 Block: pinc2.2
Z mm, Thickness
0
-10
-20
-30
-40
-100
-50
0
50
100
X mm, Circ

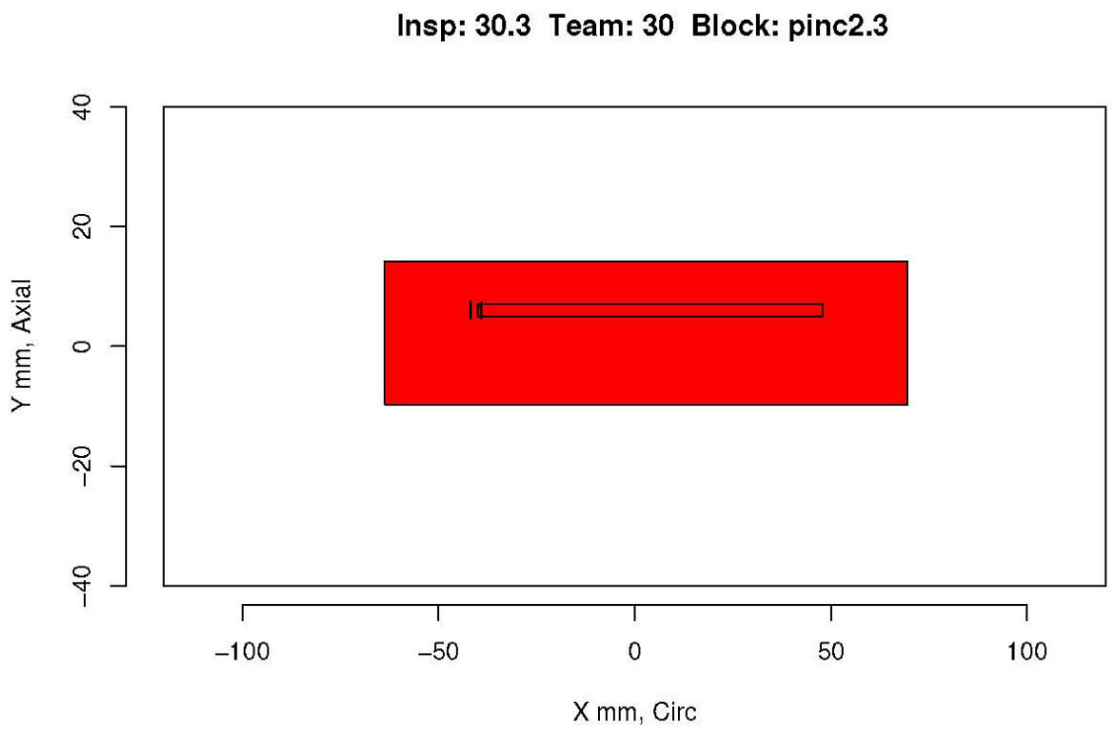
Insp: 30.3 Team: 30 Block: pinc2.3
Y mm, Axial
40
20
0
−20
−40
−100
−50
0
50
100
X mm, Circ

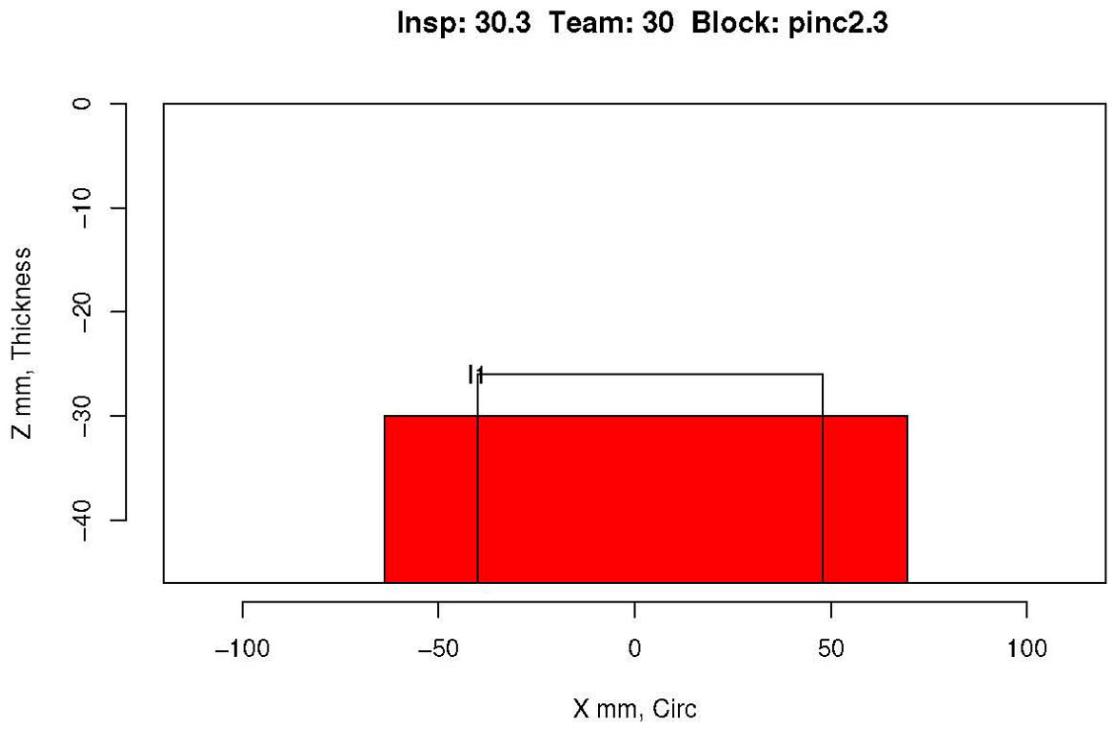
Insp: 30.3 Team: 30 Block: pinc2.3
Z mm, Thickness
0
−10
−20
−30
−40
−100
−50
0
50
100
X mm, Circ

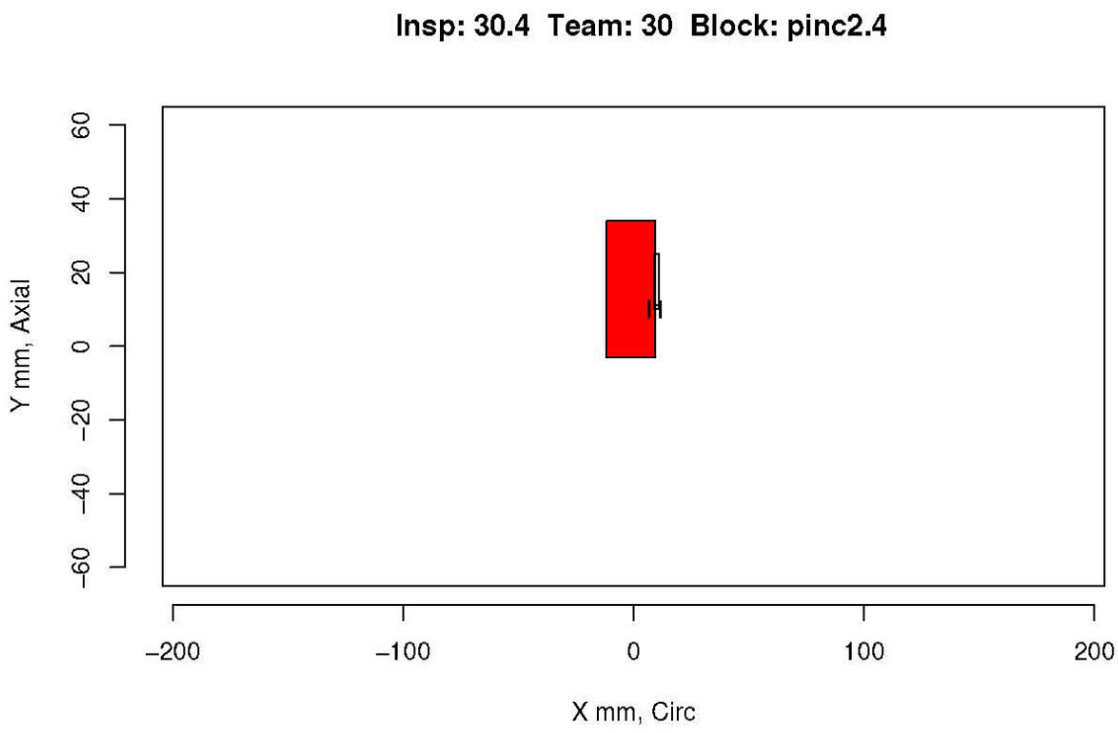
Insp: 30.4 Team: 30 Block: pinc2.4
Y mm, Axial
60
40
20
0
−20
−40
−60
−200
−100
0
100
200
X mm, Circ

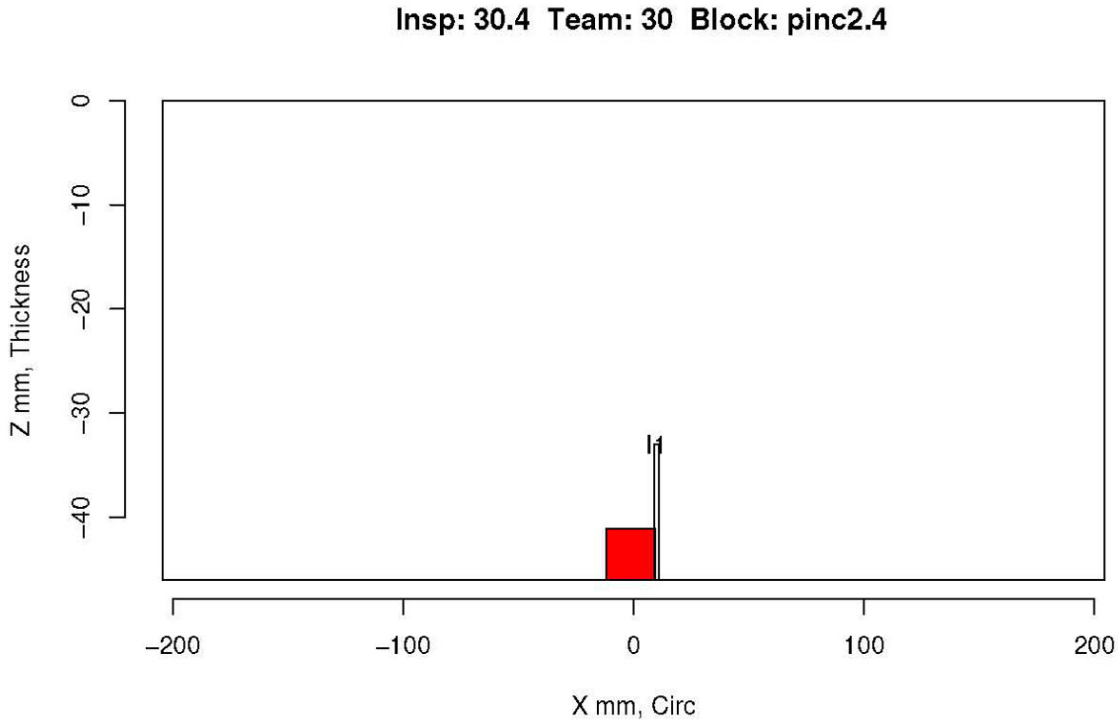
Insp: 30.4 Team: 30 Block: pinc2.4
Z mm, Thickness
0
−10
−20
−30
−40
−200
−100
0
100
200
X mm, Circ

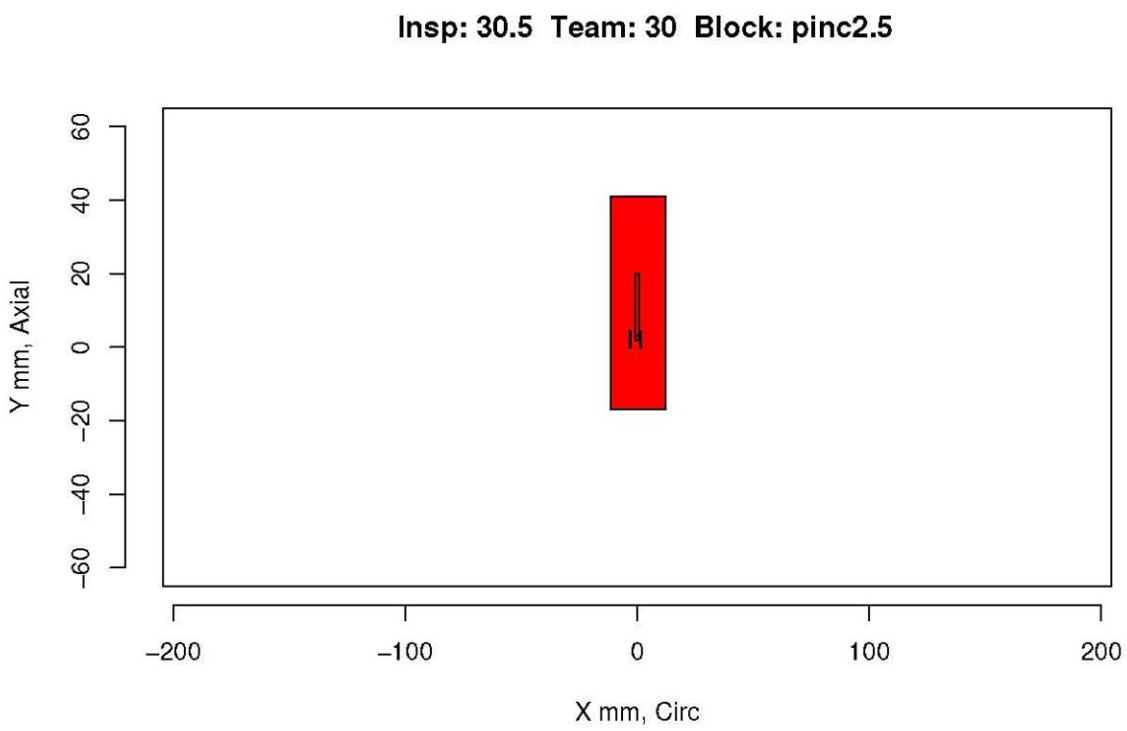
Insp: 30.5 Team: 30 Block: pinc2.5
Y mm, Axial
60
40
20
0
−20
−40
−60
−200
−100
0
100
200
X mm, Circ

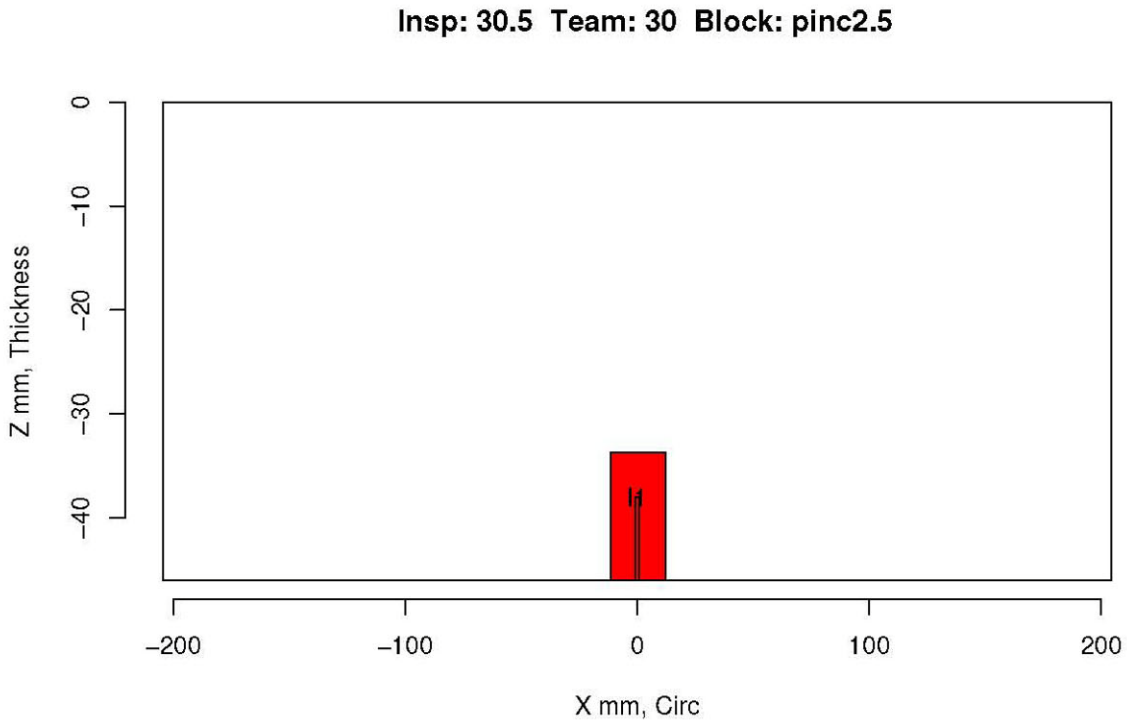
Insp: 30.5 Team: 30 Block: pinc2.5
Z mm, Thickness
0
−10
−20
−30
−40
−200
−100
0
100
200
X mm, Circ

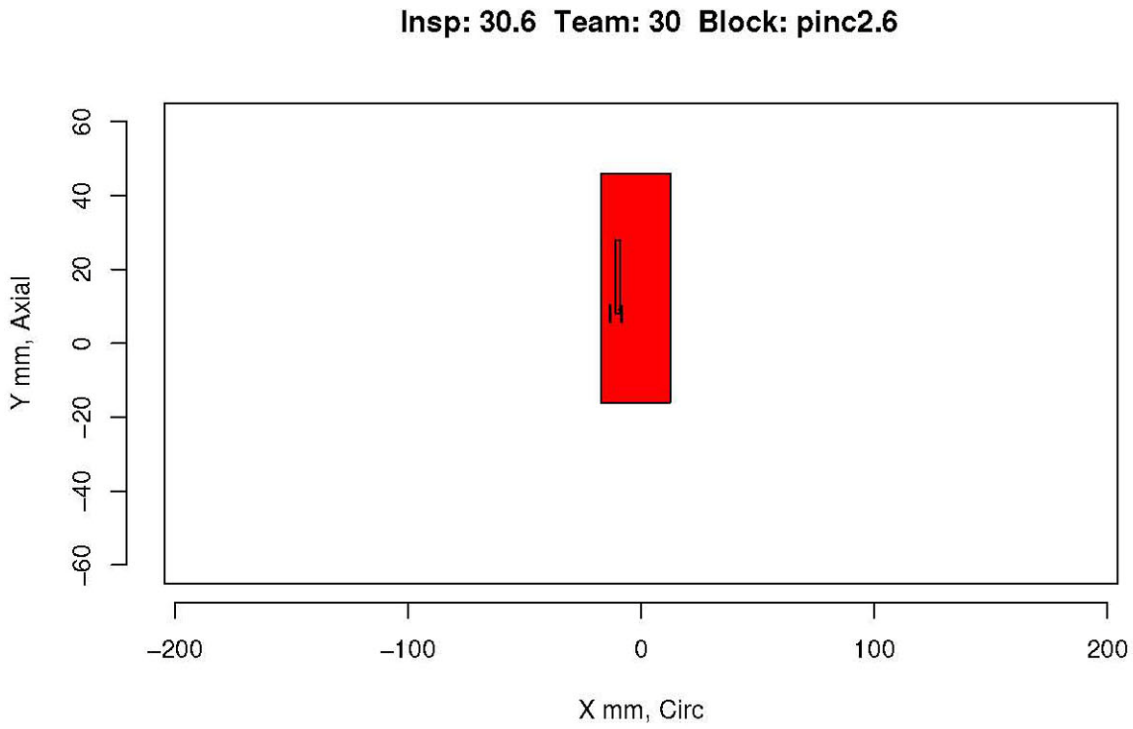
Insp: 30.6 Team: 30 Block: pinc2.6
Y mm, Axial
60
40
20
0
−20
−40
−60
−200
−100
0
100
200
X mm, Circ

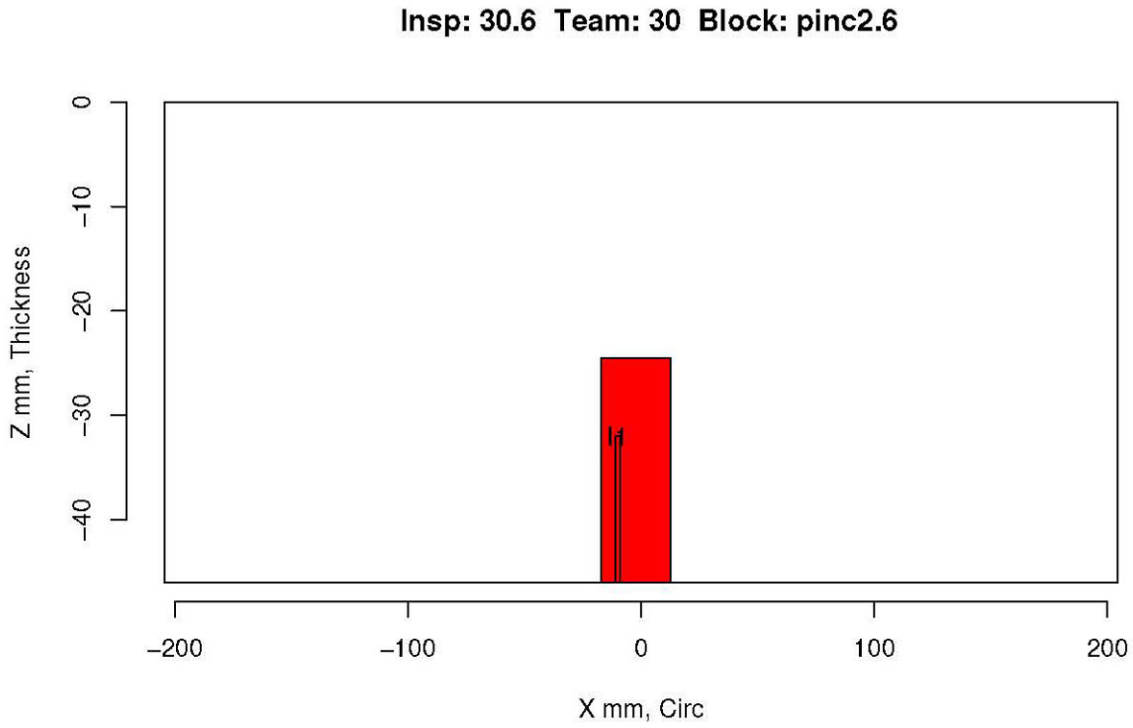
Insp: 30.6 Team: 30 Block: pinc2.6
Z mm, Thickness
0
−10
−20
−30
−40
−200
−100
0
100
200
X mm, Circ

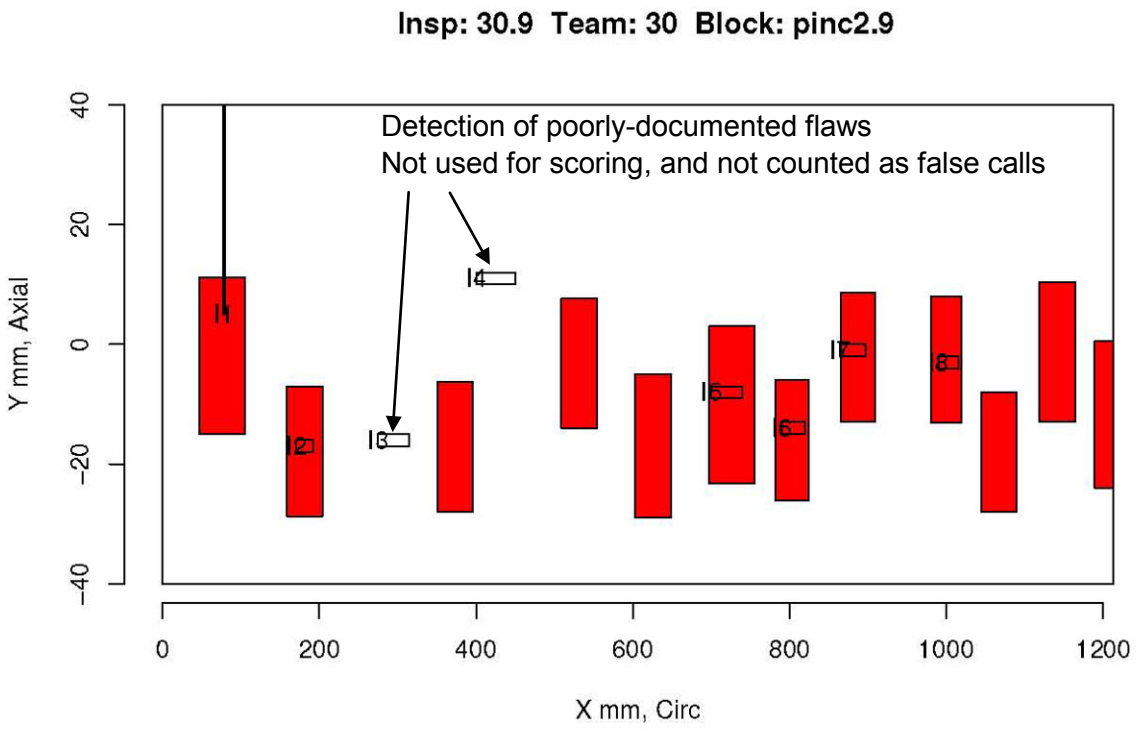
Insp: 30.9 Team: 30 Block: pinc2.9
Detection of poorly-documented flaws
Not used for scoring, and not counted as false calls
Y mm, Axial
X mm, Circ
40
20
0
-20
-40
0
200
400
600
800
1000
1200

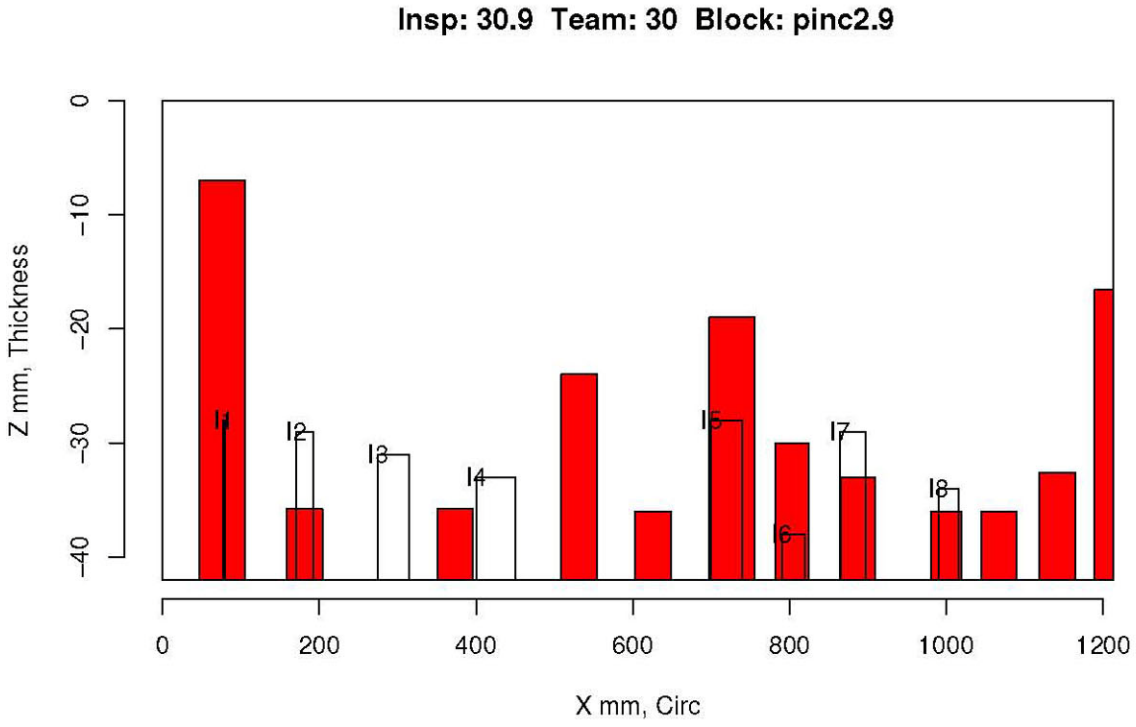
Insp: 30.9 Team: 30 Block: pinc2.9
Z mm, Thickness
X mm, Circ
0
-10
-20
-30
-40
0
200
400
600
800
1000
1200

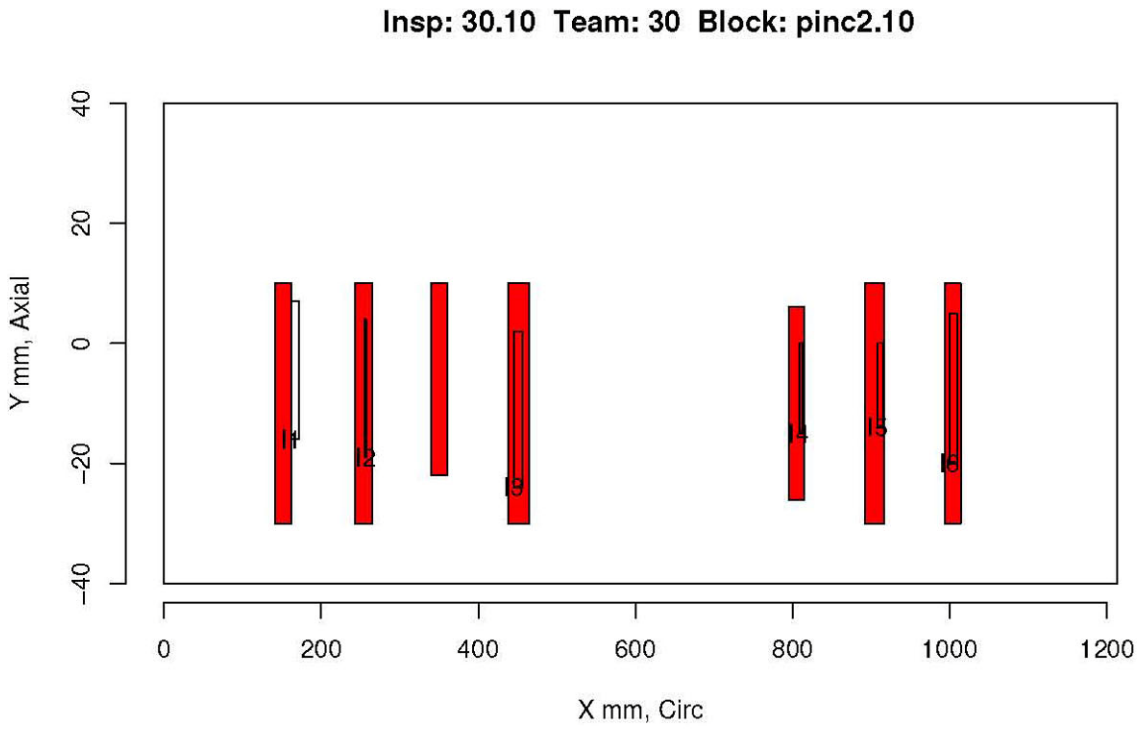
Insp: 30.10 Team: 30 Block: pinc2.10
Y mm, Axial
40
20
0
-20
-40
0
200
400
600
800
1000
1200
X mm, Circ
I1
I2
I3
I4
I5
I6

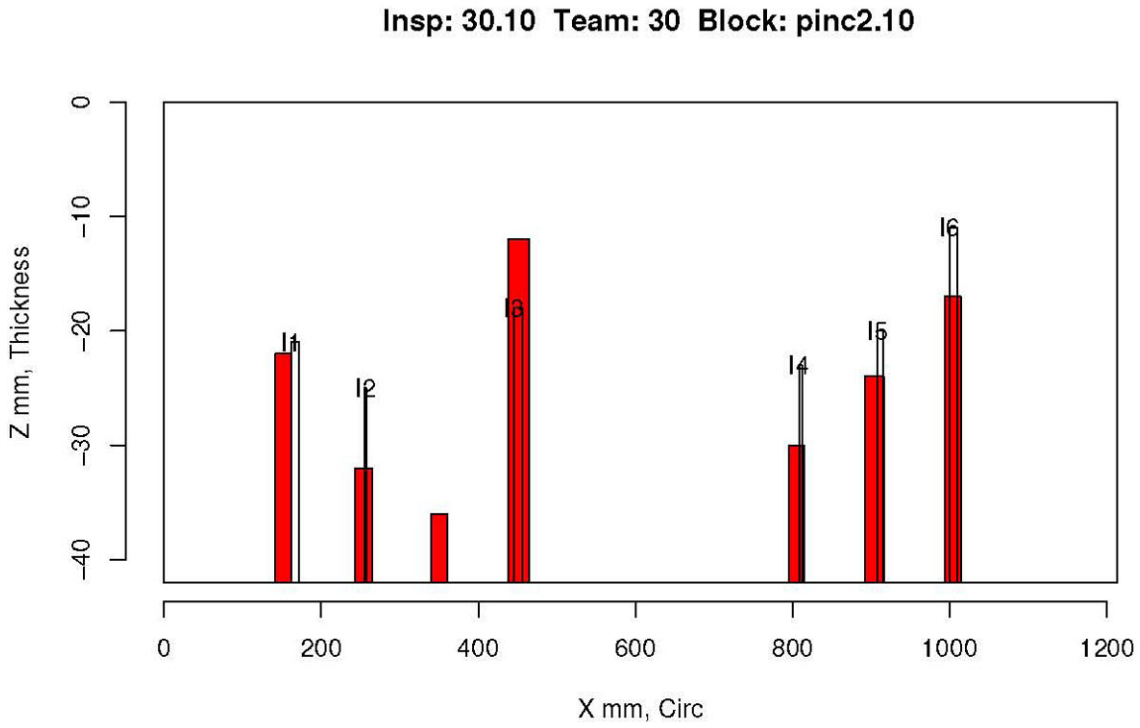
Insp: 30.10 Team: 30 Block: pinc2.10
Z mm, Thickness
0
-10
-20
-30
-40
0
200
400
600
800
1000
1200
X mm, Circ
I1
I2
I3
I4
I5
I6

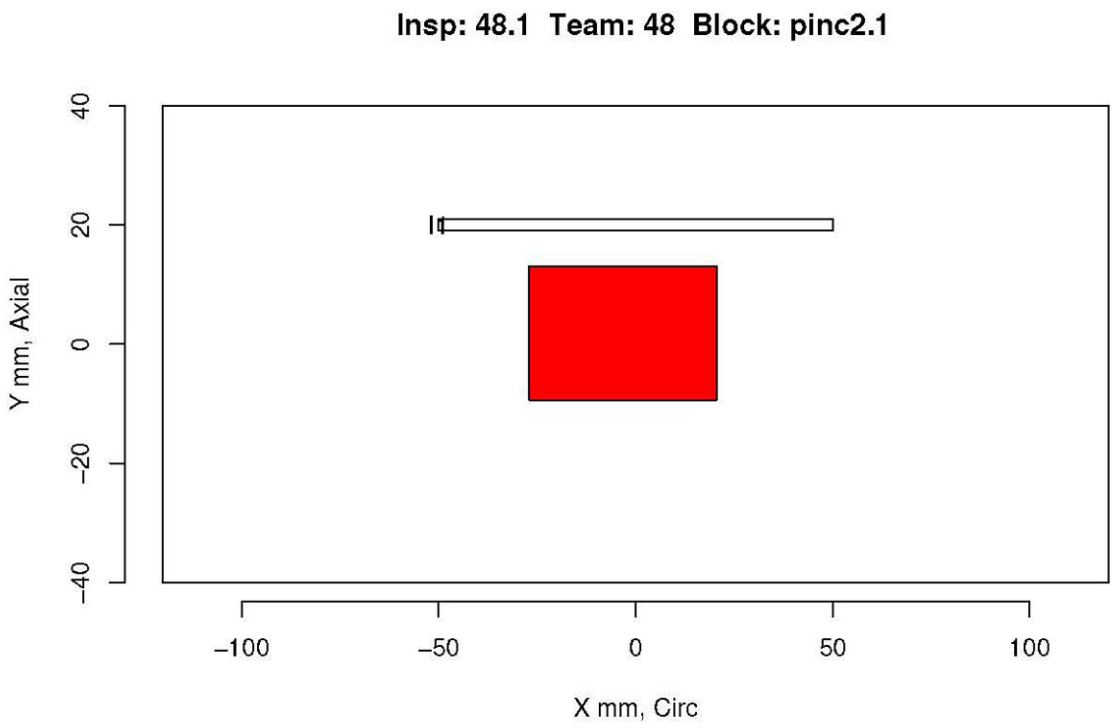
Insp: 48.1 Team: 48 Block: pinc2.1
Y mm, Axial
40
20
0
−20
−40
−100
−50
0
50
100
X mm, Circ

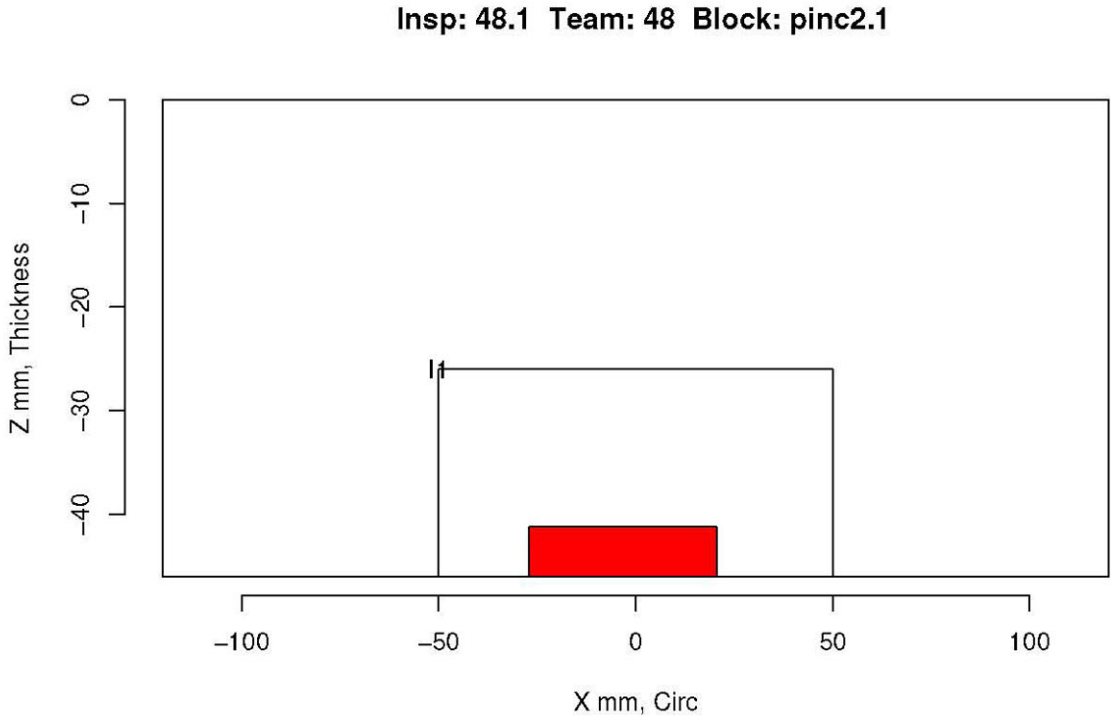
Insp: 48.1 Team: 48 Block: pinc2.1
Z mm, Thickness
0
−10
−20
−30
−40
−100
−50
0
50
100
X mm, Circ

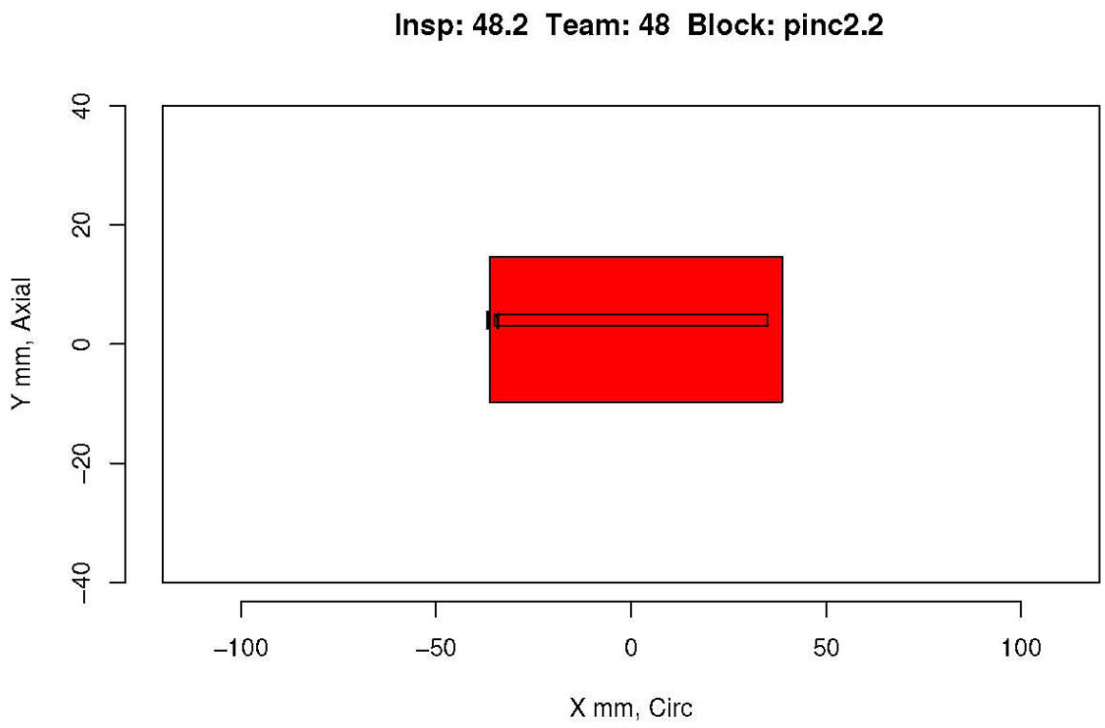
Insp: 48.2 Team: 48 Block: pinc2.2
Y mm, Axial
40
20
0
−20
−40
−100
−50
0
50
100
X mm, Circ

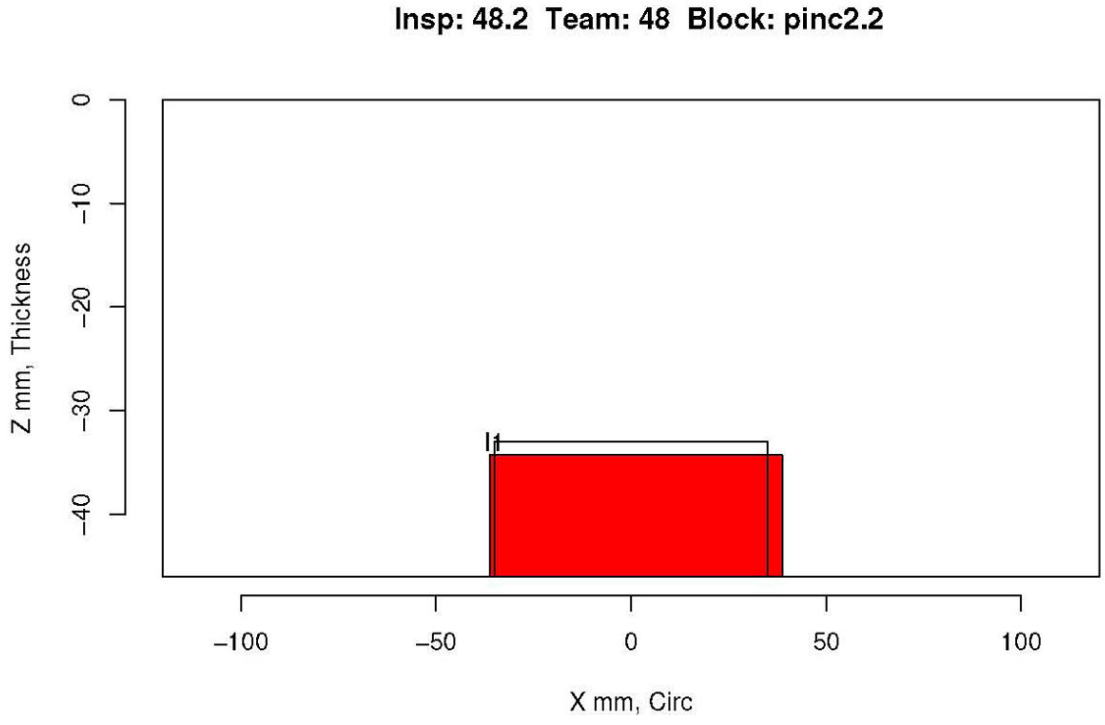
Insp: 48.2 Team: 48 Block: pinc2.2
Z mm, Thickness
0
−10
−20
−30
−40
−100
−50
0
50
100
X mm, Circ

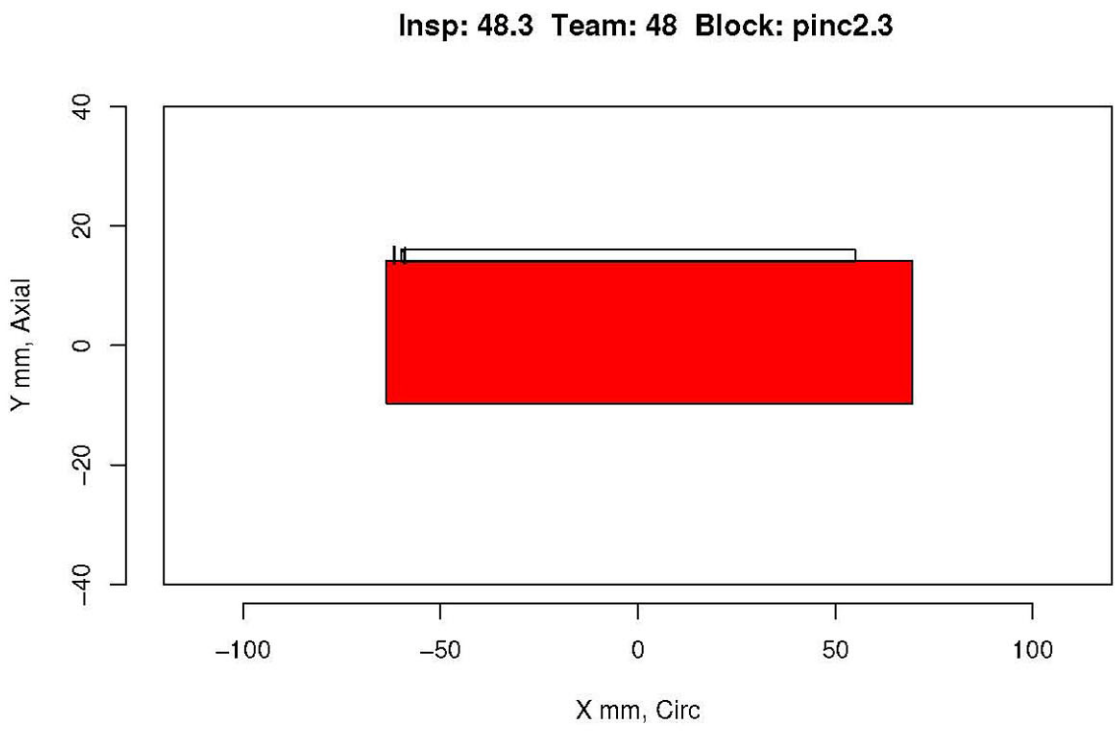
Insp: 48.3 Team: 48 Block: pinc2.3
Y mm, Axial
40
20
0
−20
−40
−100
−50
0
50
100
X mm, Circ

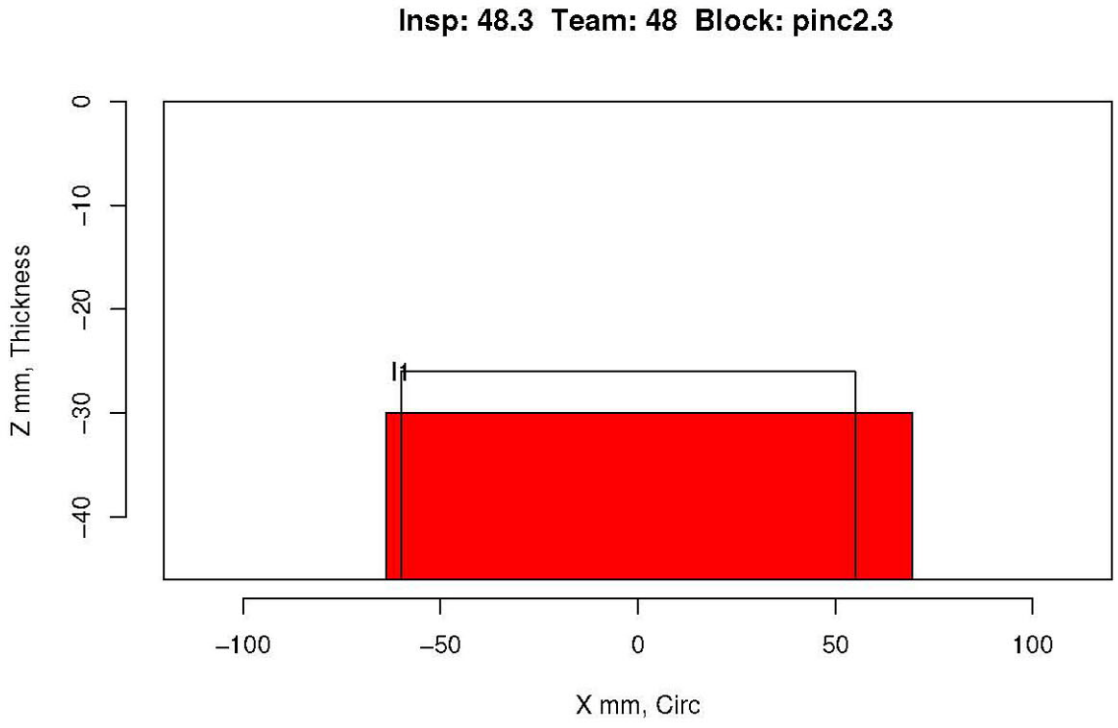
Insp: 48.3 Team: 48 Block: pinc2.3
Z mm, Thickness
0
−10
−20
−30
−40
−100
−50
0
50
100
X mm, Circ

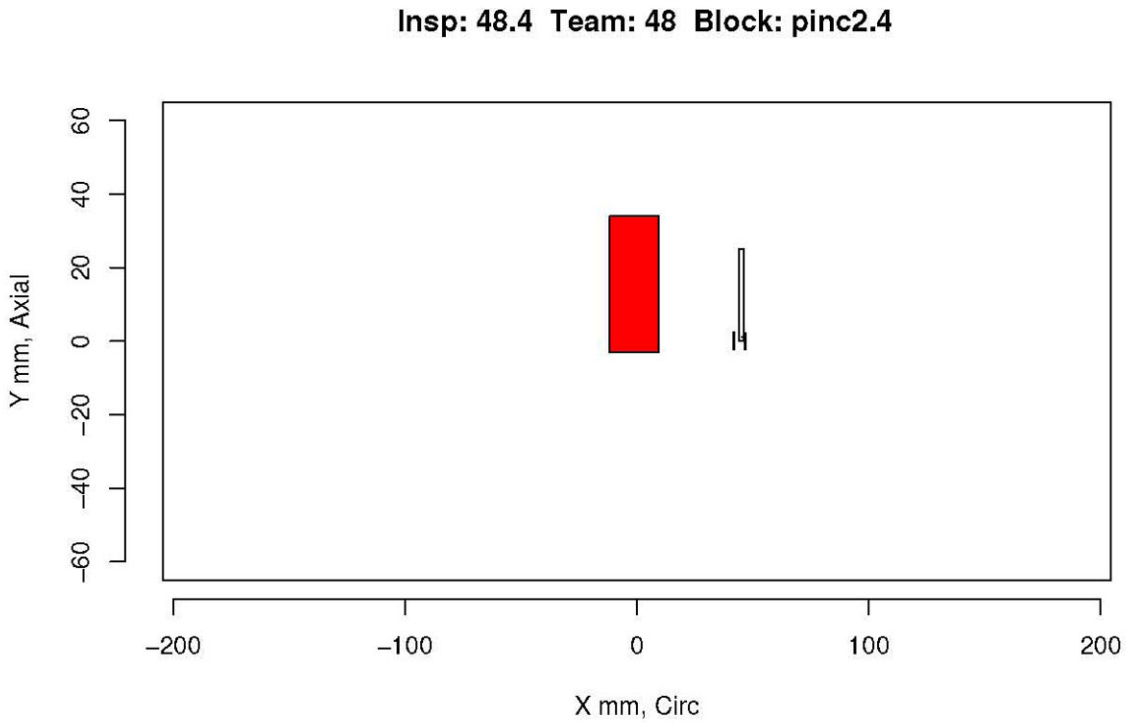
Insp: 48.4 Team: 48 Block: pinc2.4
Y mm, Axial
60
40
20
0
−20
−40
−60
−200
−100
0
100
200
X mm, Circ

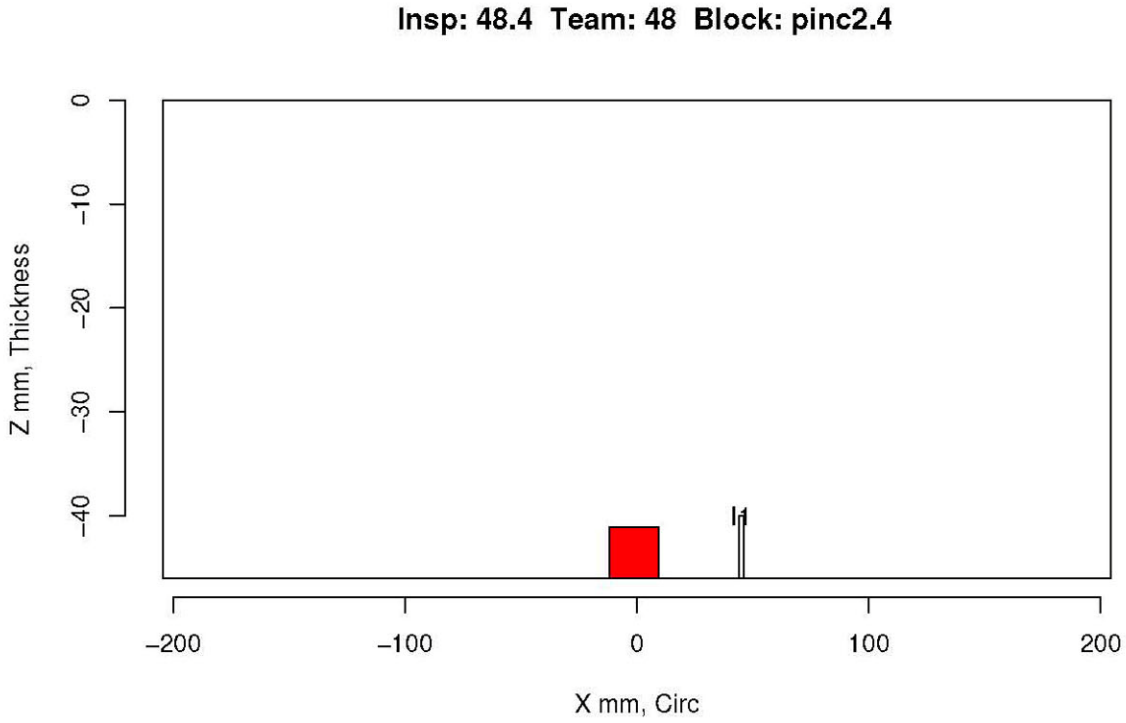
Insp: 48.4 Team: 48 Block: pinc2.4
Z mm, Thickness
0
−10
−20
−30
−40
−200
−100
0
100
200
X mm, Circ

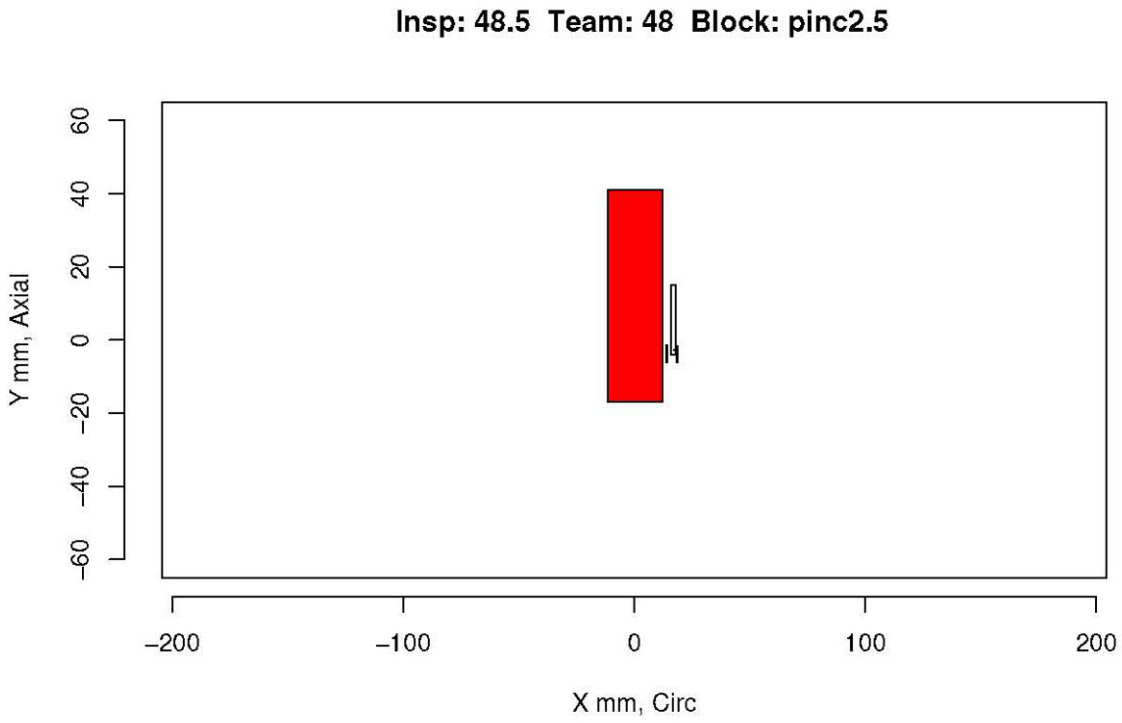
Insp: 48.5 Team: 48 Block: pinc2.5
Y mm, Axial
60
40
20
0
−20
−40
−60
−200
−100
0
100
200
X mm, Circ

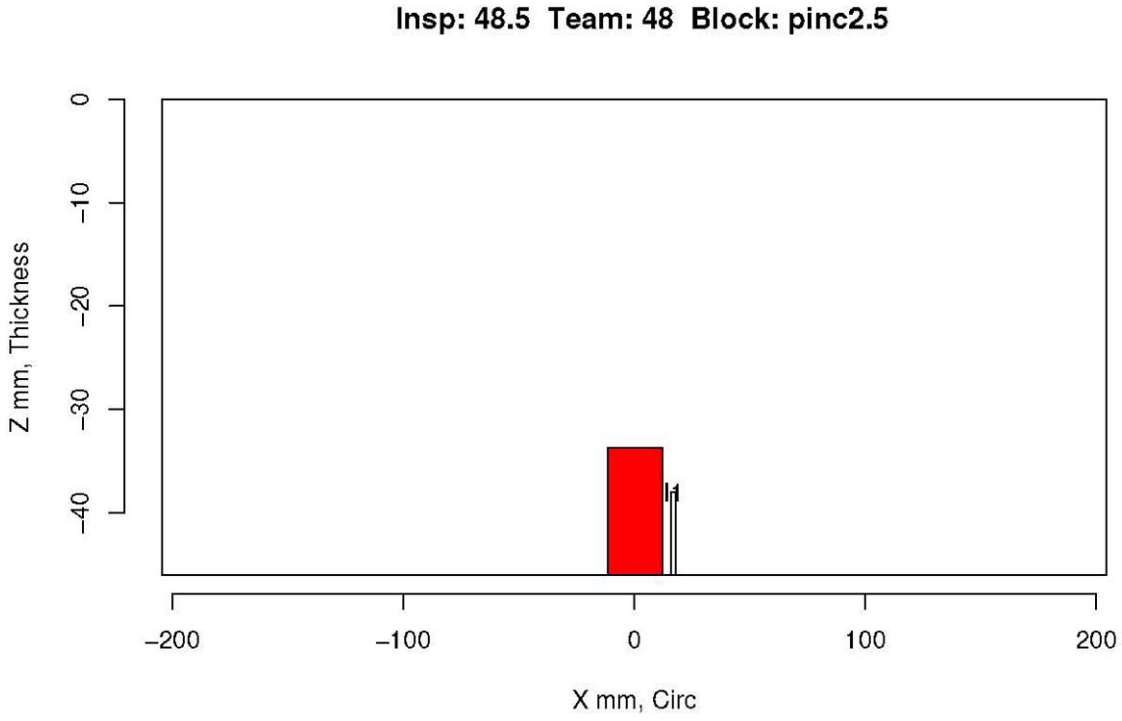
Insp: 48.5 Team: 48 Block: pinc2.5
Z mm, Thickness
0
−10
−20
−30
−40
−200
−100
0
100
200
X mm, Circ

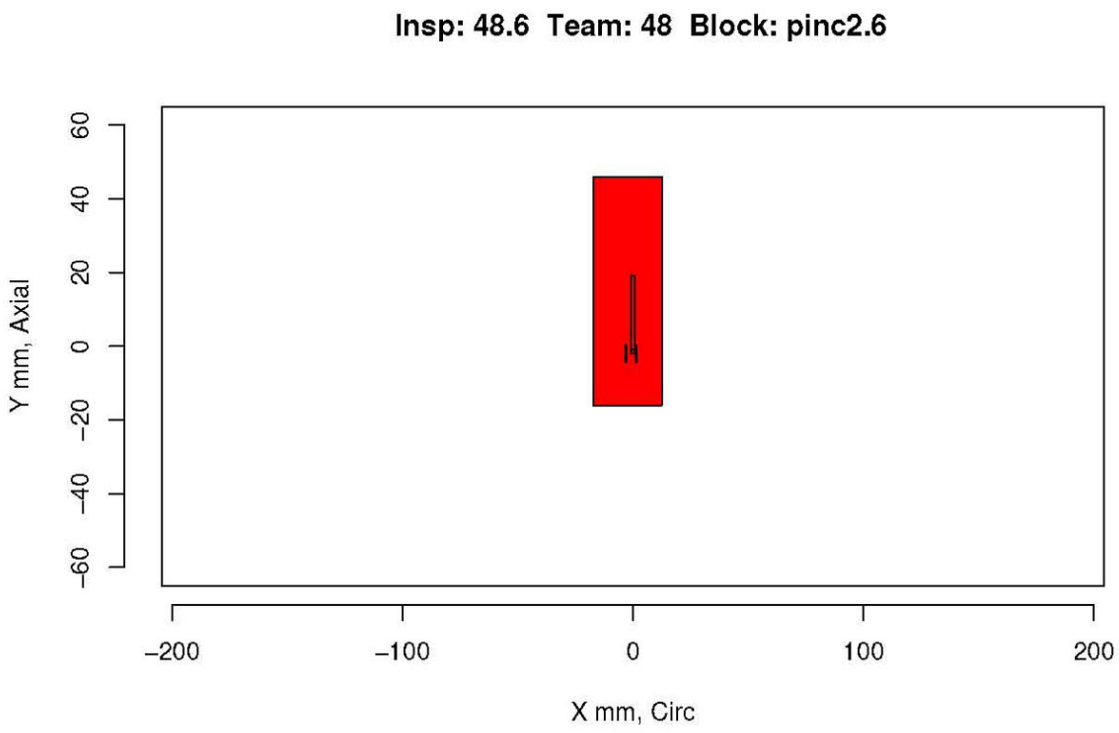
Insp: 48.6 Team: 48 Block: pinc2.6
Y mm, Axial
60
40
20
0
−20
−40
−60
−200
−100
0
100
200
X mm, Circ

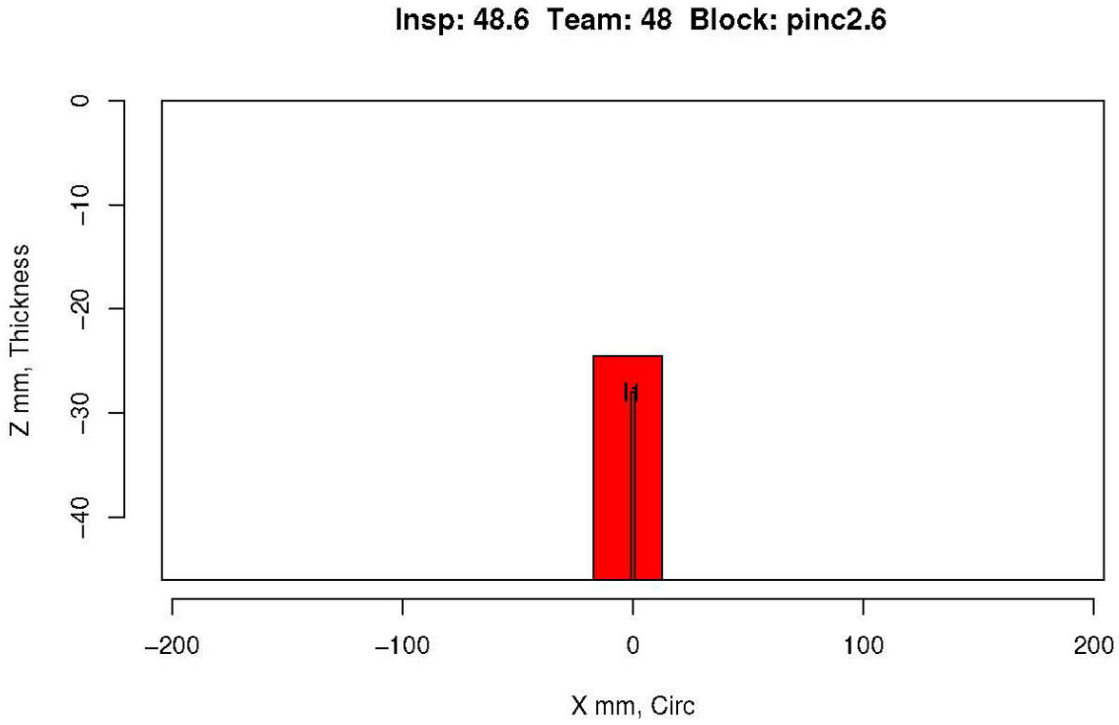
Insp: 48.6 Team: 48 Block: pinc2.6
Z mm, Thickness
0
−10
−20
−30
−40
−200
−100
0
100
200
X mm, Circ

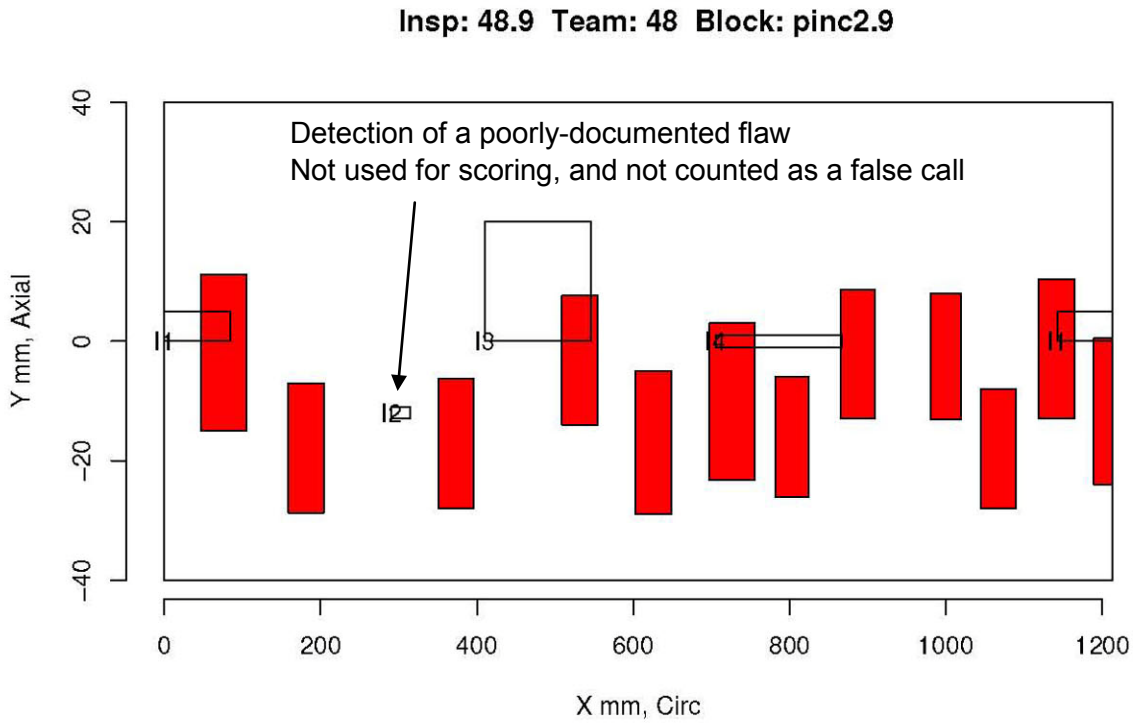
Insp: 48.9 Team: 48 Block: pinc2.9
Detection of a poorly-documented flaw
Not used for scoring, and not counted as a false call
Y mm, Axial
40
20
0
-20
-40
I1
I2
I3
I4
I1
0
200
400
600
800
1000
1200
X mm, Circ

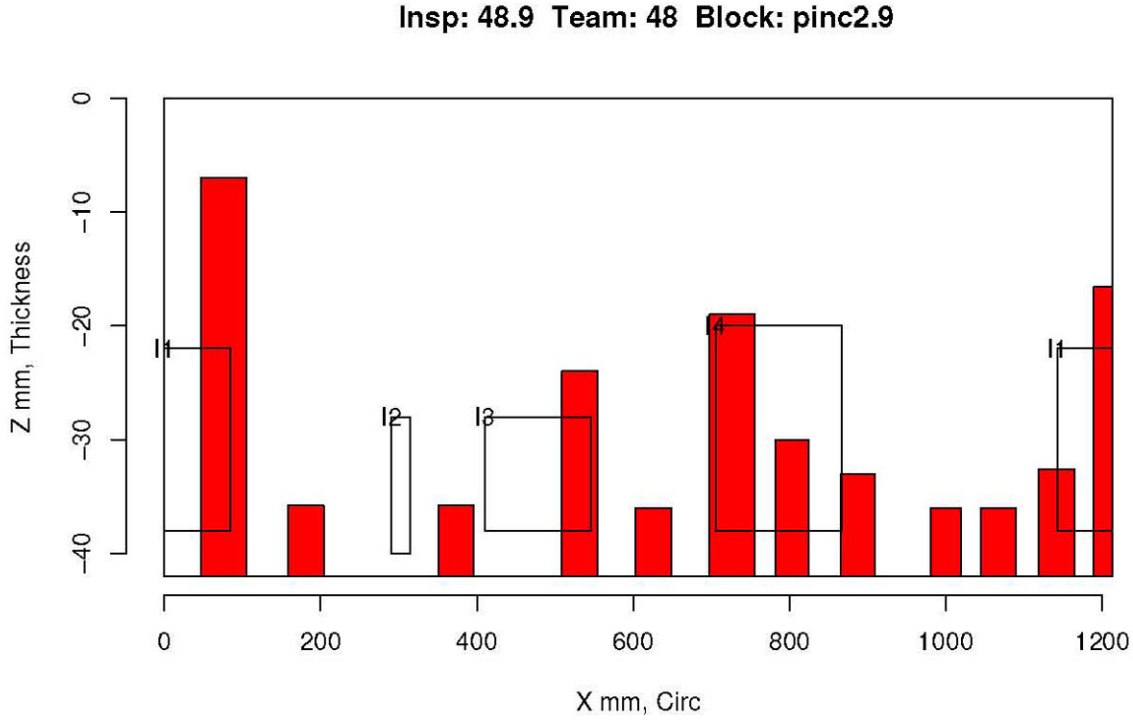
Insp: 48.9 Team: 48 Block: pinc2.9
Z mm, Thickness
0
-10
-20
-30
-40
I1
I2
I3
I4
I1
0
200
400
600
800
1000
1200
X mm, Circ

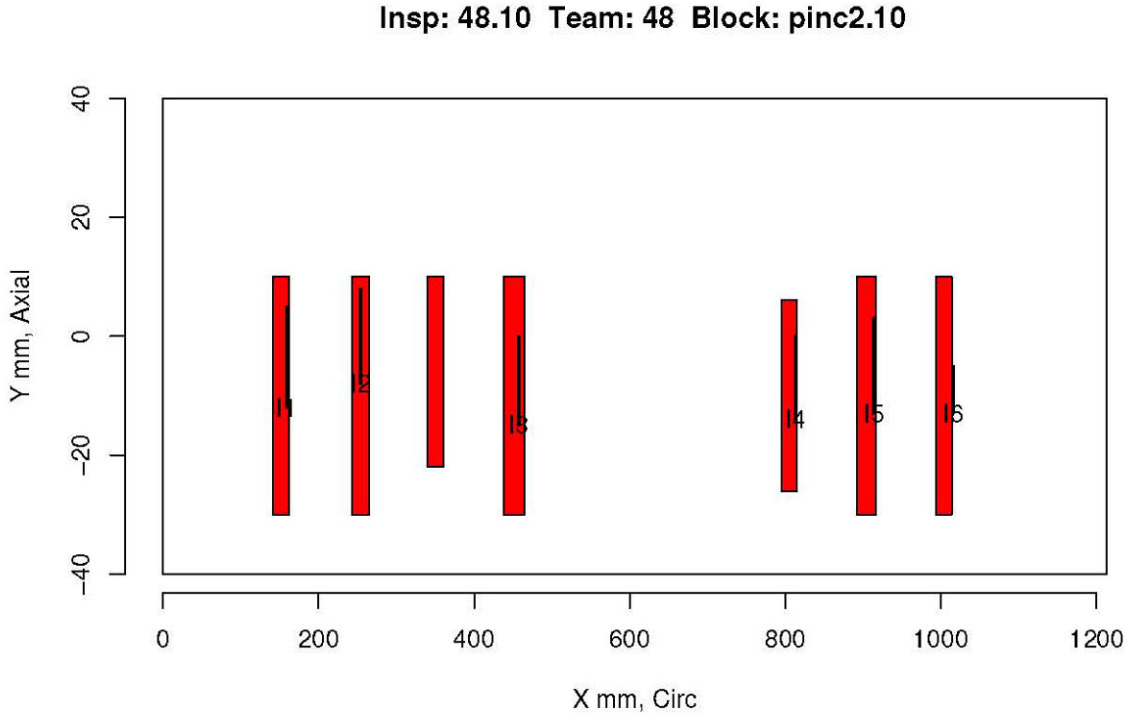
Insp: 48.10 Team: 48 Block: pinc2.10
Y mm, Axial
40
20
0
-20
-40
I1
I2
I3
I4
I5
I6
0
200
400
600
800
1000
1200
X mm, Circ

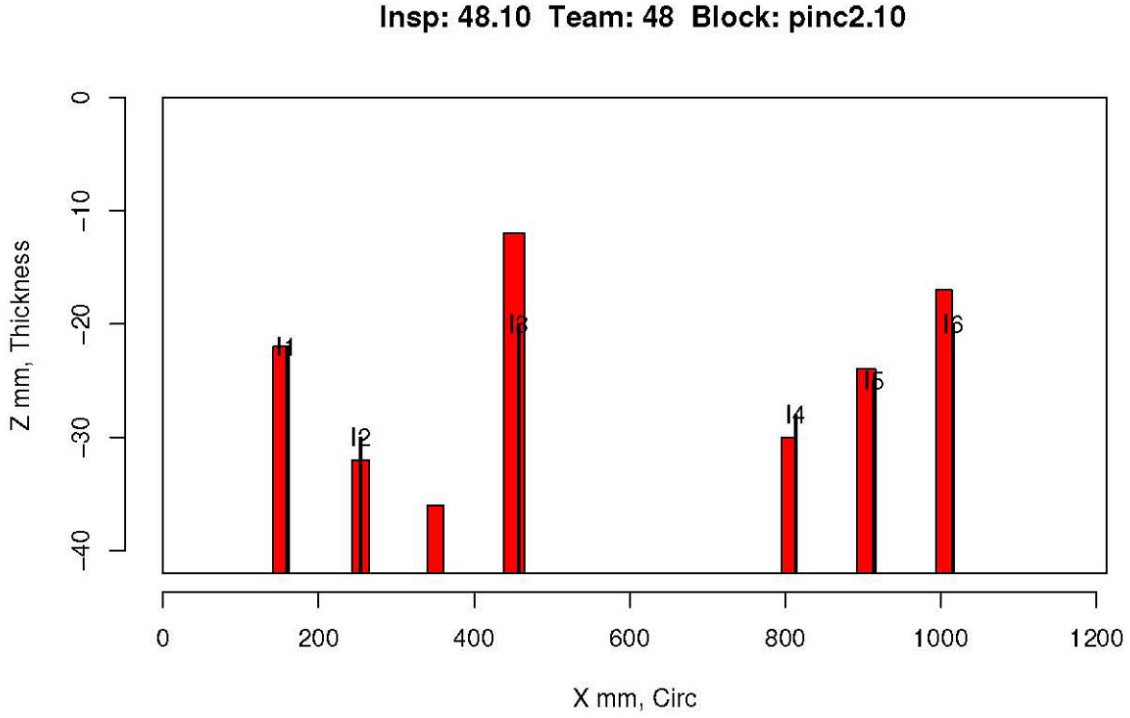
Insp: 48.10 Team: 48 Block: pinc2.10
Z mm, Thickness
0
-10
-20
-30
-40
I1
I2
I3
I4
I5
I6
0
200
400
600
800
1000
1200
X mm, Circ

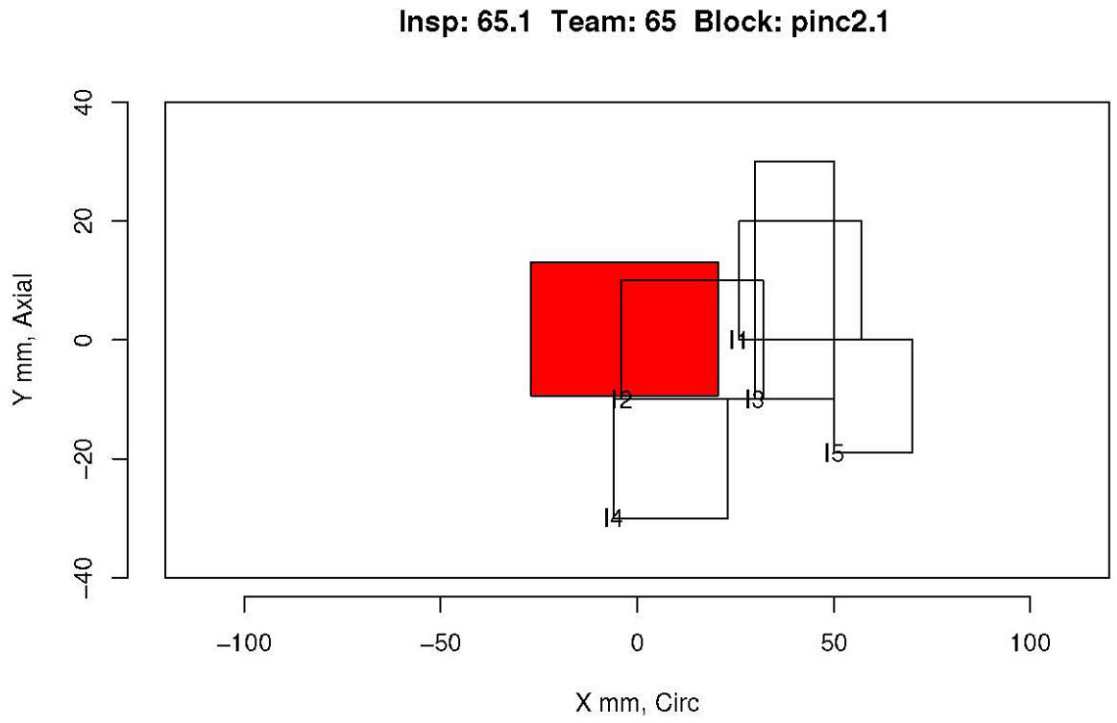
Insp: 65.1 Team: 65 Block: pinc2.1
Y mm, Axial
40
20
0
−20
−40
−100
−50
0
50
100
X mm, Circ
I1
I2
I3
I4
I5

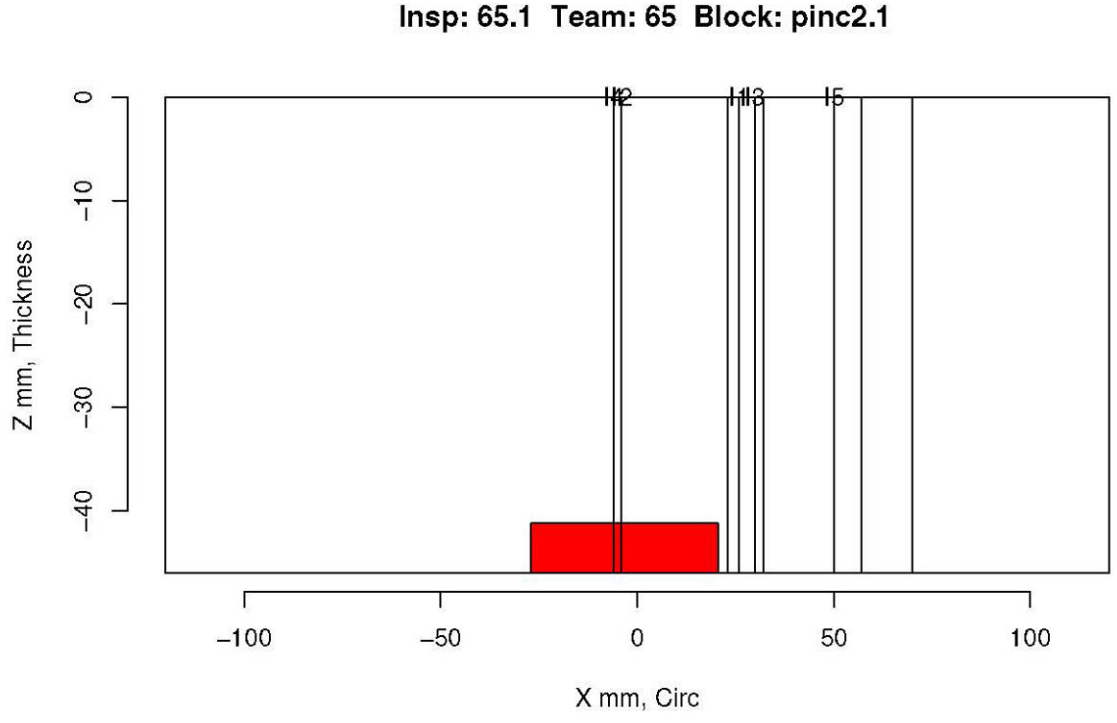
Insp: 65.1 Team: 65 Block: pinc2.1
Z mm, Thickness
0
−10
−20
−30
−40
−100
−50
0
50
100
X mm, Circ
I1
I2
I3
I5

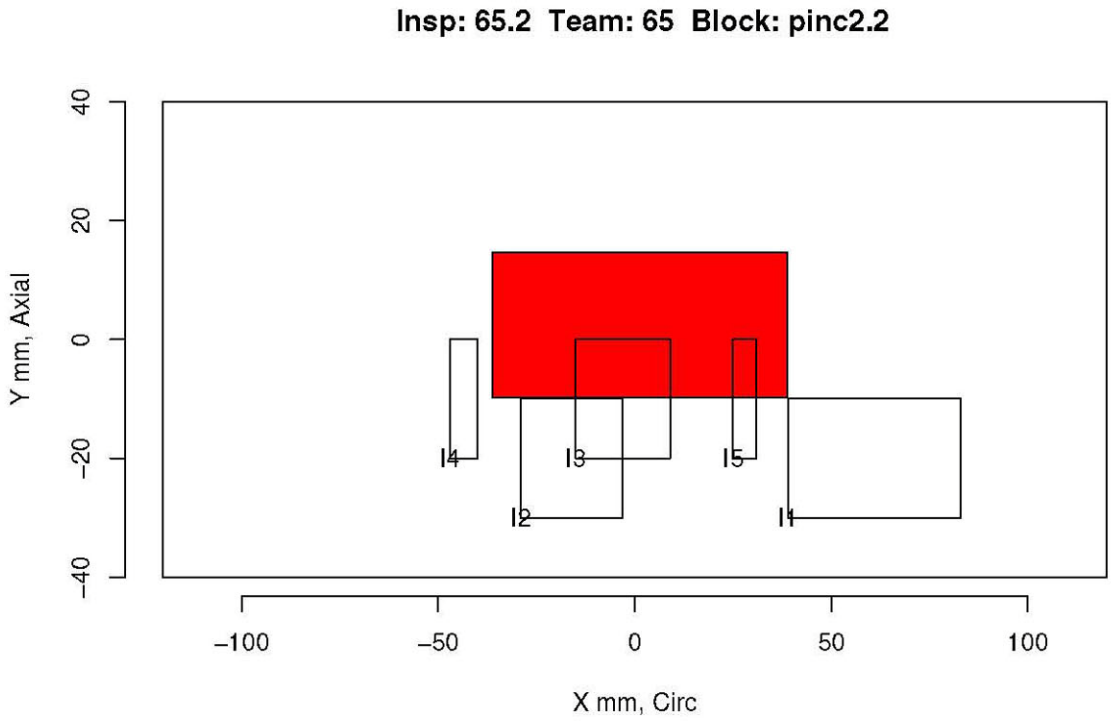
Insp: 65.2 Team: 65 Block: pinc2.2
Y mm, Axial
40
20
0
−20
−40
I4
I3
I5
I2
I1
−100
−50
0
50
100
X mm, Circ

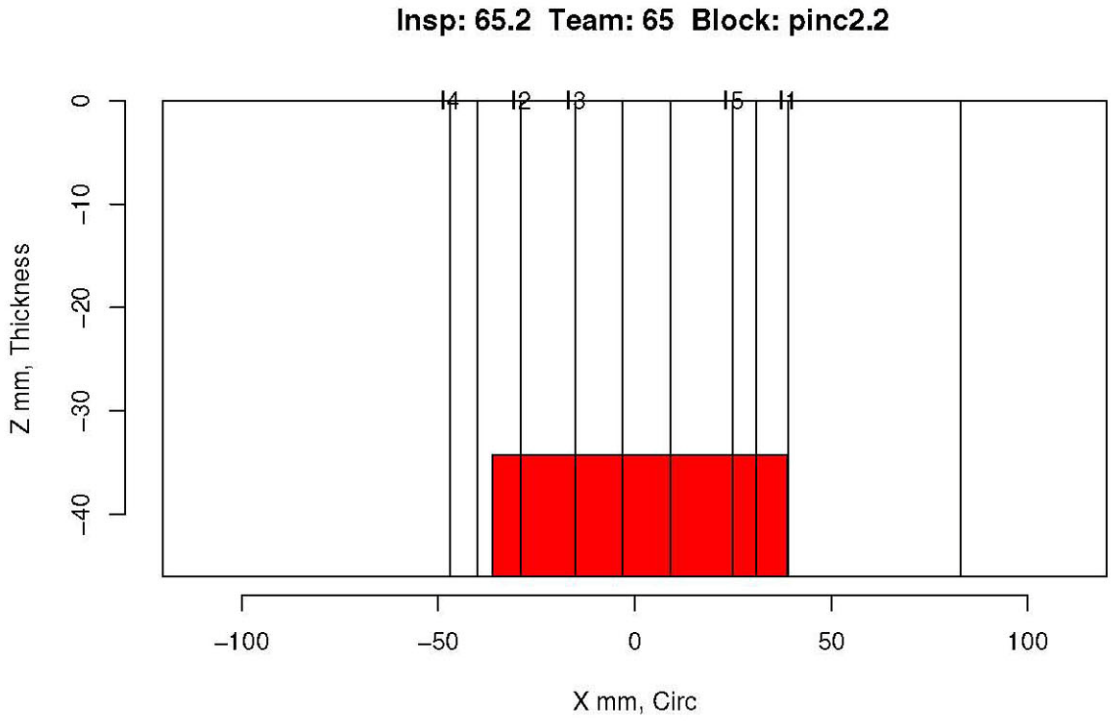
Insp: 65.2 Team: 65 Block: pinc2.2
Z mm, Thickness
0
−10
−20
−30
−40
I4
I2
I3
I5
I1
−100
−50
0
50
100
X mm, Circ

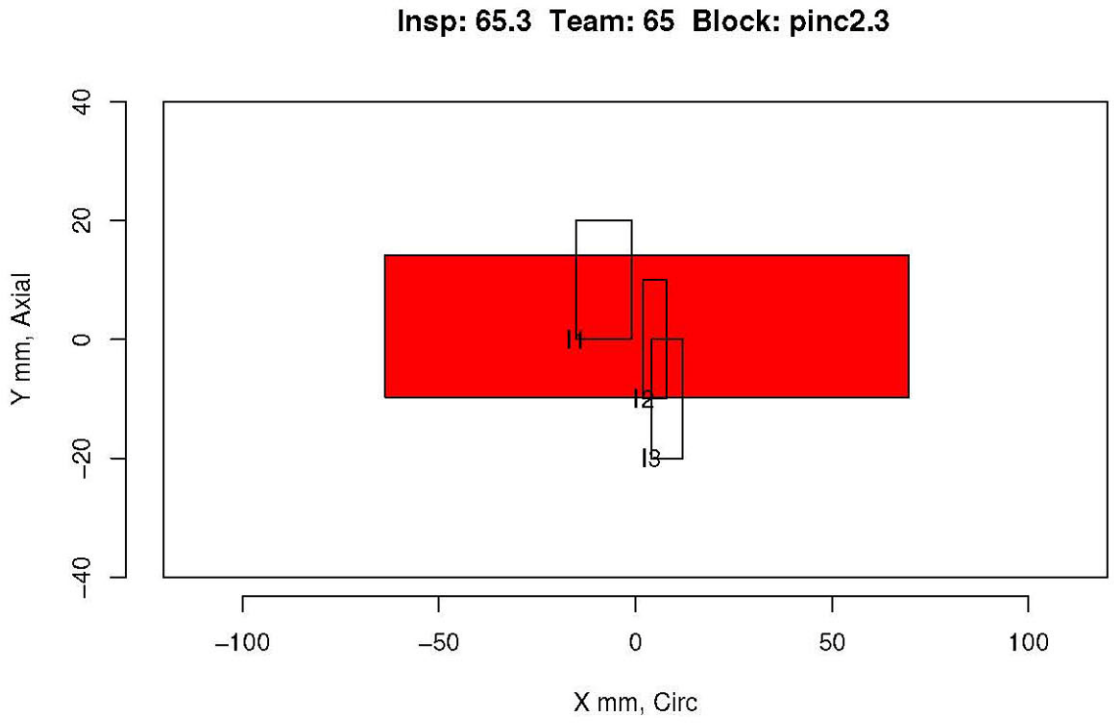
Insp: 65.3 Team: 65 Block: pinc2.3
Y mm, Axial
40
20
0
−20
−40
I1
I2
I3
−100
−50
0
50
100
X mm, Circ

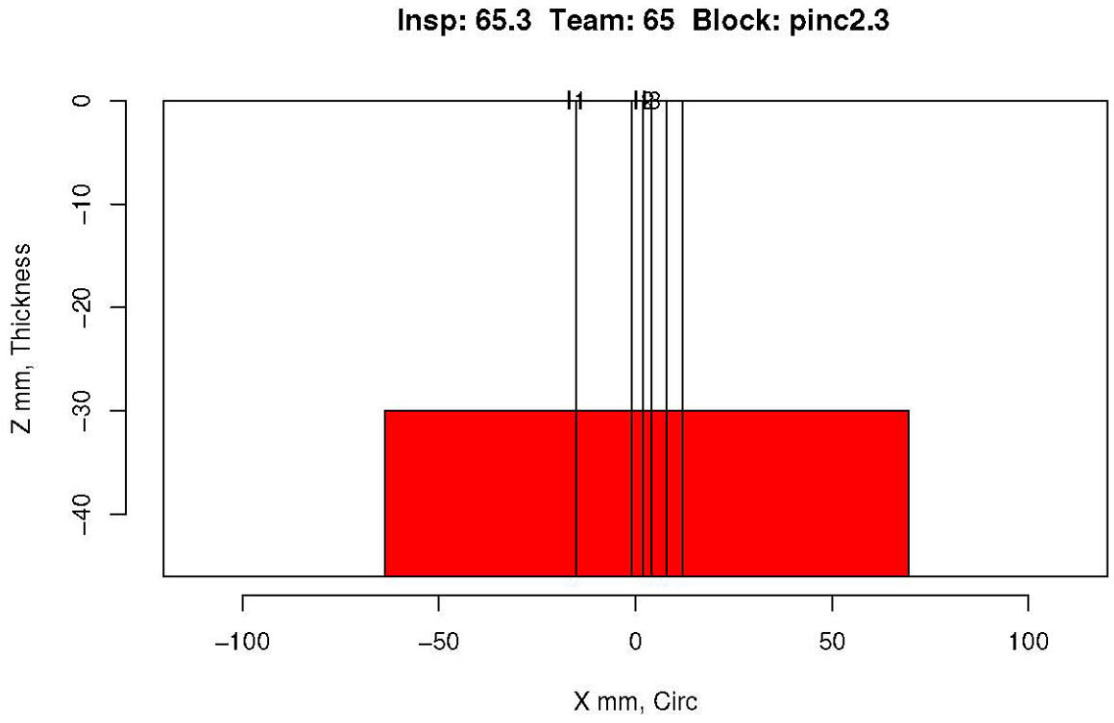
Insp: 65.3 Team: 65 Block: pinc2.3
Z mm, Thickness
0
−10
−20
−30
−40
I1
I2
I3
−100
−50
0
50
100
X mm, Circ

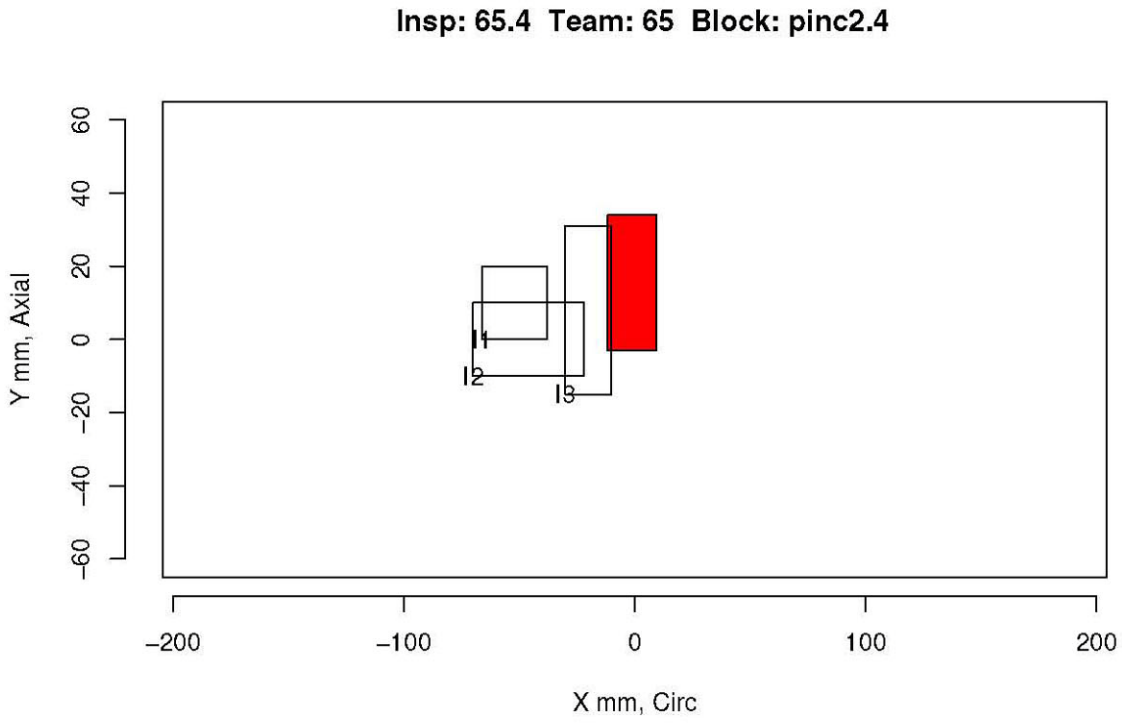
Insp: 65.4 Team: 65 Block: pinc2.4
Y mm, Axial
60
40
20
0
−20
−40
−60
I1
I2
I3
−200
−100
0
100
200
X mm, Circ

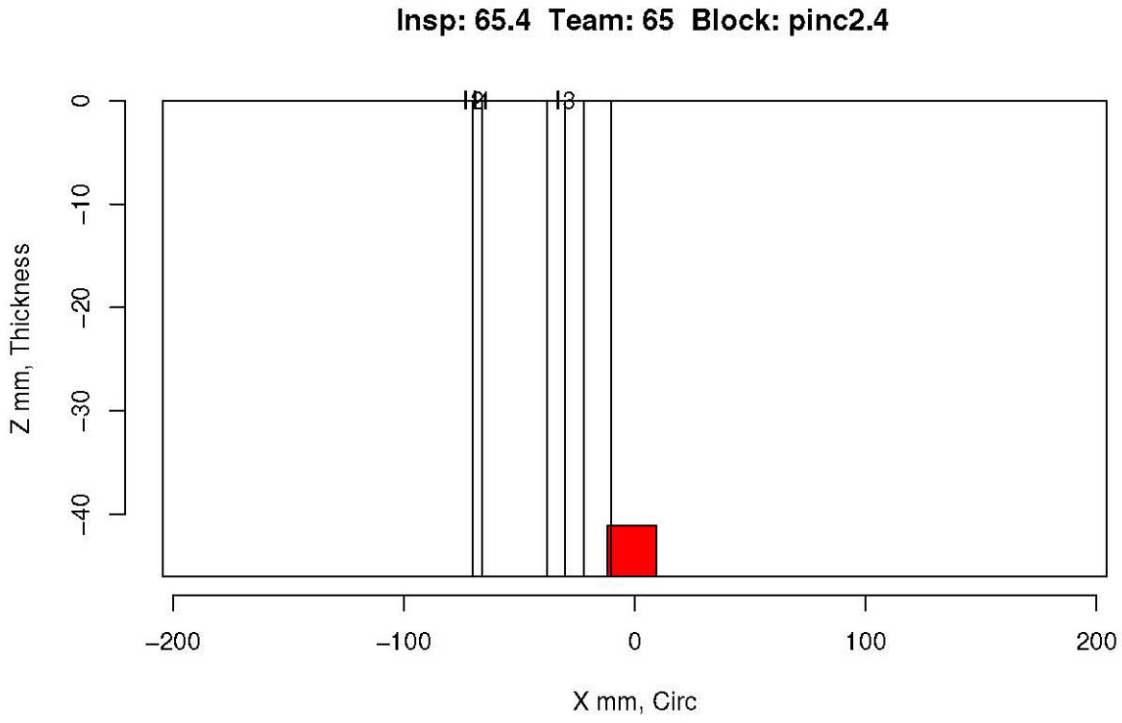
Insp: 65.4 Team: 65 Block: pinc2.4
Z mm, Thickness
0
−10
−20
−30
−40
I2
I1
I3
−200
−100
0
100
200
X mm, Circ

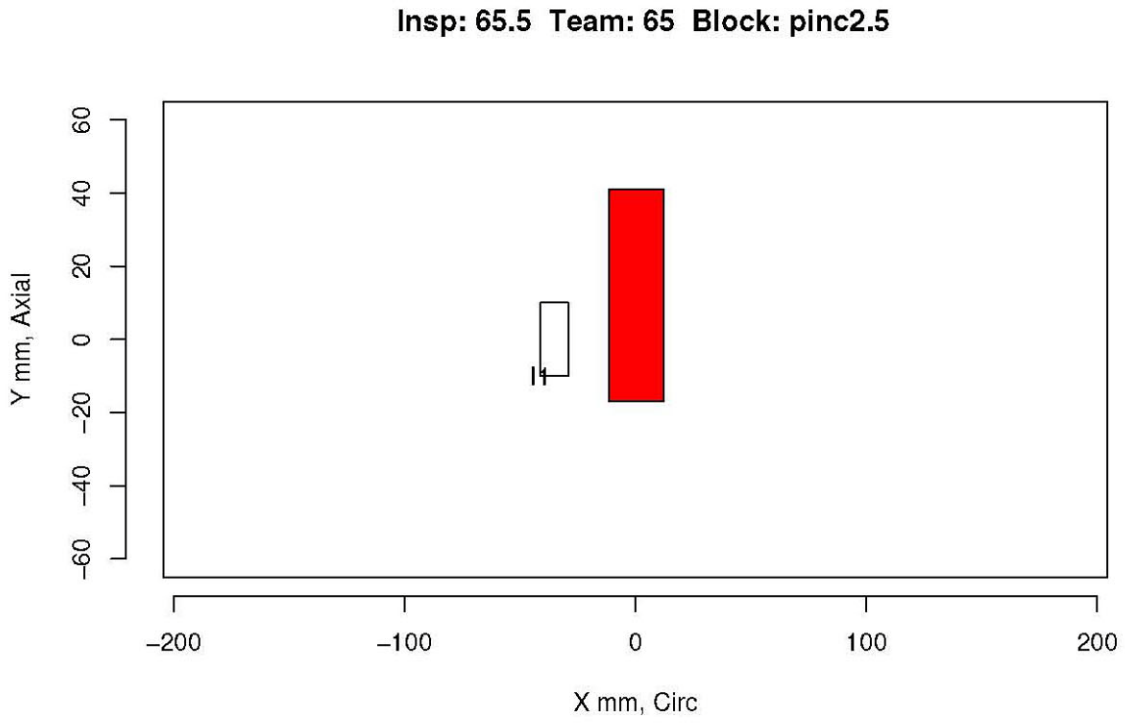
Insp: 65.5 Team: 65 Block: pinc2.5
Y mm, Axial
60
40
20
0
−20
−40
−60
−200
−100
0
100
200
X mm, Circ

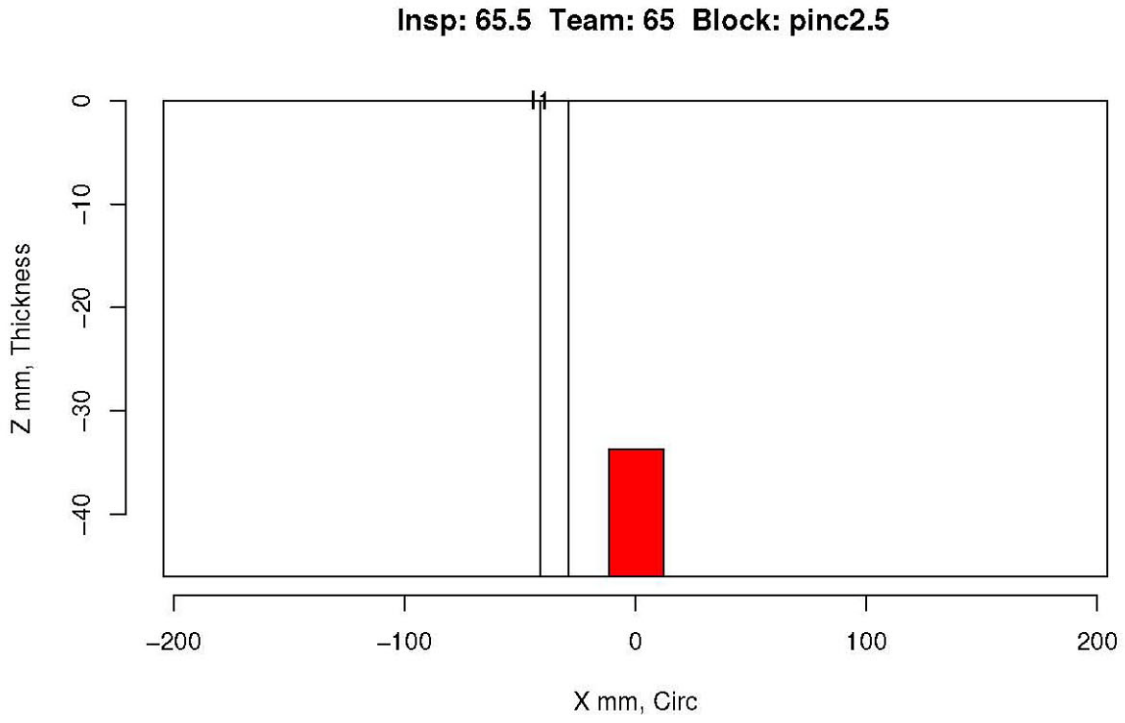
Insp: 65.5 Team: 65 Block: pinc2.5
Z mm, Thickness
0
−10
−20
−30
−40
−200
−100
0
100
200
X mm, Circ

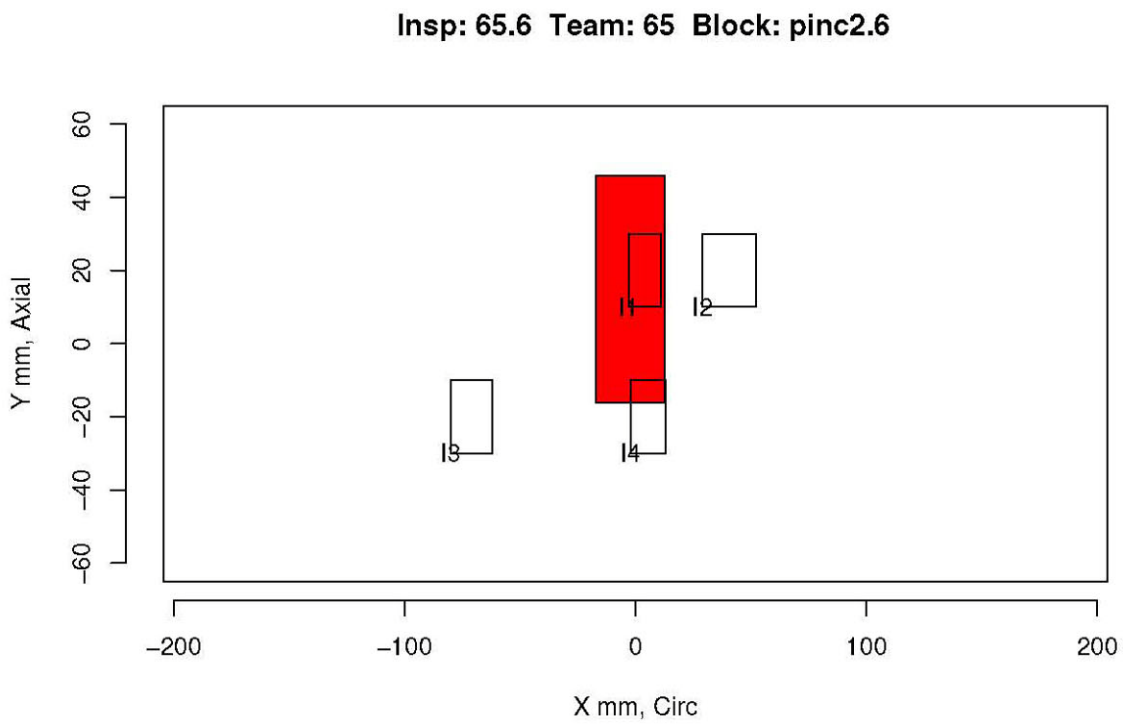
Insp: 65.6 Team: 65 Block: pinc2.6
Y mm, Axial
60
40
20
0
−20
−40
−60
I1
I2
I3
I4
−200
−100
0
100
200
X mm, Circ

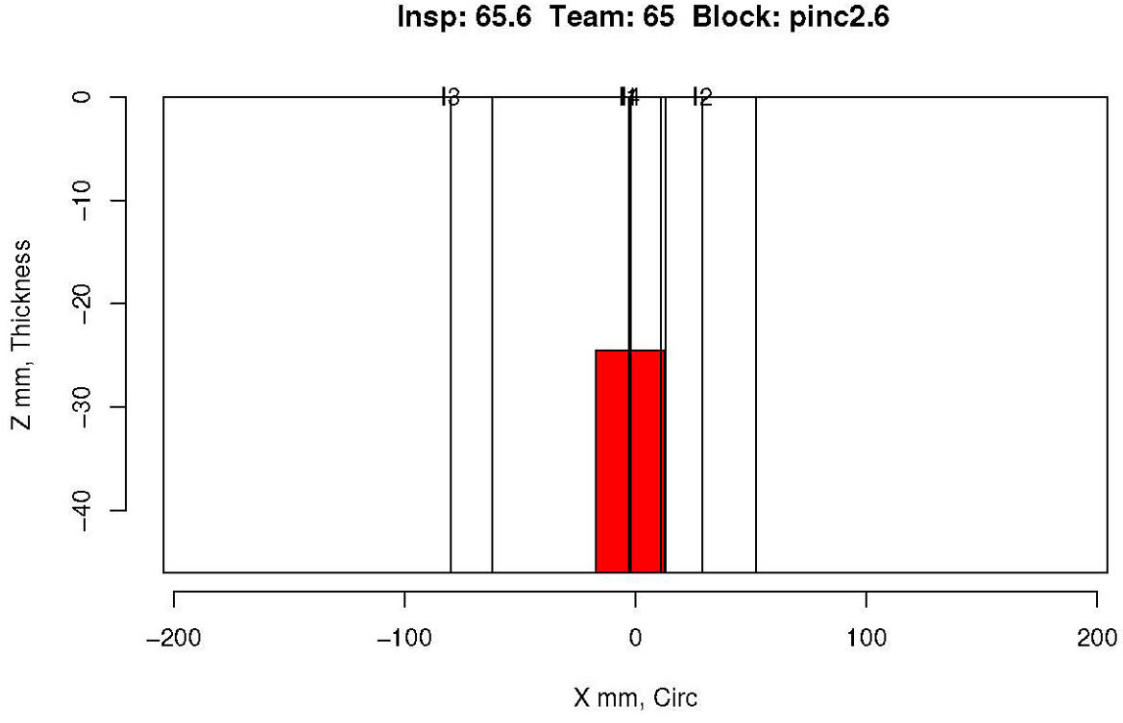
Insp: 65.6 Team: 65 Block: pinc2.6
Z mm, Thickness
0
−10
−20
−30
−40
I3
I1
I4
I2
−200
−100
0
100
200
X mm, Circ

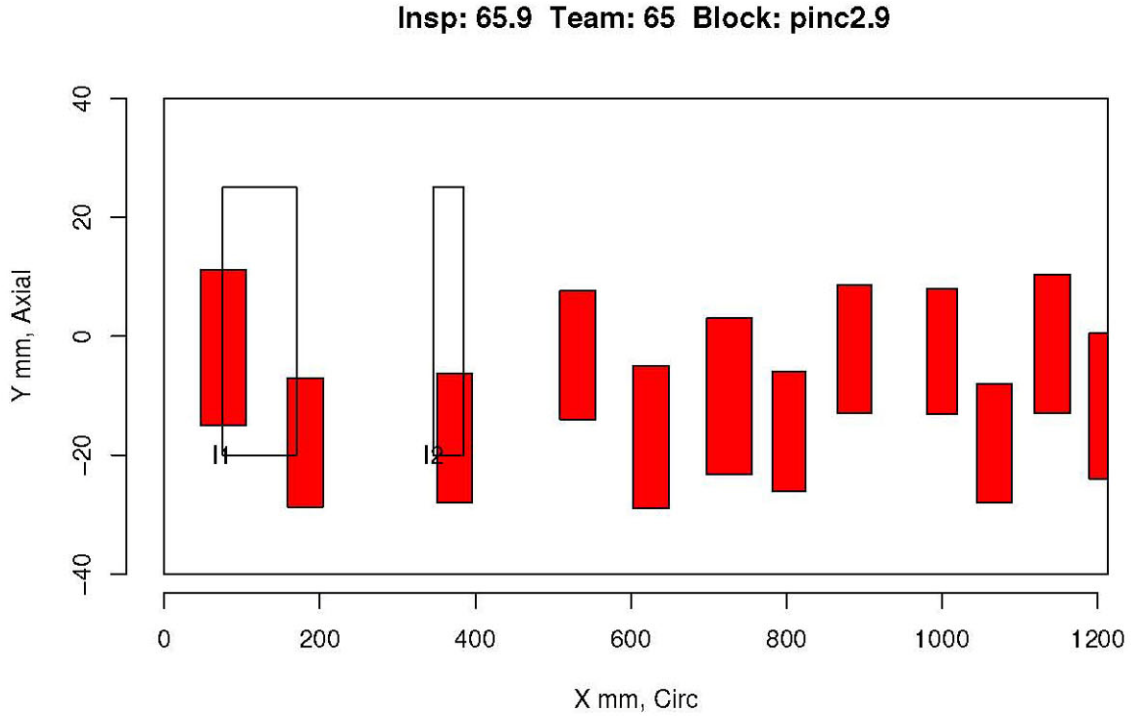
Insp: 65.9 Team: 65 Block: pinc2.9
Y mm, Axial
40
20
0
-20
-40
I1
I2
0
200
400
600
800
1000
1200
X mm, Circ

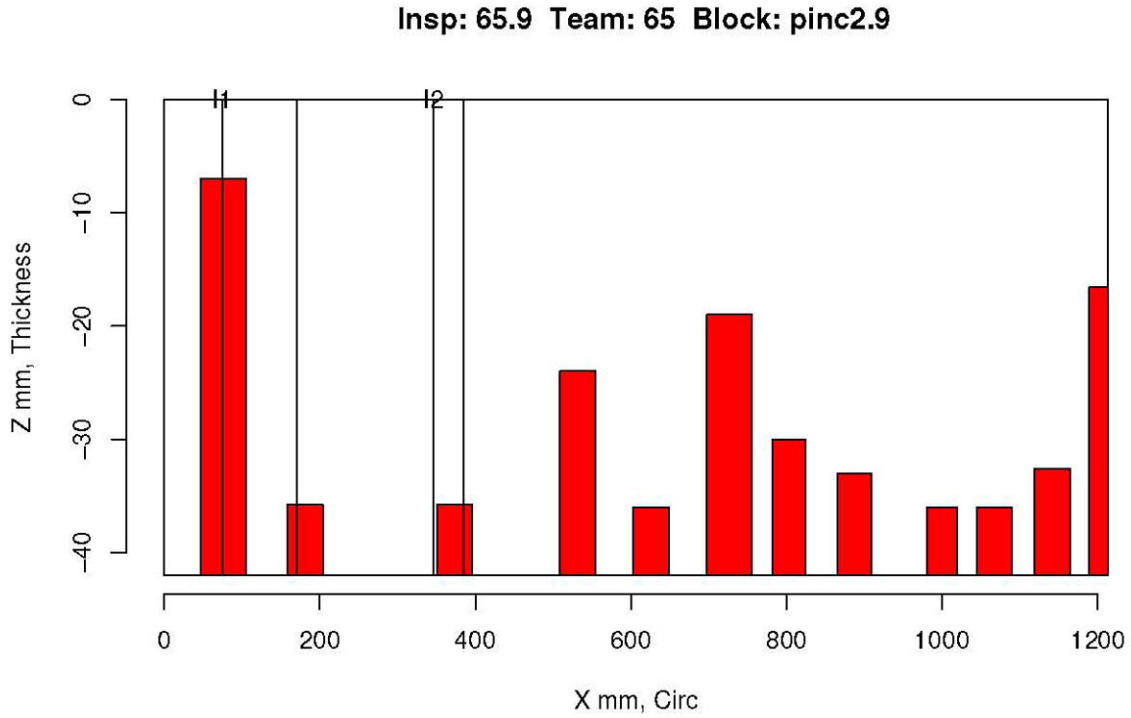
Insp: 65.9 Team: 65 Block: pinc2.9
Z mm, Thickness
0
-10
-20
-30
-40
I1
I2
0
200
400
600
800
1000
1200
X mm, Circ

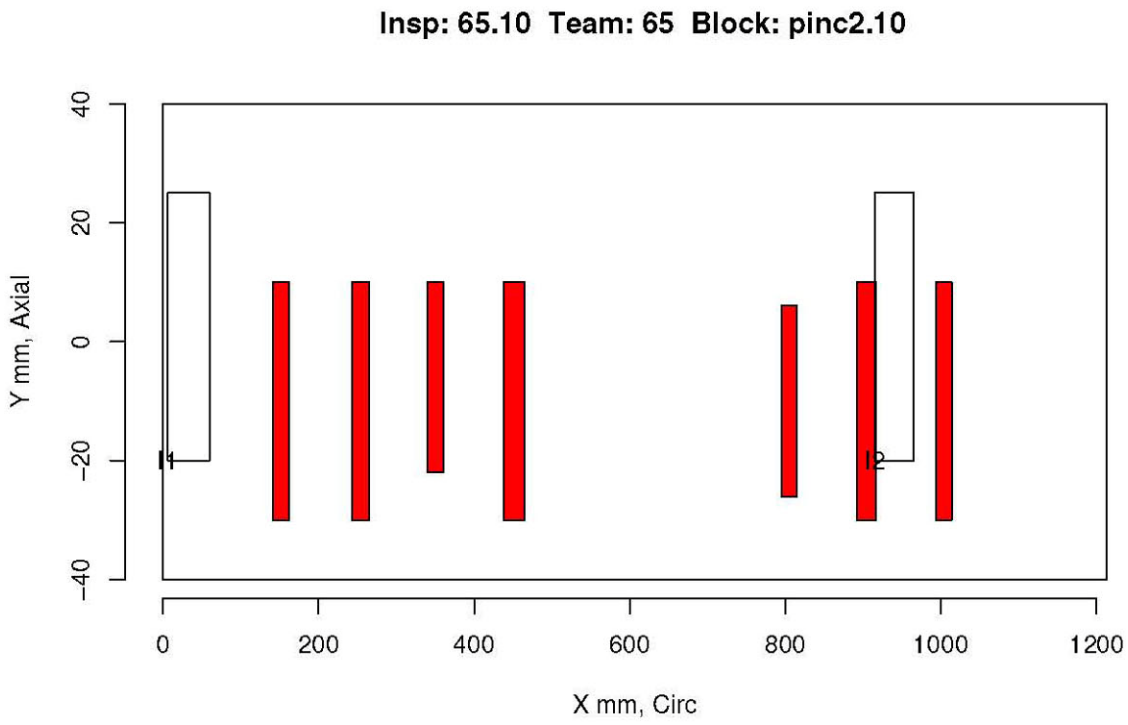
Insp: 65.10 Team: 65 Block: pinc2.10
Y mm, Axial
40
20
0
-20
-40
I1
I2
0
200
400
600
800
1000
1200
X mm, Circ

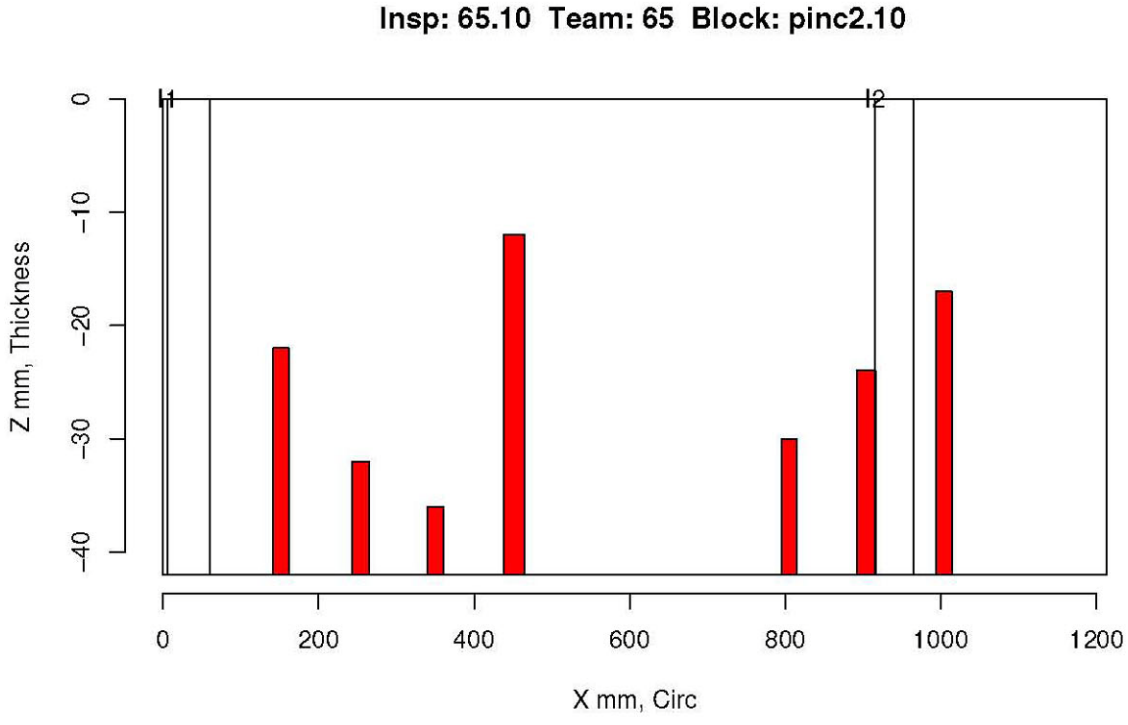
Insp: 65.10 Team: 65 Block: pinc2.10
Z mm, Thickness
0
-10
-20
-30
-40
I1
I2
0
200
400
600
800
1000
1200
X mm, Circ

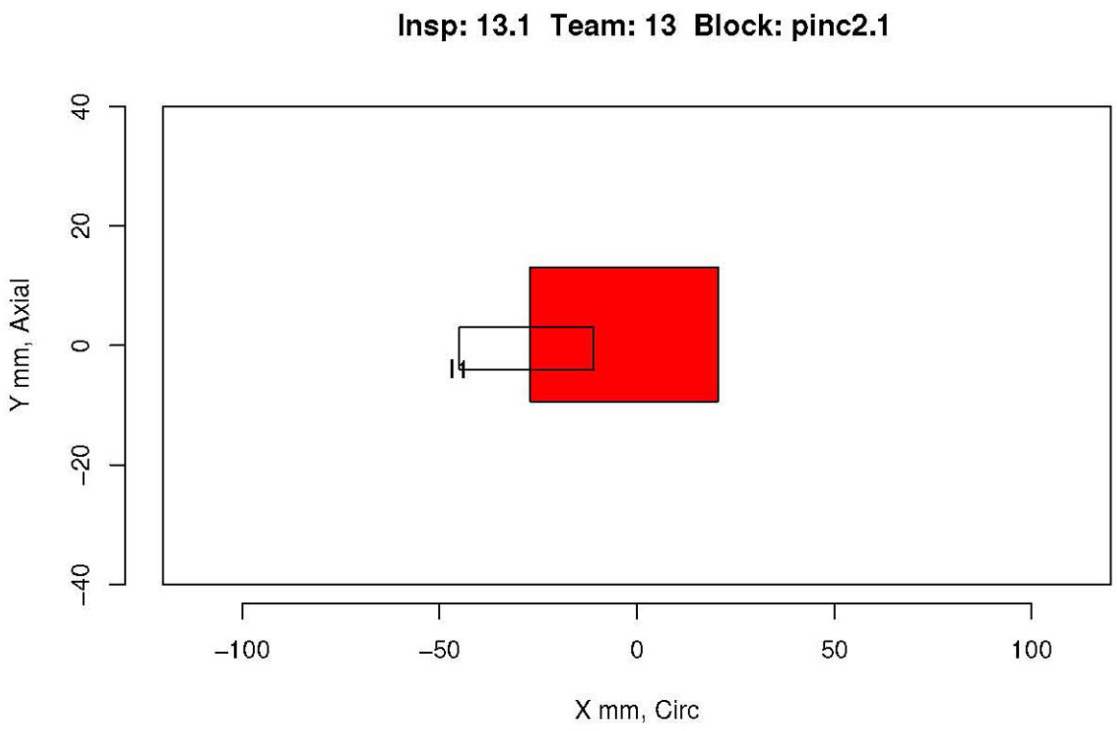
Insp: 13.1 Team: 13 Block: pinc2.1
Y mm, Axial
40
20
0
−20
−40
−100
−50
0
50
100
X mm, Circ

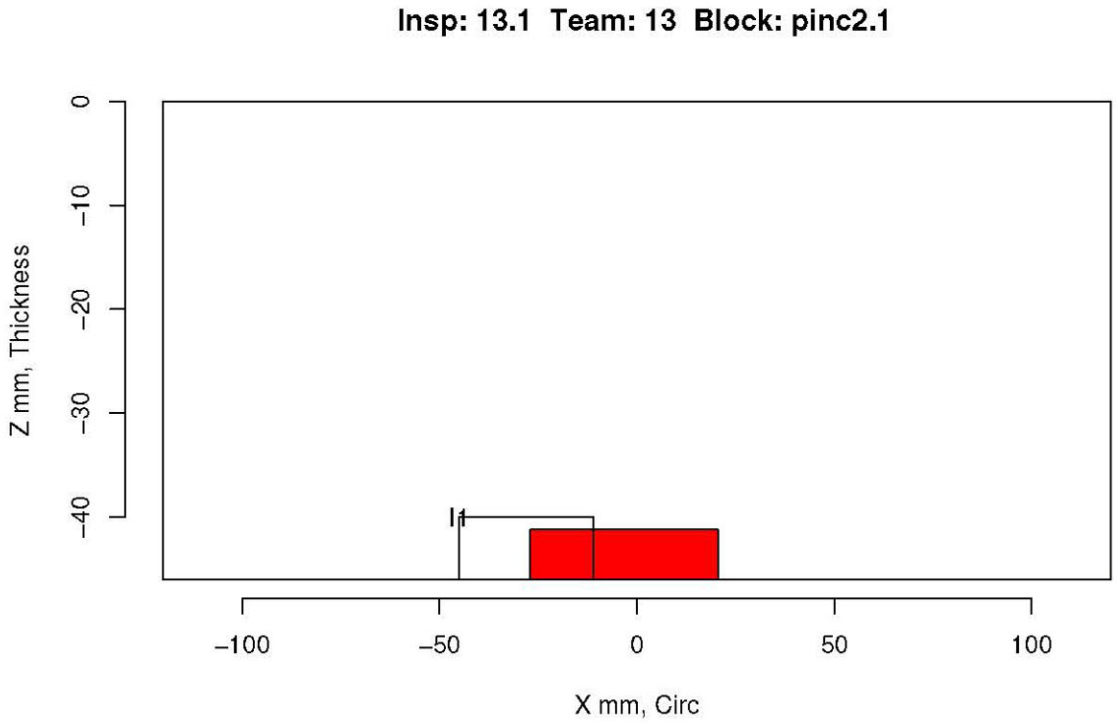
Insp: 13.1 Team: 13 Block: pinc2.1
Z mm, Thickness
0
−10
−20
−30
−40
−100
−50
0
50
100
X mm, Circ

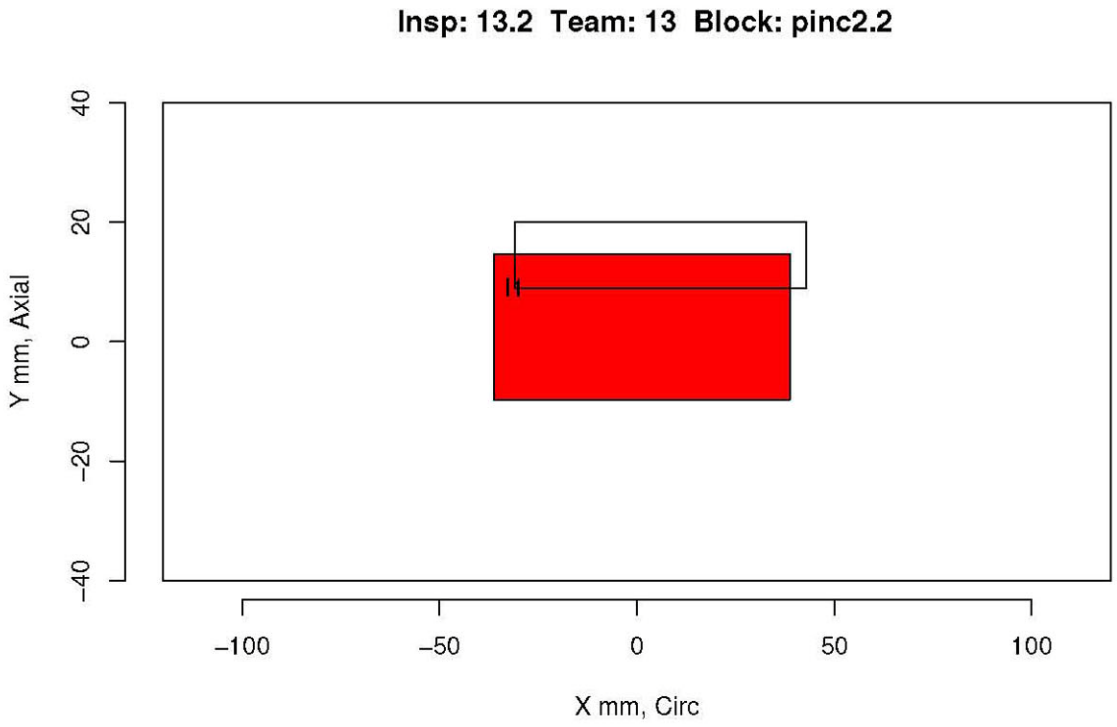
Insp: 13.2 Team: 13 Block: pinc2.2
Y mm, Axial
40
20
0
-20
-40
-100
-50
0
50
100
X mm, Circ

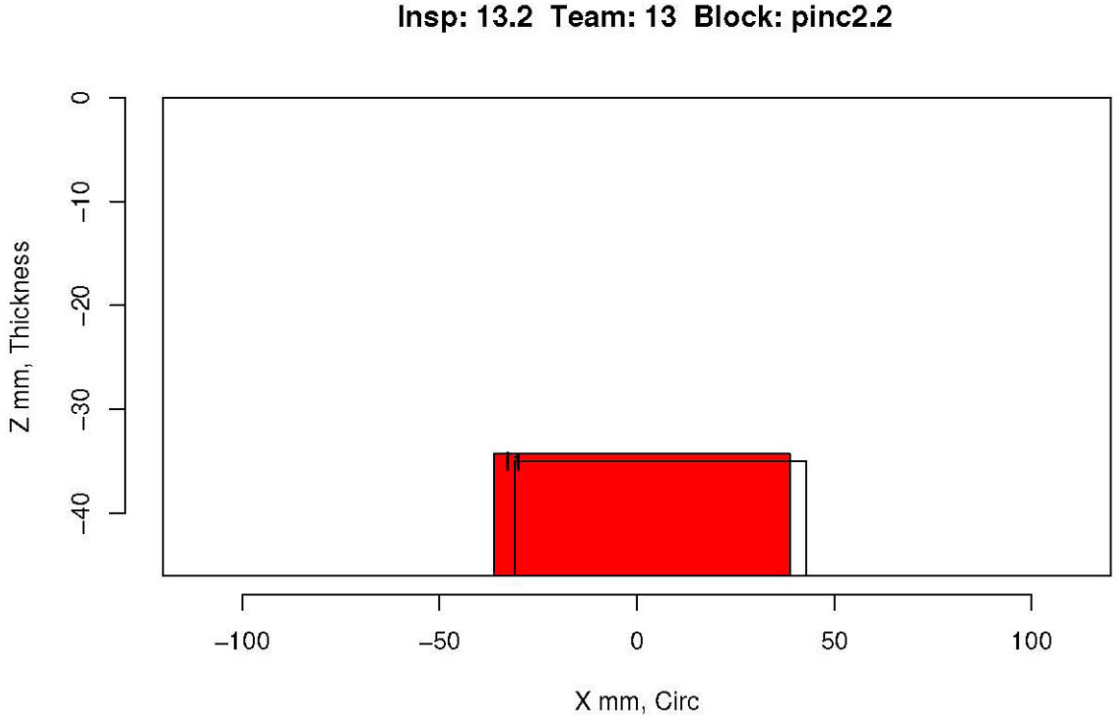
Insp: 13.2 Team: 13 Block: pinc2.2
Z mm, Thickness
0
-10
-20
-30
-40
-100
-50
0
50
100
X mm, Circ

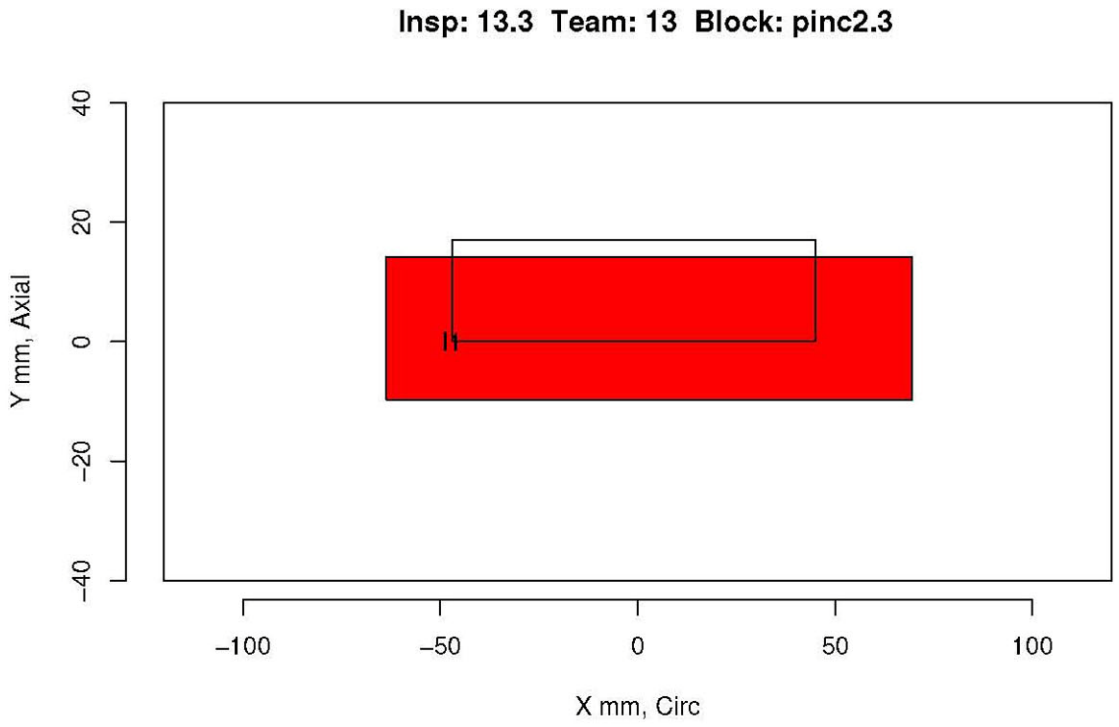
Insp: 13.3 Team: 13 Block: pinc2.3
Y mm, Axial
40
20
0
−20
−40
−100
−50
0
50
100
X mm, Circ

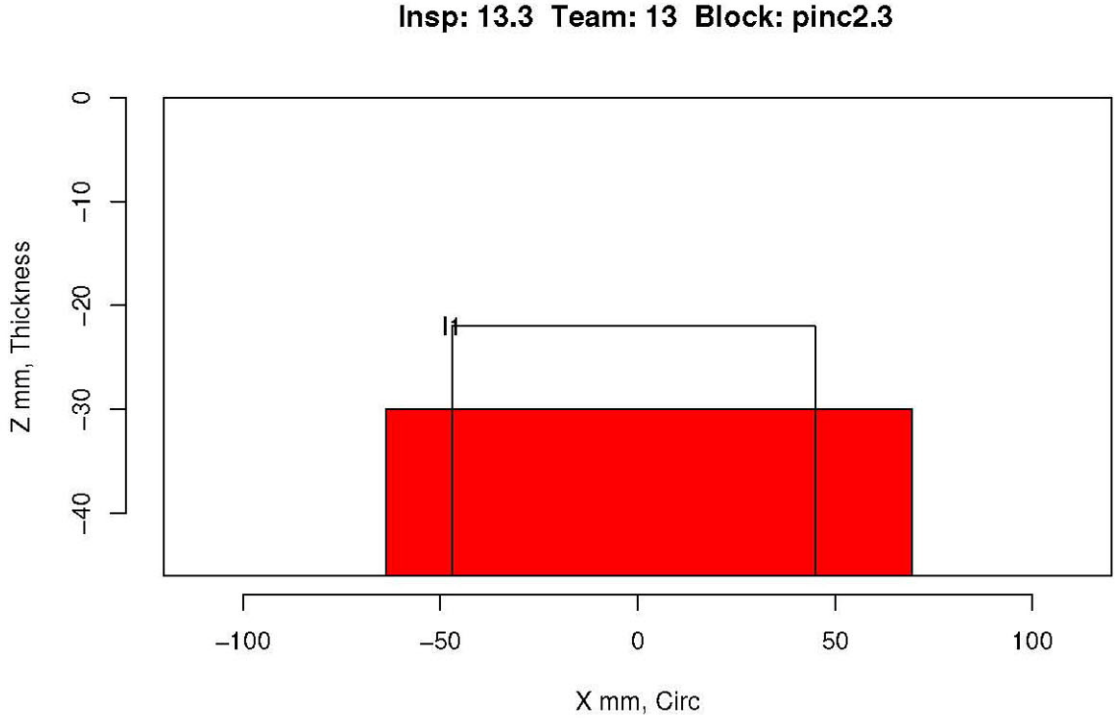
Insp: 13.3 Team: 13 Block: pinc2.3
Z mm, Thickness
0
−10
−20
−30
−40
−100
−50
0
50
100
X mm, Circ

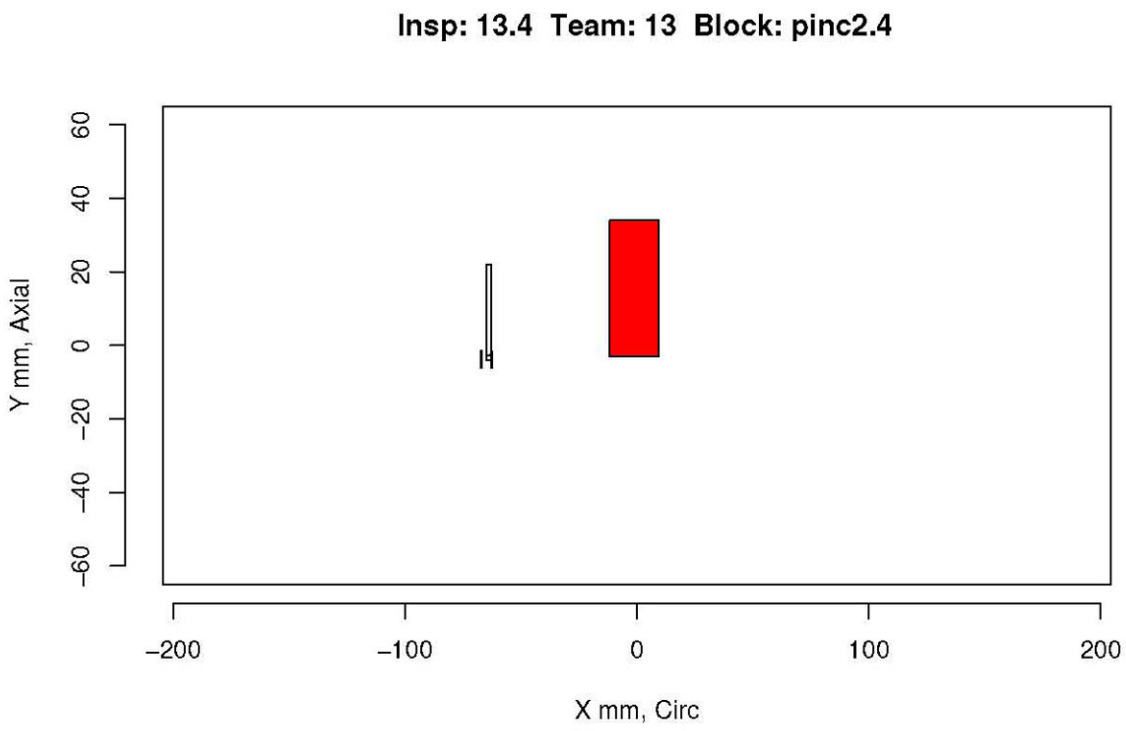
Insp: 13.4 Team: 13 Block: pinc2.4
Y mm, Axial
60
40
20
0
−20
−40
−60
−200
−100
0
100
200
X mm, Circ

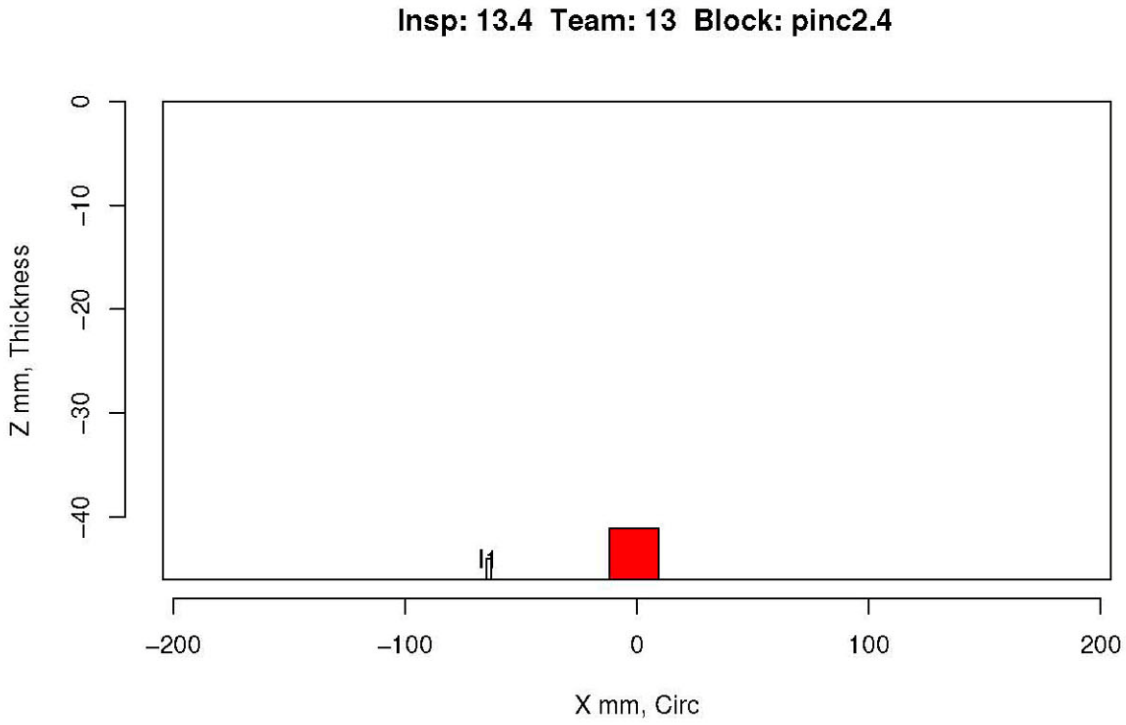
Insp: 13.4 Team: 13 Block: pinc2.4
Z mm, Thickness
0
−10
−20
−30
−40
−200
−100
0
100
200
X mm, Circ

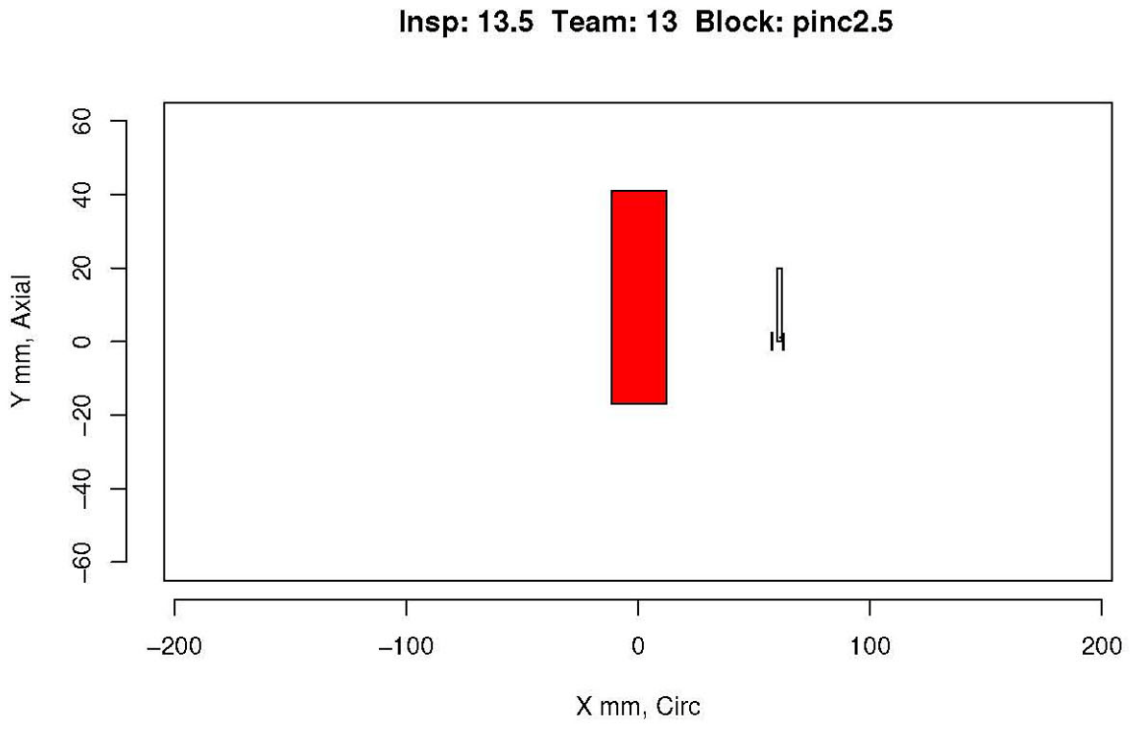
Insp: 13.5 Team: 13 Block: pinc2.5
Y mm, Axial
60
40
20
0
−20
−40
−60
−200
−100
0
100
200
X mm, Circ

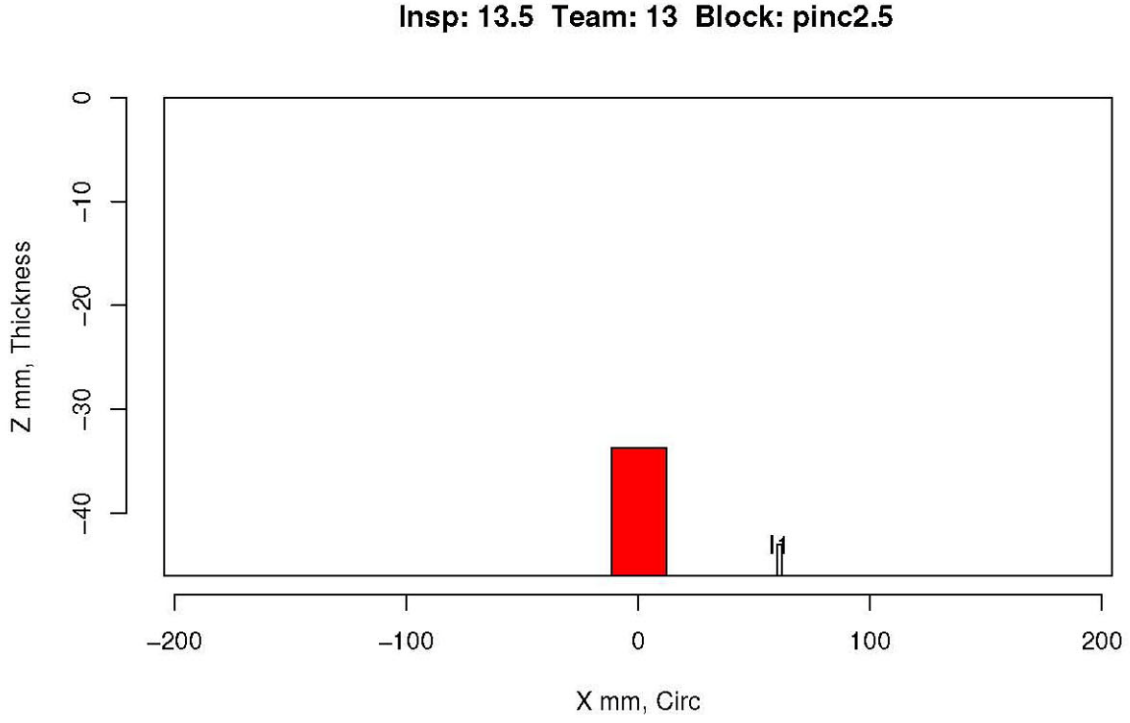
Insp: 13.5 Team: 13 Block: pinc2.5
Z mm, Thickness
0
−10
−20
−30
−40
−200
−100
0
100
200
X mm, Circ

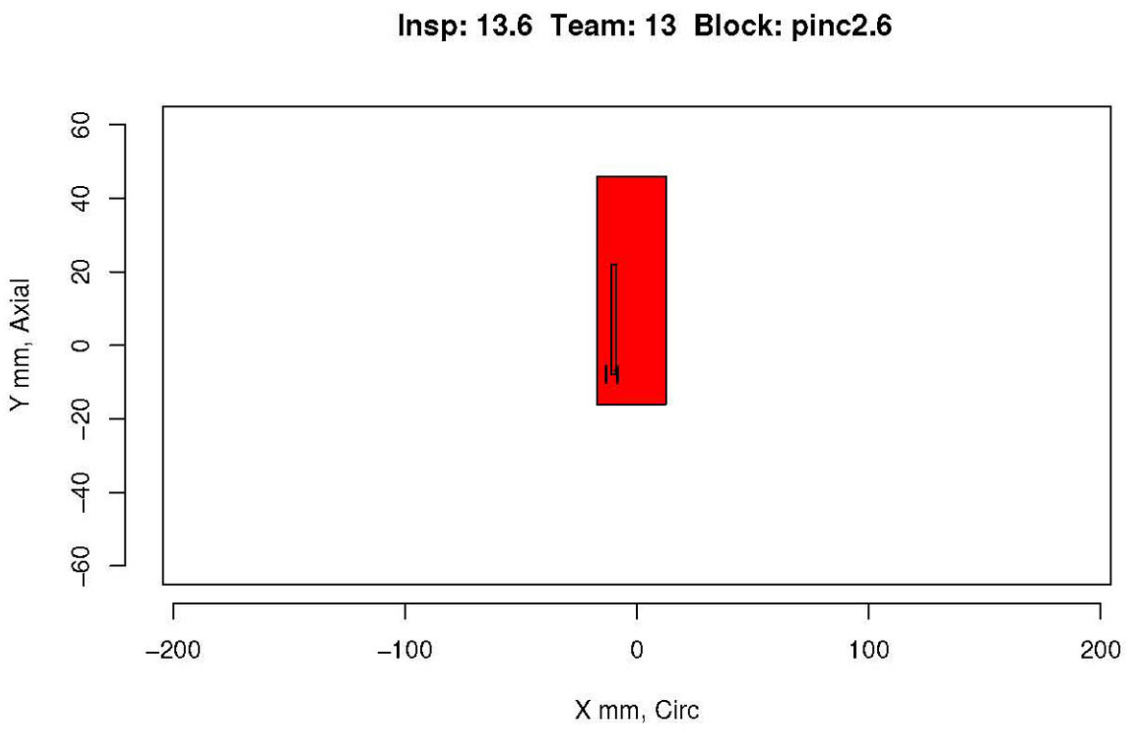
Insp: 13.6 Team: 13 Block: pinc2.6
Y mm, Axial
60
40
20
0
−20
−40
−60
−200
−100
0
100
200
X mm, Circ
I4

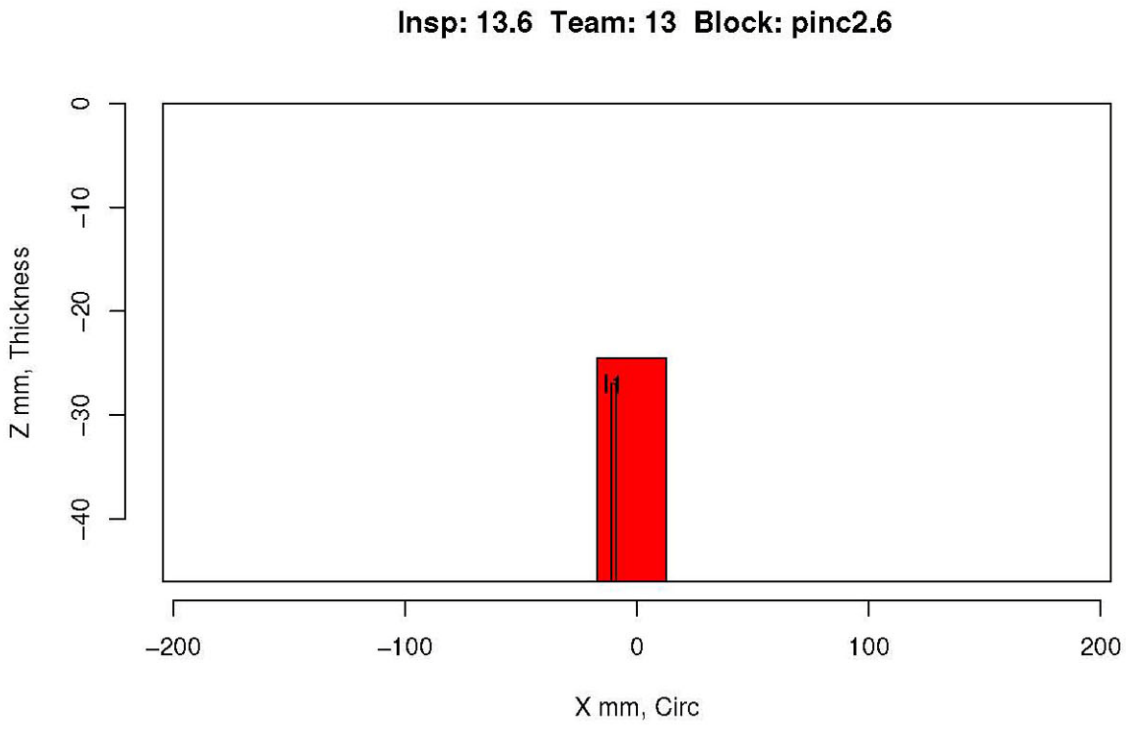
Insp: 13.6 Team: 13 Block: pinc2.6
Z mm, Thickness
0
−10
−20
−30
−40
−200
−100
0
100
200
X mm, Circ
I1

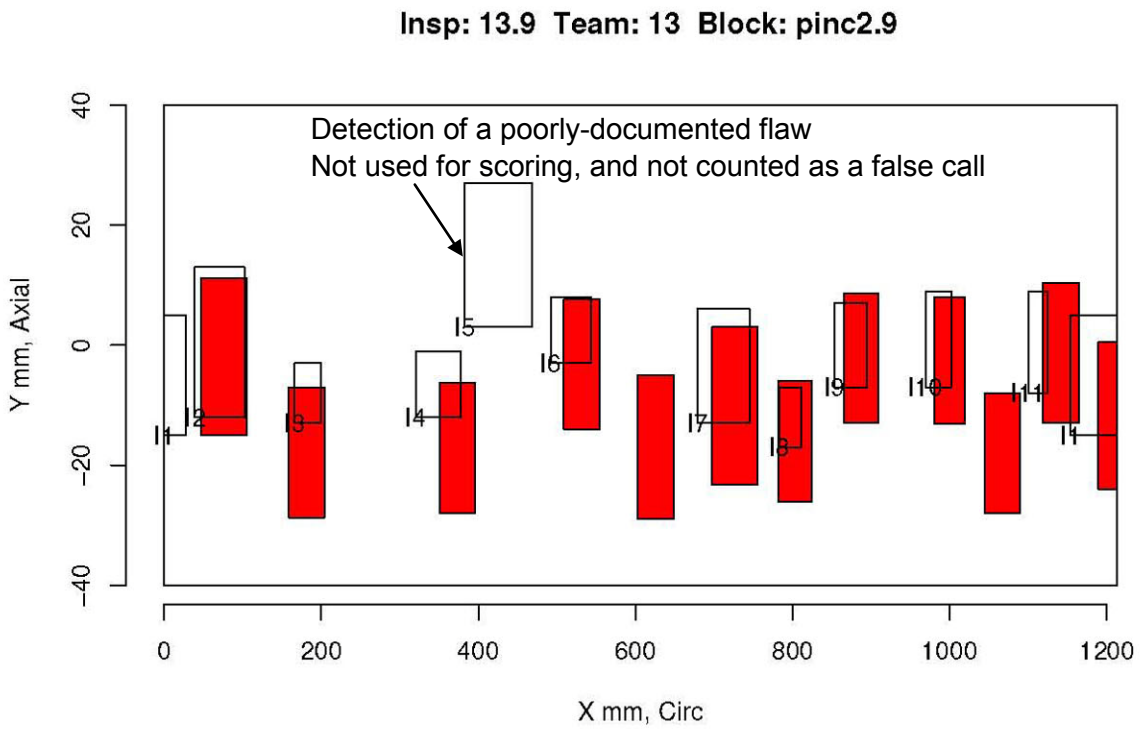
Insp: 13.9 Team: 13 Block: pinc2.9
Detection of a poorly-documented flaw
Not used for scoring, and not counted as a false call
Y mm, Axial
40
20
0
-20
-40
0
200
400
600
800
1000
1200
X mm, Circ

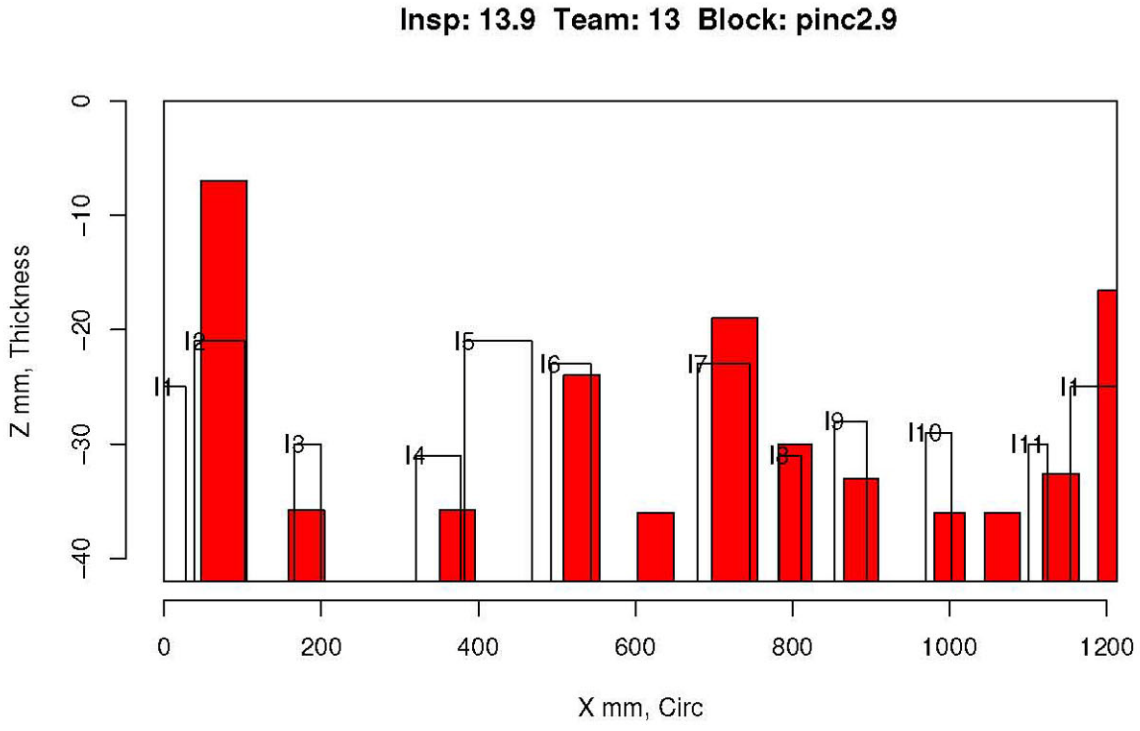
Insp: 13.9 Team: 13 Block: pinc2.9
Z mm, Thickness
0
-10
-20
-30
-40
0
200
400
600
800
1000
1200
X mm, Circ

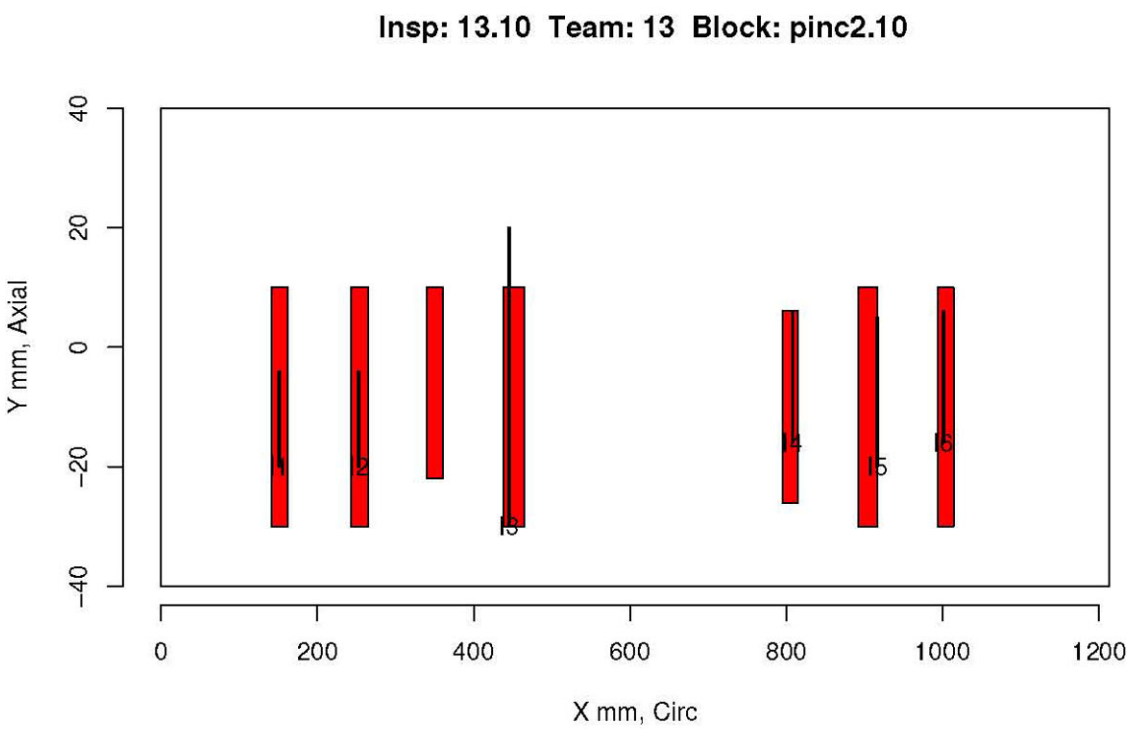
Insp: 13.10 Team: 13 Block: pinc2.10
Y mm, Axial
40
20
0
−20
−40
0
200
400
600
800
1000
1200
X mm, Circ
I1
I2
I3
I4
I5
I6

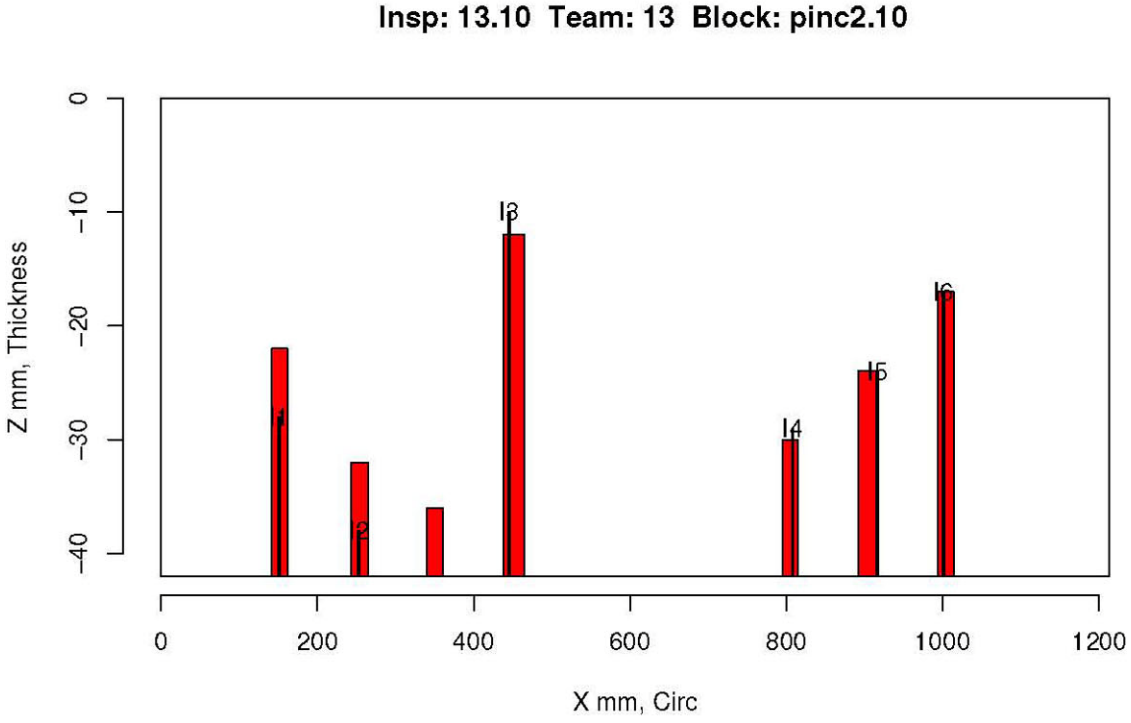
Insp: 13.10 Team: 13 Block: pinc2.10
Z mm, Thickness
0
−10
−20
−30
−40
0
200
400
600
800
1000
1200
X mm, Circ
I1
I2
I3
I4
I5
I6

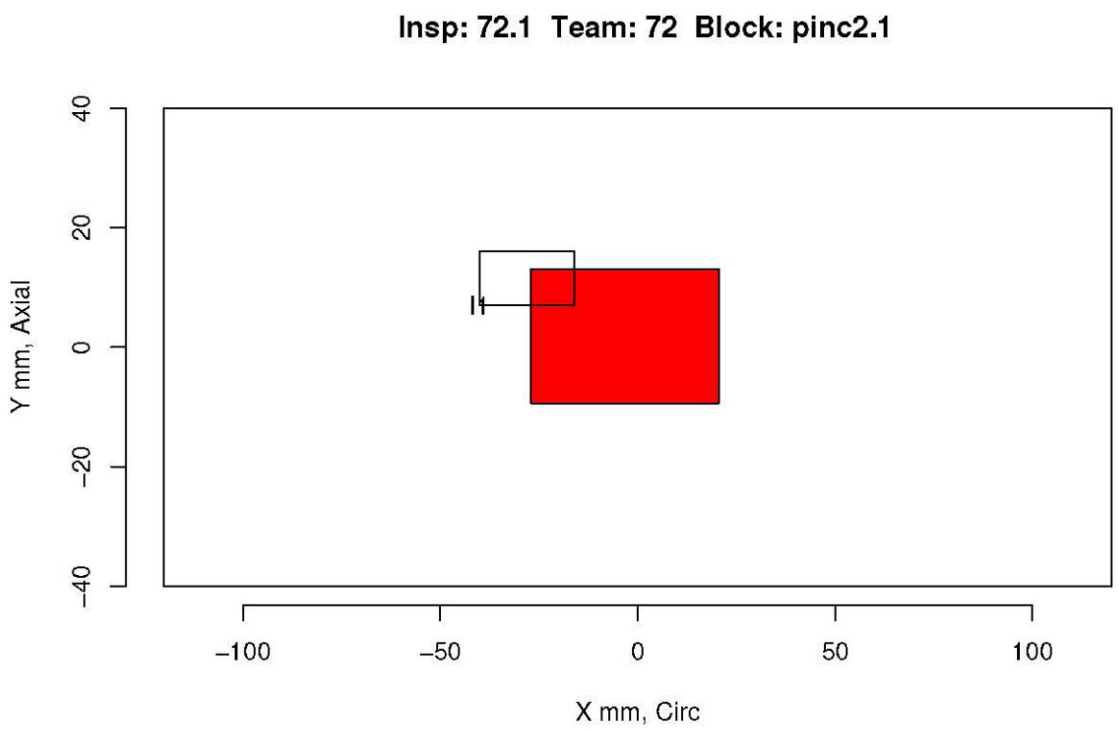
Insp: 72.1 Team: 72 Block: pinc2.1
Y mm, Axial
40
20
0
−20
−40
−100
−50
0
50
100
X mm, Circ

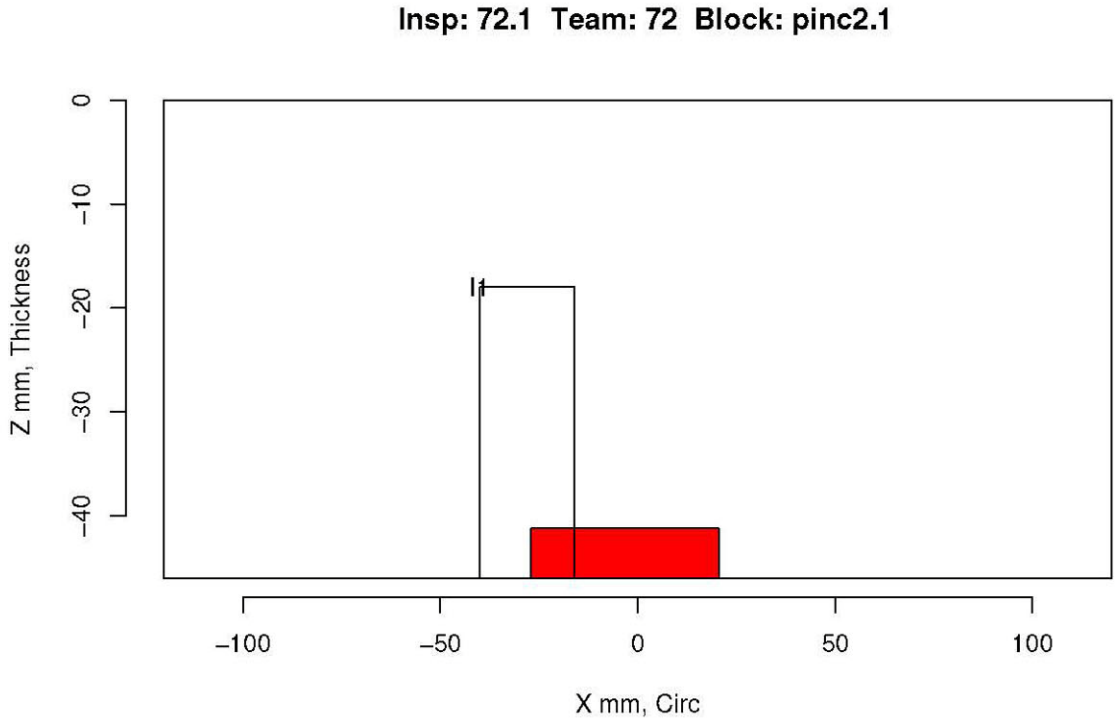
Insp: 72.1 Team: 72 Block: pinc2.1
Z mm, Thickness
0
−10
−20
−30
−40
−100
−50
0
50
100
X mm, Circ

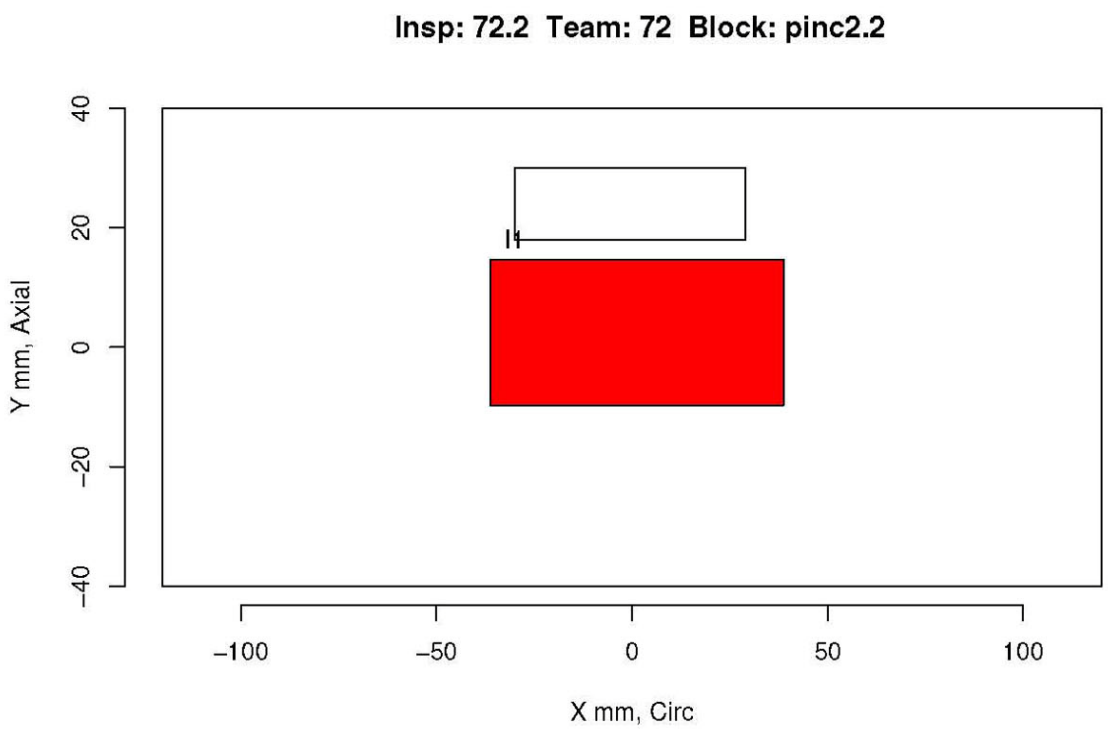
Insp: 72.2 Team: 72 Block: pinc2.2
Y mm, Axial
40
20
0
−20
−40
−100
−50
0
50
100
X mm, Circ

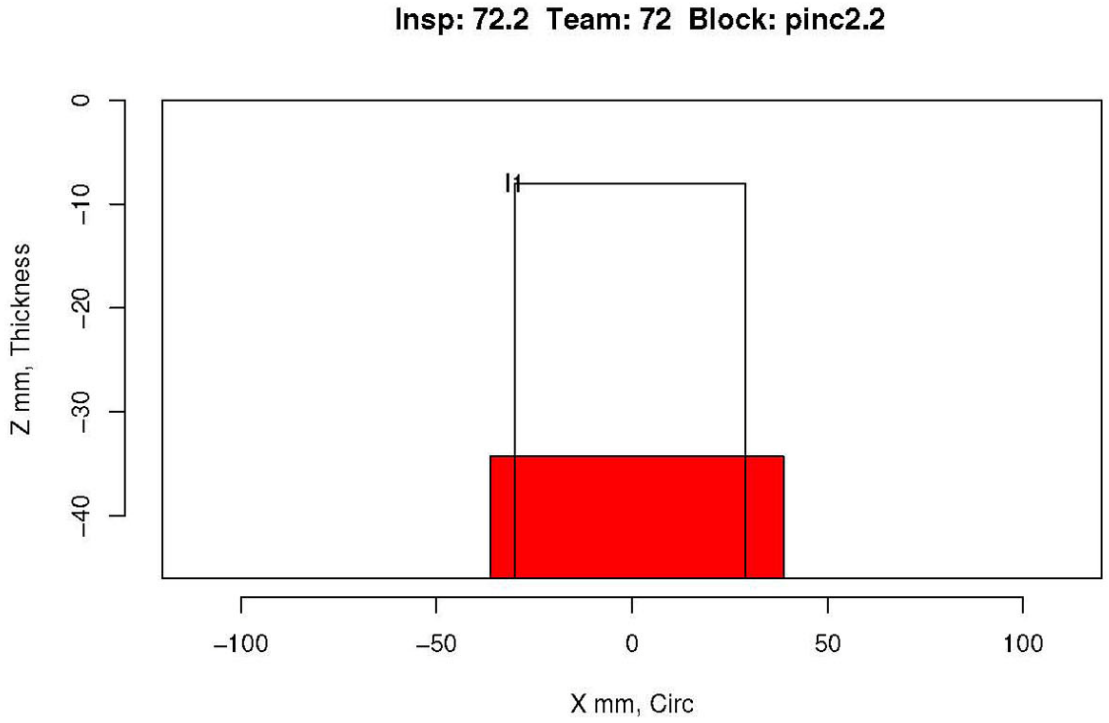
Insp: 72.2 Team: 72 Block: pinc2.2
Z mm, Thickness
0
−10
−20
−30
−40
−100
−50
0
50
100
X mm, Circ

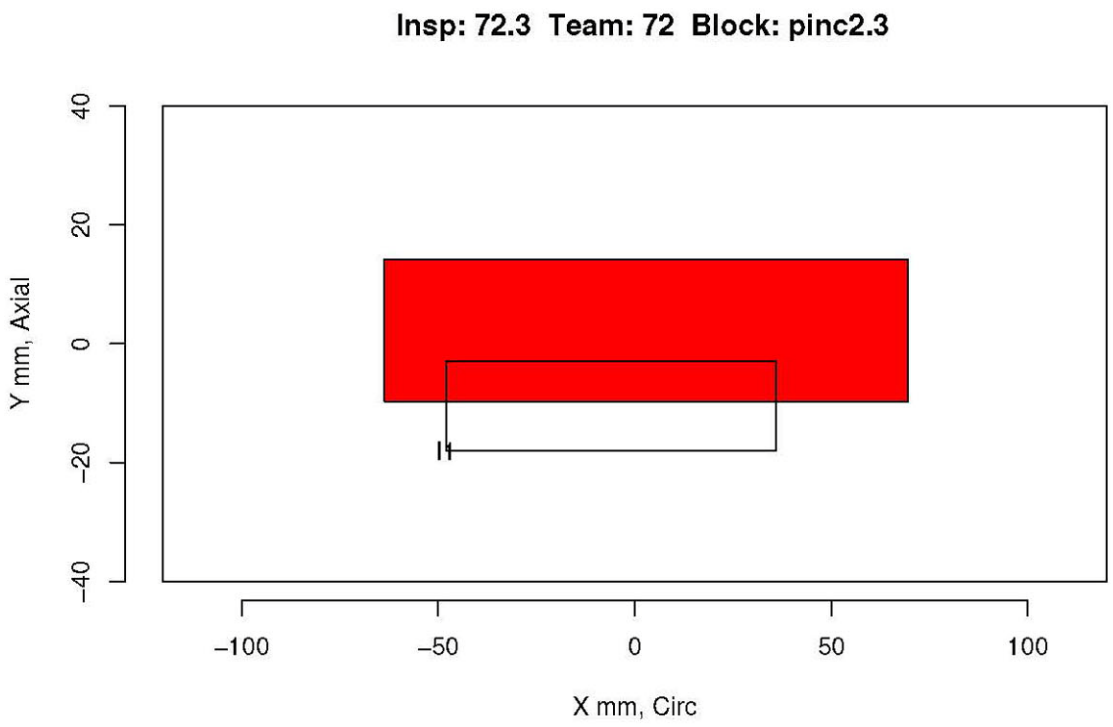
Insp: 72.3 Team: 72 Block: pinc2.3
Y mm, Axial
40
20
0
−20
−40
−100
−50
0
50
100
X mm, Circ

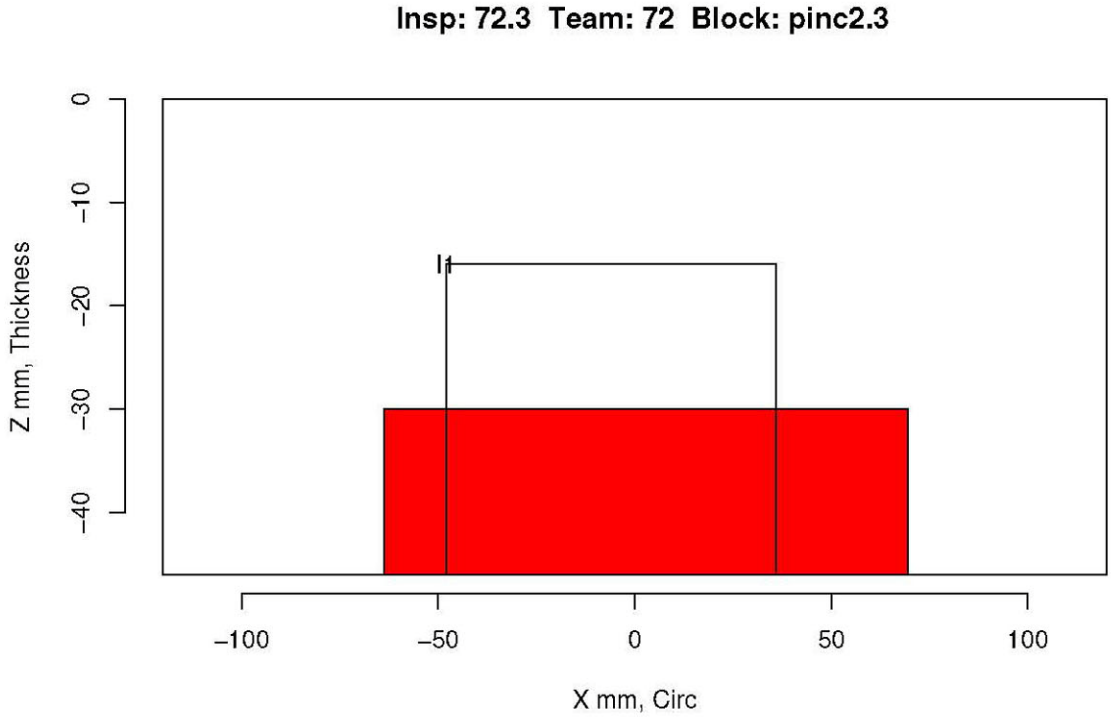
Insp: 72.3 Team: 72 Block: pinc2.3
Z mm, Thickness
0
−10
−20
−30
−40
−100
−50
0
50
100
X mm, Circ

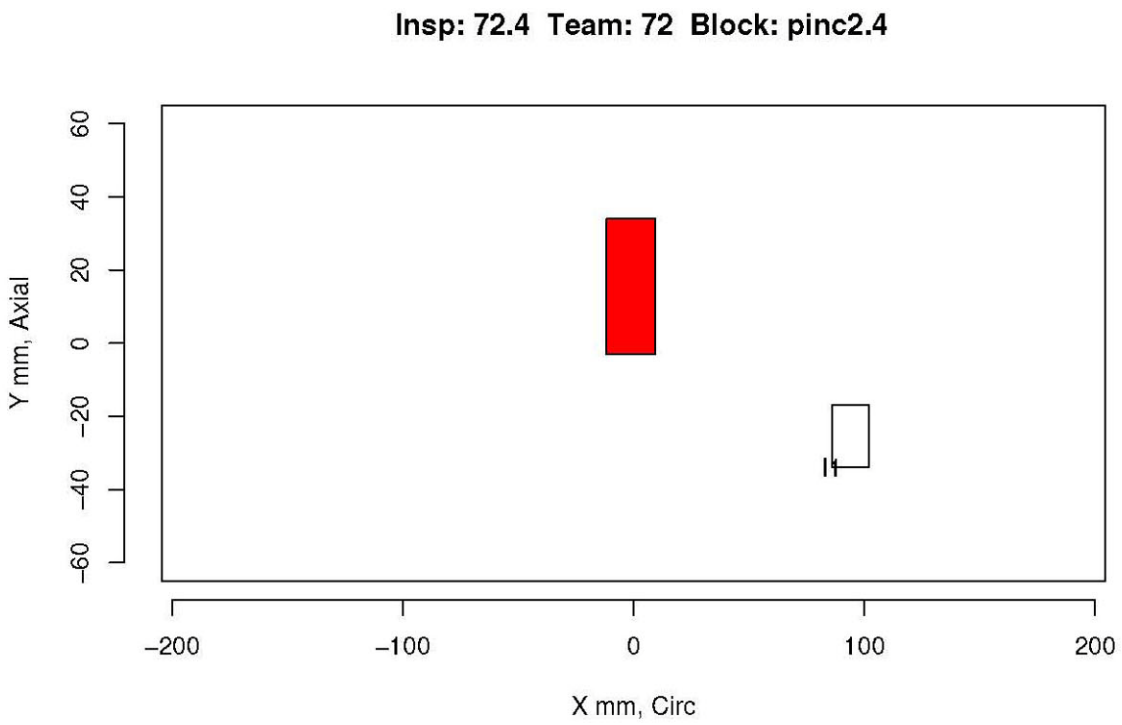
Insp: 72.4 Team: 72 Block: pinc2.4
Y mm, Axial
60
40
20
0
−20
−40
−60
−200
−100
0
100
200
X mm, Circ

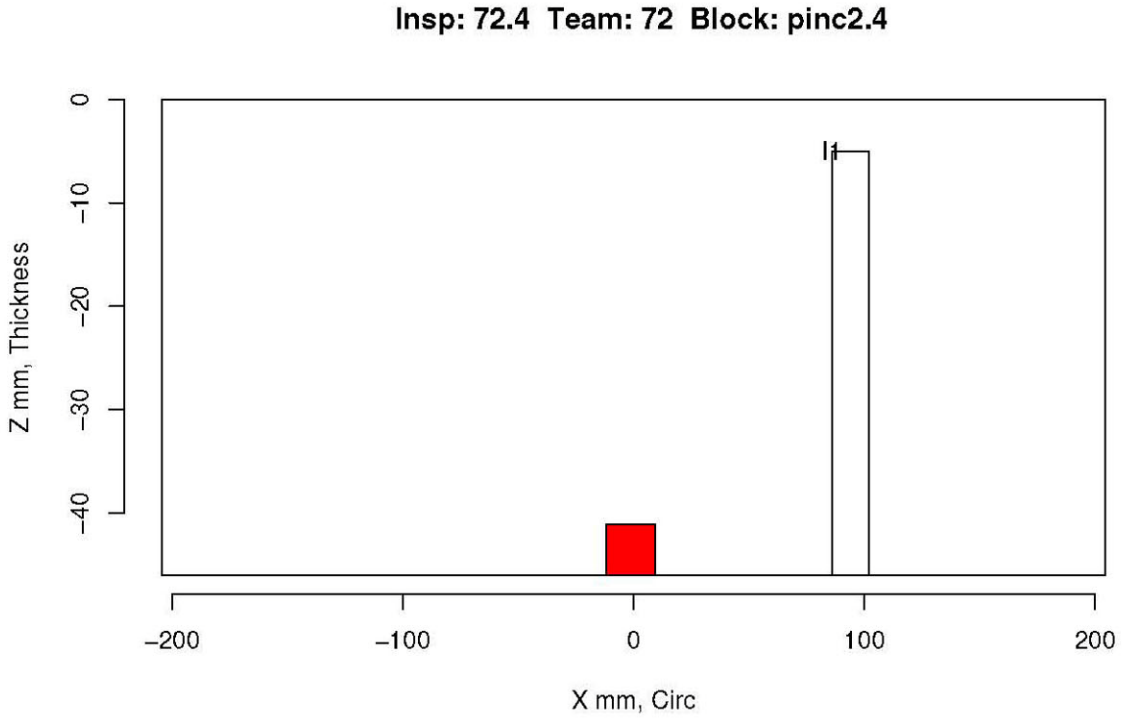
Insp: 72.4 Team: 72 Block: pinc2.4
Z mm, Thickness
0
−10
−20
−30
−40
−200
−100
0
100
200
X mm, Circ

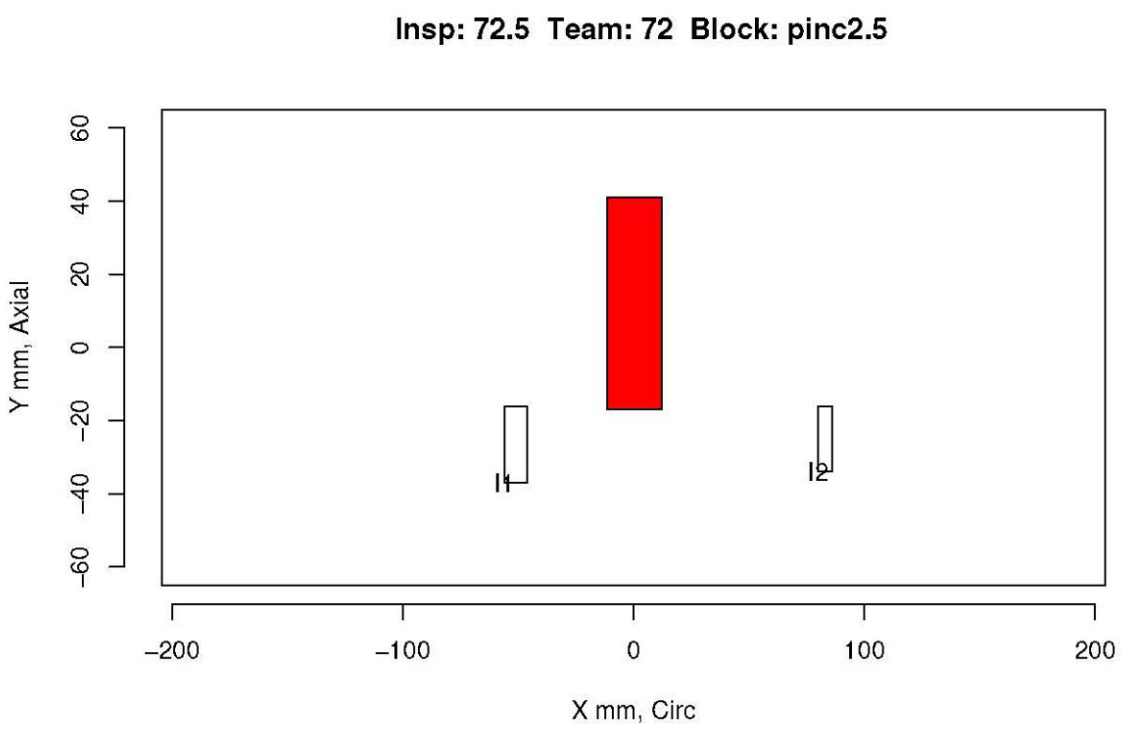
Insp: 72.5 Team: 72 Block: pinc2.5
Y mm, Axial
60
40
20
0
−20
−40
−60
I1
I2
−200
−100
0
100
200
X mm, Circ

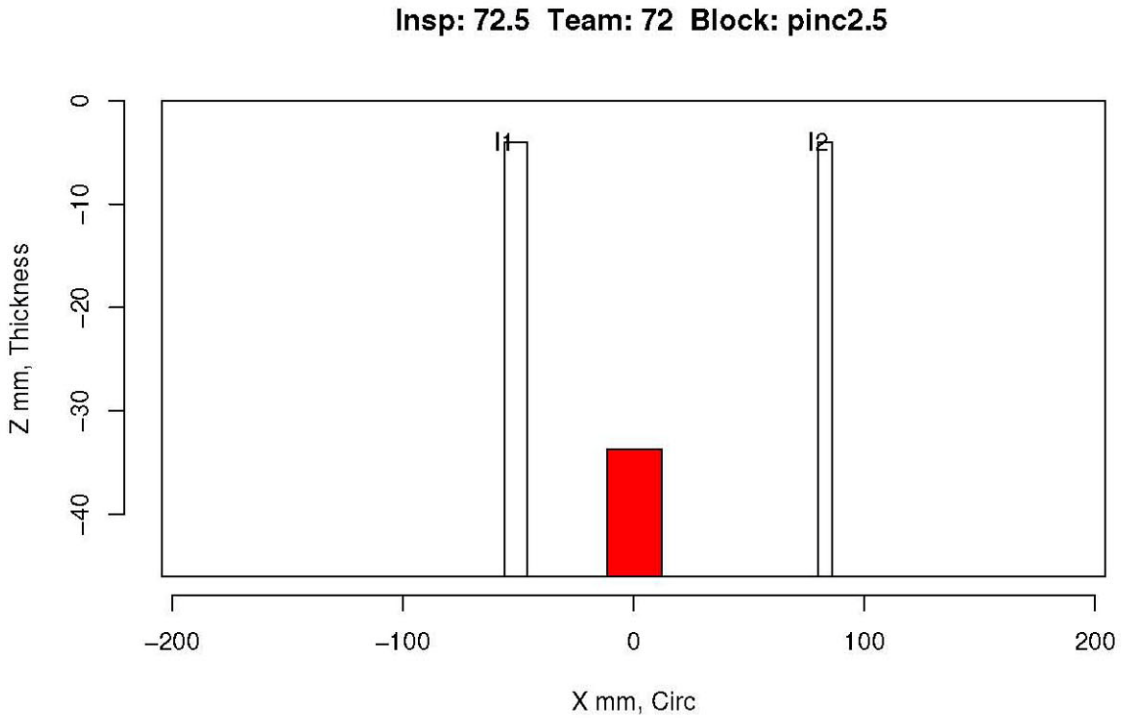
Insp: 72.5 Team: 72 Block: pinc2.5
Z mm, Thickness
0
−10
−20
−30
−40
I1
I2
−200
−100
0
100
200
X mm, Circ

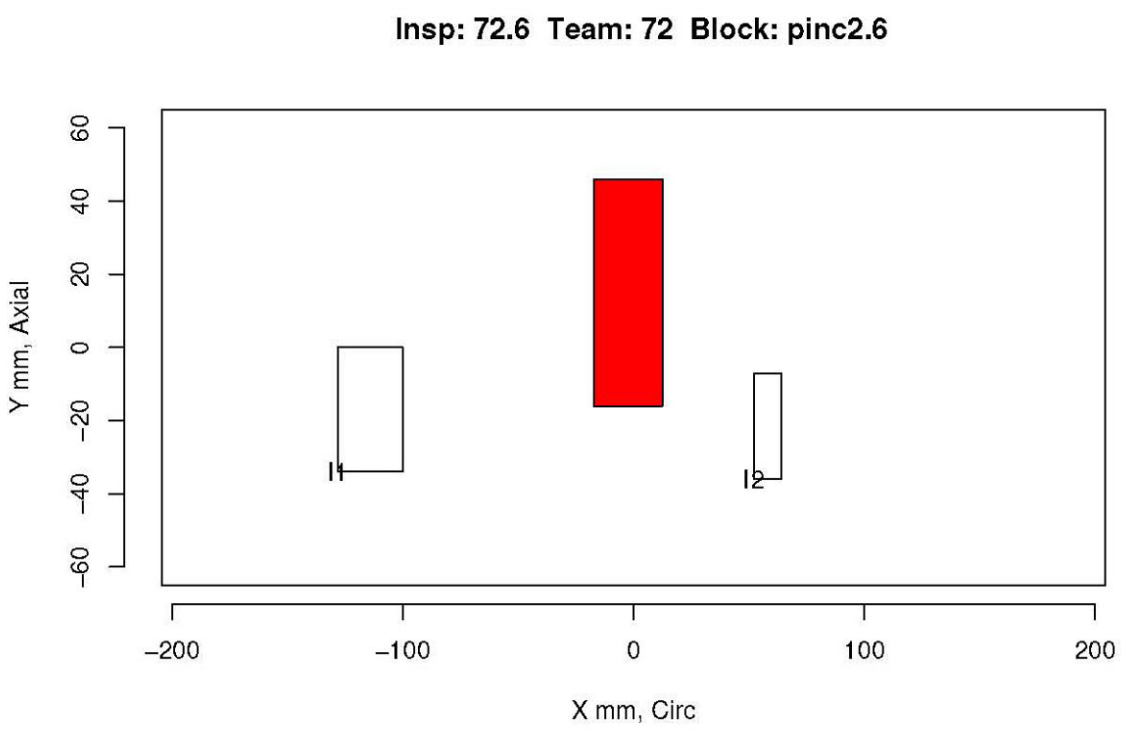
Insp: 72.6 Team: 72 Block: pinc2.6
Y mm, Axial
60
40
20
0
−20
−40
−60
I1
I2
−200
−100
0
100
200
X mm, Circ

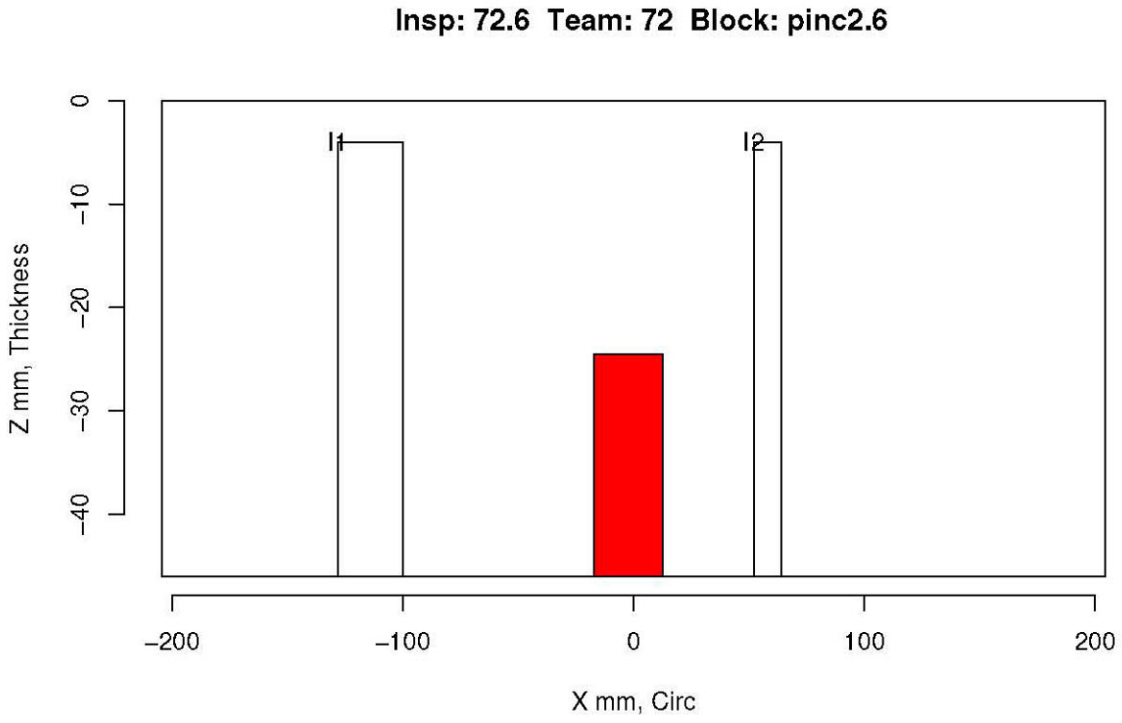
Insp: 72.6 Team: 72 Block: pinc2.6
Z mm, Thickness
0
−10
−20
−30
−40
I1
I2
−200
−100
0
100
200
X mm, Circ

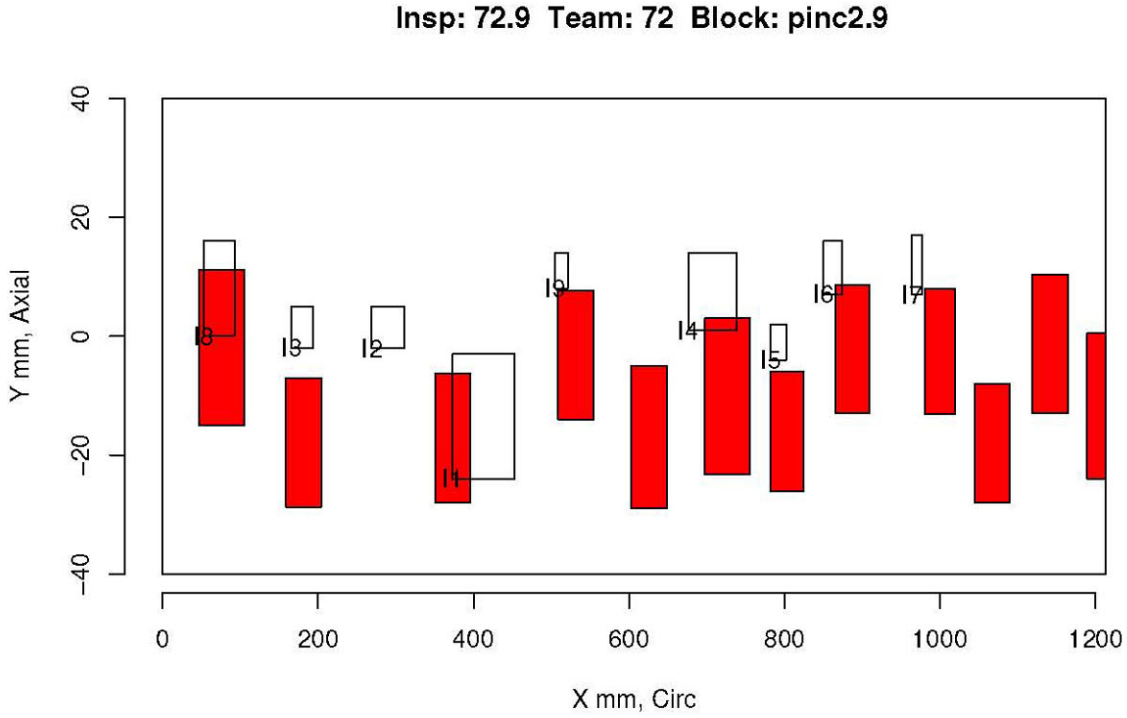
Insp: 72.9 Team: 72 Block: pinc2.9
Y mm, Axial
40
20
0
-20
-40
0
200
400
600
800
1000
1200
X mm, Circ
I8
I3
I2
I1
I9
I4
I5
I6
I7

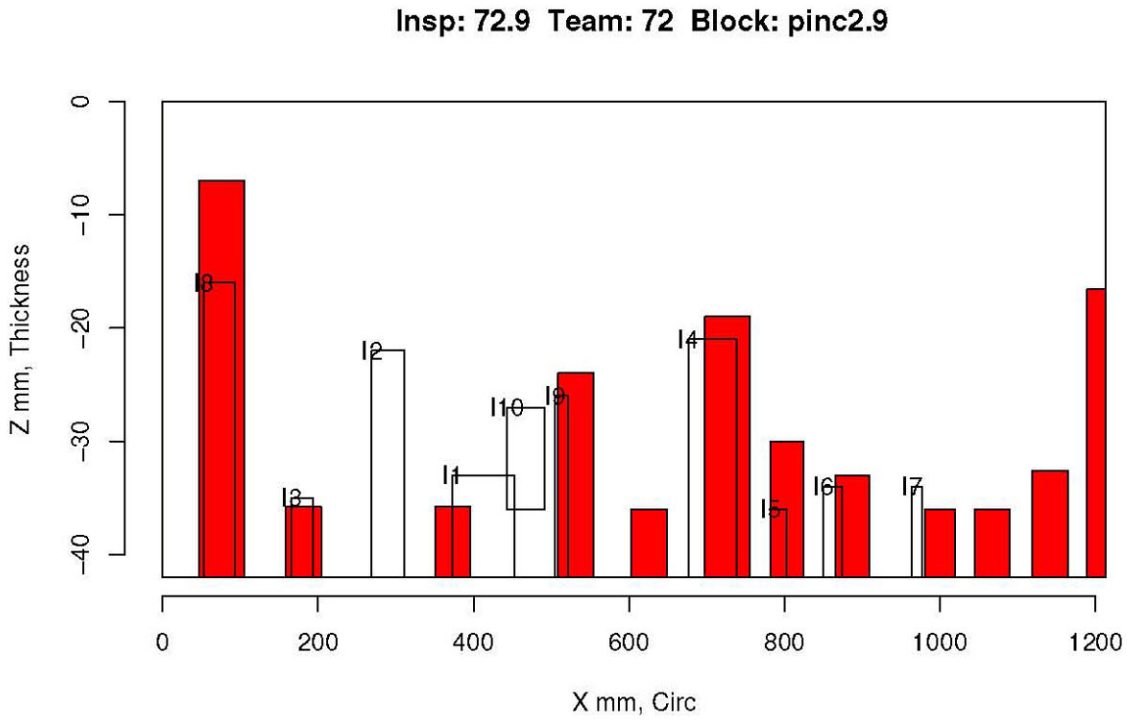
Insp: 72.9 Team: 72 Block: pinc2.9
Z mm, Thickness
0
-10
-20
-30
-40
0
200
400
600
800
1000
1200
X mm, Circ
I8
I3
I2
I1
I10
I9
I4
I5
I6
I7

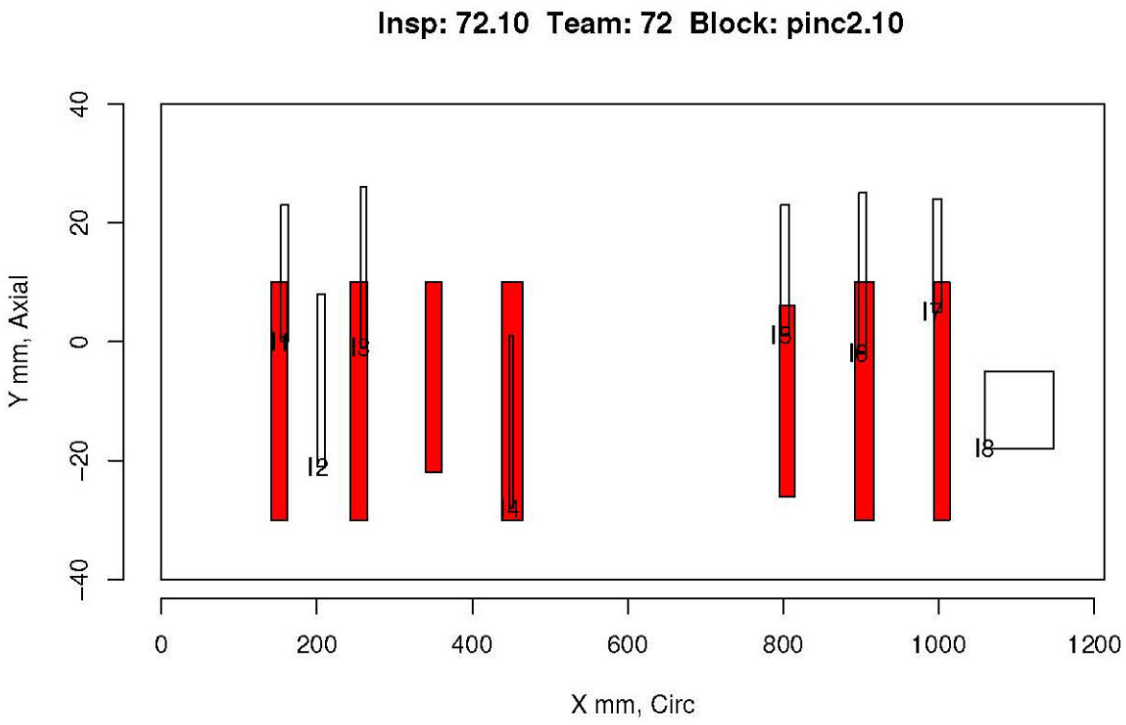
Insp: 72.10 Team: 72 Block: pinc2.10
Y mm, Axial
40
20
0
-20
-40
0
200
400
600
800
1000
1200
X mm, Circ

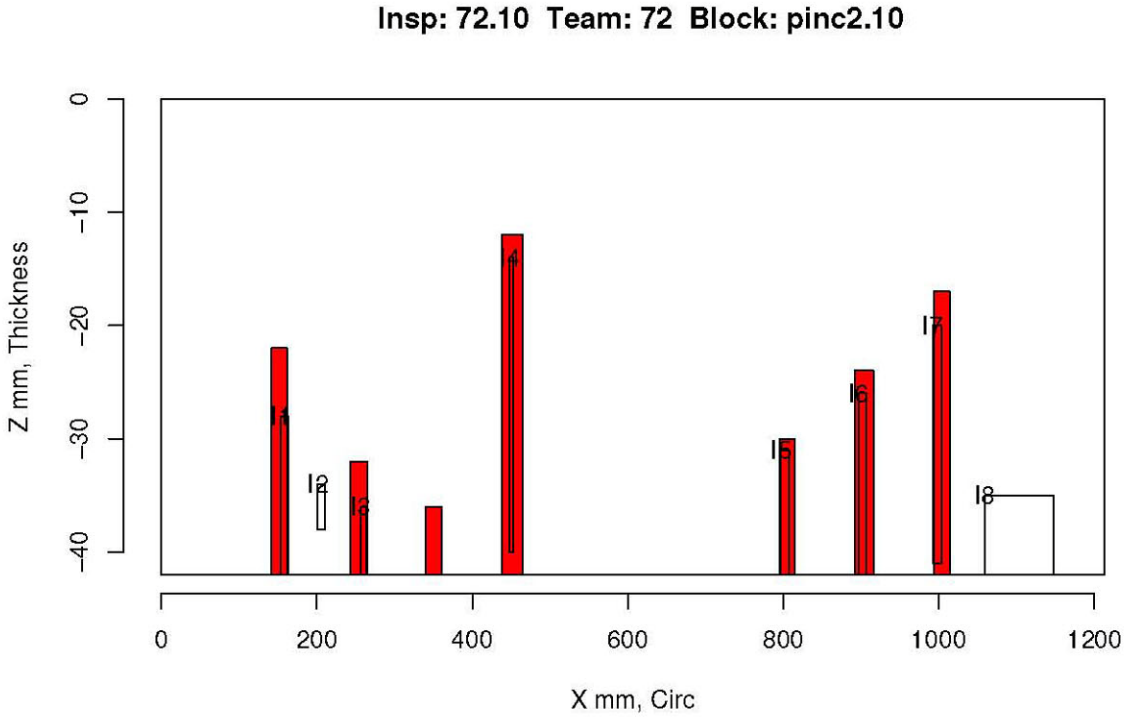
Insp: 72.10 Team: 72 Block: pinc2.10
Z mm, Thickness
0
-10
-20
-30
-40
0
200
400
600
800
1000
1200
X mm, Circ

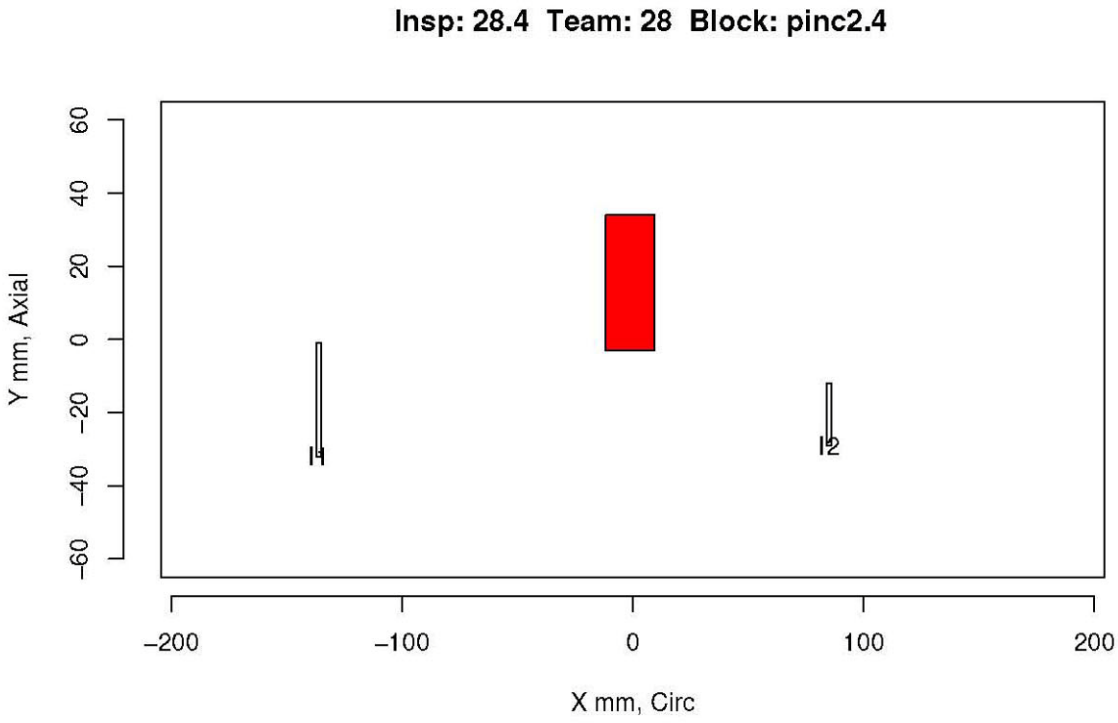
Insp: 28.4 Team: 28 Block: pinc2.4
Y mm, Axial
60
40
20
0
−20
−40
−60
I1
I2
−200
−100
0
100
200
X mm, Circ

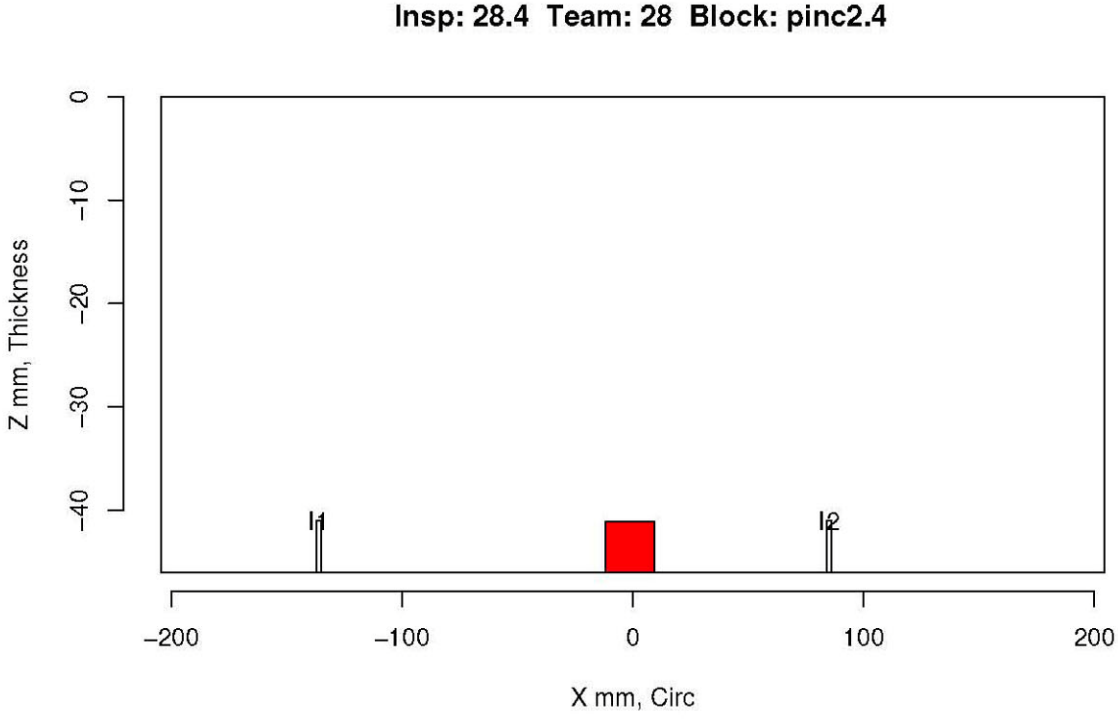
Insp: 28.4 Team: 28 Block: pinc2.4
Z mm, Thickness
0
−10
−20
−30
−40
I1
I2
−200
−100
0
100
200
X mm, Circ

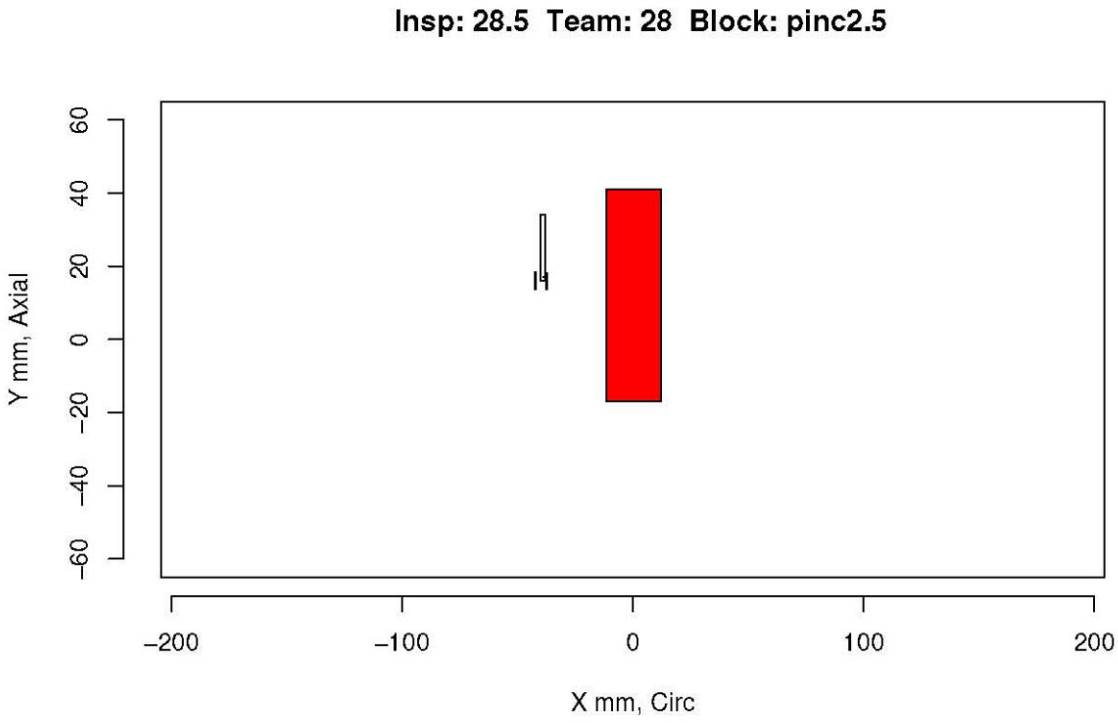
Insp: 28.5 Team: 28 Block: pinc2.5
Y mm, Axial
60
40
20
0
−20
−40
−60
−200
−100
0
100
200
X mm, Circ

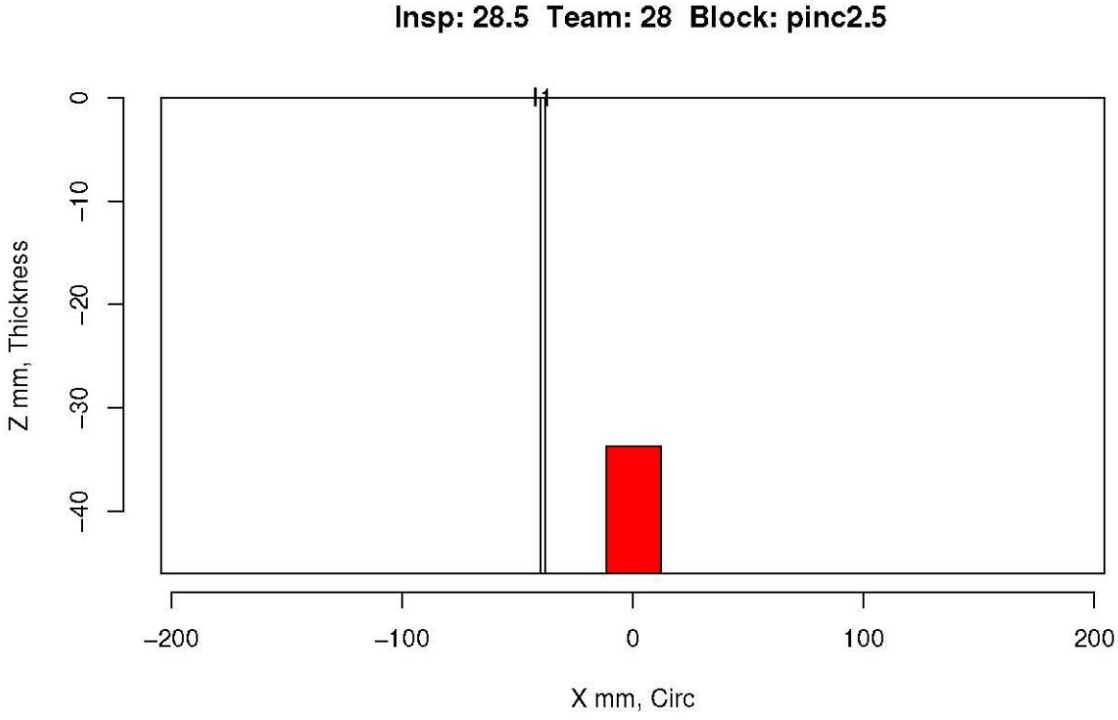
Insp: 28.5 Team: 28 Block: pinc2.5
Z mm, Thickness
0
−10
−20
−30
−40
−200
−100
0
100
200
X mm, Circ

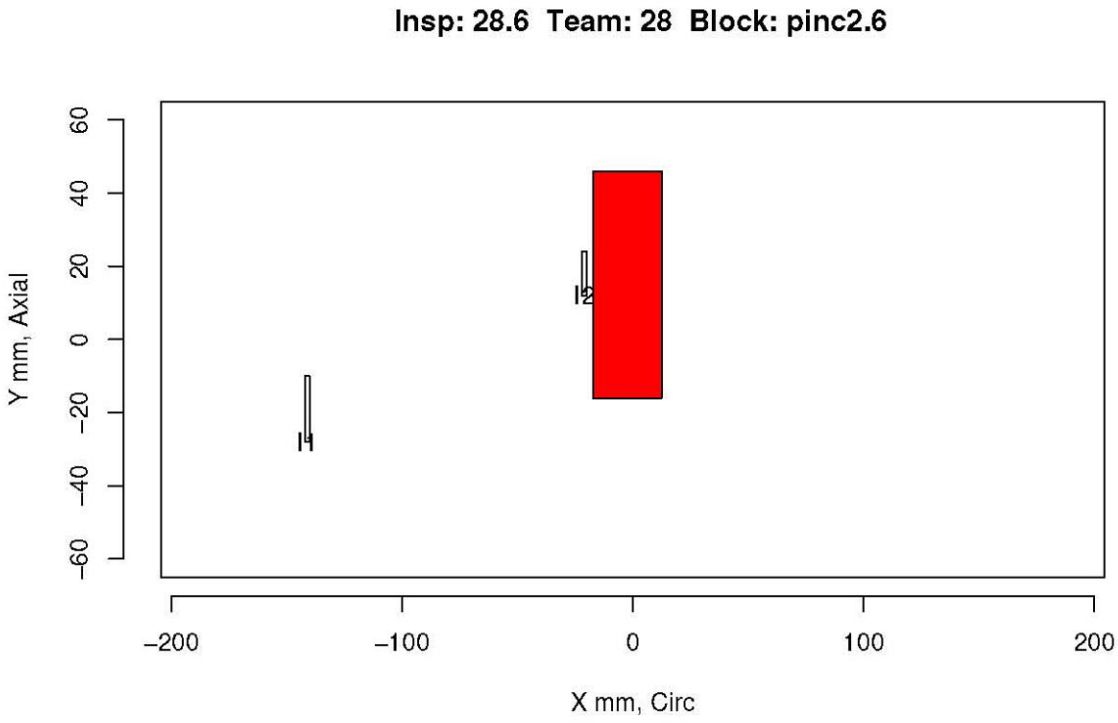
Insp: 28.6 Team: 28 Block: pinc2.6
Y mm, Axial
60
40
20
0
−20
−40
−60
I2
I4
−200
−100
0
100
200
X mm, Circ

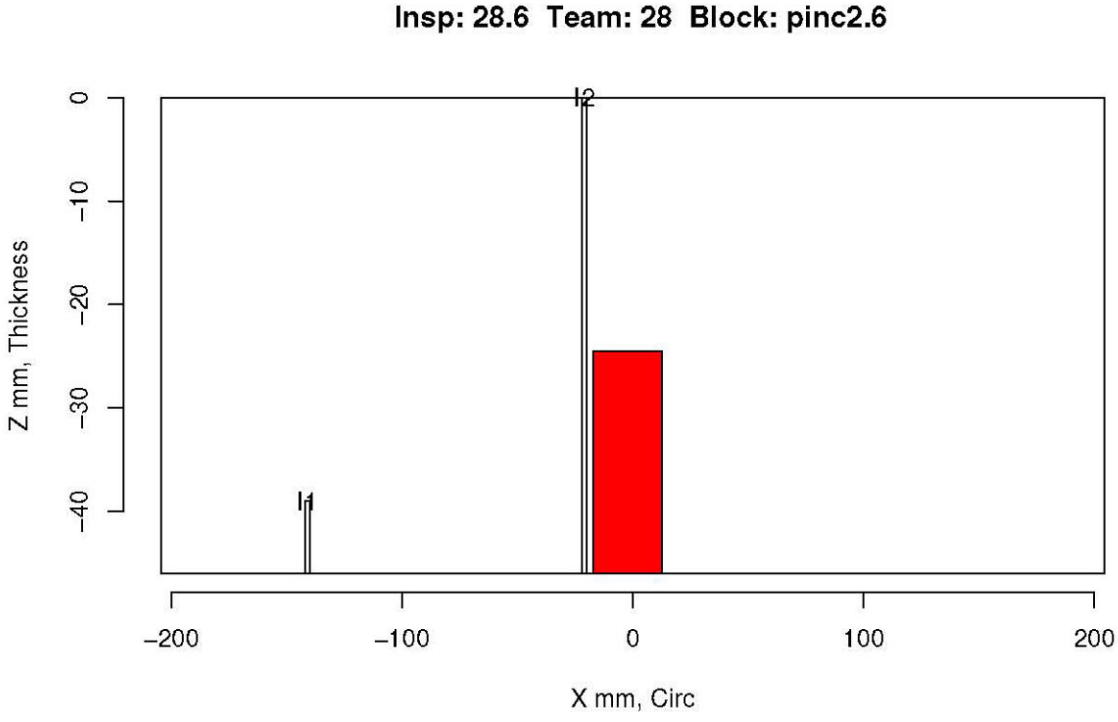
Insp: 28.6 Team: 28 Block: pinc2.6
Z mm, Thickness
0
−10
−20
−30
−40
I2
I1
−200
−100
0
100
200
X mm, Circ

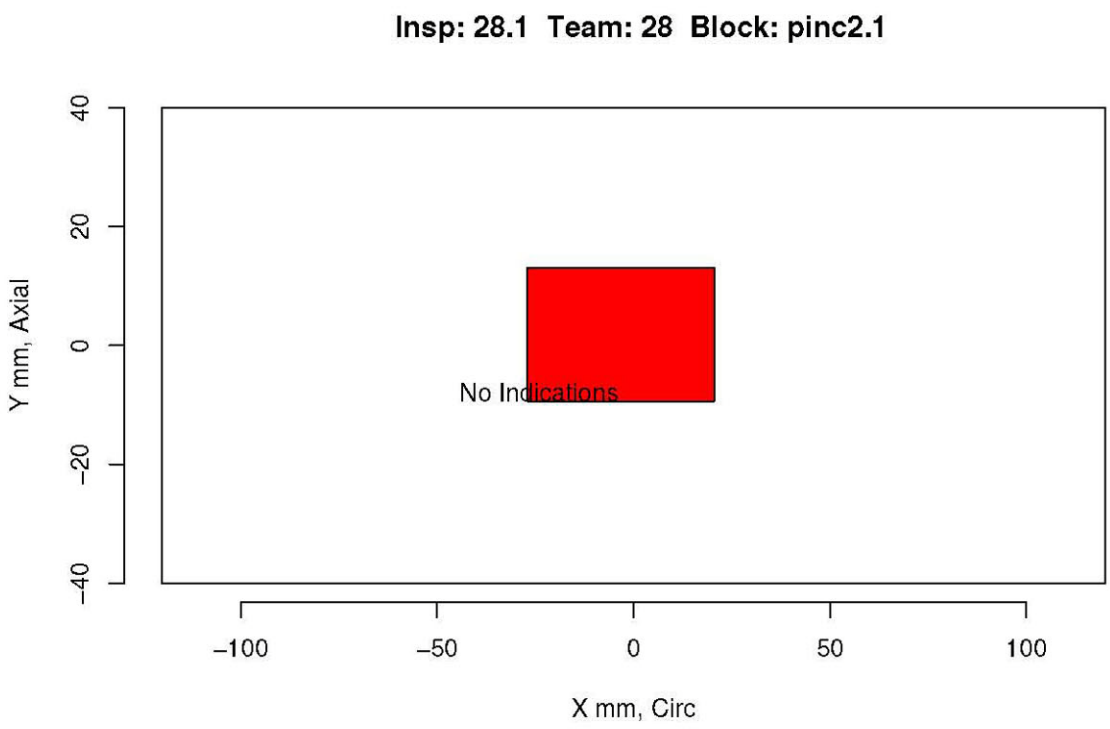
Insp: 28.1 Team: 28 Block: pinc2.1
Y mm, Axial
40
20
0
-20
-40
No Indications
-100
-50
0
50
100
X mm, Circ

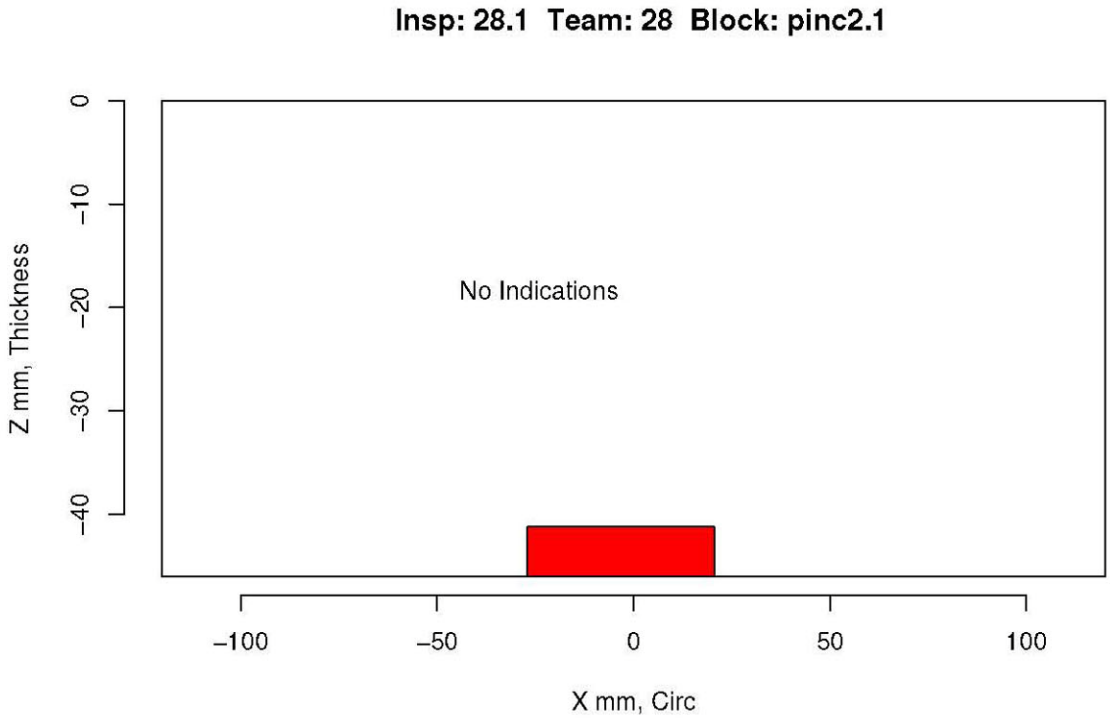
Insp: 28.1 Team: 28 Block: pinc2.1
Z mm, Thickness
0
-10
-20
-30
-40
No Indications
-100
-50
0
50
100
X mm, Circ

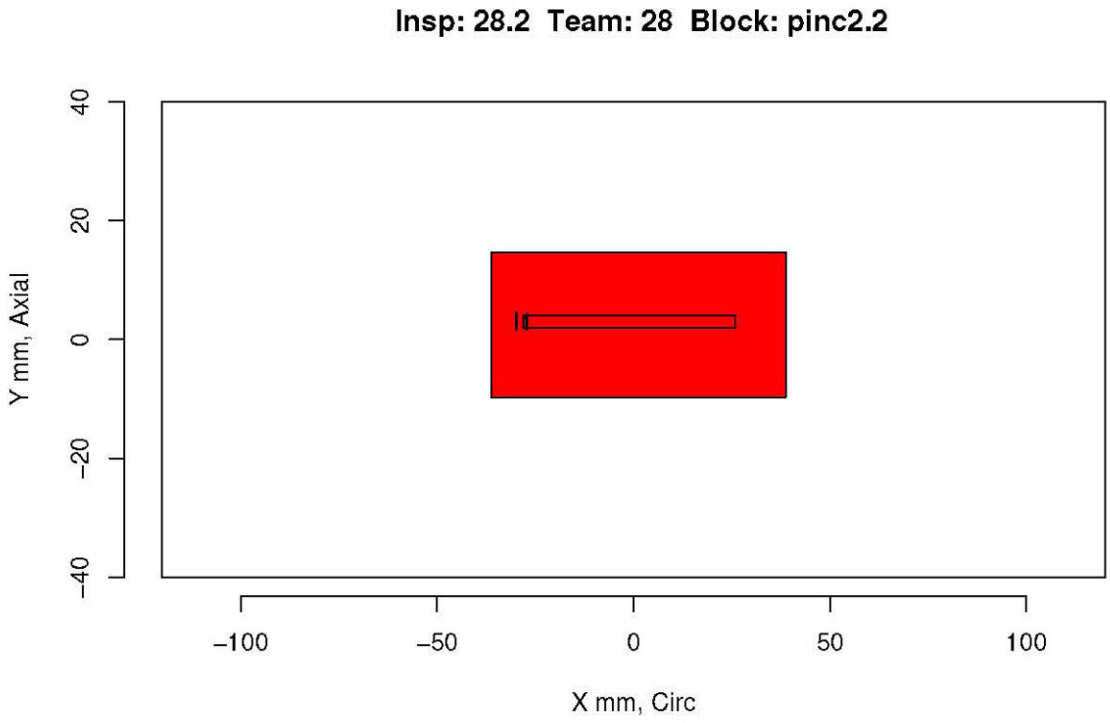
Insp: 28.2 Team: 28 Block: pinc2.2
Y mm, Axial
40
20
0
-20
-40
-100
-50
0
50
100
X mm, Circ

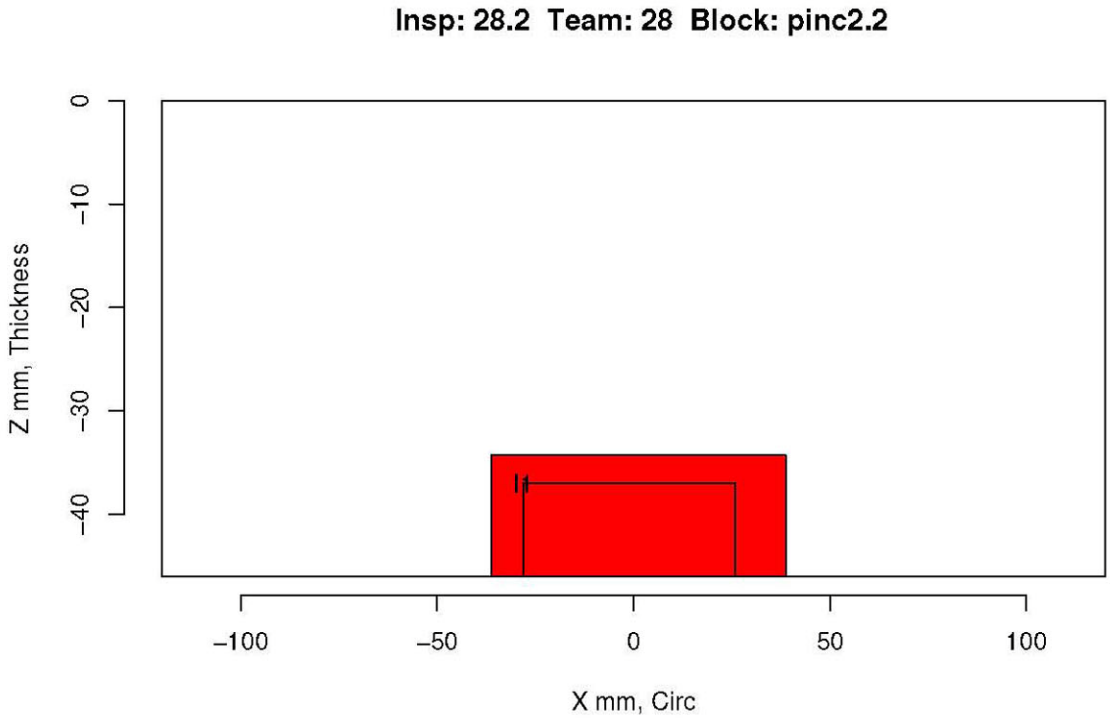
Insp: 28.2 Team: 28 Block: pinc2.2
Z mm, Thickness
0
-10
-20
-30
-40
-100
-50
0
50
100
X mm, Circ

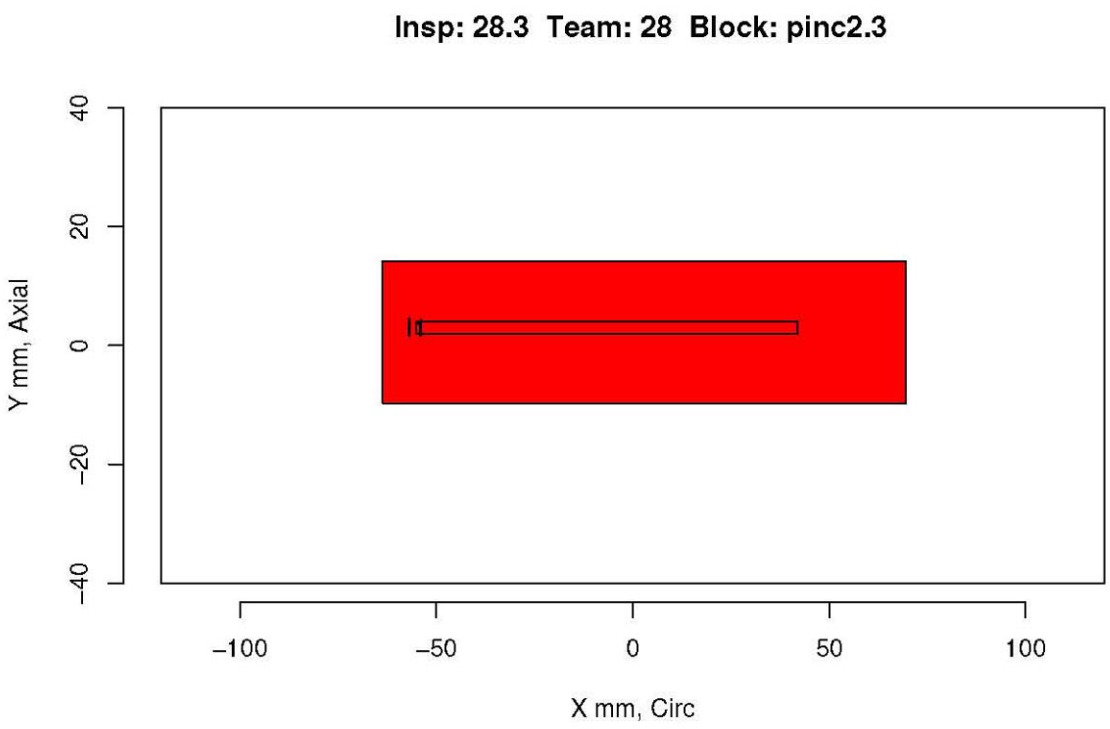
Insp: 28.3 Team: 28 Block: pinc2.3
Y mm, Axial
40
20
0
−20
−40
−100
−50
0
50
100
X mm, Circ

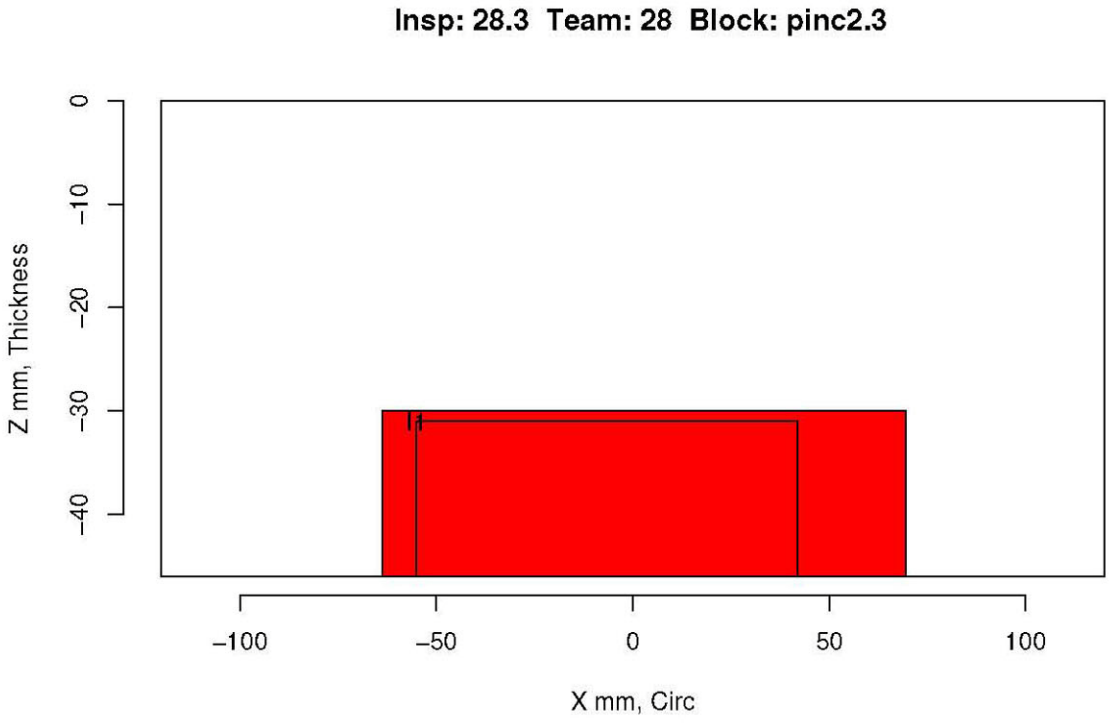
Insp: 28.3 Team: 28 Block: pinc2.3
Z mm, Thickness
0
−10
−20
−30
−40
−100
−50
0
50
100
X mm, Circ

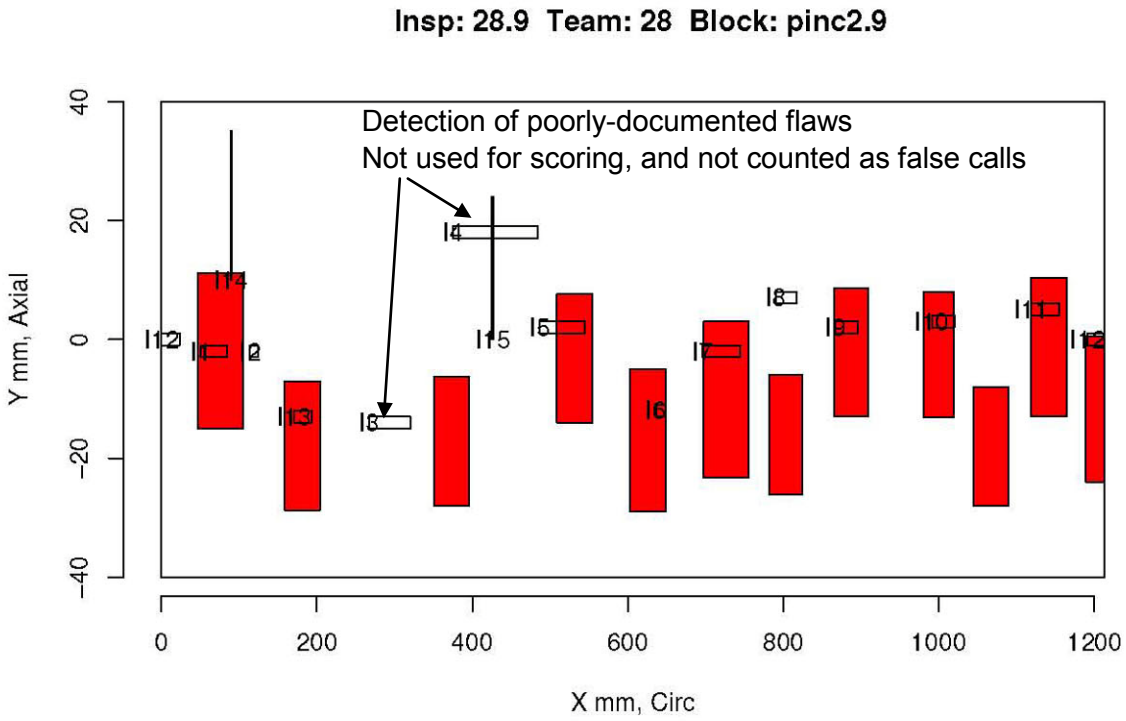
Insp: 28.9 Team: 28 Block: pinc2.9
Detection of poorly-documented flaws
Not used for scoring, and not counted as false calls
Y mm, Axial
X mm, Circ
40
20
0
-20
-40
0
200
400
600
800
1000
1200

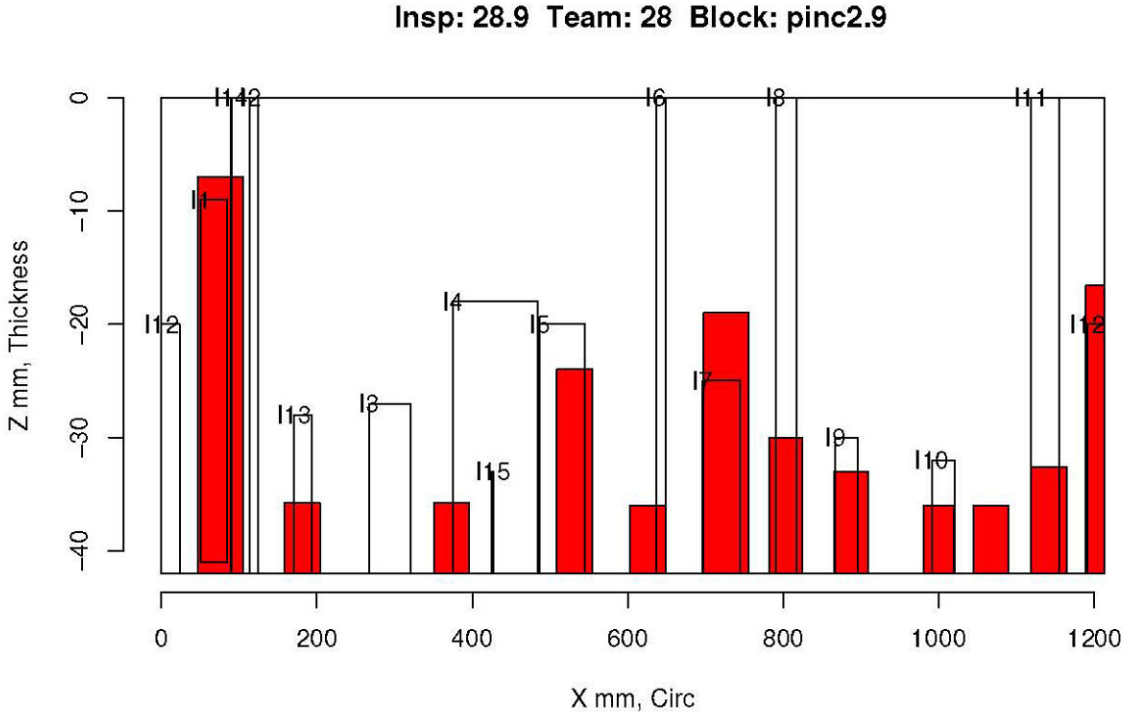
Insp: 28.9 Team: 28 Block: pinc2.9
Z mm, Thickness
X mm, Circ
0
-10
-20
-30
-40
0
200
400
600
800
1000
1200

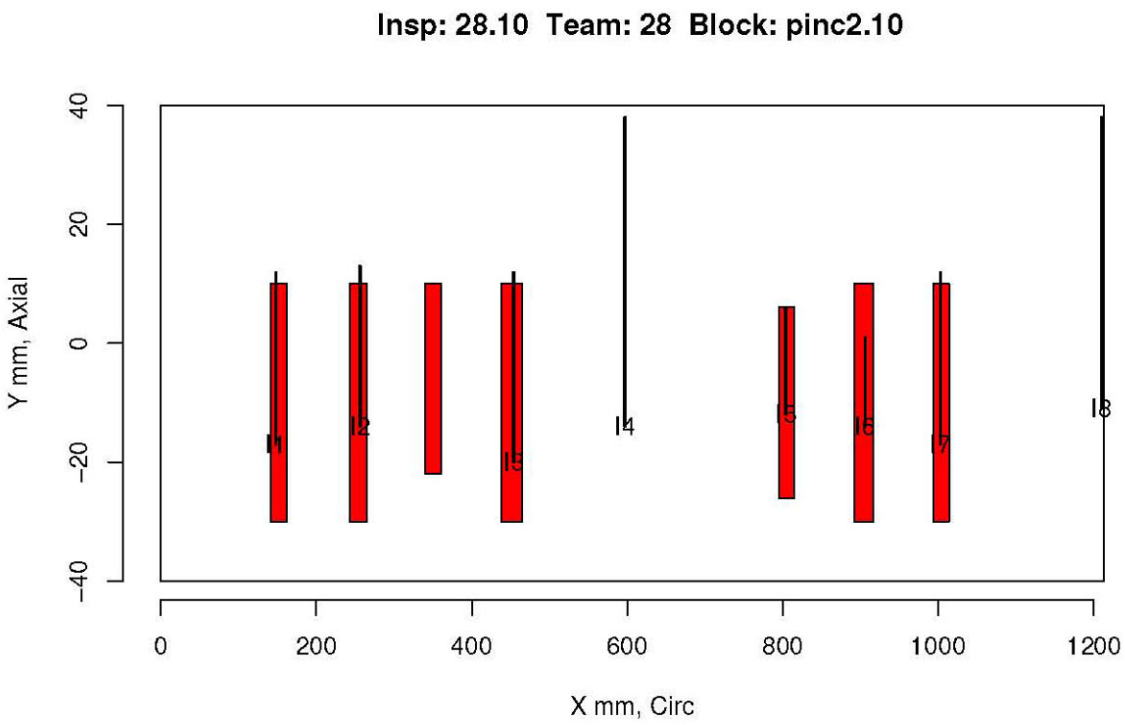
Insp: 28.10 Team: 28 Block: pinc2.10
Y mm, Axial
40
20
0
-20
-40
0
200
400
600
800
1000
1200
X mm, Circ
I1
I2
I3
I4
I5
I6
I7
I8

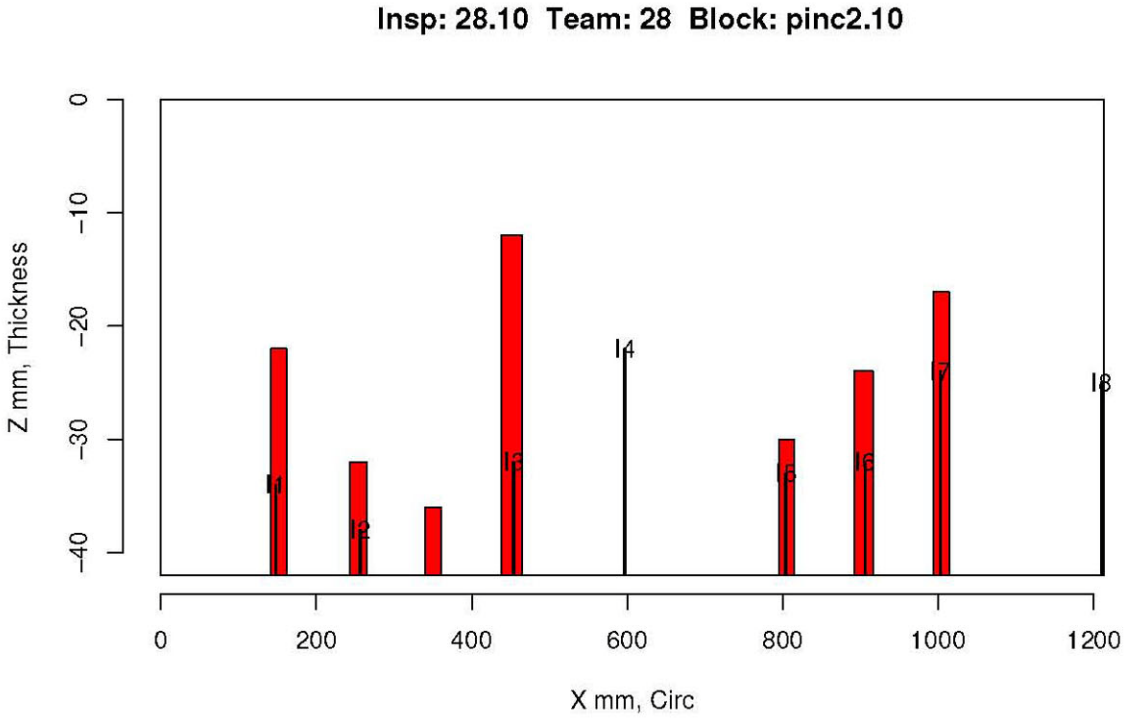
Insp: 28.10 Team: 28 Block: pinc2.10
Z mm, Thickness
0
-10
-20
-30
-40
0
200
400
600
800
1000
1200
X mm, Circ
I1
I2
I3
I4
I5
I6
I7
I8

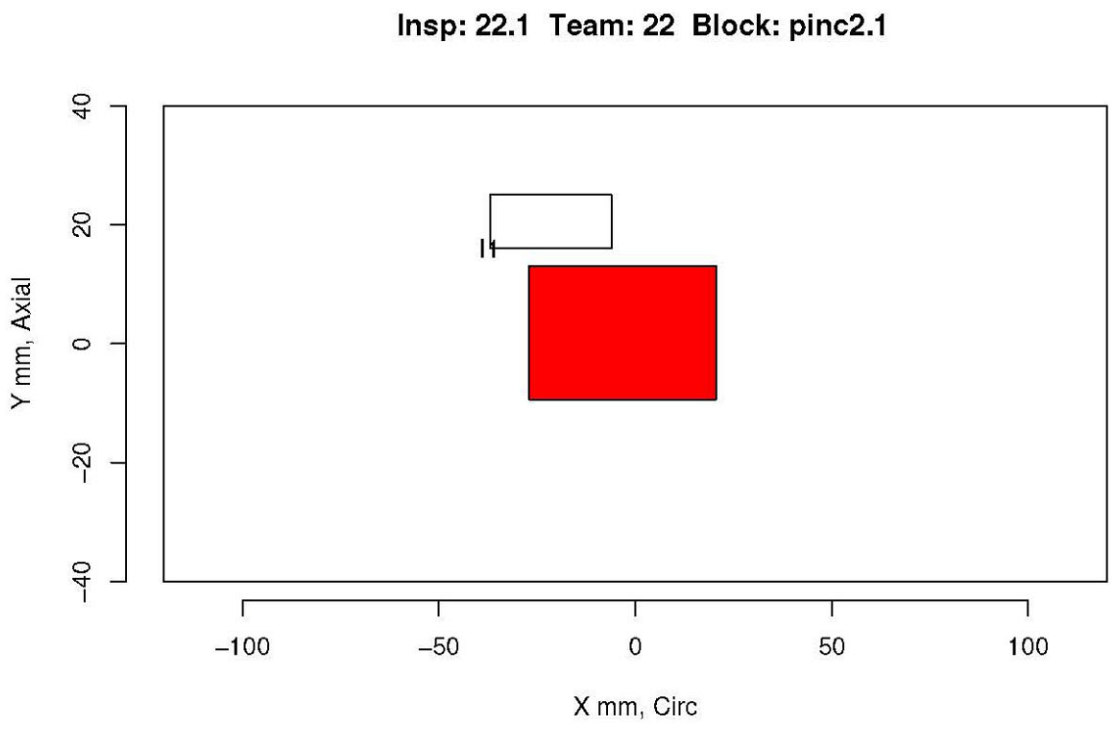
Insp: 22.1 Team: 22 Block: pinc2.1
Y mm, Axial
40
20
0
−20
−40
−100
−50
0
50
100
X mm, Circ

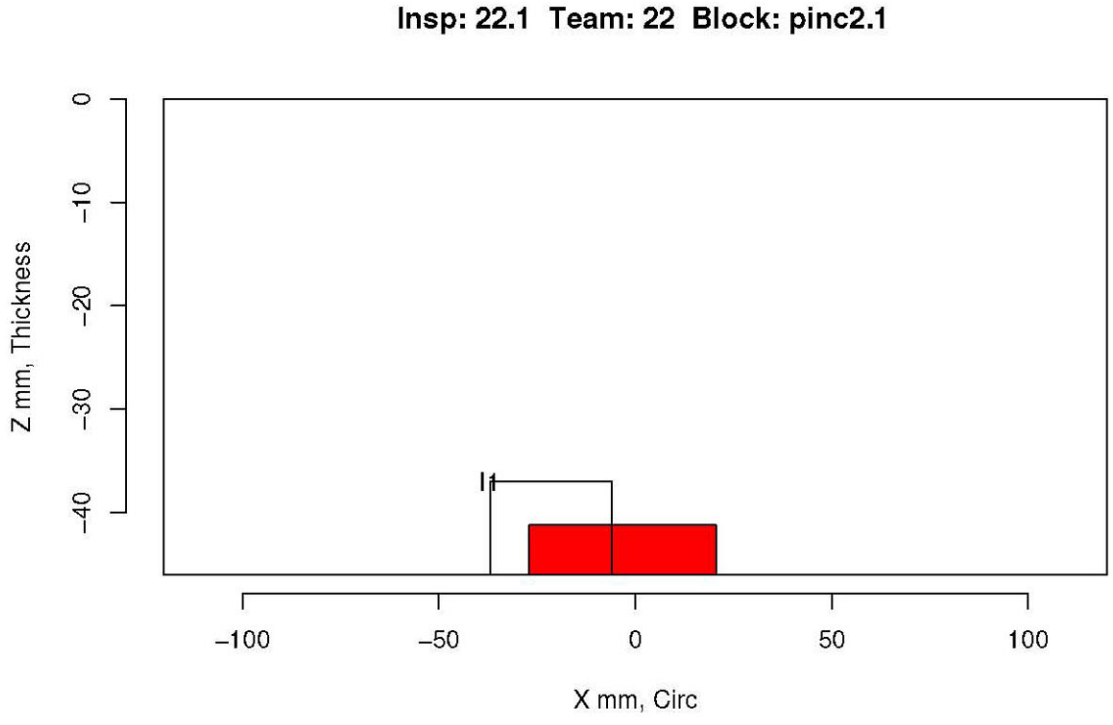
Insp: 22.1 Team: 22 Block: pinc2.1
Z mm, Thickness
0
−10
−20
−30
−40
−100
−50
0
50
100
X mm, Circ

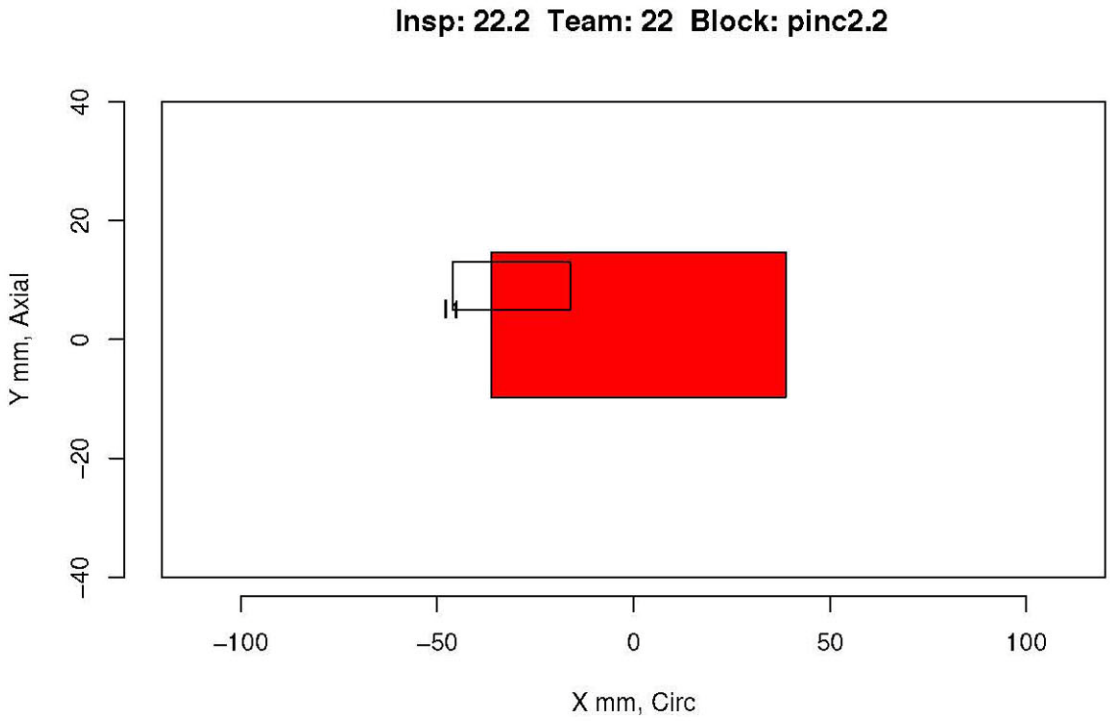
Insp: 22.2 Team: 22 Block: pinc2.2
Y mm, Axial
40
20
0
-20
-40
-100
-50
0
50
100
X mm, Circ

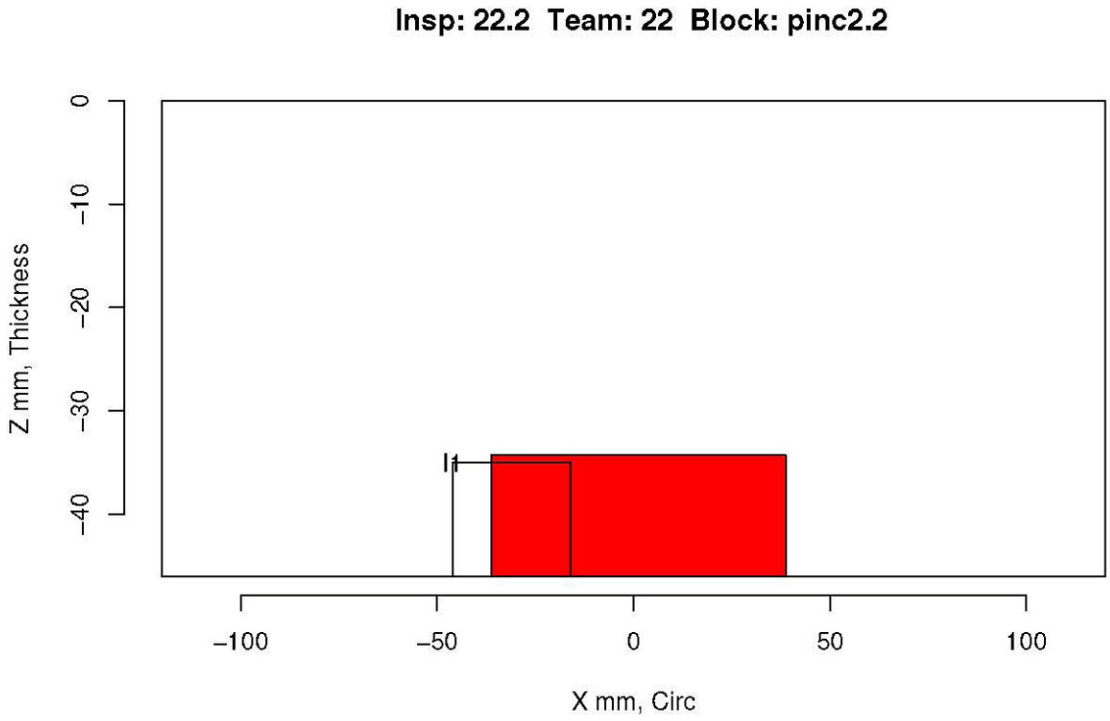
Insp: 22.2 Team: 22 Block: pinc2.2
Z mm, Thickness
0
-10
-20
-30
-40
-100
-50
0
50
100
X mm, Circ

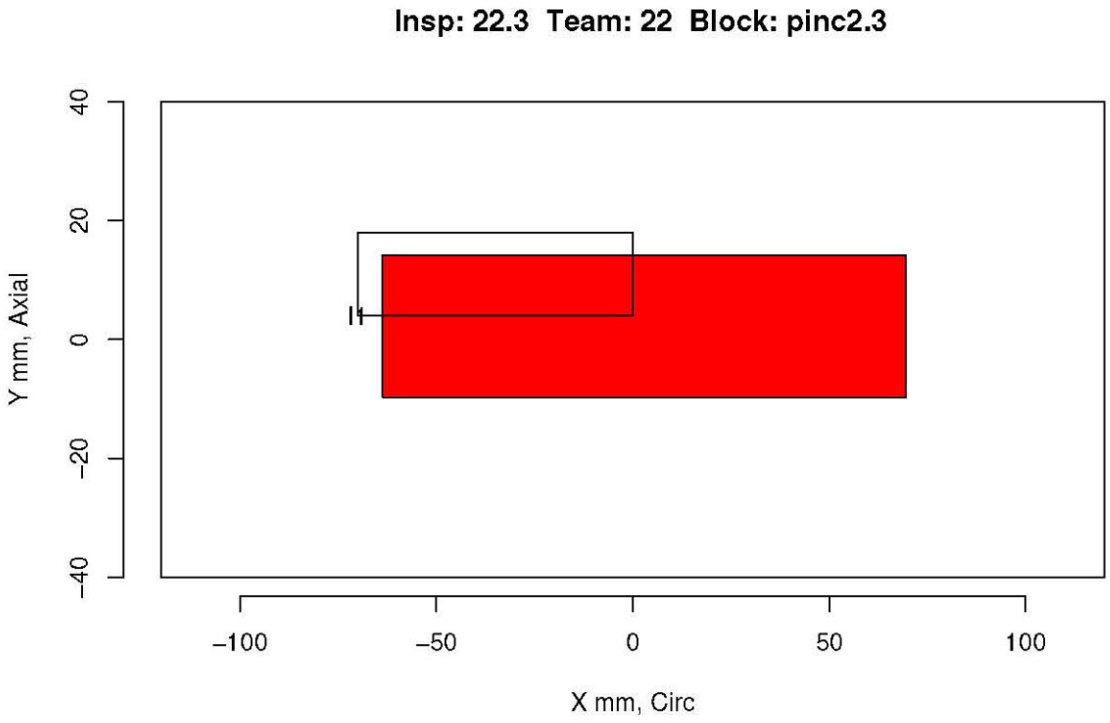
Insp: 22.3 Team: 22 Block: pinc2.3
Y mm, Axial
40
20
0
−20
−40
−100
−50
0
50
100
X mm, Circ

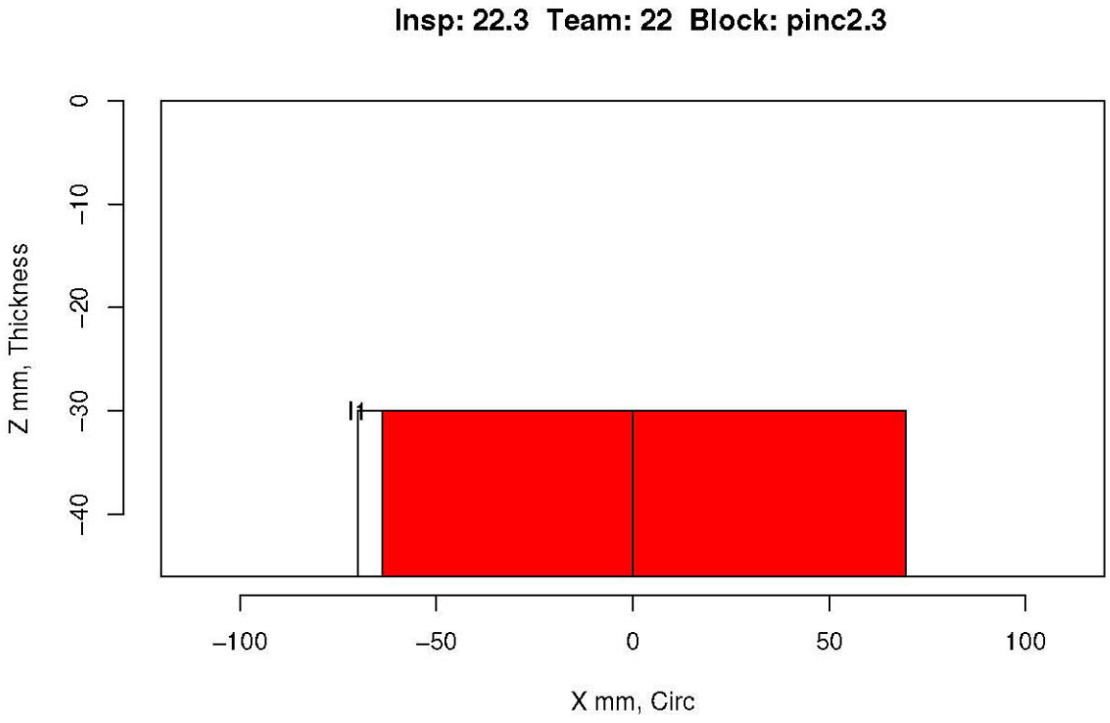
Insp: 22.3 Team: 22 Block: pinc2.3
Z mm, Thickness
0
−10
−20
−30
−40
−100
−50
0
50
100
X mm, Circ

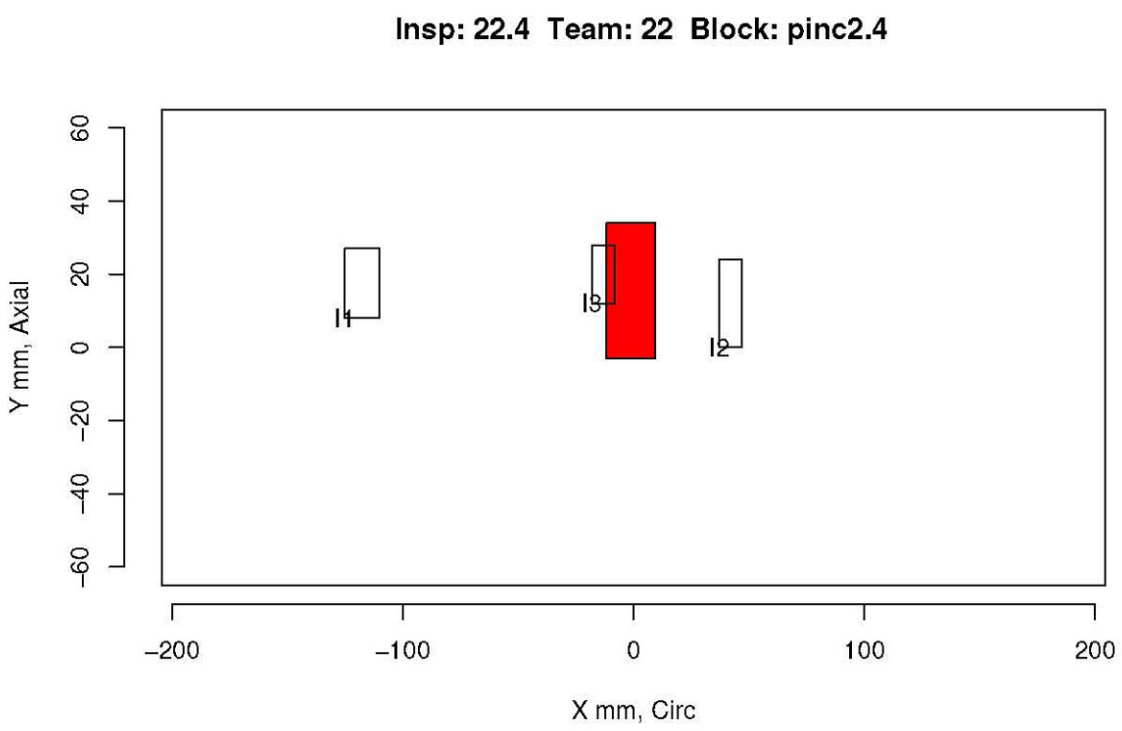
Insp: 22.4 Team: 22 Block: pinc2.4
Y mm, Axial
60
40
20
0
−20
−40
−60
I1
I3
I2
−200
−100
0
100
200
X mm, Circ

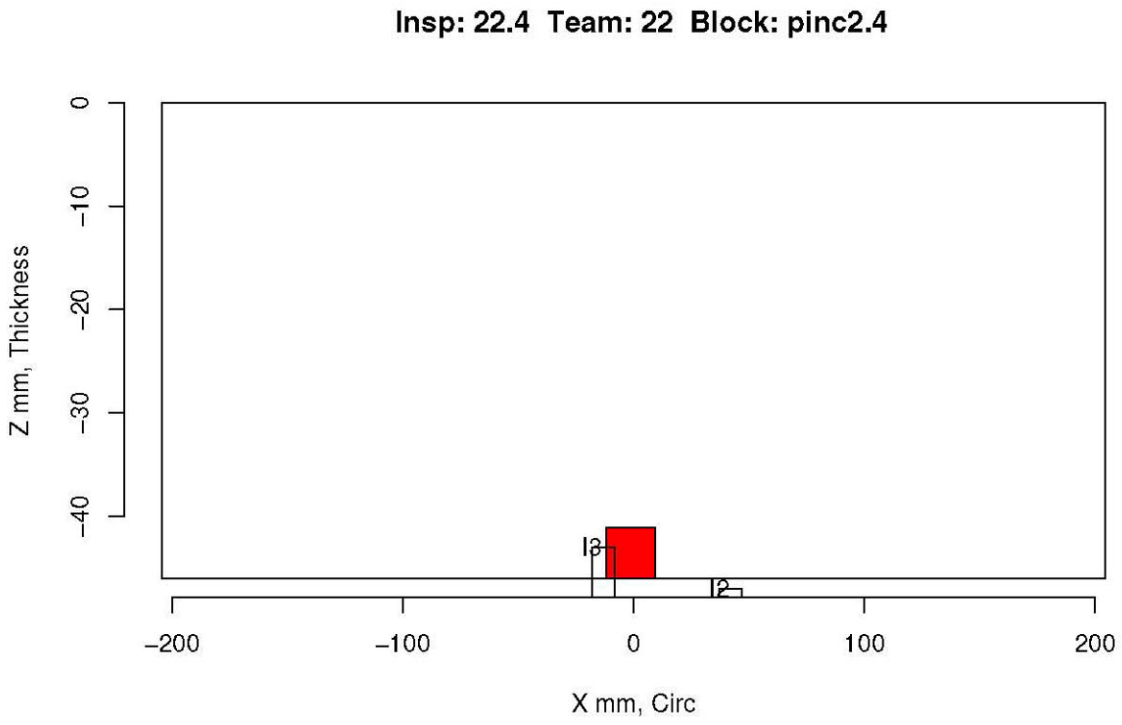
Insp: 22.4 Team: 22 Block: pinc2.4
Z mm, Thickness
0
−10
−20
−30
−40
I3
I2
−200
−100
0
100
200
X mm, Circ

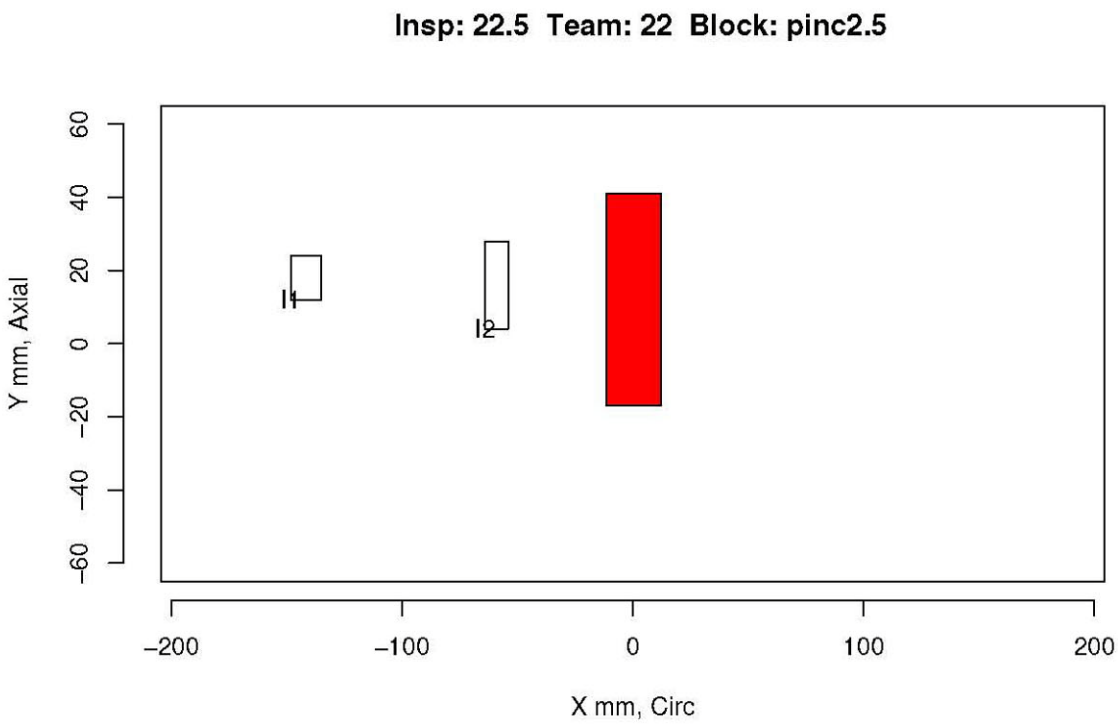
Insp: 22.5 Team: 22 Block: pinc2.5
Y mm, Axial
60
40
20
0
−20
−40
−60
I1
I2
−200
−100
0
100
200
X mm, Circ

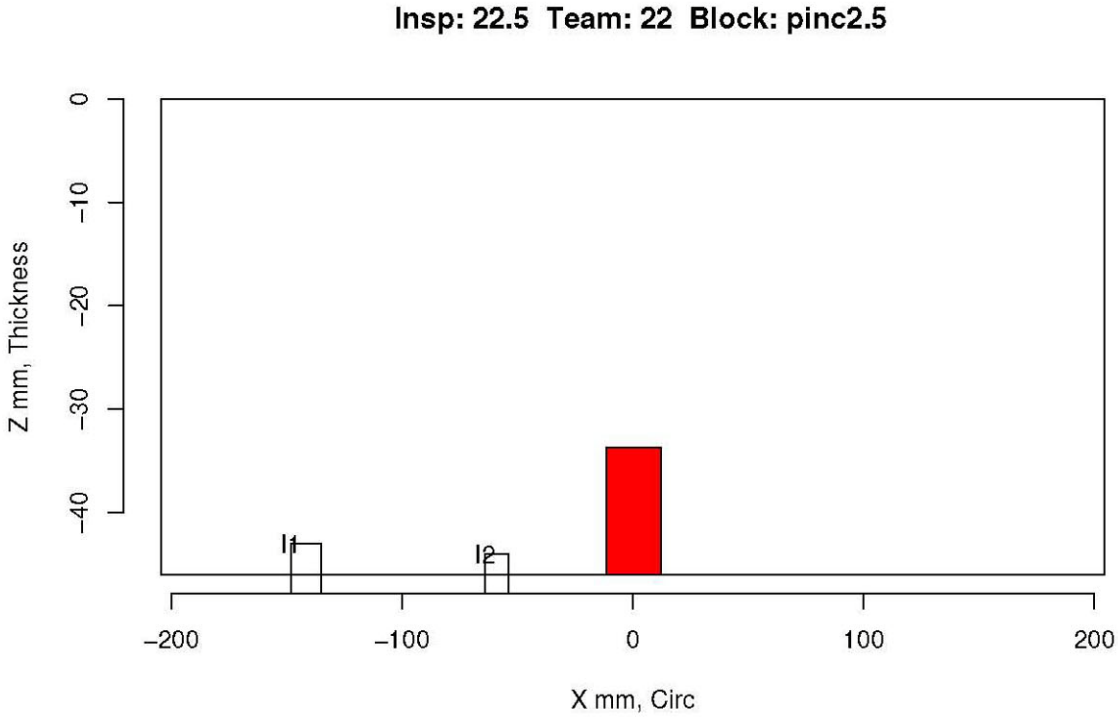
Insp: 22.5 Team: 22 Block: pinc2.5
Z mm, Thickness
0
−10
−20
−30
−40
I1
I2
−200
−100
0
100
200
X mm, Circ

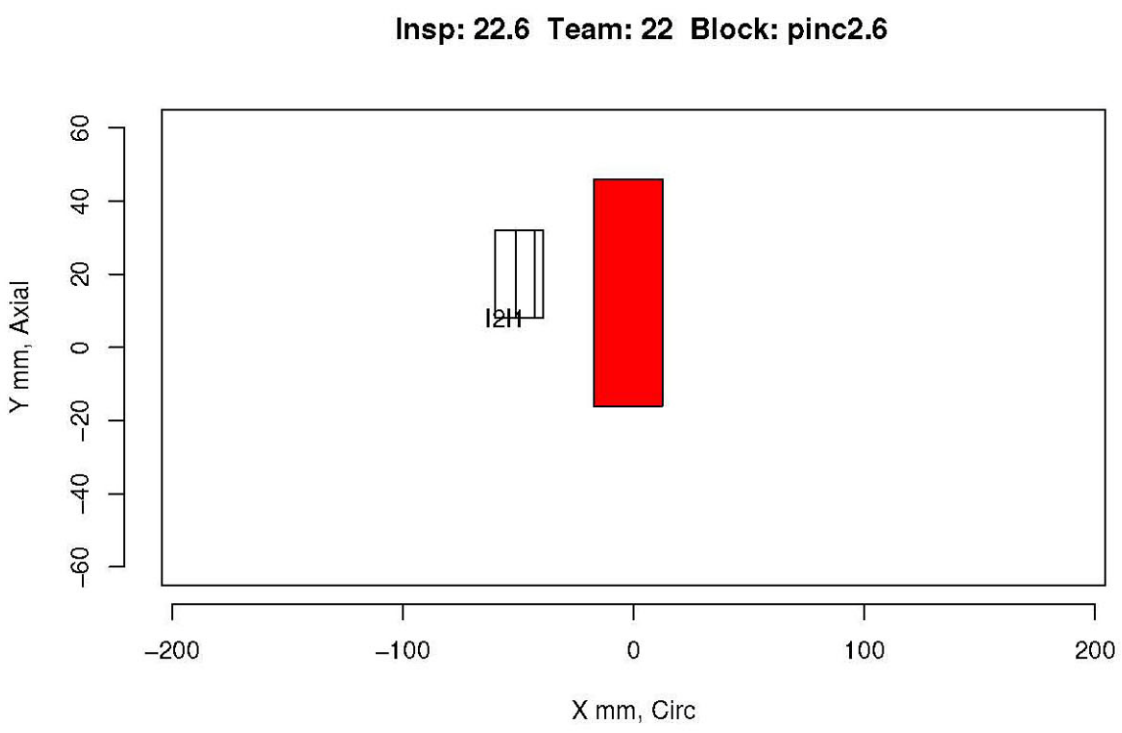
Insp: 22.6 Team: 22 Block: pinc2.6
Y mm, Axial
60
40
20
0
−20
−40
−60
I2
I1
−200
−100
0
100
200
X mm, Circ

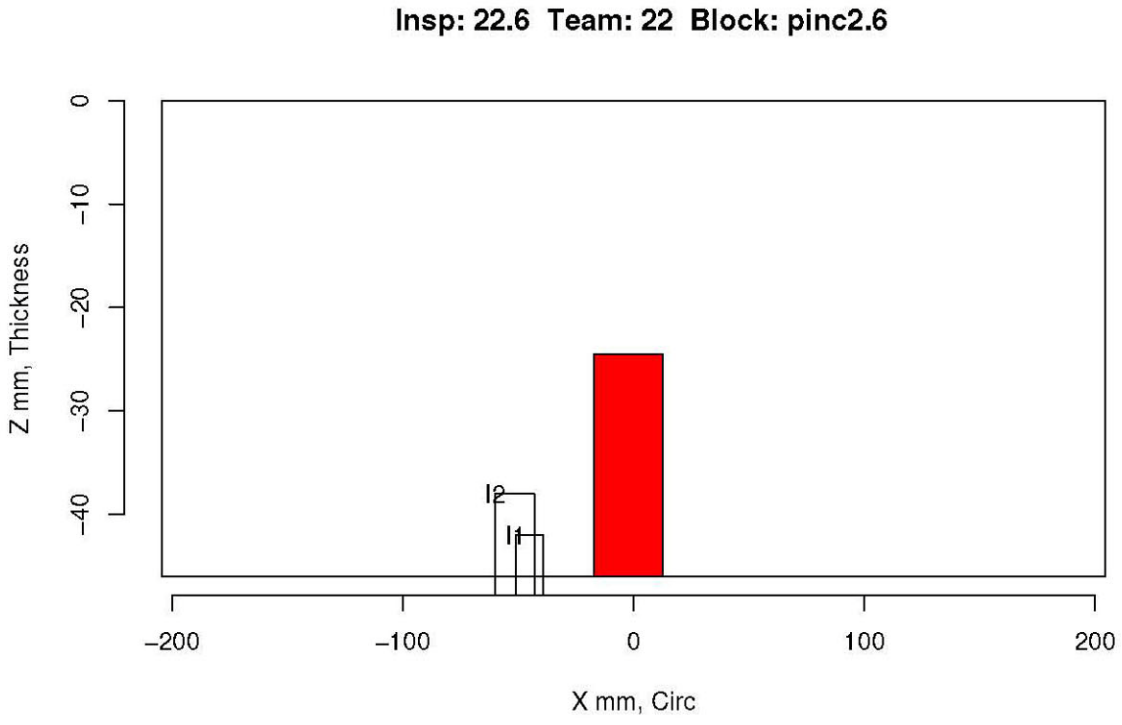
Insp: 22.6 Team: 22 Block: pinc2.6
Z mm, Thickness
0
−10
−20
−30
−40
I2
I1
−200
−100
0
100
200
X mm, Circ

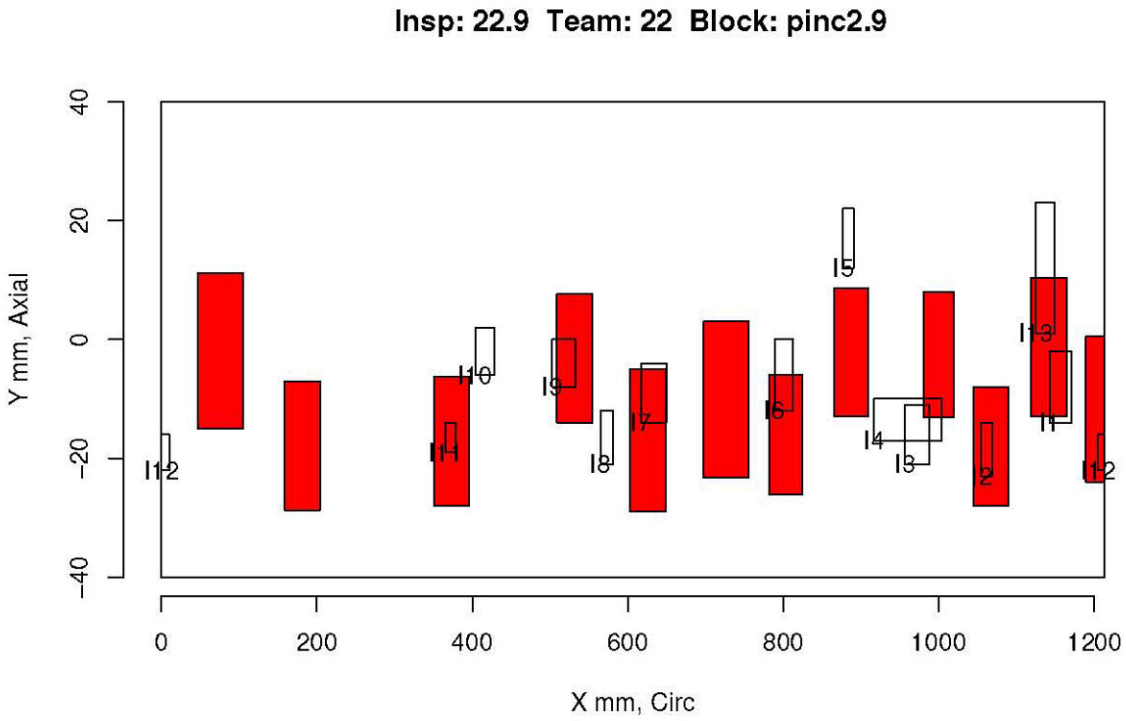
Insp: 22.9 Team: 22 Block: pinc2.9
Y mm, Axial
40
20
0
-20
-40
0
200
400
600
800
1000
1200
X mm, Circ

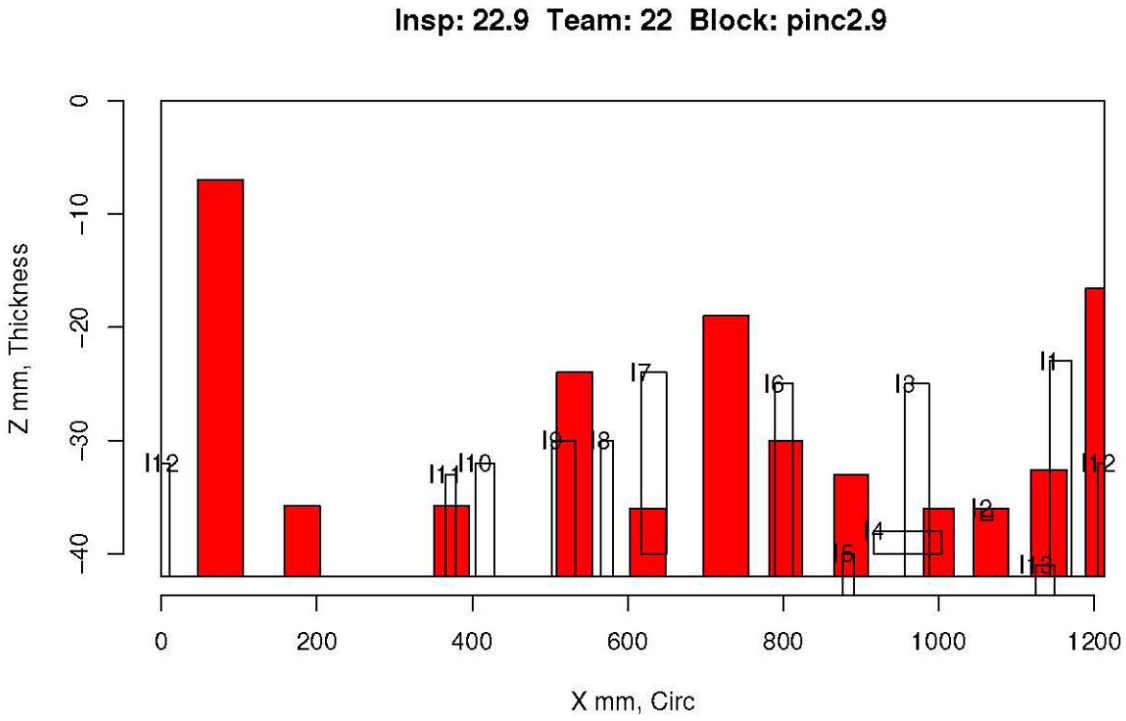
Insp: 22.9 Team: 22 Block: pinc2.9
Z mm, Thickness
0
-10
-20
-30
-40
0
200
400
600
800
1000
1200
X mm, Circ

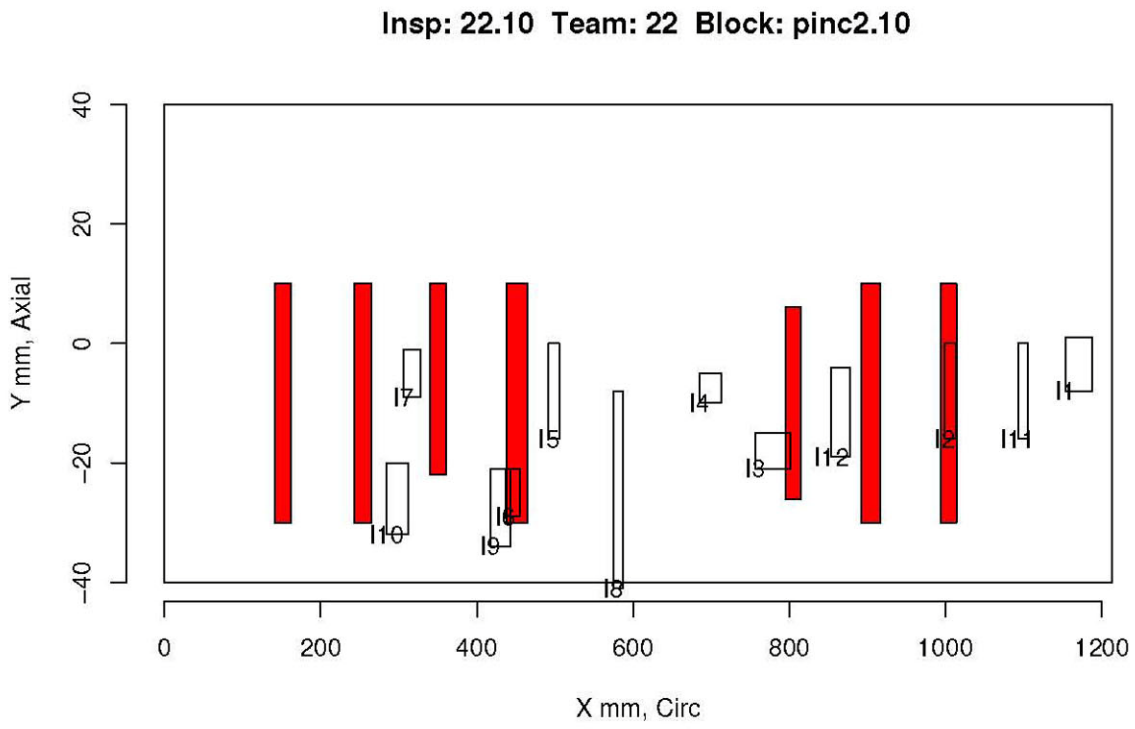
Insp: 22.10 Team: 22 Block: pinc2.10
Y mm, Axial
40
20
0
-20
-40
0
200
400
600
800
1000
1200
X mm, Circ

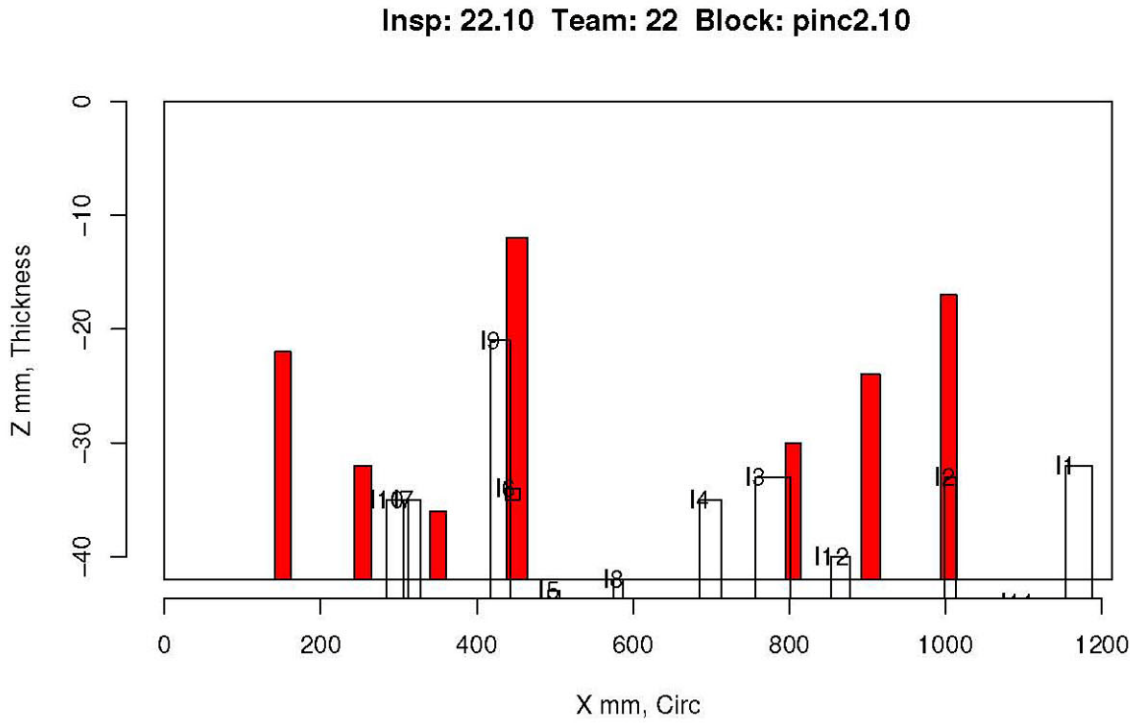
Insp: 22.10 Team: 22 Block: pinc2.10
Z mm, Thickness
0
-10
-20
-30
-40
0
200
400
600
800
1000
1200
X mm, Circ

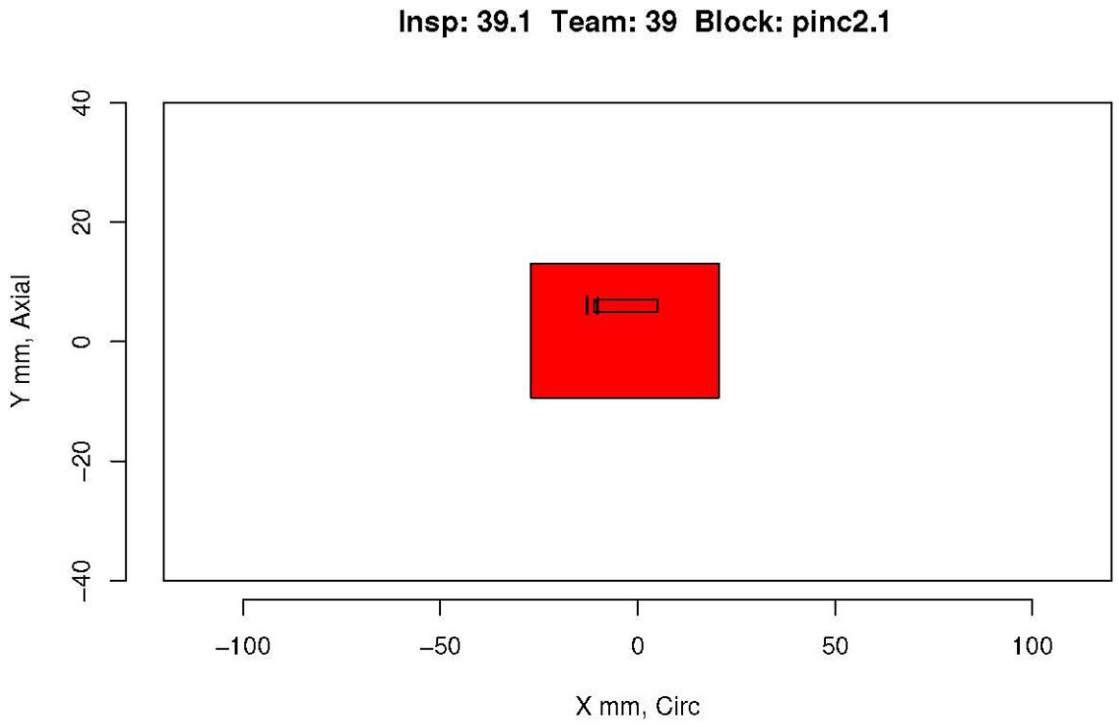
Insp: 39.1 Team: 39 Block: pinc2.1
Y mm, Axial
40
20
0
−20
−40
−100
−50
0
50
100
X mm, Circ

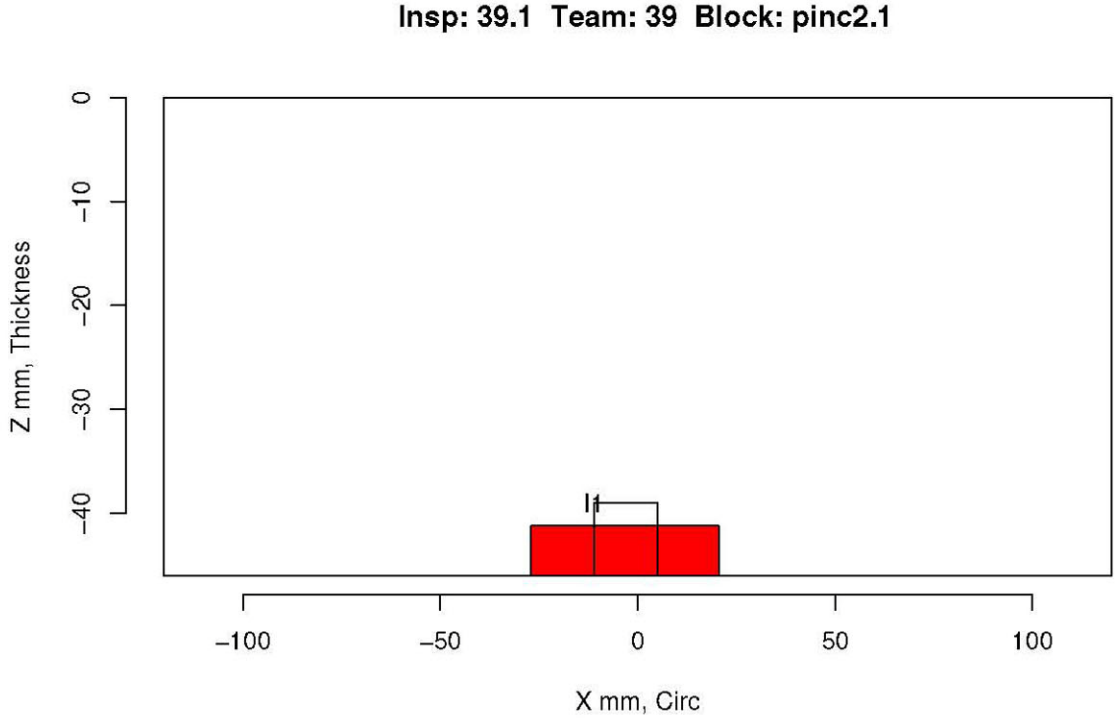
Insp: 39.1 Team: 39 Block: pinc2.1
Z mm, Thickness
0
−10
−20
−30
−40
−100
−50
0
50
100
X mm, Circ

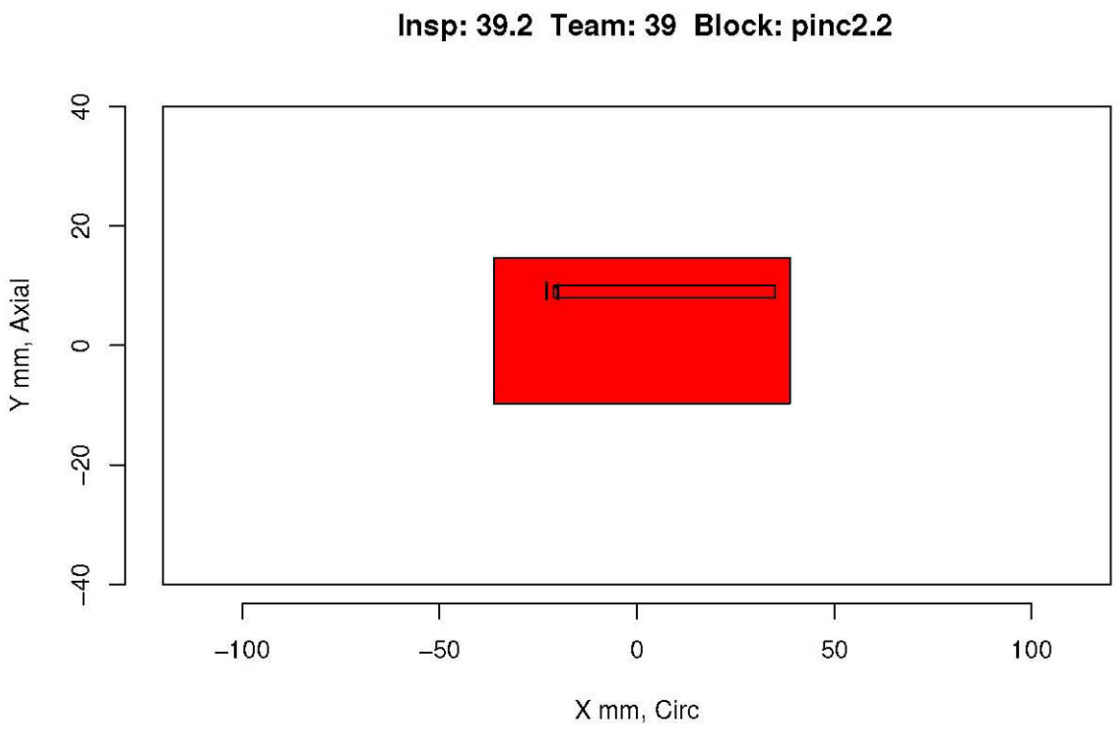
Insp: 39.2 Team: 39 Block: pinc2.2
Y mm, Axial
40
20
0
-20
-40
-100
-50
0
50
100
X mm, Circ

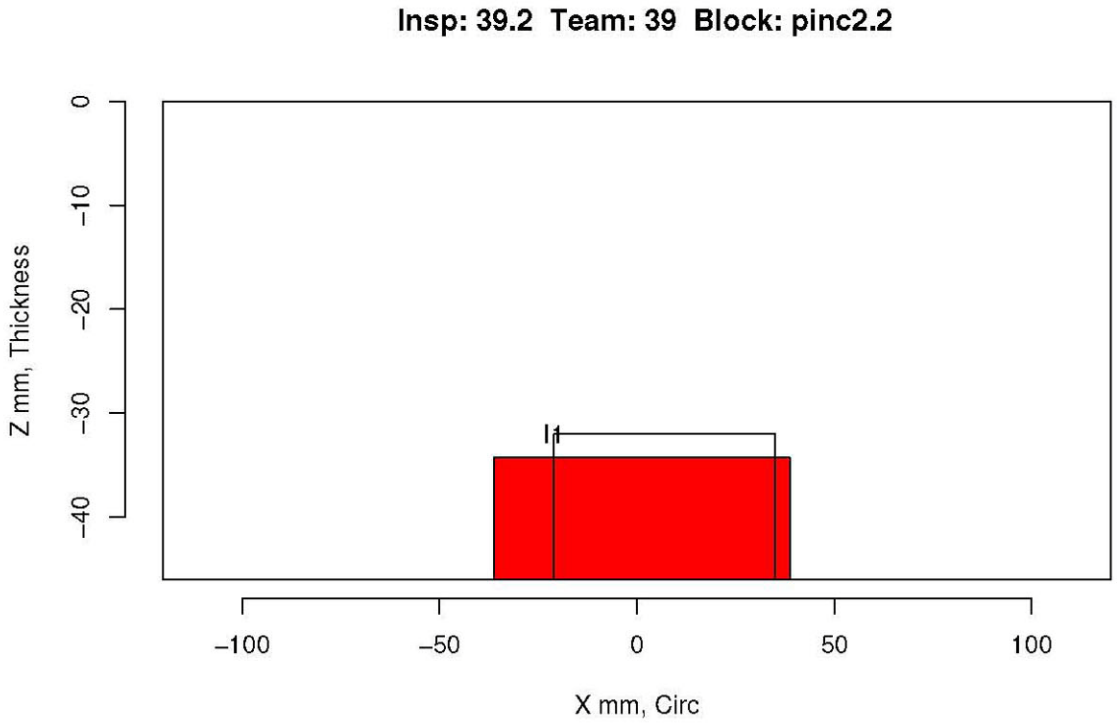
Insp: 39.2 Team: 39 Block: pinc2.2
Z mm, Thickness
0
-10
-20
-30
-40
-100
-50
0
50
100
X mm, Circ

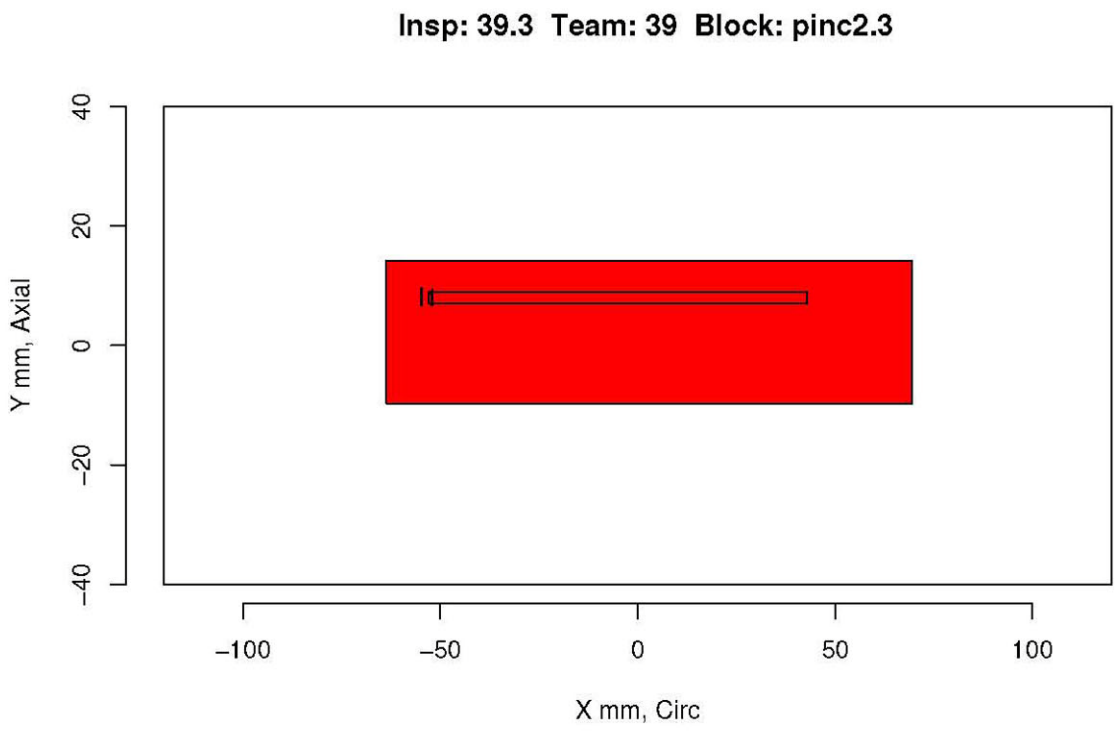
Insp: 39.3 Team: 39 Block: pinc2.3
Y mm, Axial
40
20
0
−20
−40
−100
−50
0
50
100
X mm, Circ

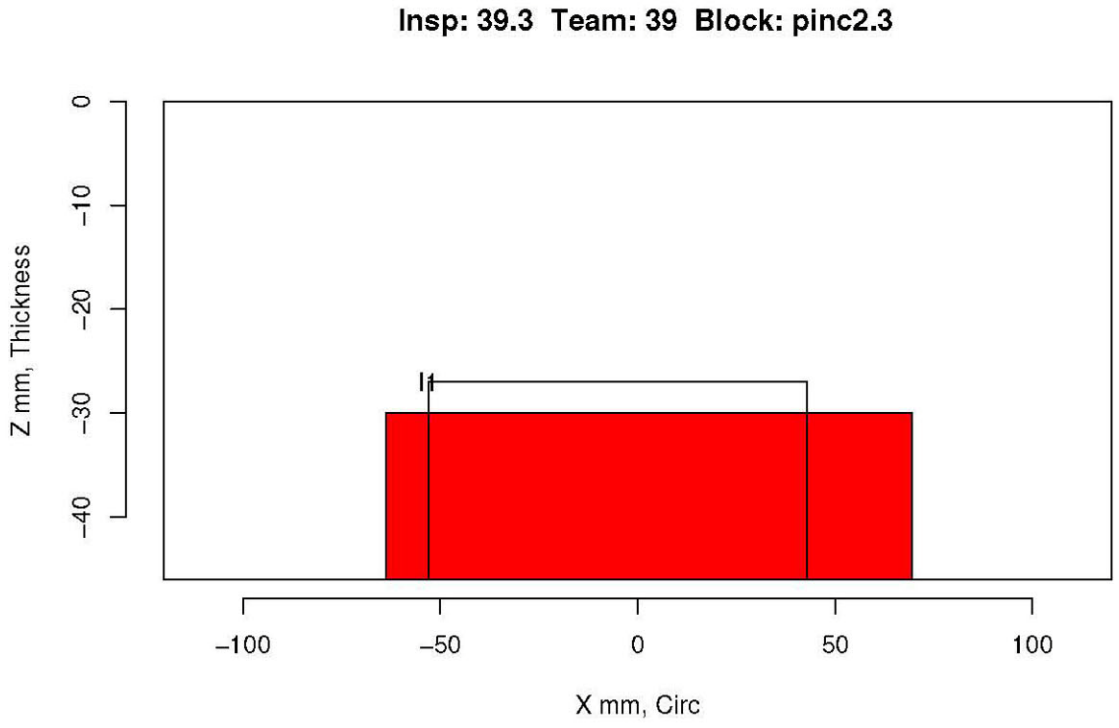
Insp: 39.3 Team: 39 Block: pinc2.3
Z mm, Thickness
0
−10
−20
−30
−40
−100
−50
0
50
100
X mm, Circ

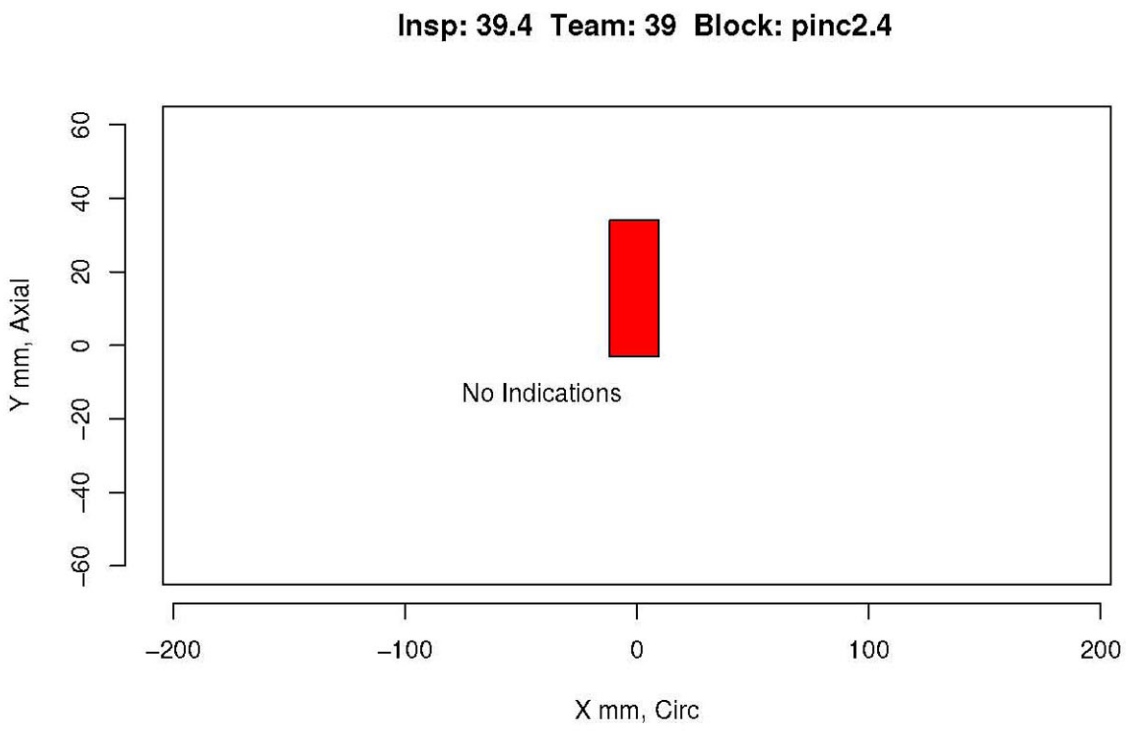
Insp: 39.4 Team: 39 Block: pinc2.4
Y mm, Axial
60
40
20
0
−20
−40
−60
No Indications
−200
−100
0
100
200
X mm, Circ

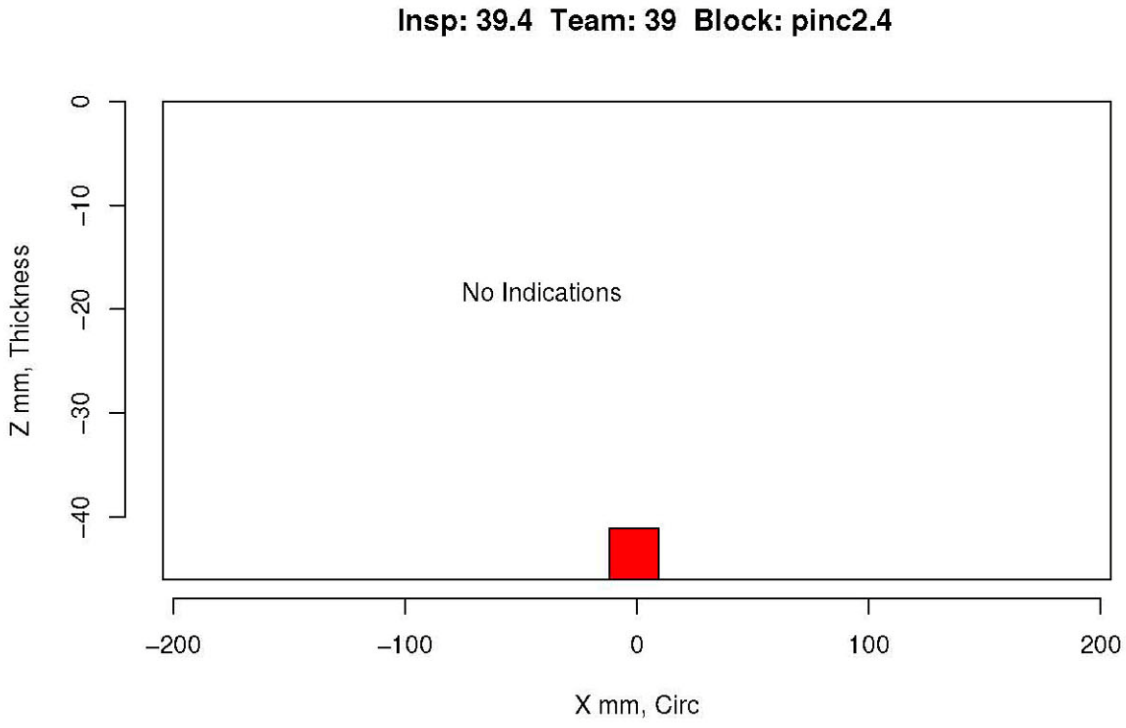
Insp: 39.4 Team: 39 Block: pinc2.4
Z mm, Thickness
0
−10
−20
−30
−40
No Indications
−200
−100
0
100
200
X mm, Circ

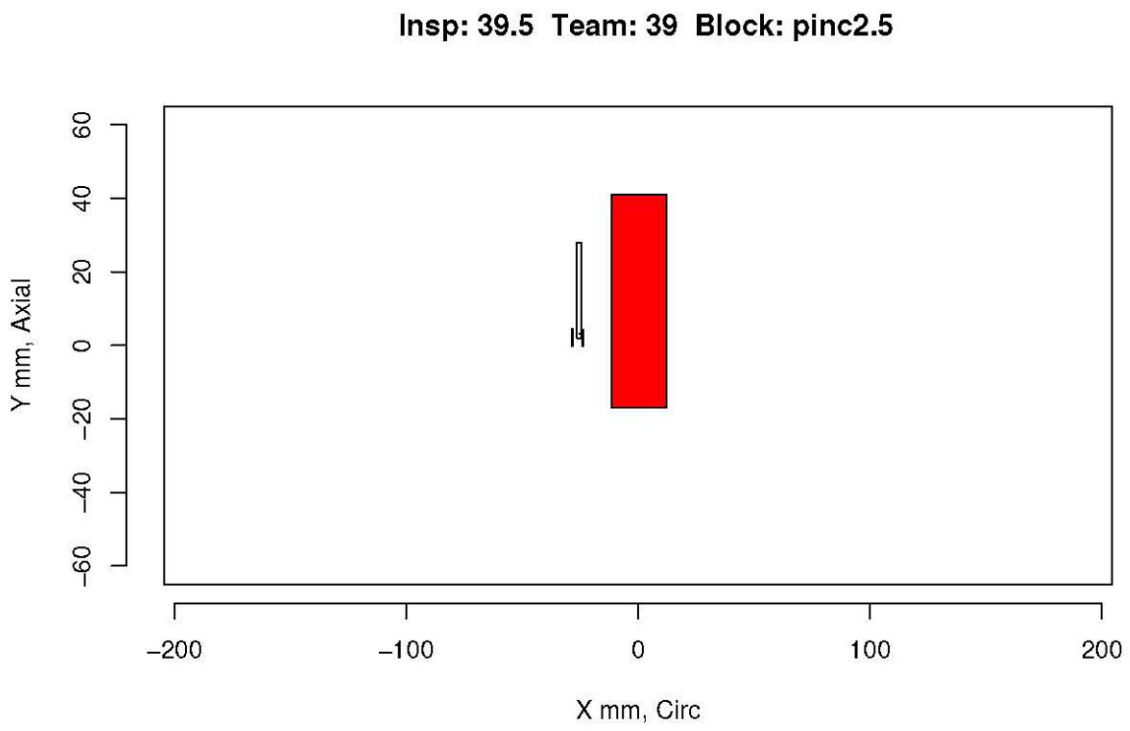
Insp: 39.5 Team: 39 Block: pinc2.5
Y mm, Axial
60
40
20
0
−20
−40
−60
−200
−100
0
100
200
X mm, Circ

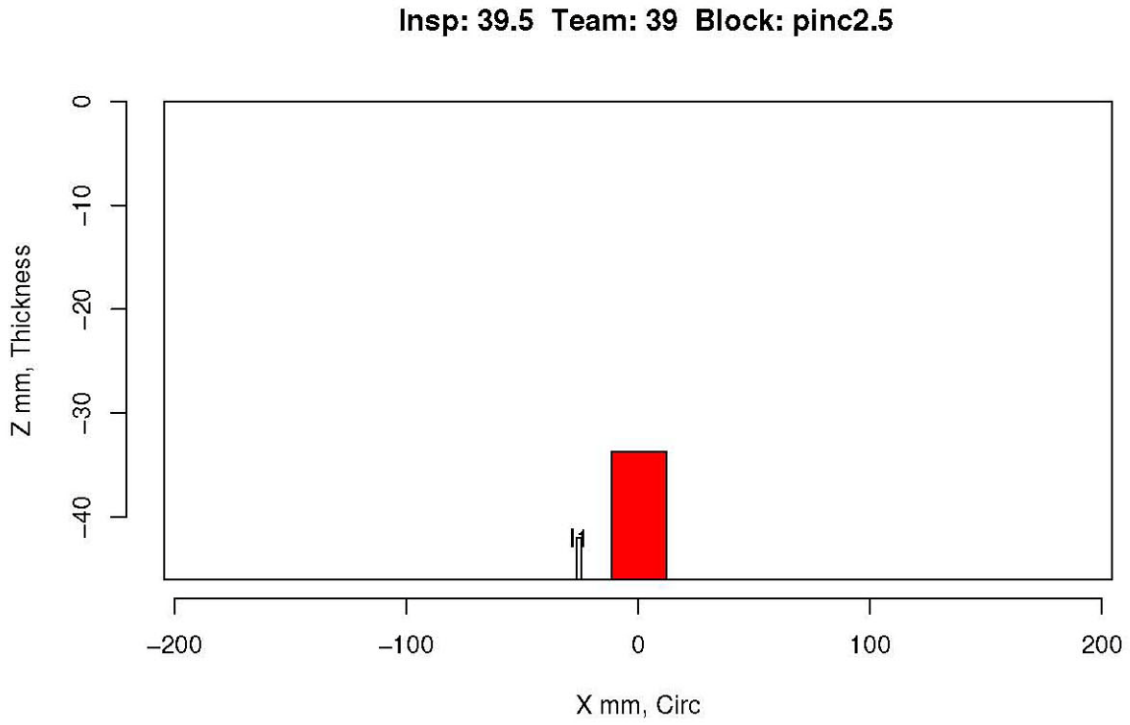
Insp: 39.5 Team: 39 Block: pinc2.5
Z mm, Thickness
0
−10
−20
−30
−40
−200
−100
0
100
200
X mm, Circ

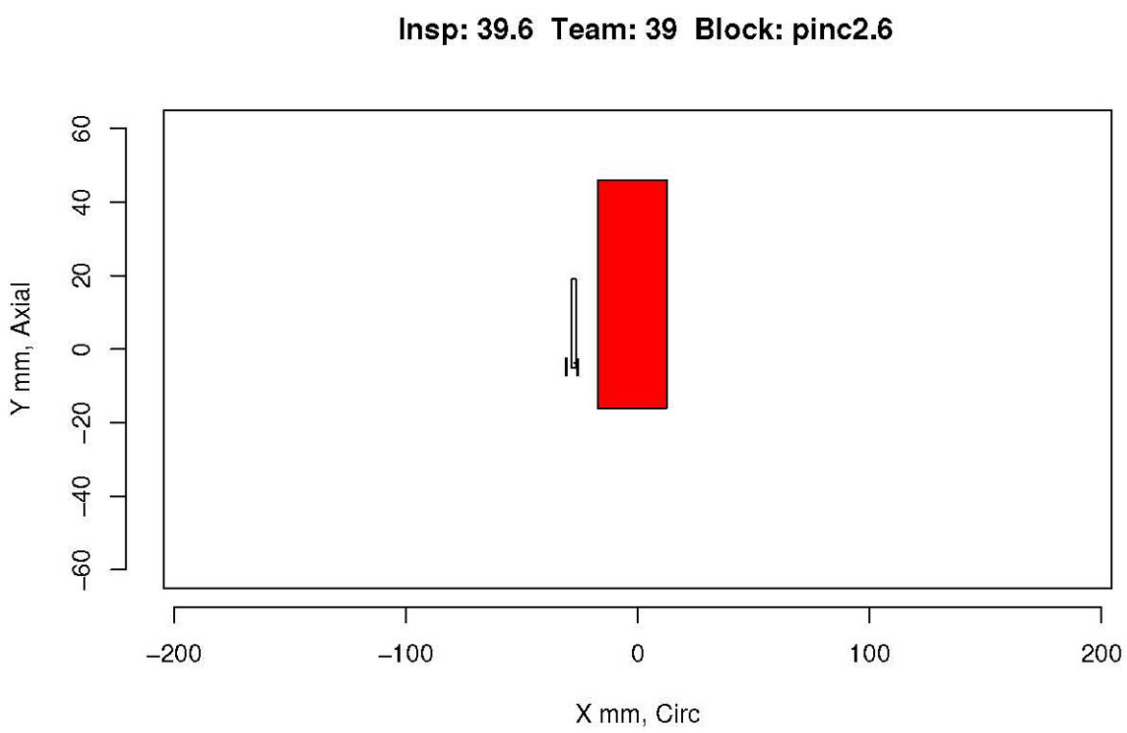
Insp: 39.6 Team: 39 Block: pinc2.6
Y mm, Axial
60
40
20
0
−20
−40
−60
−200
−100
0
100
200
X mm, Circ

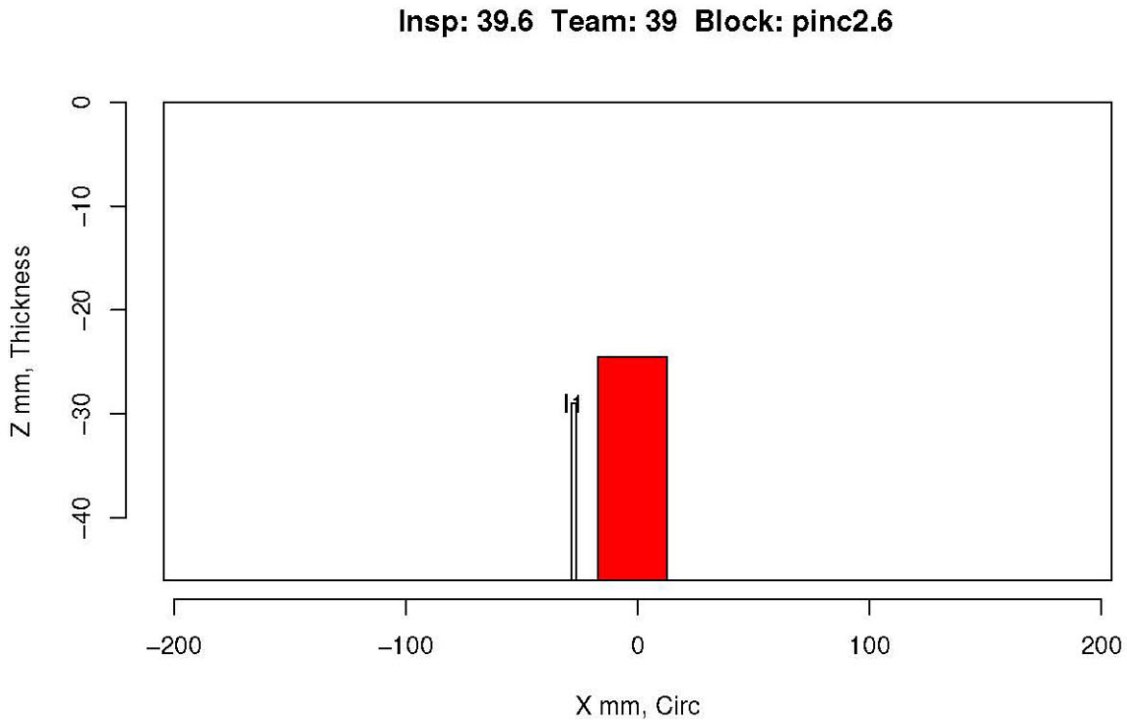
Insp: 39.6 Team: 39 Block: pinc2.6
Z mm, Thickness
0
−10
−20
−30
−40
−200
−100
0
100
200
X mm, Circ

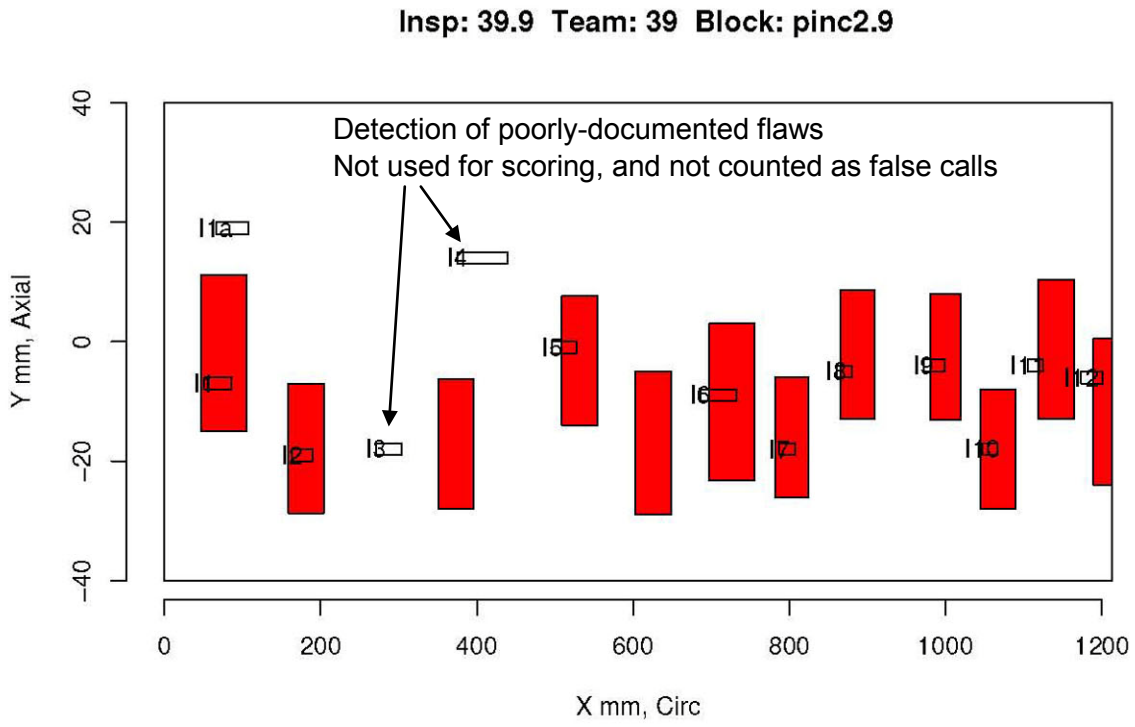
Insp: 39.9 Team: 39 Block: pinc2.9
Detection of poorly-documented flaws
Not used for scoring, and not counted as false calls
Y mm, Axial
X mm, Circ
40
20
0
−20
−40
0
200
400
600
800
1000
1200

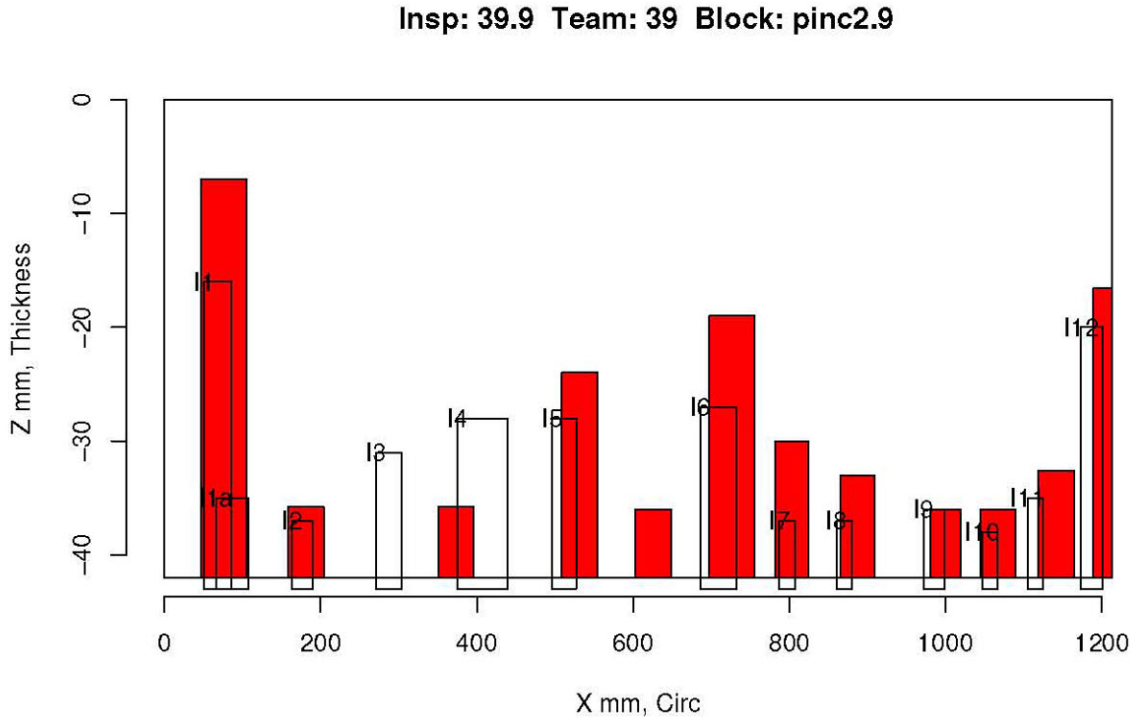
Insp: 39.9 Team: 39 Block: pinc2.9
Z mm, Thickness
X mm, Circ
0
−10
−20
−30
−40
0
200
400
600
800
1000
1200

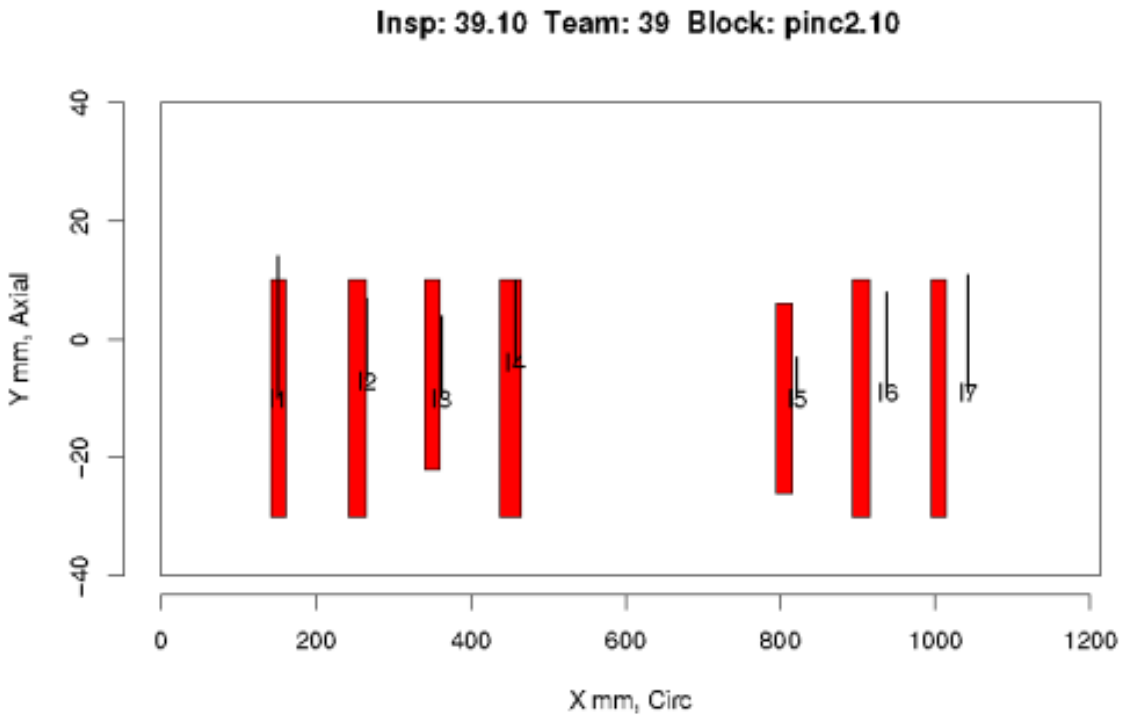
Insp: 39.10 Team: 39 Block: pinc2.10
Y mm, Axial
40
20
0
-20
-40
I1
I2
I3
I4
I5
I6
I7
0
200
400
600
800
1000
1200
X mm, Circ

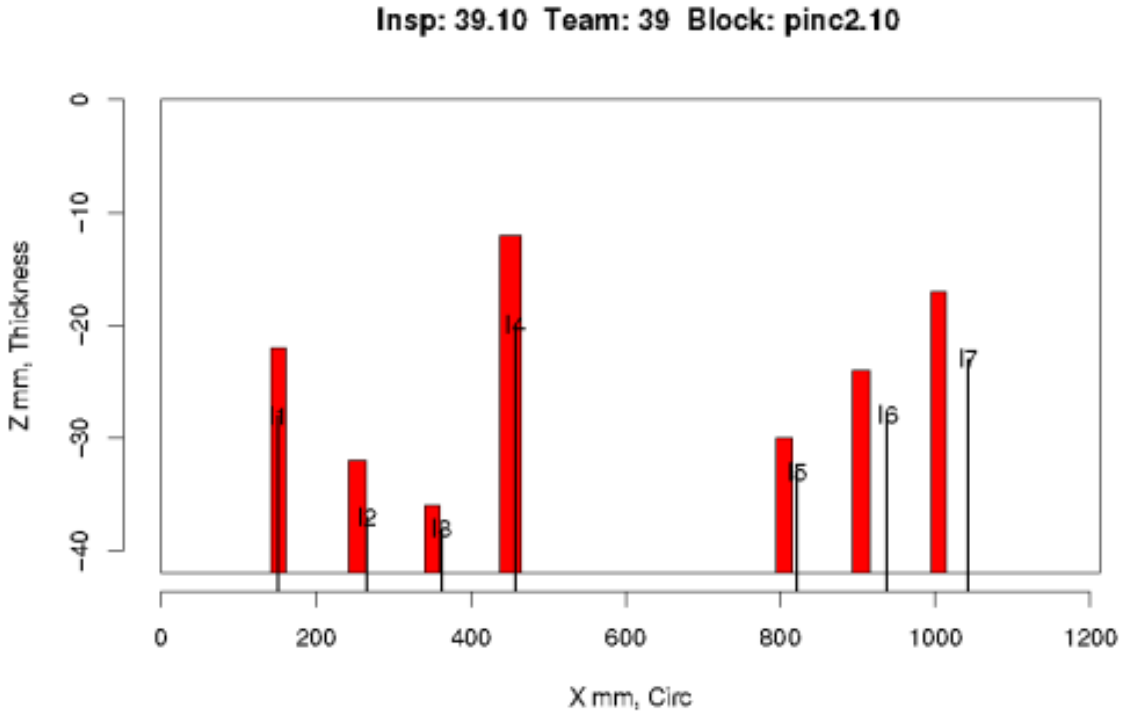
Insp: 39.10 Team: 39 Block: pinc2.10
Z mm, Thickness
0
-10
-20
-30
-40
I1
I2
I3
I4
I5
I6
I7
0
200
400
600
800
1000
1200
X mm, Circ

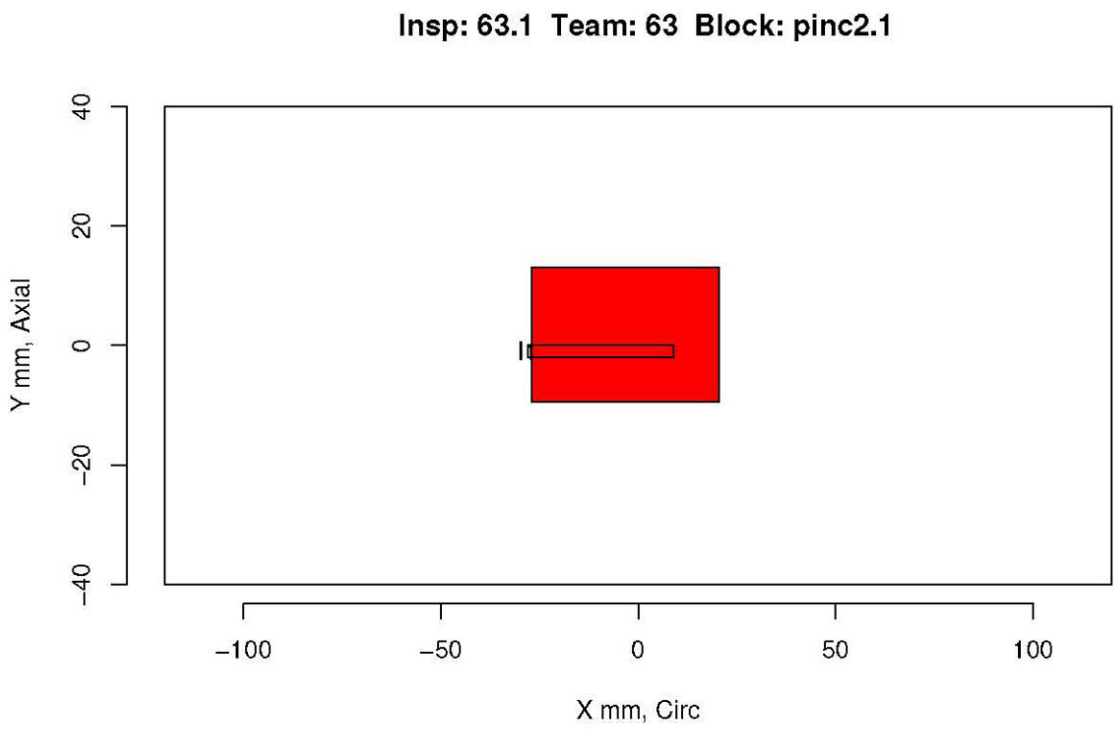
Insp: 63.1 Team: 63 Block: pinc2.1
Y mm, Axial
40
20
0
−20
−40
−100
−50
0
50
100
X mm, Circ

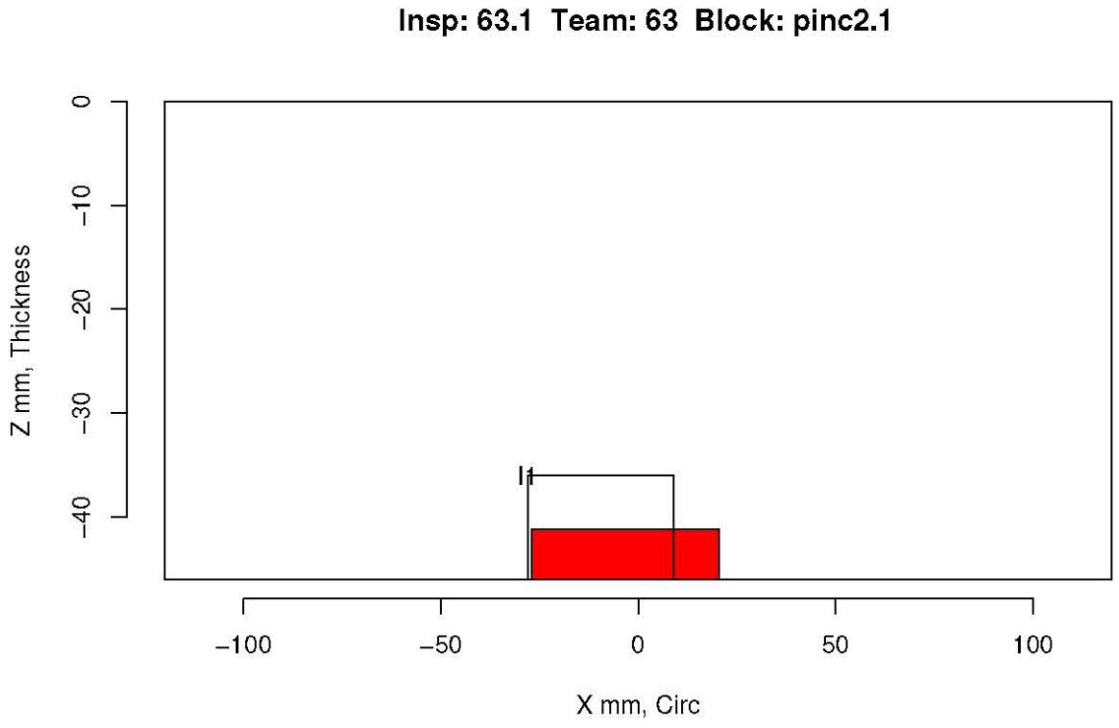
Insp: 63.1 Team: 63 Block: pinc2.1
Z mm, Thickness
0
−10
−20
−30
−40
−100
−50
0
50
100
X mm, Circ

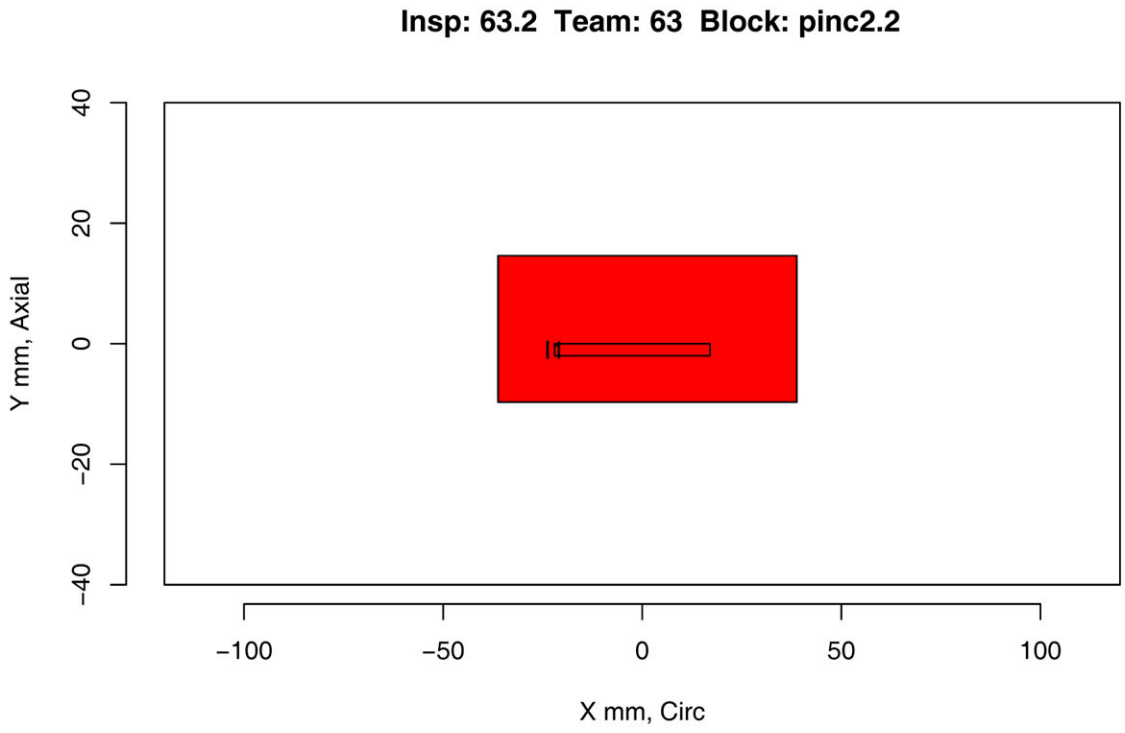
Insp: 63.2 Team: 63 Block: pinc2.2
Y mm, Axial
40
20
0
−20
−40
−100
−50
0
50
100
X mm, Circ

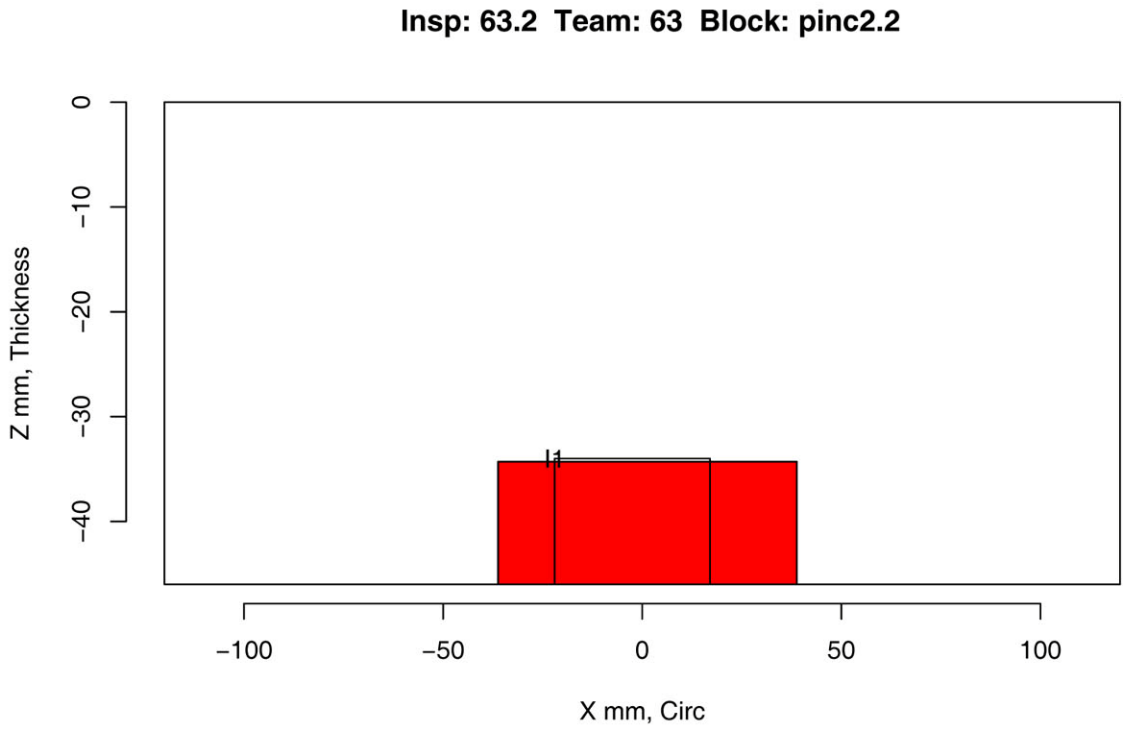
Insp: 63.2 Team: 63 Block: pinc2.2
Z mm, Thickness
0
−10
−20
−30
−40
−100
−50
0
50
100
X mm, Circ

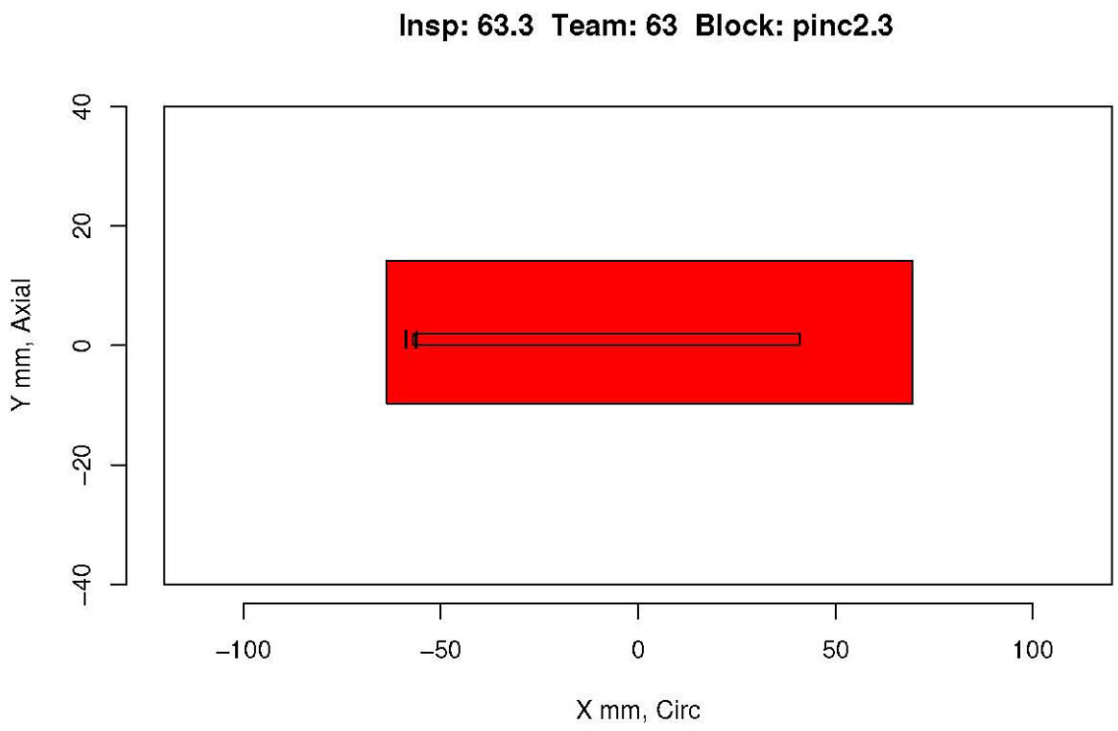
Insp: 63.3 Team: 63 Block: pinc2.3
Y mm, Axial
40
20
0
−20
−40
−100
−50
0
50
100
X mm, Circ

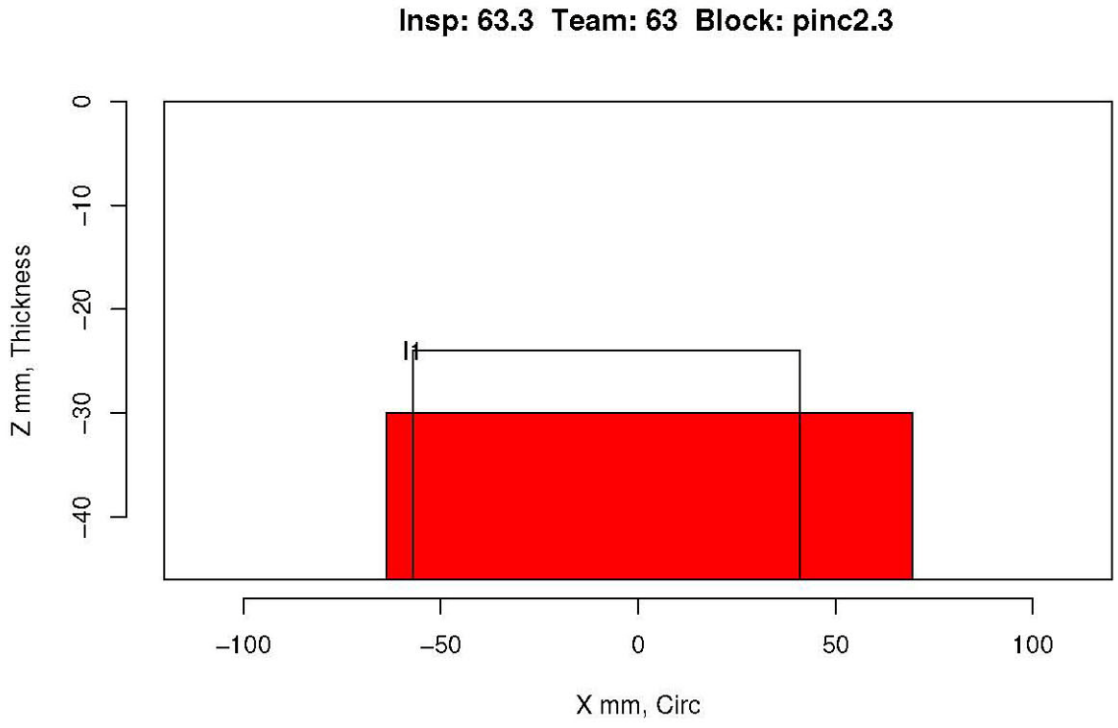
Insp: 63.3 Team: 63 Block: pinc2.3
Z mm, Thickness
0
−10
−20
−30
−40
−100
−50
0
50
100
X mm, Circ

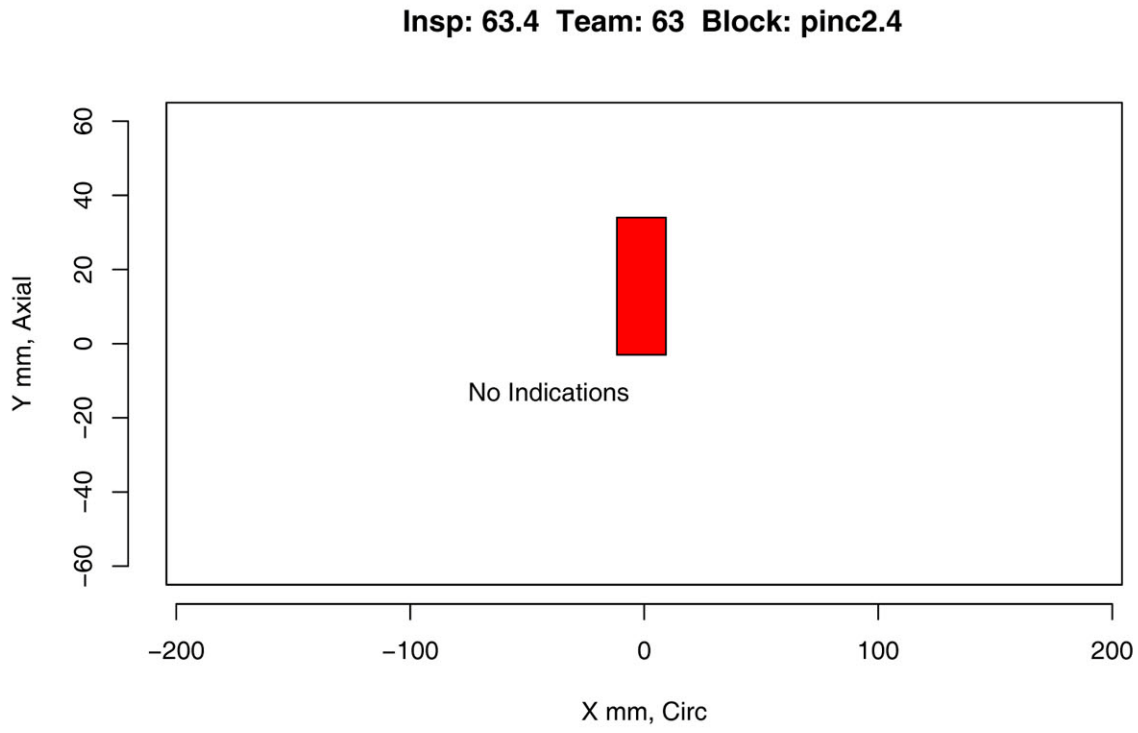
Insp: 63.4 Team: 63 Block: pinc2.4
Y mm, Axial
60
40
20
0
−20
−40
−60
No Indications
−200
−100
0
100
200
X mm, Circ

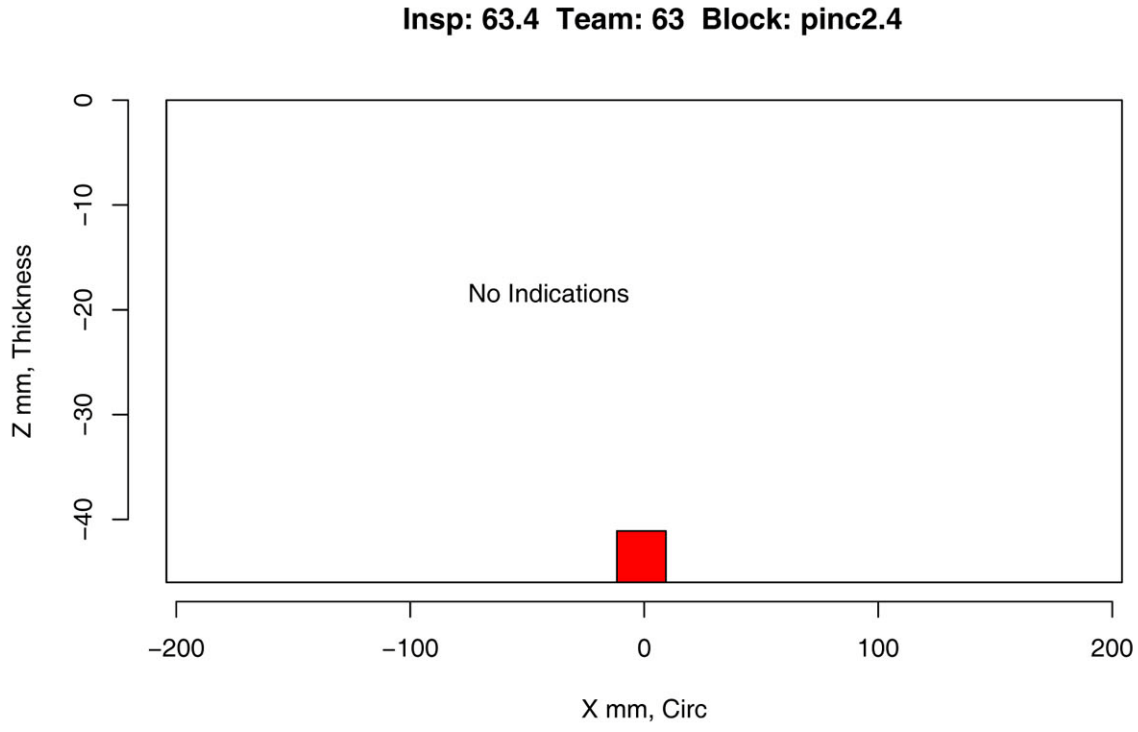
Insp: 63.4 Team: 63 Block: pinc2.4
Z mm, Thickness
0
−10
−20
−30
−40
No Indications
−200
−100
0
100
200
X mm, Circ

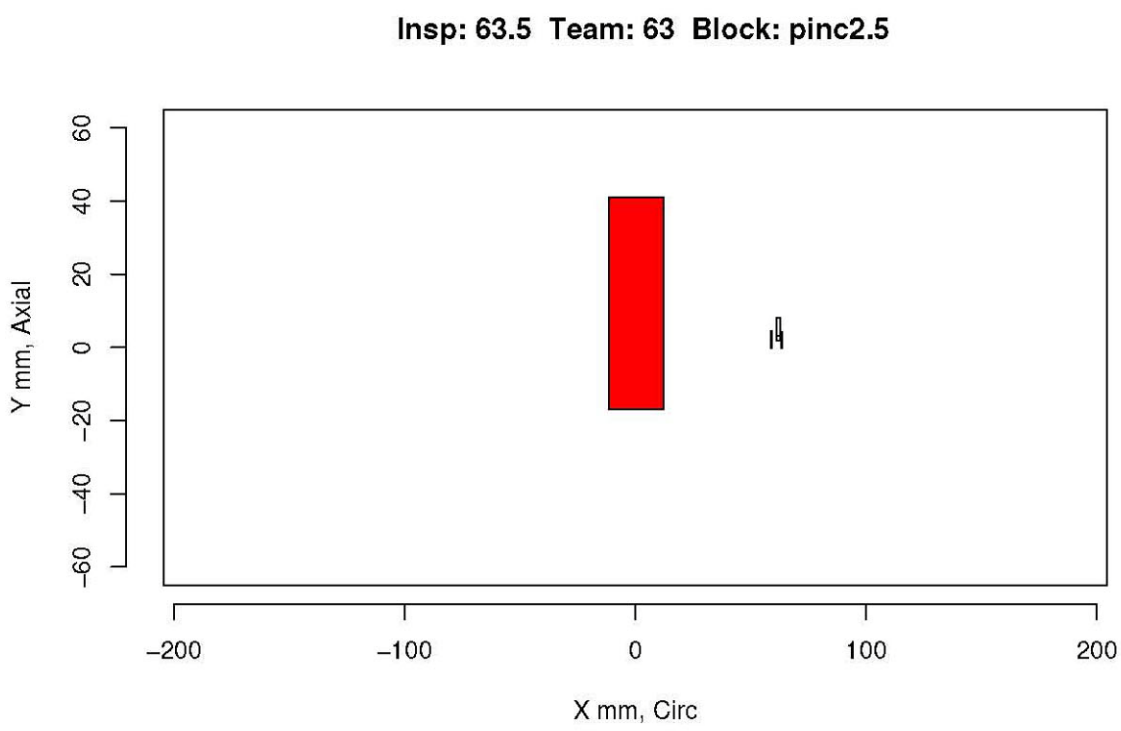
Insp: 63.5 Team: 63 Block: pinc2.5
Y mm, Axial
60
40
20
0
−20
−40
−60
−200
−100
0
100
200
X mm, Circ

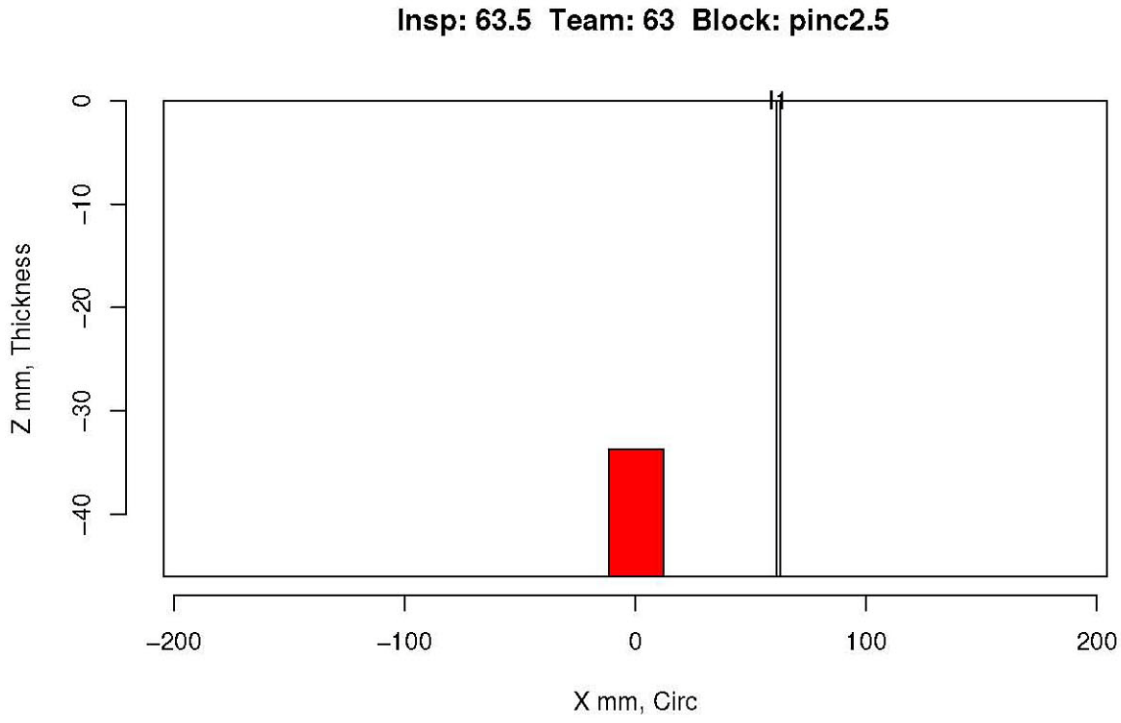
Insp: 63.5 Team: 63 Block: pinc2.5
Z mm, Thickness
0
−10
−20
−30
−40
−200
−100
0
100
200
X mm, Circ

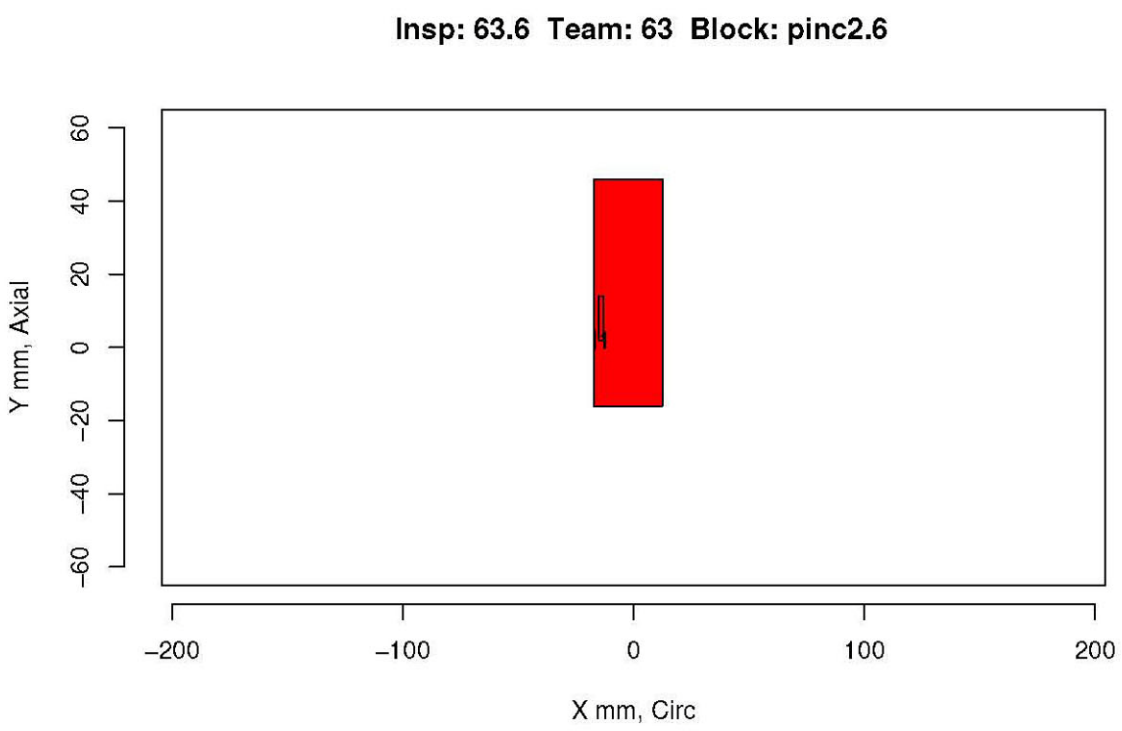
Insp: 63.6 Team: 63 Block: pinc2.6
Y mm, Axial
60
40
20
0
−20
−40
−60
−200
−100
0
100
200
X mm, Circ

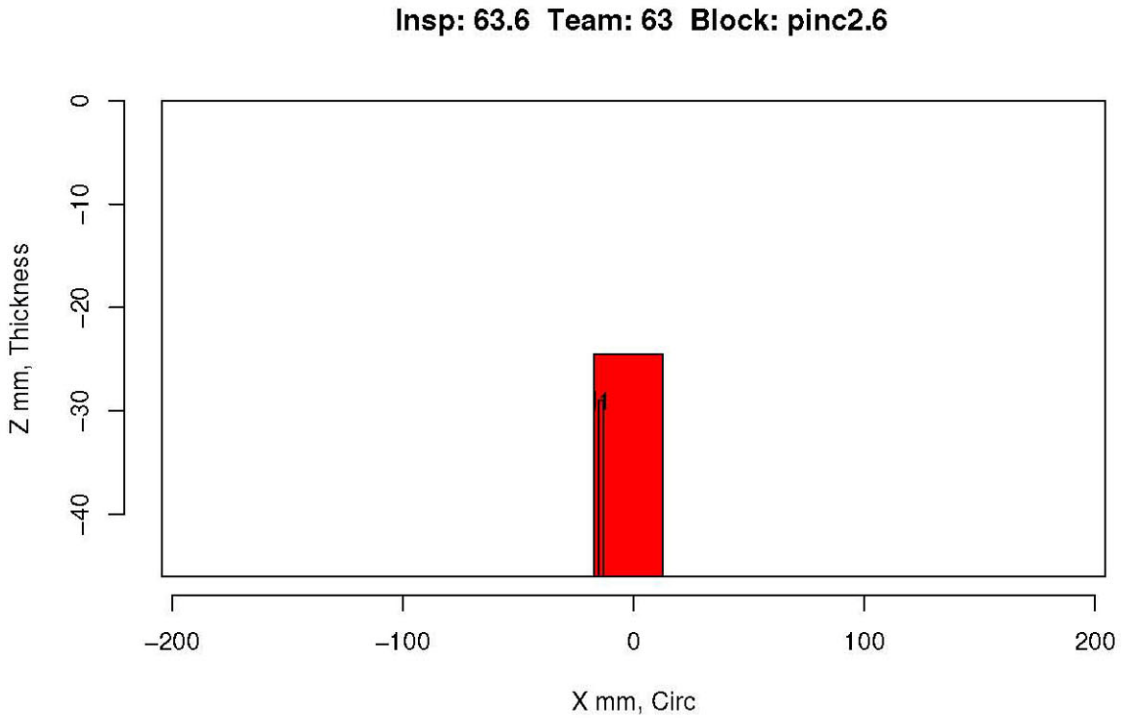
Insp: 63.6 Team: 63 Block: pinc2.6
Z mm, Thickness
0
−10
−20
−30
−40
−200
−100
0
100
200
X mm, Circ

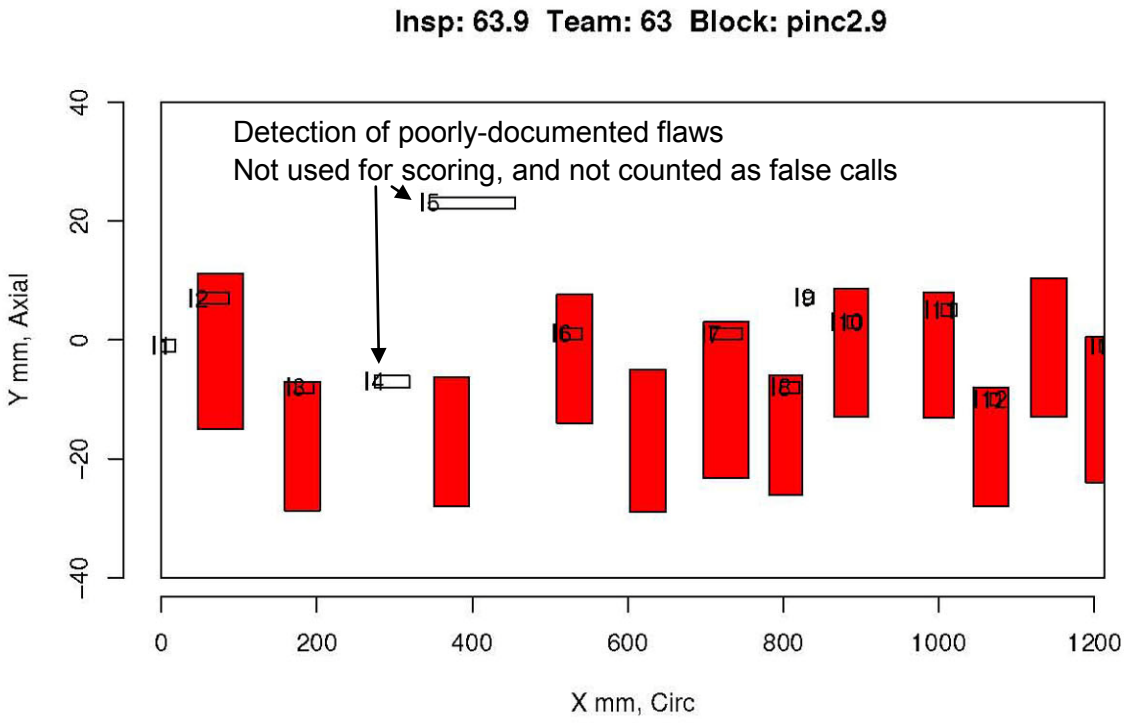
Insp: 63.9 Team: 63 Block: pinc2.9
Detection of poorly-documented flaws
Not used for scoring, and not counted as false calls
Y mm, Axial
X mm, Circ
40
20
0
-20
-40
0
200
400
600
800
1000
1200

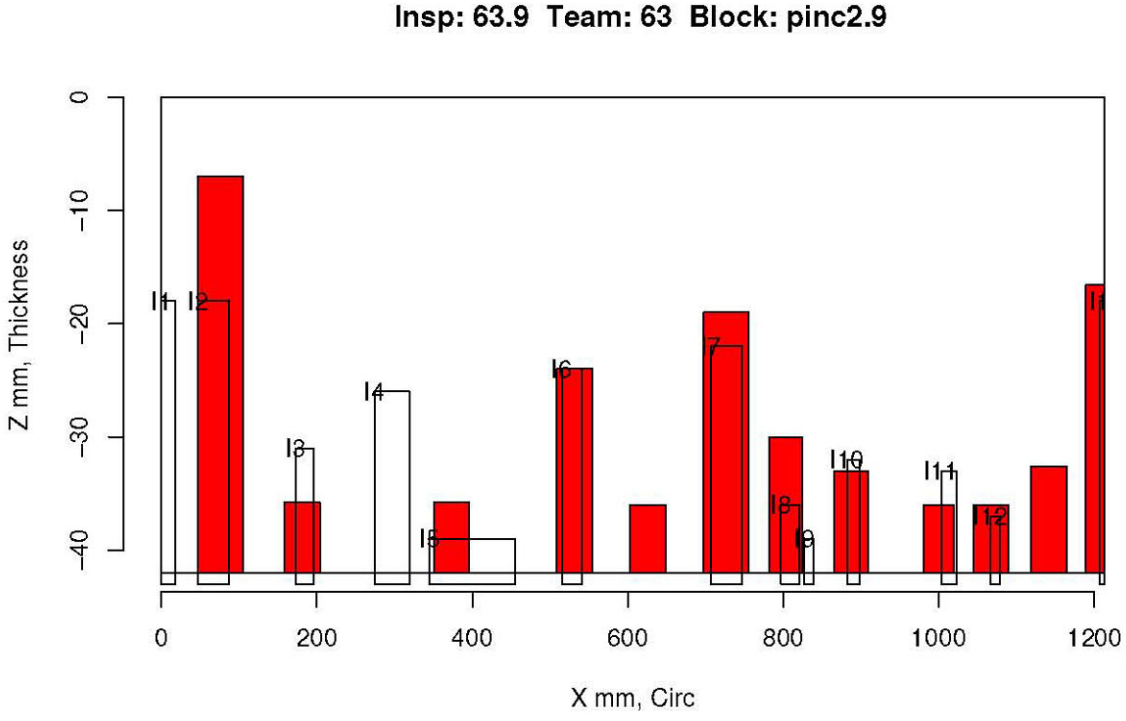
Insp: 63.9 Team: 63 Block: pinc2.9
Z mm, Thickness
X mm, Circ
0
-10
-20
-30
-40
0
200
400
600
800
1000
1200

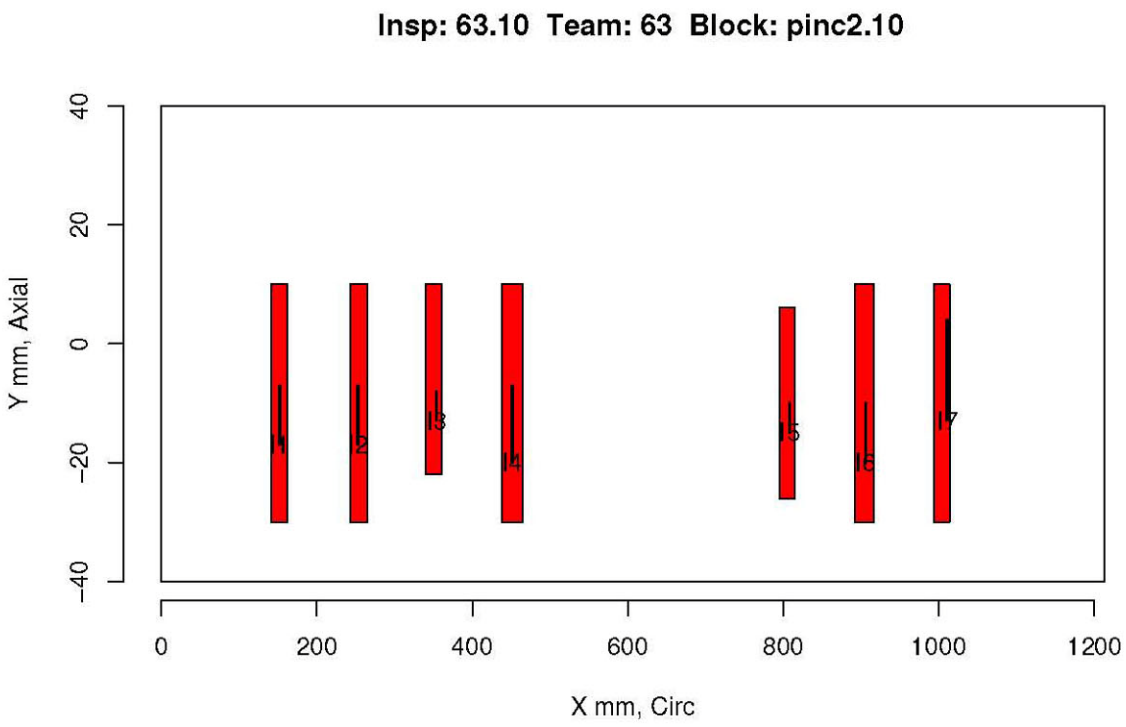
Insp: 63.10 Team: 63 Block: pinc2.10
Y mm, Axial
40
20
0
-20
-40
I1
I2
I3
I4
I5
I6
I7
0
200
400
600
800
1000
1200
X mm, Circ

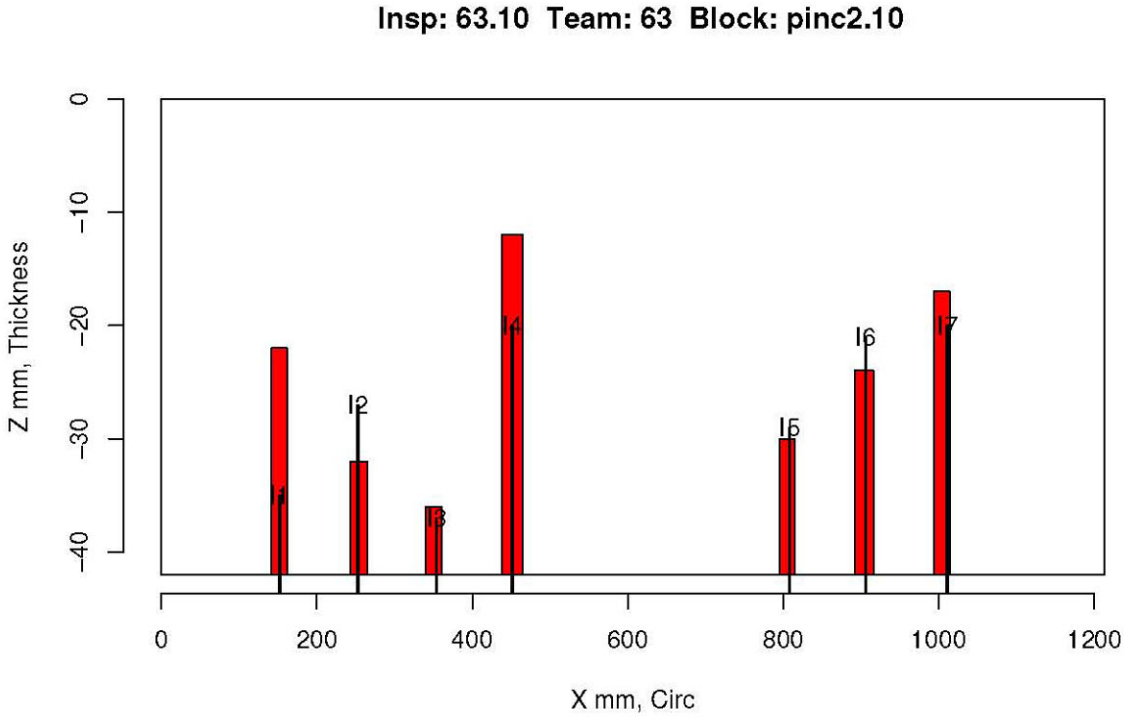
Insp: 63.10 Team: 63 Block: pinc2.10
Z mm, Thickness
0
-10
-20
-30
-40
I1
I2
I3
I4
I5
I6
I7
0
200
400
600
800
1000
1200
X mm, Circ

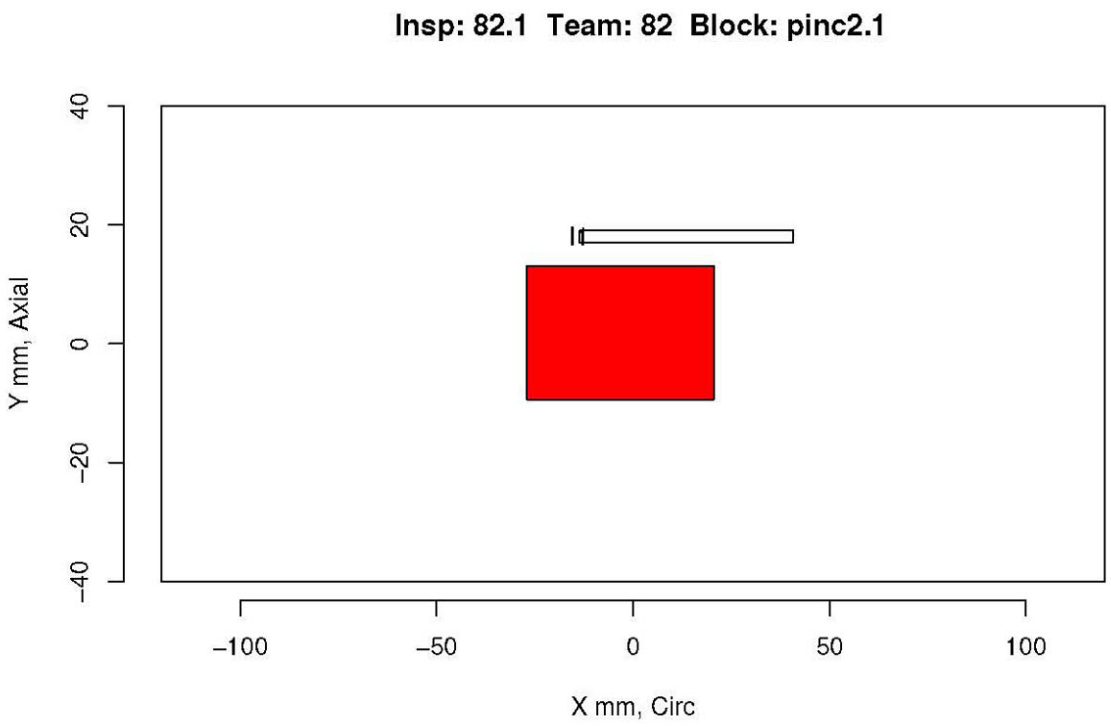
Insp: 82.1 Team: 82 Block: pinc2.1
Y mm, Axial
40
20
0
−20
−40
−100
−50
0
50
100
X mm, Circ

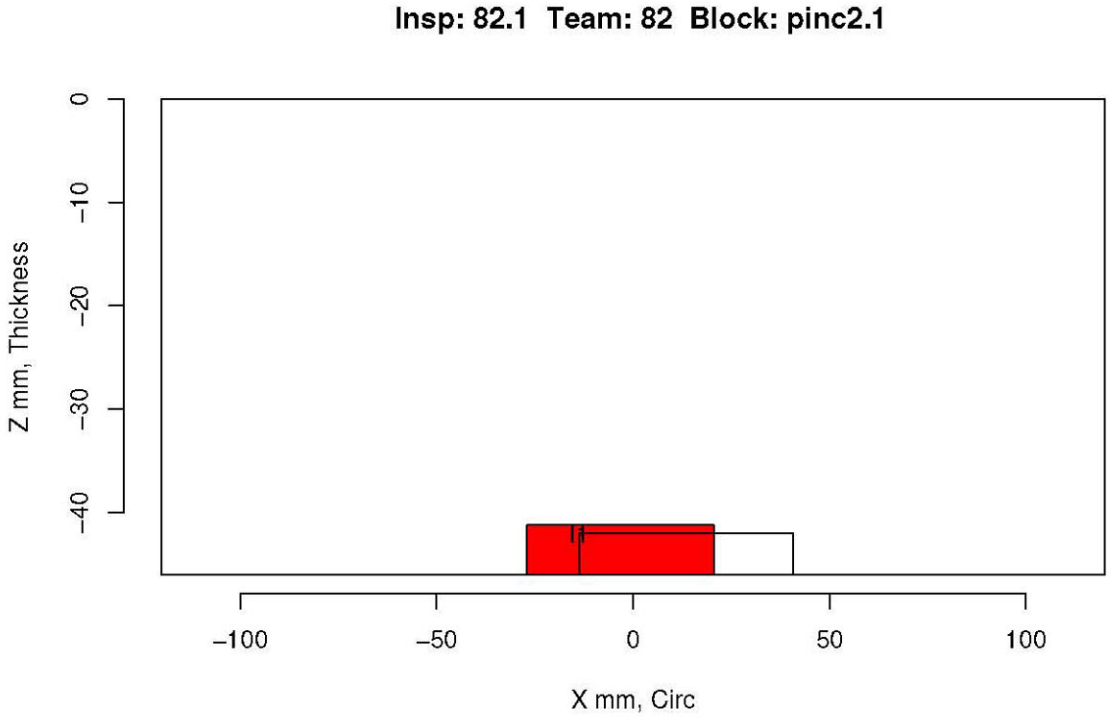
Insp: 82.1 Team: 82 Block: pinc2.1
Z mm, Thickness
0
−10
−20
−30
−40
−100
−50
0
50
100
X mm, Circ

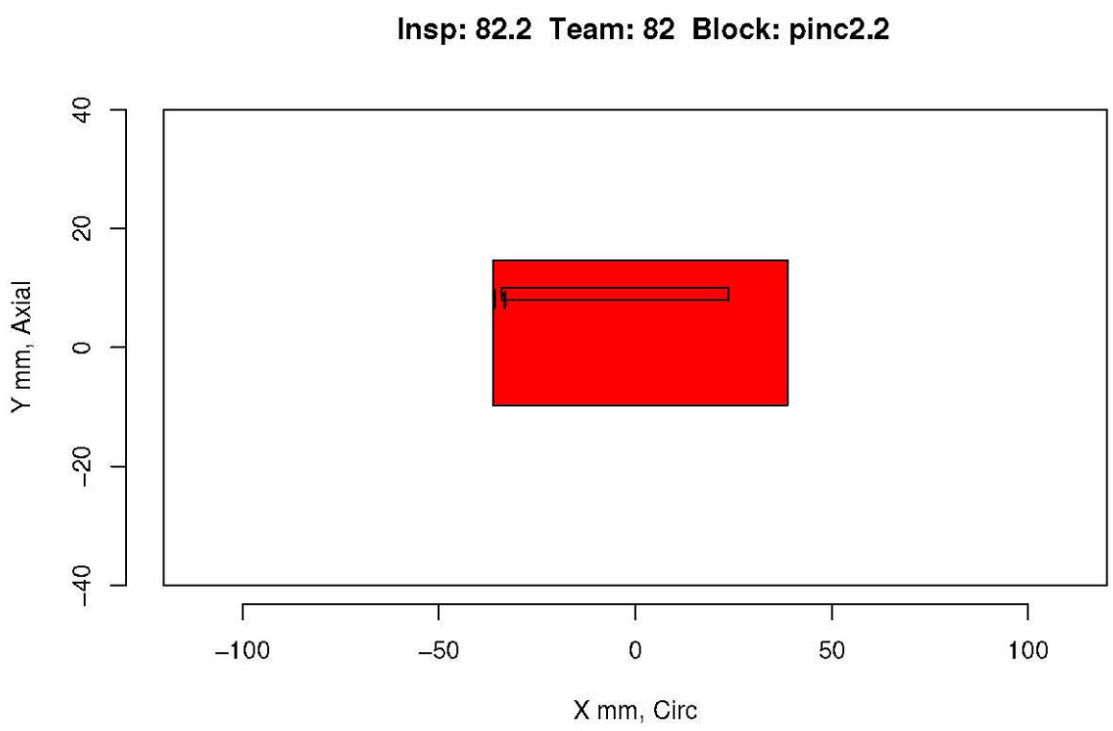
Insp: 82.2 Team: 82 Block: pinc2.2
Y mm, Axial
40
20
0
−20
−40
−100
−50
0
50
100
X mm, Circ

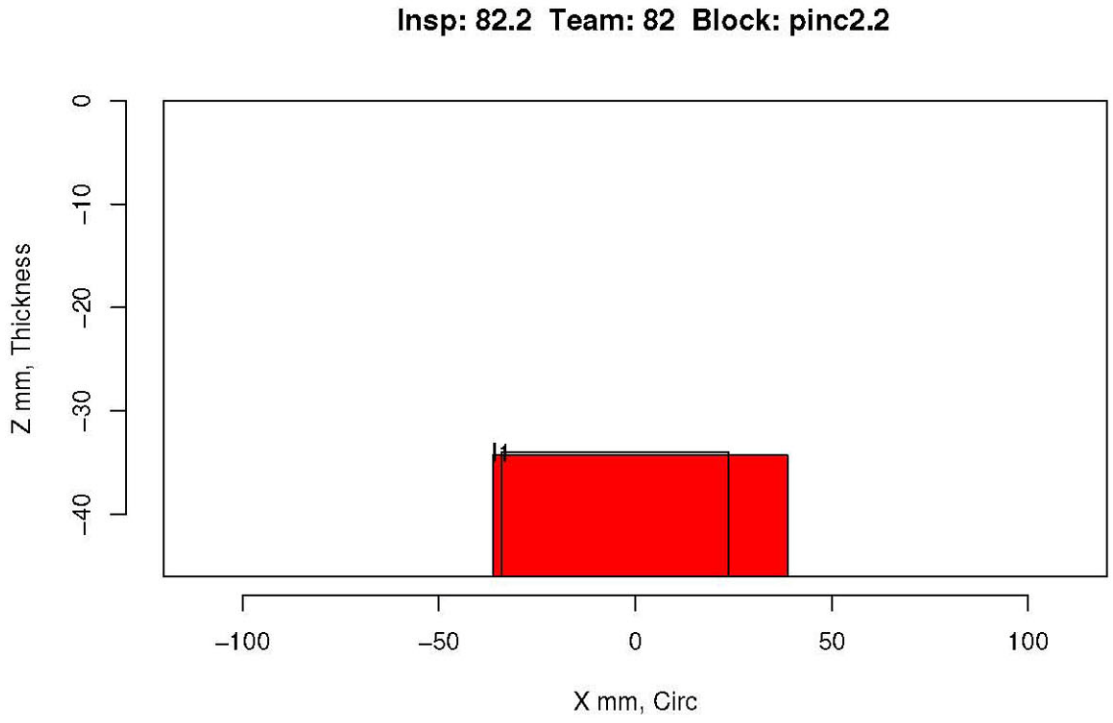
Insp: 82.2 Team: 82 Block: pinc2.2
Z mm, Thickness
0
−10
−20
−30
−40
−100
−50
0
50
100
X mm, Circ

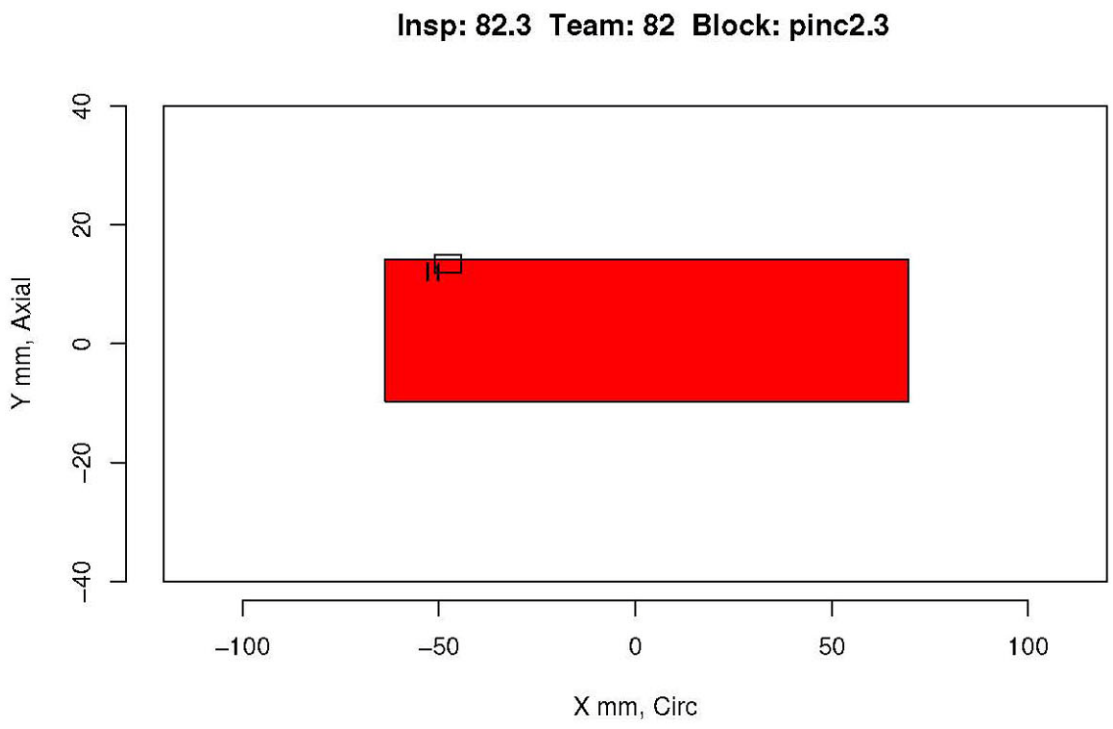
Insp: 82.3 Team: 82 Block: pinc2.3
Y mm, Axial
40
20
0
−20
−40
−100
−50
0
50
100
X mm, Circ

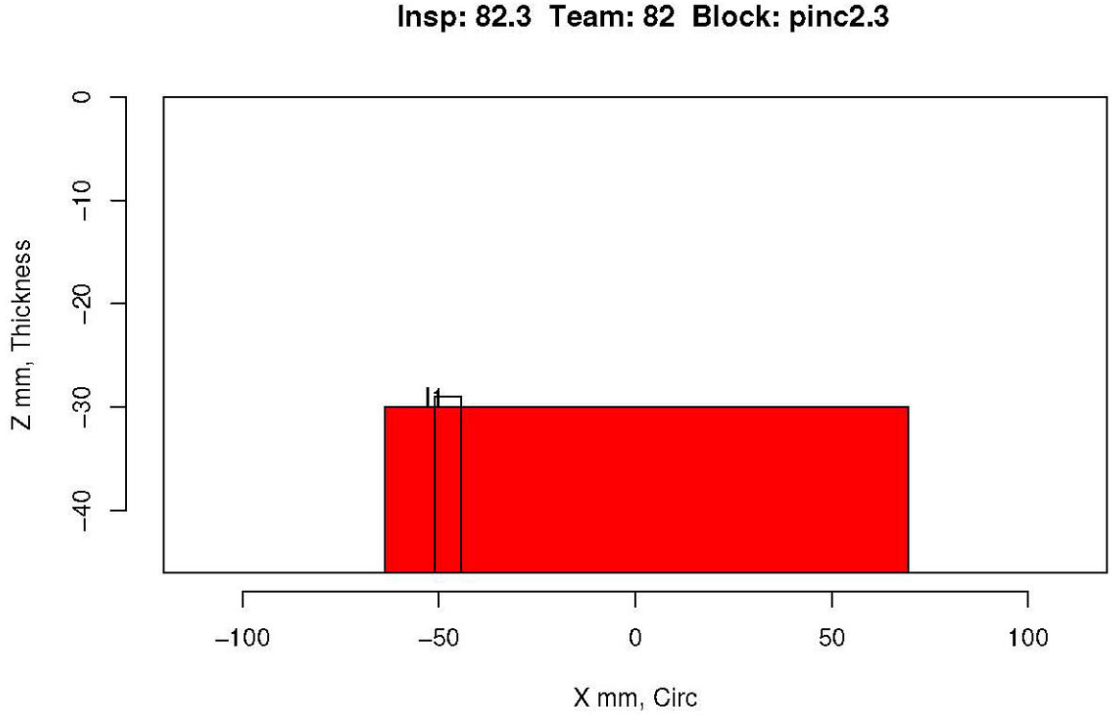
Insp: 82.3 Team: 82 Block: pinc2.3
Z mm, Thickness
0
−10
−20
−30
−40
−100
−50
0
50
100
X mm, Circ

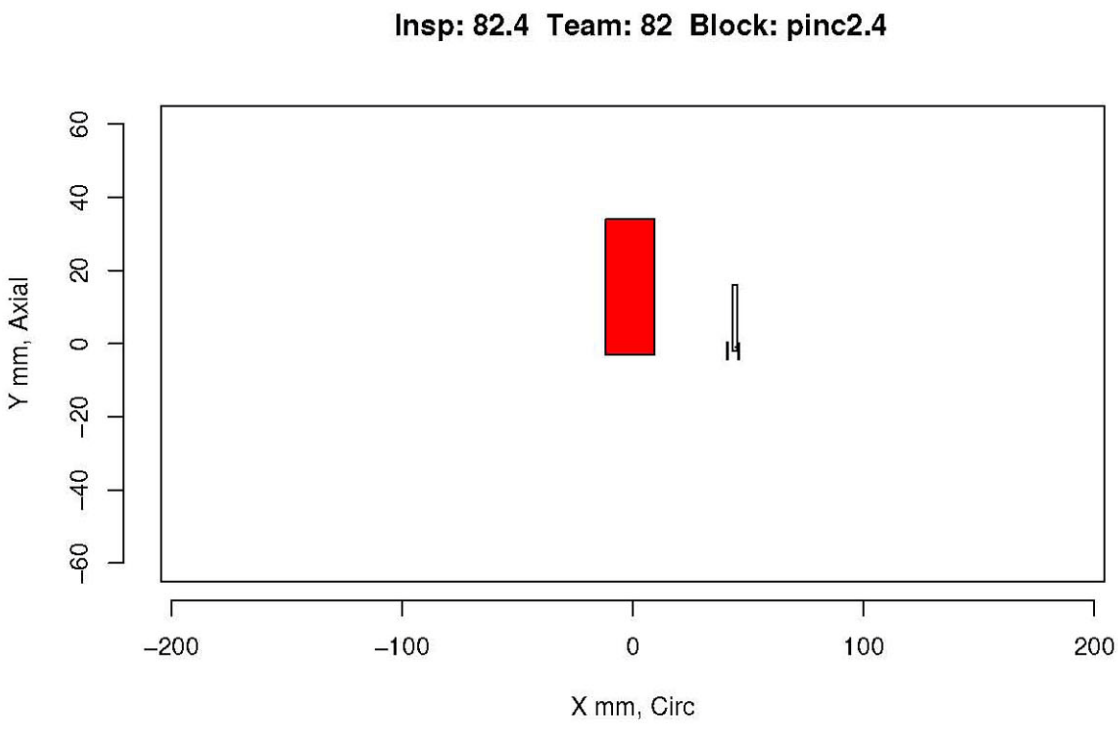
Insp: 82.4 Team: 82 Block: pinc2.4
Y mm, Axial
60
40
20
0
−20
−40
−60
−200
−100
0
100
200
X mm, Circ

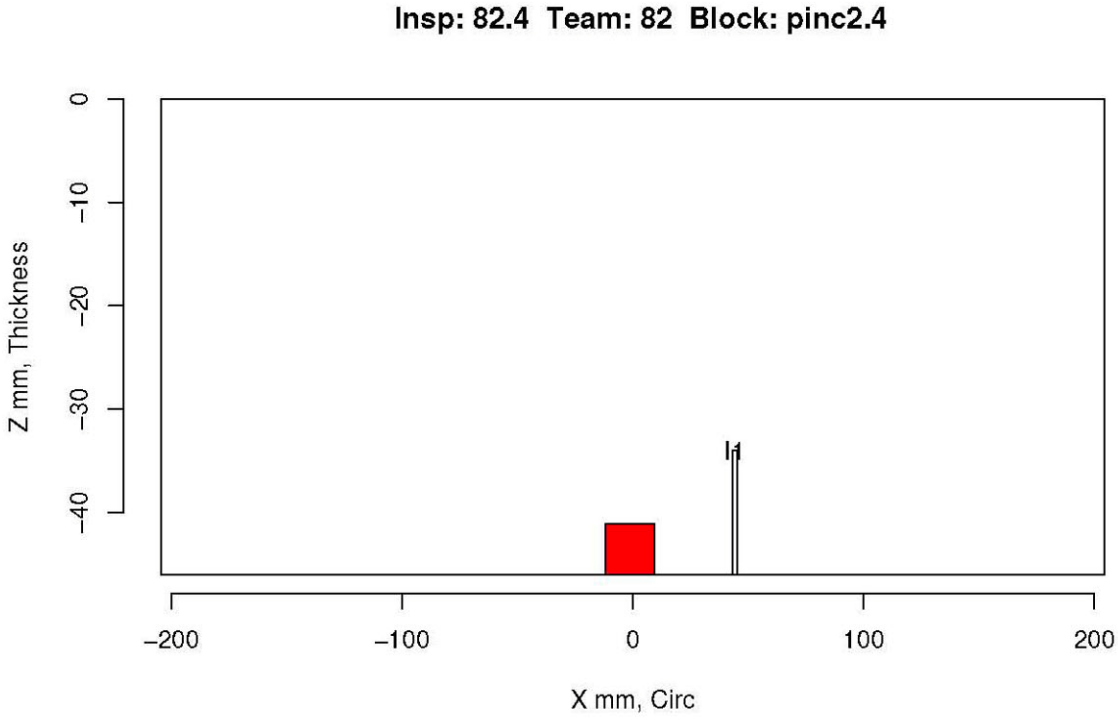
Insp: 82.4 Team: 82 Block: pinc2.4
Z mm, Thickness
0
−10
−20
−30
−40
−200
−100
0
100
200
X mm, Circ

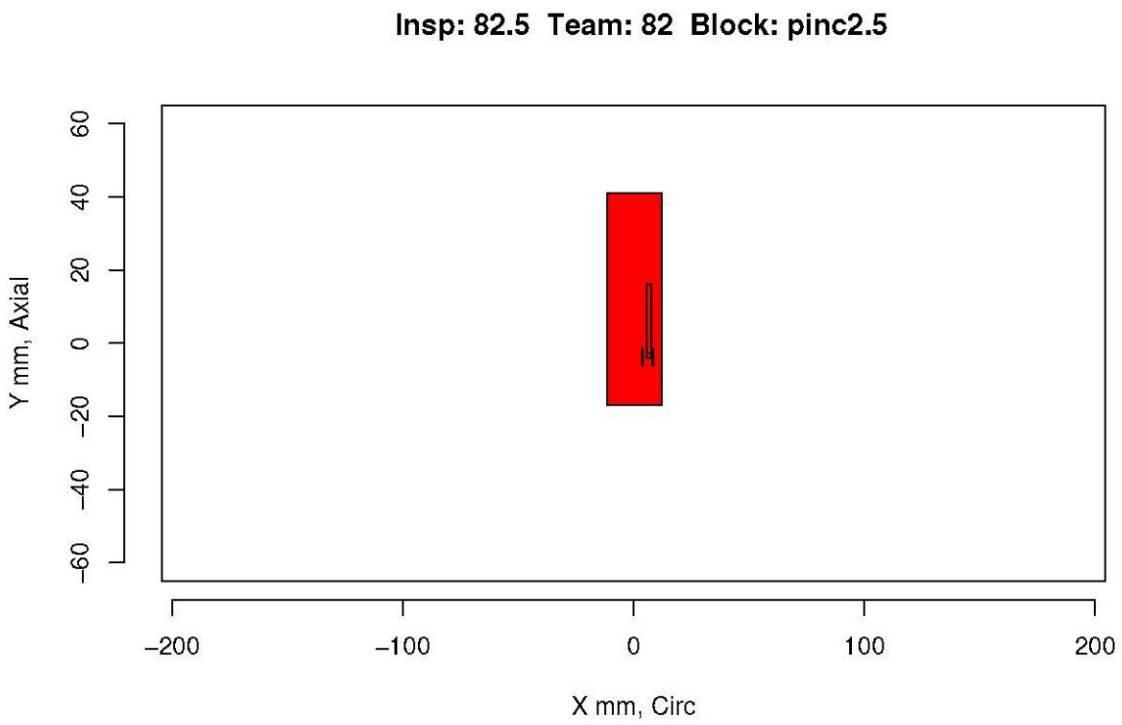
Insp: 82.5 Team: 82 Block: pinc2.5
Y mm, Axial
60
40
20
0
−20
−40
−60
−200
−100
0
100
200
X mm, Circ

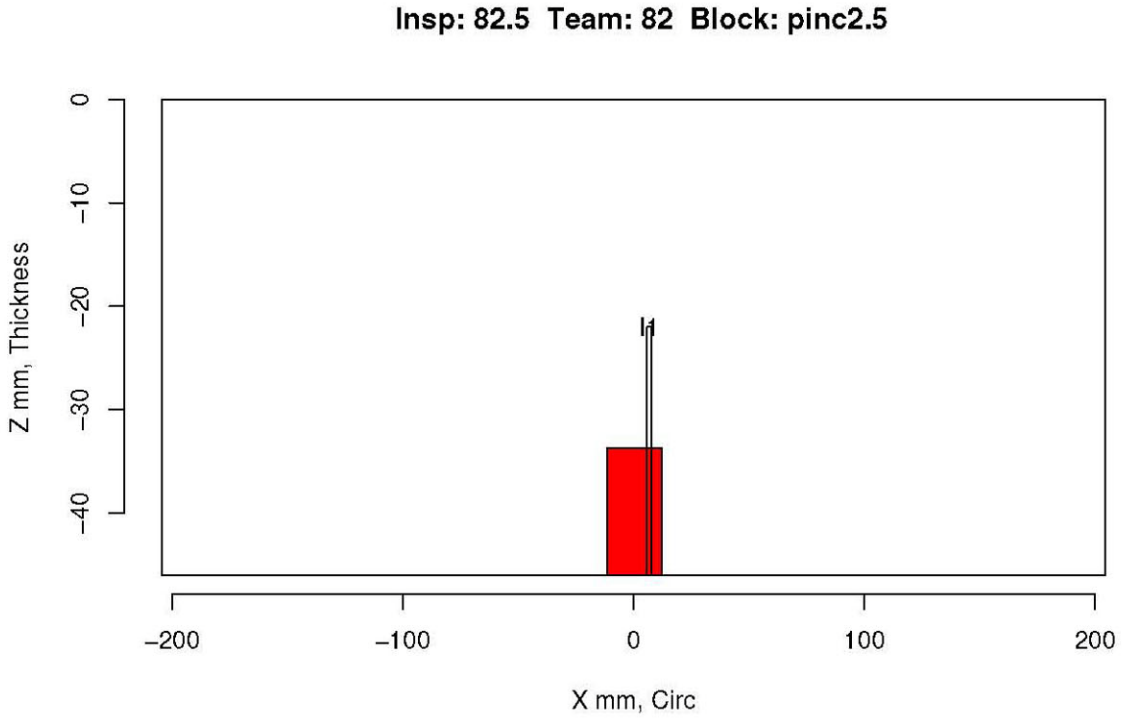
Insp: 82.5 Team: 82 Block: pinc2.5
Z mm, Thickness
0
−10
−20
−30
−40
−200
−100
0
100
200
X mm, Circ

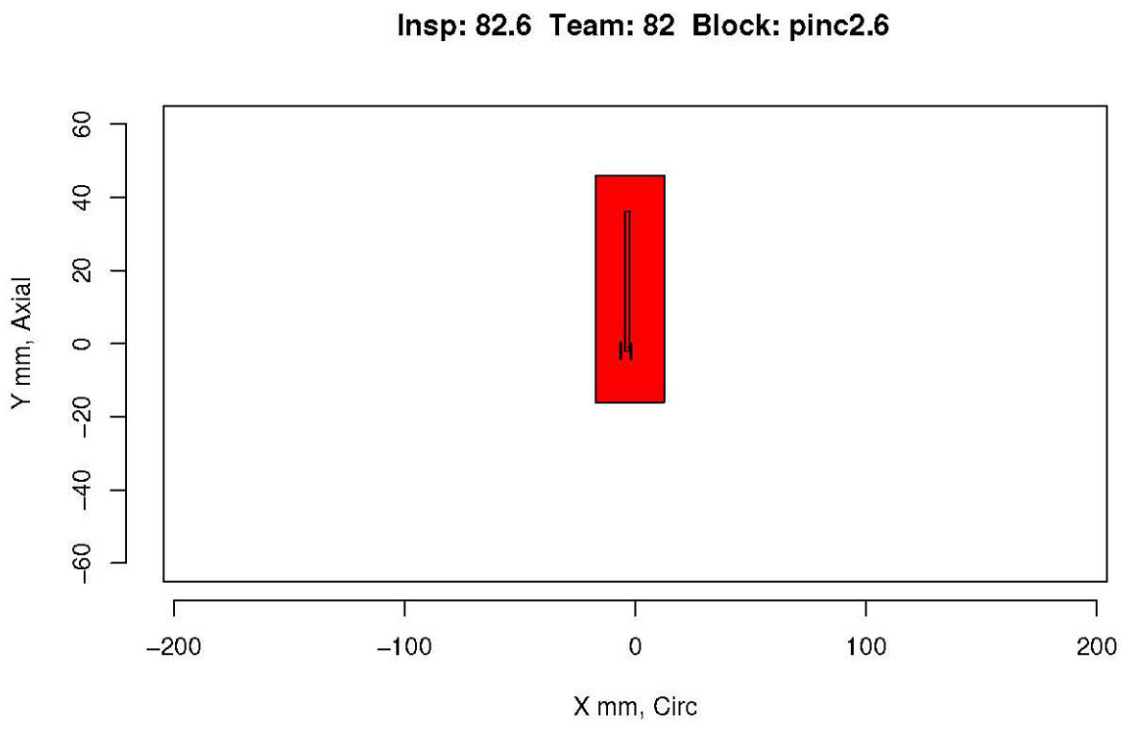
Insp: 82.6 Team: 82 Block: pinc2.6
Y mm, Axial
60
40
20
0
−20
−40
−60
−200
−100
0
100
200
X mm, Circ

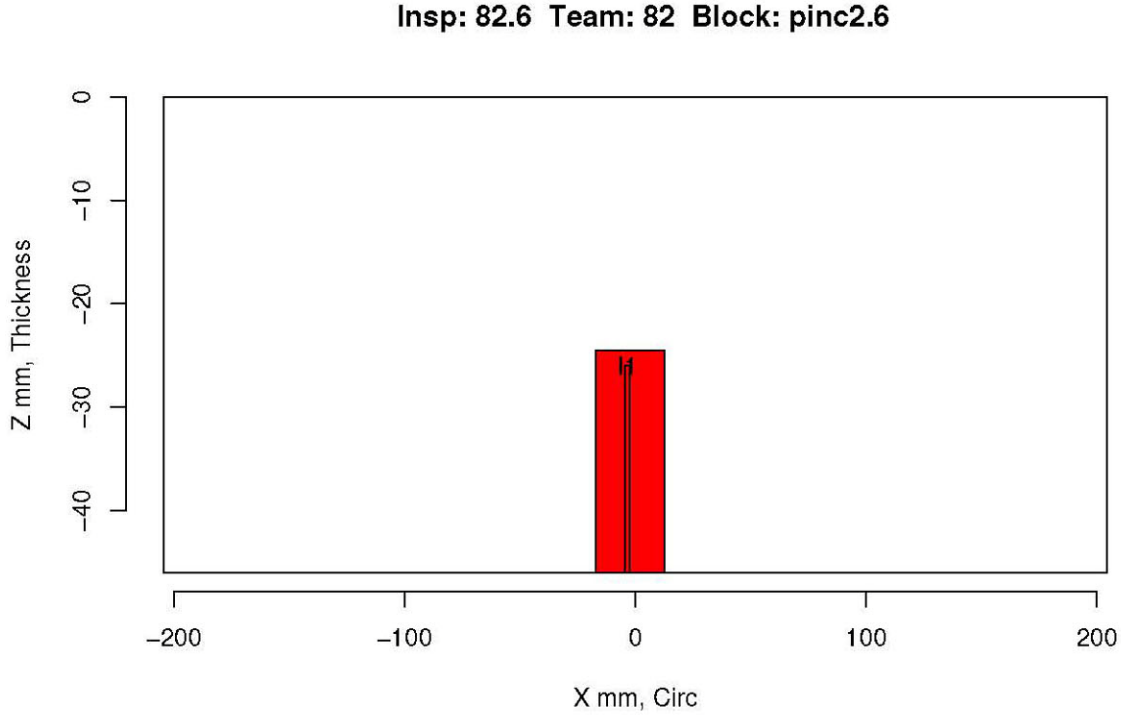
Insp: 82.6 Team: 82 Block: pinc2.6
Z mm, Thickness
0
−10
−20
−30
−40
−200
−100
0
100
200
X mm, Circ

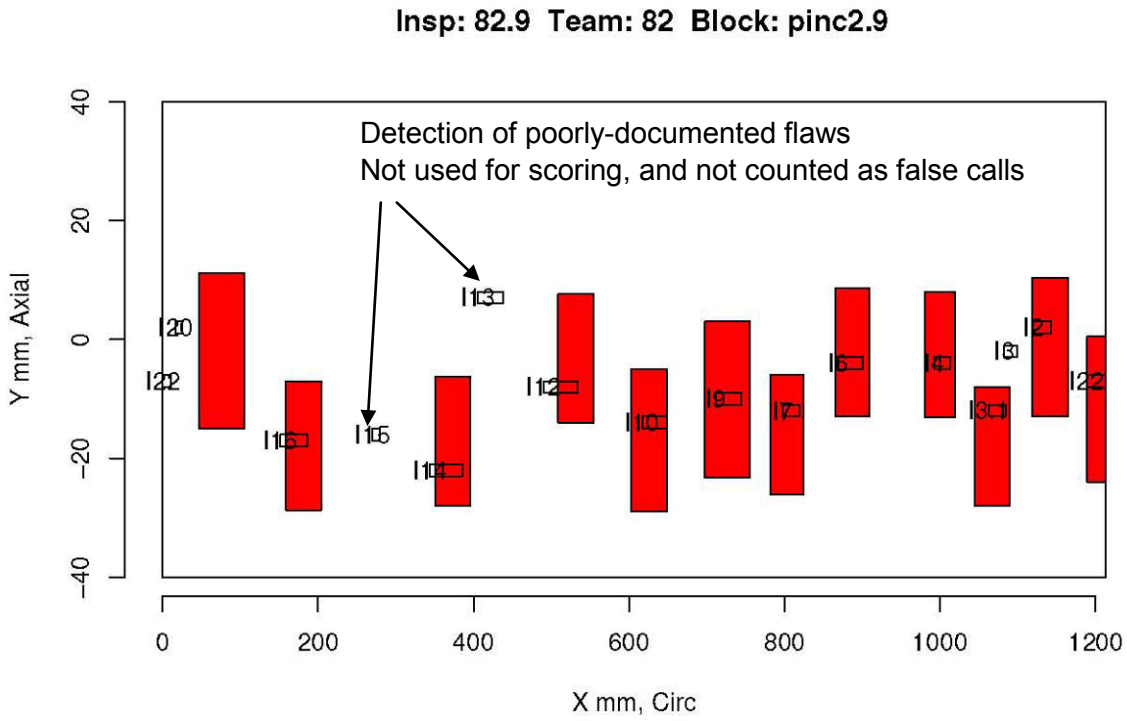
Insp: 82.9 Team: 82 Block: pinc2.9
Detection of poorly-documented flaws
Not used for scoring, and not counted as false calls
Y mm, Axial
X mm, Circ
40
20
0
-20
-40
0
200
400
600
800
1000
1200

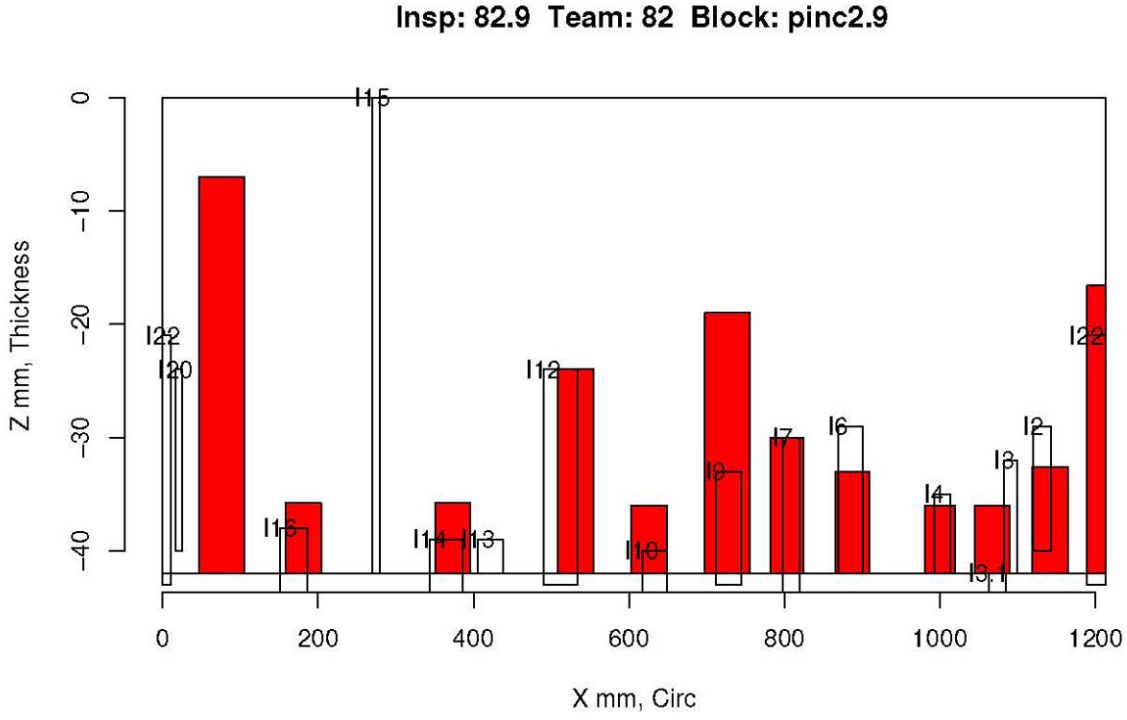
Insp: 82.9 Team: 82 Block: pinc2.9
Z mm, Thickness
X mm, Circ
0
-10
-20
-30
-40
0
200
400
600
800
1000
1200

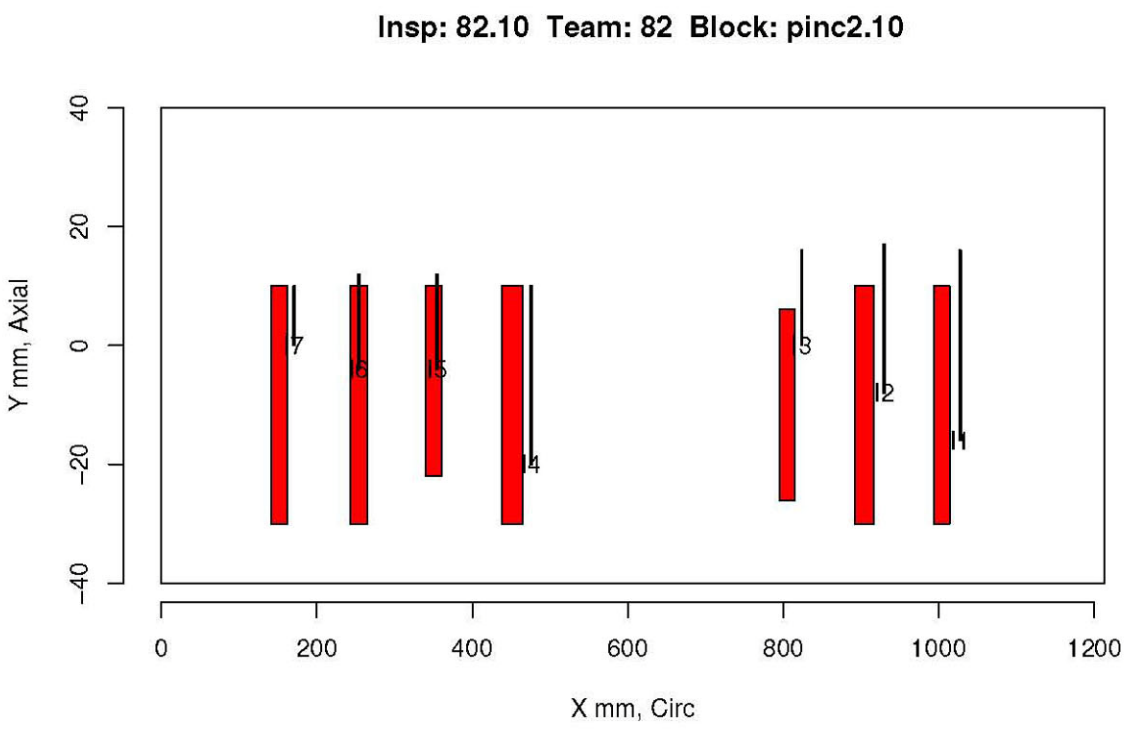
Insp: 82.10 Team: 82 Block: pinc2.10
Y mm, Axial
40
20
0
-20
-40
0
200
400
600
800
1000
1200
X mm, Circ
I7
I6
I5
I4
I3
I2
I1

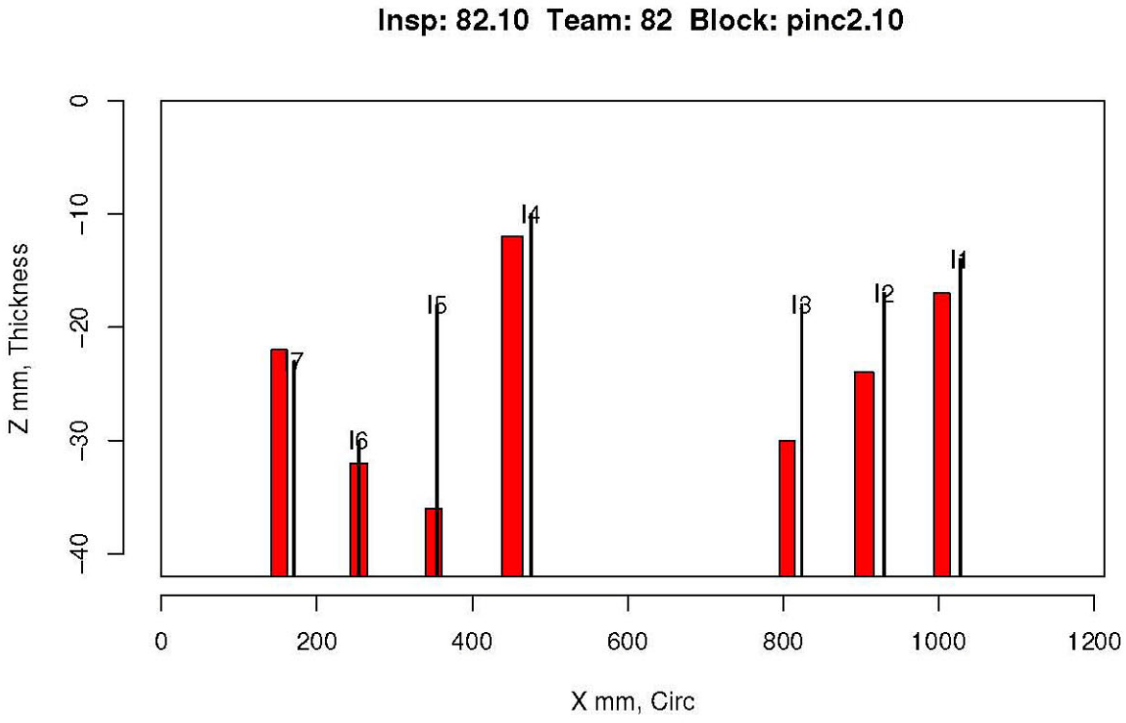
Insp: 82.10 Team: 82 Block: pinc2.10
Z mm, Thickness
0
-10
-20
-30
-40
0
200
400
600
800
1000
1200
X mm, Circ
I7
I6
I5
I4
I3
I2
I1

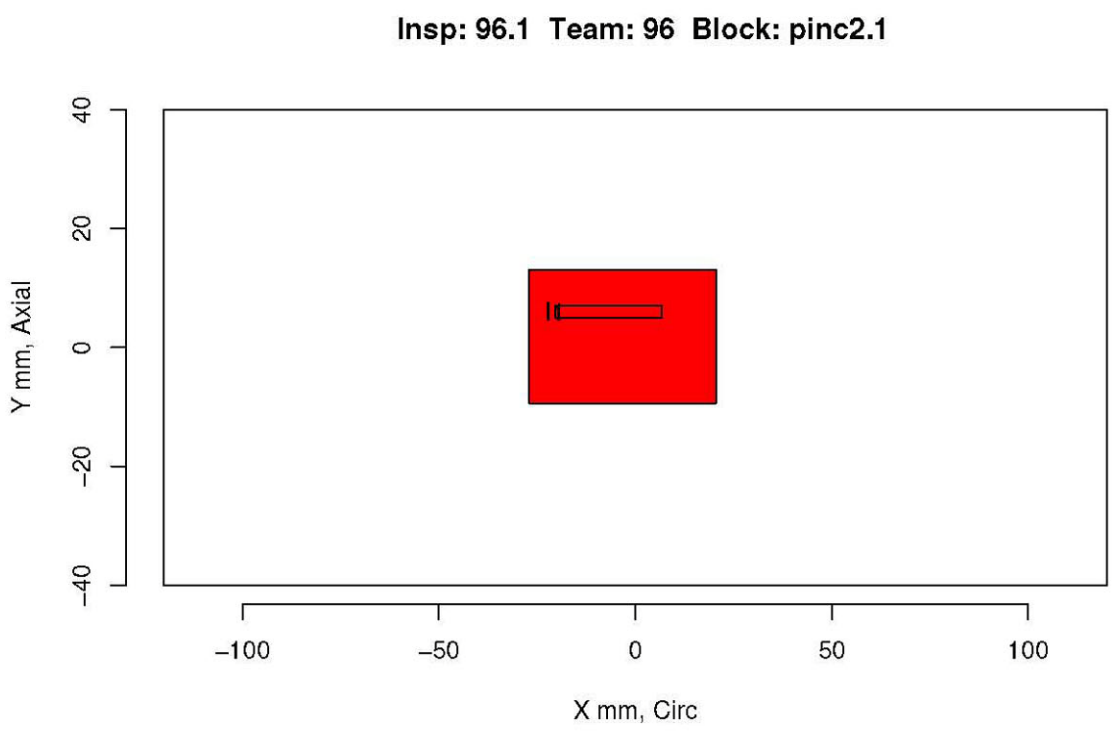
Insp: 96.1 Team: 96 Block: pinc2.1
Y mm, Axial
40
20
0
−20
−40
−100
−50
0
50
100
X mm, Circ

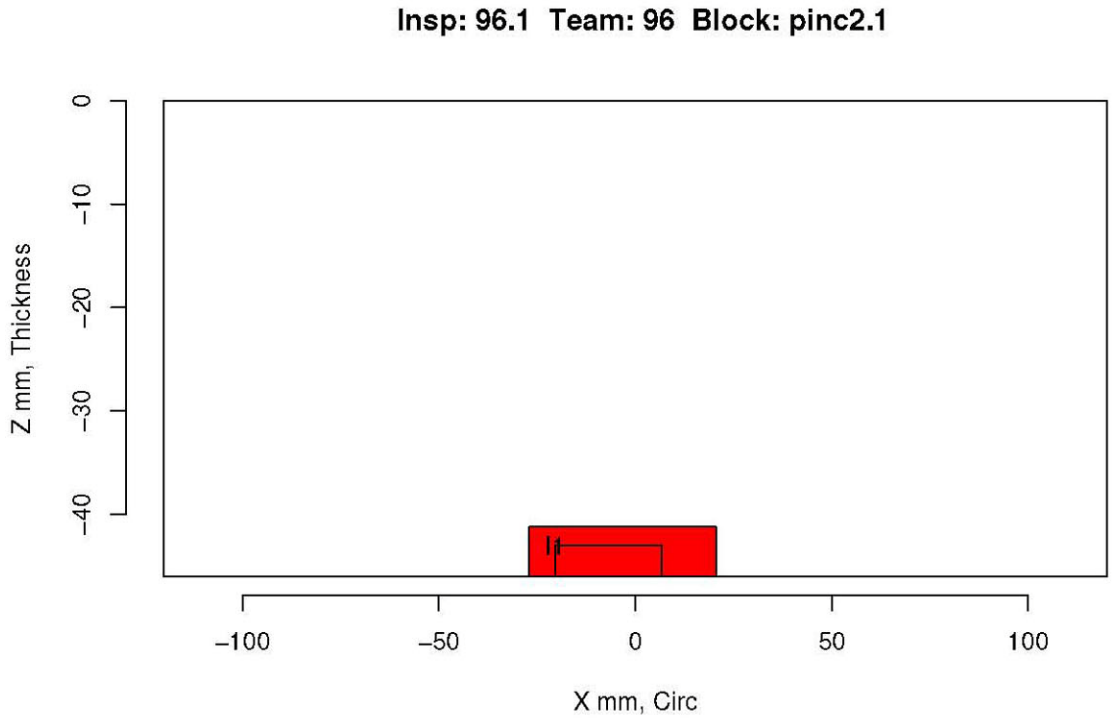
Insp: 96.1 Team: 96 Block: pinc2.1
Z mm, Thickness
0
−10
−20
−30
−40
−100
−50
0
50
100
X mm, Circ

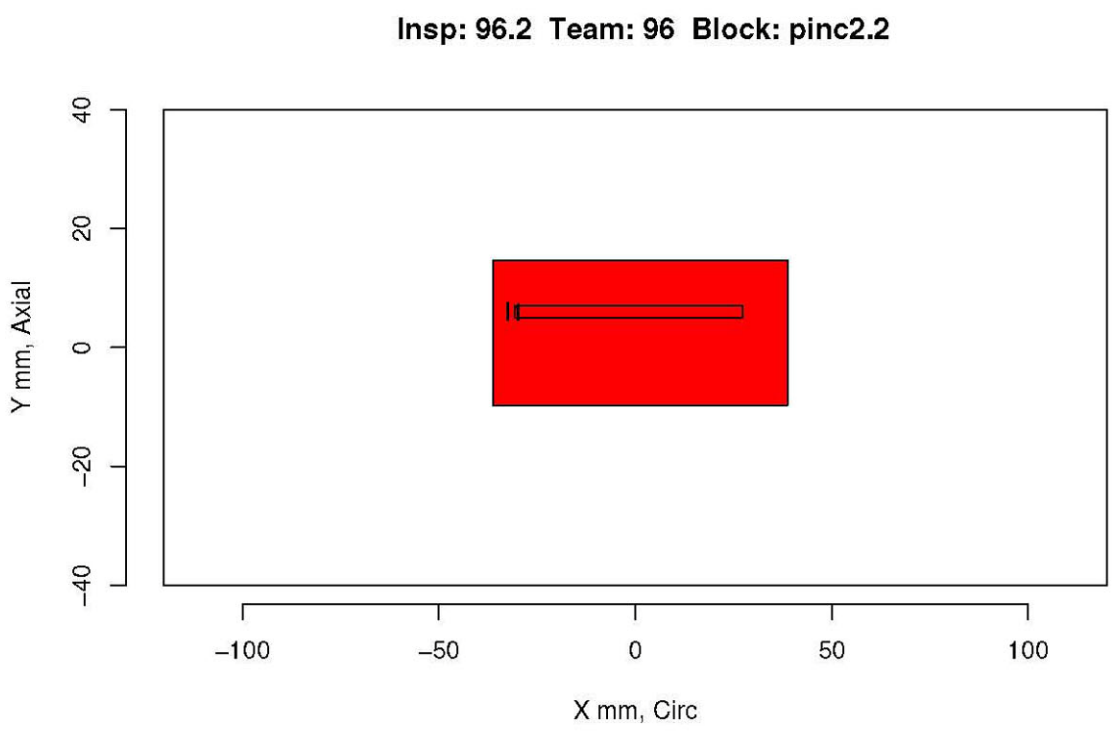
Insp: 96.2 Team: 96 Block: pinc2.2
Y mm, Axial
40
20
0
−20
−40
−100
−50
0
50
100
X mm, Circ

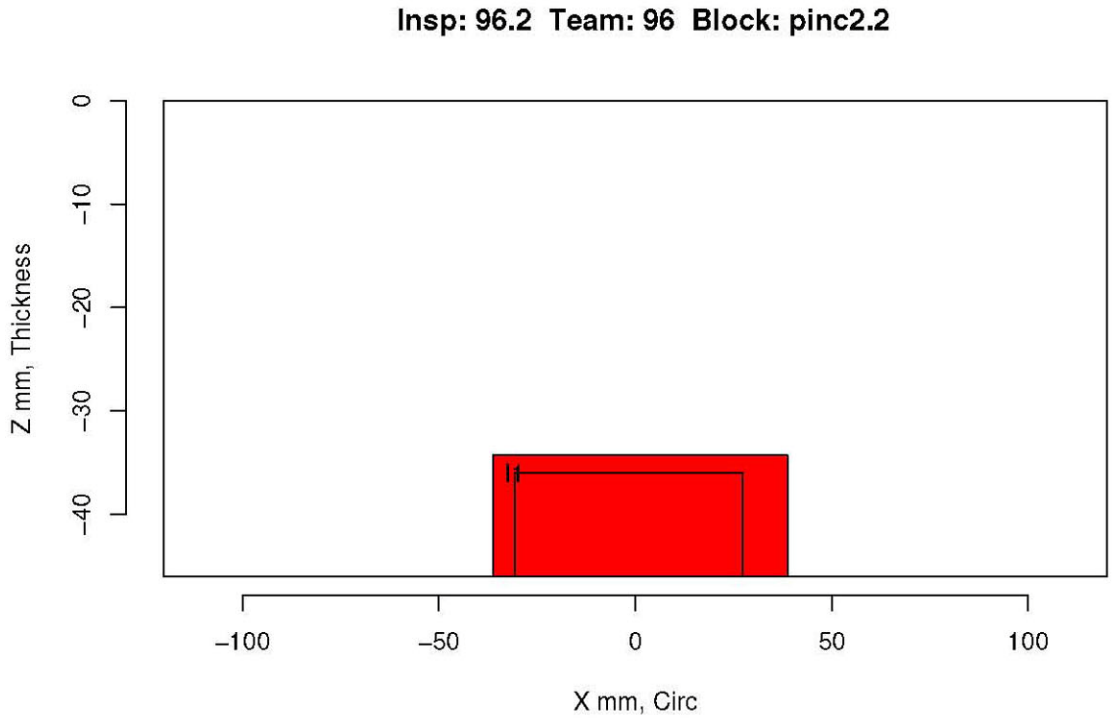
Insp: 96.2 Team: 96 Block: pinc2.2
Z mm, Thickness
0
−10
−20
−30
−40
−100
−50
0
50
100
X mm, Circ

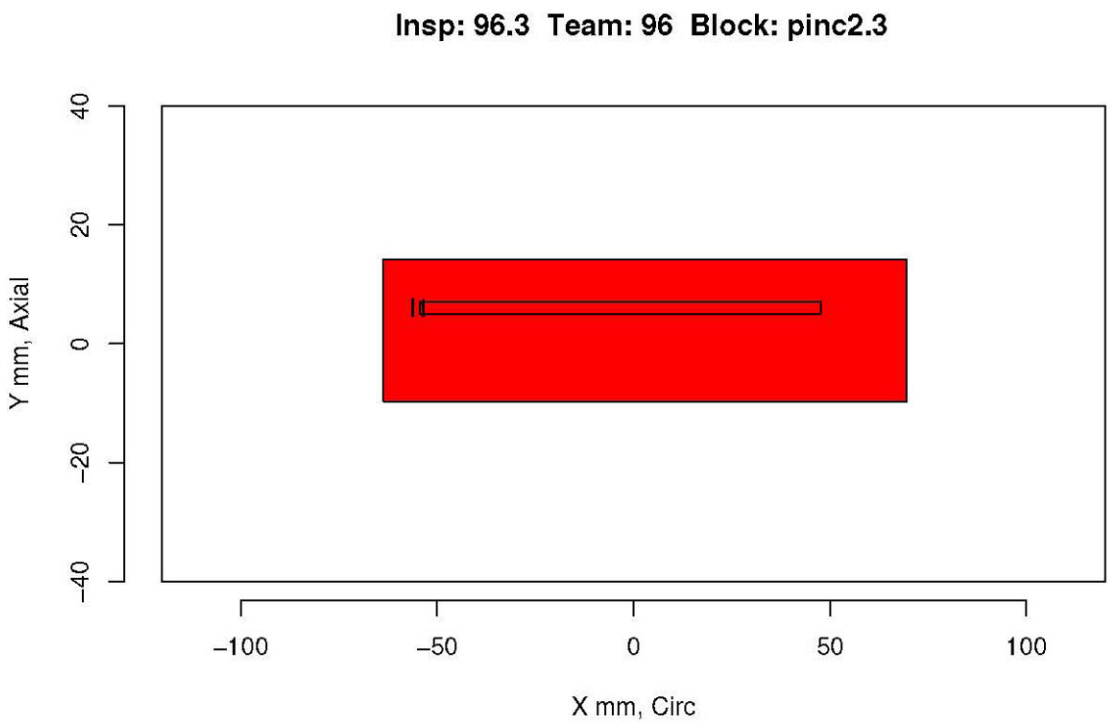
Insp: 96.3 Team: 96 Block: pinc2.3
Y mm, Axial
40
20
0
−20
−40
−100
−50
0
50
100
X mm, Circ

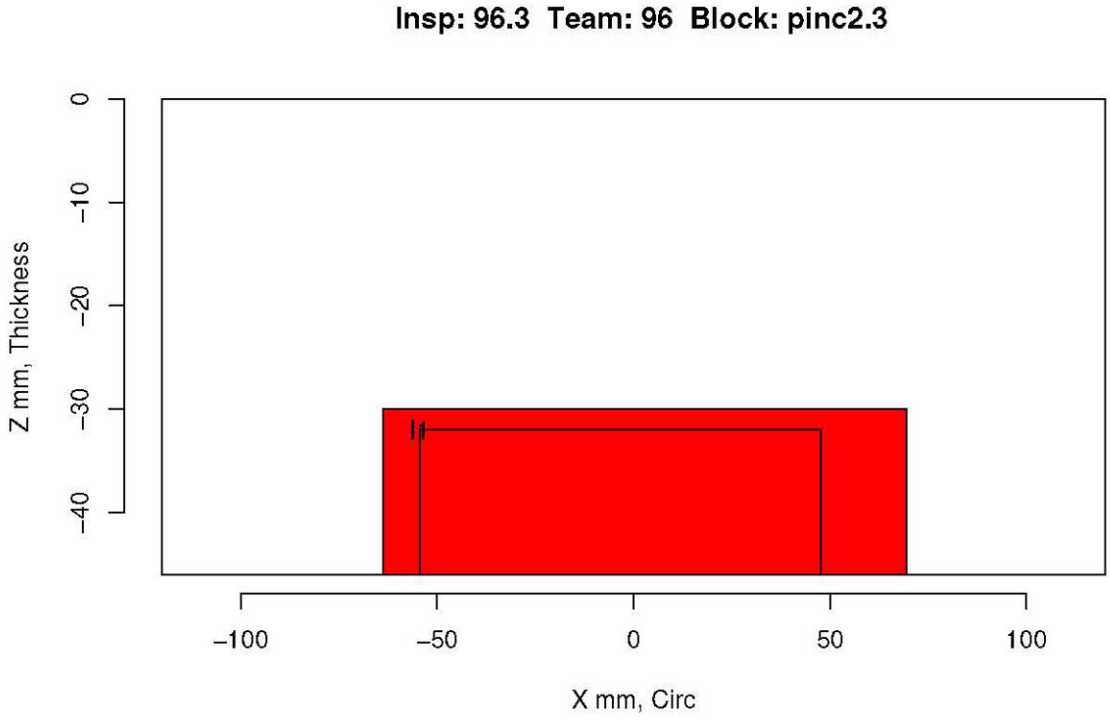
Insp: 96.3 Team: 96 Block: pinc2.3
Z mm, Thickness
0
−10
−20
−30
−40
−100
−50
0
50
100
X mm, Circ

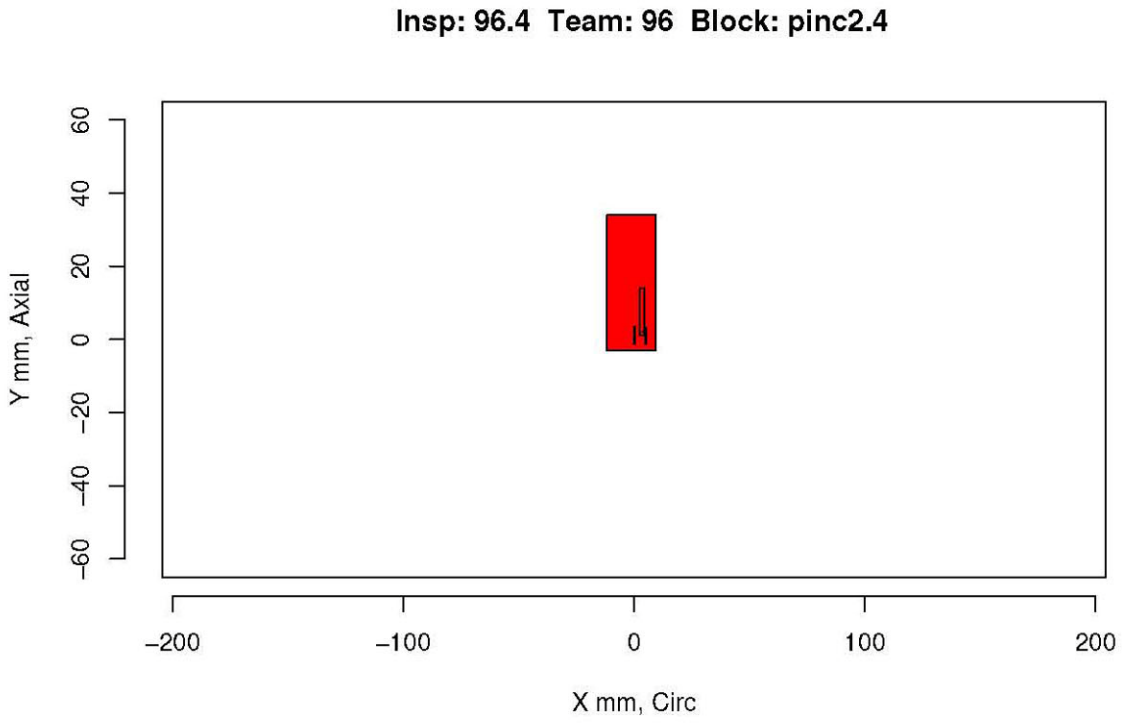
Insp: 96.4 Team: 96 Block: pinc2.4
Y mm, Axial
60
40
20
0
−20
−40
−60
−200
−100
0
100
200
X mm, Circ

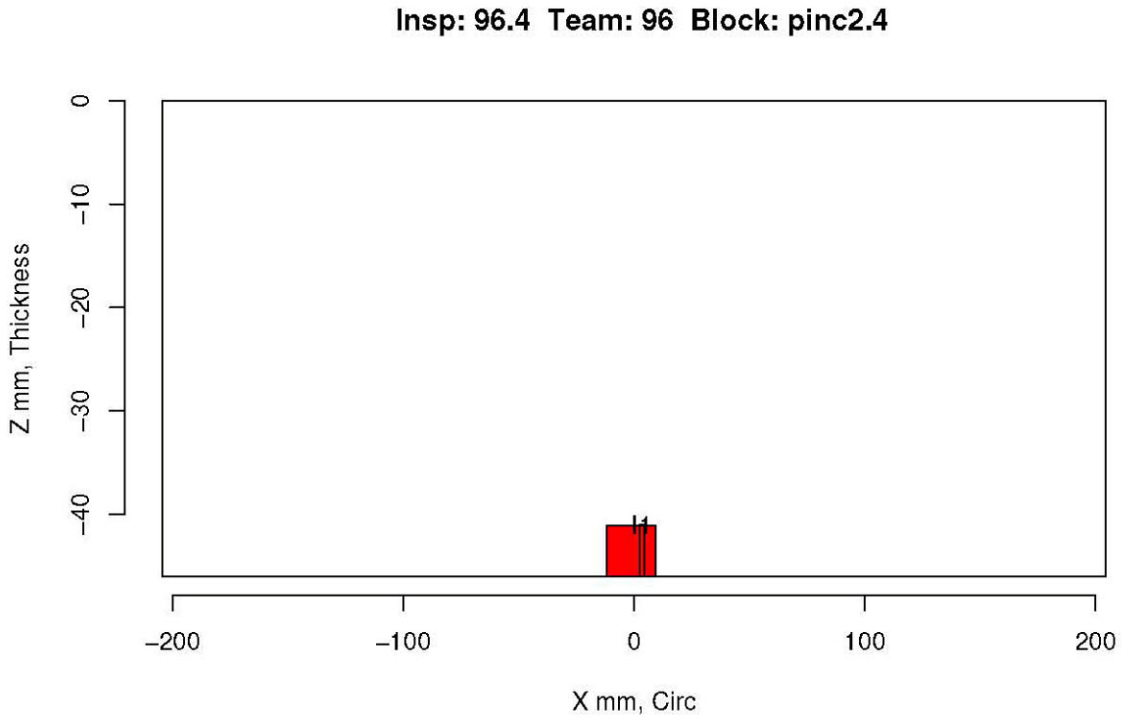
Insp: 96.4 Team: 96 Block: pinc2.4
Z mm, Thickness
0
−10
−20
−30
−40
−200
−100
0
100
200
X mm, Circ

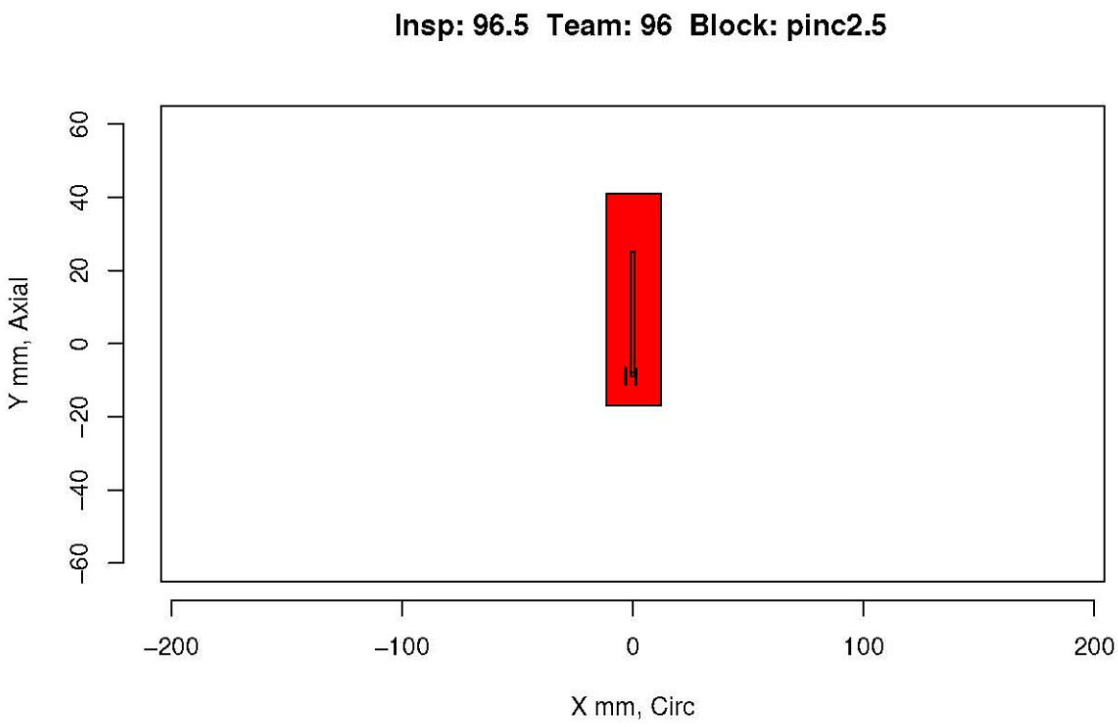
Insp: 96.5 Team: 96 Block: pinc2.5
Y mm, Axial
60
40
20
0
−20
−40
−60
−200
−100
0
100
200
X mm, Circ

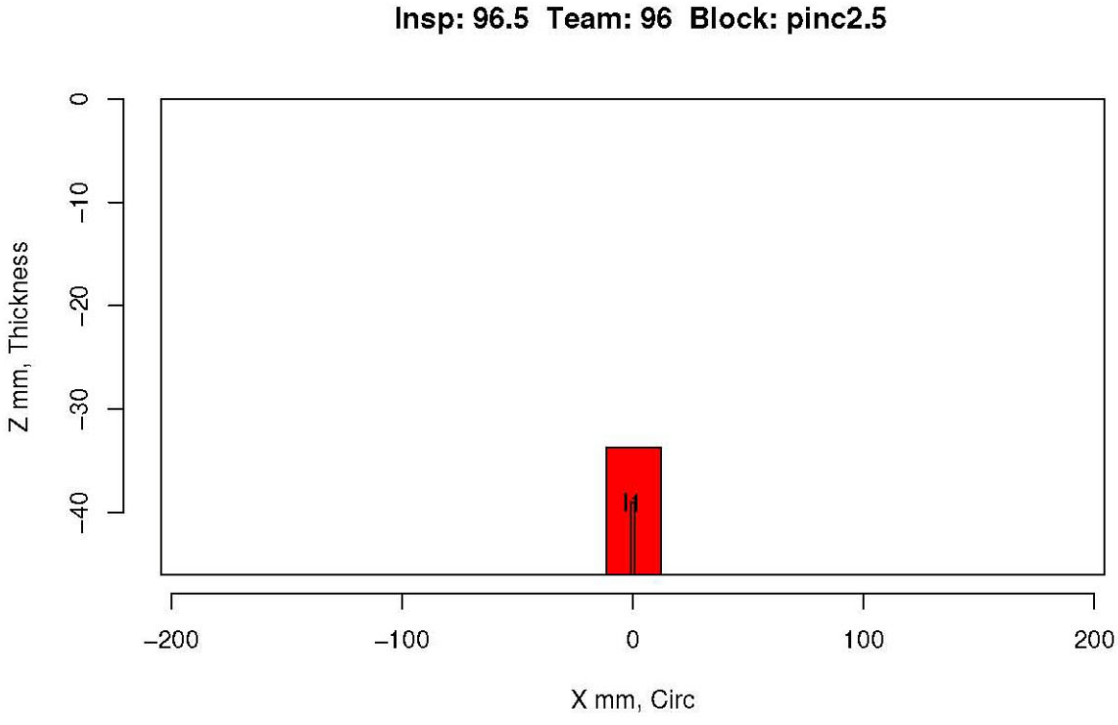
Insp: 96.5 Team: 96 Block: pinc2.5
Z mm, Thickness
0
−10
−20
−30
−40
−200
−100
0
100
200
X mm, Circ

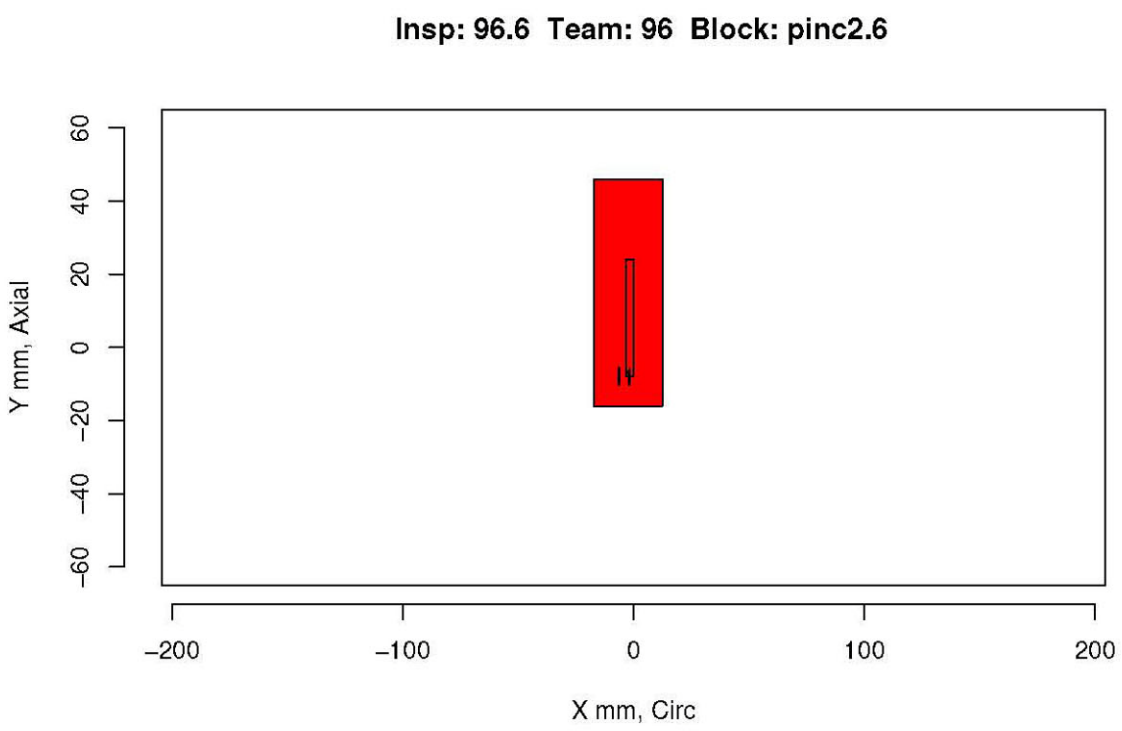
Insp: 96.6 Team: 96 Block: pinc2.6
Y mm, Axial
60
40
20
0
−20
−40
−60
−200
−100
0
100
200
X mm, Circ

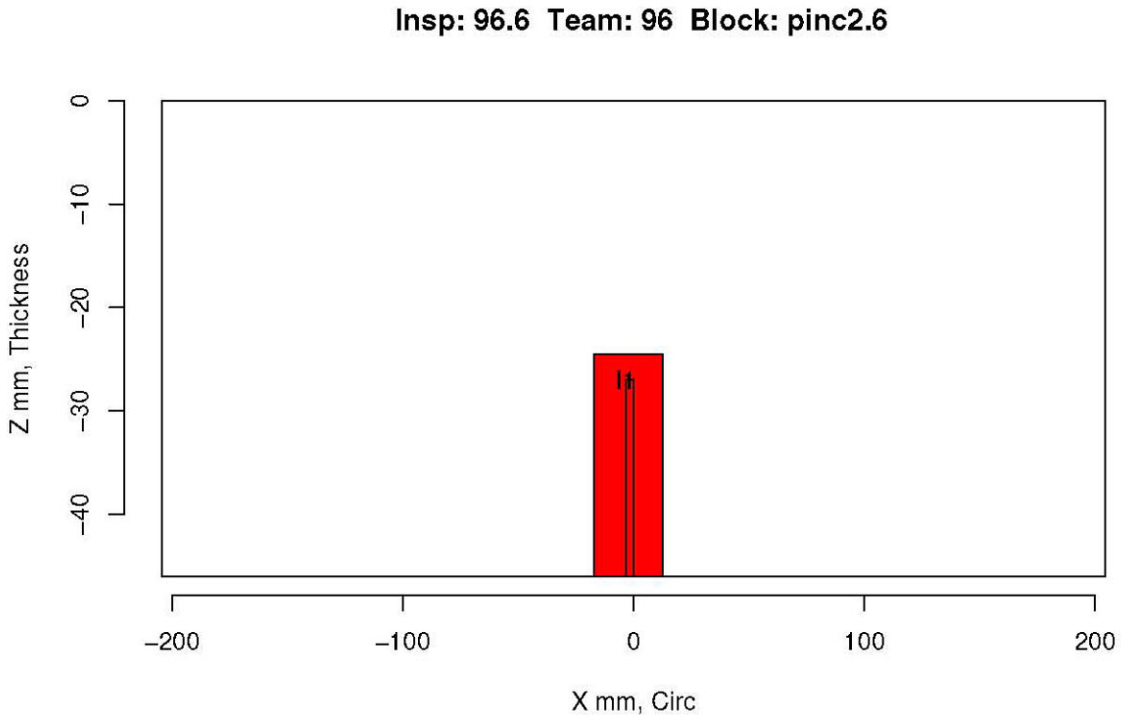
Insp: 96.6 Team: 96 Block: pinc2.6
Z mm, Thickness
0
−10
−20
−30
−40
−200
−100
0
100
200
X mm, Circ

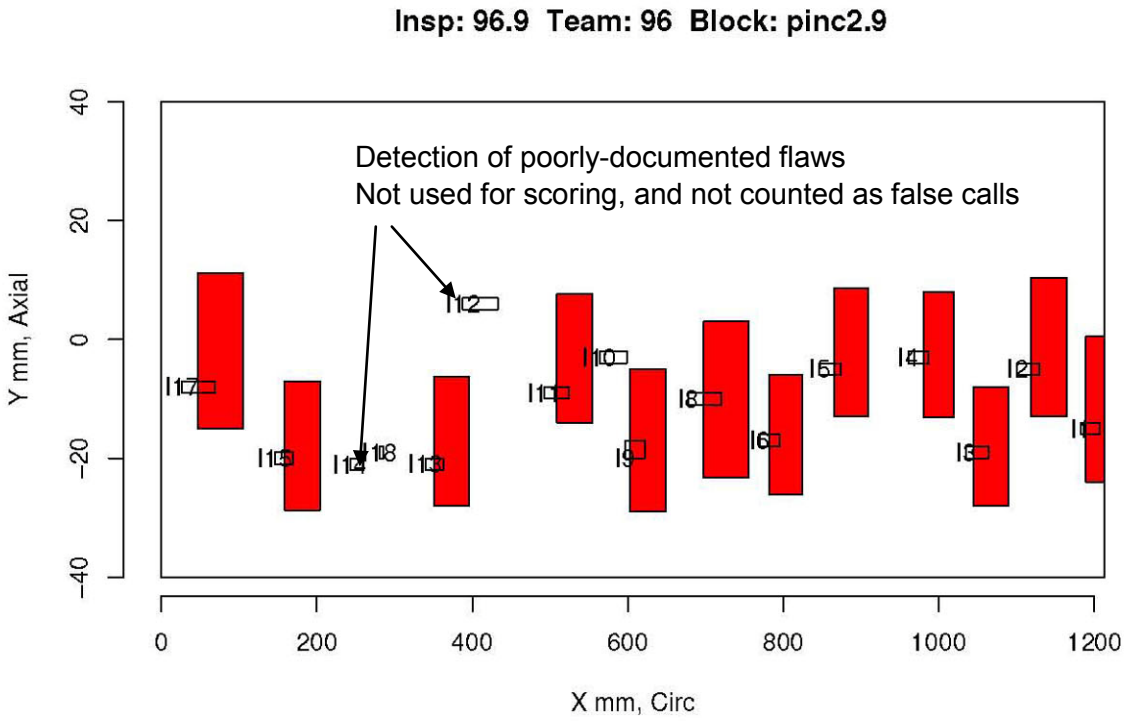
Insp: 96.9 Team: 96 Block: pinc2.9
Detection of poorly-documented flaws
Not used for scoring, and not counted as false calls
Y mm, Axial
X mm, Circ
40
20
0
-20
-40
0
200
400
600
800
1000
1200

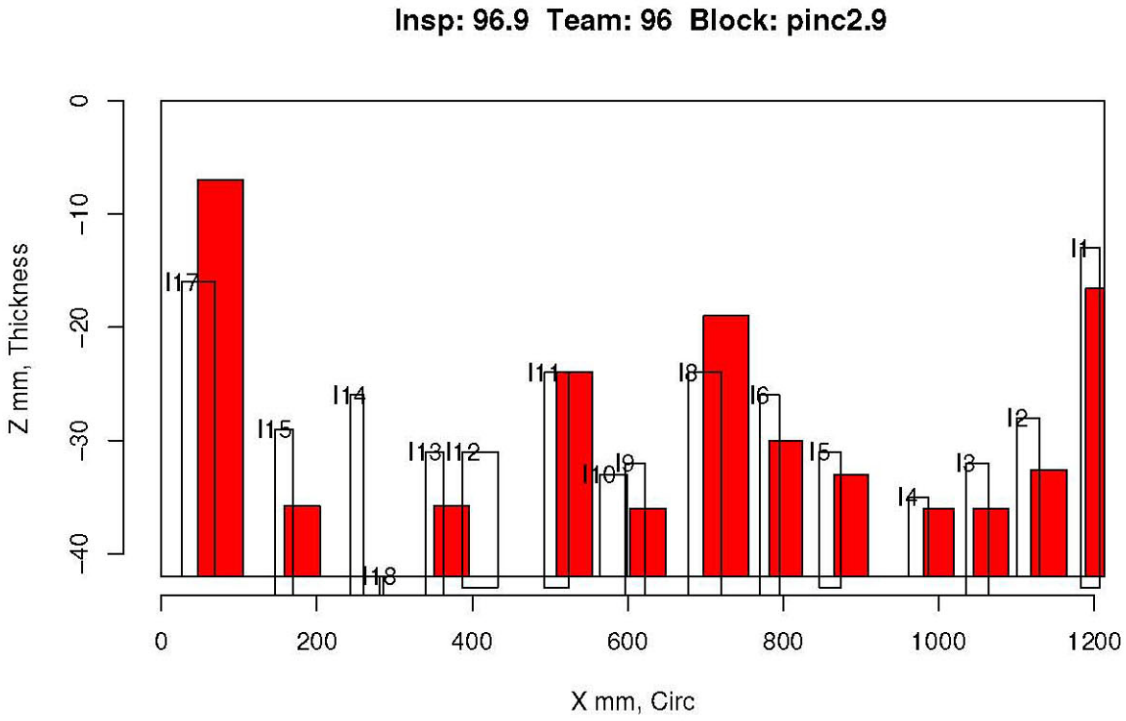
Insp: 96.9 Team: 96 Block: pinc2.9
Z mm, Thickness
X mm, Circ
0
-10
-20
-30
-40
0
200
400
600
800
1000
1200

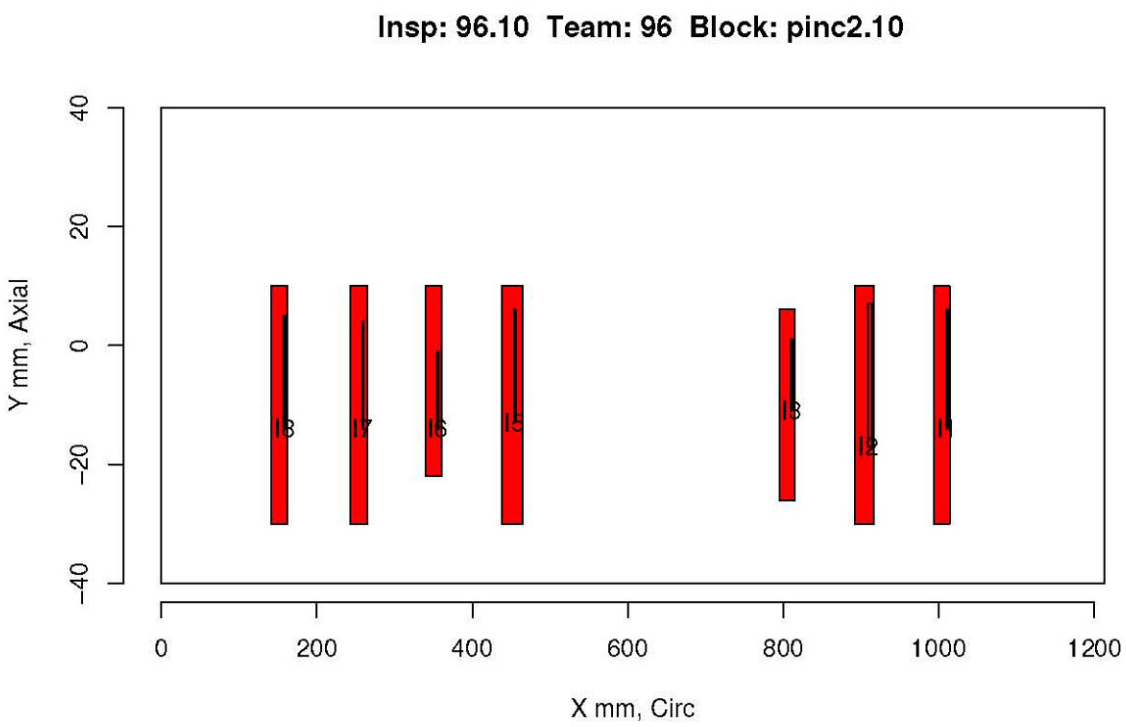
Insp: 96.10 Team: 96 Block: pinc2.10
Y mm, Axial
40
20
0
-20
-40
I3
I7
I6
I5
I3
I2
I1
0
200
400
600
800
1000
1200
X mm, Circ

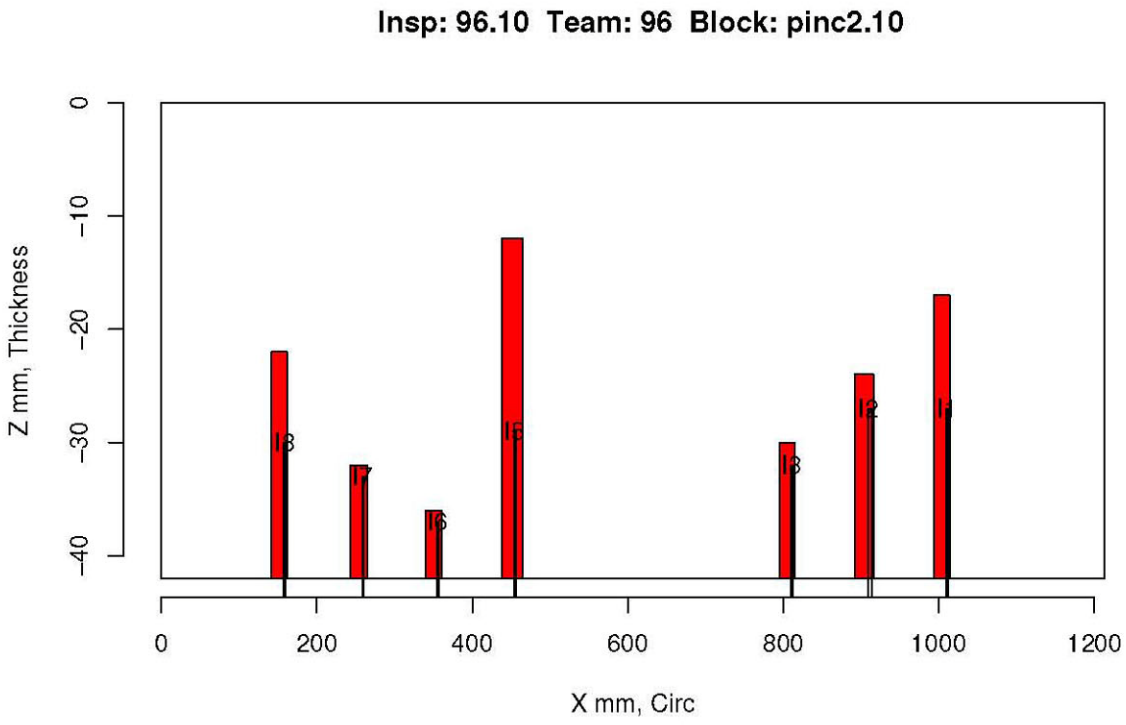
Insp: 96.10 Team: 96 Block: pinc2.10
Z mm, Thickness
0
-10
-20
-30
-40
I3
I7
I6
I5
I3
I2
I1
0
200
400
600
800
1000
1200
X mm, Circ

Appendix D

Block Hitograms for Dissimilar Metal Weld Samples

Appendix D

Block Hitograms for Dissimilar Metal Weld Samples

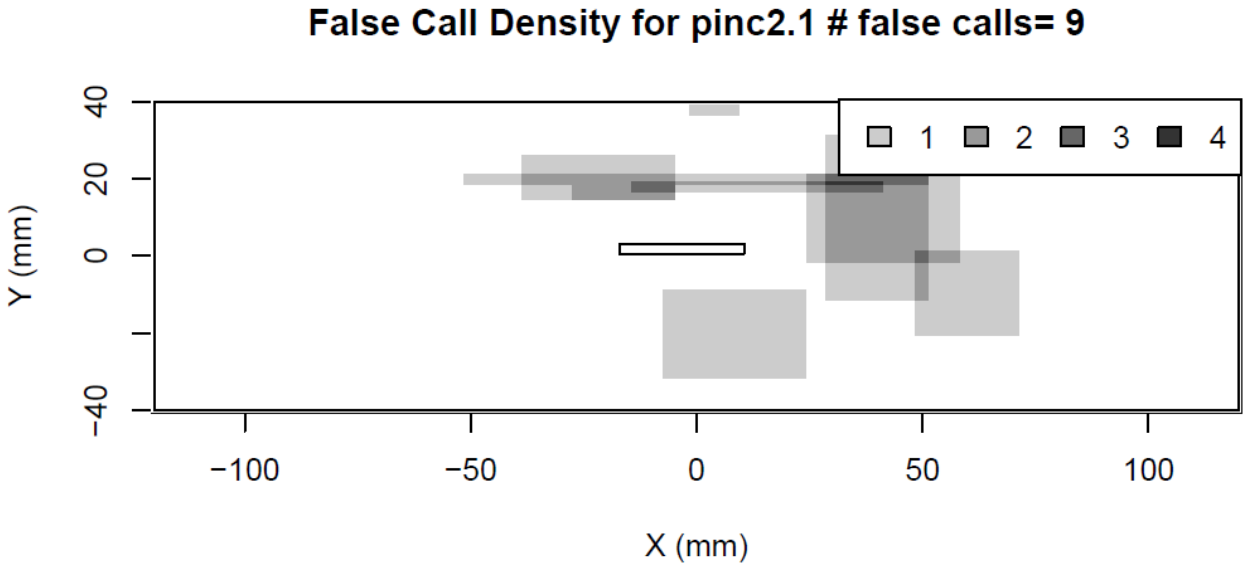

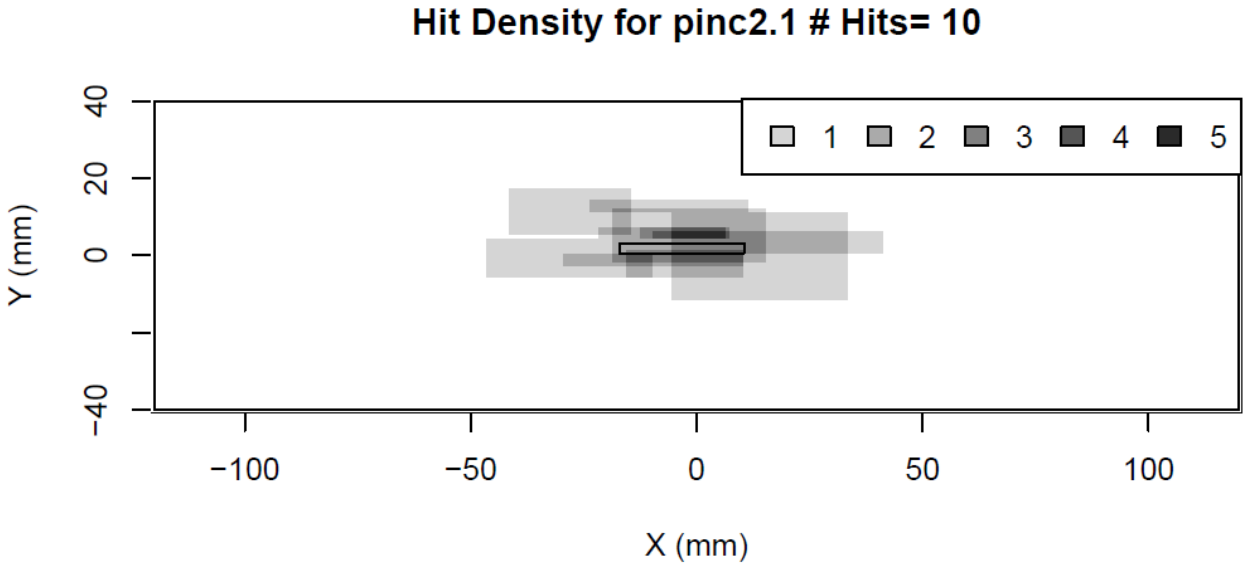

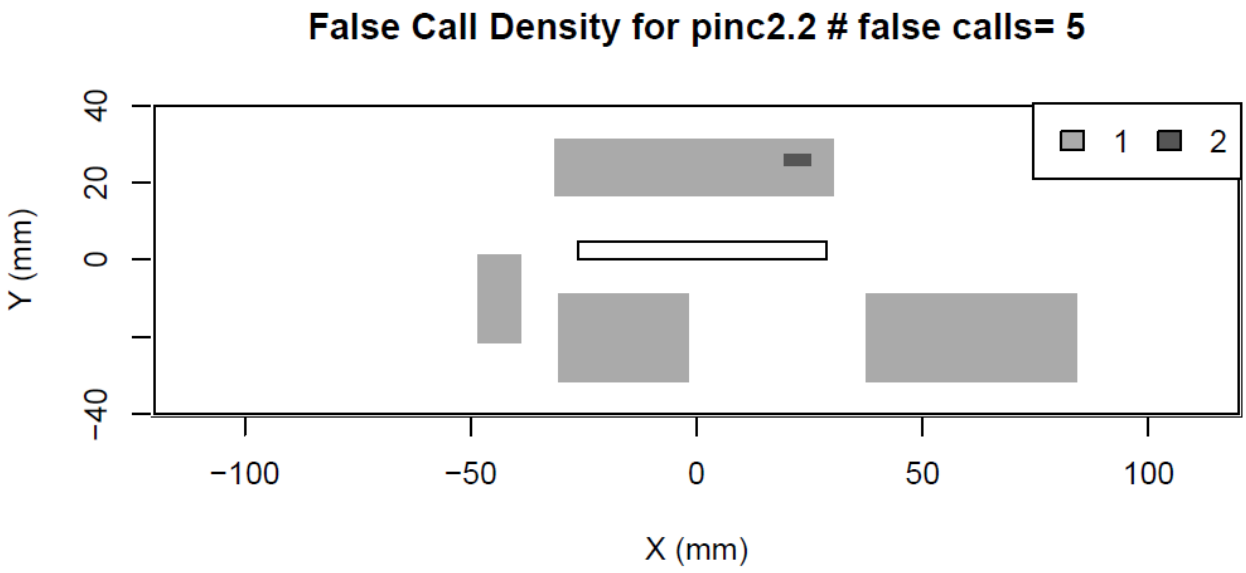
False Call Density for pinc2.2 # false calls= 5
1
2
Y (mm)
40
20
0
−40
−100
−50
0
50
100
X (mm)

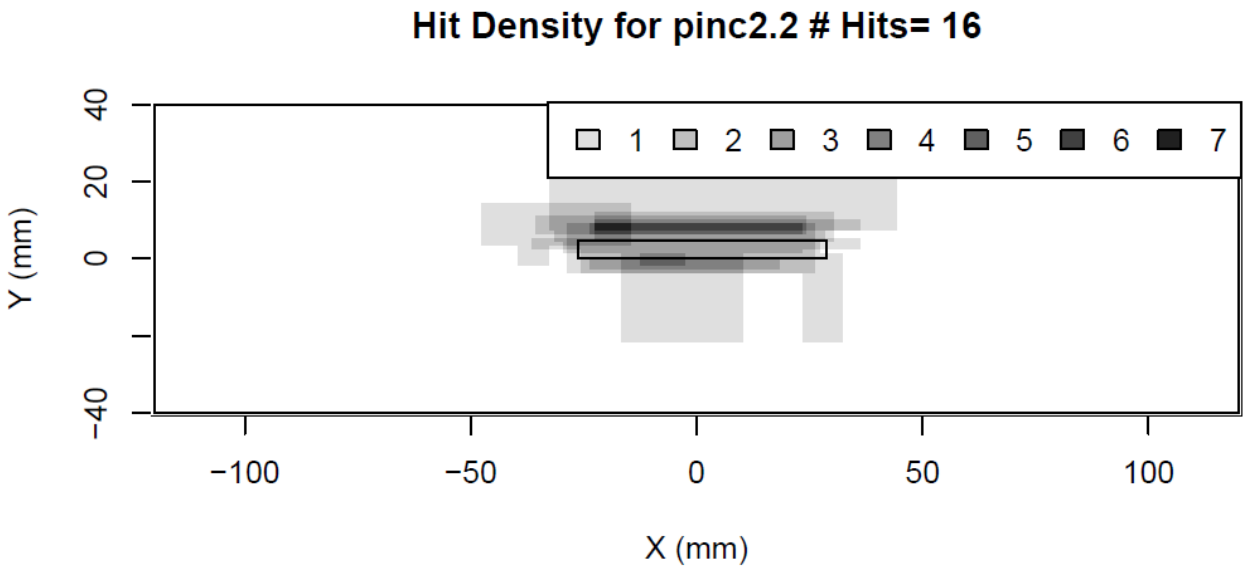
Hit Density for pinc2.2 # Hits= 16
1
2
3
4
5
6
7
Y (mm)
40
20
0
−40
−100
−50
0
50
100
X (mm)

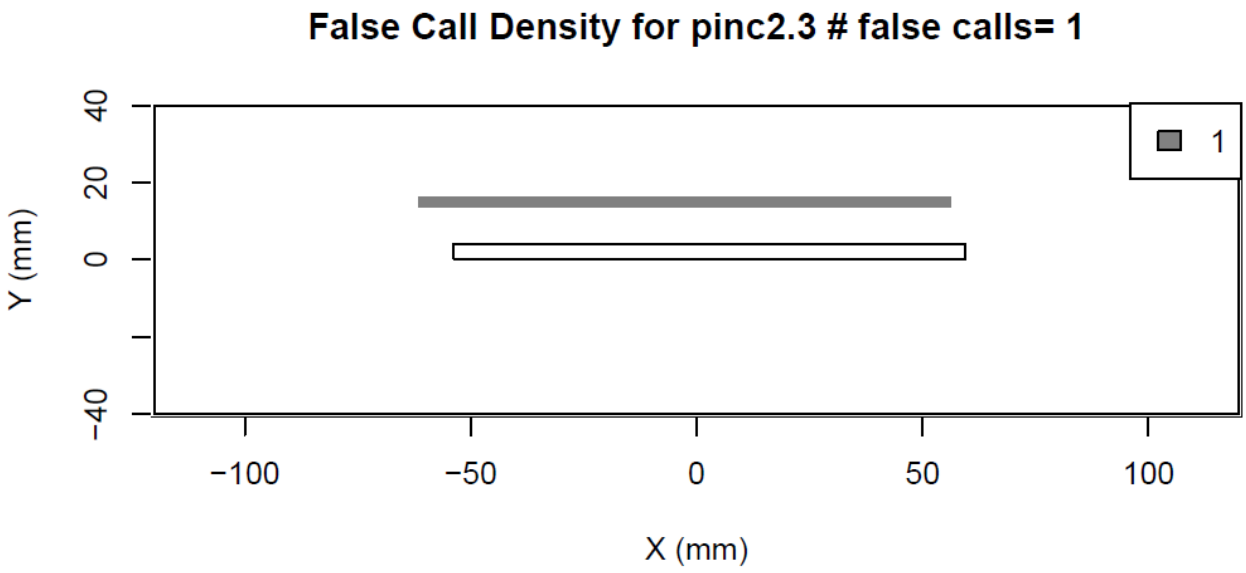
False Call Density for pinc2.3 # false calls= 1
1
Y (mm)
40
20
0
−40
−100
−50
0
50
100
X (mm)

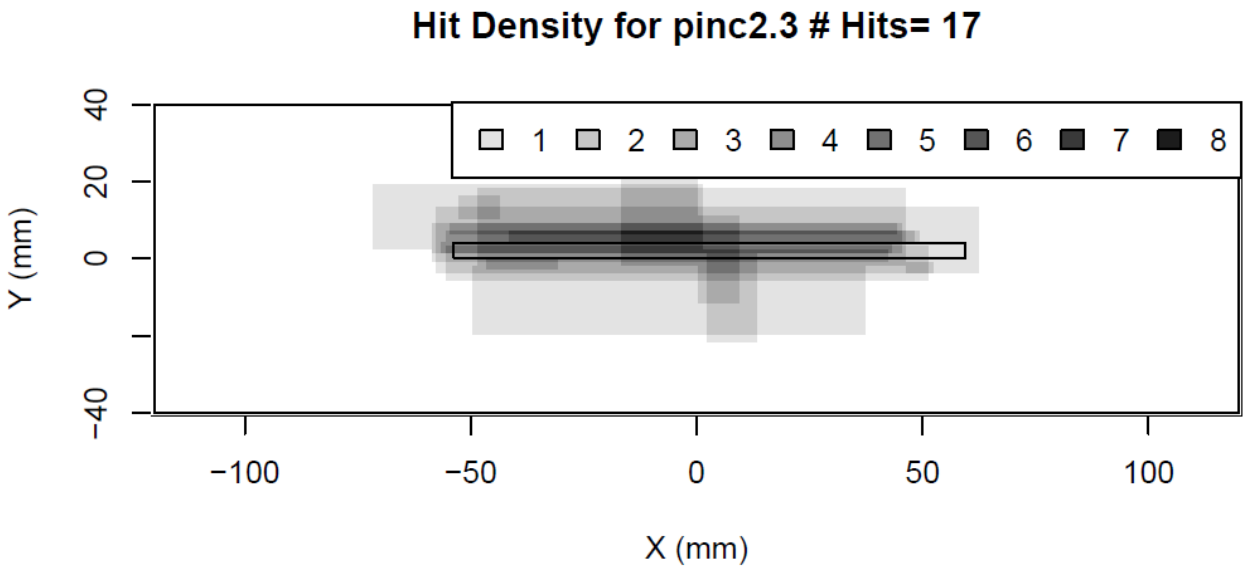
Hit Density for pinc2.3 # Hits= 17
1
2
3
4
5
6
7
8
Y (mm)
40
20
0
−40
−100
−50
0
50
100
X (mm)

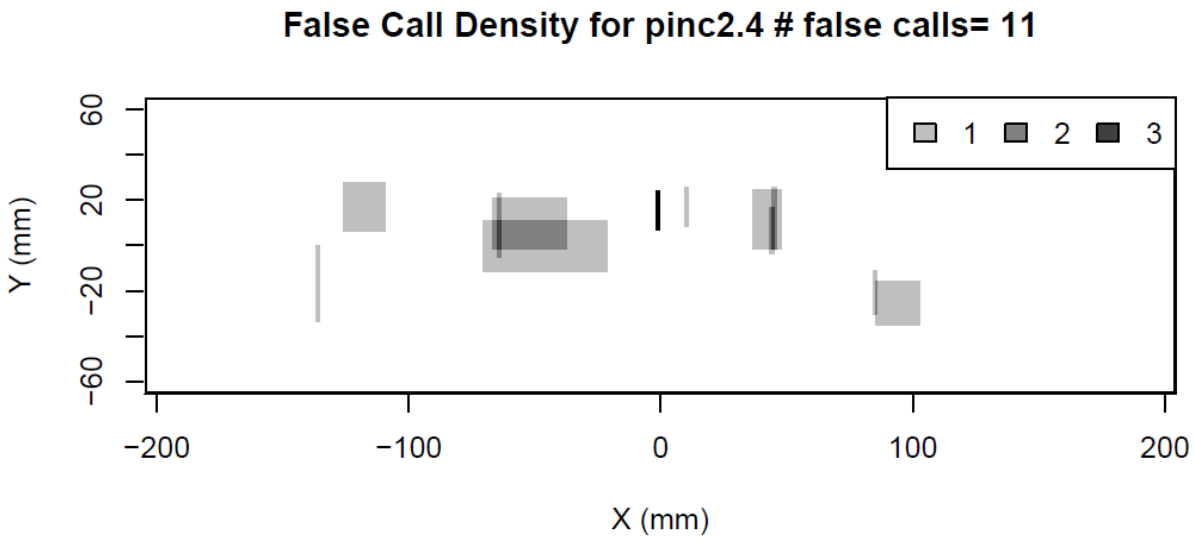
False Call Density for pinc2.4 # false calls= 11
1
2
3
Y (mm)
60
20
−20
−60
−200
−100
0
100
200
X (mm)

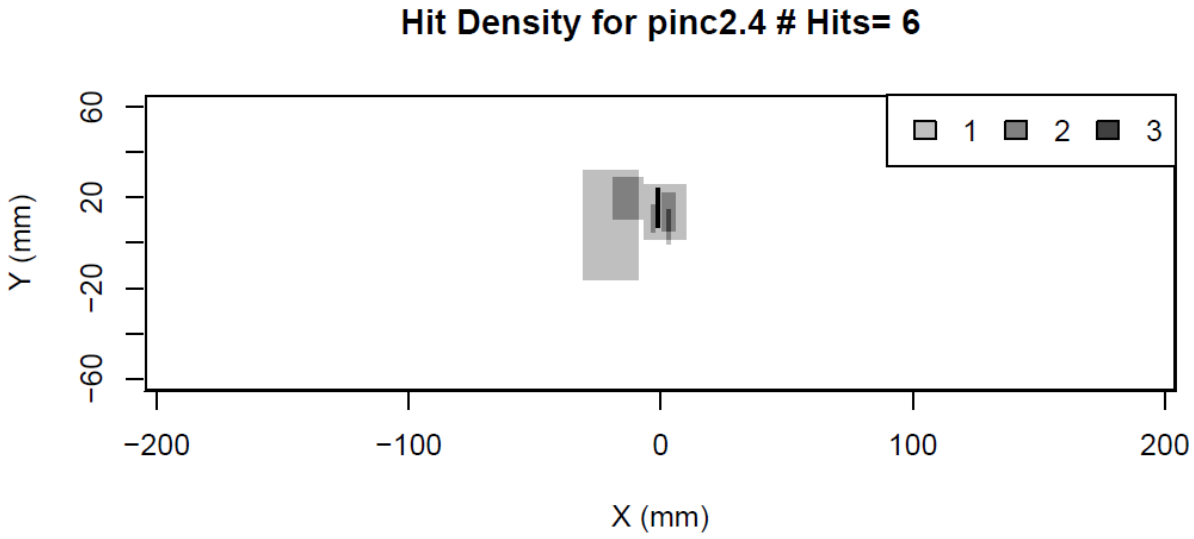
Hit Density for pinc2.4 # Hits= 6
1
2
3
Y (mm)
60
20
−20
−60
−200
−100
0
100
200
X (mm)

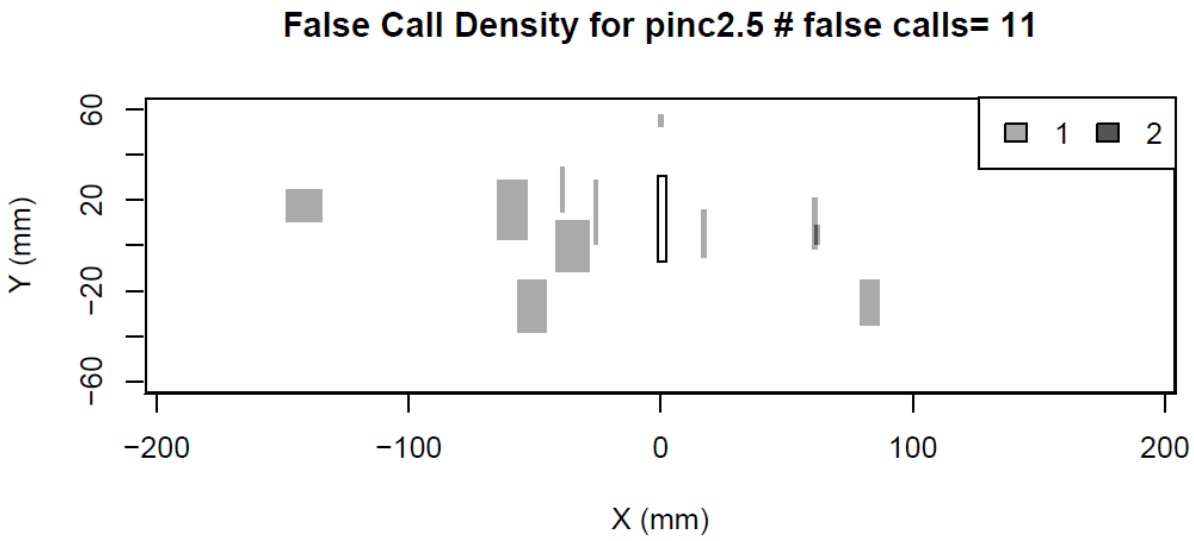
False Call Density for pinc2.5 # false calls= 11
1
2
Y (mm)
60
20
−20
−60
−200
−100
0
100
200
X (mm)

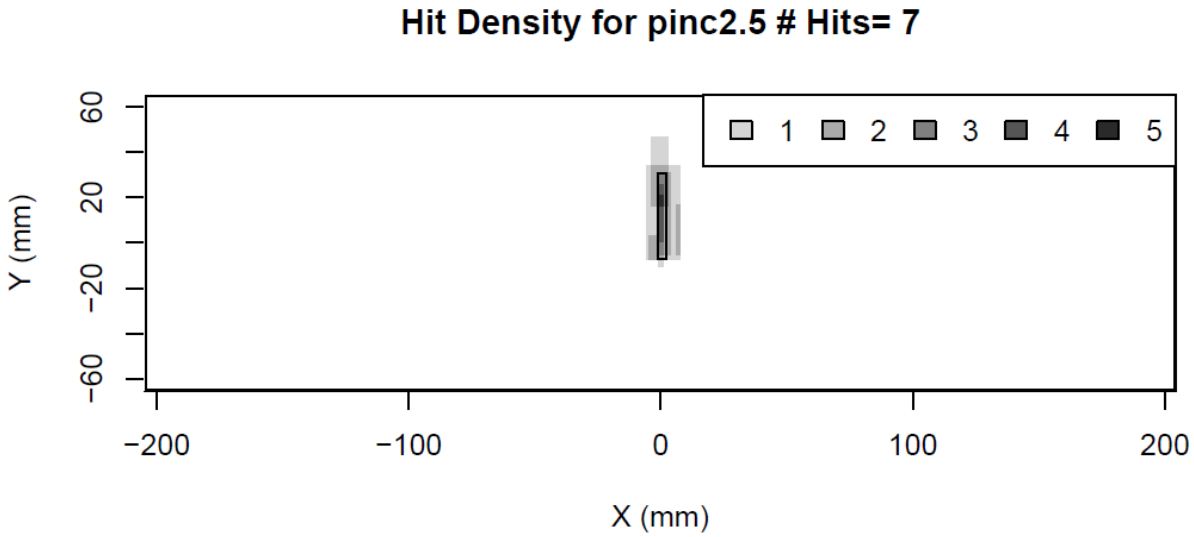
Hit Density for pinc2.5 # Hits= 7
1
2
3
4
5
Y (mm)
60
20
−20
−60
−200
−100
0
100
200
X (mm)

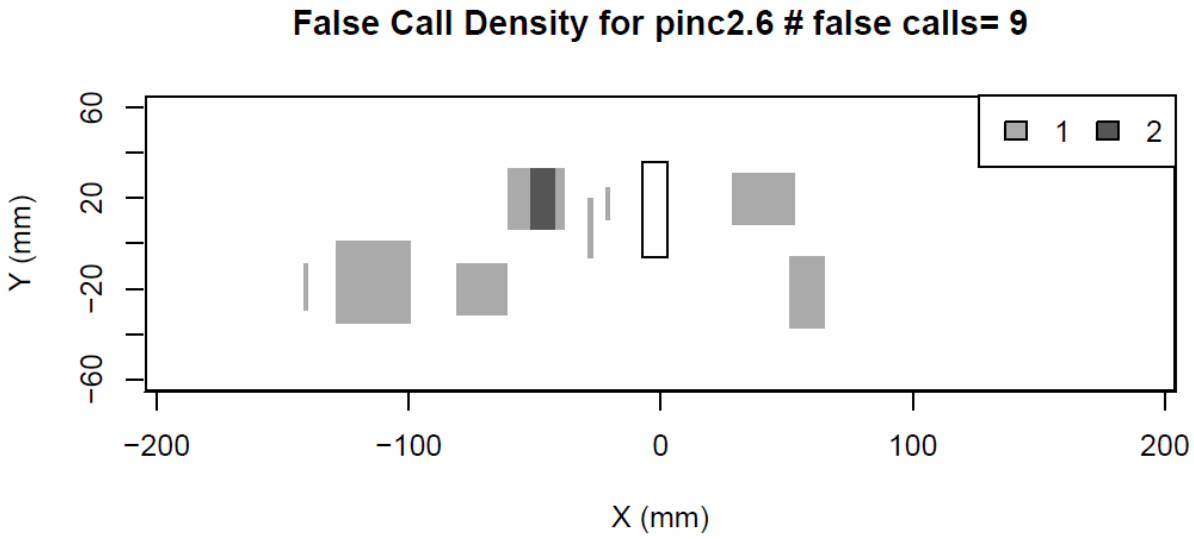
False Call Density for pinc2.6 # false calls= 9
1
2
60
20
−20
−60
Y (mm)
−200
−100
0
100
200
X (mm)

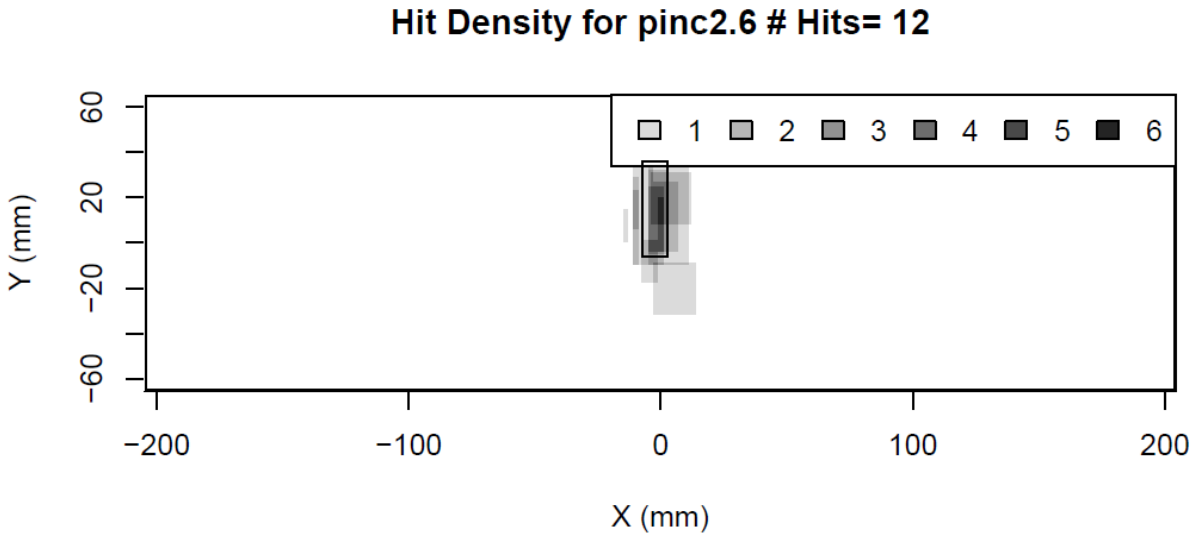
Hit Density for pinc2.6 # Hits= 12
1
2
3
4
5
6
60
20
−20
−60
Y (mm)
−200
−100
0
100
200
X (mm)

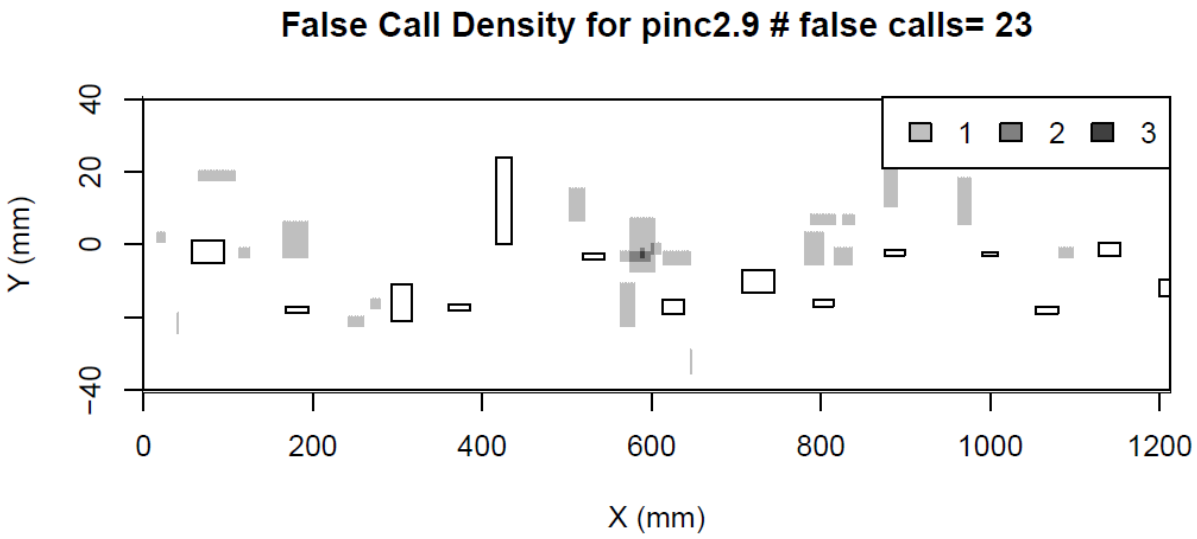
False Call Density for pinc2.9 # false calls= 23
1
2
3
Y (mm)
40
20
0
-40
0
200
400
600
800
1000
1200
X (mm)

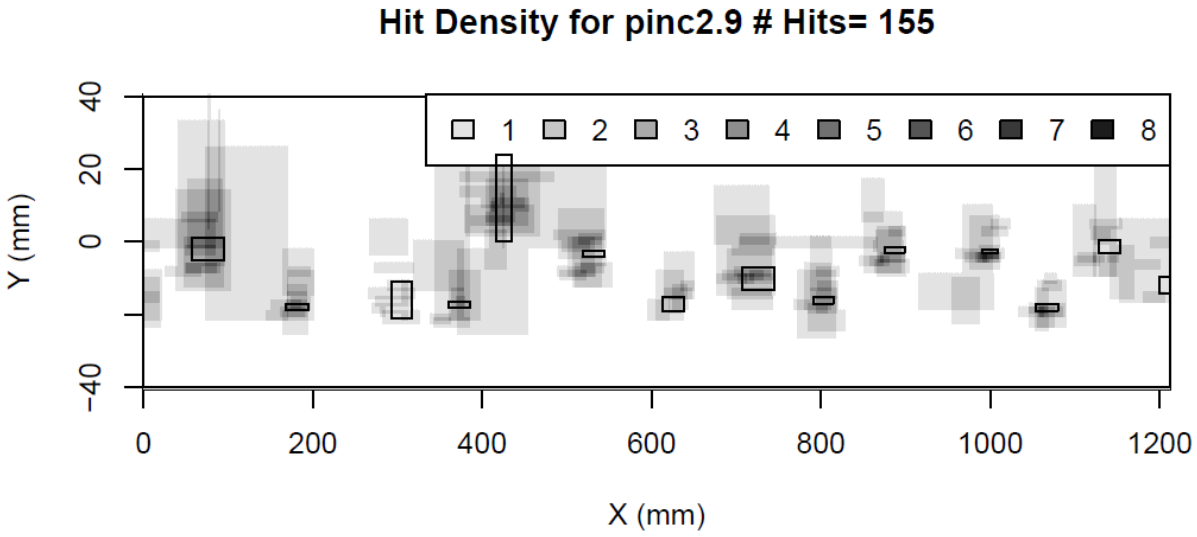
Hit Density for pinc2.9 # Hits= 155
1
2
3
4
5
6
7
8
Y (mm)
40
20
0
-40
0
200
400
600
800
1000
1200
X (mm)

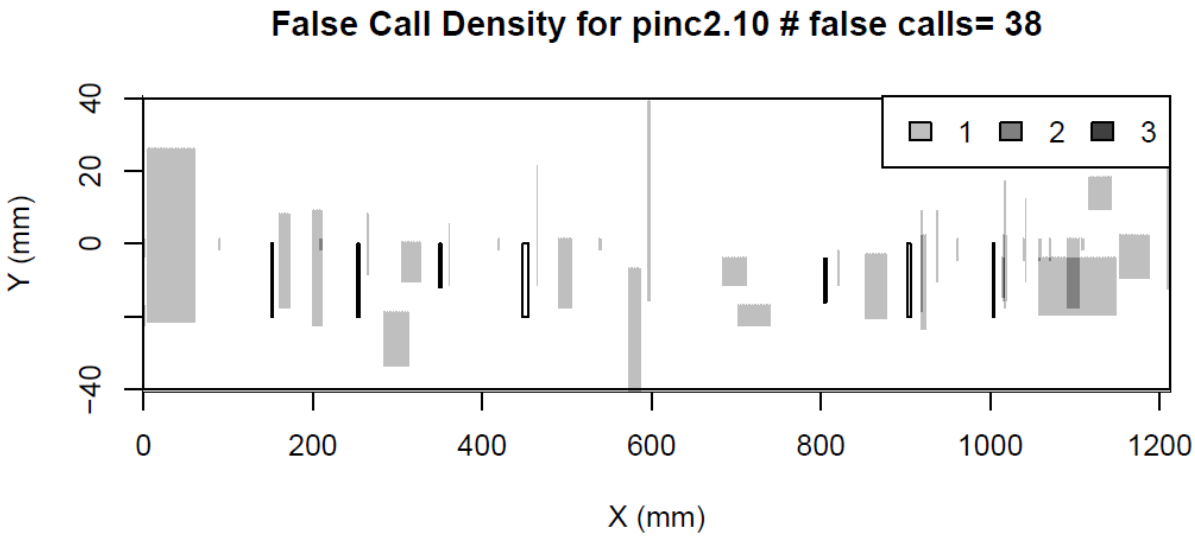
False Call Density for pinc2.10 # false calls= 38
1
2
3
Y (mm)
40
20
0
-40
0
200
400
600
800
1000
1200
X (mm)

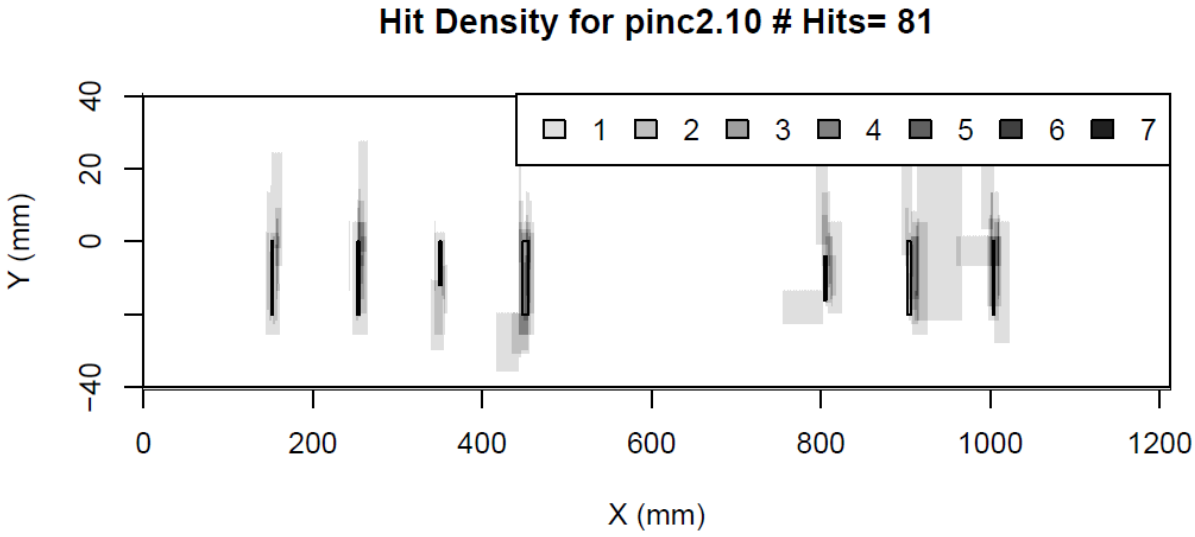
Hit Density for pinc2.10 # Hits= 81
1
2
3
4
5
6
7
Y (mm)
40
20
0
-40
0
200
400
600
800
1000
1200
X (mm)

Appendix E
Inspection Plots for Bottom-Mounted Instrumentation Samples

Appendix E

Inspection Plots for Bottom-Mounted Instrumentation Samples

Table of Contents

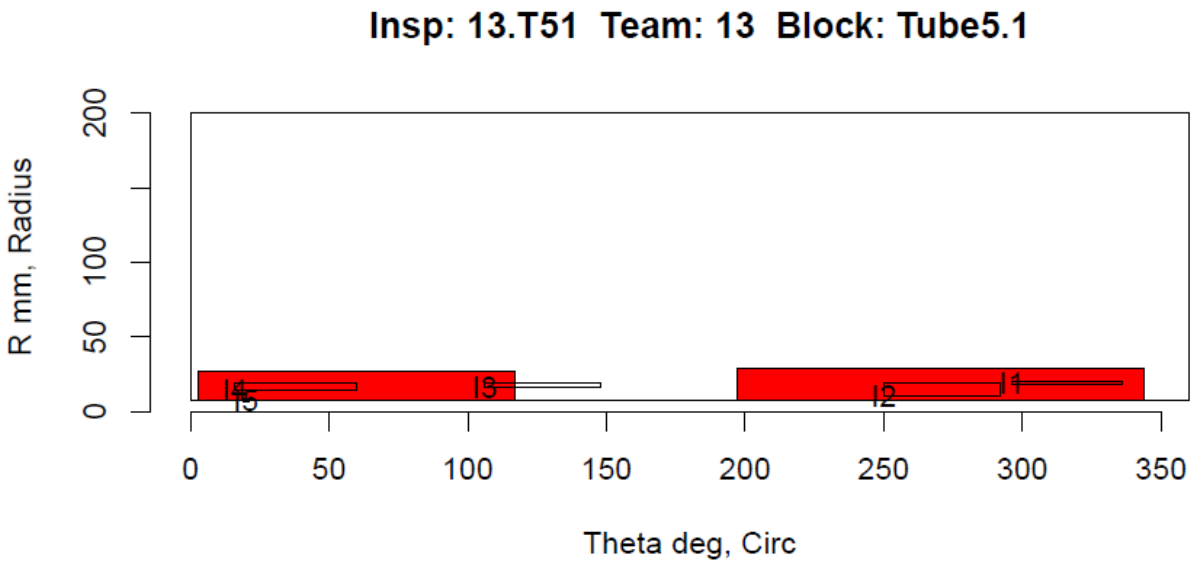
Insp: 13.T51 Team: 13 Block: Tube5.1
R mm, Radius
0
50
100
200
0
50
100
150
200
250
300
350
Theta deg, Circ
I1
I2
I3
I4
I5

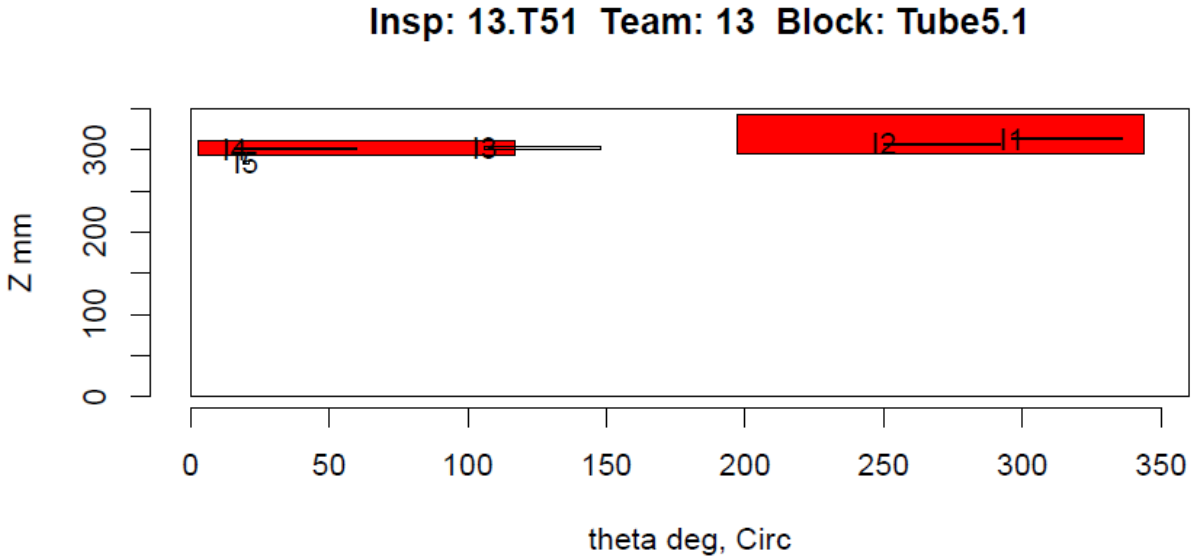
Insp: 13.T51 Team: 13 Block: Tube5.1
Z mm
0
100
200
300
0
50
100
150
200
250
300
350
theta deg, Circ
I1
I2
I3
I4
I5

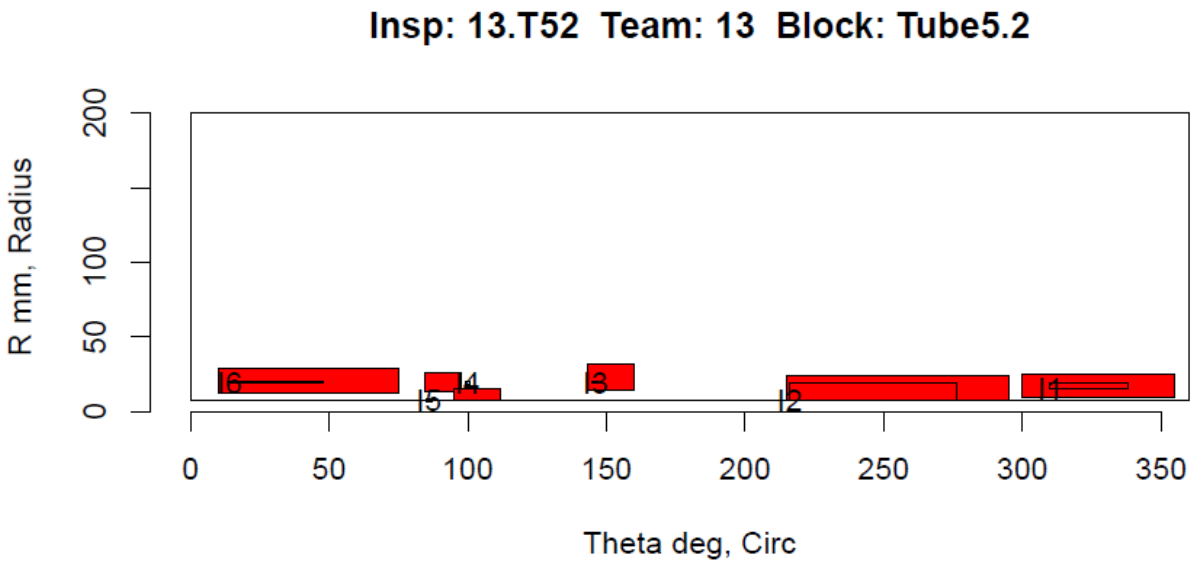
Insp: 13.T52 Team: 13 Block: Tube5.2
R mm, Radius
0
50
100
200
0
50
100
150
200
250
300
350
Theta deg, Circ
I6
I5
I4
I3
I2
I1

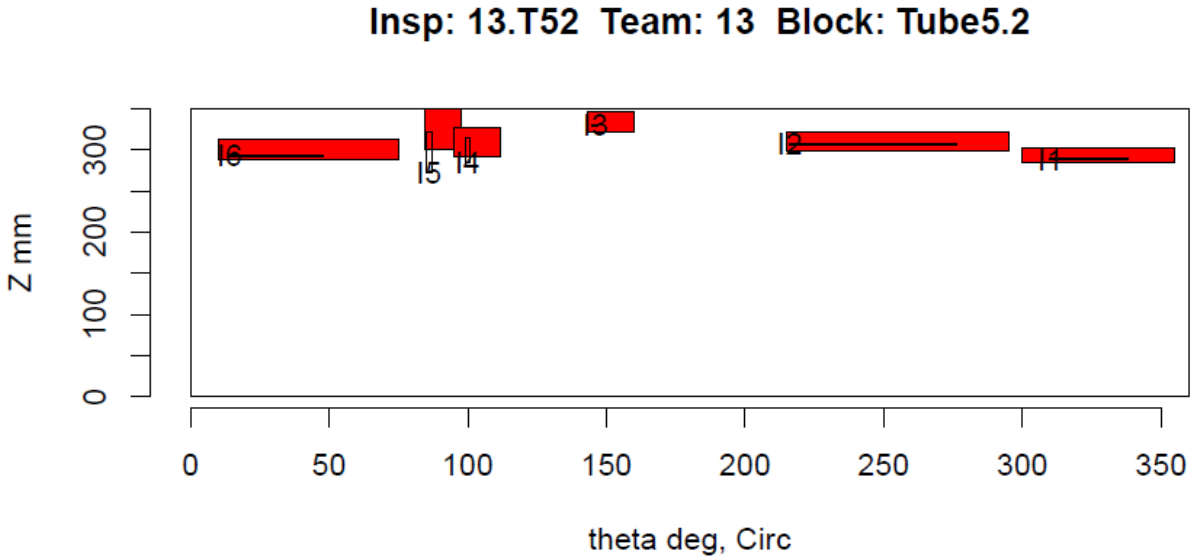
Insp: 13.T52 Team: 13 Block: Tube5.2
Z mm
0
100
200
300
0
50
100
150
200
250
300
350
theta deg, Circ
I6
I5
I4
I3
I2
I1

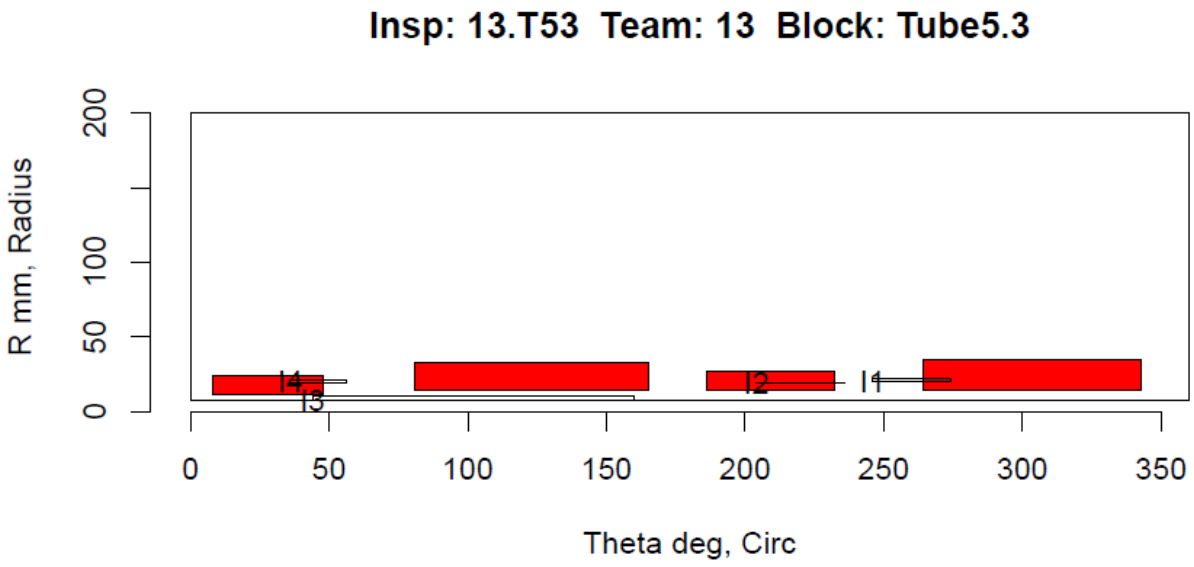
Insp: 13.T53 Team: 13 Block: Tube5.3
R mm, Radius
0
50
100
200
I4
I3
I2
I1
0
50
100
150
200
250
300
350
Theta deg, Circ

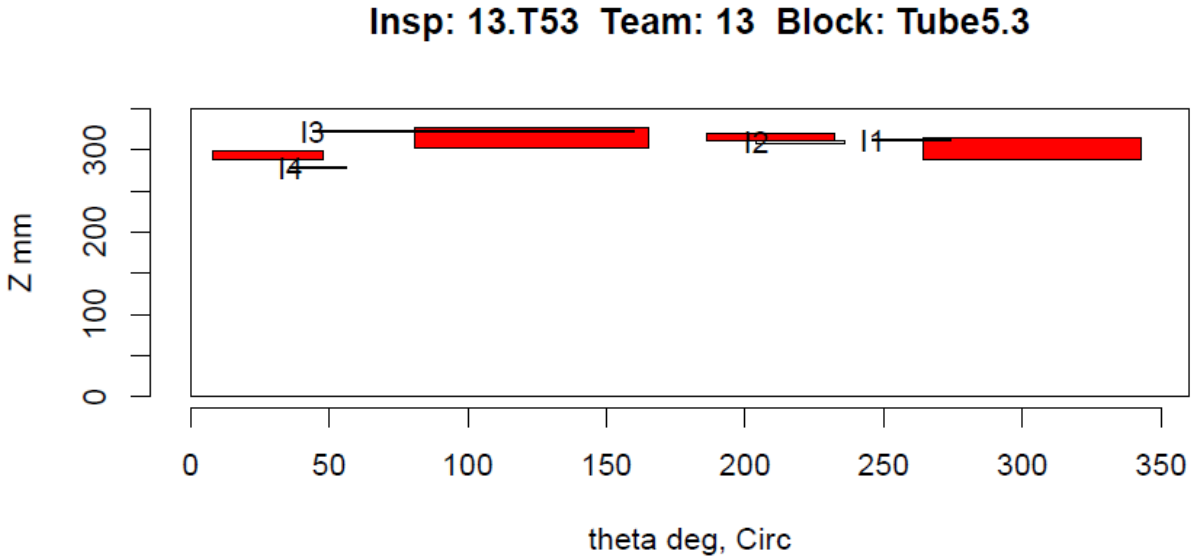
Insp: 13.T53 Team: 13 Block: Tube5.3
Z mm
0
100
200
300
I3
I4
I2
I1
0
50
100
150
200
250
300
350
theta deg, Circ

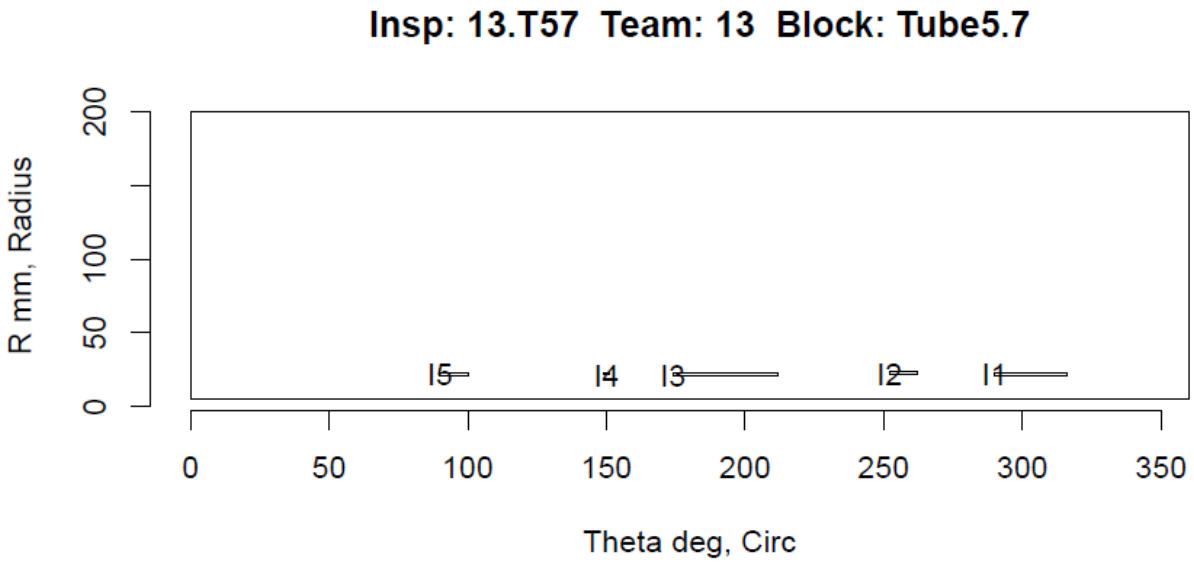
Insp: 13.T57 Team: 13 Block: Tube5.7
R mm, Radius
0
50
100
200
5
4
3
2
1
0
50
100
150
200
250
300
350
Theta deg, Circ

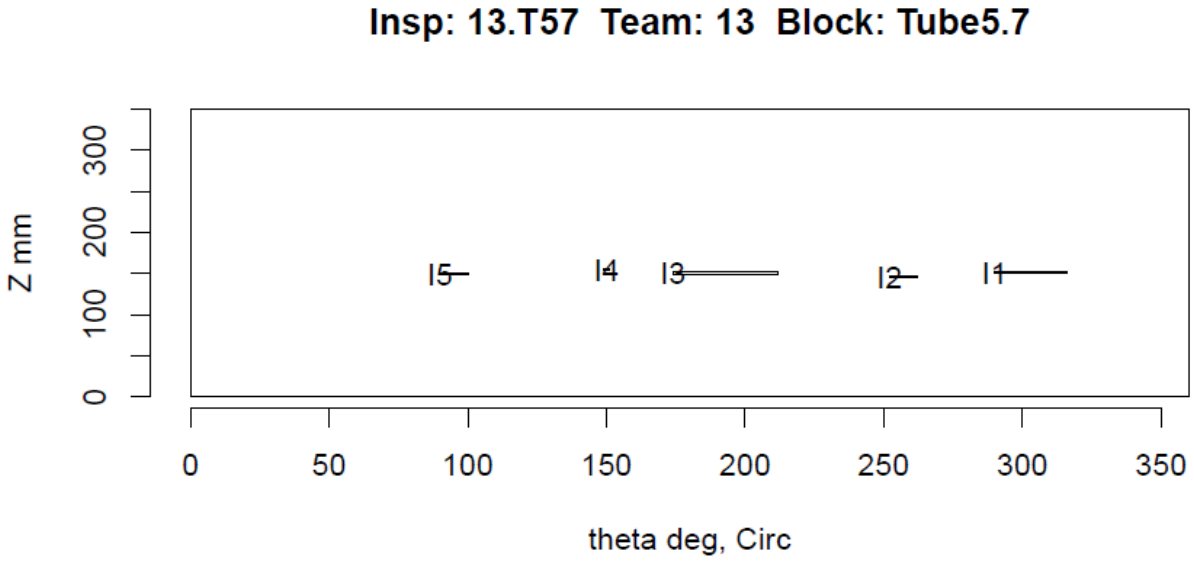
Insp: 13.T57 Team: 13 Block: Tube5.7
Z mm
0
100
200
300
5
4
3
2
1
0
50
100
150
200
250
300
350
theta deg, Circ

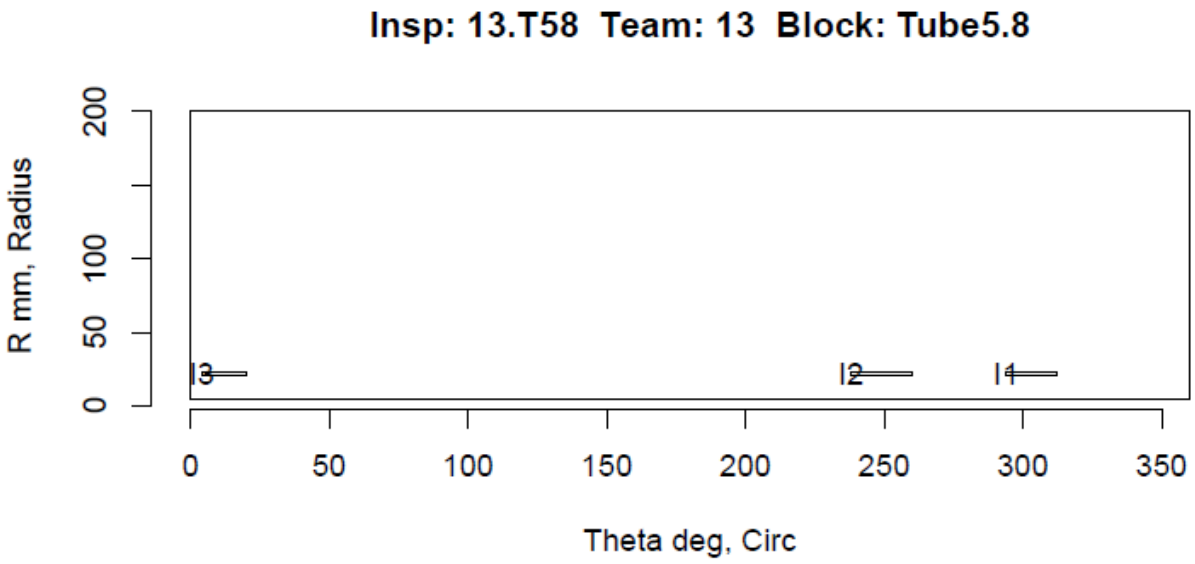
Insp: 13.T58 Team: 13 Block: Tube5.8
R mm, Radius
0
50
100
200
3
2
1
0
50
100
150
200
250
300
350
Theta deg, Circ

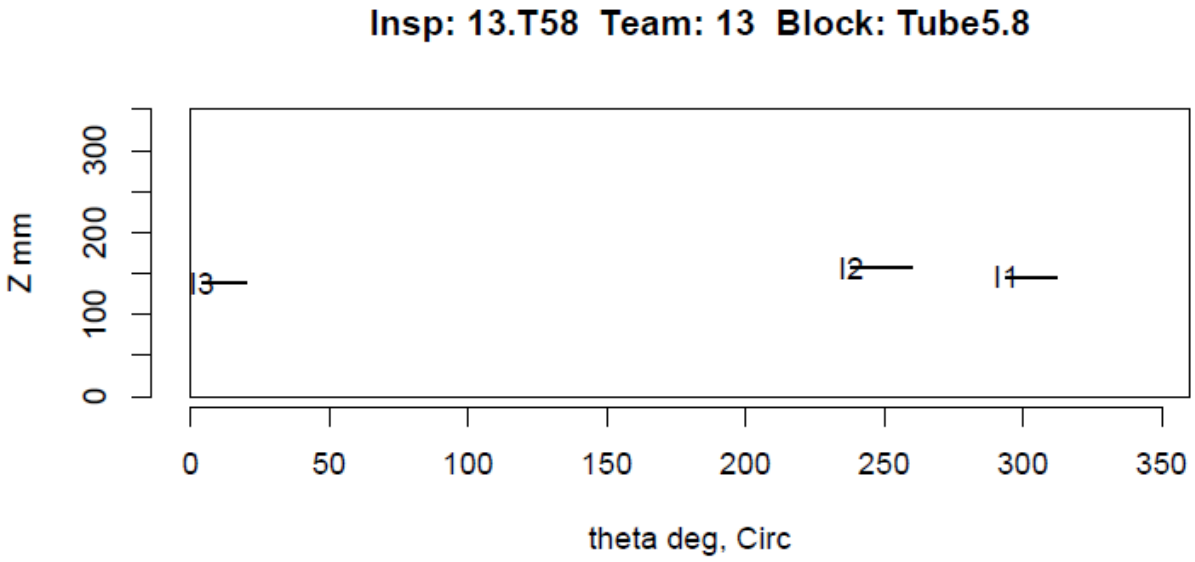
Insp: 13.T58 Team: 13 Block: Tube5.8
Z mm
0
100
200
300
3
2
1
0
50
100
150
200
250
300
350
theta deg, Circ

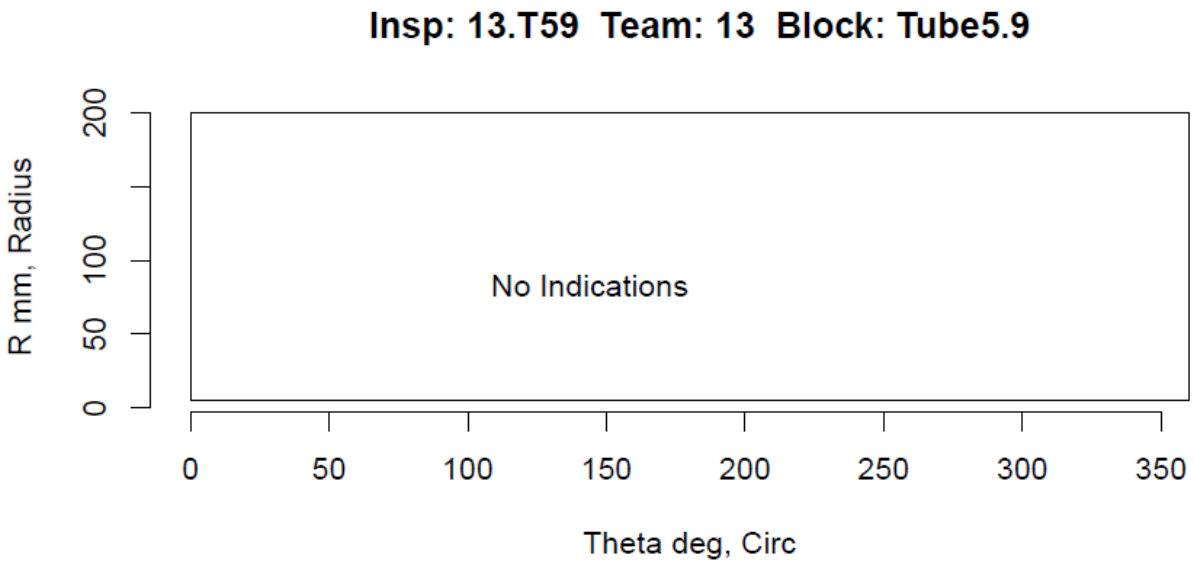
Insp: 13.T59 Team: 13 Block: Tube5.9
R mm, Radius
0
50
100
200
No Indications
0
50
100
150
200
250
300
350
Theta deg, Circ

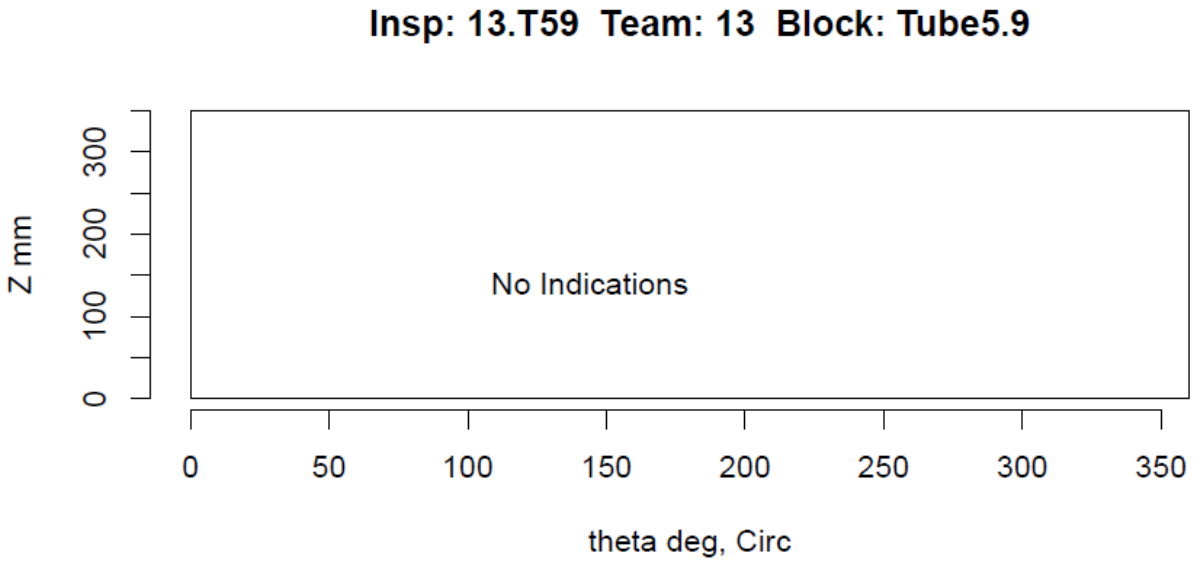
Insp: 13.T59 Team: 13 Block: Tube5.9
Z mm
0
100
200
300
No Indications
0
50
100
150
200
250
300
350
theta deg, Circ

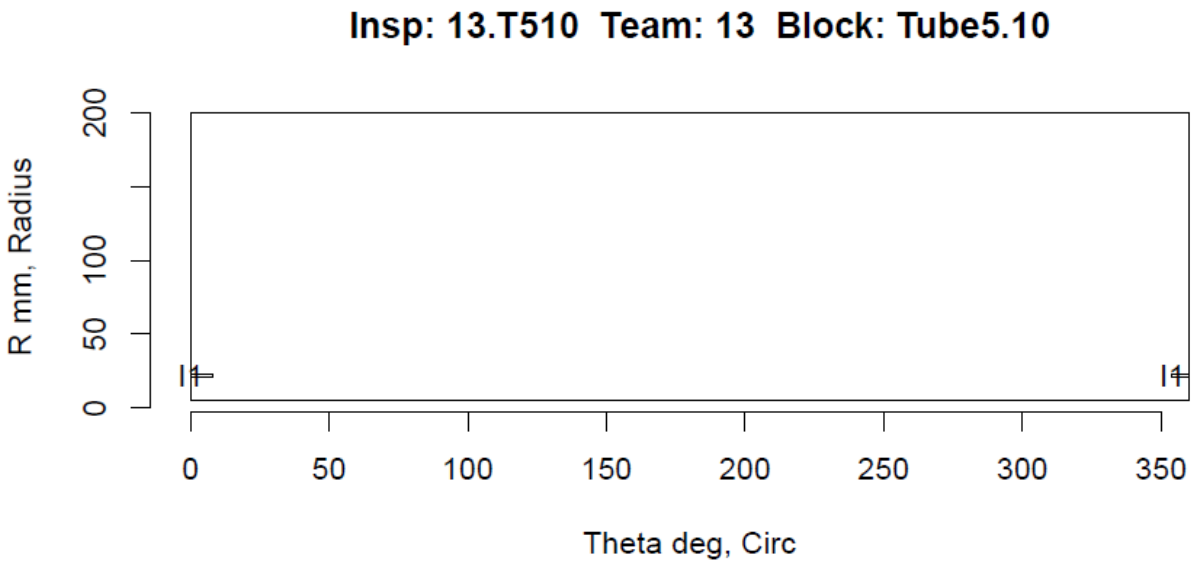
Insp: 13.T510 Team: 13 Block: Tube5.10
R mm, Radius
0
50
100
200
0
50
100
150
200
250
300
350
Theta deg, Circ

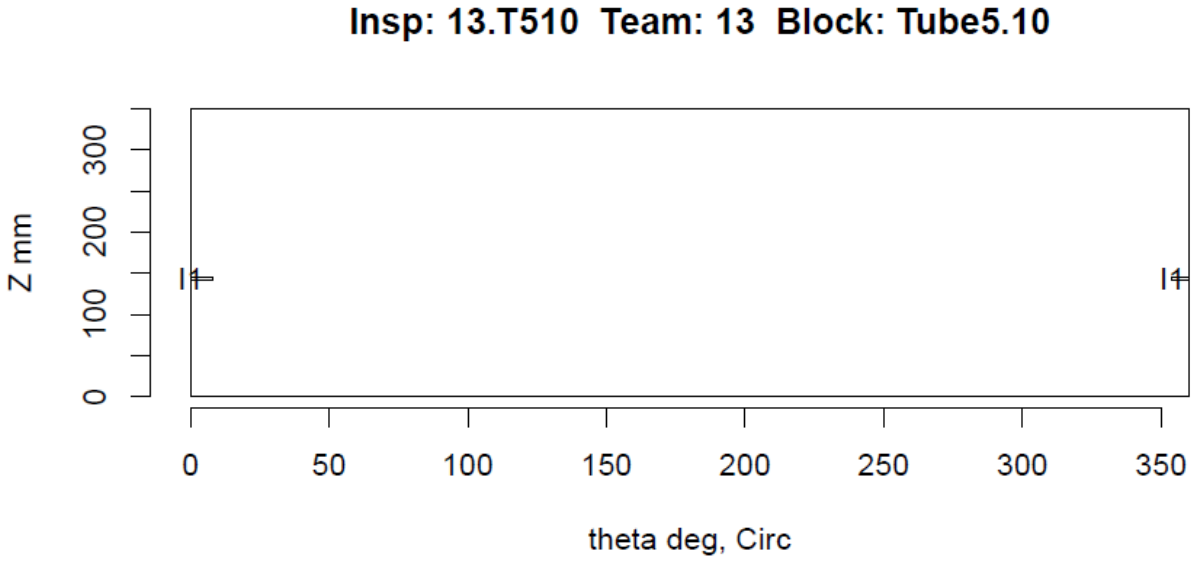
Insp: 13.T510 Team: 13 Block: Tube5.10
Z mm
0
100
200
300
0
50
100
150
200
250
300
350
theta deg, Circ

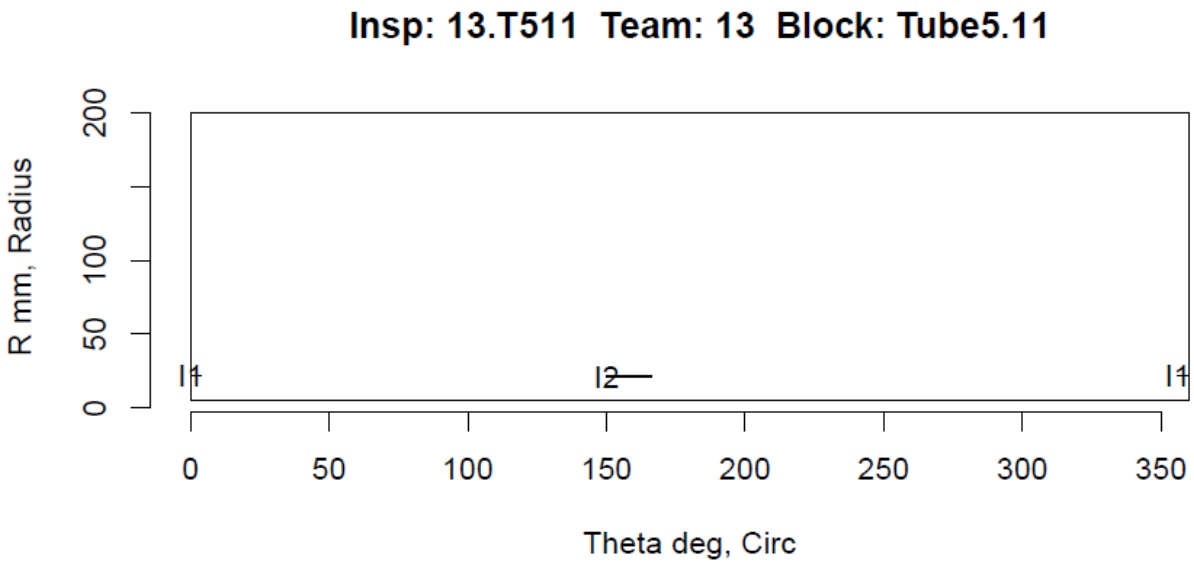
Insp: 13.T511 Team: 13 Block: Tube5.11
R mm, Radius
0
50
100
200
I1
I2
I1
0
50
100
150
200
250
300
350
Theta deg, Circ

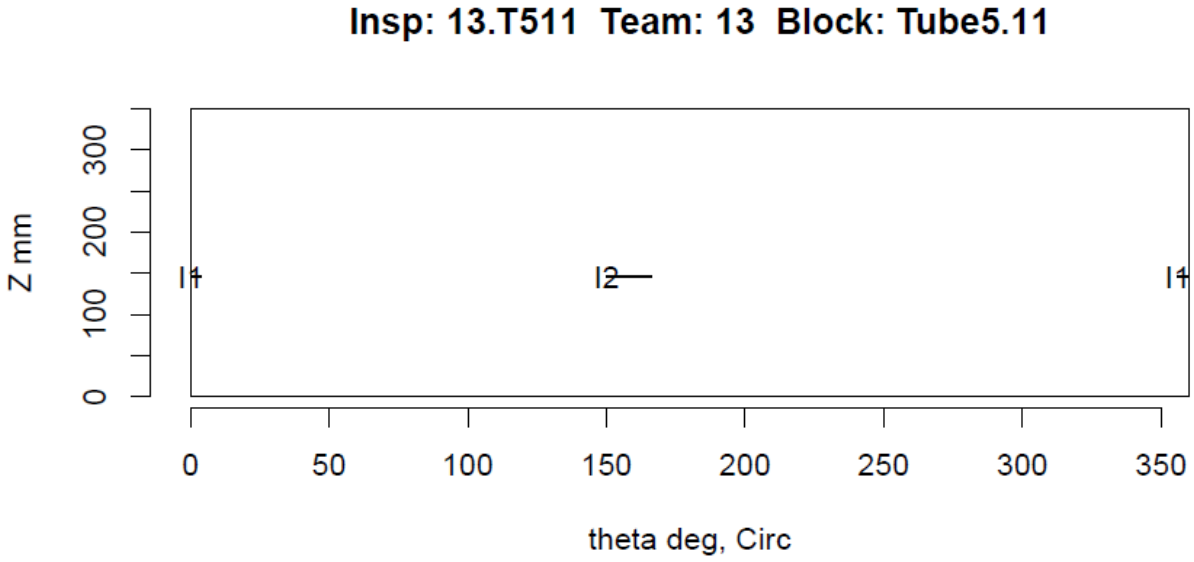
Insp: 13.T511 Team: 13 Block: Tube5.11
Z mm
0
100
200
300
I1
I2
I1
0
50
100
150
200
250
300
350
theta deg, Circ

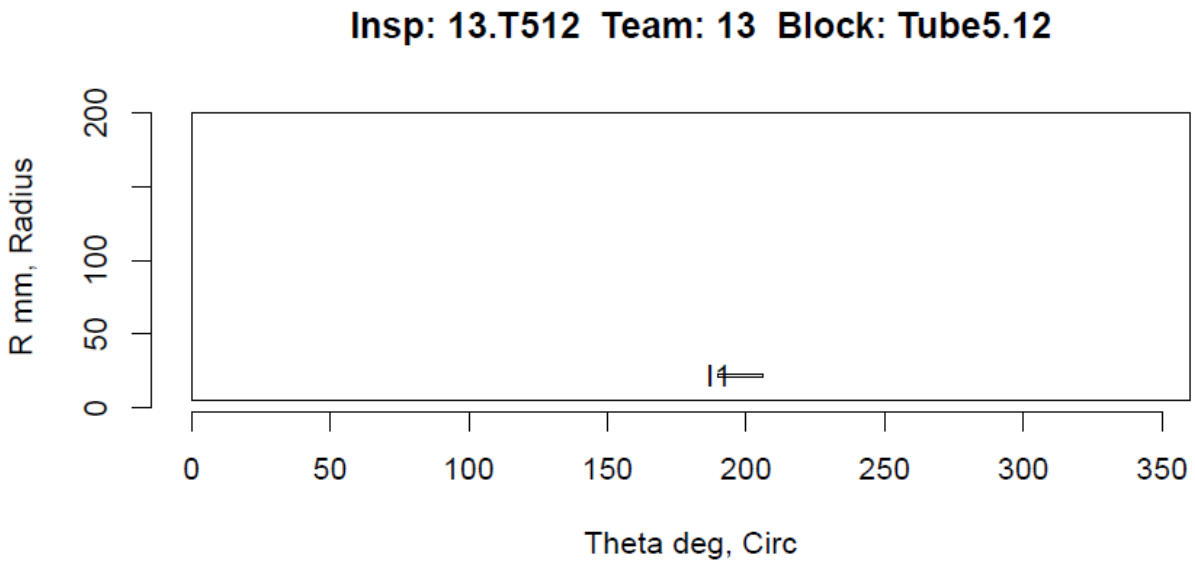
Insp: 13.T512 Team: 13 Block: Tube5.12
R mm, Radius
0
50
100
200
0
50
100
150
200
250
300
350
Theta deg, Circ

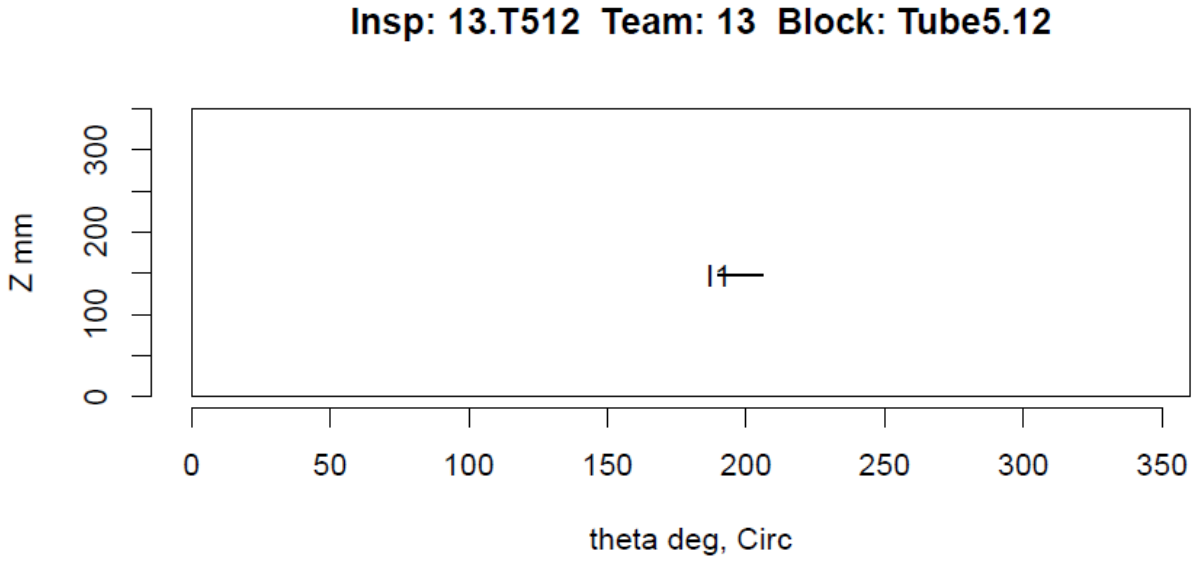
Insp: 13.T512 Team: 13 Block: Tube5.12
Z mm
0
100
200
300
0
50
100
150
200
250
300
350
theta deg, Circ

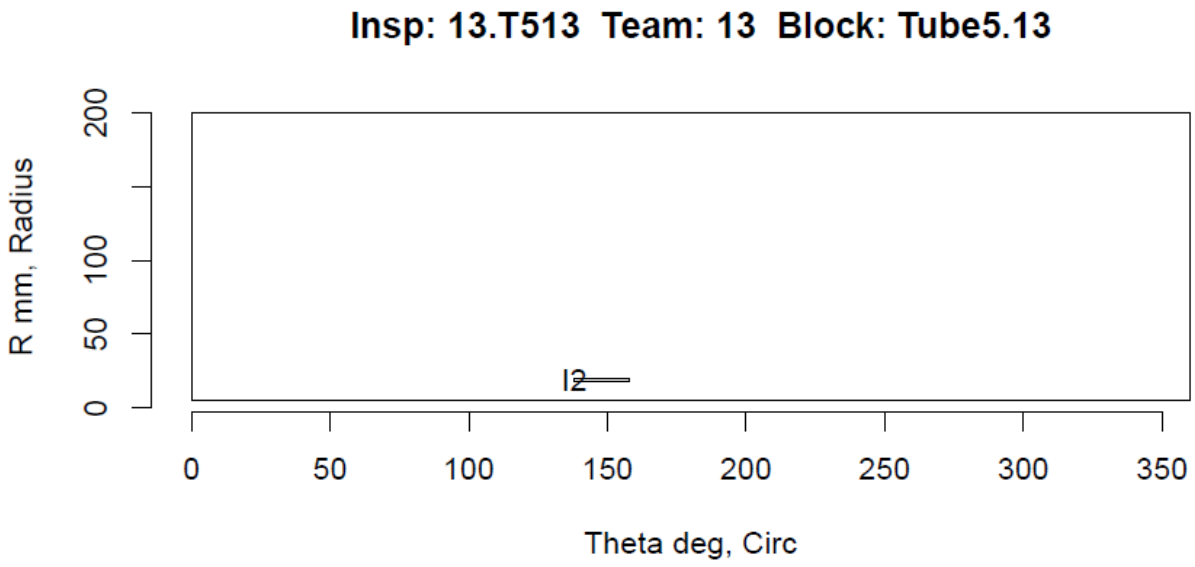
Insp: 13.T513 Team: 13 Block: Tube5.13
R mm, Radius
0
50
100
200
I2
0
50
100
150
200
250
300
350
Theta deg, Circ

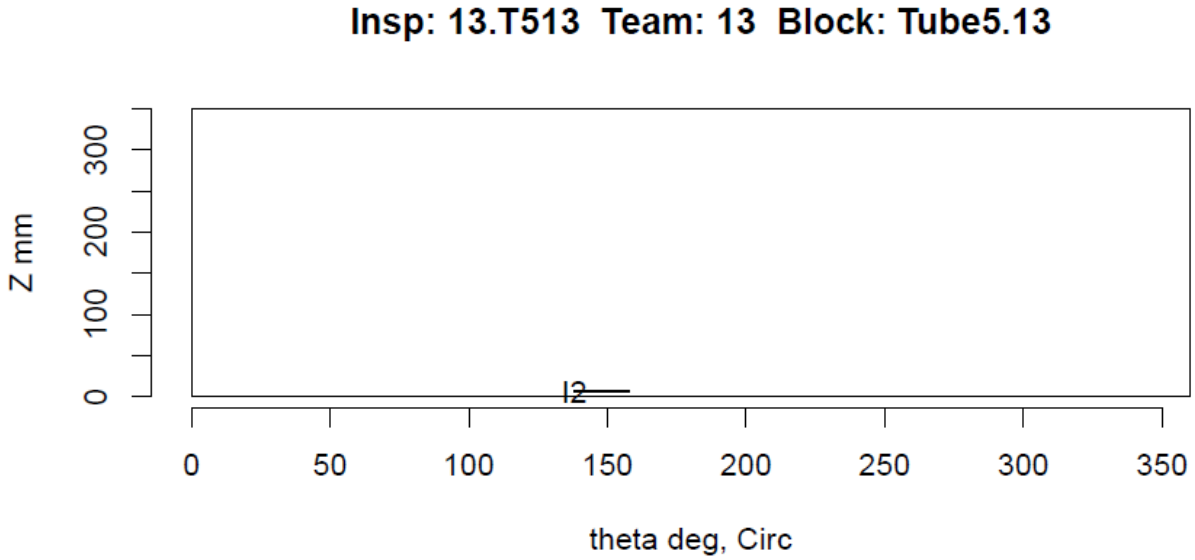
Insp: 13.T513 Team: 13 Block: Tube5.13
Z mm
0
100
200
300
I2
0
50
100
150
200
250
300
350
theta deg, Circ

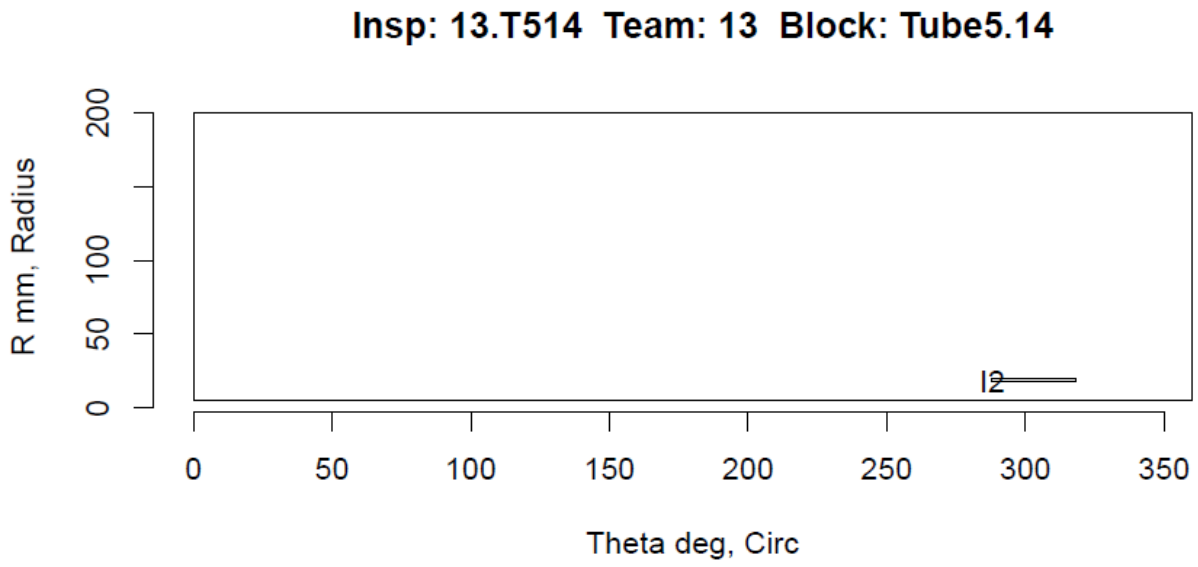
Insp: 13.T514 Team: 13 Block: Tube5.14
R mm, Radius
0
50
100
200
I2
0
50
100
150
200
250
300
350
Theta deg, Circ

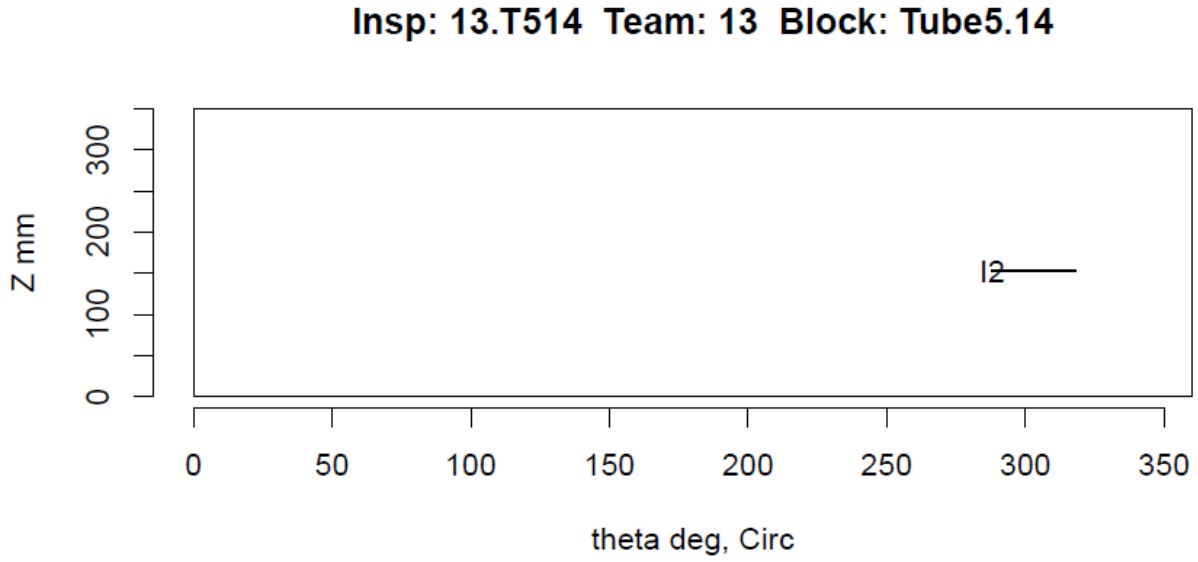
Insp: 13.T514 Team: 13 Block: Tube5.14
Z mm
0
100
200
300
I2
0
50
100
150
200
250
300
350
theta deg, Circ

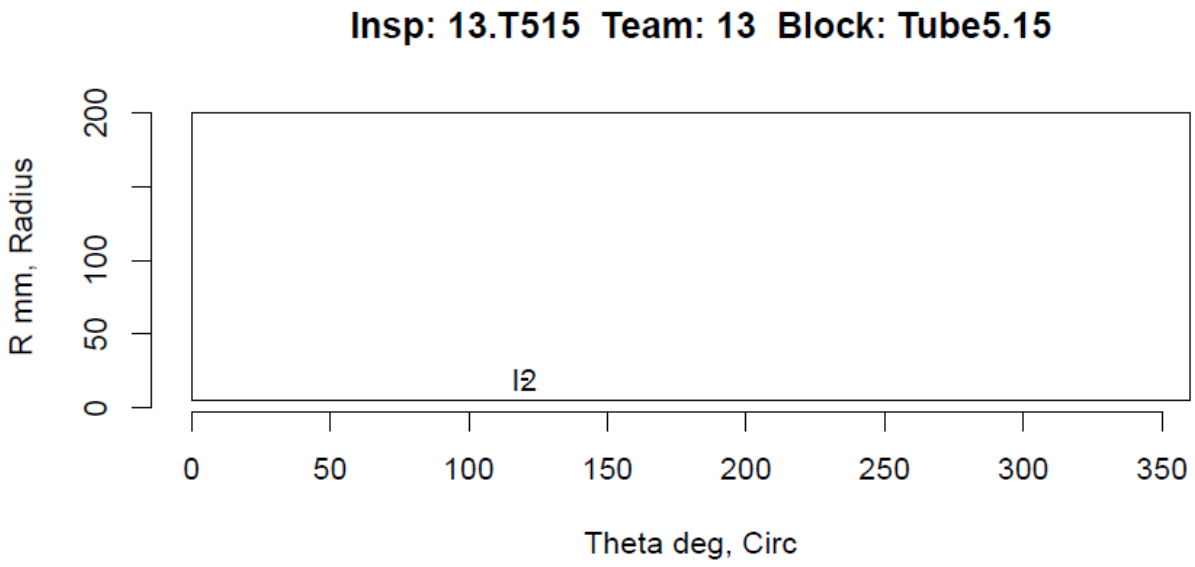
Insp: 13.T515 Team: 13 Block: Tube5.15
R mm, Radius
0
50
100
200
0
50
100
150
200
250
300
350
Theta deg, Circ

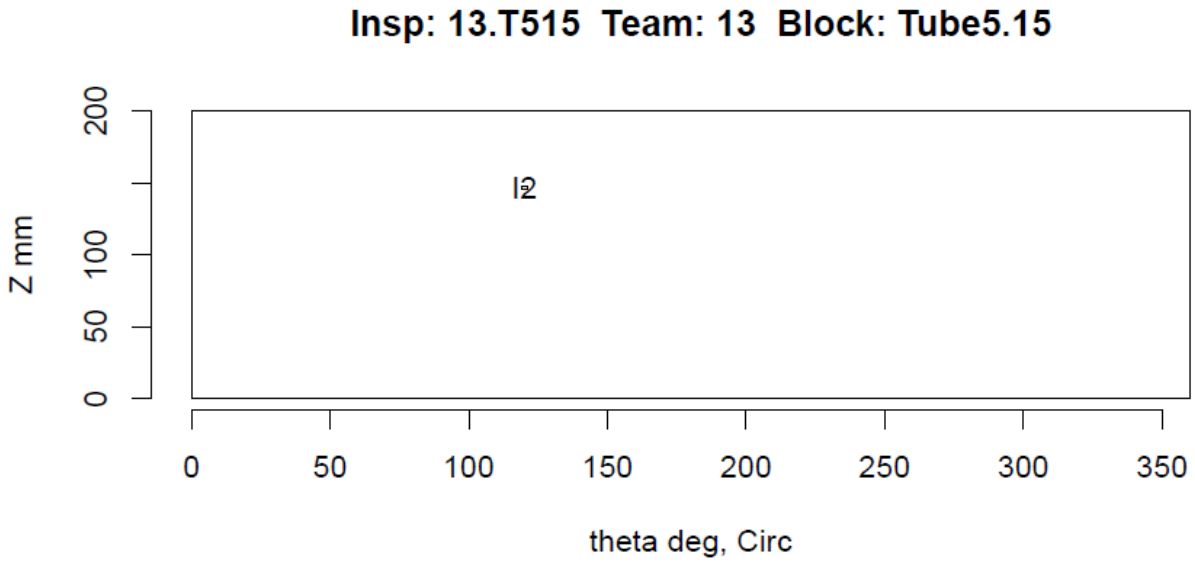
Insp: 13.T515 Team: 13 Block: Tube5.15
Z mm
0
50
100
200
0
50
100
150
200
250
300
350
theta deg, Circ

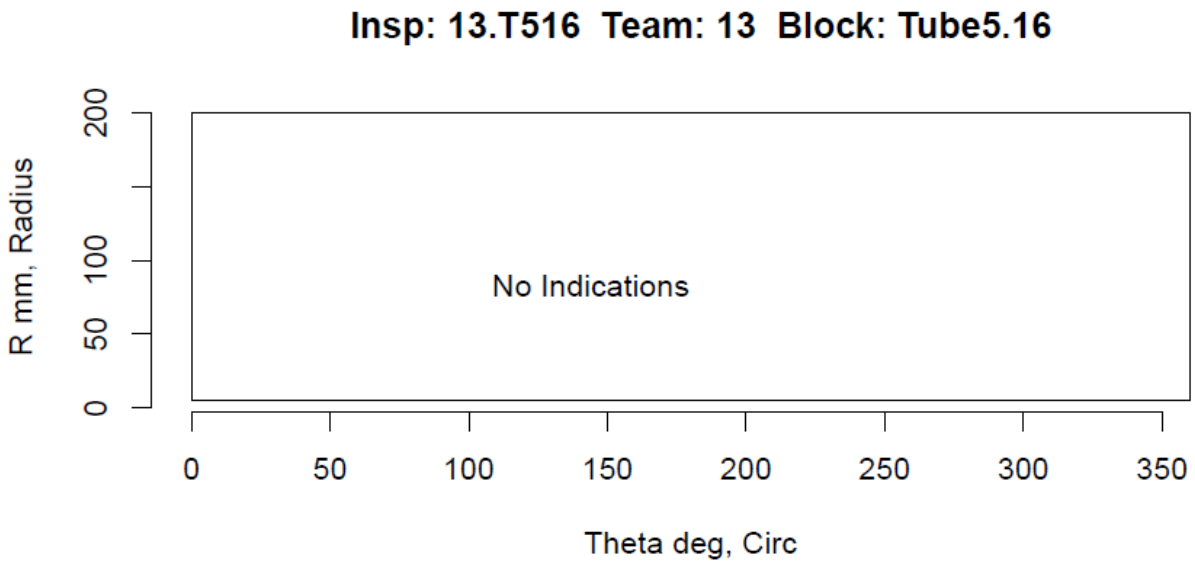
Insp: 13.T516 Team: 13 Block: Tube5.16
R mm, Radius
0
50
100
200
No Indications
0
50
100
150
200
250
300
350
Theta deg, Circ

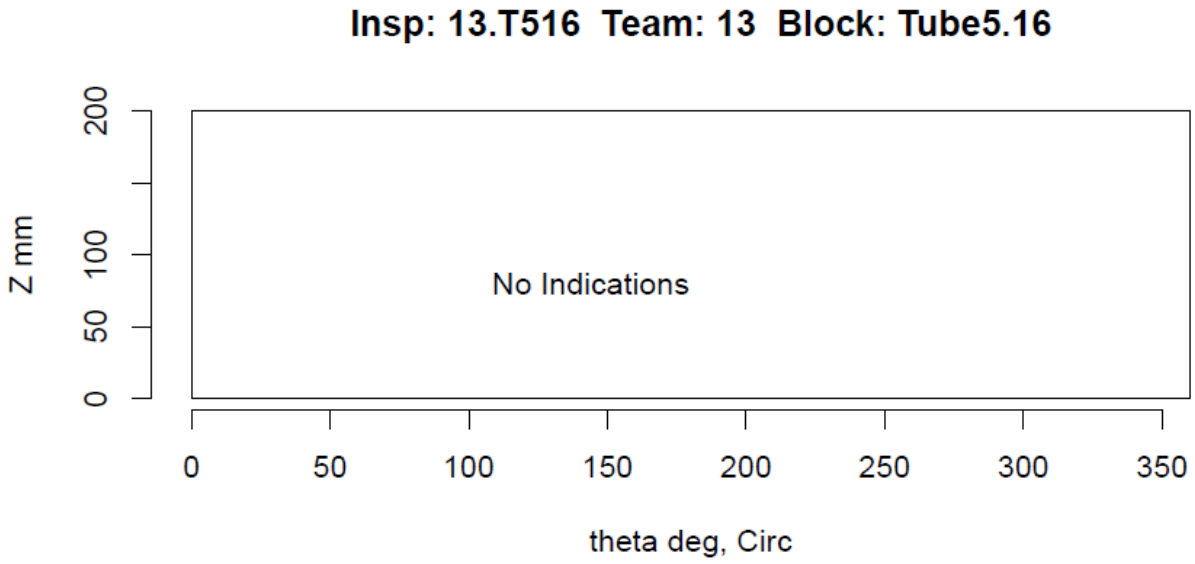
Insp: 13.T516 Team: 13 Block: Tube5.16
Z mm
0
50
100
200
No Indications
0
50
100
150
200
250
300
350
theta deg, Circ

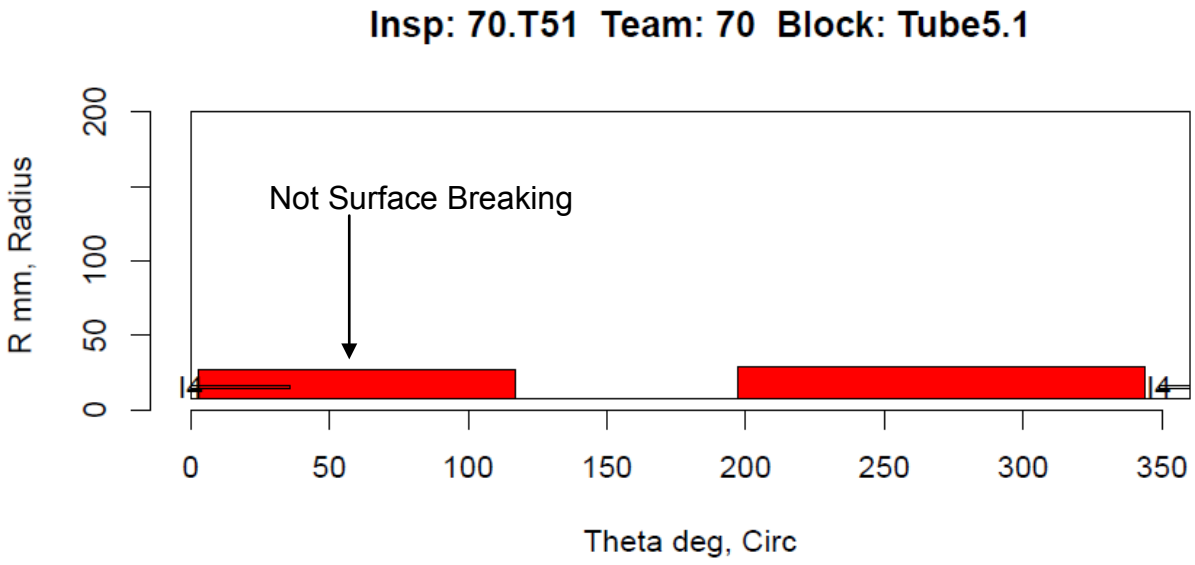
Insp: 70.T51 Team: 70 Block: Tube5.1
R mm, Radius
0
50
100
200
Not Surface Breaking
I4
I4
0
50
100
150
200
250
300
350
Theta deg, Circ

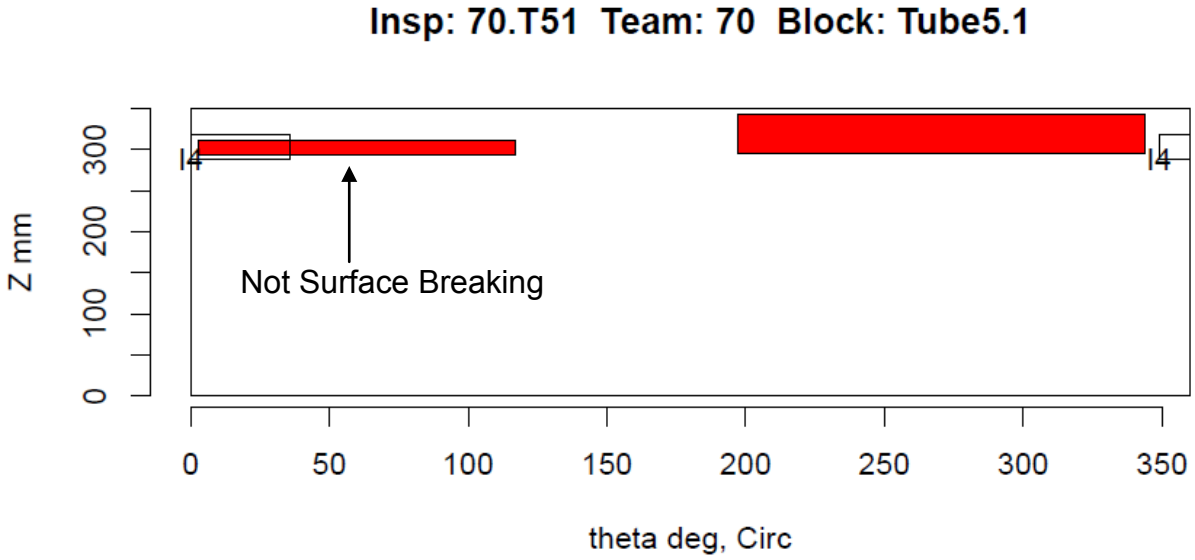
Insp: 70.T51 Team: 70 Block: Tube5.1
Z mm
0
100
200
300
I4
I4
Not Surface Breaking
0
50
100
150
200
250
300
350
theta deg, Circ

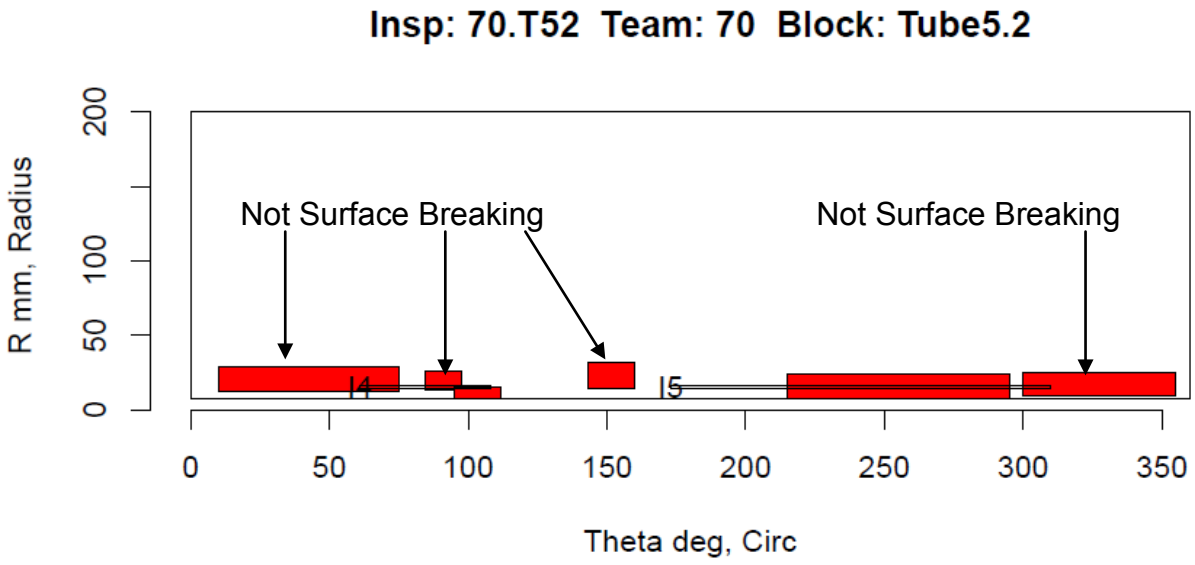
Insp: 70.T52 Team: 70 Block: Tube5.2
R mm, Radius
0
50
100
200
Not Surface Breaking
Not Surface Breaking
I4
I5
0
50
100
150
200
250
300
350
Theta deg, Circ

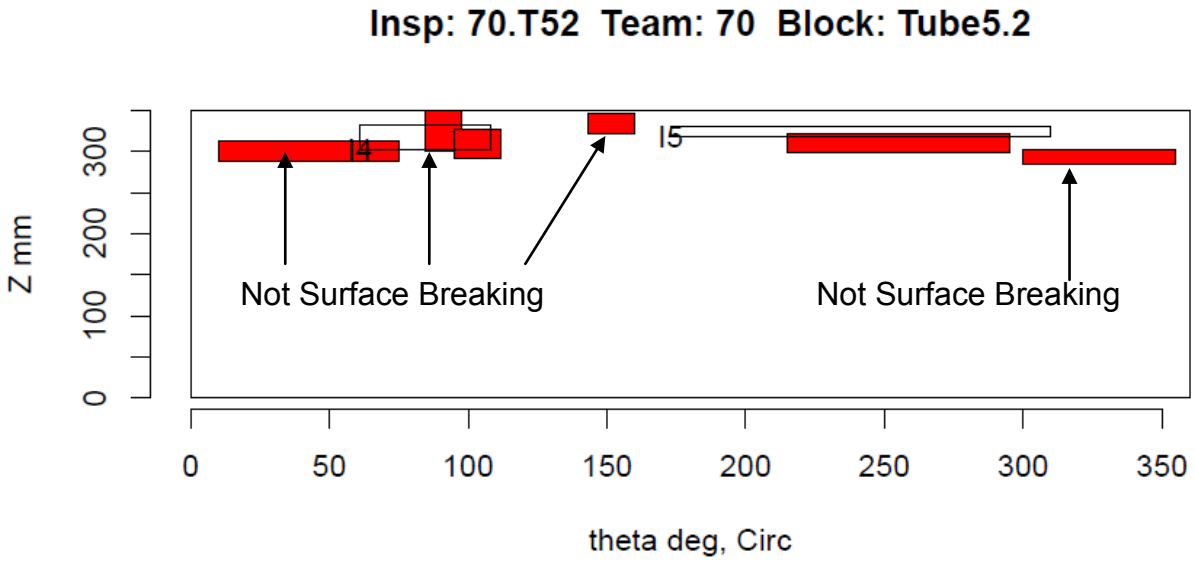
Insp: 70.T52 Team: 70 Block: Tube5.2
Z mm
0
100
200
300
I4
I5
Not Surface Breaking
Not Surface Breaking
0
50
100
150
200
250
300
350
theta deg, Circ

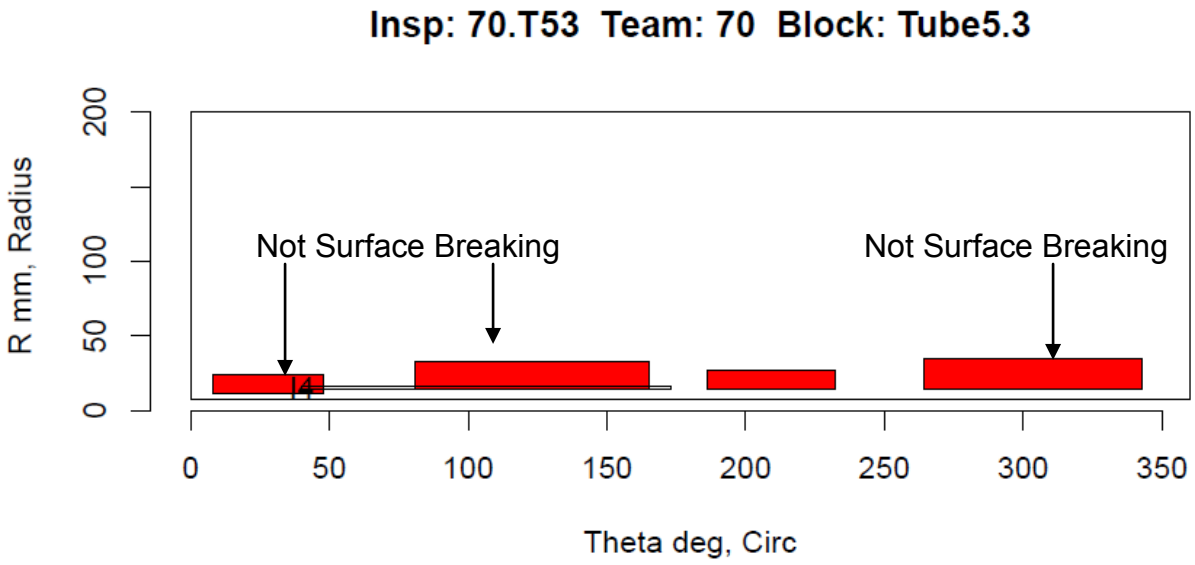
Insp: 70.T53 Team: 70 Block: Tube5.3
R mm, Radius
0
50
100
200
Not Surface Breaking
Not Surface Breaking
0
50
100
150
200
250
300
350
Theta deg, Circ

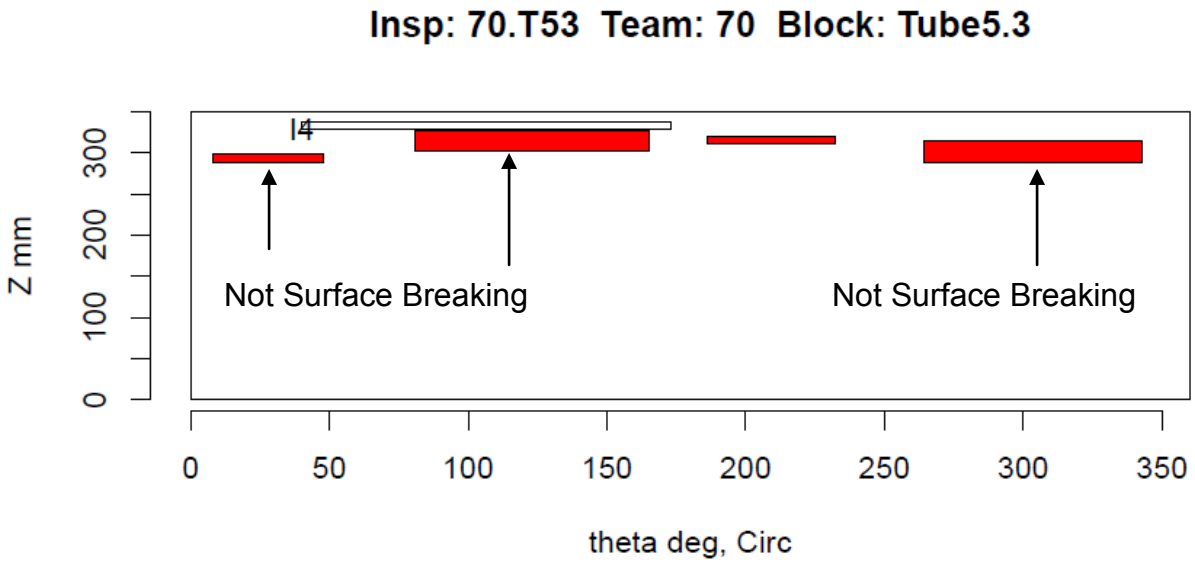
Insp: 70.T53 Team: 70 Block: Tube5.3
Z mm
0
100
200
300
Not Surface Breaking
Not Surface Breaking
0
50
100
150
200
250
300
350
theta deg, Circ

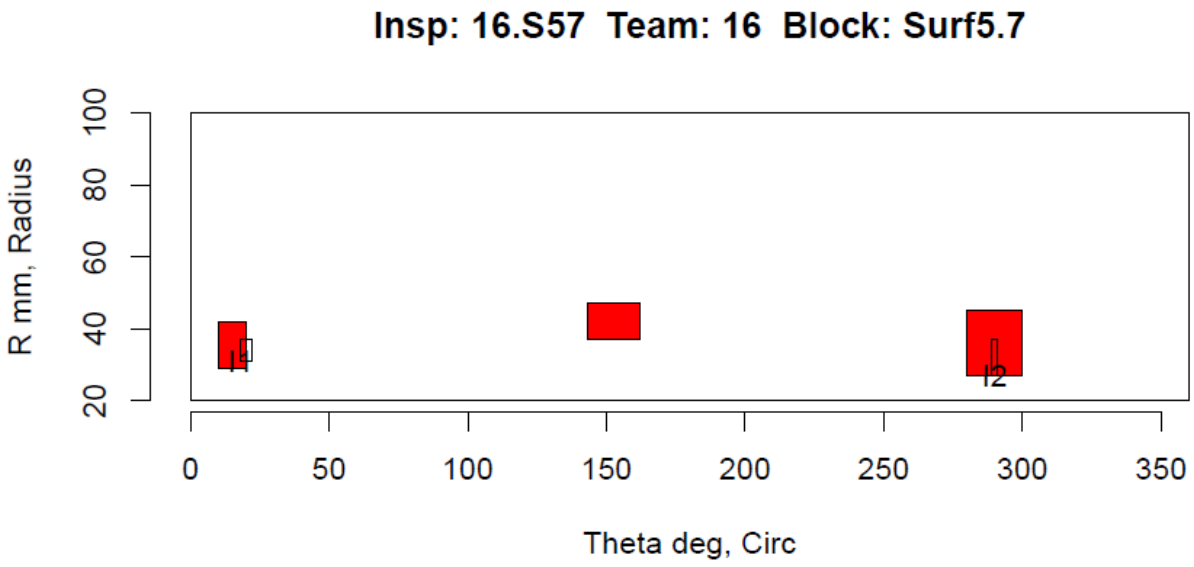
Insp: 16.S57 Team: 16 Block: Surf5.7
R mm, Radius
20
40
60
80
100
0
50
100
150
200
250
300
350
Theta deg, Circ
I1
I2

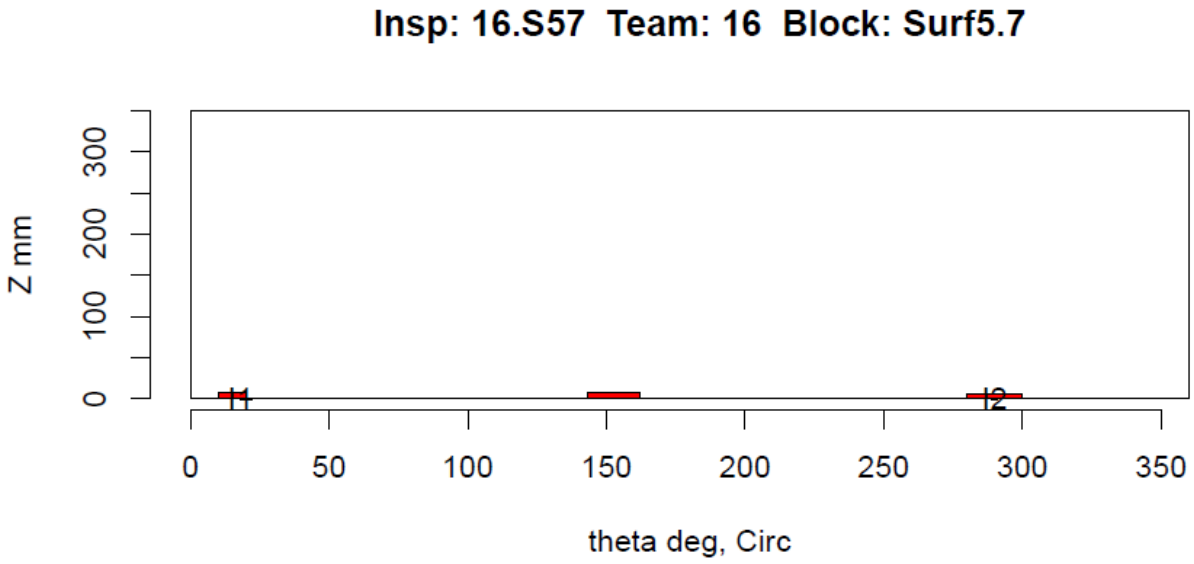
Insp: 16.S57 Team: 16 Block: Surf5.7
Z mm
0
100
200
300
0
50
100
150
200
250
300
350
theta deg, Circ
I1
I2

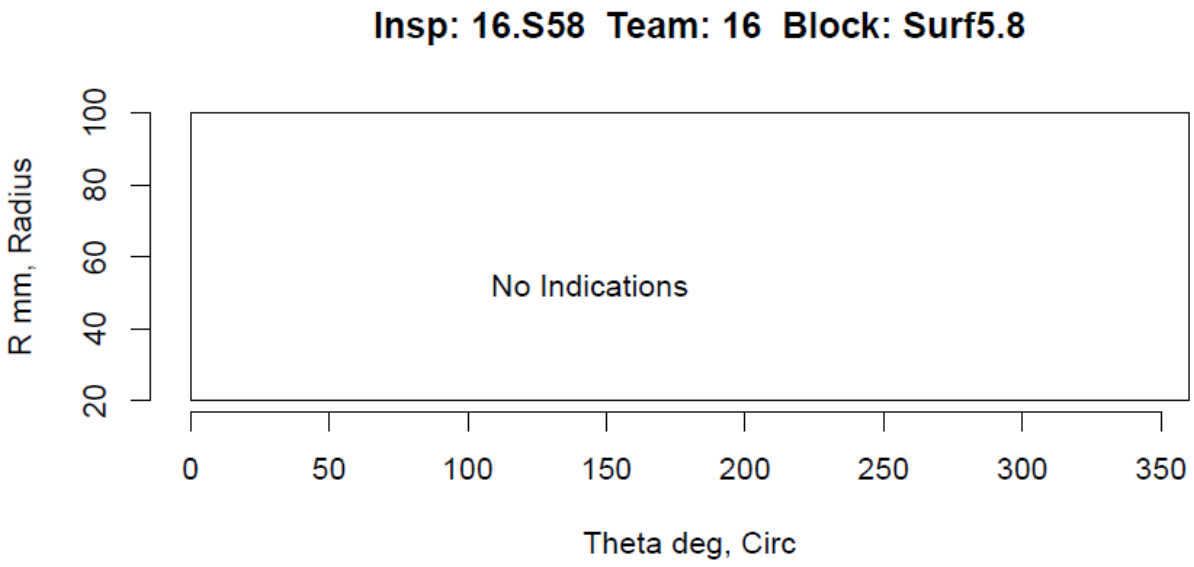
Insp: 16.S58 Team: 16 Block: Surf5.8
R mm, Radius
20
40
60
80
100
No Indications
0
50
100
150
200
250
300
350
Theta deg, Circ

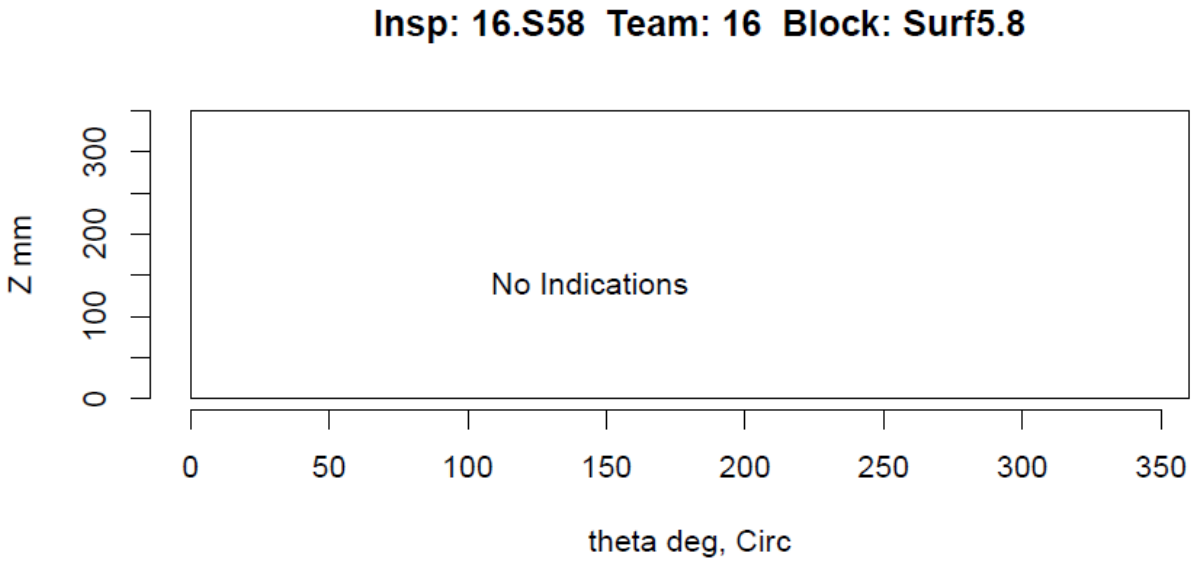
Insp: 16.S58 Team: 16 Block: Surf5.8
Z mm
0
100
200
300
No Indications
0
50
100
150
200
250
300
350
theta deg, Circ

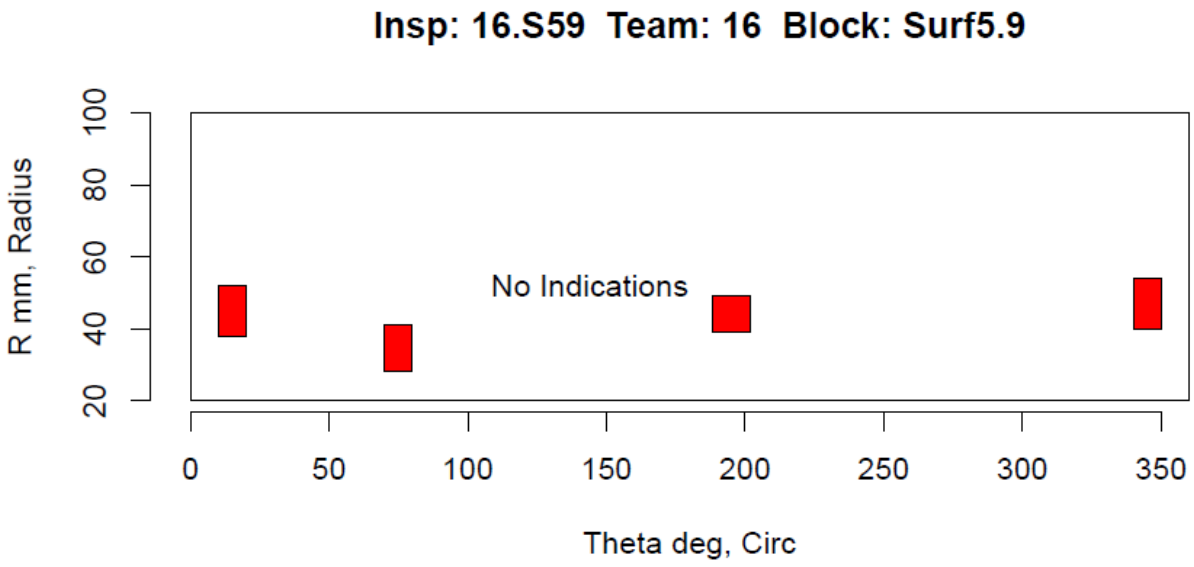
Insp: 16.S59 Team: 16 Block: Surf5.9
R mm, Radius
20
40
60
80
100
No Indications
0
50
100
150
200
250
300
350
Theta deg, Circ

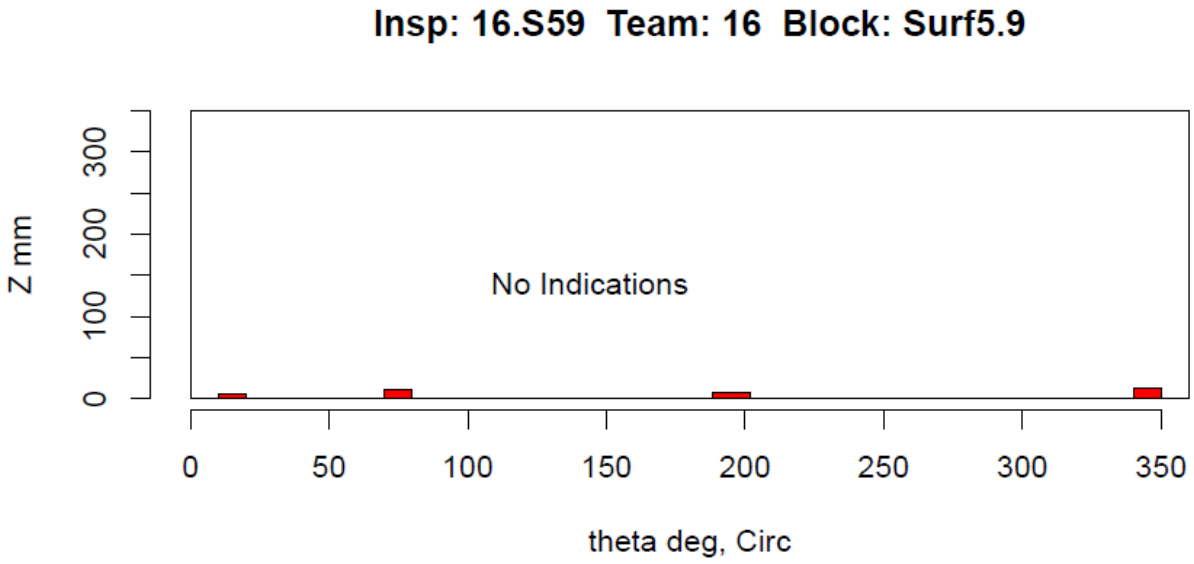
Insp: 16.S59 Team: 16 Block: Surf5.9
Z mm
0
100
200
300
No Indications
0
50
100
150
200
250
300
350
theta deg, Circ

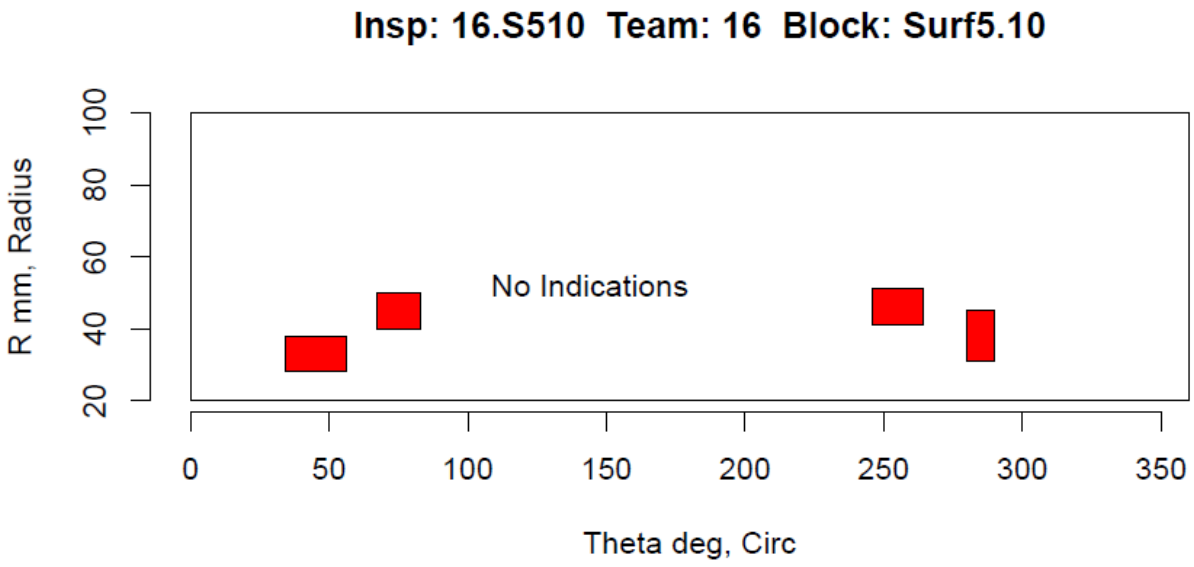
Insp: 16.S510 Team: 16 Block: Surf5.10
R mm, Radius
20
40
60
80
100
No Indications
0
50
100
150
200
250
300
350
Theta deg, Circ

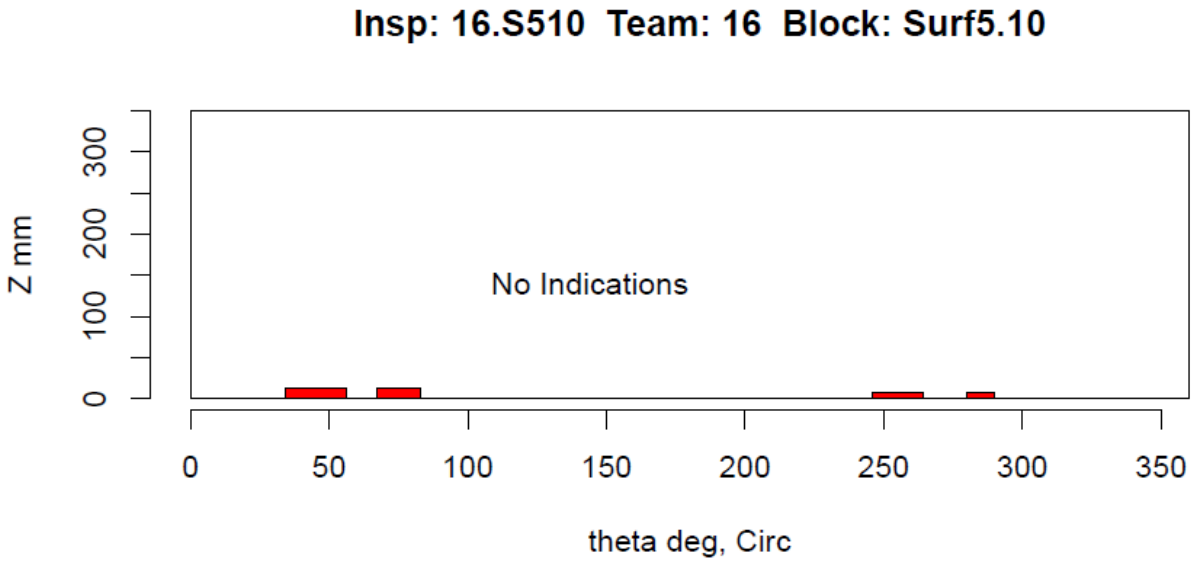
Insp: 16.S510 Team: 16 Block: Surf5.10
Z mm
0
100
200
300
No Indications
0
50
100
150
200
250
300
350
theta deg, Circ

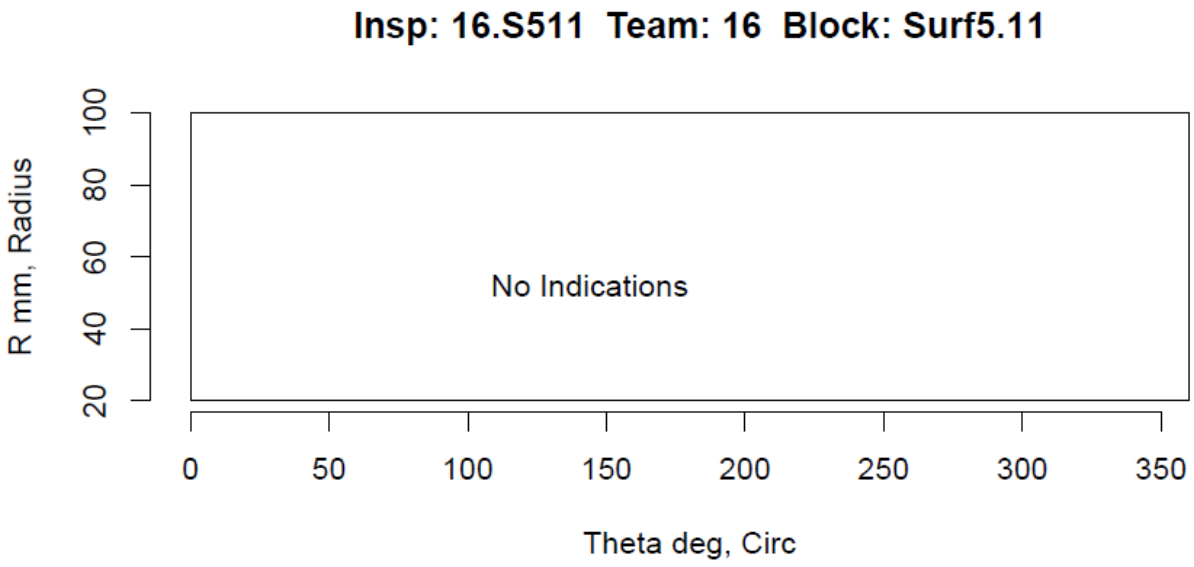
Insp: 16.S511 Team: 16 Block: Surf5.11
R mm, Radius
20
40
60
80
100
No Indications
0
50
100
150
200
250
300
350
Theta deg, Circ

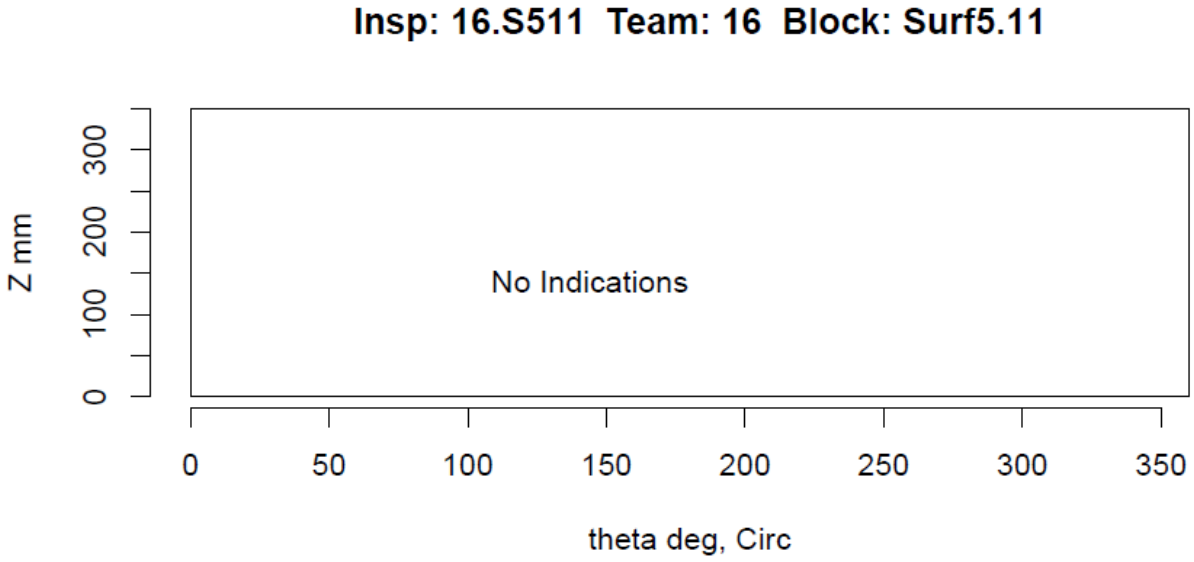
Insp: 16.S511 Team: 16 Block: Surf5.11
Z mm
0
100
200
300
No Indications
0
50
100
150
200
250
300
350
theta deg, Circ

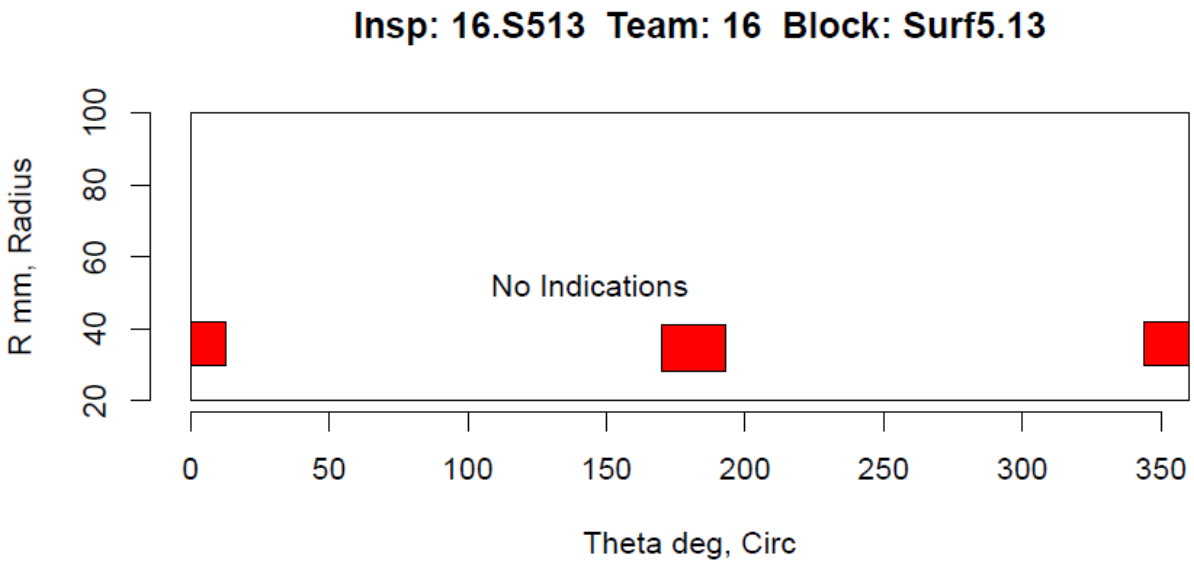
Insp: 16.S513 Team: 16 Block: Surf5.13
R mm, Radius
20
40
60
80
100
No Indications
0
50
100
150
200
250
300
350
Theta deg, Circ

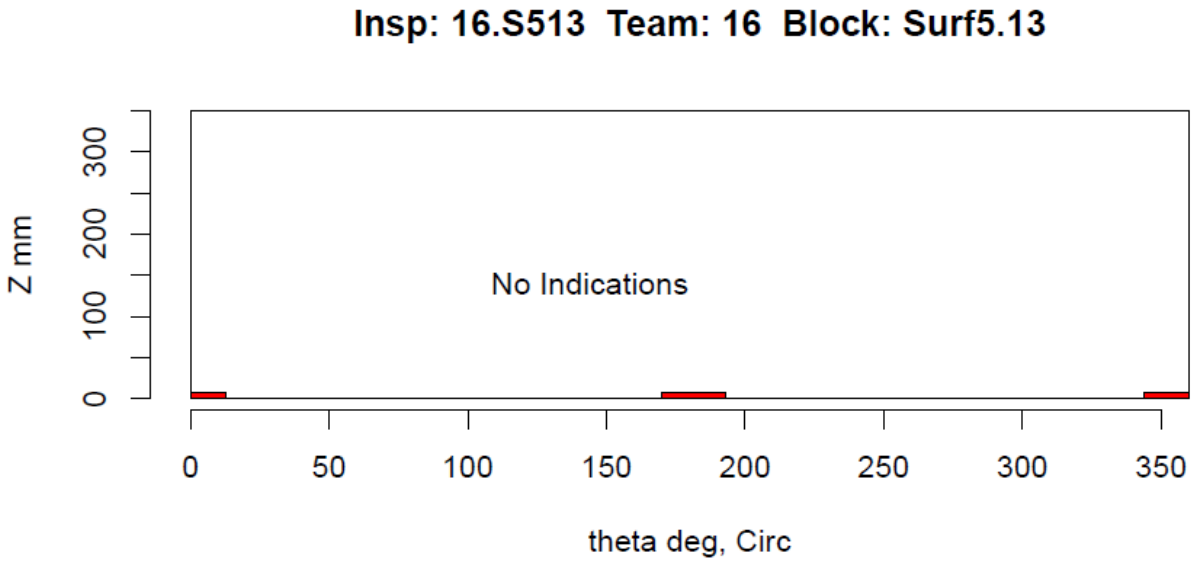
Insp: 16.S513 Team: 16 Block: Surf5.13
Z mm
0
100
200
300
No Indications
0
50
100
150
200
250
300
350
theta deg, Circ

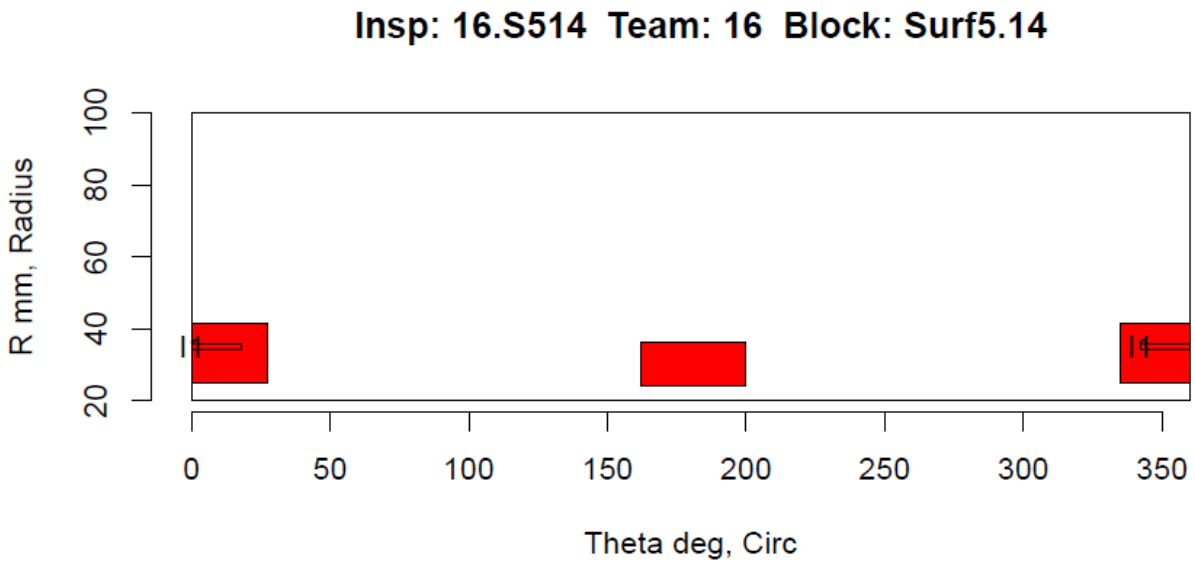
Insp: 16.S514 Team: 16 Block: Surf5.14
R mm, Radius
20
40
60
80
100
0
50
100
150
200
250
300
350
Theta deg, Circ

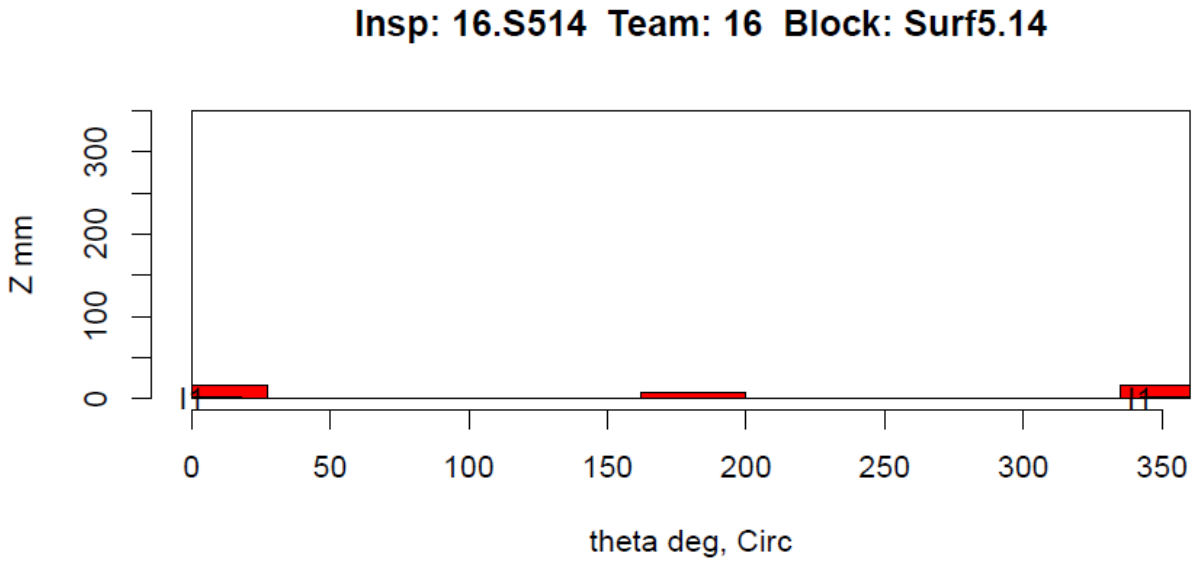
Insp: 16.S514 Team: 16 Block: Surf5.14
Z mm
0
100
200
300
0
50
100
150
200
250
300
350
theta deg, Circ

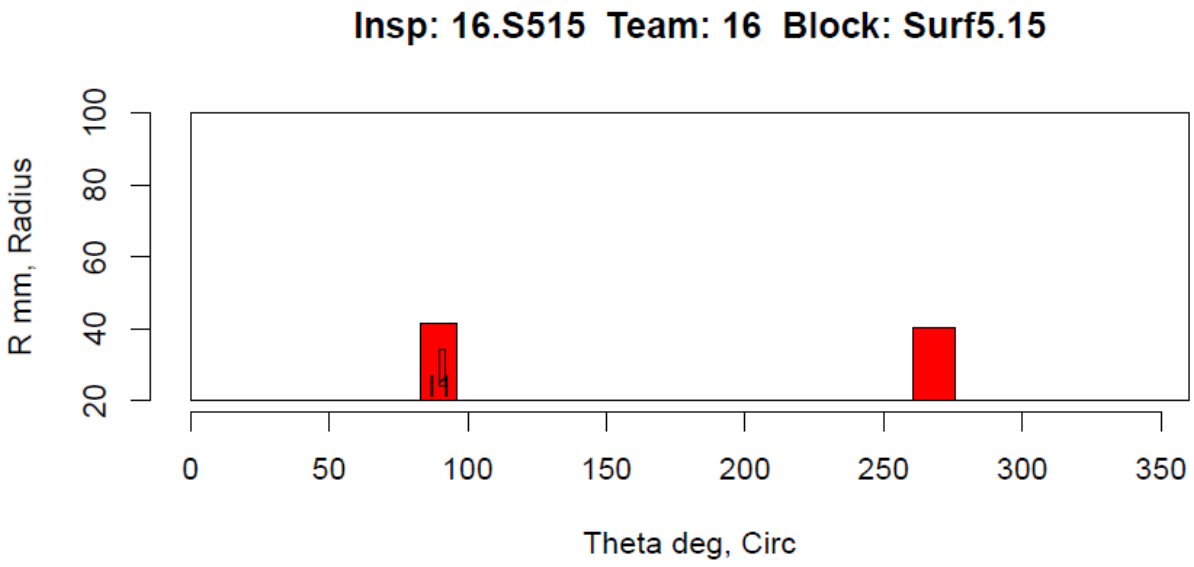
Insp: 16.S515 Team: 16 Block: Surf5.15
R mm, Radius
20
40
60
80
100
0
50
100
150
200
250
300
350
Theta deg, Circ

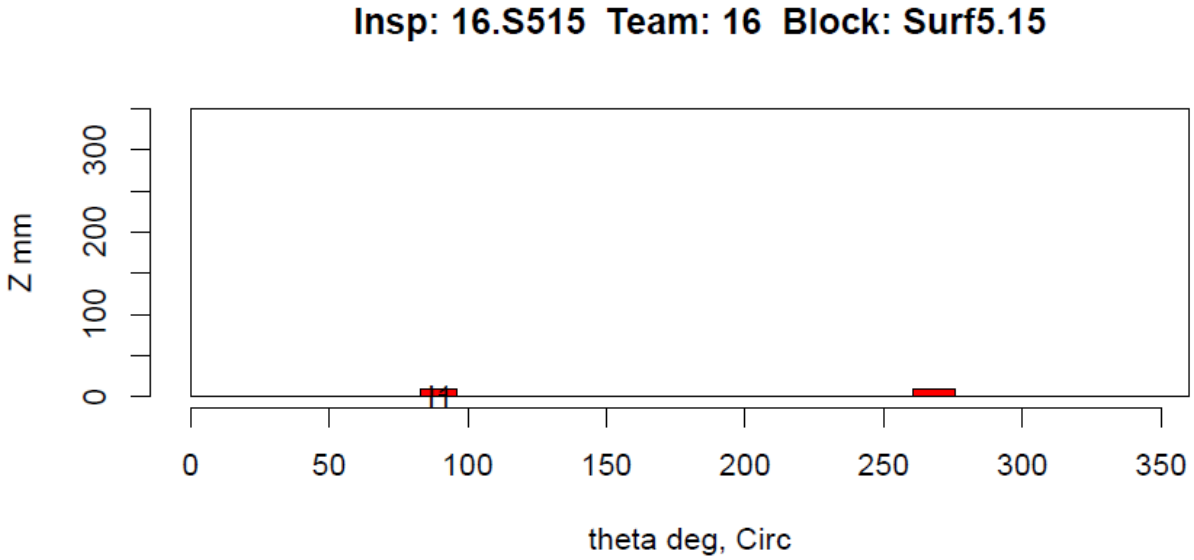
Insp: 16.S515 Team: 16 Block: Surf5.15
Z mm
0
100
200
300
0
50
100
150
200
250
300
350
theta deg, Circ

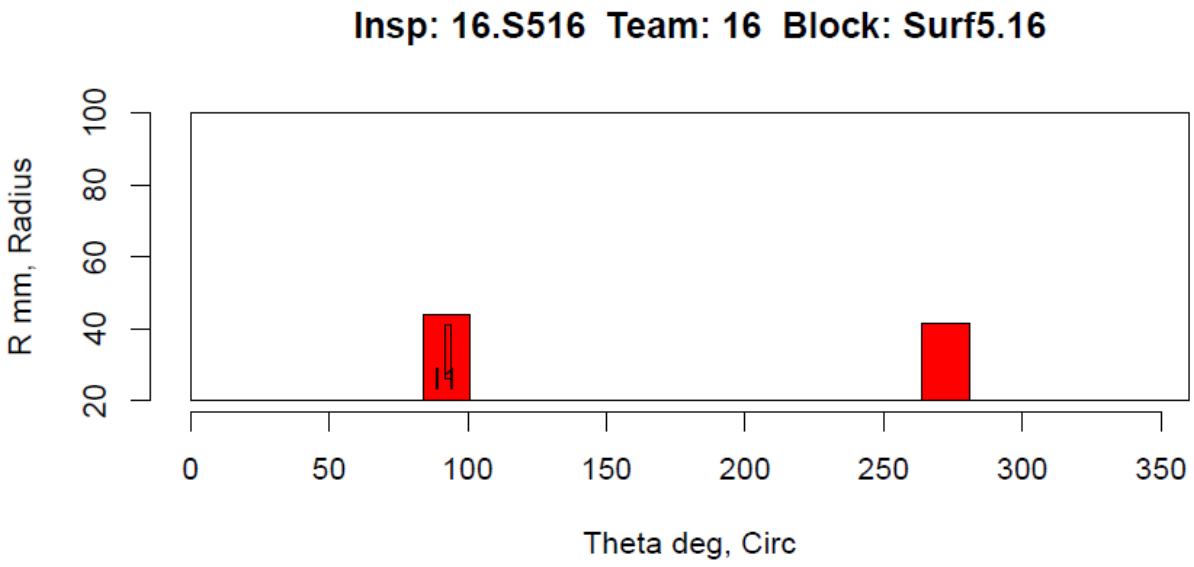
Insp: 16.S516 Team: 16 Block: Surf5.16
R mm, Radius
20
40
60
80
100
0
50
100
150
200
250
300
350
Theta deg, Circ

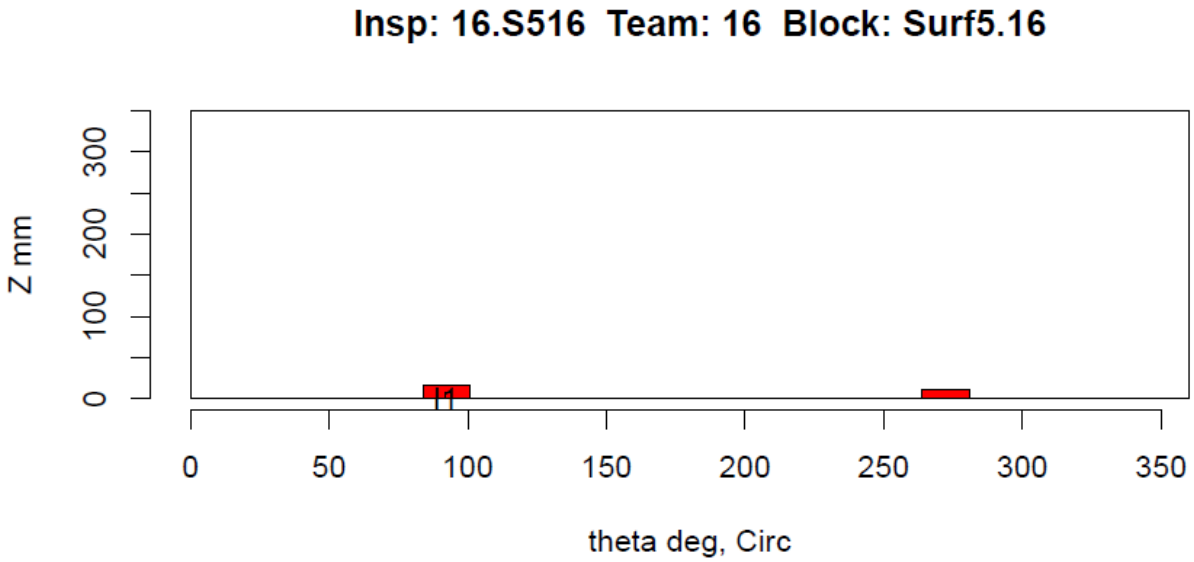
Insp: 16.S516 Team: 16 Block: Surf5.16
Z mm
0
100
200
300
0
50
100
150
200
250
300
350
theta deg, Circ

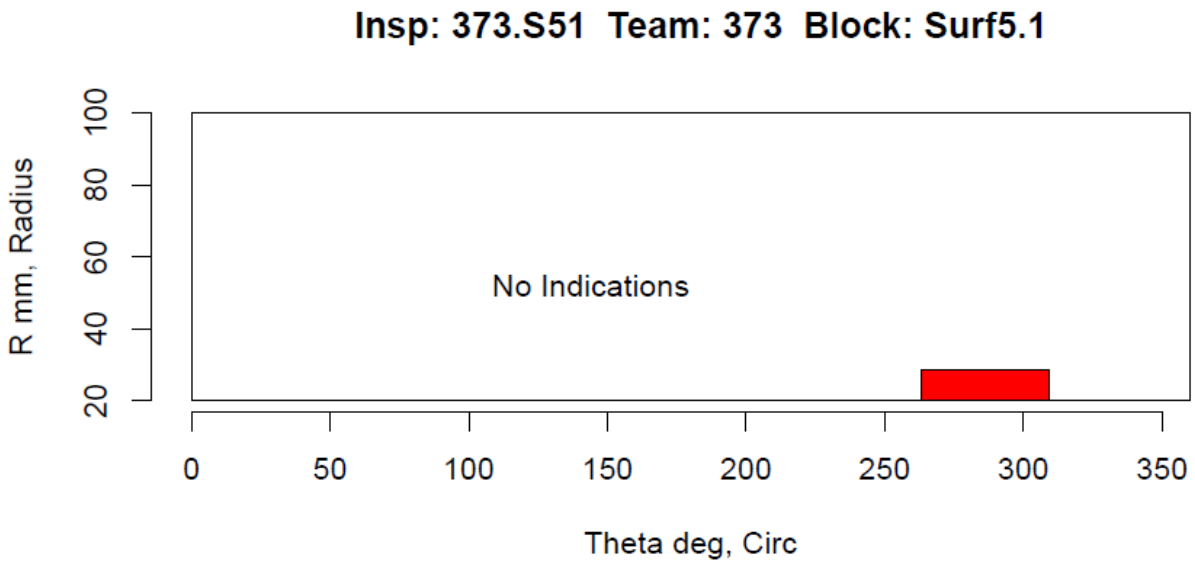
Insp: 373.S51 Team: 373 Block: Surf5.1
R mm, Radius
20
40
60
80
100
No Indications
0
50
100
150
200
250
300
350
Theta deg, Circ

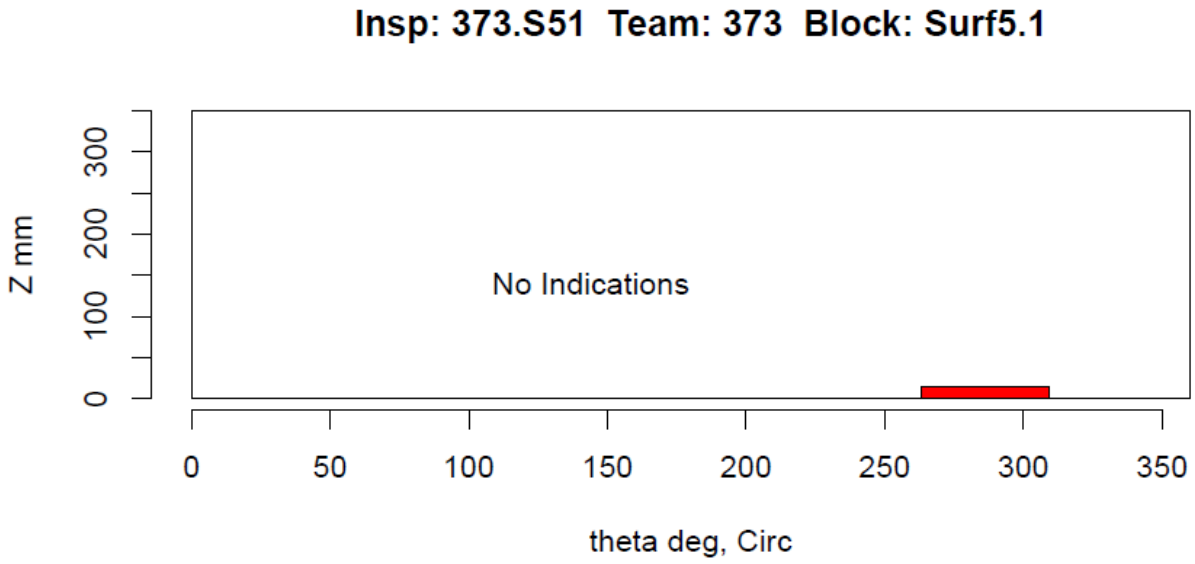
Insp: 373.S51 Team: 373 Block: Surf5.1
Z mm
0
100
200
300
No Indications
0
50
100
150
200
250
300
350
theta deg, Circ

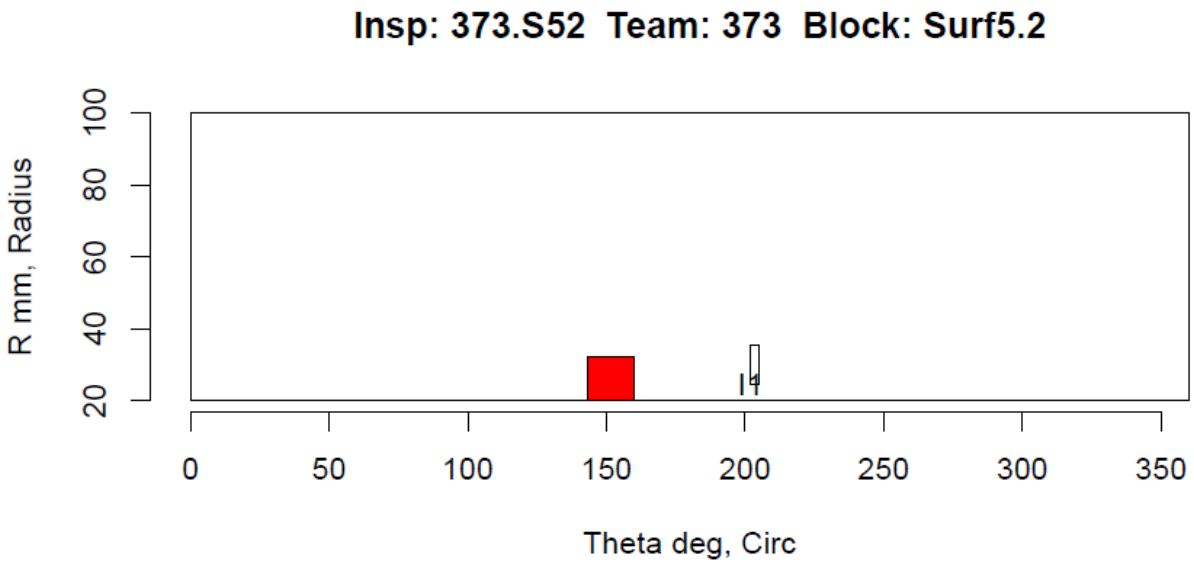
Insp: 373.S52 Team: 373 Block: Surf5.2
R mm, Radius
20
40
60
80
100
0
50
100
150
200
250
300
350
Theta deg, Circ

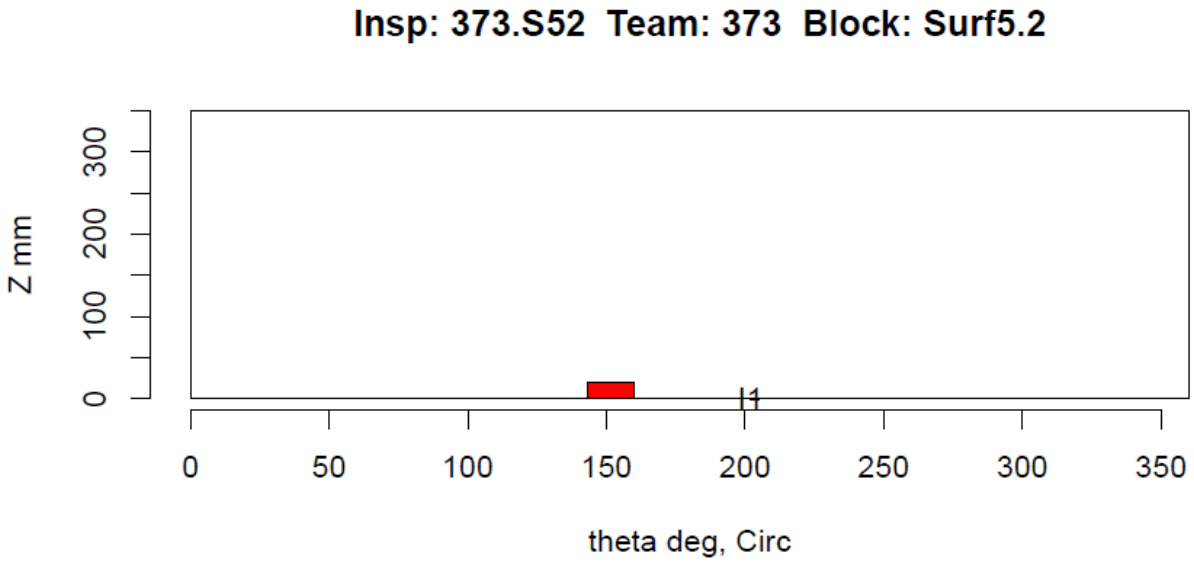
Insp: 373.S52 Team: 373 Block: Surf5.2
Z mm
0
100
200
300
0
50
100
150
200
250
300
350
theta deg, Circ

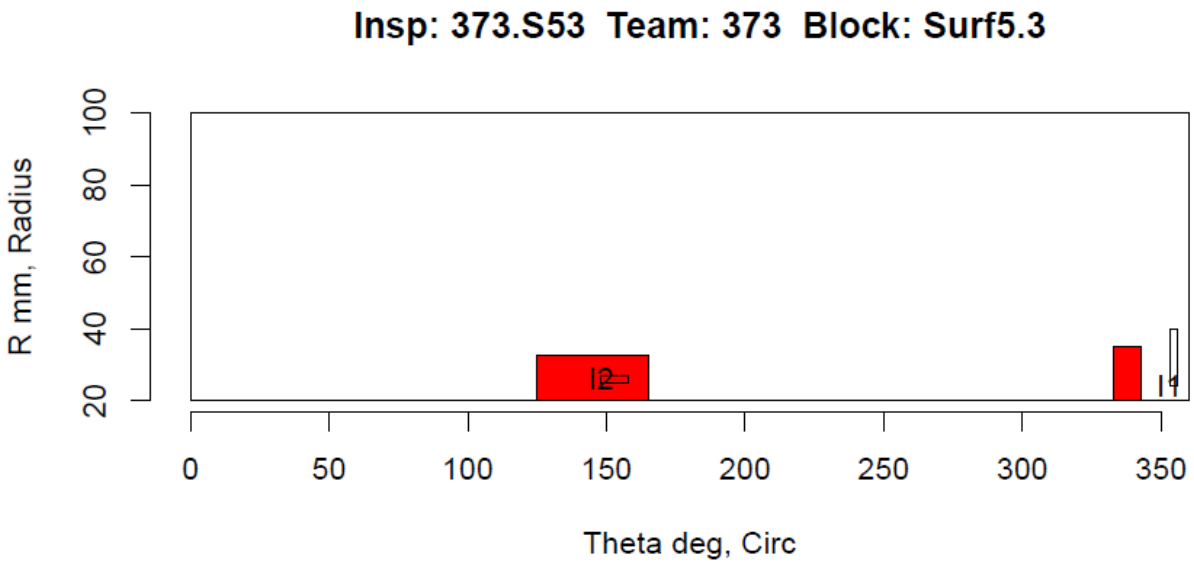
Insp: 373.S53 Team: 373 Block: Surf5.3
R mm, Radius
20
40
60
80
100
0
50
100
150
200
250
300
350
Theta deg, Circ

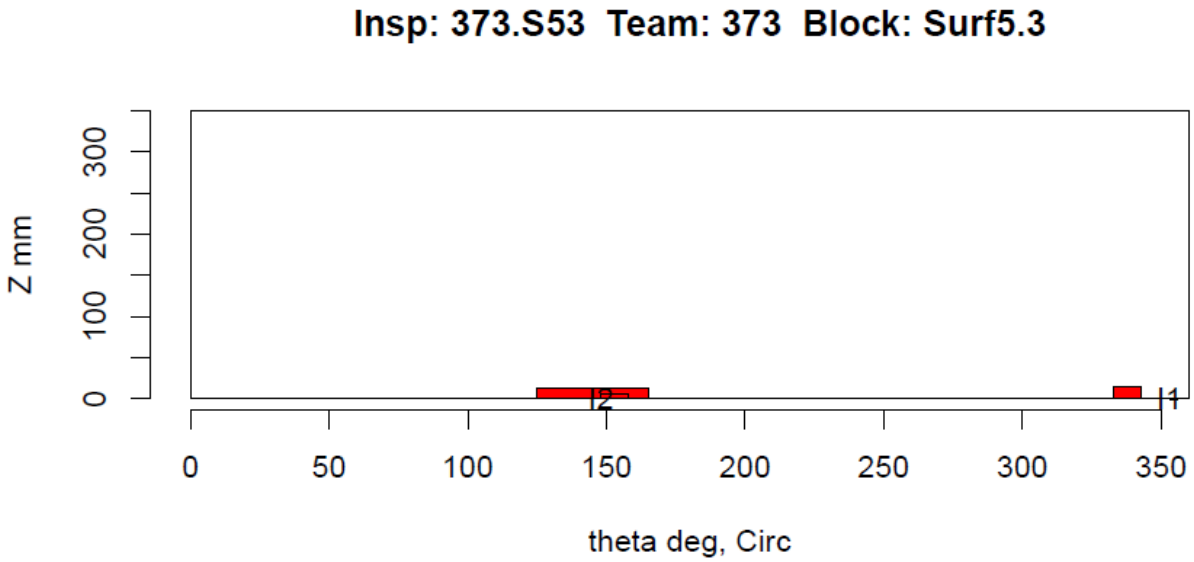
Insp: 373.S53 Team: 373 Block: Surf5.3
Z mm
0
100
200
300
0
50
100
150
200
250
300
350
theta deg, Circ

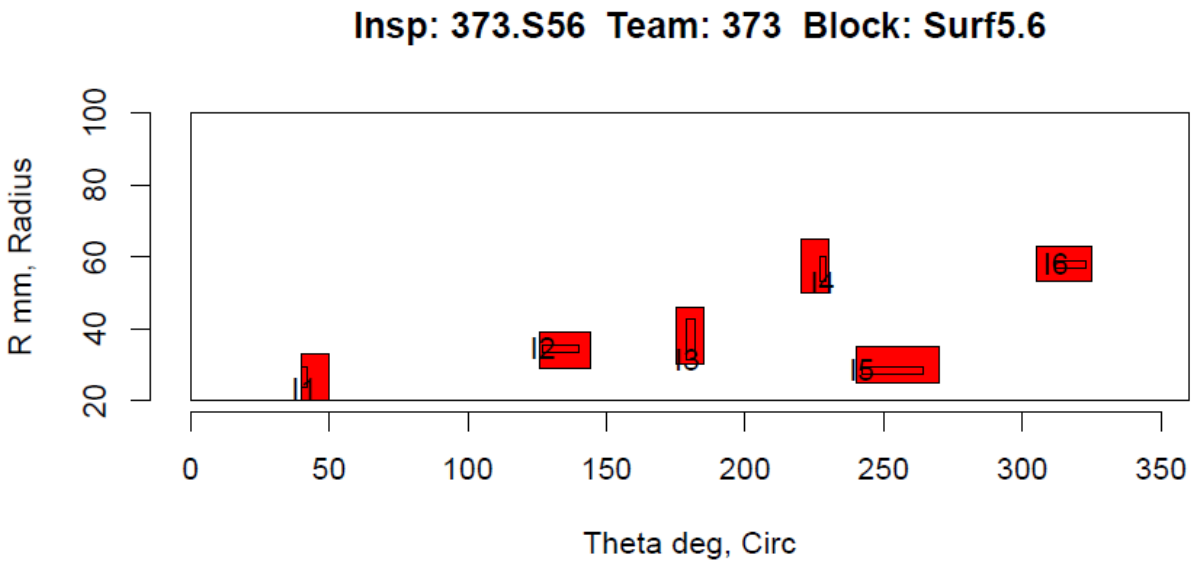
Insp: 373.S56 Team: 373 Block: Surf5.6
R mm, Radius
20
40
60
80
100
0
50
100
150
200
250
300
350
Theta deg, Circ
I1
I2
I3
I4
I5
I6

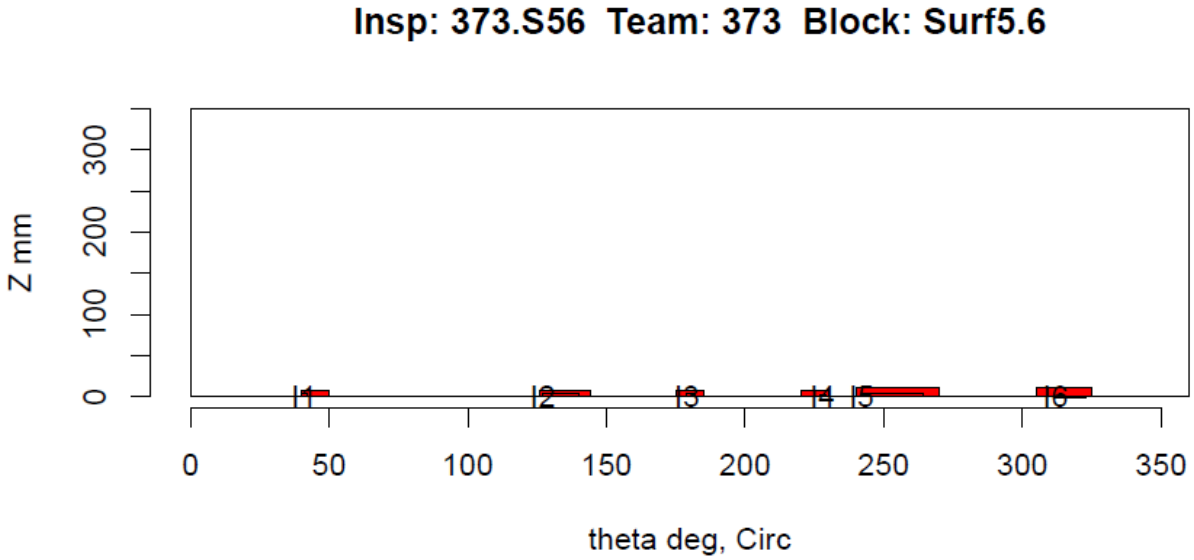
Insp: 373.S56 Team: 373 Block: Surf5.6
Z mm
0
100
200
300
0
50
100
150
200
250
300
350
theta deg, Circ
I1
I2
I3
I4
I5
I6

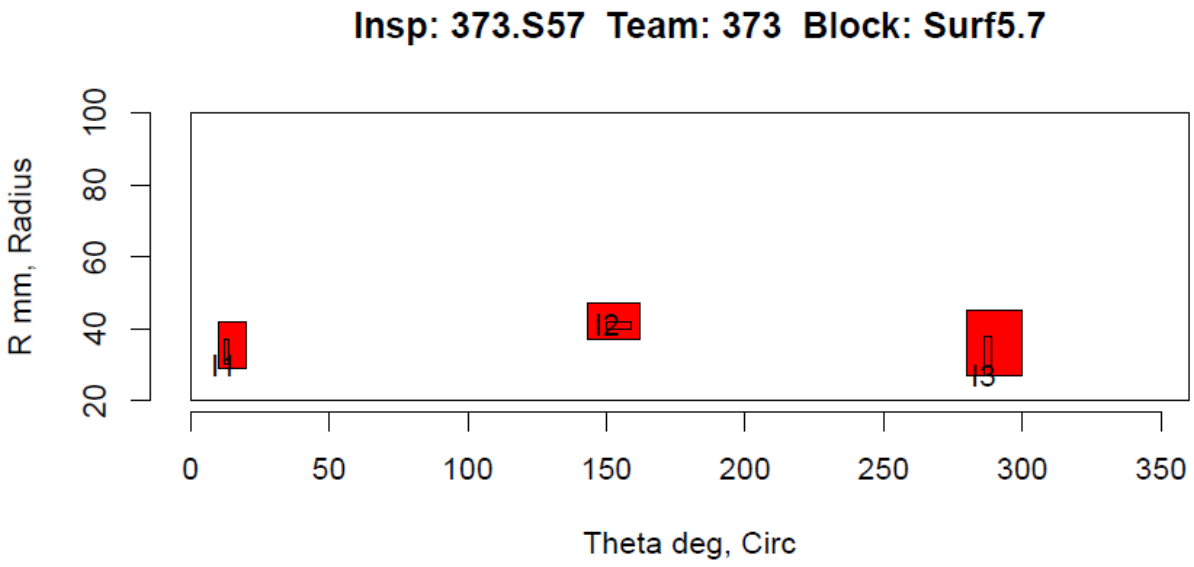
Insp: 373.S57 Team: 373 Block: Surf5.7
R mm, Radius
20
40
60
80
100
0
50
100
150
200
250
300
350
Theta deg, Circ
I1
I2
I3

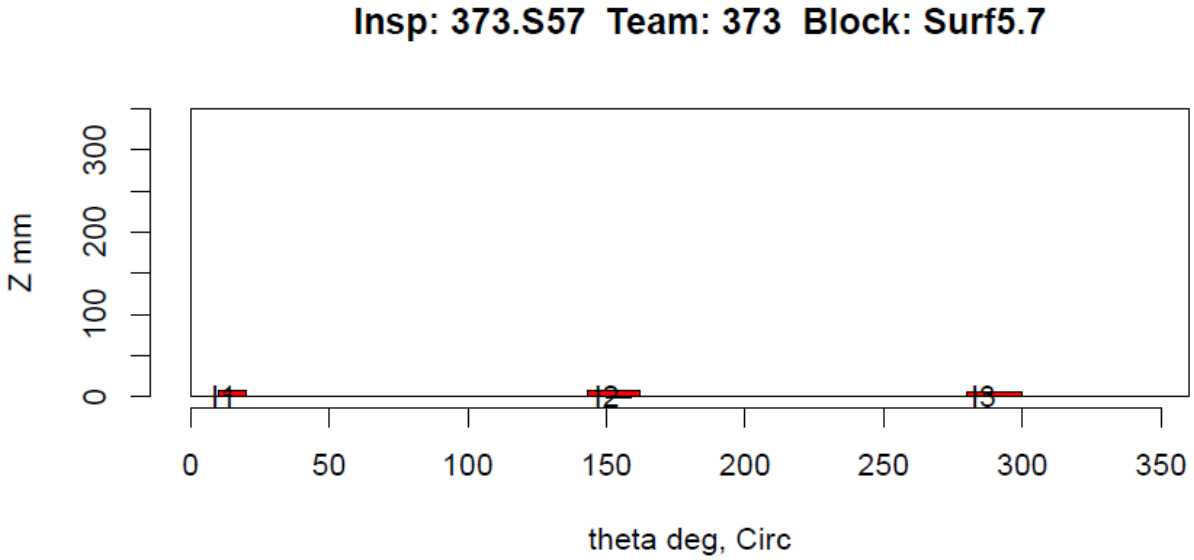
Insp: 373.S57 Team: 373 Block: Surf5.7
Z mm
0
100
200
300
0
50
100
150
200
250
300
350
theta deg, Circ
I1
I2
I3

.

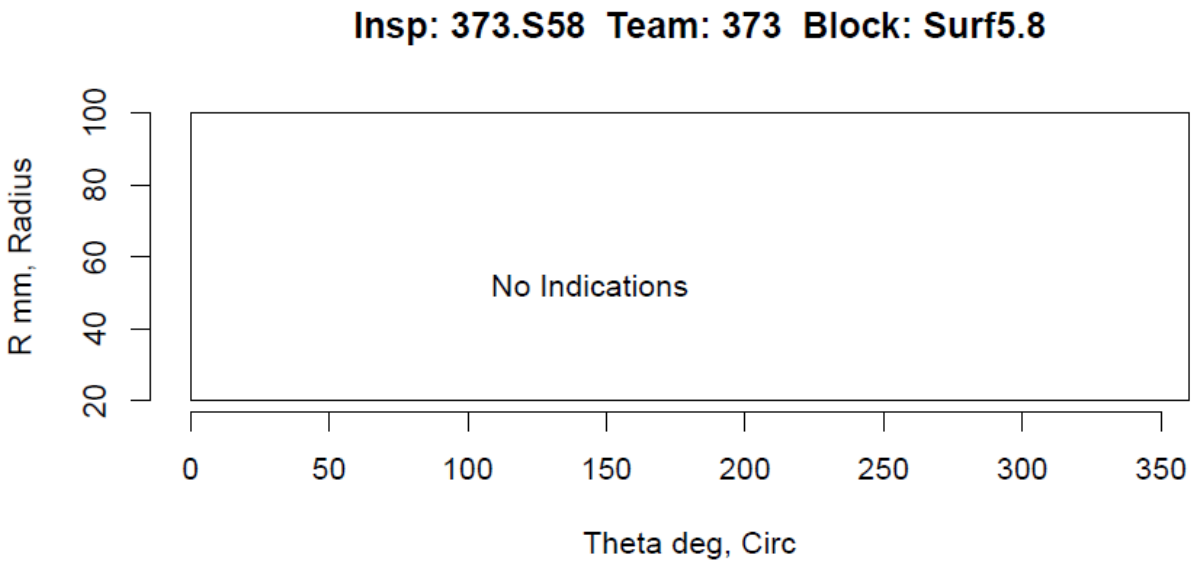
Insp: 373.S58 Team: 373 Block: Surf5.8
R mm, Radius
20
40
60
80
100
No Indications
0
50
100
150
200
250
300
350
Theta deg, Circ

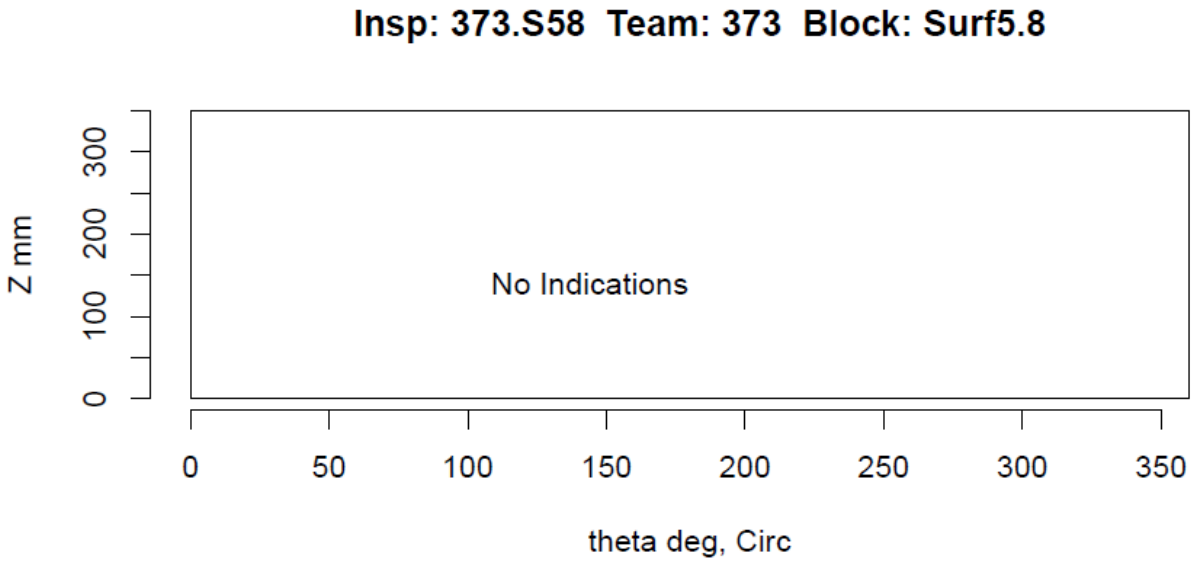
Insp: 373.S58 Team: 373 Block: Surf5.8
Z mm
0
100
200
300
No Indications
0
50
100
150
200
250
300
350
theta deg, Circ

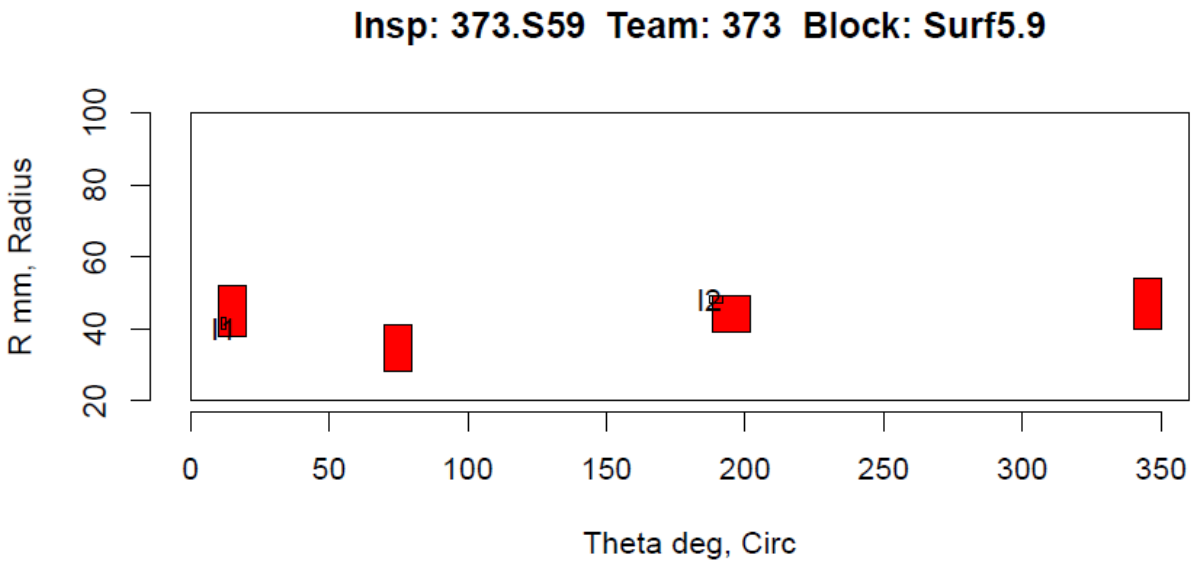
Insp: 373.S59 Team: 373 Block: Surf5.9
R mm, Radius
20
40
60
80
100
0
50
100
150
200
250
300
350
Theta deg, Circ

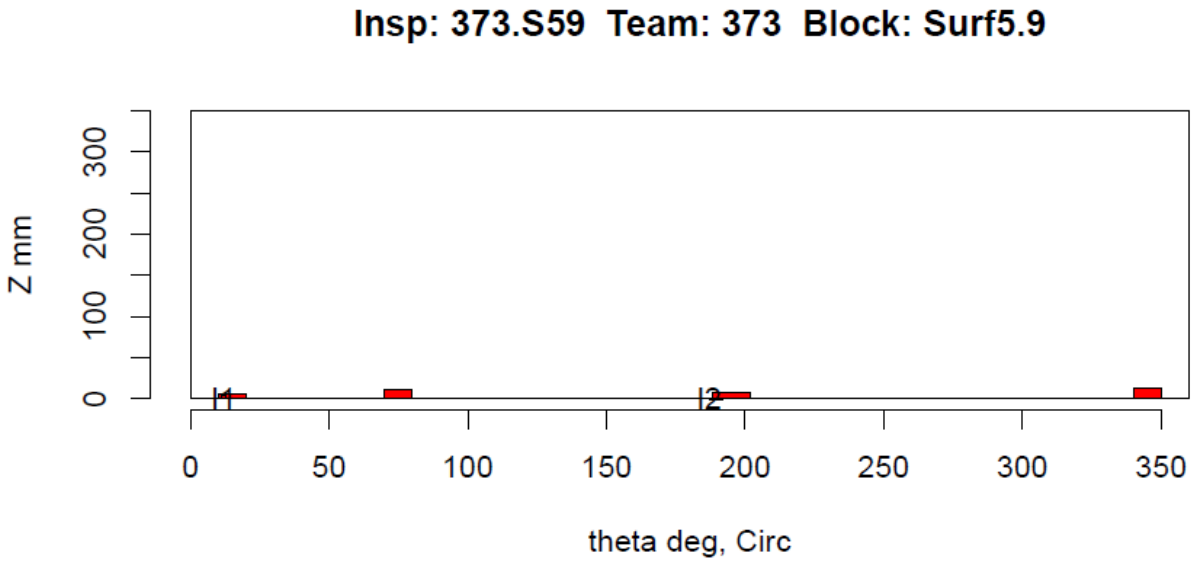
Insp: 373.S59 Team: 373 Block: Surf5.9
Z mm
0
100
200
300
0
50
100
150
200
250
300
350
theta deg, Circ

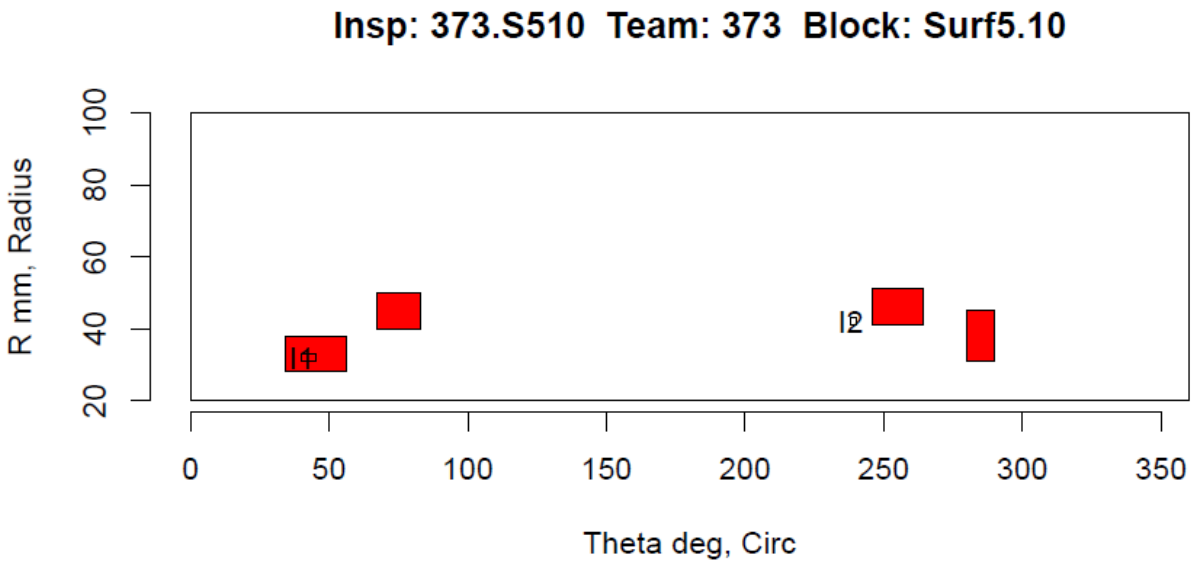
Insp: 373.S510 Team: 373 Block: Surf5.10
R mm, Radius
20
40
60
80
100
0
50
100
150
200
250
300
350
Theta deg, Circ

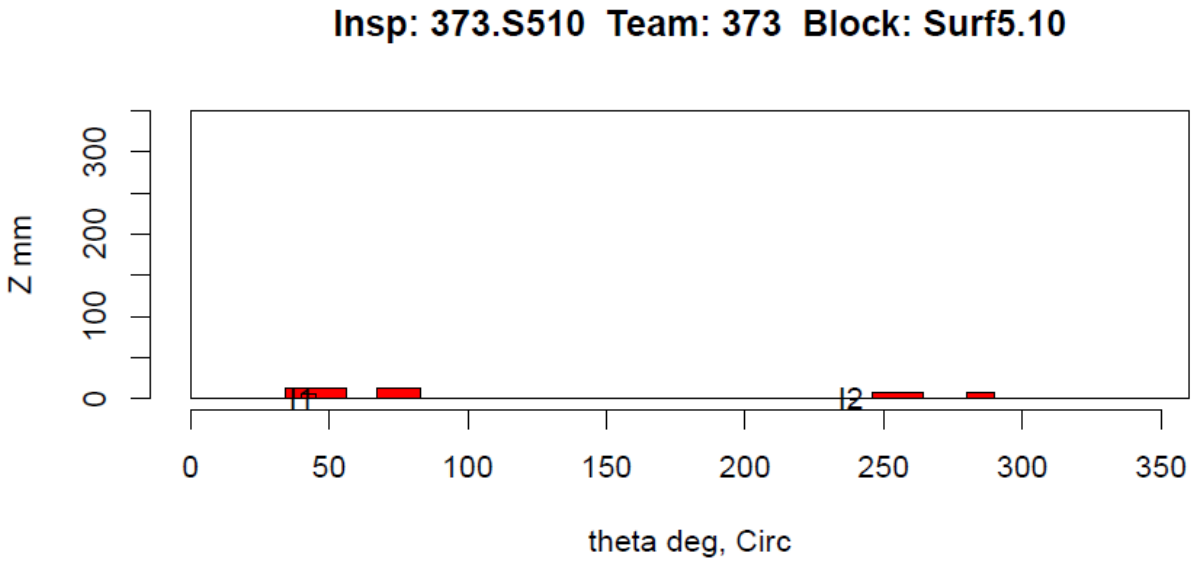
Insp: 373.S510 Team: 373 Block: Surf5.10
Z mm
0
100
200
300
0
50
100
150
200
250
300
350
theta deg, Circ

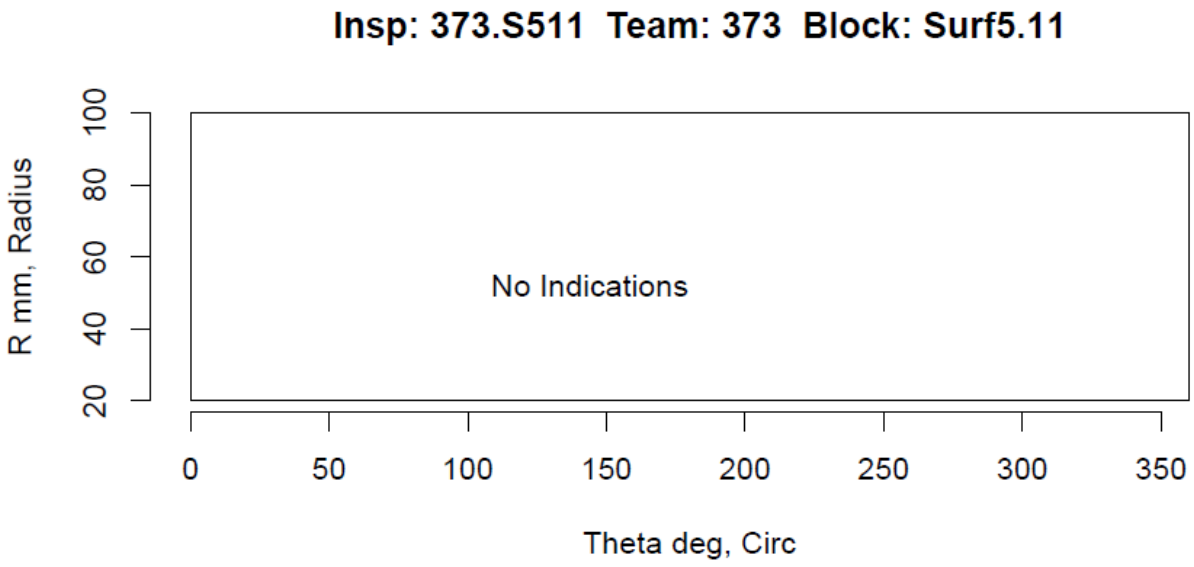
Insp: 373.S511 Team: 373 Block: Surf5.11
R mm, Radius
20
40
60
80
100
No Indications
0
50
100
150
200
250
300
350
Theta deg, Circ

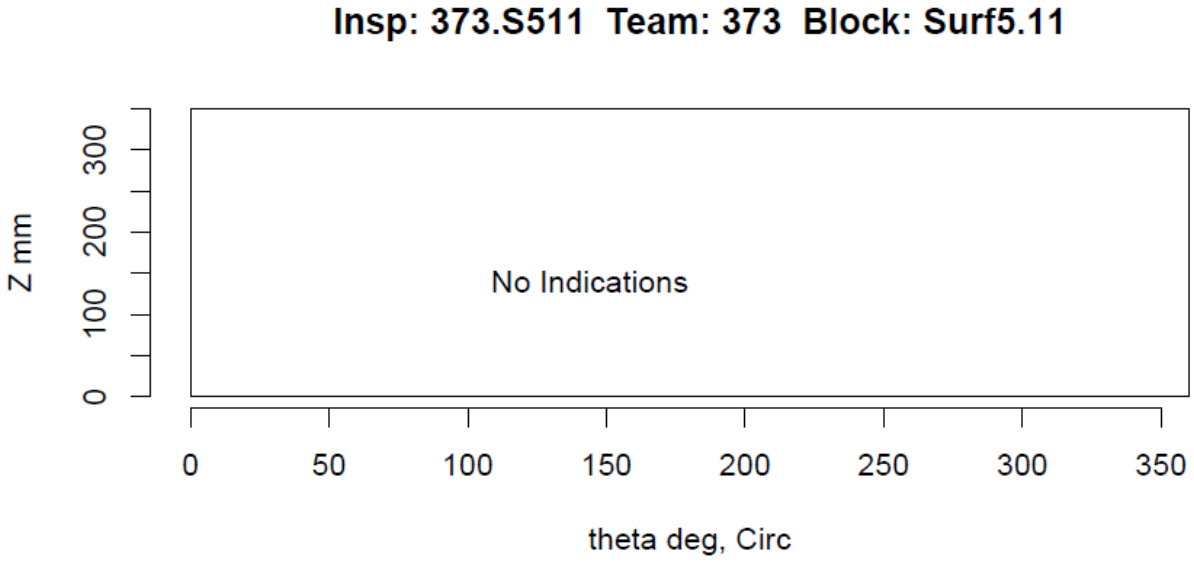
Insp: 373.S511 Team: 373 Block: Surf5.11
Z mm
0
100
200
300
No Indications
0
50
100
150
200
250
300
350
theta deg, Circ

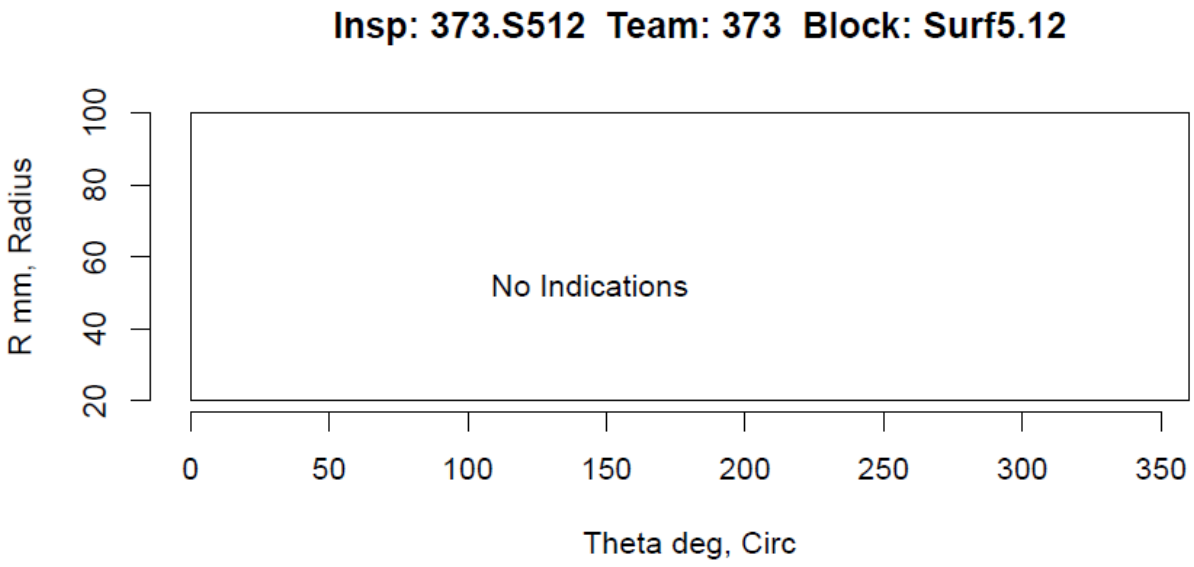
Insp: 373.S512 Team: 373 Block: Surf5.12
R mm, Radius
20
40
60
80
100
No Indications
0
50
100
150
200
250
300
350
Theta deg, Circ

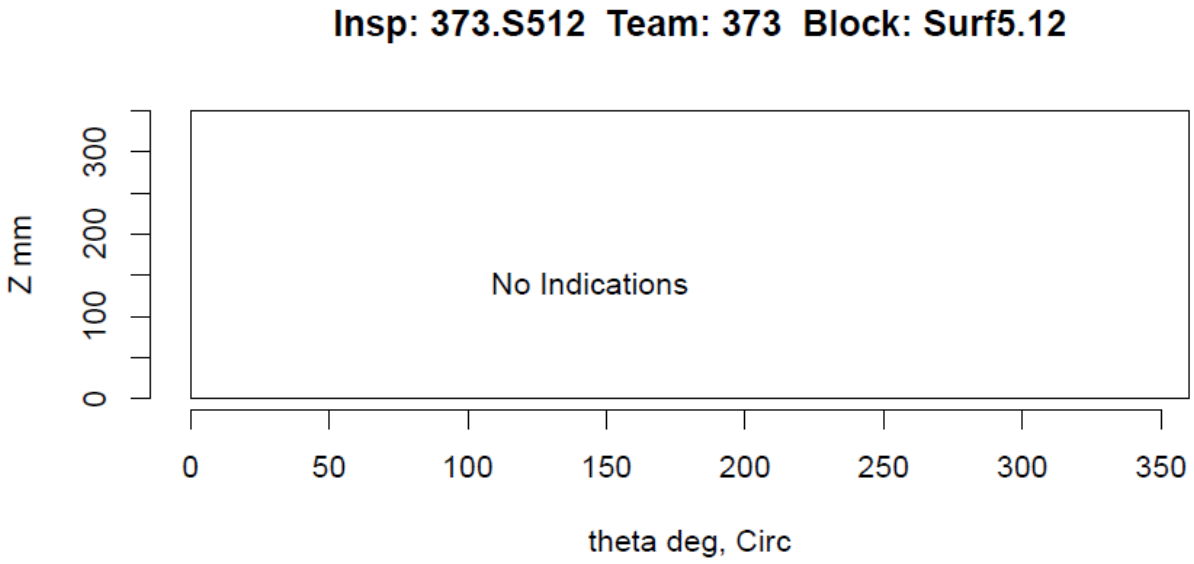
Insp: 373.S512 Team: 373 Block: Surf5.12
Z mm
0
100
200
300
No Indications
0
50
100
150
200
250
300
350
theta deg, Circ

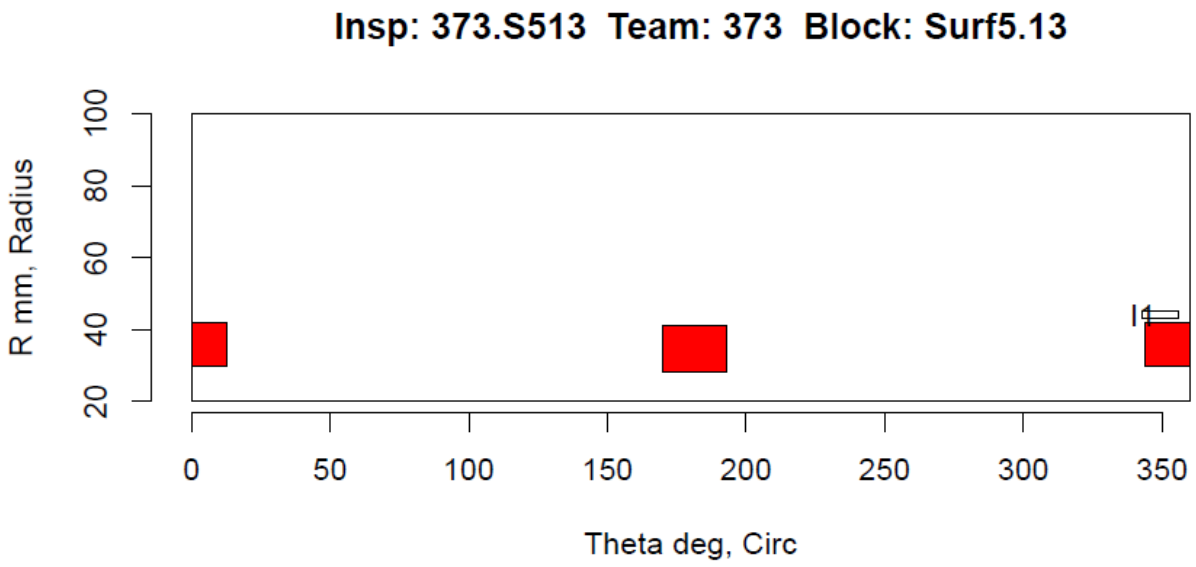
Insp: 373.S513 Team: 373 Block: Surf5.13
R mm, Radius
20
40
60
80
100
0
50
100
150
200
250
300
350
Theta deg, Circ

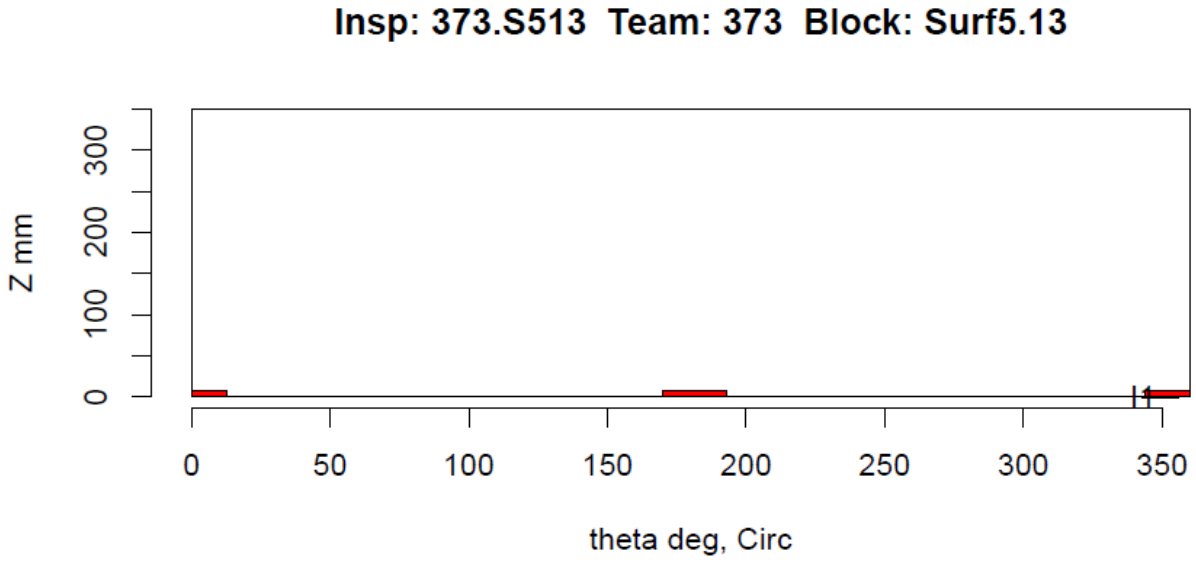
Insp: 373.S513 Team: 373 Block: Surf5.13
Z mm
0
100
200
300
0
50
100
150
200
250
300
350
theta deg, Circ

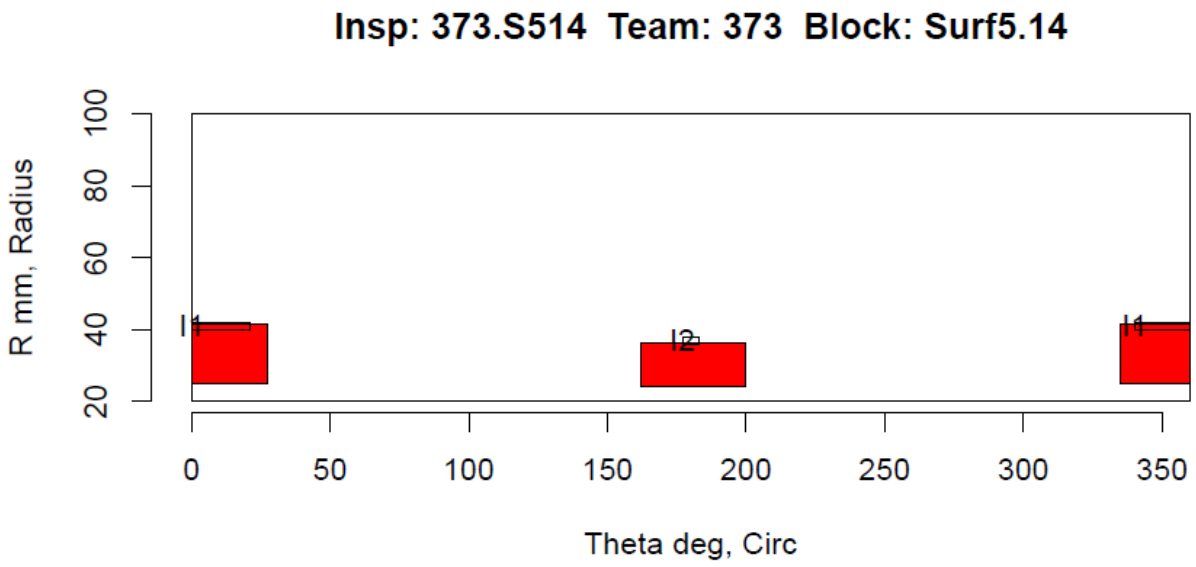
Insp: 373.S514 Team: 373 Block: Surf5.14
R mm, Radius
20
40
60
80
100
0
50
100
150
200
250
300
350
Theta deg, Circ

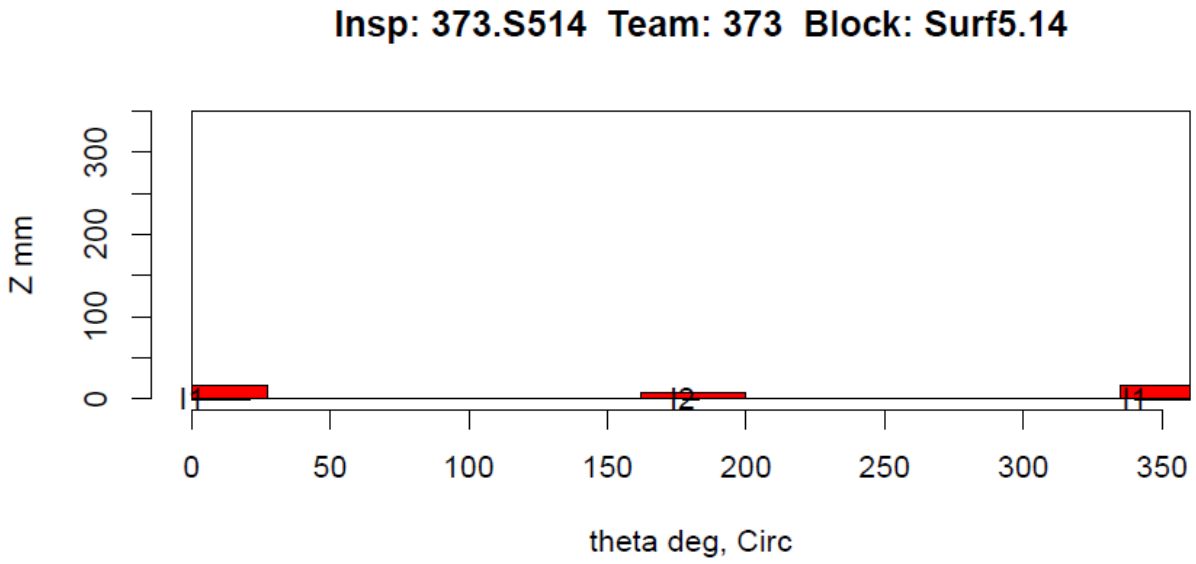
Insp: 373.S514 Team: 373 Block: Surf5.14
Z mm
0
100
200
300
0
50
100
150
200
250
300
350
theta deg, Circ

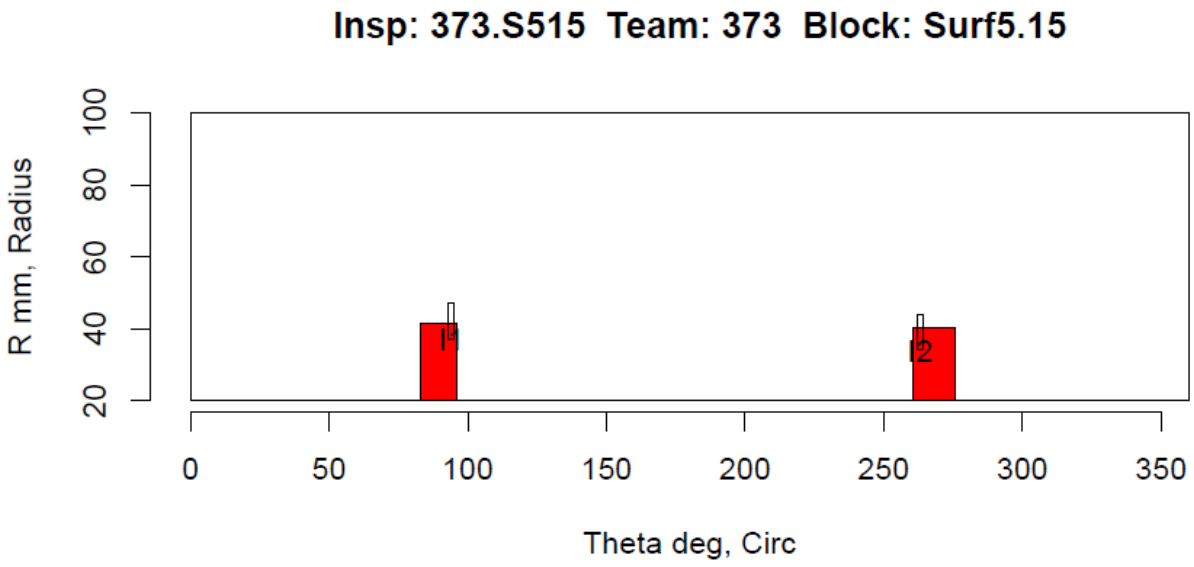
Insp: 373.S515 Team: 373 Block: Surf5.15
R mm, Radius
20
40
60
80
100
0
50
100
150
200
250
300
350
Theta deg, Circ

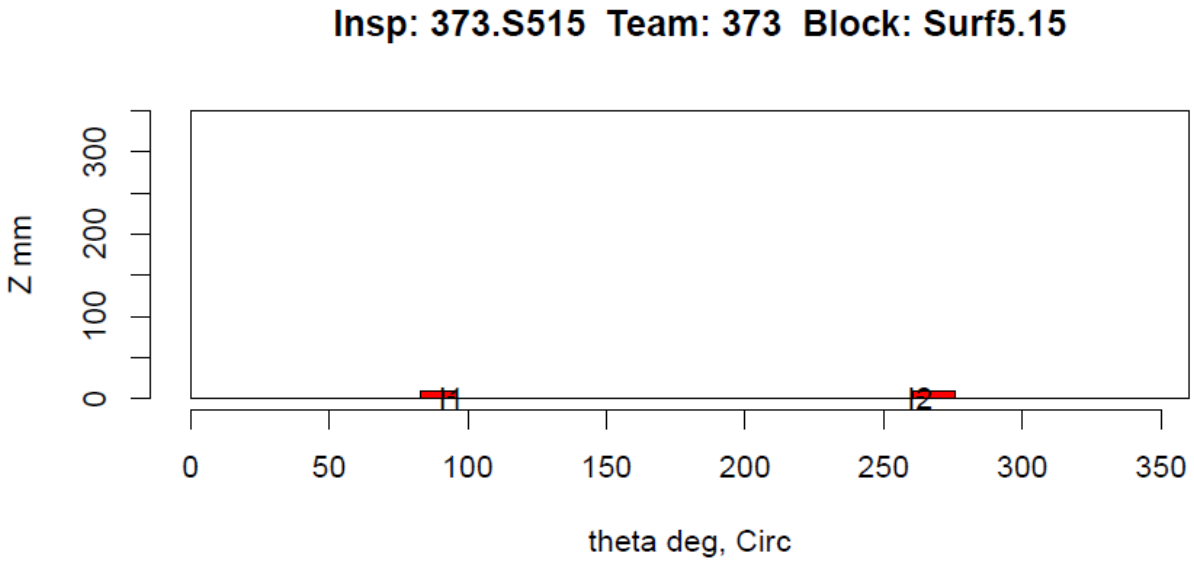
Insp: 373.S515 Team: 373 Block: Surf5.15
Z mm
0
100
200
300
0
50
100
150
200
250
300
350
theta deg, Circ

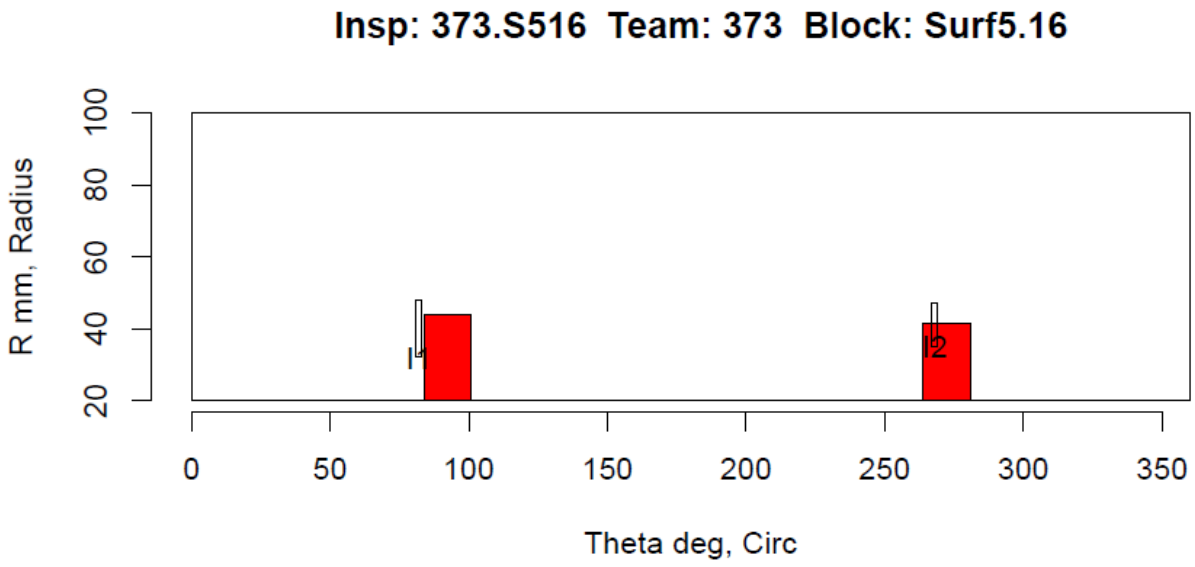
Insp: 373.S516 Team: 373 Block: Surf5.16
R mm, Radius
20
40
60
80
100
0
50
100
150
200
250
300
350
Theta deg, Circ

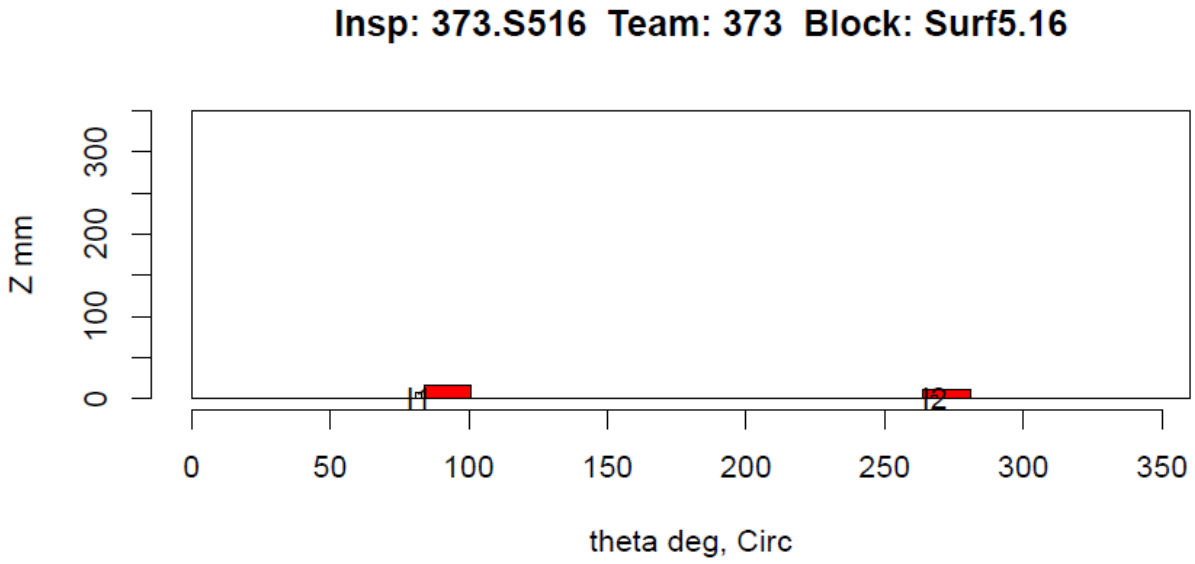
Insp: 373.S516 Team: 373 Block: Surf5.16
Z mm
0
100
200
300
0
50
100
150
200
250
300
350
theta deg, Circ

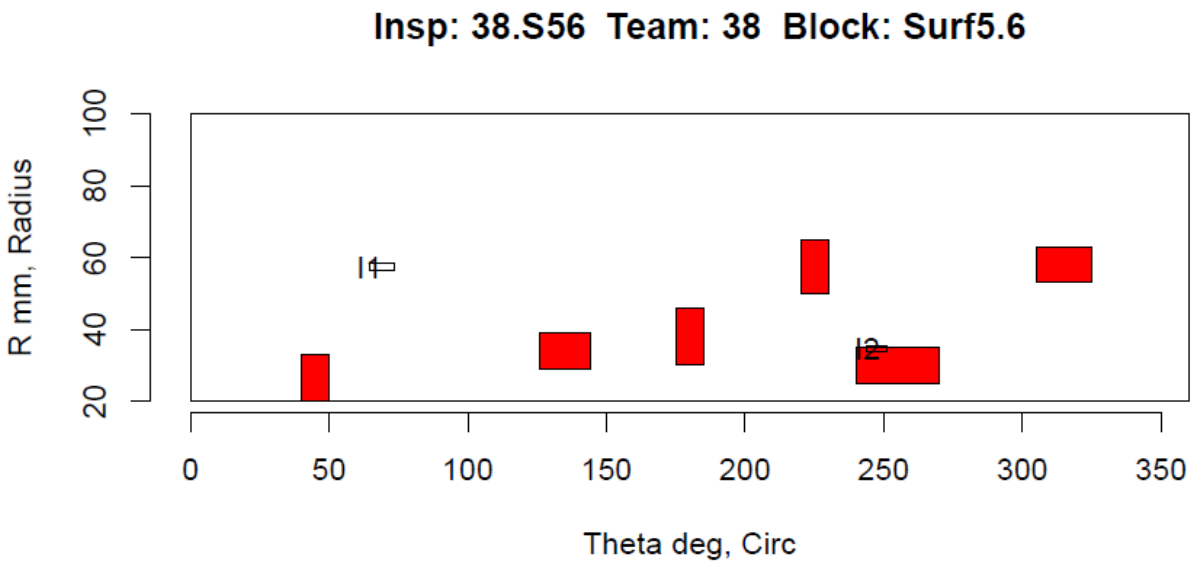
Insp: 38.S56 Team: 38 Block: Surf5.6
R mm, Radius
20
40
60
80
100
I1
I2
0
50
100
150
200
250
300
350
Theta deg, Circ

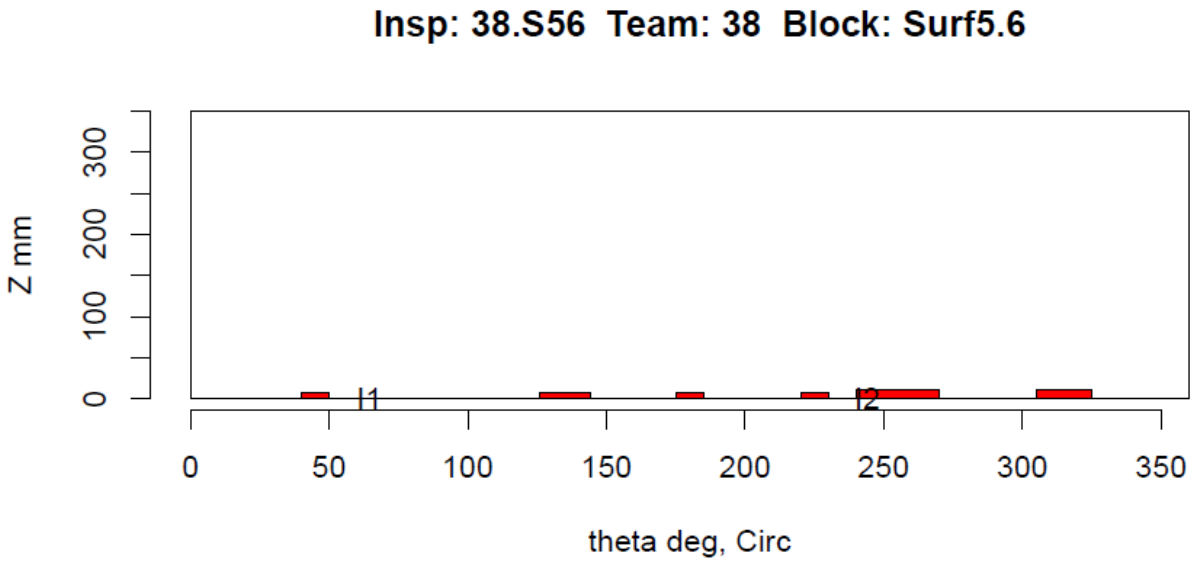
Insp: 38.S56 Team: 38 Block: Surf5.6
Z mm
0
100
200
300
I1
I2
0
50
100
150
200
250
300
350
theta deg, Circ

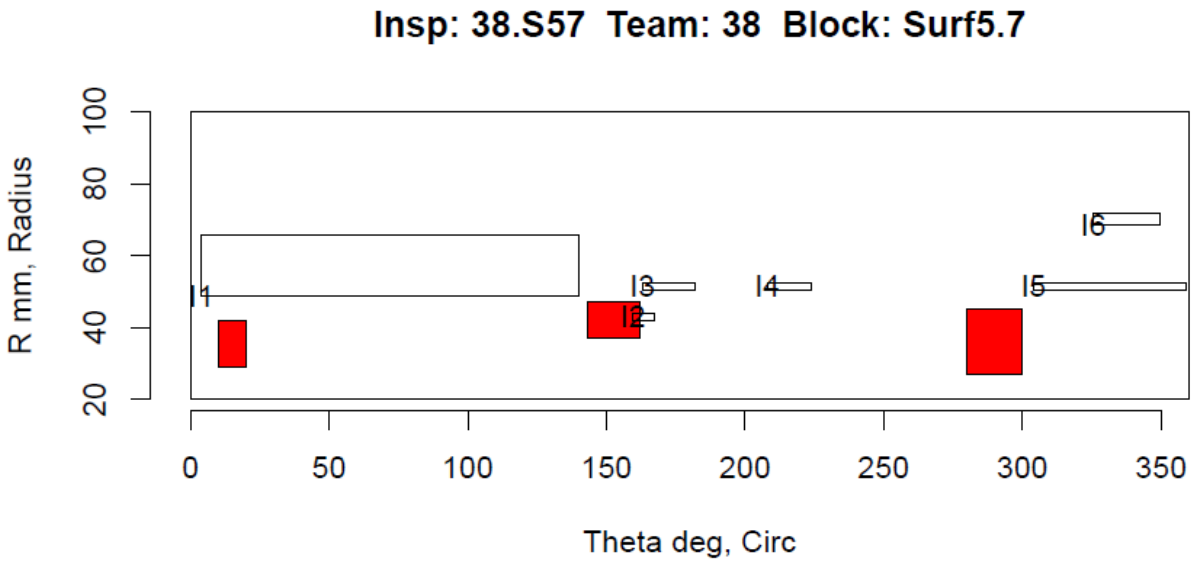
Insp: 38.S57 Team: 38 Block: Surf5.7
R mm, Radius
20
40
60
80
100
0
50
100
150
200
250
300
350
Theta deg, Circ
I1
I2
I3
I4
I5
I6

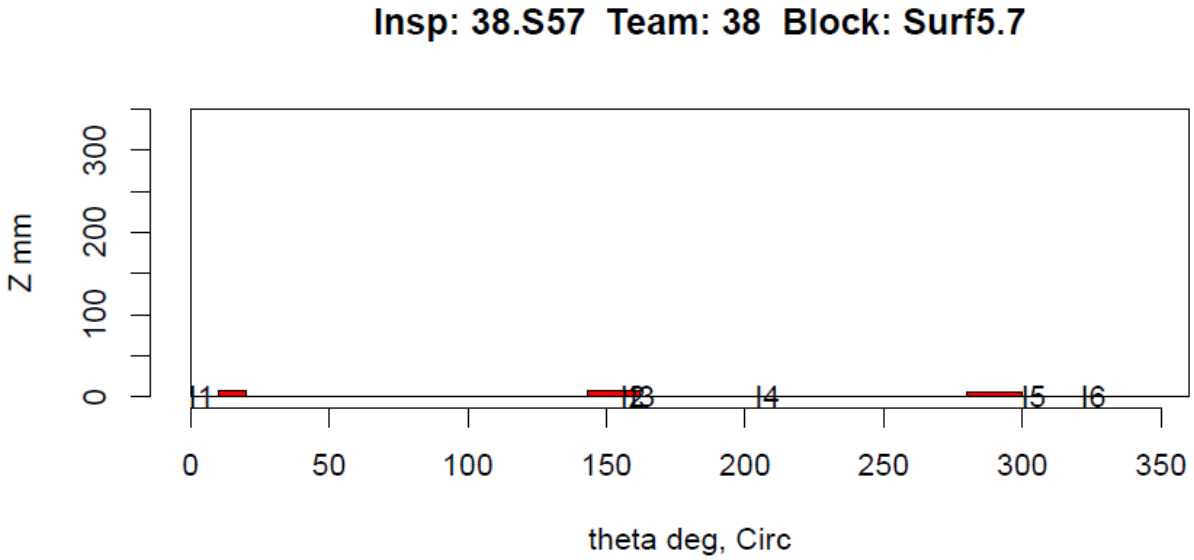
Insp: 38.S57 Team: 38 Block: Surf5.7
Z mm
0
100
200
300
0
50
100
150
200
250
300
350
theta deg, Circ
I1
I2
I3
I4
I5
I6

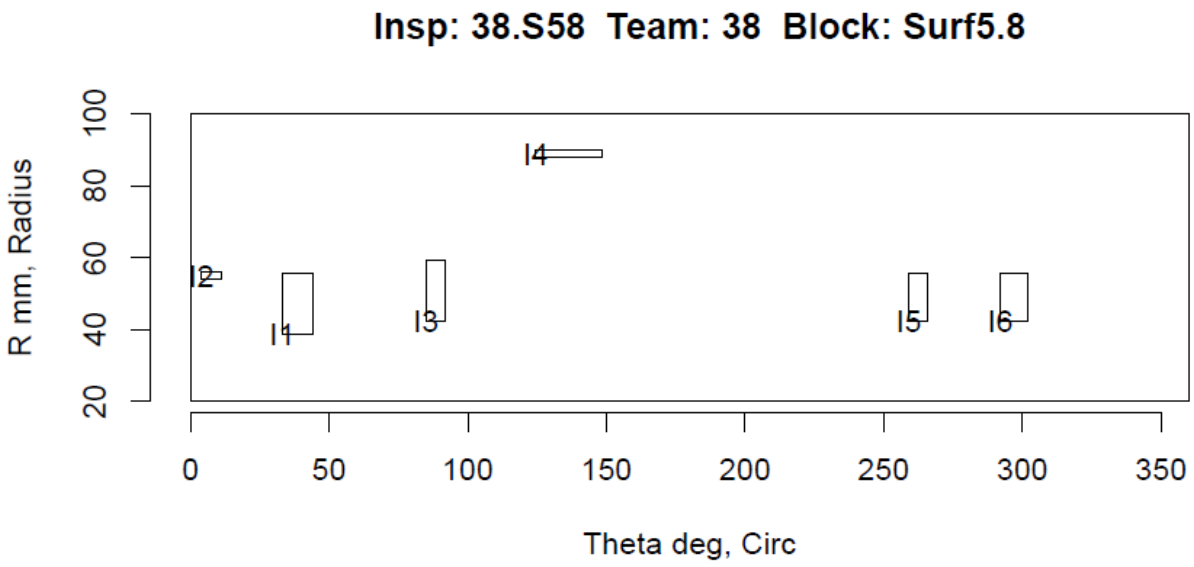
Insp: 38.S58 Team: 38 Block: Surf5.8
R mm, Radius
20
40
60
80
100
I4
I2
I1
I3
I5
I6
0
50
100
150
200
250
300
350
Theta deg, Circ

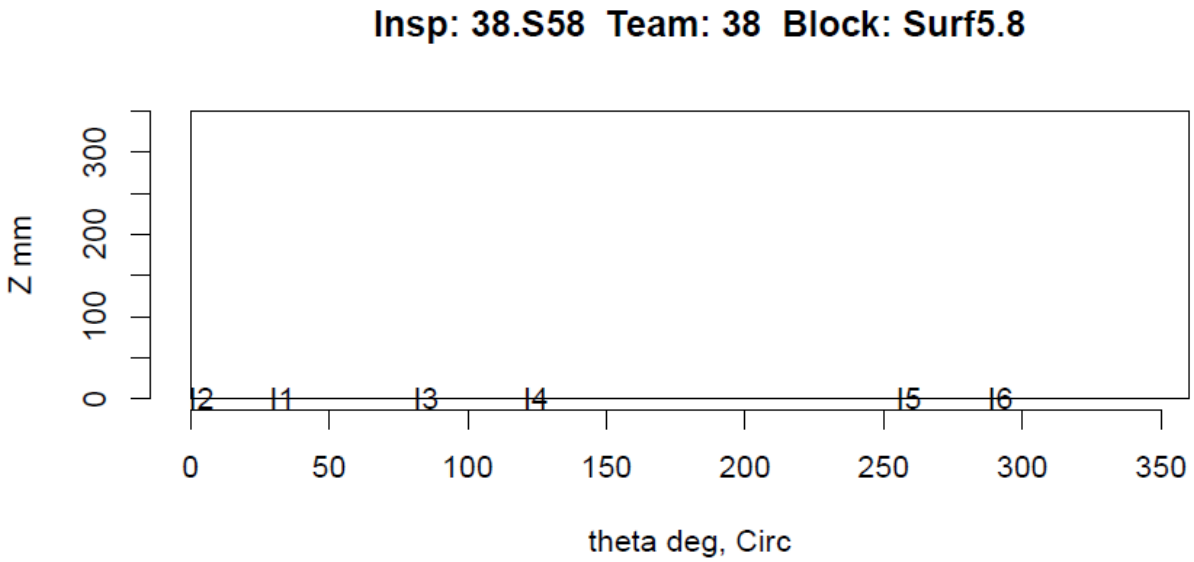
Insp: 38.S58 Team: 38 Block: Surf5.8
Z mm
0
100
200
300
I2
I1
I3
I4
I5
I6
0
50
100
150
200
250
300
350
theta deg, Circ

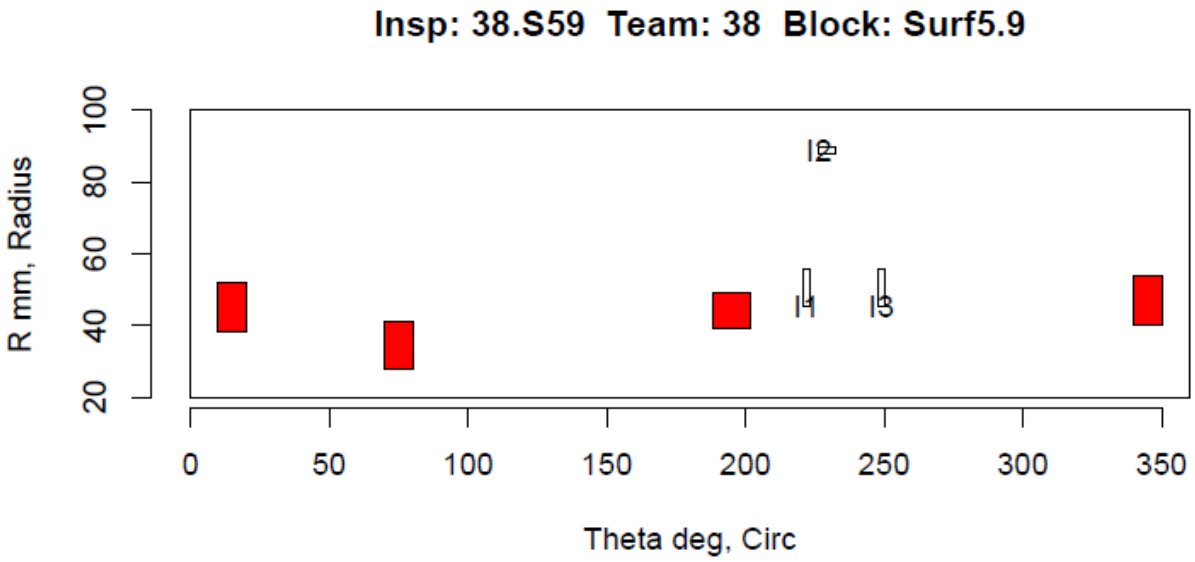
Insp: 38.S59 Team: 38 Block: Surf5.9
R mm, Radius
20
40
60
80
100
0
50
100
150
200
250
300
350
Theta deg, Circ

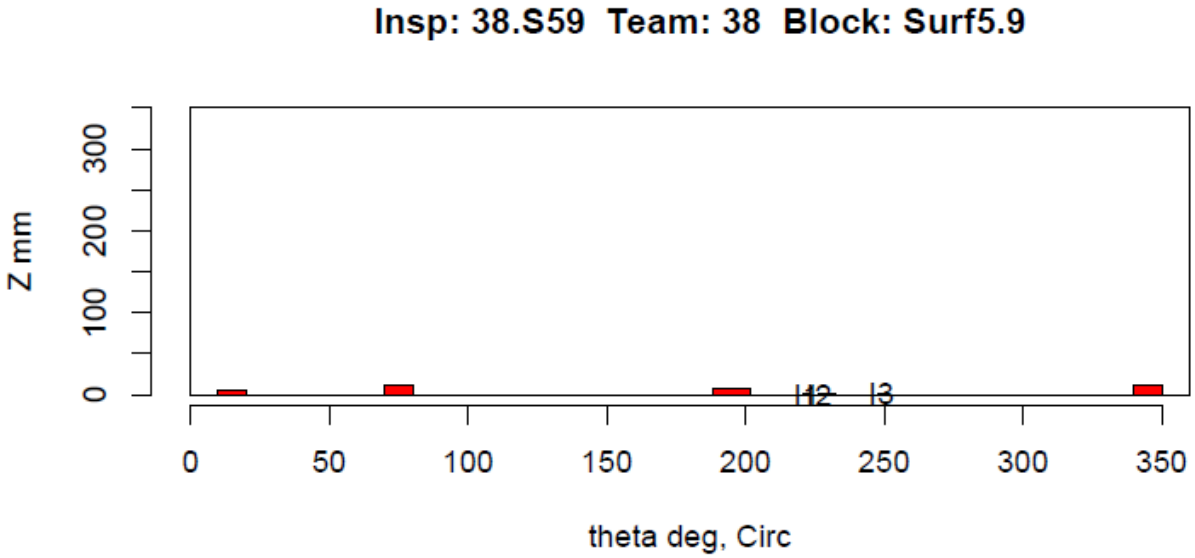
Insp: 38.S59 Team: 38 Block: Surf5.9
Z mm
0
100
200
300
0
50
100
150
200
250
300
350
theta deg, Circ

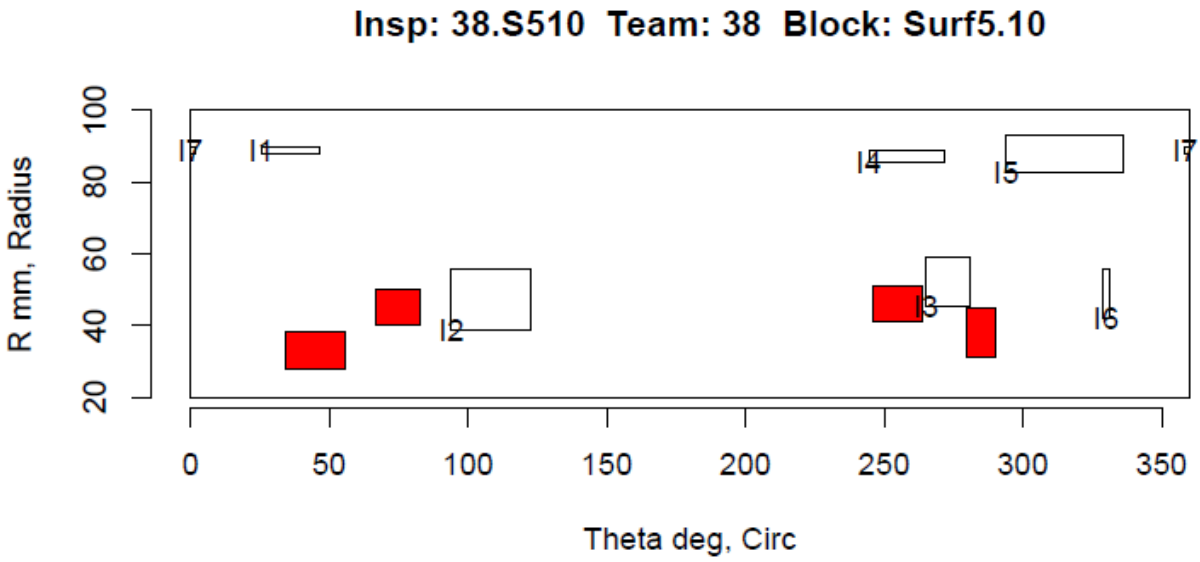
Insp: 38.S510 Team: 38 Block: Surf5.10
R mm, Radius
20
40
60
80
100
I7
I1
I2
I4
I5
I3
I6
I7
0
50
100
150
200
250
300
350
Theta deg, Circ

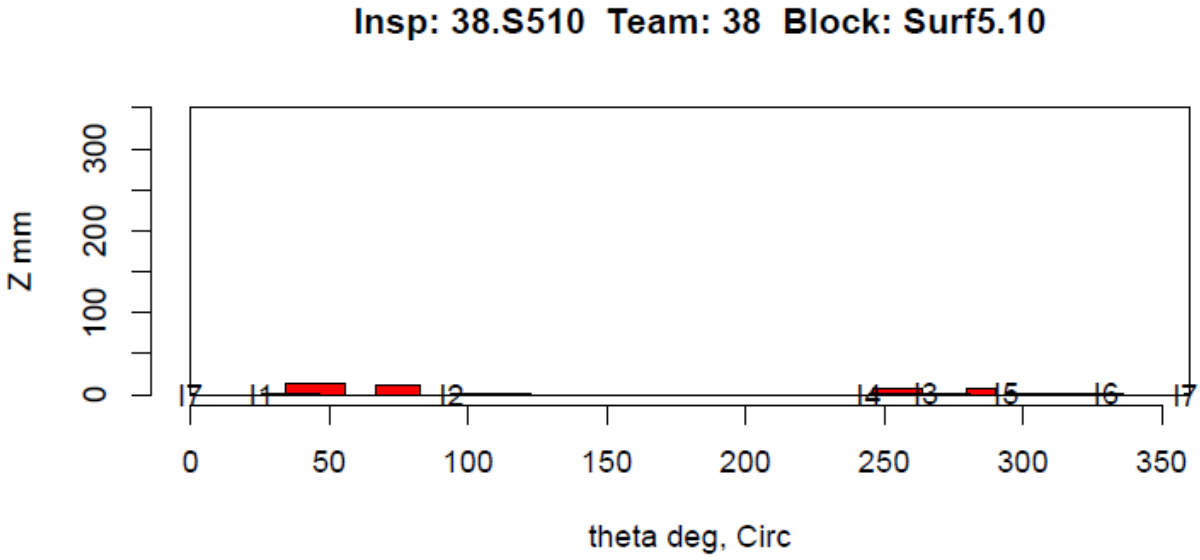
Insp: 38.S510 Team: 38 Block: Surf5.10
Z mm
0
100
200
300
I7
I1
I2
I4
I3
I5
I6
I7
0
50
100
150
200
250
300
350
theta deg, Circ

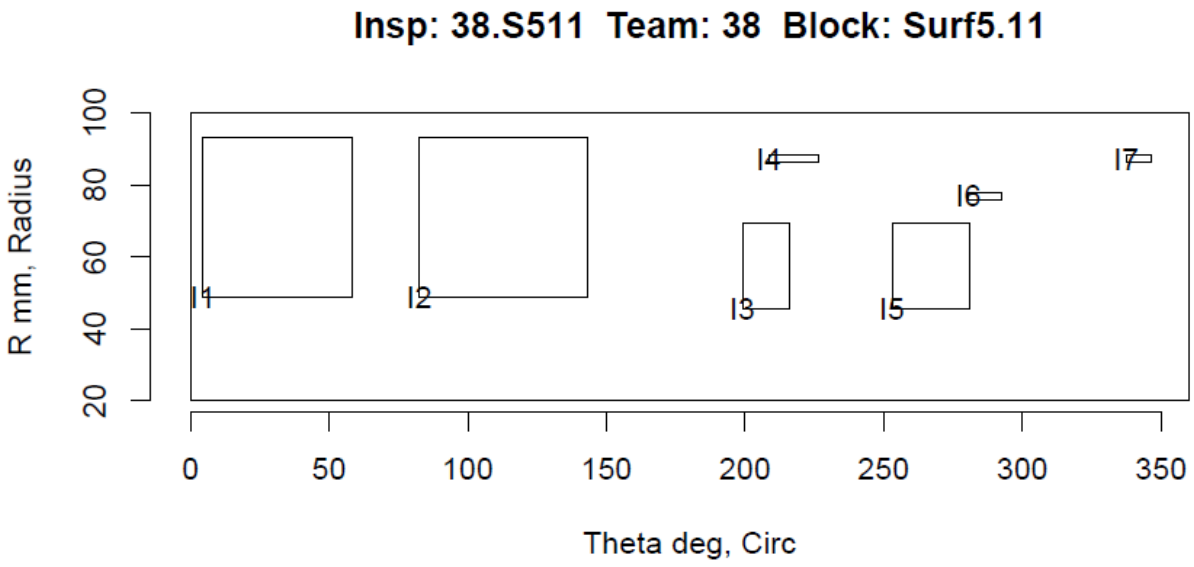
Insp: 38.S511 Team: 38 Block: Surf5.11
R mm, Radius
20
40
60
80
100
I1
I2
I3
I4
I5
I6
I7
0
50
100
150
200
250
300
350
Theta deg, Circ

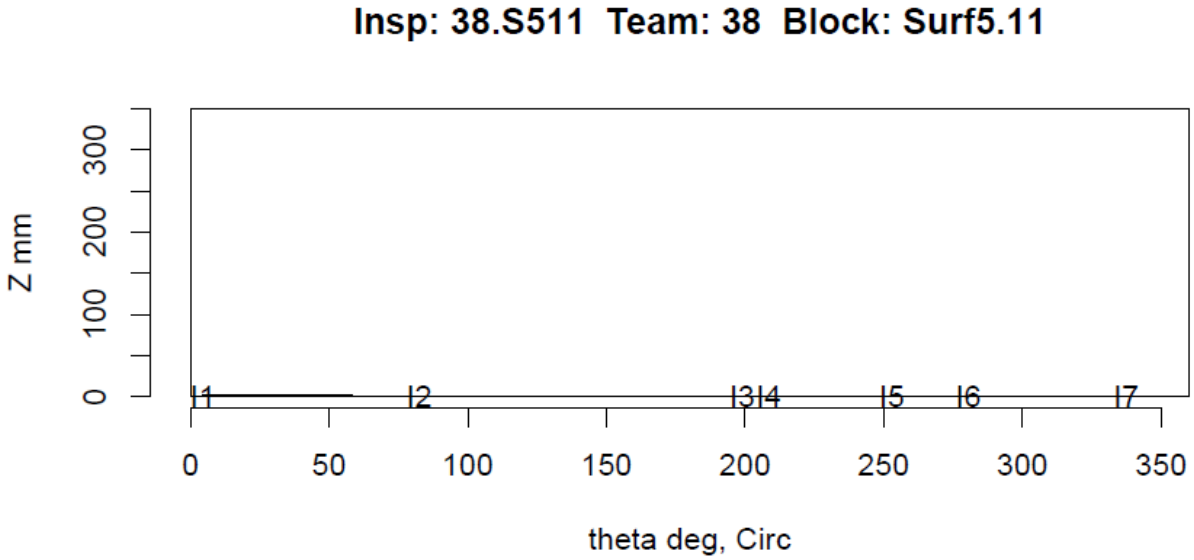
Insp: 38.S511 Team: 38 Block: Surf5.11
Z mm
0
100
200
300
I1
I2
I3
I4
I5
I6
I7
0
50
100
150
200
250
300
350
theta deg, Circ

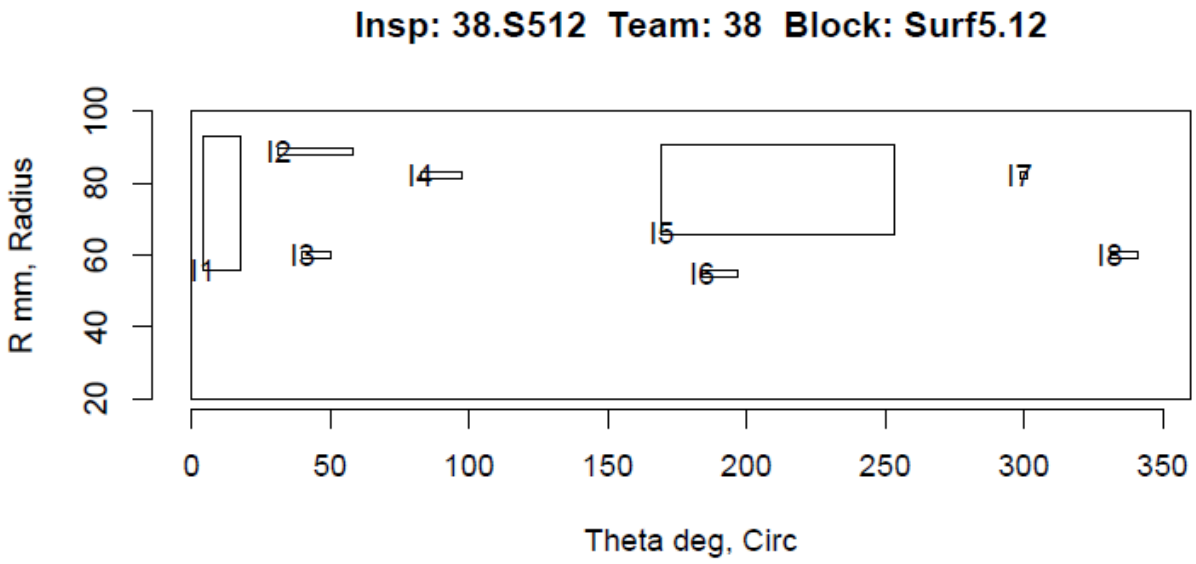
Insp: 38.S512 Team: 38 Block: Surf5.12
R mm, Radius
20
40
60
80
100
0
50
100
150
200
250
300
350
Theta deg, Circ
1
2
3
4
5
6
7
8

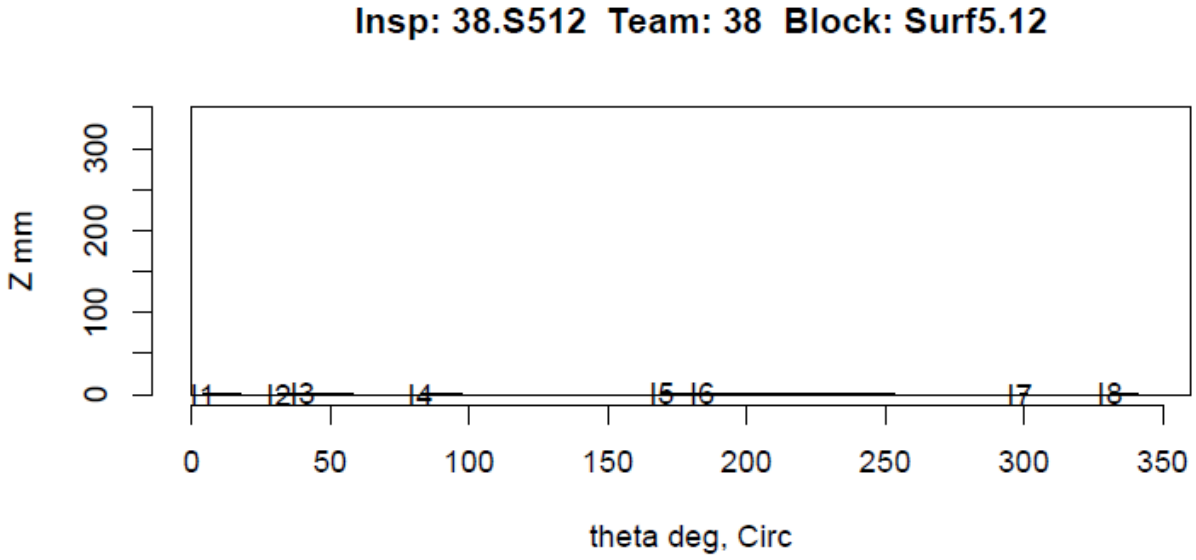
Insp: 38.S512 Team: 38 Block: Surf5.12
Z mm
0
100
200
300
0
50
100
150
200
250
300
350
theta deg, Circ
1
2
3
4
5
6
7
8

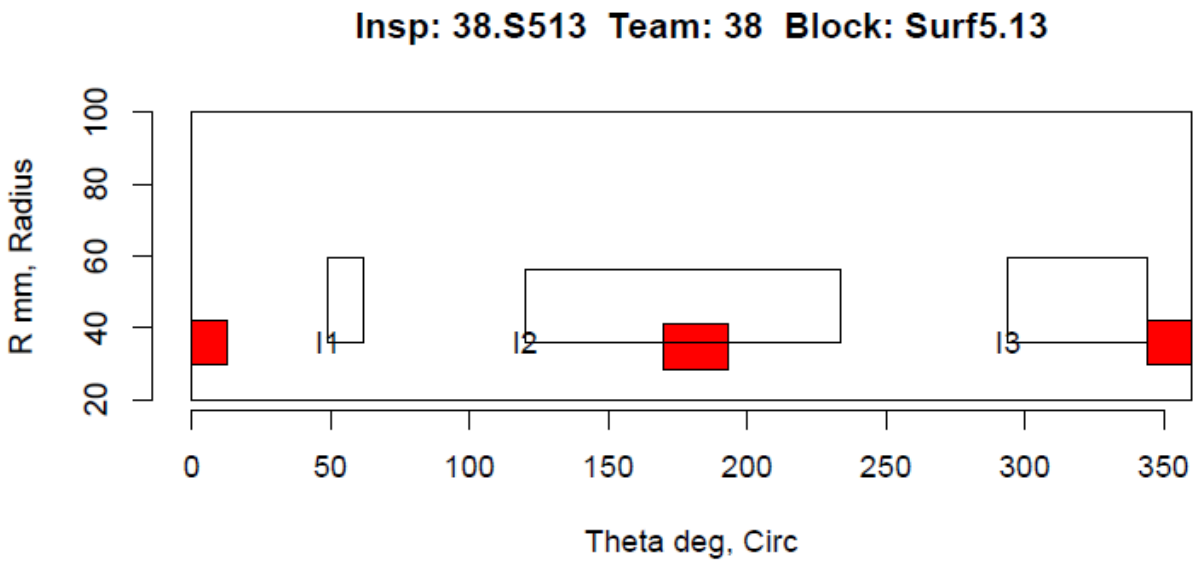
Insp: 38.S513 Team: 38 Block: Surf5.13
R mm, Radius
20
40
60
80
100
I1
I2
I3
0
50
100
150
200
250
300
350
Theta deg, Circ

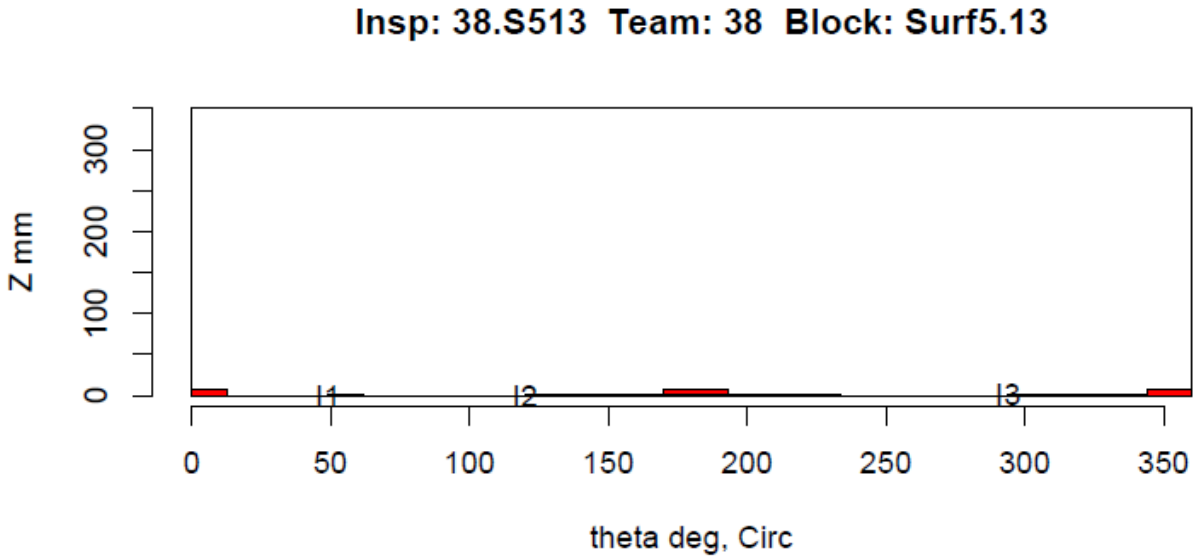
Insp: 38.S513 Team: 38 Block: Surf5.13
Z mm
0
100
200
300
I1
I2
I3
0
50
100
150
200
250
300
350
theta deg, Circ

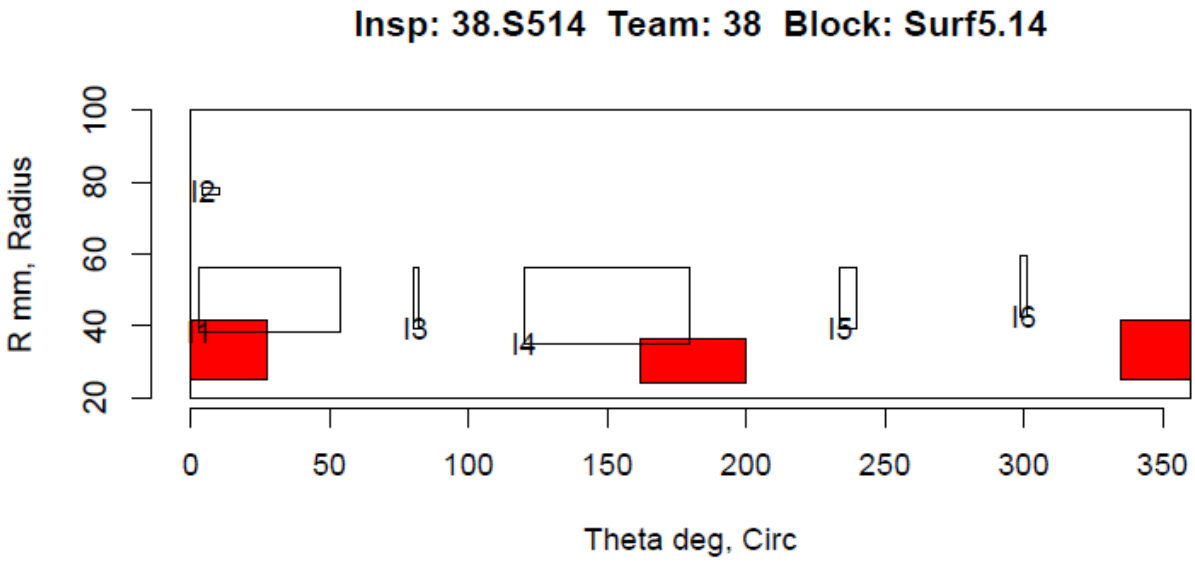
Insp: 38.S514 Team: 38 Block: Surf5.14
R mm, Radius
20
40
60
80
100
0
50
100
150
200
250
300
350
Theta deg, Circ

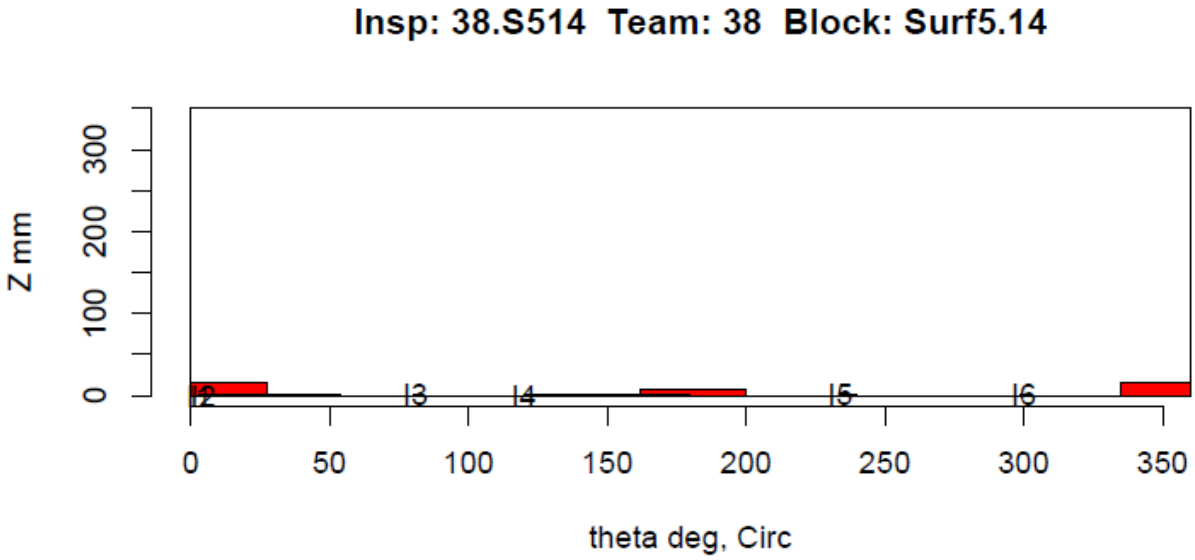
Insp: 38.S514 Team: 38 Block: Surf5.14
Z mm
0
100
200
300
0
50
100
150
200
250
300
350
theta deg, Circ

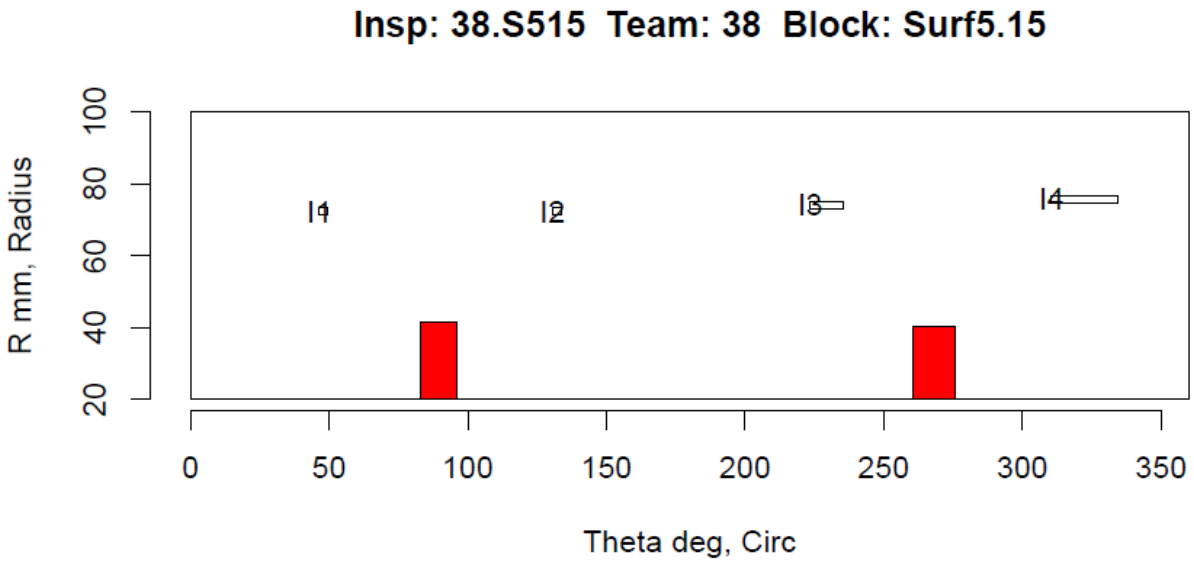
Insp: 38.S515 Team: 38 Block: Surf5.15
R mm, Radius
20
40
60
80
100
I1
I2
I3
I4
0
50
100
150
200
250
300
350
Theta deg, Circ

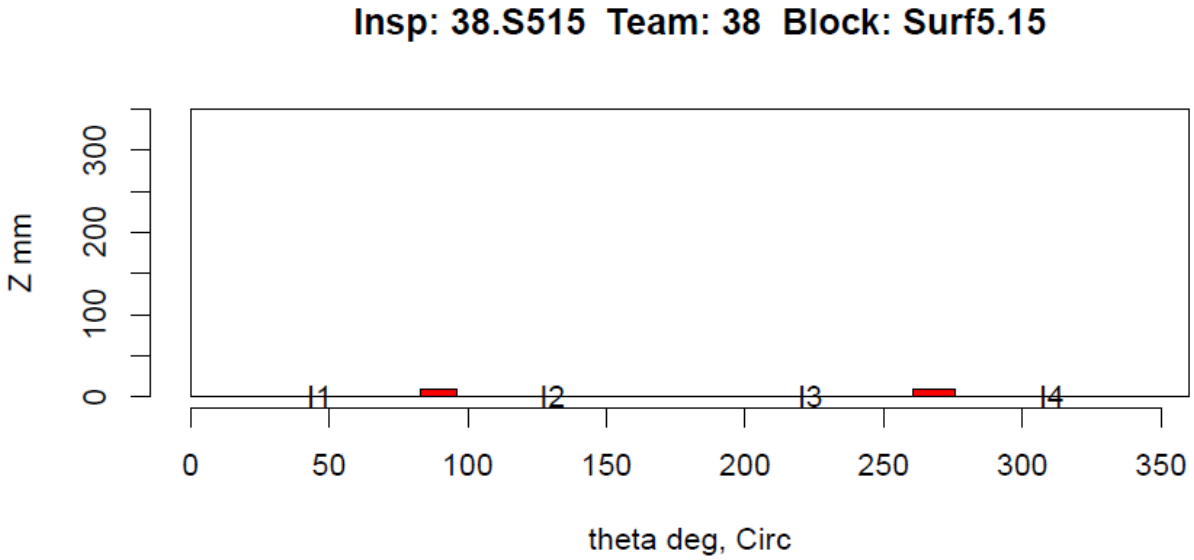
Insp: 38.S515 Team: 38 Block: Surf5.15
Z mm
0
100
200
300
I1
I2
I3
I4
0
50
100
150
200
250
300
350
theta deg, Circ

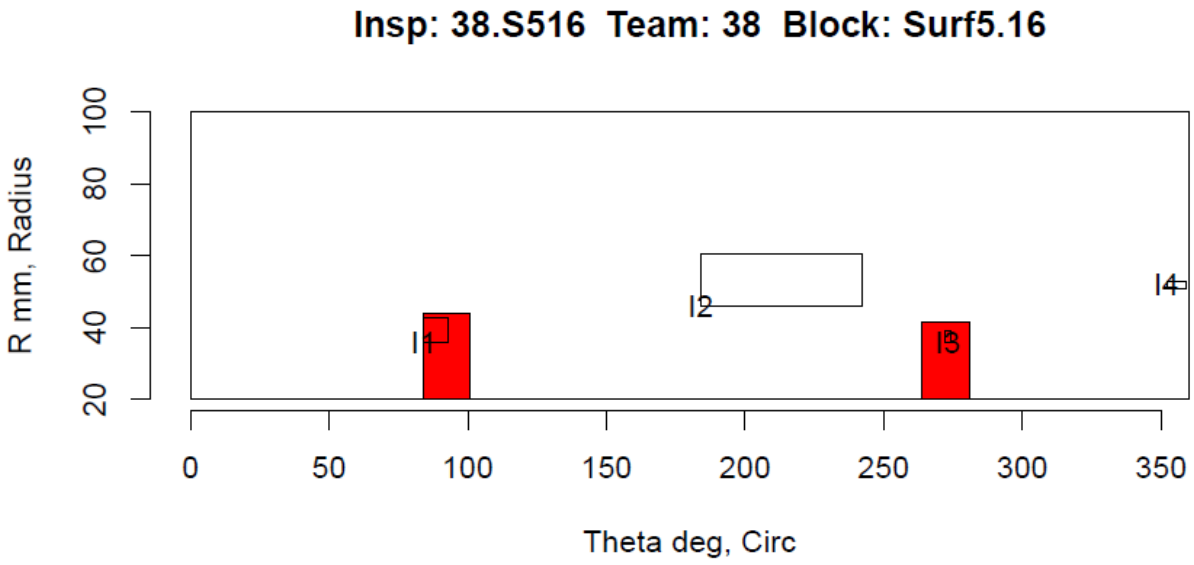
Insp: 38.S516 Team: 38 Block: Surf5.16
R mm, Radius
20
40
60
80
100
I1
I2
I3
I4
0
50
100
150
200
250
300
350
Theta deg, Circ

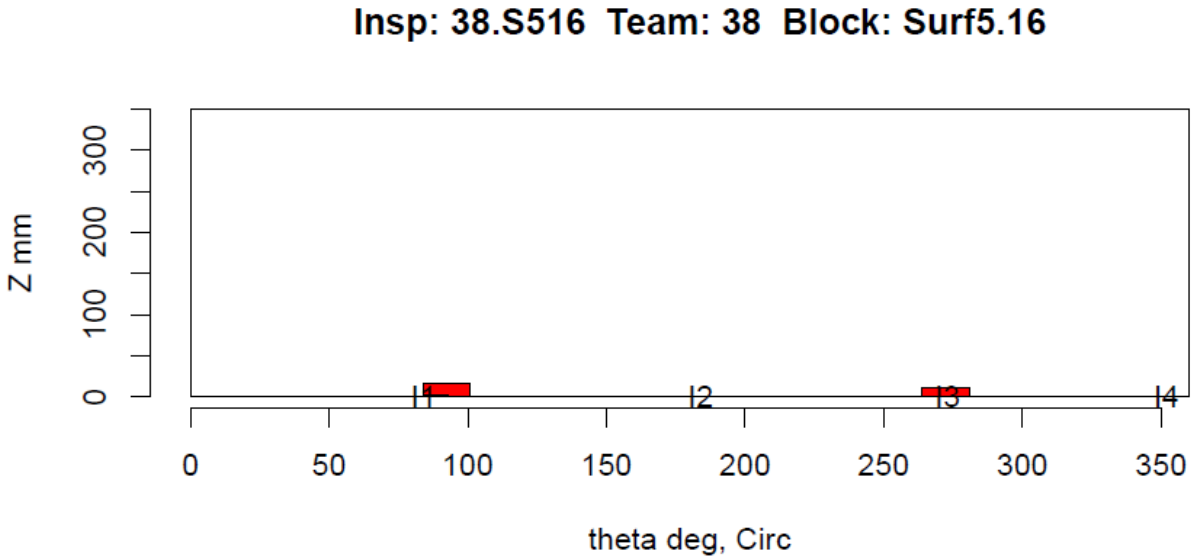
Insp: 38.S516 Team: 38 Block: Surf5.16
Z mm
0
100
200
300
I1
I2
I3
I4
0
50
100
150
200
250
300
350
theta deg, Circ

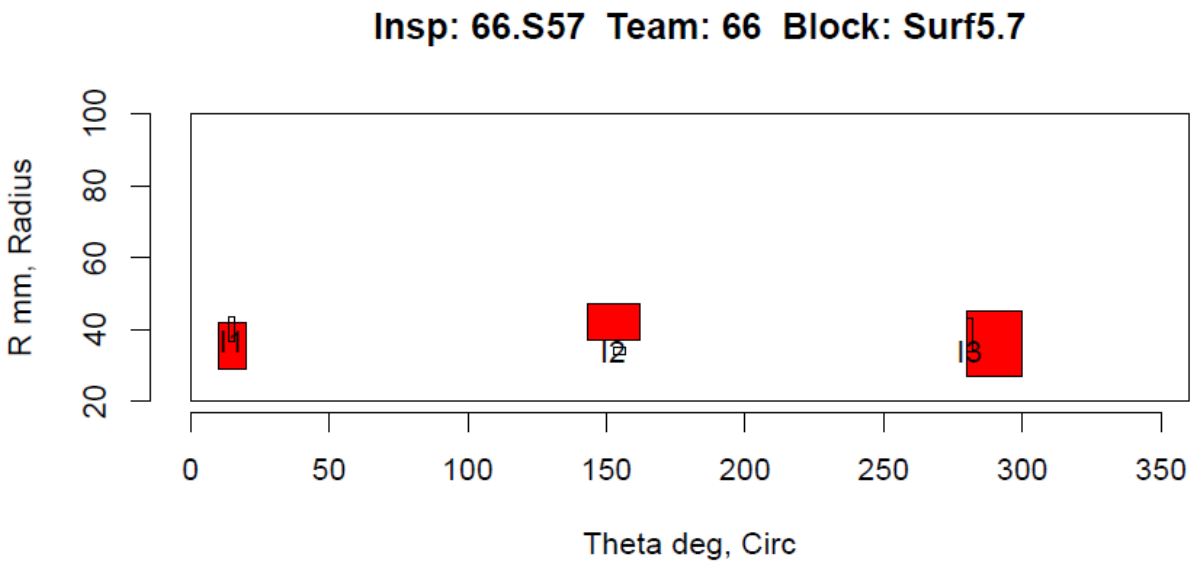
Insp: 66.S57 Team: 66 Block: Surf5.7
R mm, Radius
20
40
60
80
100
0
50
100
150
200
250
300
350
Theta deg, Circ
I1
I2
I3

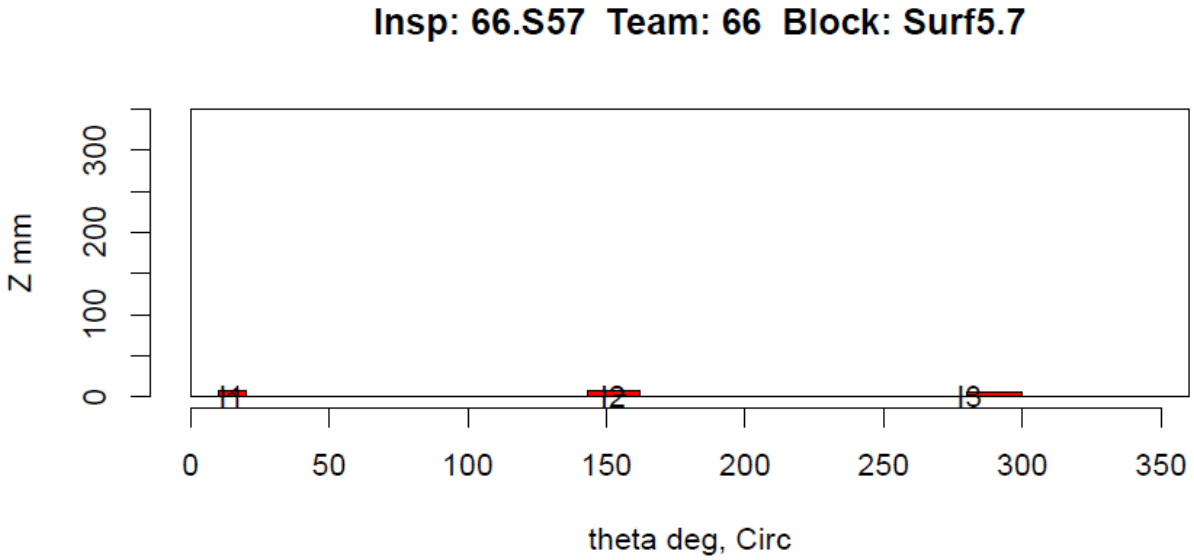
Insp: 66.S57 Team: 66 Block: Surf5.7
Z mm
0
100
200
300
0
50
100
150
200
250
300
350
theta deg, Circ
I1
I2
I3

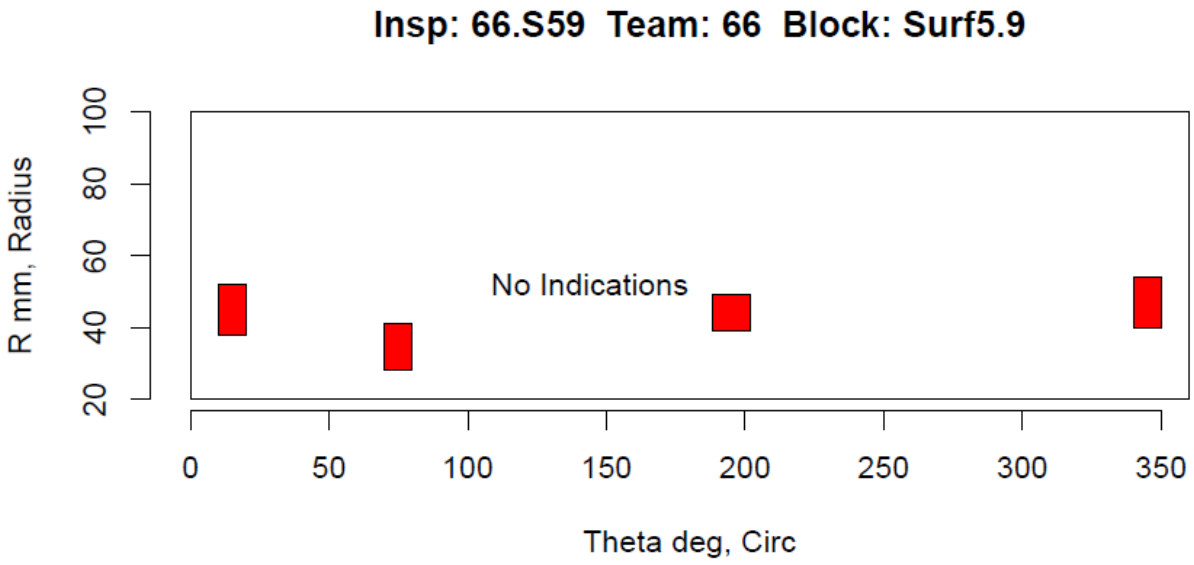
Insp: 66.S59 Team: 66 Block: Surf5.9
R mm, Radius
20
40
60
80
100
No Indications
0
50
100
150
200
250
300
350
Theta deg, Circ

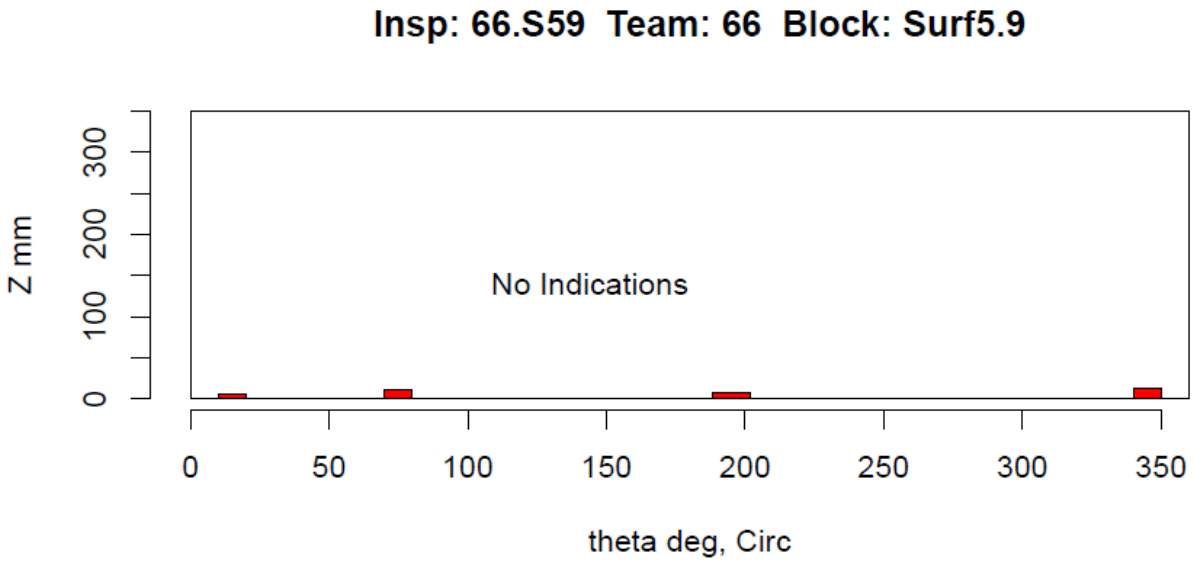
Insp: 66.S59 Team: 66 Block: Surf5.9
Z mm
0
100
200
300
No Indications
0
50
100
150
200
250
300
350
theta deg, Circ

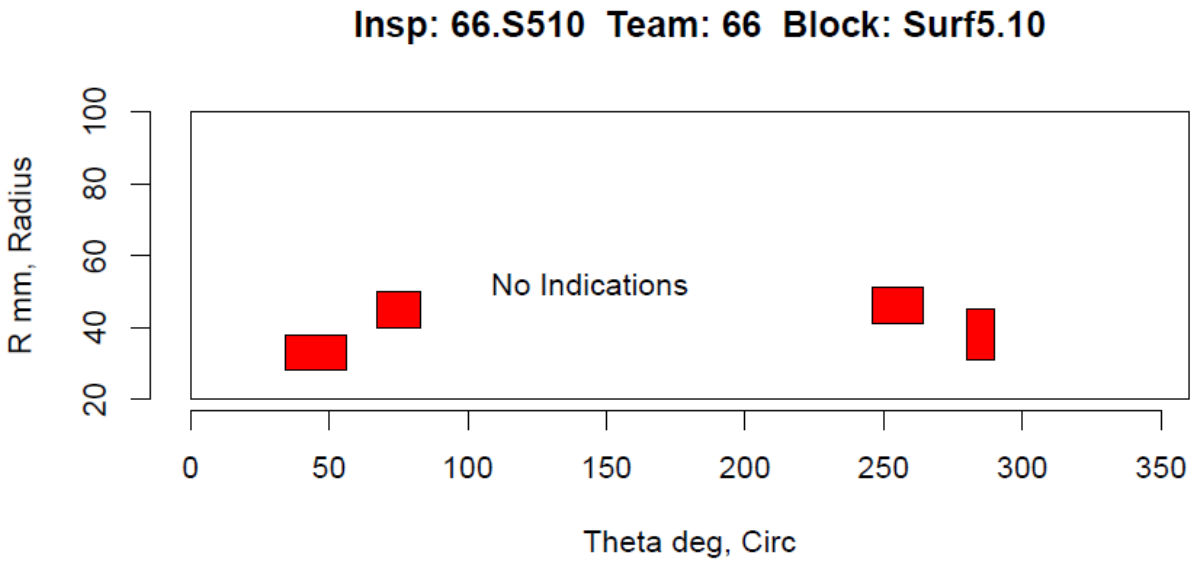
Insp: 66.S510 Team: 66 Block: Surf5.10
R mm, Radius
20
40
60
80
100
No Indications
0
50
100
150
200
250
300
350
Theta deg, Circ

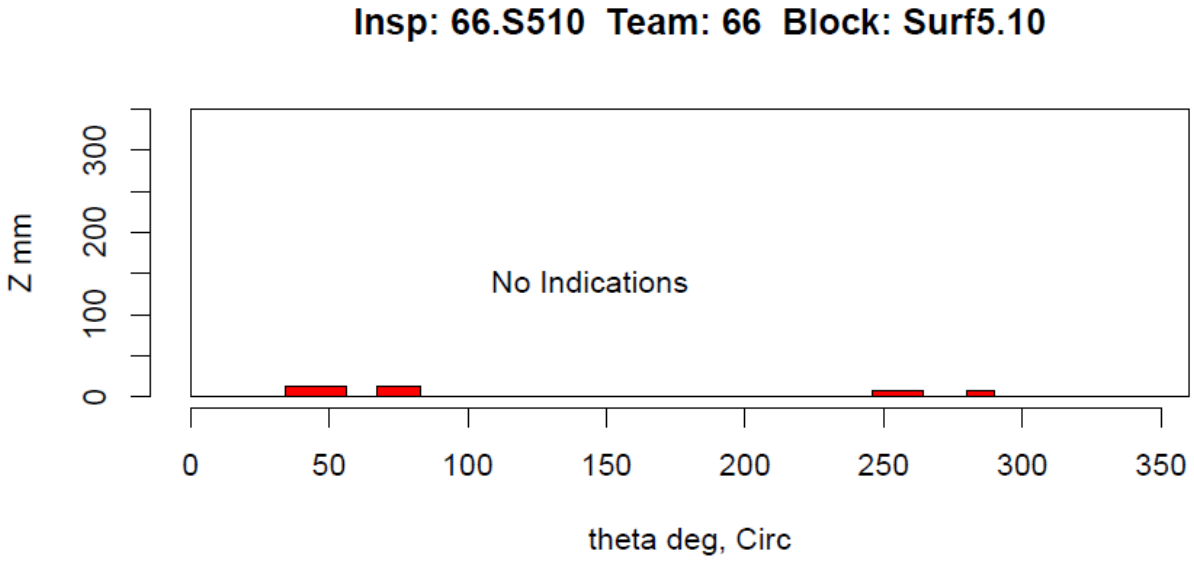
Insp: 66.S510 Team: 66 Block: Surf5.10
Z mm
0
100
200
300
No Indications
0
50
100
150
200
250
300
350
theta deg, Circ

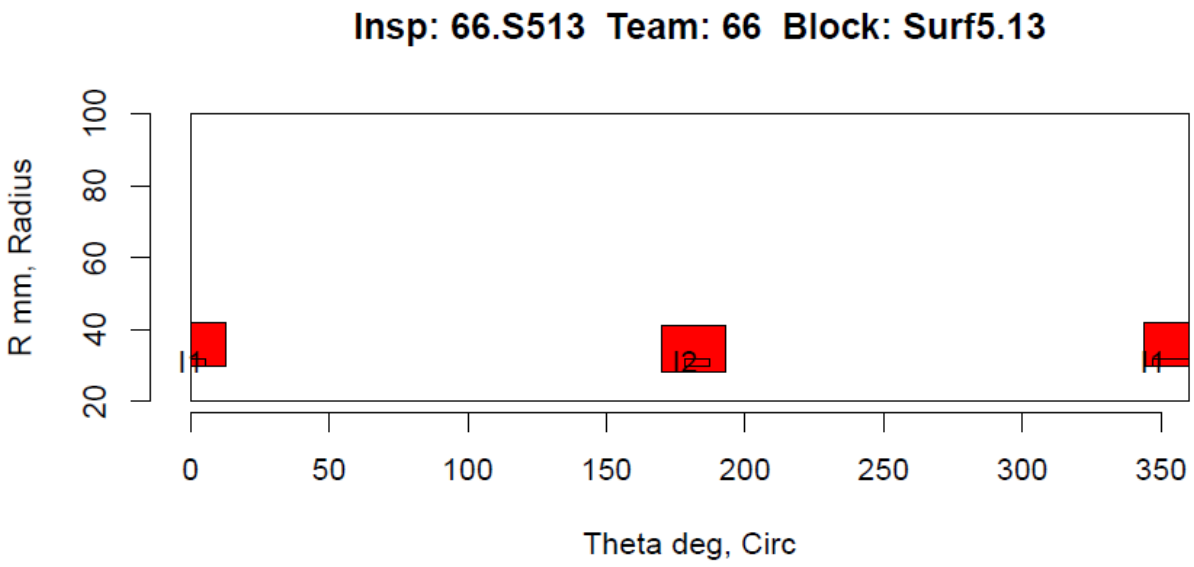
Insp: 66.S513 Team: 66 Block: Surf5.13
R mm, Radius
20
40
60
80
100
0
50
100
150
200
250
300
350
Theta deg, Circ
I1
I2
I1

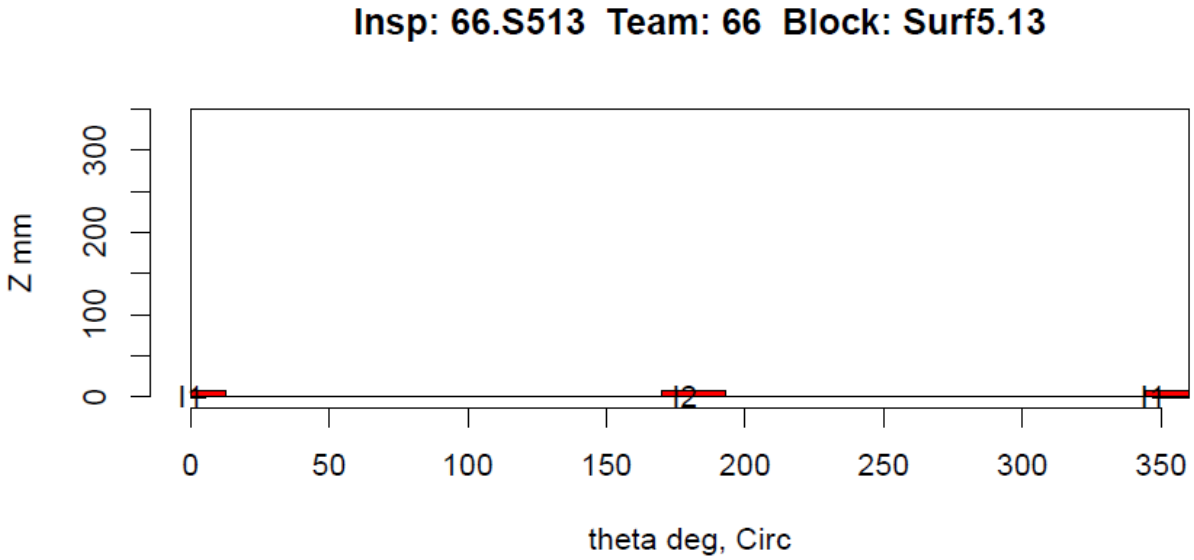
Insp: 66.S513 Team: 66 Block: Surf5.13
Z mm
0
100
200
300
0
50
100
150
200
250
300
350
theta deg, Circ
I1
I2
I1

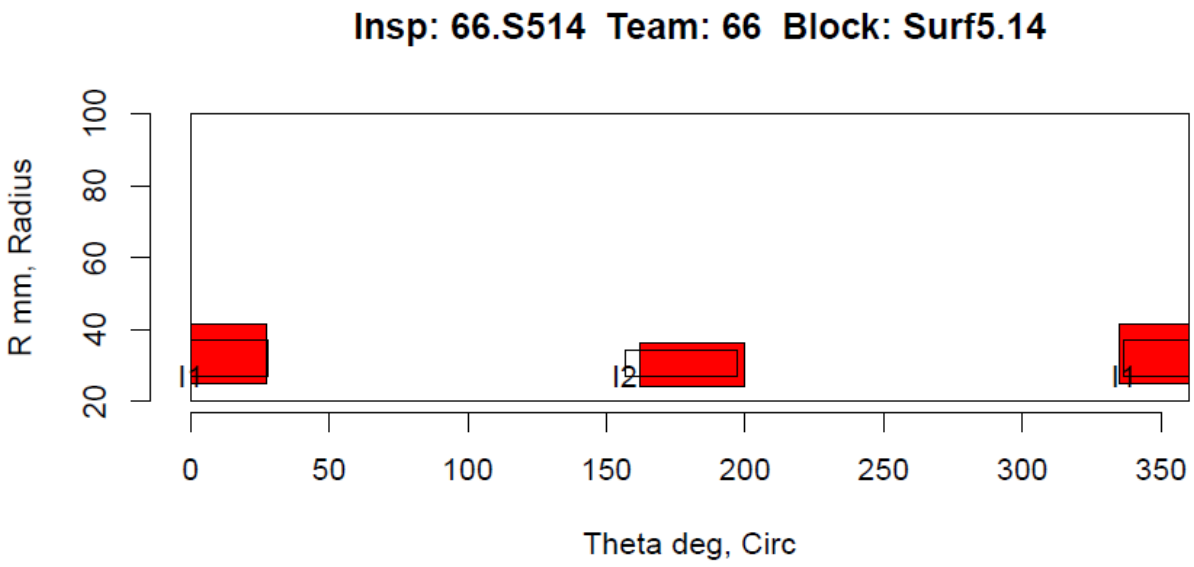
Insp: 66.S514 Team: 66 Block: Surf5.14
R mm, Radius
20
40
60
80
100
0
50
100
150
200
250
300
350
Theta deg, Circ

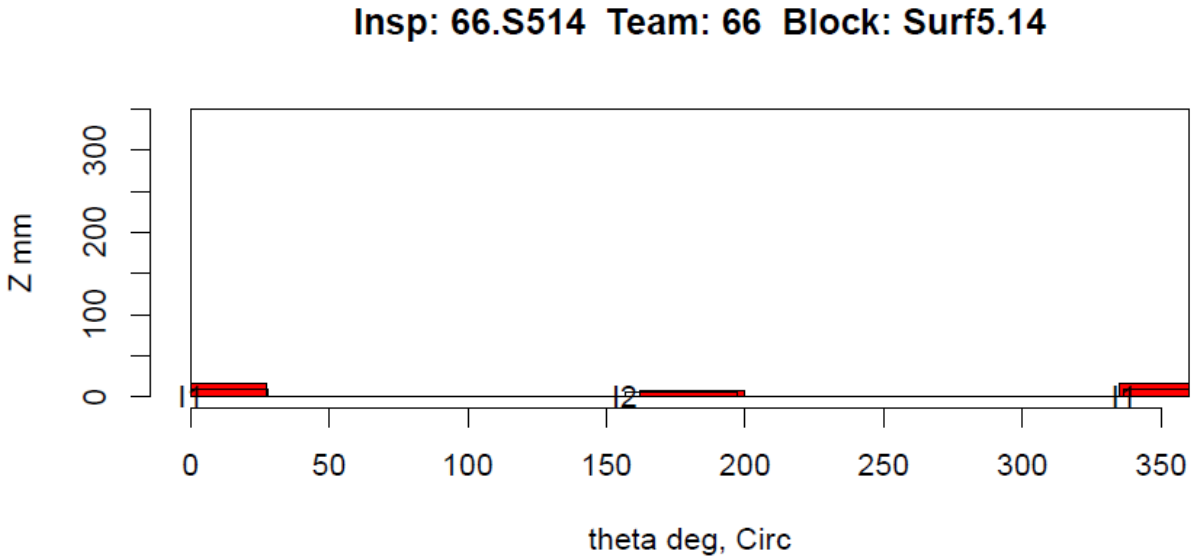
Insp: 66.S514 Team: 66 Block: Surf5.14
Z mm
0
100
200
300
0
50
100
150
200
250
300
350
theta deg, Circ

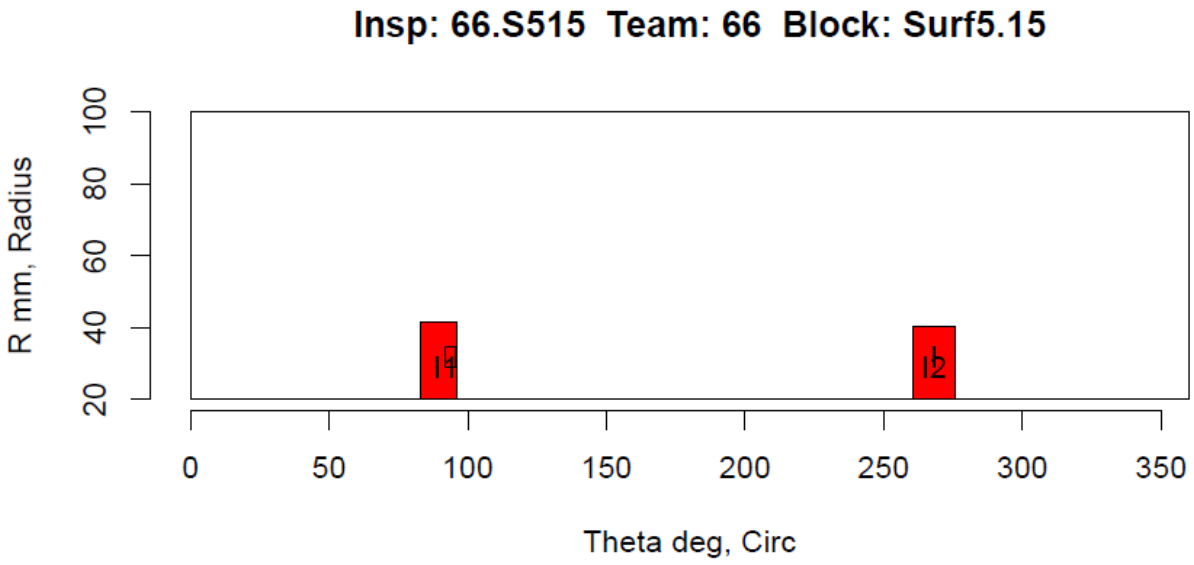
Insp: 66.S515 Team: 66 Block: Surf5.15
R mm, Radius
20
40
60
80
100
0
50
100
150
200
250
300
350
Theta deg, Circ

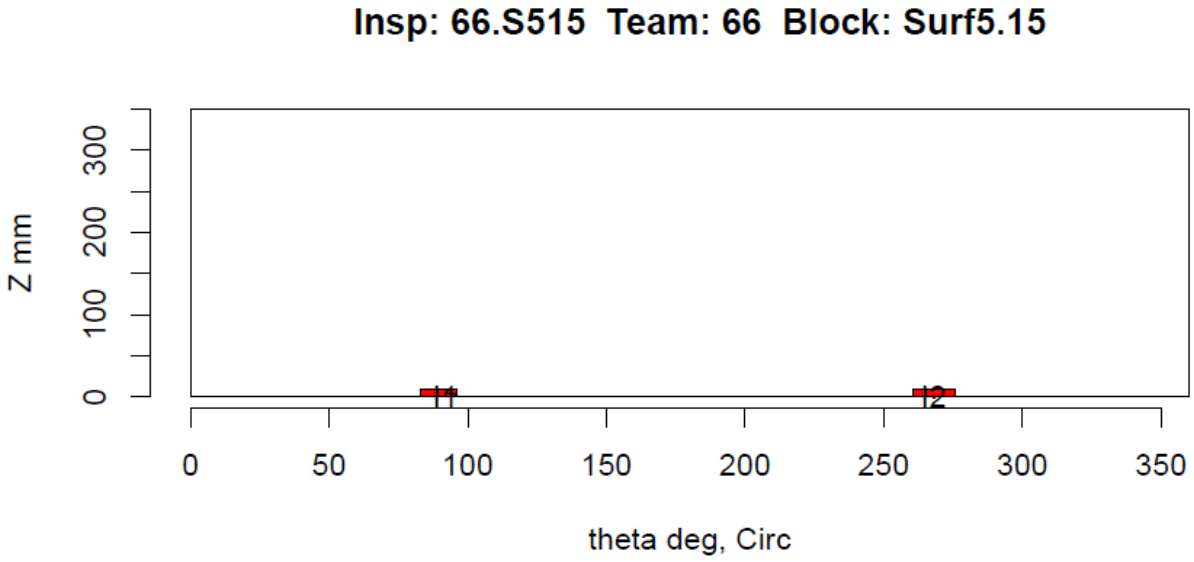
Insp: 66.S515 Team: 66 Block: Surf5.15
Z mm
0
100
200
300
0
50
100
150
200
250
300
350
theta deg, Circ

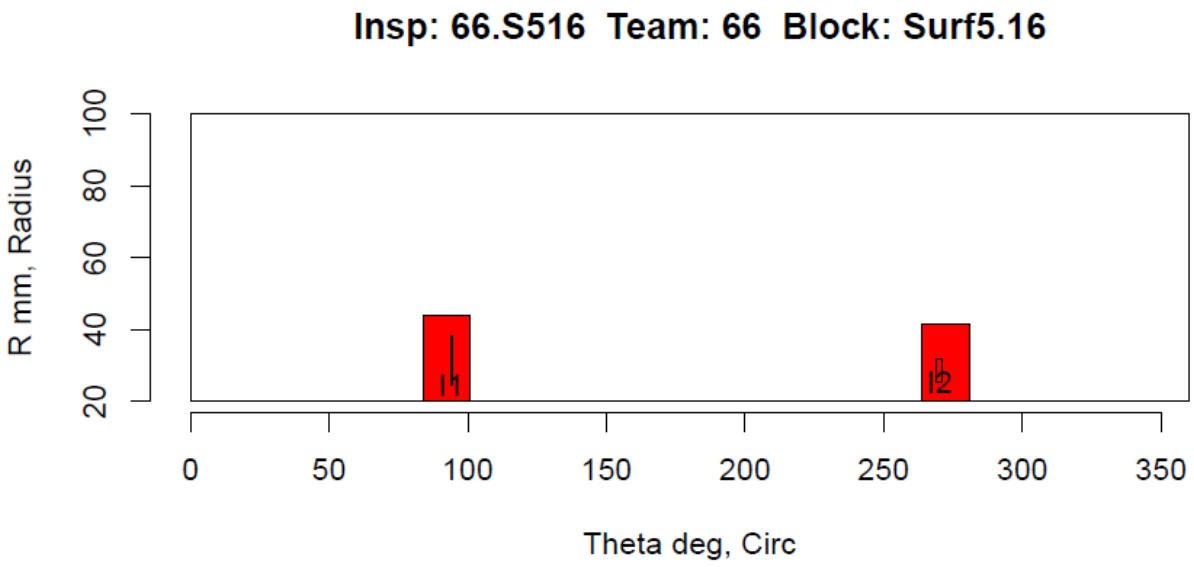
Insp: 66.S516 Team: 66 Block: Surf5.16
R mm, Radius
20
40
60
80
100
0
50
100
150
200
250
300
350
Theta deg, Circ

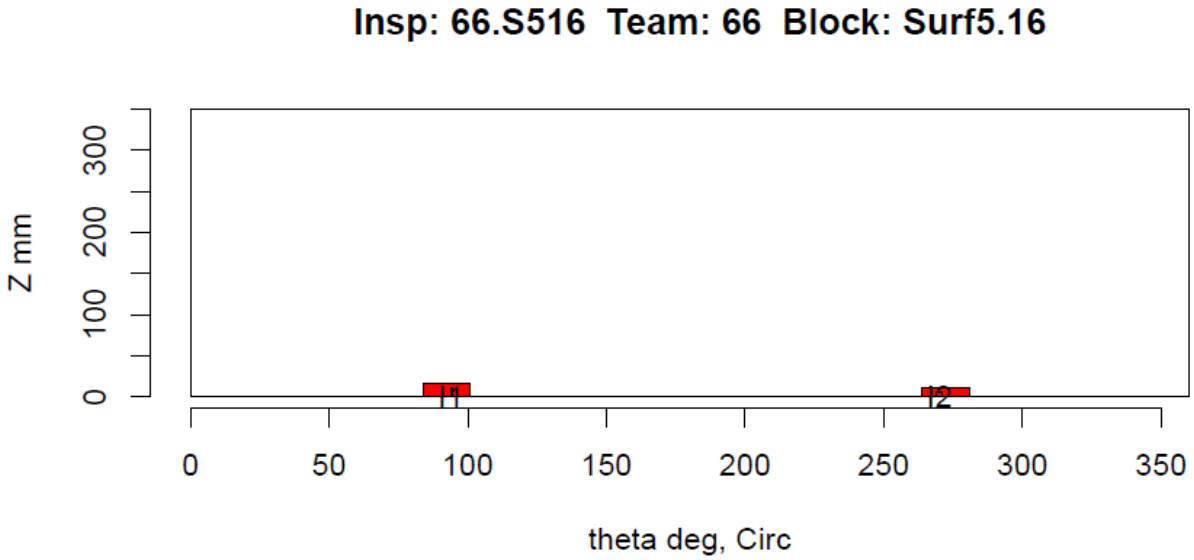
Insp: 66.S516 Team: 66 Block: Surf5.16
Z mm
0
100
200
300
0
50
100
150
200
250
300
350
theta deg, Circ

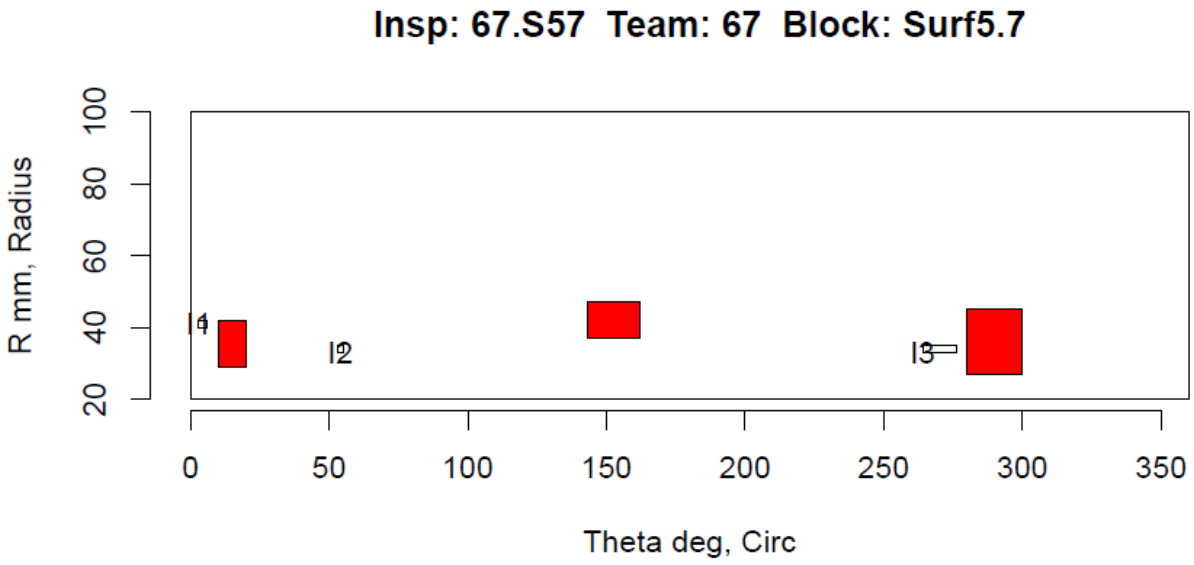
Insp: 67.S57 Team: 67 Block: Surf5.7
R mm, Radius
20
40
60
80
100
I4
I2
I3
0
50
100
150
200
250
300
350
Theta deg, Circ

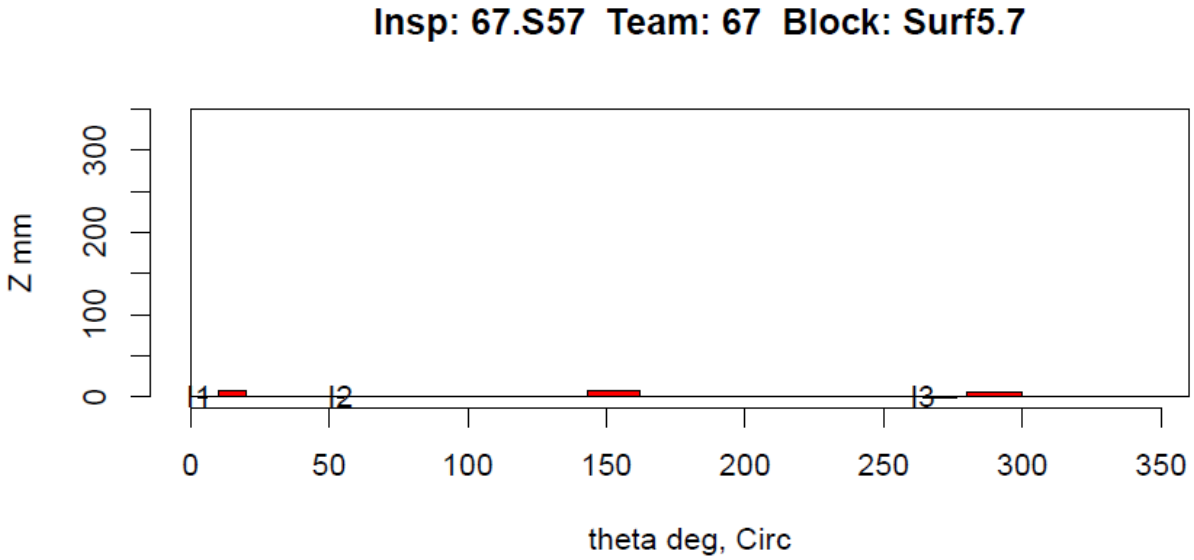
Insp: 67.S57 Team: 67 Block: Surf5.7
Z mm
0
100
200
300
I1
I2
I3
0
50
100
150
200
250
300
350
theta deg, Circ

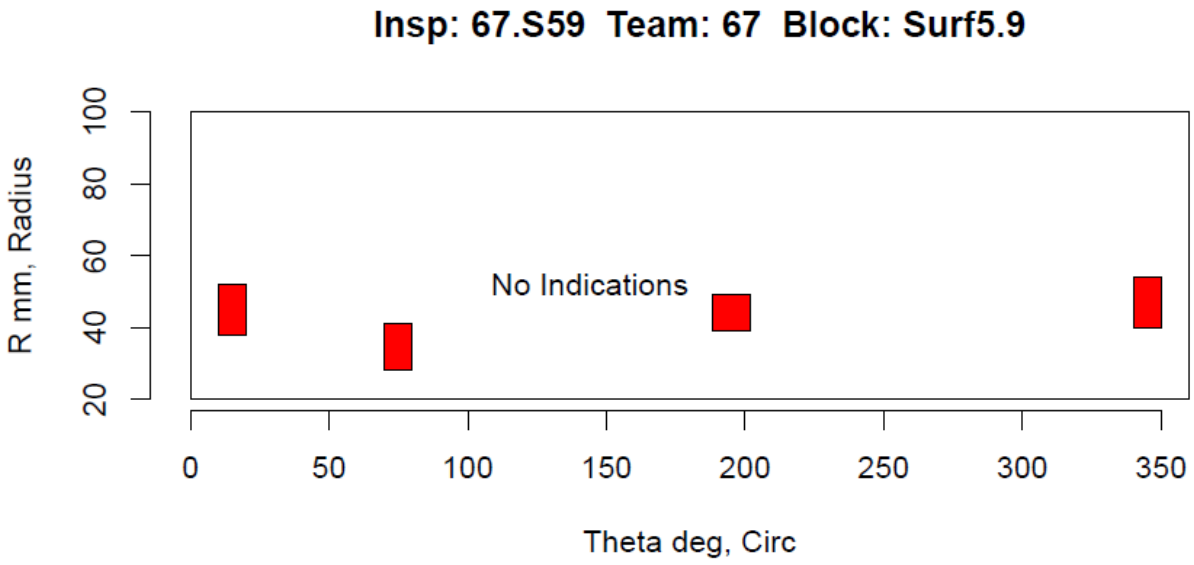
Insp: 67.S59 Team: 67 Block: Surf5.9
R mm, Radius
20
40
60
80
100
No Indications
0
50
100
150
200
250
300
350
Theta deg, Circ

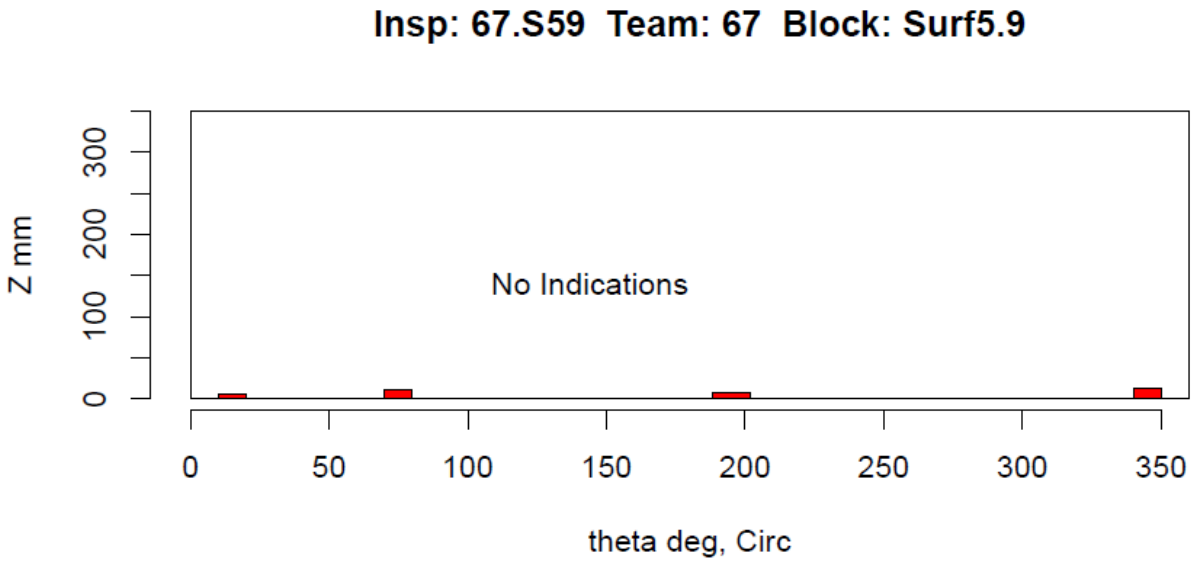
Insp: 67.S59 Team: 67 Block: Surf5.9
Z mm
0
100
200
300
No Indications
0
50
100
150
200
250
300
350
theta deg, Circ

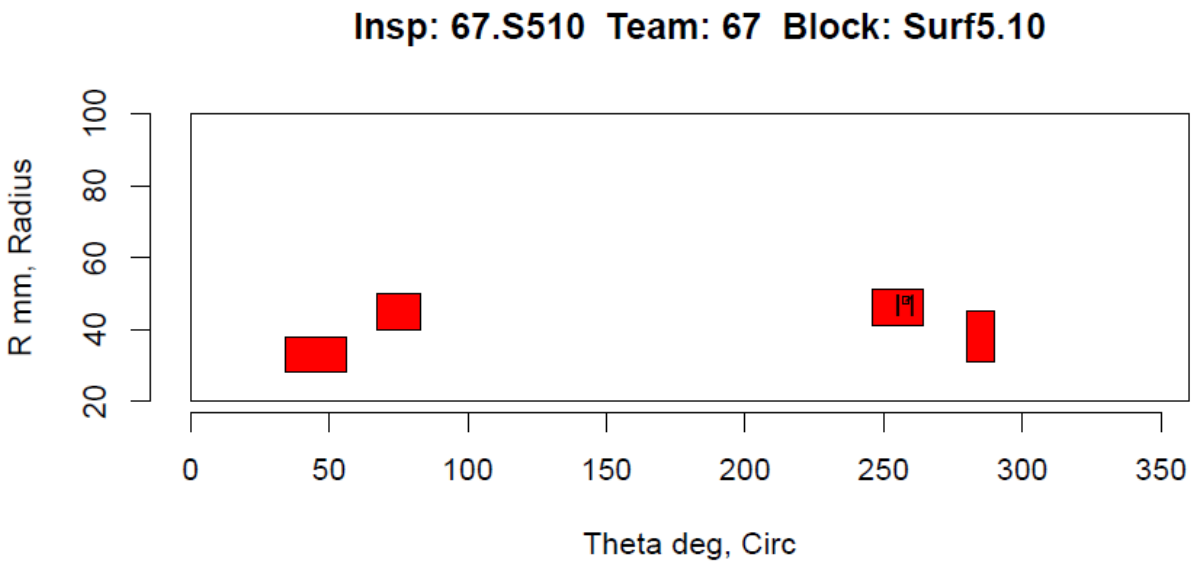
Insp: 67.S510 Team: 67 Block: Surf5.10
R mm, Radius
20
40
60
80
100
0
50
100
150
200
250
300
350
Theta deg, Circ

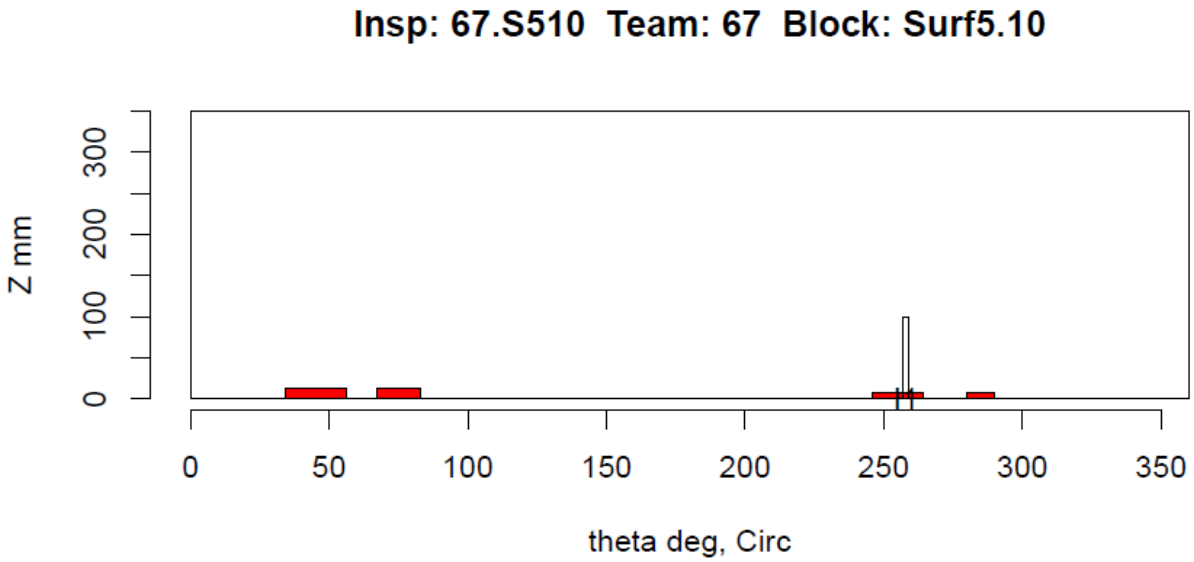
Insp: 67.S510 Team: 67 Block: Surf5.10
Z mm
0
100
200
300
0
50
100
150
200
250
300
350
theta deg, Circ

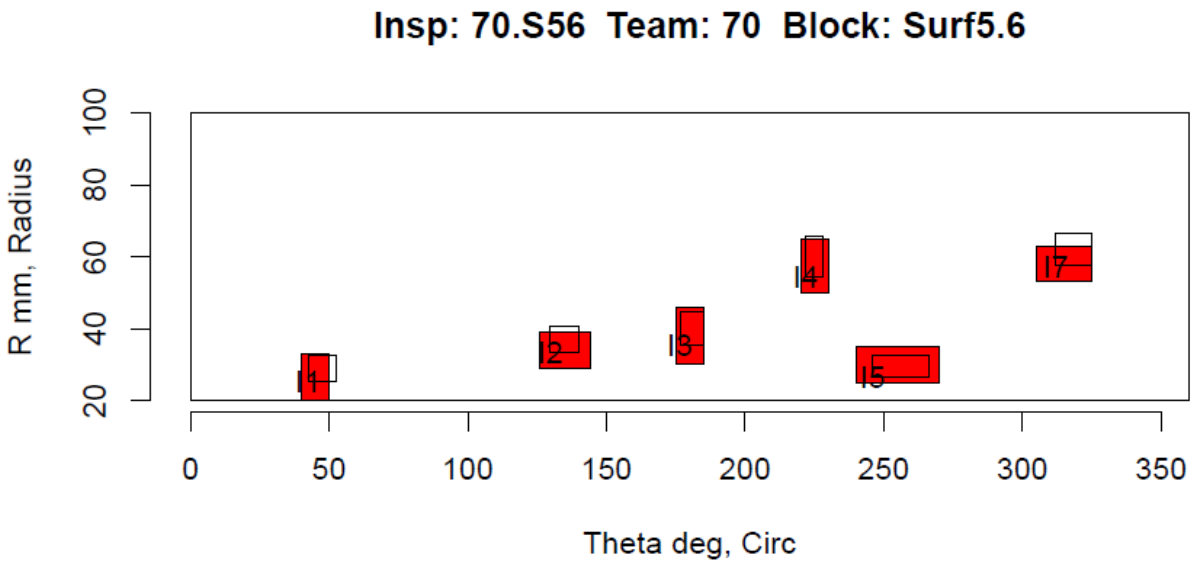
Insp: 70.S56 Team: 70 Block: Surf5.6
R mm, Radius
20
40
60
80
100
0
50
100
150
200
250
300
350
Theta deg, Circ
I1
I2
I3
I4
I5
I7

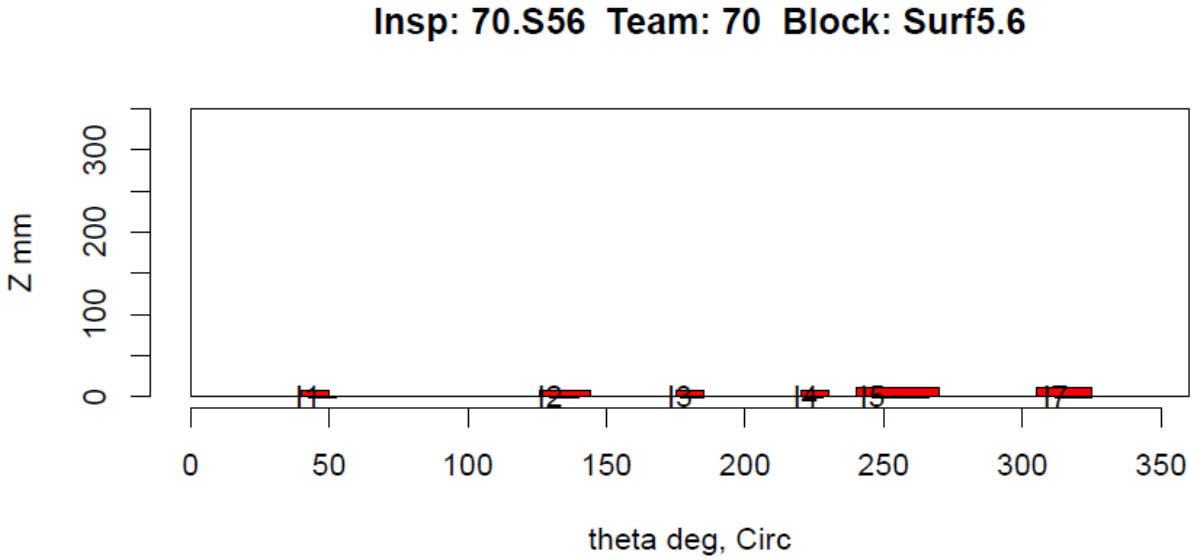
Insp: 70.S56 Team: 70 Block: Surf5.6
Z mm
0
100
200
300
0
50
100
150
200
250
300
350
theta deg, Circ
I1
I2
I3
I4
I5
I7

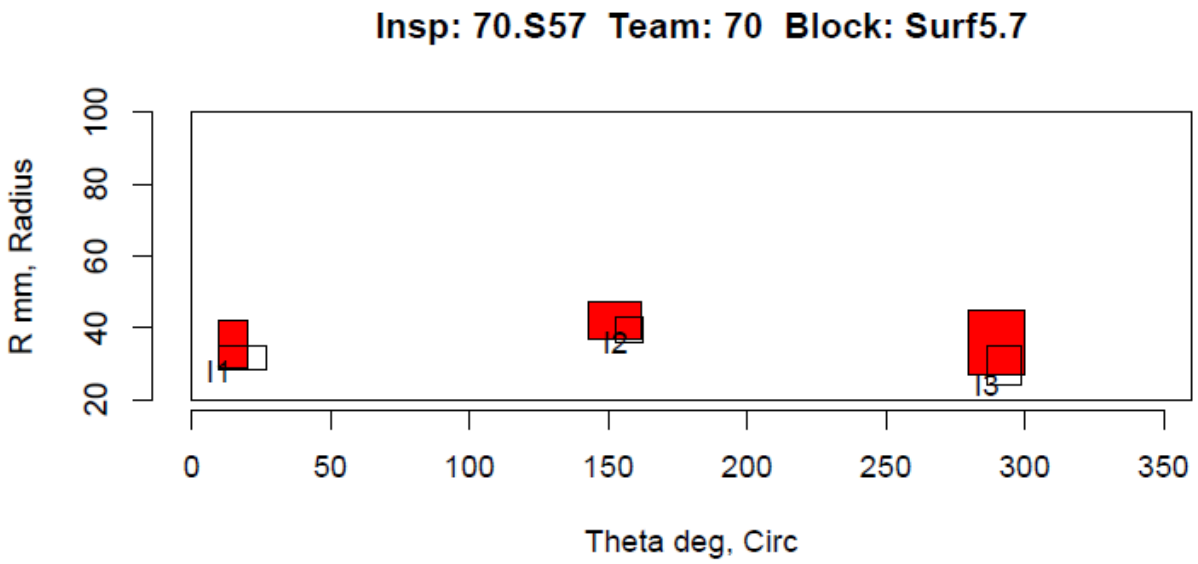
Insp: 70.S57 Team: 70 Block: Surf5.7
R mm, Radius
20
40
60
80
100
0
50
100
150
200
250
300
350
Theta deg, Circ
I1
I2
I3

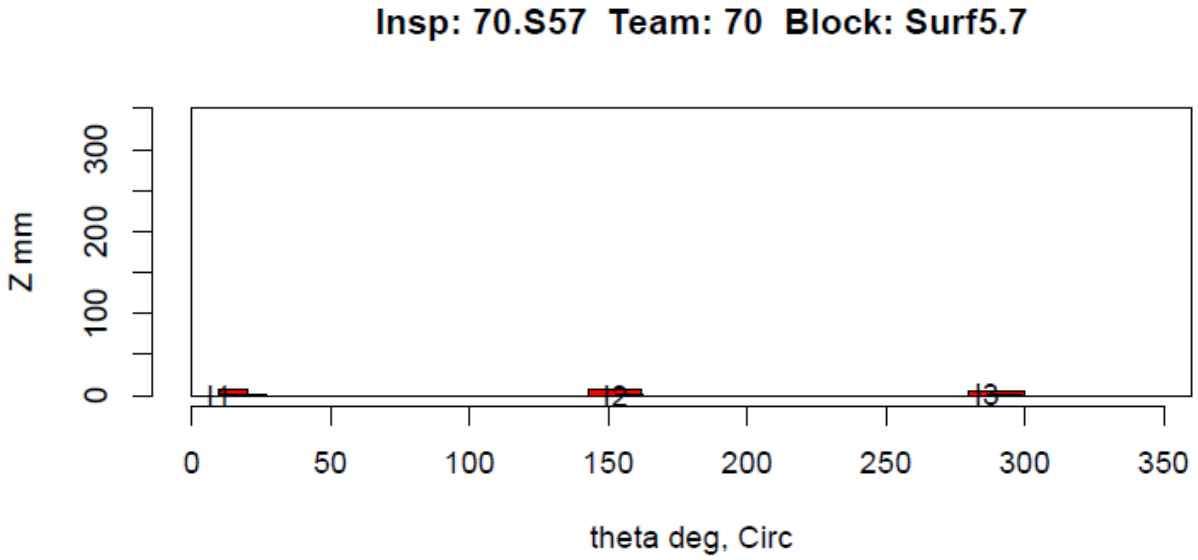
Insp: 70.S57 Team: 70 Block: Surf5.7
Z mm
0
100
200
300
0
50
100
150
200
250
300
350
theta deg, Circ
I1
I2
I3

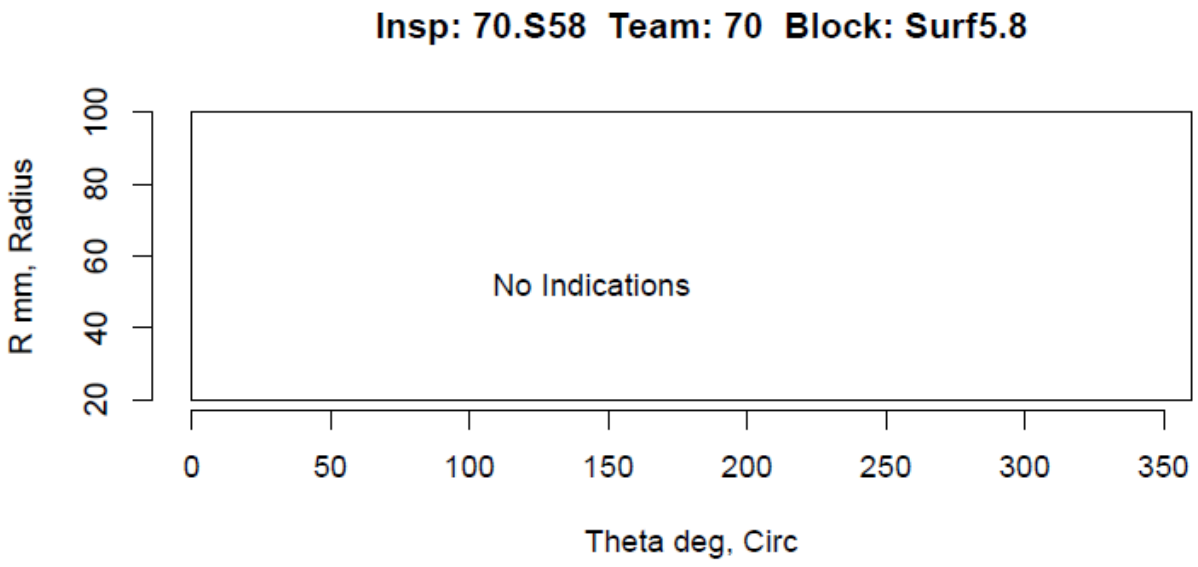
Insp: 70.S58 Team: 70 Block: Surf5.8
R mm, Radius
20
40
60
80
100
No Indications
0
50
100
150
200
250
300
350
Theta deg, Circ

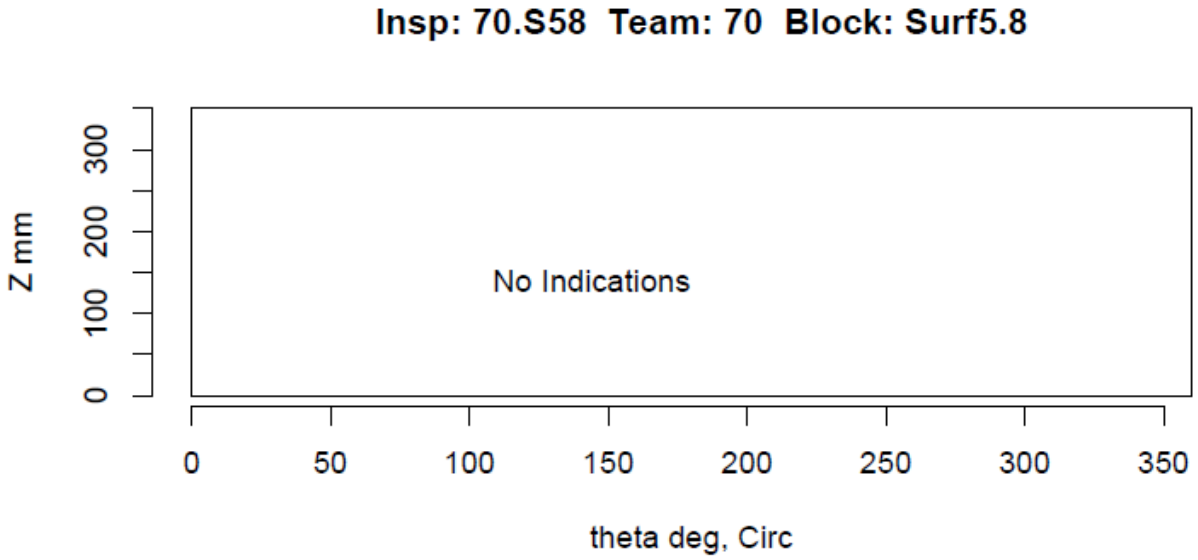
Insp: 70.S58 Team: 70 Block: Surf5.8
Z mm
0
100
200
300
No Indications
0
50
100
150
200
250
300
350
theta deg, Circ

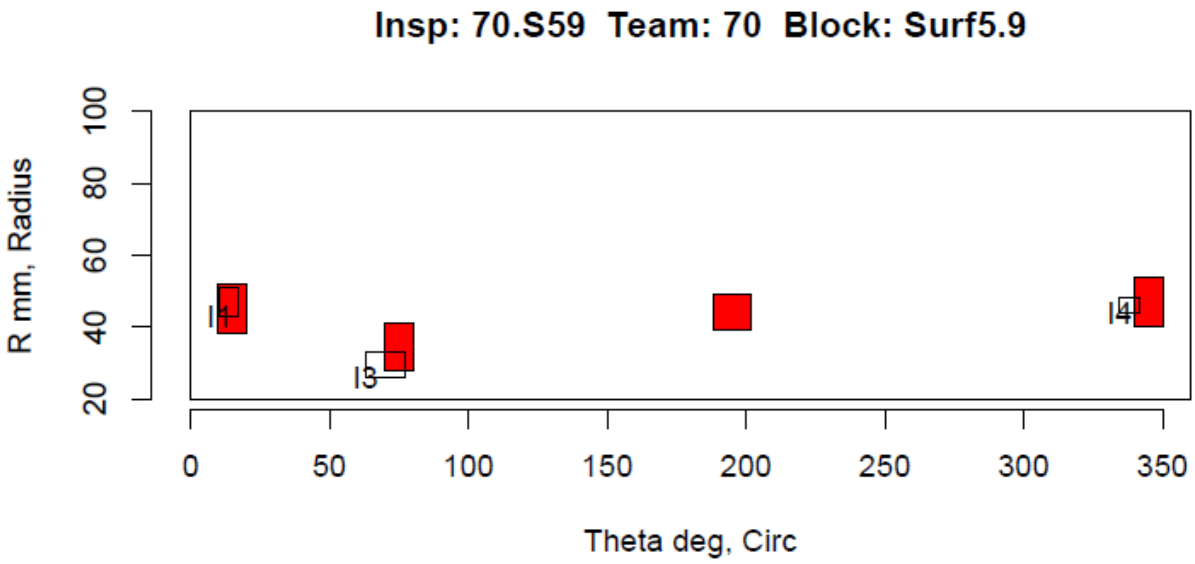
Insp: 70.S59 Team: 70 Block: Surf5.9
R mm, Radius
20
40
60
80
100
0
50
100
150
200
250
300
350
Theta deg, Circ

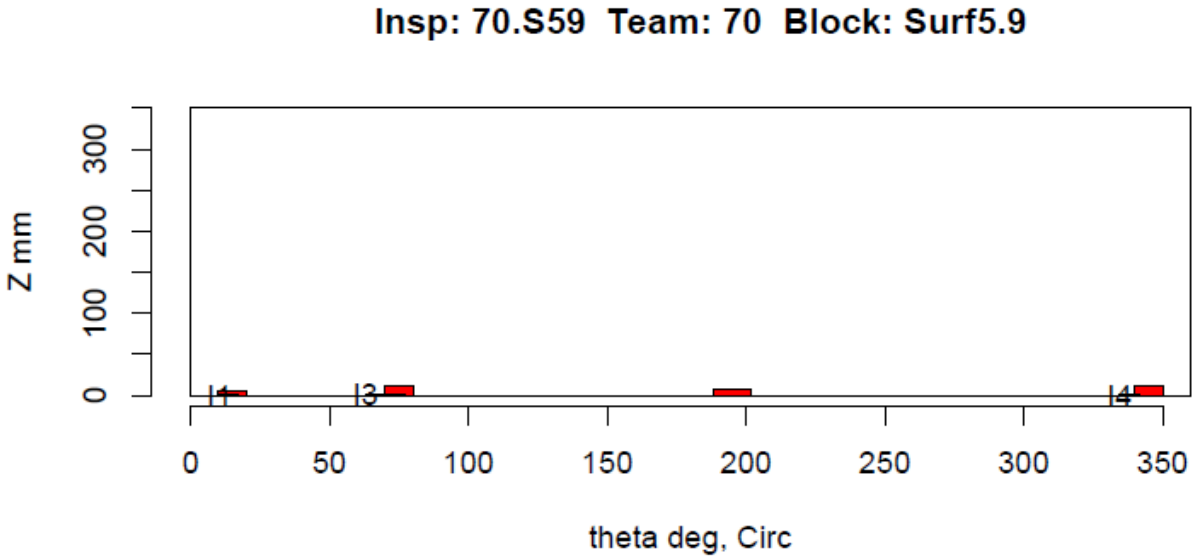
Insp: 70.S59 Team: 70 Block: Surf5.9
Z mm
0
100
200
300
0
50
100
150
200
250
300
350
theta deg, Circ

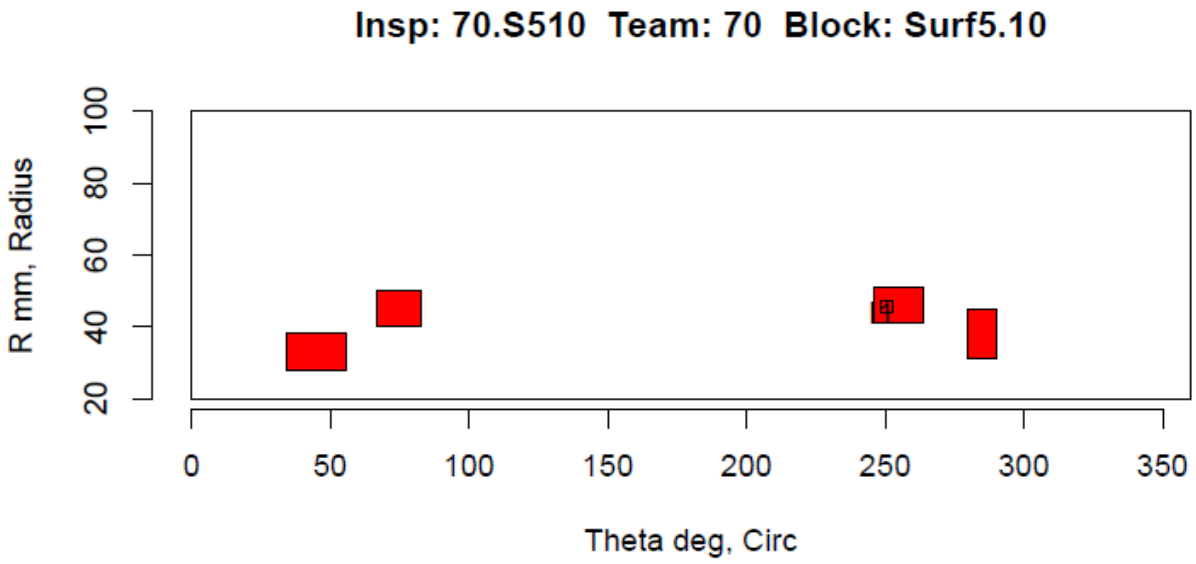
Insp: 70.S510 Team: 70 Block: Surf5.10
R mm, Radius
20
40
60
80
100
0
50
100
150
200
250
300
350
Theta deg, Circ

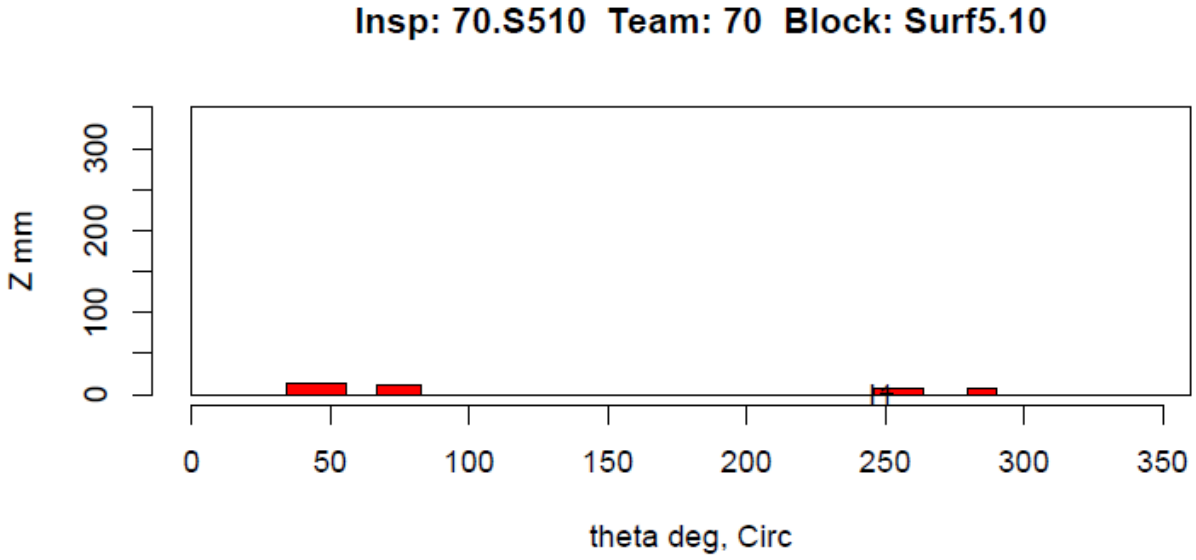
Insp: 70.S510 Team: 70 Block: Surf5.10
Z mm
0
100
200
300
0
50
100
150
200
250
300
350
theta deg, Circ

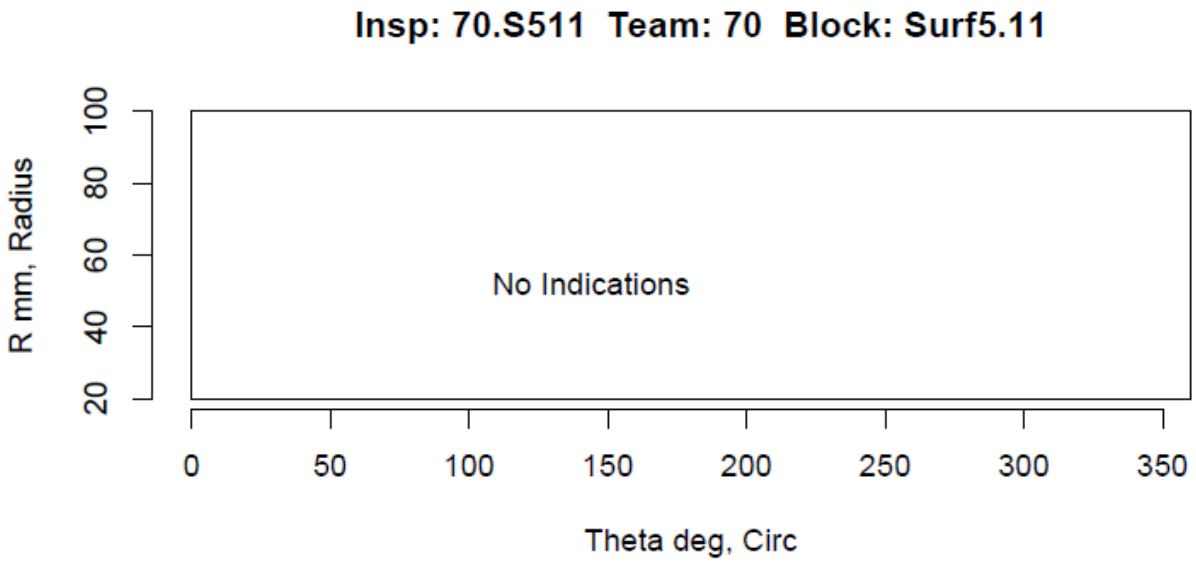
Insp: 70.S511 Team: 70 Block: Surf5.11
R mm, Radius
20
40
60
80
100
No Indications
0
50
100
150
200
250
300
350
Theta deg, Circ

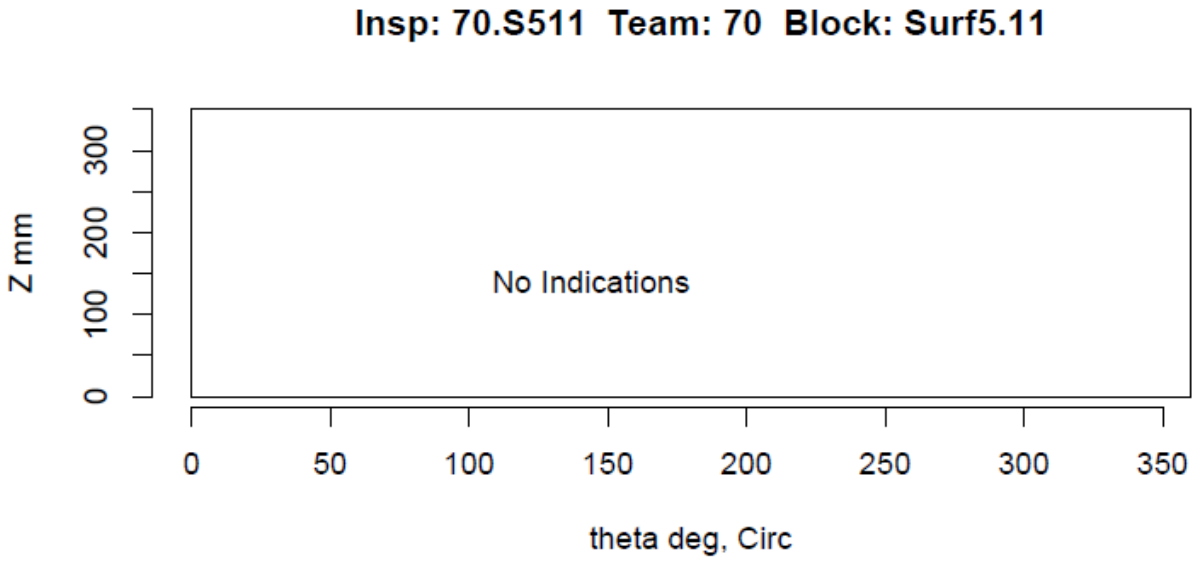
Insp: 70.S511 Team: 70 Block: Surf5.11
Z mm
0
100
200
300
No Indications
0
50
100
150
200
250
300
350
theta deg, Circ

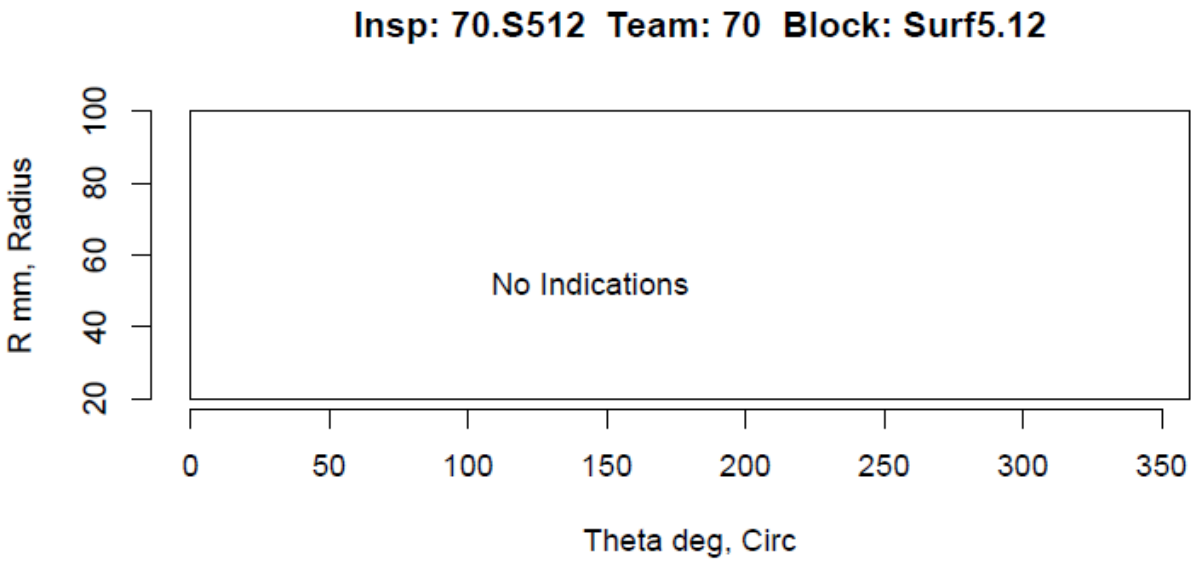
Insp: 70.S512 Team: 70 Block: Surf5.12
R mm, Radius
20
40
60
80
100
No Indications
0
50
100
150
200
250
300
350
Theta deg, Circ

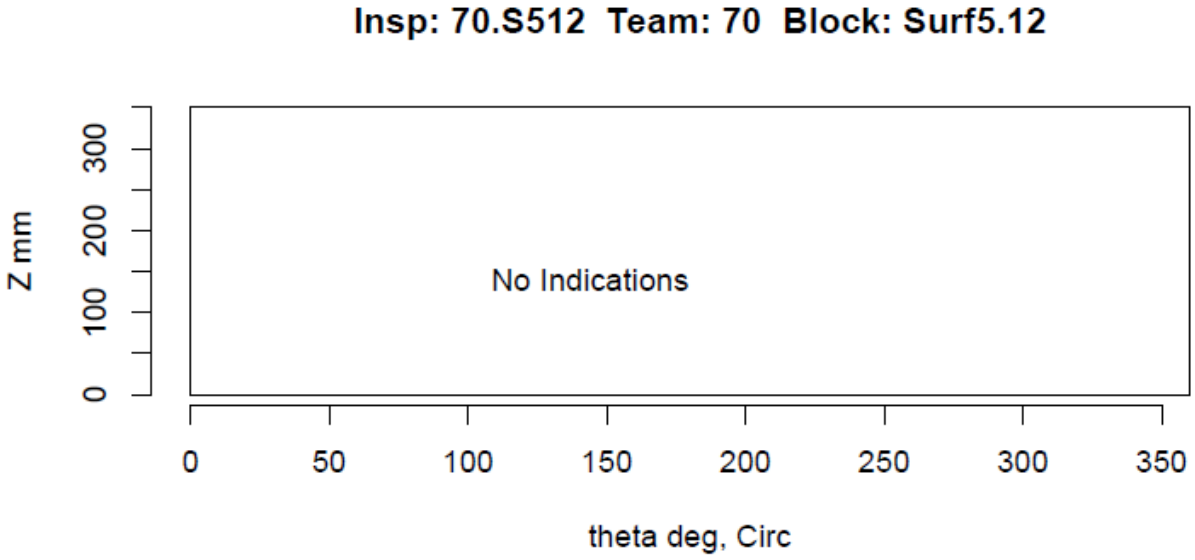
Insp: 70.S512 Team: 70 Block: Surf5.12
Z mm
0
100
200
300
No Indications
0
50
100
150
200
250
300
350
theta deg, Circ

.

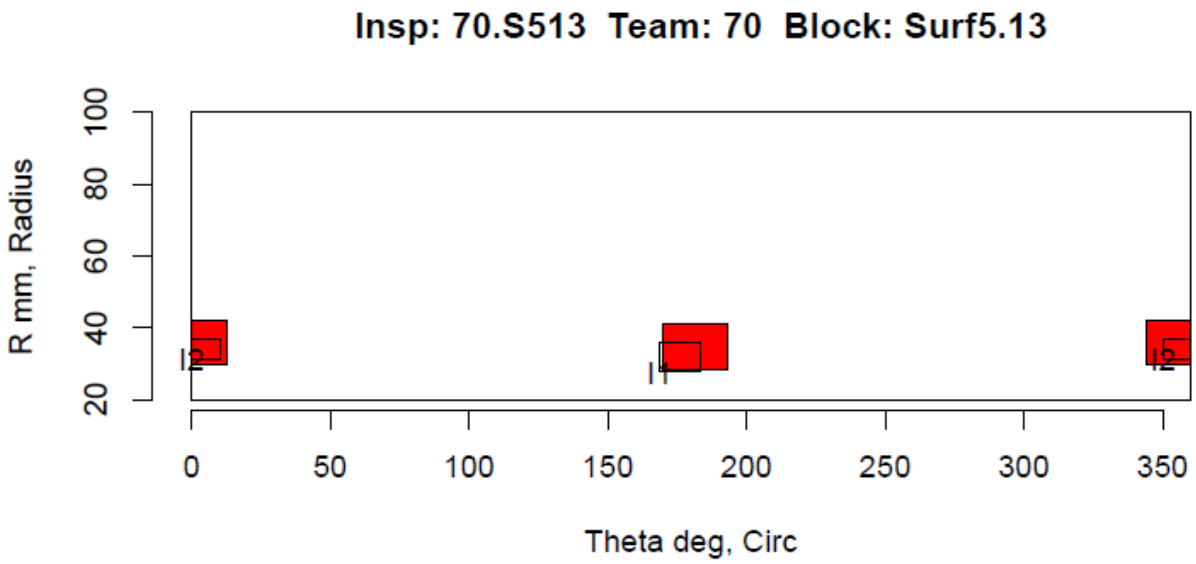
Insp: 70.S513 Team: 70 Block: Surf5.13
R mm, Radius
20
40
60
80
100
0
50
100
150
200
250
300
350
Theta deg, Circ

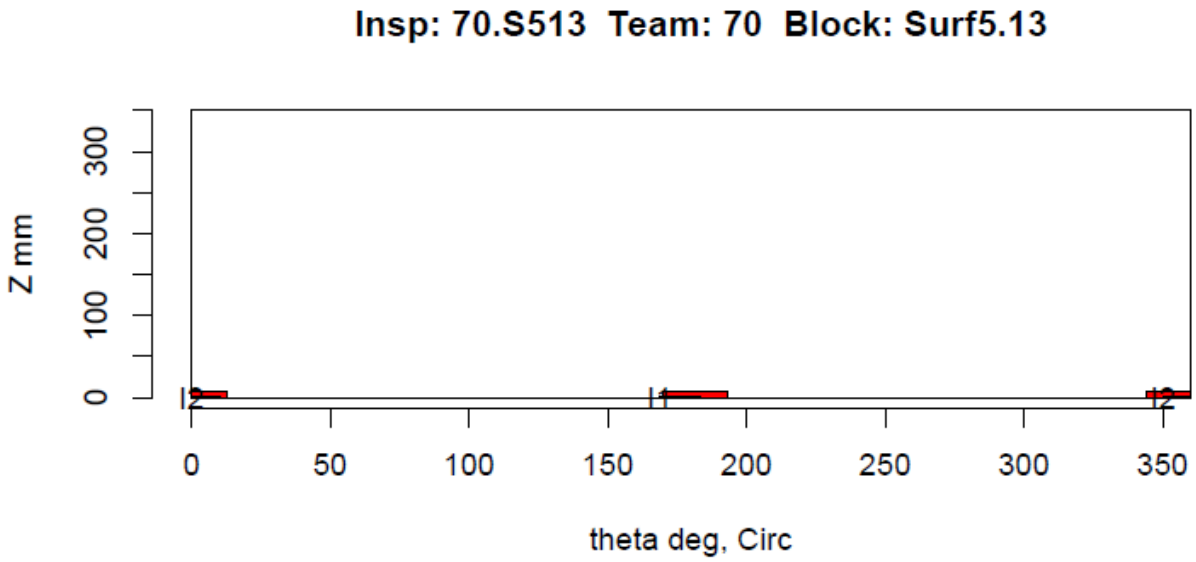
Insp: 70.S513 Team: 70 Block: Surf5.13
Z mm
0
100
200
300
0
50
100
150
200
250
300
350
theta deg, Circ

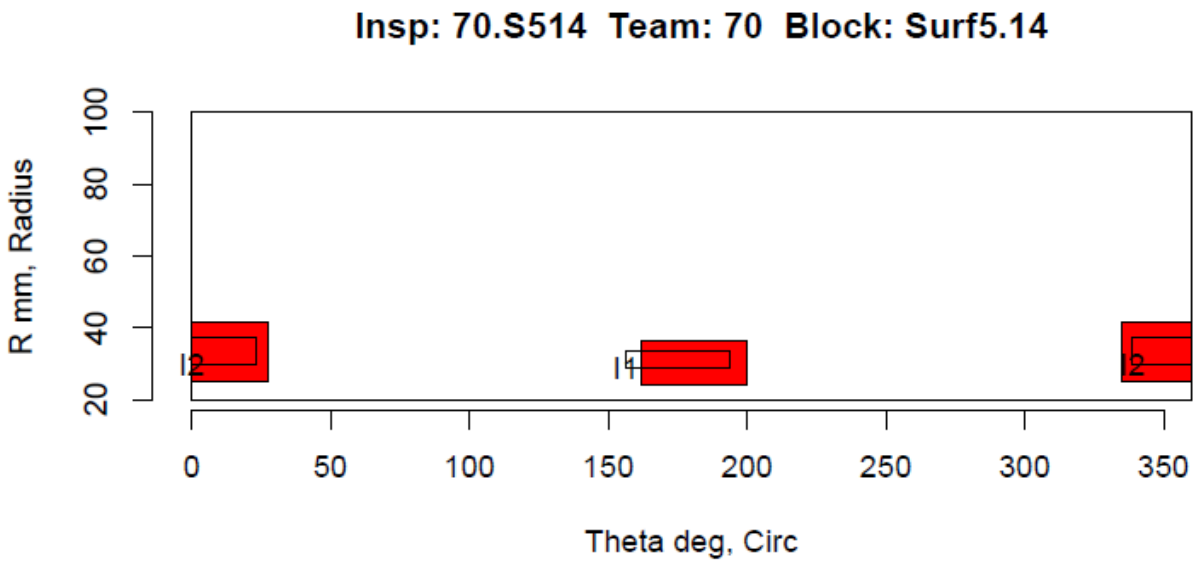
Insp: 70.S514 Team: 70 Block: Surf5.14
R mm, Radius
20
40
60
80
100
0
50
100
150
200
250
300
350
Theta deg, Circ

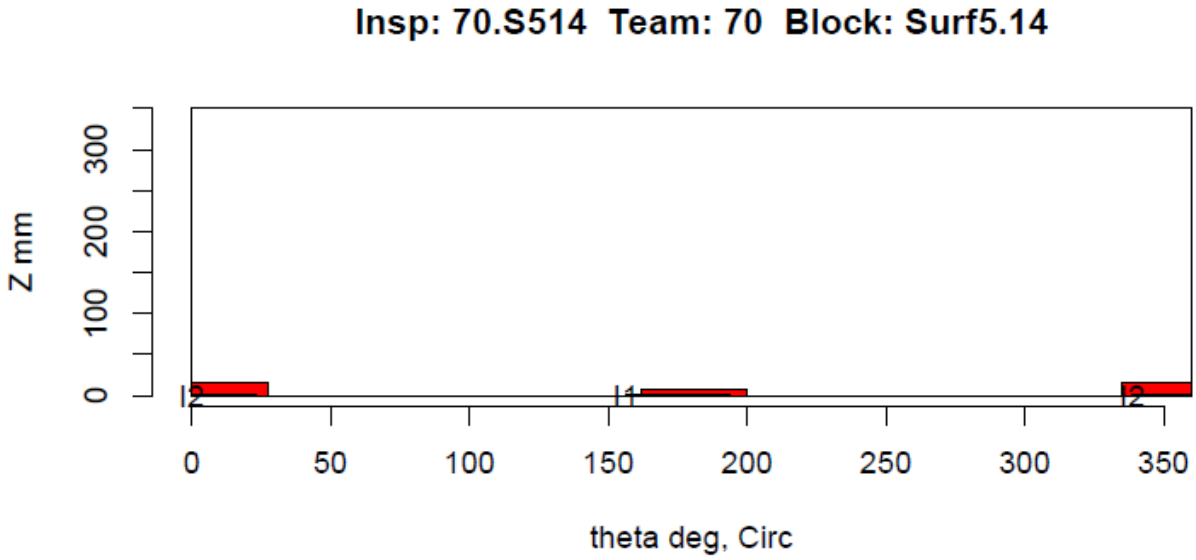
Insp: 70.S514 Team: 70 Block: Surf5.14
Z mm
0
100
200
300
0
50
100
150
200
250
300
350
theta deg, Circ

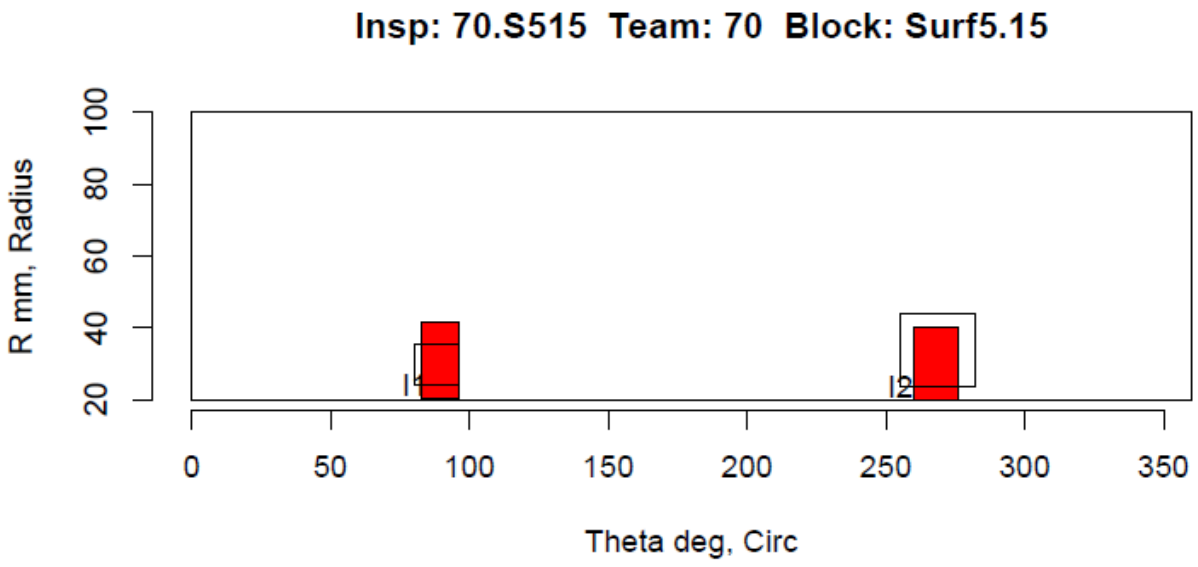
Insp: 70.S515 Team: 70 Block: Surf5.15
R mm, Radius
20
40
60
80
100
0
50
100
150
200
250
300
350
Theta deg, Circ
I1
I2

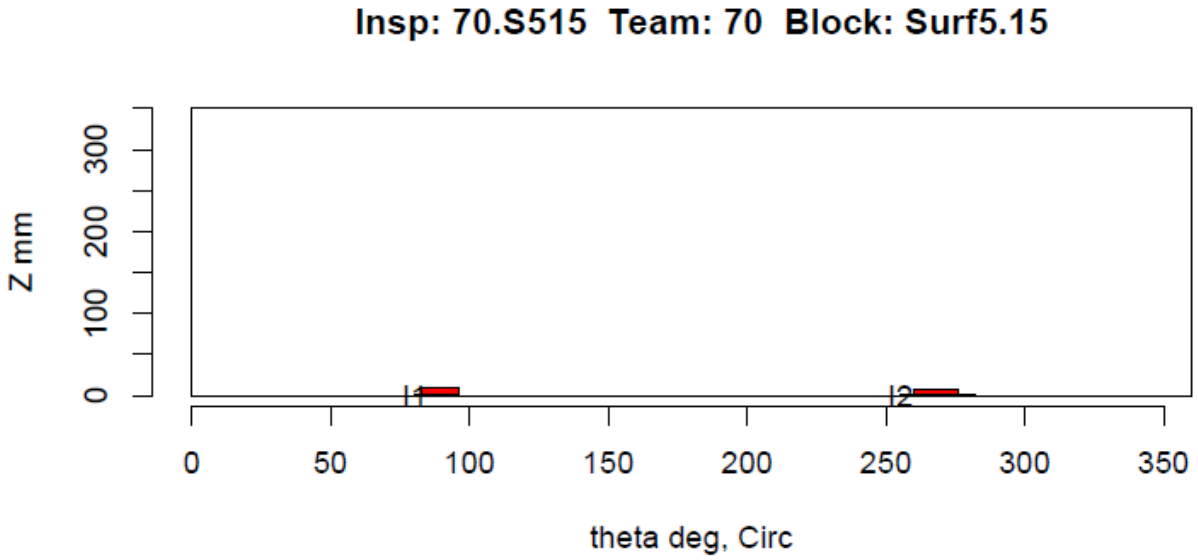
Insp: 70.S515 Team: 70 Block: Surf5.15
Z mm
0
100
200
300
0
50
100
150
200
250
300
350
theta deg, Circ
I1
I2

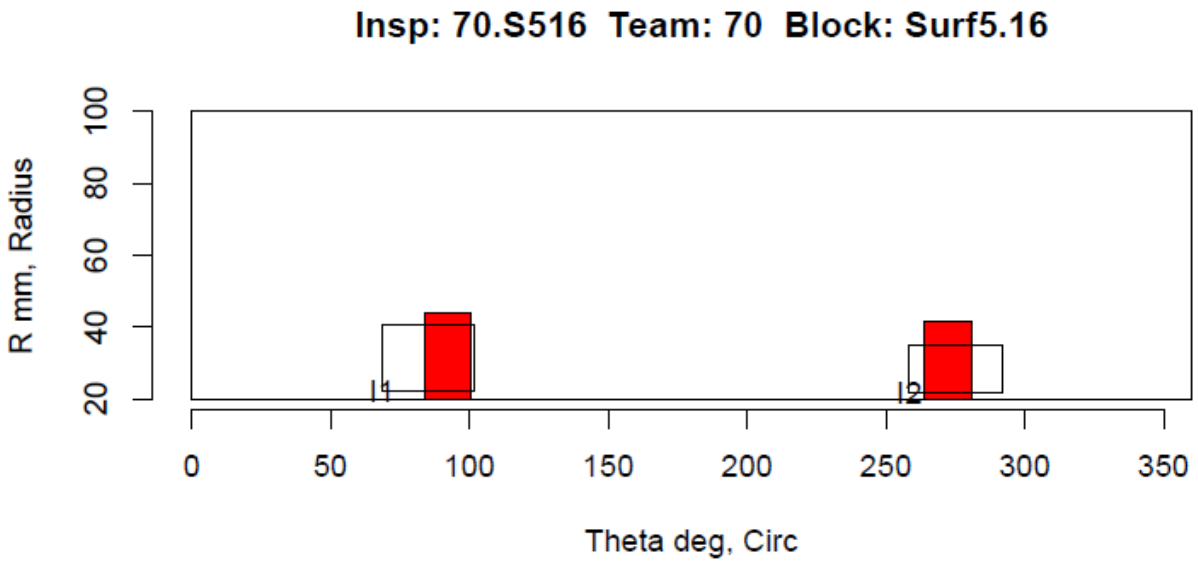
Insp: 70.S516 Team: 70 Block: Surf5.16
R mm, Radius
20
40
60
80
100
0
50
100
150
200
250
300
350
Theta deg, Circ

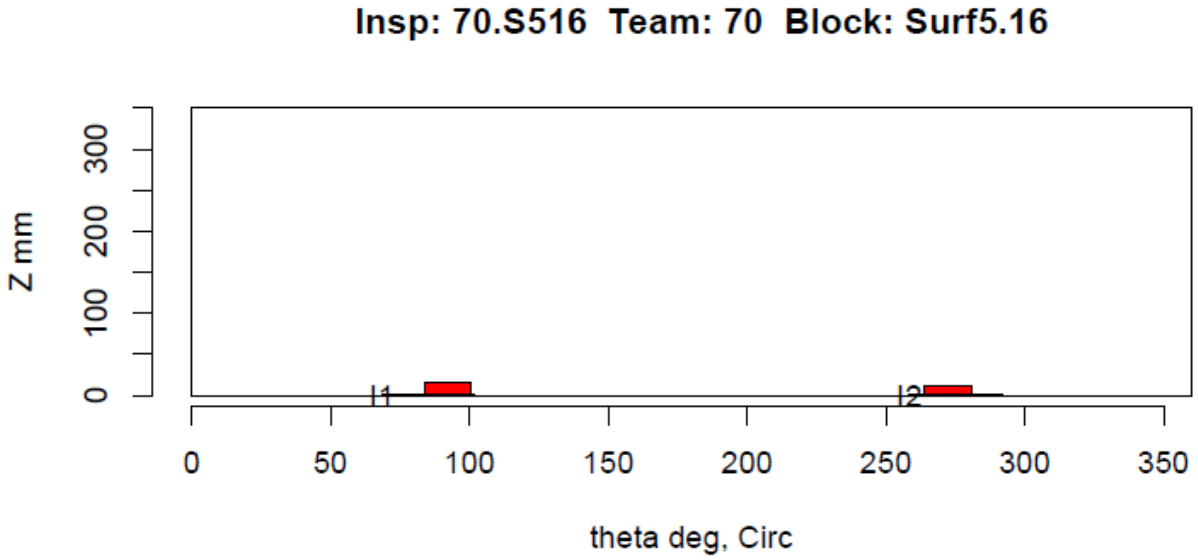
Insp: 70.S516 Team: 70 Block: Surf5.16
Z mm
0
100
200
300
0
50
100
150
200
250
300
350
theta deg, Circ

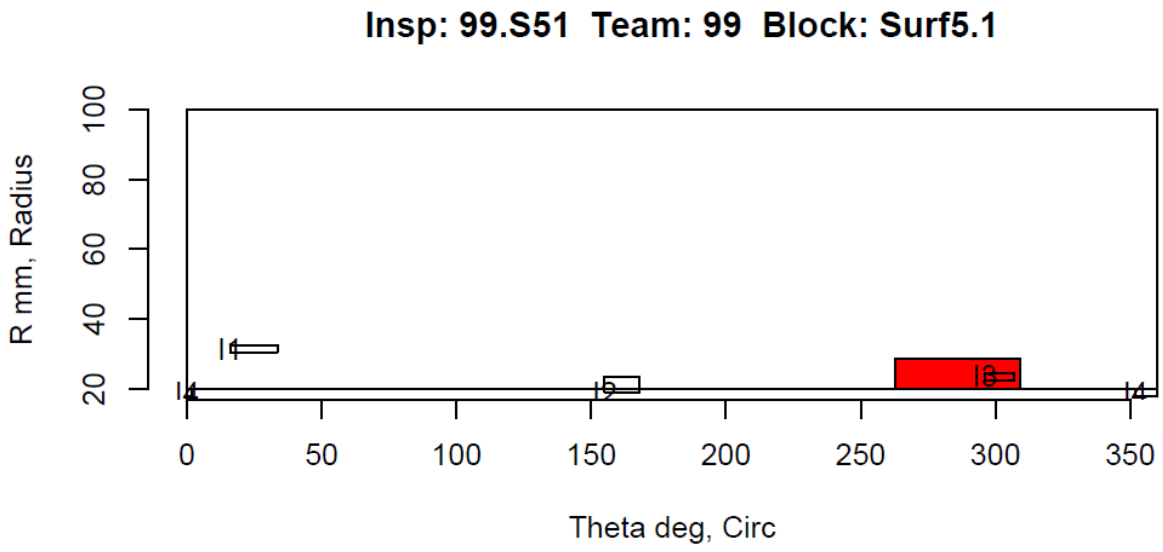
Insp: 99.S51 Team: 99 Block: Surf5.1
R mm, Radius
20
40
60
80
100
0
50
100
150
200
250
300
350
Theta deg, Circ

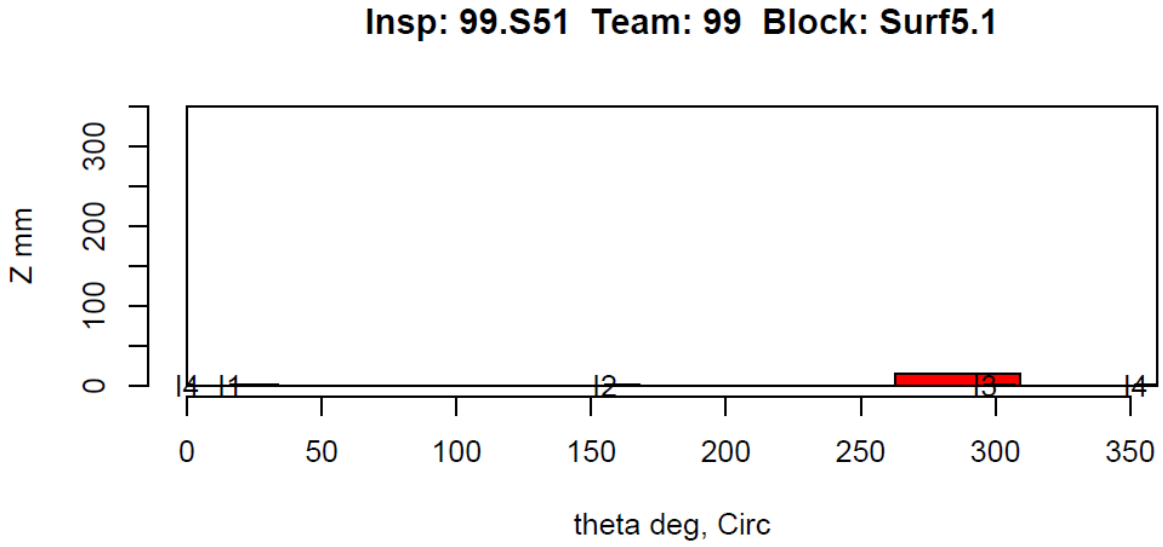
Insp: 99.S51 Team: 99 Block: Surf5.1
Z mm
0
100
200
300
0
50
100
150
200
250
300
350
theta deg, Circ

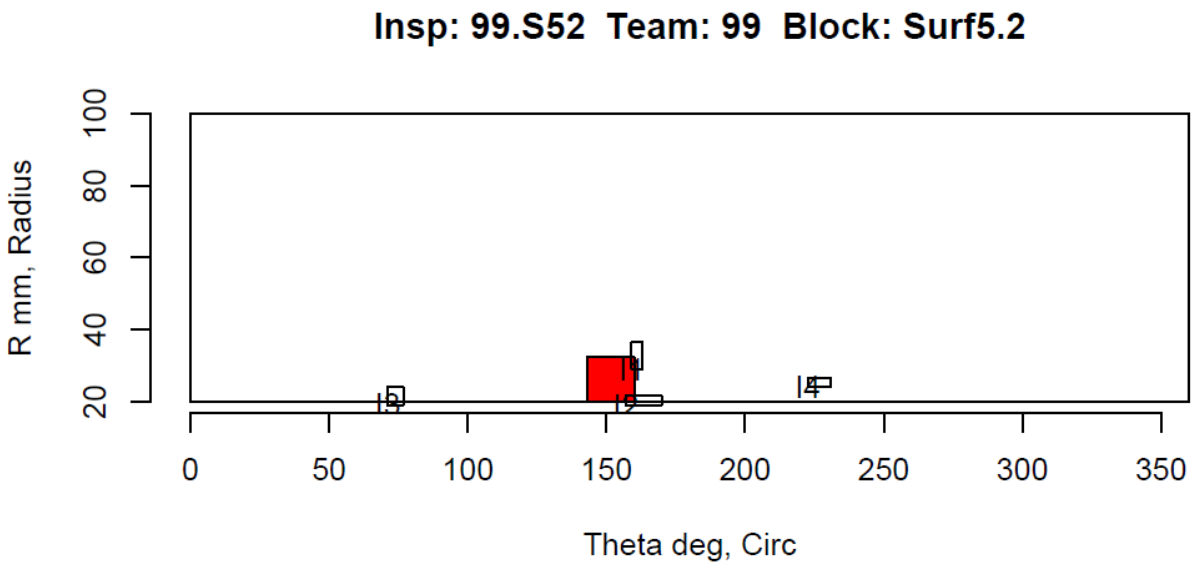
Insp: 99.S52 Team: 99 Block: Surf5.2
R mm, Radius
20
40
60
80
100
0
50
100
150
200
250
300
350
Theta deg, Circ

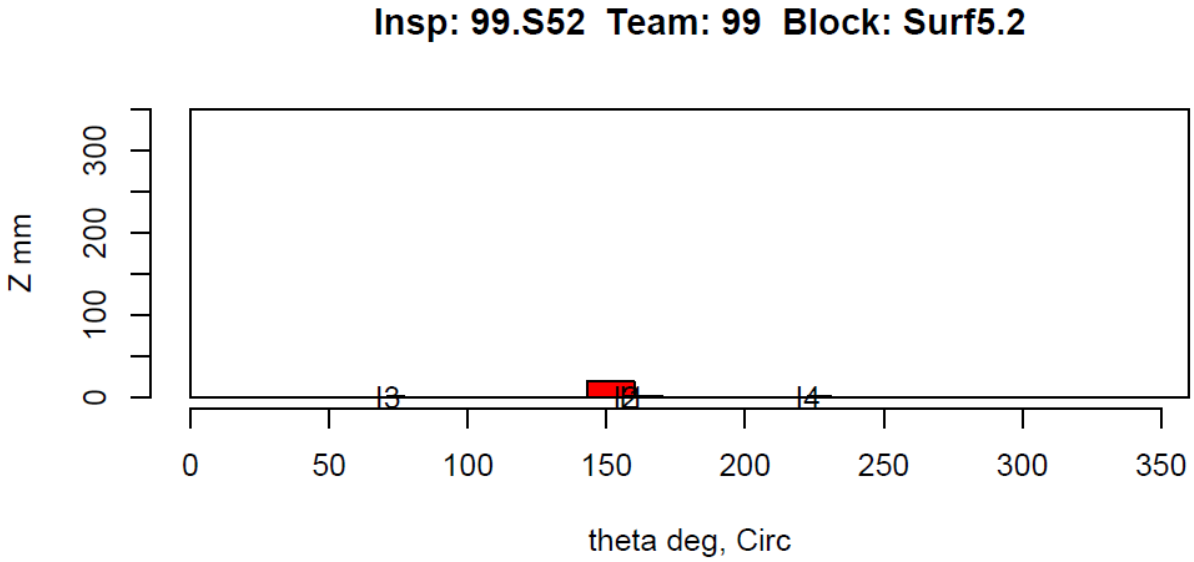
Insp: 99.S52 Team: 99 Block: Surf5.2
Z mm
0
100
200
300
0
50
100
150
200
250
300
350
theta deg, Circ

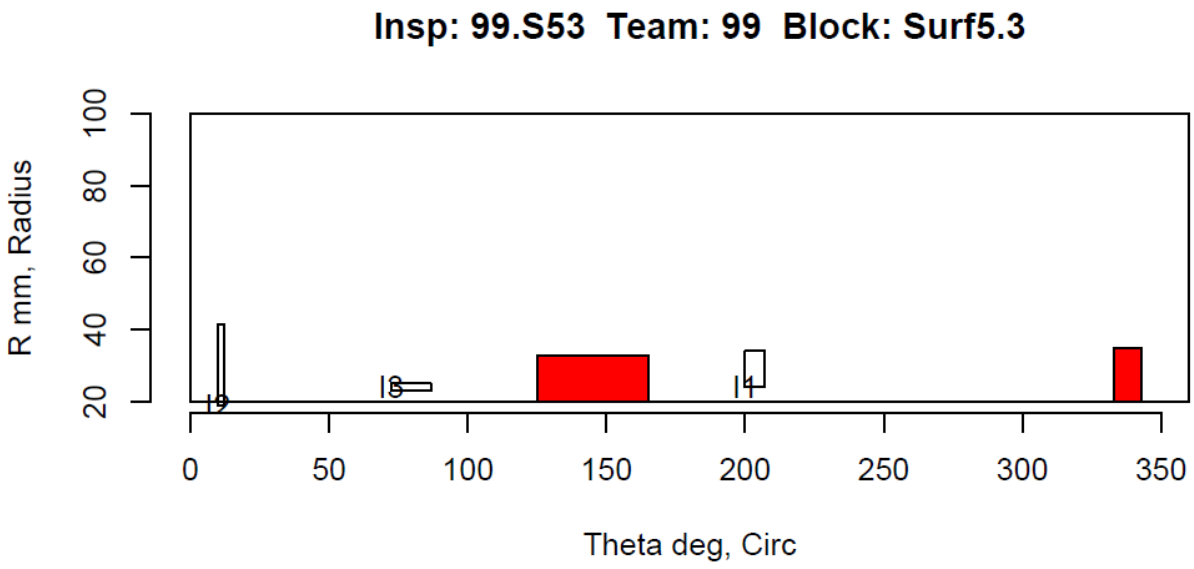
Insp: 99.S53 Team: 99 Block: Surf5.3
R mm, Radius
20
40
60
80
100
0
50
100
150
200
250
300
350
Theta deg, Circ

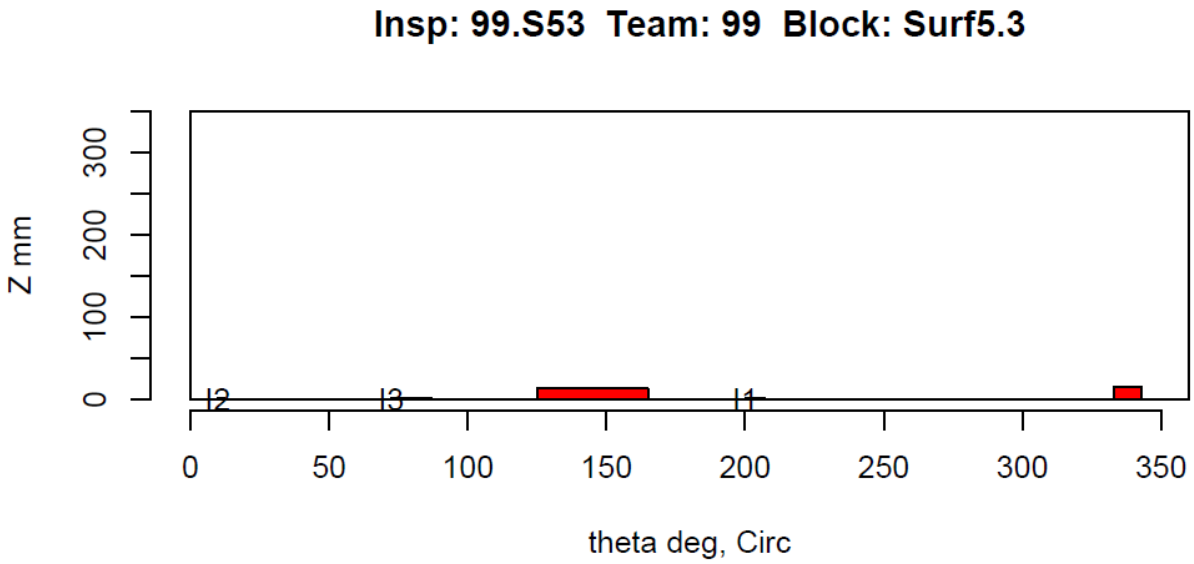
Insp: 99.S53 Team: 99 Block: Surf5.3
Z mm
0
100
200
300
0
50
100
150
200
250
300
350
theta deg, Circ

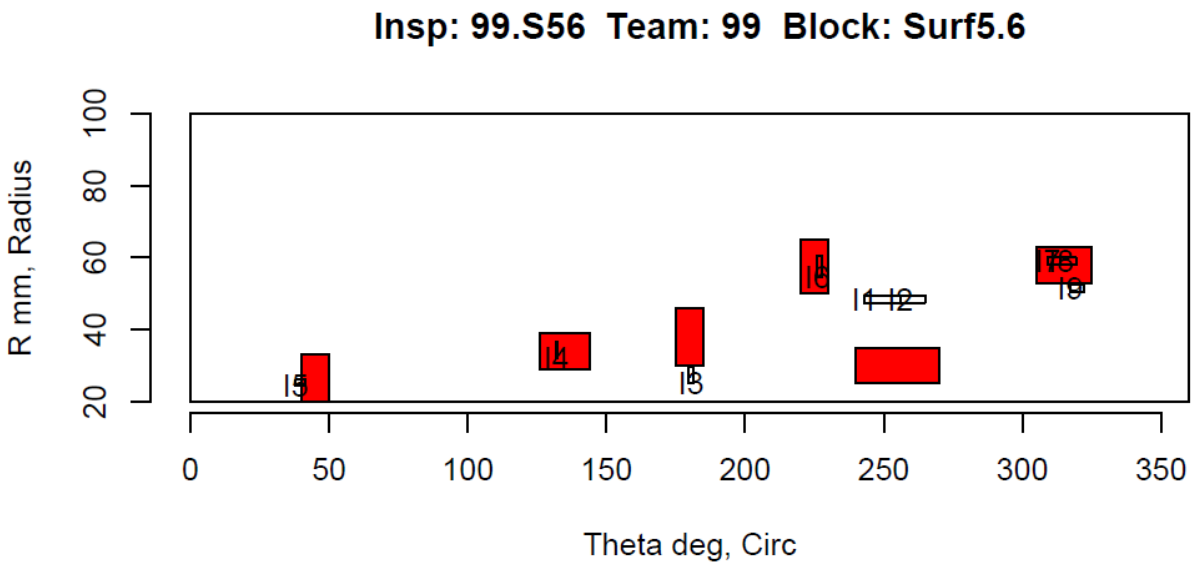
Insp: 99.S56 Team: 99 Block: Surf5.6
R mm, Radius
20
40
60
80
100
0
50
100
150
200
250
300
350
Theta deg, Circ

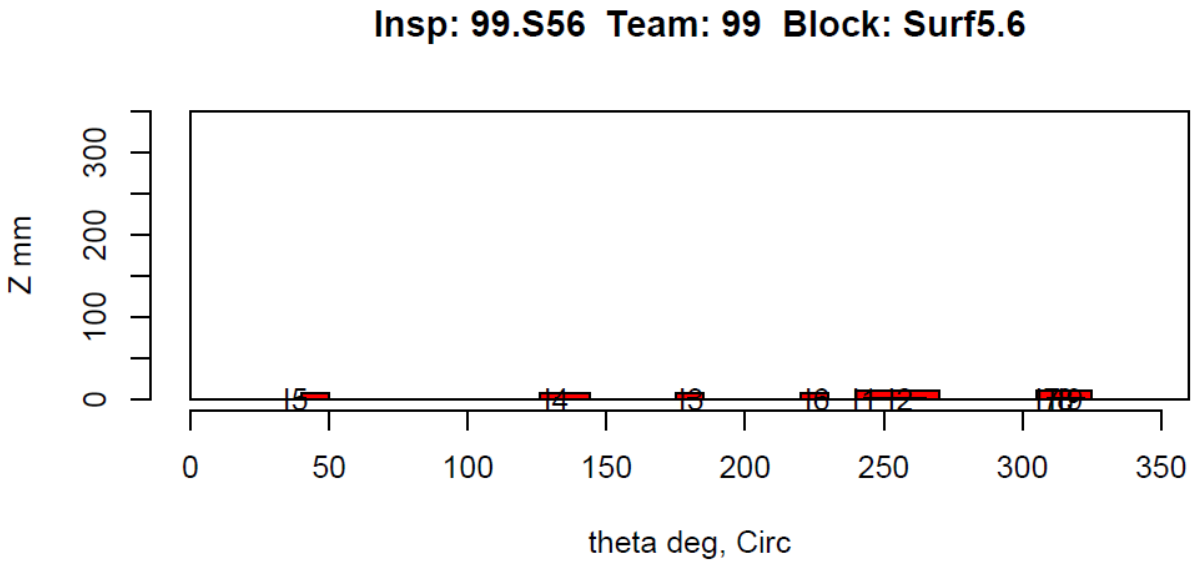
Insp: 99.S56 Team: 99 Block: Surf5.6
Z mm
0
100
200
300
0
50
100
150
200
250
300
350
theta deg, Circ

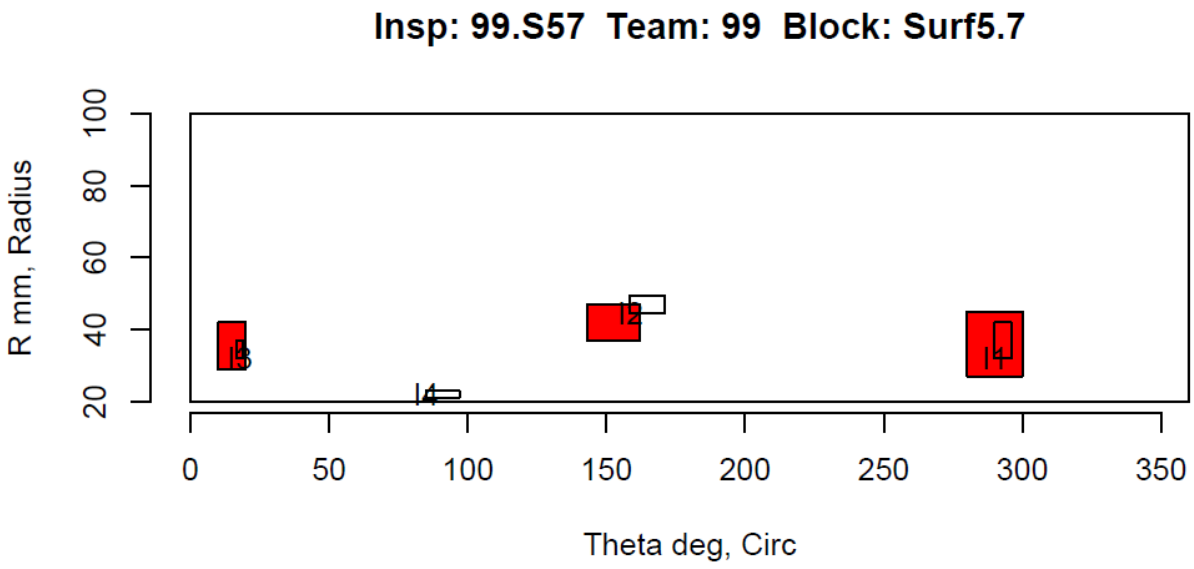
Insp: 99.S57 Team: 99 Block: Surf5.7
R mm, Radius
20
40
60
80
100
0
50
100
150
200
250
300
350
Theta deg, Circ

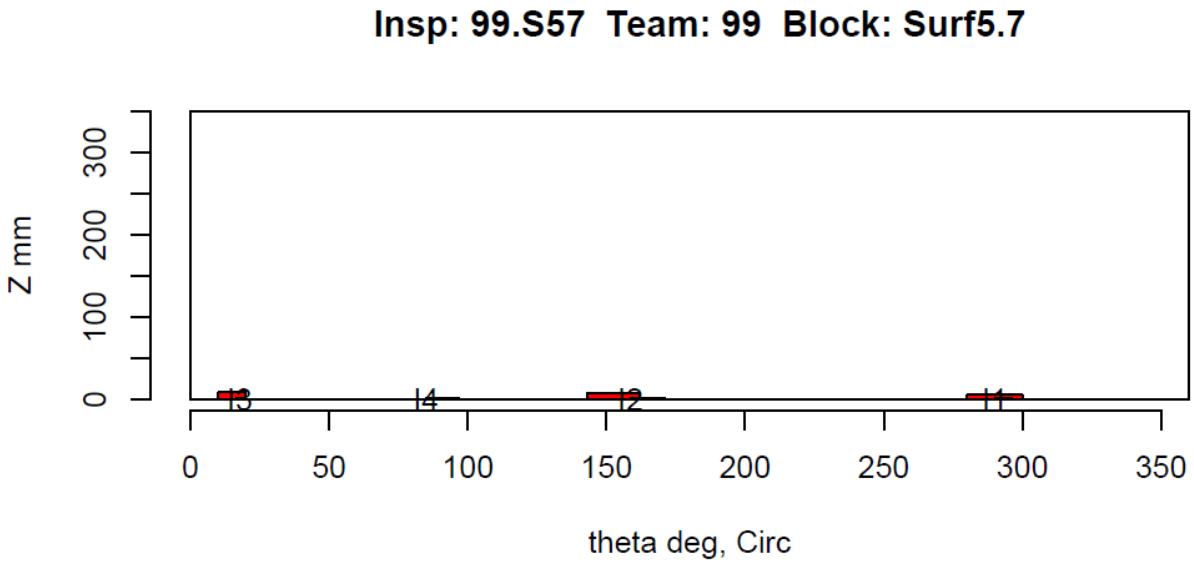
Insp: 99.S57 Team: 99 Block: Surf5.7
Z mm
0
100
200
300
0
50
100
150
200
250
300
350
theta deg, Circ

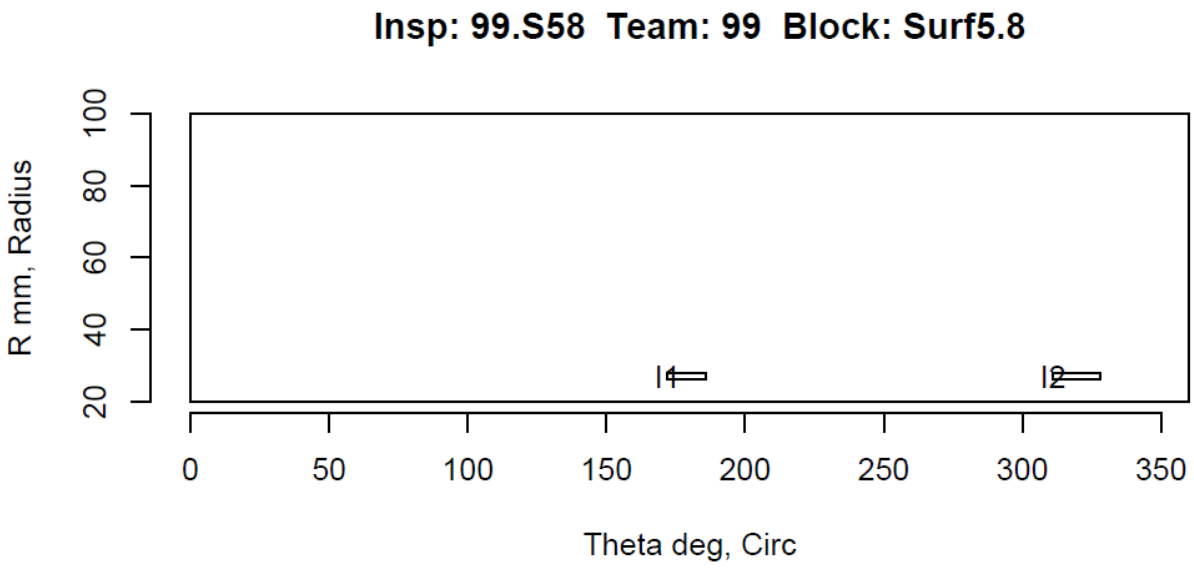
Insp: 99.S58 Team: 99 Block: Surf5.8
R mm, Radius
20
40
60
80
100
1
2
0
50
100
150
200
250
300
350
Theta deg, Circ

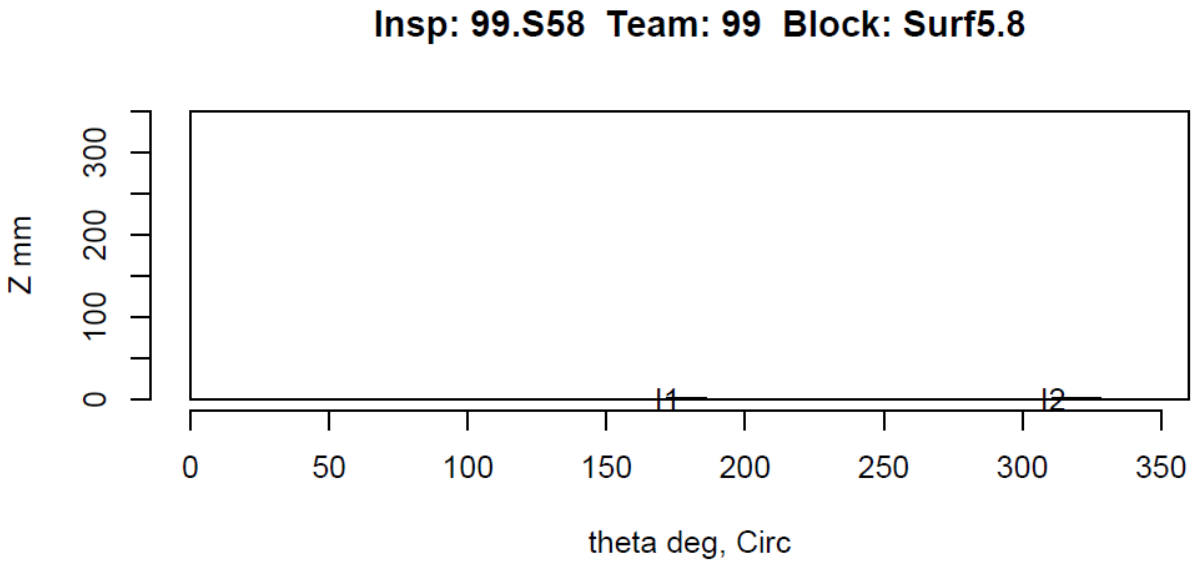
Insp: 99.S58 Team: 99 Block: Surf5.8
Z mm
0
100
200
300
1
2
0
50
100
150
200
250
300
350
theta deg, Circ

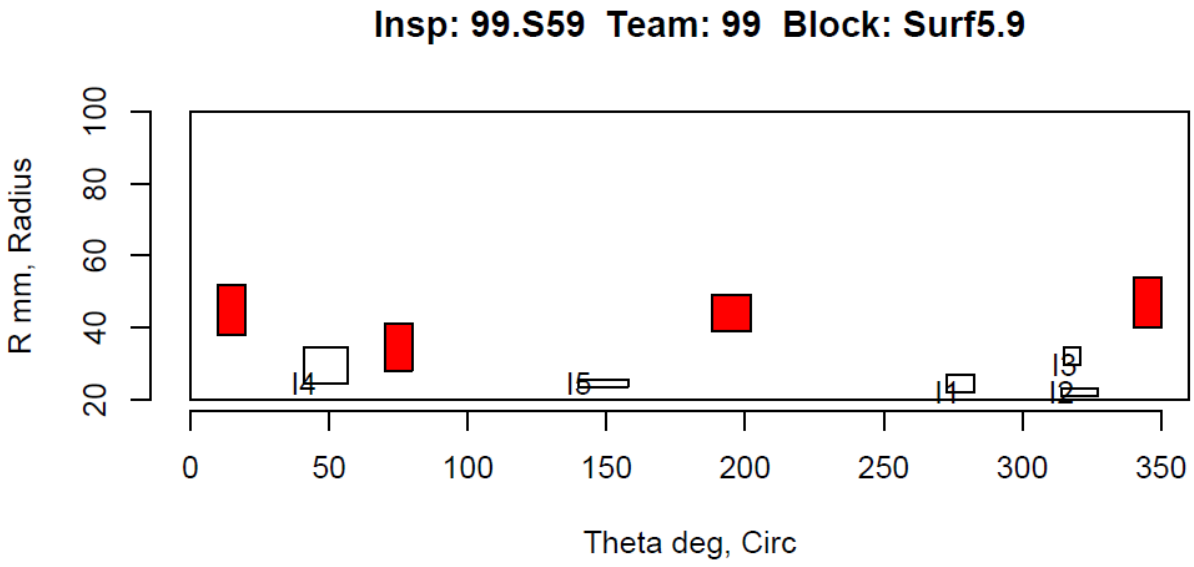
Insp: 99.S59 Team: 99 Block: Surf5.9
R mm, Radius
20
40
60
80
100
0
50
100
150
200
250
300
350
Theta deg, Circ
4
5
1
5
2

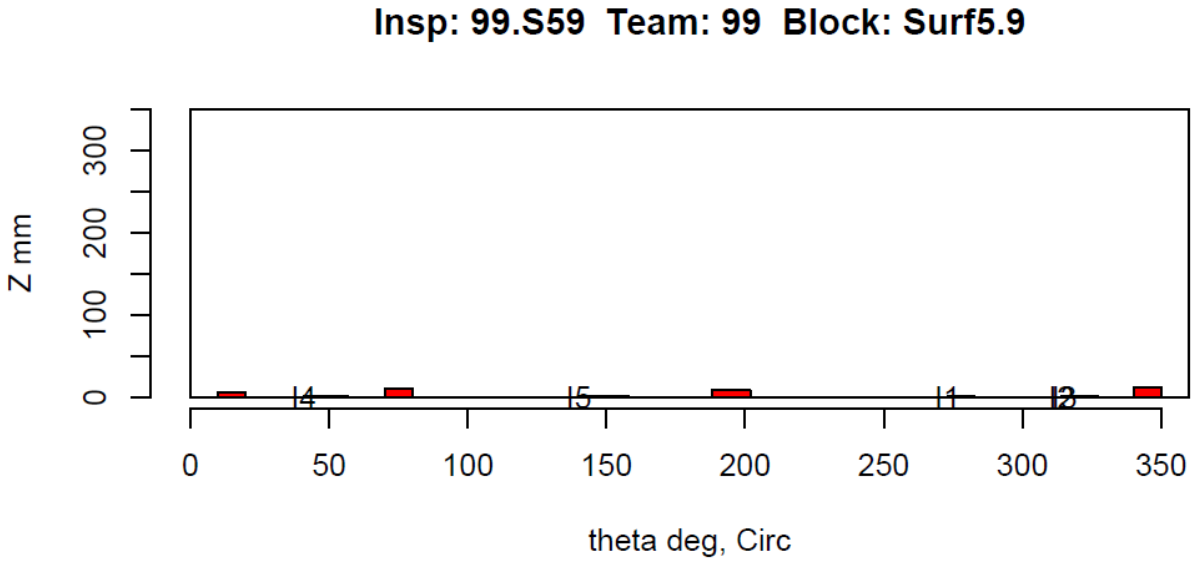
Insp: 99.S59 Team: 99 Block: Surf5.9
Z mm
0
100
200
300
0
50
100
150
200
250
300
350
theta deg, Circ
4
5
1
2

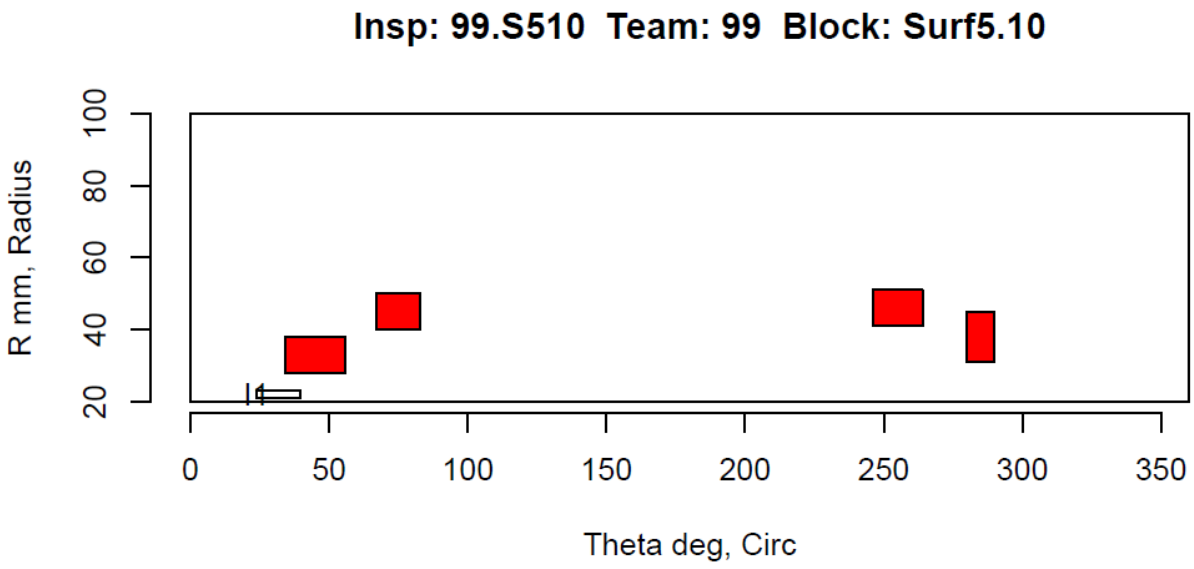
Insp: 99.S510 Team: 99 Block: Surf5.10
R mm, Radius
20
40
60
80
100
0
50
100
150
200
250
300
350
Theta deg, Circ

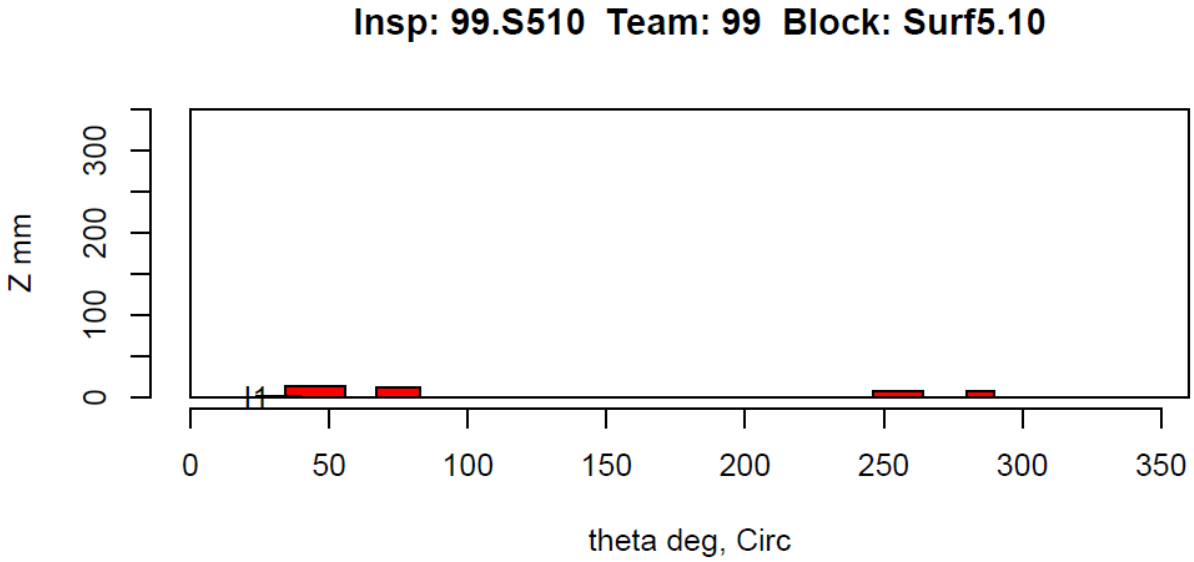
Insp: 99.S510 Team: 99 Block: Surf5.10
Z mm
0
100
200
300
0
50
100
150
200
250
300
350
theta deg, Circ

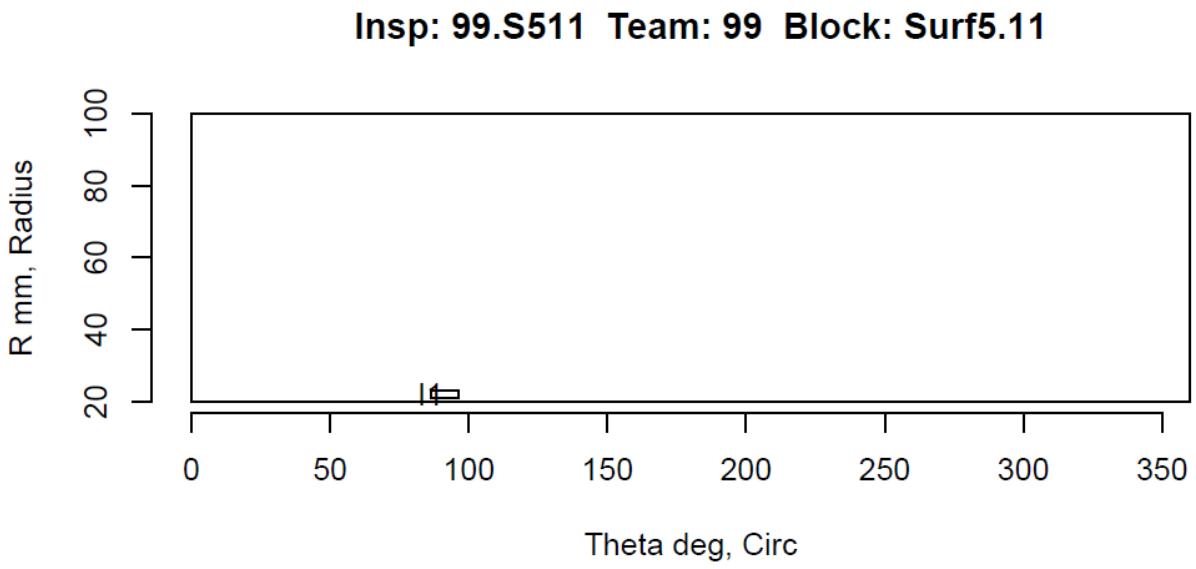
Insp: 99.S511 Team: 99 Block: Surf5.11
R mm, Radius
20
40
60
80
100
0
50
100
150
200
250
300
350
Theta deg, Circ

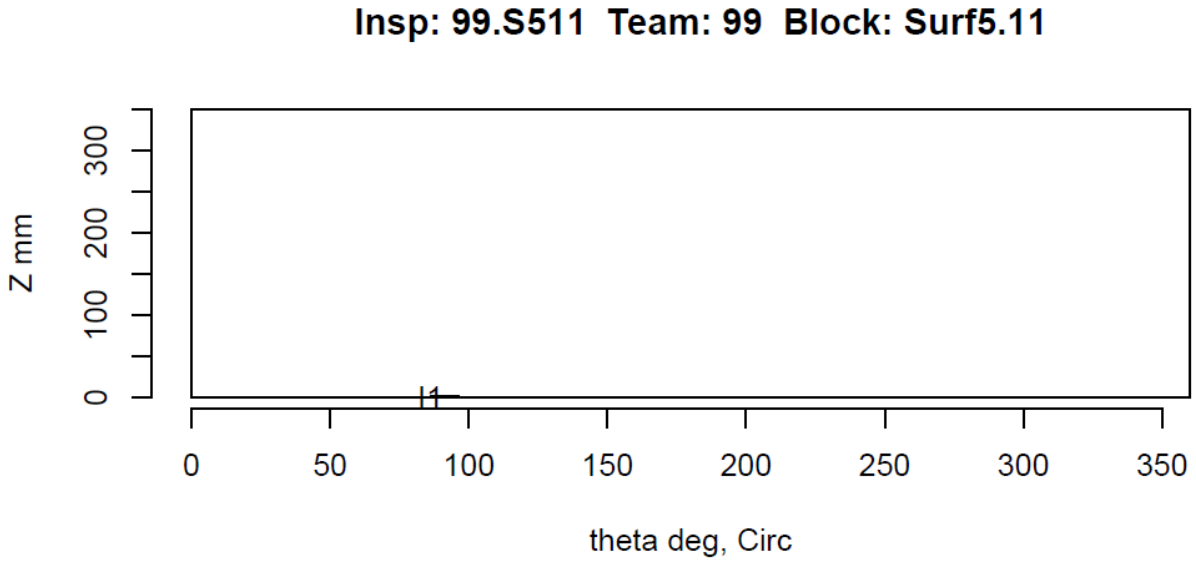
Insp: 99.S511 Team: 99 Block: Surf5.11
Z mm
0
100
200
300
0
50
100
150
200
250
300
350
theta deg, Circ

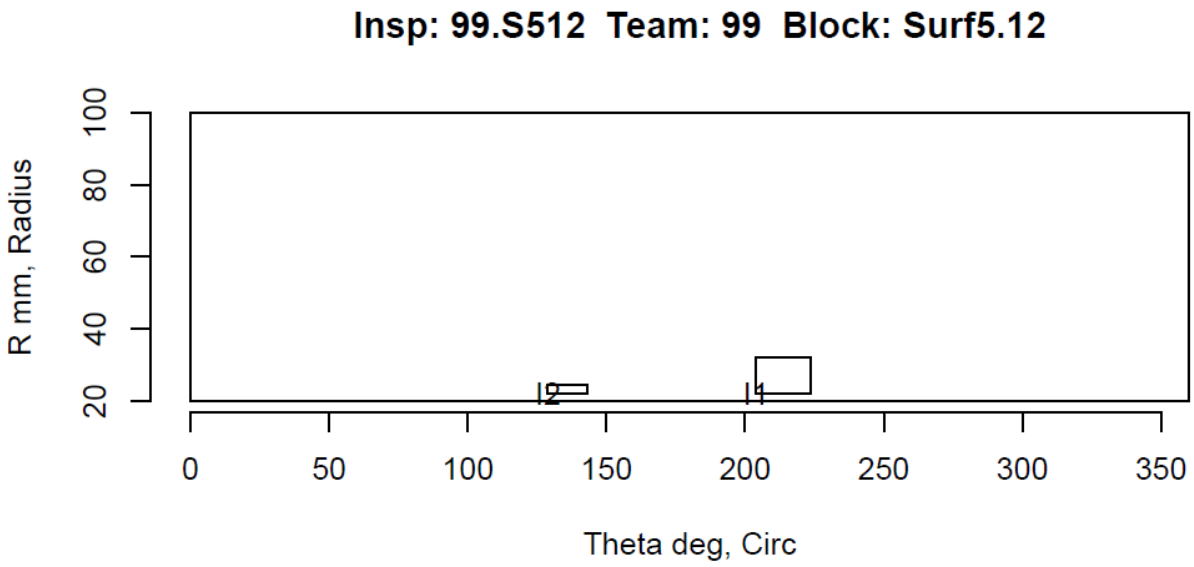
Insp: 99.S512 Team: 99 Block: Surf5.12
R mm, Radius
20
40
60
80
100
0
50
100
150
200
250
300
350
Theta deg, Circ
2
1

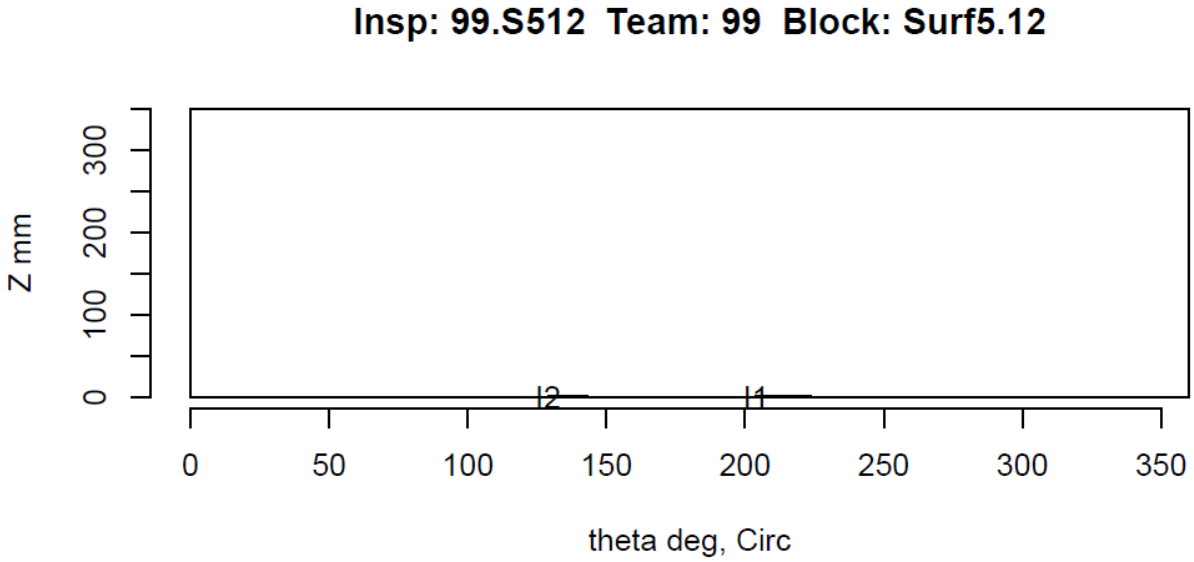
Insp: 99.S512 Team: 99 Block: Surf5.12
Z mm
0
100
200
300
0
50
100
150
200
250
300
350
theta deg, Circ
2
1

Appendix F

Block Hitograms for
Bottom-Mounted Instrumentation Tube Samples

Appendix F

Block Hitograms for
Bottom-Mounted Instrumentation Tube Samples

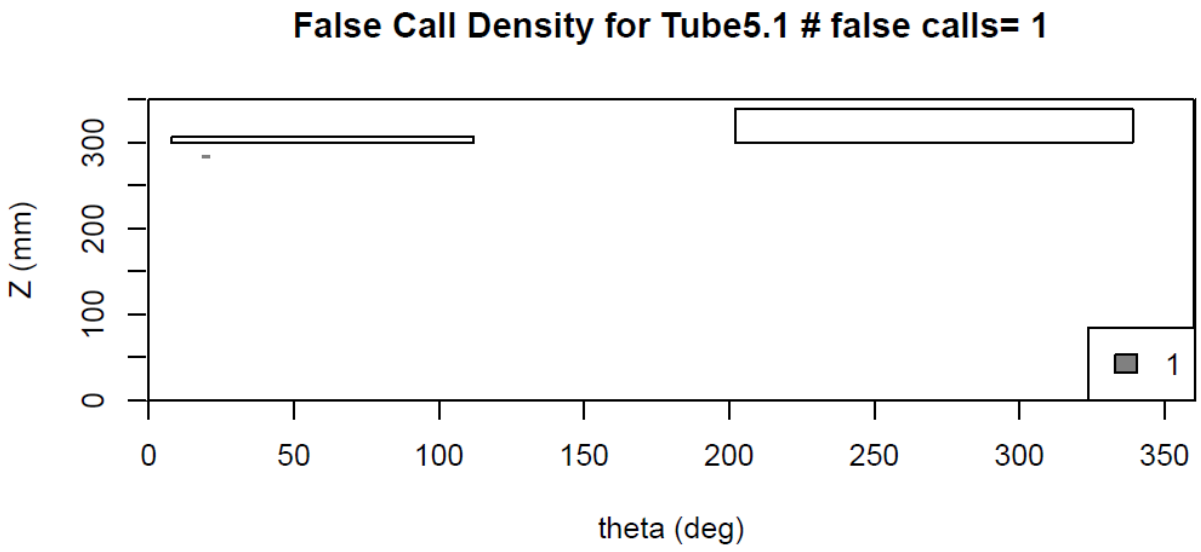
False Call Density for Tube5.1 # false calls= 1
Z (mm)
0
100
200
300
0
50
100
150
200
250
300
350
theta (deg)
1

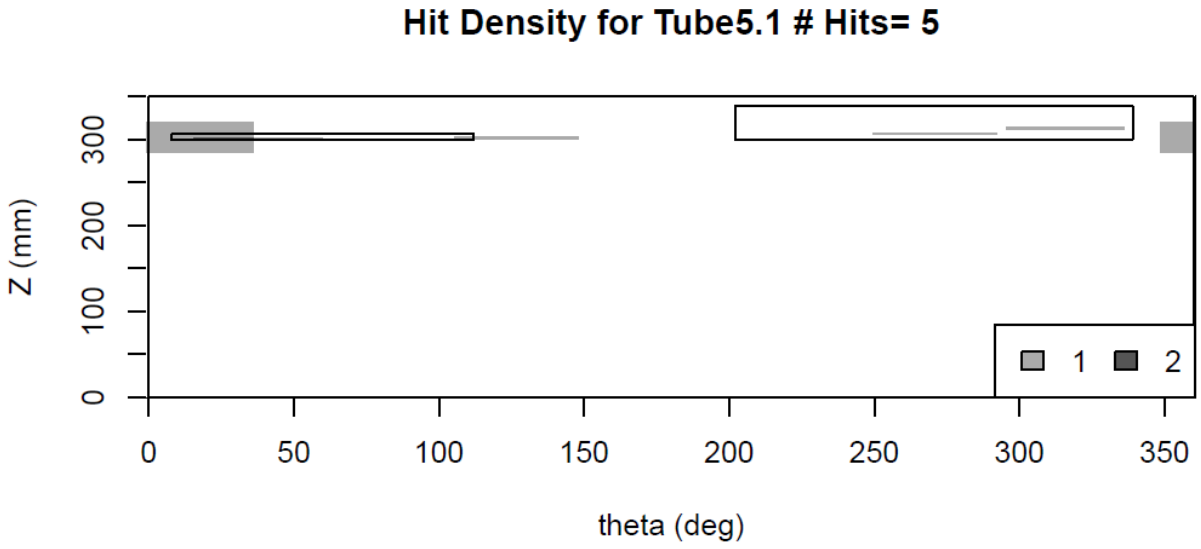
Hit Density for Tube5.1 # Hits= 5
Z (mm)
0
100
200
300
0
50
100
150
200
250
300
350
theta (deg)
1
2

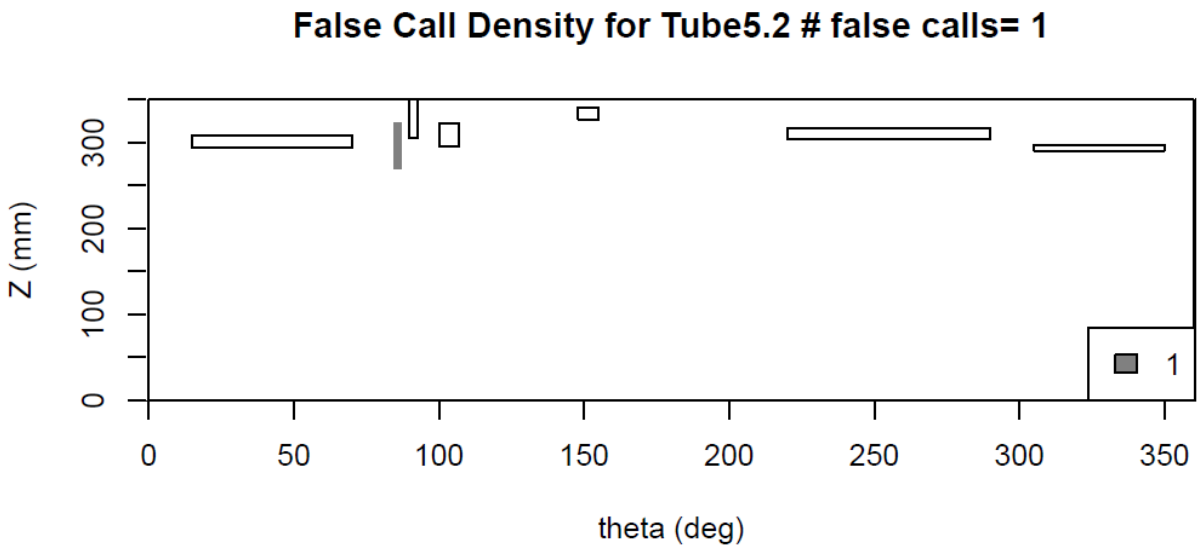
False Call Density for Tube5.2 # false calls= 1
Z (mm)
0
100
200
300
0
50
100
150
200
250
300
350
theta (deg)
1

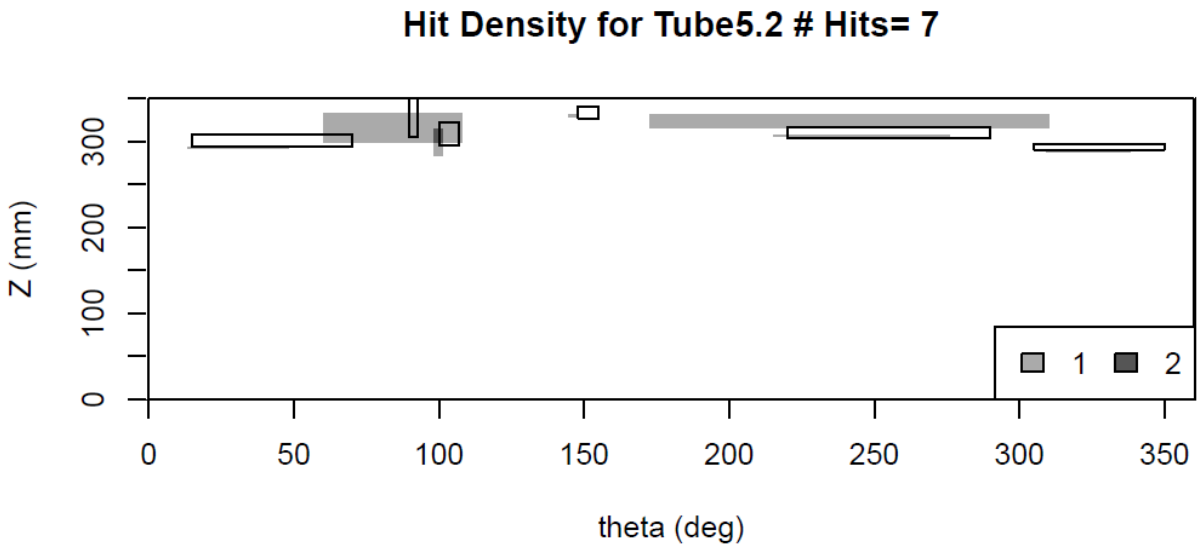
Hit Density for Tube5.2 # Hits= 7
Z (mm)
0
100
200
300
0
50
100
150
200
250
300
350
theta (deg)
1
2

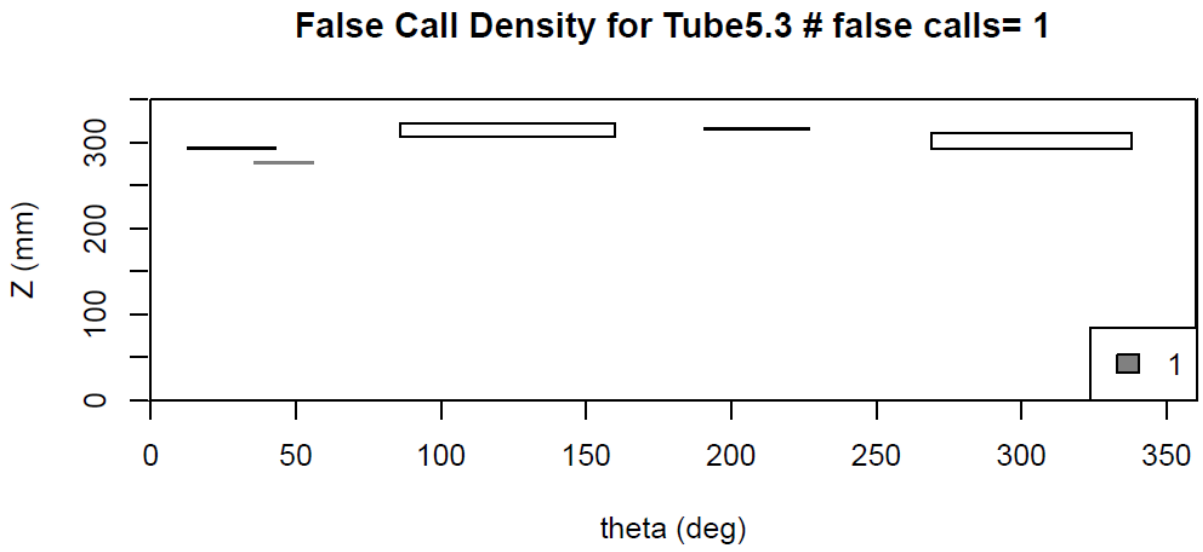
False Call Density for Tube5.3 # false calls= 1
Z (mm)
0
100
200
300
0
50
100
150
200
250
300
350
theta (deg)
1

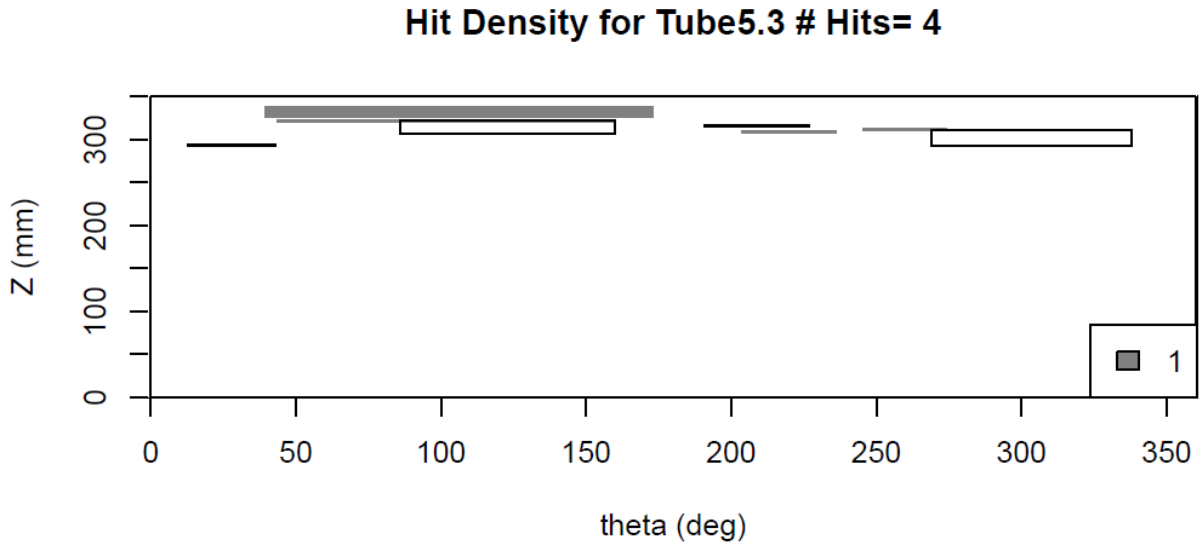
Hit Density for Tube5.3 # Hits= 4
Z (mm)
0
100
200
300
0
50
100
150
200
250
300
350
theta (deg)
1

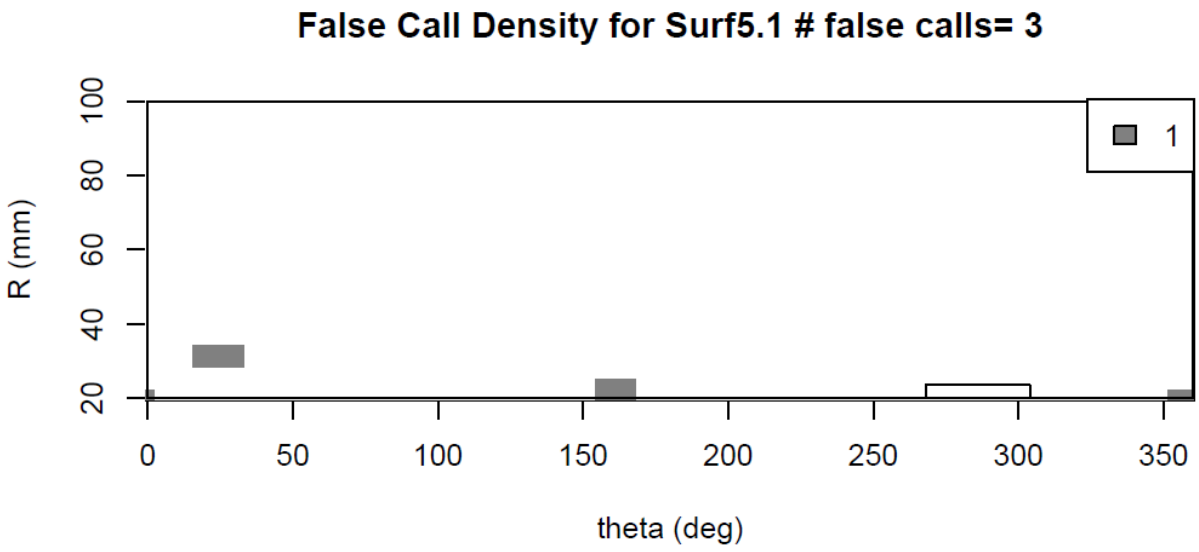
False Call Density for Surf5.1 # false calls= 3
R (mm)
20
40
60
80
100
0
50
100
150
200
250
300
350
theta (deg)
1

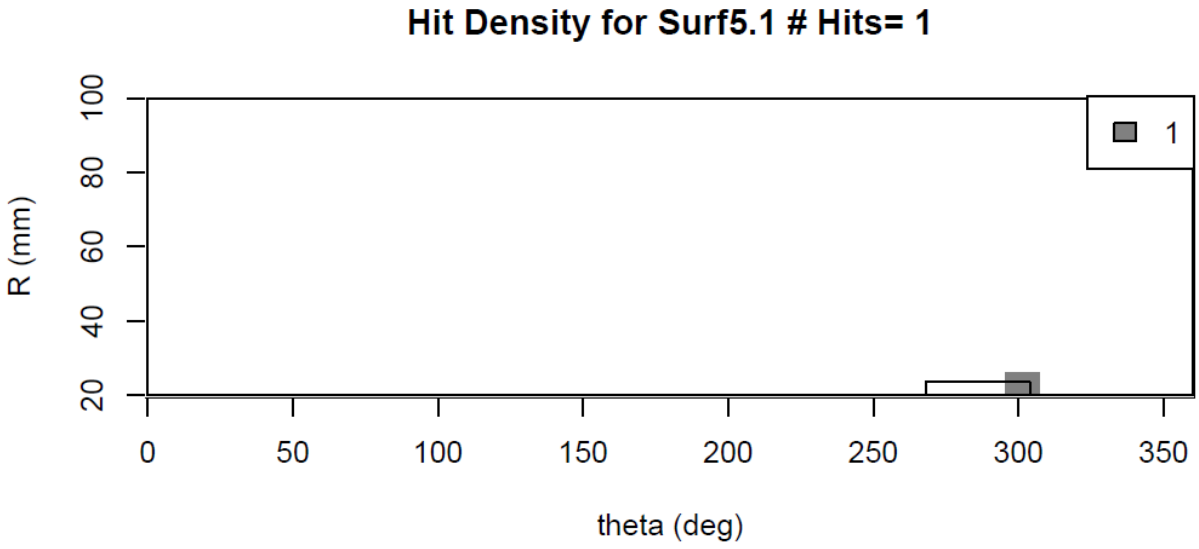
Hit Density for Surf5.1 # Hits= 1
R (mm)
20
40
60
80
100
0
50
100
150
200
250
300
350
theta (deg)
1

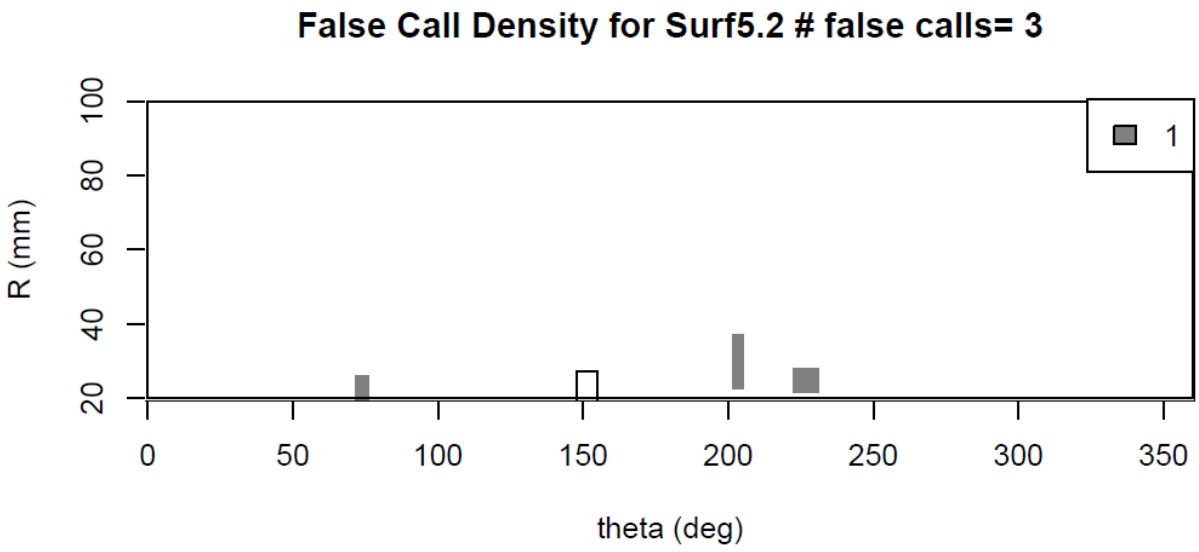
False Call Density for Surf5.2 # false calls= 3
R (mm)
20
40
60
80
100
0
50
100
150
200
250
300
350
theta (deg)
1

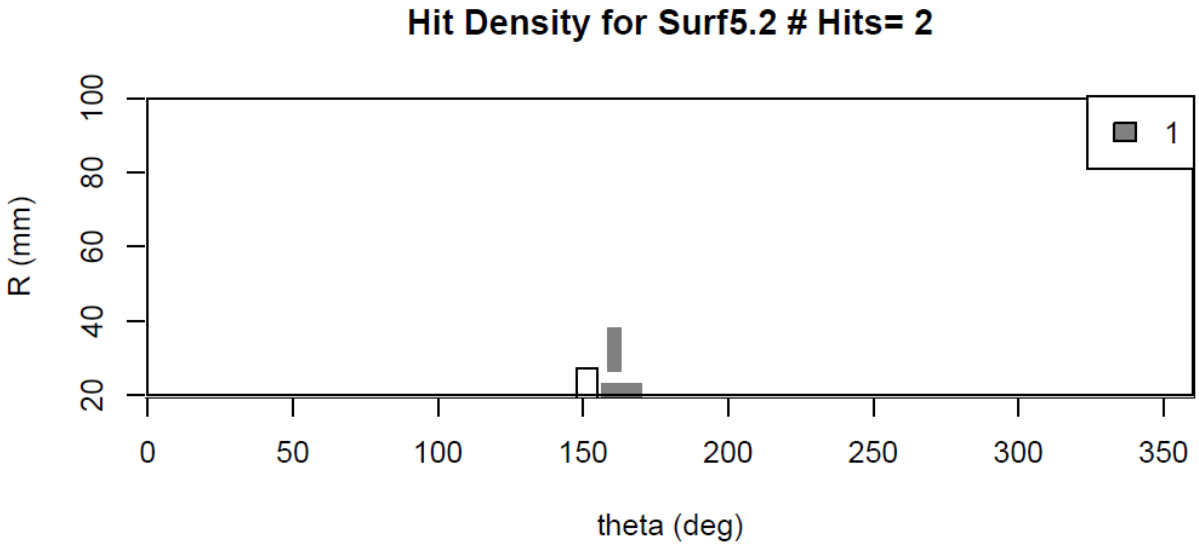
Hit Density for Surf5.2 # Hits= 2
R (mm)
20
40
60
80
100
0
50
100
150
200
250
300
350
theta (deg)
1

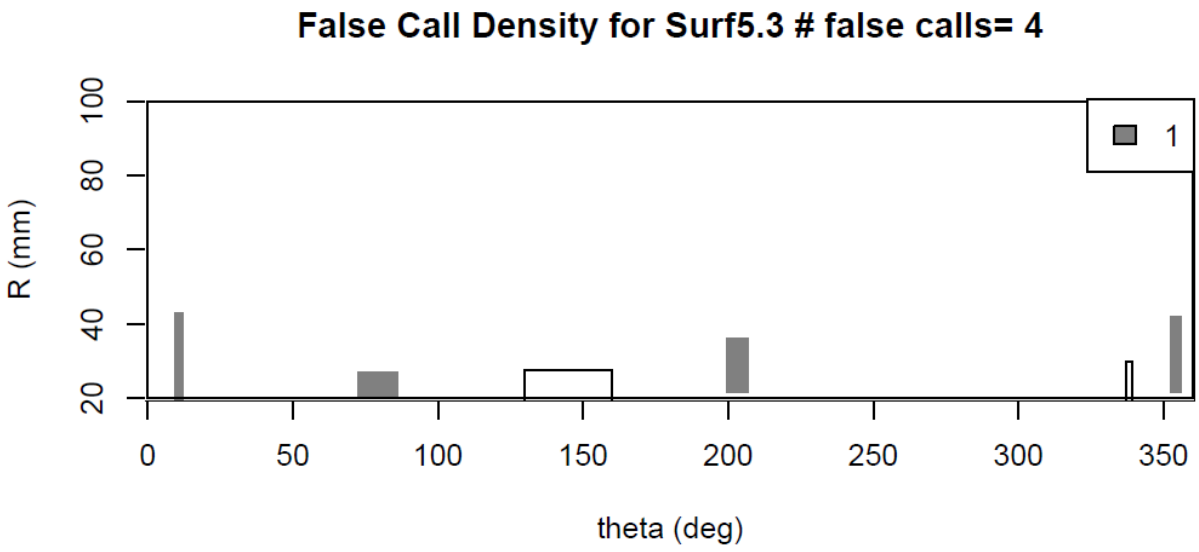
False Call Density for Surf5.3 # false calls= 4
R (mm)
20
40
60
80
100
0
50
100
150
200
250
300
350
theta (deg)
1

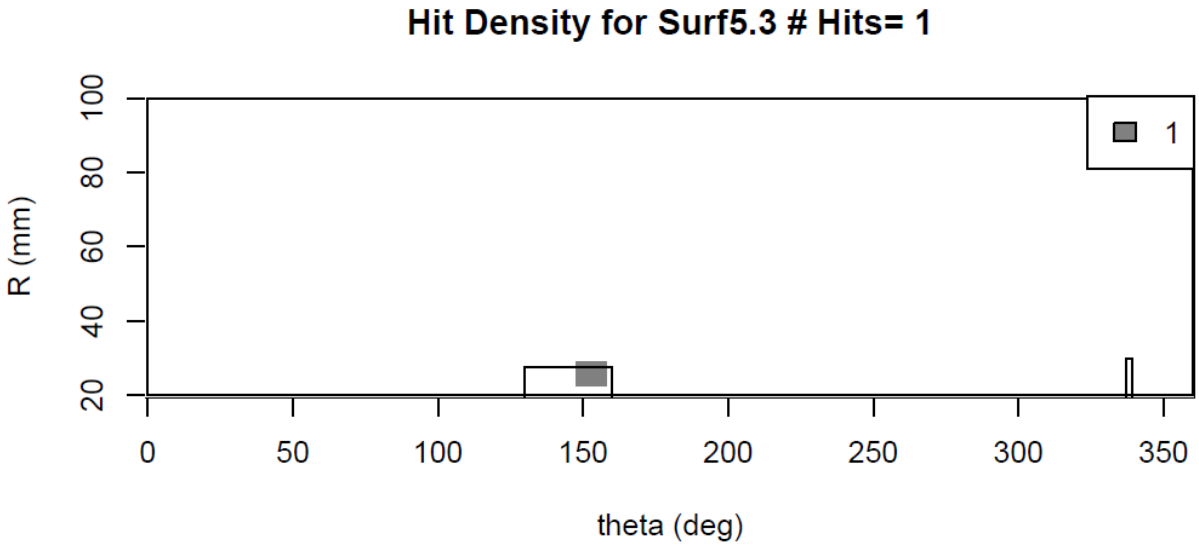
Hit Density for Surf5.3 # Hits= 1
R (mm)
20
40
60
80
100
0
50
100
150
200
250
300
350
theta (deg)
1

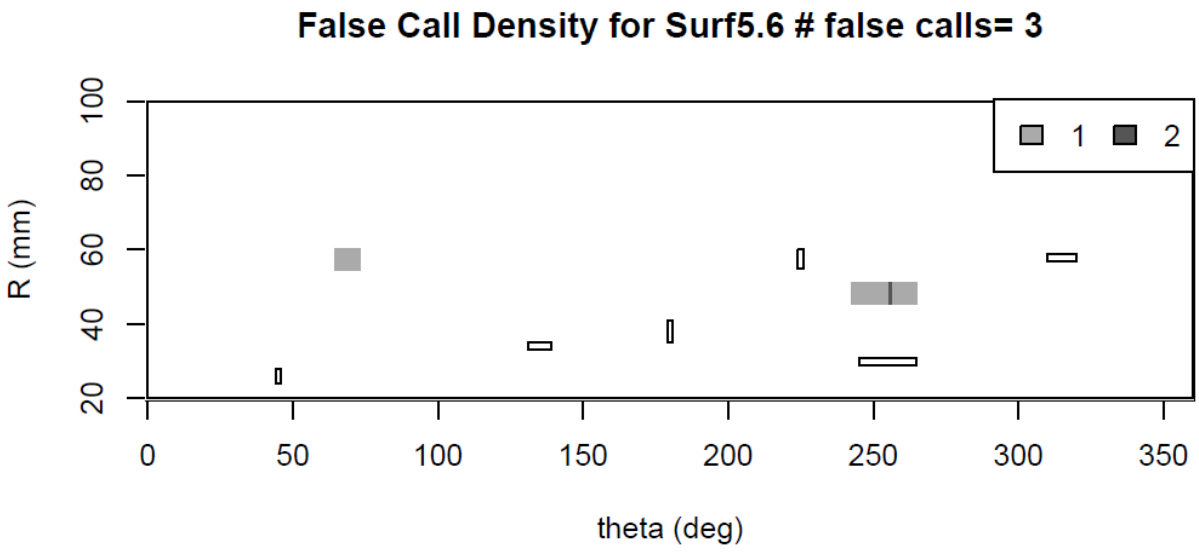
False Call Density for Surf5.6 # false calls= 3
R (mm)
20
40
60
80
100
0
50
100
150
200
250
300
350
theta (deg)
1
2

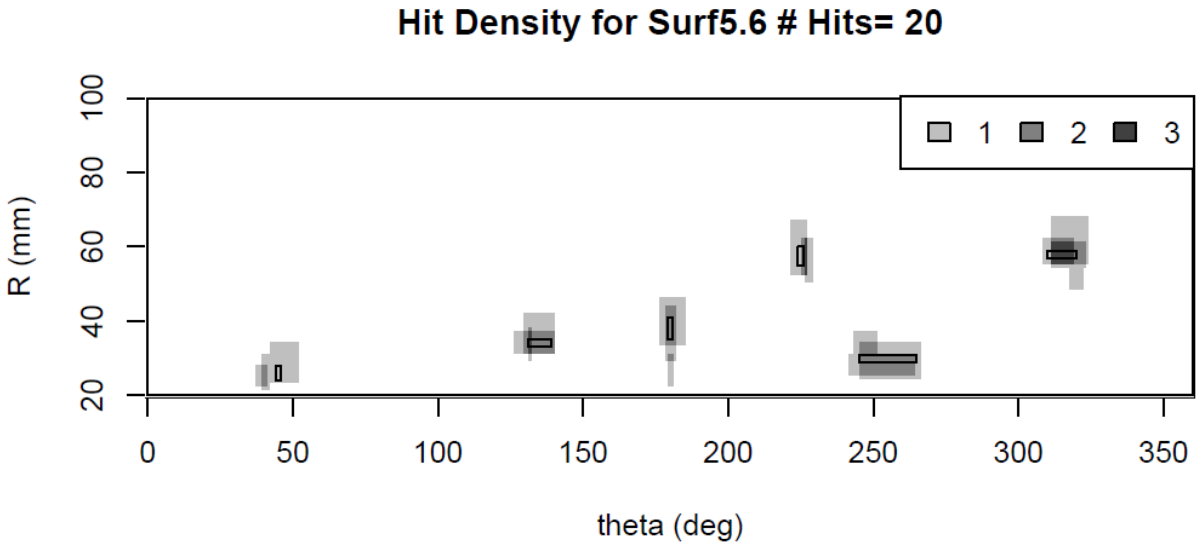
Hit Density for Surf5.6 # Hits= 20
R (mm)
20
40
60
80
100
0
50
100
150
200
250
300
350
theta (deg)
1
2
3

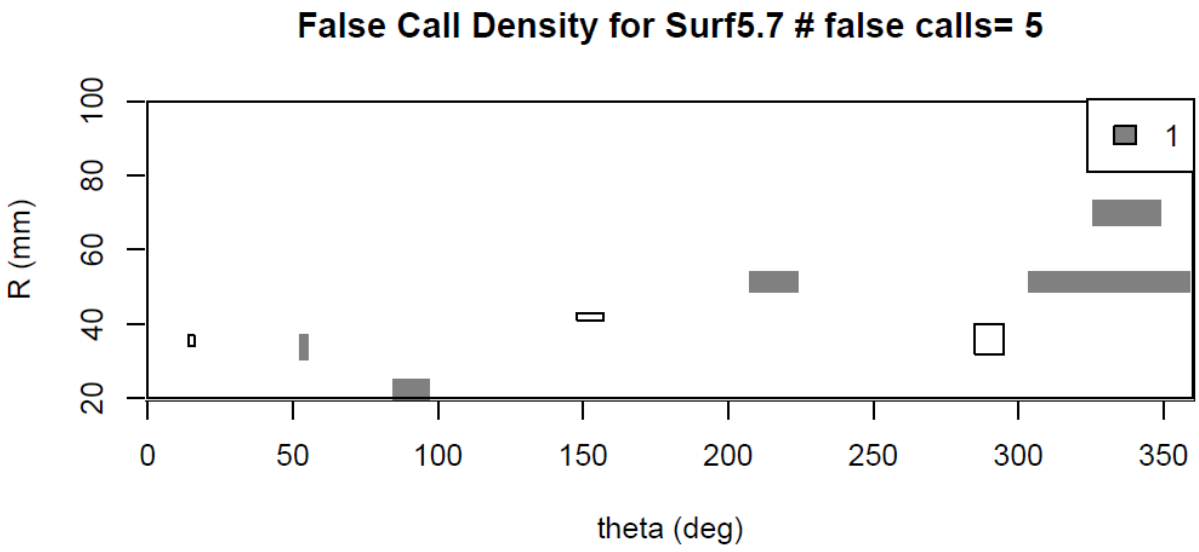
False Call Density for Surf5.7 # false calls= 5
R (mm)
20
40
60
80
100
0
50
100
150
200
250
300
350
theta (deg)
1

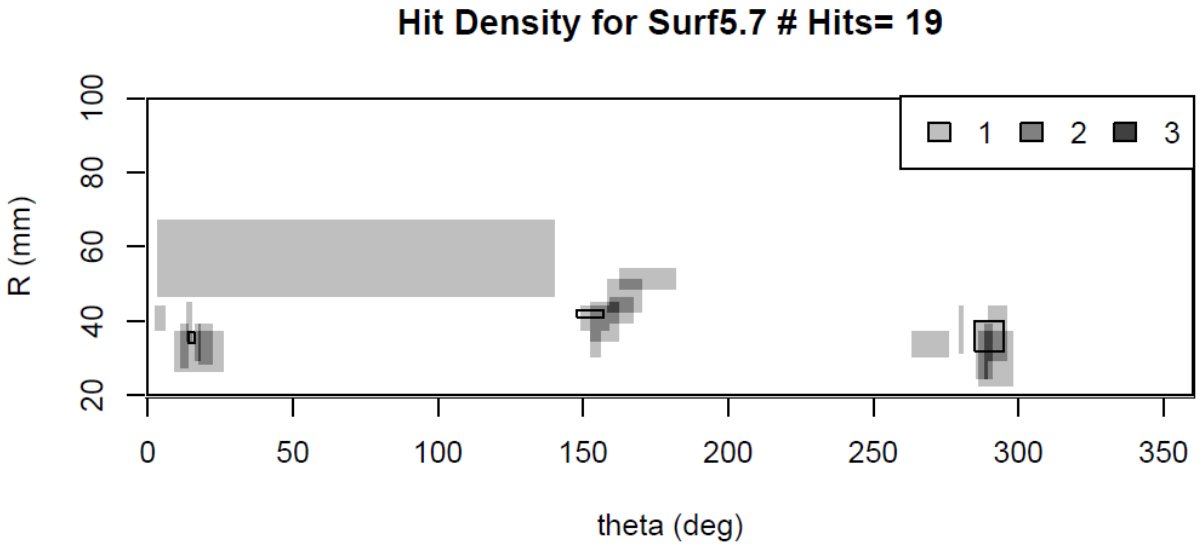
Hit Density for Surf5.7 # Hits= 19
R (mm)
20
40
60
80
100
0
50
100
150
200
250
300
350
theta (deg)
1
2
3

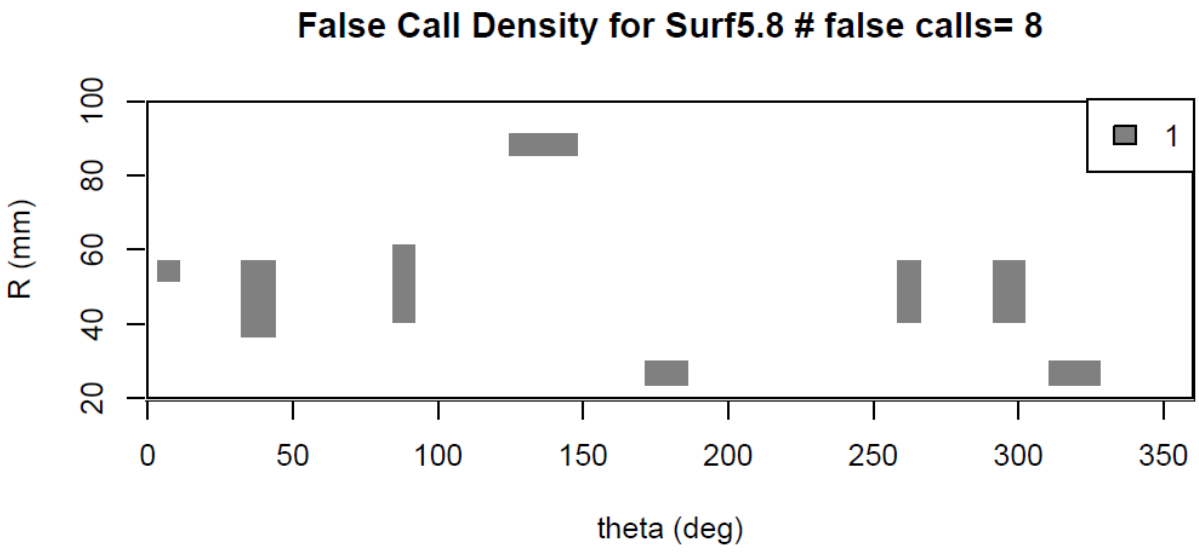
False Call Density for Surf5.8 # false calls= 8
R (mm)
20
40
60
80
100
0
50
100
150
200
250
300
350
theta (deg)
1

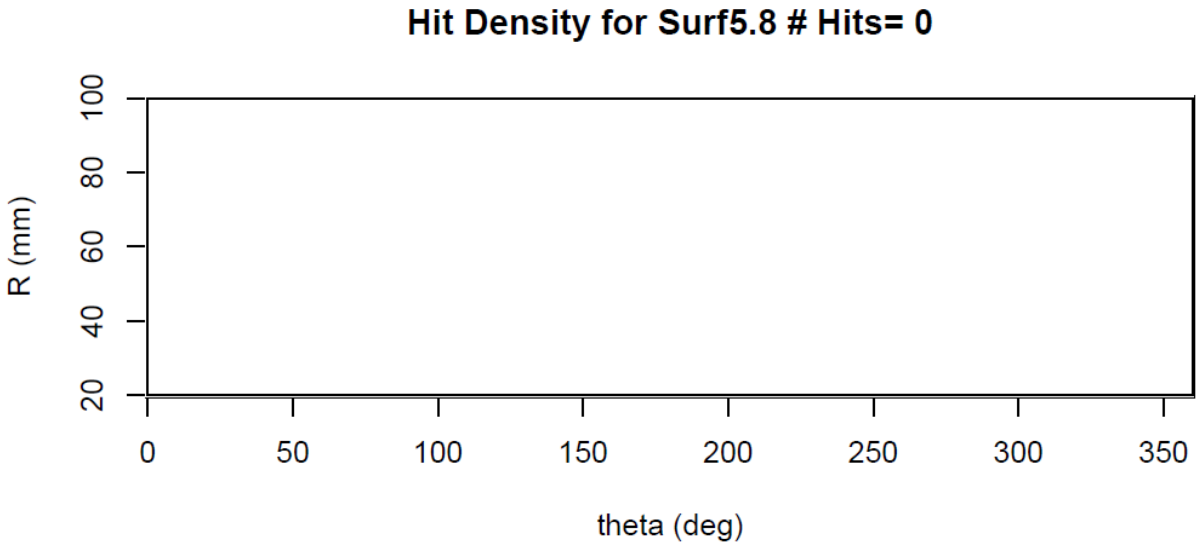
Hit Density for Surf5.8 # Hits= 0
R (mm)
20
40
60
80
100
0
50
100
150
200
250
300
350
theta (deg)

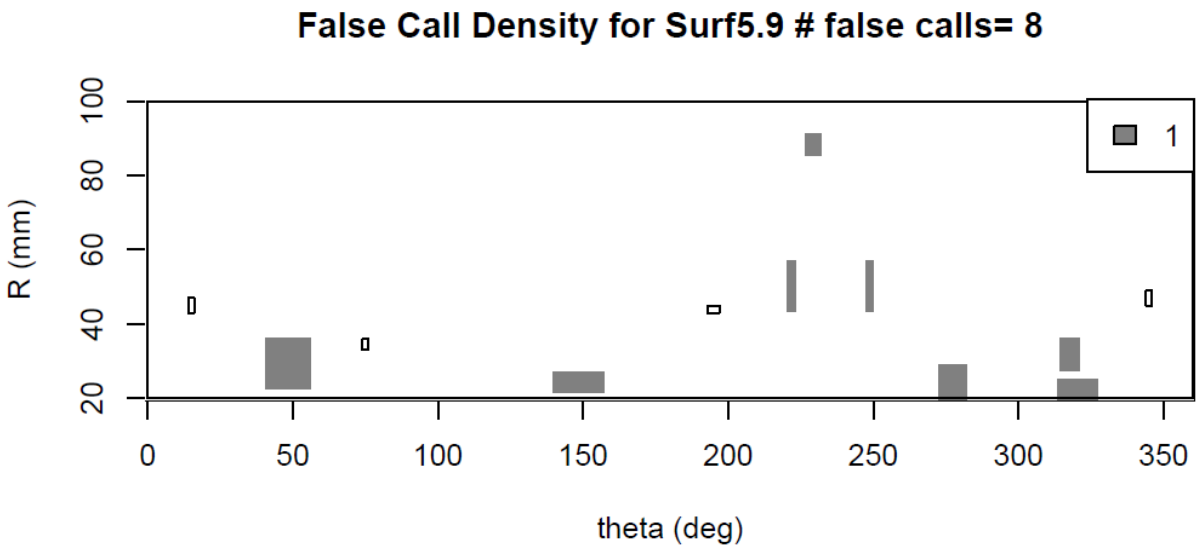
False Call Density for Surf5.9 # false calls= 8
R (mm)
20
40
60
80
100
0
50
100
150
200
250
300
350
theta (deg)
1

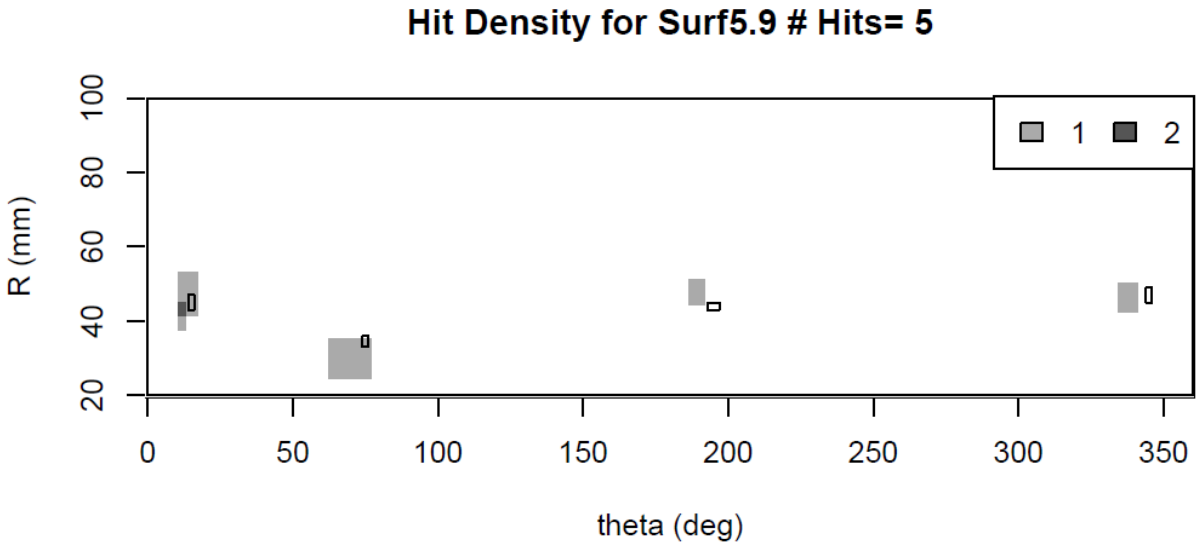
Hit Density for Surf5.9 # Hits= 5
R (mm)
20
40
60
80
100
0
50
100
150
200
250
300
350
theta (deg)
1
2

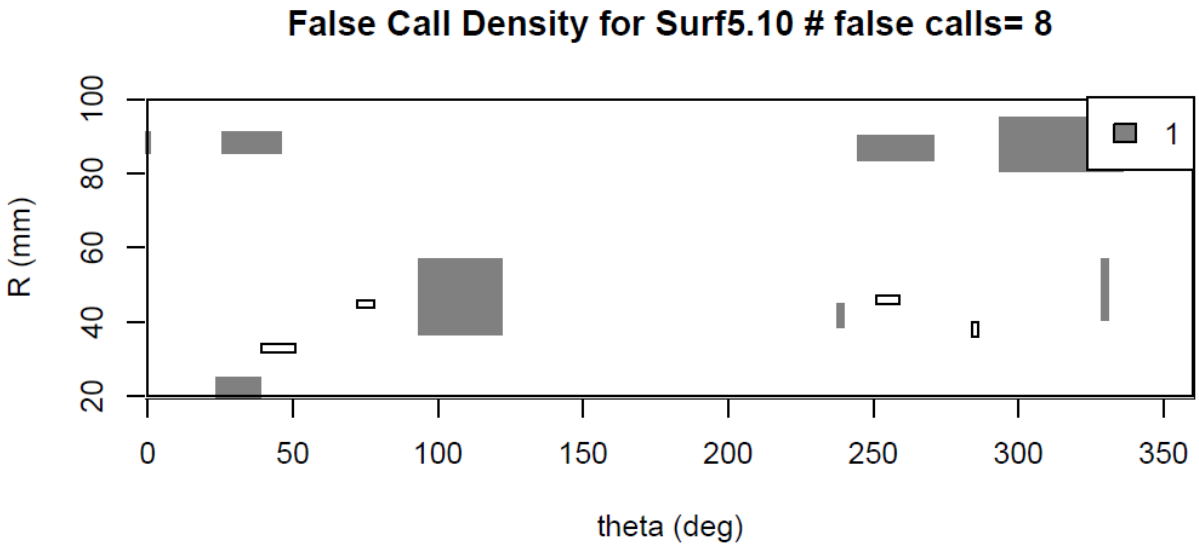
False Call Density for Surf5.10 # false calls= 8
R (mm)
20
40
60
80
100
0
50
100
150
200
250
300
350
theta (deg)
1

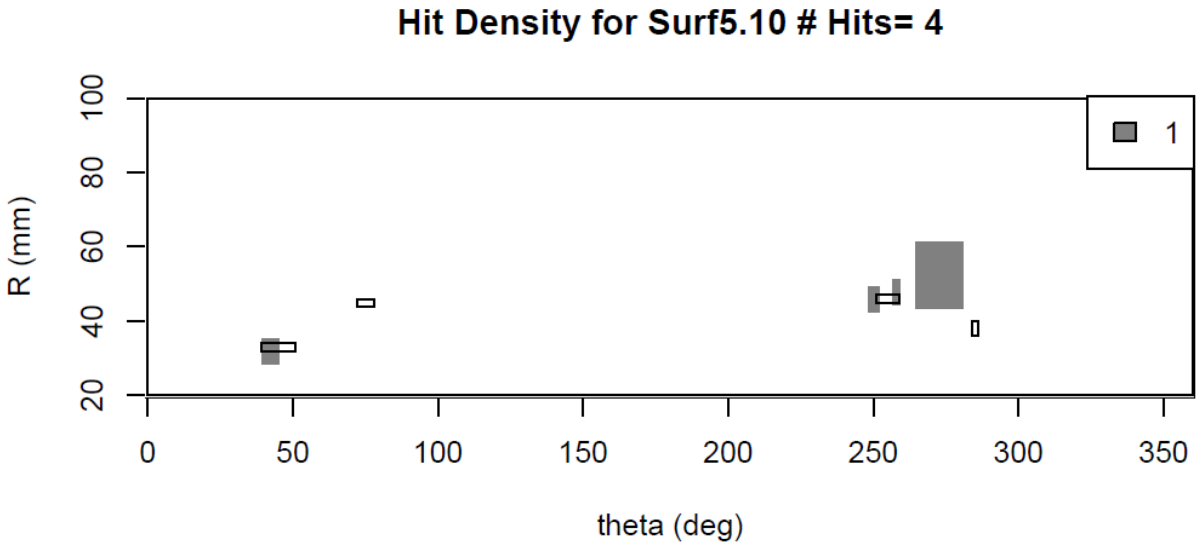
Hit Density for Surf5.10 # Hits= 4
R (mm)
20
40
60
80
100
0
50
100
150
200
250
300
350
theta (deg)
1

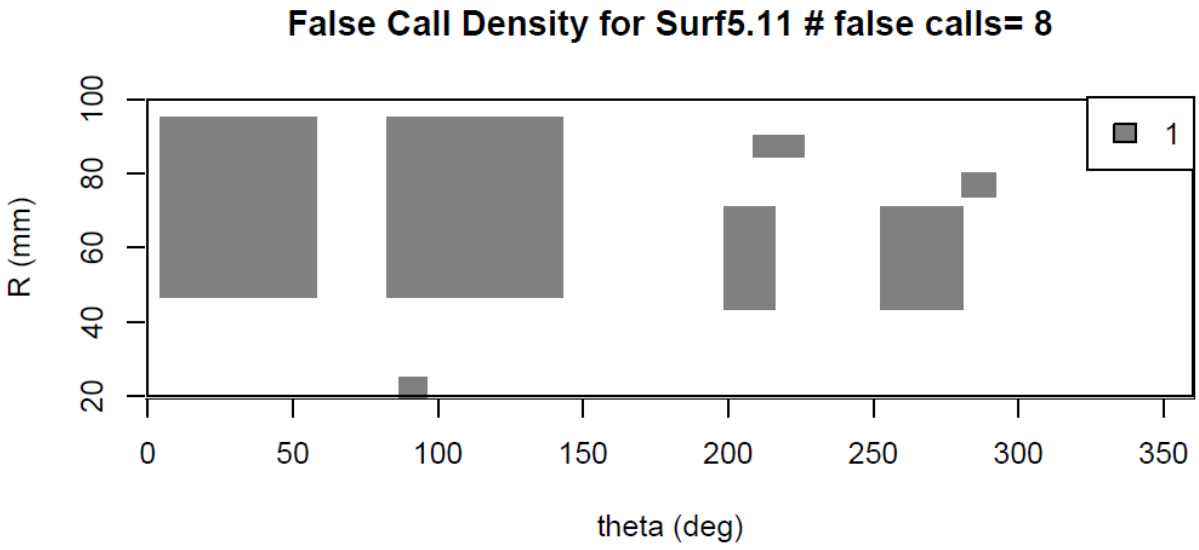
False Call Density for Surf5.11 # false calls= 8
R (mm)
20
40
60
80
100
0
50
100
150
200
250
300
350
theta (deg)
1

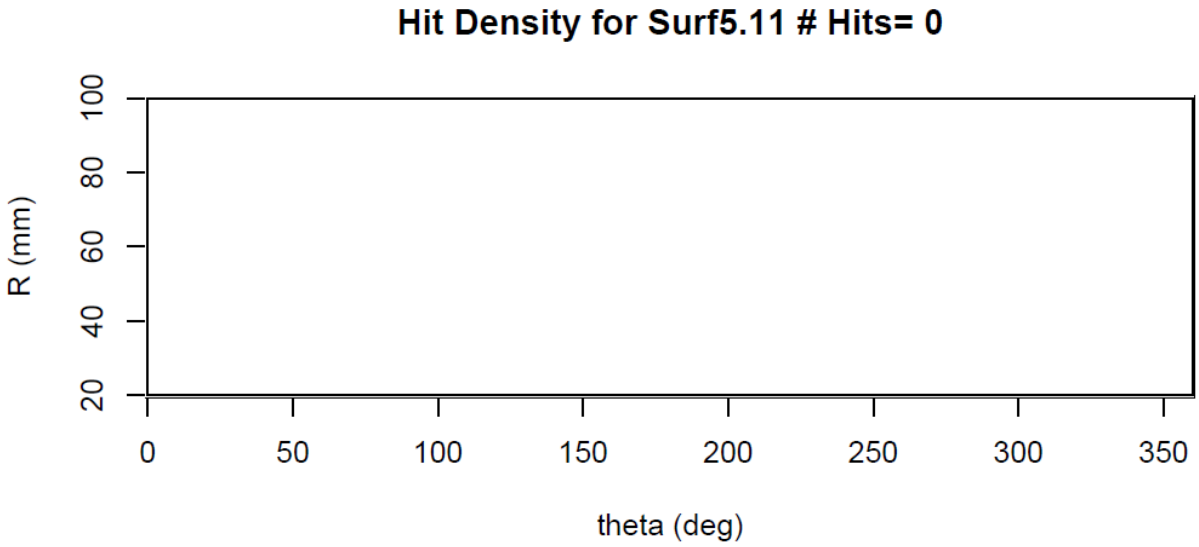
Hit Density for Surf5.11 # Hits= 0
R (mm)
20
40
60
80
100
0
50
100
150
200
250
300
350
theta (deg)

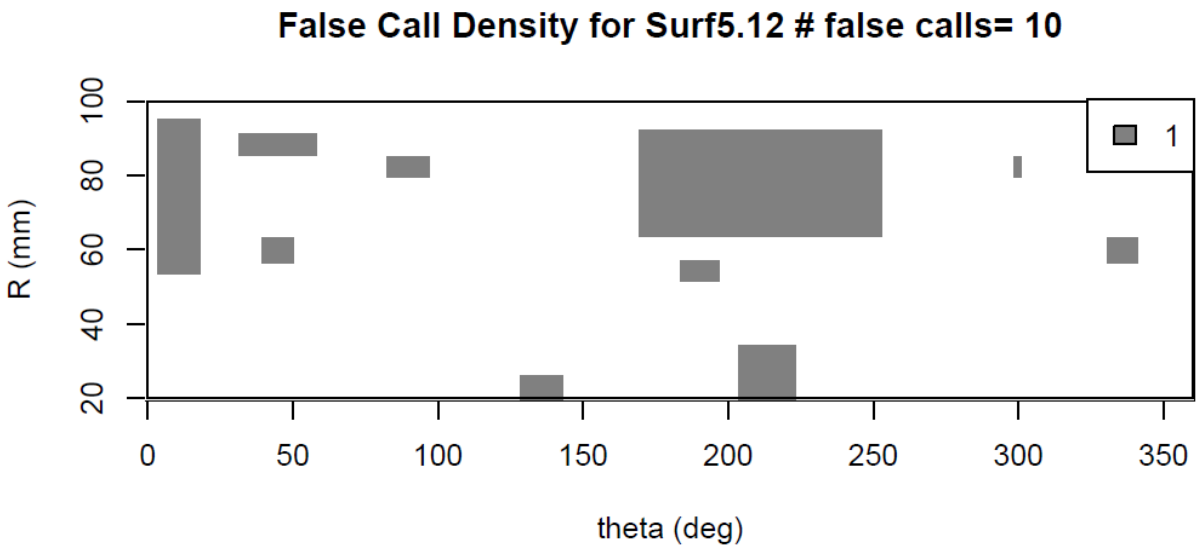
False Call Density for Surf5.12 # false calls= 10
R (mm)
20
40
60
80
100
0
50
100
150
200
250
300
350
theta (deg)
1

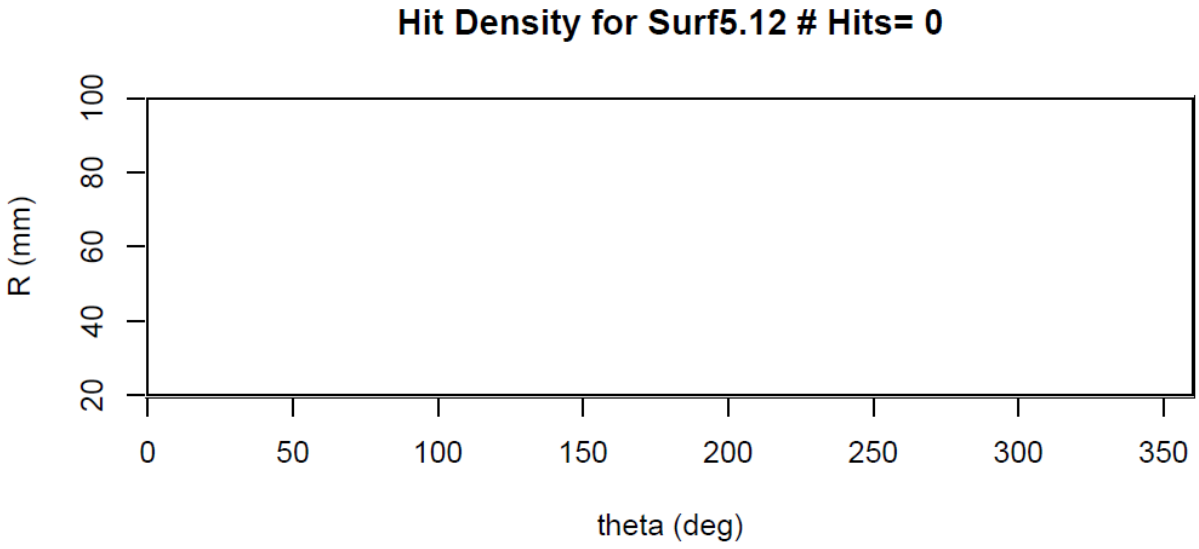
Hit Density for Surf5.12 # Hits= 0
R (mm)
20
40
60
80
100
0
50
100
150
200
250
300
350
theta (deg)

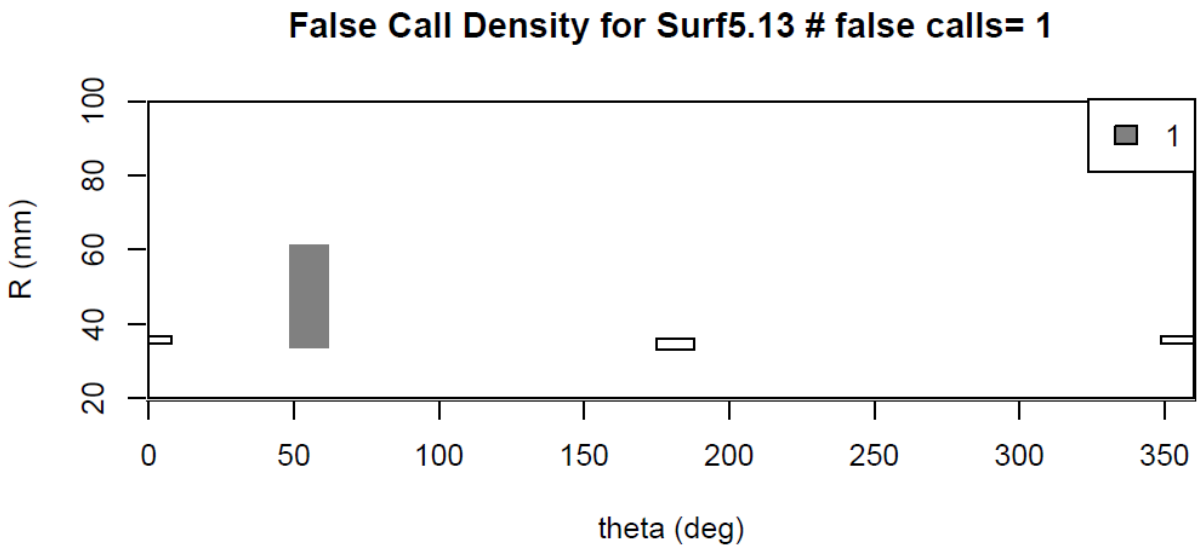
False Call Density for Surf5.13 # false calls= 1
R (mm)
20
40
60
80
100
0
50
100
150
200
250
300
350
theta (deg)
1

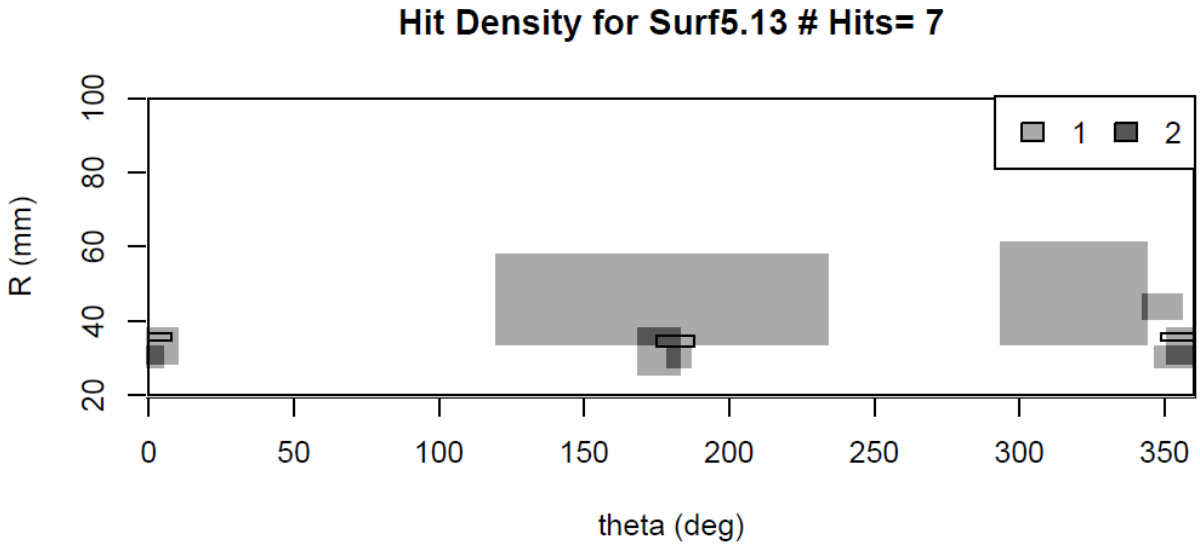
Hit Density for Surf5.13 # Hits= 7
R (mm)
20
40
60
80
100
0
50
100
150
200
250
300
350
theta (deg)
1
2

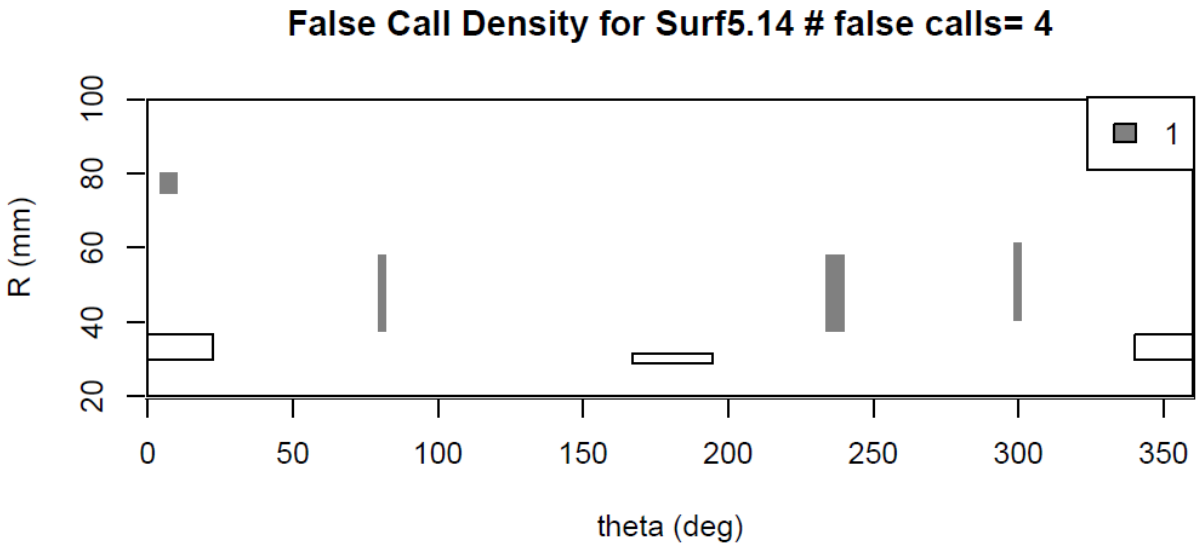
False Call Density for Surf5.14 # false calls= 4
R (mm)
20
40
60
80
100
0
50
100
150
200
250
300
350
theta (deg)
1

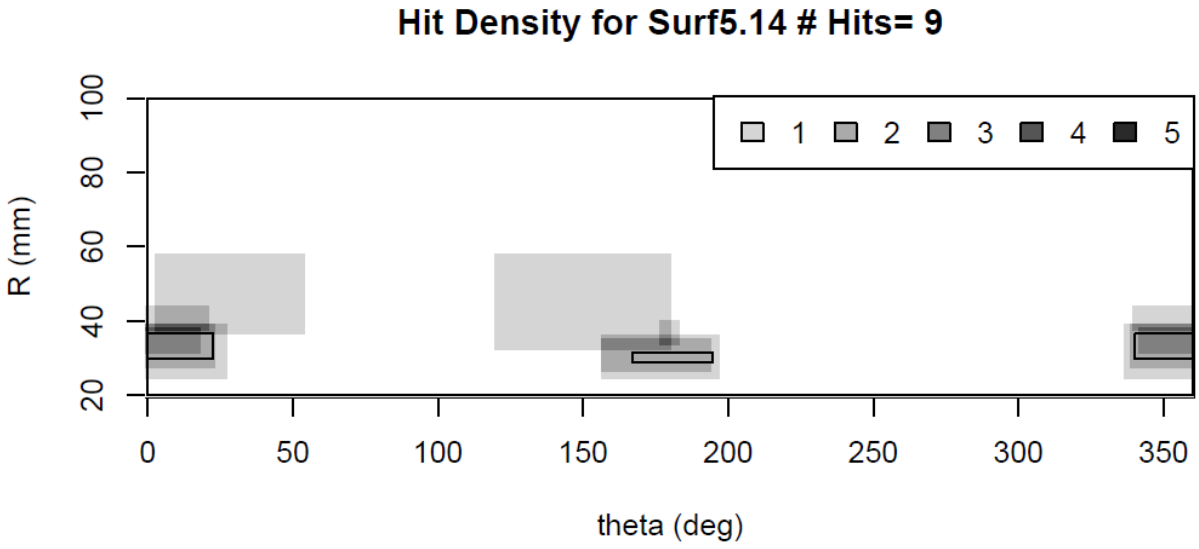
Hit Density for Surf5.14 # Hits= 9
R (mm)
20
40
60
80
100
0
50
100
150
200
250
300
350
theta (deg)
1
2
3
4
5

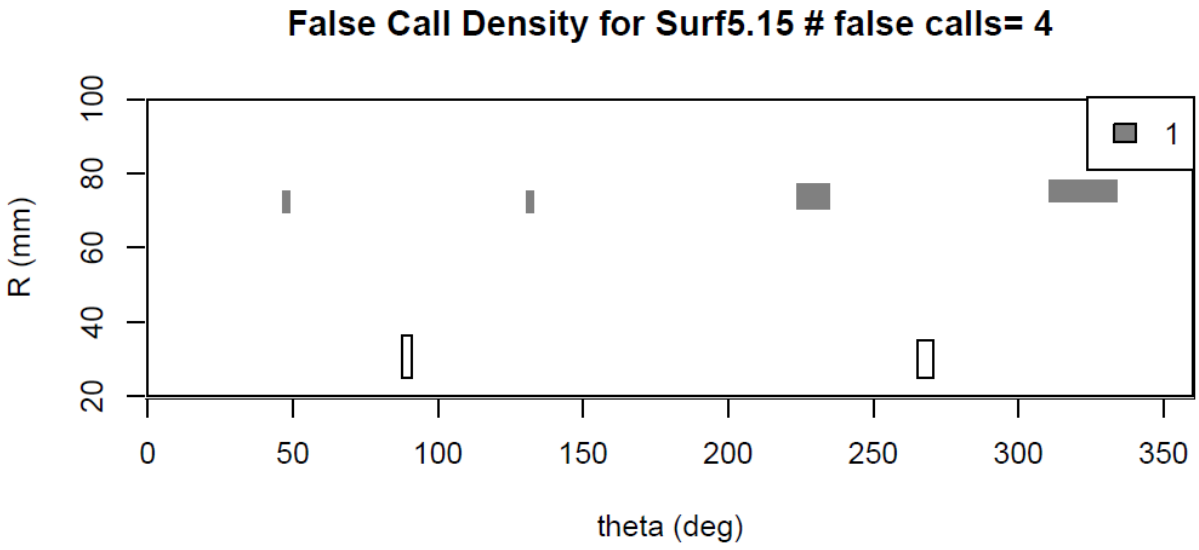
False Call Density for Surf5.15 # false calls= 4
R (mm)
20
40
60
80
100
0
50
100
150
200
250
300
350
theta (deg)
1

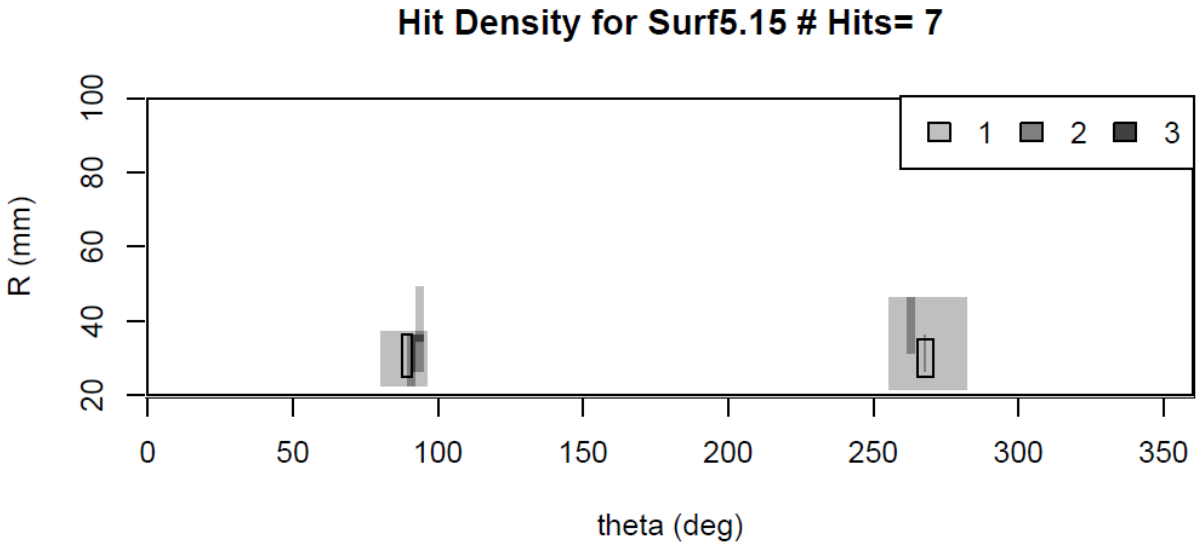
Hit Density for Surf5.15 # Hits= 7
R (mm)
20
40
60
80
100
0
50
100
150
200
250
300
350
theta (deg)
1
2
3

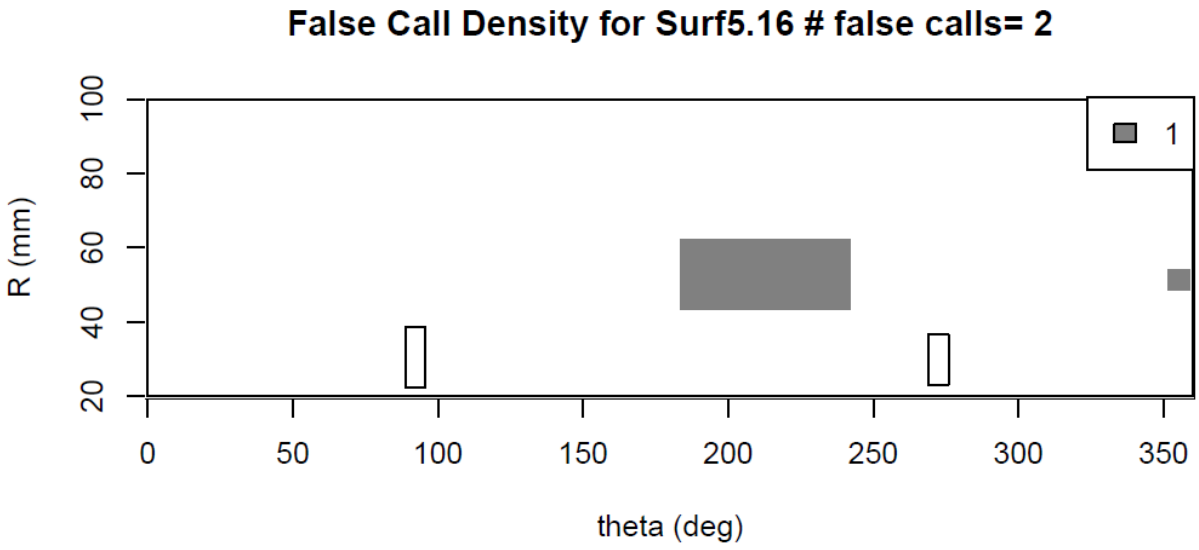
False Call Density for Surf5.16 # false calls= 2
R (mm)
20
40
60
80
100
0
50
100
150
200
250
300
350
theta (deg)
1

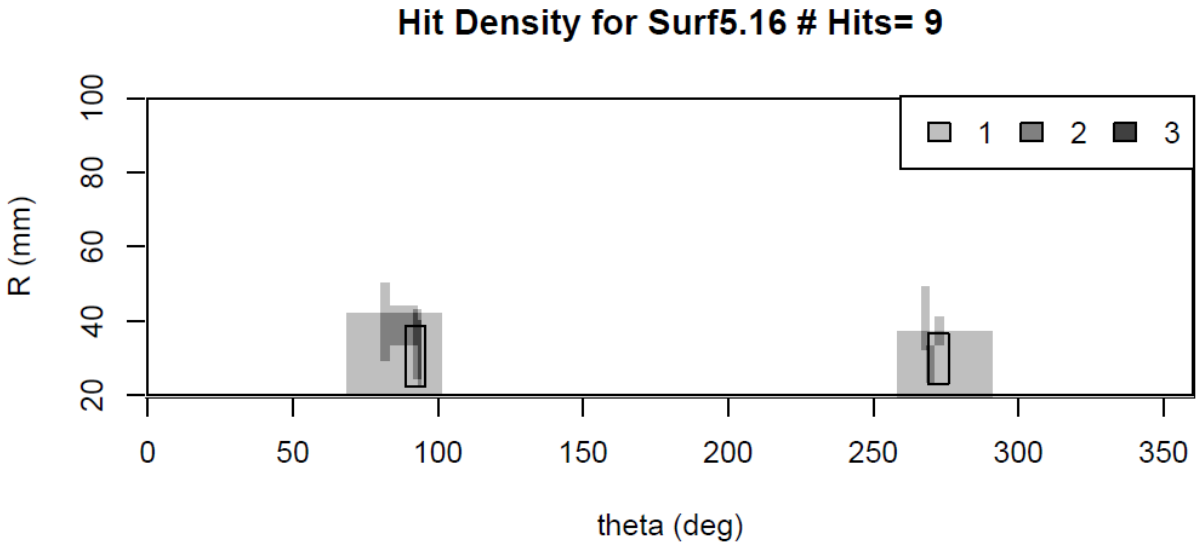
Hit Density for Surf5.16 # Hits= 9
R (mm)
20
40
60
80
100
0
50
100
150
200
250
300
350
theta (deg)
1
2
3

Appendix G

PINC Data Compilation

Appendix G

PINC Data Compilation

AF Pardini
R Mathews

Sample	Flaw	Angle	PNNL ECT Magnitude
5.6	Flaw 1	45	0.72
5.6	Flaw 2	135	1.74
5.6	Flaw 3	180	1.07
5.6	Flaw 4	225	1.25
5.6	Flaw 5	255	NR
5.6	Flaw 6	315	1.44
5.7	Flaw 1	15	2.35
5.7	Flaw 2	165	1.67
5.7	Flaw 3	300	2.32
5.9	Flaw 1	15	0.51
5.9	Flaw 2	75	NR
5.9	Flaw 3	195	NR
5.9	Flaw 4	345	1.33
5.10	Flaw 1	45	2.69
5.10	Flaw 2	75	1.79
5.10	Flaw 3	225	NR
5.10	Flaw 4	255	1.9
5.10	Flaw 5	285	NR
5.10	Flaw 6	315	1.96
5.13	No. 1-1	0	2.45
5.13	No. 1-2	180	1.62
5.14	No. 2-1	0	3.92
5.14	No. 2-2	180	1.39
5.15	No. 3-1	90	2.94
5.15	No. 3-2	270	4.01
5.16	No. 4-1	90	4.42
5.16	No. 4-2	270	7.08
Japan EDM 1	Largest	NA	1.69
Japan EDM 2	Largest	NA	2.43
Japan Ref. 1	Largest	NA	1.76
Japan Ref. 2	Largest	NA	3.52
Cal Std.	5 mm	NA	2.58
Cal Std.	5 mm	NA	2.44
Cal Std.	1 mm	NA	1.96
Cal Std.	1 mm	NA	1.36

Flaw	Observations	POD	ECT
Surf 5.9.2	6	0.167	0
Surf 5.9.3	6	0.167	0
Surf 5.10.3	6	0	0
Surf 5.10.5	6	0.167	0
Surf 5.9.1	6	0.333	0.51
Surf 5.6.1	4	0.75	0.72
Surf 5.6.3	4	0.75	1.07
Surf 5.6.4	4	0.75	1.25
Surf 5.9.4	6	0.167	1.33
Surf 5.14.2	4	0.75	1.39
Surf 5.6.6	4	0.75	1.44
Surf 5.13.2	4	0.5	1.62
Surf 5.7.2	6	0.833	1.67
Surf 5.6.2	4	0.75	1.74
Surf 5.10.2	6	0	1.79
Surf 5.10.4	6	0.5	1.9
Surf 5.10.6	6	0	1.96
Surf 5.7.1	6	0.667	2.35
Surf 5.13.1	4	0.75	2.45
Surf 5.10.1	6	0.167	2.69
Surf 5.15.1	4	0.75	2.94
Surf 5.14.1	4	1	3.92
Surf 5.15.2	4	0.5	4.01
Surf 5.16.1	4	0.75	4.42
Surf 5.16.2	4	0.75	7.08

G.1 Calibration/Verification Standard

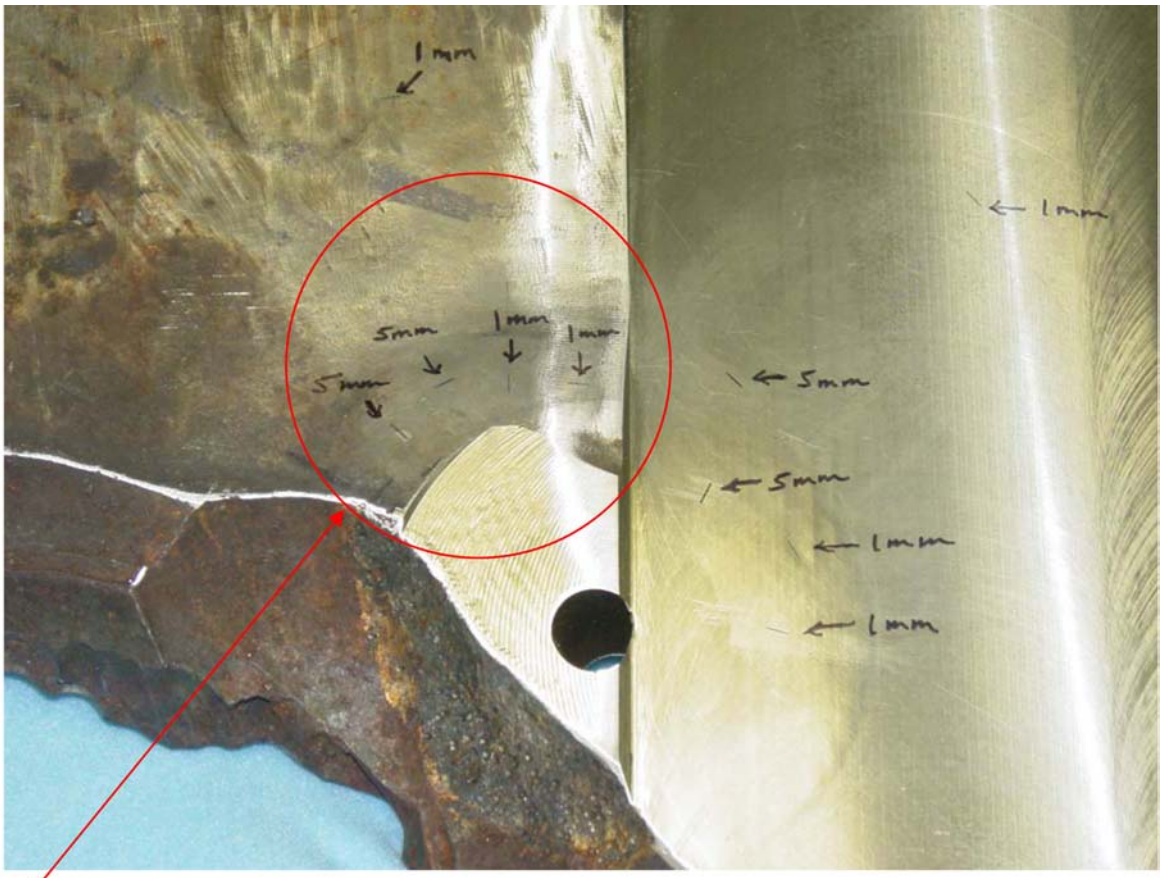

Two Larger Flaws are 4-mm Long × 5-mm Deep × 0.203-mm Wide

Two Smaller Flaws are 4-mm Long × 1-mm Deep × 0.102-mm Wide

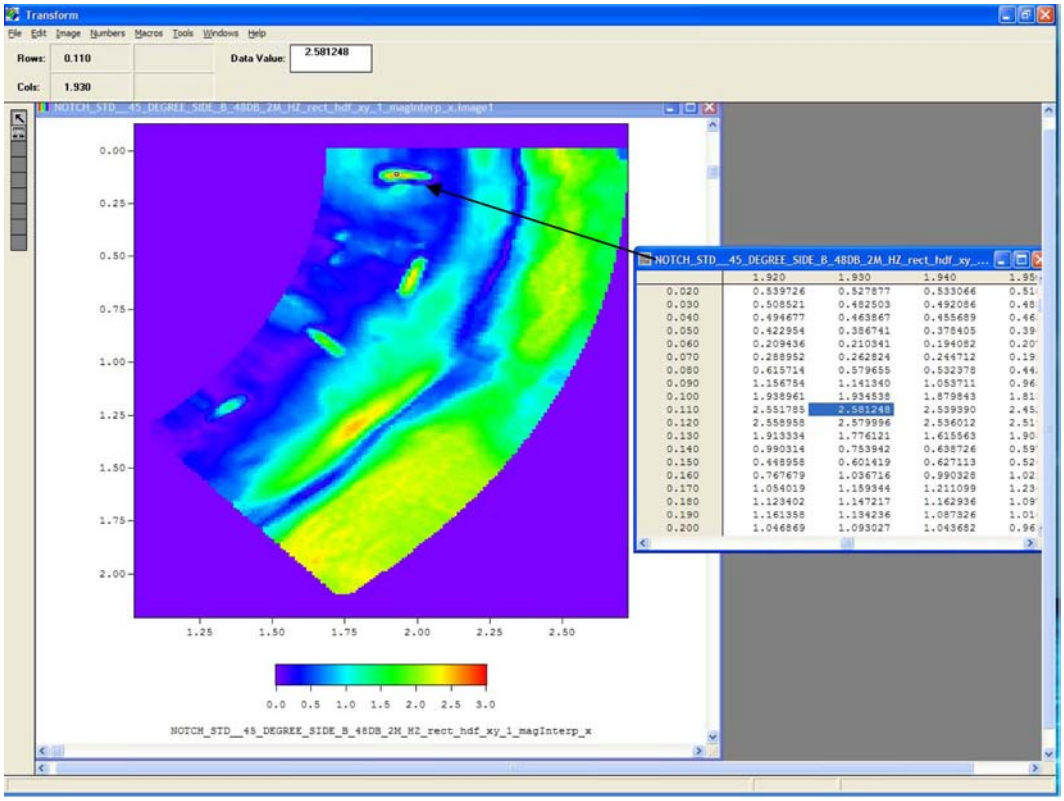
Transform
File Edit Image Numbers Macros Tools Windows Help
Rows: 0.110
Cols: 1.930
Data Value: 2.581248
NOTCH_STD__45_DEGREE_SIDE_B_48DB_2M_HZ_rect_hdf_xy_1_magInterp_x.Image1
NOTCH_STD__45_DEGREE_SIDE_B_48DB_2M_HZ_rect_hdf_xy_....
1.920 1.930 1.940
0.020 0.539726 0.527877 0.533066
0.030 0.508521 0.482503 0.492086
0.040 0.494677 0.463867 0.455689
0.050 0.422954 0.386741 0.378405
0.060 0.209436 0.210341 0.194082
0.070 0.288952 0.262824 0.244712
0.080 0.615714 0.579655 0.532378
0.090 1.156754 1.141340 1.053711
0.100 1.938961 1.934538 1.879843
0.110 2.551785 2.581248 2.539390
0.120 2.558958 2.579996 2.536012
0.130 1.913334 1.776121 1.615563
0.140 0.990314 0.753942 0.638726
0.150 0.448958 0.601419 0.627113
0.160 0.767679 1.036716 0.990328
0.170 1.054019 1.159344 1.211099
0.180 1.123402 1.147217 1.162936
0.190 1.161358 1.134236 1.087326
0.200 1.046869 1.093027 1.043682
0.00
0.25
0.50
0.75
1.00
1.25
1.50
1.75
2.00
1.25 1.50 1.75 2.00 2.25 2.50
0.0 0.5 1.0 1.5 2.0 2.5 3.0
NOTCH_STD__45_DEGREE_SIDE_B_48DB_2M_HZ_rect_hdf_xy_1_magInterp_x

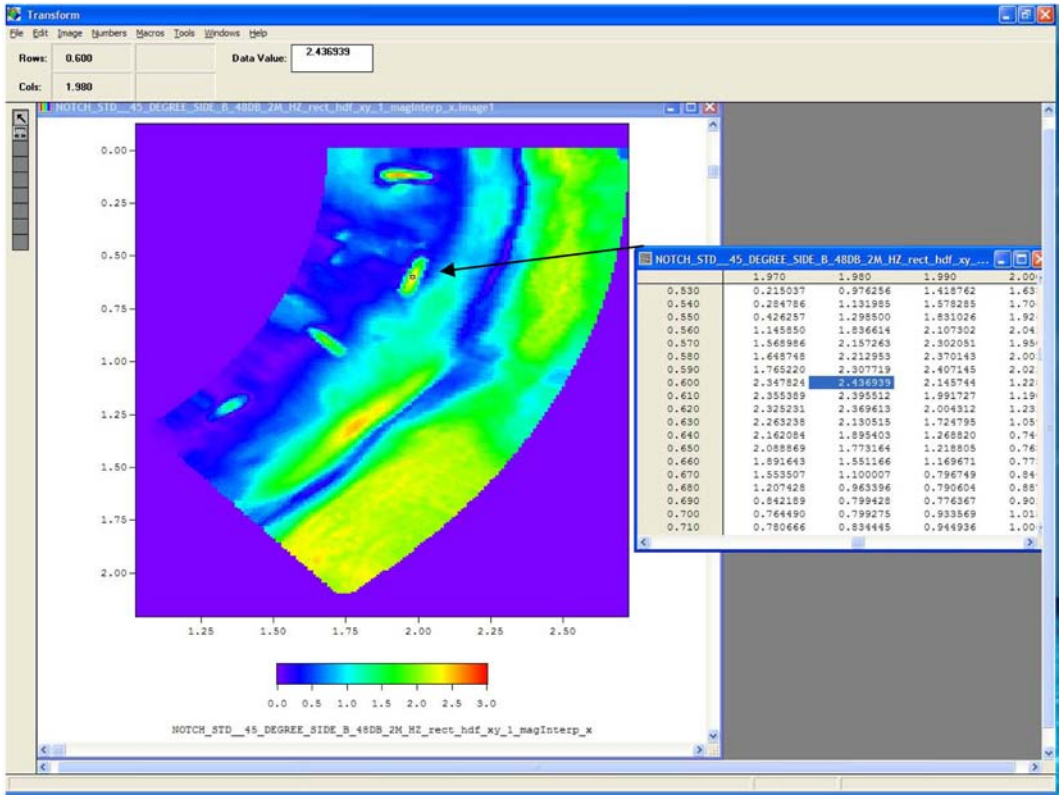
Transform
File Edit Image Numbers Macros Tools Windows Help
Rows: 0.600
Cols: 1.980
Data Value: 2.436939
NOTCH_STD__45_DEGREE_SIDE_B_48DB_2M_HZ_rect_hdf_xy_1_magInterp_x.Image1
NOTCH_STD__45_DEGREE_SIDE_B_48DB_2M_HZ_rect_hdf_xy_....
1.970 1.980 1.990
0.530 0.215037 0.976256 1.418762
0.540 0.284786 1.131985 1.578285
0.550 0.426257 1.298500 1.831026
0.560 1.145850 1.836614 2.107302
0.570 1.568986 2.157263 2.302051
0.580 1.648748 2.212953 2.370143
0.590 1.765220 2.307719 2.407145
0.600 2.347824 2.436939 2.145744
0.610 2.355389 2.395512 1.991727
0.620 2.325231 2.369613 2.004312
0.630 2.263238 2.130515 1.724795
0.640 2.162084 1.895403 1.268820
0.650 2.088869 1.773164 1.218805
0.660 1.891643 1.551166 1.169671
0.670 1.553507 1.100007 0.796749
0.680 1.207428 0.963396 0.790604
0.690 0.842189 0.799428 0.776367
0.700 0.764490 0.799275 0.933569
0.710 0.780666 0.834445 0.944936
0.00
0.25
0.50
0.75
1.00
1.25
1.50
1.75
2.00
1.25 1.50 1.75 2.00 2.25 2.50
0.0 0.5 1.0 1.5 2.0 2.5 3.0
NOTCH_STD__45_DEGREE_SIDE_B_48DB_2M_HZ_rect_hdf_xy_1_magInterp_x

G.2 PINC 5.7

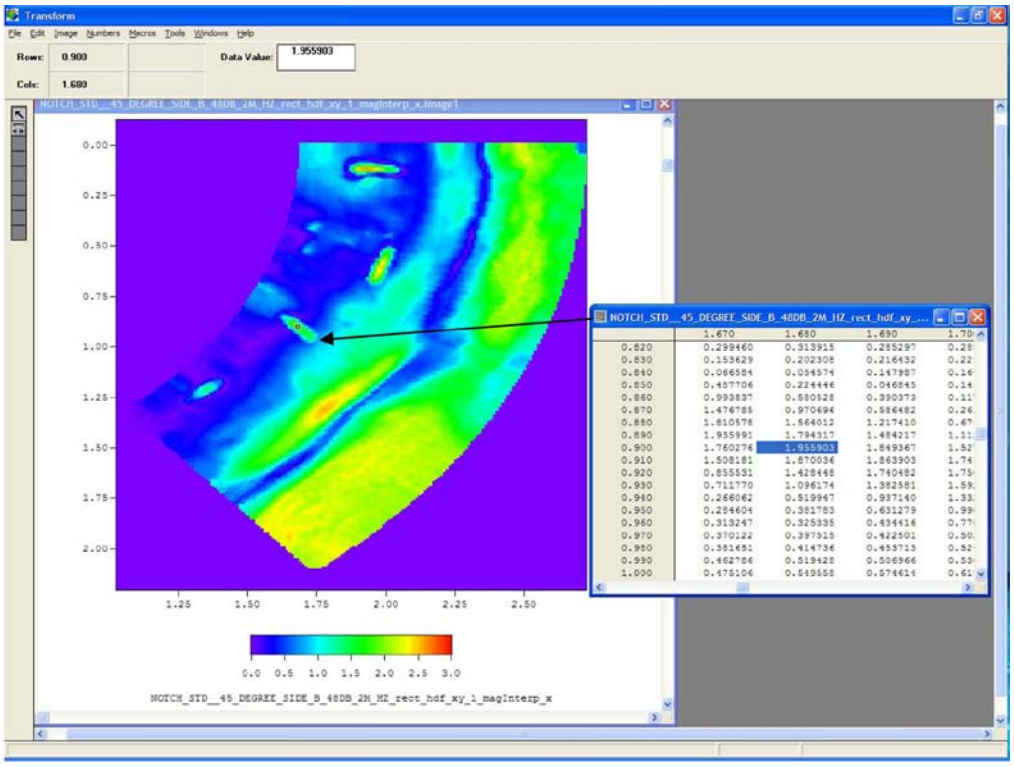
Transform
File Edit Image Numbers Macros Tools Windows Help
Rows: 0.900
Data Value: 1.955903
Cols: 1.680
NOTCH_STD__45_DEGREE_SIDE_B_48DB_2M_HZ_rect_hdf_xy_1_magInterp_x.image1
NOTCH_STD__45_DEGREE_SIDE_B_48DB_2M_HZ_rect_hdf_xy_....
1.670 1.680 1.690
0.820 0.299460 0.313915 0.285297
0.830 0.153629 0.202308 0.216432
0.840 0.066584 0.054574 0.147987
0.850 0.487706 0.224446 0.046845
0.860 0.993837 0.580528 0.390373
0.870 1.476785 0.970694 0.586482
0.880 1.810578 1.564012 1.217410
0.890 1.935991 1.794317 1.484217
0.900 1.760276 1.955903 1.849367
0.910 1.538181 1.870034 1.863903
0.920 0.855531 1.428448 1.740482
0.930 0.711770 1.096174 1.382581
0.940 0.266062 0.519947 0.937140
0.950 0.284604 0.381783 0.631279
0.960 0.313247 0.325335 0.434416
0.970 0.370122 0.397515 0.422501
0.980 0.381651 0.414736 0.453713
0.990 0.462786 0.519428 0.506966
1.000 0.475106 0.549558 0.574614
0.00 0.25 0.50 0.75 1.00 1.25 1.50 1.75 2.00
1.25 1.50 1.75 2.00 2.25 2.50
0.0 0.5 1.0 1.5 2.0 2.5 3.0
NOTCH_STD__45_DEGREE_SIDE_B_48DB_2M_HZ_rect_hdf_xy_1_magInterp_x

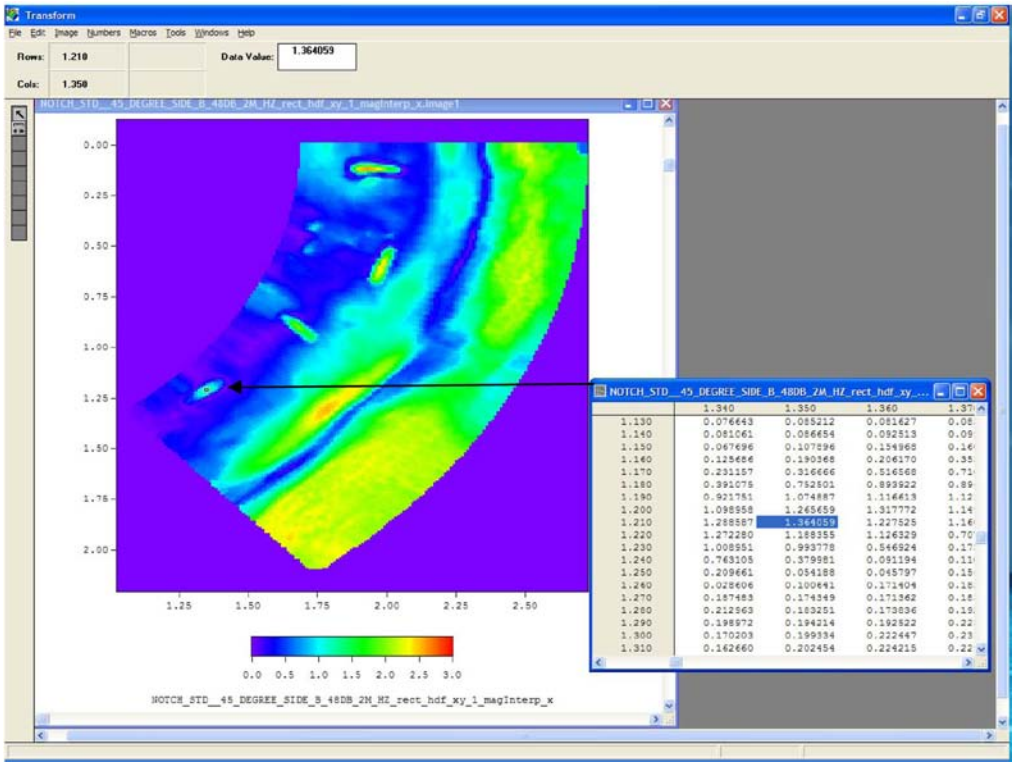
Transform
File Edit Image Numbers Macros Tools Windows Help
Rows: 1.210
Data Value: 1.364059
Cols: 1.350
NOTCH_STD__45_DEGREE_SIDE_B_48DB_2M_HZ_rect_hdf_xy_1_magInterp_x.image1
NOTCH_STD__45_DEGREE_SIDE_B_48DB_2M_HZ_rect_hdf_xy_....
1.340 1.350 1.360
1.130 0.076443 0.085212 0.081627
1.140 0.081061 0.086654 0.092513
1.150 0.067696 0.107896 0.154965
1.160 0.125656 0.190368 0.206170
1.170 0.231157 0.316666 0.516568
1.180 0.391075 0.752501 0.893922
1.190 0.921751 1.074887 1.114613
1.200 1.098958 1.265659 1.317772
1.210 1.288587 1.364059 1.227525
1.220 1.272280 1.188355 1.126329
1.230 1.008951 0.993778 0.566924
1.240 0.763105 0.379981 0.091194
1.250 0.209661 0.054188 0.045797
1.260 0.028606 0.100641 0.171404
1.270 0.187483 0.174349 0.171362
1.280 0.212963 0.183251 0.173836
1.290 0.198972 0.194214 0.192822
1.300 0.170203 0.199334 0.222447
1.310 0.162660 0.202454 0.224215
0.00 0.25 0.50 0.75 1.00 1.25 1.50 1.75 2.00
1.25 1.50 1.75 2.00 2.25 2.50
0.0 0.5 1.0 1.5 2.0 2.5 3.0
NOTCH_STD__45_DEGREE_SIDE_B_48DB_2M_HZ_rect_hdf_xy_1_magInterp_x

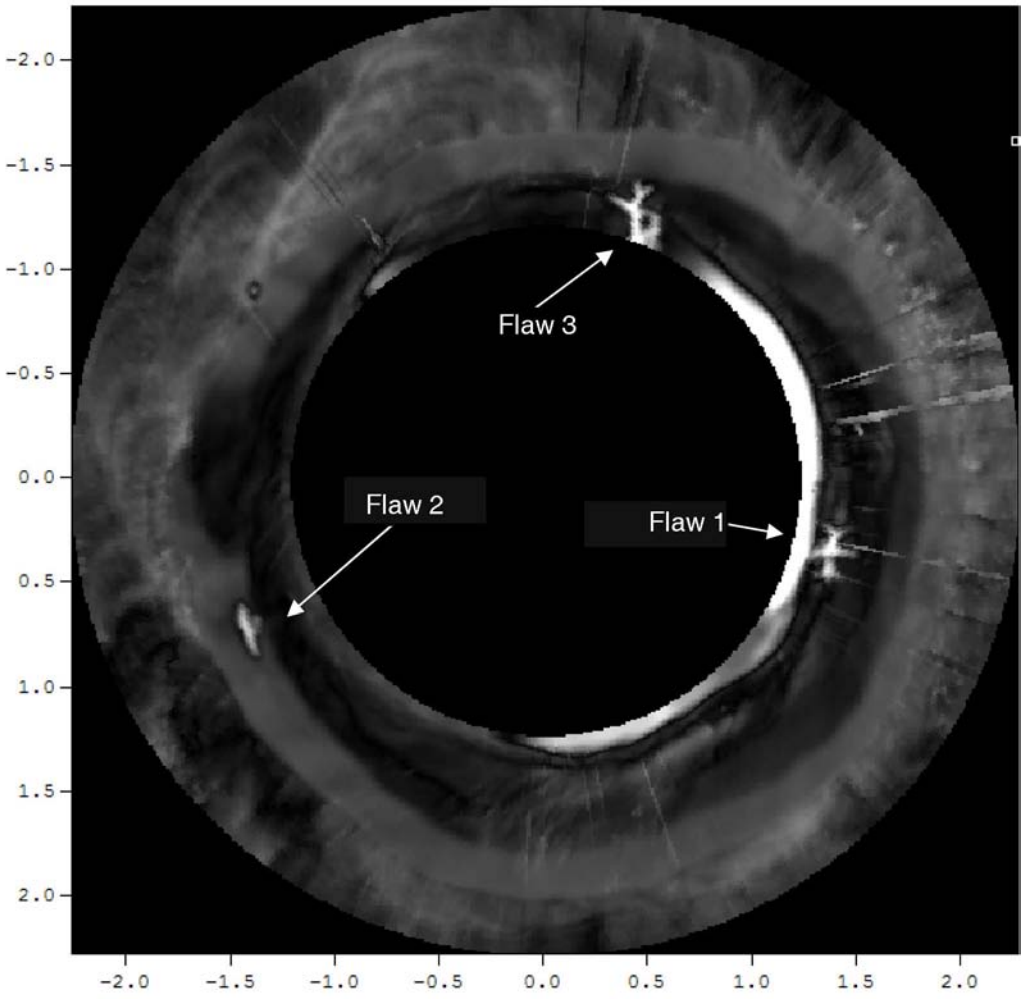

0.000.250.500.751.001.251.501.752.00

PINC_5_7_RADIAL_360_SCAN_1A_12_19_07_rect_hdf_xy_1_magInterp

G.2.1 Flaw 3

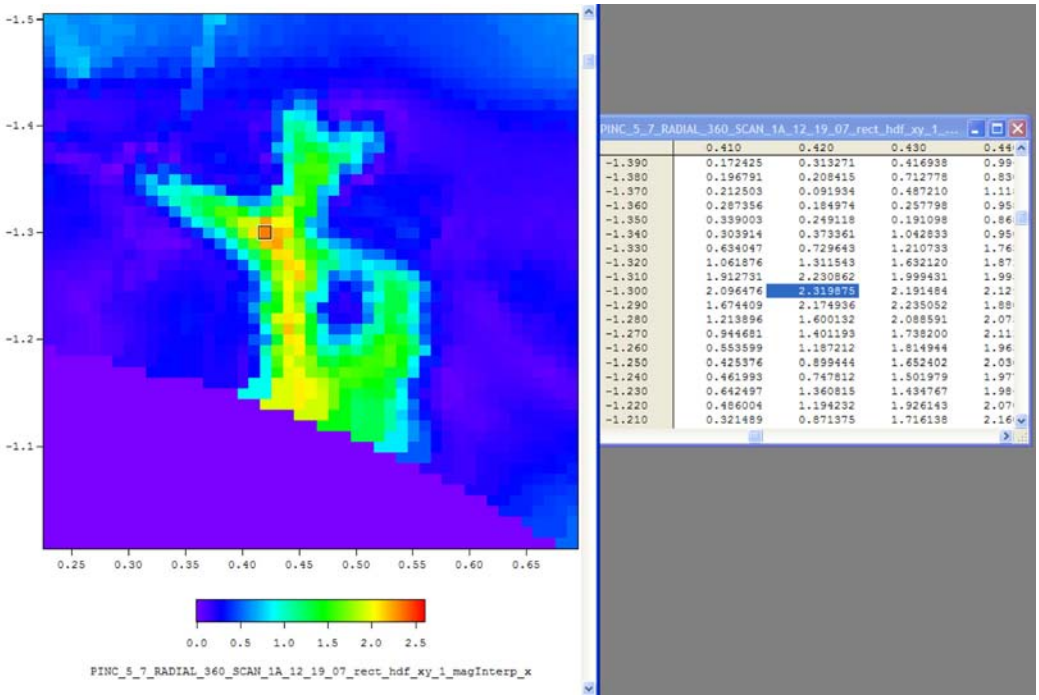

G.2.2 Flaw 1

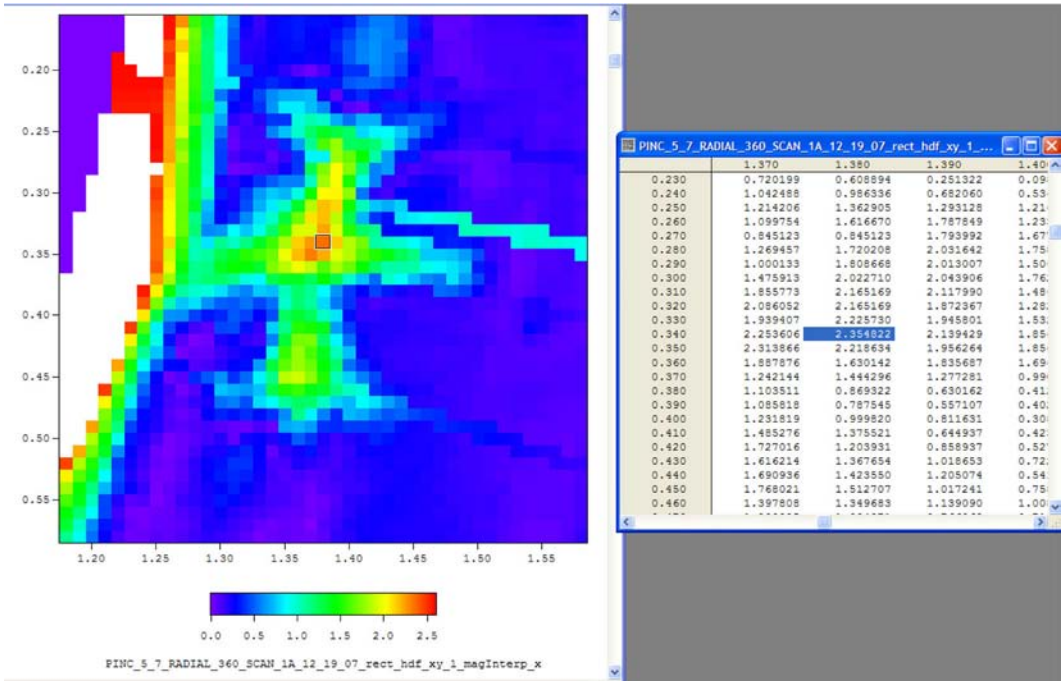

G.2.3 Flaw 2

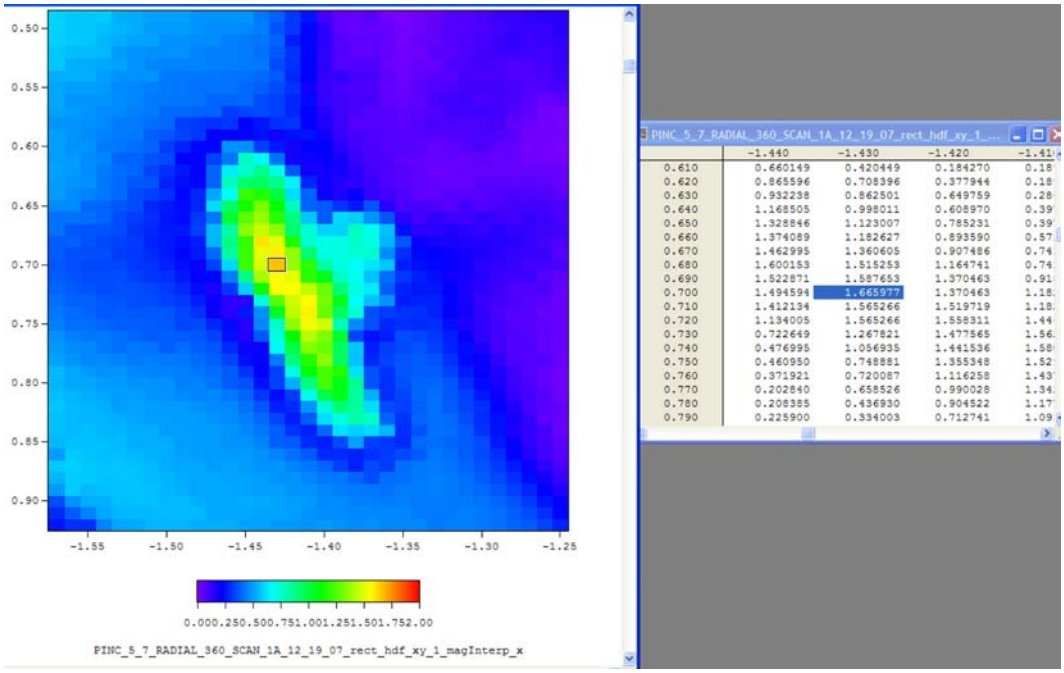
0.50
0.55
0.60
0.65
0.70
0.75
0.80
0.85
0.90
-1.55
-1.50
-1.45
-1.40
-1.35
-1.30
-1.25
0.000.250.500.751.001.251.501.752.00
PINC_5_7_RADIAL_360_SCAN_1A_12_19_07_rect_hdf_xy_1_magInterp_x
PINC_5_7_RADIAL_360_SCAN_1A_12_19_07_rect_hdf_xy_1_...
-1.440 -1.430 -1.420 -1.41
0.610 0.660149 0.420449 0.184270 0.18
0.620 0.865596 0.708396 0.377944 0.18
0.630 0.932238 0.862501 0.649759 0.28
0.640 1.168505 0.998011 0.608970 0.39
0.650 1.328846 1.123007 0.785231 0.39
0.660 1.374089 1.182627 0.893590 0.57
0.670 1.462995 1.360605 0.907486 0.74
0.680 1.600153 1.515253 1.164741 0.74
0.690 1.522871 1.587653 1.370463 0.91
0.700 1.494594 1.665977 1.370463 1.18
0.710 1.412134 1.565266 1.519719 1.18
0.720 1.134005 1.565266 1.558311 1.44
0.730 0.722649 1.267821 1.477565 1.56
0.740 0.476995 1.056935 1.441536 1.58
0.750 0.460950 0.748881 1.355348 1.52
0.760 0.371921 0.720087 1.116258 1.43
0.770 0.202840 0.658526 0.990028 1.34
0.780 0.208385 0.436930 0.904522 1.17
0.790 0.225900 0.334003 0.712741 1.09

G.3 PINC 5.8

No flaws were identified in PINC 5.8. A fabricated area was, however, identified and shown in the following image.

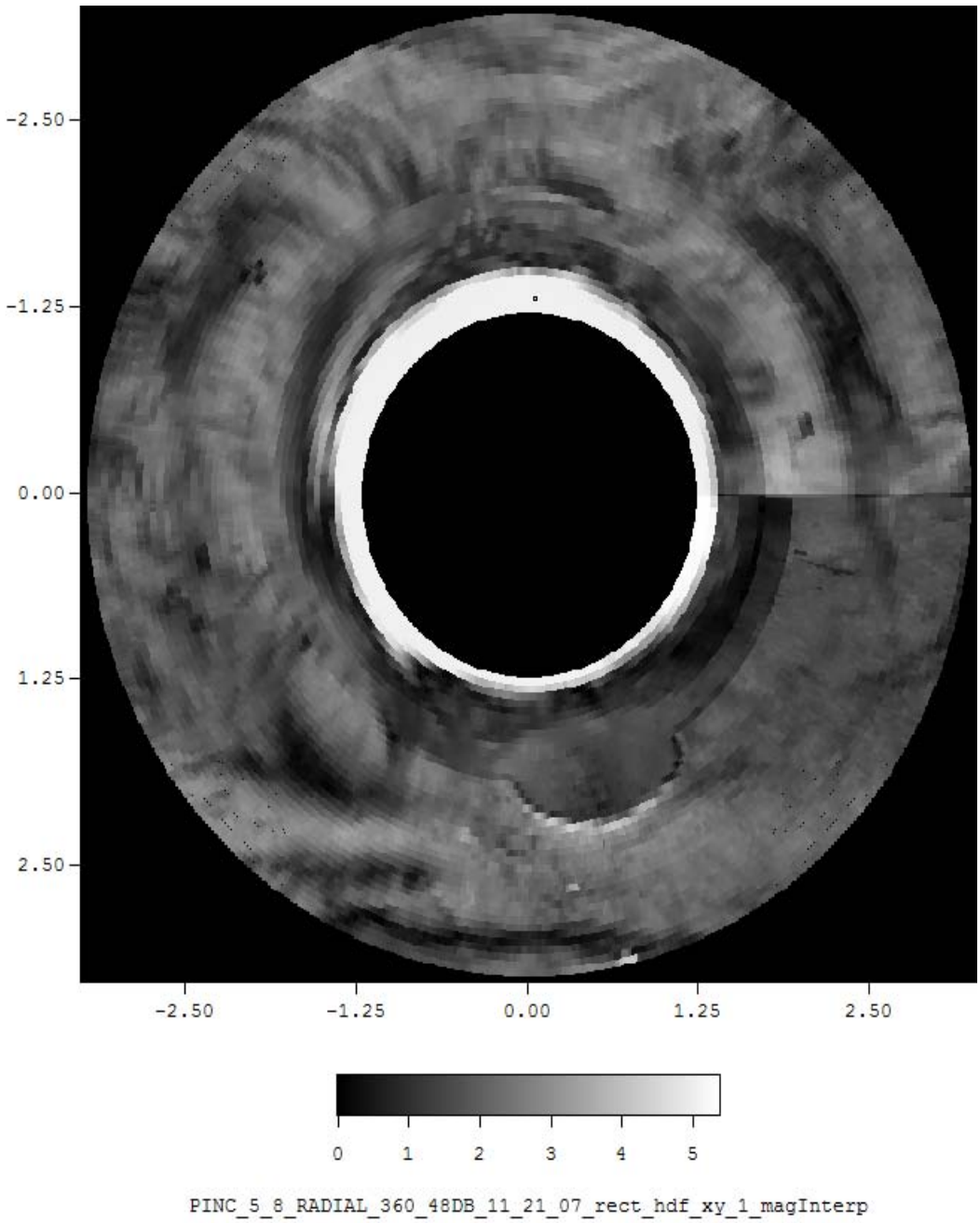

G.4 PINC 5.9

Two flaws were visible on PINC 5.9. The image below shows the magnitude of the edge of the fabrication.

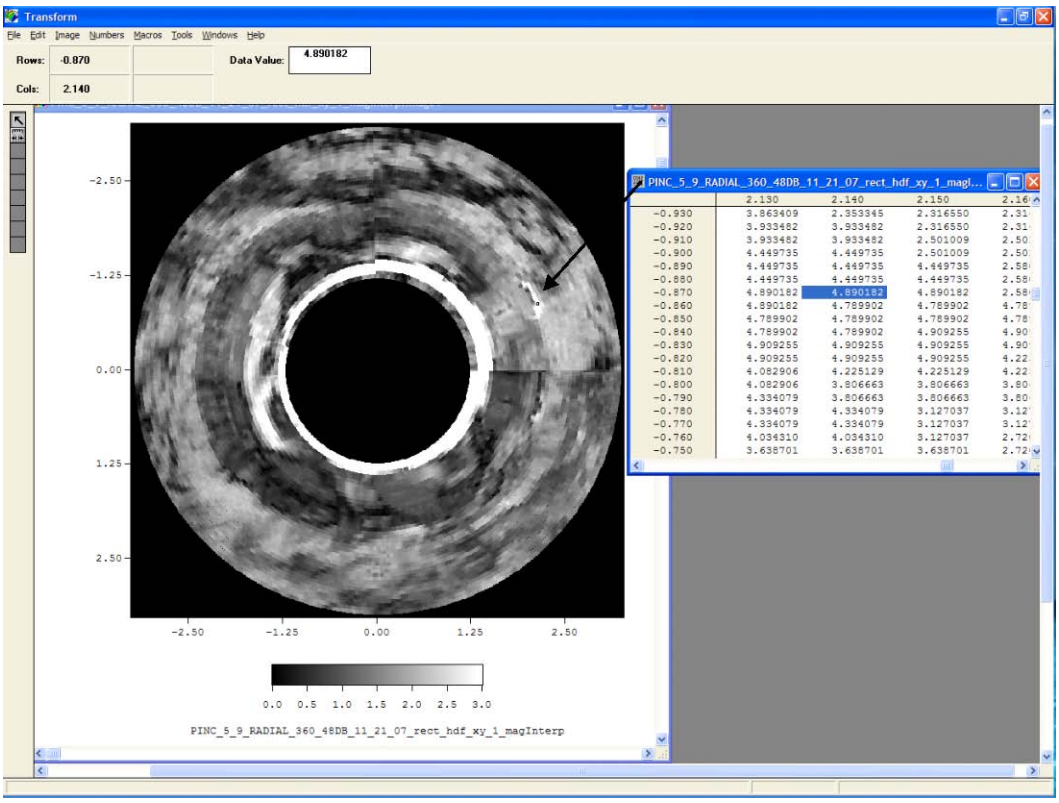

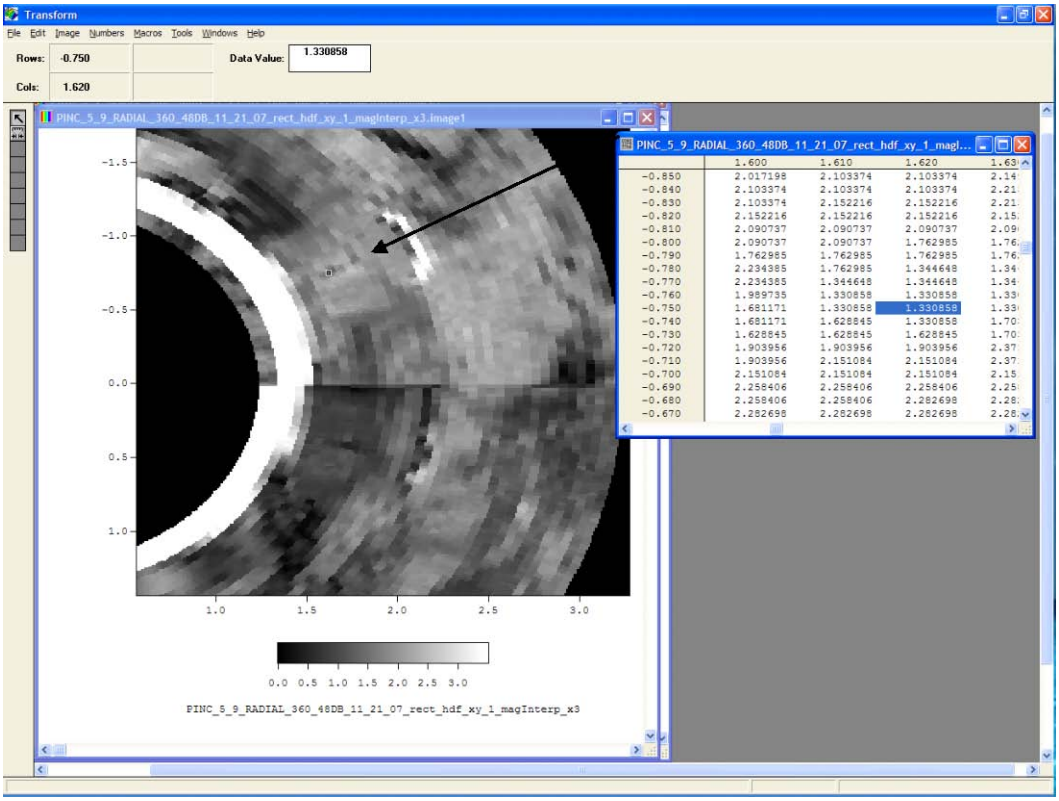
Transform
File Edit Image Numbers Macros Tools Windows Help
Rows: -0.750
Cols: 1.620
Data Value: 1.330858
PINC_5_9_RADIAL_360_48DB_11_21_07_rect_hdf_xy_1_magInterp_x3.image1
PINC_5_9_RADIAL_360_48DB_11_21_07_rect_hdf_xy_1_magInterp_x3

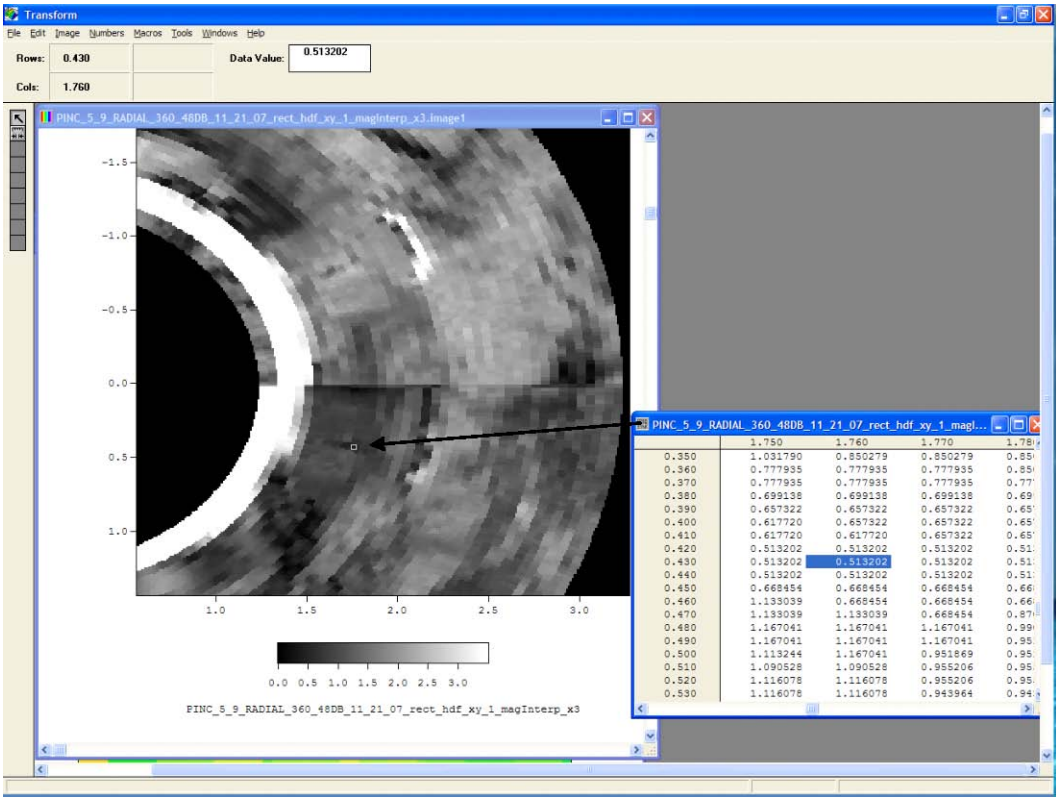
Transform
File Edit Image Numbers Macros Tools Windows Help
Rows: 0.430
Cols: 1.760
Data Value: 0.513202
PINC_5_9_RADIAL_360_48DB_11_21_07_rect_hdf_xy_1_magInterp_x3.image1
PINC_5_9_RADIAL_360_48DB_11_21_07_rect_hdf_xy_1_magInterp_x3

G.5 PINC 5.10

General magnitude of the fabrication area.

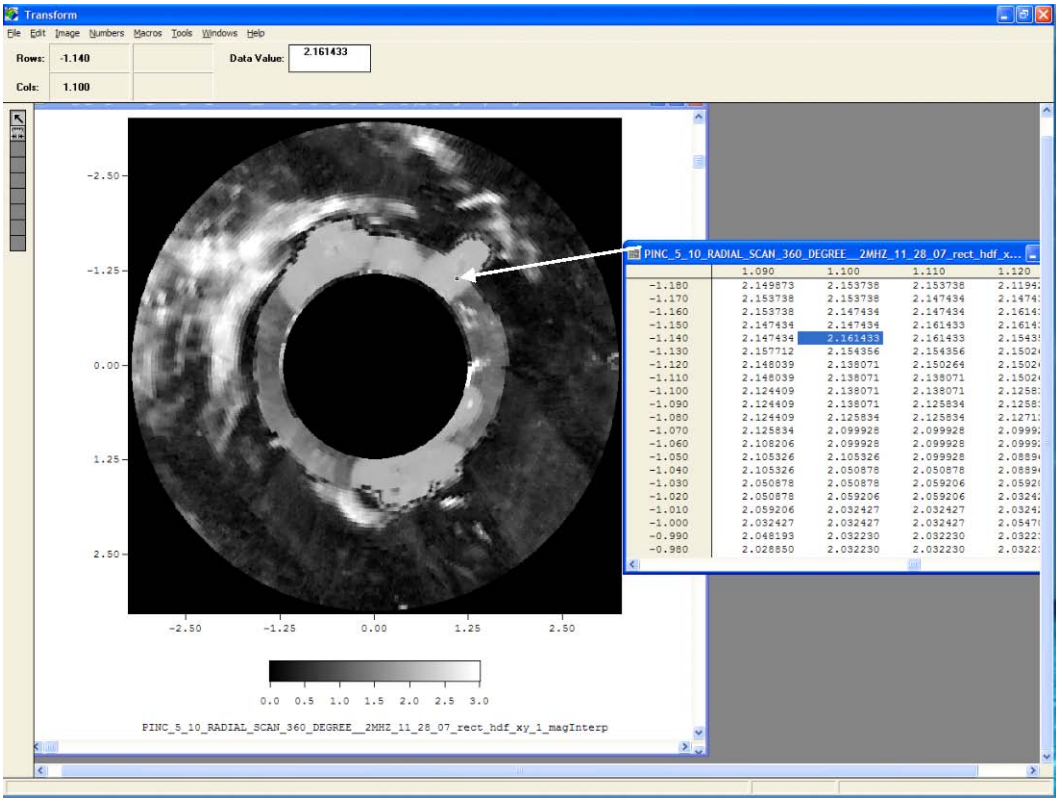

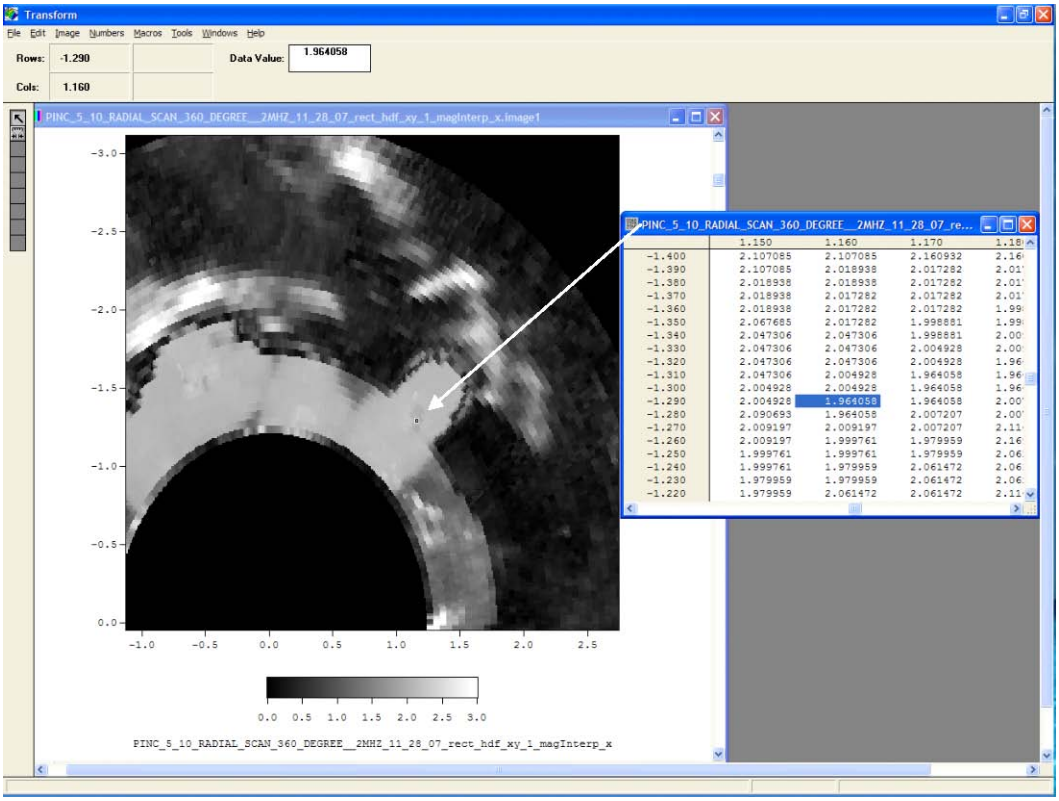
Transform
File Edit Image Numbers Macros Tools Windows Help
Rows: -1.290
Cols: 1.160
Data Value: 1.964058
PINC_5_10_RADIAL_SCAN_360_DEGREE__2MHZ_11_28_07_rect_hdf_xy_1_magInterp_x.image1
PINC_5_10_RADIAL_SCAN_360_DEGREE__2MHZ_11_28_07_re...
PINC_5_10_RADIAL_SCAN_360_DEGREE__2MHZ_11_28_07_rect_hdf_xy_1_magInterp_x

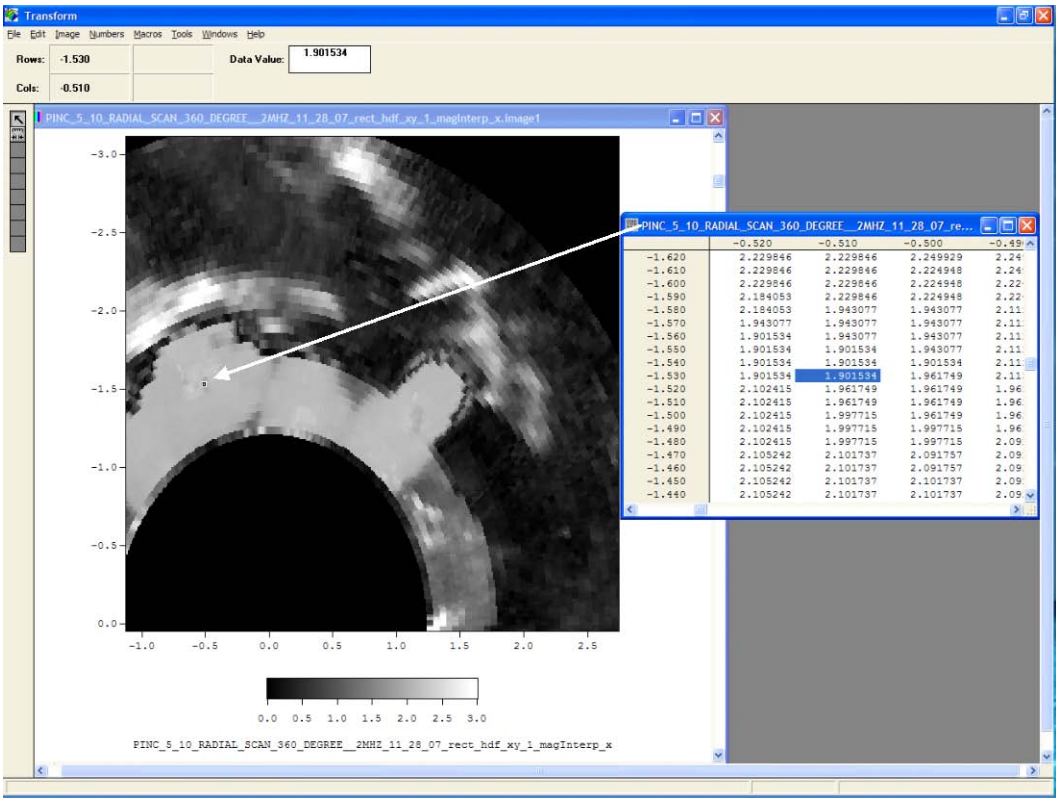
Transform
File Edit Image Numbers Macros Tools Windows Help
Rows: -1.530
Cols: -0.510
Data Value: 1.901534
PINC_5_10_RADIAL_SCAN_360_DEGREE__2MHZ_11_28_07_rect_hdf_xy_1_magInterp_x.image1
PINC_5_10_RADIAL_SCAN_360_DEGREE__2MHZ_11_28_07_re...
PINC_5_10_RADIAL_SCAN_360_DEGREE__2MHZ_11_28_07_rect_hdf_xy_1_magInterp_x

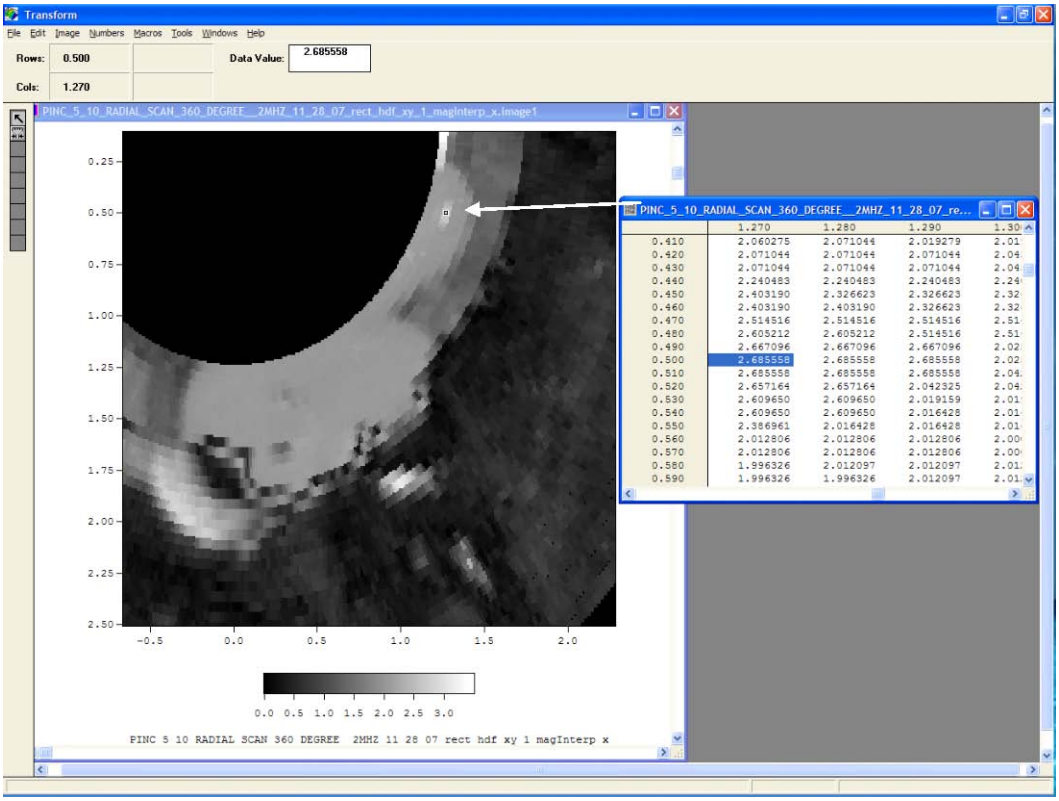
Transform
File Edit Image Numbers Macros Tools Windows Help
Rows: 0.500
Cols: 1.270
Data Value: 2.685558
PINC_5_10_RADIAL_SCAN_360_DEGREE__2MHZ_11_28_07_rect_hdf_xy_1_magInterp_x.Image1
PINC_5_10_RADIAL_SCAN_360_DEGREE__2MHZ_11_28_07_re...
PINC 5 10 RADIAL SCAN 360 DEGREE 2MHZ 11 28 07 rect hdf xy 1 magInterp x

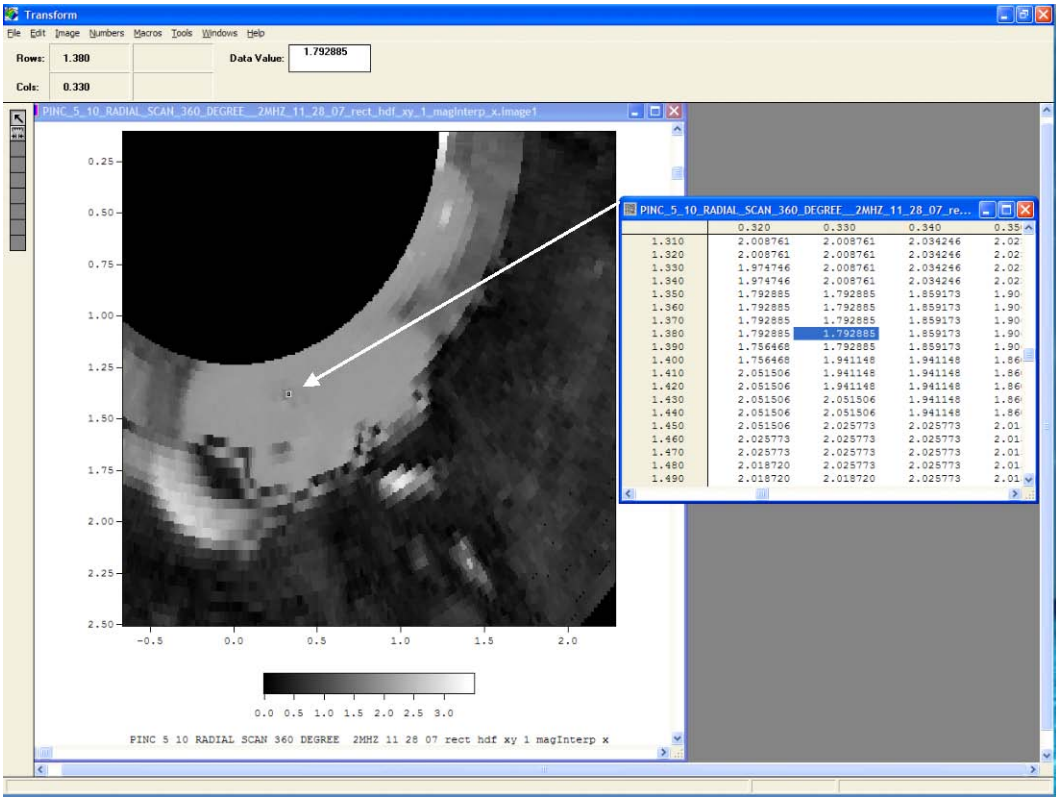
Transform
File Edit Image Numbers Macros Tools Windows Help
Rows: 1.380
Cols: 0.330
Data Value: 1.792885
PINC_5_10_RADIAL_SCAN_360_DEGREE__2MHZ_11_28_07_rect_hdf_xy_1_magInterp_x.Image1
PINC_5_10_RADIAL_SCAN_360_DEGREE__2MHZ_11_28_07_re...
PINC 5 10 RADIAL SCAN 360 DEGREE 2MHZ 11 28 07 rect hdf xy 1 magInterp x

Here is another image that we used in a different report which shows six flaws. It is a stretch to say you can see them all unless you know what you are looking for. In the example shown above, we point to a different area for the flaw location. We would need to zero in on the flaw and scan at high resolution to identify.

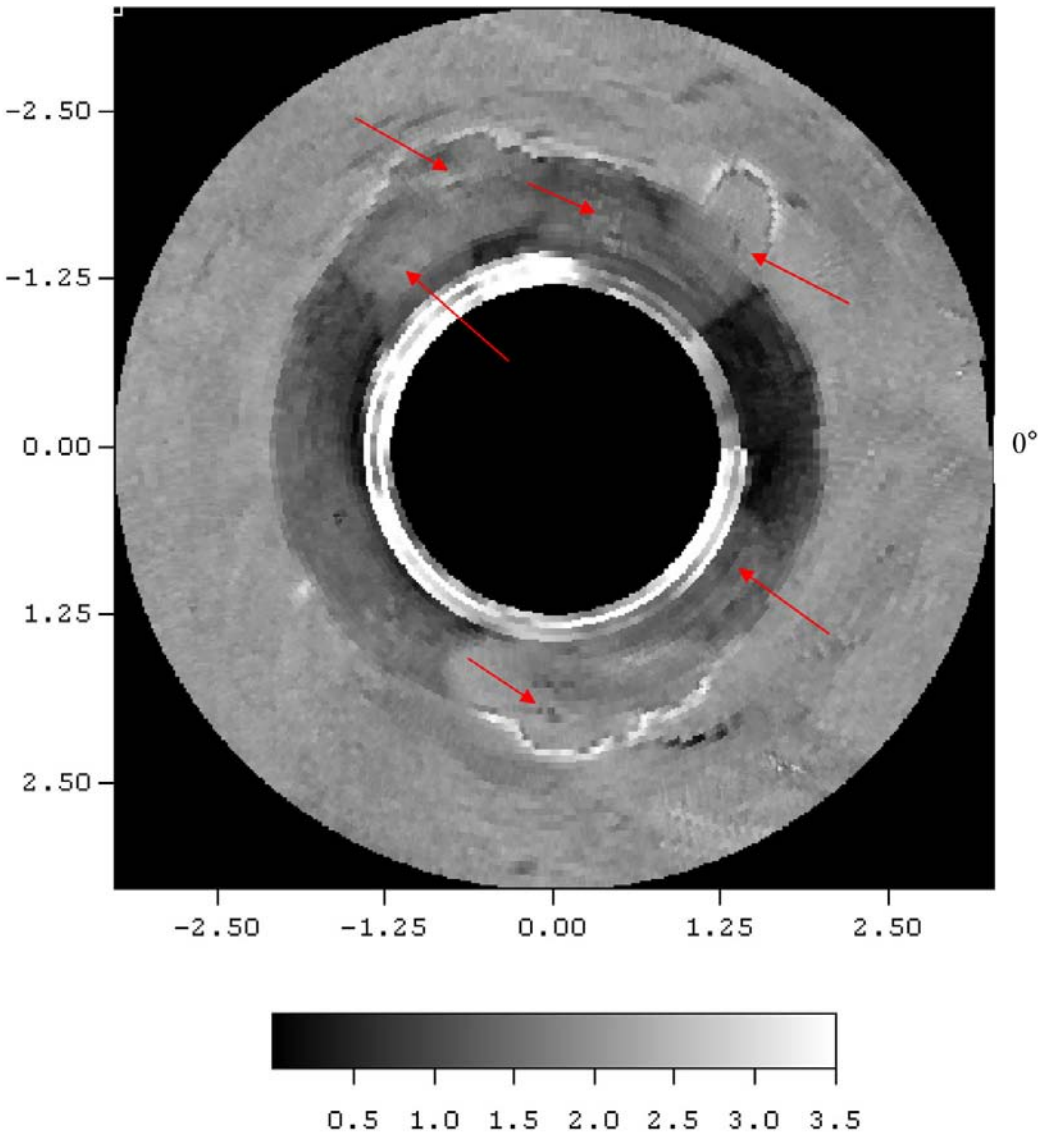

G.6 PINC 5.11

General area magnitude.

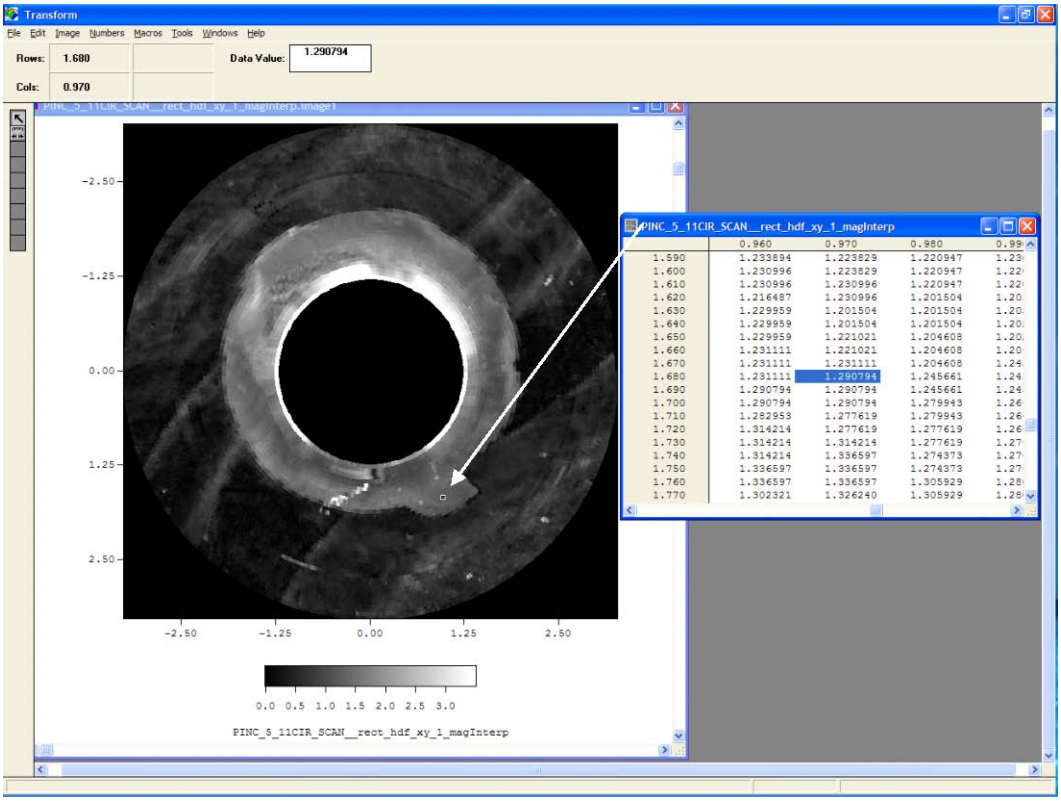

G.7 PINC 5.12

General area magnitude.

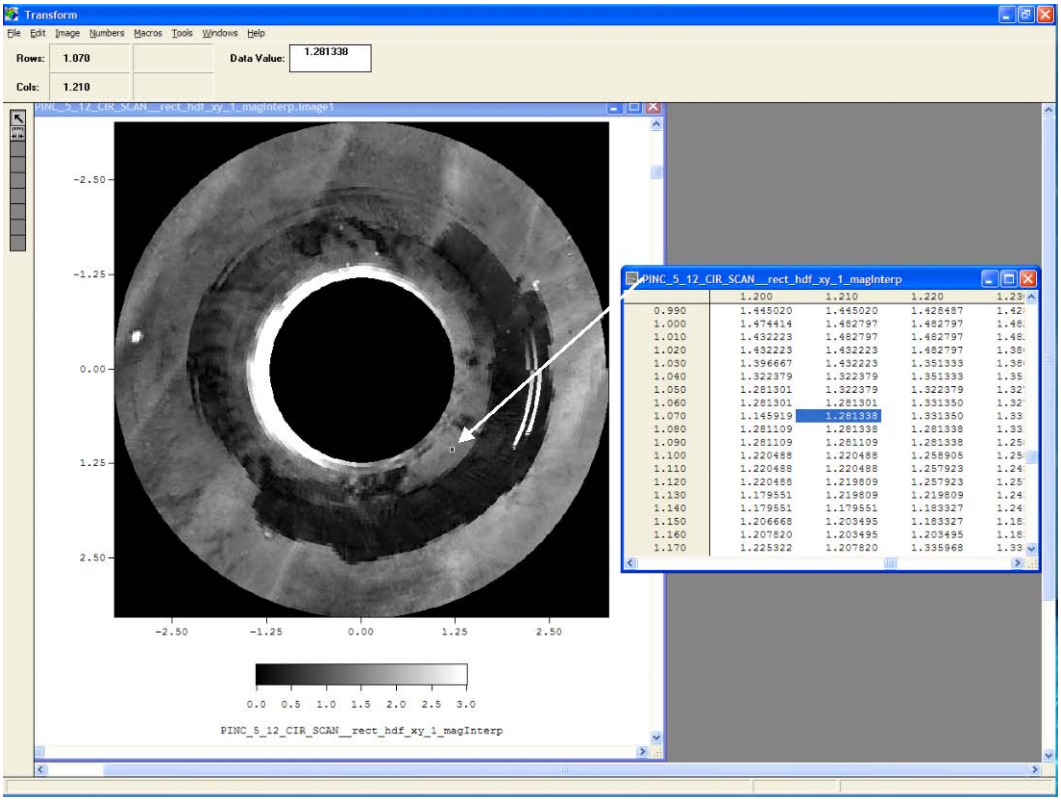

G.8 PINC 5.6

Six indications were identified.

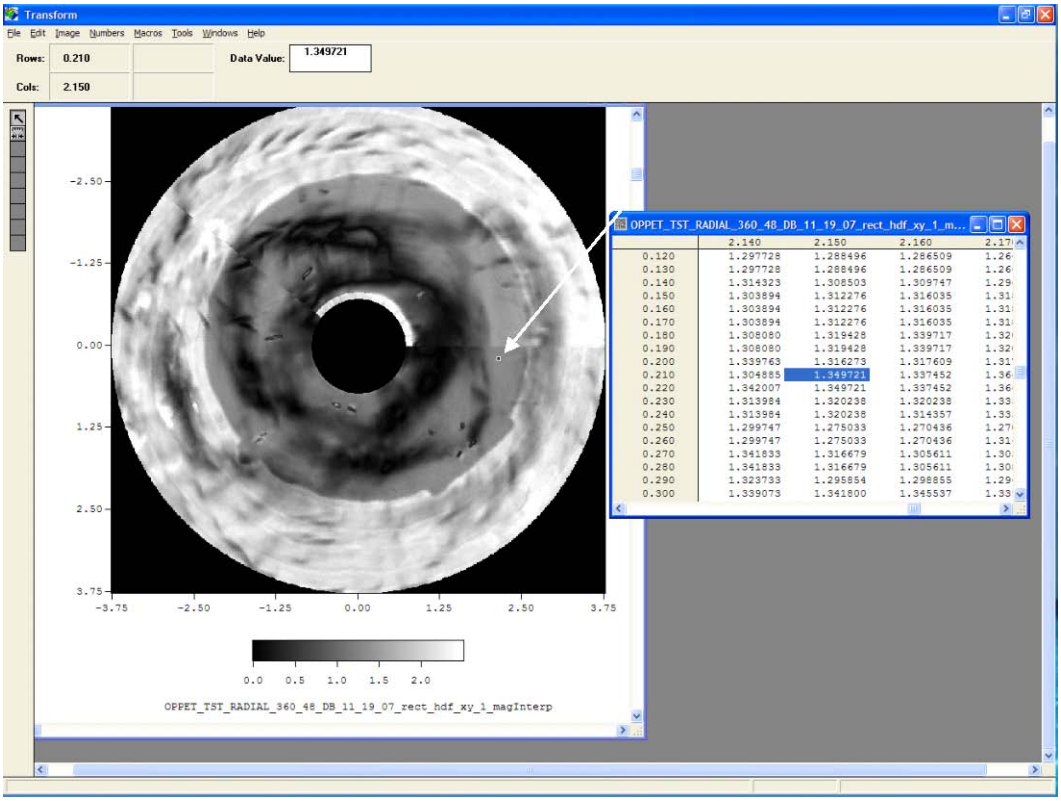

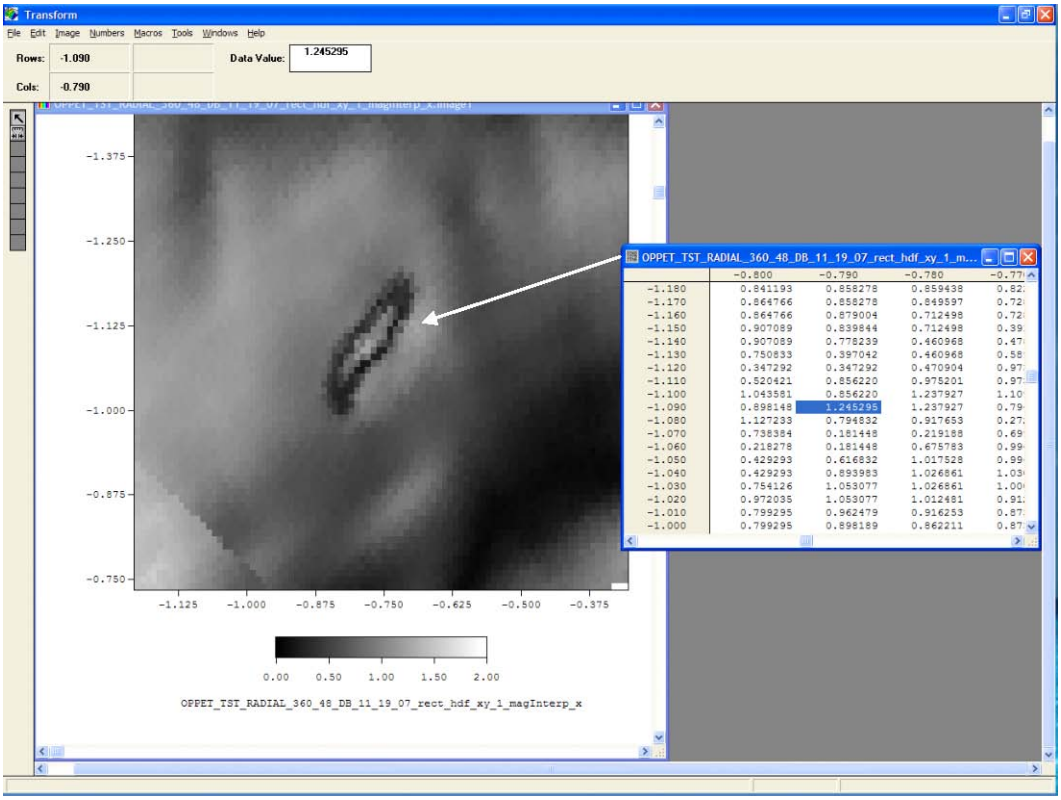
Transform
File Edit Image Numbers Macros Tools Windows Help
Rows: -1.090
Cols: -0.790
Data Value: 1.245295
OPPET_TST_RADIAL_360_48_DB_11_19_07_rect_hdf_xy_1_m...
OPPET_TST_RADIAL_360_48_DB_11_19_07_rect_hdf_xy_1_magInterp_x

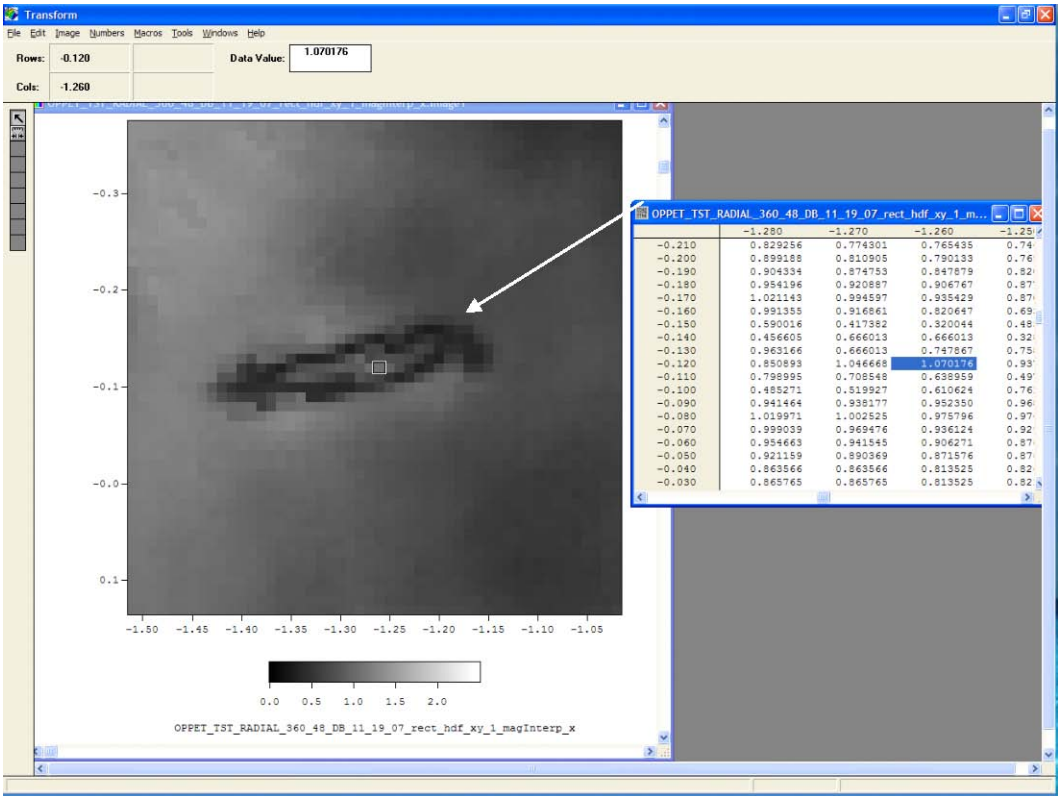
Transform
File Edit Image Numbers Macros Tools Windows Help
Rows: -0.120
Cols: -1.260
Data Value: 1.070176
OPPET_TST_RADIAL_360_48_DB_11_19_07_rect_hdf_xy_1_m...
OPPET_TST_RADIAL_360_48_DB_11_19_07_rect_hdf_xy_1_magInterp_x

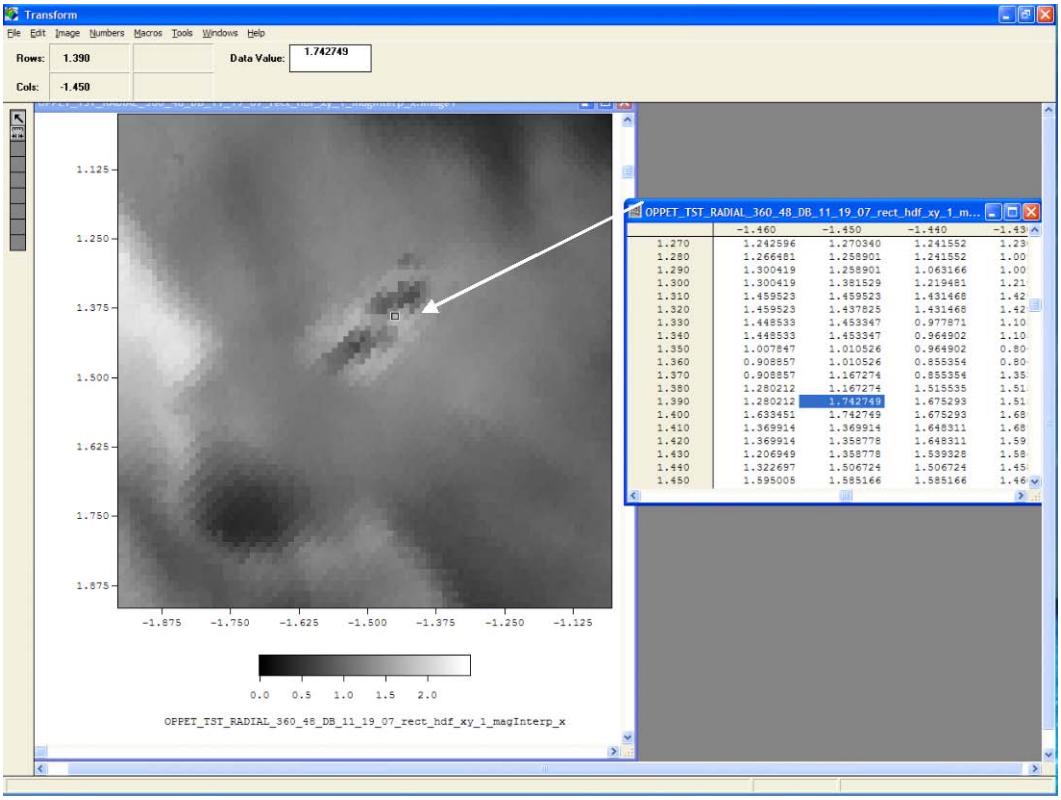
Transform
File Edit Image Numbers Macros Tools Windows Help
Rows: 1.390
Cols: -1.450
Data Value: 1.742749
OPPET_TST_RADIAL_360_48_DB_11_19_07_rect_hdf_xy_1_magInterp_x

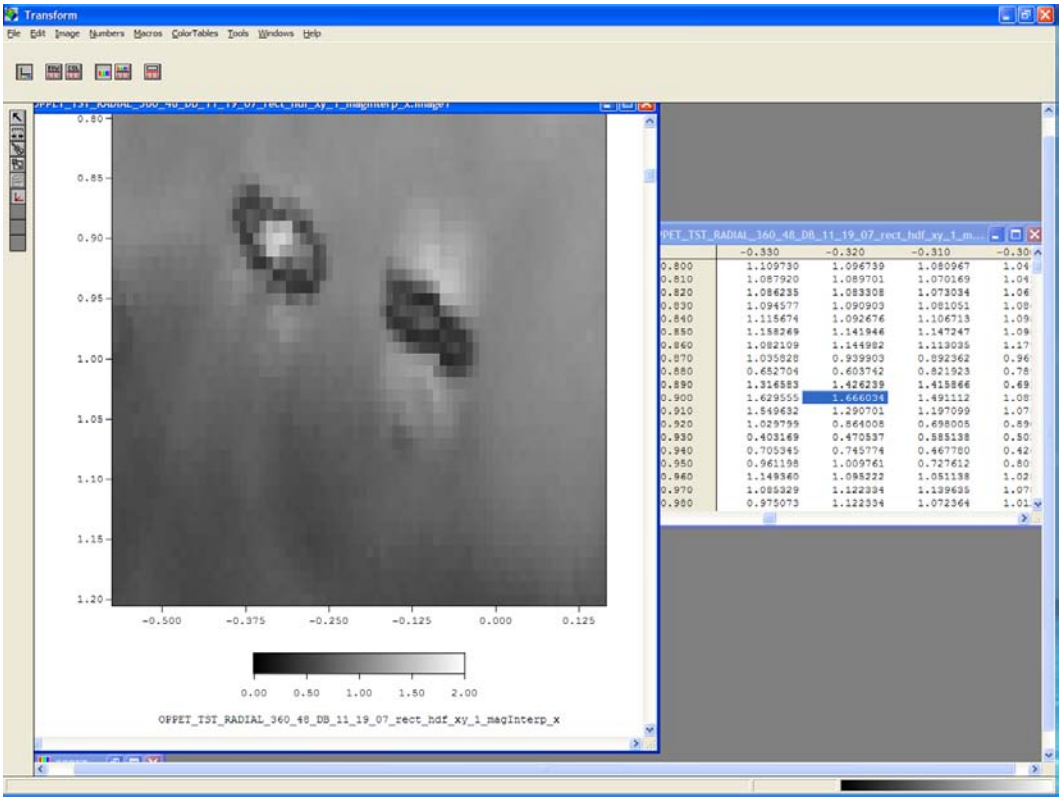
Transform
File Edit Image Numbers Macros ColorTables Tools Windows Help
OPPET_TST_RADIAL_360_48_DB_11_19_07_rect_hdf_xy_1_magInterp_x

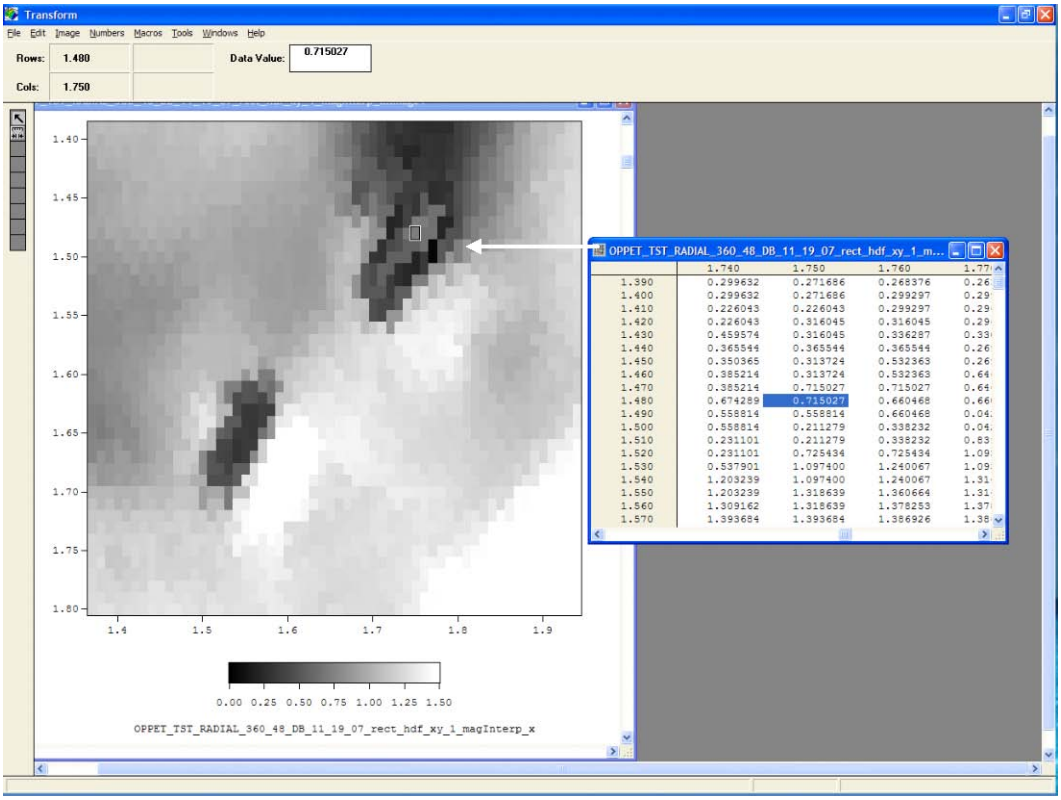
Transform
File Edit Image Numbers Macros Tools Windows Help
Rows: 1.480
Cols: 1.750
Data Value: 0.715027
OPPET_TST_RADIAL_360_48_DB_11_19_07_rect_hdf_xy_1_m...
OPPET_TST_RADIAL_360_48_DB_11_19_07_rect_hdf_xy_1_magInterp_x

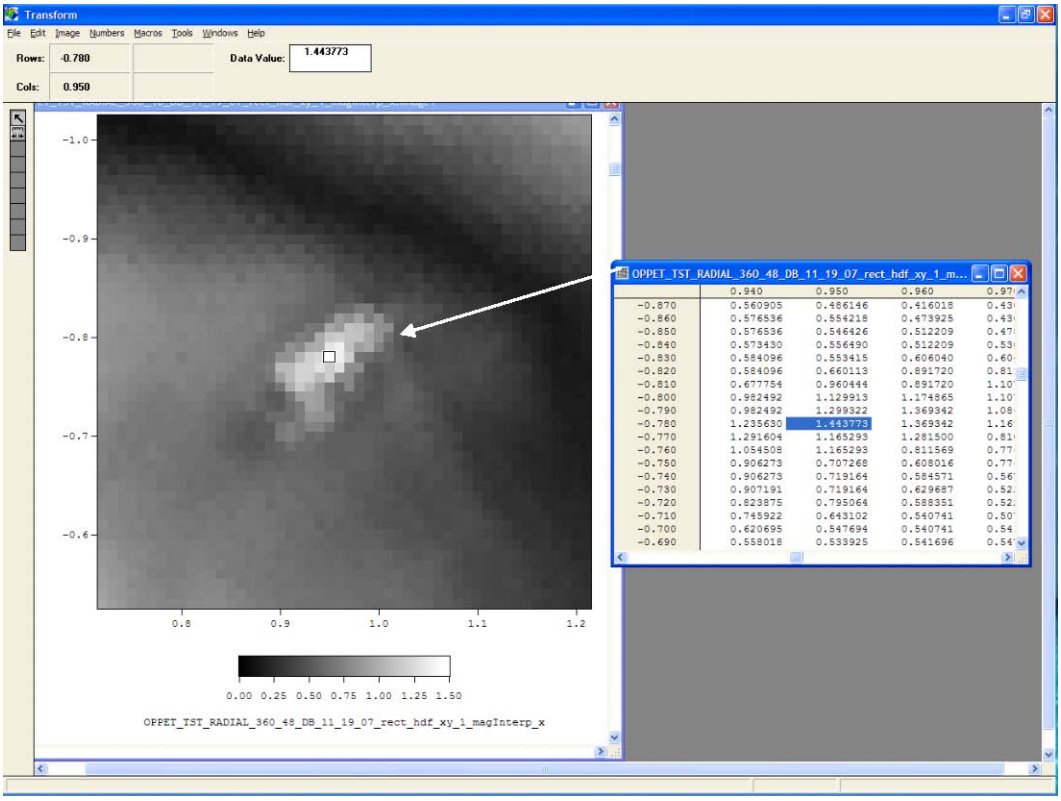
Transform
File Edit Image Numbers Macros Tools Windows Help
Rows: -0.780
Cols: 0.950
Data Value: 1.443773
OPPET_TST_RADIAL_360_48_DB_11_19_07_rect_hdf_xy_1_m...
OPPET_TST_RADIAL_360_48_DB_11_19_07_rect_hdf_xy_1_magInterp_x

G.9 Japanese Samples

G.9.1 EDM Sample Block 1

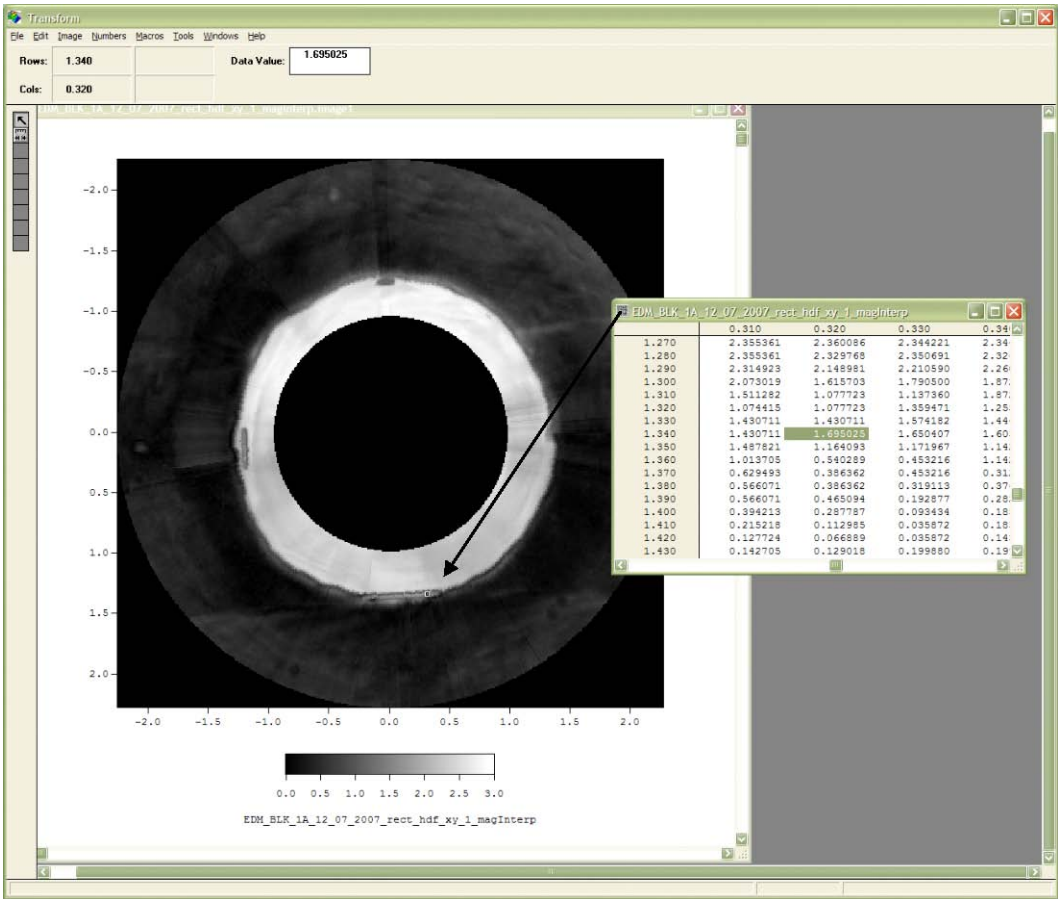

G.9.2 EDM Sample Block 2

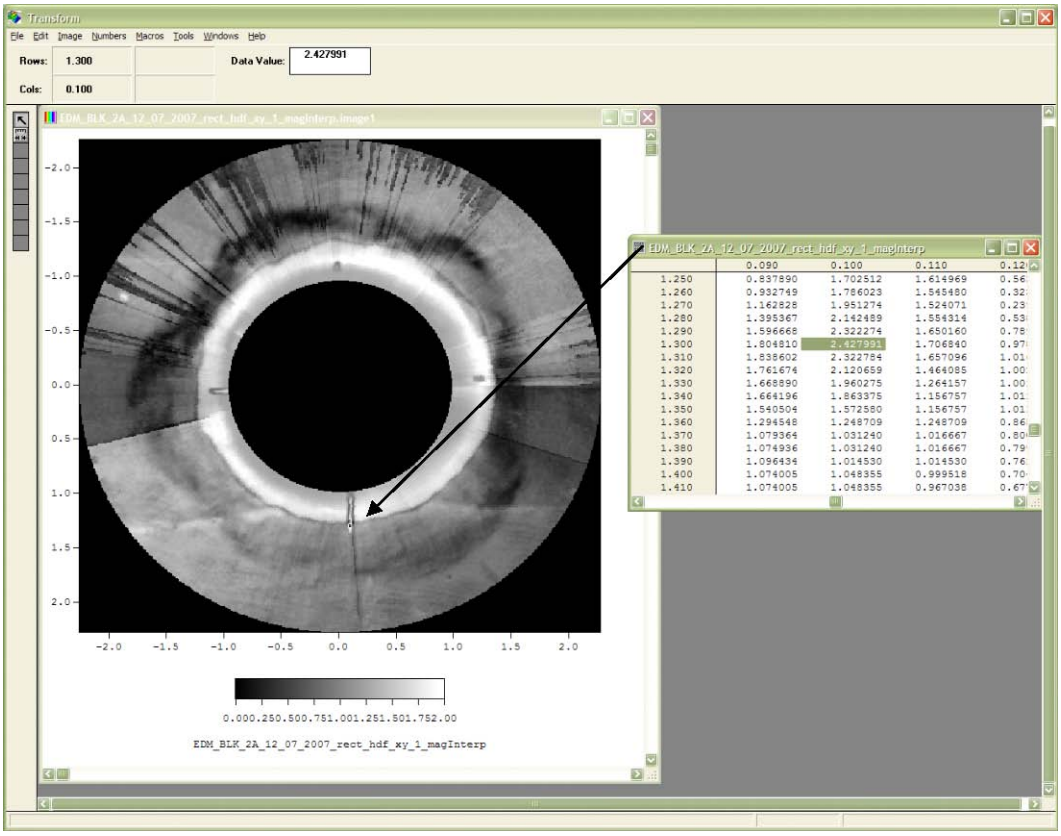

G.9.3 Reference Block 1

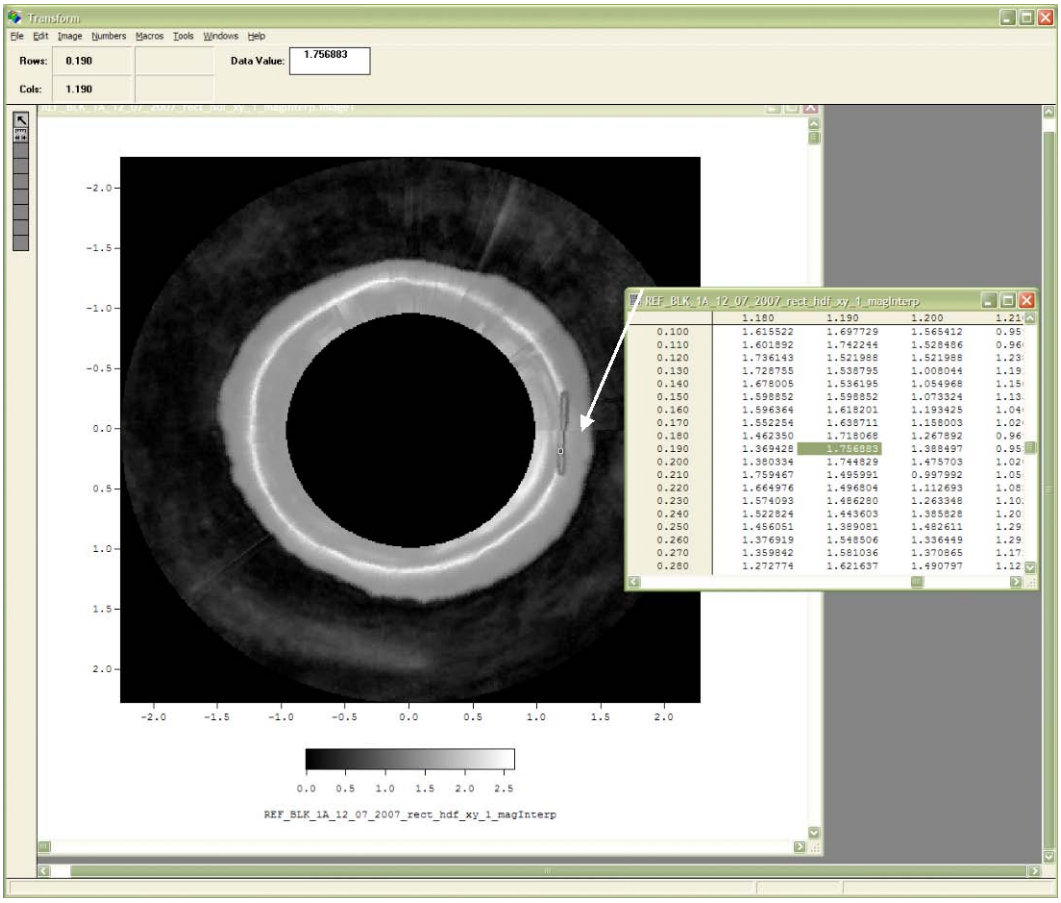

G.9.4 Reference Block 2

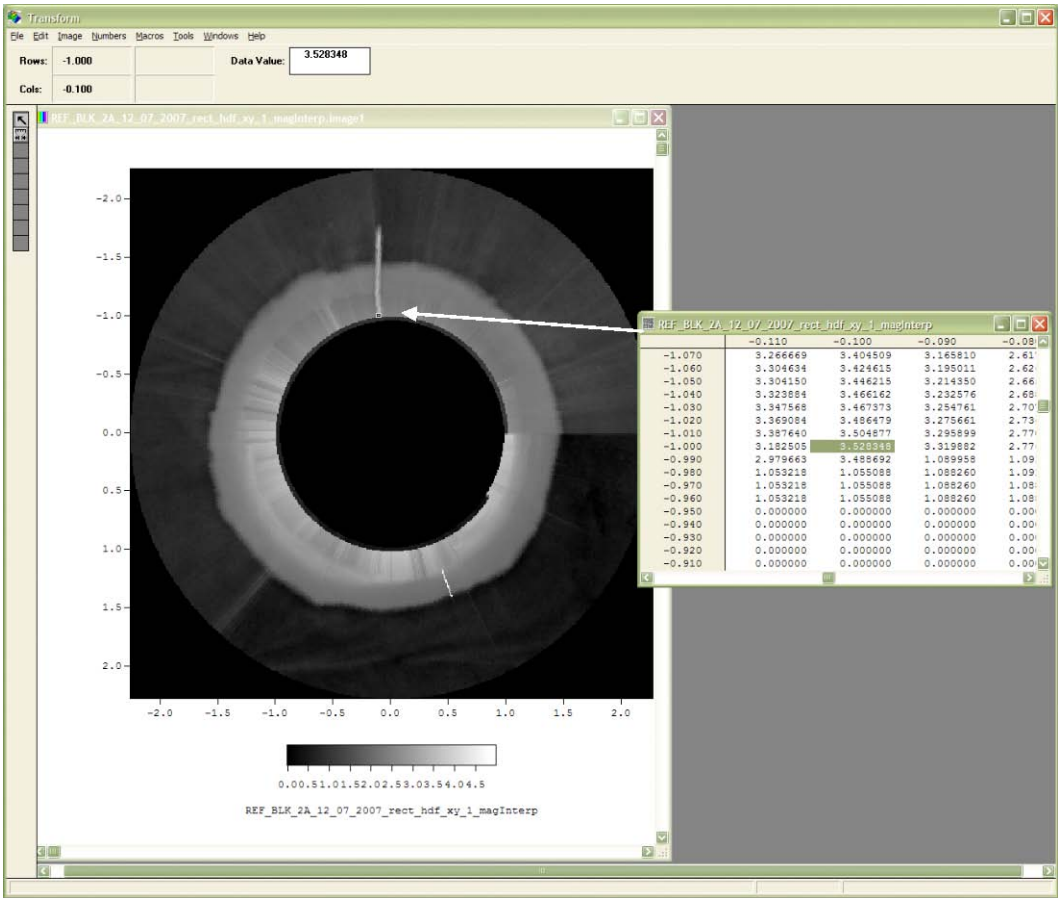

G.10 PINC 5.13


NO1


No. 1-1
60
70
80
90
100
MADE IN JAPAN

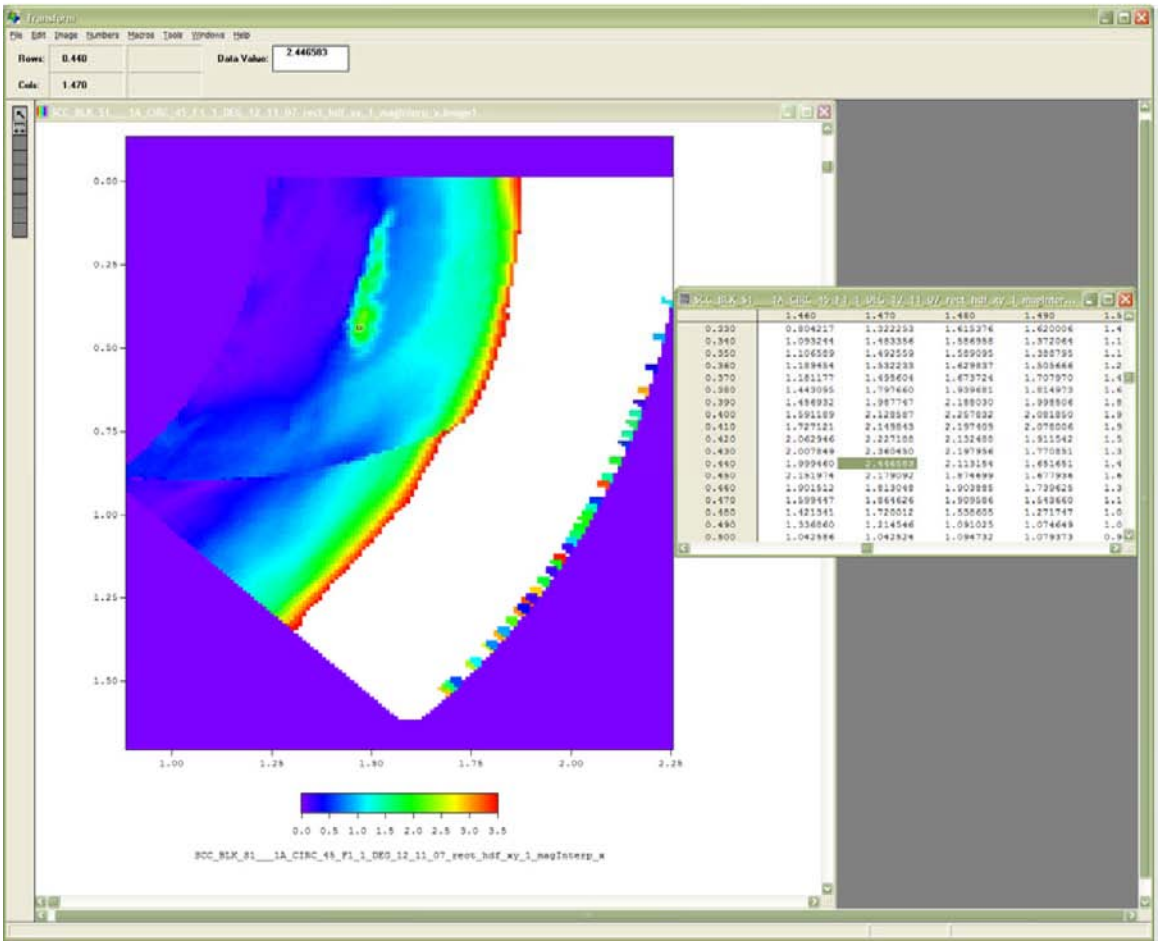
Data Value:
2.446583
Rows:
0.440
Cols:
1.470

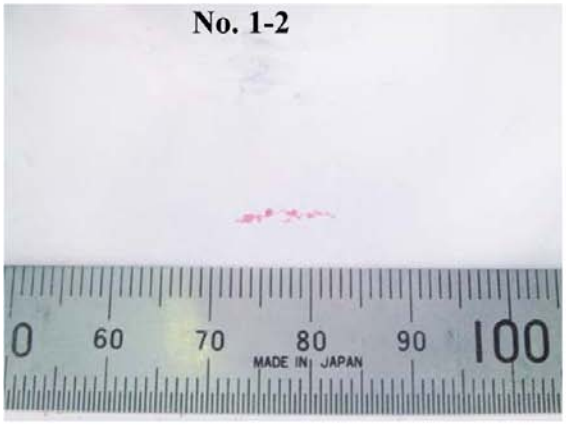
No. 1-2
0
60
70
80
90
100
MADE IN JAPAN

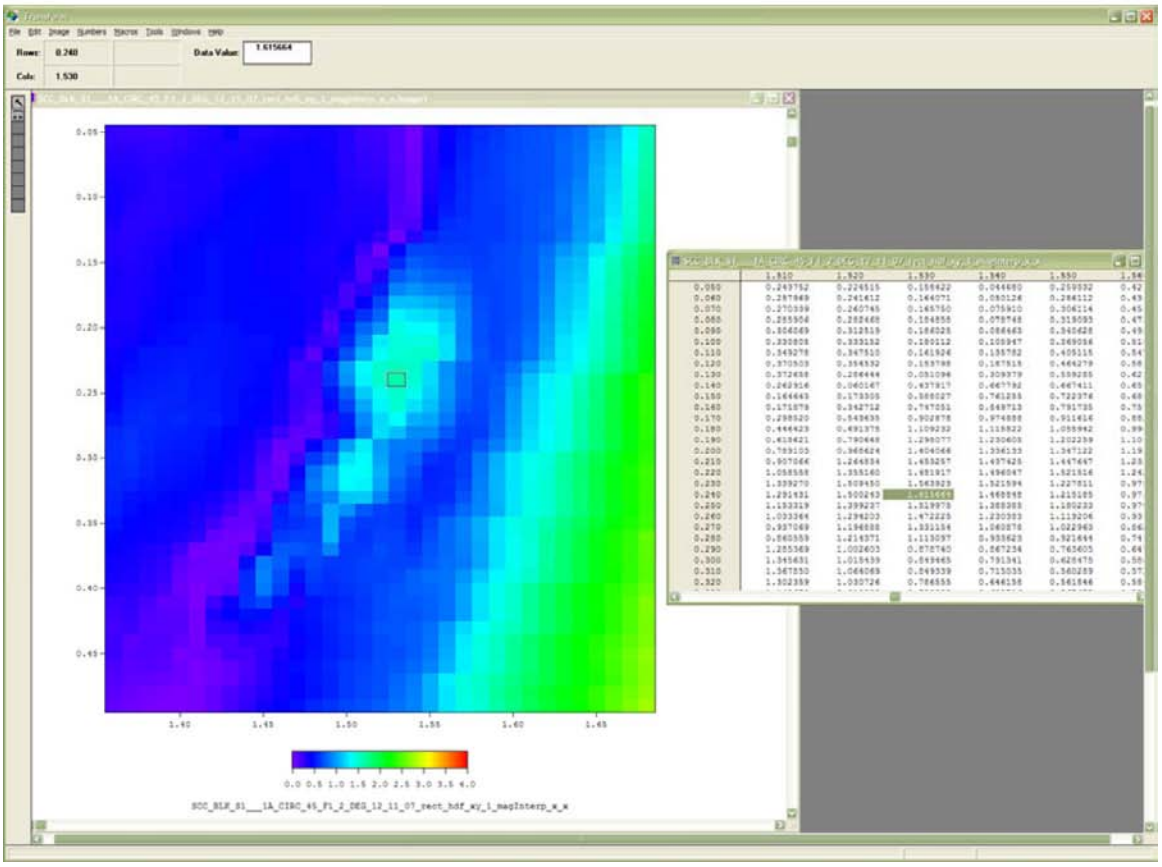

G.11 PINC 5.14


N02

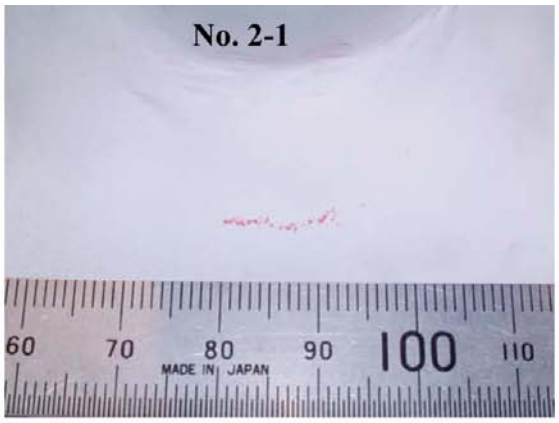
No. 2-1
60
70
80
90
100
110
MADE IN JAPAN

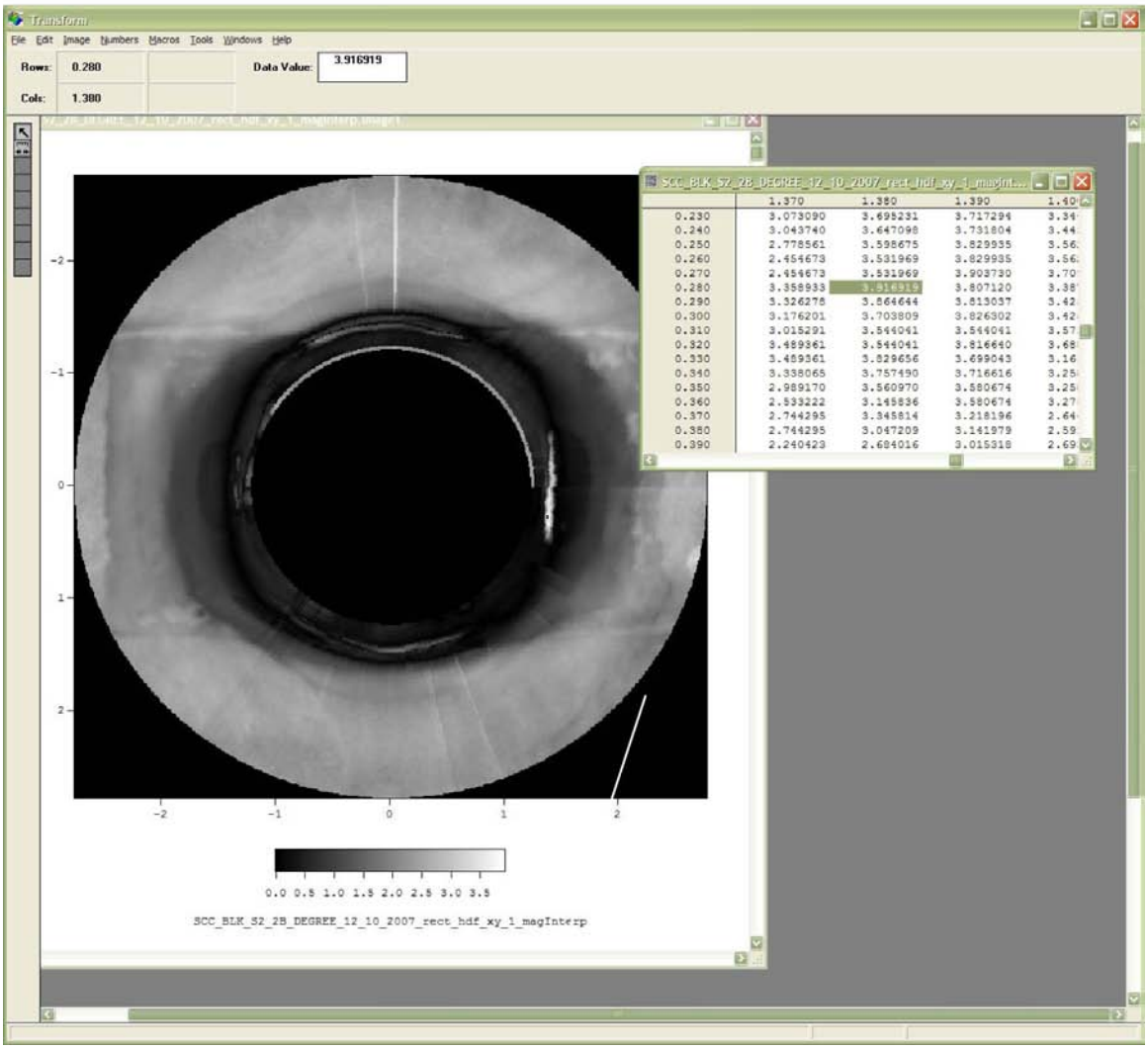
Transform
File Edit Image Numbers Macros Tools Windows Help
Rows: 0.280
Cols: 1.380
Data Value: 3.916919
SCC_BLK_S2_2B_DEGREE_12_10_2007_rect_hdf_xy_1_magInterp
0.0 0.5 1.0 1.5 2.0 2.5 3.0 3.5

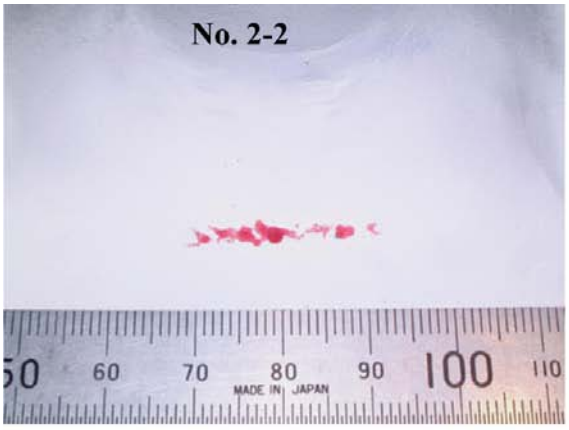
No. 2-2
50
60
70
80
90
100
110
MADE IN JAPAN

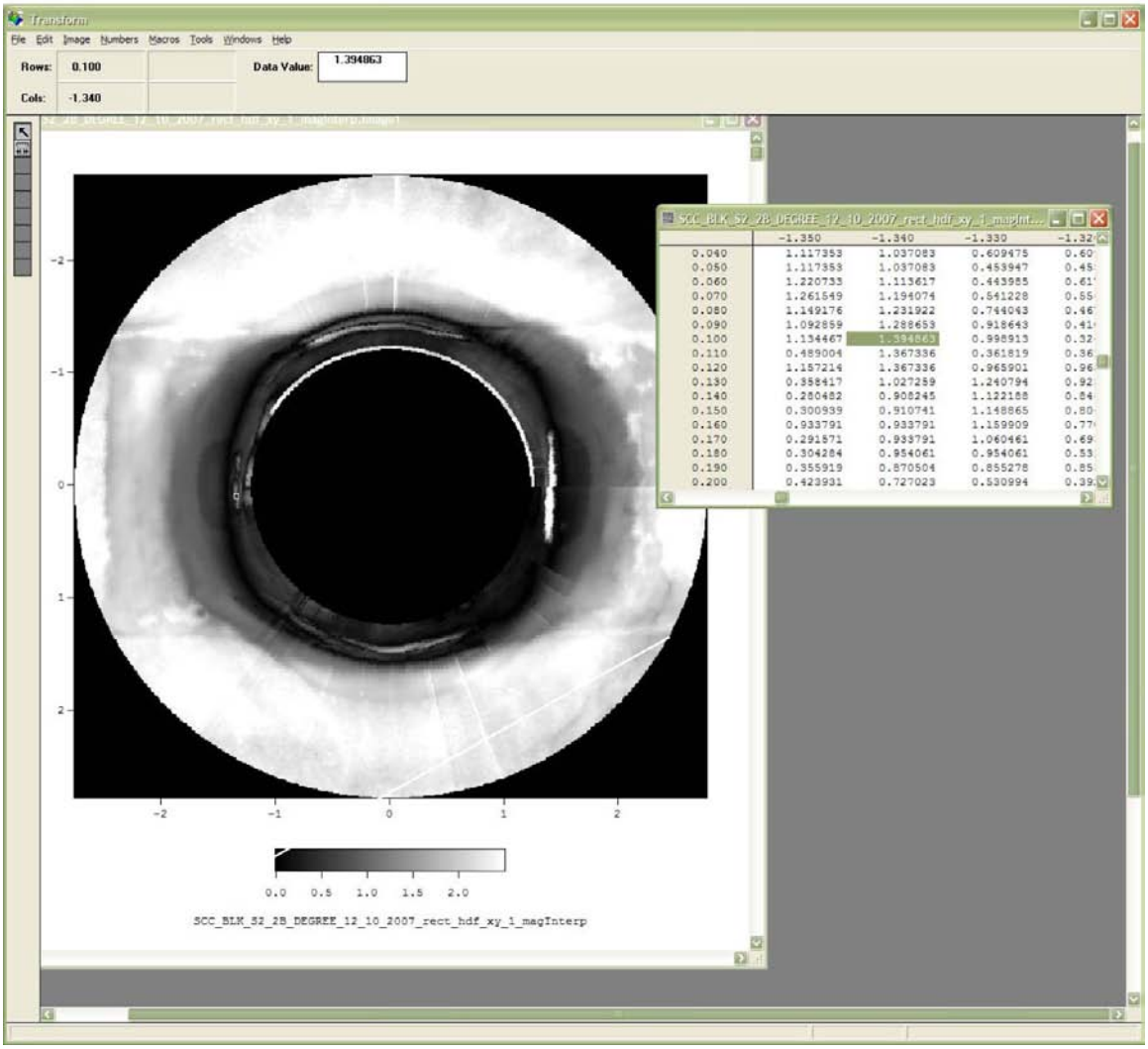
Transform
File Edit Image Numbers Macros Tools Windows Help
Rows: 0.100
Cols: -1.340
Data Value: 1.394863
SCC_BLK_S2_2B_DEGREE_12_10_2007_rect_hdf_xy_1_magInterp
-1.350 -1.340 -1.330
0.040 1.117353 1.037083 0.609475
0.050 1.117353 1.037083 0.453947
0.060 1.220733 1.113617 0.443985
0.070 1.261549 1.194074 0.541228
0.080 1.149176 1.231922 0.744043
0.090 1.092859 1.288653 0.918643
0.100 1.134467 1.394863 0.998913
0.110 0.489004 1.367336 0.361819
0.120 1.157214 1.367336 0.965901
0.130 0.358417 1.027259 1.240794
0.140 0.280482 0.908245 1.122188
0.150 0.300939 0.910741 1.148865
0.160 0.933791 0.933791 1.159909
0.170 0.291571 0.933791 1.060461
0.180 0.304284 0.954061 0.954061
0.190 0.355919 0.870504 0.855278
0.200 0.423931 0.727023 0.530994
0.0 0.5 1.0 1.5 2.0
SCC_BLK_S2_2B_DEGREE_12_10_2007_rect_hdf_xy_1_magInterp

G.12 PINC 5.15

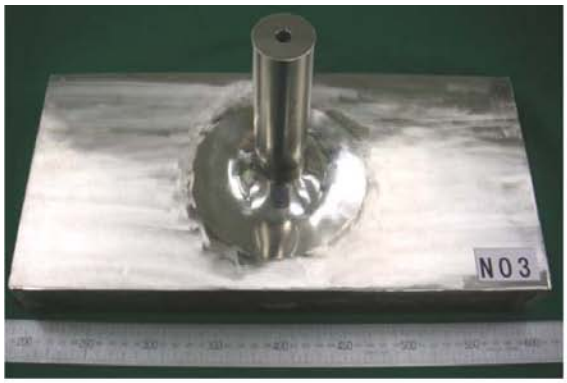
N03

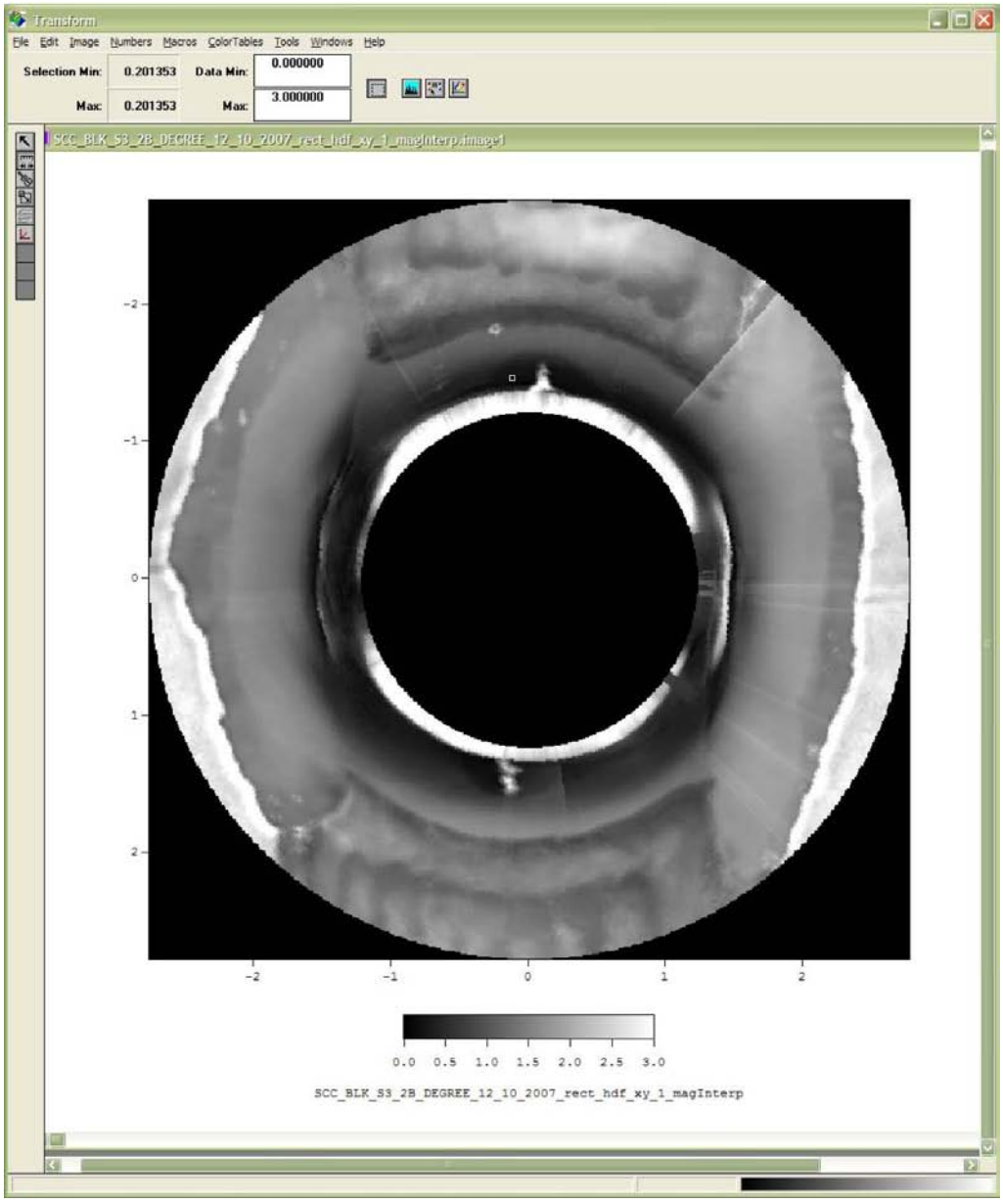
Transform
File Edit Image Numbers Macros ColorTables Tools Windows Help
Selection Min: 0.201353
Max: 0.201353
Data Min: 0.000000
Max: 3.000000
SCC_BLK_S3_2B_DEGREE_12_10_2007_rect_hdf_xy_1_magInterp.image1
-2
-1
0
1
2
0.0 0.5 1.0 1.5 2.0 2.5 3.0
SCC_BLK_S3_2B_DEGREE_12_10_2007_rect_hdf_xy_1_magInterp

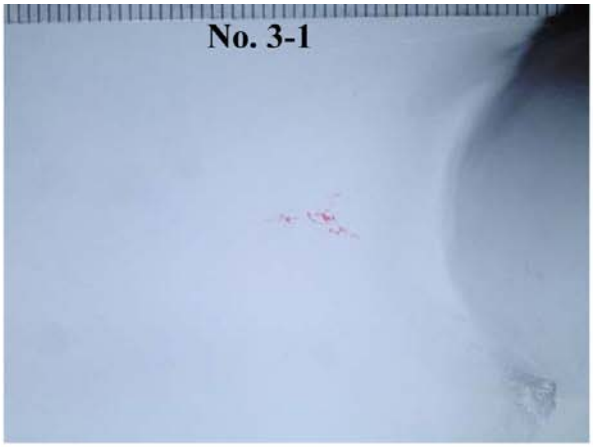
No. 3-1

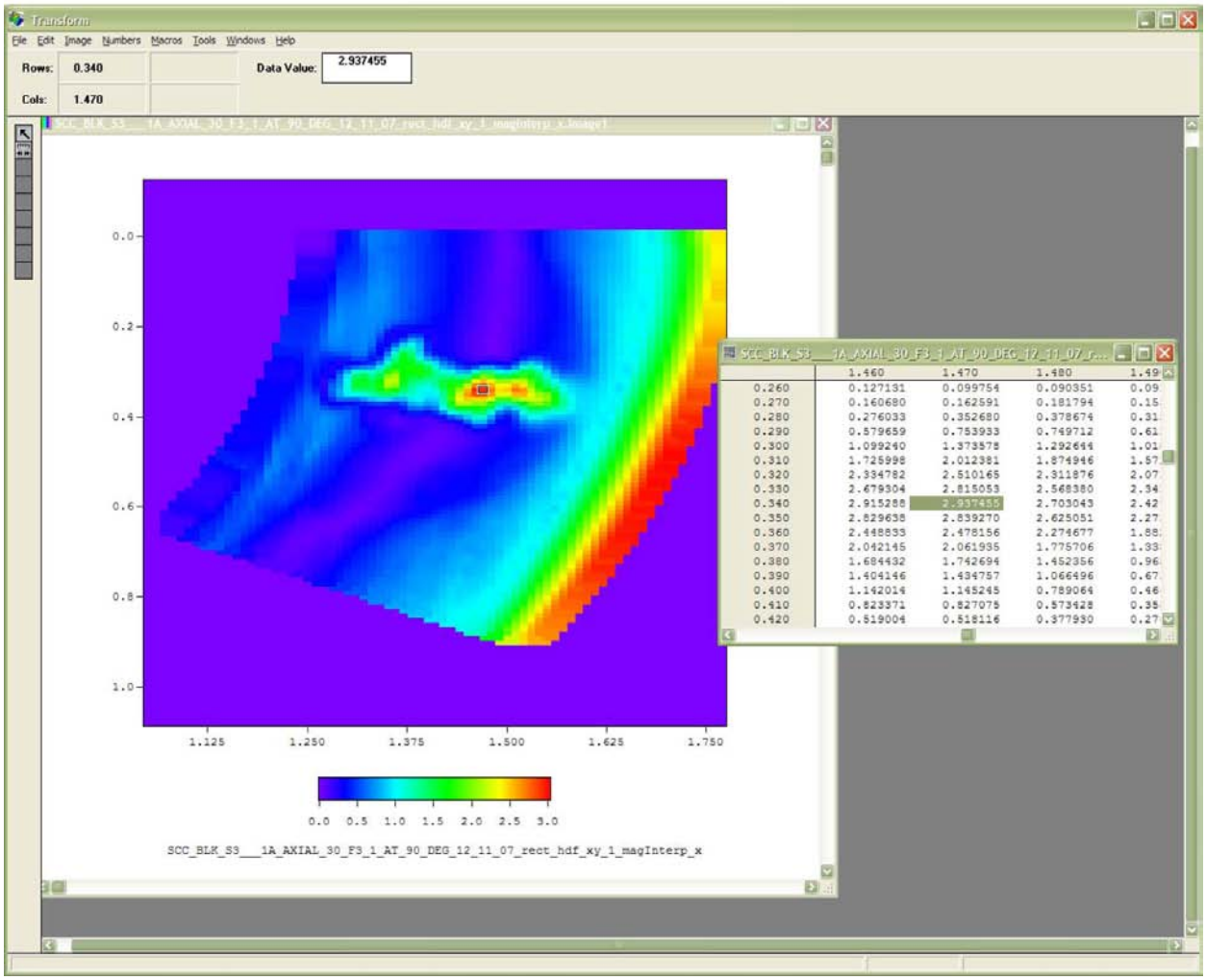
Transform
File Edit Image Numbers Macros Tools Windows Help
Rows: 0.340
Cols: 1.470
Data Value: 2.937455
0.0
0.2
0.4
0.6
0.8
1.0
1.125
1.250
1.375
1.500
1.625
1.750
0.0 0.5 1.0 1.5 2.0 2.5 3.0
SCC_BLK_S3___1A_AXIAL_30_F3_1_AT_90_DEG_12_11_07_rect_hdf_xy_1_magInterp_x
SCC_BLK_S3___1A_AXIAL_30_F3_1_AT_90_DEG_12_11_07_r...
1.460 1.470 1.480 1.49
0.260 0.127131 0.099754 0.090351 0.09
0.270 0.160680 0.162591 0.181794 0.15
0.280 0.276033 0.352680 0.378674 0.31
0.290 0.579659 0.753933 0.749712 0.61
0.300 1.099240 1.373578 1.292644 1.01
0.310 1.725998 2.012381 1.874946 1.57
0.320 2.334782 2.510165 2.311876 2.07
0.330 2.679304 2.815053 2.568380 2.34
0.340 2.915288 2.937455 2.703043 2.42
0.350 2.829638 2.839270 2.625051 2.27
0.360 2.448833 2.478156 2.274677 1.88
0.370 2.042145 2.061935 1.775706 1.33
0.380 1.684432 1.742694 1.452356 0.96
0.390 1.404146 1.434757 1.066496 0.67
0.400 1.142014 1.145245 0.789064 0.46
0.410 0.823371 0.827075 0.573428 0.35
0.420 0.519004 0.518116 0.377930 0.27

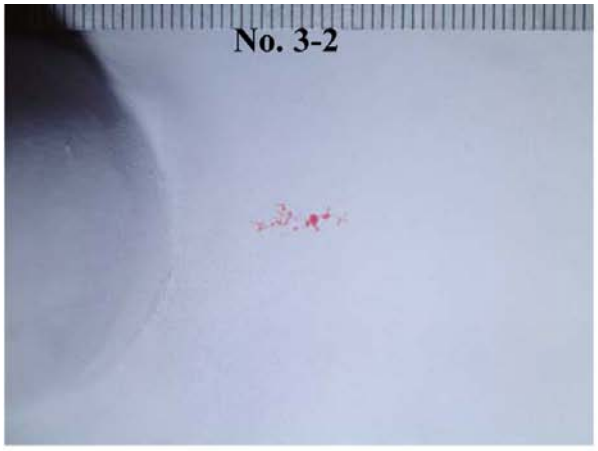
No. 3-2

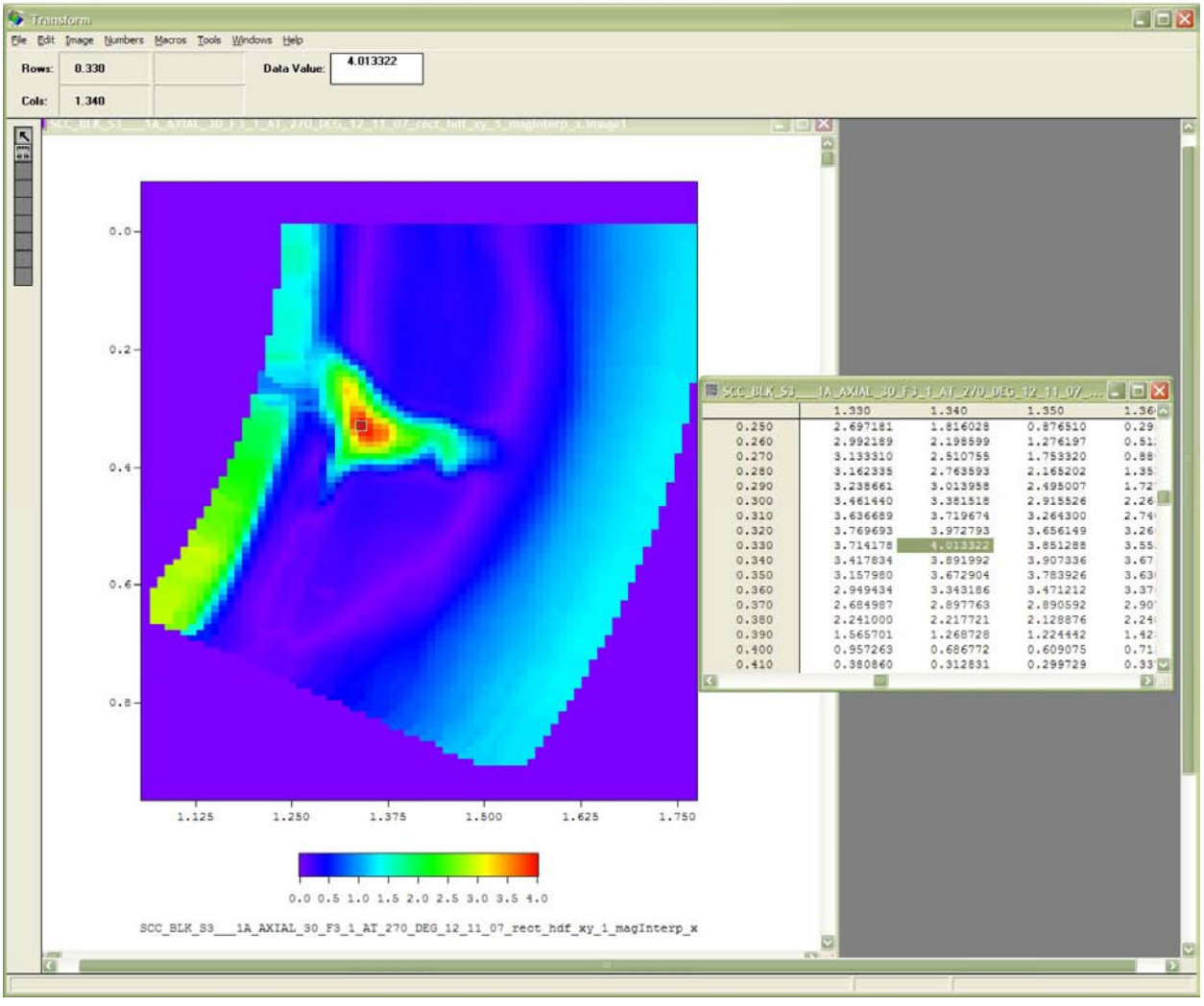
Transform
File Edit Image Numbers Macros Tools Windows Help
Rows: 0.330
Cols: 1.340
Data Value: 4.013322
0.0
0.2
0.4
0.6
0.8
1.125 1.250 1.375 1.500 1.625 1.750
0.0 0.5 1.0 1.5 2.0 2.5 3.0 3.5 4.0
SCC_BLK_S3___1A_AXIAL_30_F3_1_AT_270_DEG_12_11_07_rect_hdf_xy_1_magInterp_x
1.330 1.340 1.350
0.250 2.697181 1.816028 0.876510
0.260 2.992189 2.198599 1.276197
0.270 3.133310 2.510755 1.753320
0.280 3.162335 2.763593 2.165202
0.290 3.238661 3.013958 2.495007
0.300 3.461440 3.381518 2.915526
0.310 3.636689 3.719674 3.264300
0.320 3.769693 3.972793 3.656149
0.330 3.714178 4.013322 3.851288
0.340 3.417834 3.891992 3.907336
0.350 3.157980 3.672904 3.783926
0.360 2.949434 3.343186 3.471212
0.370 2.684987 2.897763 2.890592
0.380 2.241000 2.217721 2.128876
0.390 1.565701 1.268728 1.224442
0.400 0.957263 0.686772 0.609075
0.410 0.380860 0.312831 0.299729

G.13 PINC 5.16

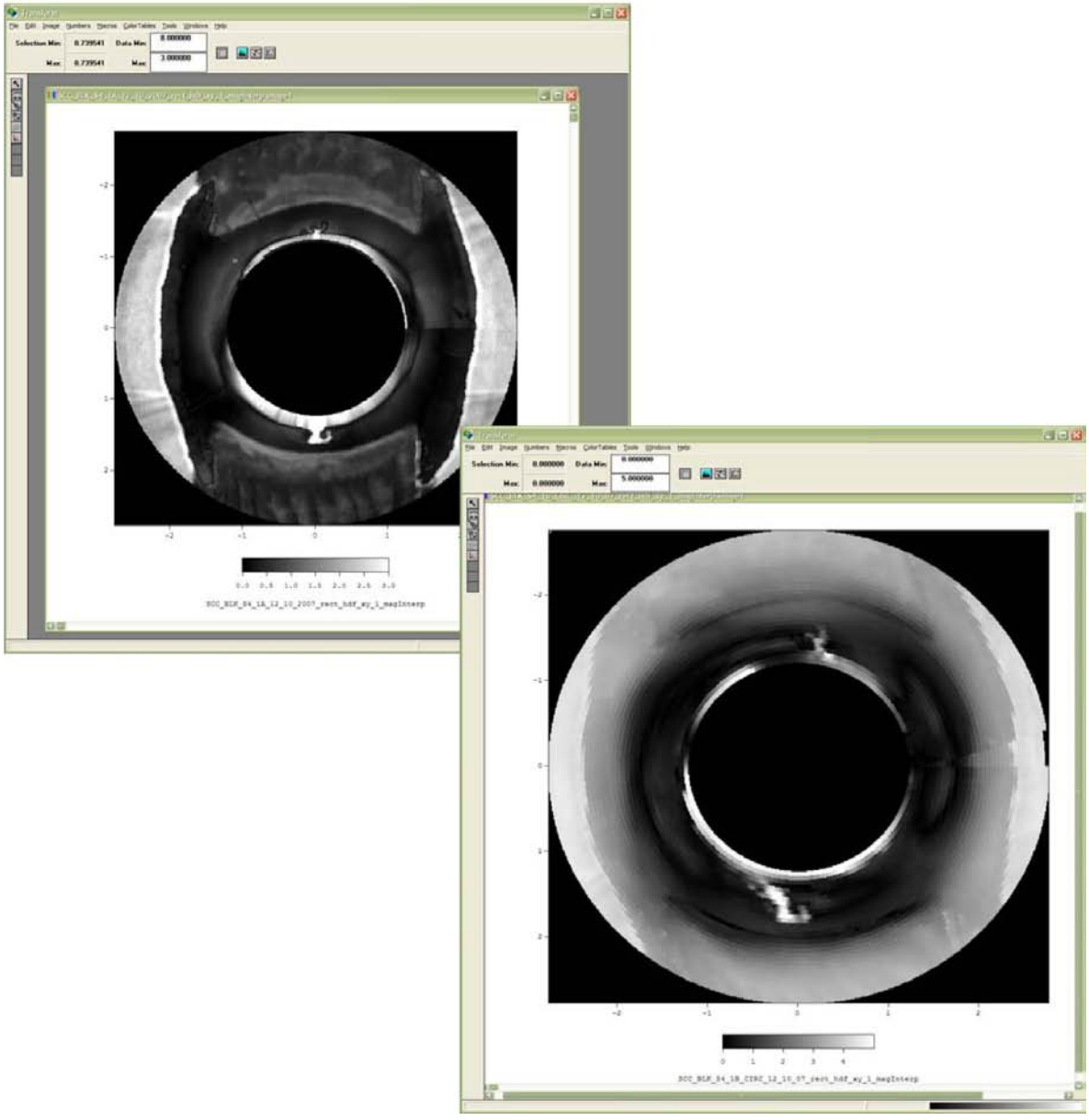

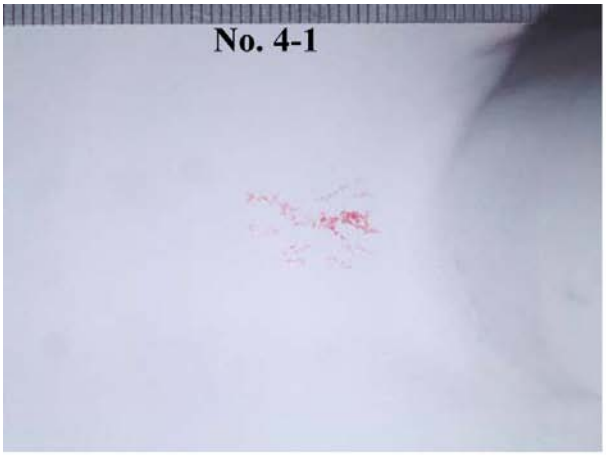
No. 4-1

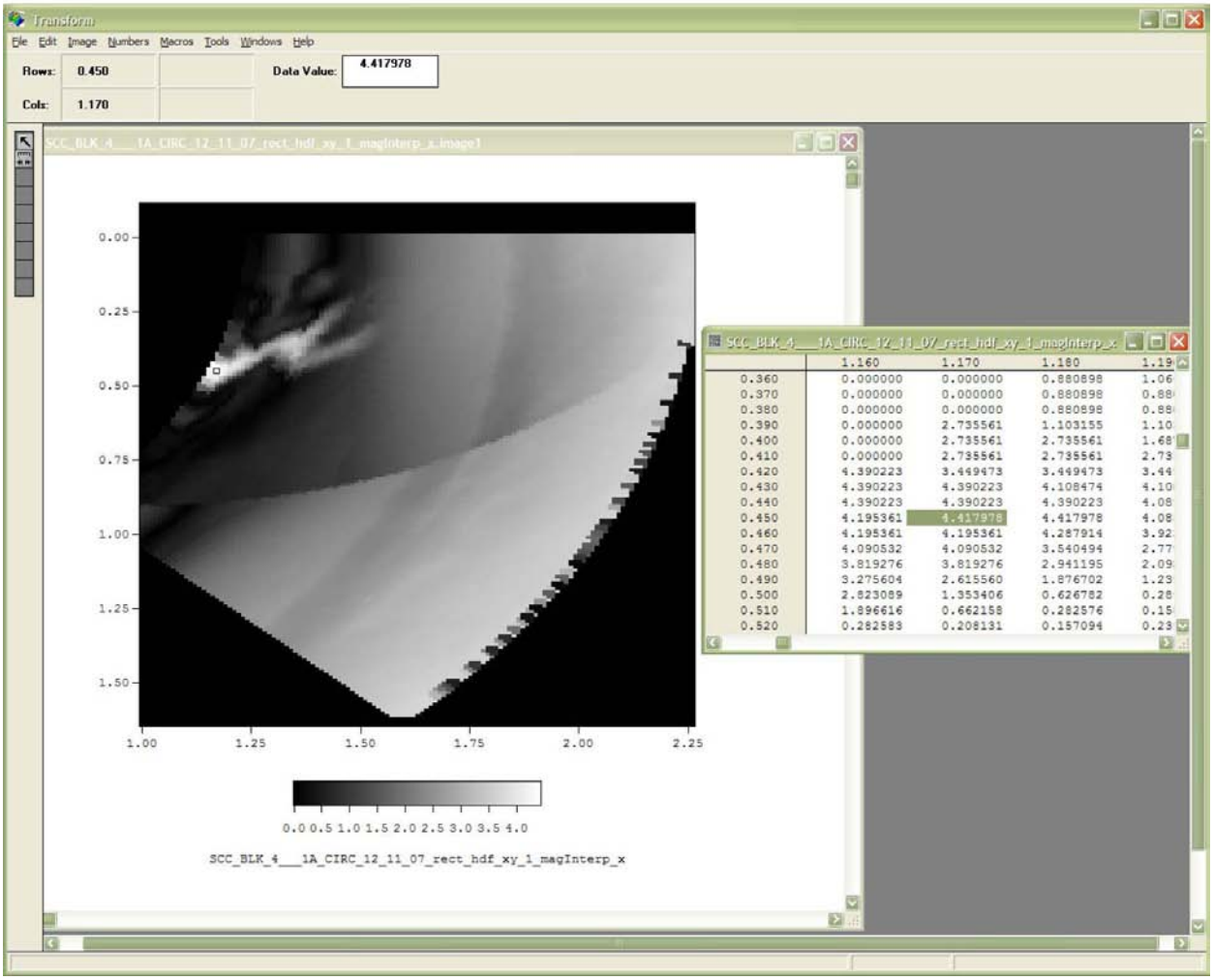
Transform
File Edit Image Numbers Macros Tools Windows Help
Rows: 0.450
Cols: 1.170
Data Value: 4.417978
SCC_BLK_4___1A_CIRC_12_11_07_rect_hdf_xy_1_magInterp_x.image1
0.00
0.25
0.50
0.75
1.00
1.25
1.50
1.00 1.25 1.50 1.75 2.00 2.25
0.0 0.5 1.0 1.5 2.0 2.5 3.0 3.5 4.0
SCC_BLK_4___1A_CIRC_12_11_07_rect_hdf_xy_1_magInterp_x
SCC_BLK_4___1A_CIRC_12_11_07_rect_hdf_xy_1_magInterp_x
1.160 1.170 1.180 1.19
0.360 0.000000 0.000000 0.880898 1.06
0.370 0.000000 0.000000 0.880898 0.88
0.380 0.000000 0.000000 0.880898 0.88
0.390 0.000000 2.735561 1.103155 1.10
0.400 0.000000 2.735561 2.735561 1.68
0.410 0.000000 2.735561 2.735561 2.73
0.420 4.390223 3.449473 3.449473 3.44
0.430 4.390223 4.390223 4.108474 4.10
0.440 4.390223 4.390223 4.390223 4.08
0.450 4.195361 4.417978 4.417978 4.08
0.460 4.195361 4.195361 4.287914 3.92
0.470 4.090532 4.090532 3.540494 2.77
0.480 3.819276 3.819276 2.941195 2.09
0.490 3.275604 2.615560 1.876702 1.23
0.500 2.823089 1.353406 0.626782 0.28
0.510 1.896616 0.662158 0.282576 0.15
0.520 0.282583 0.208131 0.157094 0.23

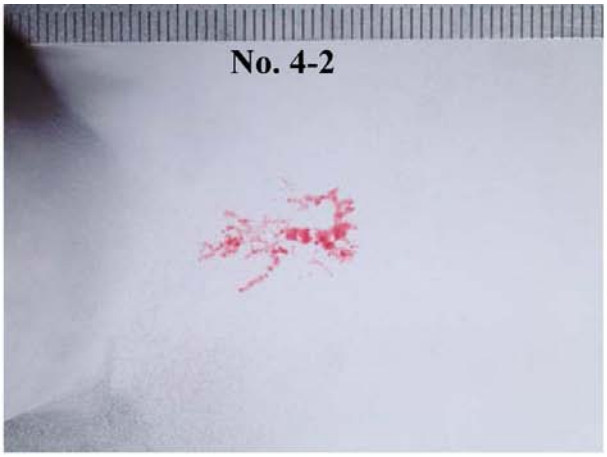
No. 4-2

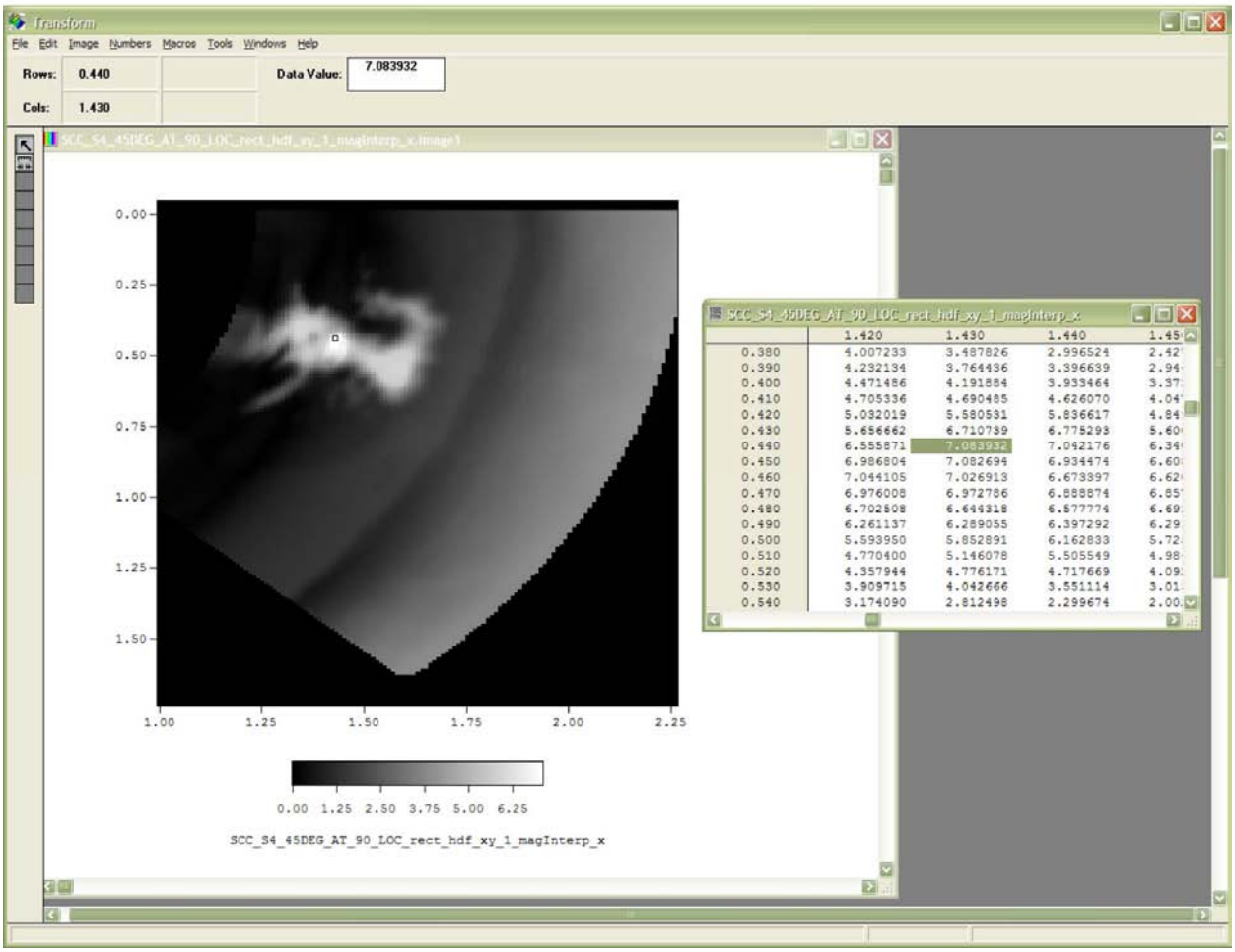
Transform
File Edit Image Numbers Macros Tools Windows Help
Rows: 0.440
Cols: 1.430
Data Value: 7.083932
0.00
0.25
0.50
0.75
1.00
1.25
1.50
1.00 1.25 1.50 1.75 2.00 2.25
0.00 1.25 2.50 3.75 5.00 6.25
SCC_S4_45DEG_AT_90_LOC_rect_hdf_xy_1_magInterp_x
1.420 1.430 1.440
0.380 4.007233 3.487826 2.996524
0.390 4.232134 3.764436 3.396639
0.400 4.471486 4.191884 3.933464
0.410 4.705336 4.690485 4.626070
0.420 5.032019 5.580531 5.836617
0.430 5.656662 6.710739 6.775293
0.440 6.555871 7.083932 7.042176
0.450 6.986804 7.082694 6.934474
0.460 7.044105 7.026913 6.673397
0.470 6.976008 6.972786 6.888874
0.480 6.702508 6.644318 6.577774
0.490 6.261137 6.289055 6.397292
0.500 5.593950 5.852891 6.162833
0.510 4.770400 5.146078 5.505549
0.520 4.357944 4.776171 4.717669
0.530 3.909715 4.042666 3.551114
0.540 3.174090 2.812498 2.299674

Appendix H

U.S. Plant Field Experience with Alloy 600 Cracking

Appendix H

U.S. Plant Field Experience with Alloy 600 Cracking[a]

Operating Unit	Date of PWSCC Discovery	Method of Discovery	Affected Component or System
Vermont Yankee	1986/04	Ultrasonic examination of the N5A and N5B core spray safe-end-to-nozzle welds indicated intergranular stress-corrosion cracking (IGSCC).	Core spray nozzle weld
San Onofre 3	1986/02	Visual – A pressure boundary leak was observed in a ¾-inch diameter pressurizer level instrument nozzle. Dye penetrant testing was utilized and revealed a crack extending from the end of the nozzle inside the pressurizer outward through the RCS pressure boundary.	Pressurizer instrument nozzle
St. Lucie 2	1987	Assumed visual - During the replacement of four pressurizer steam-space instrument nozzles, it was determined that two nozzles had cracks but there was no evidence of leakage.	Pressurizer instrument nozzles
ANO-2	1987/04	Leakage Testing - the licensee declared an unusual event and initiated a reactor shutdown as a result of a suspected reactor coolant system pressure boundary leak of approximately 60 drops per minute from the area of the pressurizer vessel lower head. It was determined that the leakage source was the heater sleeve for the X1 pressurizer heater. Because of this leakage, there was some corrosion damage to the carbon steel pressurizer shell.	Pressurizer heater sleeve
Calvert Cliffs 2	1989/05	Assumed visual - an inservice inspection of the Unit 2 pressurizer revealed evidence of reactor coolant leakage from 28 of the 120 pressurizer vessel heater penetrations and one upper level nozzle. No evidence of leakage was found on the Unit 1 pressurizer heater penetrations or pressure/level penetrations. Additional inspections using dye penetrant and eddy current tests of 28 Unit 2 and 12 Unit 1 heater sleeves were conducted. Three sleeves from Unit 2 were destructively examined. All cracks were axial and determined to have minimal safety significance.	Pressurizer heater sleeves and level nozzle

(a) This table uses information from NUREG-1823 titled *U.S. Plant Experience With Alloy 600 Cracking and Boric Acid Corrosion of Light-Water Reactor Pressure Vessel Materials* published in April 2005. Appendix A of this NUREG provides an excellent summary of U.S. and foreign Alloy 600 cracking experience.

Operating Unit	Date of PWSCC Discovery	Method of Discovery	Affected Component or System
ANO-1	1990/12	Leakage - A potential reactor coolant system leak in the area of a pressurizer upper-level instrumentation nozzle was identified. During a follow-up inspection, it was verified that a very small leak existed at the nozzle. Nondestructive testing was conducted which confirmed the existence of a small axial crack in the nozzle inner surface which breached the outside diameter of the nozzle at the toe of the nozzle-to-vessel weld.	Pressurizer instrumentation nozzle
San Onofre 3	1992/02	Liquid Penetrant - During refueling outage cycle 6, a dye penetrant examination of the pressurizer vapor space level instrument nozzles revealed the presence of a through-wall crack. The examination was attributable to boric acid crystals being found near the nozzle previously. The leaking nozzle was replaced with a new nozzle made of Alloy 690. Liquid penetration testing was conducted on the three remaining vapor space nozzles. Much smaller indications on two of the three nozzles were revealed in these tests. These three nozzles were also replaced with nozzles fabricated with Alloy 690.	Pressurizer vapor space level instrument nozzles
Palo Verde 1	1992/01	Leakage - A pressure boundary leak was discovered in the pressurizer steam-space nozzle. A pad weld was put in place in order to stop the reactor coolant leakage. PWSCC is believed to be the cause of the leakage.	Pressurizer steam-space nozzle
San Onofre 2	1992/03	Assumed visual - An inspection on Unit 2 pressurizer vapor space level instrument nozzles was conducted. Boric acid crystals were found at two of the nozzles. An interim repair of the Unit 2 nozzles with Alloy 690 was implemented prior to startup. Inspection of the remaining water and vapor space nozzles showed no signs of leakage.	Pressurizer vapor space level instrument nozzles
St. Lucie 2	1993/03	Visual - Water was discovered dripping onto the floor in containment near the pressurizer. Visual inspection revealed that four upper instrument nozzles were leaking at the entry fitting to the pressurizer. Liquid penetrant and eddy current test revealed axial cracking in the four steam-space nozzles extending into the surrounding weld area.	Pressurizer instrument nozzles
Palisades 1	1993/10	Assumed visual - inspection of the pressurizer upper temperature nozzle penetration TE-0101 was found to be leaking. Subsequent inspection of the lower temperature nozzle penetration TE-0102 was also found to be leaking. The leaks were attributable to cracking in the Alloy 600 nozzle material.	Pressurizer temperature nozzle
Palisades 1	1993/09	Visual - Plant personnel identified a leak in the power operated relief valve line near the nozzle connection to the pressurizer. The crack initiated in the heat-affected zone of the power-operated relief valve Alloy 600 safe end. NDE and visual inspection revealed a circumferential crack approximately 3 inches in length (about 30 percent of the circumference).	Relief valve

Operating Unit	Date of PWSCC Discovery	Method of Discovery	Affected Component or System
D.C. Cook 2	1994	Eddy Current - During the cycle 10 refueling outage in 1994, eddy current testing examination was performed on 71 of the 78 vessel head penetrations. The testing showed crack indications in penetration number 75. Three indications were found with lengths of 9 mm, 16 mm, and 45 mm. These indications were axial in orientation and were closely spaced. The 3 indications were located near the 160-degree location on the high side. The 45-mm crack was located near the J-groove weld, but was mostly below the weld.	VHP
Calvert Cliffs 1	1994/03	Assumed visual - Boron deposits were located on the pressurizer heater sleeve B-3 after removing insulation. On February 23, 1994, after removing more insulation, boron deposits were also discovered on pressurizer heater sleeve FF-1. Boroscopic and eddy current tests revealed a circumferential bulge approximately 0.5 inch long and 0.019 inch high (diametrical) in the area of the boric acid leaks. The leakage area showed evidence of surface metal smearing and cold work.	Pressurizer heater sleeve
St. Lucie 2	1994/02	Visual - Boric acid was observed on the exterior of the pressurizer steam-space C instrument nozzle during an inspection. Dye penetrant was utilized and identified indications at the A, B, and C steam-space instrument nozzle welds. The D instrument nozzle weld was acceptable. The unacceptable cracks were in the “J” weld between the Alloy 690 nozzle (replaced in 1993) and the clad on the inside of the pressurizer.	Pressurizer instrument nozzles
San Onofre 3	1995/07	Assumed visual - During inspection of the Alloy 600 and 690 (see the March 1992 event for Alloy 690 installation) instrument nozzles, one pressurizer level instrumentation nozzle was found with a small amount of boric acid crystals and oxidation present. Dye penetrant testing indicated crack initiation in the heat-affected zone of the weld butter. The Alloy 690 pressurizer nozzle piece interior did not have indications of PWSCC.	Pressurizer level instrumentation nozzle
San Onofre 3	1995/07	Radio Chemistry - Radio-chemistry evaluation confirmed that RCS weepage had occurred on two hot leg instrument nozzles. The accessible exterior of the two RCS hot leg nozzles were replaced with new Alloy 690 nozzles. The access to the interior of the RCS hot leg piping prevents welding from the inside of the RCS. Therefore the old nozzles were cut off half way through the RCS hot leg materials and the new nozzles were welded to the exterior of the RCS pipe.	RCS hot leg instrument nozzles
St. Lucie 2	1995/10	Visual - During a routine RCS visual leak check, an apparent boric acid buildup was discovered on the “B” side RCS hot leg instrument nozzle. Further investigation confirmed that pressure boundary leakage had previously occurred.	RCS hot leg instrument nozzle

Operating Unit	Date of PWSCC Discovery	Method of Discovery	Affected Component or System
San Onofre 3	1997/04	Not Specified, presumably visual as above - During a routine inspection, four hot leg RCS nozzles were found to have leaks and a fifth was suspected of leaking. It was suspected that the leakage was attributable to cracks through the nozzle in the heat-affected zone of the partial penetration weld on each of the instrument nozzles.	RCS instrument nozzle
San Onofre 3	1997/07	Not Specified, presumably visual as above - RCS nozzles were inspected and one hot leg spare RTD thermowell nozzle had an increased amount of white residue. An isotopic analysis determined the residue was boric acid from the RCS. PWSCC was believed to be the root cause of the leaks reported. It was believed that the leakage came from a crack in the heat-affected zone of the partial penetration weld on each of the instrument nozzles.	RCS instrument nozzle
San Onofre 2	1997/03	Visual - Steam was observed emanating from the pressurizer. It was concluded that the leak was caused by PWSCC of Alloy 600 type materials of the pressurizer liquid temperature thermowell nozzle. The crack was oriented parallel to the long axis of the nozzle.	Pressurizer temperature nozzle
Hope Creek 1	199/09	Presumably visual - A leak was discovered on core spray nozzle safe-end weld #N5BSE associated with the “A” core spray subsystem. The N5BSE weld was nondestructively tested in the previous refueling outage. This NDE test had been improperly evaluated and the crack had been unrecorded. The cause of the through-wall leakage has been attributed to IGSCC in the Alloy 182 weld metal.	Core spray nozzle weld
Calvert Cliffs 1	1998	Ultrasonic Testing - Unit 1 heater sleeves were nickel plated in 1994. One nickel plated heater sleeve (B-1) was found leaking during the 1998 refueling outage. Ultrasonic testing revealed a short axial indication.	Pressurizer heater sleeve
San Onofre 2	1998/01	Visual - A steam leak was discovered at an upper-level instrument nozzle on the pressurizer. A dye penetrant test of the nozzle proved that the Alloy 690 nozzle did not contain a leak pathway. Ultrasonic examination of the vessel shell was performed to look for defects in the shell material. No defects were found. Because no leak path was found in the nozzle or shell material, it was postulated that the crack was in the Alloy 600-type weld filler material of the nozzle.	RCS nozzles
Calvert Cliffs 2	1998/07	Visual - A steam leak was discovered at an upper-level instrument nozzle on the pressurizer. A dye penetrant test of the nozzle proved that the Alloy 690 nozzle did not contain a leak pathway. Ultrasonic examination of the vessel shell was performed to look for defects in the shell material. No defects were found. Because no leak path was found in the nozzle or shell material, it was postulated that the crack was in the Alloy 600-type weld filler material of the nozzle.	Pressure level tap

Operating Unit	Date of PWSCC Discovery	Method of Discovery	Affected Component or System
San Onofre 3	1999	Eddy Current Testing - A cracked heater sleeve was identified by eddy current testing. The heater had failed, swelled, and stuck within the sleeve. The flaw was approximately 40 percent through-wall on the inner diameter of the sleeve near the attachment weld.	Pressurizer heater sleeve
Waterford 3	1999/02	Visual - During a routine visual inspection, evidence of reactor coolant system leakage was found on two Alloy 600 instrument nozzles located on the top head of the pressurizer. The leakage was in the annulus area where the nozzle penetrates the pressurizer head. The nozzles are welded on the Inner diameter of the pressurizer and joined to instrument valves RC-310 and RC-311.	Pressurizer instrument nozzles
Waterford 3	1999/02	Visual - Evidence of boric acid leakage was found on three nozzles. One was on the RCS hot leg number 1 resistance temperature detector (RTD) nozzle, a second was on the RCS hot leg number 1 sampling line, and a third was on the RCS hot leg number 2 differential pressure instrument nozzle.	RCS hot leg instrument nozzle
Duane Arnold 1	1999/11	Ultrasonic - Two indications of IGSCC were identified in weld RRB-F002. One indication was approximately 44 percent through-wall and the other was approximately 65 percent through-wall. The inspection was expanded and a 65-percent through-wall crack was found in weld RRD-F002. These two F002 welds were repaired by completing weld overlays using Alloy 52. The cause of the cracking was IGSCC in the Alloy 182 weld metal.	Recirculation riser welds
Palo Verde 1	1999/10	Leakage - Evidence of an RCS pressure boundary leakage was discovered. The leakage was discovered at two Alloy 600 nozzles, one in each of the RCS hot legs. One was at the nozzle upstream of Valve RCV0285 in the line to a steam generator number 2 differential pressure instrument. The other was at the nozzle upstream of Valve RCV-277 in the line to a steam generator number 1 differential pressure instrument. The leakage was discovered in the form of small deposits of boron accumulated around the circumference of the nozzles. Isotopic analysis of the boron accumulation detected only long-lived radionuclides, indicating that it has taken more than 3 years for the reactor coolant to migrate through the nozzle weld and wall thickness.	RCS hot leg valves
ANO-1	2000/02	Visual - A flawed weld was identified on an instrument connection to the reactor coolant system Loop “A” hot leg piping. Once the insulation had been removed, leakage was discovered on five other nozzles. Further investigation using NDE revealed that leakage was occurring through flaws in the partial penetration weld. Both axial and circumferential flaws were found. There was also a subsurface flaw found in a seventh nozzle.	RCS hot leg instrumentation
ANO-2	2000/07		RCS hot leg instrument nozzle

Operating Unit	Date of PWSCC Discovery	Method of Discovery	Affected Component or System
ANO-2	2000/07	Visual - Boron residue was discovered on the reactor coolant system pressurizer heater power cables. The boron came from leaks in heaters B2 and D2. B2 is on backup heater bank 4, and D2 is on backup heater bank 6. After removing insulation from the pressurizer, the licensee discovered 10 additional pressurizer heater sleeves that had previous leakage. Eddy current testing on two of the heater sleeves indicated that there was a single, through-wall, axial crack in both sleeves below the J-groove weld. These cracks initiated from the inside surface of the sleeves. Ultrasonic testing showed no cracks in the shell base metal.	Pressurizer heater sleeve
ONS-1	2000/11	Visual - During a visual inspection of the top surface of the reactor pressure vessel head, small amounts of boric acid deposited on the vessel head surface was discovered. These deposits appeared to be located at the base of five unused thermocouples and the Nozzle #21 weld at points where they all penetrate the RPV head surface. On December 4, an eddy current test was performed on the inside surface of the eight thermocouple nozzles and revealed axial crack-like indications on the ID of the nozzles in the vicinity of the partial penetration weld. Dye penetrant testing on Nozzle #21 identified two very small pin-hole indications running at a slightly skewed angle across the fillet weld.	VHP Weld and thermocouple nozzles
Waterford 3	2000/10	Visual - During a bare metal inspection, boric acid was found on two of the three MNSA clamps that had been installed on hot leg nozzles during refueling outage 9. These clamps had been installed as temporary repairs until a permanent repair could be made during refueling outage 10. The MNSA clamp leakage could have been caused by the flange not being flat against the pipe. The leak could have also arisen from a brief leakage while the clamps seated.	RCS hot leg mechanical nozzle seal assembly clamps
Ft. Calhoun	2000/10	Visual - During a walkdown inspection, leakage was detected from the lower pressurizer liquid space temperature Nozzle #TE-108 was detected.	Pressurizer temperature nozzle
Waterford 3	2000/10	Visual - During a bare metal inspection of the pressurizer heater sleeve number F-4, a small amount of boric acid residue was discovered.	Pressurizer heater sleeve
Palo Verde 2	2000/10	Visual - During an inservice inspection, reactor coolant system pressure boundary leakage was discovered. The leakage was discovered at pressurizer heater nozzle sleeve A06. The leakage was detected in the form of small deposit of boron accumulation on the sleeve. Eddy current testing indicated linear axial cracking.	Pressurizer heater sleeve

Operating Unit	Date of PWSCC Discovery	Method of Discovery	Affected Component or System
V.C. Summer	2000/10/7	Visual - 100 to 200 pounds of boric acid was identified in the “A” hot leg area of the reactor vessel. The potential leak area was identified on the first weld off the reactor vessel at the nozzle-to-pipe connection of the Loop “A” hot leg. Ultrasonic and eddy current inspection together with visual inspection identified the flaw as axially oriented and about 3 inches in length. The flawed weld was removed and a new weld made of Alloy 52/152 material was utilized. Subsequent cleaning and destructive examination of the salvaged pipe section revealed also a short (about one inch) circumferential crack located in the weld that may have branched from the axial flaw, or may have nucleated as a separate defect.	Primary system hot leg
St. Lucie 1	2001/04	Visual - Leakage was discovered on a pipe-to-nozzle connection on line I-3/4-RC-126. This line was determined to be the “B” RCS hot leg instrument nozzle connection for differential pressure (D/P) transmitter PDT-1121D.	RCS hot leg instrument nozzle
ONS-2	2001/04	Visual - A preliminary reactor head visual inspection on April 28, 2001, revealed small amounts of boron residue surrounding nozzles 4, 16, 18, and 30. Subsequent surface dye penetrant test inspections of the weld area and nozzle outside diameter identified several axial cracks on four VHP nozzles that initiated near the toe of the fillet and propagated radially into the nozzle materials as well as axially along the outer diameter surface. Eddy current tests revealed two shallow axial flaws on Nozzle #16 and craze cracking on all four VHP nozzles’ inner diameter surface. The ultrasonic testing confirmed the existence of some axial cracks with one short outer diameter initiated circumferential crack on VHP 18. The circumferential flaw was OD initiated, extended 11 percent through-wall, and was 1.26 inch in length.	VHP and VHP Weld
ONS-3	2001/12	Visual - During a visual inspection of the reactor vessel VHP nozzles, leakage indications were discovered as evidenced by minor boric acid buildup around 4 VHP nozzles. Nondestructive examination of the suspected nozzles revealed that 7 of the 69 total nozzles required repair. Five of these seven nozzles had a leak pathway to the top of the reactor vessel head. Some of the indications were in the nozzles themselves, while other indications extended slightly into the weld. Most of the cracking was axial in nature, however, there was one circumferential flaw found in Nozzle #2 above the J-groove weld.	VHP and VHP Weld

Operating Unit	Date of PWSCC Discovery	Method of Discovery	Affected Component or System
ONS-3	2001/02	Visual - during a visual inspection of the reactor vessel VHP nozzles, small amounts of boron residue surrounding the base of several control rod drive mechanism head penetrations was discovered. The boric acid deposits were identified around nozzles 3, 7, 11, 23, 28, 34, 50, 56, and 63. Subsequent surface dye penetrant test inspections of the weld areas and outside diameter identified several deep axial cracks that initiated near the toe of the fillet weld and propagated radially into the nozzle materials as well as axially along the outer diameter surface. Ultrasonic testing confirmed the existence of deep cracks in all nine leaking VHP nozzles. Of these 47 original crack indications, 19 were OD-initiated flaws that were not through-wall. There were 16 flaws that were OD-initiated through-wall cracks. There were nine circumferential flaws, with one being ID-initiated and the rest being OD-initiated. Two of the outer diameter circumferential flaws were above the J-groove weld. Finally, there were also three ID-initiated non-through-wall cracks.	VHP and VHP Weld
Palo Verde 1	2001/03	Visual - During visual inspection of the RCS piping, boric acid residue was discovered on the Alloy 600 RCS hot leg thermowell 1JRCETW0121HB. The visual indications were characterized as white streaks fanning out from the hot leg and continuing up the taper of the thermowell with some buildup on the top of the tapered portion.	RCS hot leg thermowell
ANO-1	2001/03	Visual - During a routine visual inspection of the reactor vessel head area, boric acid crystals were discovered. On March 24, 2001, eddy current testing and ultrasonic testing revealed a reactor coolant solution pressure boundary leak. The leak was identified in the wall of Nozzle #56. The UT data indicated that the crack was on the downhill side of the nozzle and extended approximately 0.8 inch below the weld and upward to approximately 1.0 inch above the weld. The depth of the crack was approximately 0.2 inch.	VHP

Operating Unit	Date of PWSCC Discovery	Method of Discovery	Affected Component or System
North Anna 2	2001/11	Visual - A through-wall leak on Nozzle #63 was observed. This event was treated as a through-wall leak based on the qualified visual inspection results and liquid penetrant examination. A portion of the weld around Nozzle #63 was excavated to a depth of approximately 1" of weld metal. The liquid penetrant exam of this excavation showed 12 indications located at the outside edge of the weld almost the full length of the excavation, which turned into the weld at the uphill and downhill ends of the excavation. Six of the recorded cracks were transverse to the weld, while the other six were parallel. Eddy current testing revealed a crack 31mm in length in the area of the attachment weld. Ultrasonic testing of the same crack revealed that it was less than 1 mm in depth and 14 mm in length. Nozzle #51 also had nearby boric acid residue on the reactor vessel head. A liquid penetrant test revealed 12 indications at the toe of the weld. Five of these indications were parallel while the rest were transverse. Eddy current testing of the nozzle's weld revealed six axial indications. These axial cracks were less than 2 mm in depth and ranged from 6 to 24 mm in length. Similarly, Nozzle #62 was also investigated. This nozzle had eight indications at the toe of the weld. Two of the cracks were parallel and six were transverse. Eddy current testing revealed two axial indications. The dimensions were 74 mm and 42 mm in length, while being less than 2 mm and less than 1 mm in depth, respectively.	VHP Weld
Crystal River 3	2001/10	Visual - During a visual inspection of the reactor vessel VHP, boric acid buildup was discovered around Nozzle #32. Ultrasonic testing performed on Nozzle #32 revealed two through-wall axial cracks. These cracks extended from the bottom of the nozzle to above the J-groove weld. These two axial cracks then joined a circumferential crack above the J-groove weld. The circumferential flaw was about 90° and 50 percent through-wall. There was another circumferential flaw below the J-groove weld which extended 30° and was approximately 75 percent through-wall.	VHP

Operating Unit	Date of PWSCC Discovery	Method of Discovery	Affected Component or System
TMI-1	2001/10	Visual - During a visual inspection of the reactor vessel VHP nozzles, boric acid buildup was discovered around 8 different thermocouple nozzles. Liquid penetrant testing and ultrasonic testing identified through-wall indications on three VHP nozzles. These engineering evaluations concluded that the indications at Nozzles #44, 35, and 37 indicate a reactor coolant system pressure boundary leaks. During later examinations of the reactor vessel head, Nozzles #29 and 64 were shown to contain RCS pressure boundary leaks. The VHP nozzles were repaired by initially rolling the nozzle above the J-groove weld, and then machining the lower portion of the VHP nozzle including portions of the J-groove weld. A new pressure boundary weld was formed between the VHP nozzle and the RPV head low-alloy steel at the location above the previous J-groove weld and below the rolled nozzle area. A surface remediation inducing compressive stresses was performed after the repair. The thermocouples were repaired by cutting them approximately 1 inch from the outside surface of the RPV head. The remaining nozzle portion inside the RPV head was machined out of the head.	VHP
Palo Verde 3	2001/09	Visual - Evidence of RCS leakage was discovered. The leakage was discovered in an RCS hot leg temperature nozzle. The RCS hot leg nozzle was located in the RTD nozzle for an inservice temperature detector (Loop #1, equipment ID: 3JRCETW112HD). The leakage was identified by the discovery of boron deposits accumulated around the circumference of the hot leg nozzle.	RCS hot leg temperature nozzle
Palo Verde 3	2001/09	Visual - Evidence of reactor coolant leakage was discovered. The leak was from a pressurizer heater sleeve nozzle. The pressurizer heater sleeve leakage is located at pressurizer heater B17. The leakage was identified by the discovery of boron deposits accumulated around the circumference of the pressurizer. There was no evidence of leakage during the last refueling outage.	Pressurizer heater sleeve
Catawba 2	2001/09	Visual - A walk down of the SG 2B lower head bowl drain indicated boron residue buildup on the ½-inch piping immediately below the SG. The root cause of the SG 2B bowl drain leak was PWSCC of Alloy 600 material.	SG bowl drain

Operating Unit	Date of PWSCC Discovery	Method of Discovery	Affected Component or System
ONS-1	2002/04	Visual - A qualified visual inspection of the Unit 1 reactor vessel head was conducted. Two penetrations had very slight amounts of boron accumulations. Ultrasonic testing was then performed on the penetrations and revealed partial through-wall outside diameter cracks for nozzles 1, 7, and 8. There were five flaws and a potential leak path identified in Nozzle #7. There was one axial flaw but no leak path identified in Nozzle #8. Nozzle #1 showed three minor indications in a region of rough weld contour. Liquid dye-penetrant was then used to examine these three nozzles. PT revealed two axial flaws in the original weld on Nozzle #7. PT was also used on Nozzle #1 and there were no recordable or rejectable PT indications.	VHP and VHP Weld
ANO-2	2002/04	Visual - Six heater sleeves were found to be leaking in the pressurizer. Five of the leaking heater sleeves were discovered on April 15, 2002, while the other was found on April 30, 2002. On April 15, boron deposits were discovered on five pressurizer heater sleeve penetrations. On April 30, boron residue was observed around the sixth pressurizer heater sleeve. Since similar events had occurred in the July 2000 outage, no NDE was conducted.	Pressurizer heater sleeve
Millstone 2	2002/02	Visual - Pressurizer heater penetrations and pressurizer instrument nozzle penetration were examined with visual inspection. Two heater sleeves showed indications of minor leakage because of the boron precipitates discovered on the outside of the penetrations. The cause of this event is through-wall cracks in the two pressurizer heater sleeves.	Pressurizer heater sleeves
Davis-Besse	2002/02/16	Visual - During machining to facilitate repair of nozzle #3, the licensee found that the nozzle had tipped, with the CRDM flange (located above the head) contacting the flange of an adjacent CRDM. The licensee cleaned the surface of the RPV head and found a large cavity adjacent to nozzle #3, where the RPV head base material had been corroded down to the stainless steel cladding. Subsequent investigation revealed an additional much smaller degraded area near nozzle #2, located within the wall thickness (no cladding was exposed).	Reactor pressure vessel top head

Operating Unit	Date of PWSCC Discovery	Method of Discovery	Affected Component or System
ANO-1	2002/10	Visual - A routine visual inspection was performed on the reactor vessel head area. Small boric acid crystal nodules were found around the area of control rod drive mechanism Nozzle #56. On the downhill side of the nozzle, boric acid residue was located, extending 180° around the nozzle annulus area, with a small boric acid nodule at the most downhill point. Nondestructive examination (NDE) revealed indications of cracking in the nozzle, which was the cause of the boric acid residue. NDE of all the nozzles revealed indications of non-through wall cracks in six other nozzles, and a likely porosity weld defect in another. The leaking Nozzle #56 had been repaired during the previous outage. The new crack indications were located just outside the previous weld repair zone. The previous repair technique was the embedded flaw repair. It is believed that the same nozzle failed because the previous repair did not isolate the 182 weld, which is a susceptible material to PWSCC in the pressurized-water reactor (PWR) environment.	VHP and VHP Weld
ONS-2	2002/10	Visual - Evidence of through-wall leakage was discovered on seven VHP penetrations. These penetrations were Nozzles #8, 9, 19, 24, 31, 42, and 67. None of these nozzles had been previously repaired. Additional nozzle head penetrations were masked by boric acid deposits suspected of being from separate sources of leakage. NDE was used to characterize the cracking. No circumferential cracks were reported and 10 VHPs (#11, 15, 19, 21, 24, 31, 33, 36, 38, and 42) with axial cracks were found.	VHP
Surry 1	2001/10-11	Not specified assumed Visual - Through-wall indications of the J-groove weld were identified on VHP Nozzles #27 and 40. On November 2, 2001, indications of flaws in the penetration welds were also uncovered on Penetrations #65, 47, 69, and 18.	VHP Weld

Operating Unit	Date of PWSCC Discovery	Method of Discovery	Affected Component or System
North Anna 2	2002/09	Visual - Boric acid residue was discovered during a bare metal visual inspection of the reactor vessel head on September 14, 2002. It appears that Nozzles #21 and 31 had exhibited some leakage, as evidenced by boric acid residue on the reactor vessel head. Four additional penetrations were suspected of leaking, and several penetrations were masked with boric acid residue. Of the 59 J-groove weld penetrations that were inspected using eddy current testing (ET), 57 were identified with crack-like indications. The ET identified at least one indication of a 6-mm crack in about 83 percent of the J-groove welds. During the previous year's outage, no boric acid residue was discovered. The six nozzles (N2-51, 53, 55, 57, 62, and 63) that could not be inspected with ET had their welds inspected using liquid penetrant tests (PTs). Three of these penetrations (N2-51, 62, and 63) had been previously repaired with weld overlay of the J-groove. Each of the six penetrations that were inspected with PT had evidence of rejectable indications. Eddy current examinations of the J-groove welds showed indications of axial and circumferential cracking with respect to the welding direction. The range in length was from 0.12 inch to 7.0 inches. Some longer flaws were recorded, but they actually comprise a series of small flaws with very short distances between. Eddy current testing of the inside diameter surface showed twenty of thirty-five penetration tubes had axial indications. These indications were believed to be less than 0.12 inch deep. Four nozzles (#21, 31, 51, and 63) showed evidence of a leak path in the shrink fit area between the vessel head and the tube. Nozzles #51 and 63 had been identified as leaking in the Fall of 2001. Repairs of these penetrations had been improperly applied because the weld overlay repair did not extend out far enough to cover the previous NDE indications. The six penetration welds inspected with PT had greater than 1/16-inch linear flaw indications. The licensee replaced the reactor vessel head instead of making multiple repairs.	VHP and VHP Weld

Operating Unit	Date of PWSCC Discovery	Method of Discovery	Affected Component or System
ONS-3	2003/04	Visual - During a visual inspection of the reactor vessel head on May 2, 2003, evidence of possible through-wall leakage was observed on two VHP penetrations. The locations of these penetrations are Nozzles #4 and 7. Nozzle #4 contained a very thin white coating while nozzle 7 appeared to have a small accumulation of boron on the head adjacent to the annulus region. Approximately 6 to 8 additional nozzles-to-head penetrations were masked by deposits from a component cooling system leak above the RV head and were unable to be inspected. Prior refueling outage RVH inspection videotapes showed that the Nozzle #7 deposits were not associated with a new leak but rather were remnants from a prior outage leak and repair where the boron residue had not been removed. The Nozzle #4 boron deposits were similar to previous RVH leaks. The apparent root cause of the nozzle leak is PWSCC.	VHP
St. Lucie 2	2003/04	Visual - During a refueling outage, a defect in Nozzle #72 was found. St. Lucie Unit 2 had approximately 14.0 effective degradation years at the start of the 2003 refueling outage, therefore, this plant has a high susceptibility in accordance with Order EA-03-009. Visual inspection of the reactor pressure vessel was clean, with no evidence of leakage from the 102 RPVH penetrations or wastage on the RPVH surface. The UT inspection identified an axial crack in CEDM Nozzle #72. The defect outer diameter connected and extended into the nozzle and into the J-groove weld between the nozzle and reactor vessel head. The defect was an axial flaw, 0.28 inch deep and 0.96 inch long on the downhill side of the penetration. On May 2, 2003, a second defect was identified in CEDM Nozzle #18. The defect is also outer diameter connected and described as axial. It extended into the nozzle and through the J-groove weld between the nozzle and reactor vessel head. This second defect measured 0.26 inch deep and 2.98 inches long. It was also located on the downhill side of the penetration. Neither flaw extended through the wall of the nozzle. Neither nozzle had any evidence of leakage from the annulus between the nozzle and the reactor pressure vessel head associated with the indications.	CEDM and CEDM weld
North Anna 1	2003/03	Visual - Unit 1 entered a scheduled refueling outage. During this outage, visual inspection was performed on the reactor vessel head. On March 4, 2003, an apparent reactor vessel head through-wall leak was noted on Nozzle #50. The inspection was a follow-up to a previous inspection in 2001. Boric acid residue was found approximately ½ inch in diameter on the lower side of the penetration-to-head transition. There were no signs of wastage on the reactor vessel head.	VHP

Operating Unit	Date of PWSCC Discovery	Method of Discovery	Affected Component or System
Palo Verde 3	2003/03	Visual - Engineering personnel performing preplanned visual examinations of reactor coolant system piping discovered boric acid on the RCS hot leg instrument nozzle and a pressurizer heater sleeve. There was boric acid residue discovered on the backup pressurizer heater sleeve A01. Eddy current testing on the heater sleeve suggested that the cracking was axial in nature.	RCS hot leg instrument nozzle
D.C. Cook 2	2003/05	Not Specified - Craze cracking indications were found on a reactor pressure vessel head penetration May 17, 2003. Shallow indications were found on the inside diameter of Nozzle #74 during the reactor head inspection. These indications are closely spaced d inch below the J-groove weld. Initial calculations showed a crack depth of 0.117 inch. There was no through-wall leakage detected. These same cracking indications were found during the 2002 refueling cycle and have not shown any significant growth. This report was retracted because it was determined that the craze cracking indications in Nozzle 74 of the Unit 2 RPV head do not represent a seriously degraded principal safety barrier of the nuclear power plant.	Vessel head penetration
TMI-1	2003/11	Not specified visual assumed - An inspection of the pressurizer heater bundle identified a primary leak at the lower pressurizer heater bundle diaphragm plate. Boric acid residue was found between the diaphragm plate and the cover plate. Initially the leak was thought to be coming from a seal weld. Nondestructive examination (NDE) determined that the leak path was through the edge of the pressurizer heater bundle diaphragm plate, and that there were six indications. Four of these indications were surface flaws not associated with a through-wall crack. The heater bundle was initially repaired by depositing a seal weld over the areas of the pressurizer heater bundle diaphragm plate. A leak was revealed in later testing at normal operating pressure and temperature. Because of this leak, the lower pressurizer heater bundle assembly including the pressurizer heater bundle cover plate was replaced with a new heater bundle assembly.	Pressurizer heater sleeve
Waterford 3	2003/10	Not specified Visual assumed - Evidence of leakage was detected on nozzle RCIPT- 0106B, which is a pressure transmitter that taps off of the reactor coolant system hot leg #2. The leakage was located in the annulus area where the nozzle penetrates the head. Nozzle RC-IPT-0106B was corrected with a permanent partial nozzle welded repair.	RCS hot leg instrument nozzle

Operating Unit	Date of PWSCC Discovery	Method of Discovery	Affected Component or System
Pilgrim 1	2003/10	Visual - reactor coolant leakage was detected in a reactor vessel nozzle-to-cap weld. The crack was contained within the Alloy 182 weld metal. After the nozzle was initially welded to the cap, defects were detected and the weld was repaired. The leakage was believed to be attributable to a crack left in the weld materials during the previous repair procedure. The repair procedure utilized a weld overlay technique with Alloy 52.	Reactor vessel nozzle to cap weld
Crystal River 3	2003/10	Visual - During a routine visual inspection of the upper-level instrument tap nozzles, very small reactor coolant leaks were found on Nozzles RC-1-LT1, RC-1-LT2, and RC-1-LT3. The leakage evidence for RC-1-LT1 and RC-1-LT3 consisted of stains and boric acid residue. The evidence on RC-1-LT2 consisted only of stains on the pressurizer carbon steel shell. There was no evidence of leakage on any of the similar pressurizer nozzles. The last unidentified leak rate completed prior to plant shutdown was 0.15 gpm.	Pressurizer level nozzle
Millstone 2	2003/10	Visual - Two leaking pressurizer heater penetrations were identified. These two pressurizer heaters, along with the two degraded pressurizer heaters found in the previous outage, were planned to be removed during the current outage. Ultrasonic testing determined that the flaws were axial in nature.	Pressurizer heater sleeves
Waterford 3	2003/10	Visual - Evidence of leakage was detected on pressurizer heater sleeves C-1 and C-3. The leakage was later determined to be boric acid.	Pressurizer heater sleeve
ONS-1	2003/09	Visual - During a scheduled bare metal visual inspection on September 23, 2003, possible evidence of a through-wall leak on two VHPs (Nozzles #6 and 16) and one thermocouple penetration (Nozzle #7) was observed. The thermocouple had been repaired (plugged) in December 2000. Reactor coolant leakage prior to the unit shutdown varied between 0.15 and 0.24 gallon per minute.	VHP and thermocouple penetration
South Texas Project Unit 1	2003, Spring	Visual – The licensee identified apparent boron deposits on the lower RPV head near two BMIs.	Lower reactor pressure vessel head
Palo Verde 3	2004/02	Visual - Engineering personnel were performing a visual examination of the RCS piping and discovered boric acid residue on the A03 pressurizer heater sleeve. The visual observation was characterized as a small white buildup of boron residue around the heater sleeve as the sleeve enters the pressurizer bottom head. There was no residue running down the outside of the sleeve, and there were no signs of dripping, spraying, puddles of liquid or liquid running down the nozzle or pressurizer. The residue appeared to be dry.	Pressurize heater sleeve

Operating Unit	Date of PWSCC Discovery	Method of Discovery	Affected Component or System
Susquehanna 1	2004/03	Not Specified - During a routine inspection an indication was discovered on the N1B penetration. This reactor vessel penetration is associated with the reactor recirculation B loop. The crack had been detected during previous outages, however, it was not designated as a crack. The crack was circumferential and was approximately 50 percent through-wall. The length of the crack was roughly 2.2 inches (approximately 7 percent of the diameter).	Recirculation weld
Catawba 2	2004/09	Visual - The steam generator bowl drain for the 2A, 2C, and 2D steam generators were visually inspected. Leakage was found on the 2C and 2D SG bowls. The leakage occurred sometime after the previous refueling outage, because the bowls were clean at that time. Dye penetrant exams were conducted on 2D which identified indications. The root cause of the leakage was determined to be PWSCC. The cracks initiated in the gap between the pipe coupling and the Alloy 600 weld metal buildup. This area is in contact with primary water at a temperature of approximately 617 °F.	SG bowl drain
Oconee 1 and 3		Visual - identified small amounts of boron accumulation at the base of CRDM nozzle 21 and several T/C nozzles.	CRDM Nozzle